

AD-A158 920

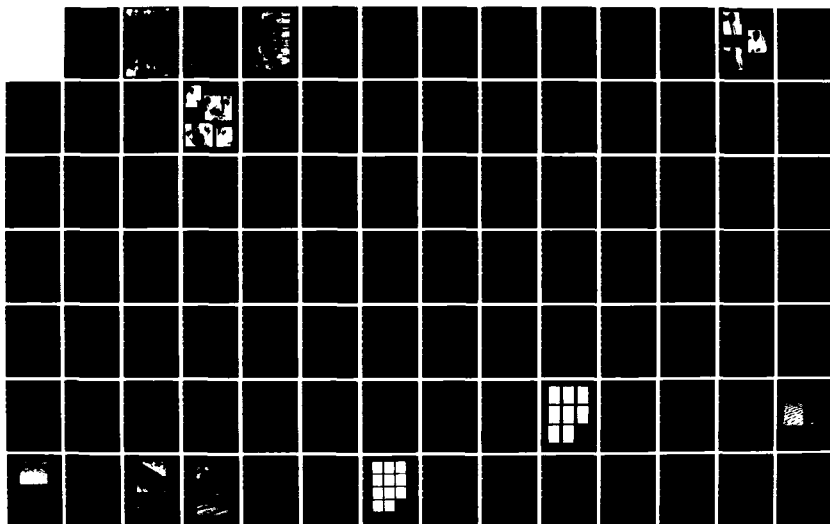
SYMPOSIUM OF NAVAL HYDRODYNAMICS (14TH) HELD AT ANN  
ARBOR MICHIGAN ON AUGUST 23-27 1982(U) OFFICE OF NAVAL  
RESEARCH ARLINGTON VA M P TULIN ET AL. 1982

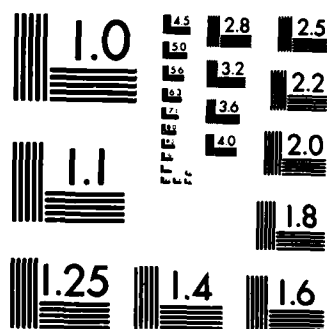
01/13

UNCLASSIFIED

F/G 20/4

NL





MICROCOPY RESOLUTION TEST CHART  
NATIONAL BUREAU OF STANDARDS-1963-A



85 8 26

FILE

This document has been approved  
for public release and since the  
distribution is unlimited.

National Academy Press

85 8 26

DTIC

AUG 10 1985



*National Academy Press*

The National Academy Press was created by the National Academy of Sciences to publish the reports issued by the Academy and by the National Academy of Engineering, the Institute of Medicine, and the National Research Council, all operating under the charter granted to the National Academy of Sciences by the Congress of the United States.



1

Fourteenth Symposium

# NAVAL HYDRODYNAMICS

Propeller-Related Problems  
Cavitation  
Nonlinear Free-Surface Problems  
Viscous Fluid Problems

sponsored jointly by

OFFICE OF NAVAL RESEARCH

UNIVERSITY OF MICHIGAN, ANN ARBOR

NAVAL STUDIES BOARD

of the

NATIONAL RESEARCH COUNCIL

DTIC  
ELECTE  
S AUG 29 1985 D  
A

NATIONAL ACADEMY PRESS  
Washington, D.C. 1983

This document has been approved  
for release and sale, its  
distribution is unlimited.

Partial support for the publication of these Proceedings was provided by the Office of Naval Research of the Department of the Navy. The content does not necessarily reflect the position or the policy of the Navy, the U.S. Government, or the National Research Council, and no endorsement should be inferred. In the interest of timely publication, the individual authors' papers are presented here as received and with minimal editorial attention.

Available from:

Naval Studies Board  
National Research Council  
2101 Constitution Avenue  
Washington, D.C. 20418

Printed in the United States of America

PROGRAM COMMITTEE

T. Francis Ogilvie, Chairman  
*Massachusetts Institute of Technology*

George F. Carrier  
*Harvard University*

Michael G. Parsons  
*University of Michigan*

Ralph D. Cooper  
*Flow Research Company*

Robert Whitehead  
*Office of Naval Research*

Choung M. Lee  
*Office of Naval Research*

Lee M. Hunt  
*National Research Council*

SYMPOSIUM AIDES

Virginia Konz  
Jeanette Vecchio  
*University of Michigan*

Mary G. Gordon  
Elizabeth A. Lucks  
Judy Sul  
*National Research Council*



A - Action For	
WHS - GRAS	<input checked="" type="checkbox"/>
DTIC - FOS	<input type="checkbox"/>
Unpublished	<input type="checkbox"/>
JUL 17 1964	
BY _____	
DISSEMINATION _____	
APPROVED BY _____	
Dist _____	
A-1	

## Foreword

The Office of Naval Research, the National Research Council, and the University of Michigan jointly sponsored the Fourteenth Symposium on Naval Hydrodynamics, which was held in Ann Arbor, Michigan, on August 23-27, 1982. An international symposium of this scope requires careful planning, intense effort, and extraordinary cooperation among sponsors, organizers, and participants. The success of the Ann Arbor symposium reflects positively on the efforts and dedication of a larger group of people than can be acknowledged here.

The technical program for the symposium consisted of eight sessions focusing on four areas of current interest to naval hydrodynamicists: propeller-related problems, cavitation, nonlinear free-surface problems, and viscous fluid problems. The authors of the thirty-two papers that were presented were drawn from the international community of ship hydrodynamics research scientists, with eleven countries represented on the technical program. In total, more than twenty countries were represented at the symposium.

As previously stated, many people contributed in many ways to the success of the Fourteenth Symposium on Naval Hydrodynamics. It is not possible to quantify the value of each contributor's input, but certainly much credit must go to Professor T. Francis Ogilvie of the Massachusetts Institute of Technology, who served as chairman of the Program Committee and spent many hours ensuring an outstanding group of technical papers for the symposium. Professor Ogilvie was ably assisted by the other members of the Program Committee: Dr. Choung M. Lee of the Office of Naval Research, Professor George F. Carrier of Harvard University, Mr. Lee M. Hunt of the National Research Council Naval Studies Board, Mr. Ralph D. Cooper of Flow Research Company, and Professor Michael G. Parsons of the University of Michigan. Professor Parsons, who is chairman of the Naval Architecture Department at the University of Michigan, and Professor Robert F. Beck of that department were responsible for the local arrangements at Ann Arbor and did an outstanding job in providing a pleasant and constructive scientific and social atmosphere for the symposium. They were assisted by Mrs. Virginia Konz and Ms. Jeanette Vecchio from their administrative staff. A successful symposium would not have been possible without the overall coordination, planning, and administration provided by Mr. Lee M. Hunt, executive director of the Naval Studies Board, and his staff, Mrs. Elizabeth A. Lucks, Mrs. Mary G. Gordon, and Mrs. Judy Sul. Dr. Choung M. Lee provided enthusiastic and dedicated support for all phases of symposium planning and organization and will remain as the focal point at the Office of Naval Research for future symposia.

Finally, a special and personal expression of gratitude is extended to Mr. Ralph D. Cooper, to whom this symposium was dedicated, for his advice, counsel, and help, which has been freely given and invaluable.

Robert Whitehead  
Group Leader, Fluid Dynamics  
Office of Naval Research

vii

## CONTENTS

Foreword

v

Robert Whitehead, Office of Naval Research

Introductory Addresses

Address by RADM Leland S. Kollmorgen

1

Address by Dr. Robert A. Frosch

3

Address by Dr. Charles G. Overberger

5

Banquet Speeches

7

SESSION I: NONLINEAR FREE-SURFACE PROBLEMS

An Exact Theory of Gravity Wave Generation by Moving Bodies, Its Approximation,, and Its Implications;

19

Marshall P. Tulin

Strong Nonlinear Characteristics of Steep Surface Gravity Waves;

53

Ming-Yang Su and Albert W. Green

Binnie Waves ;

89

Chia-Shun Yih

Three-Dimensional Nonlinear Long Waves Due to Moving Surface Pressure;

103

De-Ming Wu and Theodore Y. Wu

SESSION II: CAVITATION

Travelling Bubble Cavitation Noise Measurements ;

133

V. Shanmuganathan and V.H. Arakeri

Cloud Cavitation: Theory ;

165

G.L. Chahine

Viscous Effects on the Stability of Cavitating Line Vortices ;

195

Jaakko V. Pylkkänen

Nuclei and Cavitation

215

Jean-Pierre Le Goff and Yves Lecoffre

SESSION III: NONLINEAR FREE-SURFACE PROBLEMS

A Numerical Approach to Nonlinear Ship Motion ;

245

Tor Vinje, Xie Maogang and Per Brevig



- Slowly-Varying and Mean Second-Order Wave Forces on Ships and Offshore Structures; 279  
R.G. Standing and N.M.C. Dacunha

- Experimental Study on Second-Order Forces Acting on Cylindrical Body in Waves; 319  
Yusaku Kyojuka

- Slender-Body Calculations of Large-Amplitude Ship Motions; 383  
Douglas J. Loeser, Dick K. Yue and Nils Salvesen

SESSION IV: NONLINEAR FREE-SURFACE PROBLEMS AND CAVITATION

- Prediction of Relative Motion of Ships in Waves; 417  
Choung M. Lee, John F. O'Dea and William G. Myers

- Relative Motion Components for a Mathematical Form in Regular Waves 453  
Robert F. Beck

- Cavitation Inception Scaling by Roughness and Nuclei Generation; 507  
Jan H.J. van der Meulen and Ye Yuan-Pei

- The Role of Microbubbles on Cavitation Inception on Head Forms; 547  
S.C. Ling, S. Gowing and Y.T. Shen

SESSION V: CAVITATION AND PROPELLER-RELATED PROBLEMS

- Cavitation Erosion Tests with Oscillating Foil Section; 583  
Claus F.L. Kruppa and Gero R. Sasse

- Comparison of Computational and Experimental Unsteady Sheet Cavitation; 613  
Fred Stern

- Theoretical Treatment of Unsteady Cavitation on Ship Propeller Foils; 653  
Hirosaki Isshiki and Mitsunori Murakami

- The Numerical Prediction of Unsteady Sheet Cavitation on High Aspect Ratio Hydrofoils 733  
Robert J. Van Houten

SESSION VI: PROPELLER-RELATED PROBLEMS

- Hydrodynamic Pressure Measurements on a Ship Model Propeller. 787  
A.G.P. Versmissen and Wim van Gent

Flow Field Computations for Non-Cavitation and Cavitating  
Propellers 823  
Justin E. Kerwin

The Effects of Hull Pitching Motions and Waves on Periodic  
Propeller Blade Loads; 861  
Stuart D. Jessup and Robert J. Boswell

Analytical Prediction of Pressures and Forces on a Ship Hull 915  
Due to Cavitating Propellers ;  
Paul Kaplan, James Bentson and Moshe Benatar

#### SESSION VII: VISCOUS FLUID PROBLEMS

A Streamline Curvature Method for Computing the Flow Near 953  
Ship Sterns  
Lars Larsson and Lars-Erik Johansson

Some Aspects of Thick Three-Dimensional Boundary Layers 999  
V.C. Patel

A Streamline-Iteration Method for Calculating Turbulent Flow 1041  
Around the Stern of a Body of Revolution and Its Wake  
Zhou Lian-di

Reynolds Number Scaling of Velocities in Axisymmetric 1071  
Turbulent Boundary Layers  
David W. Coder

#### SESSION VIII: VISCOUS FLUID PROBLEMS

Application of the Vortex-Lattice Concept to Flows with 1089  
Smooth-Surface Separation  
D. Fredd Thrasher

Investigation of Stern Flow Field by Boundary Layer Suction 1135  
Technique  
Ichiro Tanaka and Toshio Suzuki

Calculation Method for Separated Flows with Applications to 1151  
Oscillatory Flow Past Cylinders and Roll Damping of Barges  
P.W. Bearman, M.J. Downie and J.M.R. Graham

Vortex Shedding Around Two-Dimensional Bodies at High Reynolds 1171  
Number  
Odd M. Faltinsen and Bjornar Pettersen

Previous Books in the Naval Hydrodynamics Series 1215

List of Participants 1217



DR. CHARLES G. OVERBERGER



Rear Admiral LELAND S. KOLLMORGEN, USN



ROBERT A. FROSCH

# Introductory Address

Rear Admiral LELAND S. KOLLMORGEN, USN

On behalf of the Office of Naval Research, I am pleased to join in the welcome of participants to the Fourteenth Symposium on Naval Hydrodynamics.

It is gratifying for us at ONR to have once again worked with our friends at the National Academy of Sciences in cosponsoring and organizing this symposium. It is an association that began with the first symposium in 1956 and is recognized as effective and mutually productive.

I take special pleasure in expressing my appreciation to the third cosponsor and host to the symposium, the University of Michigan, for providing such hospitable surroundings--the sun is scheduled for early this afternoon.

The University of Michigan in general and the Naval Architecture Department in particular play a major role in the Navy's pursuit of excellence in hydrodynamics research. The Office of Naval Research is a major supporter of academic research and graduate education both through its contract research program and by such direct means as the ONR graduate fellowship program. It is significant that naval architecture is included as one of the selected fields of study for the fellowship program. It is appropriate then that we join forces in the organization of this symposium to disseminate the results of the latest research.

Since the first symposium, the international nature of the biennial series has been consciously and effectively maintained. The meetings themselves have been held in six countries other than the United States. Speakers at the symposia have been invited from wherever outstanding research in naval hydrodynamics is being performed.

This meeting is no exception, with speakers from nine countries other than the United States and participants from a total of twenty-three countries. This international hydrodynamics research community is in keeping with the true international nature of the sea upon which the world depends.

Men have challenged the sea for many centuries. Much of early science dealt with the sea, navigation, and commerce; man's curiosity early on focused on putting men to sea on ships. Virtually all of the significant advances in ship hydrodynamics research for the past three decades have been reported at these symposia, which have served as the source of inspiration for new and innovative ideas and concepts.

As an example, two symposia in this series have had as a theme unconventional high-performance craft such as hydrofoils, air cushion vehicles, surface effects ships, and small waterplane area twin hull (SWATH) ships. Operational and prototype vehicles have been developed on the basis of the results of research presented at these meetings. Further, the application of modern numerical methods to the field of ship hydrodynamics has been fostered by your participation, and other meetings have led directly to improved performance and reduced fuel consumption for ships and weapons through drag reduction.

We can add bulbous bows, bow flares, and high-performance propellers to the list of advances that were reported here in their early stages of development. I am reminded also that the controllable reversible pitch propeller on our Spruance Frigates is a Danish design.

Although we have learned much, all of the participants at this meeting realize that there is much yet to be done.

New and increasingly stringent demands are being placed on the Navy's ships, submarines, and underwater systems. The explosive costs of energy make it even more imperative that our ships operate efficiently in every phase of their operation to conserve fuel and reduce costs. Advances in many other technologies increase the pressure for yet better performance of both our vessels and our weapons.

The performance of ships in high sea states and inclement weather is a continuing challenge. We must be able to accurately project performance before our ships are actually built and put to sea. Because of the wide variation in sea conditions around the globe and the importance of accurate wave measurements, it is extremely important to have open international exchanges such as those that occur in these symposiums. These exchanges are beneficial to all participants.

In concert with the changing nature of science and our nation's needs, the Office of Naval Research itself is changing, as it must to remain a viable and responsive supporter of the operational Navy's mission of national defense. There is ever-increasing pressure to focus research in areas that promise real payoff and progress.

Our research funds must be used carefully to continue to provide a solid foundation of basic research that is relevant to the operational needs of the Navy. This is as true for hydrodynamics as it is for all other areas of science.

I am constantly aware of our inability to progress in various areas because of our lack of fundamental understanding of physical phenomena--three-dimensional flows among them. I am pleased to see a paper on hull-propeller interaction and hopeful that a new generation of computers will make these complex problems more tractable.

Please accept my best wishes for a productive symposium and success in your future research endeavors.

# Introductory Address

ROBERT A. FROSCH  
National Research Council

I am delighted to welcome you to the Fourteenth Symposium on Naval Hydrodynamics on behalf of the Naval Studies Board of the National Research Council. The Board is a sponsor of this Symposium together with the Office of Naval Research.

As most of you know, the National Academy of Sciences was founded by Congressional charter early in the 1860s under the administration of President Abraham Lincoln. It was chartered by the Congress as an honorific body, which is in addition required to give advice on scientific and technological matters to any agency of the U.S. Government that may request it. During the 1960s the National Academy of Engineering was organized under the charter of the National Academy of Sciences to serve the same functions for engineering that the Academy of Sciences had been set up to perform for the sciences. In 1970 the Institute of Medicine was chartered by the Academy to deal with problems of provision of health services to all sectors of our society.

The National Research Council is the operating arm of the National Academy system. Through its boards and committees it taps the scientific and engineering expertise of the nation to advise the Government as the charter of the Academy requires. Another measure the Academy uses for providing advice and for keeping up with the growth and advances in science and engineering is the sponsorship of symposia such as this.

It is a pleasure for the Naval Studies Board to join with ONR in the sponsorship of this symposium. Both ONR and the National Research Council have shared for a long time a belief in the fundamentally international character of ideas, and the consequent importance of sharing views on scientific concepts and their possible applications. No country or particular group has a monopoly on creativity. It is particularly the case that in matters of the oceans we are all sharers of this vast global resource and must share its problems.

A global interest in common problems and in devising scientific approaches to their solutions is evident in the challenging program that has been arranged for this occasion. I am sure that the papers and the discussions that follow them will refresh everyone's ideas and lead to a better understanding of how certain problems of Naval Hydrodynamics can be solved.

I congratulate you on the opening of this important symposium and share with you the anticipation of an exciting meeting.

# Introductory Address

DR. CHARLES G. OVERBERGER  
The University of Michigan

Admiral Kollmorgen, Dr. Frosch, ladies and gentlemen: on behalf of President Harold T. Shapiro and the Regents of the University of Michigan, I would like to welcome you to Ann Arbor and to the University.

We are very pleased to be able to host the Fourteenth Symposium on Naval Hydrodynamics. Since the first symposium held in 1956 in Washington, D.C., which many of you here this morning attended, this series of symposia has been a significant contributor to the growth of an important scientific field. We were, therefore, eager to cosponsor the Fourteenth Symposium with the Office of Naval Research and the Naval Studies Board of the National Research Council.

The University of Michigan at Ann Arbor is a particularly appropriate place to hold this Symposium. The College of Engineering has a rich tradition in experimental and theoretical naval hydrodynamics through the Department of Naval Architecture and Marine Engineering, the Department of Mechanical Engineering and Applied Mechanics, and the Department of Atmospheric and Oceanic Sciences. We have been teaching naval architecture and marine engineering here for more than 100 years. Last year the Department of Naval Architecture and Marine Engineering celebrated the centennial of the arrival at the University of a young Naval officer named Mortimer Cooley. Cooley had been sent here by the U.S. Navy to teach "iron shipbuilding and steam engineering" for four years. In fact, he remained with the University for 47 years, serving 24 of them as Dean of Engineering.

Naval hydrodynamics has been an important area of study and research here throughout these years. Since 1960, 22 Ph.D.'s have been earned in hydrodynamics within the Department of Naval Architecture and Marine Engineering alone. Many of those graduates are here for this symposium; five will be presenting papers during the week.

The University is proud of its excellent Department of Naval Architecture and Marine Engineering, which will serve as your host for the Symposium. The department has the largest undergraduate enrollment in the nation plus remarkable strength over the full spectrum of marine-related academic activity. It covers fields from marine systems economics through hydrodynamics to marine engineering and offers strong programs on all levels from the bachelor's degree through the Ph.D.. Its faculty has a vital commitment to both teaching and research.

The University is now in the middle of the first major modernization of the Ship Hydrodynamics Laboratory in more than 20 years, an effort specifically directed toward improving the fundamental research capability of the facility. There will be an opportunity for you to visit the towing tank during an open house tomorrow evening, and you are cordially invited to avail yourselves of it.

In closing, I welcome you again to the University of Michigan and express the hope of all of us that you have a successful and rewarding symposium.





# Banquet Address

MARSHALL TULIN

The very first Symposium on Naval Hydrodynamics convened in Washington, D.C., during September 1956, 26 years ago. The banquet site was a small ballroom in the late Roger Smith Hotel near the intersection of 18th Street and Pennsylvania Avenue, N.W. The appointed speaker was that charming person and distinguished mathematician who, for many decades, was a one-man civilian faculty at the Royal Naval College, Greenwich, and who helped to educate a generation of fine British naval constructors, Professor L. M. Milne-Thomson. He created consternation among the organizers of that symposium when, upon walking into the ballroom, he asked, "Where is my blackboard?" A small portable blackboard was hastily procured, and at the end of the dinner he gave a fine lecture on "Some Problems and Methods in Hydrodynamics," much more easily appreciated now in print than it was then at that late hour by that well-fed audience.

Milne-Thomson began by pointing out that "Hydrodynamics, as an exact science, started with Archimedes. It is true that he treated the particular case of zero velocity, but his work remains today a correct piece of applied mathematics and, indeed, a great achievement for the time." I might add that the great Greek's exact result in his context reduces our low-speed, moderate-speed, whatever-speed theories to insignificance. And I might further remind you that Archimedes promptly left his famous principle in the bathtub and dashed naked into the street to achieve immediate publication of his results.

I feel a little bit in such a situation at the moment. But I have in fact the very pleasurable task of lauding one among us, and I am honored to be chosen to perform it. In addition, there are a few remarks I would like to publish, ex-bathtub, on behalf of most of us here, but I will hold them until I close.

This twenty-sixth year is as close as we will come to a silver anniversary meeting of this Symposium on Naval Hydrodynamics on these shores. We have met in some alluring foreign capitals, and we have touched both the Atlantic and Pacific shores of this huge land. It therefore seems appropriate to me that our silver anniversary meeting, if I may call it that, is being held at this great American university in our vast and mythic Midwest. Soon after arriving here I had a chance to read that fascinating, even exciting, booklet "Naval Architecture and Marine Engineering at the University of Michigan, 1881-1981" in which I learned of the early importance here of the U.S. naval officer Mortimer Cooley and the Scottish emigre Herbert Sadler, two ships engineers. These two men, who be-

tween them held the post of Dean of Engineering for 33 years between 1904 and 1937, not only created and developed the University's School of Naval Architecture, but had enormous influence on the powerful Engineering School which has existed here for a long time. The booklet also confirmed my own impressions of the role of their successors--Dick Couch, Harry Benford, Francis Ogilvie, and now Mike Parsons--in creating the strong and internationally known department that exists today.

We who are alumni of the David Taylor Model Basin are not organized as such, but we certainly feel a family connection. And it is with the greatest pride that we observed the success, first of Dick Couch and then of Francis Ogilvie, in creating this department. It not only trains its students superbly in the ancient art of ship design, but it is now well known for high quality research in ship hydrodynamics, as evidenced by Bob Beck's fine paper on the scientific determination of free-board presented at this meeting. We have just missed the department's centennial last year, but congratulations to you both as well as to all the others involved, and let us wish Mike Parsons the best of luck in future. Francis Ogilvie obviously did so well here that our eastern cousins saw fit to snatch him away as a department head. It is surely not unfitting that we take this opportunity to wish him a happy and always convergent voyage as Department Head at MIT.

We are now all basking in that fine Midwestern hospitality that has such a direct and personal quality. If you will allow me, I will thank all the hosts here--Mike, Bob Beck, Bob Latorre, Dick and Francis, and their gracious wives--for the wonderful arrangements and warm reception. And to our Office of Naval Research hosts Bob Whitehead and Sara, Choung Lee, and their partners in this, Lee Hunt of the Naval Studies Board of the National Research Council, and his support, Elizabeth Lucks, Judy Sul, and Dixie Gordon. Thanks to all of you from all of us.

I had thought for a while before coming here that it just might be necessary for us to celebrate in anonymity that certain person to whom this symposium is being dedicated--much the way we celebrate the authors of the Holy Scriptures or the Nordic Sagas or Beowulf--such is his personal modesty and aversion to formal recognition. But I was relieved to hear the ice broken and the name of Ralph Cooper spoken aloud during the first session here. Ralph, this is something we all want to see done, so please humor us and sit back and enjoy, if you possibly can.

The patriarch Abraham negotiated with God that He would spare Sodom and Gomorrah if Abraham could find 50 righteous men living there. Failing to deliver, Abraham renegotiated the number to 10. But still he failed, and the cities were destroyed. Now God did find one righteous man in those biblical cities: his name was Lot. And when God bothers to look around Washington, D.C., I am relieved to know that he will at least find Ralph Cooper.

Has any of us during Ralph's long service for the Navy at ONR ever doubted even for a second his devotion to the Navy and to the research community both in the United States and overseas, of which we are all a part? Have we not all somehow been affected by his unfailing graciousness and accessibility? Have we not benefitted from his earnest interest in our work, and, as a result, felt both eager and pleased to participate in the Navy's program? And has not that program profited from his broad understanding of naval hydrodynamics, his open-mindedness toward new things, and his discriminating appraisals? He stands as an epitome of public service in the technical sector, steadfast in his devotion, and devoid of any thought of personal gain.

I have been chosen to praise him here in view, I am sure, of our long personal friendship, and I can assure you that he is as gracious and modest and wise in private as he is in carrying out his duties. But let me tell you a bit about his history. He was born and raised in Jacksonville, Florida, and educated in mechanical engineering at the Georgia Institute of Technology and at Columbia University where he took his M.S. degree. In between he attended the U.S. Navy's steam school at Newport, Rhode Island, and served as an officer in a destroyer flotilla in the Pacific and for a while in Tinian, China. He arrived at Langley Field, NACA, sometime in the late 1940s and began to work in a hypersonic tunnel group in the east area. It was there that we met. At Langley, Ralph--like all of us--was under the influence of some great aerodynamicists and aeronautical engineers, among them Antonio Fervì, A. Buremann, Carl Kaplan, I.E. Garrick, I. Katzoff, A. von Doenhoff, and John Stuck, and younger scientifically-minded colleagues like Clinton E. Brown, Bernard Budiansky, and Coleman Donaldson. There were many others: it was a rich and thriving hive.

In the early 1950s I reported to Ralph from Washington that there were two very good Chinese restaurants in that city, both Mandarin. It was an attraction lacking and much missed in Newport News at the time, so Ralph joined me at the David Taylor Model Basin in a group called Turbulence and Frictional Resistance Research. We worked on some theoretical problems together, including the resistance of cylinders in unsteady axial motion, and the effect of non-uniform approach flow on lifting line theory. And we did a series of experimental studies, both in towing tanks and in a low turbulence wind tunnel that we had designed and built for our purposes. We also had the good sense to buy a superb hot film anemometer from a young genius at Rouse's wonderful Institute in Iowa. His name was C.S. Ling, and he is attending this Symposium. Ralph attended a course in hot-wire techniques given by Lester Kovasznay at Johns Hopkins University, at which many other people later to become well known for turbulence research were also present. G.I. Taylor, later to be knighted, visited the David Taylor Model Basin in the early 1950s to discuss the possibility of detecting submarine wakes by measurement of turbulence, a possibility that had

been put forward by Francois Frenkiel. After listening to Taylor, we realized that it would be a good idea to make measurements of the turbulence in the far wake of an axially symmetric body. Ralph undertook the task in our low turbulence wind tunnel using Ling's hot-film anemometer and the techniques Ralph had learned from Kovasznay. Today Ralph's DTMB report on this work is often quoted in the literature. Frederick Todd, then Director of the Hydrodynamics Laboratory at DTMB, directed our attention to the problem of designing studs for transition tripping on ship models. Ralph carried out systematic tests, and as a result we introduced the use of large diameter but very flat discrete studs to replace wires and sand strips on ship models for turbulence stimulation; those tests were conducted both in the old 140-foot basin in the basement of the DTMB and in a smaller but very useful tank that we had for our own use. At DTMB Ralph fell under the spell and romance of research on ships, and under the influence of the great experts and younger colleagues there. I can mention Georg Weinblum, Lou Landweber, Herman Lerbs, Bill Cummins, Phil Eisenberg, Murray Strasberg, and Hugh Fitzpatrick, among others. And we had constant contact with great and talented visitors such as G.I. Taylor, whose visit and its consequences I have already mentioned.

In retrospect, it is hard to imagine a better preparation for Ralph's career as a Scientific Program Manager at ONR than his apprenticeship at those two great U.S. Laboratories: Langley (NACA) and Carderock (DTMB).

During his tenure at ONR as Head of the Fluid Dynamics Program, Ralph became Mister Hydrodynamics, closely assisted by Stanley Doroff, and we can all thank him for the continued vigor of the program there, of which this Symposium series is an essential part. It has enriched our technical lives and promoted growth in understanding of problems vital to the performance of naval ships and weapons systems in such areas as speed and powering, seakeeping, maneuvering, noise, detection, and weapons effects.

Research seldom produces immediate gains, and for that reason it requires faith and courage to support it. It is easy to doubt, and there are, unfortunately, constant doubters to defend against and, if possible, to convert. But it is inconceivable that the modern fleet could perform in all important details as effectively as it must without the thousands of individual contributions from research that have been woven bit by bit through decades into the technology the fleet requires. It is almost a thankless job. So Ralph, be assured of the admiration and affection of the scientific community that you have served so well over the last 20 odd years, and be assured, too, of your remarkable success.

Now, ladies and gentlemen, let us rise and express our personal appreciation.

In concluding, allow me, Archimedes-like, to do a little shouting in the streets. I wonder, do many of you share my

sense of a crisis in research in our field of naval hydrodynamics? First of all, it has become more and more difficult to obtain support for even clearly relevant research in hydrodynamics. Furthermore, both government laboratory personnel and those of us outside in universities and industry who are supporting government programs with our efforts know that it is almost impossible to obtain support for what Bob Frosch called "irrelevant research," no matter how skilled the scientist seeking that support. I refer to Dr. Frosch's remarks at the opening ceremony here stressing the importance of "irrelevant research." I commend those remarks to your consideration, coming as they do from a former Assistant Secretary of the Navy for R&D and the current vice-president for Research for the General Motors Corporation.

The crisis regarding support leads to another crisis about which we should be equally concerned. It concerns the participation in our affairs of outstanding scientists, both experimentalists and applied mathematicians from neighboring fields, from whom we can learn how to raise our own standards and expectations as to what we can achieve and how. They can offer us much needed critiques in both the fluid dynamic and applied mathematics aspects of our work. At the first symposium in this great series in 1956 there were present (I exclude a few prominent scientists who are present here today) Batchelor, Benjamin, Birkhoff, Bleich, Carrier, Clauser, Cole, Corrsin, Dryden, Ellis, Gilborg, Greenspan, Herzfeld, Imai, Kennard, Liebanoff, Kovasznay, Laporte, Lighthill, Lin, Longuet-Higgins, MacColl, Munk, Plesset, Rott, Rouse, Schubauer, Sears, Stewart, Stoker, van Dyke, Whitham.

I will speak frankly. Let us avoid isolating ourselves and suffering the tinge of the second-class. I was not happy to hear Admiral Kollmorgen in his opening remarks here suggest, if I understood him, that we have not succeeded in understanding the problem of propeller-wake interaction as well as aerodynamics experts might. I happen not to believe this, but neither do I believe that we cannot do better. Such serious problems deserve the best by way of scientific and logical approaches, the most accurate observations, the highest level of mathematics, and, finally, responsible computing.

Forgive me for this somewhat portentous ending. And thank you for joining with me in our modest tribute to Ralph Cooper.

'Til Hamburg in '84.

# Banquet Address Response

RALPH D. COOPER

As most of you know, I rank high on the list--probably at the very top--of poor public speakers, and out of consideration for audiences I have avoided, whenever I could, being placed in the position of speaking in public.

The first faint alarm about my present predicament sounded in Tokyo two years ago at the conclusion of the Thirteenth Symposium on Naval Hydrodynamics when I was overwhelmed by the announcement that the Fourteenth Symposium was to be held in my honor. During most of the intervening two years I tried rather unsuccessfully to suppress this unpleasant prospect. I do not mean the prospect of the great honor that is being bestowed upon me of which I am keenly aware, but the prospect of these poor comments that I am now inflicting upon an unsuspecting and undefended audience. However, I was moved from faint alarm to abject terror when Bob Whitehead casually remarked to me several months ago that Marshall was going to deliver the after-dinner talk at the banquet of the Fourteenth Symposium and then suggested that I might want to say a few words in reply. Can you imagine living for two months with the knowledge that you would have to follow Marshall to the podium under these circumstances?

After much thought--as a matter of fact, I have probably thought of little else day or night since that conversation with Bob--I was unavoidably led to the speculation, now sadly confirmed, that I would be the object of very complimentary comments that would be at best highly exaggerated or more probably downright untrue.

To defend myself, to set the story straight, and to see that the credit and the blame are placed where they properly belonged, I decided to try to trace the events and circumstances that have resulted in my appearing before you tonight.

Being a sort of a fluid dynamicist, I am, of course, greatly concerned with continuity and consequently had some difficulty in deciding where to start my story. I finally decided to begin the story with the start of my work at the Langley Research Center of the old National Advisory Committee for Aeronautics almost 35 years ago. Among the people that I soon met there were Marshall Tulin and Morton Cooper--both of whom play central roles in the tortuous saga I am about to disclose to you--who had arrived some years before. We became good friends, drawn together by our mutual professional interests and other activities like playing bridge and tennis, and organizing parties.

Marshall soon took a temporary leave of absence to pursue graduate studies at Brown University, where one of his principal teachers, if I remember correctly, was George Carrier--the same George Carrier who has participated in the Organizing Committee for the last several Symposia on Naval Hydrodynamics as a representative of the National Academy of Sciences. One summer, I think it was in the late 1940s, C. C. Lin

offered a course in boundary-layer theory at Brown that, in addition to Marshall, attracted Lou Landweber and Phil Eisenberg from the David Taylor Model Basin. Before they returned to Carderock, Lou and Phil told Marshall to let them know if he ever wanted a job. Shortly thereafter, he let them know and went to work at the David Taylor Model Basin. He knew that I was interested in moving to a more cosmopolitan area, and so when a position opened at the David Taylor Model Basin he put in a good word for me, and I too was soon working at the David Taylor Model Basin.

Those were great days for me. A number of friends and colleagues at the Model Basin from those days are in the audience here today. In addition to Lou and Marshall, they are Dick Couch, John Breslin, and Bill Morgan. A charming account of those days can be found in the introduction to Lou's recent Weinblum Memorial Lecture, which will appear in the December issue of the Journal of Ship Research.

At that time, as many of you know, Marshall was working on the first of his many major scientific contributions to naval hydrodynamics--the linearized theory of cavity flows. During that same period, Marshall also made several other lesser-known contributions. One of them might be described as a time and motion study. He invented the speed run. Marshall and I were in a common carpool in those days, and the point of the speed run was for the driver of the car to go from the Model Basin to the center of Washington--a distance of some 10 or 12 miles--during the afternoon rush hour in the shortest time possible. Of course, to ensure a common basis of comparison of the drivers' skills, the same automobile had to be used in making a speed run. Naturally, my car was chosen for this dubious honor. I no longer remember the winning time, but I do remember it was held by Marshall. Only the gods know why or how we escaped arrest or accident.

Marshall's second lesser-known contribution of this period was more in the nature of number theory. He had perfected an intricate procedure for playing the horses. I will not bore you with the details of this procedure, lest you be tempted to try it with the same disastrous results. Not only did our horses never win, we never even got to see the beautiful animals in action. We frequently encountered Alec Tachmindji on these excursions to the local tracks. He was another colleague from those days at the Model Basin and also an aficionado of the horses. He must have thought that we were mad indeed, though he very pointedly but politely never pressed us for an explanation of our strange behavior at the track.

To get on with the main point of the story, Phil went to the Office of Naval Research in the mid-1950s, and after a short time Marshall joined him. Shortly, with the help of the National Academy of Sciences, they organized the First Symposium on Naval Hydrodynamics, which was held in 1956 and which was, of course, immensely successful and justly famous in several respects.

Not long after this Marshall went to the London Office of the Office of Naval Research for several years, and Phil asked me to come to the Office of Naval Research to help fill the void created by Marshall's departure. I arrived at the Office of Naval Research in time to play a minor role in the Second Symposium on Naval Hydro-

dynamics, which had been organized by the same team as the first--namely, Phil, Marshall, and the National Academy of Sciences. While in ONR London, Marshall conceived the idea of holding the Third Symposium on Naval Hydrodynamics in Europe and even worked out the technical program in considerable detail. About a year before the meeting was to take place, Marshall returned to Washington, and he and Phil left the Office of Naval Research and started Hydrohautics. It fell to Stanley Doroff and me to carry out the plan for the Third Symposium on Naval Hydrodynamics that Marshall had initiated. By a stroke of great good fortune, we were able to collaborate in that endeavor with the Netherlands Ship Model Basin led by Drs. van Lammeren and van Manen. Dyck van Manen is, of course, in the audience tonight. The result was the Scheveningen meeting, and the pattern for the Symposium on Naval Hydrodynamics was firmly established and followed faithfully thereafter.

There is a little story I wish to share with you about the preparations for this meeting. You may recall that one of the first serious studies on the sexual behavior of man was written by an eminent social scientist named Havelock-Ellis, the bearer of one of a number of impressive hyphenated British names that are occasionally encountered. One day while on a European tour to promote and organize the Third Symposium on Naval Hydrodynamics, I visited George Wood of the National Academy of Sciences, who was temporarily assigned to La Specia, Italy. I was excitedly and enthusiastically describing the plans for the Third Symposium to him, and at one point I said, "Of course, you know that we are dedicating the symposium to Sir Thomas Havelock." George replied, "Oh yes, didn't he write something with a fellow called Ellis?" To this day I do not know whether George was pulling my leg or not.

But to return to the story I started to tell you. At about this time--early in the 1960s--Mort Cooper also decided to leave the Langley Research Center, and he joined me at the Office of Naval Research where he very ably managed the aerodynamics portion of the fluid dynamics program. About five or six years ago, the leader of another department of the Office of Naval Research was in the process of hiring a new scientific officer. He asked Mort and me to assist him in making a selection from a long list of impressive candidates. The qualifications of one candidate stood out head and shoulders above all others, and we each independently gave him a strong recommendation. He was, of course, ultimately hired. His name is Robert Whitehead.

Just before I left the Office of Naval Research, Bob joined the Fluid Dynamics Program, and he became the leader of the group when I did leave. Subsequently, Bob recruited the able services of Choung Lee to lead a portion of the hydrodynamics program, including responsibility for these Symposia on Naval Hydrodynamics.

The story is almost, but not quite, over. Mort Cooper retired from the Office of Naval Research a number of months before I did. A symposium in his honor was organized by the aerodynamics community, led by Tuncer Cebeci of the State University of California at Long Beach. Inspired by this honor tendered him, he made a similar suggestion to Bob Whitehead on my behalf. Since Bob was not going to



attend the Tokyo Symposium on Naval Hydrodynamics, he assigned to Lee Hunt the task of persuading whoever was selected to organize the Fourteenth Symposium to dedicate it to me. Francis Ogilvie very graciously agreed to this, the announcement in Tokyo resulted, and here I am, standing before you, engaged in public speaking.

That completes a rather long and complex story, and I thank you for the serious attention you have given to it. The moral of this story, of course, is absolutely clear--one cannot be too careful about whom one chooses for one's friends.

And now, ladies and gentlemen, will you join me in a toast: to the Symposia on Naval Hydrodynamics--past, present, and future!

*Session I*

# NONLINEAR FREE- SURFACE PROBLEMS

# An Exact Theory of Gravity Wave Generation by Moving Bodies, Its Approximation, and Its Implications

Marshall P. Tulin\*, HYDRONAUTICS, Incorporated

## ABSTRACT

The purpose of this paper is to present an analytic theory of wave generation by moving bodies sufficiently rigorous and in such a form that reliable conclusions may be drawn regarding the nature, appearance, and importance of non-linear effects, and through which better understanding of their mechanism may be acquired.

In this theory, the two dimensional steady gravity wave problem is cast in the form of a first order linear differential equation in a complex domain leading to exact solutions. In this equation, the dependent variable is the complex function  $v^3$ , where  $v$  is the so-called complex velocity. The independent variable is a complex function representing a slightly strained  $\Psi$  space, where  $\Psi$  is the complex potential. The straining is  $O(\theta^2)$ , where  $\theta$  is the local angle of the free surface, and is determined in terms of the solution through quadrature.

In the case of steep progressive waves, the exact solution (in the variables described above) is precisely the exponential function. Even in the second order version of this exact theory, which is equivalent to the theory of Davies (1951), a limiting wave naturally appears with included angle  $120^\circ$ .

In the case of waves made by a submerged body or by a pressure distribution acting on the free surface, the exact solution has the form of superimposed waves of continuously changing effective wave number, explicitly related to the "nonwave" disturbance due to the moving body or pressure distribution. In the case of a submerged body, it is shown that both the primary wave generation and the modulation of wave length are caused by the local pressure gradient normal to the free surface in excess of the normal pressure gradient which would exist in a free wave given the velocity there.

It is shown that both "weak" and "strong" nonlinear regimes exist.

In the latter, which occurs when the "nonwave" disturbance is sufficiently large, discrete waves arise at critical points on the surface, whose steepness is of order  $(\kappa)^{+1/2}$  where  $\kappa$  is the wave number. Therefore the existence of solutions in the strong regime for sufficiently

\*now: Presidential Professor of Ocean Engineering; University of California at Santa Barbara

small Froude number is brought into question.

In the weakly nonlinear regime, where the "nonwave" disturbance is of small  $O(\epsilon)$ , waves become exponentially small as  $\kappa$  increases. Various approximations to the exact solution for the far downstream wave are given. An approximation valid in the regime  $1 \ll \kappa \ll \epsilon^{-2}$  is systematically derived and is shown equivalent to both the so-called "slow-ship" theories of Inui-Kajitani (1977) and Dawson (1977).

## I. INTRODUCTION

It has been long understood that non-linear effects in water wave behavior are of great practical importance, and are even crucial to the existence and understanding of many observed phenomena — for example, the solitary wave, progressive wave instability, breaking. The subject of these non-linear effects is very far from closed. In fact, only within the last decade or two, a great deal of attention has been devoted to the calculation and understanding of very basic waves (steady, two-dimensional solitary waves and steep progressive waves), and most remarkable results obtained, as in a sequence of papers by M. S. Longuet-Higgins, and by L. W. Schwartz, and Chen and Saffman, etc.; these and others have been reviewed very recently by L. W. Schwartz and J. D. Fenton (1982).

During the same period (the last decade) increasing attention has been devoted to non-linear effects related to the wave resistance of ships. These effects include those which occur in the case of steady two-dimensional progressive waves, and others in addition. Among these, the non-linear interaction between the propagating waves and the "current" field around thick ships may be of particular importance. A number of recent theories of ship wave resistance have attempted to account for these interactions, including those theories in the "slow-ship" category, wherein the "current" field is taken to be that assumed to exist in the limit of zero Froude number (the double-model flow).

It seems fair to say that all of these non-linear ship theories rest on assumptions whose validity are difficult to judge quantitatively. Indeed the problem is awesome, as there are a variety of non-linear effects occurring at one and the same time, and some of them are not even sufficiently clarified from the point of view of mechanism. A review of the simpler case of progressive waves alone shows how surprisingly complex are the phenomena revealed through theory during the last decade.

In this situation it seemed desirable to have an analytic theory of wave generation by moving bodies sufficiently rigorous and in such a form that reliable conclusions could be drawn regarding the nature, appearance, and importance of non-linear effects, and through which better understanding of their mechanism could be acquired. Despite the three-dimensionality of the real ship wave problem, it was felt that even such a theory restricted to two-dimensional flow would

afford important progress. At the least, it would allow for comparison with the two-dimensional versions of the various three-dimensional approximate theories. At the best, it would point the way toward the construction of more rigorous or appropriate three dimensional theories.

The opportunity for such an analytic theory presents itself through the formulation of the steady gravity wave boundary condition in complex notation, utilizing a particular choice of dependent and independent variables. The form of Bernoulli's equation from which this development springs was first presented by Levi-Civita (1925) and it was later used by Davies (1951,52) as the basis for a calculation method for steep progressive waves. In this development, Davies started with a very useful approximation of Levi-Civita's boundary condition. The same approximation was later used by Packham (1952) to produce a closed form solution for the solitary wave.

What we have realized here is that the dependent variable  $v^3$  ( $v$  is the complex velocity), implicit in the earlier approximate works of Davies, et. al, can be shown exactly to obey a linear first order differential equation in a complex space,  $\zeta$ , slightly strained (of order [slope]<sup>2</sup>) from the space  $\Psi = \bar{\phi} + i \bar{\psi}$ , where  $\Psi$  is the usual complex potential. The mapping  $\Psi \rightarrow \zeta$  depends upon the solution  $v(\zeta)$ . As a result, while the exact solution may be given in formal terms, the calculation of explicit results depends upon iteration of the mapping  $\Psi \rightarrow \zeta$ .

The important thing about this theory is that it seems to present within a single expression, formally linear, all of the non-linear effects. Of particular interest is the appearance in the governing differential equation of an analytic function ( $Q + \Omega$ ) representing both the source of waves in the flow and of the modulation in their length as they propagate. In the case of an imposed pressure distribution on the free surface, the function  $\Omega$  is given in terms of that pressure distribution, and for a submerged body  $Q$  is given in terms of the flow about the body, in both cases making use of the Cauchy integral. And, finally we are able to give physical significance to the function ( $Q + \Omega$ ) in terms of the normal pressure gradient on the free surface.

The importance of having an analytical theory of the kind presented here seems justified by the revelation that for sufficiently strong disturbances (as represented by the max. value of  $Q$  on the free surface) waves arise at discrete points on the free surface which are mathematically distinct from the waves arising in linear theory or in the "weakly" non-linear regime. In this "strongly" non-linear regime, for example, these particular waves do not become exponentially small with decreasing Froude number, but rather tend to unbounded steepness as  $F \rightarrow 0$ .

Here we have derived the theory in the case of flow in water of unbounded depth and extracted a certain number of results. It remains for the future to utilize it for explicit computations. Furthermore, it would seem clear that the theory can be extended to the case of finite depth, to study solitary waves (as Packham (1952) has done already) as well as shallow water waves, as begun by Davies (1951) in

the case of progressive waves. If this were to be done, it might prove useful for improved understanding of flows near the critical speed in shallow water, where non-linear effects are of the essence.

In addition, the present results, which confirm the low speed (weakly non-linear) theories of Inui-Kajitani (1977) and Dawson (1977), at the same time suggest weakly non-linear approximations which would not be limited to low speed applications.

## II. DERIVATION - FROM THE FREE SURFACE CONDITION TO THE FLOW FIELD: COMPLEX FUNCTION APPROACH

We consider a free surface (S) on which in some region we allow the possibility for a pressure  $p$  to be imposed. A steady inviscid flow exists beneath the free surface. Then (Bernoulli's Equation):

$$q^2/2 + gy = q_\infty^2/2 - p/\rho \quad [\text{on } S] \quad [1]$$

where  $q$  is the local flow speed,  $y$  the local vertical ordinate of [S];  $g$  the acceleration of gravity;  $p$  the imposed local pressure on [S];  $\rho$  the fluid density and  $q_\infty$  a reference speed.

In addition the flow is irrotational, so that a velocity potential  $\phi$  exists (as usual  $\vec{V} = \nabla\phi$ , where  $\vec{V}$  is the local velocity vector,  $q = |\vec{V}|$ ), and then:

$$\frac{1}{2} \frac{\partial q^2}{\partial \phi} + \frac{g}{q} \sin\theta = - \frac{1}{\rho} \frac{dp}{d\phi} \quad [\text{on } S]$$

or

$$\frac{\partial \bar{q}^3}{\partial \bar{\phi}} + 3\kappa \sin\theta = -3\bar{q} \frac{d\bar{p}}{d\bar{\phi}} \quad [\text{on } S] \quad [2]$$

where:

$\kappa = \ell g/q_\infty^2$ ;  $\bar{q} = q/q_\infty$ ;  $\bar{p} = p/\rho q_\infty^2$ ; and  $\bar{\phi} = \phi/\ell q_\infty$ ;  $\theta$  is the local angle of  $\vec{V}$  to the horizontal, or  $\sin^{-1} dy/ds$ , where  $s$  is the length along the surface streamline, and  $\ell$  is a characteristic length scale, which non-dimensionalizes all lengths appearing hereafter.

We note that [2] can be written:

$$\frac{\partial \bar{q}^3}{\partial \bar{\phi}} + \kappa \sin 3\theta + (4\kappa \sin^3\theta) = -3\bar{q} \frac{d\bar{p}}{d\bar{\phi}} \quad [\text{on } S] \quad [3]$$

or

$$\frac{\partial \ln \bar{q}^3}{\partial \bar{\phi}} + \frac{\kappa \sin 3\theta}{\bar{q}^3} + \frac{4\kappa \sin^3\theta}{\bar{q}^3} = - \frac{3}{\bar{q}^2} \frac{d\bar{p}}{d\bar{\phi}} \quad [\text{on } S] \quad [4]$$

We specialize now to the case of two-dimensional flows in the physical plane defined by  $z = x + iy$ . Therefore a complex potential exists,  $\Psi = \bar{\phi} + i\bar{\psi}$ , where  $\bar{\psi} = 0$  on [S].

Then [4] can be written in complex function notation:

$$R \left[ \frac{d \ln G}{d \bar{\Psi}} - \kappa i G^{-1} + \kappa T G^{-1} \right] = R [\Omega(\Psi)] \quad \bar{\psi} = 0 \quad [5]$$

where:

$G = \bar{v}^3 = \bar{q}^3 e^{-3i\theta}$ ;  $\bar{v} = \bar{q} e^{-i\theta} = v/q_\infty$ ; subscript o refers to  $\bar{\psi} = 0$ ;  
R means "the real part of" (and I, "the imaginary part of").

$$R[\Omega(\Psi_o)] = - \frac{3}{\bar{q}_o^2} \frac{dp_o}{d\bar{\phi}_o} \quad [6]$$

$$R[T(\Psi_o) \cdot G^{-1}(\Psi_o)] = \frac{4 \sin^3 \theta_o}{\bar{q}_o^3} = \left\{ R [i G_o^{-1/3}] \right\}^3 \quad [7]$$

We can write [5] as:

$$R \left[ \frac{1}{G} \left\{ \frac{dG}{d\bar{\Psi}} - G\Omega(\Psi) - \kappa i + \kappa T(\Psi) \right\} \right] = 0 \quad \bar{\psi} = 0 \quad [8]$$

Two cases may be distinguished. If [ ] in [8] is regular for  $\bar{\psi} < 0$  (beneath the free surface), then of necessity:

$$\frac{1}{G} \left\{ \frac{dG}{d\bar{\Psi}} - G\Omega(\Psi) - \kappa i + \kappa T(\Psi) \right\} = -\kappa^* i \quad \text{everywhere for } \bar{\psi} < 0 \quad [9]$$

where  $\kappa^*$  is a real constant.

Far below the free surface we take the following limits:

$$q \rightarrow q_\infty; T(\Psi) \rightarrow 0; \Omega \rightarrow 0$$

Then,  $\kappa^* \equiv \kappa$ , and [9] becomes:

$$\frac{dG}{d\bar{\Psi}} + G[i\kappa - \Omega(\Psi)] = \kappa i - \kappa T(\Psi) \quad [10]$$

The assumptions made above correspond to the case of flow without a body or bottom beneath the free surface.

If, however, [ ] in [8] is not regular everywhere for  $\bar{\psi} < 0$ , then:

$$\frac{1}{G} \left\{ \frac{dG}{d\bar{\Psi}} - G\Omega(\Psi) - \kappa i + \kappa T(\Psi) \right\} = \kappa i + Q(\Psi) \quad \text{everywhere for } \bar{\Psi} < 0 \quad [11]$$

where,

$$R[Q(\Psi)] = 0 \quad \text{on } \bar{\Psi} = 0 \quad [12]$$

and  $Q$  represents the effect of a body or bottom beneath the free surface. We consider here only the effect of a body.

Far below the free surface we take  $Q(\Psi) \rightarrow 0$ . Then,

$$\frac{dG}{d\bar{\Psi}} + G[\kappa i - \Omega(\Psi) - Q(\Psi)] = \kappa i - \kappa T(\Psi) \quad [13]$$

or finally,

$$\frac{dF}{d\bar{\Psi}} + F[\kappa i - Q(\Psi) - \Omega(\Psi)] = Q(\Psi) + \Omega(\Psi) - \kappa T(\Psi) \quad [14]$$

where

$$F = G - 1 \quad [15]$$

and we note that  $F$  vanishes far from the free surface, and thus represents the disturbance to the flow  $q_\infty$ .

The ordinary differential equation [14] defines the flow created on and beneath the free surface by a pressure distribution on the free surface (represented by  $\Omega$ ), and/or by a body beneath the free surface (represented by  $Q$ ). This equation for  $F$  already represents a variety of non-linear wave effects, even without the function  $T$ , which itself represents additional non-linearities of higher order (of order  $\epsilon^3$ , where  $\epsilon$  is the amplitude of  $F$ ).

Further, the higher order non-linear effects due to  $T$  may be incorporated in mapping  $\Psi \rightarrow \zeta = \xi + i\eta$  so that [14] becomes:

$$\frac{dF}{d\zeta} + F[\kappa i - Q(\zeta) - \Omega(\zeta)] = Q(\zeta) + \Omega(\zeta) \quad [16]$$

where

$$\frac{d\zeta}{d\bar{\Psi}} = 1 + \frac{T}{iF - (\Omega + Q)(F + 1)} = 1 + O(\epsilon^2) \quad [17]$$

and  $\Omega + Q = O(\epsilon)$ .

Alternatively, [17] may be written



$$\frac{d\zeta}{d\Psi} = 1 - \frac{\kappa T}{dF/d\zeta} = 1 - \frac{\kappa T}{dG/d\zeta}$$

[18]

$$= 1 - \frac{\kappa T}{dF/d\Psi + \kappa T} = 1 - \frac{\kappa T/G}{\frac{d \ln G}{d\Psi} + \kappa T/G}$$

In the case of periodic waves, [16] takes a very simple form. This classic problem is treated in the next section, where a limiting wave arises naturally. This example serves to demonstrate that in any particular case, it must be verified that the solutions given by [16] are physically realizable.

The mapping defined by [17] represents a straining of the  $\Psi$  space which increases as  $\epsilon^2$ . In the next section we show that for progressive waves a stretching occurs in the transformation  $z \rightarrow \Psi \rightarrow \zeta$  such that

$$\frac{\lambda}{\ell} = \frac{2\pi}{\kappa} [1 + O(A^2)] \quad [19]$$

where  $\lambda$  is the wave length in the physical plane, and  $A$  is proportional to the wave amplitude.

The dependence of  $T$  on  $\epsilon^3$  suggests that its effect on the solution may be included in a complete solution of [14] or [16] through iteration. Even in its neglect, however, the essential non-linearities would seem captured not only in essence, but in a reasonably quantitative way, provided that the additional stretching represented by [19] is kept in mind. A feasible way is therefore opened up for the effective study of wave generation including non-linearities, which is the purpose of this work.

### III. THE PERIODIC WAVE IN DEEP WATER. THE CALCULATION OF $\lambda$

The progressive wave has been treated with improved accuracy, starting with Stokes (1847) and continuing through Michell, Havelock, Davies (1951), Schwartz, and Longuet-Higgins; see Schwartz and Fenton (1982). It has a special importance for us since the flow in the physical plane asymptotically far downstream of a surface or submerged disturbance in deep water will tend toward a purely progressive wave. Indeed, the wave resistance of the disturbance is simply related to the asymptotic wave amplitude. It is additionally important as its treatment here allows us to derive some necessary results (the calculation of  $\lambda$ , for example) and to understand the workings of the present theory.

The motion is unforced,  $\Omega = Q = 0$ , and the wave originates at

infinity as a solution of:

$$\frac{dF}{d\Psi} + i\kappa F = -\kappa T \quad [20]$$

which becomes,

$$\frac{dF}{d\zeta} + i\kappa F = 0 \quad (\zeta = \xi + i\eta) \quad [21]$$

upon the transformation,

$$\frac{d\zeta}{d\Psi} = 1 - i \left( \frac{T}{F} \right) \quad [22]$$

If the amplitude of  $F$  is  $A$ , then the free surface condition [3] or [4] shows that  $T/F = O(A^2)$ .

An appropriate solution of [21] is, of course:

$$F = -Ae^{-i\kappa\zeta(\Psi)} ; \quad G = 1 - Ae^{\kappa\eta} e^{-i\kappa\xi} \quad [23]$$

or,

$$q^3 = \left[ (1 + A^2 e^{2\kappa\eta}) - 2Ae^{\kappa\eta} \cos\kappa\xi \right]^{1/2} \quad [24]$$

$$\tan 3\theta = -Ae^{\kappa\eta} \sin\kappa\xi / (1 - Ae^{\kappa\eta} \cos\kappa\xi)$$

Take that a wave crest exists for  $z = \Psi = \zeta = 0$ , where:

$$q_{\text{crest}} = [1 - A]^{1/3} \quad [25]$$

Therefore a limiting wave occurs for  $A \equiv 1$ , for which the slope at the crest is (found from [24] by the application of L'Hospital's rule):

$$\theta_{\text{crest}} \rightarrow \pm \pi/6 \text{ for } \zeta \rightarrow 0 \mp \quad [26]$$

corresponding to the well known result: a limiting wave with an included angle at the crest of  $120^\circ$ .

The overall dimensions, length  $\lambda$  and total amplitude  $H$ , of the wave are found by integration of the definition,  $G^{1/3} = d\Psi/dz$ , in the form:

$$\kappa \left( \frac{\lambda}{2} + iH \right) = \int_0^{\bar{\Phi}(\xi = \pi/\kappa)} \frac{d\bar{\Phi}_0}{[1 - Ae^{\kappa\eta} e^{-i\kappa\xi}]^{1/3}} \quad [27]$$

The role and importance of  $T$  may be understood by examining solutions of [20], neglecting  $T$  altogether, which are correct to second order in  $A$ :

$$F = -Ae^{-i\kappa\Psi} + O(A^3) \quad [28]$$

The wave shape and overall dimensions in this case are readily found through the easily derived relation:

$$\kappa dz = 3i \int \frac{v dv}{(v^3 - 1)} =$$

$$i \ln \frac{v - 1}{\sqrt{v^2 + v + 1}} + \sqrt{3} \tan^{-1} \frac{2v + 1}{\sqrt{3}} + \text{const.} \quad 29$$

where,

$$v = (1 - Ae^{-i\kappa\bar{\Phi}})^{1/3}$$

from which it can be calculated that for the limiting wave in this approximation:

$$H/\lambda = 1/2\pi \quad ! \quad 30$$

which may be compared with Stokes' value:  $H/\lambda = 0.142 \sim 1/7$ . Further we note that the included angle at the wave crest in this approximation is  $120^\circ$  as in the exact theory. Wave forms calculated according to this second order theory have been computed from [29] and have been compared to the calculations of Schwartz (1964). In this comparison the crests in both cases are found to steepen and the troughs to flatten with increasing wave amplitude. In the Schwartz calculations, the wavelength shortens with increasing amplitude while in the second order case here the wavelength is independent of wave amplitude.

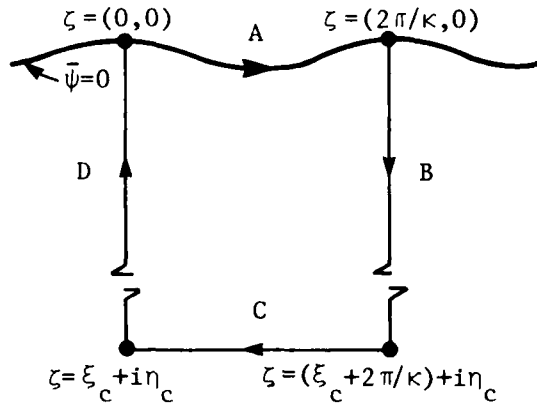
The transform  $\Psi \rightarrow \zeta$  corresponds both to a "stretching" and "wrinkling" of the  $\Psi$  plane, increasing as  $A^2$ . The "wrinkling" only modifies the wave distortion already present to second order (and which culminates in a limiting wave), while the "stretching" introduces shortening of wavelength, as deduced below.

Integrating the transformation [22] over one wave-length, from crest to crest,

$$\xi_o(\lambda) - \bar{\phi}_o(\lambda) = -R \left\{ i \int_o^{\bar{\phi}(\lambda)} \left( \frac{T}{F} \right)_o \cdot d\bar{\phi}_o \right\} =$$

$$I \left\{ \int_o^{\bar{\phi}(\lambda)} \left( \frac{T}{F} \right)_o d\bar{\phi}_o \right\} \quad [31]$$

The integral in [31] may be evaluated by contour integration, making use of Cauchy's theorem. We take the contour shown below (left):



The integral along the contour is zero, since the integrand is analytic within and upon the contour. The integrals along B and D cancel each other because of the periodicity of the wave. Therefore:

$$I \int_o^{\bar{\phi}(\lambda)} \left( \frac{T}{F} \right) d\bar{\phi}_o = -I \int_C \left( \frac{T}{F} \right) d\psi = -I \int_{C(\eta_c \rightarrow -\infty)} \left( \frac{T}{G} \right) \cdot \frac{1}{F} d\bar{\phi} \quad [32]$$

since  $G(\downarrow) \rightarrow 1$ . The integrand in the last integral above may be evaluated making use of a representation of  $T/G$  in terms of its definition, eg. [7]:

$$T/G = \sum_{n=1}^{\infty} iA_n e^{-in\kappa\psi} \quad [33]$$

where, (see [7]):

$$R \left\{ T/G \right\}_o = \frac{4\sin^3\theta_o}{\bar{q}_o^3} = \sum_{n=1}^{\infty} A_n \sin n\kappa\bar{\phi} \quad [34]$$

and where the real coefficients  $A_n$  may be found by Fourier integration. For example,

$$A_1 = \frac{\kappa}{\pi} \int_0^{2\pi/\kappa} \left( \frac{4 \sin^3 \theta_0}{\bar{q}_0^3} \right) \cdot \sin \kappa \bar{\phi}_0 \, d\bar{\phi}_0 \quad [35]$$

Combining [33] with the solution  $F = -A e^{-i\kappa\zeta(\Psi)}$  and using that  $\zeta \rightarrow \Psi$  for  $\eta_c \rightarrow -\infty$ :

$$\begin{aligned} & -I \int_{C(\eta_c \rightarrow -\infty)} \left( \frac{T}{G} \right) \cdot \frac{1}{F} \, d\bar{\phi} = \\ & -R \int_0^{\bar{\phi}(\lambda)} \sum_{n=1}^{\infty} \left( \frac{A_n}{A} \right) e^{-i(n-1)\kappa \bar{\phi}} \cdot e^{(n-1)\kappa \eta_c} \, d\bar{\phi} = \\ & \quad (\eta_c \rightarrow -\infty) \\ & = -\frac{A_1}{A} \cdot \bar{\phi}(\lambda) \end{aligned} \quad [36]$$

or, finally, substituting in [31], and making use of the fact that as  $\bar{\psi} \rightarrow -\infty$ ,  $\bar{\phi}(\lambda) = \bar{\phi}_0(\lambda) = \lambda/\ell$ :

$$\xi_0(\lambda) = \frac{2\pi}{\kappa} = \frac{\lambda}{\ell} (1 - A_1/A)$$

or, [37]

$$\frac{\lambda}{\ell} = \frac{2\pi}{\kappa} / (1 - A_1/A)$$

where  $A_1$ , given by [35] is  $O(A)$ . Therefore,  $\lambda = \frac{2\pi}{\kappa} (1 + O(A^2))$ . Inspection of [35] shows that  $A_1 < 0$ , so that  $\lambda$  decreases with increasing wave amplitude, as was first pointed out by Stokes.

Finally, we point out that the second order solution may be improved by iteration, although we beg questions of convergence, using the transform:

$$\zeta_0(\bar{\phi}_0) = \bar{\phi}_0 - i \int_0^{\bar{\phi}_0} \left( \frac{T}{G} \right) \cdot \frac{G}{F} \, d\bar{\phi}_0 \quad [38]$$

$$\zeta_o(\bar{\phi}_o) = \bar{\phi}_o - i \left\{ \int_0^{\bar{\phi}_o} \frac{T}{G} d\tilde{\phi}_o + \int_0^{\bar{\phi}_o} \frac{T}{G} \frac{1}{F} d\tilde{\phi}_o \right\}$$

$$\zeta_o(\bar{\phi}_o) = \bar{\phi}_o - i \left\{ \int_0^{\bar{\phi}_o} \sum_{n=1}^{\infty} i A_n e^{-in\kappa\tilde{\phi}_o} d\tilde{\phi}_o - \sum_{n=1}^{\infty} i \frac{A_n}{A} e^{-i\kappa(n\tilde{\phi}_o - \zeta_o)} d\tilde{\phi}_o \right\}$$

[39]

where in the first approximation  $\zeta_{o_1} = \phi_{o_1}$  etc.

#### IV. WAVES PRODUCED BY A PRESSURE DISTRIBUTION ON THE FREE SURFACE

We return now to our main purpose: the exploration of non-linearities associated with the free surface response to moving disturbances. First we consider the pressure distribution moving on the free surface. We will be able to compare the results with the recent calculations of Doctors' and Dagan (1980) based on an assortment of other approximations. Here:

$$\frac{dF}{d\Psi} + F[\kappa i - \Omega] = \Omega - \kappa T \quad [14], \text{ as shown earlier}$$

or

$$\frac{dF}{d\zeta} + F[\kappa i - \Omega] = \Omega \quad [40]$$

where, the transform  $\Psi \rightarrow \zeta$  is given by:

$$\frac{d\zeta}{d\Psi} = 1 + \frac{i\kappa T}{\kappa i F - \Omega(F+1)} = 1 + O(\epsilon^2) \quad [41]$$

the pressure field given by  $\Omega$  being taken  $O(\epsilon)$ . Recall that,

$$R[\Omega(\bar{\phi}_o)] = -\frac{3}{\bar{q}_o^2} \frac{d\bar{p}_o}{d\bar{\phi}_o} \quad [6]$$

Again, the space  $\zeta$  corresponds to the space  $\Psi$  "stretched and wrinkled" by the waves themselves.

An appropriate exact solution of [40], (no waves far upstream) is:

$$F = \int_{-\infty}^{\zeta} \Omega(\bar{\zeta}) e^{-i\kappa \int_{\bar{\zeta}}^{\zeta} [1 + \frac{i}{\kappa} \Omega(\tilde{\zeta})] d\tilde{\zeta}} d\bar{\zeta} \quad [42]$$

This simple solution represents on the free surface  $\zeta_o$  a linear summation of elemental waves  $\delta F(\zeta; \bar{\zeta})$  originating at  $\zeta = \bar{\zeta}$ :

$$F(\zeta_o) = \int_{-\infty}^{\zeta_o} \delta F(\zeta_o; \bar{\zeta}_o) d\bar{\zeta}_o \quad [43]$$

where the elemental wave is given by,

$$\delta F = \Omega(\bar{\zeta}_o) e^{-i\kappa(\zeta_o - \bar{\zeta}_o)} + \int_{\bar{\zeta}_o}^{\zeta_o} \Omega(\tilde{\zeta}_o) d\tilde{\zeta}_o \quad [44]$$

so that the amplitude and phase of the elemental wave is shifted over the region it travels downstream, the shift depending on the integral over the pressure disturbance,

$$\int_{\bar{\zeta}_o}^{\zeta_o} \Omega(\tilde{\zeta}_o) d\tilde{\zeta}_o ,$$

so that the phase shift over one wave length is measured by:

$$\frac{\lambda}{\lambda_o} = 1 - I \left[ \int_0^{\zeta_o^{(\lambda)}} \frac{\Omega(\tilde{\zeta}_o) d\tilde{\zeta}_o}{2\pi} \right]$$

where  $\lambda_o$  is the unshifted wave length  $2\pi/\kappa$ .

The amplitude  $A(\infty)$  of the wave far downstream is given by:

$$A(\infty) = |F_\infty| = \text{ampl} \int_{-\infty}^{+\infty} \Omega(\bar{\zeta}_o) e^{+i\kappa \bar{\zeta}_o + \int_{\bar{\zeta}_o}^{\infty} \Omega(\tilde{\zeta}_o) d\tilde{\zeta}_o} d\bar{\zeta}_o$$

$$= \text{ampl} \int_{-\infty}^{+\infty} \Omega(\bar{\zeta}_0) e^{\int_{\bar{\zeta}_0}^{\infty} \Omega(\bar{\zeta}_0) d\bar{\zeta}_0} \cdot e^{+i\kappa \left\{ \bar{\zeta}_0 + I \int_{\bar{\zeta}_0}^{\infty} \frac{\Omega(\bar{\zeta}_0) d\bar{\zeta}_0}{\kappa} \right\}} d\bar{\zeta}_0 \quad [45]$$

The wave resistance,  $D$ , associated with a pressure disturbance,  $p$ , on the surface is,

$$D = - \int p \, dy_0 = - \int p(\zeta) \frac{dy_0}{d\zeta} \cdot d\zeta_0 \quad [46]$$

We have made calculations to second order ( $\zeta \equiv \Psi$ ) for a pressure patch treated by Doctors and Dagan (1980), hereafter referred to as D&D. The results are shown as Figure (1). The second order calculation are seen to agree very closely with the second order theory of D&D based on a regular expansion of  $\phi$  in the physical plane.

#### V. WAVES PRODUCED BY A SUBMERGED BODY

In the case where the flow is not unlimited beneath the free surface (submerged body and/or finite depth), we have shown that:

$$\frac{dF}{d\Psi} + F[\kappa i - Q(\Psi)] = Q(\Psi) - \kappa T(\Psi) \quad [14]$$

where

$$R[Q(\bar{\Phi}_0)] \equiv 0$$

This may again be transformed into the exact equation:

$$\frac{dF}{d\zeta} + F[\kappa i - Q] = Q \quad [47]$$

where the transform  $\Psi \rightarrow \zeta$  is given by:

$$\frac{d\zeta}{d\Psi} = 1 + \frac{\kappa T}{\kappa i F - Q(F+1)} = 1 + O(\epsilon) \quad [48]$$

the field  $Q$  due to the submerged body being taken  $O(\epsilon)$ .



An appropriate exact solution of [47], (no waves for upstream) is

$$F = \int_{-\infty}^{\zeta} Q(\bar{\zeta}) e^{-i\kappa \int_{\bar{\zeta}}^{\zeta} [1 + \frac{1}{\kappa} Q(\tilde{\zeta})] d\tilde{\zeta}} d\bar{\zeta} \quad [49]$$

For the solution on the free surface,  $\zeta = \zeta_0$ , the solution is:

$$F(\zeta_0) = \int_{-\infty}^{\zeta_0} iQ_1(\bar{\zeta}_0) e^{-i\kappa \int_{\bar{\zeta}_0}^{\zeta_0} [1 - \frac{1}{\kappa} Q_1(\tilde{\zeta}_0)] d\tilde{\zeta}_0} d\bar{\zeta}_0 \quad [50]$$

since  $Q(\zeta_0) = iQ_1(\zeta_0)$ , the real part being null. The amplitude of the wave far downstream is:

$$A(\infty) = \text{ampl} \int_{-\infty}^{+\infty} iQ_1(\bar{\zeta}_0) e^{+i\kappa [\bar{\zeta}_0 + \int_{\bar{\zeta}_0}^{\infty} \frac{Q_1}{\kappa}(\tilde{\zeta}_0) d\tilde{\zeta}_0]} d\bar{\zeta}_0 \quad [51]$$

An exact alternate solution is:

$$F(\bar{\phi}_0) = \int_{-\infty}^{\bar{\phi}_0} [iQ_1(\phi_0) - \kappa T(\phi_0)] e^{+i \int_{\phi_0}^{\bar{\phi}_0} [\kappa - Q_1(\tilde{\phi}_0)] d\tilde{\phi}_0} d\phi_0 \quad [52]$$

where

$$A(\infty) = \text{ampl} \int_{-\infty}^{+\infty} [iQ_1 - \kappa T] e^{+i\kappa [\bar{\phi}_0 + \int_{\bar{\phi}_0}^{\infty} \frac{Q_1}{\kappa}(\tilde{\phi}_0) d\tilde{\phi}_0]} d\bar{\phi}_0 \quad [53]$$

We shall use the latter to consider in a little more detail the flow over a submerged body, and in particular to define and give meaning to the important function  $Q_1(\bar{\phi}_0)$ , which drives the wave field.

# VI. ON THE CALCULATION OF $Q_1(\bar{\phi}_0)$

The waves produced by a submerged body are seen to comprise in  $\zeta$  space a linear superposition of elemental waves driven by the function  $Q_1(\phi_0)$ . Here we give a method for its calculation, and in the next section (VII) we reveal its physical meaning — a major result of this work.

We imagine a submerged body,  $S$ , without circulation (for simplicity). The flow in the physical plane is shown as Figure 2a. It transforms into the complex potential plane as shown in Figure 2b. The slit at  $\bar{\psi} = -h$  for  $0 < \bar{\phi} < \ell$  represents a distribution of flow singularities (of  $F$ ). The flow may be extended, we assume, into the region  $\bar{\psi} > 0$  where a slit again exists for  $\bar{\psi} = +h$ , as shown in Figure 2b. In this latter representation, there are no singularities on the free surface itself. On the slit in the upper half plane we anticipate two separate singularity systems: one for  $0 < \bar{\phi} < \ell$  is an image of the system at  $\bar{\psi} = -h$ , and the other extends from  $\bar{\phi} = 0$  to infinity downstream and is wavelike; it is the latter which creates the waves on the free surface. We shall not necessarily calculate these singularity systems, but we shall use the fact that they exist as shown.

We wish to find wave-like solutions which decay with depth and are regular for  $\bar{\psi} < 0$ , and we must define  $Q$  appropriately. Since  $F$  can be singular only on the slit  $A$  for  $\bar{\psi} < 0$ , then the same must be true of  $Q$  (in view of [14]). Since  $Q$  is soft [i.e.,  $Q(\phi, 0) = iQ_1(\phi, 0)$ ], we know, too, that  $Q(\bar{\psi})$  can furthermore, only be singular in the upper half plane on the slit  $B$ , the image of  $A$ .

We may thus, in general, write for  $Q$  (Cauchy's Theorem):

$$Q(\bar{\psi}) = \frac{1}{2\pi i} \int_A \frac{Q(A)d\bar{\psi}}{\bar{\psi} - \bar{\psi}} + \frac{1}{2\pi i} \int_B \frac{Q(B)d\bar{\psi}}{\bar{\psi} - \bar{\psi}} \quad [54]$$

which can also be written:

$$Q(\bar{\phi}, \bar{\psi}) = \frac{i}{2\pi} \int_0^\ell \left[ \frac{\delta Q^*}{(\bar{\phi} - \bar{\phi}) - i(h + \bar{\psi})} + \frac{\delta Q(B)}{(\bar{\phi} - \bar{\phi}) + i(h - \bar{\psi})} \right] d\bar{\phi} \quad [55]$$

where

$Q^* = [Q(A)_{\text{upper}} - Q(A)_{\text{lower}}]$ , represents the jump in  $Q$  across the slit  $A$ , a complex quantity. [56]

It is easy to see that for  $Q(\phi_0)$  to be purely imaginary, then  $\delta Q(B) = \overline{\delta Q^*}$ , (where the overbar here denotes the complex conjugate), so that finally,

$$Q(\bar{\phi}, \bar{\psi}) = \frac{i}{2\pi} \int_0^\ell \left[ \frac{\delta Q^*}{(\bar{\phi} - \bar{\phi}) - i(h + \bar{\psi})} + \frac{\overline{\delta Q^*}}{(\bar{\phi} - \bar{\phi}) + i(h - \bar{\psi})} \right] d\bar{\phi} \quad [57]$$

and

$$Q_i(\bar{\phi}, 0) = I \left\{ \frac{i}{\pi} \int_0^\ell \frac{\overline{\delta Q^*} d\bar{\phi}}{[(\bar{\phi} - \bar{\phi}) + ih]} \right\} = \frac{i}{\pi} R \left\{ \int_0^\ell \frac{\delta Q^*}{[(\bar{\phi} - \bar{\phi}) - ih]} d\bar{\phi} \right\} \quad [58]$$

We need now only use the definition of  $Q$  implicit in [14] in order to define  $Q^*$ ; solving for  $Q$ :

$$Q = \frac{dF/d\bar{\psi} + \kappa iF + \kappa T}{(1 + F)} = \frac{d\ln G}{d\bar{\psi}} + i\kappa - \frac{i\kappa}{G} + \frac{\kappa T}{G} \quad [59]$$

This completes our definition of  $Q_i(\bar{\phi}, 0)$ , eqs. [58], [56], and [59], which is now stated in terms of the flow on the submerged body.

For its interpretation we imagine the flow created solely by a surrogate submerged body,  $S_s$ , whose singularities on the slit A correspond exactly to those on the real body  $S$ ; therefore, as the depth of submergence increases  $S_s \rightarrow S$ . For this body:

$$Q_s(\bar{\phi}, 0) = \frac{i}{2\pi} \int_0^\ell \frac{\delta Q^* d\bar{\phi}}{[(\bar{\phi} - \bar{\phi}) - ih]} \quad [60]$$

So, that, comparing [60] with [58], and using [59]:

$$Q_i(\bar{\phi}_o, 0) = 2I \left\{ Q_s(\bar{\phi}_o, 0) \right\}$$

$$Q_i(\bar{\phi}_o, 0) = -6 \frac{d\theta_s(\bar{\phi}_o)}{d\bar{\phi}_o} + 2\kappa \left( 1 - \frac{\cos 3\theta_s(\bar{\phi}_o)}{\bar{q}_s^3(\bar{\phi}_o)} \right) + 2I \left\{ \kappa \frac{T}{G} \right\} \quad [61]$$

This explicit relation allows for the calculation of  $Q_i(\bar{\phi}_o, 0)$  and therefore the wave field, given knowledge of  $F$  on the slit A (surrogate body). In an iterative solution,  $F$  could first be taken as calculated for the isolated body (in the case where the body is sufficiently submerged), or in the double model flow (for large  $\kappa$ ).

For large  $\kappa$  we note, see [61] that:

$$Q_1(\bar{\phi}_0, 0) \sim 2\kappa \left\{ \left( 1 - \frac{\cos 3\theta_s(\bar{\phi}_0)}{\bar{q}_s^3(\bar{\phi}_0)} \right) + O(\theta^3) \right\} \quad [61a]$$

where F on A would correspond to the double model flow.

# VII. ON THE PHYSICAL INTERPRETATION OF $Q_1(\bar{\phi}_0)$ . HOW WAVES ARE GENERATED.

The function  $Q_1(\bar{\phi}_0)$  can be given additional important meaning in the following way. The flow is inviscid, so that Bernoulli's equation applies everywhere. Therefore:

$$\frac{\partial q^2/2}{\partial n} + g \frac{\partial y}{\partial n} = - \frac{1}{\rho} \frac{\partial p}{\partial n} \quad [62]$$

where  $n$  is the unit normal to the surface. Equation [62] can also be written:

$$\frac{\partial \bar{q}^3}{\partial \bar{\psi}} + 3\kappa \cos \theta = -3\bar{q} \frac{\partial \bar{p}}{\partial \bar{\psi}} \quad [63]$$

or,

$$\frac{\partial \ln \bar{q}^3}{\partial \bar{\psi}} + \frac{3\kappa \cos 3\theta}{\bar{q}^3} + \frac{3\kappa(\cos \theta - \cos 3\theta)}{\bar{q}^3} = - \frac{3}{\bar{q}^2} \frac{\partial \bar{p}}{\partial \bar{\psi}} \quad [64]$$

or,

$$I \left\{ + \frac{d \ln G}{d \Psi} - \frac{3\kappa I}{G} - \frac{\kappa T(\Psi)}{G} \right\} = I \{ i P(\Psi) \} \quad [65]$$

where

$$R \{ P(\Psi) \} = \frac{3}{\bar{q}^2} \frac{\partial \bar{p}}{\partial \bar{\psi}} \quad \text{on } \bar{\psi} = 0 \quad [66]$$

$$I \left\{ \frac{T}{G} \right\} = \frac{3(\cos \theta - \cos 3\theta)}{\bar{q}^3} \quad \text{on } \bar{\psi} = 0 \quad [67]$$

or

$$I \left\{ \frac{d \ln G}{d \Psi} - \frac{3 \kappa i}{G} - i P - \kappa \frac{\tau}{G} \right\} = 0 \quad \text{on } \bar{\Psi} = 0 \quad [68]$$

This can finally be written:

$$\frac{dG}{d\Psi} + iG[3\kappa - P + iM] = 3\kappa i + \kappa \tau \quad [69]$$

where,

$$I[M(\Psi)] = 0 \quad \text{on } \bar{\Psi} = 0$$

In the case of a free wave,  $P = P_w$ ,  $M \equiv 0$ , and [69] can be compared with the earlier equation [13], with the result that:

$$P_w = 2\kappa - \frac{2\kappa}{G} + \frac{i\kappa(\tau + T)}{G} \quad [70]$$

Hereafter we write:

$$P = P_w + P^*$$

so that  $P^*$  is a measure of the motion induced normal pressure gradient in excess of that existing in a free-wave.

Therefore [69] can be written:

$$\frac{dG}{d\Psi} + iG[\kappa - P^* + iM] = \kappa i - \kappa T \quad [71]$$

which compares with Equation [13] ( $\Omega \equiv 0$ ):

$$\frac{dG}{d\Psi} + iG[\kappa + iQ] = \kappa i - \kappa T$$

On  $\bar{\Psi} = 0$ , these become:

$$\frac{dG}{d\bar{\Psi}} + iG[\kappa - P_r^* - iP_1^* + iM_r] = \kappa i - \kappa T$$

$$\frac{dG}{d\bar{\Psi}} + iG[\kappa - Q_1] = \kappa i - \kappa T$$

so that, comparing these relations:

$$M_r(\bar{\phi}_0) = P_r^*(\bar{\phi}_0) \quad \text{and} \quad Q_i(\bar{\phi}_0) = P_r^*(\bar{\phi}_0)$$

and, finally:

$$Q(\Psi) = iP^*(\Psi); \quad M(\Psi) = -Q(\Psi)$$

or, in the case where  $\Omega$  also exists:

$$Q(\Psi) + \Omega(\Psi) = iP^*(\Psi); \quad M(\Psi) = -Q(\Psi) \quad [72]$$

As a result, the wave driving function  $Q_i(\bar{\phi}_0) + \Omega_i(\bar{\phi}_0)$  can be given the following physical interpretation:

$$Q_i(\bar{\phi}_0) + \Omega_i(\bar{\phi}_0) = P_r^*(\bar{\phi}_0), \text{ and noting [66]}$$

$$Q_i(\bar{\phi}_0) + \Omega_i(\bar{\phi}_0) = \frac{3}{q^3} \left( \frac{\partial \bar{p}}{\partial n} - \frac{\partial \bar{p}}{\partial n} \bigg|_w \right) \quad \bar{\psi} = 0 \quad [73]$$

which reveals that in the case of a submerged body; the wave field originates in an unbalance of the normal pressure gradient on the free surface; i.e., in the excess of the normal pressure gradient over that in a free wave.

Note that in the case of a surface pressure distribution, waves originate, in addition to those due to  $\Omega_i$ , in the imposed pressure distribution itself (those due to  $\Omega_r$ ).

#### VIII. STRONG AND WEAK NONLINEAR REGIMES. ASYMPTOTIC BEHAVIOR ( $\kappa \rightarrow \infty$ ); AND OTHER APPROXIMATIONS. COMPARISON WITH OTHER THEORIES.

It is implicit in the exact result, [47], that the generation of waves by a submerged body involves both weak and strongly nonlinear effects, depending on the maximum value of  $Q_i(\phi_0)/\kappa$ . The regimes correspond to:

$$\text{WEAK NONLINEAR : } Q_i(\phi_0)_{\max} < \kappa$$

$$\text{STRONG NONLINEAR: } Q_i(\phi_0)_{\max} > \kappa$$

This can readily be seen from the following form for the exact result, [47]:

$$\frac{dF_o}{d\zeta_o^*} + i\kappa F_o = \frac{i Q_{1o}}{[1 - Q_{1o}/\kappa]} \quad [74]$$

whose solution is:

$$F_o = e^{-i\kappa\zeta_o^*} \int_{-\infty}^{\zeta_o^*} \frac{i Q_{1o}}{[1 - Q_{1o}/\kappa]} e^{+i\kappa\tilde{\zeta}_o^*} d\tilde{\zeta}_o^* \quad [75]$$

where  $\zeta_o^*$  is the map of  $\zeta$  given by:

$$\frac{d\zeta_o^*}{d\zeta_o} = [1 - Q_{1o}/\kappa] \quad [76]$$

It is apparent that both the solution, [75], and the mapping [76] experience singularities at the point on the free surface where  $Q_{1o}(\phi_o) = \kappa$ . We can in fact show that in the asymptotic case ( $\kappa \rightarrow \infty$ ) that discrete waves arise at such points. These waves are entirely a product of the strongly nonlinear effect.

The Strongly Non-linear Regime.

We write the amplitude of the far downstream wave as, see [53]:

$$A(\infty) = \text{ampl.} \int_{-\infty}^{+\infty} [i Q_{1o}(\bar{\phi}_o) - \kappa T(\bar{\phi}_o)] \cdot e^{+i\kappa f(\bar{\phi}_o)} d\bar{\phi}_o \quad [77]$$

where:

$$f(\bar{\phi}_o) = \bar{\phi}_o + \int_{\bar{\phi}_o}^{\infty} Q_{1o}(\tilde{\phi}_o)/\kappa d\tilde{\phi}_o$$

and note that:

$$\frac{df}{d\bar{\phi}_o} = [1 - Q_{1o}(\bar{\phi}_o)/\kappa] \quad [78]$$

Note that for large  $\kappa$  (low speed), the wave amplitude  $A(\infty)$  will

cease to be of exponential order in  $\kappa$  if the first derivative of the arg.  $e^{i\kappa f(\phi_0)}$  is zero within the range of integration (real values of  $\phi_0$ ). That is, see [78], if a value of  $\phi_0^*$  exists such that:

$$Q_1(\phi_0^*) = \kappa \quad [79]$$

At such critical points ( $\phi_0 = \phi_0^*$ ), strong waves arise which may be estimated by asymptotic integration (the method of stationary phase) [77].

For large  $\kappa$ , we note (see [61a]) that through  $O(\epsilon^2)$ , the critical point corresponds to the condition:

$$\bar{q}_s^3(\phi_0^*) > 2 \cos 3 \theta_s(\phi_0^*) \quad [80]$$

where we recall that the subscript  $s$  corresponds to the flow about the surrogate body. Note that this condition does not explicitly involve the wave number  $\kappa$ .

As a result of [80], if  $\bar{q}_s(\max)$  on  $\bar{\psi}_s = 0$  exceeds the value  $2^{1/3}$ , then of necessity one or more critical points must exist. In addition, if  $|\theta_s|$  reaches the value  $\pi/6$ , then of necessity critical points must also exist.

Imagine a submerged body  $S$ . As its depth increases,  $q_s \rightarrow 1$ ,  $\theta_s \rightarrow 0$  everywhere, so that at a sufficient depth no critical points exist on the free surface, and the flow corresponds to the weakly non-linear regime. For smaller depths, however, critical points will generally exist, and the flow corresponds to the strongly non-linear regime.

In this case, the method of stationary phase applied to [77], yields:

$$A(\infty) \sim \text{ampl.} \sum_n \frac{\sqrt{2\pi} \left[ \kappa(i - T(\phi_{0n}^*)) \right]}{\left[ \frac{dQ_1}{d\phi_0}(\phi_{0n}^*) \right]^{1/2}} \cdot e^{i[\kappa f(\phi_{0n}^*) \pm \pi/4]} \quad [81]$$

where the upper or lower sign is to be taken in the exponential according as  $dQ_1/d\phi_0$  at the critical point,  $\phi_{0n}^*$ , is positive or negative. Beyond the first appearance of strong waves note that  $n$  must be even.

Since  $dQ_1/d\phi_0$  at the critical point is  $O(\kappa)$ , then [81] shows that in the strongly non-linear regime:

$$A(\infty) \sim \kappa^{1/2} \quad [82]$$

a result which implies that wave slopes are  $O(\kappa^{1/2})$  and wave amplitudes are  $O(\kappa^{-1/2})$ . We recall, however, that physically realizable waves do not exist for  $A > 1$ , so that [82] implies that in the strongly nonlinear regime, for sufficiently small Froude numbers (large  $\kappa$ ), a physically



realizeable solution does not exist.

### The Weak Regime

We seek the reduction of the exact result [77] to approximate non-linear forms valid in the weak regime for sufficiently small disturbances; these allow comparison with several existing non-linear theories. The latter are usually expressed in physical plane variables, so we begin by writing [77] in the form:

$$\text{Exact; } A(\infty) = (\kappa\epsilon) \left\{ \text{ampl.} \int_{-\infty}^{+\infty} \left[ i\bar{Q}_{10} - \epsilon^2 \bar{T}_0 \right] e^{i\kappa f_0(x)} [1+u_0(x)] [1+y_0'^2] dx \right\} \quad [83]$$

where:  $x$  is the horizontal space coordinate, non-dimensionalized by the characteristic length  $\ell$ ;  $\bar{Q}_{10} = Q_{10}/(\kappa\epsilon)$  and  $\bar{T}_0 = T_0/\epsilon^3$  are both  $O(1)$ .

In the first approximation (making use that  $y_0' = O(\epsilon)$ ):

$$\epsilon^2 \ll 1; \quad A(\infty) \approx (\kappa\epsilon) \left\{ \text{ampl.} \int_{-\infty}^{+\infty} i\bar{Q}_{10} e^{i\kappa f_0(x)} [1+u_0(x)] dx + O(\epsilon^2) \right\} \quad [84]$$

where  $(1+u_0)$  is the horizontal component of  $\bar{q}_0$ .

To proceed further it is necessary to expand the terms in the exact expression for  $Q_{10}$ , [61], with the result:

$$\bar{Q}_{10} = \frac{6}{\epsilon} \left[ u_{s_0} + (\kappa r_{s_0})^{-1} \right] + O(\epsilon) \quad [85]$$

where  $r_{s_0}$  is the radius of curvature of the streamline  $\bar{\psi}_s = 0$ , positive when concave from beneath and where  $(1+u_{s_0})$  is the horizontal component of  $\bar{q}_{s_0}$ .

Substituting [85] in [84] yields a further approximation:

$$\kappa\epsilon^2 \ll 1; \quad \epsilon^2 \ll 1; \quad A(\infty) \approx \text{ampl.} \left\{ \int_{-\infty}^{+\infty} 6i [u_{s_0} + (r_{s_0}\kappa)^{-1}] \cdot e^{+i\kappa \int_{-\infty}^{\bar{x}_0} [1-6\{u_{s_0} + (r_{s_0}\kappa)^{-1}\}][1+u_0] d\bar{x} + O(\kappa\epsilon^2)} d\bar{x}_0 \right\} + O(\kappa\epsilon^2) \quad [86]$$

wherein we have not made any a priori assumptions regarding the magnitude of  $\kappa$ . Note that the requirement  $\kappa\epsilon^2 \ll 1$  arises from the approximation of the exponential argument, and that the quantities appearing may be evaluated at  $y = 0$  in place of  $\psi = 0$ .

Further we examine the low speed weakly non-linear regime:  $\kappa \gg 1$ ;  $\kappa\epsilon^2 \ll 1$ . In this case the surrogate submerged body,  $S_s$ , approaches the submerged half of the double model,  $S_d$ , corresponding to the flow beneath a rigid plane. In this case:

$$\begin{aligned} u_s(x_0) &= u_d(x_0)/2 + O(\epsilon/\kappa) \\ u_o(x_0) &= u_d(x_0) \\ (r_{s_o} \kappa)^{-1} &= O\left(\frac{\epsilon}{\kappa}\right) \end{aligned} \quad [87]$$

where  $[1 + u_d(x_0)]$  is the speed on the rigid plane beneath which  $S_d$  is submerged.

Substituting [87] in [86] we obtain the low speed weakly non-linear approximation:

$$\kappa\epsilon^2 \ll 1; \quad \kappa \gg 1;$$

$$A(\infty) \approx 3 \cdot \text{ampl} \left\{ \int_{-\infty}^{+\infty} i u_d(\tilde{x}_0) \cdot e^{i\kappa \int_{-\infty}^{\tilde{x}_0} [1 - 2u_d(\tilde{x}_0)] d\tilde{x}_0} d\tilde{x}_0 \right\} + O(\kappa\epsilon^2) + O(\epsilon) \quad [88]$$

This virtually corresponds to the version of the theory of Inui-Kajitani (1977), derived in the two-dimensional case by Doctors and Dagan (1980), where it is shown by numerical application to a surface pressure distribution that I-K closely corresponds to the second-order regular expansion theory. The difference is that  $A(\infty) = \text{ampl. } F$  while the corresponding RHS in I-K is  $\text{ampl. } v$ ; it is easily shown that  $F = 3(v - 1) + O(\epsilon^2)$ , so that [88] and I-K may be considered identical.

We now prepare for a comparison with the three dimensional theory of Charles Dawson (1977). The low-speed, weakly non-linear approximation, [88], implies the following differential equation in the complex domain, for the complex velocity  $v = d\psi/dz$ :

$$\kappa\epsilon^2 \ll 1; \quad \kappa \gg 1;$$

$$\frac{dv}{dz} + i\kappa v[1 + 2iU(z)] = \kappa U(z) \quad [89]$$

where:  $z = x + iy$ , where  $y = 0$  corresponds to the free surface,

$$\text{and } R\{U_d(x,0)\} = 0; \quad I\{U_d(x,0)\} = u_d(x,0) \quad [90]$$

Therefore,  $-iU(z)$  is the double model complex velocity. On  $y = 0$ :

$$\kappa \varepsilon^2 \ll 1; \quad \kappa \gg 1;$$

$$\frac{dv}{dx} + i\kappa v [1 - 2u_d(x)] = i\kappa u_d(x) \quad [91]$$

which leads eventually to the solution [88]; therefore proving our contention about [89].

Now we consider the solution for  $v$  to be composed of the double model flow plus a wave-like perturbation,  $\tilde{v}$  of  $O(1/\kappa)$ , with a perturbation potential  $\phi$ ; i.e.  $v = -iU(z) + \tilde{v}$ . We find for  $\tilde{v}$ , after substitution in [91]:

$$\kappa \varepsilon^2 \ll 1; \quad \kappa \gg 1;$$

$$\frac{d\tilde{v}_0}{dx} + i\kappa \tilde{v}_0 [1 - 2u_d(x)] = -\frac{du_d}{dx} - i\kappa u_d(1 - 2u_d) \quad [92]$$

or, in scalar notation ( $y = 0$ ); taking the real part:

$$\kappa \varepsilon^2 \ll 1; \quad \kappa \gg 1;$$

$$\tilde{\phi}_{xx} + \kappa \tilde{\phi}_y [1 - 2u_d(x)] = -u_{dx}(x) \quad [93]$$

Dawson's three dimensional equation, written in our notation except that his  $\ell$  is the length along the double model streamlines on  $y = 0$ ; and setting  $u_d(x) = \phi_{dx}$ , is:

$$\phi_{d\ell}^2 \tilde{\phi}_{\ell\ell} + \left( \phi_{d\ell}^2 \tilde{\phi}_\ell \right)_\ell + \kappa \tilde{\phi}_y = 0 \quad [94]$$

We put [93] and [94] in comparative form by re-arrangement and by neglecting some terms of  $O(\varepsilon^2)$  in each equation:

$$[93] \rightarrow (1 + 2u_d) \tilde{\phi}_{xx} + \kappa \tilde{\phi}_y = -(1 + 2u_d) u_{dx} \quad [95]$$

$$[94] \rightarrow (1 + 2u_d) \tilde{\phi}_{\ell\ell} + \kappa \tilde{\phi}_y = -(1 + 2u_d + 2\tilde{\phi}_\ell) u_{d\ell} \quad [96]$$

where  $u_d$  in [96] is the speed along  $\ell$  on the free surface in the double model flow.

Since  $\tilde{\phi}_\ell/u_d = O(1/\kappa)$ , these eqn's may be taken as identical in the present approximation:  $\kappa \varepsilon^2 \ll 1$ ,  $\kappa \gg 1$ .

With regard to the weakly non-linear straining technique introduced by Guilloton (1964), we note that [92] may be written in the form

(y = 0):

$$\frac{d\tilde{v}_0}{dx'} + 1\kappa\tilde{v}_0 = -u_{dx}, -1\kappa u_d (1 - 2u_d) \quad [97]$$

$$\frac{dx'}{dx} = [1 - 2u_d(x)] \quad [98]$$

implying that the low speed, weakly non-linear solution may be obtained as the solution of the linearized equation, [97], with the solution re-interpreted according to the straining [98]. In the low speed application of straining a' la Guilloton, however,  $dx'/dx = [1 - u_d(x)]$ . The present result, [98], therefore confirms the observation of Doctors-Dagan that Guilloton underestimates by half the straining necessary, and that [98] applies, as implied by Inui-Kajitani.

In summary, we have found that the present low speed, weakly non-linear approximation of the exact theory [83], is identical with both Inui-Kajitani and Dawson within the approximations involved, and limited to the speed range defined by  $1 \ll \kappa \ll \epsilon^{-2}$ . It would be remiss not to point out here that Dawson was anticipated by Ogilvie (2d; 1968) and then by Dagan (3d; 1972a,b), and later by others; see Tulin (1978). The present analysis therefore confirms and provides comment on the approximation first proposed by Ogilvie and now so well known as low speed theory.

The most important comment to make is that for given  $\epsilon$ , no matter how small, this so-called low speed theory is not valid for sufficiently low speeds. It is a theory valid for low, but not too low speeds! Perhaps it would best be thought of as a moderate speed theory, especially where moderate is used in the context of real ship speeds. This distinction illuminates the difference between this moderate speed theory and the very low speed theory of Keller (1974;78) based on rays. The two theories may or may not overlap in any particular case.

At very low speeds, in the sense meant by Keller in his works, the waves on a submerged body become exponentially small in the weakly non-linear case, although they may be calculated by using the appropriate integral, [84]. In Keller's ray theory these waves have disappeared, as he contends that only in the case of a body intersecting the surface do waves originate at very low speeds, and then only at singularities on the waterline. However, we have also found here finite waves originating on the surface in the case of very low speeds, even for a submerged body, but only in the strongly non-linear regime; these do not seem to have been anticipated in any previous theory, and their practical significance remains to be shown.

Finally we should point out that a weakly non-linear approximation, but not limited to moderate speeds, is given by [86], and applies, provided that  $\kappa\epsilon^2 \ll 1 \ll 1/\epsilon^2$ . In its application we should point out that the surrogate body flow involved in the integrand may be realized as the arithmetic mean of the double model plus free model flows (in the latter,  $u_{sf} \equiv 0$  on  $y = 0$ ).

## ACKNOWLEDGMENTS

This work has been carried out under Contract No. N00014-80-C-0669 with the Fluid Dynamics Branch of the Office of Naval Research, Navy Dept., and I wish to express gratitude to Mssrs. Ralph Cooper and Stanley Doroff for their early encouragement and support of my work on ship waves and to Drs. Robert Whitehead and Chung Lee for its continuation.

I wish to thank colleagues at Hydronautics and particularly to C. C. Hsu, and also to Prof. Yingzhong Liu (during his stay as a visitor from Shanghai Jiaotong University), for their helpful discussions and calculations. Prof. Liu is entirely responsible for the calculations presented as Figure 1.

And finally I wish to thank my old friend Prof. Gideon Dagan of Tel Aviv University for illuminating discussions, particularly related to the comparison between this theory and others in the weakly nonlinear regime.

## REFERENCES

- Dagan, G. (1972a). A study of the nonlinear wave resistance of a two-dimensional source generated body, Hydronautics Technical Report, 7103-2.
- Dagan, G. (1972b). Small Froude number paradoxes and wave resistance at low speeds, Hydronautics Technical Report, 7103-4.
- Davies, T. V. (1951). The theory of symmetrical gravity waves of finite amplitude, Proc. Roy. Soc. A, 208, 475.
- Dawson, C. W. (1977). A practical computer method for solving ship wave problems, Second International Conference on Numerical Ship Hydrodynamics, Berkeley, 30.
- Doctors, L. J., and Dagan, G. (1980). Comparison of nonlinear wave-resistance theories for a two-dimensional pressure distribution, J. Fluid Mech., 98, 3, 647.
- Guilloton, R. (1964). L'Etude theorique du bateau en fluide parfait, Assn. Technique Maritime et Aeronautique, Paris Bull., 64, 537.
- Inui, T., and Kajitani, H. (1977). A study on local nonlinear free surface effects in ship waves and wave resistance, 25th Anniversary Colloquium of the Institute fur Schiffbau, Hamburg.
- Keller, J. B. (1974). Wave patterns of nonthin or full bodied ships, Proc. 10th Symp. Naval Hydro. ONR, Navy Dept. Washington, D.C. 543.
- Keller J. B. (1979). The ray theory of ship waves and the class of streamlined ships, J. Fluid Mech., 91, 3, 465.
- Levi-Civita, T. (1925). Math. Ann. 93, 264.
- Ogilvie, T. F. (1968). Wave resistance: the low speed limit, Report 002, Dept. of Naval Architecture, Univ. Mech., Ann Arbor.
- Packham, B. A. (1952). The theory of symmetrical gravity waves of finite amplitude, Proc. Roy. Soc.(A), 208, 475.

- Schwartz, L. W. (1974). Computer extension and analytic continuation of stokes expansion for gravity waves, J. Fluid Mech., 62, 3, 553.
- Schwartz, L. W., and Fenton, J. D. (1982). Strongly nonlinear waves, Ann. Rev. Fluid Mech., 14, 39.
- Stokes, G. G. (1847). On the theory of oscillatory waves, Trans. Cambridge Philos. Soc., 8, 441.
- Tulin, M. P. (1978). Ship wave resistance-a survey, Proc. 8th U.S. Nat'l. Congress Appl. Mech., UCLA, Los Angeles, 217.

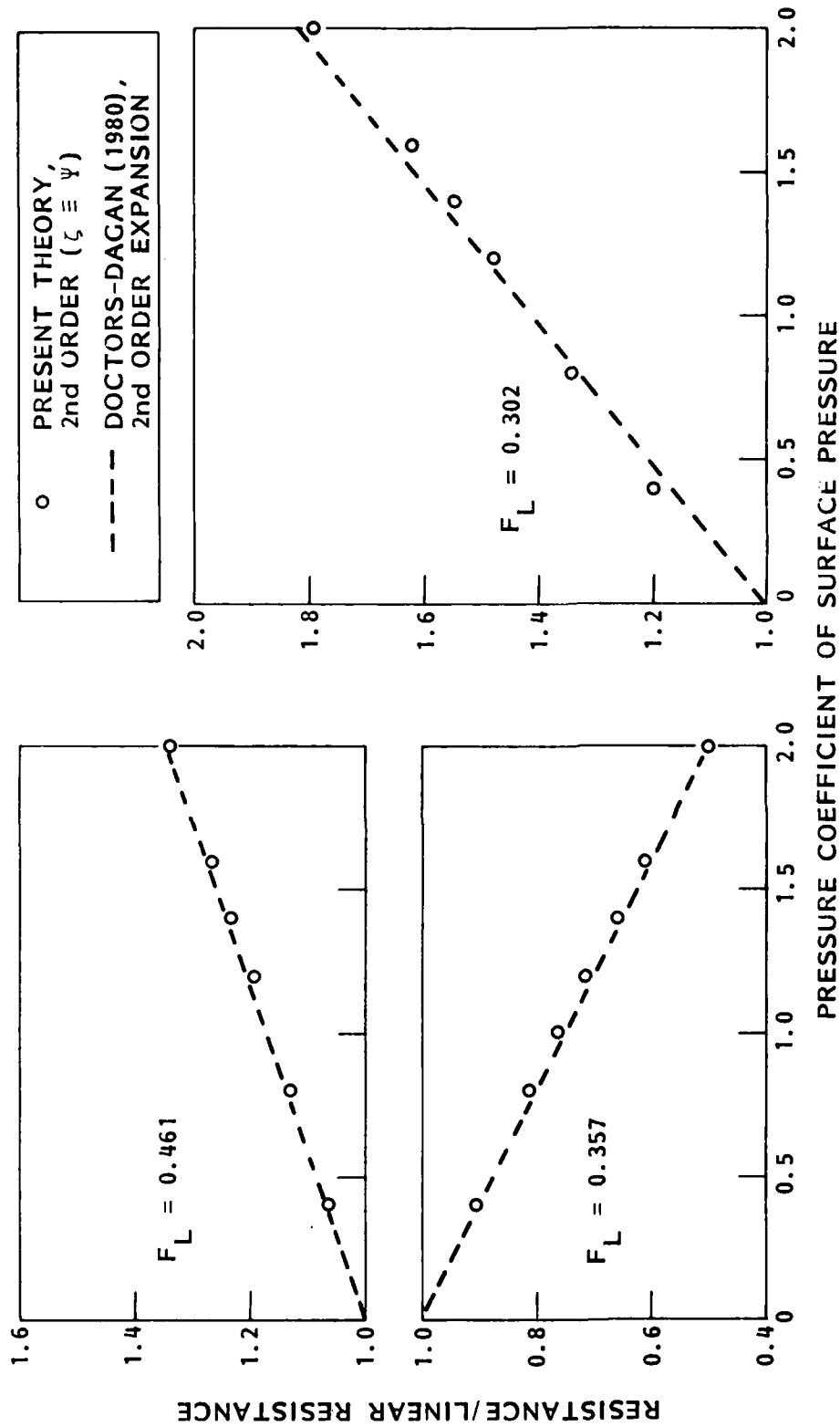


FIGURE 1 - A COMPARISON OF THE WAVE RESISTANCE OF A SURFACE PRESSURE DISTRIBUTION

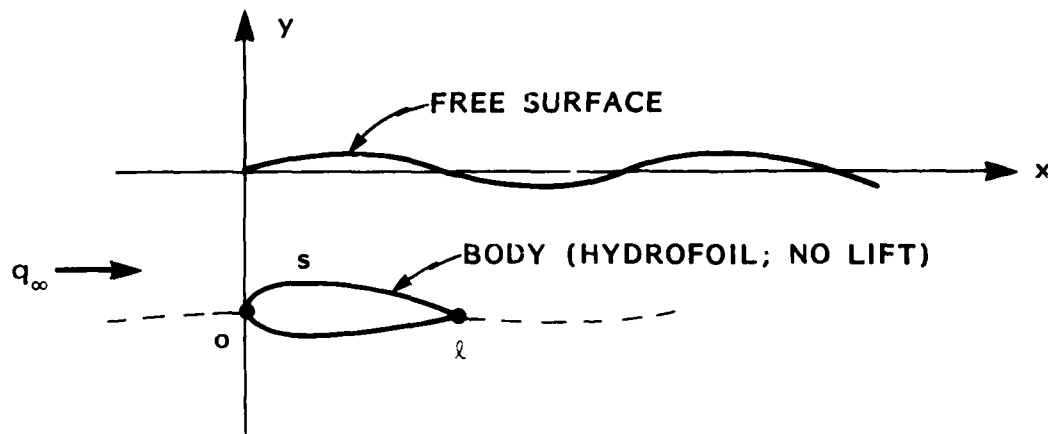


FIGURE 2a - PHYSICAL PLANE

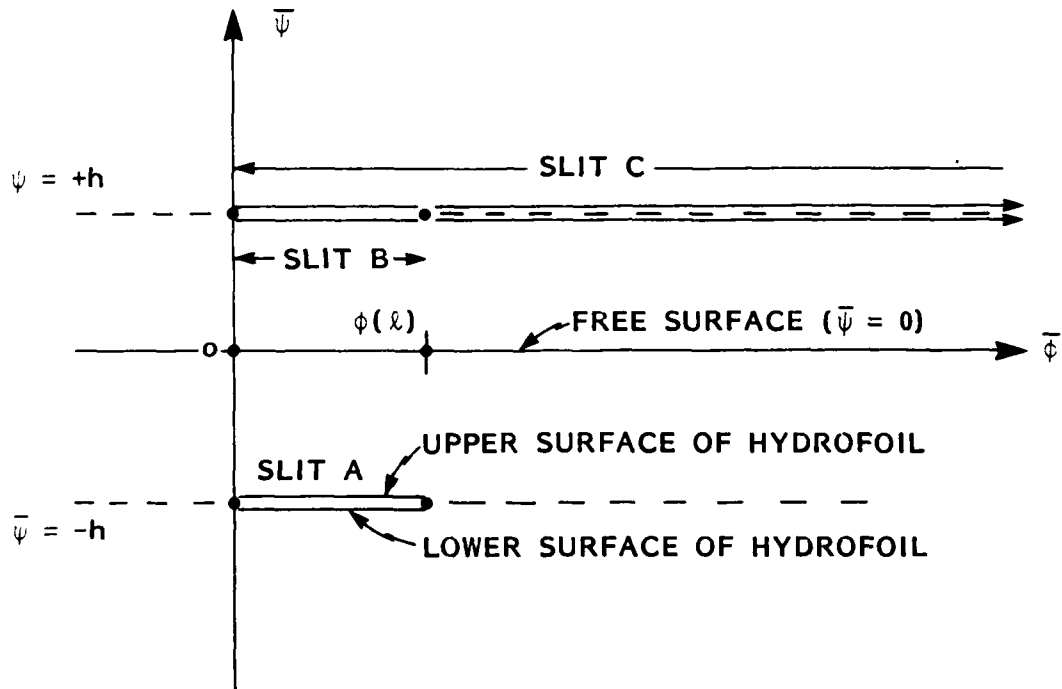


FIGURE 2b - EXTENSION OF THE PHYSICAL PLANE INTO ENTIRE COMPLEX POTENTIAL PLANE



## Discussion

T.F. Ogilvie (Massachusetts Institute of Technology)

The theory presented applies only to pressure distributions and/or submerged bodies. I assume that there are smoothness restrictions on the allowable pressure distributions. How then do you apply or even interpret your results for surface-piercing bodies?

E. Baba (Mitsubishi Heavy Industries)

The author should be commended for his efforts in making clear the relationship among the free-surface conditions related to the problems for weakly nonlinear regime, i.e., the author's, Inui-Kajitani's and Dawson's. My comment is about the position where the free-surface condition is satisfied. The author's free-surface condition is satisfied on the free surface. On the other hand, Dawson's one is satisfied not on the free surface but on the symmetrical plane for double-body flow, and, further, a term proportional to the second derivative of the double-body velocity potential with respect to the depthwise variable ( $y$ ) is missed in a sense of a Taylor expansion about the symmetrical plane. To the discussor's experience in calculating wave resistance in low Froude numbers, a contribution from this additional term is important, as discussed in the depth study meeting in Izu that followed the Washington workshop on ship wave resistance computations in 1979. The discussor would like to hear the author's view on this point.

L.J. Doctors (University of New South Wales)

The discussor was pleased to see the excellent agreement between the present theory and that of Doctors and Dagan (to second order) displayed in Figure 1. Could Dr. Tulin compare the two methods in terms of ease of use and expected accuracy at higher orders?

Can he also comment on why the theory at second order already predicts a limiting included overt angle of  $120^\circ$ --a result that one would expect should only appear at much higher orders.

Finally, one knows that perturbation theory, when applied to the traveling pressure-patch problem with pressure taken as the small parameter, will break down if a spray jet occurs--such as occurs at the bow of a planing surface. Can the present theory overcome this weakness?

A.T. Chwang (University of Iowa)

I would like to ask two questions: First, in your paper you used "surrogate" body instead of the actual body in the calculation. Would

you please explain what is meant by "surrogate" body? Second, have you compared your solution with other known solutions such as solitary waves or solitons?

### Author's Reply

M.P. Tulin (Hydronautics, Inc.)

To T.F. Ogilvie

As the discussor perceives, the part of the theory pertaining to surface pressure distributions may, in principle, be utilized in the case of a two-dimensional body intersecting the free surface, and it would be worthwhile to pursue such calculations and observe the phenomena that could emerge--strong wave generation, non existence, etc. In deriving the theory, no explicit assumptions were made about the smoothness of the pressure distribution. The apex of the problem would be to specify a pressure distribution resulting in a physically meaningful body and free surface, but this does not require strong smoothness everywhere. It is clear, for example, that if a body with a corner under water (cigar-box) were sought, the pressures would not be differentiable immediately at the corner. In all probability, the form of the pressure at and just downstream of the stagnation point would be crucial in its specification and might require some subtle considerations.

To E. Baba

Dr. Baba has raised an interesting and important question. Certainly a theory unlimited on the high-speed end should consider the effect raised. As for the moderate-speed theory, I would like more time to consider the question carefully; but my belief now is that Dawson's theory, neglecting the term cited by Dr. Baba, is correct to the order specified in my paper (two dimensions). Whether the term would appear in a theory accurate to lower speeds than Dawson used is doubtful.

To L.J. Doctors

The "second" order version of my exact theory is inconsistent in the sense that the approximation neglects some third-order terms (slope) in a regular expansion of Bernoulli's equation but not others (speed), it is for this reason that it yields the limiting wave, whereas a regular second order expansion does not. I do not yet know just how a spray jet might emerge and be treated within the framework of this theory, and it would be most interesting to study that question in detail.

To A.T. Chwang

The surrogate body flow in the plane of the complex potential possesses singularities only on the slit in the lower half plane representing the real submerged body, and nowhere else. On that slit the values of  $F$  are precisely the same as for the real submerged body flow. Therefore, the difference between the surrogate and the real body flow is that the latter includes the effect of images in the upper half plane, while the former does not (unbounded flow). As for the effect of bottom boundaries, I have not treated that case, but it would be most interesting to do so. It is certainly possible to obtain cnoidal and solitary progressive waves in this approach, as Davies and Packham have already done in approximations that are second order in my theory (the solitary wave solution of Packham has been shown to compare extremely well with the numerical solution of Lenau).

## Strong Nonlinear Characteristics of Steep Surface Gravity Waves

Hing-Yang Su, Oceanographer, Physical Oceanography Branch  
Albert W. Green, Head, Physical Oceanography Branch  
Naval Ocean Research and Development Activity  
NSTL Station MS 39529

Results of an extensive series of experiments on strong nonlinear properties of deep water gravity waves are summarized. The experiments were conducted in a large outdoor basin (1 x 100 x 340 m) and a long indoor wave tank (3.6 x 3.6 x 134 m). The waves were produced by a mechanical wavemaker. Effects of wave steepness ( $0.1 < ak < 0.34$ ) are analyzed for both wave trains and packets. Waves with moderate to large steepness are found to be subject to two fundamentally different types of subharmonic instabilities and two kinds of bifurcations.

Dynamical processes observed in these experiments include three-dimensional wave breaking, directional energy spreading, nonlinear energy transfer for narrow spectra, formation/interactions of envelope solitons, and formation of three-dimensional compact wave groups.

The experimental results plus additional analyses of oceanic wave group characteristics provide evidence that the strong interactions of ocean waves can be significant mechanisms for energy transfer. These newly recognized characteristics of gravity waves may have significant relevance to ship dynamics and offshore platforms in storm seas.

## I. INTRODUCTION

In the last two decades several theories about the stability and interactions of finite amplitude surface waves have been presented. (See Yuen and Lake, 1982). Many of the theoretical predictions have been verified to some extent by recent experimental results, but in several cases experiments have provided descriptions of phenomena that defy theoretical analysis at this time. In this paper we shall concentrate on describing experimental results that have given some valuable insights about the evolution of wave trains and wave groups, particularly in providing clearer understanding of the processes and forcing conditions that may exist in high sea states.

These results could aid designers in improving predictions of ship performance. One property of nonlinear wave dynamics that may be of particular interest to naval architects is the high coherency of the highest waves within a wave group. For many purposes it is sufficient to consider that the surface wave field is represented by a narrow-band Gaussian process that can be used in realistic simulations of ship hull response. The occurrence of coherent wave groups, particularly in high sea states, could present critical forcing situations that are not represented by simple statistical forcing models.

In the following sections we summarize the results of recent experimental work directed toward improving the description of the nonlinear dynamics of surface waves. In §2 we describe results of observations of two-dimensional wave instabilities and the formation of envelope solitons. These two-dimensional instabilities are also intimately related to a rapid change in the carrier frequency of wave groups and wave trains. In §3 we present results of observations of three-dimensional wave instabilities and bifurcation processes that occur for steep wave trains. A feature of wave instabilities that has not been described previously is the interaction of two- and three-dimensional instabilities; some of our results that give evidence for this type of interaction are briefly outlined. In §4 we describe statistical analyses of extensive wave data sets obtained during stormy periods in the Gulf of Mexico. We examine the occurrence of contiguous high waves that are members of an identifiable wave group. The joint probability distribution and correlation of contiguous high waves will be discussed. The dependence of wave groupiness on the peakedness of the wave spectra are examined. In §5 we attempt to relate some of the experimental and theoretical results to phenomena in natural ocean waves. These phenomena include wave breaking, formation of giant waves, short crestedness of natural waves and power spectra evolution. The results of our experimental work clarify and help to explain some of these complicated processes. In §6 we make a brief review of pertinent theoretical results which can partially elucidate some of the wave evolution processes that we have observed.

## II. THE EVOLUTION OF TWO-DIMENSIONAL WAVES: EXPERIMENTAL RESULTS

Benjamin and Feir (1967) presented clear evidence that finite amplitude wave trains are subject to a two-dimensional instability which is manifested by rapid growth of side-band components of the basic carrier wave. The growth of the side-band components progressively modulates the initial carrier; as the growth of the instability advances the upper side-band component attenuates while the lower frequency side-band grows. Distinct wave groups are formed in this process and the maximum wave height within a group may be double the initial wave height. An example of this type of wave train evolution is given in Figure 1, where  $a_0 k_0 = 0.15$  and the carrier frequency of the wave train  $f_0 = 1.23$  Hz. In this example the time series of water surface elevation at 61 m ( $59\lambda_0$ ) contains wave groups composed of about 7 waves. The higher waves occur at the leading edges of these groups with maximum wave heights 90% greater than the initial wave train. Modulation intensity decreases noticeably at the 76.2 m station with eventual reconstitution of a near-uniform wave train at the  $x = 106.7$  m station.

Wave power spectra for this example are shown in Figure 2. Note that the side-band components are visible at station  $x = 30.5$  m, and at  $x = 91.5$  m the lower side-band component of the instability has variance equal to variance of the carrier wave component at  $f_0$ . Meanwhile, the higher side-band component ( $f_2$ ) decreases appreciably. By the time the wave train evolves and proceeds to station  $x = 106.7$  m ( $104\lambda_0$ ), the lower side-band component ( $f_1$ ) has almost twice the variance of the  $f_0$  component. The majority of the carrier wave energy is transferred to  $f_1$ . It appears that the Benjamin-Feir instability is a precursor of the frequency downshift that accompanies the energy transfer from the carrier mode to the lower frequency mode. This frequency downshift occurs for waves with steepness,  $a_0 k_0 \gtrsim 0.1$ . It is clearly not a process described by the presently available theories. (Su, 1982b; Lake et al., 1977).

Another experimental result of interest is the formation of wave groups that remain essentially unchanged as they propagate. These experimental observations, to some extent, correspond with "envelope solitons", wave groups with invariant envelopes. Note examples in Figures 3 and 4. In Figure 3, we find that the wave packet has separated into a set of distinct envelope solitons by station  $x = 61$  m. Frequency dispersion causes the lower frequency harbingers to lead the envelope solitons which appear to maintain their shapes after separation from the initial packet. The leading envelope soliton contains the bulk of the energy of the original wave packet. The leading solitons generally have carrier frequencies that are lower than the initial carrier frequency, while trailing waves have frequencies nearer the initial packet carrier frequency. The maximum magnitudes of the frequency shifts relative to  $f_0$  are roughly equal to the initial steepness ( $a_0 k_0$ ), or  $(1 - f_1 f_0^{-1}) \approx a_0 k_0$ , where  $f_1$  is the most rapidly growing lower side-band of the

Benjamin-Feir instability.

As the number of waves in the initial packet ( $N_W$ ) increase, there is a higher probability that some envelope solitons or simple groups will collide. Examples of collisions of wave packets are shown in Figure 4 where  $a_0 k_0 = 0.15$ ,  $f_0 = 1.23$  Hz and  $N_W = 60$ .

At early stages the wave packet is subjected to modulations that are roughly symmetric about the center of the evolving packets in the range  $x = 6.1$  m to  $x = 42.7$  m. At subsequent stations the more intense modulations are biased toward the front of the packet (Fig. 4,  $x = 61.0$  m to  $91.5$  m). We believe that the asymmetric modulations are due to the collisions of wave groups of different carrier frequencies. (Su, 1982c).

### III. EXPERIMENTAL RESULTS OF THREE-DIMENSIONAL WAVES

Several types of three-dimensional surface wave patterns were observed to evolve from finite amplitude wave trains with initial steepness  $0.16 \lesssim a_0 k_0 \lesssim 0.34$ . Most of these observations were made in an outdoor basin  $1 \times 100 \times 340$  m. A 16 m long plunger-type wavemaker was used to generate waves that are initially uniform and 2-dimensional. Some smaller scale experiments were carried out in a deeper, narrower indoor tank  $3.6 \text{ m} \times 3.6 \text{ m} \times 134 \text{ m}$ .

#### A. Skew Bifurcation of Stokes Waves

For  $0.16 \lesssim a_0 k_0 \lesssim 0.18$ , finite amplitude wave trains (similar to Stokes waves) are found to bifurcate into three-dimensional patterns which propagate oblique to the primary direction of the initial waves generated by the wavemaker. A typical case with  $a_0 k_0 = 0.17$  serves as an illustration of the 3-dimensional pattern that appears to be similar to a "skew bifurcation" of Stokes waves (see Figure 5). The rather complex three-dimensional wave field has been divided into five phases:

- (a) finite amplitude (Stokes-like) waves,
- (b) skew bifurcation,
- (c) interactions of the skew bifurcation,
- (d) low frequency wave modulations, and
- (e) modulation of skew bifurcated waves.

Figure 6 presents two examples of skew-bifurcated waves; the initial long-crested waves with wavelength  $\lambda_0$  evolve into short-crested waves. Results of our experiments show that the crest lengths of the skew bifurcated waves ( $\lambda_s$ ) and their propagation directions, lie in the ranges:

$$2.5\lambda_0 < \lambda_s < 3.5\lambda_0$$

$$15^\circ < \psi < 20^\circ.$$

The average value of  $\lambda_s$  and  $\psi$ , are approximately  $3\lambda_0$  and  $18^\circ$ , respectively. The group velocities of the skew wave patterns  $C_{p,s}$  in the initial wave direction is

$$C_0/35 \lesssim C_{p,s} \lesssim C_0/65$$

which is small compared with the group velocity of small-amplitude waves,  $C_0/2$ . The skew wave patterns appear to be almost stationary to an observer standing on the wavemaker.

The upper central portion of Figure 7 gives an example of the interactions between two crossing skew wave patterns. This interaction produces compact diamond-shaped wave packets whose pattern is similar to the form of a narrow band two-dimensional wavenumber spectrum illustrated by Longuet-Higgins (1976). In the stage after the most intense interactions of the skewed bifurcating waves, a pair of skewed wave patterns emerge without apparent distortion of envelope shape.

Next the skew-bifurcated waves undergo the modulational instability that appears to be of the Benjamin-Feir type. Instability-induced modulations can be seen in the upper portion of Figure 7. The temporal records (Figure 8) of surface displacement at six locations clearly show the development of the instabilities. Low frequency modulations at about  $1/50$  the frequency of the primary waves are due to the progressive skewed wave pattern which has a small group speed. The shorter modulation period (about 6 wave periods) superimposed on the longer modulations are caused by the Benjamin-Feir instability. A more detailed description of the results of observations of the skew wave pattern can be found in Su (1982a).

#### B. Symmetric Bifurcation of Stokes Waves

When the range of wave steepness is  $0.25 < a_0 k_0 < 0.35$ , the characteristics of evolution of initially uniform wave trains are different from those discussed above. The evolution of these steeper waves can be described by five stages. A typical example described here has  $a_0 k_0 = 0.32$  (Figure 9). The stages are:

- (a) Three-dimensional instability,
- (b) Symmetric bifurcation,
- (c) Spilling wave breaking,
- (d) Radiation of oblique wave groups, and
- (e) Frequency downshift.

Figures 9 and 10 should be noted in order to understand the brief description of each stage.

Figure 10a shows a small portion of the wavemaker together with the first few waves with small perturbations (roughness). In Figure 10b distinct small-scale perturbations are superimposed on the larger waves; these disturbances are evidence of incipient three-dimensional instabilities on the steep waves. At this stage small-scale breaking occurs near the crests of the primary waves. The multiple disturbances are quickly sorted out, and highly regular, crescent-



shaped wave forms emerge at the beginning of the next stage (Figure 10c); these crescent-shaped waves are the result of symmetric bifurcation of the steep primary waves and a superimposed three-dimensional instability. The bifurcated waves in most cases have wavelengths that are twice the primary  $\lambda_0$ . This configuration of the symmetric bifurcation occurs in nine out of ten experiments in this range of  $a_0 k_0$ . Note in Figure 11a that there is a  $\frac{1}{2}\lambda_{BC}$  shift of the pattern in alternating rows of waves, when the symmetric bifurcation is dominant.  $\lambda_{BC}$  is the crestwise wavelength of the symmetric bifurcated wave.

In about one out of ten experiments another configuration occurs and is characterized by a length scale of  $3\lambda_0$  (Figure 11b). Note that every third row of waves has a  $\frac{1}{2}\lambda_{BC}$  crestwise shift with respect to the other two rows. The least frequently observed configuration (about 1% of experiments) has a length scale of  $4\lambda_0$  and is qualitatively similar to the first configuration, except that there are two identical patterns followed by two  $\frac{1}{2}\lambda_{BC}$  shifted patterns (Figure 11c) (Su, 1982a).

In the next stage spilling wave breaking occurs in the centers of the crescents (Figure 10d) as the symmetric bifurcation intensifies. Capillary waves radiate away from the "breakers" in a wide range of directions. Adjacent waves appear to interact strongly. Air entrainment occurs as the spilling breakers form. Following this phase, the wave train evolves into two regimes: (1) wave groups radiating away from the primary waves propagating at an angle of about  $30^\circ$  (Figure 10f) and modulating the primary wave train, their source appears to be related to the symmetric bifurcation process and the fully developed state of the three-dimensional instability; (2) wave groups travelling in the direction of the primary waves (Figure 10e) and appearing to be undergoing a transition similar to a well developed Benjamin-Feir instability accompanied by a rapid decrease of the primary wave frequency. The frequency downshift in the final stage may be as large as 25% of  $f_0$  (Su, Bergin, Harler and Ilyrick, 1982).

Figures 12 and 13 show the time series of surface fluctuations and the corresponding power spectra at ten stations. Modulations due to the three-dimensional instability are first visible at  $x = 12.2$  m in Figure 13. At stations,  $x = 30.5$  m and  $x = 36.6$  m, we see the alternate high and low wave crests which are the indications of symmetric bifurcated waves. In the next two stations ( $x = 42.7$  m and  $x = 48.8$  m), the most dominant modulation is four wave periods; this corresponds to the transition from three- to two-dimensional waves. The two-dimensional wave modulations produce the lower frequency envelope modulations at station ( $x = 67.1$  m).

### C. Interactions of Two- and Three-Dimensional Instabilities

We have described the experimental results of wave evolution as if the two- and three-dimensional instabilities were not co-existent and not subject to interactions. These phenomena are coincident, although

their growth rates differ according to  $a_0 k_0$ . In fact, both classes of instability influence each other during the evolution of wave trains and packets. In this section we describe some results of these interactions.

One particularly important effect of the interactions of the instabilities is found in the relation of initial steepness ( $a_0 k_0$ ) to relative growth of wave amplitude. Figure 14 shows the variation of the amplitude amplification factor, defined as  $(a_m/a_0)$ , for  $0.09 < a_0 k_0 < 0.20$ , where  $a_m$  is the largest wave amplitude observed at the maximum modulation in each run of experiments at a fixed  $a_0 k_0$ , with initial amplitude  $a_0$ .  $(a_m/a_0)$  is the relative maximum wave height growth in the wave evolution due to the Benjamin-Feir type instability. From the theoretical analysis of this type of instability (Longuet-Higgins, 1978), we would expect  $(a_m/a_0)$  to increase monotonically for  $a_0 k_0 < 0.20$ .

A remarkable feature of the observed variation (Figure 14) is that  $(a_m/a_0)$  reaches a maximum value;  $(a_m/a_0) \approx 1.9$  for  $a_0 k_0 \approx 0.14$ . Additionally, at the stage of maximum amplitude of the wave envelopes  $a_0 k_0 \times a_m/a_0 = 0.27$  ( $0.14 \leq a_0 k_0 \leq 0.2$ ), i.e., the "effective steepness" ( $a_m k_0$ ) reaches its maximum. This "effective steepness" puts the steepest waves into a range ( $a_0 k_0 > 0.25$ ) in which the three-dimensional instability limits the amplitudes of two-dimensional disturbances. The impact of the three-dimensional instability is clearly demonstrated in Figure 14. Su (1982b) and Irlville (1982) reported the observations of three-dimensional crescent-shaped breaking waves during the interval of maximum wave train modulation for  $a_0 k_0 \gtrsim 0.18$ . For wave packet modulations, Su (1982c) reported similar observations for  $a_0 k_0 \gtrsim 0.14$ .

In short, effects of interactions between these two types of instabilities may be summarized as follows. The three-dimensional instability appears to be enhanced in the steeper waves by the presence of the two-dimensional instability. Breaking dissipation accompanying the evolution of the crescent-shaped patterns, which results from three-dimensional instability, appears to limit the amplitude attained by the two-dimensional instability. The two-dimensional unstable waves reach a maximum steepness of only about 75% of the theoretical steepness limit, 0.443. Additionally, some effects of finite depth of water on both two- and three-dimensional instabilities are presented by Su, Bergin, Ilyrick and Roberts (1982).

#### IV. PROPERTIES OF STORM WAVE GROUPS

##### A. Introduction

In this section we describe some analyses of wave data taken in storm conditions. The results provide new insights into the ways nonlinear dynamics influence the formation of wave groups. A wave group is defined here to be a sequence of waves with heights exceeding

a threshold chosen to be the significant wave height ( $H_s$ ). This definition differs from the classical version that characterizes the "group" as an envelope of waves with nearly the same frequency. Marine folklore abounds with accounts of higher waves occurring more frequently in groups than singly. Recently this lore has been compared with quantitative analyses of ocean wave records. In the past decade it has been recognized that the occurrence of wave groups can be of considerable importance in operation and design of marine vehicles and offshore structures.

The presence of wave groups in wind seas is usually considered to be a consequence of the narrowness of the spectral bandwidth. The "groupiness" of wind seas has received very little analysis compared with standard wave spectral investigations. Greater attention has been devoted to understanding the processes that contribute to narrow spectral bandwidth and groupiness of wave data from rapid growth stages. We suggest that §2 and §3 contain some keys for explanation of these phenomena; in those sections we noted that wave trains and packets evolve into wave groups.

In an attempt to seek physical reasons for this phenomenon, as well as recognizing that wave trains/packets have natural tendency to evolve into more stable wave groups (§2 and §3), we now think it may be justifiable to propose that the narrow bandwidth of wave spectra is a consequence of existence of abundant wave groups in storm seas (generally considered to be strictly random processes). In any case, we shall show that these two wave characteristics are closely related.

The field data used here were collected by a consortium of several oil companies with offshore platforms in the Gulf of Mexico during 1969-1971. The data include passages of three hurricanes (Ward, 1974). Here we shall use only those portions of wave records with significant wave height ( $H_s$ ) greater than 2 m and with individual waves ( $H_i$ ) determined by the zero up-crossing method. Nearly 50,000 waves are included in this analysis. (Su, Bergin and Bales, 1982).

The peakedness parameter,  $Q_p$ , introduced by Goda (1970) is a useful measure for (relative) narrowness of the wave spectrum,  $E(f)$ :

$$Q_p = \frac{2}{m_0^2} \int_0^\infty f E^2(f) df, \quad (1)$$

where  $m_0$  is the zeroth moment of  $E(f)$ . Larger  $Q_p$  corresponds to narrower  $E(f)$ . Wave records have been separated according to the growth stage (increasing  $H_s$ ), or the decay stage (decreasing  $H_s$ ), so that possible differences in the statistical properties between these two stages of ocean waves can be studied.

## B. Correlation of Successive Wave Heights

Table 1 gives the correlation  $[R(j)]$  of successive wave heights for lags of  $j$  waves,  $j = 1, 2, 3$  and 4, for the stages of growth, decay and the combination of the two. The mean of  $R(1) > 0.32$  is

higher than the one-lag auto-correlation of a narrow band Gaussian process (Goda, 1970) for all the cases. The assumption that  $R(-1) = R(1)$  can be justified by the symmetry of the joint probability distribution of wave heights. We find that up to three successive waves are well correlated. We found little difference in the  $R(1)$ 's between the stages of growth and decay in comparison with the rather large difference (0.30 vs. 0.20) reported earlier by Rye (1974). More recently, Arhan and Ezraty (1978) obtained  $R(1) = 0.297$  for a data set of about 26,000 storm waves collected in the North Sea, which compares more favorably with the present result than that of Rye (1974).

To show the dependence of  $R(1)$  on the bandwidth of wave spectra, a scatter diagram of hourly  $R(1)$  vs. the corresponding  $Q_p$  is given in Figure 15. Although there is considerable scatter, the diagram indicates an approximately linear dependence between  $R(1)$  and  $Q_p$ :

$$R(1) \approx 0.2 (Q_p - 1) \quad (2)$$

### C. Probability Distribution of Group Lengths

The number of successive waves with  $H_i \geq H_s$  is defined here as the length of a wave group ( $L_1$ ), while the number of successive waves with  $H < H_s$  is defined as the group separation ( $L_2$ ). The combined number of waves for a pair of contiguous wave group and group separation,  $L = L_1 + L_2$ , will be called the total length of a wave group. Table 1 gives the probability distribution of  $L_1 = 1, 2, 3$  and 4,  $p(L_1)$ , plus the mean and standard deviation of  $L_1$ ,  $L_2$  and  $L$  for the stages of growth, decay and the combination of the two.

Assuming statistical independence of wave heights, Goda (1970) computed  $p(L_1 = 2) = 0.116$ . This is smaller than the value of 0.198 calculated from the field data; we surmise from this that waves with  $H_i \geq H_s$  tend to group together, rather than propagate singly. Our analysis shows small differences in  $L_1$ ,  $L_2$  and  $L$ , for the stages of growth and decay in comparison with those reported by Rye (1974).

Figure 16 is a scatter diagram of hourly  $L_1$  vs. corresponding  $Q_p$ . Also shown on the figure is a curve obtained by Goda (1976) based on a computer simulation using the JONSWAP spectra. This curve seems to represent a fairly good approximation for the mean of  $L_1$  vs.  $Q_p$ . An approximate linear relationship for these wave group parameters is

$$L_1 = 0.2 Q_p + 0.9. \quad (3)$$

Eliminating  $Q_p$  from (2) and (3) yields

$$L_1 = R(1) + 1.1 \quad (4)$$

### D. Joint Distribution of Successive Wave Heights

For sake of brevity we shall not present the details of the joint distribution of successive wave heights. Specifically, we mention

results of computations of the ratio of  $H_i$  to the expected value of  $H_{i+1}$  from the joint distribution. If  $H_i$  and  $H_{i+1}$  were independent, the expected value of  $H_{i+1}/\sqrt{m_0}$  would be 2.51 under the assumption of Rayleigh distribution of wave heights; note the straight dashed line in Figure 17. Statistics of the field wave data shows that successive waves with  $H_i/\sqrt{m_0} > 4$  have a higher correlation than smaller waves. This fact further justifies our choice of  $H_i \geq H_5$  for defining wave groups.

## V. COMPARISONS OF LABORATORY AND OCEAN WAVES

So far we have presented results of wave measurements from the laboratory and wind seas. The organized wave trains and packets in the laboratory experiments have features that we can relate to phenomena frequently seen in ocean waves, such as short crestedness, spilling breakers and directional spreading. The strong visual similarity of natural and laboratory waves inspires us to propose that the phenomena are governed by the same processes.

Before discussing the similarities, we should mention differences between laboratory and ocean waves. The laboratory waves come from a spatially compact, coherent source that creates Stokes-like waves. Harmonics of the finite amplitude waves are phase locked. Ocean wind waves are generated by randomly distributed turbulent atmospheric forcing that appears to act directly only as long as the wave phase speed is less than the wind speed. Another obvious difference is wavelength; the laboratory waves are on the  $O(1 \text{ m})$ , whereas their visual oceanic counterparts are typically somewhat longer and further from the gravity-capillary regime. Although we could describe more differences, such as boundary effects and effects of dissipative turbulence, we refer the reader to Su (1982a,b) for more extended discussions.

### A. Short-Crestedness and Directional Spreading

Deep ocean waves, particularly in growing seas, are usually short crested; the crestlength is on the order of the wavelength. The short crests can be attributed to modulations produced by waves travelling in different directions, instabilities or bifurcations. Nature probably allows all of these phenomena a range of admixtures, but the laboratory experiments give some sharp focus on wave instabilities and bifurcations. The added acuity allows us to see that even small perturbations on waves of moderate  $ak$  create rapidly growing instabilities. The compounding of two- and three-dimensional instabilities, and bifurcations create short-crested waves.

Oceanic waves are not generated by a coherent source, nonetheless the perturbations will be present and the most unstable modes will amplify. These two-dimensional growth processes will modulate the waves to form groups containing waves steep enough to accelerate the growth of the three-dimensional instability and, finally, breaking.

Weak resonant interactions possibly complement wave instabilities. The laboratory results give clear evidence that bifurcations and three-dimensional instabilities lead to breaking waves and spreading of energy away from the primary wave direction.

In growing seas dominant waves may often have  $ak = 0.14$  to  $0.18$ , the range in which modulational instabilities grow rapidly, so it appears reasonable to surmise that the ocean wave instabilities lead to short-crestedness. The generation of short crested waves spreads the directional power spectrum. The experiments also show that three-dimensional wave breaking may be an additional source of directional spreading of wave energy.

## B. Wave Breaking in Deep Water

We have been impressed by the apparent similarity of the spilling breakers seen in the experiment and white-capping deep sea breaking waves. In the laboratory we found that wave breaking is the result of three-dimensional instabilities and symmetric bifurcations. Analyses of storm wave records show that many waves have sufficient  $ak$  to trigger the sequence of these types of instabilities and bifurcations.

More indirect evidence of the physical similarity of these processes comes from the group properties of storm waves; it appears that wave groups contribute to the most energetic bands of the spectra. The probabilities of occurrence of these groups exceeds that of a narrow band Gaussian process. From this we surmise that modulational instabilities and bifurcations tend to reinforce phase locking of wave components; this also exists in ocean waves and leads to wave breaking. Donelan, Longuet-Higgins and Turner (1972) observed that oceanic wave breaking appears to happen most often at periods twice the dominant wave period. This is consistent with the experimental results of the three-dimensional breaking waves in the most frequent configuration of the symmetric bifurcation (§III).

## C. Giant Waves

We now add another example of evidence for strongly nonlinear wave evolution. This concerns the so-called "giant" waves encountered in the Aghulas Current and, less frequently, other regions of the oceans. These types of abnormally high waves have been described by Hallory (1974) and Hamilton (1980). Results of our experiment that appear to bear on this phenomenon are the observations of rapid growth of wave height due to modulational instability. The giant waves appear to be in small groups that arise as a result of rapid changes in the wind or current field through which large amplitude swell passes. Swell entering the Aghulas Current from the south (with  $ak = 0.08$ ) increases steepness as it interacts with the opposing current. The increase in steepness to  $ak = 0.12$  is sufficient to bring the swell into a range where rapid growth of modulational instabilities creates wave packets containing some large steep waves.

In the laboratory we found that the modulational instability could create waves with heights two times that of the initial waves. Intense modulation can also occur as a result of rapid and intense change of wind speed and direction in the presence of swells, such as in the case of the passage of a squall line (Hamilton, 1980). The abrupt wind change rapidly generates waves that may increase the steepness of the initial wave field by the process of long-short wave interactions. These instabilities could be the sources of anomalous waves. Although the connections of the laboratory and oceanic processes are tenuous at this stage, the roles of nonlinear instabilities and bifurcations in ocean wave evolution seem to be important.

#### D. Implications to Naval Hydrodynamics

As efforts progress in numerical simulations of hull response, it is clear that the representations of the forcing field, such as waves and currents, need to be accurate. The occurrence of wave groups complicates the response model by introducing conditions that require the model to have memory for several wave periods. For example, a ship underway in heavy seas may momentarily be loaded by water trapped on the open decks. This status could be precarious for a damaged vessel since there is a significant probability that the first intense wave will be followed by another. The second wave could have somewhat greater impact than the first, due to the mass of water added by the first wave.

### VI. APPLICABLE THEORIES

#### A. Applicability of Theories

Throughout this paper we have described our observations in terms of instabilities and bifurcations. This terminology has been chosen to describe processes that have similarities with recent theoretical results. All of these theories have assumed that the initial wave trains or packets have finite amplitudes. The instabilities arise from the presence of relatively small perturbations to the wave field. The theoretical results that are based on small perturbation analyses are not strictly applicable to our observations in every case, since the observed perturbations are not always small. The nonlinear wave evolution resulting from finite amplitude disturbances is different from the theoretical assumptions. Later stages in the development of the transitional phenomena, such as irreversible frequency downshift, wave breaking and the self-limiting of instabilities at finite amplitudes are not in the scope of present theory. Nevertheless, the theoretical results have given valuable aid in developing working analogies of complex phenomena. Mathematical methods currently being developed in other branches of physics, renormalization theory for example, may eventually overcome the major mathematical problems and

quantitatively describe the natural phenomena (See Dewitt, 1982 for examples).

## B. Wave Instabilities

Benjamin and Feir (1967) showed that two-dimensional Stokes waves were subject to instabilities when perturbations at higher or lower frequency side bands were introduced. Experimentally, these side-band instabilities are observed as modulations of the carrier wave, hence the term "modulational instabilities". Longuet-Higgins (1978) extended the Benjamin-Feir theory to all waves of large amplitude. Modulational instabilities of this class have been observed (§2) and are the source of the incipient modulations of wave trains and packets.

Three-dimensional instabilities of steep waves have been predicted by McLean, et al. (1980) and McLean (1981). This type is most clearly manifested as the dominant instability for  $a_0 k_0 > 0.3$ , although it is present for small steepness. This instability has the critical feature of phase locking with the primary wave, so it must travel at the phase speed of the carrier waves. Observations of the crescent-shaped, three-dimensional instabilities correspond closely with the theoretical predictions of symmetric bifurcations given by Saffman and Yuen (1981). There are some clear differences, however. The observed waves break and appear to dominate the carrier waves.

Saffman and Yuen (1980) predicted a second class of bifurcated waves, the skew bifurcations mentioned in §3. Our observations confirm existence of this phenomenon and are quantitatively consistent with several features, such as angle of divergence of the wave vector relative to the primary, but the group speed differs.

In our experiments we found that the intense modulational instabilities created wave packets containing waves with  $ak$  large enough to trigger the three-dimensional instabilities. The small perturbation analyses of the present theories do not include these forcing conditions. Generally, it is clear that many of the qualitative and some of the quantitative theoretical results are consistent with our observations.

## C. Envelope Solitons

Another important observation in the experiments is that wave packets tend to sort themselves out into smaller packets of near-permanent form, described here as envelope solitons. This packet fissioning into envelope solitons was predicted for waves of small  $a_0 k_0$  by Zakharov and Shabat (1972). The main features of their theory agree well with observations with small  $a_0 k_0$ ; however, for waves with  $a_0 k_0 > 0.1$  the leading, most energetic envelope solitons are found to have carrier frequencies lower than the initial main carrier. The nonlinear homogeneous Schrödinger equation, which is the basis for the Zakharov and Shabat analysis does not admit



solutions with permanently frequency-downshifted waves (Yuen and Lake, 1975; Lake et al., 1977). Presently there is no theory that explains the frequency-downshifting information of envelope solitons.

#### D. Frequency Downshifting

One of the most interesting features of our experimental results is the observation that waves with  $a_0 k_0 > 0.1$  shift energy from the initial carrier wave to a lower frequency component. The energy is transferred to wave components with a frequency corresponding to the lower side band mode of the modulational instability (Benjamin and Feir, 1967; Longuet-Higgins, 1978). This energy extraction from the primary wave may continue until the carrier is almost totally absorbed by the lower side band. Exchange of energy among frequency components is predicted by Hasselmann (1962) as a result of weakly nonlinear resonant wave interactions (Phillips, 1960). Due to the assumptions of small steepness and long interaction times, the weak resonant theory is not applicable to wave evolution in the ranges of  $ak$  in storm seas and in our experiments. In addition, an important simplifying assumption used in the theory is that the phase relationships among the interacting field are random. As we have noted, this assumption has limited validity due to the apparent phase locking of components in wave packets with  $ak \gtrsim 0.1$ .

#### VII. CONCLUSIONS

We have described several nonlinear wave processes that have been observed recently. The initial wave steepness ranged from 0.1 to 0.34. The general features of these processes correspond well with predicted instabilities and bifurcations, but significant advances in theories will be needed to explain the observed frequency downshifting, energy transfer and dissipation. The tendency of moderate-to-steep waves to form phase locked groups was observed in the laboratory and in oceanic storms. Several characteristics of the ocean waves are very similar to the laboratory waves, so we suggest that comparable processes are working in both domains, but considerable work will be required to quantify this conclusively. The existence of wave groups of large-amplitude could be a threat to ship survival in extreme seas, particularly when the vessel is damaged or disabled. We shall be able to make more accurate predictions of sea state and ship response to heavy seas, if we can improve our understanding of these strong nonlinear wave phenomena.

The high incidence of wave groups of higher waves in storms should be considered in formulation of new statistical theories of deep water waves. Existence of these components with strong interactions compels us to suggest that the weak multiwave resonant interactions may not be the major source for the wave-wave energy transfer. Sporadic, but strong interactions should also be included in the energy budget.

## REFERENCES

- Arhan, M. and R. Ezraty. (1978). Statistical Relations Between Successive Wave Heights. Oceanologica ACTA, Vol. 1, No. 2, pp. 151-158.
- Benjamin, T.B. and J.E. Feir. (1967). The disintegration of wave trains on deep water. Part I. Theory. J. Fluid Mech. 27 pp. 417-30.
- Dewitt, R.J. (1982). Self Consistent Effective Medium Parameters for Nonlinear Random Ocean Internal Waves. Doctoral Dissertation, University of Illinois at Urbana-Champaign, Department of Physics, 136 pp.
- Donelan, H., H.S. Longuet-Higgins and J.S. Turner. (1972). Periodicity in whitecaps. Nature, 239. pp. 449-450.
- Goda, Y. (1970). Numerical Experiments on Wave Statistics with Spectral Simulations. Rept. Port and Harbour Res. Inst., Japan, Vol. 9, No. 3, pp. 3-57.
- Goda, Y. (1976). On Wave Groups. Proc. BOSS '76 Conf. Trondheim, Norway.
- Hamilton, G.D. (1980). Buoy Capsizing Wave Conditions. Mariners Weather Log, 24, (3). pp. 165-173.
- Hasselmann, K. (1962). On the nonlinear energy transfer in a gravity wave spectrum. Part 1. J. Fluid Mech., 12, pp. 418-500.
- Lake, B.H., H.C. Yuen, H. Rungtaldier, and H. Ferguson. (1977). Nonlinear deep water waves. Theory and experiments. Part 2. Evolution of a continuous wave train. J. Fluid Mech. (83), p. 49.
- Longuet-Higgins, H.S. (1978). The instabilities of gravity waves of finite amplitude in deep water. II. Subharmonics. Proc. R. Soc. London Ser. A. 360. pp. 489-505.
- Longuet-Higgins, H.S. (1976). On the nonlinear transfer of energy in the peak of a gravity-wave spectrum: a simplified model. Proc. R. Soc. Lond. A., 247, pp. 311-328.
- McLean, J.H., Y.C. Ma, D.U. Martin, P.G. Saffman and H.C. Yuen. (1980). A new type of three-dimensional instability of finite amplitude waves. Phys. Rev. Letters, 46, pp. 817-820.
- McLean, J.H. (1981). Instabilities of finite-amplitude water waves on deep water. J. Fluid Mech., 114, pp. 315-330.
- Hallory, J.K. (1974). Abnormal Waves on the South East Coast of South Africa. Int. Hydrographic Rev. 51 (2), pp. 99-129.
- Melville, J. (1982). The instability and breaking of deep-water waves. J. Fluid Mech., 115, pp. 165-185.
- Phillips, O.M. (1960). On the dynamics of unsteady gravity waves of finite amplitude. Part 1. J. Fluid Mech. (9) pp. 183-217.
- Rye, H. (1974). Wave Group Formation Among Storm Waves. Proc. of 14th Coastal Engineering Conf., Vol. 1, pp. 164-183.
- Saffman, P.G. and H.C. Yuen. (1980). A new type of three-dimensional deep-water waves of permanent form. J. Fluid Mech. Vol. 101, pp. 797-808.

- Saffman, P.G. and H.C. Yuen. (1981). Three-dimensional deep-water waves. II. Computation of steady symmetric wave patterns. To appear in J. Fluid Mech.
- Su, H.Y. (1982a). Three-dimensional deep-water waves. 1. Experimental measurement of skew and symmetric wave patterns. To appear in J. Fluid Mech.
- Su, H.Y. (1982b). Long-time evolution of deep-water surface wave trains of moderate steepness. Submitted to J. Fluid Mech.
- Su, H.Y. (1982c). Evolution of groups of gravity waves with moderate to high steepness. Submitted to Phys. Fluids.
- Su, H.Y., M. Bergin, R. Myrick and J. Roberts. (1982). Experiments on Shallow-Water Grouping and Breaking. Proc. First Int. Conf. on Meteorology and Air/Sea Interaction of the Coastal Zone. The Hague, Netherlands.
- Su, H.Y., M.T. Bergin and S.L. Bales. (1982). Characteristics of Wave Groups in Storm Seas. Proc. Ocean Structural Dynamics Symposium '82, Corvallis, Oregon.
- Su, H.Y. and A.W. Green. (1981). Experimental Studies of Strong Nonlinear Interactions of Deep-Water Gravity Waves. Proc. IUCM Symp. on Wave Dynamics and Radio Probing of the Ocean Surface. May, 1981. Miami, Florida.
- Su, H.Y., M. Bergin, P. Marler and R. Myrick. (1982). Experiments on nonlinear instabilities and evolution of steep gravity wave trains. To appear in J. Fluid Mech.
- Ward, E.G. (1974). Ocean Data Gathering Program - An Overview. Offshore Technology Conf., Houston, Texas, pp. 771-780.
- Yuen, H.C. and B.M. Lake. (1982). Nonlinear Dynamics of Deep-Water Gravity Waves. Advances in Applied Mechanics, Vol. 22. pp. 67-229, Academic Press.
- Yuen, H.C. and B.M. Lake. (1975). Nonlinear deep water waves. Theory and experiment. Phys. Fluids (18) pp. 956-960.
- Zakharov, V.E. and A.B. Shabat. (1972). Exact theory of two-dimensional self-focusing and one-dimensional self-modulating waves in nonlinear media. Sov. Phys. JETP 34:62-69.

Table 1. Statistics of Wave Groupiness with Comparisons

Source	Growth or Decay	Group Length Distribution				Group Length		Group Separation		Total Group Length	Wave Height Correlation			
		$l_1=1$	$l_1=2$	$l_1=3$	$l_1=4$	mean	s.d.	mean	s.d.		R(1)	R(2)	R(3)	R(4)
This study	G	.724	.192	.059	.017	1.40	.776	10.44	9.42	11.84	.324	.066	-.000	-.021
	D	.699	.205	.069	.020	1.43	.774	10.81	9.73	12.24	.340	.079	.023	.015
	G&D	.713	.198	.064	.018	1.41	.775	10.61	9.56	12.02	.329	.070	.008	-.008
Goda, 1970	(-5)power	.8	.2	.05	.01									
	Random	.866	.116	.015	.002	1.15								
Rye, 1974	G					1.41	.69	8.05	6.63	9.46	0.30			
	D					1.26	.51	7.26	5.70	8.52	0.20			
	G&D	.76	.185	.05	.01	1.35	.61	7.71	6.23	9.06	0.24			
	Random					1.15	.42	7.46	6.95	8.61				
Arhan & Ezraty, 1978	G&D										.297	.051	.036	
	=3.3										.298	.113	.043	
	=1.0										.163	.02	.02	

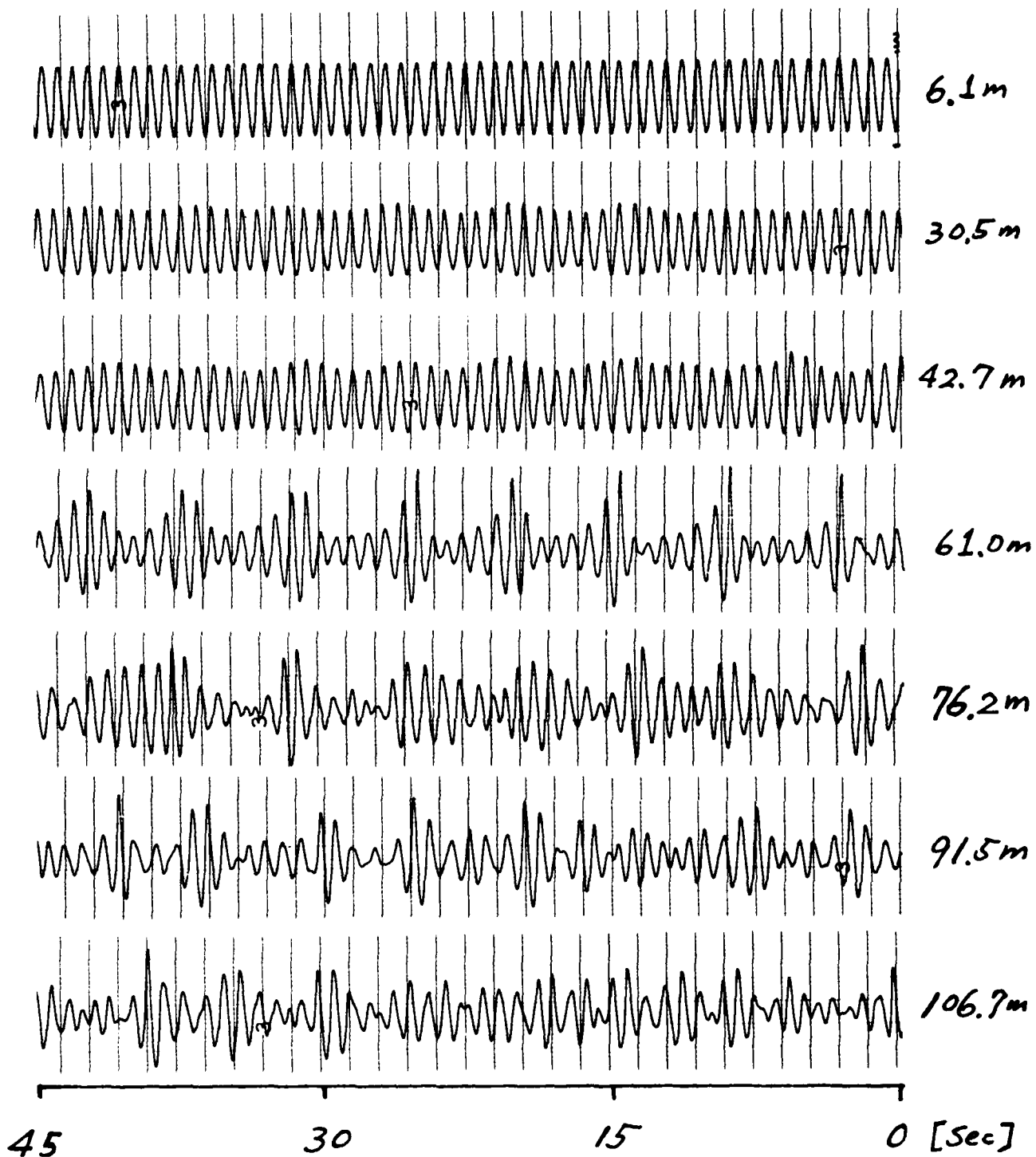


Figure 1. The space-time evolution of a continuous wave train with an initial steepness,  $a_0 k_0 = 0.15$  and  $f_0 = 1.23$  Hz.

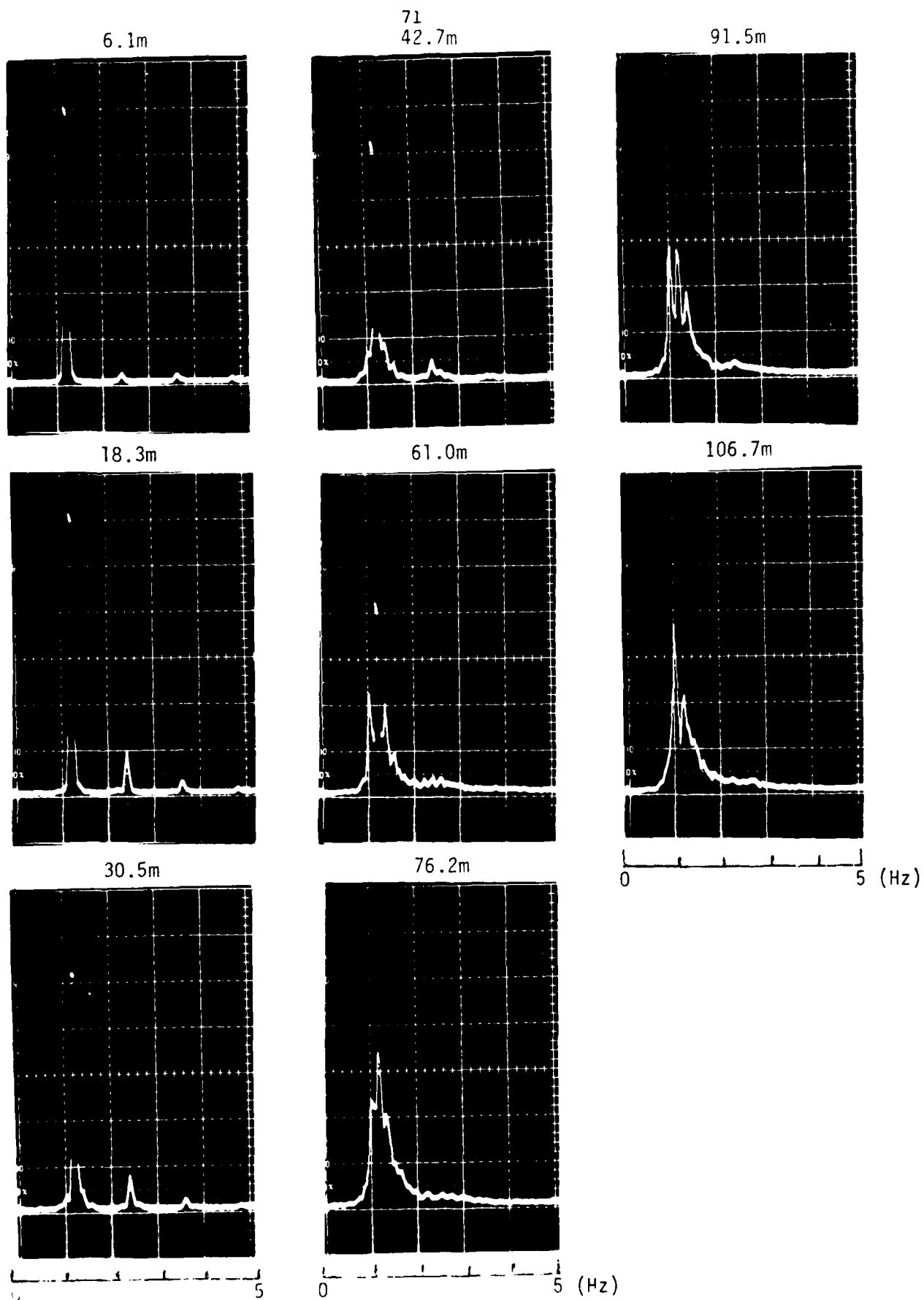


Figure 2. The variance spectra of surface fluctuations at the stations described in Figure 1.

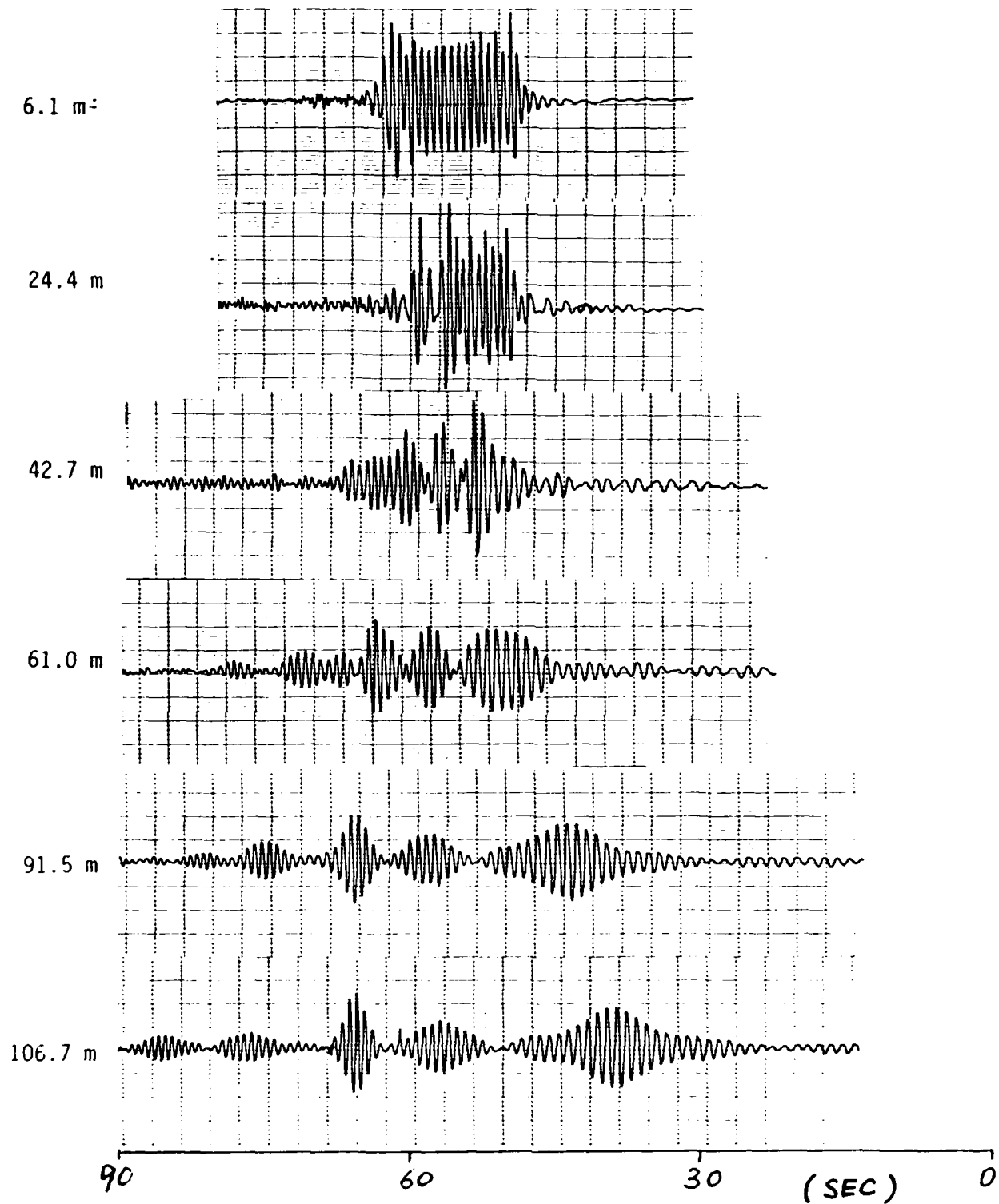


Figure 3. Time series of surface displacements at six stations for a moderate steepness wave packet ( $N_w = 20$ ,  $a_0 k_0 = 0.22$ ,  $\lambda_0 = 0.82$  m and  $f_0 = 1.15$  Hz). The packet fissions to form five distinct envelope solitons (61 m).

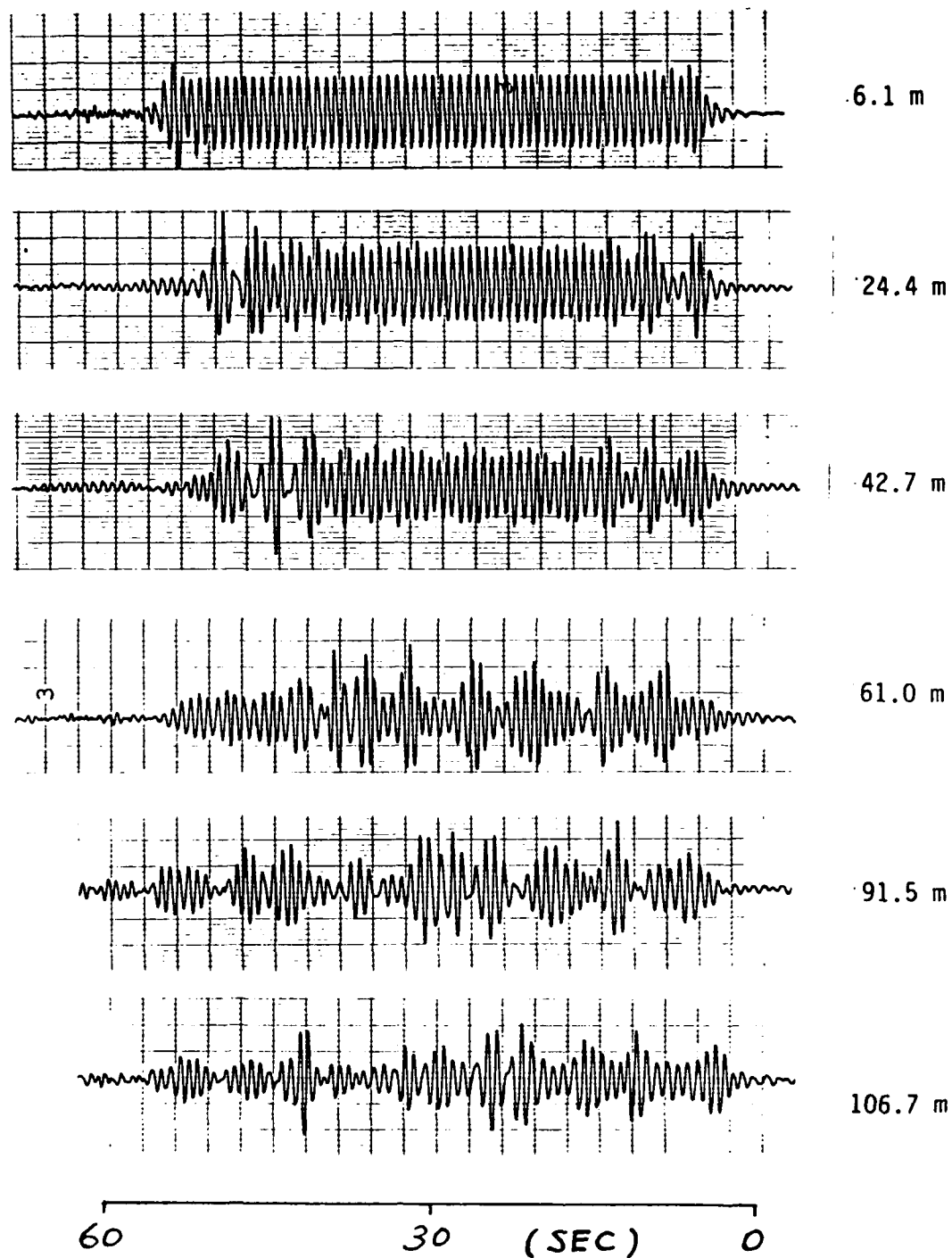


Figure 4. The evolution of long wave packets includes packet collisions that occur as the lower frequency fission products pass through the higher frequency, slower packets.

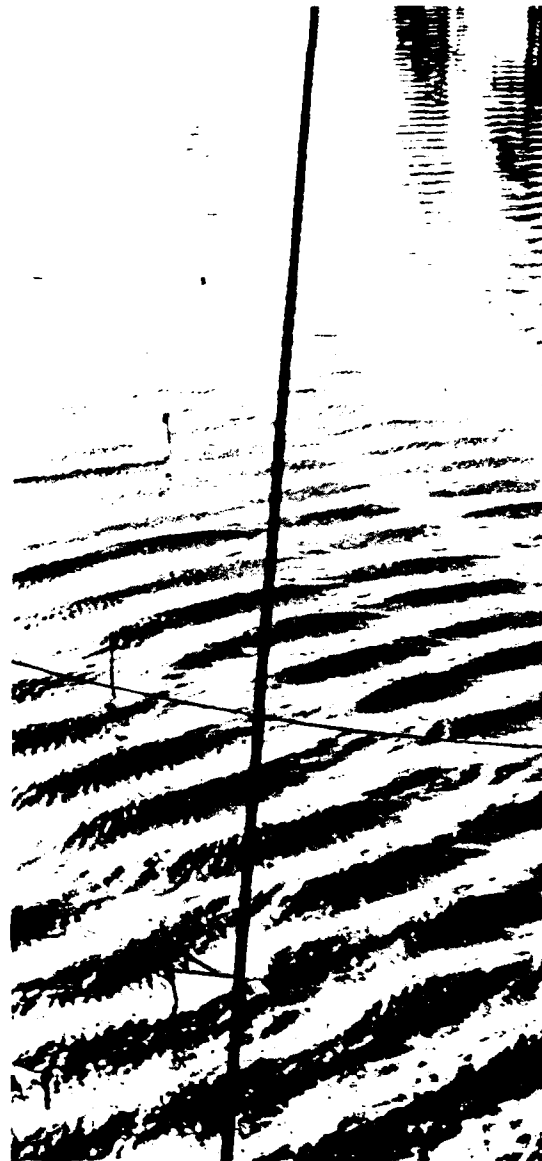




Figure 5. Skew wave patterns result from bifurcations of wave trains in (a). The skew wave patterns appear in (b) as straight, alternating bands of high and low amplitude. In region (c) interference bands occur due to interactions of the two crossing skew wave patterns. In zone (d) Benjamin-Feir-type modulations of the skew waves are apparent. In (e) the Benjamin-Feir-type modulations of the primary waves.



(a)



(b)

Figure 6. Two examples of skew bifurcated wave patterns; waves propagate from the lower right to the upper left.

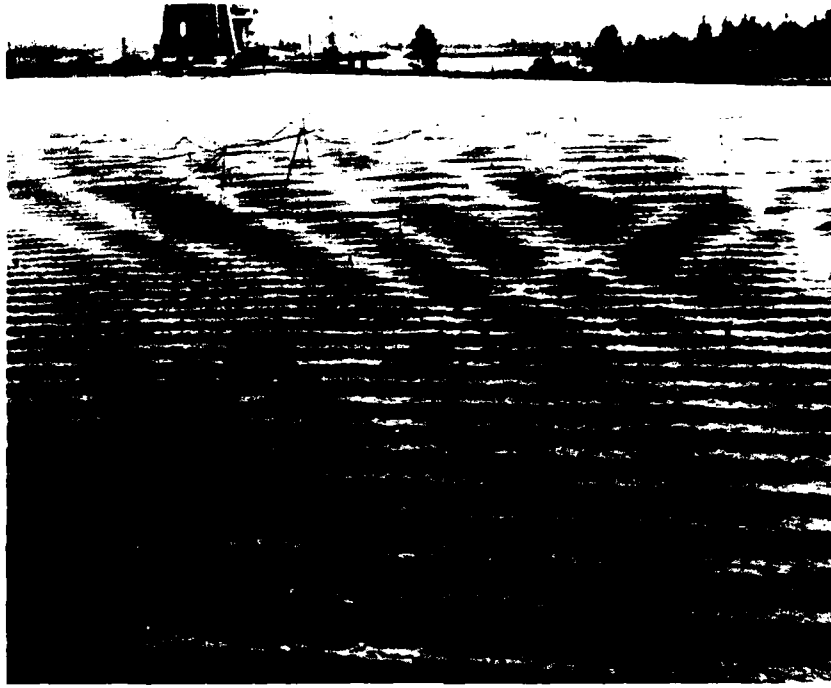


Figure 7. An example of interaction of crossing skew wave patterns that generate compact diamond-shaped wave packets.

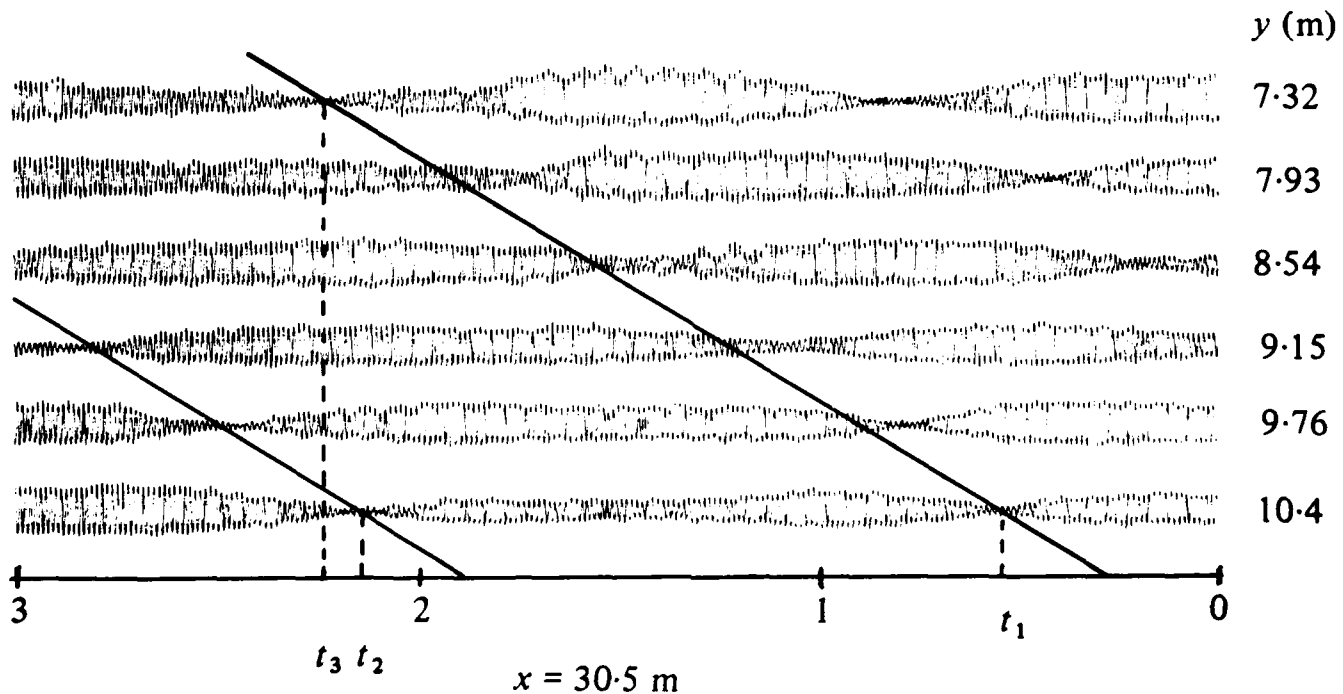


Figure 8. Temporal records of wave height variations for the skew bifurcated wave patterns with  $a_0 k_0 = 0.17$ .

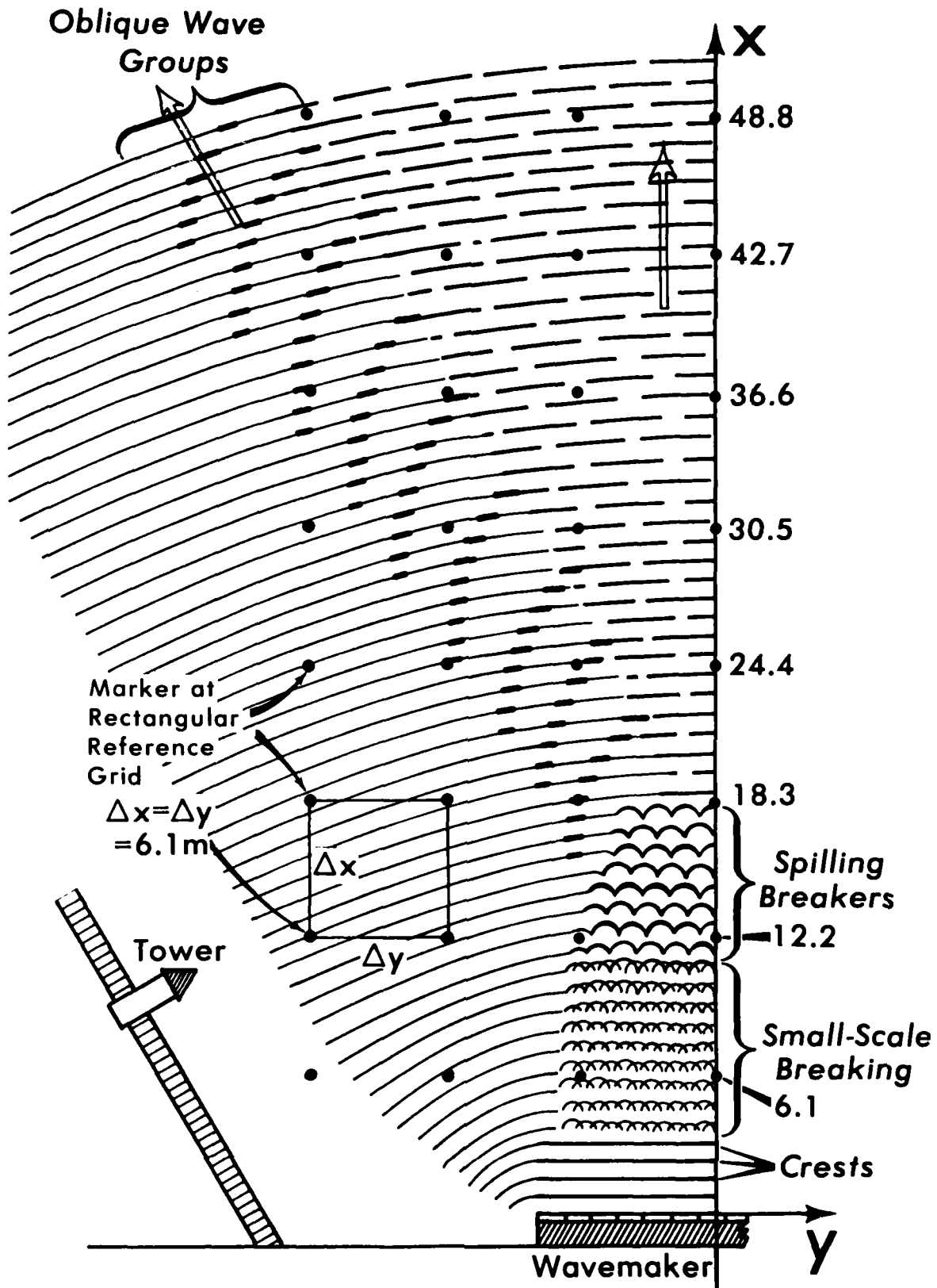


Figure 9. A schematic diagram of phases of three-dimensional evolution of a steep wave train ( $a_0 k_0 = 0.32$ ,  $f_0 = 1.55\text{ Hz}$ ,  $\lambda_0 = 65\text{ cm}$ ).

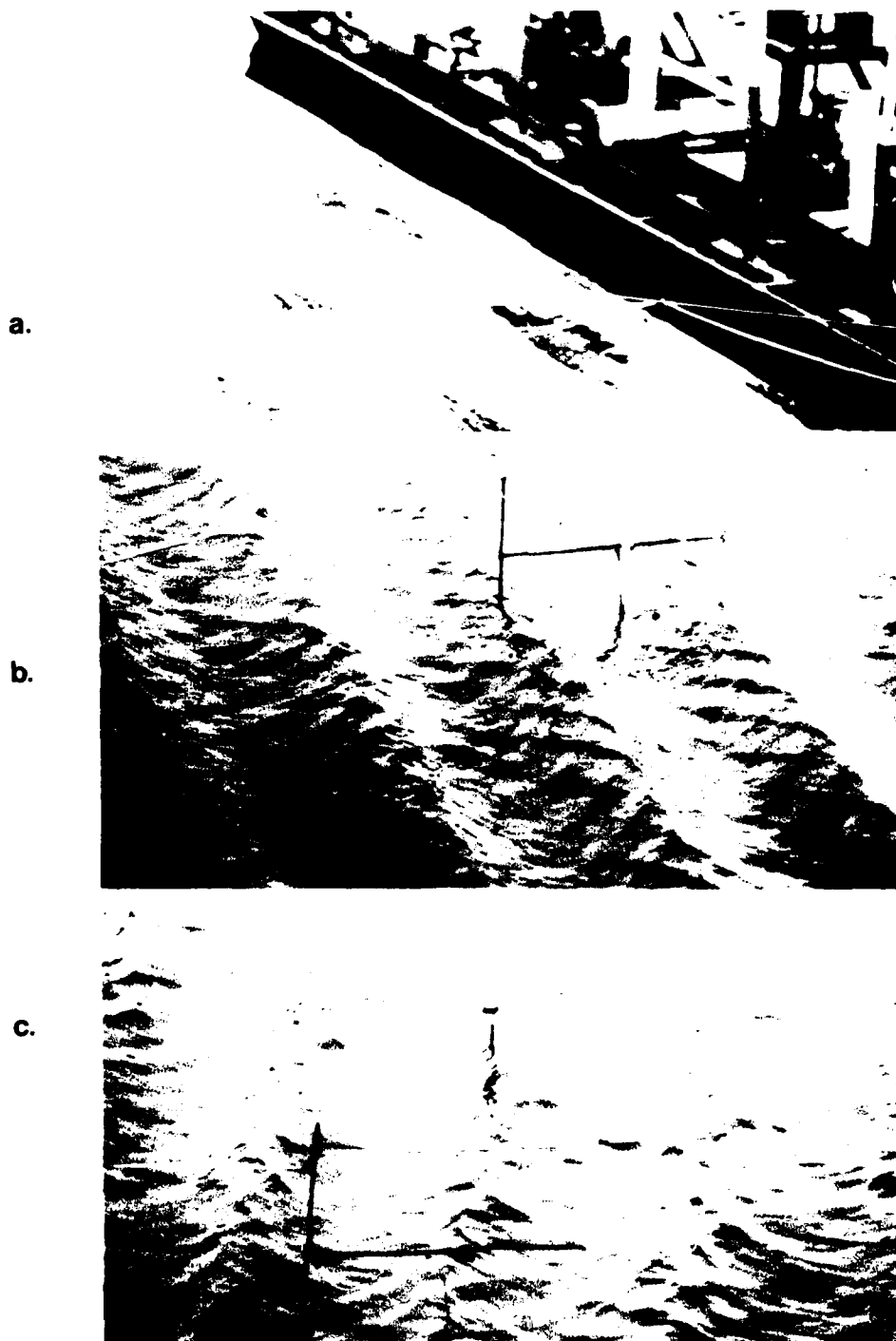


Figure 10. A sequence of photographic images corresponding to the phases of the three-dimensional evolution of a steep wave trains ( $a_0 k_0 = 0.32$ ,  $f_0 = 1.23$  Hz): (a) the initial uniform wave train, (b) at  $x = 20$  ft., and (c) at  $x = 40$  ft., examples of the growth of the three-dimensional perturbations (d) at  $x = 60$  ft., the symmetric bifurcation forms crescent-shaped spilling breaking waves, (e) at  $x = 80$  ft., showing intense two-dimensional modulation preceding the frequency downshift, and (f) at  $x = 120$  ft., the oblique wave groups radiate from the transition of the spilling breakers.

d.



e.



f.



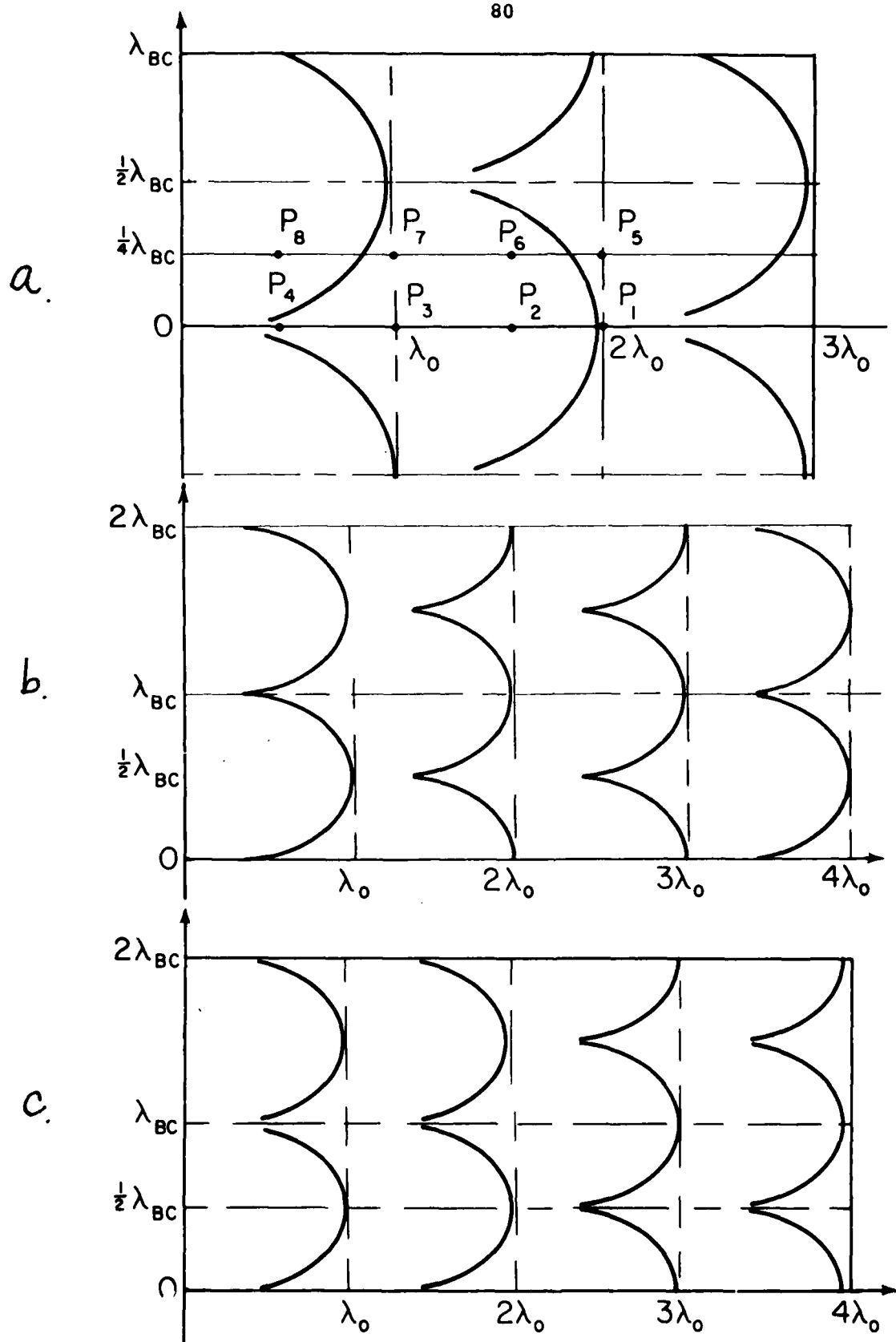


Figure 11. Three observed configurations of symmetric bifurcations from steep wave trains with  $0.25 < a_0 k_0 < 0.34$ : (a) with the periodicity of two primary waves, (b) with the periodicity of three primary waves, and (c) with the periodicity of four primary waves.

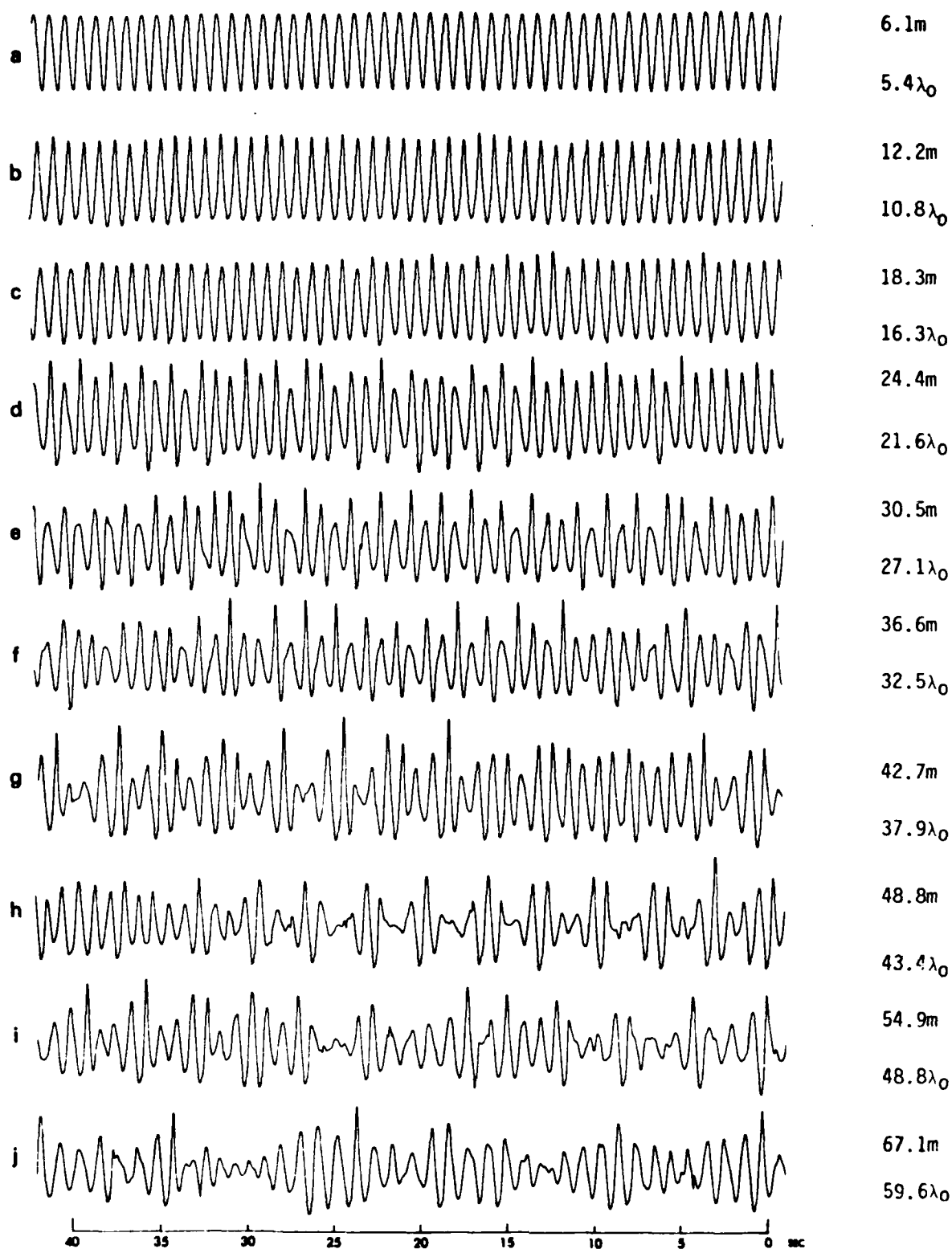


Figure 12. Time series of surface displacement of a wave train at stations along a tow tank;  $a_0 k_0 = 0.30$ ,  $f_0 = 1.15$  Hz,  $\lambda_0 = 1.12$  m.



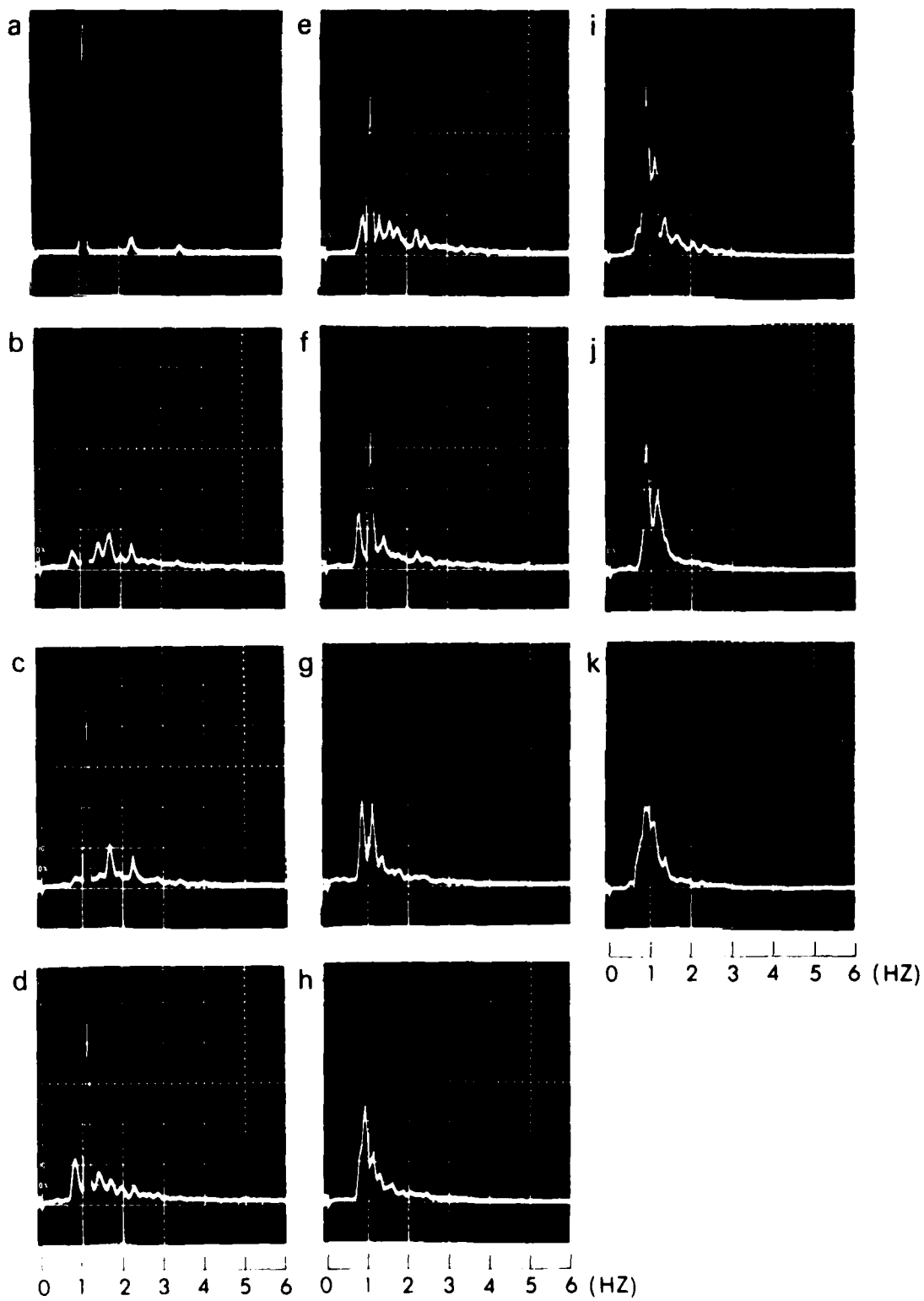


Figure 13. Variance spectra at the corresponding stations in Figure 12.

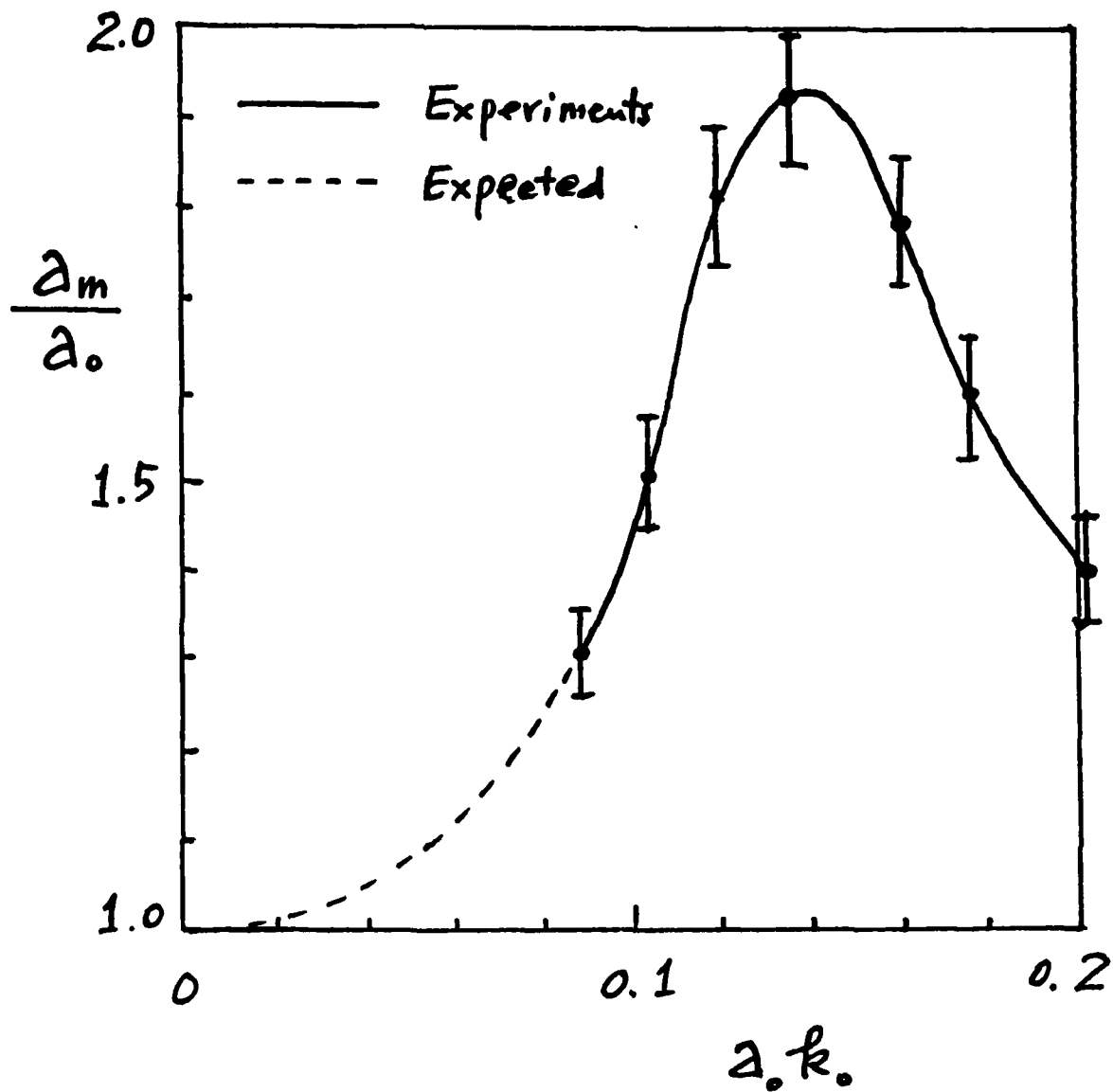


Figure 14. Dependence of the amplitude amplification factor ( $a_m/a_0$ ) on the initial wave steepness ( $a_0 k_0$ ).

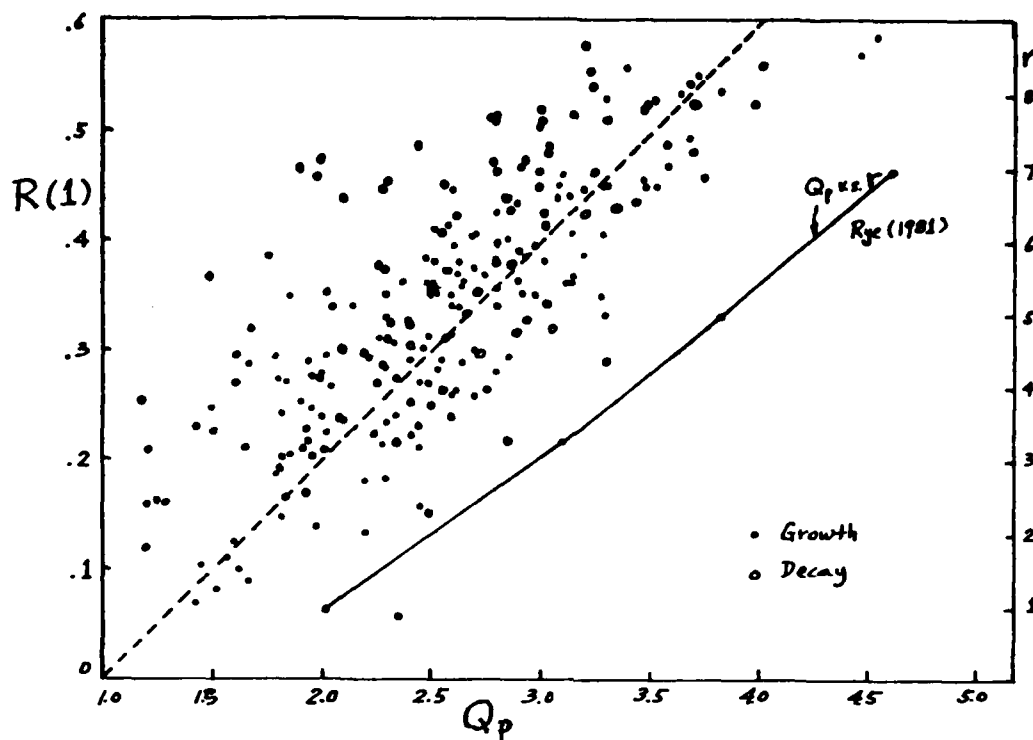


Figure 15. Scatter diagram of correlation of wave heights vs. peakedness parameter for the stages of growth and decay, respectively.

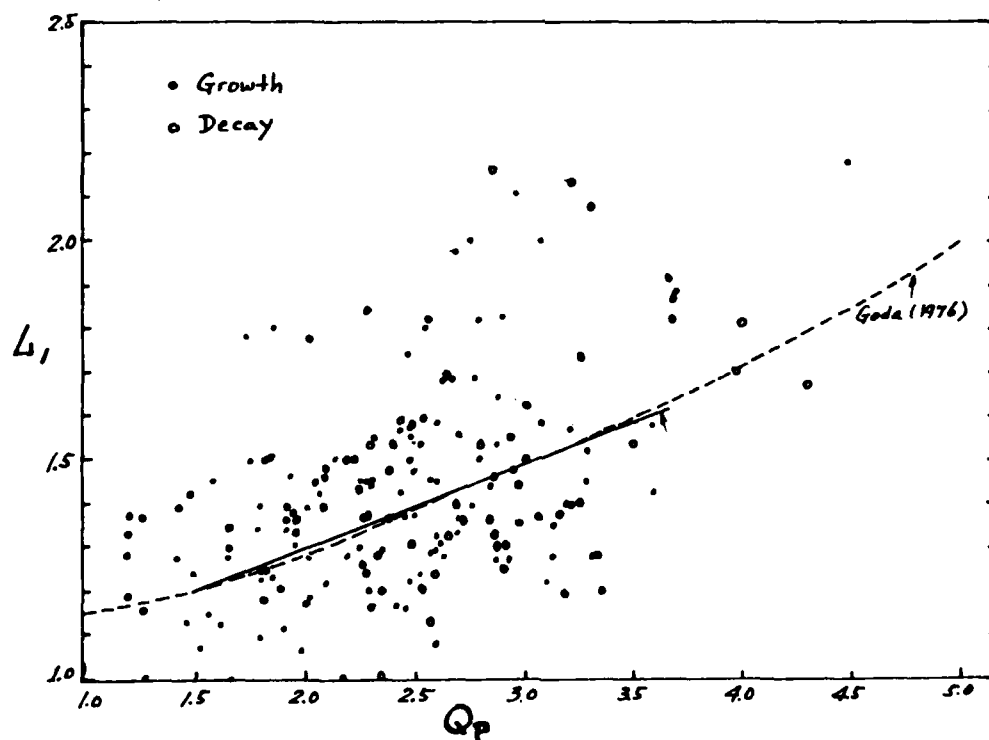


Figure 16. Scatter diagram of mean group length,  $L_1$ , vs. peakedness parameter,  $Q_p$ .

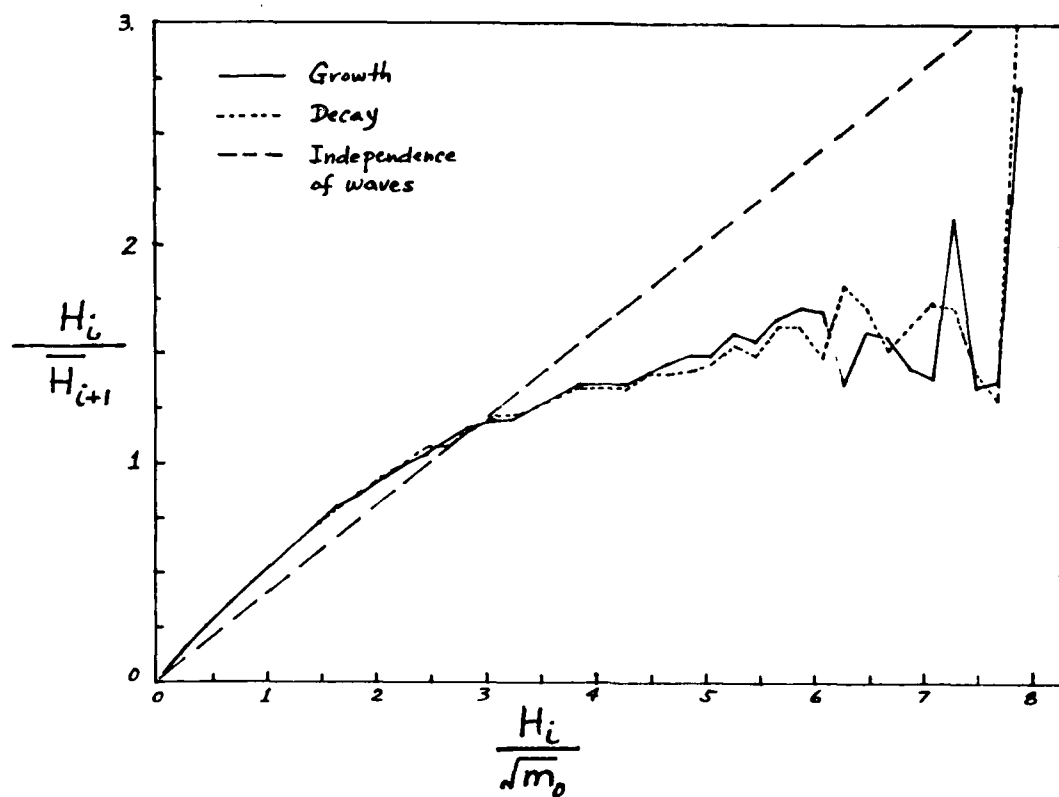


Figure 17. The ratio of  $H_i/H_{i+1}$  vs.  $H_i/\sqrt{m_0}$  for the stages of growth and decay. The dash line would be the expected curve if waves are completely independent.

## Discussion

A.T. Chwang (University of Iowa)

In one of your earlier slides you showed the evolution of envelope solitons. However, they are not arranged in descending order in amplitude. We know that a soliton with larger amplitude propagates faster than one of smaller amplitude. I presume if you measure further downstream you will find the envelope solitons will arrange in descending order in amplitude. My second question concerns the interaction of waves. I would expect that the resultant wave would have an amplitude greater than the sum of two incident waves. However, your slides indicate otherwise. Would you please explain? Perhaps the result depends on the oblique angle of the two incident waves.

B. Johnson (U.S. Naval Academy)

Would you expect the same results if the wavemaker generated a perfect Stokes wave with no harmonic distortion introduced by the wavemaker? In other words, is it possible to separate the observed instabilities into those caused by the imperfect motion of the mechanical wavemaker and those predicted by Benjamin and Feir?

How time and wind dependent are your outdoor results? Do the observed phenomena appear the same so long as the wind speed is below a certain value? Do you use a wind-speed criterion above which experiments are not undertaken? This information would be useful to other outdoor seakeeping and maneuvering basins.

O. Sarda (University of Iowa)

Would Dr. Su tell us briefly about the measurement system and if the data set was obtained in analog form only (as is seen from the figures) or in digital form, a form convenient for storage and analysis, also.

M.P. Tulin (Hydronautics, Inc.)

My comment supplements the remark that wave steepness is not limited by the occurrence of the Stokes limiting wave but by instabilities beginning earlier. Duncan and I have found the same to be true in the case of waves produced by a moving hydrofoil, where breaking usually begins on the first wave to the rear at a maximum wave slope of  $17-18^\circ$  (rather than  $30^\circ$ ) and seems to be associated with two-dimensional instabilities of the type calculated by Longuet-Higgins.

## Author's Reply

M.-Y. Su (NORDA)

To A.T. Chwang

Your statement of descending order in amplitude of envelope solitons evolving from a wave packet is correct. The example I show in the presentation is still in the process of evolution, in which the middle envelope soliton has not reached its final stage yet. In our experiments, which are not presented here, there are cases that demonstrated exactly what you described.

Your second question is believed to refer to Figure 14 in which the amplitude amplification versus wave steepness is shown. The increase versus wave amplitude here is due to nonlinear instability of the Benjamin-Feir type but not superposition of two wave trains. As such, the amplitude amplification factor can be smaller than 2.

To B. Johnson

We have purposely used two quite different types of plunger shapes for studying the instability problems of both two-dimensional and three-dimensional phenomena. No basic difference has been found. As such, we could state that these phenomena are independent of the specific characteristics of the wavemaker.

Since our large basin is outdoors we need to wait for calm weather to conduct experiments. In our locality, we can often expect such conditions to prevail during the early morning and late afternoon. Normally, wind speed is less than 1 m/sec for our experiments. The phenomena with which we are concerned here are mainly due to subharmonic perturbation and/or bifurcations, which are not affected by the small wind waves at the superharmonic scales.

To O. Sarda

The wave data (i.e., surface elevation) are measured by up to 20 capacitance wave gauges simultaneously. The data are digitized on-line at a normal rate of 40 samples per second and recorded on magnetic tapes. To produce the time series of wave evolution as shown in the presentation, these digital data are converted back to analog form and plotted. Other wave characteristics are all processed digitally.

To M. Tulin

The breaking waves investigated by Longuet-Higgins and Coblet is two dimensional in nature, while the breaking waves in our experiments presented here are due to a new kind of three-dimensional instability.

# Binnie Waves

by

Chia-Shun Yih

The University of Michigan

## Abstract

Surface waves created by water flowing in an open channel with vertical side-walls and variable width are considered and analytical solutions given. It is shown that there are infinitely many Froude numbers, depending on the wavenumber of the channel-width variation and on the transverse wavenumber, at which the amplitude of one of the wave components becomes infinite. These critical Froude numbers are interpreted physically. The waves created generally have a diamond pattern.

The case of channels of variable depth as well as variable width is then investigated and the solutions given. Finally, internal waves are treated briefly and some results presented.



AD-A158 928

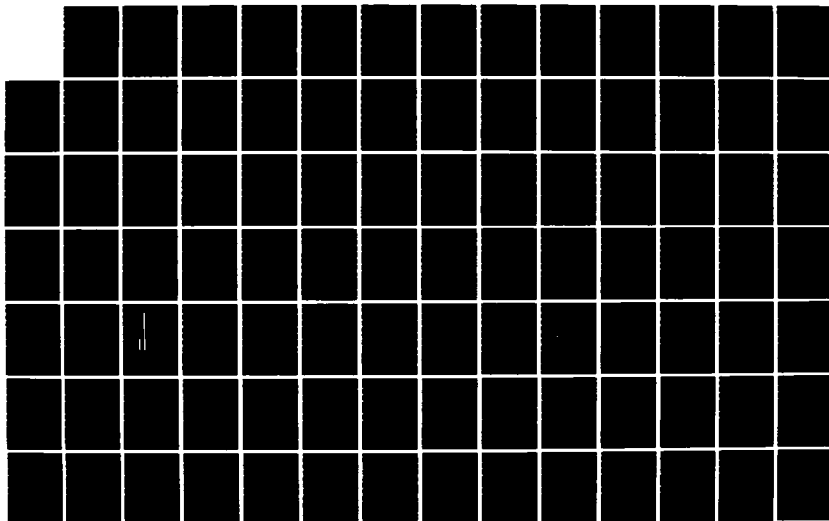
SYMPOSIUM OF NAVAL HYDRODYNAMICS (14TH) HELD AT ANN  
ARBOR MICHIGAN ON AUGUST 23-27 1982(U) OFFICE OF NAVAL  
RESEARCH ARLINGTON VA M P TULIN ET AL 1982

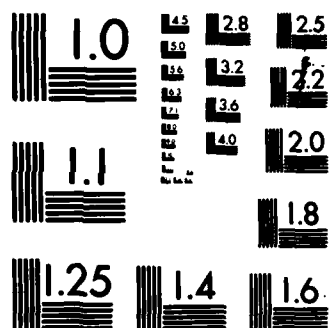
2/13

UNCLASSIFIED

F/G 28/4

NL





MICROCOPY RESOLUTION TEST CHART  
NATIONAL BUREAU OF STANDARDS-1963-A

## I. INTRODUCTION

More than two decades ago Binnie (1960) observed self-induced surface waves in a channel with vertical corrugated side-walls. The longitudinal wavelengths of these waves were observed to be an integral multiple of the basic wavelength of the wall corrugation, and there were transverse wavenumbers as well, so that the waves observed have a diamond pattern in general. I believe that although there are papers in the literature dealing with corrugated walls Binnie's paper is the only one that deals with dispersive waves, which are much more interesting and richer in substance than the nondispersive sound waves.

In his brief analysis Binnie treated the side-walls as straight. In doing so he necessarily did not reveal the mechanism by which his waves are created and the amplitudes of the many wave components, each with a different transverse wavenumber, are determined. His corrugated walls serve merely to provide the basic longitudinal wavelength.

In this paper Binnie's waves will be given a more complete analysis and the analytical solutions presented. The waviness of the side-walls will be taken fully into account. It is found that resonance occurs at an infinite number of critical Froude numbers (or internal Froude numbers for the case of internal waves), at which the amplitude of one of the wave components becomes infinite. The critical Froude numbers are given a physical interpretation which illuminates their significance. For a given Froude number, there is in general one wave component with the maximum amplitude, and this component must be what Binnie observed. The analysis given here is capable of predicting which component will be dominant at a given Froude number.

The case of variable depth (as well as variable width) will then be considered, and similar analytical results given. Finally, internal waves in a channel with vertical side-walls and variable width will be briefly treated, and the results for the special case of two fluid layers of equal depth presented.

## II. FORMULATION OF THE PROBLEM

The theory will be constructed on the assumption of irrotational flow. Let  $x$ ,  $y$ , and  $z$  denote Cartesian coordinates measured in units of  $L$ , which is the half-width of the channel at some section, and let  $U$  be the mean velocity in the  $x$ -direction. Then the velocity components  $u$ ,  $v$ , and  $w$ , for the directions of increasing  $x$ ,  $y$ , and  $z$ , respectively, will be measured in units of  $U$  and the velocity potential  $\phi$  will be measured in units of  $UL$ . We shall then treat the Cartesian coordinates, the velocity components, and  $\phi$  as dimensionless.

We have

$$(u, v, w) = (\phi_x, \phi_y, \phi_z), \quad (1)$$

where the subscripts denote partial differentiation. Since the fluid is assumed incompressible,  $\phi$  satisfies the Laplace equation

$$\phi_{xx} + \phi_{yy} + \phi_{zz} = 0. \quad (2)$$

Let the displacement of the free surface above its mean position (or the plane of the free surface if there were no flow) be denoted by  $\zeta$ , measured in units of  $L$ . Then the kinematic condition of the free surface is

$$u\zeta_x + v\zeta_y = w, \quad (3)$$

and the Bernoulli equation written for the free surface is

$$u^2 + v^2 + w^2 + 2F^{-2}\zeta = \text{constant}, \quad F^2 = U^2/gL. \quad (4)$$

Combining (3) and (4), and using (1), we have the free-surface condition

$$(\phi_x \frac{\partial}{\partial x} + \phi_y \frac{\partial}{\partial y})(\phi_x^2 + \phi_y^2 + \phi_z^2) + 2F^{-2}\phi_z = 0. \quad (5)$$

If the dimensional mean water depth is  $h$ , and

$$d = \frac{h}{L}, \quad (6)$$

then the condition at the bottom is

$$\phi_z = 0 \quad \text{at} \quad z = -d \quad (7)$$

The condition at the side-walls is

$$\phi_n = 0 \quad (8)$$

where  $n$  is measured in a direction normal to the side-walls. Equation (2), (5), (7), and (8) govern the fluid motion in the channel.

### III. A TRANSFORMATION FOR THE CHANNEL SHAPE

So far we have not accounted for the variation of the channel width. This variation is represented by the transformation

$$x + iy = \alpha + i\beta + a \sin k(\alpha + i\beta)$$

or

$$\begin{aligned} x &= \alpha + a \sin k\alpha \cosh k\beta, \\ y &= \beta + a \cos k\alpha \sinh k\beta, \end{aligned} \quad (9)$$

where  $k$  is the wavenumber of the channel-width variation, and  $a$  its amplitude. The Jacobin of the transformation is

$$J = \frac{\partial(x,y)}{\partial(\alpha,\beta)} = 1 + 2ak \cos k\alpha \cosh k\beta + a^2 k^2 (\cos^2 k\alpha + \sinh^2 k\beta). \quad (10)$$

The boundary of the channel is given by  $\beta = \pm 1$ .

In terms of  $\alpha$ ,  $\beta$ , and  $z$ , (2) and (5) become

$$\frac{1}{J}(\phi_{\alpha\alpha} + \phi_{\beta\beta}) + \phi_{zz} = 0, \quad (11)$$

and

$$\frac{1}{J}(\phi_{\alpha} \frac{\partial}{\partial \alpha} + \phi_{\beta} \frac{\partial}{\partial \beta}) [\frac{1}{J}(\phi_{\alpha}^2 + \phi_{\beta}^2) + \phi_z^2] + 2F^{-2} \phi_z = 0 \quad (12)$$

The condition (7) remains the same, but (8) is now replaced by

$$\phi_{\beta} = 0 \text{ at } \beta = \pm 1. \quad (13)$$

The governing system now consists of (11), (12), (13), and (7).

## VI. SOLUTION OF THE PROBLEM

It is evident that the amplitude of the waves produced by the channel-width variation is proportional to the amplitude of that variation. Hence we assume

$$\phi = \phi_0 + a\phi_1 + a^2\phi_2 + \dots \quad (14)$$

Since in the absence of any width variation the flow is just a uniform flow in the  $x$  or  $\alpha$  direction, it is evident that

$$\phi_0 = \alpha. \quad (15)$$

Substituting (14) and (15) into (11) and (12), and sorting out the terms of first order in  $a$  (Remember that  $J$  contains  $a$ ,  $\alpha$ , and  $\beta$ .), we have

$$\phi_{1\alpha\alpha} + \phi_{1\beta\beta} + \phi_{1zz} = 0 \quad (16)$$

$$\phi_{1\alpha\alpha} + F^{-2}\phi_{1z} = -k^2 \sin k\alpha \cosh k\beta. \quad (17)$$

The solution satisfying (16), (7), and (13) is, since  $\cosh k\beta$  is even in  $\beta$ ,

$$\phi_1 = \sum_{n=0}^{\infty} B_n \sin k\alpha \cos n\pi\beta \cosh \gamma_n(z+d), \quad (18)$$

where

$$\gamma_n = (k^2 + n^2\pi^2)^{1/2} \quad (19)$$

and  $B_n$  is determined by (17). The result is

$$B_n C_n = -k^2 \int_{-1}^1 \cos n\pi\beta \cosh k\beta \, d\beta = \frac{2(-1)^{n+1} k^3 \sinh k}{\gamma_n^2}, \quad (20)$$

where

$$C_n = -k^2 \cosh \gamma_n d + F^{-2} \gamma_n \sinh \gamma_n d. \quad (21)$$

To the order  $a$ , then,  $\zeta$  is determined from (4) to be

$$\zeta = -ak^{-1} \cos k\alpha \sum_{n=0}^{\infty} B_n \gamma_n \sinh \gamma_n d \cos n\pi\beta \quad (22)$$

which gives a diamond pattern for the free-surface displacement. In obtaining (22), we have made use of the result

$$\phi_x^2 + \phi_y^2 = \frac{1}{J}(\phi_\alpha^2 + \phi_\beta^2),$$

as well as (20), which gives the Fourier coefficients for  $\cosh k\beta$ . The free-surface displacement is shown in Figure 1 for one half wave-length of the channel-width variation.

Note that as  $C_n \rightarrow 0$ ,  $B_n \rightarrow \infty$ . The infinite number of values of  $F$  given by  $C_n = 0$  then are critical values, at which resonance occurs. For  $C_n = 0$ ,

$$F^2 = \frac{\gamma_n^2 \tanh \gamma_n d}{k^2 \gamma_n},$$

or

$$\frac{k}{\gamma_n} U = \left( \frac{g h \tanh \gamma_n d}{\gamma_n d} \right)^{1/2}. \quad (23)$$

In (23),  $k/\gamma_n$  is the cosine of the angle between the  $\alpha$ -direction and the direction normal to the wave fronts of the slanted waves with wavenumber  $\gamma_n d$  (which is the wavenumber non-dimensionalized with the length  $h$  instead of the length  $L$ ), and the right-hand side is precisely the wave speed of these waves. Thus, the  $n$ -th critical value of  $U$  is such that its component normal to the fronts of the waves with wave-

number  $\gamma_{nd}$  is equal to their wave speed. When  $U$  has such a value, the amplitude of the  $\gamma_n$ -waves (with wavenumber  $\gamma_n$  or  $\gamma_{nd}$ , depending on the length scale used to non-dimensionalize the wavenumber) becomes infinite, and resonance occurs. This is reminiscent of the resonance that occurs when a layer of water flows over a wavy bottom with a speed equal to the speed of waves with the same wavenumber as the bottom. But now there are infinitely many critical values of  $U$ , and slanted waves are involved, so that the resonance is somewhat more subtle.

Higher approximations can be carried out systematically. For the sake of brevity we shall refrain from doing so, but shall mention that at the second approximation two new longitudinal wavenumbers will be produced: zero and  $2k$ . The former give no finite critical values for  $U$ , whereas the latter does -- in much the same way that the basic longitudinal wavenumber  $k$  gives rise to such critical values, as shown in the foregoing. At the third approximation the new wavenumber  $3k$  is brought forth, which gives rise to another set of critical values for  $U$ . Thus there are infinitely many sequences of critical values of  $U$ , each sequence consisting of an infinite number of such critical values.

## V. CHANNELS WITH VARIABLE WIDTH AND DEPTH

Since natural streams have variable depth, often with a maximum depth much smaller than their width, we shall use the shallow-water theory to deal with the case of variable depth. We shall retain the meanings of the symbols used so far, but  $d$  now is given by

$$d = 1 - \beta^2. \quad (24)$$

The total (dimensionless) depth is

$$D = d + \zeta, \quad (25)$$

and the equation of continuity is

$$\frac{\partial}{\partial x} (D\phi_x) + \frac{\partial}{\partial y} (D\phi_y) = 0, \quad (26)$$

and the Bernoulli equation for the free surface is

$$\phi_x^2 + \phi_y^2 + 2F^{-2}\zeta = \text{constant}, \quad (27)$$



where  $\phi_z^2$  is neglected, in consistency with the shallow-water theory. Converting (26) and (27) to the  $\alpha$ - $\beta$  coordinates, we have

$$(d\phi_\beta)_\beta + d\phi_{\alpha\alpha} + \phi_\alpha \zeta_\alpha = 0, \quad (28)$$

and

$$\frac{1}{J}(\phi_\alpha^2 + \phi_\beta^2) + 2F^{-2}\zeta = \text{constant}, \quad (29)$$

where  $J$  is given by (10).

Using (10), (14), (15), and (29), we have

$$\zeta_\alpha = -aF^2\phi_{1\alpha\alpha} - aF^2k^2 \sin k\alpha \cosh k\beta + O(a^2). \quad (30)$$

Substituting (14), (15), (24), and (30) into (28), extracting terms of order  $a$ , and writing

$$\phi_1 = \sin k\alpha f(\beta), \quad (31)$$

we obtain

$$[(1 - \beta^2)f']' + [k^2F^2 - k^2(1 - \beta^2)]f = F^2k^2 \cosh k\beta, \quad (32)$$

where the primes indicate differentiation with respect to  $\beta$ . Equation (32) is singular at  $\beta = \pm 1$ . What is needed is a nonsingular solution of (32). This solution can always be found, but if  $k^2$  is not small compared with 1 much computation is needed. Fortunately for most natural streams  $k^2$  is small, permitting a simple calculation.

Consider the equation

$$[(1 - \beta^2)G']' + [\lambda - k^2(1 - \beta^2)]G = 0, \quad (33)$$

and seek nonsingular solutions of this equation. Let

$$\lambda = \mu_0 + k^2\mu_1 + k^4\mu_2 + \dots, \quad (34)$$

$$G = g_0 + k^2 g_1 + k^4 g_2 + \dots \quad (35)$$

Substituting (34) and (35) into (33), and collecting terms not containing  $k$ , we obtain the Legendre equation for  $g_0$ . For a nonsingular solution, then,

$$\mu_0 = n(n+1), \quad g_0 = P_n(\beta), \quad (36)$$

where  $P_n(\beta)$  is the  $n$ -th Legendre polynomial in  $\beta$ . Collecting terms of order  $k^2$ , we obtain

$$Lg_1 \equiv [(1 - \beta^2)g_1']' + n(n+1)g_1 = (1 - \beta^2)g_0 - \mu_1 g_0. \quad (37)$$

First, the requirement that  $g_1$  be nonsingular demands that the right-hand side of (37) be orthogonal to  $g_0$ . (To prove this statement, one needs only to multiply (37) by  $g_0$  and integrate, by parts if necessary, between  $-1$  and  $1$ .) This determines  $\mu_1$  and  $g_1$  in principle. In practice it is easier to use the formulas on page 115 of Jahnke and Emde (1945), for instance, and obtain

$$L \left\{ \frac{1}{6+4n} (\beta^2 P_n - \frac{2n}{2n-1} \beta P_{n-1}) \right\} = -\beta^2 P_n + \frac{2n^2+2n-1}{(2n+3)(2n-1)} P_n,$$

so that

$$g_1 = \frac{1}{6+4n} (\beta^2 P_n - \frac{2n}{2n-1} \beta P_{n-1}), \quad (38)$$

$$\mu_1 = 1 - \frac{2n^2+2n-1}{(2n+3)(2n-1)}. \quad (39)$$

For a given  $n$ , we shall denote the corresponding  $\lambda$  and  $G$  by  $\lambda_n$  and  $G_n$ , respectively. Since the right-hand side of (32) is even, we have  $n = 2m$ , where  $m$  is an integer, including zero, and

$$f(\beta) = \sum_{m=0}^{\infty} B_{2m} G_{2m}. \quad (40)$$

Substituting this into (32), and using the orthogonality of the eigenfunctions  $G_{2m}$ , we obtain

$$B_{2m} (k^2 F^2 - \lambda_{2m}) \int_{-1}^1 G_{2m}^2 d\beta = F^2 k^2 \int_{-1}^1 \cosh k\beta G_{2m} d\beta, \quad (41)$$

which determine  $B_{2m}$ . Then (40), (31), and

$$\phi = \alpha + a\phi_1$$

give the solution up to  $O(a)$ . We note that stopping at terms of  $O(k^2)$  involves an error of  $O(k^4)$ , which for  $k = 1/4$  is negligible, and for  $k = 1/2$  is of the order of 0.06.

Let the two integrals in (41) be denoted by  $I_1$  and  $I_2$  ( $I_1$  for the left-hand side), we obtain the following table, for  $n$  up to 4.

TABLE 1. Values of Integrals

k	n	0	2	4
1/4	$I_1$	2.014	0.399	0.222
	$I_2$	2.028	0.006	0.000
1/2	$I_1$	2.056	0.395	0.222
	$I_2$	2.114	0.022	0.000

For  $k^2 F^2 = \lambda_{2m}$ ,  $m = 0, 1, 2, \dots$ , there is again resonance. The physical interpretation for these critical values is analogous to that for the case of vertical side-walls, but the arguments lose some sharpness due to the fact that the Legendre polynomials cannot be easily combined with  $\sin k\alpha$  or  $\cos k\alpha$  to form a sine or cosine function which is easily seen to represent waves.

## VI. INTERNAL WAVES

Since it is easier to create internal waves of large amplitudes, internal waves created in channels of variable width by flowing water will be briefly discussed. The solution for internal waves so created

can be obtained by the same approach as described in Sections 2-4. The results for the case of two layers of fluid of the same depth  $h$  and with density  $\rho'$  for the upper layer and density  $\rho$  for the lower layer will be given here, because they are obtainable from (18) - (22) upon simple modifications of coefficients. If in the  $C_n$  the  $F^{-2}$  is replaced

by  $F_i^{-2} = \frac{\rho - \rho'}{\rho + \rho'} F^{-2}$ , and then the  $B_n$  determined by (20) is multiplied by

$\frac{\rho - \rho'}{\rho + \rho'}$ , (18) and (22) will give the solutions for  $\phi$  (of the lower layer)

and  $\zeta$ . As for  $\phi'$ , the velocity potential for the upper layer, it is

$$\phi' = - \sum_{n=0}^{\infty} B_n \sin k\alpha \cos n\pi\beta \cosh \gamma_n (z - d), \quad (42)$$

where  $B_n$  is the modified  $B_n$  obtained by the process mentioned in the fore-going.

Finally, we note that the theory is not merely for supercritical flows, and that when  $k$  is large waves of large amplitude can occur even at subcritical speeds. The figure given in this paper is for supercritical speeds, for the  $F$  would be larger than 1 if it were based on the mean depth, and the pattern agree qualitatively with that obtained from the classical shallow-water theory at supercritical speed and for vertical side walls. But this should not obscure the fact that the present theory is for all Froude numbers, however large or small.

We note also that Binnie (1960) observed time-periodic oscillations in his waves. These are freely propagating waves with longitudinal wavelengths which are integral multiples of the wave length of the corrugation and transverse wave numbers (denoted by  $n$  here). They are not bound to the corrugations studied in this paper, and their production is presumably due to some mechanism of instability not discussed here.

#### ACKNOWLEDGMENT

This work has been supported by the Office of Naval Research. Marc Ingber assisted the author by producing the figures in the table.

#### REFERENCES

1. Binnie, A.M. (1960). Self-induced waves in a conduit with corrugated walls. I. Experiments with water in an open horizontal channel with vertically corrugated sides. *Proc. Roy. Soc. A*, 259, 18-27.
2. Jahnke, E. and F. Emde, Table of Functions, Dover, New York, 1945.

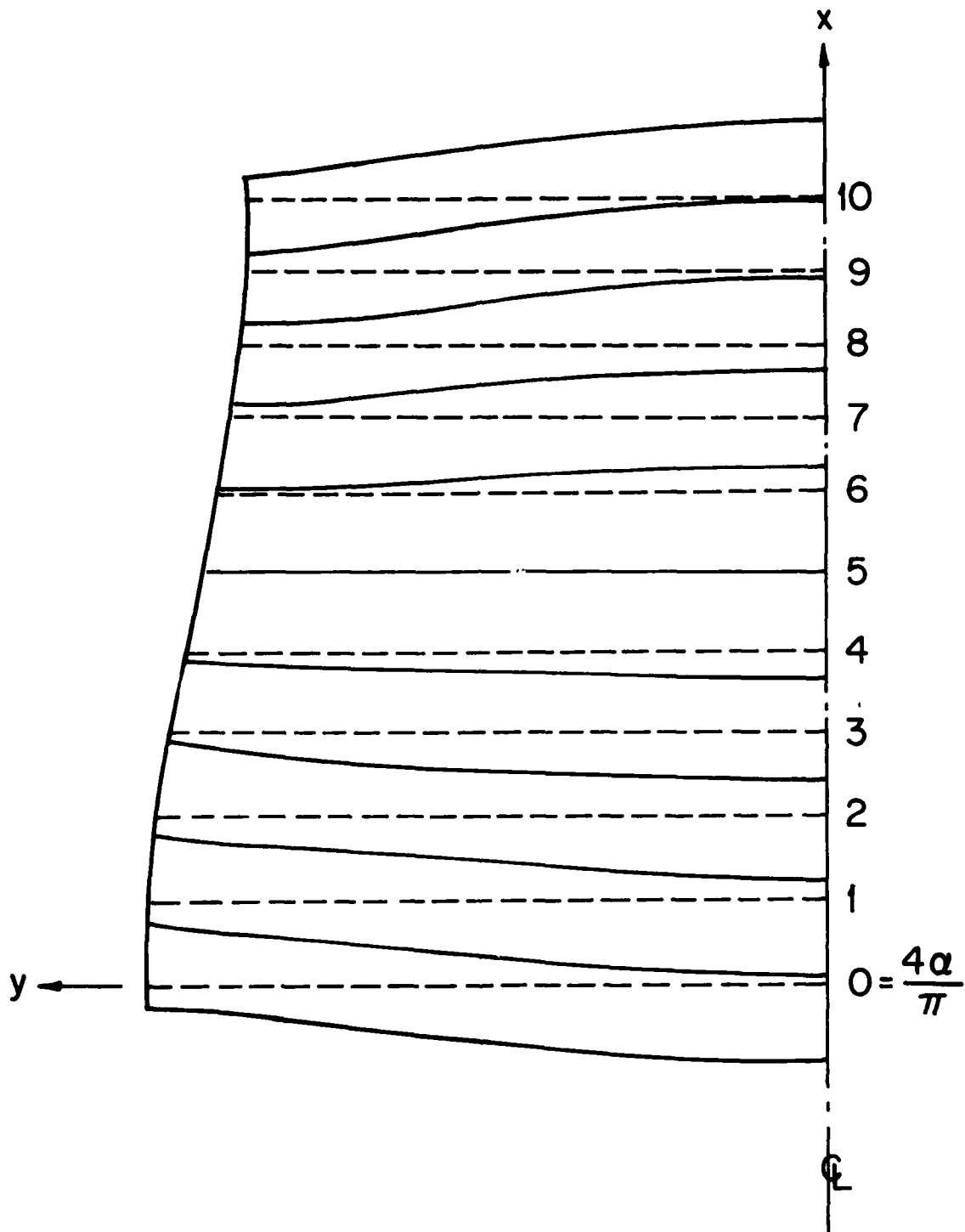


Figure 1. Graphs showing the free surface, at  $F = 2$ ,  $k = 0.4$ ,  $d = 0.2$ . The maximum dimensionless  $\zeta/a$  is 0.242, at  $k\alpha = \pi$  (or  $4\alpha/\pi = 10$ ) and  $\beta = 0$ . On  $k\alpha = 0.5\pi$ ,  $\zeta = 0$ . The dimensionless  $\zeta/a$  is plotted above or below the dotted lines. The figure can be reflected across the planes  $\alpha = 0$  and  $\beta = 0$  sequentially to produce the free surface for a whole wavelength and for the whole channel.

## Discussion

A.T. Chwang (University of Iowa)

Regarding the question of resonance, I would imagine that for a simply divergent or convergent channel with straight side walls, there would be a continuous spectrum of resonant frequencies. Would you please comment on it and tell me if I am wrong.

L.J. Doctors (University of New South Wales)

Professor Yih takes into account the effect of the wavy channel walls by means of the transformation given by Equation (9).

Since the amplitude of the waviness in the wall is considered to be small, it would also seem possible to represent this effect by means of a source distribution on the walls. To first order, this source distribution would be constant with respect to depth below the free surface but vary along the channel.

Could Professor Yih comment on this approach and compare it with his own? It should be added that an infinite set of image source distributions would be required--as is usual with tank problems.

E. Palm (University of Oslo)

Since the driving mechanism for the waves is revealed mathematically in the form of a forcing term in the free-surface boundary conditions, should not these waves formally be closely related to waves due to pressure applied on the free surface?

## Author's Reply

C.-S. Yih (University of Michigan)

To T. Chwang

For a divergent or convergent channel one can use a different conformal mapping from Equation (9) in my paper, and then the solution would involve Fourier integrals with a continuous spectrum in  $k$ , with the Fourier coefficients to be determined. The very interesting thing is that the value of  $k$  that, if discrete, would cause resonance, will now give the lee-wave (which, in general, has diamond patterns) components after the contraction or expansion.

To L.J. Doctors

Professor Doctors is right in saying that the effect of the wavy wall can be represented by sources and sinks. The strengths of these sources and sinks are independent of depth to the zeroth order, i.e., if the effect of surface waves is ignored, but will vary with depth already in a first-order calculation. For large composite wave number  $\gamma_n$ , this variation is confined to a thin layer near the free surface. For  $n = 0$  and  $k$  (the longitudinal wave number) very small, the variation will be weak.

If the variation of the channel width is periodic but otherwise arbitrary, one can use a Fourier series in my approach, and if it is not periodic, under certain restrictions a Fourier integral can be used. I prefer this approach to using sources and sinks, because it is simpler and more elegant, if I may say so. While the method of sources and sinks can always be applied, it is cumbersome. Among other things, one has to calculate for and trace out the boundary shape from the source-sink distribution, which is a nuisance.

To E. Palm

Professor Palm rightly perceives the analogy of the driving mechanism given in my paper with a pressure distribution applied at the free surface of water flowing in a straight channel. Indeed, Equation (17) indicates this analogy, with the right-hand side, which arises in a roundabout way from the variation in channel width, standing for the fictitious pressure distribution.

# Three-Dimensional Nonlinear Long Waves Due to Moving Surface Pressure

De-Ming Wu\* and Theodore Y. Wu  
California Institute of Technology  
Pasadena, California 91125

This is a continuing study of long waves generated in shallow water by a moving surface pressure disturbance; the method takes both the nonlinear and dispersive effects into account for the subcritical, transcritical and supercritical regimes. The long wave model adopted here is the one recently developed by Wu (1979, 1981), which is of the Boussinesq class but generalized to allow two horizontal dimensions of wave propagation in water of both temporally and spatially varying depth. A finite-difference numerical method has been developed to solve this general class of unsteady, three-dimensional, nonlinear long wave problems. A simple approximate open-boundary condition has been found to work effectively and successfully as a 'radiation condition' in suppressing nonphysical wave reflections from the open boundary into the domain of interest. A series of numerical examples will be presented to illustrate the theoretical predictions. They include a particular test case of a steady two-dimensional disturbance for which an exact solution is readily available for comparison. The Froude number  $F_h = U / \sqrt{gh}$  (based on the moving pressure velocity  $U$  and water depth  $h$ ) chosen for the computation ranges from 0.4 through 1.4, which typically covers the transcritical regime. Some salient new features of the wave profile and wave resistance can be attributed to nonlinear and dispersive effects.

A new feature of particular interest is that after a free-surface pressure disturbance is kept moving at a transcritical speed for a sufficiently long time, a solitary wave will emerge just ahead of the disturbance, and finally surges away from the disturbance to propagate ahead as a free solitary wave. The process seems to continue almost periodically. The central problem considered here may have applications to air-cushion vehicle, ship motion in shallow water, and possibly also to problems of meteorological interest.

\*On academic leave from the Harbin Shipbuilding Engineering Institute, Harbin, China.



## I. INTRODUCTION

In 1834 John Scott Russell (1838, 1845) was the first to observe the 'singular and beautiful phenomenon' that a 'wave of a large solitary elevation' formed, surged ahead free from a boat, when the boat drawn by a pair of horses suddenly stopped. Thereafter the wave continued its own course along a channel without change of form and speed. This keen observation of Russell and his subsequent pioneering experimental studies stimulated much strong interest as shown notably by Boussinesq (1871, 1877), Rayleigh (1876), and Korteweg & de Vries (1895). These early contributions of great significance opened an important chapter of hydrodynamics. In the past two decades, a renewed interest in long waves has been intense, and can be traced back to the discovery of Zabusky & Kruskal (1965) indicating that solitary waves invariably emerge in the asymptotic solution of the Korteweg-de Vries equation. The literature has been numerous and rich, and we refer the interested reader to recent reviews, e. g. by Miles (1980), Yuen & Lake (1982) where earlier reviews can also be found.

In naval architecture and ocean engineering, it has long been known under the name of shallow-water effect and restricted-water effect (with side wall constraints) that flow configurations and trim of ships moving in a shallow and restricted water present a striking contrast to those of ships sailing in open deep sea (see e. g., Kinoshita 1954; Inui 1954; Graff, Kraft & Weinblum 1964; Kirsch 1966; Graff & Binek 1969; and review by Wu 1972). The flow field of a ship sailing in shallow water undergoes drastic changes of finite amplitude from a wave type to an entirely different type as the 'depth Froude number'  $F_h = U/\sqrt{gh}$  (based on ship speed  $U$  and water depth  $h$ ) increases from the subcritical ( $F_h < 1$ ) to supercritical regime ( $F_h > 1$ ). In the transcritical regime ( $F_h \approx 1$ ), the nonlinear effects become so predominant that a nonlinear theory is necessary to yield a valid solution, as demonstrated by Lea & Feldman (1972) who developed a method of systematic matched asymptotic expansions to evaluate the nonlinear effects on ship resistance, sinkage and trim.

It is generally believed that both the nonlinear and dispersive effects must be accounted for in a balanced manner to solve transcritical ship problems. Regarding the contention that a strong interplay of nonlinear and dispersive effects may exist in transcritical ship motion, considerable light has been shed by the recent discovery of Huang, Sibul & Wehausen (1982). In their towing tank experiment with a ship model (a Series 60, block 80 hull, though the hull shape was said to have little to do with the observed phenomenon) in very shallow water (about 0.5 ft), they found that approximately two-dimensional waves spanning across the tank were generated, one after another, to move down the tank ahead of the model. The longer the run, the more of them appear. This has led the authors to conjecture that "the motion does not approach a steady state, but that solitons will continue to be generated as long as the model keeps moving".

To facilitate our calculations of the nonlinear and dispersive effects on the generation and evolution of long waves, we take here a

new approach based on the layer-mean transport equations introduced by Wu (1979, 1981). This set of equations was derived by averaging the three-dimensional Euler equations along the vertical axis across the water layer and then expressed, through expansion for long waves, in terms of the water surface displacement and layer-mean velocity potential. They admit two possible forcing functions, one being the free-surface pressure disturbance and the other due to the vertical displacement of the floor supporting the water layer, both of which assume the form compatible with the long water waves they generate. This nonlinear dispersive long-wave model has been applied by Lepelletier (1981) for calculating harbor oscillations and by Schember (1982) to study propagation and evolution of three-dimensional tsunami-like long waves in coastal water. We undertake here a study of the generation of long waves by traveling free-surface pressure disturbances and report some preliminary results.

## II. THE NONLINEAR DISPERSIVE LONG-WAVE MODEL

The problem of our central interest is concerned with the generation and propagation of three-dimensional long gravity waves of finite amplitude that can propagate in two horizontal dimensions  $\underline{r} = (x, y)$  in a layer of water whose initial free surface, when unperturbed at time  $t = 0$ , is at  $z = 0$  and whose floor is at a prescribed depth  $z = -h(\underline{r}, t)$ . The forcing functions responsible for generating waves will include the free-surface pressure distribution  $p_0(\underline{r}, t)$  acting over the displaced water surface at  $z = \zeta(\underline{r}, t)$  and the unsteady movement of the water floor given by  $z = -h(\underline{r}, t)$ . The surface pressure may be used to represent disturbances of meteorological and naval architectural nature such as in applications to air-cushion vehicle and ships, while the floor movement can simulate tsunami-genic disturbances of the ocean floor. In our exposition, however, these forcing functions will be confined to such a type that the resulting waves will have lengths,  $\lambda$ , primarily large compared with the characteristic water depth,  $h_0$ , and will have typical amplitude,  $a$ , small relative to  $h_0$ , i. e.,

$$\alpha = a/h_0 \ll 1, \quad \epsilon = h_0/\lambda \ll 1. \quad (1)$$

(The condition of  $\epsilon \ll 1$  holds for long waves by definition.) Further, we shall concentrate our attention to the case when the magnitude of  $\alpha$  relative to  $\epsilon^2$ , known as the Ursell number, is of order unity,

$$Ur = \alpha/\epsilon^2 = a\lambda^2/h_0^3 = O(1). \quad (2)$$

The gravity waves satisfying conditions (1) and (2) will be said to belong to the "Boussinesq class". It signifies the case in which the

nonlinear effects causing the waves to steepen forward, at a rate proportional to  $\alpha$ , are comparable in importance with the opposite tendency, due to the dispersive effects by which waves of longer lengths travel at greater velocities by a margin proportional to  $\epsilon^2$ .

For the theoretical model capable of representing appropriately the long waves generated in shallow water by this general class of forcing functions we adopt the one recently developed by Wu (1979, 1981, his equations (41) and (42)):

$$\zeta_t + \nabla \cdot [(h + \zeta) \nabla \bar{\phi}] = -h_t + \nabla \cdot \left\{ \left[ \frac{h}{2} (h_t + \nabla \cdot (h \nabla \bar{\phi})) - \frac{h^2}{3} \nabla^2 \bar{\phi} \right] \nabla h \right\}, \quad (3)$$

$$(\bar{\phi})_t + \frac{1}{2} (\nabla \bar{\phi})^2 + g\zeta + \frac{1}{\rho} p_0 = \frac{h}{2} \frac{\partial}{\partial t} [h_t + \nabla \cdot (h \nabla \bar{\phi})] - \frac{h^2}{6} \nabla^2 \bar{\phi}_t. \quad (4)$$

Here,  $\nabla$  represents the two-dimensional vector operator  $\nabla \equiv \partial/\partial \underline{r} = (\partial/\partial x, \partial/\partial y)$  with respect to the position vector  $\underline{r} = (x, y)$  in the horizontal plane, and  $\bar{\phi}$  denotes the layer-mean value of the original velocity potential  $\phi(x, y, z, t) = \bar{\phi}(\underline{r}, z, t)$  as defined by

$$\bar{\phi}(\underline{r}, t) = \frac{1}{\eta} \int_{-h}^{\zeta} \phi(\underline{r}, z, t) dz, \quad (\eta = h + \zeta). \quad (5)$$

The velocity potential  $\phi$  and its layer mean  $\bar{\phi}$  are related by

$$\phi - \bar{\phi} = -(z + \frac{1}{2}h)[h_t + \nabla \cdot (h \nabla \bar{\phi})] - \frac{1}{2}(z^2 - \frac{1}{3}h^2)\nabla^2 \bar{\phi}. \quad (6)$$

From this relation one can readily deduce the velocity distribution as  $(\phi_x, \phi_y, \phi_z)$  and the pressure field from the Bernoulli equation,

$$\frac{1}{\rho} p = -gz - \phi_t - \frac{1}{2} (\phi_x^2 + \phi_y^2 + \phi_z^2). \quad (7)$$

In the sequel, the fluid density,  $\rho$ , and the gravitational constant,  $g$ , will be normalized to unity and reinstated whenever needed for clarification.

The above set of basic equations (3) and (4) may be regarded as to form a generalized Boussinesq class in view of the new feature of the medium being now inhomogeneous (due to the spatial and temporal variation of  $h$ ) and the added dimension of wave propagation.

Strictly speaking, the consistency of the expansion procedures (see Wu, 1979) employed in deriving (3) and (4) also requires that

$$|h_t|/c < O(\alpha), \quad |\nabla h| < O(1), \quad |p_o|/\rho c^2 < O(\alpha), \quad (c^2 = gh_o), \quad (8)$$

where  $c = (gh_o)^{1/2}$  represents the typical wave velocity. Under this limiting condition, the basic equations (3) and (4) are both valid with an error term of  $O(\alpha\epsilon^4, \alpha^2\epsilon^2)$ , as shown by Wu (1979).

Various long-wave models can be extracted directly from (3) and (4), as their subgroups, under special simplifying assumptions. If the nonlinear terms are dropped from (3) and (4), we have the linear dispersive long-wave model. On the other hand, if the dispersive effects (given by the terms involving third-order derivatives of  $\bar{\phi}$ ) are neglected, we have the nonlinear, nondispersive long-wave model which may be regarded as the generalized Airy wave model. Finally, when both the nonlinear and dispersive effects are neglected, we obtain the simplest case of linear, nondispersive long-wave model,

$$\zeta_t + h\nabla^2\bar{\phi} = -h_t + \nabla \cdot \left(\frac{1}{2}hh_t\nabla h\right), \quad (9)$$

$$\bar{\phi}_t + g\zeta = -\frac{1}{\rho}p_o + \frac{1}{2}hh_{tt}. \quad (10)$$

Before we proceed with detailed comparison between these models, we note that the integrals of (9) and (10) are particularly simple when the extraneous disturbances are of the form

$$p_o = p_o(x-Ut), \quad h = h_o - h_1(x-Ut) \quad (h_o = \text{const.}), \quad (11)$$

each representing a right-running wave with velocity  $U$ . From (9) and (10) it is readily found that for  $p_o$  alone,

$$\zeta = \frac{1}{U^2 - c^2} \frac{h_o}{\rho} p_o(x-Ut) \quad (c = \sqrt{gh_o}), \quad (12a)$$

and for the case of  $p_o \equiv 0$ , but with  $h_1$  given by (11),

$$\zeta = \frac{U^2}{U^2 - c^2} \{h_1(x-Ut) + \frac{1}{2} h_0^2 h_1''(x-Ut)\} , \quad (12b)$$

where the primes denote differentiations with respect to the argument. The above solutions are classical (aside from the term with  $h''$  in (12b) which arises from the present refinement, see Lamb, 1932, Art. 177); they indicate that  $\zeta$  is similar in form to the traveling disturbances and is in the same phase with the disturbance, or the opposite, according as  $U > c$  or  $U < c$ , except for the critical speed ( $U = c$ ) at which  $\zeta$  becomes undefined. They further imply zero wave resistance since no waves are radiated from the traveling disturbances. We shall see that these drastic departures of the solution from our physical experience are stemmed from the oversimplifications of the last model, especially for the subcritical and transcritical speeds.

### III. THE BASIC NUMERICAL METHOD

In view of the basic form of (3) and (4) being the simple wave equation (to the leading order in the absence of extraneous disturbances), the numerical techniques developed here for computation of solutions to equations (3) and (4) are further extensions of those typically used to yield implicit solutions to the wave equations as represented in finite-difference form. Implicit methods are chosen to allow for larger time steps and to reduce the growth of spurious numerical errors of large wave numbers. In general, our computation of  $\zeta$  and  $\bar{\phi}$  for various problems governed by the basic equations (3) and (4) will be handled as an initial-boundary value problem in order to avoid the difficulty due to the lack of an exact or accurate 'radiation condition' for evaluating the data at an open boundary.

We describe first the numerical method we have developed for the computation of two-dimensional nonlinear dispersive waves (in the  $(x, z)$  plane) over a sufficiently large region  $\mathcal{R}$  fixed in the absolute frame of reference (fixed with respect to the undisturbed fluid). The fluid medium is assumed to be unbounded in both directions of the  $x$ -axis. For a prescribed pressure disturbance  $p_0(x, t)$ , assumed to be finite in extent,  $\bar{\phi}$  and  $\zeta$  assume the initial values  $\bar{\phi} \equiv 0$ ,  $\zeta = -p_0$  and  $\zeta \equiv 0$  outside the distribution of  $p_0$ , as in the state of static equilibrium. For  $t > 0$ , the pressure disturbance progresses along the free surface with a given velocity. The basic equation (3) and (4) are then solved with suitable boundary conditions (to be discussed below) by a time advancing and finite-differencing scheme. In advancing  $\zeta$  and  $\bar{\phi}$  in time steps, we apply the modified Euler method following a two-step predictor-corrector procedure, with iteration, while the spatial derivatives are approximated by central differences. For all the interior nodes (the boundaries are exceptions as will be discussed later), nodal values of  $\zeta_i^n$  and  $\bar{\phi}_i^n$  (with the usual notation:

$\zeta_i^n = \zeta(i\Delta x, n\Delta t)$  at time step  $t = n\Delta t$  are first used to determine a set of provisional values  $\zeta_i^{n+1}$  and  $\phi_i^{n+1}$  according to the formula

$$\zeta_i^{n+1} = \zeta_i^n - \Delta t Z_i^n, \quad (13a)$$

$$Z_i^n = \frac{1}{4\Delta x^2} (\zeta_{i+1}^n - \zeta_{i-1}^n)(\bar{\phi}_{i+1}^n - \bar{\phi}_{i-1}^n) + \frac{1}{\Delta x^2} (1 + \zeta_i^n)(\bar{\phi}_{i+1}^n - 2\bar{\phi}_i^n + \bar{\phi}_{i-1}^n), \quad (13b)$$

$$\begin{aligned} \bar{\phi}_i^{n+1} = \bar{\phi}_i^n + (1 + \frac{2\epsilon^2}{3\Delta x^2})^{-1} \{ \frac{\epsilon^2}{3\Delta x^2} (\bar{\phi}_{i+1}^{n+1} + \bar{\phi}_{i-1}^{n+1} - \bar{\phi}_{i+1}^n - \bar{\phi}_{i-1}^n) \\ - \Delta t [F_i^n + p_{oi}^n] \}, \end{aligned} \quad (14a)$$

$$F_i^n = \frac{1}{8\Delta x^2} (\bar{\phi}_{i+1}^n - \bar{\phi}_{i-1}^n)^2 + \zeta_i^n, \quad (14b)$$

where  $\epsilon = h/L$ ,  $L$  being the extent of the  $p_o$  distribution. We note that (14) is an implicit scheme, involving an iteration procedure. These provisional values are then used to evaluate a set of corrected values  $\zeta_i^{n+1}$  and  $\bar{\phi}_i^{n+1}$  at  $t = (n+1)\Delta t$  from the formula

$$\zeta_i^{n+1} = \zeta_i^n - \frac{\Delta t}{2} \{ Z_i^{n+1} + Z_i^n \}, \quad (15)$$

$$\begin{aligned} \bar{\phi}_i^{n+1} = \bar{\phi}_i^n + (1 + \frac{2\epsilon^2}{3\Delta x^2})^{-1} \{ \frac{\epsilon^2}{3\Delta x^2} (\bar{\phi}_{i+1}^{n+1} + \bar{\phi}_{i-1}^{n+1} - \bar{\phi}_{i+1}^n - \bar{\phi}_{i-1}^n) \\ - \frac{\Delta t}{2} [F_i^{n+1} + F_i^n + p_{oi}^{n+1} + p_{oi}^n] \}. \end{aligned} \quad (16)$$

Similar to (14), (16) is an implicit scheme with iteration. The above formulas, (13)-(16), hold only for the case of uniform depth ( $h = \text{const.}$ ), but can be readily modified to be applicable to the general case.

In regard to the condition that should be required for the open boundary nodes, we could avoid the issue, at least in an initial stage, by taking a sufficiently large computation region  $\mathcal{R}$  such that  $\bar{\phi}$  and  $\zeta$  outside  $\mathcal{R}$  can be considered insignificant. However, the need of an adequate open-boundary condition (also called the 'radiation

condition' by some authors) will sooner or later arise, especially when  $\mathcal{R}$  is to be kept as small as desired. A proper open-boundary condition must satisfy the following prerequisites. First, it must be sufficiently transparent, i. e., nonobstructing to allow all the physical phenomena generated in the region  $\mathcal{R}$  to pass through the open boundary without suffering appreciable numerical (nonphysical) reflections at the boundary back into  $\mathcal{R}$ . Second, when numerical errors attributable to an imperfect open-boundary condition cannot be further reduced to a desired limit, they must not affect the stability and convergence of the entire computational scheme, or contaminate the interior data beyond an acceptable level. For nonlinear water wave problems it is especially challenging because of the presence of other possible solutions, admissible to the Laplace equation for  $\phi$ , that propagate with infinite velocity. Various approximate open-boundary conditions have been proposed for different types of problems (see, e. g., Orlanski 1976, its modified scheme used by Chan 1977 and Yen et al. 1977; Bai 1977; also see the review by Yeung 1982). There is however no absolutely satisfactory answer to this difficult problem and research efforts still continue.

In order to assess the various existing open-boundary conditions together with a few new ones that were examined during this work, we have applied them to two test cases, in both of which the exact solution of the corresponding steady state was obtained (one of them will be presented in the next section) for comparison with the large time asymptotic limit of the numerical solutions reached by using the different boundary conditions. Based on the result of this extensive search, we have found that the following open-boundary condition,

$$Q_t + cQ_x = 0 \quad c = \pm (gh_o)^{1/2}, \quad (17)$$

where  $Q = \bar{\phi}$  and  $\bar{\phi} = \zeta$ , and the  $\pm$  sign is so chosen at each boundary node as to make the local wave leave the region  $\mathcal{R}$ , has worked effectively and successfully in all the cases attempted. This is basically different from the Orlanski scheme and its variations, for by their rule the local phase velocity  $c$  of exit waves must be numerically evaluated from using the nodal data adjacent to the boundary point. This is also different from Sommerfeld's radiation condition since condition (17) does not differentiate between the eventual long waves and transient waves of larger wave numbers. Crude as it may appear, condition (17) nevertheless has produced the best result, as will be seen later, of all the open-boundary conditions tested. In specific detail, the present numerical representation of (17) adopts an 'upstream differencing' for a downstream boundary point and a 'downstream differencing' for an upstream boundary point,

$$\zeta_{IMX}^{n+1} = (1 + \frac{\Delta t}{\Delta x})^{-1} [\zeta_{IMX}^n + \frac{\Delta t}{\Delta x} (\zeta_{IMX-1}^{n+1} + \zeta_{IMX-1}^n - \zeta_{IMX}^n)], \quad (18)$$

and with a similar equation for  $\bar{\phi}$ . Here in (18), the subscript IMX denotes the downstream open boundary node.

In the interest of keeping the computation region as small as necessary, we have further devised a technique employing a 'step-shifting region'. This is a region which remains fixed with respect to the absolute frame as before, only now with its boundary shifted forward by one interval length  $\Delta x$  after  $N$  time steps (i. e. choosing  $\Delta t = \Delta x / (NU)$  to keep up with the moving disturbance. The same basic equations and open-boundary conditions are used as before (for fixed boundaries) except that new boundary values will now be required at the new upstream boundary node after each shift. It is convenient to choose the upstream boundary point far enough to keep flow variables infinitesimal there. Thus, for supercritical cases, it suffices to set  $\zeta_1^{n+1} = 0$  and  $\phi_1^{n+1} = \phi_1^n$  for all  $n$ . In the subcritical case it has proven successful to determine the new boundary values by interpolating the nodal values at the previous time step and using the approximate phase velocity  $c = \sqrt{gh_0}$ .

#### IV. STATIONARY WAVES GENERATED BY SURFACE PRESSURE DISTURBANCE

An interesting special case is the two-dimensional stationary waves generated by a steady surface pressure, namely  $p_0 = P(x+Ut)$ , moving over a layer of water of uniform depth. After a suitable Galilean transformation from the absolute frame to the moving-disturbance frame, (3) and (4) become

$$U\zeta + (1 + \zeta)u = 0,$$

$$Uu + \frac{1}{2}u^2 + \zeta - \frac{1}{3}Uu_{xx} + P = 0,$$

in which  $u$ ,  $\zeta$  and  $P$  are functions only of  $x$ , and we have set  $h = 1$ . Upon eliminating  $\zeta$  from the above two equations, we obtain

$$u_{xx} = \frac{3}{U} \frac{1}{(U+u)} \left[ \frac{1}{2}u^3 + \frac{3}{2}Uu^2 + (U^2 - 1)u \right] + \frac{3}{U} P(x). \quad (19)$$

In the absence of disturbance,  $P \equiv 0$ , the above equation has solutions of the form

$$u = A \operatorname{sech}^2 \{k(x - Ut)\} \quad A = \frac{4}{3} U k^2 h^2, \quad (20)$$



provided  $U > 1$  (i. e.  $U > c = (gh)^{1/2}$ ), that is, in the supercritical regime. For given  $U$  and  $P(x) \neq 0$ , (19) can be integrated numerically if appropriate boundary values are prescribed at a certain point upstream of  $P(x)$ , e. g. by giving  $u$  and  $u_x$  at a point  $x_1$ . For low subcritical speeds, such as  $U < 0.5$ , it can be seen that  $\zeta$  just upstream of the leading edge of  $P(x)$  is negligibly small. Hence a very accurate solution of  $\zeta$  can be obtained by integrating (19) downstream from the leading edge ( $x = 0$ ) of  $P(x)$  with the boundary conditions  $\zeta = 0$  and  $\zeta_x = 0$  (i. e.  $u = 0$  and  $u_x = 0$ ) at  $x = 0$ .

## V. TRAVELING PRESSURE DISTURBANCES

As the first example of an initial value problem of a traveling disturbance we consider the following surface pressure distribution for  $t > 0$ ,

$$p_o(x, t) = p_{om} \frac{1}{2} \left[ 1 - \cos\left(2\pi \frac{x+Ut}{L}\right) \right] \quad (0 < (x+Ut) < L), \quad (21)$$

with

$$h = \text{const.} = 1, \quad F_h = U/\sqrt{gh} = U = 1/\sqrt{2\pi} = 0.3989, \quad p_{om} = 0.01, \\ L = 1, \quad (22)$$

and  $p_o = 0$  elsewhere as well as for  $t < 0$ . For the initial values we assign, as stated before,  $\zeta = -p_o(x, 0)$  and  $\bar{\phi} \equiv 0$  at  $t = 0$ . The transient motion resulting from the application of this  $p_o$  was computed by applying the present numerical scheme, as explained in the previous section, to equations (3) and (4) over the region  $-20 < x < 10$ , with

$$\Delta x = 0.2, \quad \Delta t = \Delta x/4U. \quad (23)$$

The numerical result is replotted in figure 1, so that the wave train remains fixed with respect to  $p_o$ , for the dimensionless time  $t = UT/L$  up to 10. Also shown in figure 1 is the steady limit computed by numerical integration of (19) for the present  $p_o$  by following the procedure described earlier, here with  $\Delta x = 0.01$ . By comparison, the leading wave of the unsteady wave train is seen to have approached the steady limit by  $t = 10$ , and the tendency is to have the subsequent waves grow in magnitude, thereby gaining in speed to approach the steady limit in consecutive order. Since the steady limit is known to be accurate, this comparison further affords a critical examination of the error due to any imperfectness of the open-boundary condition (17) used here, which in this case is extremely small.

The wave resistance,  $D_W$ , experienced by the surface pressure (per unit width) has the coefficient

$$C_{DW} = D_W / \rho g h L = - \frac{1}{\rho g h L} \int_0^L p_o(x, t) \frac{\partial \zeta}{\partial x} dx . \quad (24)$$

The corresponding result of  $C_{DW}$  is given in figure 2. We see that  $C_{DW}$  oscillates while gradually approaching its steady limit.

#### A. Pressure Disturbance of Opposite Signs

To examine the different features of long waves generated by surface pressure disturbances of opposite signs for the case when the nonlinear effects become appreciable, we consider again the distribution (21), now with

$$U = 0.4 , \quad p_{o_m} = 0.3 \quad \text{and} \quad p_{o_m} = -0.3 , \quad (25)$$

respectively. The results of these two cases, executed numerically again by using (23) and as shown in figures 3 and 4, exhibit clearly the nonlinear effects as the waves in both cases have sharper crests and flatter troughs, than in the case of sinusoidal waves corresponding to much smaller  $p_{o_m}$ , thus displaying finite departure from the antisymmetry as would be expected on linear theory argument. These waves are seen to resemble the free cnoidal waves as solutions of the KdV equation.

Figure 5 shows that the wave resistance coefficient,  $C_{DW}$ , of the negative pressure disturbance ( $p_{o_m} = -0.3$ ) oscillates with time more strongly, about a considerably greater mean, than the  $C_{DW}$  of the positive pressure disturbance ( $p_{o_m} = 0.3$ ). The basic mechanism underlying these distinctive features between positive and negative surface pressures is not well understood, though it is discernible from figures 3 and 4 that the water surface has a steeper slope under the negative surface pressure than that under the positive one.

#### B. Pressure Disturbances at Supercritical Speeds

We now proceed to investigate the long waves generated by surface pressure disturbances at supercritical speeds by adopting again the distribution given by (21), now with

$$U = 1.2, \quad p_{0m} = 0.3 \quad \text{and} \quad p_{0m} = -0.3 \quad (26)$$

respectively. The numerical execution was based on  $\Delta x = 0.2$ ,  $\Delta t = \Delta x / U$ . As shown in figures 6 and 7, the forcing disturbance advances quickly from its initial position, drawing the trailing waves increasingly longer and displacing the water surface ahead of it over a wide extent. In the meantime, the waves generated in the initial stage have not had much time to have propagated away from their original position. It is also quite clear that the free surface underneath the pressure distribution undergoes a rather slow change in amplitude and phase. On the other hand, the corresponding wave resistance coefficient decays rapidly to small values after its first peak, then gradually approaching zero, as can be seen from figure 8.

In order to estimate the rate of approach of the solution to its steady limit (a rate which may have a strong dependence on the Froude number), we compare the large time solutions corresponding to  $U = 1.2$  and  $1.4$  respectively, subject to otherwise the same pressure disturbance as given by (21). From figure 9 we see that the closer the  $U$  to 1, the slower is this rate of approach (see the data at  $t = 48$  for comparison). We therefore may expect that it would take very long time to reach the steady limit when  $U$  is very close to 1, if the limit exists. This case will be examined in more detail in the next section.

In figure 10, we demonstrate a comparison between nonlinear dispersive and linear dispersive models for the case of  $U = 1.2$ ,  $p_{0m} = 0.1$  and  $h = 0.5$ . Although the two limiting solutions are similar in form, the linear theory underestimates the wave amplitude by a margin as large as 30 %.

Finally, we point out that, as can be seen from figures 9 and 10, the present open-boundary condition is evidently very effective in handling the physical processes near the open boundary, especially when  $\zeta$  and  $\phi$  are of finite amplitude at the downstream boundary for  $t < 20$ , a situation which usually presents a severe test. Only with this early success was the computation possible to continue to very long times as shown.

## VI. TRANSCRITICAL DISTURBANCES

On physical ground, both the nonlinear and dispersive effects are expected to play essential roles in the transcritical regime. On one hand, the continued rate of working by the traveling disturbance will contribute to increasing the mechanical energy of the nearby fluid. If we base our argument on linear dispersive wave theory, we see that the energy so accumulated can radiate only towards downstream because of the group velocity of long waves being slightly less than their phase velocity. This will imply that it will become

increasingly more difficult to radiate the accumulated energy away from the disturbance as the velocity of a traveling disturbance,  $U$ , approaches the critical value, which is  $c = (gh)^{1/2}$ . On the other hand, it is feasible that the flow energy accumulated about the disturbance may evolve, under the joint action of nonlinear and dispersive effects, into waves of finite amplitude that can radiate in different ways.

To investigate this interesting problem, we consider the case of the  $p_o(x, t)$  distribution of (21) with

$$U = 1.0, \quad p_{o_m} = 0.1, \quad h = 0.5. \quad (27)$$

The numerical result for  $\zeta$ , obtained with  $\Delta x = 0.2$ ,  $\Delta t = 0.2$  and as shown in figure 11, exhibits an exceedingly interesting phenomenon. The transient wave underneath the  $p_o$  distribution continues to grow in magnitude and starts at time about  $t = 24$  to form an inflected peak just ahead of  $p_o$ , which shortly thereafter surges ahead to run away as a soliton. At a later time about  $t = 48$ , a second inflected peak forms to surge ahead as the second soliton. Since its separation, the first soliton has continued to grow in magnitude, and accordingly accelerates further ahead. At  $t = 56$ , it becomes so large that its breaking can be an open question. Other than the prospects of exchanging energy between the main wave train and the 'run-away solitons', these solitary waves appear in every aspect like free solitons, for their excess mass is all distributed above the original water level (at  $z = 0$ ). On the downstream side, the wave train also grows in amplitude, length and group size, thereby gaining in phase velocity while moving forward following the forcing disturbance. The profile oscillates across  $z = 0$  and resembles the cnoidal waves.

It is interesting to note that by comparison with the corresponding results of wave resistance variations shown in figure 12, the run-away solitons appear to emerge at the instant when the wave resistance instantaneously reaches a maximum, i. e.  $C_{DW} = 0.02126$  at  $t = 19.2$  for the first and  $C_{DW} = 0.02301$  at  $t = 44.6$  for the second soliton. Immediately after the separation of a soliton from the main wave train, the wave resistance decreases to reach a minimum, then increases as the next soliton is being conceived.

The interesting phenomenon just presented has been found to manifest over a region in the transcritical regime, as demonstrated in figure 13 for the case of

$$U = 0.9, \quad p_{o_m} = 0.1, \quad h = 0.5. \quad (28)$$

The time period of formation of consecutive solitons in this case appears to be considerably shorter than that at the critical speed, e. g.,  $t \approx 16$  in this case versus  $t \approx 24$  at  $U = 1$  for the first

soliton to emerge. This comparison would suggest that the characteristic time scale for this transcritical phenomenon perhaps reaches a maximum at the critical speed. As a remark concerning the computational error incurred in this case, the dashed lines near the boundaries delineate more accurate results obtained by using a greater region of computation. The error is thus seen to remain confined only to a narrow region next to the boundary.

To isolate the nonlinear effects, we present in figure 13 a comparison with the corresponding results based on linear dispersive model. The contrast is drastic. The unique phenomenon of soliton separation does not seem to occur at all on linear theory. This therefore lends a strong evidence that the phenomenon arises only from the interaction between the nonlinear and dispersive effects.

The wave resistance coefficients corresponding to the two theories are shown in figure 14. The  $C_{DW}$  predicted by the linear dispersive model increases with time, with no asymptote in sight.

In concluding our exposition, we note that the new phenomenon of soliton separation predicted by the present nonlinear dispersive model appears to be very much like the experimental discovery of Huang, Sibul & Wehausen (1982), notwithstanding the different circumstances that the source of disturbance was a ship model in the experiment and is a two-dimensional surface pressure at hand. The history of formation of run-away solitons, the cnoidal-wave-like train of waves following the forcing disturbance and the transient waves further downstream in the two cases are very much alike in all the qualitative features. Evidently, this newly discovered phenomenon has a rich content yet to be brought out by further studies. Perhaps it has a fundamental basis common with the 'singular and beautiful phenomenon' first interviewed by John Scott Russell.

#### Acknowledgment

We take pleasure in expressing our gratitude to Professor John V. Wehausen for the benefits received from reading his scholarly works over the years, and especially having the seeding stimulus given by him in his lecture on the subject at the 1982 Hamburg Festkolloquium cited in the text. We also wish to express our deep appreciation to Mr. Ralph D. Cooper for his wise and able service bestowed on our professional community while at the Office of Naval Research, the Department of the Navy, throughout the decades. This is a token of our warmest thanks and tribute to both of them.

This study is supported jointly by ONR Contract N00014-76-C-0157 and N00014-82-K-0443, NR 062-737 and NSF Grants PFR 77-16085 and MEA-8118429. The numerical computations have been executed at the Booth Computing Center, California Institute of Technology.

# References

- Bai, K. J. 1977 A localized finite-element method for steady, three-dimensional free-surface flow problems. Proc. 2nd Int. Conf. Numer. Ship Hydrodyn., Berkeley, Calif., 78-87.
- Boussinesq, M. J. 1871 Theorie générale des mouvements qui sont propagés dans un canal rectangulaire horizontal. Acad. Sci. Paris, Comptes Rendus 73:256-60.
- Boussinesq, M. J. 1877 Essai sur la théorie des eaux courantes. Mem. présentés par divers Savants à L'Acad. Sci. Inst. France (séries 2) 23:1-680; 24:1-64.
- Chan, R. K. C. 1977 Finite difference simulation of the planar motion of a ship. Proc. 2nd Int. Conf. Numer. Ship Hydrodynamics., Berkeley, Calif., 39-52.
- Graff, W., Kracht, A. M. & Weinblum, G. 1964 Some extensions of D. W. Taylor's standard series. Trans. SNAME 72:374.
- Graff, W. & Binek, H. 1969 Untersuchung des Modelltankeinflusses an einem Flachwasserschiff. Forschungsberichte des Landes Nordrhein-Westfalen nr. 1986.
- Huang, De-bo, Sibul, O. J., & Wehausen, J. V. 1982 Ships in very shallow water. Festkolloquium - Dedication to Professor Karl Wieghardt. March 1982, Institut für Schiffbau der Universität Hamburg.
- Inui, T. 1954 Wave-making resistance in shallow sea and in restricted water. J. Japan Soc. Naval Arch. 76:1-10.
- Kinoshita, M. 1954 On the restricted-water effect on ship resistance. J. Japan Soc. Naval Arch. 76:173-214.
- Kirsch, M. 1966 Shallow water and channel effects on wave resistance. J. Ship Res. 10:164.
- Korteweg, D. J. & de Vries, G. 1895 On the change of form of long waves advancing in a rectangular canal and on a new type of long stationary waves. Phil. Mag. 39:422-443.
- Lamb, H. 1932 Hydrodynamics. 6th ed. Cambridge Univ. Press.
- Lea, G. K. & Feldman, J. P. 1972 Transcritical flow past slender ships. Proc. Ninth Symp. on Naval Hydrodynamics, 2:1527-1541, Aug. 20-25, 1972. Paris (ed. R. Brard & A. Castera) ACR-203, Office of Naval Research, Arlington, Va.
- Lepelletier, T. G. 1981 Tsunamis-Harbor oscillations induced by nonlinear transient long waves. Ph.D. thesis, Calif. Inst. of Technology, Pasadena, Calif.
- Miles, J. W. 1980 Solitary waves. Ann. Rev. Fluid Mech. 12: 11-43, Annual Reviews Inc., Palo Alto, Calif.
- Orlanski, I. 1976 A simple boundary condition for unbounded hyperbolic flows. J. Comput. Phys. 21:251-269.
- Rayleigh, Lord 1876 On waves. Phil. Mag. 1:257-279. Sci. Pap. 1:251-271.
- Russell, J. S. 1838 Report of the Committee on Waves. Rep. Meet. Brit. Assoc. Adv. Sci. 7th, Liverpool, 1837, 417-496. John Murray. London.

- Russell, J. S. 1845 Report on waves. Rep. Meet. Brit. Assoc. Adv. Sci. 14th, York, 1844, 311-390. John Murray, London.
- Schember, H. R. 1982 A new model for three-dimensional nonlinear dispersive long waves. Ph. D. thesis, Calif. Inst. of Technology, Pasadena, Calif.
- Wu, T. Y. 1972 Blockage. Proc. 13th Intern. Towing Tank Conf. Berlin/Hamburg, Sept. 1972. 1:124-131.
- Wu, T. Y. 1979 On tsunami propagation - evaluation of existing models. In TSUNAMIS - Proc. National Science Foundation Workshop (ed. L. S. Hwang & Y. K. Lee) 110-149. Tetra Tech Inc., Pasadena, Calif.
- Wu, T. Y. 1981 Long waves in ocean and coastal waters. Proc. ASCE, J. Eng. Mech. Div. 107, EM3, 501-522.
- Yen, S. M., Lee, K. D., Akai, T. J. 1977 Finite element and finite difference solutions of nonlinear free surface wave problems. Proc. 2nd Int. Conf. Numer. Ship Hydrodyn., Berkeley, Calif., 305-318.
- Yeung, R. W. 1982 Numerical methods in free-surface flows. Ann. Rev. Fluid Mech. 14:395-442. Palo Alto, Annual Reviews Inc.
- Yuen, Y. C. & Lake, B. M. 1982 Nonlinear dynamics of deep-water gravity waves. Advances in Appl. Mech. (ed. C. -S. Yih) 22:68-226, Academic Press, Inc., New York.
- Zabusky, N. J. & Kruskal, M. D. 1965 Interaction of 'solitons' in a collisionless plasma and the recurrence of initial states. Phys. Rev. Lett. 15:240-243.

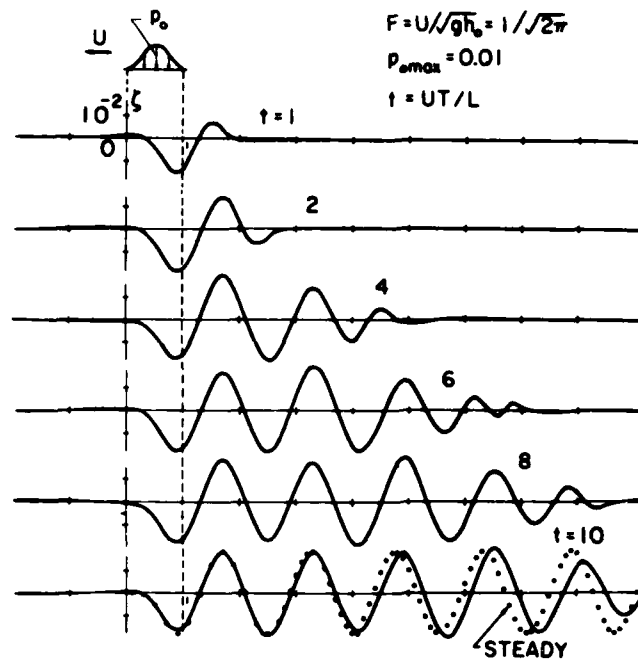


FIGURE 1. Generation of a wave train by the surface pressure distribution given by equation (21), traveling at Froude number  $F_h = U = (2\pi)^{-1/2}$ .  $p_{0m} = 0.01$  (based on  $\rho gh$ ): — unsteady theory ( $\Delta x = 0.2$ ,  $\Delta t = 0.125$ ); o o o steady limit (by numerical integration of (19) with  $\Delta x = 0.01$ ).

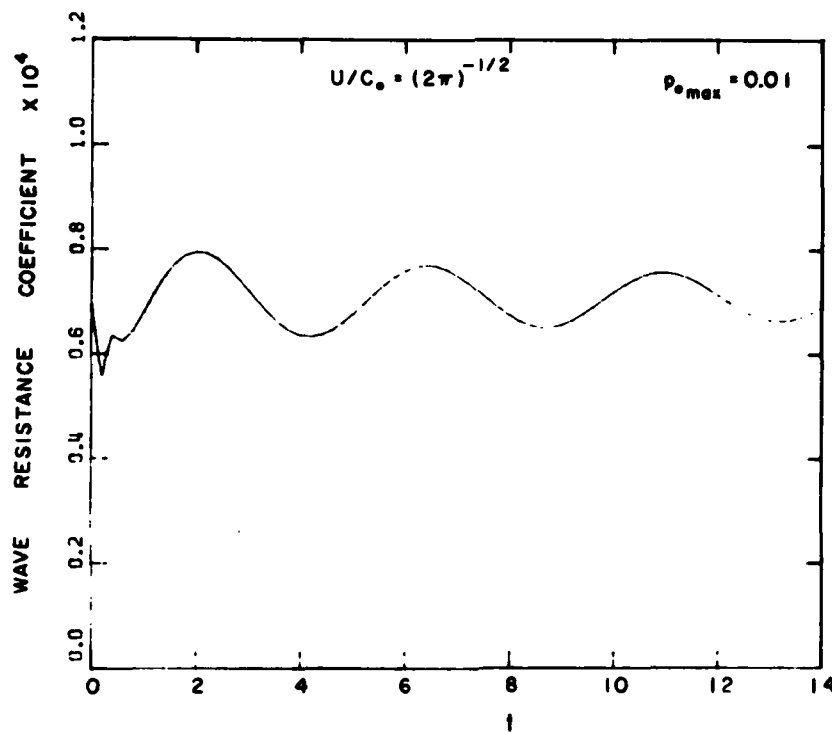


FIGURE 2. Wave resistance coefficient (defined in (24)) corresponding to the surface pressure prescribed by (21) and (22).



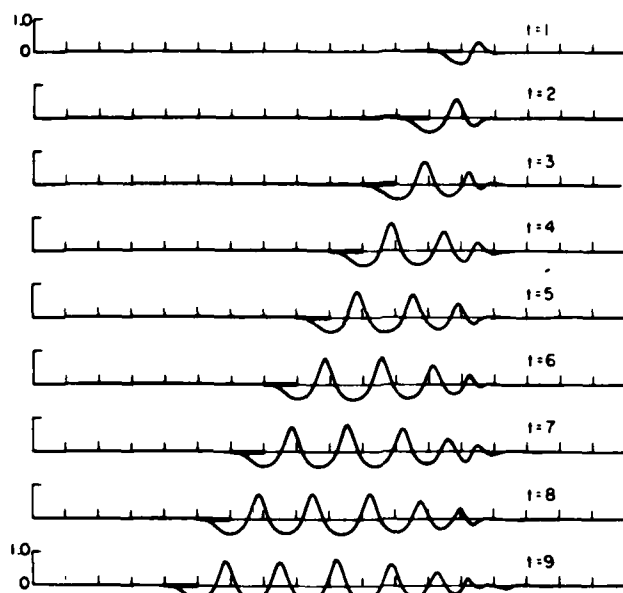
$U = 0.4, \quad p_{o\max} = 0.3$ 


FIGURE 3.

Wave generation by the surface pressure prescribed by (21),  $p_{om} = 0.3$ , at Froude number  $F_h = U = 0.4$ .

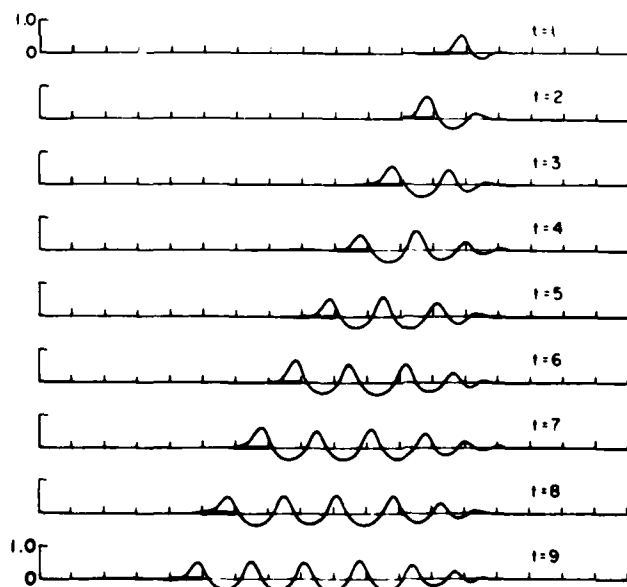
 $U = 0.4, \quad p_{o\max} = -0.3$ 


FIGURE 4.

Wave generation by the surface pressure prescribed by (21),  $p_{om} = -0.3$ ,  $F_h = U = 0.4$ .

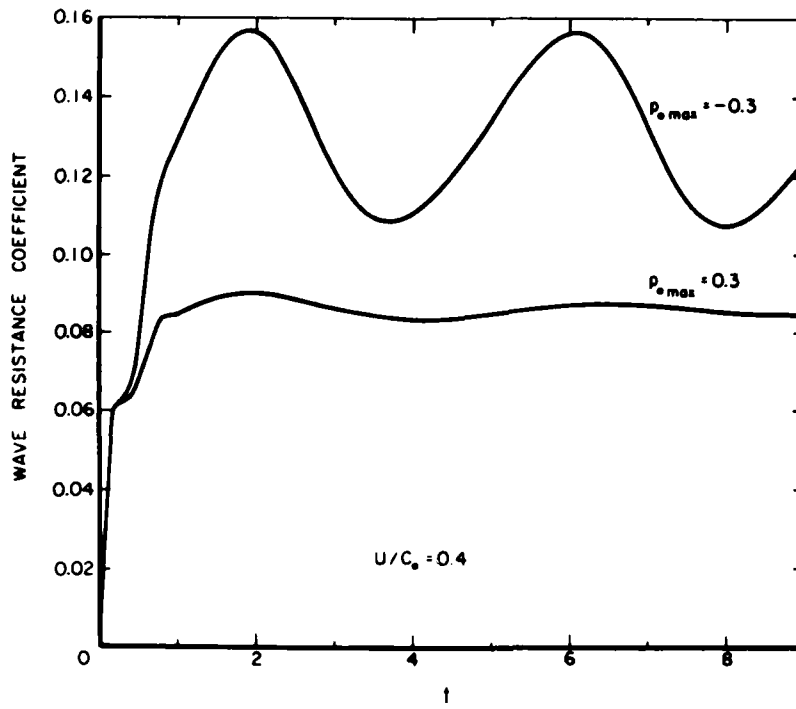


FIGURE 5. Wave resistance coefficients corresponding to the surface pressure distributions given for figures 3 and 4.

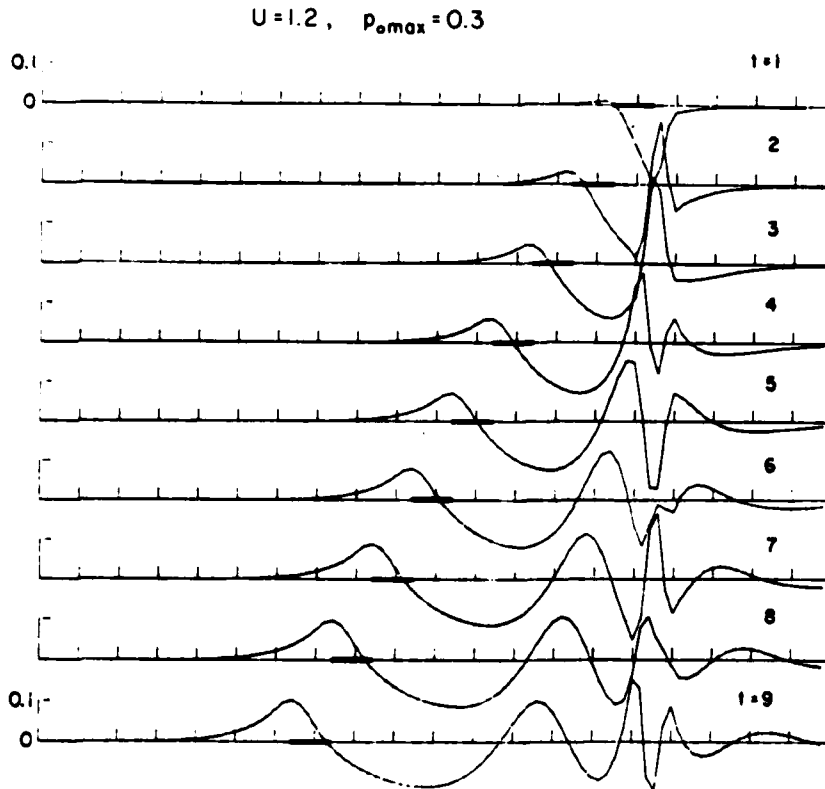


FIGURE 6. Wave generation at supercritical speed  $U = F_h = 1.2$  by the  $p_o(x, t)$  given by equation (21), with  $p_{om} = h_0 = 0.3$ .

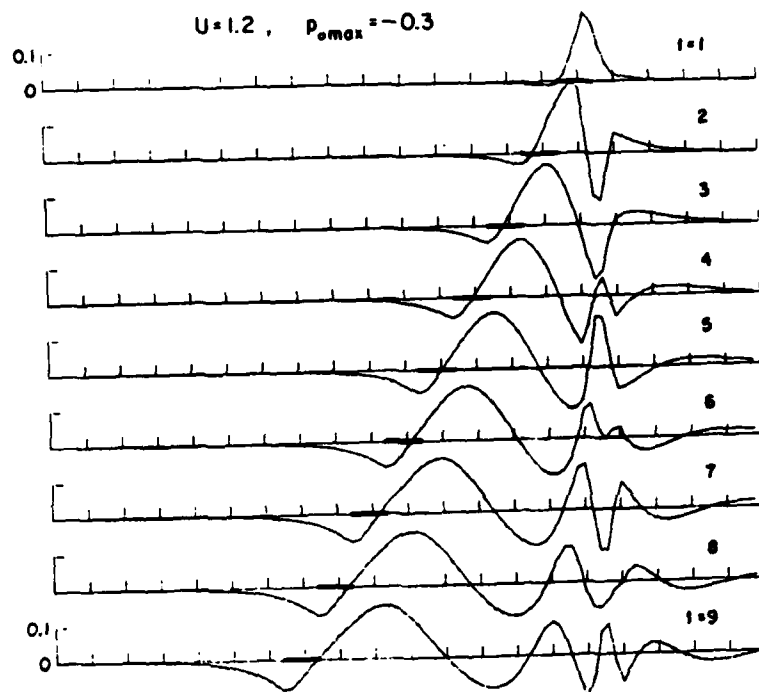


FIGURE 7. Wave generation at supercritical speed  $U = F_h = 1.2$  by the  $p_0(x, t)$  given by equation (21), with  $p_{0m} = -0.3$ .

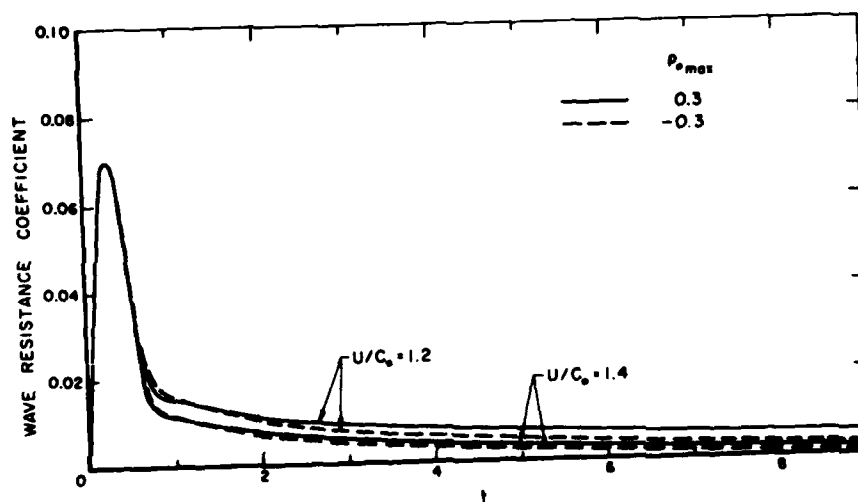


FIGURE 8. Wave resistance coefficients corresponding to the surface pressure distributions prescribed for figures 6 and 7.

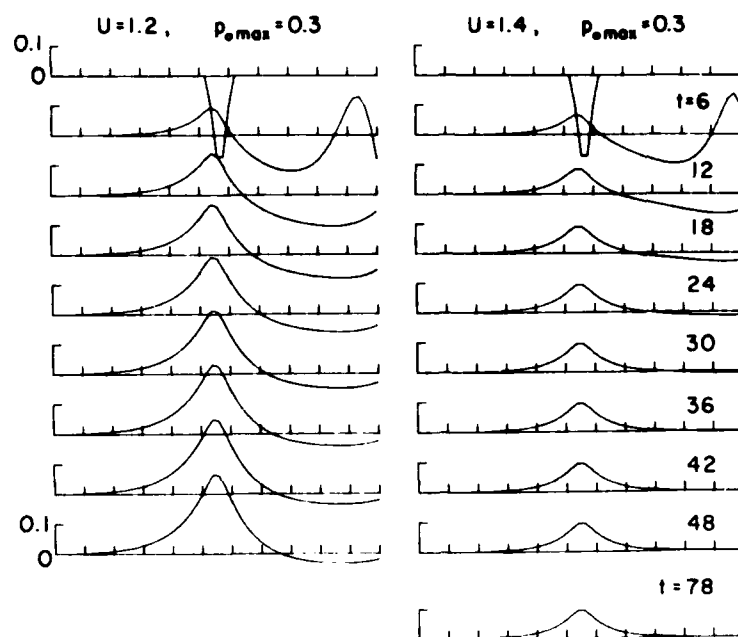


FIGURE 9. Large time asymptotic waves at supercritical speeds at  $U = F_h = 1.2$  and  $1.4$ .

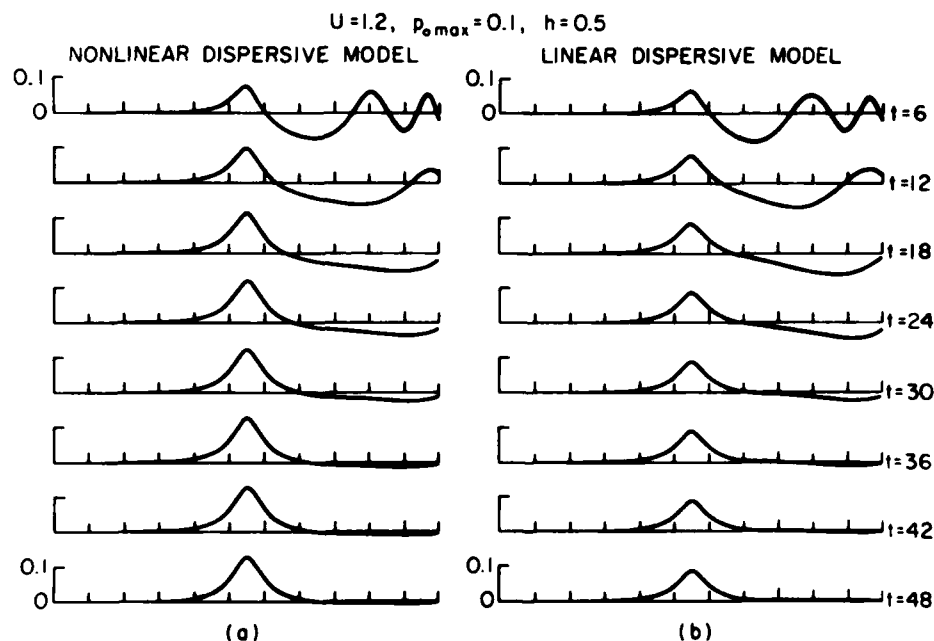


FIGURE 10. Comparison between nonlinear dispersive model and linear dispersive model at the supercritical speed of  $U = F_h = 1.2$ ;  $p_{0m} = 0.1$ .

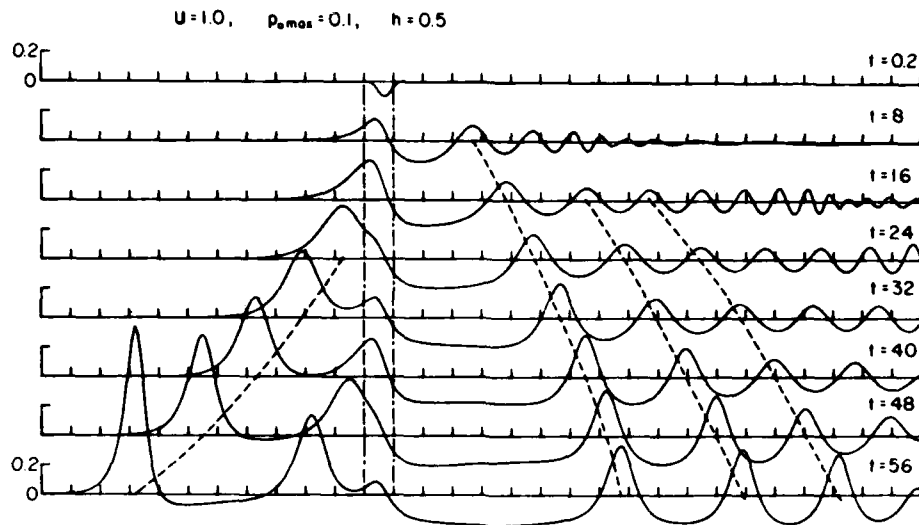


FIGURE 11. Interplay of nonlinear and dispersive effects at the critical speed  $U = F_h = 1$ . The large time solution shows solitary waves being generated to propagate upstream as free waves. Two such 'run-away solutions' can be seen shortly after  $t = 24$  and 48.

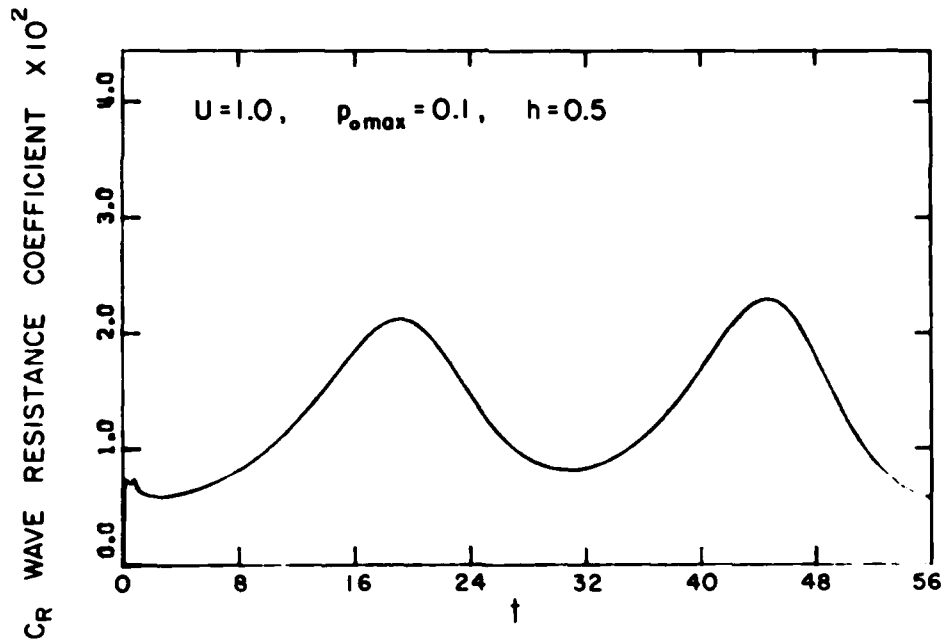


FIGURE 12. Variation of wave resistance experienced by the surface pressure disturbance at the critical speed. The run-away solitons appear to emerge at the temporal maxima of the wave resistance (compare with figure 11).

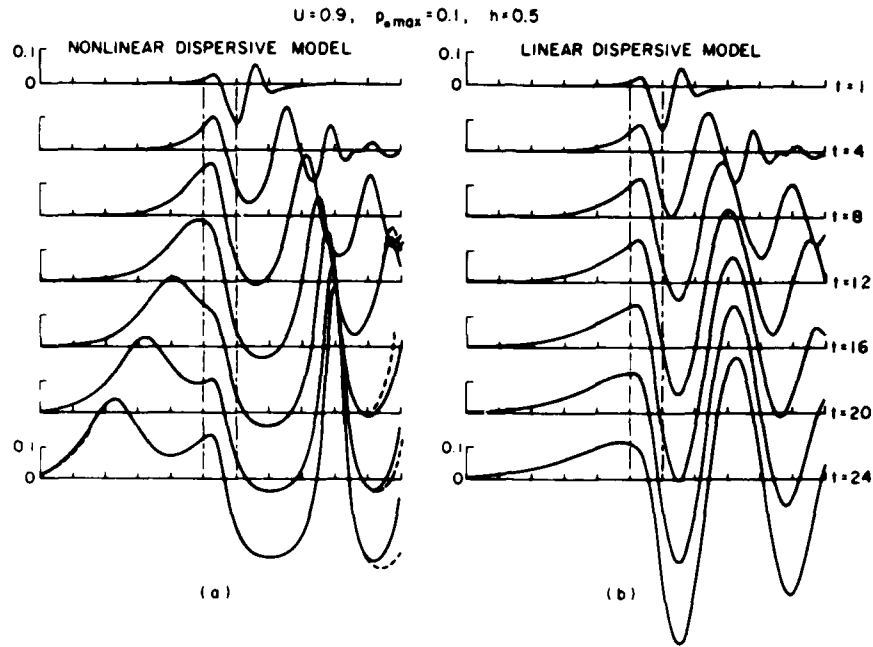


FIGURE 13. Comparison between nonlinear dispersive model and linear dispersive model at the high subcritical speed of  $U = F_h = 0.9$ ;  $p_{0m} = 0.1$ . — · — the range of  $p_0(x, t)$ ;  $\frac{h}{h}$  — — numerical results from using a greater region of computation.

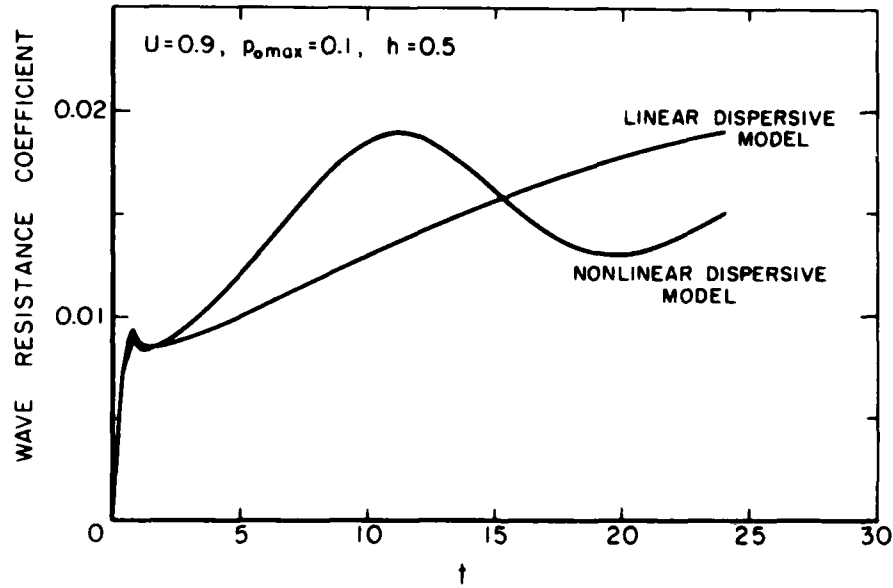


FIGURE 14. Wave resistance as predicted by nonlinear dispersive and linear dispersive theories.

## Discussion

A.M. Ferguson (University of Glasgow)

The results of some recent shallow-water tests conducted at the University of Glasgow Hydrodynamics Laboratory may be of interest.

These tests concerned the reactions of a bulk carrier in shallow water approaching a shoaling sandbank. The reaction of interest was that a singular transverse wave was noted well ahead of the model. When this wave, or pressure front, reached the shoaling sandbank, the model responded with an increase in trim by the head, then oscillated in pitch in the manner of a damped spring. This reaction was amplified when the bow of the model reached and passed over the sandbank.

I would be interested in the author's comments.

W.C. Webster (University of California)

Dr. Wu mentioned some experiments that were conducted at the University of California at Berkeley. In those experiments a ship model was towed at a constant speed in shallow water. During these experiments the following remarkable phenomena were observed:

1. A train of waves was generated at the bow. These waves separated from the bow and ran ahead of the ship.
2. These waves were, as far as we could tell, two dimensional. That is, they did not change shape across the tank. This is the only situation I know of whereby two-dimensional waves result from a full three-dimensional flow.
3. "Running away" waves were generated at speeds well below  $F_r = 1$  to speeds corresponding to  $F_r \approx 1.4$ . This latter result is consistent with solitary wave theory.

I suggest that the good agreement between Wu's two-dimensional theory and our experiments lies in the fact that only two-dimensional waves are created. Perhaps the appropriate three-dimensional equations admit only two-dimensional upstream wave patterns.

S.M. Yen (University of Illinois)

I would like to compliment the authors for their success in developing a method to implement the open boundary condition for the nonlinear moving surface-pressure problem. The direct application of Orlandi's method at the open boundary could lead to several computational difficulties that have to be dealt with carefully. These

difficulties include the accurate numerical calculation of advection speed and the control of high-frequency errors. It would be of interest to apply a simple model of the open boundary condition as suggested by the authors. However, it requires the determination of the typical advection for the problem to be solved.

Colleagues in atmospheric sciences have also studied methods to implement the open boundary condition in solving the atmospheric gravity-wave problems. They have also found that the best way to apply the advection equation at the open boundary is to use the typical advection speed for problems in which this speed is known. The authors' findings presented in this paper are, therefore, in accord with that of the colleague in atmospheric sciences.

### Author's Reply

T.Y. Wu and D.-M. Wu

To A.M. Ferguson

We would like to thank Dr. Ferguson for bringing a very interesting experimental observation to our attention. We believe that the phenomenon stated is closely related to the general problem at hand. As the bulk carrier model approached the shoaling sandbank, the sandbank could be regarded as a source of providing a disturbance, unsteady with respect to the carrier model, which should then be able to usher in a singular transverse wave precursing ahead of the model, as observed, provided the Froude number was within a transcritical range. Based on our finding here that the wave resistance experienced by a progressing disturbance should vary with time even when the progressing velocity is kept fixed at a near-critical speed, one might expect that a self-propelling model could respond with oscillations in motion (like what was observed) in similar operational state with respect to the criticality of the speed of the progressing forcing function. It is especially of interest to note that the salient features are common to the forerunning wave in this case and those described by Professor Webster in his discussion. That is, these waves all appear with a transverse wave front ahead of a three-dimensional disturbance.

To W.C. Webster

We very much appreciate having Professor Webster's contribution to summarize the experimental findings obtained by the University of California at Berkeley team. It complements effectively the comparison between theory and experiment that we had merely enough time to present only the case of the Froude number  $U = 0.90$  (see Figure A.1). Likewise we take note that, interestingly, while the forcing agency is



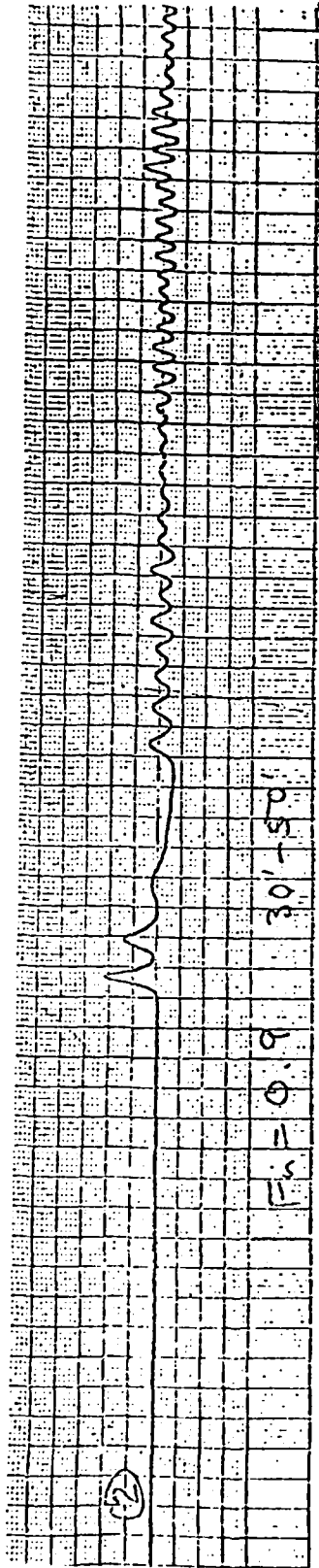
a three-dimensional and slender ship model for the experiment and is a two-dimensional surface-pressure disturbance employed in theoretical calculation, the resulting runaway solitons are nevertheless two dimensional in both cases and have almost the same main features in their evolution and propagation. We hope we can pursue together further comparative studies between theory and experiment, especially in regard to this issue.

To S.M. Yen

We wish to thank Professor Yen for providing valuable information about the practice of applying Orlanski's method and the emergence of some new methods developed by researchers in atmospheric science. Various computational difficulties associated with application of Orlanski's method may not be its intrinsic shortcoming. In the present case, where we have also experienced similar difficulties, the field equations are, however, basically different from those for which Orlanski's method was originally proposed. We are further delighted to learn, for the first time, that some new methods, apparently quite similar to the one we have just developed through our studies, have been found successful in serving as the open boundary condition for numerical computation of problems in atmospheric science.

Nevertheless, we should like to stress the importance and need of a thorough understanding of the nature of the "open boundary condition" for problems involving wave phenomena. The validity of the condition must necessarily require satisfaction of certain criteria ensuring the convergence and stability of the numerical scheme and, if possible, by having a definite error estimate. We have been able to secure only a limited success in estimating the error of our open boundary condition, through some numerical experimentation.

Experiment



Long Wave Theory

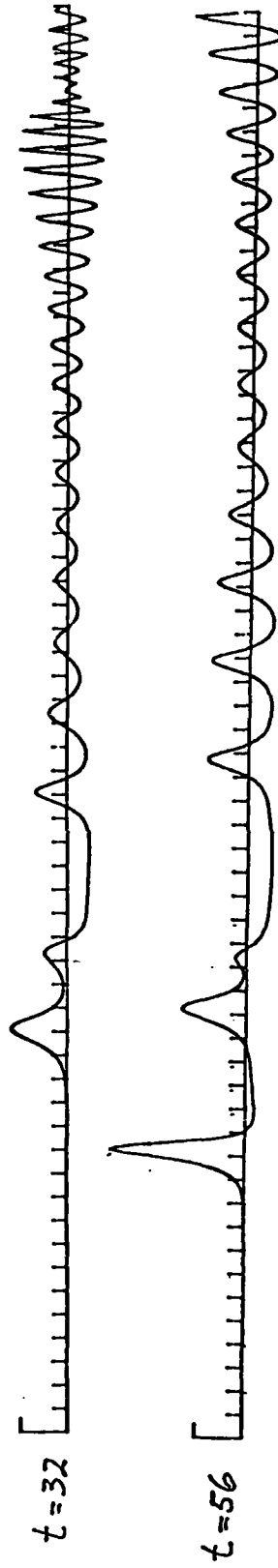


FIG. A.1

*Session II*

# CAVITATION

# Travelling Bubble Cavitation Noise Measurements

V. Shanmuganathan and V.H. Arakeri  
Indian Institute of Science, Bangalore, India

## ABSTRACT

An effectively controlled uniform travelling bubble cavitation at all free stream conditions was made possible by seeding the flow with artificial nuclei by electrolysis generated within the boundary layer of the test bodies. The cavitation inception and noise data were obtained on three test bodies having different pressure distribution and boundary layer characteristics. The cavitation noise data have been presented in the non-dimensional form.

## 1. INTRODUCTION

A cavitation nucleus when subjected to sufficient tension, will expand as a vapour bubble until it experiences a positive pressure at which point it will reverse the process and collapse. This volume change makes the cavitation bubble to act as a monopole in radiating sound. The acoustic characteristics of noise radiated from a single cavitation bubble growth and collapse process has been analytically first computed by Fitzpatrick and Strasberg (1956). Some of the important conclusions from their work are that at low frequencies the cavitation noise spectral density,  $S$  increases like  $f^4$  where  $f$  is the frequency, reaches a peak at value of  $f$  approximately equal to reciprocal of the bubble lifetime and finally decays like  $f^{-2/5}$  at higher frequencies if the liquid is assumed to behave incompressibly throughout the history of bubble dynamics. However, the decay at high frequencies is predicted to be much stronger like  $f^{-2}$  if the compressibility effects of the liquid are taken into account. Some of the early experimental studies in particular those of Jorgensen (1961) did confirm the qualitative aspects of the prediction due to Fitzpatrick and Strasberg (1956).

In real flows, cavitation zone consists of several cavitation bubbles growing and collapsing randomly distributed in space and time. In this situation it would be pertinent to ask whether the information obtained from single bubble dynamics could be useful at all in predicting cavitation noise from a cavitating zone. The answer to the above, to some extent is contained in the work of Morozov (1969) who has shown that if the cavitation bubbles can be assumed to be independent random events, then the spectral density of cavitation noise from a cavitation

zone is given by the product of  $S$ , the spectral density of a single cavitation bubble noise event and  $N$ , the average number of cavitation noise events per unit time. Therefore, in principle the qualitative aspects of cavitation noise from a cavitation zone would be expected to be similar to those of a single bubble cavitation event discussed earlier. In addition, it would be justifiable to use the important parameters characterising single bubble cavitation noise in describing noise from an arbitrary cavitation zone in non-dimensional terms. The ultimate aim finally being the derivation of appropriate scaling laws for cavitation noise as successfully done by Strasberg (1977) in one instance. By scaling here we mean the extrapolation of cavitation noise measurements under given conditions to different conditions with geometrical similarity maintained. If the scaling laws derived on the basis of analysis of single bubble cavitation noise are to be successful, then we should expect that the phenomenon of cavitation itself scales properly with bubble dynamics considerations alone. For example, we should expect then that the relative extent of cavitation should simply scale with the cavitation number,  $\sigma$ . However, it is well known now that this is not found to be true and in particular we may cite the work of Blake et al. (1977) who found that on the same body at otherwise identical physical conditions (like same  $\sigma$ , free stream velocity etc) different types and extent of cavitation was observed depending upon whether boundary layer was tripped or not tripped at the leading edge of the foil. In turn this reflected in noise measurements as well. Thus, the scale effects which may influence the inception process would be naturally expected to be carried over to the scaling of cavitation noise itself. In some cases this difficulty can partially be overcome as for example suggested by Strasberg (1977), Blake et al. (1977) and Thompson and Billet (1977) to use the parameter  $\sigma/\sigma_i$  (the ratio of cavitation number to the cavitation number at inception) rather than just  $\sigma$ .

However, this procedure may not account for all the effects due to variation in nuclei content as well as differences in real fluid flow characteristics. These effects are now well documented for example by Acosta and Parkin (1975), Arakeri (1979), Arndt (1981), Holl (1970), etc., and will not be elaborated further. Due to the complex nature of scaling of cavitation inception process itself it would be difficult to attribute the observed scale effects on cavitation noise either to the scale effects on the inception process or to the effects which are inherent to the noise generation. This necessarily indicates a need to conduct cavitation noise measurements where controlled cavitation can be generated.

In recent years there have been several investigations reported (Albrecht and Bjorheden 1975, Noordzij 1976, Kodama et al. 1979) where such control has been attempted by artificially seeding the flow with electrolysis bubbles which act as free stream nuclei. Similarly Arakeri and Acosta (1973) reported studies where electrolysis was used to generate artificial nuclei at the surface of a headform. In comparing the two methods of seeding the flow it is to be noted that free stream nuclei

are subject to the so-called "screening effect" first pointed out by Johnson and Hsieh (1966). In view of this, in the present work, the seeding of the nuclei by electrolysis from electrode in the nose of the headform was preferred. Thus, the primary scope of the present work was to study the scaling of travelling bubble cavitation noise with cavitation number, free stream velocity, etc., following the work of Blake et al. (1977) however with controlled generation of cavitation.

## 2. EXPERIMENTAL METHODS

### 2.1 Test Facility

The experiments were carried out in the High Speed Water Tunnel of the Indian Institute of Science, Bangalore. The test section of this facility is that of a closed jet type with an inner diameter of 381 mm and an overall length of 1524 mm. In this test section, a test body of maximum diameter of 50 mm would not essentially experience any blockage effect. The maximum attainable velocity in the test section is 30 m/s though the experiments were carried out up to a velocity of 17 m/s only. The pressure inside the system can be varied from 0.34 to 2.5 atmospheres by controlling the pressure above the free surface of an air chamber connected to the settling section of the tunnel circuit. An important feature of this facility is that it has a resorber which will drive back into the solution, the air bubbles liberated in the tunnel circuit. Though there is no deaeration system, the water is filtered through a filtering unit and treated with alum.

### 2.2 Test Models

The test models chosen for these experiments were Schiebe nose, Hemispherical nose and NSRDC the details of whose geometry are given in Figure 1. These test bodies have recently been used for cavitation inception studies for example by Gates and Acosta (1978) and Carroll (1981). The experiments were primarily carried on the Schiebe nose whose contour is generated by the potential flow solution to a distributed source disc oriented normally to a uniform flow. The coordinates of this body were taken from Gates (1979). This model geometry was chosen for the reasons that it does not have a laminar separation and it has a low natural incipient cavitation number,  $\sigma_i$  approximately equal to 0.4 though its  $C_{pmin} = -0.75$ . This large difference between  $\sigma_i$  and  $C_{pmin}$  provides a wide range of  $\sigma$  where the seeding of flow with artificial nuclei would be expected to be quite effective.

Experiments were also conducted on a hemispherical nose which has altogether different shape of pressure distribution even though about the same  $-C_{pmin}$  value as the Schiebe nose. Over the range of present tests hemispherical nose was expected to exhibit laminar separation as compared to the absence of the same on the Schiebe nose over the identical Reynolds number range. A series of tests were first made without tripping the boundary layer on the hemispherical nose. However, some additional tests on a different hemispherical nose were made by tripping the boundary layer by intentionally keeping the electrode ring (see Figure 3) about 0.1 mm protruding out of the surface. This was effective in eliminating laminar

separation (judged on the basis of observed type of cavitation at inception) at a velocity of about 11 m/s.

A limited number of tests were conducted using a NSRDC nose whose pressure distribution is almost similar to that of Schiebe nose though the  $-C_{pmin}$  value is somewhat higher. The theoretical pressure distributions in the absence of wall effects for all the three models are shown in Figure 2. All the models were made of plexiglass for reasons to be indicated later and extreme care was exercised in fabrication of the same. The models were inspected for their accuracy on an optical projection equipment at nominal magnification of 10X. The models were mounted in the test section securely with a three bladed sting support as shown schematically in Figure 4.

### 2.3 Nuclei Generation

Hydrogen bubbles which served as artificial nuclei in the present experiments were produced by electrolysis from a stainless steel ring of 25 mm diameter and 1 mm thickness imbedded in the nose of the body at  $s/D$  roughly equal to 0.25. Schematic details of the mounting of the ring was imbedded in a plexiglass plug in the nose of an otherwise stainless steel body. However, it was found that as soon as a potential was applied across the ring and tunnel wall the electrolysis bubbles were generated not only on the ring but also on the surface of the model due to its proximity. In view of this, it was finally decided to make the entire model out of plexiglass. The ring was electrically connected to the negative pole of a D.C. power supply by a cable passing through an internally drilled hole in the model and its support system. Differing levels of D.C. voltages in the range of 0-60 volts were applied between the terminals to generate electrolysis bubbles.

### 2.4 Noise Measurements

The noise measurements were made with the help of a flush mounted pressure transducer (Celesco LC 71) whose sensitive surface is of 0.208" diameter and resonant frequency is 150 kHz. Barker (1976) mounted the transducer in a flooded cavity behind a thin diaphragm which was flush with the test section. This was done to eliminate background noise from wall pressure fluctuations caused by the turbulent wall boundary layer. In the present work such an arrangement was not found to be necessary since the primary interest was the measurement of cavitation noise as compared to Barker (1976) who was interested in the measurement of radiated flow noise as well. The location of the transducer relative to the model is shown in Figure 4. The signal from the transducer was fed into a B & K Level Recorder via a Precision Conditioning Amplifier, a Measuring Amplifier and a Third Octave Filter. The data from calibrated charts were reduced to give sound pressure levels and spectral density using standard methods. The measurements were made in the frequency range of 2 to 100 kHz with an averaging time of 1 sec. We must note that this is the minimum averaging time and increases to a higher value at lower frequencies. Attempts were made in the present work to ascertain the reverberation characteristics of the test section following the method

suggested by Blake et al. (1977). However, difficulties were experienced primarily since the LC 71 was not as sensitive as a hydrophone and the projector used (B & K Hydrophone 8100) had a poor projection efficiencies at lower frequencies. As a result below about 20 kHz the signal to noise ratio in particular at distances of the order of 1 m turned out to be quite poor. In view of this the present measurements remain uncorrected for the possible reverberation effects.

## 2.5 Nuclei Measurements

In order to get an idea about the nuclei size and population, Laser Scattering method was adopted. The optical set up in the present work was very much similar to the one initially used by Keller (1972). The laser beam from Spectra Physics Helium-Neon laser tube was made to graze through the boundary layer of the model and was focused at a point slightly above the stainless steel ring from which the nuclei were generated. The light scattered was collected at  $90^\circ$  by a photomultiplier tube of DISA Make and the signal was fed into a GOULD's Storage Oscilloscope. The pulse height and the number of pulses were obtained from the stored oscilloscope trace typically over a 50 sec period which could be expanded. At the time of writing this paper, the calibration of the laser light scattering set up was not completed.

## 2.6 General Test Procedure

Before commencing the experiments, the water was deaerated by running the tunnel at low speed, pulling high vacuum over the free surface of the air chamber in the tunnel circuit and allowing the model to cavitate heavily. Then air collected in the resorber was released by opening the air vent. Now and then the air content was measured using Biochem Oxygen Analyser. This was repeated until the air content was brought down to roughly 25 percent of saturation at atmospheric conditions.

The water velocity in the test section was kept at a specified value and the tunnel pressure was then gradually reduced until the bubble became visible on the model under the stroboscopic illumination. This was done without electrolysis at different voltages to study the effect of electrolysis and its voltage on the cavitation inception.

At a given water velocity, the pressure was reduced in steps and at each pressure the noise spectra were obtained with and without electrolysis. The electrolysis voltage was kept at 9 V for almost all of the tests and the data were collected in the velocity range of 8.6 m/s to 17 m/s. The range of  $\sigma$  variation at each speed was between 0.4 and 0.7.

## 3. RESULTS

The results from nuclei measurements by Laser Scattering are shown in Figure 5. This gives qualitatively an idea about the effect of electrolysis on nuclei distribution. It is evident that by electrolysis many larger sized nuclei were introduced in the flow. Though there were



as many as 30 nuclei of the size corresponding to a pulse height of 0.0 to 0.2 V in the flow when there was no electrolysis they could not initiate cavitation probably because their size might have been less than the critical radius. Once the electrolysis was switched on many number of nuclei whose size corresponds to the pulse height greater than 0.2 V were generated and readily triggered travelling bubble cavitation at a  $\sigma$  of about 0.6. As noted previously, the laser light scattering set up was not calibrated and hence it is not possible to assign bubble sizes to the respective voltage levels shown in Figure 5. However, we might note that even before selecting the location of electrolysis ring position etc., extensive theoretical estimation of the expected bubble sizes at detachment from the electrolysis ring were made. This was on the basis of balance of various forces acting on the bubble submerged within the laminar boundary layer. From this analysis it was estimated that the electrolysis bubble sizes are in the range of 30 microns at a free stream velocity of about 12 m/s.

Figure 6 shows the influence of electrolysis voltage on the noise spectrum at a  $\sigma$  value of 0.61 on the hemispherical nose. With the electrolysis on, there is a substantial increase in Sound Pressure Level (SPL) as much as 20 dB at certain frequencies, when compared to that without electrolysis. As shown in the figure generally the sound pressure spectrum varied when the electrolysis voltage was changed. At 2.5 V the SPL at a given frequency was generally the maximum and gradually decreased as the voltage was increased. One feature which might explain this dependence was the fact that at lower voltages the cavitation bubbles were generally larger and its number density was less; however, at larger voltages the bubbles were smaller but the number density was greater. In view of these observations most of the tests in the present work was limited to electrolysis voltage of 9 V which was a compromise between excessive bubble density and consistency in appearance of stable cavitation zone.

The incipient cavitation number,  $\sigma_i$  variation with velocity for the three test bodies with electrolysis is shown in Figure 7. In all cases the type of cavitation at inception was the travelling bubble type. Without electrolysis on the Schiebe nose at lower velocities (below about 12 m/s) the type of cavitation at inception observed was the travelling bubble type. At a higher velocity of about 14 m/s the type changed to travelling patch with generally inception numbers being lower. In any case it is apparent that the inception cavitation numbers without electrolysis are significantly lower than those with electrolysis. Figure 8 shows the dependence of inception cavitation number with change in the electrolysis voltage at a given velocity. The  $\sigma_i$  values increase with increase in the electrolysis voltage though generally marginally.

The influence of cavitation number on the spectral densities for the Schiebe body is shown in Figure 9. Here the spectral density of radiated noise is defined as  $10 \log \bar{p}_s^2(f, \Delta f) / \Delta f$  where  $\bar{p}_s^2(f, \Delta f)$  is the effective mean square pressure in the one-third octave band width

$\Delta f$  at the centre frequency  $f$ . The spectral densities so defined are converted to decibel values by referring to a pressure of one micro pascal. The spectral density variation with  $\sigma$  for selected centre frequencies for the Schiebe body are shown in Figure 10. It is clear that at all the centre frequencies cavitation noise first increases with lowering of  $\sigma$ , reaches a maximum at a certain  $\sigma$  and then decreases with further reduction in  $\sigma$ . The influence of velocity on the spectral densities for the Schiebe body is shown in Figure 11. It is clear that at all frequencies the spectral density increases with increase in velocity as also shown in Figure 12 at certain selected centre frequencies. The non-dimensional representation of the noise data for the Schiebe body is shown in Figure 13. The method used in non-dimensionalising the results is fully considered in a later section.

The influence of cavitation number and velocity on the spectral densities for the hemispherical nose (untripped) are shown in Figures 14 and 15 respectively. The non-dimensional representation of the noise data for this body is shown in Figure 16.

The influence of cavitation number on the spectral densities for the hemispherical nose (tripped) are shown in Figure 17. The non-dimensional representation of the noise data for this tripped body is shown in Figure 18. Finally, selected noise data for all the test bodies in a non-dimensional form are shown in Figure 19.

#### 4. DISCUSSION OF RESULTS

##### 4.1 Cavitation Inception

As expected there is a dramatic difference in the value of incipient cavitation number for the Schiebe nose with and without electrolysis. The difference between  $\sigma_i$  and  $C_{pmin}$  is of the order of 0.15 with electrolysis whereas it is of the order of 0.375 without electrolysis. In addition to this the cavitation pattern at inception with electrolysis was of travelling bubble type and being uniform around the headform. As compared to this, without electrolysis the cavitation pattern at inception was extremely unsteady sometimes being of the travelling bubble type and at other times being of travelling patch type. There was also no uniformity of cavitation pattern around the headform. It is to be pointed out that noise measurements without electrolysis would have been extremely difficult due to the unsteady nature of cavitation without utilising significantly larger averaging times than that utilised presently. This general description was found to be true for the other two models as well namely hemispherical nose (tripped) and the NSRDC nose. In the latter case without electrolysis several spot type cavities appeared at relatively low velocities ( $\sim 10$  m/s) and in many instances these persisted even with electrolysis thus interfering with noise measurements. It is for this reason that only limited cavitation noise measurements have been presented for the NSRDC nose.

One significant point to be noted from the results of Figure 7 is that for the three test bodies with electrolysis the  $\sigma_i$  value does not depend strongly on the velocity and the type of cavitation at inception did not vary with change in velocity. Thus, the velocity scale effect on the  $\sigma_i$  normally observed has been eliminated by the use of artificially seeding the flow with nuclei in the boundary layer.

The effect of increasing the electrolysis voltage seems to have only a small effect on the inception cavitation number as shown in Figure 8. This may not be entirely surprising since on present bodies the electrolysis bubbles are dynamically detached from the electrode surface before they get a chance to fully grow on the surface. Thus, it appears that the detachment size is primarily governed by dynamic considerations than electrolysis considerations. Physically though it was observed that the number density of cavitation bubbles did increase the absence of quantitative results from the laser light scattering set up further discussion on the inception results would only be speculative in nature. However, it is interesting to note that the difference between  $-C_{pmin}$  and  $\sigma_i$  values is considerably larger for the Schiebe body than the other two headforms.

#### 4.2 Cavitation Noise

It is clear from Figures 9, 14, and 17 that the dependence of cavitation noise spectral density on  $\sigma$  is quite complex. In general as shown in detail in Figure 10 the spectral density first increases with decrease in  $\sigma$ , reaches a peak around  $\sigma = 0.5$  (for the Schiebe nose) and then decreases for  $\sigma$  values less than 0.5. At different centre frequencies the behaviour though qualitatively similar does not seem to show any consistent quantitative trend. Results similar to ours have previously been observed at least qualitatively in a limited region of  $\sigma$  by Lesunovskii et al. (1969). However, our findings are in contradiction to the observations of Blake et al. (1977) and more recently by Hamilton (1981) who observe that cavitation noise level keeps on increasing with decrease in  $\sigma$ . It is possible that had they gone to lower  $\sigma$ 's than indicated in above references they may have observed similar trend as ours. It is to be pointed out that from single bubble dynamics considerations it is expected that cavitation noise level would keep on increasing with decrease in  $\sigma$  since it is predicted that the maximum bubble size would increase with decreasing  $\sigma$  (see for example Baiter 1974). Then the present observations suggest that the single bubble dynamics considerations may not be accurate in predicting radiation of cavitation noise from a cavitation zone thickly populated with vapour bubbles. Such considerations necessarily ignore possible interference effects which may influence the bubble dynamics aspects. In addition, the presence of cavitation bubbles in sufficient density near to the solid surface may alter the effective pressure distribution since basically the flow will see a modified test body.

The effect of velocity on the noise radiated due to cavitation on the Schiebe body is shown in Figure 11. It is clear that at all centre

frequencies the level increases quite sharply with increase in the magnitude of the free stream velocity. The results in Figure 12 show that the dependence of the level of cavitation noise on velocity can be expressed in the form,  $\bar{p}_s^2 = KU_m^m$ . In present work the value of  $m$  was found to vary between about 5.3 to 7.2 depending on the centre frequency (see Figure 12). It is to be noted that Blake et al. (1977) estimated the value of  $m$  to be about 3-4. Single bubble dynamics considerations (see for example Hamilton 1981) suggest that the value of the exponent should be 2.4 ignoring the compressibility effects of the liquid medium. It is not at all clear at this stage as to the reasons for the higher values of the exponent found in the present work at least at the  $\sigma$  value of 0.56 for the Schiebe body. On the untripped hemispherical nose possessing laminar separation the dependence of spectral density on the velocity is found to be somewhat different as shown in Figure 15 as compared to the trend observed for the Schiebe body as shown in Figure 11. This may be entirely due to the viscous effects associated with the presence of laminar separated region on this body.

#### 4.3 Non-dimensional Representation of Spectral Density

The spectral density can be non-dimensionalised following Blake et al. (1977) using the parameters of single bubble dynamics such as maximum radius of the bubble  $R_m$  and collapse time  $\tau_0$ . The maximum radius of the bubble can be approximately estimated from Strasberg's (1956) relationship

$$R_m = \left[ \frac{1}{2} U_\infty^2 (-\sigma - C_{pmin}) \right]^{1/2} t'$$

where  $t'$  is the residence time, i.e., the duration in which the bubble is in the region where the local pressure is less than the vapour pressure. It is given by

$$t' = \frac{1}{U_\infty (1 - \bar{C}_p)^{1/2}}$$

where  $\bar{C}_p$  is the space averaged static pressure coefficient.

The distance 'l' along the surface of the model in which the local pressure is less than the vapour pressure, is determined from the intercept of the constant  $\sigma$  line with the pressure distribution curve  $C_p$  vs  $s/D$ .

A rough estimate of  $\tau_0$  can be made using Rayleigh's relationship

$$\tau_0 = 0.915 R_m \left( \frac{\rho}{P_\infty - P_v} \right)^{1/2}$$

$$\text{i.e., } \tau_0 = 0.915 \frac{R_m}{U_\infty} \left( \frac{2}{\sigma} \right)^{1/2}$$

Analogous to one used by Fitzpatrick and Strasberg (1956) Blake et al. (1977) have given the spectral density in the non-dimensional form as

$$S(f \tau_0) = \frac{\bar{p}_s^2 (f, \Delta f)}{\Delta f} \frac{v \tau_0 r^2}{R_m^4 P_\infty}$$

Here  $v \tau_0$  is the total lifetime of the bubble including growth, initial collapse and rebounding times expressed in multiples of  $\tau_0$ . Blake et al. (1977) have suggested that the value of  $v$  should be taken approximately equal to 3. In the absence of any experimental study on the bubble dynamics in the present work the value of  $v$  was chosen to be the same as that used for example by Blake et al. (1977).

For the Schiebe body the non-dimensionalized spectral density for various combinations of the free stream parameters is shown in Figure 13. It can be seen that the collapse of data is quite good for non-dimensional frequency parameter value of up to about 4. At higher values of  $f \tau_0$  the scatter is found to be quite high comparatively. It is presumed that this unexpected spread is due to the peak found in almost all the noise spectra at a centre frequency of 63 kHz as shown for example in Figure 11 for the Schiebe body. The reasons for this peak in the absence of bubble splitting phenomenon of the type observed by Blake et al. (1977) are not clear. For the hemispherical nose, in particular for the tripped case the collapse of data (Figure 18) was generally similar to that for the Schiebe body just discussed. For the untripped case the scatter was somewhat greater even at low values of  $f \tau_0$  and in particular for the data at lower velocities. Again one may suspect the role of laminar separated region whose length varies with velocity to at least partly be responsible for these observations. As shown in Figure 19 the attempted collapse of cavitation noise data from all the three test bodies at selected combination of free stream parameters is found to be only adequately good. Again the observed peak in the spectral densities at 63 kHz seems to distort the collapse.

## 5. CONCLUSION

It is found that seeding the flow with artificial nuclei has an important effect on cavitation inception, type of cavitation and resulting noise. One important observation was that with artificial nuclei the cavitation inception number did not show a strong dependence on velocity on three different test bodies having different hydrodynamic characteristics which otherwise would not have been the case. In addition, the cavitation observed was that of the travelling bubble type which was steady and uniform around the headform. This was helpful in obtaining systematic cavitation noise data at various free stream conditions. Cavitation noise spectral densities showed a complex behaviour with  $\sigma$ ; initially the levels increased with decrease in  $\sigma$ , and after reaching a peak they subsequently decreased in levels with further decrease in  $\sigma$ . Within the range of velocities in the present tests the cavitation noise spectral densities showed a rather sharp increase with increase in  $U_\infty$ . The mean square sound pressure was found to be proportional to  $U_\infty^m$  with  $m$  values ranging from 5.3 to 7.2 at different centre frequencies. The presentation of the noise data in normalized coordi-

nates showed the collapse to be quite good (within 5 dB) at non-dimensional frequency values of  $f\tau_0$  less than about 4. At higher  $f\tau_0$  values the spread was rather high being of the order 10-15 dB. The present results could have been viewed with greater confidence had the reverberation corrections been applied to the cavitation noise data. In any case these corrections would not influence our findings on the dependence of cavitation noise on free stream parameters like  $\sigma$  and  $U_\infty$ .

#### ACKNOWLEDGEMENTS

The financial support for this study has been provided by the Electronics Commission, Government of India which is gratefully acknowledged.

#### REFERENCES

- Acosta, A.J. and B.R. Parkin (1975). Cavitation inception - A selective review, *J. Ship Res.* 19, 4, 193.
- Albrecht, K. and O. Bjorheden (1975). Cavitation testing of propellers in a free surface tunnel utilising micro air bubble control, *J. Fluids Engg.* 97, 523.
- Arakeri, V.H. (1979). Cavitation inception, *Proc. Indian Acad. Sci.* 2, 2, 149.
- Arakeri, V.H. and A.J. Acosta (1973). Viscous effects in the inception of cavitation on axisymmetric bodies, *J. Fluids Engg.* 95, 519.
- Arndt, R.E.A. (1981). Cavitation in fluid machinery and hydraulic structures, *Annual Review of Fluid Mechanics*, 13, 273.
- Baiter, H.J. (1974). Aspects of cavitation noise, *Netherlands Ship Model Basin*, Publ. No. 490.
- Barker, S.J. (1976). Measurements of hydrodynamic noise from submerged hydrofoils, *J. Acoust. Soc. Am.* 59, 1095.
- Blake, W.K. et al. (1977). Cavitation noise and inception as influenced by boundary layer development on a hydrofoil, *J. Fluid Mech.* 80, 617.
- Carroll, J.A. (1981). Observations of the effects of boundary layer and nuclei on cavitation of axisymmetric bodies, *Penn. State Univ. TM* No. 81-60.
- Fitzpatrick, H.M. and M. Strasberg (1956). Hydrodynamic source of sound, *First Symp. on Naval Hydrodynamics ONR Washington*.
- Gates, E.M. and A.J. Acosta (1978). Some effects of several free stream factors on cavitation inception on axisymmetric bodies, *Twelfth symp. on Naval Hydrodynamics ONR Washington*.
- Gates, E.M. et al. (1979). Cavitation inception and nuclei distributions. *Joint ARL/CIT experiments, California Institute of Technology*, Rep. No. E 244.1.
- Hamilton, M.F. (1981). Travelling bubble cavitation and resulting noise, *Penn. State Univ. TM* No. 81-76.
- Holl, J.W. (1970). Nuclei and cavitation, *J. Basic Engg.*, Dec., 681.
- Johnson, V.E. and T. Hsieh (1966). The influence of the trajectories of gas nuclei on cavitation inception *Sixth Symp. on Naval Hydrodynamics ONR Washington*.
- Jorgensen, D.W. (1961). Noise from cavitating submerged water jet, *J. Acoust. Soc. Am.* 33, 1334.
- Keller, A. (1972). The influence of the cavitation nucleus spectrum on cavitation inception investigated with a scattered light counting

- method, J. Basic Engg., Dec., 917.
- Kodama, Y. et al. (1979). The effect of nuclei on the inception of bubble and sheet cavitation on axisymmetric bodies, Int. Symp. on Cavitation Inception, ASME, 75.
- Lesunovskii, V.P. and V. Khokha Yu (1969). Characteristics of the noise spectrum of hydrodynamic cavitation on rotating bars in water, Sov. Phy. Acoust., 14, 474.
- Morozov, V.P. (1969). Cavitation noise as a train of sound pulses generated at random times, Sov. Phy. Acoust., 14, 361.
- Noordzij, L. (1976). Some experiments on cavitation inception with propellers in NSMB depressurized towing tank, Int. Shipbldg. Prog., 23, 1.
- Strasberg, M. (1977). Propeller cavitation noise after 35 years of study, Proc. ASME Symp. Noise and Fluids Engg., 89.
- Thompson, D.E. and M.L. Billet (1977). Initial investigation of stationary hydrofoil cavitation and cavitation noise scaling, Penn. State Univ. TM No. 77-323.

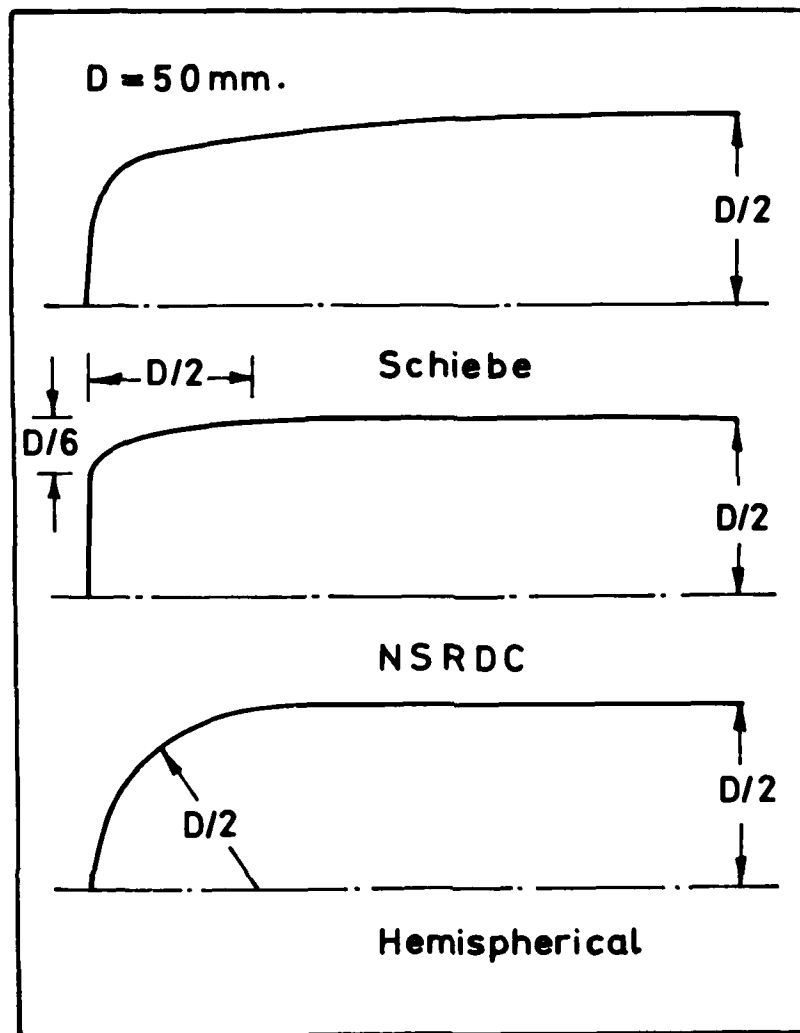


Figure1—Geometry of the Test Bodies



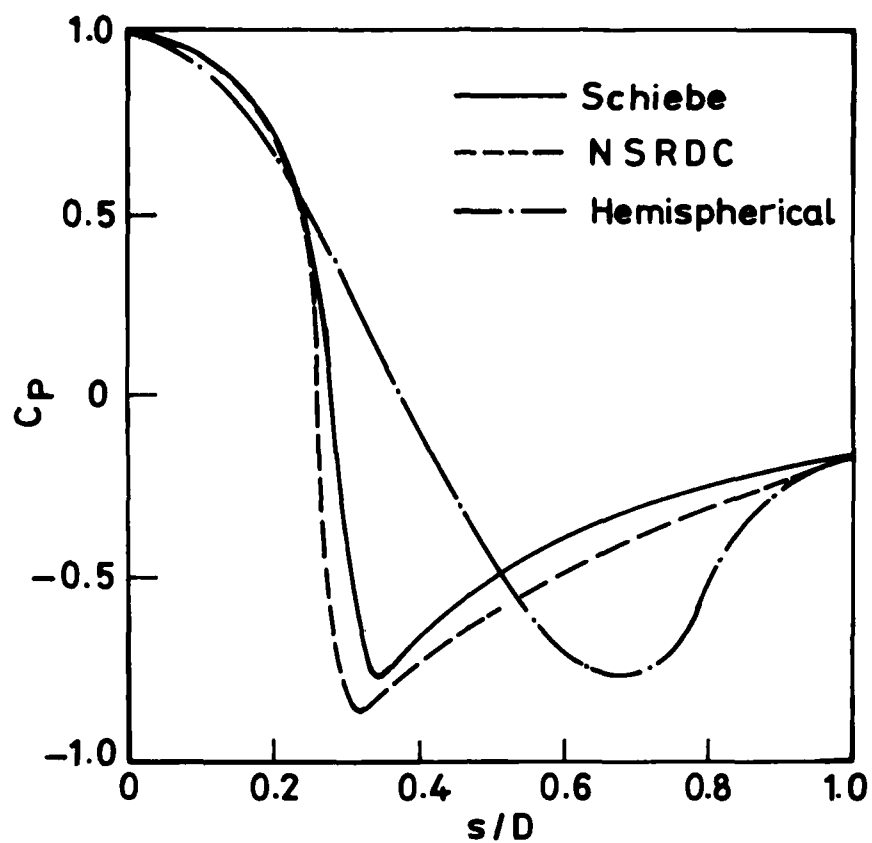


Figure 2—Theoretical Pressure Distributions

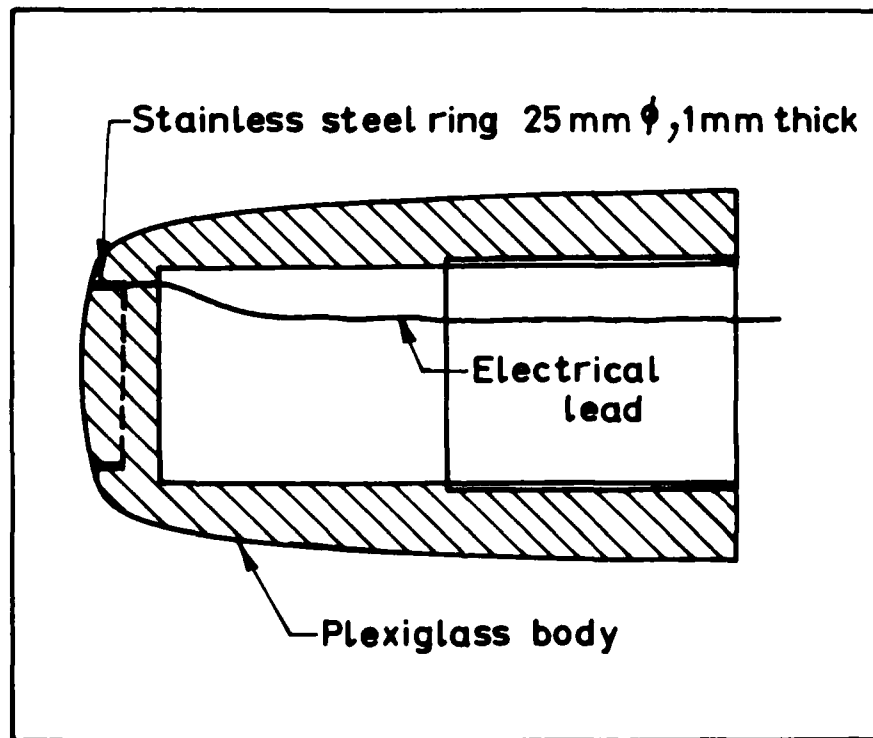


Figure 3—Schematic Sketch Showing the Electrolysis Ring.

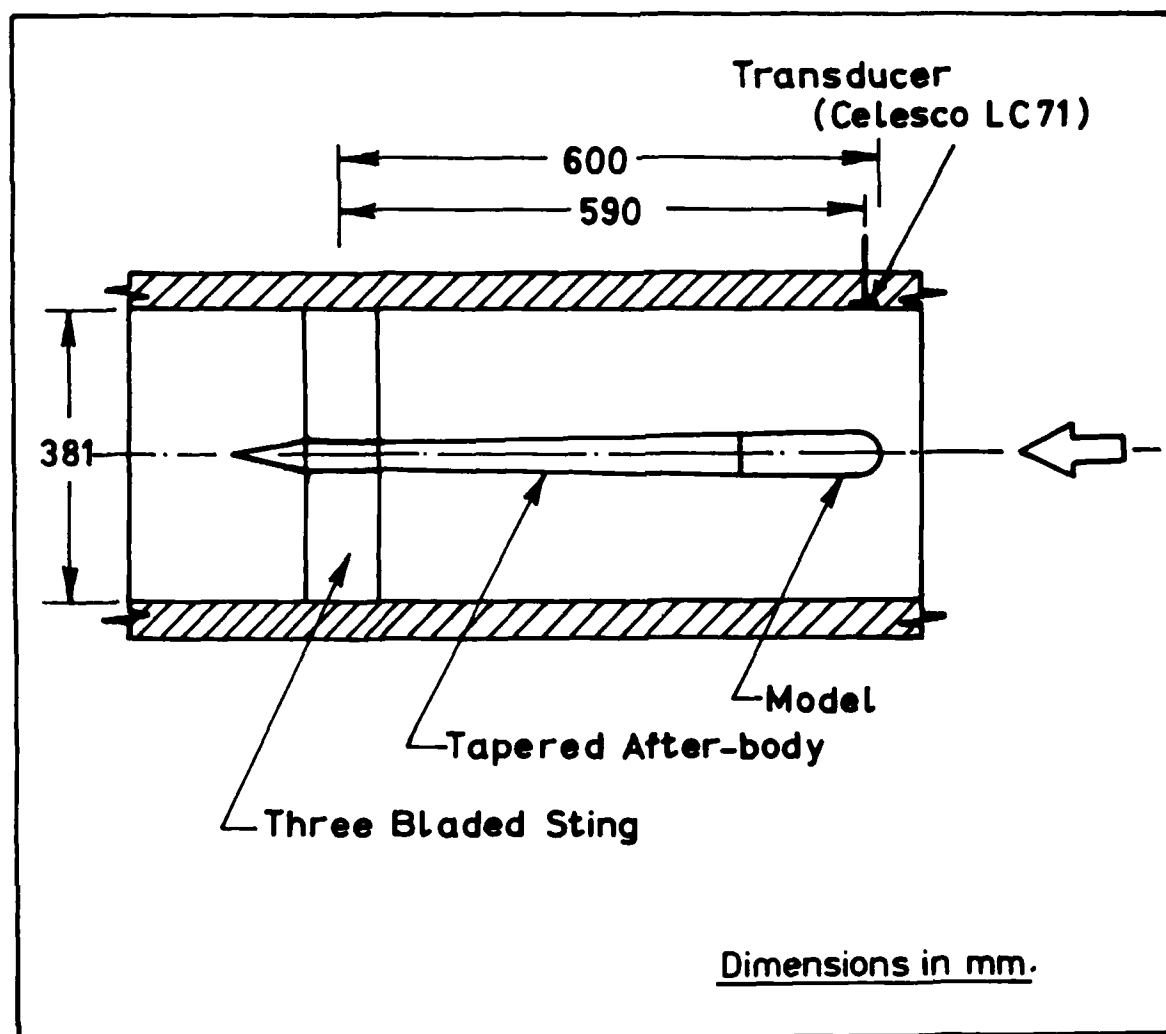


Figure 4 - Schematic Sketch Showing the Location of Transducer and Test Body in the Test Section.

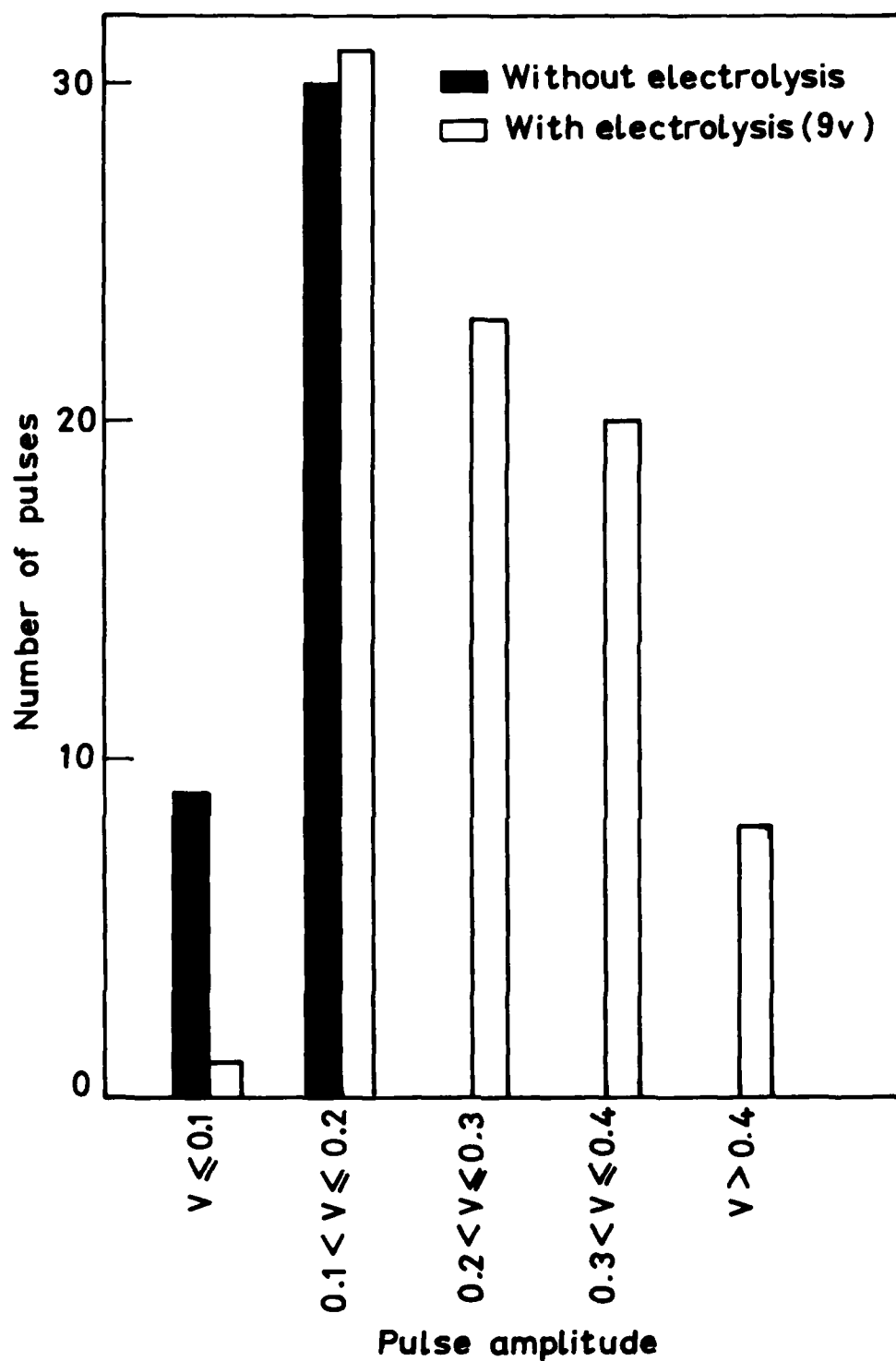


Figure 5-Effect of Electrolysis on Nuclei Population.

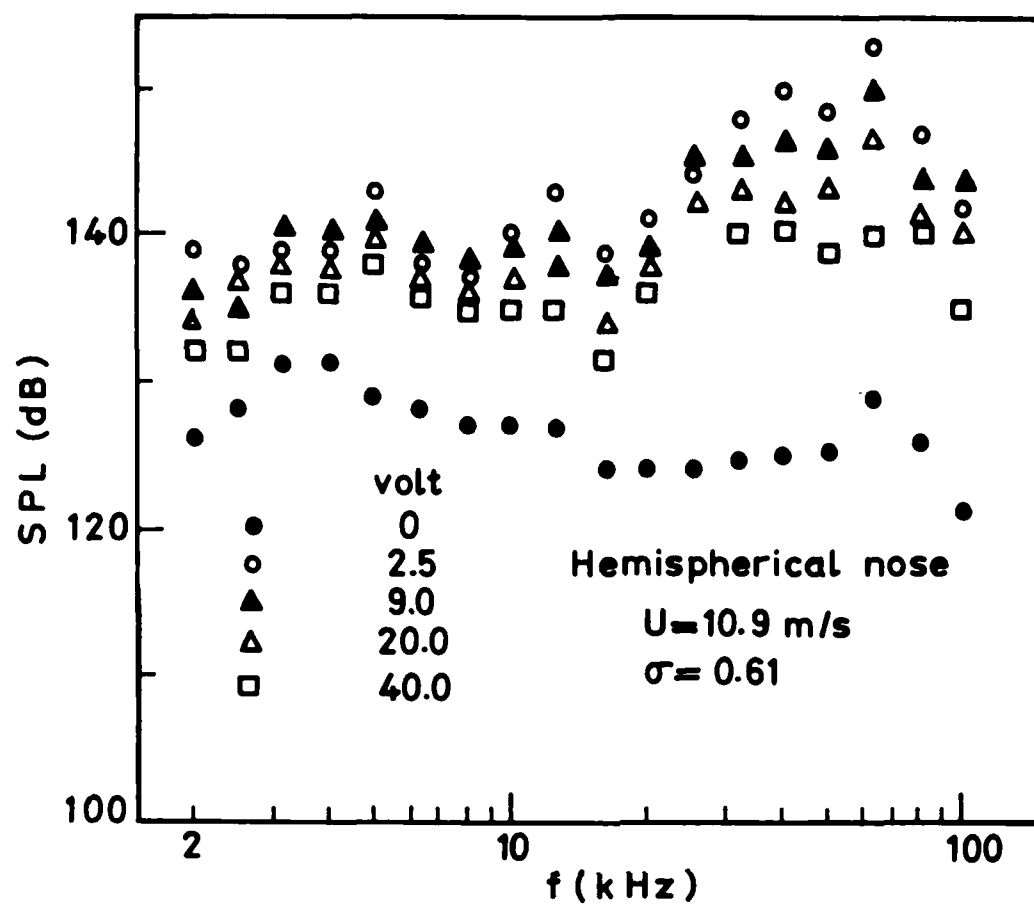


Figure 6—Influence of Electrolysis Voltage on Noise Spectrum

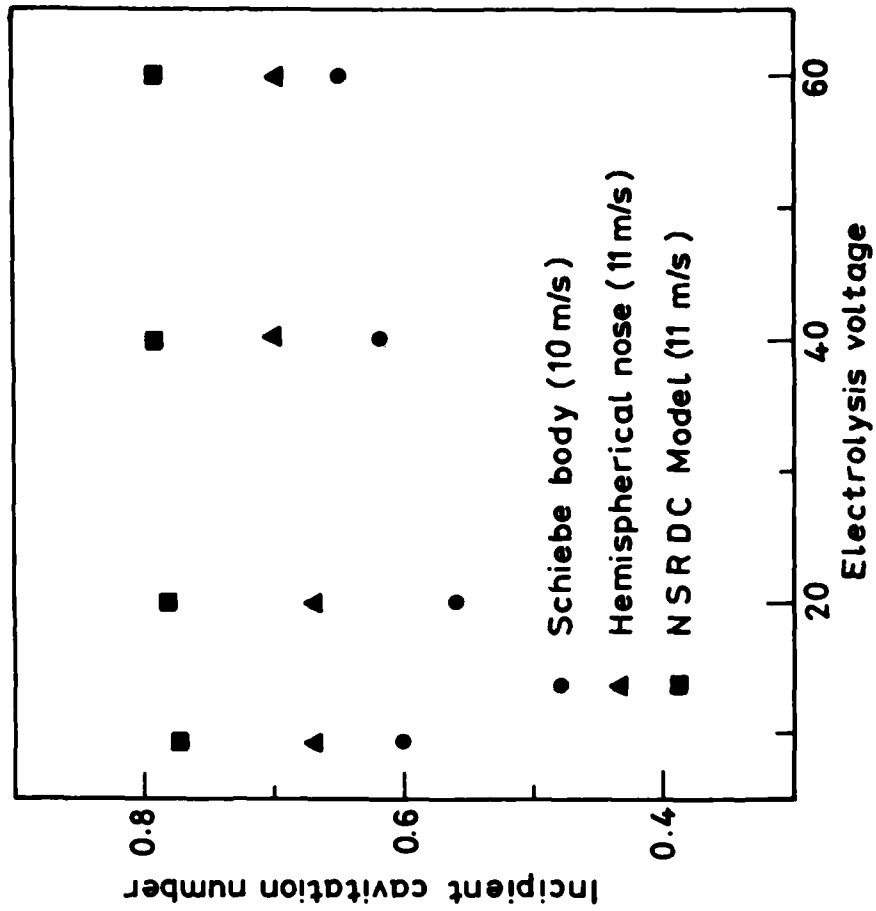


Figure 8 - Incipient Cavitation Number Vs Electrolysis Voltage.

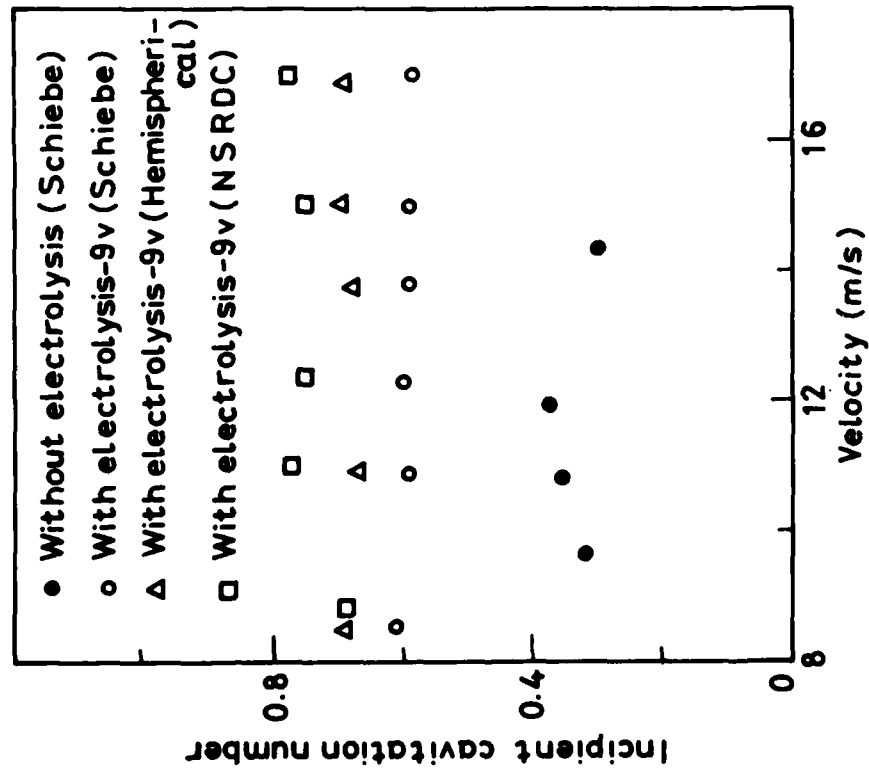
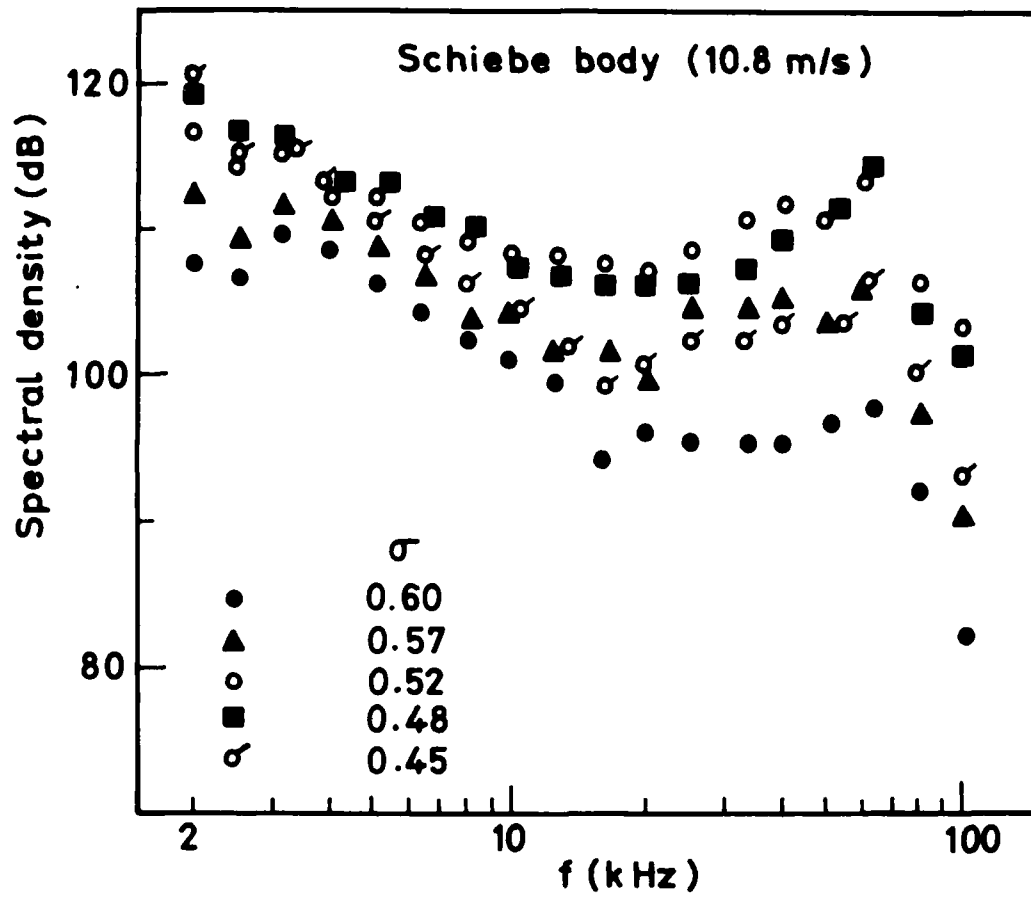


Figure 7 - Incipient Cavitation Number Vs Velocity.



**Figure 9—Influence of Cavitation Number on Spectral Densities for Schiebe Body.**

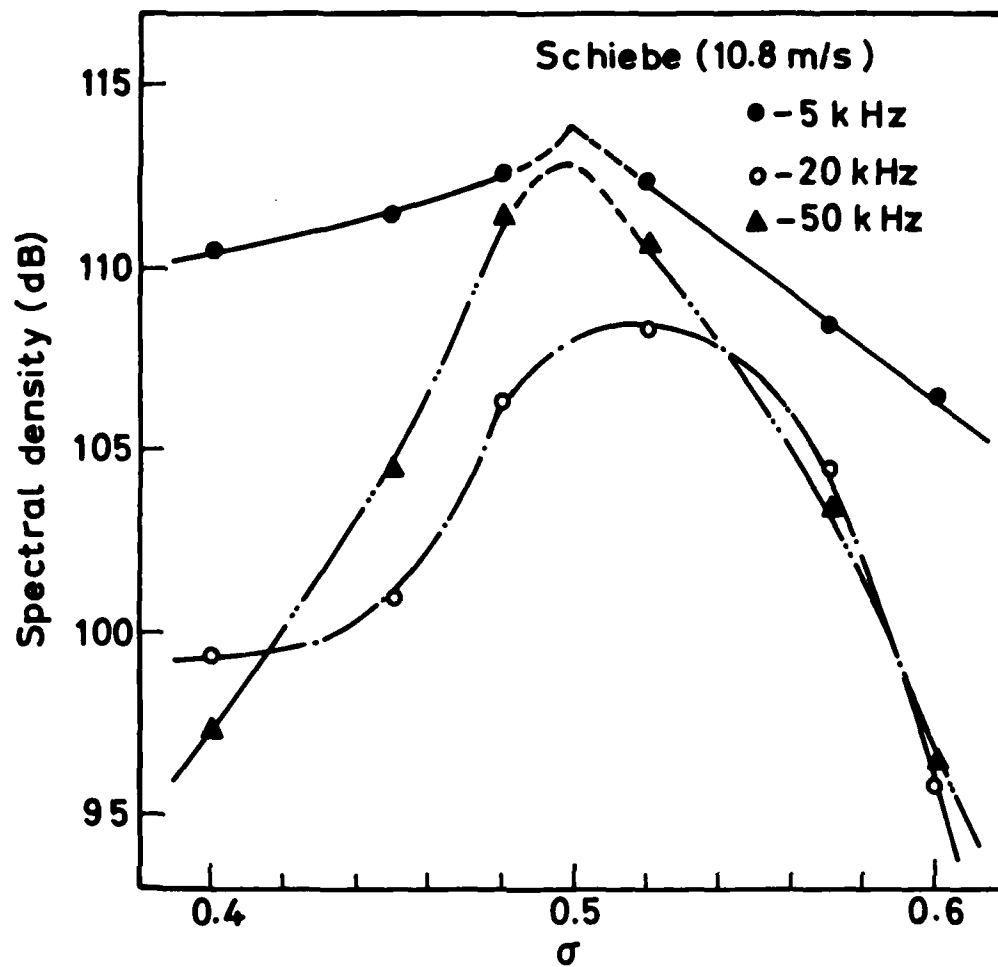


Figure 10—Influence of Cavitation Number on Spectral Densities at Different Central Frequencies on Schiebe Body.

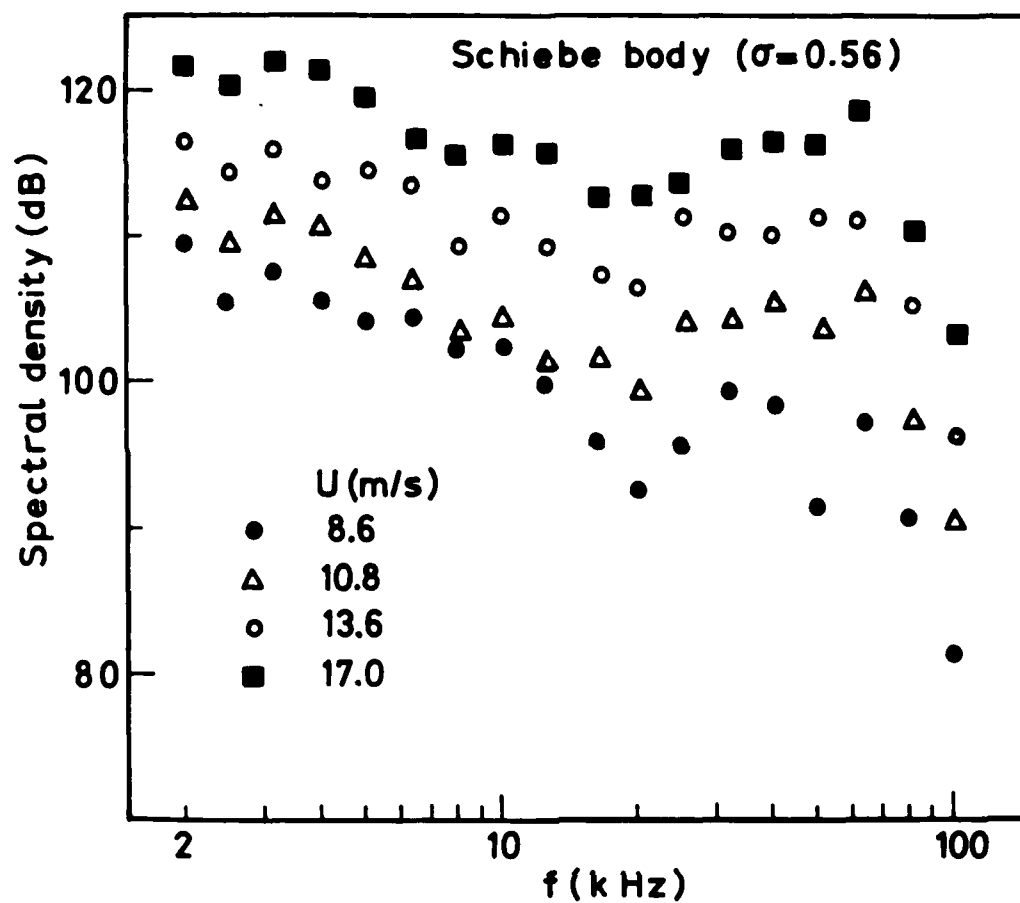


Figure 11—Influence of Velocity on Spectral Densities for Schiebe Body.



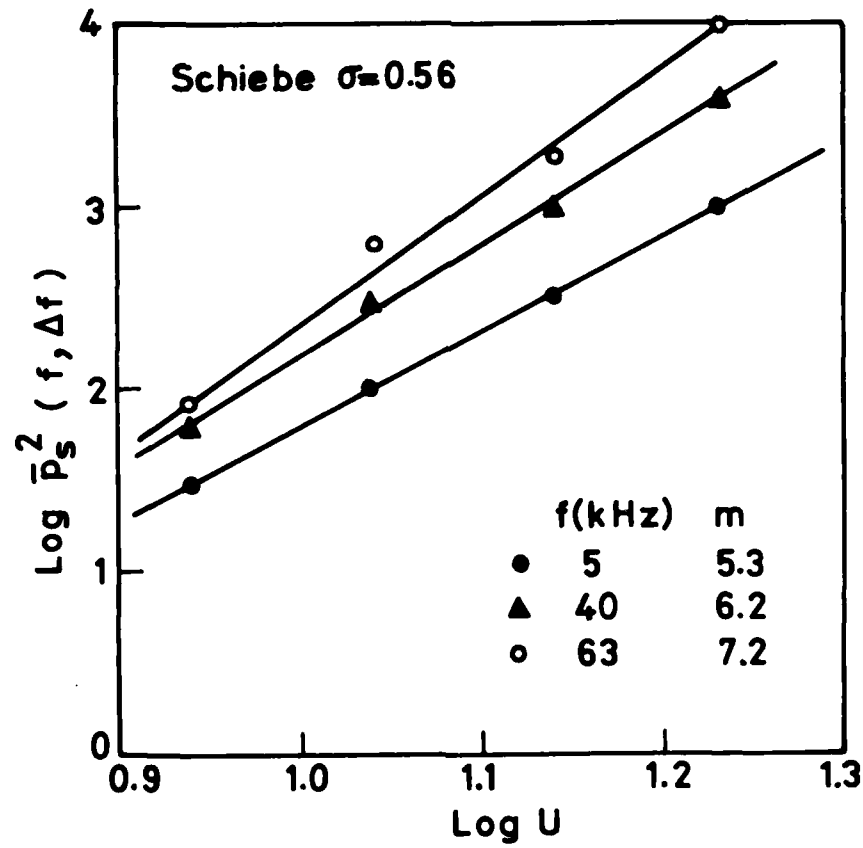


Figure 12—Influence of Velocity on Mean Square of Sound Pressure at Different Centre Frequencies on Schiebe Body.

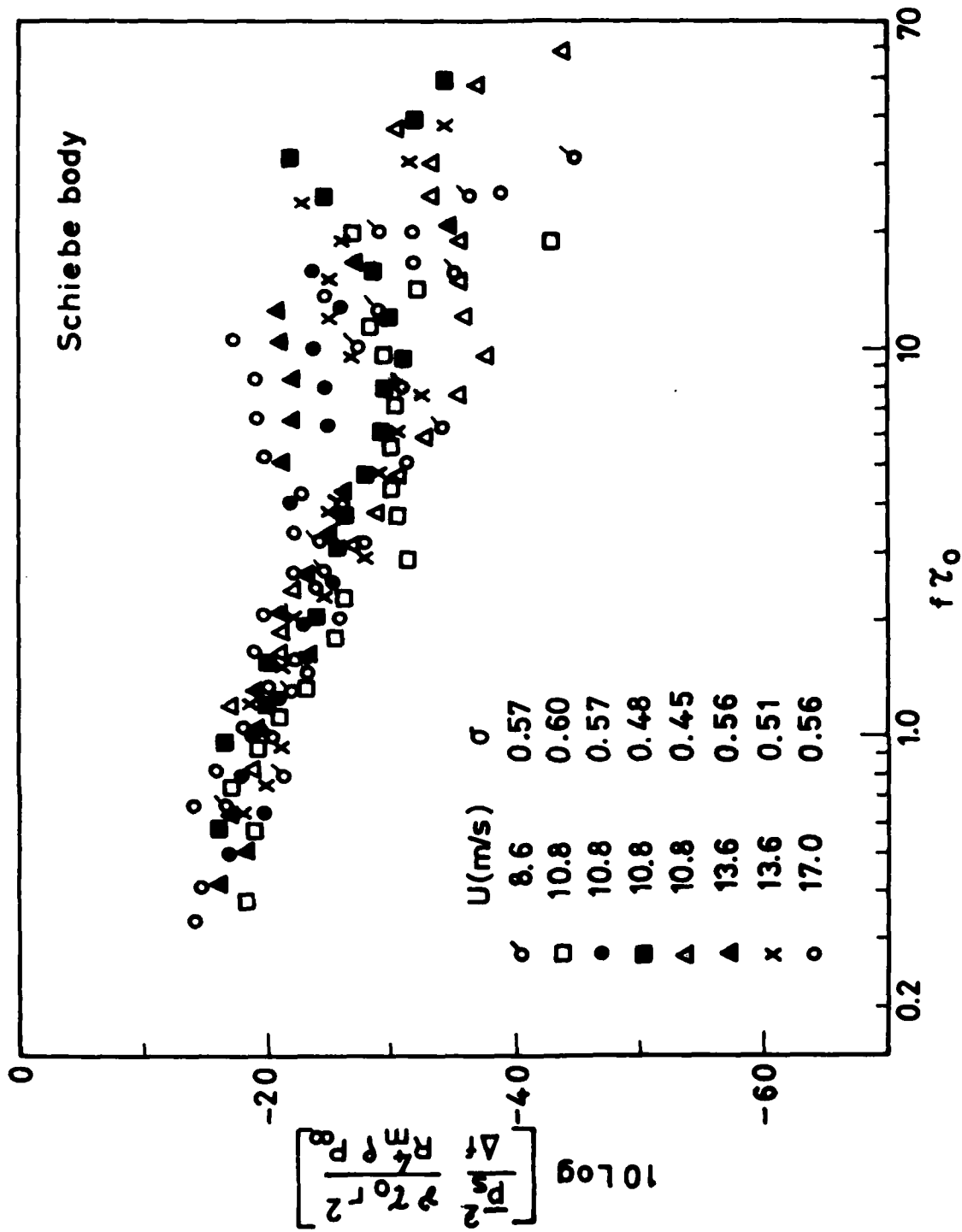


Figure 13—Non-dimensional Spectral Densities for Various Conditions on Schiebe Body.

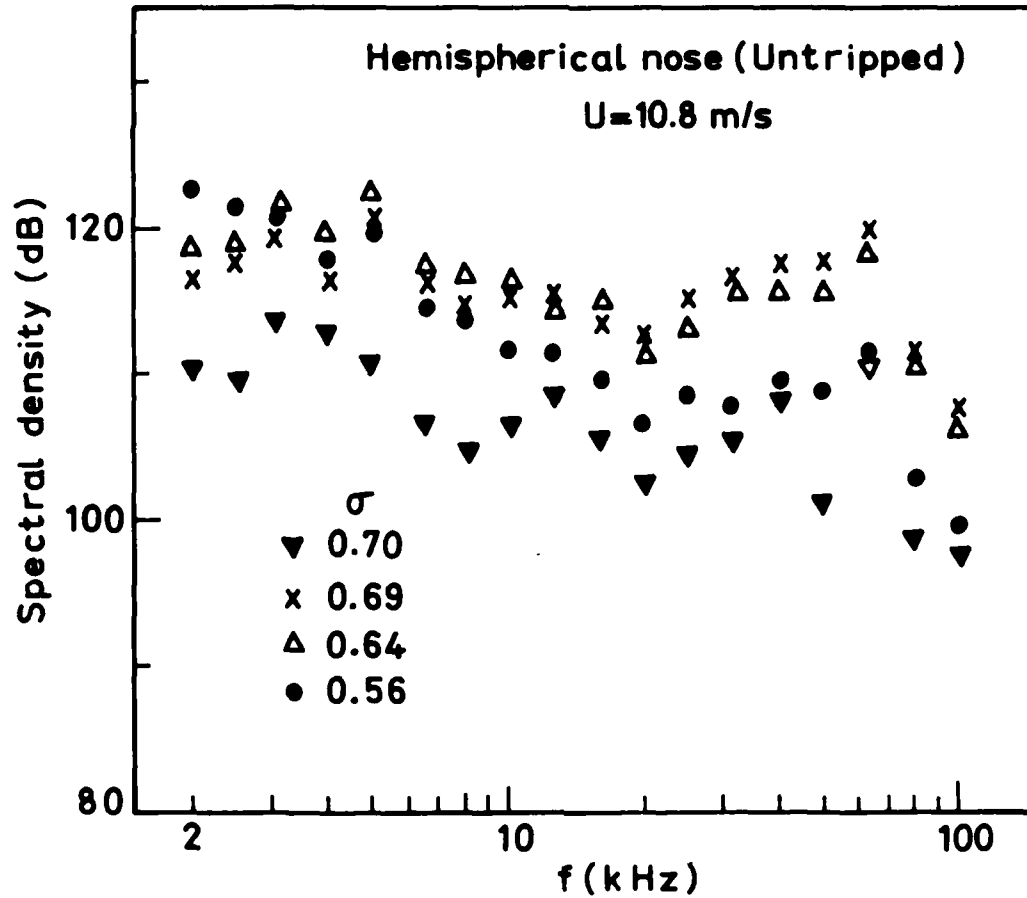


Figure 14—Influence of Cavitation Number on Spectral Densities for Hemispherical Nose (untripped).

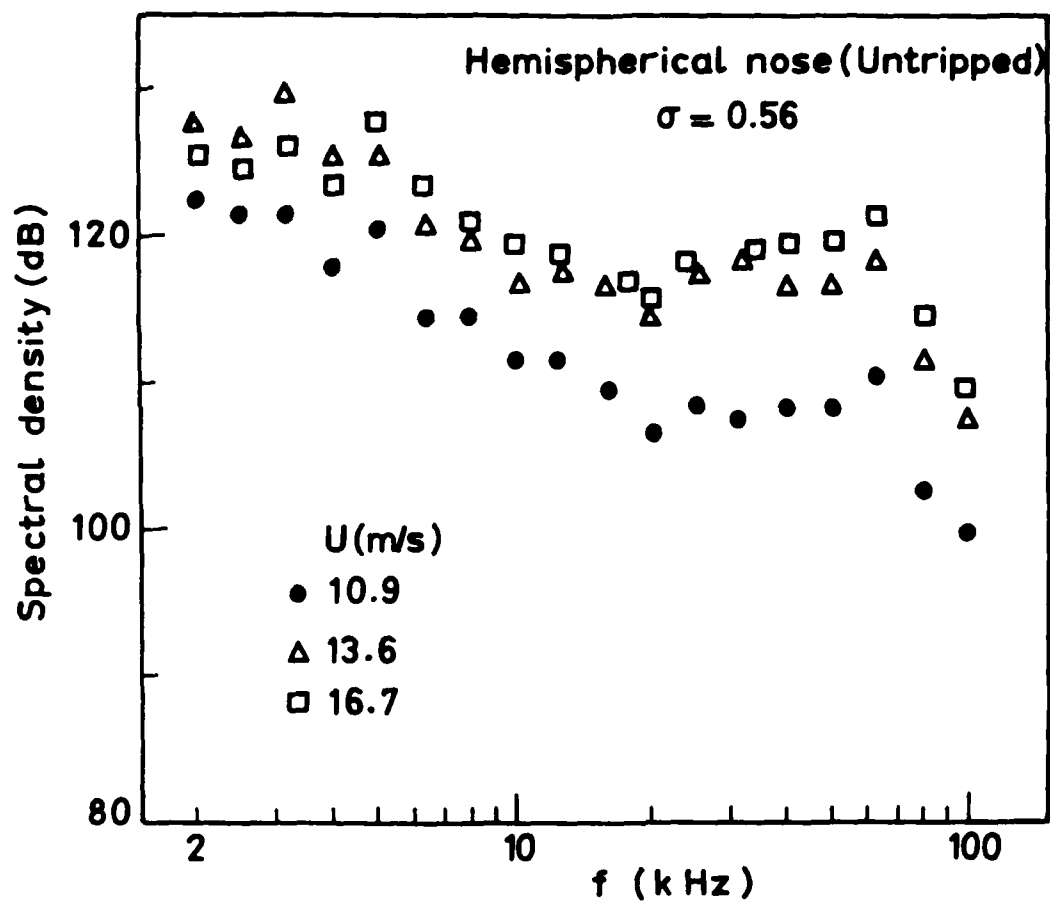


Figure 15—Influence of Velocity on Spectral Densities for Hemispherical Nose (untripped).

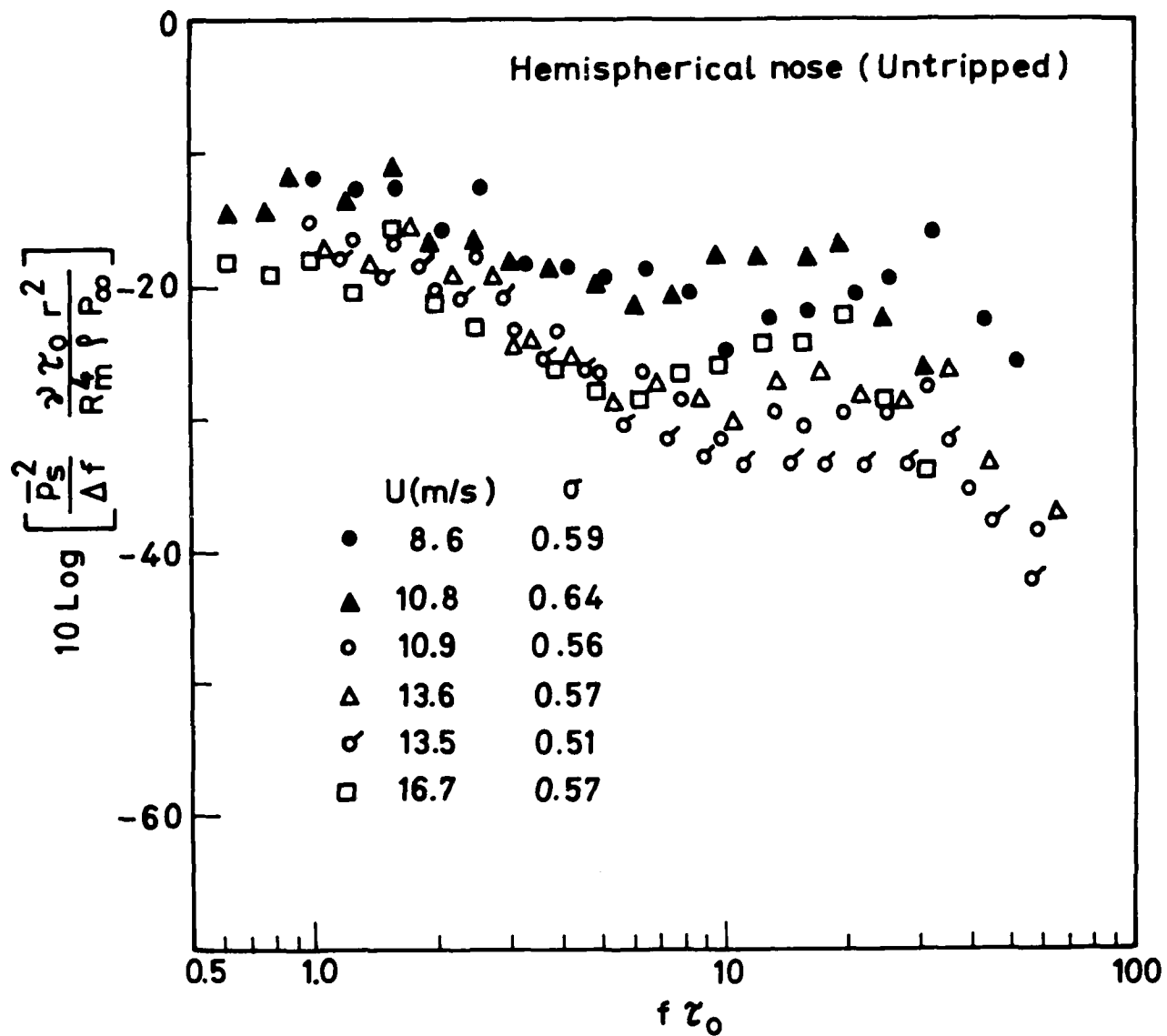


Figure 16—Non-dimensional Spectral Densities for Various Conditions on Hemispherical Nose (untripped).

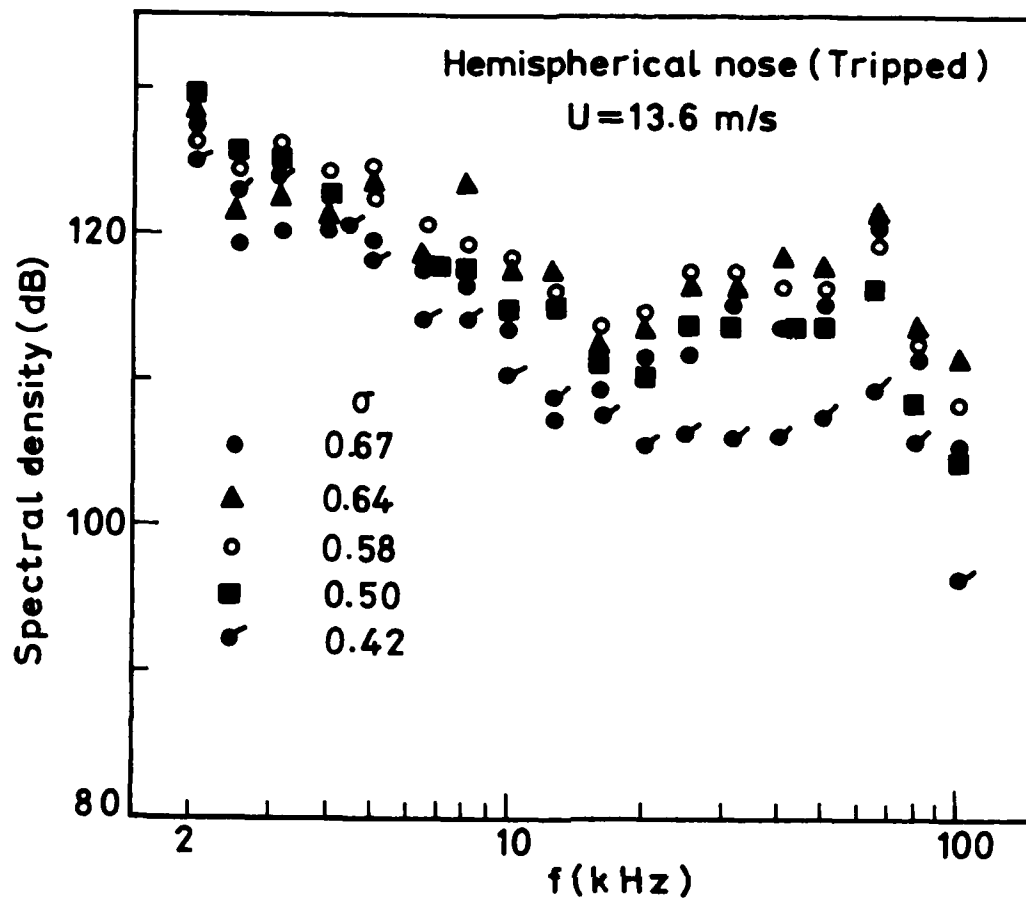
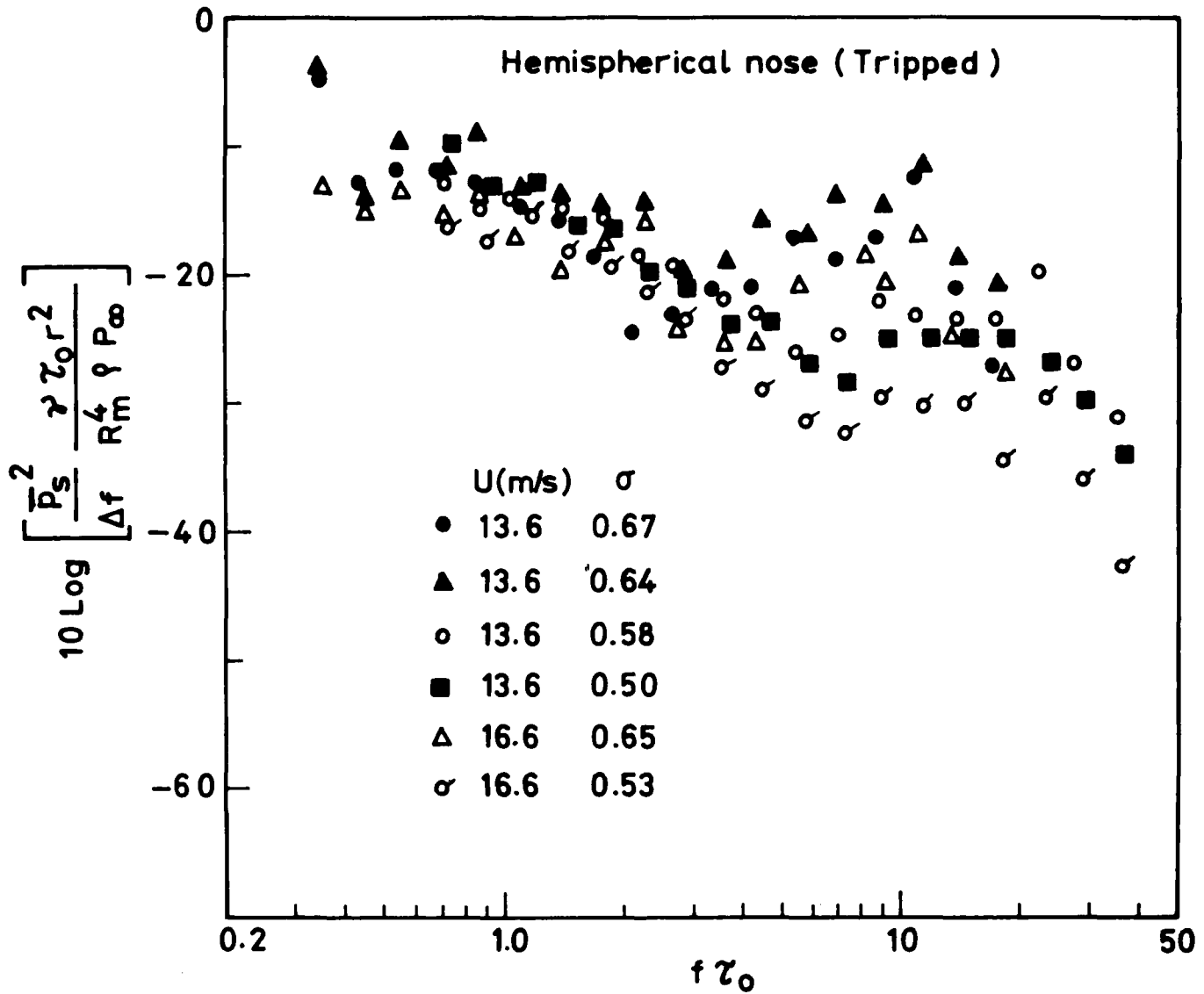


Figure 17—Influence of Cavitation Number on Spectral Densities for Hemispherical Nose (Tripped).



**Figure 18—Non-dimensional Spectral Densities for Various Conditions on Hemispherical Nose (Tripped).**

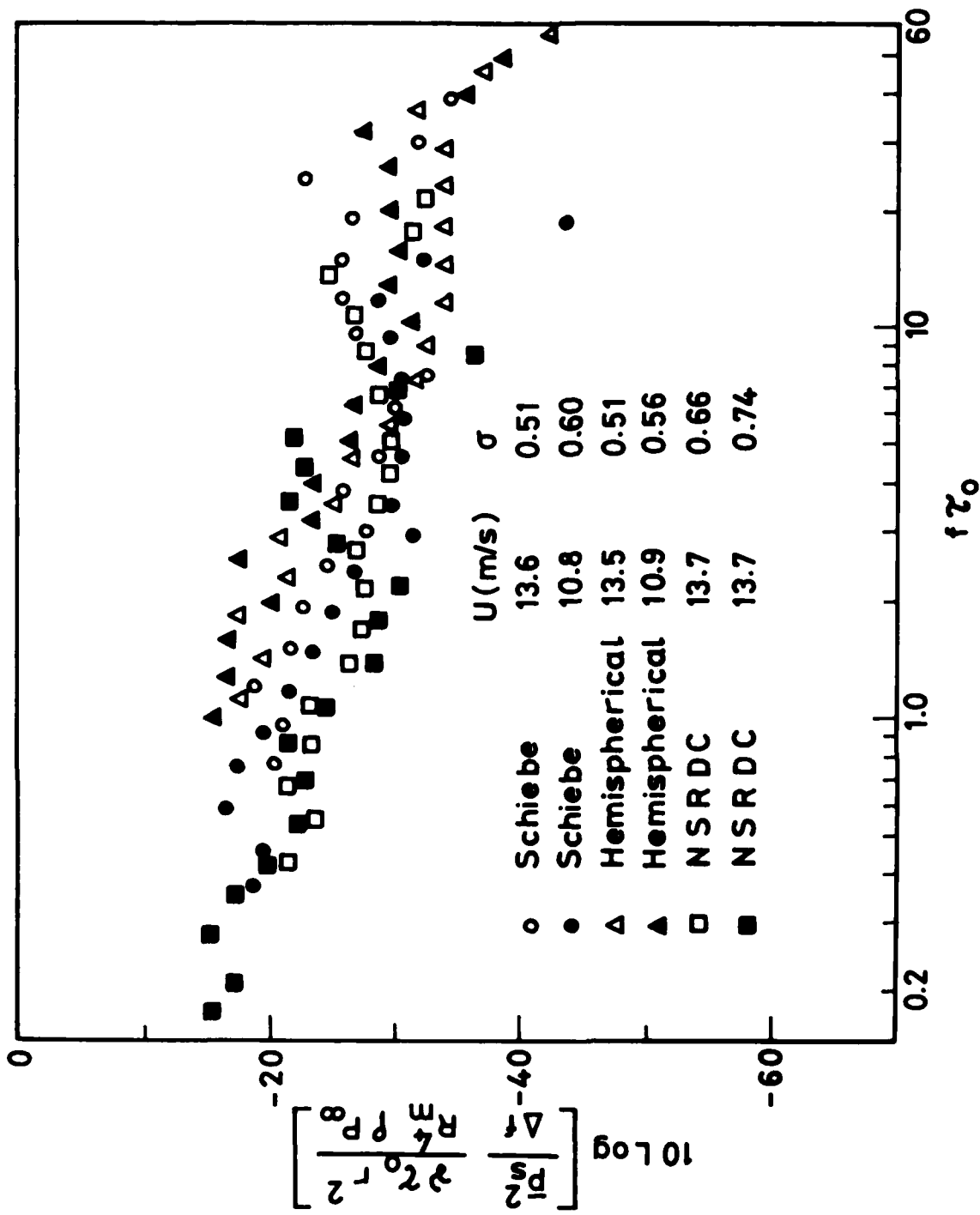


Figure 19—Non-dimensional Spectral Densities for Various Conditions on Three Test Bodies.



## Discussion

T.T. Huang (DTNSRDC)

Does your bubble-seeding technique (electrolysis) trip the boundary layer? If so, how much increase in noise is caused by the tripping itself. The increase of microbubble population will cause an increase of the occurrence of bubble cavitation events. Further increase of microbubble population, the interaction of individual bubble cavitation, and the noise associated with the interaction become important. Based on your data, can you address this interaction problem?

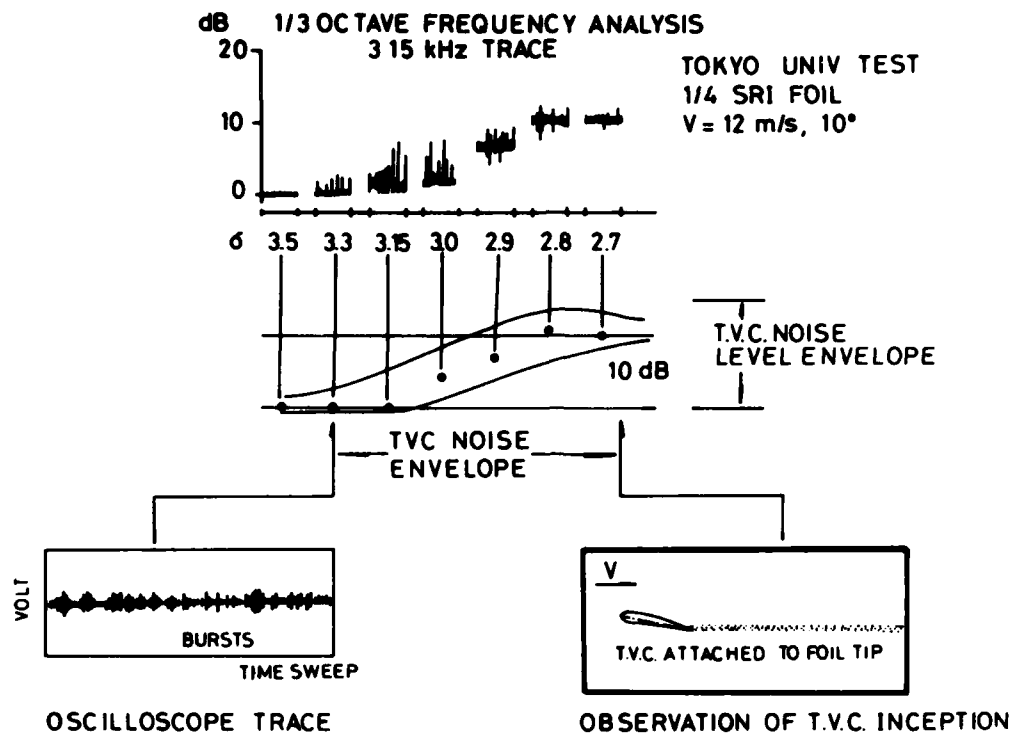
On a large-scale body, traveling bubble cavitation becomes less important. Do you intend to extend your research to cover the noise associated with sheet and attached cavitation?

R. Latorre (University of Michigan)

Several years ago I attempted to measure the cavitation noise during inception on an ITTC headform tested in the cavitation tunnel of the Ship Research Institute, Mitaka, Japan. Unfortunately, cavitation formed on the mounting sting, which tended to mask the inception noise. At lower  $\sigma$  there was a good correspondence with the visual observation of cavitation inception and the increase in the noise signal. Did the authors find a similar correspondence?

Regarding Section 4.2, the cavitation noise from a tip vortex cavity shed from three-dimensional hydrofoils and rotating propellers<sup>1-4</sup> also increased with lowered  $\sigma$ , reached a maximum, and then decreased with further reduction in  $\sigma$ . This has been characterized as a tip vortex cavitation noise envelope shown in Figure 1. At the peak noise level, what were typical cavitation patterns on the head form? With tip vortex cavitation the noise level decreased with the formation of the vortex cavity.

In Section 4.3 the authors have used  $\gamma = 3.0$  and noted that above nondimensional frequency values of 4, the data have a large spread. Did they attempt to use another  $\gamma$  value, and, if so, what was the result on the data collapse? On the other hand, the authors indicate the noise level  $\sim kU^m$ , where  $m$  is 5.3 to 7.2 in the present work and was 3-4 for another researcher. This difference might be a difference in the cavitation pattern and type. Could the authors provide sketches of the cavitation pattern on the head and associated noise?



## References:

1. Latorre, R. "Experimental Study of Model Propeller Tip Vortex Cavitation Noise," *Acoustica*, Vol. 47, No. 2, 1981, pp. 132-141.
2. Latorre, R. "Propeller Tip Vortex Cavitation Noise Inception," *Proceedings Propellers '81 Symposium*, SNAME, May 1981, pp. 319-334.
3. Latorre, R. "Study of Tip Vortex Cavitation Noise from Foils," *International Shipbuilding Progress*, Vol. 27, No. 307, 1980, pp. 66-85.
4. Latorre, R. "TVC Noise Envelope--An approach to Tip Vortex Cavitation Noise Scaling," *Journal of Ship Research*, Vol. 26, No. 1, March 1982, pp. 65-75.

## Author's Reply

V. Shanmuganathan and V. Arakeri

To R. Latorre

The authors wish to thank Prof. Robert Latorre for his useful discussion on their paper.

As indicated in Section 3.0, though there was cavitation on the strut supporting the model in the present work, there was a substantial increase in the SPL, as much as 20 dB at certain frequencies when the electrolysis was on, and there was a good correspondence between the onset of cavitation on the model and increase in noise level at all values.

With electrolysis on, the type of cavitation was that of traveling bubble only at all conditions. Also, the SPL was lower at very low cavitation numbers when the extent of cavitation became larger.

Even from the theoretical solution of the Rayleigh-Plesset equation, the value of  $\gamma$  was found to be around 3. Hence the authors did not choose to use any other value of  $\gamma$  in normalizing the data. With regard to Prof. Latorre's suggestion that the difference in  $m$  value between the present experiments and those of Blake could be due to the difference in the type of cavitation, it is to be pointed out that in both cases the type of cavitation observed was that of traveling bubble; however, the complications arising due to bubble splitting, etc. present in Blake's experiments was not possible and observed in the present experiments. In addition, in the present work, the extent of cavitation scaled uniformly with the cavitation number owing to nuclei seeding, whereas this would not be ensured in the Blake experiments. These differences may perhaps be responsible for the observed differences in the value of  $m$ .

# Cloud Cavitation: Theory

G. L. Chahine, HYDRONAUTICS, Incorporated

## ABSTRACT

The collapse of a bubble cloud, due to a change in the surrounding pressure, is considered, first, by using a single perturbation theory. The interaction of any individual cavity with the rest of the cloud is modelled using matched asymptotic expansions in powers of the ratio between the characteristic bubble radius and interdistance. Up to the third order, the problem is shown to be equivalent to the interaction of two cavities of different collapsing strengths. The numerical results obtained with a symmetrical repartition of bubbles on a spherical shell show that the influence of the other bubbles in the cloud on the collapse of a particular bubble is to reduce the driving pressure during most of the collapse time, thus delaying the implosion, and then to dramatically increase this pressure producing a violent end of the collapse. The pressure released is then orders of magnitude higher than with an isolated bubble. This pressure, which is being imposed on an area of the same size as the whole cloud, could explain the high erosion rates and bending of foil trailing edges. In the second part, a continuum medium approach of the cloud is considered in order to extend the validity of the preceding approach to higher void fraction and to enable to account for the compressibility of the bubbly medium.

## I. INTRODUCTION

The design criteria for high-speed ship propellers involve trade-offs between efficiency and cavitation, and strength and vibration of the propeller. Operating in ship wakes at relatively low cavitation numbers, the propeller will, at least intermittently, cavitate, inducing erosion of the blades, loss of efficiency, noise, vibration, and occasionally structural failure of nearby plating. These harmful effects are mainly due to the collapse of unsteady cavities. These include individual bubbles as well as sheet cavities and "clouds" (Figure 1).

Adequate and increasingly sophisticated theories for individual bubble growth and collapse exist (see the reviews by Plesset and Prosperetti, 1977 and Hammitt, 1980). While the transition to sheet

cavity is not well-understood, a large number of experimental observations of sheet cavitation are available (Shen and Peterson, 1979, Bark and Barlekom, 1979), and a steady, then unsteady, theory for sheet cavitation was recently developed (Tulin, 1980 and Tulin and Hsu, 1980). Downstream of a "steady" sheet cavity a region of high population of tiny bubbles can be observed and is especially known to be associated with erosion. However, as concluded from observations by Tanabayachi and Chiba (1977), an unsteady sheet cavity is required for the formation of coherent clouds of very fine bubbles. These clouds are either detached from the frothy mixture at the trailing end of the unsteady sheet, or generated in a finite region of the liquid downstream of the unsteady sheet where significant fluctuating pressures exist.

As the pressures generated by single bubble collapse are not strong enough to explain the intense erosion in the subject region, and the high forces needed, for example, to bend the trailing edge, cloud cavitation has been held responsible since Van Manen's (1963) work. This is supported experimentally by a very close correlation between the dynamics of these clouds and the sharpest and highest pressure pulses detected on an oscillating hydrofoil (Bark and Barlekom, 1979). Similar phenomena have been observed with ultrasonic cavitation (Hanson and Mørch, 1980).

Apart from some information on the frequency of generation of cloud cavitation, the experimental observations and measurements are very qualitative and do not allow at the present time, any quantitative predictions. In addition, the lack of understanding of the dynamics of such cavities makes it impossible to explain any scaling effects and to correct for them. Theoretical and fundamental studies are thus needed as guidance for future design and experimentation.

To our knowledge, since the early work of Van Wijngaarden (1964) only a few publications by Mørch (1977, 1980, and 1982) and Hanson and Mørch (1980) have dealt theoretically with the problem of "collective bubbles collapse" or "cavity cluster collapse." However a large amount of literature has been devoted to the modeling of bubble-liquid mixture behavior, using either a continuum medium approach or a "two-fluid" approach (Zwick, 1959; Van Wijngaarden, 1972, 1976, 1980, 1982; Zuber, 1964; Ishii, 1975). In order to explain the phenomenon of propeller blades bent at the trailing edge, Van Wijngaarden (1964) considered the case of a uniform layer of cavities on a solid wall. He studied its unidimensional collective collapse when the surrounding fluid is suddenly exposed to a pressure increase. He derived the continuity and momentum equations for the layer, neglecting the convective and dissipative terms and assuming that the volume fraction of gas is small enough to authorize such approximations. However, he took into account the individual bubble radial motion and translation, neglecting viscous effects. Solving the derived system of equations, Van Wijngaarden found a considerable increase of the pressure along the wall due to collective effects.

Mørch (1977, 1980), concerned with ultrasonic cavitation fields, considered the collapse of a hemispherical "cluster" near a wall, which by symmetry, he extended to the case of a spherical cloud. He

characterized the cloud only by its radius and a uniform volume fraction,  $\alpha$ , constant in time, and developed the following model. A pressure rise in the liquid leads to the formation of a shock wave on the "cloud boundary". The shock moves toward the cloud center leaving no bubbles behind it and thus constitutes the cloud boundary at each time. The collapse time of a spherical cloud is found to be  $\sqrt{\alpha}$  times the Rayleigh collapse time of a spherical bubble of the same initial radius. Although a very interesting approach, especially for the calculation of the collapse time, this model (like Rayleigh's model for spherical bubble collapse) is incapable, in its present state, of adequately calculating the pressure field. At the end of the collapse the cloud radius is zero and the velocities and pressures are infinite, since the model does not allow the bubbles to contain noncondensables. In addition, the main physical assumption (presence of a shock wave dividing the space in two regions one containing bubbles which do not sense the pressure variations until a later time stage, and another one where all bubbles have collapsed) is valid only for relatively high void fractions. The case of a spherical single cavity of the same size as the whole cloud is the perfect extreme example of the domain of validity of this approach. Hanson and Mørch (1980) and Mørch (1982) extended the same model to a cylindrical cloud and a layer of bubbles on a solid plate.

We present in this paper first a singular perturbation theory (Chahine, 1981) which will allow us to compute the pressure field and the cloud dynamics for the growth and collapse of a cloud composed of a finite number of bubbles. In the second part of the paper we will discuss a continuum medium approach for a bubble cloud collapse.

## II. SINGULAR-PERTURBATION THEORY

The following approach is applicable to a cloud of bubbles of low void fraction. Provided that the characteristic size of a bubble in the cloud,  $r_{b0}$ , is small compared to the characteristic distance between bubbles,  $l_0$ , we can assume in absence of initial relative velocity between the bubble and the surrounding fluid that each of the individual bubbles reacts, in first approximation, to the local pressure variations spherically as if isolated. To the following order of approximations, interactions between bubbles induce bubble motion and deformation and are taken into account. This approach is an extension of the earlier studies by Chahine and Bovis (1981) and Bovis and Chahine (1981) on the collapse of a bubble near a solid wall and a free surface, later presented more generally for nonspherical bubbles by Chahine (1982).

Since the problem possesses two different geometrical scales,  $l_0$  and  $r_{b0}$ , we can consider two subproblems: one concerned with the macroscale and the other one with the microscale. The "outer problem" is that considered when the reference length is set to be  $l_0$ . This problem is concerned with the macrobehavior of the cloud, and the bubbles appear in it only as singularities. The "inner problem" is

that considered when the lengths are normalized by  $r_{b0}$  and its solution applies to the vicinity of the considered individual bubble of center  $B^i$ . The presence of the other bubbles, all located at infinity in the "inner problem", is sensed only by means of the matching condition with the "outer problem". That is to say, physically the boundary conditions at infinity for the "inner problem" are obtained, at each order of approximation, by the asymptotic behavior of the outer solution in the vicinity of  $B^i$ . Mathematically, one has to match term by term the inner expansion of the outer solution with outer expansion of the inner solution, using the same asymptotic sequence in the two expansions.

#### A. Bubble Radius Variations

The determination of the flow field and the dynamics of any of the individual bubbles,  $B^i$ , is accessible once the boundary conditions at infinity in the corresponding "inner region" are known. Here we imposed the restrictive assumption that the void fraction is low enough so that the information about the variation of the ambient pressure around the cloud,  $P_\infty(t)$ , is transmitted to the microscale in a time scale much shorter than the bubble collapse time. Therefore, in the absence of a slip velocity between the considered bubble and the surrounding fluid and when interactions are neglected, the only boundary condition at infinity is the imposed pressure variation  $P_\infty(t)$ . The "inner problem" is therefore spherically symmetrical and its solution is given by the well-known Rayleigh-Plesset equation. With the assumption that the liquid is inviscid and incompressible this equation can be written as follows:

$$a_0 \ddot{a}_0 + \frac{3}{2} \dot{a}_0^2 = -\bar{P}_\infty(t) + \bar{P}_{g0}(a_0^{-3k} - 1) + W_e^{-1}(1 - a_0^{-1}) \quad (1)$$

In this equation, where the superscript  $i$  is omitted for convenience,  $a_0^i(t)$  is the radius of the bubble  $B^i$  normalized by  $r_{b0}$ . The times are normalized by the Rayleigh time based on  $r_{b0}$  and  $(P_0 - P_v)$ . All pressures are normalized by  $(P_0 - P_v)$  where  $P_0$  is the initial pressure, and  $P_v$  the vapor pressure.  $W_e$  is the Weber number and  $\bar{P}_{g0}$  the initial normalized gas pressure in the bubble. The noncondensable gas pressure inside the bubble,  $P_g$ , is assumed to have a polytropic behavior,  $P_g a_0^{3k} = \text{cte}$ .

When interactions cannot be neglected, still assuming that an "inner region" enclosing the bubble  $B^i$  can be defined, the boundary conditions at infinity can be much more complex than in the preceding paragraph. First, as we will see in paragraph 3, the macroscale pressure in the cloud at  $B^i$ ,  $P(B^i, t)$ , can be very different from the imposed far field pressure  $P_\infty(t)$  and depends indeed on the bubble location in the cloud. Second, a relative velocity between the bubble and the surrounding fluid,  $\underline{U}(B^i, r, t)$  can exist causing the bubble to be non-spherical. Both  $P$  and  $\underline{U}$  can be determined only by solving the equations of motion of the two-phase medium as presented in paragraph 3. Here we will limit ourselves to a small perturbation theory whose interest will be to give the behavior of the solution when the perturbation grows continuously. In that case  $P(B^i, t)$ , which is the

---

\* underlined quantities are vectors

driving pressure for the collapse of the bubble  $B^i$ , is only a perturbation of the imposed far field pressure,  $P_\infty(t)$ , and  $U(B^i, r, t)$  is a perturbation of the spherical velocity due to the bubble volume variation.

If we assume that the liquid flow is irrotational, we can define a velocity potential for the macroscale ("outer problem"),  $\phi(B^i, t)$ , and a velocity potential for the microscale ("inner problem"),  $\phi_1(B^i, r, t)$  both satisfying the Laplace equation. The matching condition between these two potentials expresses the at-infinity conditions for  $\phi_1$ , and replaces the conditions on  $P(B^i, t)$  and  $U(B^i, r, t)$ . Using the results obtained with the interaction of two bubbles and the property of addition of potential flows, this condition can be written:

$$\lim_{r \rightarrow \infty} \phi_1(B^i, r, t) = - \sum_{j=1}^N \left[ \left( \frac{\ell_{ij}^0}{\ell_{ij}^0} \right) \left( \epsilon q_0^j + \epsilon^2 q_1^j + \epsilon^3 q_2^j + \dots \right) + \right. \\ \left. + \left( \frac{\ell_{ij}^0}{\ell_{ij}^0} \right)^2 \left( \epsilon^2 q_0^j + \epsilon^3 q_1^j + \dots \right) r \cos \theta^{ij} + \right. \\ \left. + \left( \frac{\ell_{ij}^0}{\ell_{ij}^0} \right)^3 \left( \epsilon^3 q_0^j + \dots \right) r^2 P_2(\cos \theta^{ij}) + \dots \right] \quad (2)$$

where the superscript (j) denotes quantities corresponding to the other bubbles,  $B^j$ .  $\ell_{ij}^0$  is the initial distance between the bubble centers  $B^i$  and  $B^j$ .  $\theta^{ij}$  is the angle  $MB^iB^j$  and  $r$  the distance  $B^iM$ , where  $M$  is a field point in the fluid (see Figure 2).  $P_n(\cos \theta)$  is the Legendre polynomial of order  $n$  and argument  $\cos \theta$ .  $q_n^j$  is the correction of order  $\epsilon^n$  of the strength,  $q_0^j = \dot{a}_0^j (a_0^j)^2$ , of the source representing the first-approximation spherical oscillations of the bubble  $B^j$ .

Expressed in physical terms (velocities, pressures), the boundary condition (2) states that the first order correction,  $O(\epsilon)$ , to the non-perturbed spherical behavior of the bubble  $B^i$  is a spherical modification of the collapse driving pressure. This would introduce, as for two bubbles, a spherical correction of the variations  $a_0^i(t)$ . At the following orders new corrections of the uniform pressure appears, as well as a velocity field accounting for a slip velocity between the bubble and the surrounding fluid. Again, as in the two-bubble case, this induces a spherical correction and a nonspherical correction of the bubble shape. Therefore, one can show that the equation of the surface of the bubble  $B^i$  can be written in the form:

$$R^i(\theta^{ig}, t) = a_0^i(t) + \epsilon a_1^i(t) + \epsilon^2 \left[ a_2^i(t) + f_2^i(t) \cdot \cos \theta^{ig} \right] + \\ + \epsilon^3 \left[ a_3^i(t) + f_3^i(t) \cos \theta^{ig} + g_3^i(t) P_2(\cos \theta^{ig}) \right] + \dots, \quad (3)$$



Where the direction  $B^i G^i$  (see figure 2) from which is measured the angle  $\theta^{ij}$  is compounded from all the  $\theta^{ij}$  and is obtained using Equation (7) presented below. Writing the nonspherical boundary conditions on the bubble wall and expanding  $\theta_i$  in spherical harmonics one obtains the following differential equations for the successive corrections of  $a_o^i(t)$  given by (1). Superscripts(i) are omitted for convenience:

$$\begin{aligned}
 a_o \ddot{a}_1 + 3\dot{a}_o \dot{a}_1 + a_1 F_o(a_o, W_e, P_{go}, K) &= -\sum_j \left( \frac{\ell_o}{\ell_o^{ij}} \right) \dot{q}_o^j, \\
 a_o \ddot{a}_2 + 3\dot{a}_o \dot{a}_2 + a_2 F_o + F_1(a_o, a_1, W_e, P_{go}, K) &= -\sum_j \left( \frac{\ell_o}{\ell_o^{ij}} \right) \dot{q}_1^j, \\
 a_o \ddot{a}_3 + 3\dot{a}_o \dot{a}_3 + a_3 F_o + F_2(a_o, a_1, a_2, W_e, P_{go}, K) &= -\sum_j \left( \frac{\ell_o}{\ell_o^{ij}} \right) \dot{q}_2^j, \\
 a_o \ddot{d}_2 + 3\dot{a}_o \dot{d}_2 &= -\sum_j 3 \left( \frac{\ell_o}{\ell_o^{ij}} \right)^2 (\dot{a}_o q_o^j + a_o \dot{q}_o^j), \\
 a_o \ddot{d}_3 + 3\dot{a}_o \dot{d}_3 + 3F_3(a_o, a_1) \dot{d}_2 &= -\sum_j 3 \left( \frac{\ell_o}{\ell_o^{ij}} \right)^2 (\dot{a}_o q_1^j + a_o \dot{q}_1^j + F_3 q_o^j), \\
 a_o \ddot{g}_3 + 3\dot{a}_o \dot{g}_3 - (\ddot{a}_o - 6/W_e a_o^2) g_3 &= -\sum_j 5 \left( \frac{\ell_o}{\ell_o^{ij}} \right)^3 (a_o^2 \dot{q}_o^j + 2a_o \dot{a}_o q_o^j).
 \end{aligned} \tag{4}$$

In these equations  $F_o, F_1, F_2, F_3$  are known functions depending on the physical constants,  $W_e$  and  $P_{go}$ , and on the calculated preceding orders of approximation. The deformations  $f_2, f_3$  of the bubble  $B^i$  and the motion of its center toward  $B^j$ ;  $\ell_2, \ell_3$ ; have been replaced by  $d_2, d_3$  which indicate the total motion of the point  $E_i$  toward  $B_i$  (Figure 2).

$$\dot{d}_2 = \dot{f}_2 - \dot{\ell}_2; \quad \dot{d}_3 = \dot{f}_3 - \dot{\ell}_3 \tag{5}$$

When all the initial radii of the bubbles in the cloud are identical, the right-hand sides of Equation (4) are the same as those for the two-bubble case right-hand sides multiplied by one of the geometrical constants  $c_1, c_2, c_3$ :

$$\begin{aligned}
 c_1 &= \sum_j (\ell_o / \ell_o^{ij}), \\
 c_2 &= \sum_j (\ell_o / \ell_o^{ij})^2 \cdot \cos \theta^{ij},
 \end{aligned} \tag{6}$$

$$c_3 = \sum_j (\ell_o / \ell_o^{1j})^3 \cdot p_2 (\cos \theta^{1j}) \quad (6)$$

We can now compute the behavior of  $B^1$  by solving the obtained differential equations (1 and 4) using a multi-Runge-Kutta procedure. The behavior of the whole cloud can then be obtained. This appears at first to be a very long task. However, noting that if  $a_o(t)$  is the nondimensional solution for a bubble of unit initial radius, the solution  $a_o^1$ , for a bubble of normalized initial radius  $\lambda$  is such that,  $a_o^1(\lambda t) = \lambda a_o(t)$ , the right-hand sides of (4) can be easily computed when  $\lambda$ s are known.

Indeed the whole problem can be reduced to the case of two interacting bubbles of different sizes. The comparison of equations (4) with those obtained in the case of two-bubbles shows that the  $N$  bubbles in the cloud other than  $B^1$  can be replaced by a unique bubble of strength  $q_n^{ig}$ , located at  $G^1$ , a distance  $\ell_o^{ig}$  from  $B^1$  in the direction defined by the angle  $MB^1G^1 = \theta^{ig}$ . As this equivalent bubble should induce the same pressures and velocities as defined by (2), its location and strength are obtained by the equations:

$$q_n^{ig} / \ell_o^{ig} = \sum_{j=1}^N q_n^j / \ell_o^{1j} \quad ,$$

$$\epsilon_{ig} \cdot q_n^{ig} / (\ell_o^{ig})^2 = \sum_{j=1}^N \epsilon_{ij} \cdot q_n^j / (\ell_o^{1j})^2 \quad , \quad (7)$$

where  $\epsilon_{ig}$  and  $\epsilon_{ij}$  are respectively unit vectors of the directions  $B^1G^1$  and  $B^1B^j$  (Figure 1), and  $n$  is the order of approximation. These equations define the angle  $\theta^{ig}$ , and the direction in which  $d_n^1(t)$  is measured in equation (4).

#### B. Pressure Field

For a given  $P_\infty(t)$ , equation (1) can be solved for the variations of the bubble radius,  $a_o^1(t)$ . This allows the subsequent determination of the pressure field around the bubble  $B^1$ , of center  $B^1$ , by the use of:

$$P_o(B^1, r, t) = P_\infty(t) + (2 a_o \dot{a}_o^2 + a_o^2 \ddot{a}_o) / r - a_o^4 \dot{a}_o^2 / 2r^4 \quad ,$$

where  $r$  is the distance between  $B^1$  and a given point  $M$  in the fluid.

The following corrections of  $P_o$  are obtained once the successive orders of the problem are solved. The nondimensional outer problem,  $\Phi$ , can be written:

$$\Phi(M, t) = -\sum_i \left[ \frac{\tilde{q}_o^i}{r^i} + \epsilon \frac{\tilde{q}_1^i}{r^i} + \epsilon^2 \frac{\tilde{q}_2^i}{r^i} + \epsilon^3 \left( \frac{\tilde{q}_3^i}{r^i} - \frac{\tilde{h}_2^i}{r^{i/2}} \cos \theta^{ig} \right) + O(\epsilon^3) \right] \quad , (8)$$

where bars denote nondimensional "outer" quantities, and tildes non-dimensional "inner" quantities.

$$\bar{\Phi} = \bar{\Phi} T/r_{b0}, \quad \tilde{q}_n^i = q_n^i \cdot T/r_{b0}^3, \quad \bar{r}^i = r^i/\ell_0. \quad (9)$$

$T$  is the characteristic time of the bubble collapse and  $r^i$  is the distance between a field point  $M$  and  $B^i$ . The Bernoulli equation enables one to calculate  $P$  using (8). We can write nondimensionally:

$$\bar{p}(M, \bar{t}) = \frac{P(M, t) - P_\infty(t)}{\Delta p} = -\epsilon \frac{\partial \bar{\Phi}}{\partial \bar{t}} - \frac{1}{2} \epsilon^4 \left| \nabla \bar{\Phi} \right|^2. \quad (10)$$

$\Delta p$  is the amplitude of the pressure driving the collapse and  $\bar{t} = t/T$ , where

$$T = r_{b0} \sqrt{\rho/\Delta p}. \quad (11)$$

In the following, we will consider as an illustration a uniform field of bubbles; any bubble has the same geometrical position relative to the others, and thus the same behavior. The general expression (8) simplifies considerably to become:

$$\begin{aligned} \bar{p}(M, \bar{t}) = & (\epsilon \dot{\tilde{q}}_0 + \epsilon^2 \dot{\tilde{q}}_1 + \epsilon^3 \dot{\tilde{q}}_2 + \epsilon^4 \dot{\tilde{q}}_3) \sum_i \left( \frac{1}{\bar{r}^i} \right) + \\ & - \epsilon^4 \dot{\tilde{h}}_2 \sum_i \left( \frac{\cos \theta_i}{\bar{r}^{i2}} \right) - \epsilon^4 \frac{\tilde{q}_0^2}{2} \cdot \left| \nabla \sum_i \left( \frac{1}{\bar{r}^i} \right) \right|^2 + O(\epsilon^3). \end{aligned} \quad (12)$$

In this expression, the summations are geometrical constants similar to  $c_1, c_2, c_3$  (6). Thus, once the dynamical bubbles behavior is known as well as their distribution the pressure field is determined.

#### c. Examples: Spherical Shell of Bubbles

As an illustration of the method presented above let us consider a distribution of bubbles centered on the surface of a sphere and which have the same position relative to each other. We will study the bubble behavior and the pressure generated for two types of ambient pressure variations with time: a) the classical case of a sudden positive pressure jump of amplitude  $\Delta p$ , b) the case of a sudden pressure drop,  $\Delta p$ , followed by a return to the initial pressure after a time period  $\Delta T$  during which the minimum pressure is kept constant.

In figure 3, the results of five different computations for case a), are compared, expansions being conducted up to  $\epsilon^3$ . The ratio,  $\epsilon = r_{b0}/\ell_0$ , was kept constant and at a value of 0.05. The cases of two, three and twelve bubbles of centers located on the surface of a sphere are presented together with that of an isolated bubble. The

fifth case is an intermediate situation between the configurations of three and twelve bubbles. This case is arbitrary and is only determined by the choice of  $c_1$ ,  $c_2$ , and  $c_3$ . In each case the variation with time of the distance,  $B^i E^i$ , (Figure 2) between the extreme point on a bubble  $E^i$ , and its initial center,  $B^i$ , is chosen to represent the bubble dynamics. Taking the bubble collapse in an unbounded fluid as reference, it is easy to see from Figure 3 how increasing the number of bubbles changes the dynamics of the one studied. We can observe first that, during the early slow phase of the implosion process, the collapse is significantly delayed. At any given nondimensional time the distance between  $B^i$  and  $E^i$  (and simultaneously the bubble characteristic size) is greater when the number,  $N$ , of interacting bubbles increases. Then, in the final phase of the implosion the tendency is reversed: the phenomenon speeds up and, in a shorter total implosion time, the final velocity of the motion is higher when  $N$  increases. As we will see later, this effect can be easily explained by accounting for the modification of the driving pressure of the collapse of any bubble due to the dynamics of the other bubbles.

Figure 4 shows the behavior of the bubbles in the case of a pressure variation of type b. The cases of an isolated bubble and two, three, five and twelve bubbles are investigated again, and the variations of  $B^i E^i$  with time are plotted. The ratio  $\epsilon$ , and the duration  $\Delta T$ , of the pressure drop are kept constant and at the particular values of 0.1 and 0.8 respectively. Here, as in the preceding figure, noticeable changes can be observed when the degree of interaction increases. First, the growth is slowed down and retarded in comparison with the isolated case. Then, the collapse is accelerated and as a result the total implosion time decreases with an increase in the number of bubbles,  $N$ . While for  $N = 2$ , the total implosion time is greater than that of an isolated bubble, for  $N = 12$  the time is significantly smaller. As we will see below this acceleration of the collapse makes the generated pressures at the end of the collapse higher than for the single bubble case.

Figure 5 compares for the same cloud configuration (twelve bubble,  $\epsilon = 0.1$ ) the bubble behavior for three values of the duration,  $\Delta T$ , of the pressure drop. The greater  $\Delta T$  is, the longer the bubble is allowed to grow. As a result the maximum size it attains is bigger, but its lifetime is smaller. Thus, the resulting collapse is much stronger.

To examine the observations made above let us compare the imposed ambient pressure with the variations of the pressure generated at a distance  $\ell_0$  from a collapsing bubble in an infinite medium. As we can see from Figure 6, the perturbation pressure, i.e. the difference between the pressure at  $\ell_0$  and the far-field pressure, is negative for  $t < 0.75$ . As a result a fictitious bubble placed at the distance  $\ell_0$  from this spherical bubble will sense a less important and more gradual increase in the surrounding pressure. In the considered case, instead of a sudden nondimensional jump of the pressure from 0 to 1,  $P$  surges only to 0.84, then rises slowly, not attaining 1 until  $t > 0.75$ . This would affect the bubble dynamics exactly as observed in Figure 3, namely a less violent start of the collapse. As a result, we find at

the end of this process a larger bubble than would be observed in an infinite medium. This, added to the fact that in the later stages ( $t \approx 0.75$ ) the driving pressure increases up to 2.25 times the far-field pressure, makes the subsequent end of collapse much more violent.

The same type of observation is made in the case of a finite-time pressure drop. In the first time period,  $T$ , the pressure sensed at a distance  $\ell_0$  from the bubble center,  $B_0$ , is higher than the imposed one. As a result a second fictitious bubble placed at this distance from  $B_0$  would have a slower growth during  $\Delta T$ . This phenomena is however reversed in the second phase as an expansion wave is generated by the growing bubble  $B_0$ . In the third and last phase a compression wave increases the driving pressure for collapse making this one more intense. In the presence of several bubbles the effects described above are amplified. Figure 7 is an example of this for the case of twelve bubbles. Plotted are the pressures generated during the bubble history at two locations: a) the center of the cloud and b) the center of one bubble,  $B^i$ , in its absence. These pressures are compared with those generated during the growth and collapse of an isolated bubble at a distance equal to the spherical cloud radius. The corresponding bubble radius variation with time is that represented in Figure 5 (12 bubbles  $T = 0.6$ ). The high pressure surge at the end of the collapse will be considered in the following.

Figure 8 is a collection of the results obtained in several cases studied. The maximum nondimensional pressure generated during the cloud collapse are represented versus the number of bubbles in the cloud. The cumulative effect is obvious since the values obtained vary in a several orders of magnitude range. The numbers represented should not be considered accurate since other scales for times, pressures and lengths are needed at the end of the collapse. Instead, they are presented here to give an indication of how tremendous pressures can be generated with an increasing number of interacting bubbles, and to give an idea of the trend of this increase. In this figure, the maximum pressures are given at the cloud center,  $C$ , at the center of a bubble,  $B^i$ , if it was removed, and at a distance  $r_{b0}$  from  $B^i$ .

The important role played by the gas content of the bubbles is to be emphasized. Increasing  $P_{g0}$  from 0.1 to 0.2 reduces dramatically the generated pressures. This comes mainly from the fact that the cushioning effect of the gas reduces significantly the velocities attained at the end of the implosion.

Another very interesting observation from figure 8 is that the maximum pressures generated at the end of the collapse is much lower for a pressure drop of finite duration followed by a recompression in comparison with the pressure jump case. This effect is not due to the apparent higher gas content in this case. Indeed, the value of  $P_g$  to consider for comparison purposes should be for all cases the minimum gas pressure,  $P_{gmin}$ , which exists at the start of the collapse when the bubble has its maximum volume. For the case of twelve bubbles for example and a pressure drop ( $\Delta T = 0.8$ ,  $P_{g0} = 0.53$ ) the value of  $P_{gmin}$  is 0.07. The effective gas content is thus smaller, and the observed pressure drop is intrinsically related to the imposed pressure

function.

This observed pressure attenuation can be explained by the fact that the cumulative effect of the other bubbles on the initial phase of the dynamics of the considered bubble is of opposite nature for the two pressure cases. In the pressure jump case the presence of other bubbles reduces initially the effective driving pressure of the bubble collapse thus preventing the bubble size from being small in the later phase when the collapse pressure surge occurs (see Figure 6). Conversely, the initial cumulative effect in the case of a finite time pressure drop is to reduce the bubble growth thus reducing the bubble size when the pressure surge occurs.

Another parameter on the value of the maximum pressure generated is the duration of the pressure drop. This effect is shown in Figure 9 for twelve bubbles and  $\epsilon = 0.1$ . The previous type of reasoning when applied to the gas pressure leads us to believe that the increase of the maximum pressure with  $\Delta T$  is mainly due to a decrease in the effective initial gas content at the start of the collapse since the maximum bubble radius increases with  $\Delta T$ .

### III. CONTINUUM MEDIUM APPROACH

One major assumption of the theoretical approach as used in the preceding section is that, in first approximation the imposed ambient pressure is assumed to be instantaneously transmitted to the vicinity of each bubble in the cloud. Therefore, both the compressibility of the bubbly medium and the influence of the liquid motion generated by the other bubbles on the dynamics of the bubble considered were neglected in the first order approximation. This limits the validity of the study to very low void fractions. The incompressibility assumption is valid as long as the fluid velocity does not approach the speed of sound. For single bubble dynamics this does not usually happen until the final phase of the collapse. Here, however, two factors contribute to limit the validity of the assumption. First, the rate of implosion is higher and second, more important, the velocity of sound drops considerably when the void fraction increases. This underlines the need to account for the behavior of the cloud as a whole in order to determine a more accurate value of the local pressure driving the collapse of the individual bubbles. In addition this would have the advantage of limiting, for the following orders of approximations, the number of bubbles directly influencing the considered one. Indeed, the asymptotic theory shows that the effective parameter of the expansions is  $\epsilon c_1$ , (where  $c_1$ , defined by (6), is a direct function of the number of bubbles), rather than  $\epsilon = r_{b0}/\ell_0$ . Introducing a motion equation for the bubbly medium would limit the number of influencing bubbles to those in the direct vicinity of the considered one, through a time delay of the propagation of the information from one bubble to another. In summary, if we account for a motion equation in the cloud medium the first order approximation of the preceding approach becomes more accurate and as a consequence the following corrections will be

smaller making the approach valid for higher void fractions,  $\alpha$ .

#### A. Classical Description

Basically the classical methods used to describe a two-phase medium are not much different from the singular perturbation method we presented above. The final description deals just with the macroscale of the cloud. However, this description is obtained by averaging the various physical quantities defined in the microscale. The two phase medium is assumed to be constituted of "particles" containing the host liquid and few bubbles. This "particle" is small enough to be able to distinguish the gaseous and liquid constituents, but large enough to enable one to define significant volume average quantities in the two-phase continuum. Therefore, each "particle" appears in the macroscale as a fluid point  $M$  allotted various physical and kinematic properties:  $\alpha(M,t)$  is the local void fraction,  $\rho_m(M,t)$  is the local medium density,  $\underline{U}_m(M,t)$  is the velocity and  $P_m(M,t)$  the pressure,....etc. In such a volume averaging description, if  $V_p$  is the volume of the particle,  $X(M,t)$  the considered average quantity and  $x(m,t)$  its local value in the microscale, we have the following definition:

$$X(M,t) = \frac{1}{V_p} \int_P x(m,t) dV \quad (13)$$

The density of the medium is therefore defined by the relation:

$$\rho_m(M,t) = \rho_\ell [1 - \alpha(M,t)] + \rho_g(M,t) \alpha(M,t), \quad (14)$$

where  $\rho_g(M,t)$  is defined by (13). The liquid is assumed to be incompressible and  $\rho_\ell$  constant. The void fraction,  $\alpha(M,t)$ , is defined as the relative volume of gas in the particle. Usually  $\rho_g \alpha$  is neglected and the density of the medium is written:

$$\rho_m(M,t) \approx \rho_\ell [1 - \alpha(M,t)] \quad (15)$$

If  $\underline{U}_\ell(M,t)$  is the average velocity of the liquid in the particle and  $\underline{U}_g(M,t)$  the average velocity of the gas, we obtain comparable results to (14) and (15):

$$\rho_m \underline{U}_m = \rho_\ell \underline{U}_\ell (1 - \alpha) + \rho_g \underline{U}_g \alpha, \quad (16)$$

$$\rho_m \underline{U}_m \approx \rho_\ell \underline{U}_\ell (1 - \alpha), \quad (17)$$

and combining with (15),

$$\underline{U}_m \approx \underline{U}_\ell \quad (18)$$

The continuity equation is obtained by writing the mass conservation of a volume of the bubbly medium followed during its motion. Using the average quantities defined above we can write:

$$\frac{d}{dt} \int_{V(t)} \rho_m dV = \int_{V(t)} \left[ \frac{d\rho_m}{dt} + \rho_m \nabla \cdot \underline{U}_m dV \right] = 0 \quad (19)$$

Here the material derivative pertains to the medium velocity  $\underline{U}_m$ , or with our assumptions to  $\underline{U}_\ell$  (see (18)).

$$d/dt = \partial/\partial t + \underline{U}_\ell \cdot \nabla \quad (20)$$

As Equation (19) is valid for any volume  $V$ , we obtain the general equation:

$$\frac{\partial \rho_m}{\partial t} + \nabla \cdot (\rho_m \underline{U}_m) = 0 \quad , \quad (21)$$

where  $\rho_m$  is defined by either (14) or (15).

A similar equation can be written concerning the number of bubbles,  $n(M,t)$ . Neglecting any complete bubble disappearance or sudden generation, as well as bubble splitting and coalescence we can write:

$$\frac{Dn}{Dt} + n \nabla \cdot \underline{U}_g = 0 \quad , \quad (22)$$

the material derivative being defined as:

$$D/Dt = \partial/\partial t + \underline{U}_g \cdot \nabla \quad (23)$$

The momentum equation of the bubbly medium can be obtained in the same manner by using the momentum equations of both constituents in the microscale and integrating over the "particle" volume  $V_p$ . If we neglect the viscous forces, this can be written:

$$\int_{V_p} \left[ \rho_i \frac{d\underline{U}_i}{dt} + \nabla p_i \right] dV = 0 \quad , \quad (24)$$

the index  $i$  designating the liquid or the gaseous phase depending on the position of the element of volume  $dV$  in the microscale. If we account for the incompressibility of the liquid this equation becomes:

$$\rho_\ell (1 - \alpha) \frac{d\underline{U}_\ell}{dt} + \rho_g \alpha \frac{D\underline{U}_g}{Dt} - \rho_g \int_{V_p} \underline{U}_g \cdot \nabla \underline{U}_g dV + \int_{V_p} \nabla p_i dV = 0 \quad (25)$$

If we neglect the gas contribution to the momentum, and we account for



(18) we obtain the following approximate classical momentum equation:

$$\rho_\ell (1 - \alpha) \frac{d\mathbf{U}_m}{dt} + \nabla P_m = 0, \quad (26)$$

where it is assumed that

$$\int_V \nabla p_i dV = \int_A p_i \underline{n} ds \approx V_p \cdot \nabla P_m. \quad (27)$$

The only equation left is that giving the bubble translation velocity,  $\mathbf{U}_g$ , which reflects the interaction between the two phases of the bubbly medium. The study of this equation is a whole subject of research in itself. Several contributions exist which have dealt with more and more complicated situations. To quote some without trying to be extensive we can add to the above references Johnson and Hsieh (1966), Landweber and Miloh (1980), Van Wijngaarden (1976,b), Van Beek (1981). When viscous drag is neglected a very interesting general expression for the motion of a deformable bubble in a nonuniform potential flow was derived by Landweber and Miloh (1980). If we admit, however, that the liquid flow around an isolated bubble is linearly accelerated, and that the bubble remains in first approximation spherical, we can write, neglecting the bubble mass, a simpler equation as follows:

$$\frac{D\mathbf{U}_g}{Dt} - 3 \frac{D\mathbf{U}_\ell}{Dt} = 3 \frac{a_0}{a_0} (\mathbf{U}_\ell - \mathbf{U}_g). \quad (28)$$

In this equation the virtual mass of the bubble is considered to be  $2/3 \pi a_0^3 \rho_\ell$  and the material derivative is related to the bubble velocity as discussed by Prosperetti and Van Wijngaarden (1976).

When other bubbles are present in the flow corrections are to be introduced in this expression, following Landweber's calculations. Van Wijngaarden (1976,a) and Van Beek (1981) performed similar corrections for a rigid sphere and obtained the expression:

$$\frac{d}{dt} \left[ \frac{1}{2} (1 + \zeta) (\mathbf{U}_g - \mathbf{U}_\ell) \right] = (1 - \alpha) \frac{d}{dt} \mathbf{U}_\ell, \quad (29)$$

where  $\zeta$  is a correction to the added mass of the sphere due to the presence of the cloud. They gave, however, respectively the values  $(2.78 \alpha)$  and  $(-0.225 \alpha)$  for  $\zeta$ .

#### B. Micromorphic Continuum Description

In classical continuum mechanics the fluid is described geometrically by a field point  $M$  and kinematically by a velocity field  $\mathbf{U}(M)$ . The averaging approach of the cloud medium, as described in the preceding paragraph, is in this sense classical. However, when a medium contains microstructure, as is the case for a bubbly medium, a more refined description can be obtained by assigning to  $M$ , in

addition to the macroscale velocity,  $\underline{U}(M)$ , other quantities which reflect the microscale behavior in the "particle". In a first gradient theory, in addition to the velocity field,  $\underline{U}(m)$ , a field of the gradients of relative velocities in the microscale scale,  $\underline{X}$ , is added which defines kinematically the medium\*. The description can be further refined by using higher order gradient theories. Germain (1973) considered such approaches and, using the method of virtual power, was able to derive the equation of motion of the continuum medium accounting for the macrostresses,  $\underline{\sigma}$ , and the microstresses,  $\underline{S}$ .

In a first gradient theory the velocity in the microscale can be written as

$$\underline{U}'(m) = \underline{U}(M) + \underline{X}(M) \cdot \underline{Mm} \quad . \quad (30)$$

Consequently the acceleration,  $\underline{\Gamma}'$ , of  $m$  is derived and, by equating at dynamical equilibrium the virtual power of all the internal and external forces acting on the considered particle (volume  $V_p$ ) to the material derivative of the virtual power of mass velocity of  $V_p$ , one obtains a dynamical equation of the medium relating  $\underline{S}$ ,  $\underline{\alpha}$ , and  $\underline{\Gamma}'$ .

To define  $\underline{X}$  we consider the motion on a scale which is of the same order as the microstructure. To do so for a bubble cloud, let us divide the cloud medium into fluid "cells" each enclosing an isolated bubble. In addition, we assume for simplicity that the bubble center of mass and the "cell" center of mass coincide at the considered time. Let  $\underline{U}(M)$  be the velocity in  $M$  induced by the rest of the cloud in absence of the bubble, and  $\underline{V}(B)$  the velocity of the bubble center,  $B$ .  $\underline{U}(M)$  would be the value of the velocity field assigned to  $M$  in a classical fluid mechanics description.

The bubble radius is  $a_0$  and its variations with time are given by (1). This radial motion of the bubble surface induces at a point  $m$  of the cell (Figure 10) a velocity of value  $(u_r \cdot \underline{e}_r')$ , where  $\underline{e}_r'$  is the unit vector of the direction  $Mm$ . The total velocity  $\underline{u}'$ , at  $m$  is:

$$\underline{u}'(m) = \underline{U}(M) + \frac{\dot{a}_0 a_0^2}{r'^2} \cdot \underline{e}_r' + \nabla \left[ \frac{a_0^3}{2r'^2} (\underline{U}(M) - \underline{V}(B)) \cdot \underline{e}_r' \right] + \dots (31)$$

where  $r'$  is the distance between  $M$  and  $m$ . The second term in this expression is a source term due to the spherical bubble oscillations, while the last term,  $\underline{u}''$ , is a dipole due to the slip velocity between the spherical bubble and the fluid, and could include first order corrections of the bubble shape. For further corrections for non-sphericity of the bubble, other terms (singularities of higher orders) have to be included. By differentiating (31) with respect to time and space one can define an acceleration vector,  $\underline{\Gamma}'$ , and a strain rate tensor,  $\underline{D}'$ . Following Germain's approach, and using the principle of virtual powers, one could then derive an equation of motion of the cloud medium. We decided instead to start with a first gradient

\* A double underlined quantity is a tensor.

theory and replace (31) by its Taylor expansion. We follow in doing so the first calculations done by Michelet (1980) in his graduate thesis.

The basic approximation used in this linearization approach is based on the fact that Equation (31) is only valid in the liquid portion of the "cell" ( $r \geq a_0$ ). It seems therefore logical to write the velocity in  $m$ , close to the bubble boundary, as a Taylor expansion of the value of  $u'$  computed on a point of the bubble surface,  $S$ , (Figure 10). This has the advantage of eliminating the singularity of (31) for  $r' = 0$ . The obtained expression for  $\underline{u}'(m)$  is then:

$$\underline{u}'(m) \approx \underline{U}(M) + \left[ 3a_0 + 4V_t \cos\theta - r' \left( 2 \frac{\dot{a}_0}{a_0} + 3 \frac{V_t}{a_0} \cos\theta \right) \right] \underline{e}_r + \left[ 2 V_t \sin\theta - \frac{3}{2a_0} r' V_t \sin\theta \right] \underline{e}_\theta, \quad (32)$$

where  $V_t = |\underline{V}(B) - \underline{U}(M)|$ .

When  $V_t$  is not accounted for, the expression of  $u'(m)$  reduces to a form comparable to (30), which is much easier to interpret than equation (32). In that case we obtain:

$$\underline{u}'_0(M') \approx \underline{U}(M) + \underline{X} \cdot \underline{Mm} + \underline{\alpha} \cdot \underline{e}_r', \quad (33)$$

where  $\underline{X}$  and  $\underline{\alpha}$  are both tensors assigned to  $M$  and defined as:

$$\underline{X} = -2 \frac{\dot{a}_0}{a_0} \underline{I}, \quad \underline{\alpha} = 3 a_0 \underline{I}. \quad (34)$$

We notice that in comparison to (30), which describes a first gradient homogeneous deformation, in (33) there is in addition to the gradient tensor,  $\underline{X}$ , a tensor  $\underline{\alpha}$  reflecting the presence of a source in the cell. Equation (32) reflects in addition to this the presence of a dipole. It could be written as

$$\underline{u}'(M') \approx \underline{U}(M) + \underline{X} \cdot \underline{Mm} + \underline{X}' \cdot \frac{|\underline{Mm}|}{a_0} \underline{e}_z + \underline{\alpha} \underline{e}_r + \underline{\alpha}' \underline{e}_z + \left( 6V_t \cos\theta - \frac{9}{2a_0} r' V_t \cos\theta \right) \underline{e}_r, \quad (35)$$

where  $\underline{e}_z$  is the unit vector of the direction of  $\underline{U}$  and  $\underline{V}$ ;  $\underline{X}'$  and  $\underline{\alpha}'$  play the same role as  $\underline{X}$  and  $\underline{\alpha}$  but are applied just to the direction of the translation. The last inhomogeneous term is more difficult to put in simple form.

From the expression (32) we can now compute the acceleration, then apply the principle of virtual power, to obtain the equation of

motion. Here again in absence of translation velocity  $V_t$ , the results are simpler to interpret. In absence of viscous effects these results can be written as follows:

$$\rho_m \left[ \frac{dU}{dt} + 3 \underline{K} \left( \ddot{a}_o - 2 \frac{\dot{a}_o^2}{a_o} \right) \right] = -\nabla p, \quad (36)$$

where  $\underline{K}$  depends unfortunately on the cell geometry,

$$\rho_m \underline{K} = \int_V \rho_i \underline{e}_r dV \quad (37)$$

If the cell and the bubble are symmetrical with regard to the center of mass  $M$ , then  $\underline{K} \equiv 0$ , and (37) reduces to the classical equation of motion, (26). Although it is unfortunate that the cell shape seems to play a role in the model,  $\underline{K}$  might rather reflect an effect of the non-sphericity of the bubble.

When  $V_t$  is taken into account a whole series of "inertia" integrals like (37) appear in the calculations. In order to see what such a model might indicate we considered the case of a spherical bubble in a spherical cell. In this case the motion equation becomes:

$$\rho_m \left\{ \frac{dU}{dt} + \frac{\dot{a}_o}{a_o} \left[ 3 + \frac{3}{4} \frac{R}{a_o} - 6 \frac{a_o}{R} + O(\alpha) \right] (\underline{V} - \underline{U}) \right\} = -\nabla p. \quad (38)$$

Here,  $R$  is the radius of the cell, and if we write  $R \approx a_o \alpha^{-1/3}$ , we have the unusual result:

$$\rho_m \left\{ \frac{dU}{dt} + 3 \frac{\dot{a}_o}{a_o} \left[ \alpha^{-1/3} \left( \frac{1}{4} + \alpha^{1/3} - 2 \alpha^{2/3} + \dots \right) \right] (\underline{V} - \underline{U}) \right\} = -\nabla p \quad (39)$$

This surprising result (dependence on  $\alpha^{-1/3}$ ) might be compared with that obtained for the apparent viscosity of a bubbly flow, which is  $4\mu/3 \cdot \alpha^{-1}$ . (Batchelor (1967), Van Wijngaarden (1972)). We recognize however that the present model is in its infancy and should be carefully checked before any conclusions are drawn. In addition, due to the linearization of the velocity field (first gradient theory) this model loses its validity for low  $\alpha$ s.

#### C. Case of a spherically symmetrical cloud

Let us consider a finite size spherical cloud of bubbles and define its radius,  $R(t)$ , at time  $t$ , as the position of the last outer shell of bubbles. The space is therefore divided into two regions.

For  $r > R(t)$ , the medium is an incompressible liquid of density  $\rho_l$ , while the interior of the sphere,  $r \leq R(t)$ , is filled with a two-phase medium which can be defined as in the preceding paragraphs. Let us consider here the classical approach and define at a point  $M(r)$ , a radial liquid velocity  $u_l(r, t)$  and a radial bubble translation velocity  $u_g(r, t)$ . Similarly we define a local void fraction  $\alpha(r, t)$ , density  $\rho_m(r, t)$ , bubble radius  $a_0(r, t)$ , number density  $n(r, t)$ , and medium velocity  $u_m(r, t)$ . The matching between the two media, states that at  $r = R(t)$  there is continuity of velocities and pressures:

$$\dot{R}(t) = u_g(r, t) \quad , \quad (40)$$

$$P_l(R, t) = \lim_{r' \rightarrow \infty} p'(R, r', t) \quad ,$$

where  $r'$  is the distance in the microscale between a bubble center and a cell field point. The continuity and momentum equations in the liquid medium ( $r > R(t)$ ) are easy to solve and give, after neglecting viscous effects:

$$u_l(r) = \dot{V}_g / 4\pi r^2 \quad , \quad (41)$$

$$\frac{\partial P_l}{\partial r} = -\frac{\rho_l}{4\pi} \left[ \frac{\ddot{V}_g}{r^2} - 2 \frac{\dot{V}_g^2}{r^5} \right] . \quad (42)$$

$V_g$  is the total volume of the bubbles in the cloud

$$V_g = 4\pi \int_c^R \alpha r^2 dr \quad (43)$$

Inside the bubbly medium, due to the spherical symmetry, the continuity equation also gives

$$u_l(r, t) = \frac{\dot{V}_g(r)}{4\pi r^2} ; \quad r < R(t) \quad , \quad (44)$$

with

$$V(r) = 4\pi \int_0^r \alpha(x, t) x^2 dx \quad . \quad (45)$$

If we are interested in the problem of the collapse of the cloud under an imposed ambient pressure variation,  $P_\infty(t)$ , (41) can be integrated between the cloud radius and infinity to give:

$$-P_\infty(t) + P_l(R) = \frac{\rho_l}{4\pi} \left[ \frac{\ddot{V}_g}{R} - \frac{1}{2} \frac{\dot{V}_g^2}{R^4} \right] \quad (46)$$

Using (40),  $P_0(R)$  can be related to the behavior of any individual bubble of radius  $a_0$  in the last outer shell of the cloud, using equation (1). Equation (43) becomes:

$$-P_\infty(t) + P_v + P_{g_0} \left( \frac{a_0}{a} \right)^{3k} = \frac{\rho_l}{4\pi} \left[ \frac{\ddot{v}_g}{R} - \frac{1}{2} \frac{\dot{v}_g^2}{R^4} + a_0 \ddot{a}_0 + \frac{3}{2} \dot{a}_0^2 \right]. \quad (47)$$

The cloud radius motion can be obtained by using an equation of the bubble motion, for instance (25) or (26). In the simplest case equation (25) gives the following second relation between  $R$ ,  $a_0$  and  $v_g$ :

$$\ddot{R} + 3 \frac{\dot{a}_0}{a_0} \dot{R} = \frac{3}{4\pi R^2} \left[ \ddot{v}_g - \frac{\dot{v}_g^2}{2R^3} + \frac{\dot{a}_0}{a_0} \dot{v}_g \right]. \quad (48)$$

A third equation, in addition to (47) and (48), is needed to solve for  $R$ ,  $a_0$  and  $v_g$ . Without an assumption on a proportionality between  $v_g(t)$  and  $a_0(t)$  or without penetrating the cloud and solving for all  $a_0(r,t)$  to determine  $v_g$  there is no hope of solving the problem. We do not think the proportionality assumption is generally justifiable even if at  $t = 0$  all bubbles in the cloud have the same size, since  $P(r,t)$  would not generally be the same for any location  $r$  at a subsequent time. This need to solve the whole problem is to be expected and is very important because it shows that defining the cloud by just one parameter, as a unique void fraction, is not sufficient to describe its dynamics. Number and bubble size distribution are other important variables to consider. An exception to this reasoning is the case of a cloud which possesses a high enough void fraction in order for a shock wave to form at  $R(t)$  and separate the two media described here. Such an interesting model has been described by Mørch (1982).

#### IV. CONCLUSIONS

We have considered in this paper the collapse of a cloud of bubbles submitted to a change in the ambient pressure. Two types of models were presented. The first model, valid for low void fraction is an asymptotic approach based on the fact that the bubble radius is small compared to its distance from neighboring bubbles. This single perturbation method allowed us to write a system of differential equations which enables one to describe any bubble motion and deformation knowing the geometrical and size distributions of the bubbles. As a consequence the whole flow and pressure field can be determined. As an illustration a few cases of symmetrical bubble distributions on a spherical shell were considered and showed interesting results. Even for very low void fractions, collective bubble collapse can generate pressures orders of magnitude higher than those produced by single bubble collapse. This would tend to explain the observed high erosion intensities and the bending of trailing edges. The cumulative effect

comes from the fact that the interaction increases the driving pressure of collapse of each individual bubble. This augments the violence of its implosion and thus the interaction with the other bubbles. Thus, each bubble ends its collapse not under the effect of a pressure of the same order as the ambient, but orders of magnitude higher. This cumulative effect would not exist if the void fraction is high enough for the cloud to behave as a single bubble. The study showed again the importance of gas content in the bubble and the history of the ambient pressure variations.

The second approach is a continuum approach and is undertaken in order to extend the validity of the study to higher void fractions. We principally pointed out the difficulties and suggested a way of improving the averaging methods by accounting for the singular nature of the bubbly medium under collapse conditions. To do this we used a first gradient theory for the flow field and a micromorphic structure for the bubbly medium. A correction of order  $\alpha^{-1/3}$  appears in the motion equation of the bubbly medium when the bubble radial oscillation and translation velocity are not negligible. We showed finally for a spherical cloud, with a classical continuum medium approach that it is not possible to easily solve the problem without imposing an assumption of a relationship between the behavior of the total gas volume in the cloud and that of an individual bubble. The knowledge of the local behavior of the bubbles in the cloud and thus of the local characteristics of the cloud (i.e., void fraction, bubble number density) seems necessary for solving the problem.

This work was supported by the Naval Sea Systems Command, General Hydromechanics Research Program administered by the David Taylor Naval Ship Research and Development Center under contract number N00014-82-C-009. My thanks are due to M. P. Tulin who raised my interest in this fascinating subject and to Ph. Genoux, from DRET, Paris, for fruitful discussions and help in calculations for the continuum medium approach.

## V. REFERENCES

- Bark, G., and Van Barlekom, W. B. (1979). Experimental investigations of cavitation noise, 12th Symposium on Naval Hydrodynamics, 470.
- Batchelor, G. K. (1967). An introduction to fluid dynamics, Cambridge, the University Press.
- Bovis, A. G., and Chahine, G. L. (1981). Etude asymptotique de l'interaction d'une bulle oscillante avec une surface libre voisine, J. de Mécanique, 20, 3, 537
- Chahine, G. L. (1981). Asymptotic theory of collective bubble growth and collapse, Proc. 5th International Symp. on Water Column Separation, IAHR, Obernach, Germany.
- Chahine, G. L. (1982). Experimental and asymptotic study of non-spherical bubble collapse, Appl. Sci. Res., 38, 187.
- Chahine, G. L., and Bovis, A. G. (1981). Pressure Field Generated by nonspherical bubble collapse, Cavitation Erosion in Fluid

- Systems, ASME, New York, 27.
- Germain, P. (1973). The method of virtual power in continuum mechanics, Part 2: Microstructure, SIAM J. Appl. Math. 25, 3, 556.
- Hammitt, F. G. (1980). Cavitation and multiphase flow phenomena, McGraw Hill International Book Company.
- Hansson, I., and Mørch, K. A. (1980). The dynamics of cavity clusters in ultrasonic (vibratory) cavitation erosion, J. of Applied Physics, 51, 4651.
- Ishii, M. (1975). Thermo-fluid dynamic theory of two-phase flow, Eyrolles, Paris.
- Johnson, V. E., and Hsieh, T. (1966). The influence of the trajectories of gas nuclei on cavitation inception, Proc. 6th Naval Hydrodynamics Symp., Washington, D.C.
- Landweber, L., and Miloh, T. (1980). Unsteady Lagally theorem for multipoles and deformable bodies, J. Fluid Mech. 96, 33.
- Michelet, M. G. (1980). Etude des milieux micromorphiques, ENSTA, Filière de Recherche Post-Scolaire, rapport de DEA No. 2.
- Mørch, K. A. (1977). Concerted collapse of cavities in ultrasonic cavitation, Proc. Acoustic Cavitation Meeting, London, 62.
- Mørch, K. A. (1980). On the collapse of cavity clusters in flow cavitation, Proc. 1st International Conference on cavitation and inhomogeneities in Underwater Acoustics, Springer Series in Electrophysics, 4, 95.
- Mørch, K. A. (1982). Energy considerations on the collapse of cavity clusters, Appl. Sci. Res. 38, 313.
- Plesset, M. S., and Prosperetti, A. (1977). Bubble dynamics and cavitation, Annual Review J. Fluid Mech. 9, 145.
- Prosperetti, A., and Van Wijngaarden (1976). On the characteristics of the equation of motion for a bubbly flow and the related problem of critical flow, J. Eng. Math. 10, 2.
- Shen, Y. T., and Peterson, F. B. (1979). Unsteady cavitation on an oscillating hydrofoil, 12th Symposium on Naval Hydrodynamics, 362.
- Tanabayashi, H., and Chiba, N. (1977). Unsteady cavitation of oscillating hydrofoil, Mitsubishi Technical Bulletin 117, Mitsubishi Heavy Industries, Ltd., Tokyo, Japan.
- Tulin, M. P. (1980). An analysis of unsteady sheet cavitation, 1980 ITTC Conference, Ann Arbor, Michigan.
- Tulin, M. P., and Hsu, C. C. (1980). New applications of cavity flows theory, 13th Symposium on Naval Hydrodynamics, Tokyo, Japan.
- Van Beek, P. C. W. (1981).  $O(\alpha)$  - accurate equation of motion for a liquid-bubble dispersion, Technische Hogeschool Delft. Report 81-18. Department of Mathematics and Informatics.
- Van Manen, J. D. (1963). Bent trailing edges of propeller blades of high powered single screw ships, International Shipbuilding Progress, 10, 101, 3.
- Van Wijngaarden, L. (1964). On the collective collapse of a large number of gas bubbles in water, Proc. 11th International Cong. of Appl. Mechanics, Springer, Berlin, 854.
- Van Wijngaarden, L. (1972). One-dimensional flow of liquids containing small gas bubbles, Annual Review of Fluid Mech., 4, 369.



- Van Wijngaarden, L. (1976,a). Hydrodynamic interaction between bubbles in a dilute gas bubble liquid mixture, J. Fluid. Mech., 77, 1, 27.
- Van Wijngaarden, L. (1976,b). Some problems in the formulation of the equations for gasliquid flows. Theor. and Appl. Mech., ed. W. T. Koiter, North Holland Publishing Company.
- Van Wijngaarden, L. (1980). Sound and shock waves in bubbly liquids, Proc. 1st International Conference on Cavitation and Inhomogeneities in Underwater Acoustics, Springer Series in Electrophysics, 4, 127.
- Van Wijngaarden, L. (1982). Bubble interaction in liquid/gas flows, Appl. Sci. Res., 38, 331.
- Zuber, N. (1964). On the dispersed two-phase flow in the laminar flow regime, Chem. Eng. Sci., 19, 897.
- Zwick, S. A. (1959). Behavior of small permanent gas bubbles in a liquid, J. Math and Phys., 37, 339.

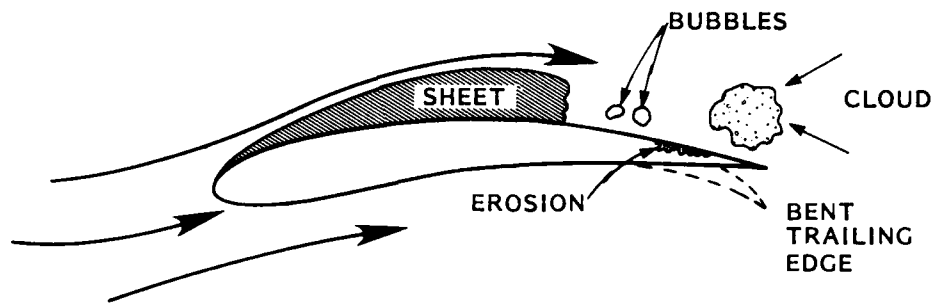


FIGURE 1 - TYPES OF CAVITATION ON FOIL

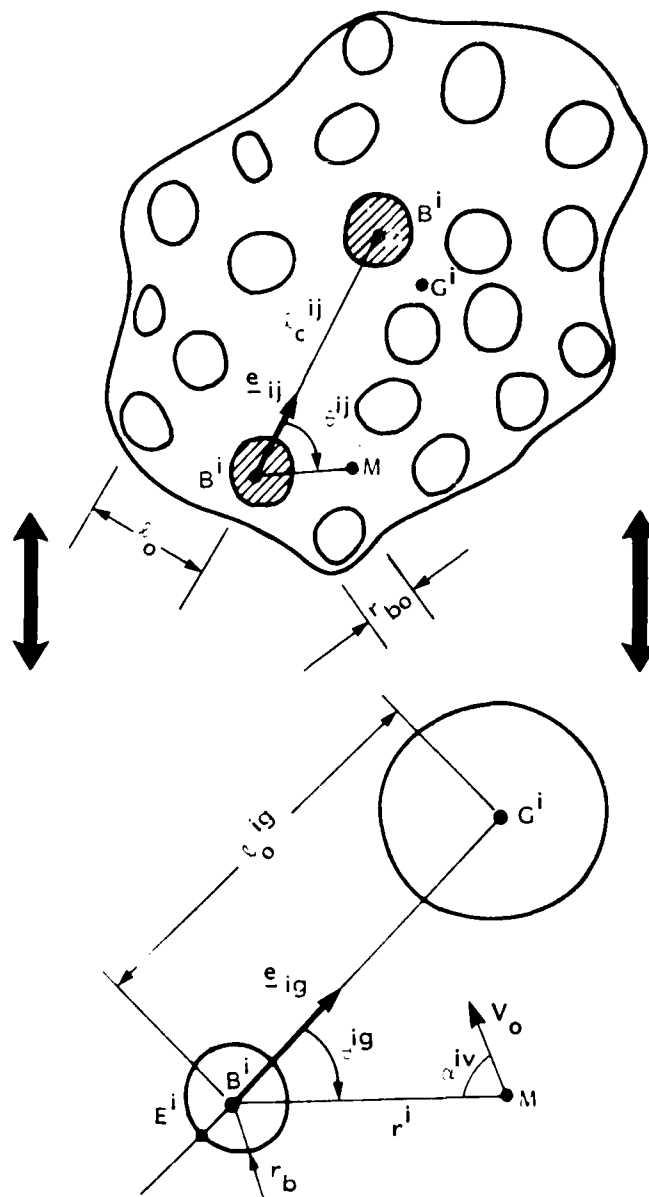


FIGURE 2 - MULTIBUBBLE INTERACTION EQUIVALENCE CONCEPT

AD-A158 920

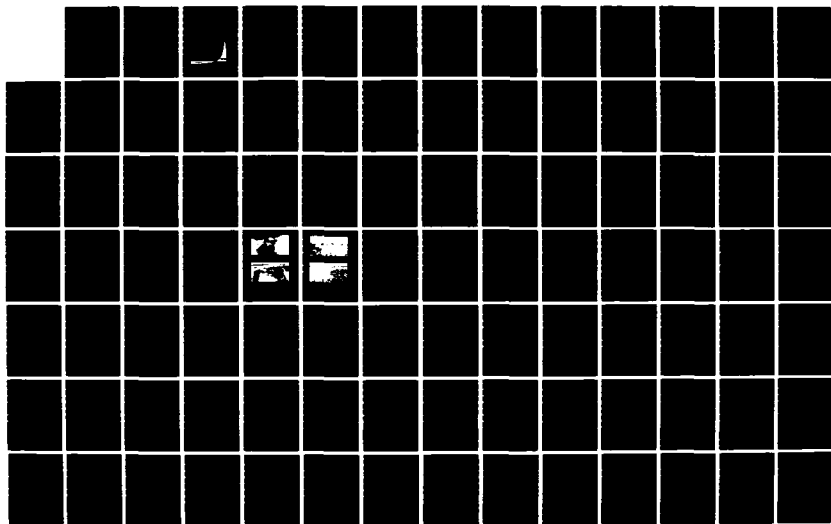
SYMPOSIUM OF NAVAL HYDRODYNAMICS (14TH) HELD AT ANN  
ARBOR MICHIGAN ON AUGUST 23-27 1982(U) OFFICE OF NAVAL  
RESEARCH ARLINGTON VA M P TULIN ET AL. 1982

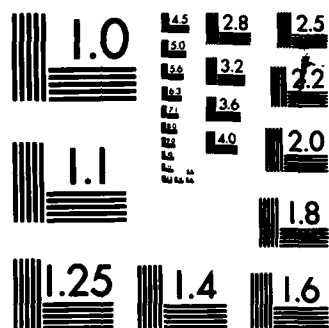
3/13

UNCLASSIFIED

F/G 20/4

NL





MICROCOPY RESOLUTION TEST CHART  
NATIONAL BUREAU OF STANDARDS-1963-A

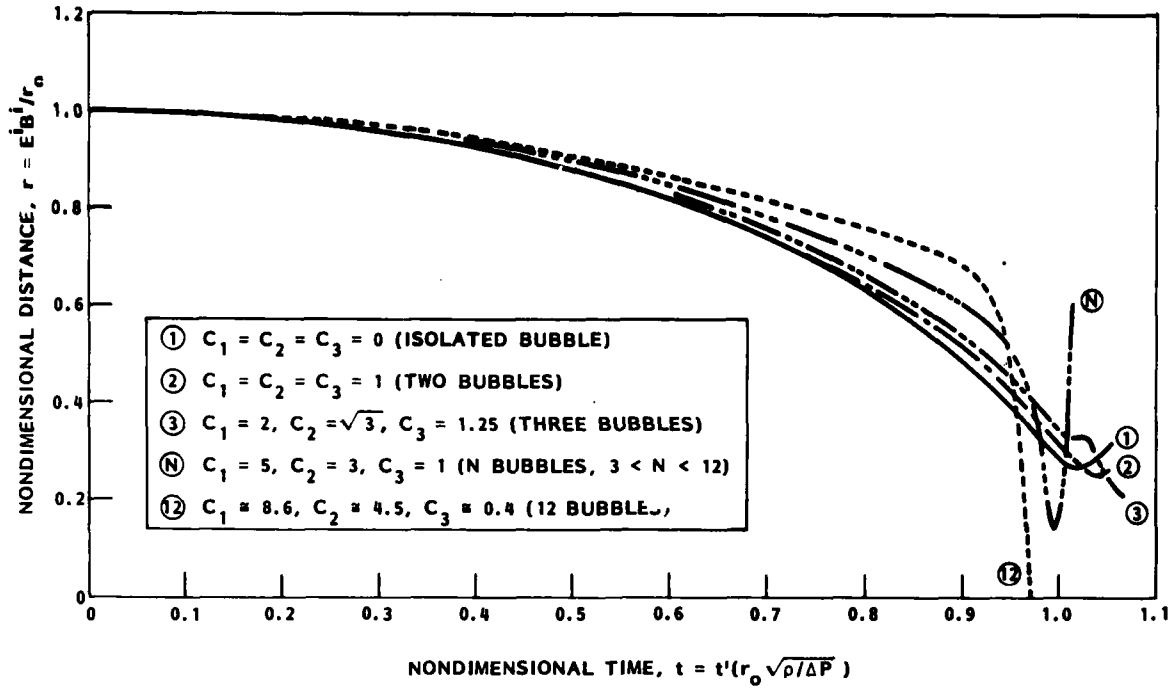


FIGURE 3 - MOTION OF THE BUBBLE WALL TOWARD THE CLOUD:  $\epsilon = 0.15$ ,  $P_{g0} = 0.1$ ,  $K = 1.4$ , POSITIVE PRESSURE STEP

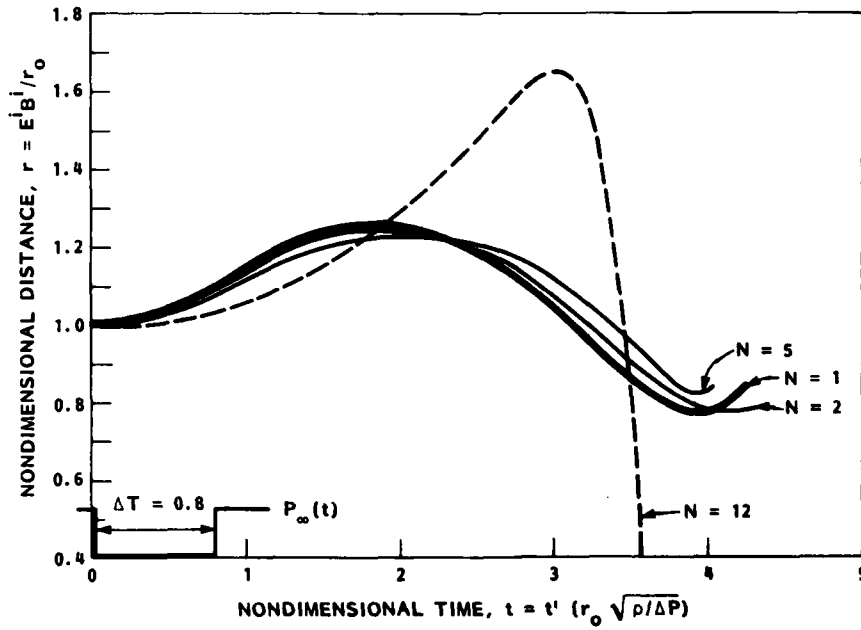


FIGURE 4 - MOTION OF THE BUBBLE WALL TOWARD THE MULTIBUBBLE CLOUD CENTER  $W_c = 100$ ,  $P_{g0} = 0.53$ ,  $K = 1.4$ ,  $\epsilon = 0.1$ , DURATION OF THE PRESSURE DROP  $\Delta T = 0.8$ .

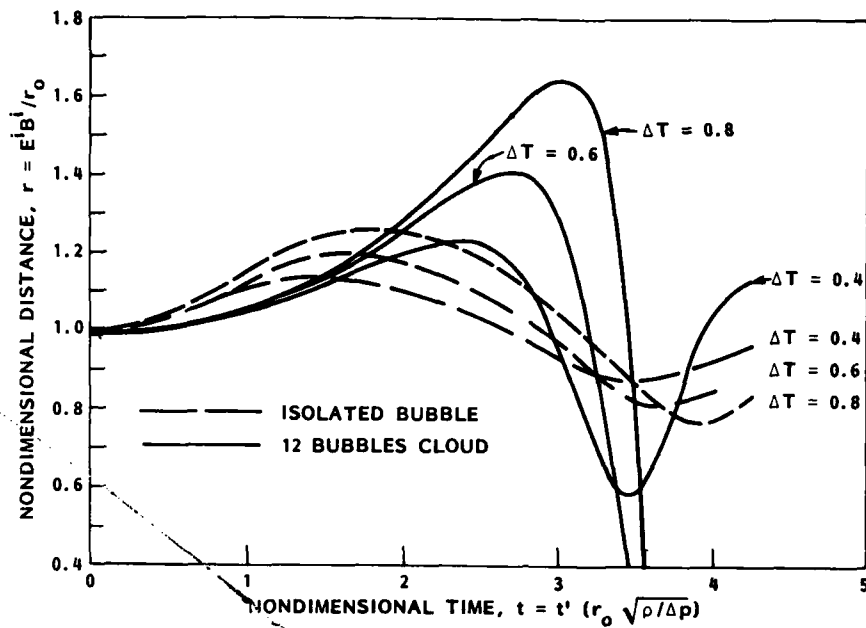


FIGURE 5 - INFLUENCE OF THE PRESSURE DROP DURATION ON THE BUBBLE WALL MOTION TOWARD THE CLOUD CENTER,  $W_e = 100.$ ,  $P_{g_0} = 0.53$ ,  $K = 1.4$ ,  $\epsilon = 0.1$ ,  $N = 12$

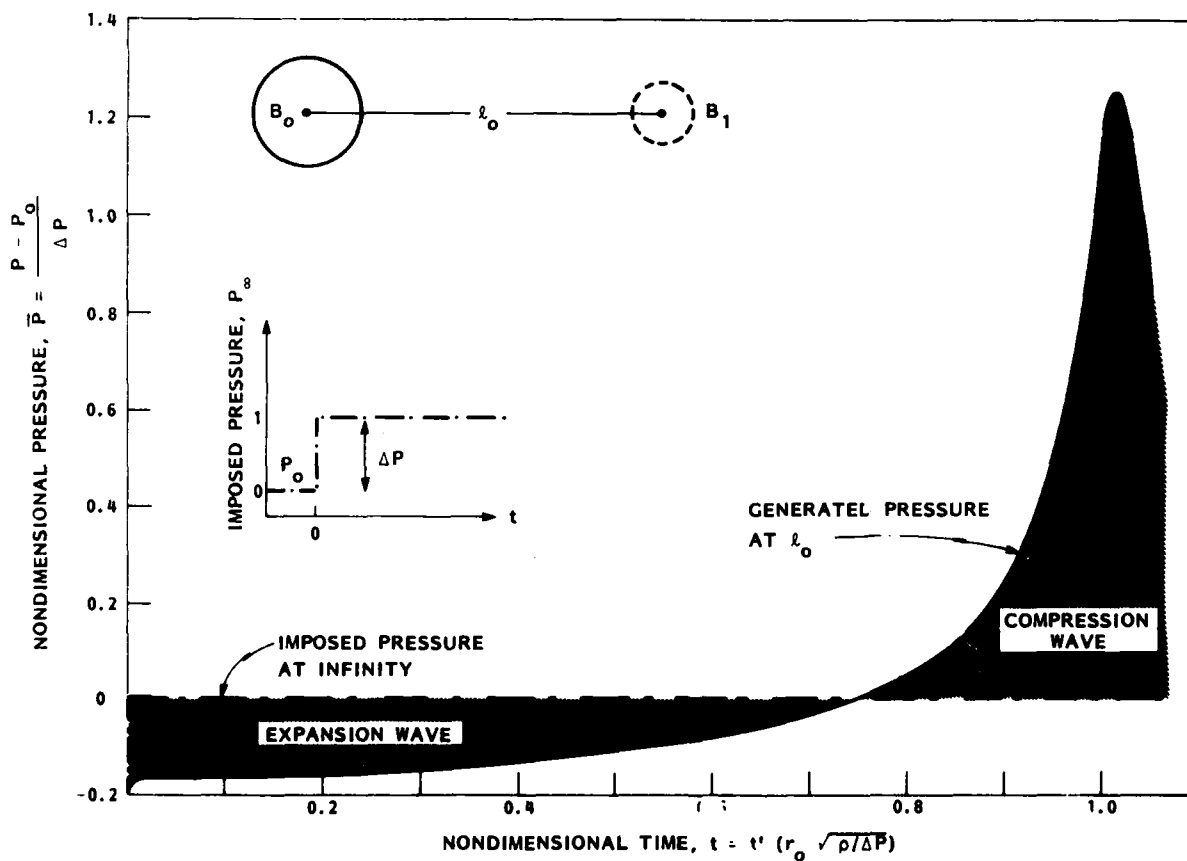


FIGURE 6 - PRESSURE VARIATION VERSUS TIME AT A DISTANCE  $l_0$  FROM AN ISOLATED SPHERICAL BUBBLE  
 $P_{g_0} = 0.1$ ,  $W_e = 100.$ ,  $\epsilon = r_0 / l_0 = 0.33$

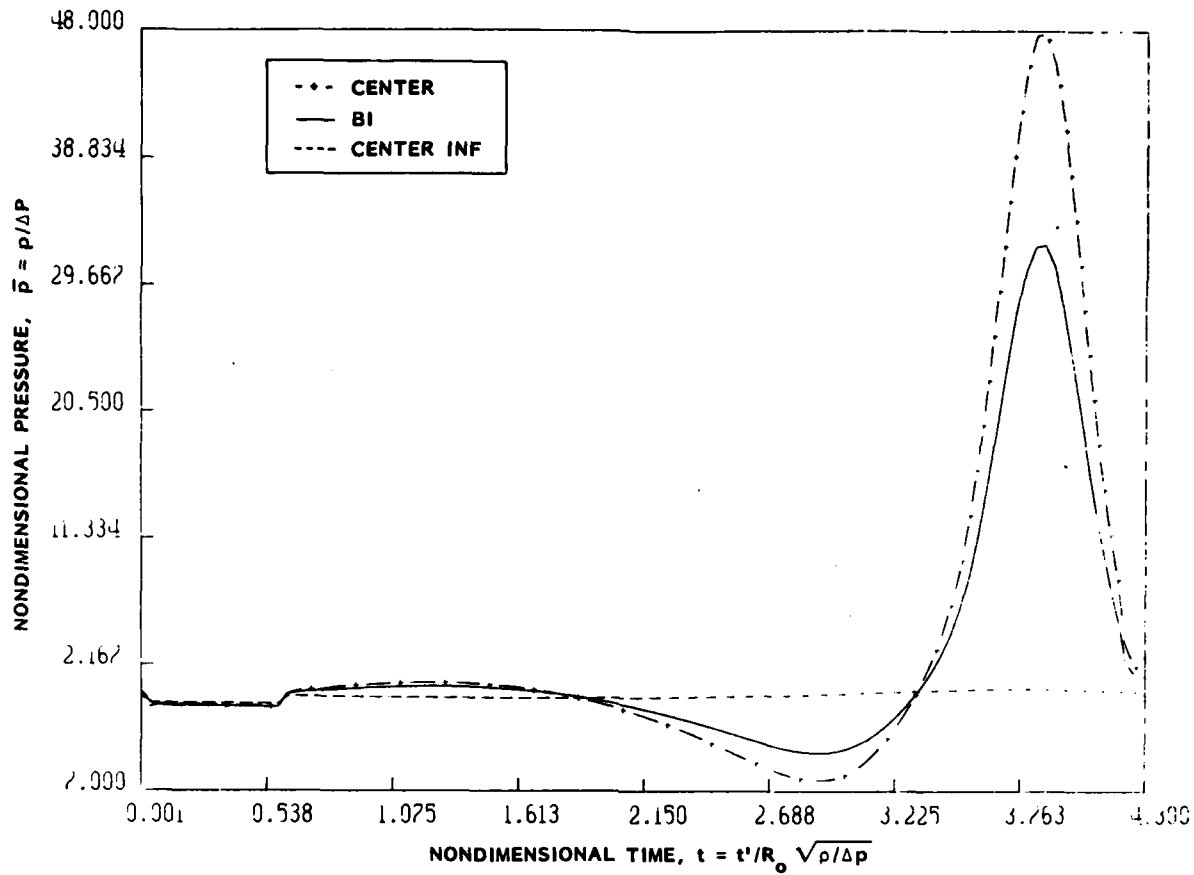


FIGURE 7 - PRESSURE VERSUS TIME AT DIFFERENT LOCATIONS,  
 $\epsilon = 0.1$ ,  $W_e = 100.$ ,  $\bar{p}_{g_0} = 0.54$ ,  $K = 1$ , 12 BUBBLES,  
 $\Delta T = 0.6$

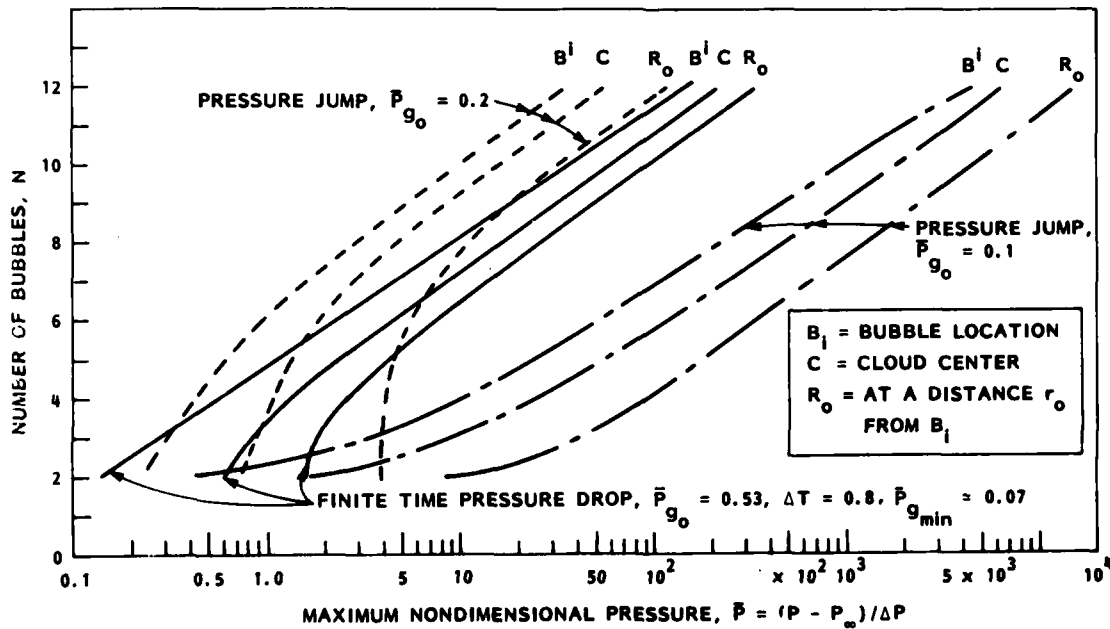


FIGURE 8 - VARIATION WITH THE NUMBER OF BUBBLES OF THE  
 MAXIMUM PRESSURES GENERATED,  $W_e = 100$ ,  $\epsilon = 0.1$

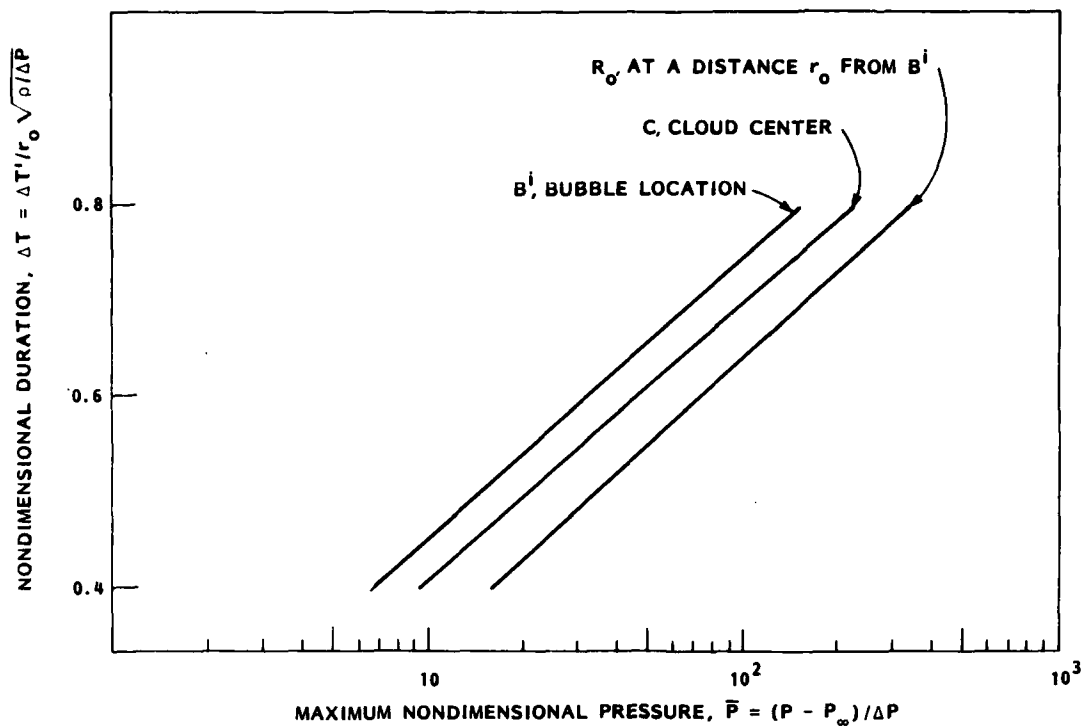


FIGURE 9 - VARIATION WITH THE AMBIENT PRESSURE DROP DURATION,  $\Delta T$ , OF THE MAXIMUM PRESSURES GENERATED,  $\bar{P}_{g_0} = 0.53$ ,  $W_e = 100.$ ,  $\epsilon = 0.1$ ,  $N = 12$

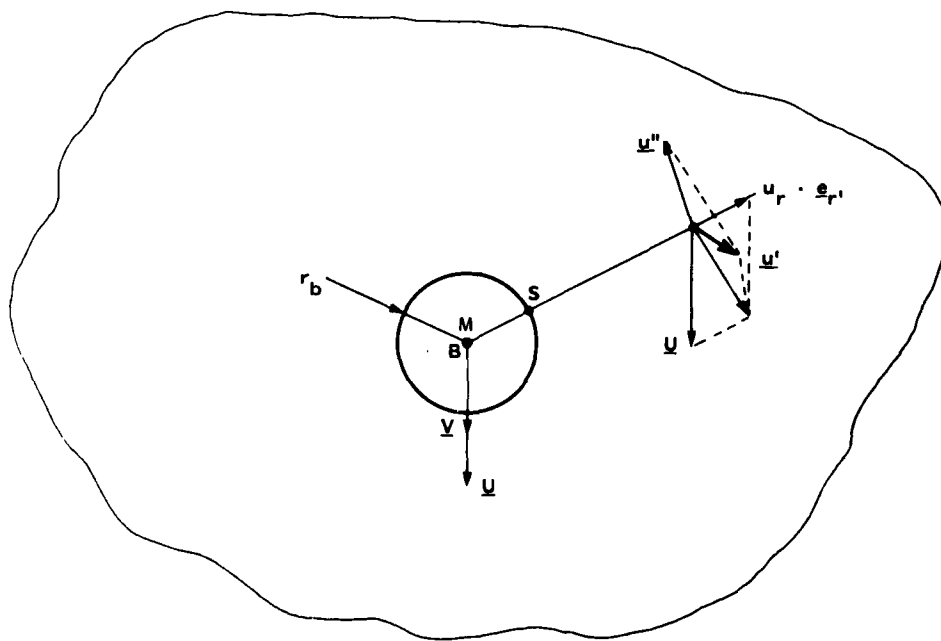


FIGURE 10 - SCHEMATIC OF A FLUID CELL



## Discussion

E.A. Weitendorf (Hamburg Ship Model Tank)

Is it possible to derive advices for practical propeller cavitation tests if cloud cavitation occurred?

It is imaginable that advices for the propeller designer who has to avoid cloud cavitation as far as possible are already included in the findings of the author. For instance, is it the right way for avoiding the cloud cavitation that the pressure on the profile at the end of the sheet cavitation should change as rapidly as possible to positive pressure values by increasing the profile curvature? I would like to know the opinion of the author on this problem.

R. Latorre (University of Michigan)

The author is to be congratulated for isolating the interaction of a bubbly continuum to a basic bubble-bubble model.

To continue the development of this model it appears the author can introduce the compressibility of the medium by modifying the time scale of the pressure propagation among the bubbles. Has he a suggestion of how this might be treated?

My second comment concerns the mass exchange across the bubble boundary. Recently, Prosperetti<sup>1</sup> introduced a generalized equation based on the Rayleigh-Plesset equation that includes non-Newtonian behavior of the liquid and mass exchange process at the bubble interface.

$$RU_1 + \frac{3}{2} U_1^2 - \frac{T}{\rho_1} 2U_1 + T \frac{1}{\rho_b} - \frac{1}{\rho_1} = \frac{1}{\rho_1} P_i - P_\infty - \frac{2\sigma}{R} + 3 \int_R^\infty r^{-1} \tau_{rr} dr \quad (1)$$

where R	bubble radii
$U_1$	radical liquid velocity at cavity interface
$P_i$	pressure in the bubble
$P_\infty$	pressure at infinity
$\tau_{rr}$	stress in fluid
$r$	distance from center
$T$	mass flux
$\rho_1$	fluid density
$\rho_b$	bubble density

Prosperetti<sup>1</sup> indicated that Equation (1) is useful when the mass flux can be computed independently of conditions within the bubble. It appears that this model might be useful in treating the final stage of the bubble collapse where the bubbles may break down into a group of smaller bubbles. Does the author's numerical study suggest what changes would result from using Equation (1)? I would be happy to hear his comments on the utility of this modification.

## References

- <sup>1</sup> Prosperetti, A. "A Generalization of the Rayleigh-Plesset Equation of Bubble Dynamics," Phys. Fluids Vol. 25, No. 3, March 1982, pp. 409-410.

## Author's Reply

G.L. Chahine (Hydronautics, Inc.)

To E.A. Weitendorf

Obviously, my paper considers, theoretically, the dynamics of an existing bubble cloud in a given pressure field, without attempting to address the very important practical problem of propeller design in order to avoid cloud cavitation. However, without considering the cloud inception problem, I agree with Dr. Weitendorf that some conclusions may be drawn from the results of the paper. Figures 5 and 9, for example, reinforce his suggestion concerning a rapid positive pressure increase behind the sheet cavity. Indeed, reducing  $\Delta T$ , the pressure drop duration, reduces the bubble growth and its rate of collapse (Figure 5) as well as the pressures generated following the collapse (Figure 9). An order-of-magnitude difference in these pressures can be seen for  $\Delta T$  dropping from 0.8 to 0.4. A similar conclusion can be drawn concerning the amplitude of the pressure drop and the increase to which the cloud is submitted. This is expressed by the value of the nondimensional parameter  $\bar{P}_{g0}$ , with  $\bar{P}_{g0}$  small meaning either high-pressure variations or low initial gas pressure. When  $\bar{P}_{g0}$  is increased ( $\Delta P$  decreased) the generated pressures are very significantly reduced (Figure 8). This suggests a practical propeller design that minimizes the pressure fluctuation behind the sheet cavity, besides reducing its spatial extent. This might mean increasing the curvature and reducing the pitch angle. Another idea would be the injection of gas bubbles in the concerned region in order to increase  $\bar{P}_{g0}$ .

To R. Latorre

The second part of my paper (continuum approach) treats the two-phase medium as a continuum and derives the basic equations needed to describe the propagation of information (pressures, velocities) inside the cloud and answers Dr. Latorre's first question.

The inclusion in the model of the mass exchange across the boundary of the bubble and non-Newtonian effects is an interesting suggestion but has the drawbacks of complicating, for instance, the numerical procedure of the first approach. For inertia-controlled bubbles, the mass exchange is negligible as it takes place at a much slower rate. Viscoelastic effects included in the Rayleigh-Plesset model have been shown theoretically to be negligible for spherical bubbles.<sup>1</sup> In addition, experimental evidence,<sup>2</sup> confirming earlier results about spherical bubbles, showed that significant viscoelastic effects are observed only when the bubble departs from sphericity.

### References

1. Chahine, G.L. "Etude asymptotique des oscillations et du collapse des bulles de cavitation," Thèse de Docteur-Ingenieur, University Paris VI, 1974.
2. Chahine, G.L. "Experimental and Asymptotic Study of Nonspherical Bubble Collapse," Appl. Sci. Res., Vol. 38, pp. 187-197, 1982.

# Viscous Effects on the Stability of Cavitating Line Vortices

Jaakko V. Pylkkänen  
Helsinki University of Technology  
Ship Hydrodynamics Laboratory  
Finland

## ABSTRACT

A semi-empirical theory is presented to investigate the effect of viscosity on the stability of cavitating line vortices. The emphasis is on the formulation and the analytical aspects of the problem. No numerical results are available.

In the case of the flow of a trailing vortex far downstream, viscous action leads to an increased pressure at the axis, and so to an axial deceleration of the core fluid. Correspondingly, in the present approach, the cavity pressure is considered as a function of the axial coordinate. The actual dependence is based on a paper of Batchelor. In order to simplify the derivations the cavity diameter is assigned a constant value. Thus the pressure balance on the boundary between the cavity and the fluid demands the inclusion of a fictitious surface tension component as a function of the axial coordinate. This formulation of the problem makes it possible to apply the linear spatial stability theory. The real and fixed disturbance frequency can be considered as representing the nonuniform wake. It is found that the cavitating line vortex is spatially stable everywhere except at one point where the stability is neutral. An analytical formula involving exponential integrals determines the coordinate of this special station. The above analysis is repeated for the case of compressible fluid. Assuming both low wave and Mach numbers the same conclusions are still valid.

## NOTATION

B	mathematical abbreviation
C <sub>subscript</sub>	unknown to be determined
c	speed of sound
D <sub>subscript</sub>	mathematical abbreviation

$F_{TpD}$	mathematical abbreviation
$H_m$	$= H_m^{(1)}$ , Hankel function of first kind
$H, H_S$	defined by Eqs. (3.5) and (5.8)
$i$	$= \sqrt{-1}$
$K_m$	modified Bessel function of second kind
$k$	$= \omega/c$
$k[X]$	defined by Eq. (3.7)
$L, L_S$	defined by Eqs. (2.12) and (5.3)
$\ell[X]$	defined by Eq. (3.8)
$M$	Mach number
$m$	helicity number
$P$	defined by Eq. (4.13)
$p$	pressure
$p_d$	vapour pressure in cavity
$p_{dD}[X]$	additional pressure due to viscosity
$p_0$	static pressure at infinity
$\Delta p$	pressure jump across the boundary
$R_E$	radius of cavity
$r$	radial coordinate in $(r, \theta, x)$ set
$S_r$	Strouhal number
$T_s$	surface tension
$T_{sD}[X]$	fictitious surface tension
$t$	time
$V_\Omega$	$= \Omega R_E$
$w_E$	axial velocity

$W_{\text{subscript}}$	averaged axial velocity in Ch. 4
$X$	$= \epsilon X$
$X_{\text{NS}}$	coordinate of neutrally stable position
$x$	axial coordinate in $(r, \theta, x)$ set
$Y$	integration variable
$\beta$	defined by Eq. (5.5)
$\Gamma$	circulation
$\gamma$	Euler's constant
$\epsilon$	small parameter
$\eta$	radial disturbance of cavity boundary
$\eta_0, \eta_1$	defined by Eq. (2.9)
$\theta$	angular coordinate in $(r, \theta, x)$ set
$\chi$	fast variable defined by Eq. (2.10)
$\kappa$	$= d\chi(X)/dx$
$\nu$	kinematic viscosity
$\Xi$	defined by Eq. (2.10)
$\xi$	variable defined by Eq. (4.12)
$\rho$	fluid density
$\phi$	disturbance velocity potential
$\phi_0, \phi_1$	defined by Eq. (2.8)
$\phi_{1H}, \phi_{1B}$	defined by Eq. (2.22)
$\phi^*$	adjoint of $\phi$
$\Omega$	angular velocity
$\omega$	real and fixed disturbance frequency
$O$	one writes $f(\epsilon) = O(\delta(\epsilon))$ as $\epsilon \rightarrow 0$ if $\lim_{\epsilon \rightarrow 0} \{f(\epsilon)/\delta(\epsilon)\} < \infty$

## 1. INTRODUCTION

A cavitating tip vortex affects the pressure field around a naval screw propeller. The pressure amplitudes in front of and directly above the propeller are decreased (Weitendorf, 1977). Large pressure fluctuations are caused by the breakdown of a cavitating tip vortex (English, 1980). The purpose of the present paper is to investigate the spatial stability of a cavitating axisymmetric vortex and estimate the longitudinal position of the stations where instabilities occur.

There exist several papers dealing with the stability of a cylindrical vortex enclosing a central core in an inviscid flow (Ffowcs Williams and O'Shea, 1970), (Morozov, 1974), (Narain and Uberoi, 1973), (Pylkkänen, 1981), (Uberoi et al., 1972). To account for diffusion in the fluid around trailing vortices the axisymmetric Navier - Stokes equations have been calculated numerically by Bovis (Bovis, 1980), (Bovis, 1981). Further, several authors have dealt with the stability of boundary layers of rotating axisymmetric bodies. With minor modifications they could serve as models for a corresponding investigation in the case of a tip vortex. All these studies demand a numerical evaluation. In the case of slowly diverging jets the problem of the spatial stability has been attacked by Garg & Round (Garg and Round, 1978) and Plaschko (Plaschko, 1979). The viscous flow in a diverging duct poses a similar spatial stability problem (Eagles and Weissman, 1975). Nayfeh has studied the connection between temporal and spatial stability of boundary layers from a more general point of view (Nayfeh, 1980), (Nayfeh and Padhye, 1979).

The present problem consists of a spatial stability investigation in the context of slow changes in the boundary conditions. The governing equations of the flow and the boundary conditions define a cylindrical cavity surrounded by a potential vortex advancing at a constant speed. In contrast to the studies mentioned above, the goal here is to obtain analytical expressions. Thus a simple model for the effect of viscosity is needed. It is assumed that the vapour pressure in the cavity depends on the axial coordinate. The actual shape of this positive pressure gradient is based on a paper of Batchelor (Batchelor, 1964), (Uberoi, 1979). By assigning a constant radius to the cavity the mathematical aspect of the problem becomes much simpler. Consequently the condition of the pressure balance on the cavity boundary demands the inclusion of a fictitious surface tension component. These assumptions make it possible to perform an analytic stability investigation. It will be found that at one axial station the flow is spatially neutral. Finally the calculations are repeated by allowing for the compressibility of the fluid.

The flow field is characterized as follows. The axial velocity  $W_E$  represents the speed of advance of the foil. The azimuthal velocity  $V_\Omega$  at the boundary of the cavity (at the radius  $R_E$ ) is due to the cross flow at the tip. The entire fluid is taken to be inviscid and incompressible.

## 2. PROBLEM FORMULATION

In cylindrical coordinates  $(x, r, \theta)$  the mean flow is given by

$$(2.1) \quad (W_E, 0, \Omega \frac{R_E^2}{r} = V_\Omega \frac{R_E}{r}).$$

Since the fluid is inviscid and irrotational outside the vortex core, the perturbation velocity potential satisfies the Laplace equation

$$(2.2) \quad \nabla^2 \phi = 0 \text{ for } r \geq R_E + \eta(x, \theta, t),$$

where  $\eta(x, \theta, t)$  is the disturbance of the cavity boundary, and  $t$  denotes time. The kinematic and dynamic boundary conditions are (Narain and Uberoi, 1973)

$$(2.3) \quad \phi_r = (\phi_x + W_E) \eta_x + \frac{1}{r^2} (\phi_\theta + V_\Omega R_E) \eta_\theta + \eta_t \text{ on } r = R_E + \eta,$$

$$(2.4) \quad -\rho \left\{ \phi_t + \frac{1}{2} [\phi_r^2 + (W_E + \phi_x)^2 + \frac{1}{(R_E + \eta)^2} (\phi_\theta + V_\Omega R_E)^2] \right\} + p_d + p_{dD}(x) \\ = \frac{T_s + T_{sD}(x)}{R_E} \left\{ 1 - \frac{R_E}{[\eta_x^2 + (\eta_\theta / (R_E + \eta))^2 + 1]} \right\}^{3/2} \left[ \frac{1}{(R_E + \eta)} \left( 1 + 2 \left[ \frac{\eta_\theta}{R_E + \eta} \right]^2 + \eta_x^2 \right) \right. \\ \left. - \frac{1 + \eta_x^2}{(R_E + \eta)^2} \eta_{\theta\theta} - \left( 1 + \left[ \frac{\eta_\theta}{R_E + \eta} \right]^2 \right) \eta_{xx} + \frac{2 \eta_\theta \eta_x \eta_{\theta x}}{(R_E + \eta)^2} \right\} \text{ on } r = R_E + \eta,$$

and in linearized form

$$(2.5) \quad \phi_r = W_E \eta_x + \frac{V_\Omega}{R_E} \eta_\theta + \eta_t,$$

$$(2.6) \quad -\rho \left\{ \phi_t + W_E \phi_x + \frac{V_\Omega}{R_E} \phi_\theta - \frac{V_\Omega^2}{R_E} \eta \right\} = \{T_s + T_{sD}(x)\} \left\{ \eta_{xx} + \frac{1}{2} \eta_{\theta\theta} + \frac{1}{R_E^2} \eta \right\}.$$

$T_s$  and  $p_d$  denote the surface tension acting on the vortex sheet, and the vapour pressure of the cavity, respectively. Finally the disturbances should disappear when the radial coordinate approaches infinity.

The additional pressure component  $p_{dD}(x)$  originates from the positive gradient due to viscosity. The pressure balance necessitates the inclusion of a fictitious surface tension  $T_{sD}(x)$ . The detailed form of these two quantities will be discussed in Chapter 4. The pressure  $p_{dD}(x)$  is assumed to vary only slowly in the axial direction. According to the method of multiple scales the additional variable

$$(2.7) \quad X = \epsilon x$$



is introduced. The variables  $X$  and  $x$  are called the slow and fast scales (Garg and Round, 1978). The parameter  $\epsilon$  characterizes the positive pressure gradient along the axis (Plaschko, 1979).

The disturbance velocity potential and the position of the cavity boundary are taken as

$$(2.8) \quad \phi(r, \theta, x, t) = [\phi_0(r, X) + \epsilon \phi_1(r, X)] e^{i\Xi},$$

$$(2.9) \quad \eta(\theta, x, t) = [\eta_0(X) + \epsilon \eta_1(X)] e^{i\Xi},$$

where

$$(2.10) \quad \Xi = -\omega t + m\theta + \frac{1}{\epsilon} \chi(X),$$

$$(2.11) \quad \kappa(X) = \frac{d\chi(X)}{dX}.$$

The real part of  $\kappa(X)$  is the wave number, and the imaginary part is the spatial growth rate. The real frequency  $\omega$  represents the disturbances in the base flow. In the case of a marine screw propeller, the wake field of a ship, or the variable immersion of the trailing tip vortex as a function of the angular position of the blade can be modelled in this way. For comparison, the present flow configuration corresponds to a three-dimensional boundary-layer case, where the mean flow is independent of the spanwise direction. Here the spanwise direction is replaced by the angular coordinate. Thus, as discussed by Nayfeh (Nayfeh, 1980), the helicity number  $m$  is fixed.

Substituting Eqs. (2.8) and (2.9) into the Laplace equation and the boundary conditions, and equating the coefficients of like powers of  $\epsilon$  leads to

$$(2.12) \quad \phi_0'' + \frac{1}{r} \phi_0' + \left\{ -\frac{m^2}{r^2} - \kappa^2(X) \right\} \phi_0 = L\phi_0 = 0,$$

$$(2.13) \quad L\phi_1 = -i \left\{ 2\kappa(X) \frac{\partial \phi_0(r, X)}{\partial X} + \frac{d\kappa(X)}{dX} \phi_0(r, X) \right\} = H,$$

$$(2.14) \quad \phi_0'(R_E, X) = i \{ W_E \kappa(X) - \omega + mV_\Omega / R_E \} \eta_0,$$

$$(2.15) \quad \phi_1'(R_E, X) = i \{ W_E \kappa(X) - \omega + mV_\Omega / R_E \} \eta_1 + W_E \frac{\partial \eta_0(X)}{\partial X},$$

$$(2.16) \quad -\rho \{ i \phi_0(R_E, X) [-\omega + \kappa(X) W_E + mV_\Omega / R_E] - \eta_0 V_\Omega^2 R_E^{-1} \} = \{ T_s + T_{sD}(X) \} \\ \cdot \{ \eta_0 [R_E^{-2} - m^2 R_E^{-2} - \kappa^2(X)] \},$$

$$(2.17) \quad -\rho\{i\phi_1(R_E, X)[-w+\kappa(X)W_E+mV_{\Omega}R_E^{-1}]-\eta_1V_{\Omega}^2R_E^{-1}+W_E\frac{\partial\phi_0(R_E, X)}{\partial X}\} \\ =\{T_s+T_{sD}(X)\}\{\eta_1[R_E^{-2}-m^2R_E^{-2}-\kappa^2(X)]+i[2\kappa(X)\frac{\partial\eta_0}{\partial X}+\frac{d\kappa(X)}{dX}\eta_0]\}.$$

In the above formulae a prime is used to denote  $\partial/\partial r$ . The insertion of the dynamic boundary condition in the kinematic boundary condition eliminates  $\eta$ , and in final form, the complete set of boundary conditions is

$$(2.18) \quad \phi_0'(R_E, X) + \frac{\rho\{-w+\kappa(X)W_E+mV_{\Omega}R_E^{-1}\}^2\phi_0(R_E, X)}{\rho V_{\Omega}^2R_E^{-1}-\{T_s+T_{sD}(X)\}\{R_E^{-2}-m^2R_E^{-2}-\kappa^2(X)\}} = 0,$$

$$(2.19) \quad \phi_1'(R_E, X) + \frac{\rho\{-w+\kappa(X)W_E+mV_{\Omega}R_E^{-1}\}^2\phi_1(R_E, X)}{\rho V_{\Omega}^2R_E^{-1}-\{T_s+T_{sD}(X)\}\{R_E^{-2}-m^2R_E^{-2}-\kappa^2(X)\}} \\ = \frac{-iW_E\frac{\partial}{\partial X}\phi_0'(R_E, X)}{\{-w+\kappa(X)W_E+mV_{\Omega}R_E^{-1}\}} + \frac{iW_E^2\frac{\partial\kappa(X)}{\partial X}\phi_0'(R_E, X)}{\{-w+\kappa(X)W_E+mV_{\Omega}R_E^{-1}\}^2} + \langle i\rho W_E\frac{\partial\phi_0(R_E, X)}{\partial X} \\ \cdot \{-w+\kappa(X)W_E+mV_{\Omega}R_E^{-1}\} + i[T_s+T_{sD}(X)][\frac{d\kappa(X)}{dX}\phi_0'(R_E, X) + 2\kappa(X)\frac{\partial\phi_0'(R_E, X)}{\partial X} \\ - \frac{2W_E\kappa(X)\frac{d\kappa(X)}{dX}\phi_0'(R_E, X)}{\{-w+\kappa(X)W_E+mV_{\Omega}R_E^{-1}\}}] \rangle (\rho V_{\Omega}^2R_E^{-1} - (T_s+T_{sD}(X))(R_E^{-2}-m^2R_E^{-2}-\kappa^2(X)))^{-1} = B,$$

$$(2.20) \quad \phi_0 = \frac{\partial\phi_0}{\partial r} \rightarrow 0 \quad \text{as} \quad r \rightarrow \infty,$$

$$(2.21) \quad \phi_1 = \frac{\partial\phi_1}{\partial r} \rightarrow 0 \quad \text{as} \quad r \rightarrow \infty.$$

The  $\varepsilon^1$  order problem is composed of two parts, i.e.

$$(2.22) \quad \phi_1 = \phi_{1H} + \phi_{1B},$$

where

$$(2.23i) \quad L\phi_{1H} = H,$$

$$(2.23ii) \quad \phi_{1H} = \frac{\partial \phi_{1H}}{\partial r} \rightarrow 0 \quad \text{as } r \rightarrow \infty,$$

$$(2.23iii) \quad \phi'_{1H}(R_E, X) + \frac{\rho \{-\omega + \kappa(X) W_E + m V_{\Omega} R_E^{-1}\}^2 \phi_{1H}(R_E, X)}{\rho V_{\Omega}^2 R_E^{-1} - \{T_s + T_{sD}(X)\} \{R_E^{-2} - m^2 R_E^{-2} - \kappa^2(X)\}} = 0,$$

$$(2.24i) \quad L\phi_{1B} = 0,$$

$$(2.24ii) \quad \phi_{1B} = \frac{\partial \phi_{1B}}{\partial r} \rightarrow 0 \quad \text{as } r \rightarrow \infty,$$

$$(2.24iii) \quad \phi'_{1B}(R_E, X) + \frac{\rho \{-\omega + \kappa(X) W_E + m V_{\Omega} R_E^{-1}\}^2 \phi_{1B}(R_E, X)}{\rho V_{\Omega}^2 R_E^{-1} - \{T_s + T_{sD}(X)\} \{R_E^{-2} - m^2 R_E^{-2} - \kappa^2(X)\}} = B.$$

The inhomogeneous perturbation potential  $\phi_{1H}$  satisfies the same boundary conditions as  $\phi_0$ .  $\phi_{1B}$  is obtained as a solution of the Laplace equation subject to a mixed boundary condition. If one is only interested in the stability of the flow, there is no need to evaluate  $\phi_{1B}$  further.

The boundary condition for the mean flow

$$(2.25) \quad p_d + \Delta p + p_{dD}(x) = -\frac{1}{2} \rho_0 \left\{ W_E^2 + \left( \frac{\Gamma}{2 R_E} \right)^2 \right\} + p_0,$$

where  $p_0$  denotes the static pressure at infinity,  $\Gamma$  the circulation, and

$$(2.26) \quad \Delta p = -\frac{1}{R_E} \{T_s + T_{sD}(x)\}$$

determines the radius of the cavity. Eq. (2.25) also gives the connection between the increasing pressure along the axis and the fictitious surface tension, i.e.

$$(2.27) \quad p_{dD}(x) = \frac{1}{R_E} T_{sD}(x).$$

## 3. SOLUTION

The  $\epsilon^0$  order disturbance potential and its adjoint are

$$(3.1) \quad \phi_0 = C_{m\kappa}(X) K_m(\kappa[X]r),$$

$$(3.2) \quad \phi_0^* = r C_{m\kappa}(X) K_m(\kappa[X]r),$$

where  $K_m$  is modified Bessel function of the second kind. The amplitude function  $C_{m\kappa}$  is an unknown at this stage. Inserting this solution in the dynamic boundary condition gives the dispersion relation

$$(3.3) \quad -\rho \left( -K_m(\kappa[X]R_E) \{ -\omega + \kappa(X) W_E + m V_\Omega R_E^{-1} \}^2 - \frac{V_\Omega^2}{R_E} \left\{ \frac{d}{dr} K_m(\kappa[X]r) \right\} \right) \Big|_{r=R_E} \\ = \{ T_s + T_{sD}[X] \} \{ R_E^{-2} - m^2 R_E^{-2} - \kappa^2(X) \} \left\{ \frac{d}{dr} K_m(\kappa[X]r) \right\} \Big|_{r=R_E},$$

from which the wave number and the spatial growth rate are determined.

The inhomogeneous problem (2.23) has a solution if and only if the inhomogeneous part is orthogonal to every solution of the adjoint homogeneous problem (Garg and Round, 1978), (Sauer and Szabo, 1969), i.e.

$$(3.4) \quad \int_{R_E}^{\infty} H \phi_0^* dr = 0 = \int_{R_E}^{\infty} H \phi_0 r dr.$$

Due to the fact that the disturbance boundary conditions are linearized, the lower limit in the integrals can be set at  $R_E$ . This is equivalent to approximating the material lines by stream lines in unsteady cavity problems.

The substitution of

$$(3.5) \quad H = -i \{ 2\kappa(X) K_m(\kappa[X]r) \frac{d}{dX} C_{m\kappa}(X) + 2\kappa(X) C_{m\kappa}(X) \frac{d}{dX} K_m(\kappa[X]r) \\ + \frac{d\kappa(X)}{dX} C_{m\kappa}(X) K_m(\kappa[X]r) \}$$

in Eq. (3.4) yields

$$(3.6) \quad \kappa[X] \frac{d}{dX} C_{m\kappa}(X) + \ell[X] C_{m\kappa}(X) = 0,$$

where

$$(3.7) \quad k[X] = \int_{R_E}^{\infty} r K_m(\kappa[X]r) [-2i\kappa(X) K_m(\kappa[X]r)] dr,$$

$$(3.8) \quad \ell[X] = \int_{R_E}^{\infty} r K_m(\kappa[X]r) [-i\kappa'(X) K_m(\kappa[X]r) - 2i\kappa(X) \frac{d}{dX} K_m(\kappa[X]r)] dr.$$

On integration the differential equation (3.6) gives

$$(3.9i) \quad C_{m\kappa}(X) = C_{mC} \exp \int_{X_0}^X \left\{ -\frac{\ell[Y]}{k[Y]} \right\} dY,$$

where

$$(3.9ii) \quad T_{SD}(X) = 0 \quad \text{for } X < X_0.$$

Thus the solution, to the first order of approximation, is

$$(3.10) \quad \phi = C_{mC} K_m(\kappa[X]r) \exp \left\{ -i\omega t + im\theta + \frac{i}{\epsilon} \int_{X_0}^X [\kappa(Y) + i \frac{\ell[Y]}{k[Y]}] dY \right\},$$

where

$$(3.11) \quad i \frac{\ell[X]}{k[X]} = -i \frac{\kappa'[X]}{\kappa(X)} \left\{ \frac{1}{2} + \frac{K_m^2(\kappa[X]R_E)}{(K_m'(\kappa[X]R_E))^2 - (1 + \frac{m^2}{\kappa^2(X)R_E^2}) K_m^2(\kappa[X]R_E)} \right\}.$$

The constant of integration  $C_{mC}$  can be fixed by a suitable normalization (Plaschko, 1979).

#### 4. STABILITY INVESTIGATION

For easier evaluation in the low wave number case the dispersion formula (3.3) is written as

$$(4.1) \quad \left\{ -\frac{\omega R_E}{W_E} + m \frac{V_\Omega}{W_E} + \kappa[X]R_E \right\}^2 = - \frac{\{\kappa[X]R_E\} K_m'(\kappa[X]R_E)}{K_m(\kappa[X]R_E)} \left\{ \frac{V_\Omega^2}{W_E^2} + \left( \frac{T_s}{\rho R_E W_E^2} + \frac{p_{dD}[X]}{\rho W_E^2} \right) (m^2 - 1 + \kappa^2[X]R_E^2) \right\}.$$

Introducing the mathematical abbreviations

$$(4.2) \quad D_{mK}(X) = \frac{\kappa[X] R_E K'_m(\kappa[X] R_E)}{K_m(\kappa[X] R_E)},$$

$$(4.3) \quad F_{TpD} = \frac{T_s}{\rho R_E W_E^2} + \frac{p_{dD}[X]}{\rho W_E^2},$$

the relation can be investigated preliminarily as the second order equation

$$(4.4) \quad \kappa[X] R_E = \{1 + D_{mK}(\kappa[X]) F_{TpD}(X)\}^{-1} \left\{ -\left(m \frac{V_\Omega}{W_E} - \omega \frac{R_E}{W_E}\right) \pm \left(-D_{mK}(X) \frac{V_\Omega^2}{W_E^2} - D_{mK}(X) F_{TpD}(X) \left[\left(m \frac{V_\Omega}{W_E} - \frac{R_E}{W_E}\right)^2 - m^2 + 1 - \frac{V_\Omega^2}{W_E^2}\right] - D_{mK}^2(X) F_{TpD}^2(X) [m^2 - 1]\right)^{1/2} \right\}.$$

The tip vortex of a marine screw propeller is adequately represented by the low wave number approximation ( $\kappa(X) R_E \ll 1$ ). Thus the asymptotic expressions (Abramowitz and Stegun, 1970)

$$(4.5) \quad K_0(z) = \langle -\{\ln(\frac{z}{2}) + \gamma\} \rangle + z^2 \langle \frac{1}{4} - \frac{1}{4} \{\ln(\frac{z}{2}) + \gamma\} \rangle + \dots,$$

$$K_1(z) = \frac{1}{z} + z \langle \frac{1}{2} \{\ln(\frac{z}{2}) + \gamma - \frac{1}{2}\} \rangle + \dots,$$

$$K_2(z) = \frac{1}{z^2} \langle 2 \rangle + \langle -\frac{1}{2} \rangle + \dots,$$

$$K_3(z) = \frac{1}{z^3} \langle 8 \rangle + \frac{1}{z} \langle -1 \rangle + \dots, \quad \text{for } z \rightarrow 0,$$

$$\gamma = 0.5772\dots = \text{Euler's constant},$$

are substituted in  $D_{mK}[X]$  (Eq. (4.2) and  $\{i\ell[X]/k[X]\}$  (Eq. (3.10)). One obtains

$$(4.6) \quad D_{mK}(X) \approx \{\ln(\frac{1}{2} [X] R_E) + \gamma\}^{-1} \quad \text{for } m = 0,$$

$$\approx -m \quad \text{for } m \geq 1; \quad \kappa(X) R_E \ll 1,$$

and

$$(4.7) \quad i \frac{\ell[X]}{k[X]} \approx -i \frac{\kappa'(X)}{\kappa(X)} \langle \frac{1}{2} \rangle \quad \text{for } m = 0, 1,$$

$$\approx -i \frac{\kappa'(X)}{\kappa(X)} \langle \frac{3}{2} \rangle \quad \text{for } m \geq 2; \quad \kappa(X) R_E \ll 1.$$

To order  $\epsilon^1$  the disturbances grow if the local spatial growth rate is negative, i.e.

$$(4.8i) \quad \text{Im}\{\kappa(X) + \epsilon i \frac{\ell[X]}{k[X]}\} < 0,$$

and remain neutrally stable in the case of an equality (Garg and Round, 1978). The local wave number

$$(4.8ii) \quad \text{Re}\{\kappa(X) + \epsilon i \frac{\ell[X]}{k[X]}\}$$

does not possess any  $\epsilon^1$  order correction. Thus the spatial stability is seen to depend on  $\{\kappa'[X]/\kappa[X]\}$ . On the basis of the approximations

$$(4.9i) \quad \frac{1}{\kappa[X]} \frac{d\kappa[X]}{dX} \approx \frac{\left\langle \frac{dT_{SD}(X)}{dX} \right\rangle}{\frac{K_1(\kappa[X]R_E)}{K_0(\kappa[X]R_E)} \frac{T_s + T_{SD}(X)}{\rho R_E W_E^2}} \leq 0 \text{ for } m = 0,$$

$$(4.9ii) \quad \frac{1}{\kappa[X]} \frac{d\kappa[X]}{dX} \approx \frac{\omega R_E \left\langle \frac{dT_{SD}(X)}{dX} \right\rangle}{2\rho W_E^2 \{V_\Omega - \omega(\frac{T_s + T_{SD}(X)}{\rho W_E^2})\}} \leq 0$$

$$\text{for } m = 1, \frac{V_\Omega W_E^2}{\omega} < \frac{1}{\rho} (T_s + T_{SD}(X)), \quad T_s + T_{SD}(X) \ll 1,$$

$$(4.9iii) \quad \frac{1}{\kappa[X]} \frac{d\kappa[X]}{dX} \approx \frac{1}{\rho R_E^3 W_E^2} \left\langle \frac{1 + (\frac{V_\Omega}{W_E})^2 (-2 \pm \sqrt{2})^2}{(-2 \pm \sqrt{2}) \frac{V_\Omega}{W_E} + \frac{\omega R_E}{W_E}} \right\rangle \left\langle \frac{dT_{SD}(X)}{dX} \right\rangle$$

$$\cdot \left\langle \pm \sqrt{2} \frac{V_\Omega}{W_E} + 2[2 \mp \sqrt{2}] \frac{V_\Omega}{W_E} \left( \frac{T_s + T_{SD}(X)}{\rho R_E W_E^2} \right)^{-1} \right\rangle \leq 0$$

$$\text{for } m = 2, \quad T_s + T_{SD}(X) \ll 1; \quad \kappa(X)R_E \ll 1,$$

the flow is spatially stable everywhere except at the point

$$(4.10) \quad \left\{ \frac{dT_{SD}(X)}{dX} \right\} \Big|_{X \approx X_{NS}} = 0,$$

where the stability is neutral. The axial coordinate of this station is denoted by  $X_{NS}$ . The shape of the pressure gradient curve determines it.

The papers of Uberoi (Uberoi, 1979) and Batchelor (Batchelor, 1964) contain a detailed discussion of the continual slowing-down of the azimuthal motion by viscosity. The link between the azimuthal and axial components of motion in a steady line vortex is provided by the pressure. The result is a positive axial momentum. The present approach is based on this pressure gradient dependence. An equation for the additional "cavity" pressure,  $p_{dd}(X)$ , is obtained by substituting suitable quantities in Eq. (4.6) of Batchelor. Now  $p_{dd}(X)$  is taken to be determined by

$$(4.11) \quad \frac{1}{\rho} \{p_0 - p_d - p_{dd}(X)\} - \frac{1}{2} \{W_E^2 + r^2 (2\pi R_E)^{-2}\} = \frac{r^2 W_{ED}^2}{8\nu} \frac{P(\xi)}{x},$$

where

$$(4.12) \quad \xi = \frac{W_E R_E^2}{4\nu x},$$

$$(4.13) \quad P(\xi) = \int_{\xi}^{\infty} \frac{(1 - e^{-t})^2}{t^2} dt.$$

The variable  $W_{ED}$  could be called an averaged or equivalent axial velocity in the vortex core. Two initial conditions are determined by the continuity of pressure and its derivative. In the present case the Villat-Brillouin condition at the detachment point,  $X_{OS}$ , for steady flow and constant radius of cavity demands

$$(4.14) \quad dp_{dd}(X_{OS})/dX = 0.$$

This leads to

$$(4.15) \quad X_{OS} = 0.$$

The vortex core is assumed to be initiated at the detachment station, i.e.

$$(4.16) \quad \{p_0 - p_d - \frac{\rho}{2} (W_E^2 + r^2 (2\pi R_E)^{-2})\} = \frac{\rho r^2 W_{ED}^2}{8\nu} \frac{P(\xi_{OS})}{x_{OS}},$$

where

$$(4.17) \quad P(\xi_{OS})/x_{OS} = 4\nu / \{W_E R_E^2\}.$$

An interpretation of the  $p_{dd}(X)$ -function is to consider it as a model of a vortex core of constant but negligible thickness. The unknown  $W_{ED}$  is added to satisfy the two initial conditions.



The main conceptual weakness of the present theory is the neglect of the convection of angular momentum (Uberoi, 1979). Uberoi has proposed a simple theory for a turbulent trailing vortex, which incorporates the vortex changes. His solution is

$$(4.18) \quad \Gamma(x,r)/\Gamma_0 = 1 - \left\{1 + \frac{\text{constant}_1}{\text{constant}_2} \exp[\xi_r \cdot \text{constant}_2] - 1\right\}^{-1},$$

where

$$(4.19) \quad \xi_r = (r^2/x)(W_E/\Gamma_{OS}).$$

The constants are obtained from experimental data. This flow field is not represented by a velocity potential. Thus the stability investigation must be modelled on the paper of Plaschko (Plaschko, 1979). But it can be shown, that compared with the non-cavitating flow, the existence of free surface decreases the magnitude of radial velocities in the boundary layer.

## 5. COMPRESSIBLE FLUID

By drawing on two of the references, (Morozov, 1974), (Ffowcs Williams and O'Shea, 1970), the investigation in Chapters 2-4 can be extended to include the effects of the compressibility of the fluid.

Provided the Mach ( $M = \sqrt{V_\Omega^2 + W_E^2}/c$ ) and Strouhal ( $S_r = R_E \omega/V_\Omega$ ) numbers satisfy

$$(5.1) \quad M^2 S_r^2 \ll 1, \quad M \ll 1,$$

the linearized equations of the motion for the periodic perturbation yield the Helmholtz equation

$$(5.2) \quad \nabla^2 \phi + k^2 \phi, \quad k = \omega/c \text{ for } r \geq R_E + \eta.$$

The  $\epsilon^0$  and  $\epsilon^1$  order disturbance velocity potentials are

$$(5.3) \quad \phi_0'' + \frac{1}{r} \phi_0' + \left\{-\frac{m^2}{r^2} - \kappa^2(X) + k^2\right\} \phi_0 = L_S \phi_0 = 0,$$

$$(5.4) \quad L_S \phi_1 = H_S,$$

where

$$(5.5) \quad \beta^2(X) = k^2 - \kappa^2(X).$$

The two cases,

$$(5.6i) \quad \beta(X) = \sqrt{k^2 - \kappa^2(X)} \text{ for } 0 < \kappa(X) < k,$$

$$(5.6ii) \quad \beta(X) = i\sqrt{\kappa^2(X) - k^2} \text{ for } k < \kappa(X) < \infty,$$

are to be considered separately. The boundary conditions at infinity (Eqs. (2.20), (2.21)), and on the cavity surface (Eqs. (2.18), (2.19)) remain unchanged.

The solution to the  $\varepsilon^0$  order problem, and the inhomogeneous term of the  $\varepsilon^1$  order problem are given by

$$(5.7) \quad \phi_0 = C_{m\kappa}(X) H_m^{(1)}(\beta[X]r),$$

and

$$(5.8) \quad H_S = \{-2i\kappa(X) H_m^{(1)}(\beta[X]r)\} \frac{d}{dX} C_{m\kappa}(X) + \{-i \frac{d\kappa(X)}{dX} H_m^{(1)}(\beta[X]r) - 2i\kappa(X) \frac{d}{dX} H_m^{(1)}(\kappa[X]r)\} C_{m\kappa}(X).$$

The superscript of the first kind of Hankel function  $H_m^{(1)}$  will be omitted in the following. The inhomogeneous eigenvalue problem has a solution if and only if

$$(5.9) \quad \int_{R_E}^{\infty} H_S \phi_0^* dr = 0 = \int_{R_E}^{\infty} H_S \phi_0 r dr.$$

Thus, to the first approximation, the disturbance potential is

$$(5.10) \quad \phi = C_{m\kappa} H_m(\beta[X]r) \exp\{-i\omega t + im\theta + \frac{i}{\varepsilon} \int_{X_0}^X [\kappa(Y) + i\varepsilon \frac{\ell[Y]}{\kappa[Y]}] dY\},$$

where

$$(5.11) \quad i \frac{\ell[X]}{\kappa[X]} = -i \frac{\kappa'(X)}{\kappa(X)} \left\{ -\frac{1}{2} - \left( \frac{\kappa(X)}{\beta(X)} \right)^2 + \frac{\left( \frac{\kappa(X)}{\beta(X)} \right)^2 H_m^2(\beta[X]R_E)}{(H_m'(\beta[X]R_E))^2 + \left( 1 - \frac{m^2}{\beta^2(X)R_E^2} \right) H_m^2(\beta[X]R_E)} \right\}.$$

The dispersion equation

$$(5.12) \quad \rho \frac{H_m(\beta[X]R_E)}{H_m'(\beta[X]R_E)} \{-\omega + W_E \kappa(X) + m V_{\Omega} R_E^{-1}\}^2 = -\beta(X) \left\{ \frac{\rho V_{\Omega}^2}{R_E} + (T_s + T_{SD}(X)) \cdot (R_e^{-2} + m^2 R_E^{-2} + \kappa^2(X)) \right\},$$

where

$$(5.13) \quad D_{mH}(X) = \frac{\beta[X] R_E H'_m(\beta[X] R_E)}{H_m(\beta[X] R_E)}$$

determines the local wave number and the stability parameter. When  $D_{mK}(X)$  is replaced by  $D_{mH}(X)$ , the solution given by Eq. (4.4) is still applicable.

In the low wave number flow the asymptotic expressions (Abramowitz and Stegun, 1970)

$$(5.14) \quad \begin{aligned} H_0(z) &= \langle 1 + \frac{i}{\pi} 2 \{ \ln(\frac{z}{2}) + \gamma \} \rangle + z^2 \langle -\frac{1}{4} + \frac{i}{\pi} \frac{1}{2} \{ -\ln(\frac{z}{2}) - \gamma + 1 \} \rangle + \dots, \\ H_1(z) &= \frac{1}{z} \langle \frac{i}{\pi} \{ -2 \} \rangle + z \langle \frac{1}{2} + \frac{i}{\pi} \{ \ln(\frac{z}{2}) + \gamma - \frac{1}{2} \} \rangle + \dots, \\ H_2(z) &= \frac{1}{z^2} \langle \frac{i}{\pi} \{ -4 \} \rangle + \langle \frac{i}{\pi} \{ -1 \} \rangle + \dots, \\ H_3(z) &= \frac{1}{z^3} \langle \frac{i}{\pi} \{ -16 \} \rangle + \frac{1}{z} \langle \frac{i}{\pi} \{ -2 \} \rangle + \dots, \quad \text{for } z \rightarrow 0, \end{aligned}$$

are substituted in  $D_{mH}(X)$  and  $\{i\ell[X]/k[X]\}$ . The limiting cases

$$(5.15i) \quad \beta(X) \approx k, \quad kR_E \ll 1,$$

$$(5.15ii) \quad \beta(X) \approx i\kappa(X), \quad \kappa(X)R_E \ll 1,$$

result in simple analytical formulae

$$(5.16i) \quad \begin{aligned} D_{mH}(X) &\approx \{ \ln(\frac{1}{2} k R_E) \}^{-1} & \text{for } m = 0, \\ &\approx -m & \text{for } m \geq 1, \quad \beta(X) \approx k \end{aligned}$$

$$(5.16ii) \quad \begin{aligned} D_{mH}(X) &\approx \{ \ln(\frac{1}{2} \kappa(X) R_E) \}^{-1} & \text{for } m = 0, \\ &\approx -m & \text{for } m \geq 1, \quad \beta(X) \approx i\kappa(X). \end{aligned}$$

By inserting  $\{\beta(X) = i\kappa(X)\}$  in Eq. (5.11), the derivations of Chapter 4 are recovered. The other extreme approximation  $\{\beta(X) = k\}$  leads to

$$(5.17) \quad i \frac{\ell[X]}{k[X]} \approx -i \frac{\kappa'(X)}{\kappa(X)} \langle -\frac{1}{2} + O([\frac{\kappa}{k}]^2) \rangle \quad \text{for } \kappa(X) \approx k,$$

and

$$\begin{aligned}
 (5.18) \quad \frac{\kappa'(X)}{\kappa(X)} \approx & - \frac{1}{\rho R_E W_E^2} \left( \frac{dT_{SD}(X)}{dX} \right) \left( R_E^2 \kappa^2(X) D_{mH}(X) + (m^2 - 1) D_{mH}(X) \right) \\
 & \cdot \left( 2 R_E^2 \kappa^2(X) [1 + D_{mH}(X) \frac{T_s + T_{SD}(X)}{\rho R_E W_E^2}] + R_E \kappa(X) [2 \{ m \frac{V}{W_E} - \frac{\omega R_E}{W_E} \}] + R_E^2 \kappa^2(X) \right. \\
 & \cdot \left. \left[ -\frac{V^2}{W_E^2} + (R_E^2 \kappa^2(X) - 1 + m^2) \frac{T_s + T_{SD}(X)}{\rho R_E W_E^2} \right] \right) \geq 0 \text{ for } \beta(X) \approx k.
 \end{aligned}$$

Thus it can be concluded that, as in Chapter 4, the cavitating vortex is neutrally stable only at the station defined by the condition  $\{dT_{SD}(X)/dX = 0\}$ .

## 6. CONCLUSION

For long waves the potential vortex flow outside a cavity is always temporally stable (Pylkkänen, 1981). But, because of viscosity, this result does not correspond to observations in nature. Thus the present conclusion, that the flow is spatially stable everywhere except at one point, where the stability is neutral, seems to be a more reasonable one. Also for a low Mach number flow represented by the Helmholtz equation this result is valid.

The present formulation can be extended to include the convection of angular momentum. The actual solution to this problem cannot be based on velocity potential. Earlier research indicates, that a finite area of spatial instability is to be expected now. The conclusion is that the calculated stability is highly dependent on the assumed initial conditions.

The wake field of a ship is represented by the real and fixed frequency  $\omega$ . In a linearized theory the axial coordinate of the neutrally stable position is completely independent of the wake frequency or amplitude. The local wave number is determined from the dispersion equation, and is strongly dependent on the wake frequency. The changing immersion of a tip vortex due to the variable angular position of the blade can be simulated in exactly the same way. That is, because of the assumed constant cavity radius and the linearization of the boundary conditions the details or the cause of the disturbance do not appear in the low wave number approximations.

The present theory yields simple and pronounced formulae for the mutual dependence of the variables compared with investigations based on the evaluation of full Navier-Stokes equations. This is due to the fact that the independent parameter  $p_{dd}(X)$  appears only on one of the boundary conditions, and not in the governing equation of the flow. Certainly the sophistication of the investigation could be increased in several ways, but conversely, one could easily lose the insight given by analytical results.

## ACKNOWLEDGEMENT

The author expresses his thanks to Professor V. Kostilainen for making available the facilities of the Ship Laboratory of Helsinki University of Technology. Also my thanks are due to Miss E. Heap for correcting the English text of the manuscript, and Ms. L. Söderman for the typing. The financial support of the Academy of Finland has made the present study possible.

## REFERENCES

- Abramowitz, M. and I.A. Stegun (1970). Handbook of Mathematical Functions. Dover Publications, Inc., New York.
- Batchelor, G. L. (1964). Axial flows in trailing line vortices, Journal of Fluid Mechanics 20, 645.
- Bovis, A. G. (1980). Asymptotic study of tip-vortex cavitation, in Cavitation and Polyphase Forum - ASME-Meeting. New Orleans.
- Bovis, A. G. (1981). Some results on cavitation induced by trailing vortex flows, in Euromech 146, Flows of Liquids past Bodies with Developed Cavities, Villard de Lans.
- Eagles, P. M., and M. A. Weissman (1975). On the stability of slowly varying flow: the divergent channel, Journal of Fluid Mechanics 69, 241.
- English, J. W. (1980). Cavitation induced hull surface pressures - measurements in a water tunnel, in Symposium on Propeller Induced Ship Vibration, The Royal Institution of Naval Architects, London, pp. 55-73.
- Ffowcs Williams, I. E., and S. O'Shea (1970). Sound generation by hydrodynamic sources near a cavitated line vortex, Journal of Fluid Mechanics, 43, 675.
- Garg, V. K., and G. F. Round (1978). Nonparallel effects on the stability of jet flows, Journal of Applied Mechanics 45, 717.
- Morozov, V. P. (1974). Theoretical analysis of the acoustic emission from cavitation line vortices, Soviet Physics Acoustics 19, 468.
- Narain, J. B., and M. S. Uberoi (1973). Nonlinear stability of trailing line vortices enclosing a central jet of light or dense fluid, Physics of Fluids 16, 1406.
- Nayfeh, A. H. (1980). Stability of three-dimensional boundary layers, AIAA Journal 18, 406.
- Nayfeh, A. H., and A. Padhye (1979). Relation between temporal and spatial stability in three-dimensional flow, AIAA Journal 17, 1084.
- Plaschko, P. (1979). Helical instabilities of slowly divergent jets, Journal of Fluid Mechanics 92, 209.
- Pylkkänen, J. V. (1981). Stability of a vortex enclosing a cavity, Helsinki University of Technology, Ship Hydrodynamics Laboratory Report No 21.
- Sauer, R., and I. Szabo (1969). Mathematische Hilfsmittel des Ingenieurs Teil II, Springer-Verlag, Berlin.

- Uberoi, M. S. (1979). Mechanisms of decay of laminar and turbulent vortices, Journal of Fluid Mechanics 90, 241.
- Uberoi, M. S., C. Y. Chow, and J. P. Narain (1972). Stability of coaxial rotating jet and vortex of different densities, Physics of Fluids 15, 1718.
- Weitendorf, E. A. (1977). Cavitation and its influence on induced hull pressure amplitudes, in Symposium on Offshore Propulsion Systems, Høvik.

## Closure

J.V. Pylkkanen (Helsinki University of Technology)

This closure is the author's response to the following informal question. How does the Reynolds number affect the stability? The axial coordinate of the station of neutral stability is strongly dependent on the initial condition at the detachment plane. In its turn, the initial condition is determined by the development of the boundary layer at the tip region. A free shear layer will be formed because of the different directions and different magnitudes of the boundary-layer flows originating on the suction and pressure sides of the blade. It could well be that bilge vortices are created in a very similar way. If this is really the case, use could be made of already available computational techniques.

What will happen if on one or both sides of the blade there exists also a sheet cavity? The extent of this sheet could be compared with the vapor-pressure area of the shear layer. If these two cavitating domains overlap, the sheet cavity will join the cavitating tip vortex. As an initial approximation, the sectional area of the cavitating tip vortex might be increased by the sectional area of the sheet cavity at this position.

# Nuclei and Cavitation

Jean-Pierre Le Goff  
Direction des Recherches Etudes et Techniques  
Yves Lecoffre  
NEYRTEC Company  
France

## I. ABSTRACT

This paper presents the main steps in the ten-year research programme undertaken by NEYRTEC and sponsored by D.R.E.T. concerning the influence of nuclei on cavitation.

After briefly recalling the state of the art in 1970, the details of research progress in the field of bubble cavitation are described, viz. :

- (a) initial experiments and measurement of negative pressure on a cavitating profile during bubble growth ;
- (b) theoretical model and scaling laws for nuclei populations ;
- (c) development of measuring devices and methods for controlling nuclei in hydrodynamics facilities (venturi, scattering method, microbubble seeding, dissolved gas monitoring) ;
- (d) field applications in laboratory, industrial and marine conditions.

The second part of the paper describes recent experimental work which confirmed the validity of scaling laws. The tests were made on two geometrically similar hydrofoils and two propellers in two different cavitation tunnels. The scale ratio was 1 : 6 for the foils and 1 : 2 for the propellers. The largest hydrofoil (NACA 16209) was 600 mm x 900 mm. The diameter of the largest propeller was 330 mm. During these tests, the nuclei population was adjusted according to the  $\lambda^3$  scaling laws on concentration. Forces were measured and flow visualisations were made.

The results show that :

- (a) Cavitation inception conditions are perfectly reproducible whatever the scale and the velocity ;



- (b) In developed cavitation conditions, when the  $\lambda^3$  law is applied and the  $\sigma$  values are the same, the geometries of the cavitating flows are almost identical on the small and large models (of hydrofoils or propellers). The resulting lift (and thrust) coefficients are also equal ;
- (c) Although extensive noise measurements were not made during these tests, a tremendous effect of nuclei population on radiated noise has been observed.

These results confirm that the nuclei population has a major influence on cavitation behaviour. It is thus highly recommended to control this parameter in hydrodynamic facilities and to measure it in full-scale conditions.

## II. STATE OF THE ART IN 1967

The aim of model tests is to :

- determine cavitation inception conditions,
- measure the effects of developed cavitation on force coefficients,
- predict noise and fluctuating pressures,
- evaluate the risks associated with erosion.

Theoretical treatments are not able to solve the problems completely and it is always necessary to make model tests to evaluate these effects.

It has been observed that model tests can lead to large discrepancies, either in the same facility at different times or in different facilities. The prediction of full scale cavitation behaviour thus appears to be a difficult problem.

In order to have a better understanding of the physical parameters involved, international tests have been conducted, including ITTC headform comparative experiments. The results clearly show the above-mentioned discrepancies (ref. 1).

The main parameters governing cavitation in water have long been recognised to be the gas content and the Reynolds number. Numerous studies were made in the 50's and 60's in order to assess their relative importance, but these studies were not conclusive.

The importance of water quality appeared to be evident as tests made in exactly similar flow conditions led to different results. Reynolds number effects were also recognised as the inception curves showed similar overall trends when this parameter was varied.

As an example, the well-known results of Bonnin and Hammit are given on figure 1, where cavitation inception experiments in water and sodium are compared (ref. 2).

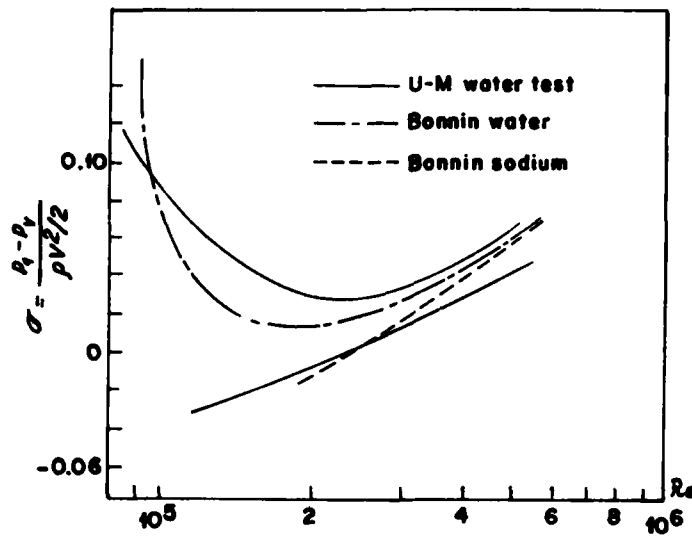


Fig. 1 - Cavitation inception in similar venturis (Ref. 1)

The main recommendations resulting from those studies were in the form of practical rules for cavitation tests :

- (a) Reynolds Number and velocity should be as high as possible in model tests.
- (b) Dissolved gas content should be as low as possible in the cavitation facility.

The second point was recommended both from a cavitation point of view and for practical purposes : a high gas content generally leads to bubble formation in test-sections, making flow visualisation impossible (Ref. 3).

Moreover in 1970, the relative importance of stream nuclei and so-called wall nuclei was not clear (Ref. 4).

Practically, as the parameters involved in cavitation were not correctly described, the laboratories used their own testing procedures to predict cavitation effects, these procedures being compared to full-scale results in an empirical way.

In many naval or industrial applications, the working  $\sigma$  values are high enough so that cavitation has no effect on performance. Thus the results obtained under normal operating conditions in model tests can be extrapolated to full-scale.

During the late sixties, the French Navy began feasibility studies on hydrofoils, with totally immersed lifting surfaces. This type of high speed craft requires the use of an automatic pilot. It is necessary to know precisely the force coefficients of the foils under non-cavitating and cavitating conditions.

For hydrofoil craft, the uncertainties obtained in conventional tests under developed cavitation conditions are unacceptable.

As the model tests of two- and three- dimensional hydrofoils had to be carried out by NEYRTEC (Sog.), it appeared necessary to develop in parallel a more basic research programme.

At the time, the main purpose of research was to be able to make reproducible tests on models and to extrapolate the results to full scale.

### III. PRELIMINARY EXPERIMENTS

The aim of the first studies was to ascertain the order of magnitude of the discrepancies on force coefficients and cavitation inception  $\sigma$  values that could be obtained in model tests depending on the procedure used.

Two types of experiments have been conducted :

- (a) cavitation inception with an orifice plate ;
- (b) lift and moment coefficient measurements on a cavitating two-dimensional hydrofoil.

During these experiments, the dissolved air content of the water in the cavitation tunnel and its time-pressure distribution were varied as well as the flow velocity and the cavitation  $\sigma$  parameter. Typical results for cavitation inception in a jet are given on figure 2 which show the general trend of the phenomenon, viz. :

- (a) cavitation inception  $\sigma_i$  increases with gas content,
- (b)  $\sigma_i$  increases with pressure drop (or velocity in the jet).

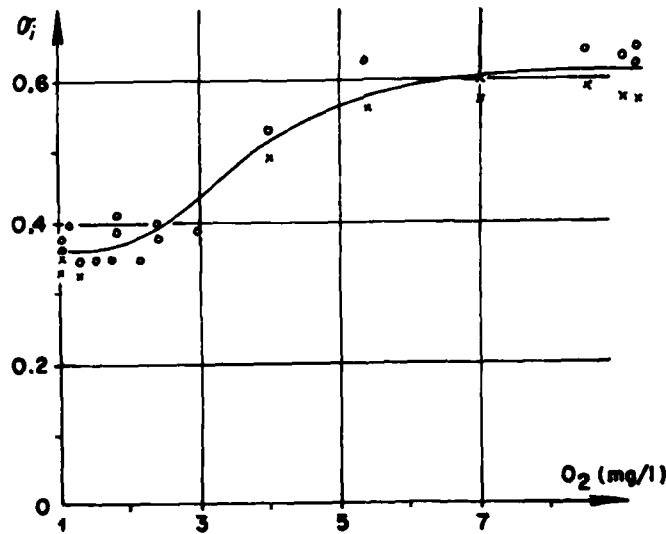


Fig. 2 - Influence of dissolved gas on cavitation inception (circular diaphragm)

The lift curves of the foil (figure 3) show that the discrepancies between lift coefficient under given overall flow conditions were dependent on the type of cavitation. When sheet cavitation appeared, no influence of the gas content was noticed ; when bubble cavitation was present, changes in lift coefficients could be as high as 50 %. The lowest lift for a given value of  $\sigma$  was always obtained with high dissolved gas concentration. It was also shown that the gas content (measured with an oxygen probe) was not the only relevant parameter as tests conducted with the same air content value gave different results.

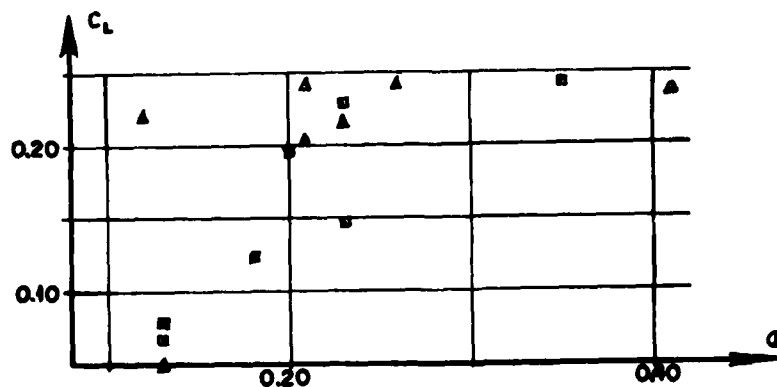


Fig. 3 - Lift of a 2-D Hydrofoil -  $\alpha = 1^\circ$ , showing the dispersion of results

It thus appeared probable that the history of the water had to be taken into account. Different explanations were proposed, most of them involving some stabilization mechanism of "nuclei" in the cavitation facility. In fact, no clear explanation was given at the time, contradictory hypotheses been presented by different authors.

#### IV. NEGATIVE PRESSURE MEASUREMENTS (1972)

As the foregoing global tests were not able to produce a practical procedure for hydrofoil testing, it was decided to seek more basic insight into the specific problem of developed bubble cavitation behaviour.

A special microscope was designed whose resolution was less than  $1\text{ }\mu\text{m}$ . Its focal length was 30 mm in water. The idea was to measure the nuclei in the water upstream from a cavitating body, outside the boundary layer.

A test section was built which consisted of two cylindrical portions built in such a way that one of them could rotate (figure 4). Bubble cavitation was produced on the cylinders and the pressure field was explored in the cavitating zone by means of a movable flush mounted pressure transducer. The main difficulty was to avoid cavitation on the pressure gauge itself.

Tests were conducted by changing the water quality by acting upon the dissolved air content in order to modify the nuclei population.

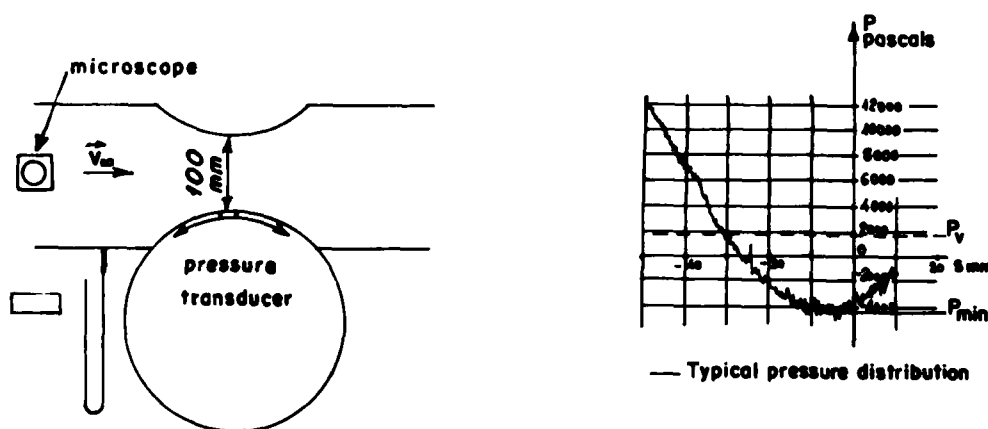


Fig. 4 - Test section

The results showed that whatever the experimental conditions (gas content), a negative pressure zone (or at least a zone where pressure was below vapour pressure) always existed at the boundary of the cavitating flow. The point of minimum pressure (generally below zero absolute) was systematically measured and the related  $C_{pmin}$  value was computed :

$$C_{pmin} = \frac{P_{min} - P_{\infty}}{1/2 \rho V_{\infty}^2} ; \quad \sigma = \frac{P_{\infty} - P_v}{1/2 \rho V_{\infty}^2}$$

For each experimental point, the number  $N$  of vapour bubbles on the profile was measured by means of high-speed photographs. The main result of the study was to show (figure 5) that the minimum  $C_p$  value for a given  $\sigma$  value was only a function of the number  $N$ , whatever the dissolved gas content and the flow velocity.

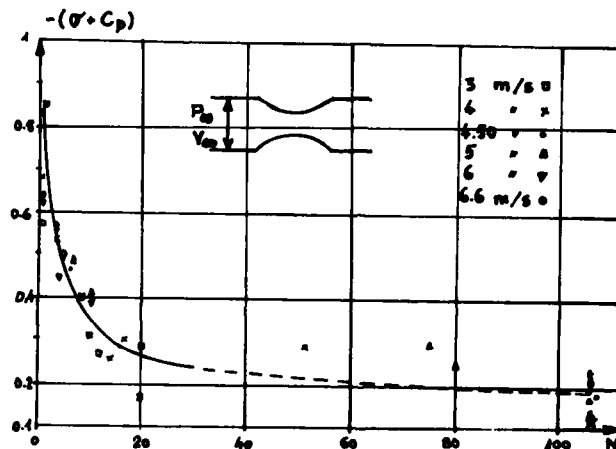


Fig. 5 - Minimum pressure coefficient on the rotating cylinder

As  $N$  increased, the  $C_{pmin}$  value was closer to the working  $\sigma$  value, that is, the pressure was closer to vapour pressure.

The geometry of the flow was also dependent on  $N$ . When the number of vapour bubbles was high for a given  $\sigma$  value, the growth of each bubble was slowed down and its maximum diameter reduced.

Moreover, high-speed movies (5 000 f/s) and instantaneous pressure measurements were recorded simultaneously. This showed that the passage of a growing bubble over the pressure transducer produced a positive pressure pulse.

Finally, the number of nuclei measured using the microscope

was compared to  $N$ . The trend was that when  $N$  increased, the number of nuclei measured, especially the big ones, also increased. These nuclei were very probably microbubbles.

## V. SCALING (1974)

### A. General behaviour of the flow

After these experiments, the overall mechanism of bubble cavitation became clearer :

1. At the leading edge of a profile, provided the  $\sigma$  value is low enough, the cavitation nuclei can create vapour bubbles. The number of bubbles generated depends on the concentration and critical pressure distribution of these nuclei.
2. Further downstream, the growth of vapour bubbles is mostly due to inertia effects. The fact that the bubbles actually grow clearly shows that the pressure outside the bubble in the liquid is below vapour pressure. If the radial velocity of the bubbles is high enough, this pressure can become negative.
3. The effect of the boundary and of neighbouring bubbles tends to slow down the rate of growth. Simultaneously, the mean pressure on the foil increases and the resulting lift decreases.

### B. Theoretical approach

From these qualitative observations, a simplified theoretical model was built whose principal aim was to specify the scaling rules from model to full-scale.

The model consisted of potential flow computation where a grid of five bubbles and their images through a plane were allowed to grow under a specified pressure at infinity  $p_{\infty}(t)$  (figure 6). In our experimental case,  $p_{\infty}(t)$  was extrapolated from subcavitating experiments for a specified  $\sigma$  value.

The result of the computation showed a reasonable agreement between the measured mean pressure and the theoretical time and space averaged calculated pressure.

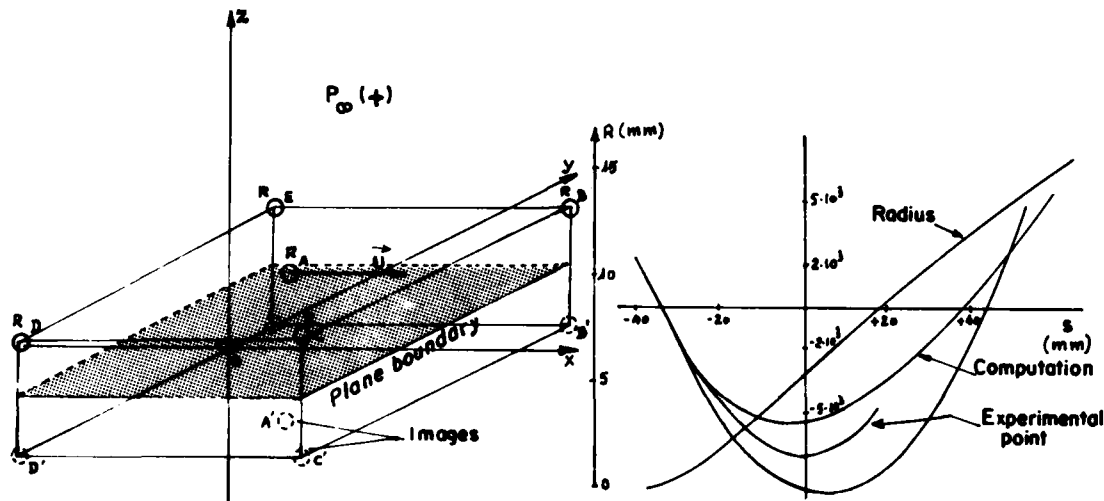


Fig. 6 - 5 bubbles model

The theoretical model is obviously not perfect, i. e. :

- (a) bubbles are assumed to be spherical ;
- (b) the radius of the five bubbles is assumed to be the same ;
- (c) boundary layer effects are not taken into account.

However, from a formal point of view, the model shows that the only relevant parameters are the  $\sigma$  value and the relative distance between bubbles and between the bubbles and the wall.

The result is that bubble cavitation effects as described by this model are only a function of  $N$  and  $\sigma$  whatever the velocity and dimensions.

#### C. Scaling of nuclei concentration

For developed cavitation conditions, the scaling rules on nuclei concentrations become obvious :

The vapour bubbles are generated from freestream nuclei and their absolute number depends on the volumetric concentration of active nuclei. As the number  $N$  of vapour bubbles has to be the same on the model and at full scale, the relative concentration must be proportional to the third power of the geometrical scale ratio  $\lambda$  :

$$\frac{C_m}{C_p} = \lambda^3$$

The smaller the scale, the higher the concentration needed.



## VI. NUCLEI CONTROL (1976)

The general explanation of the phenomenon being known, the problem was to develop practical means to control the nuclei content of water.

### A. Comparative measurement techniques

In April 1974, joint experiments were conducted at NEYRTEC where the available methods for measuring nuclei were compared, namely :

- (a) holographic method of F. B. PETERSON (NSRDC)
- (b) the scattering method of A. KELLER (Munich University)
- (c) the microscope of F. DANIEL (NEYRTEC).

The tests showed a very good correlation between the holographic and scattering methods and these appeared to be the most efficient systems for so-called "indirect measurements". Problems arose with the microscope due to difficulties in precise determination of an "effective" depth of field.

The results confirmed that the nuclei concentration would vary with the operating conditions of the cavitation tunnel in a non-controllable way (ref. 5).

### B. Artificial nucleation

It then became important to develop apparatus to generate artificial nuclei. The best way was to inject microbubbles in the water (e. g. Electrolysis, bubble filter). NEYRTEC developed a special technique by using high pressure saturated water. The study of this technique began in 1975. At that time, air and water mixtures were injected into the facility and the bubbles produced had an average diameter of 50  $\mu\text{m}$ . The system permitted an injection rate of about  $10^6$  to  $10^7$  microbubbles per second. For typical test conditions (flow rate 10  $\text{m}^3/\text{s}$ ), this leads to a nuclei concentration of 0.1 to 1 bubble per  $\text{cm}^3$ , which is a rather low concentration.

Since that time, new microbubble systems of the same type have been developed to produce up to  $10^{10}$  microbubbles/second. All exhibit a critical pressure very close to the vapour pressure and are well suited for model tests.

Simultaneously, new concepts of test facilities (pump test loops, cavitation tunnels, etc.) have been developed embodying nuclei content control systems.

### C. Venturi (direct measurements of nuclei)

The results given by indirect methods of nuclei measurements always show very large amounts of nuclei (ref. 5) - more than one thousand per cubic centimetre in the range of diameters above  $1\text{ }\mu\text{m}$ . Experimented observations on cavitation bodies show that the number of vapour bubbles is limited and that concentrations higher than 1-10 active nuclei per  $\text{cm}^3$  were difficult to explain. For this reason, it was decided to build a system in which the pressure could be controlled and the number of nuclei actually creating vapour bubbles in the specified conditions could be determined.

In 1976, NEYRTEC built a microventuri (figure 7) whose principle had first been developed at the Delft Hydraulic Laboratory by OLDENZIEL. The principle of the system consists in creating a known pressure at the venturi throat. By varying the flow rate, this pressure can be changed and become negative. For a given pressure, the number of nuclei generating vapour bubbles are counted acoustically when they collapse.

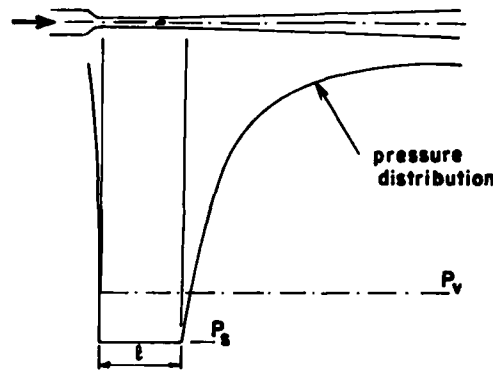


Fig. 7 - Principle of venturi system

Using this system, one is able to measure the effective nuclei distribution and determine the histogram of critical pressure versus concentration. This apparatus is built in stainless steel or nickel and so can be used with most industrial liquids like water, sodium or mercury.

#### D. Results and applications of venturi apparatus

Several tests under laboratory and industrial conditions have been conducted using the venturi system. All the results clearly showed that the nuclei population in "industrial" water is always less than expected from indirect-method measurements.

Typically, the "susceptibility" (i. e. critical pressure of weakest nuclei) of water is less than - 1 bar and the effective nuclei concentration whose critical pressure is above - 2 bars is in the range of 10 to 100 per litre. Such low critical pressures would correspond to bubbles less than 2  $\mu\text{m}$  in diameter. This confirms that the particles which are present in the water and which are measured by indirect methods do not constitute nuclei, at least in the range of practical hydrodynamic conditions.

This shows that using direct methods is the only way to measure the nuclei content in full scale conditions. However, indirect methods (e. g. scattering) can be used in test facilities when the nature of the nuclei is known. For example, NEYRTEC designed a local scattering apparatus to count the microbubbles injected into cavitation tunnels (Ref. n° 6 ). Practically, the range of concentrations that can be measured with the venturi is limited to  $10/\text{cm}^3$ . Using the scattering method, it is possible to count up to  $1\,000/\text{cm}^3$ .

NEYRTEC has used the venturi system for many different applications, e. g. :

##### (a) 1977 : Turbine tests in LAUSANNE (E.P.F.L.)

The curve (figure 8) summaries a typical test showing the efficiency- $\sigma$  curve with and without injecting artificial nuclei. The nuclei concentration was measured with the venturi. These experiments are described in reference n° 7.

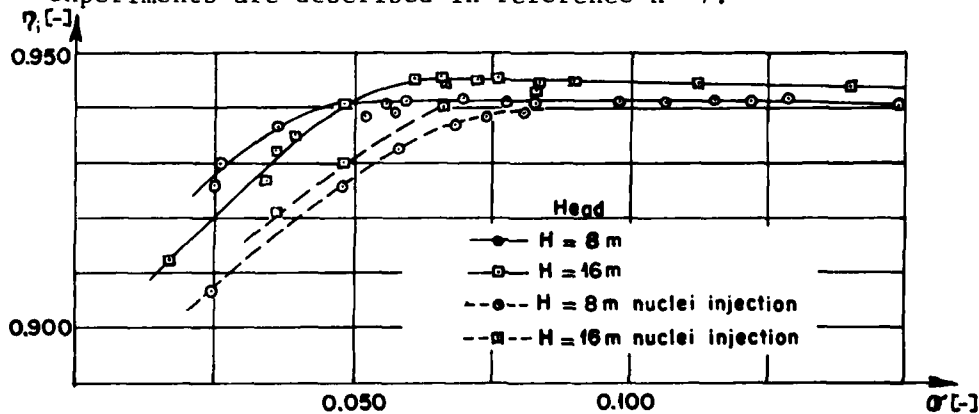


Fig. 8 - Efficiency -  $\sigma$  curves for a Francis turbine

- (b) 1978 : Joint experiments were conducted in Delft Hydraulic Laboratories. Two venturi techniques (Delft and NEYRTEC), one scattering method (KELLER), one holographic method (VAN RENESSE) and one acoustic method (JANSSEN-DELFT) were compared and a correlation of the results has been made with the cavitation noise emitted by a valve. The results confirmed the discussion above. A report of those experiments will be published in IAHR conference (Amsterdam - September 82).

During the same year, a NEYRTEC/CEA/EDF/CNRS contract showed that the nuclei content was the same in tap water and water containing large quantities of mud. The measured concentration was in both cases very low.

Figure 9 shows the large discrepancies between a scattering method and a venturi system.

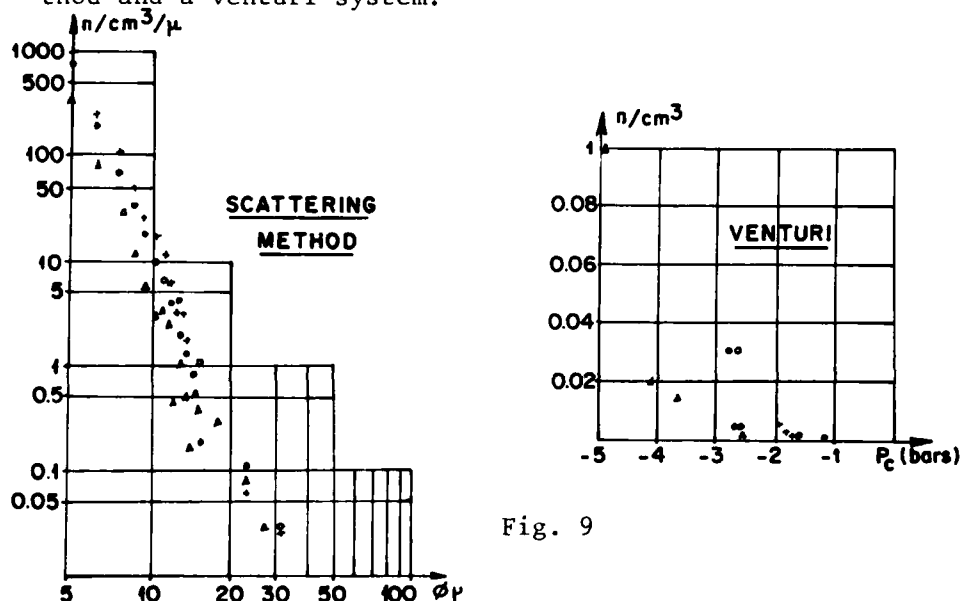


Fig. 9

- (c) 1980-1982 : In order to know the nuclei concentration in sea water and simulate it in model tests using the above-mentioned scaling laws, a special apparatus was built to measure "in situ" nuclei distributions down to 100 metres. Typical results of preliminary tests are given in figure 10. It was planned to use this system in January 1982 in a cooperative programme between the Naval Sea Systems Command and the French Navy (Bassin d'Essais de Carène).

Unfortunately, the weather made it impossible to perform successful tests.

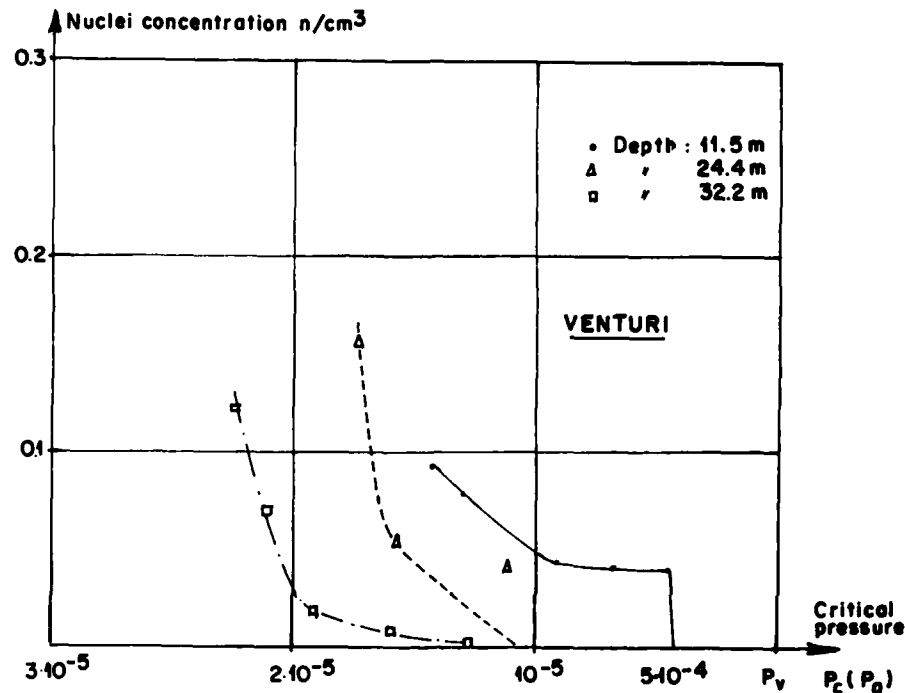


Fig. 10 - Nuclei spectrum in sea water

#### VII. VALIDATION OF SCALING LAWS (1982)

After the above-mentioned studies, it appeared important to carry out tests in industrial conditions with the following aims :

1. Verify the proposed scaling laws between full scale and models, namely :  
 $\sigma_i$  based on  $P_s$  and not on  $P_v$ .  
 nuclei concentration scaling as  $\lambda^3$ .
2. Demonstrate the operational feasibility of the techniques developed for nuclei control (artificial nuclei injection and measuring methods).
3. Give recommendations for future applications in the design and operation of cavitation facilities.

##### A. Description of the experiments

Two types of test were conducted. The first was a comparison of the lift curves and cavitation inception conditions of two geometrically similar hydrofoils.

The second type of test compared the thrust of two propellers.

The hydrofoils (NACA 16209) were two-dimensional. The larger one had a chord length of 600 mm and a width of 900 mm. The smaller one was geometrically similar at a scale of 1/6. The two cavitation test sections including the contraction and diffuser were also similar at the same scale ratio.

The propellers were installed in the big cavitation tunnel. The larger propeller had a diameter of 330 mm and the smaller a diameter of 165 mm.

During these tests, the water was seeded with artificial nuclei, the 36 injection points being equally distributed upstream from the contraction. The length allowed for mixing was sufficient to provide a homogeneous distribution of nuclei in the test section.

The lift of the hydrofoils was measured for 5 incidence values ( $-1$ ,  $0$ ,  $1$ ,  $2$  and  $3^\circ$ ) and different velocities ( $5$  to  $15$  m/s). A typical test consisted in gradually lowering the  $\sigma$  value until cavitation extended downstream from the hydrofoil. For all these tests, nucleation was systematically varied and measured by venturi and scattering methods.

Inception conditions were determined with and without injection.

The Reynolds numbers used were in the range of  $0.4 \times 10^6$  to  $1.2 \times 10^6$  for the small hydrofoil and  $3.6 \times 10^6$  to  $4.8 \times 10^6$  for the large one.

Propeller thrust was measured for different  $J$  values extending from  $0.5$  to  $0.9$ , and typical tests were similar to the ones made with hydrofoils (cavitation inception and force measurements).

Most of the tests were made with travelling bubble cavitation and high speed movies and photographs were taken throughout.

## B. Results

### 1. Cavitation inception

Cavitation inception conditions for a given geometrical configuration (same incidence angle for the foils or same  $J$  for the propellers) were exactly the same when nuclei injection was applied. In the case of the propellers, the  $\sigma_i$  value under these conditions was compared with theoretical calculations made by "Bassin d'essais des Carènes". The inception  $\sigma$  conditions were found to be very close to the minimum  $C_p$  value for  $J = 0.6$ .

These inception values did not depend on the scale, velocity, testing procedure or dissolved gas content. Of course, in this case,  $\sigma_i = \sigma_d$ .  $\sigma_d$  is the so-called desinent  $\sigma$ .

When no nuclei were seeded, the  $\sigma_i$  value was highly dependent on the overall test conditions. For example, with hydrofoils, it was possible, using highly degassed water, to perform tests at a  $\sigma$  value of 0.5 and an incidence of  $3^\circ$  without cavitation. This corresponds to highly developed cavitation and even to a drop in lift when nucleation is applied.

This clearly shows that inception conditions cannot be correctly determined if no artificial nuclei are used.

Moreover, to determine  $\sigma_i$ , which represents a limit between sub-cavitating and cavitating conditions, it is not necessary to control the number of nuclei, but only to know that a "sufficient" number of them have a critical pressure very close to the vapour pressure.

A more detailed discussion of this point can be found in ref. 7.

## 2. Developed cavitation

### Hydrofoils

The main difficulty during these tests was to obtain nuclei concentrations with the large hydrofoil which were low enough to simulate conditions corresponding to low nuclei contents with the small hydrofoil.

The  $\lambda^3$  law requires equivalent concentrations in the big cavitation tunnel which are 196 times lower than in the small one. It is practically impossible to measure such a low concentration in the big tunnel as its order of magnitude is less than :

$$1 \text{ nuclei}/10^6$$

Such a measurement is statistical in nature and difficult to interpret.

In practice, we succeeded in having no measurable nuclei in either tunnel when the tests were made in both cases with very highly degassed water.

The results of figure 11 give the  $C_L - \sigma$  curve for the big hydrofoil with and without nuclei injection.

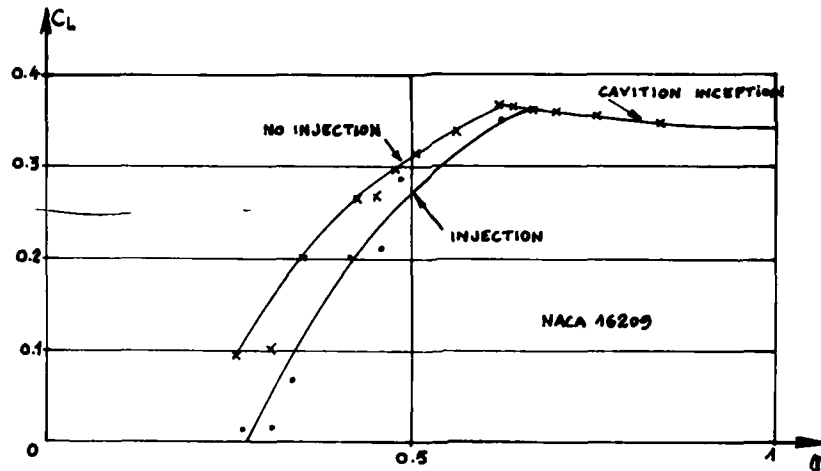


Fig. 11 - Effect of nuclei injection on the lift of the big hydrofoil  $i = 2^\circ$

On figure 12, for the same incidence, the drop ( $\Delta C_L$ ) in  $C_L$  is presented in both cases in the form :

$$\frac{\Delta C_L}{C_L \text{ subcavitating}}$$

The curves show that this drop in lift is the same when the nuclei concentrations scale as  $\lambda^3$ .

This has been verified for all the experimental points at which bubble cavitation occurred.

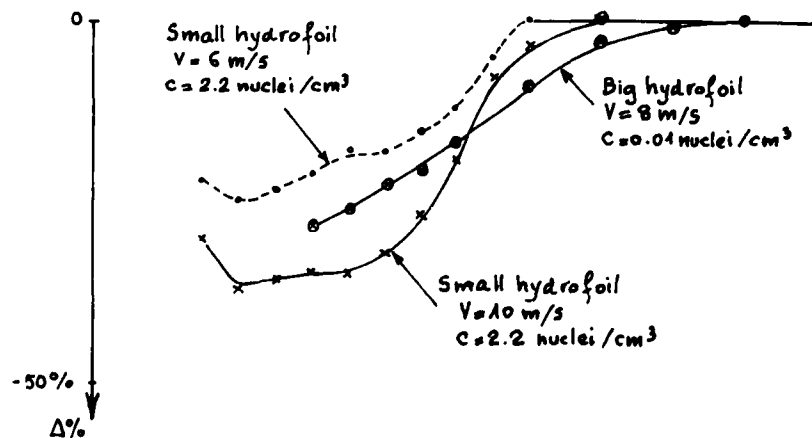


Fig. 12 - Relative drop in  $C_L$  between degazed water and water with added nuclei when concentrations are scaled as  $\lambda^3$





≈ 50 cm

Cavitation bubble on the big hydrofoil  
nuclei concentration ≈ 0

Flow  
direction

Photo 1



10 cm

Small hydrofoil  
concentration ≈ 0

Flow  
direction

Photo 2

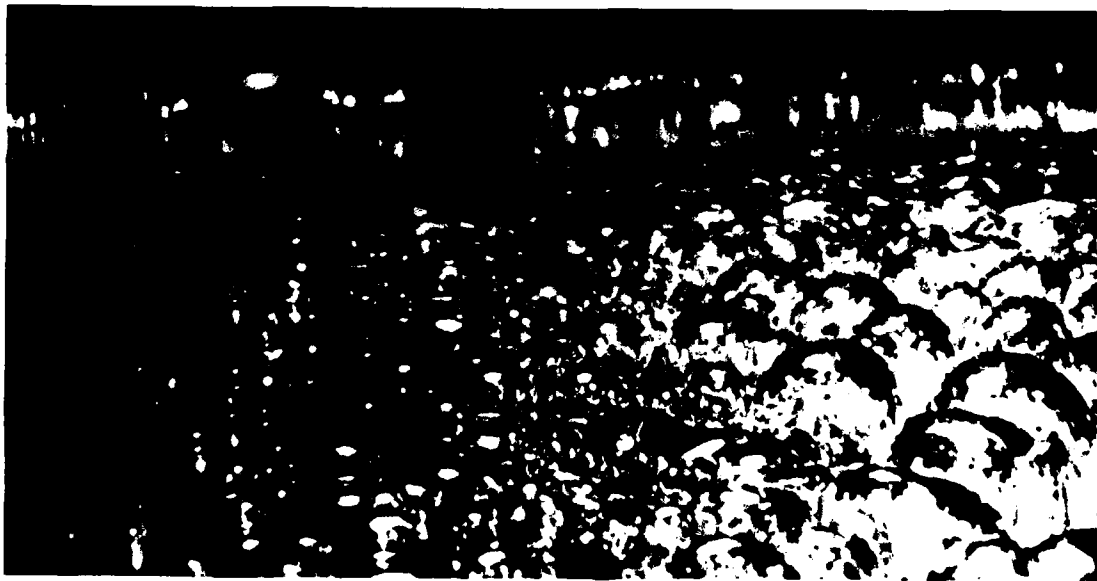


≈ 50 cm

Big hydrofoil - concentration ≈ 0.01 / cm<sup>3</sup>

Flow  
direction

Photo 3



10 cm

Small hydrofoil - concentration ≈ 2.2 / cm<sup>3</sup>

Flow  
direction

Photo 4

Photographs n° 1, 2, 3, 4 show the aspect of cavitation on the two hydrofoils. Photographs n° 1 and 2 correspond to a low nuclei concentration.

Photographs n° 3 and 4 correspond to nuclei concentrations of  $0,01/\text{cm}^3$  for the big hydrofoil and  $2,2/\text{cm}^3$  for the small one.

It is obvious that the flow geometries also scale under these conditions.

It is to be noted that the isolated bubbles shown on photograph n° 1 on the big hydrofoil with degassed water have a diameter of about 150  $\mu\text{m}$  !

It was also verified that at high incidence angles, when sheet cavitation was present, nuclei injection had no influence on the geometry of the flow or on the resulting lift.

### Propellers

The results for the propellers are very similar to those obtained with the hydrofoils.

A typical  $K_T$  curve is given on figure 13 showing the effect of nuclei injection and (for a  $J$  of 0.66) the effect of an increased number of injected nuclei.

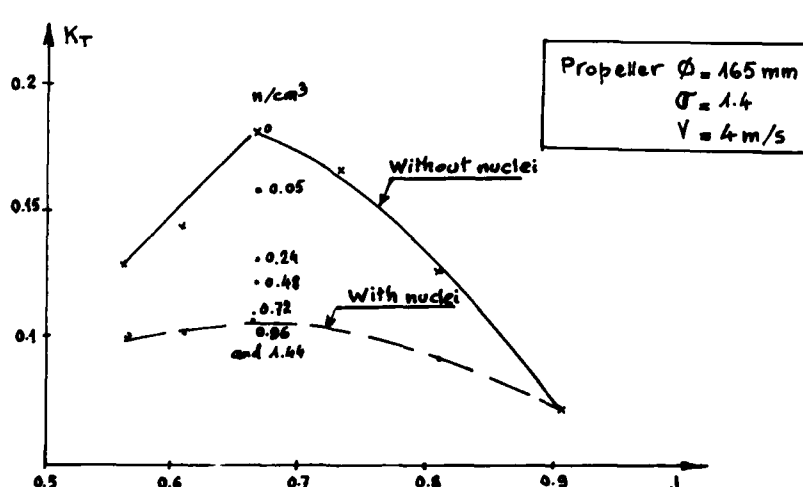


Fig. 12 -  $K_T$  curve obtained with and without nuclei

In this case also, the concentration to be injected to obtain an equivalent  $K_T$  was scaled as  $\lambda^3$  as with the profiles and the flow geometry was also similar under these conditions.

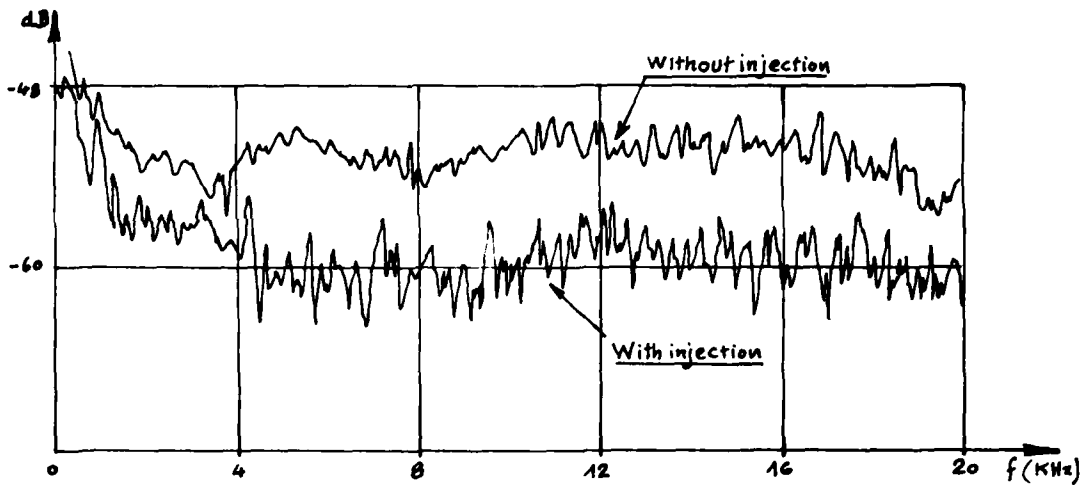


Fig. 14 - Noise emitted by the small hydrofoil with and without nuclei injection

#### Noise

Although no systematic study of the noise emitted was made, a tremendous effect of nuclei population on radiated noise was observed. The lower the concentration, the higher the noise generated.

Figure 15 gives a comparison of noise intensity recorded on the small hydrofoil at two different nuclei concentrations. The validity of making such measurements in the frequency-intensity plane could be questioned and this result must be considered only as a global effect.

## CONCLUSION

The main object of this paper was to describe experimental research work conducted at NEYRTEC from 1968 to 1982 to develop simulation procedures for cavitation scaling. Only the principal results obtained during the 15 year period are presented but these relate both to basic research and to more practical applications.

Most of the results are concerned with bubble cavitation as this is greatly influenced by nuclei populations. It is not of course sufficient to control nuclei populations to scale all aspects of cavitation behaviour perfectly. Reynolds effects still remain important because they are responsible for the type of cavitation produced. However, their influence on inception is probably not as important as previously thought.

Concerning full scale nucleation in natural waters, many questions remain to be answered about the physical and biological nature of nuclei. Currently, the only practical way of gathering the missing knowledge is to carry out in situ experiments at sea, but these are not readily performed.

Care must be taken when representing natural nucleation on models. Most of the existing water tunnels are not equipped with artificial nuclei injection systems. Full scale data are still needed under varying experimental conditions to provide practical scaling recommendations for model tests.

- Réf. 1     JOHNSON C. A.  
"Cavitation inception on Head Forms. Further tests"  
Proc. 12th ITTC Conf. Rome 1969
- Réf. 2     BONNIN, BONNAFOUX, GICQUEL  
"Comparaison des seuils d'apparition de la cavitation  
dans un tube de venturi dans l'eau et le sodium liquide"  
EdF - Bulletin de la Direction des Etudes et Recherches.  
Série A - n° 1     P. 3 - 12 - 1971
- Réf. 3     A. GORSHKOFF  
14th ITTC Ottawa 1975 P. 154  
Appendix 8 - Standards for cavitation tests.
- Réf. 4     F. B. PETERSON  
ONR Syp. Paris - 1972
- Réf. 5     F. B. PETERSON, F. DANIEL, A. KELLER and Y. LECOFFRE  
Comparative measurements of bubble and particulate  
spectra by three optical methods  
14th ITTC Conference  
Ottawa 1975
- Réf. 6     Y. LECOFFRE  
"Cavitation Tests and Nucleation Control"  
ASME Winter Annual Meeting - New-York 1979 -  
Cavitation Inception
- Réf. 7     P. HENRY, Y. LECOFFRE, P. Y. LARROZE  
Scale effects of cavitation phenomena  
Symposium AIRH 1980 TOKYO

## Discussion

V.H. Arakeri (Indian Institute of Science)

The authors have shown a vivid pictorial presentation of cavitation phenomena. Their method of seeding the flow with nuclei is most interesting and effective. However, it appeared from the film that the number density of nuclei in the flow upstream of the propeller, for example, is rather too high. It is well known that in two-phase mixtures containing water and air bubbles the speed of sound can decrease by an order of magnitude to values as low as 10 mls. In view of this, it would be interesting to know the void fraction in the flow with nuclei seeding and whether the authors feel that the compressibility effects due to the phenomena discussed are not likely to be important in their experiments.

S. Gowing (DTNSRDC)

The authors of this paper have indicated that the effect of cavitation nuclei concentrations on traveling bubble inception prediction may be properly scaled by varying the total concentrations of the nuclei according to the geometric ratio only ( $\lambda^3$ ). Research at DTNSRDC has shown model size to affect the size range of microbubbles that is eligible for cavitation. This is especially true for the case of "large" (~100- $\mu$ m) bubbles having an insufficient residence time in the low-pressure zones of small models to blow up. Would the authors please comment on their conclusions regarding the effects of size distribution of the microbubble nuclei used in scaling inception test results of different size models?

K.R. Suhrbier (Vosper Thornycroft (U.K.) Limited)

My comments refer to the discussion in Section VII and in particular to the data given in Figure 12 for the 165-mm propeller.

The effect of the nuclei seeding described on  $K_t$  is clearly very pronounced and certainly much greater than what could be achieved by simply changing the total gas content of the tunnel water. The authors' method may therefore be of interest when dealing with scale effects in the case of high-speed propellers since the coefficients of the models often tend to be too high, unless special test techniques are used.

Perhaps it would have been interesting to have seen the data for the 330-mm propeller. Presumably, the same thrust coefficient was obtained for the concentration scaled as  $\eta^3$ , rather an equivalent  $K_T$  as stated in the paper.

May I ask the authors whether they had an opportunity to correlate any model propeller test results, obtained with their procedure, with full-scale data?

E.A. Weitendorf (Hamburg Ship Model Basin)

I appreciate the photographic and movie material of the authors, hereby, one can observe the physical processes of the different tests in detail. Regarding the utilization of the venturi or of the scattered light system it should be mentioned that the first system is not suitable for the measurement of a nuclei histogram containing concentrations and diameters, since those nuclei distributions are responsible for the creation of sheet cavitation. Moreover the venturi system can only be used for very degassed water not occurring in normal cavitation tests. This means a limitation of the applicability of the venturi system when the input data for the physical process of the inception of the sheet cavitation have to be measured. Concerning the efficiency of the model Francis turbine (in Figure 8 of the paper), it would have been appreciated if a proof of these values for the prototype had been given by the authors after applying the scaling law proposed by the authors.

Finally, a word concerning the validity of the paper having the embracing title "Nuclei and Cavitation" should be made. The results given in the paper were concerned with bubble cavitation only. Until now, this type of cavitation was never observed in full scale. This bubble cavitation seems to be a physical process occurring in model tests only. All full-scale cavitation observations have revealed sheet cavitation. This means that the value of the paper in understanding the physical phenomena "Nuclei and Cavitation" is restricted, since, moreover, each type of cavitation is governed by its own scaling law.

### Author's Reply

J.P. Le Goff and Y. Lecoffre

To Mr. Arakeri

The question of changing the speed of sound in the cavitation tunnel may be an important one when artificial nuclei are applied.

In our case, the order of magnitude of the maximum microbubble flow rate was  $3 \times 10^{-5} \text{ m}^3/\text{s}$ , when the total water flow rate in the cavitation tunnel was about  $4 \text{ m}^3/\text{s}$ .

The average void fraction in the cavitation tunnel was roughly  $10^{-5}$  and cannot lead in this case to a very low speed of sound.

Note that 64,000 bubbles  $50 \mu$  in diameter have the same volume as one 2-mm bubble. Of course, the same void fraction made up of 2-mm



bubbles does not lead to the same "milky" appearance of the flow.

However, concerning the attenuation of sound even for such very low void fractions, a marked effect has been found when we tested the Sydney express propeller.

As the type of cavitation was permanent sheet cavitation, no influence of nuclei injection on performance or type of cavitation could be found. Nevertheless, the noise level measured was lower in the whole range of frequencies when microbubbles were injected.

To Mr. Gowing

When making our cavitation inception tests, we compared the results obtained with and without microbubble injection. The shift in  $\sigma_i$  values was found to be extremely large (insofar as  $\sigma_i$  can be defined when no nucleation is applied as cavitation events appear in a rather stochastic manner in this case).

When nucleation was applied (Reference 8), the  $\sigma_i$  values, incipient or desinent, were found to be the same. They were compared with calculations in the case of the propeller and were found to be very close to the  $(C_{p_{min}})$  value.

It should be noted that the propeller used was specially designed to exhibit bubble cavitation and had a smooth pressure distribution, giving the cavitation bubbles sufficient time to grow.

Concerning the tests made at a lower sigma value, where the cavitation is more developed, the nuclei are subjected to a low negative pressure. In this case, the time effect on "big nuclei" ( $>100 \mu$ ) is less pronounced.

The nuclei distribution used in most cases was in the range of 30 to  $100 \mu$  (mean diameter  $50 \mu$ ). Owing to the fact that the pressure distribution is always rather smooth in bubble cavitation, we think that such a nuclei distribution did not lead to large discrepancies in  $\sigma_i$ .

Of course, for a much smaller scale, the effects could be important.

To Mr. Suhbier

The 330-mm propeller led to equivalent results as stated in the paper, that is: same effect on cavitation appearance and same effect on the order of magnitude of the thrust when nucleation was scaled as  $\lambda^3$ .

Unfortunately, until now we have not had the opportunity to compare such model tests and sea trials. The tests described are the first ones we have made on propellers, and these have been specially designed to entrance traveling bubble cavitation for these specific experiments.

More work is necessary to make the comparisons you mention.

## References

- Y. Lecoffre and A. Bovis, "Mesure en mer et en moyens d'essais de la teneur en germes de cavitation," DRG Seminar on Advanced Hydrodynamics Facilities, Den Haag (Pays-Bas), 26-28 April 1982.

To Mr. Weitendorf

As a general comment, the principal reason why this research program was made was that very large discrepancies have been found in model cavitation tests in our laboratory.

Some of those tests concerned the development of a hydrofoil craft, and problems arose with exactly similar overall operating conditions (same tunnel, same hydrofoil, same velocity, and same sigma value). Further, it is well known that tests made in different facilities also show similar discrepancies. Thus, such discrepancies can only be due to changes in the "quality" of the water.

When testing model hydrofoils, which was, at the time, our primary concern, traveling bubble cavitation was always found at low incidence angles, and it could be shown that only this type of cavitation was influenced by nuclei content as far as lift measurements were concerned. As stated in the paper, the order of magnitude of the discrepancies found could be as high as 30 percent of the lift.

The purpose of the present study was to devise a method of making reproducible experiments. As explained in the paper, this was done by:

- o studying the traveling-bubble cavitation type and the associated scaling laws at reduced scale,
- o developing means of controlling the nuclei distribution,
- o checking that traveling-bubble cavitation actually could exist at a large scale and that the scaling laws proposed for nuclei distribution hold true.

Moreover, numerous tests made by us and others relate to other types of traveling or unsteady cavitation, where the influence of nuclei is also important, especially regarding the  $\sigma_i$  values (References 1 and 6) and the noise generated.

We do, of course, agree that each type of cavitation is governed by different scaling laws.

Concerning the use of the venturi system or the scattering method, our opinion is as follows: when the nature of nuclei is not known, which is the case for measurements in natural or industrial water, the only available instruments that can measure the nuclei population are what we call the direct ones, which are the ones in which nuclei are actually forced to cavitate under gradually changing pressure levels.

When the nature of nuclei is known, this being the case of the water used in cavitation tunnels when it is seeded with microbubbles, any method that can detect these efficient nuclei can be used (scattering, holography, venturi). The main limitation of the venturi system is obviously the density of nuclei it can measure. Practically,

the maximum measurable density lies between 5 and 10 nuclei per  $\text{cm}^3$ . In our opinion and from our measurements, this corresponds to an extremely large amount of efficient nuclei in natural water. It also corresponds to high concentrations in cavitation facilities when no artificial nucleation is applied under conventional testing conditions.

When artificial nucleation is applied, in our laboratory we use either a bypass scattering method or the venturi, depending on the microbubble concentration generated. The two methods yield similar results in the range of concentrations where they both work.

Thus, the utilization of the venturi system is not limited by the total air content (saturated or degassed water) but basically by the number of efficient nuclei present in the water, which is usually much less than  $1/\text{cm}^3$ .

Turning to the problem of the efficiency of the Francis turbine, the preliminary remarks made in this discussion are also, in our opinion, applicable.

Moreover, it should be noted that the sigma values used in industrial prototypes are normally much higher than those for which a loss in performance is measured in model tests. The main reason is to avoid erosion. Thus, direct industrial comparisons are not possible.

The main results of the tests in the Lausanne Laboratory were that the drop in efficiency due to a change in head on the model was suppressed and that the so-called standard sigma was the same for the two heads utilized (8 m and 16 m). A more detailed report of these tests can be found in Reference 7 of the paper.

The second point is that it happens quite often that severe erosion is found in prototype turbines when no apparent cavitation was obtained on the model. Applying artificial nucleation, in our opinion, reveals the zones where cavitation is likely to appear on the prototype, and, hence, possible erosion zones.

To conclude, regarding the problem of traveling bubble cavitation or any cavitation initiated by nuclei, most facilities exhibit nuclei concentration that are several orders of magnitudes too low.

*Session III*

**NONLINEAR  
FREE-SURFACE  
PROBLEMS**

# A Numerical Approach to Nonlinear Ship Motion

by

Tor Vinje, Xie Maogang\*

The University of Trondheim, Trondheim, Norway

Per Brevig

The Norwegian Hydrodynamic Laboratories, Trondheim, Norway

## ABSTRACT

A numerical method for simulation of nonlinear 2D ship motion problems is presented. The method is based on potential theory and the problem is treated as an initial value problem. The full non-linear free surface condition is assumed in an inner domain and this solution is matched along an assumed common boundary to a linear solution in the outer domain. The results agree fairly well with results from linear theory regarding a submerged cylinder in forced motion and with an incoming wave. Noticable non-linear effects, even breaking, are observed for cylinders close to the free surface.

## INTRODUCTION

Whilst linearized hydrodynamics give extremely useful prediction of the forces on and the motion of ships under normal operating conditions, the basic underlying assumptions of the theory preclude application to extreme wave heights and large motion amplitudes. Even though higher order asymptotic solutions have shown to predict well certain nonlinear phenomena, such as slow-drift oscillation of moored vessels, we are still lacking an analytic tool for prediction of extreme ship motions, such as capsizing. Even prediction of the local hydrodynamic forces acting on bow-flare sections of ships running in reasonably low waves is not covered by these asymptotic methods. To cope with these extreme cases different numerical approaches have been applied, all taking into account the non-linear free surface conditions and allowing the body to perform finite motions.

Since the early seventies the "particle-and cell" technique has been applied to these kind of problems. This method is in general a very powerful one, but the disadvantage seems to be that the material free surface is not

\* Permanent address: China Ship Scientific and Research Center, Wuxi, China.

that well described in the framework of the finite difference method to really account for large curvatures (see Nichols & Hirt (1975)). This short-coming seems to be accounted for by introducing curve-linear coordinates (see Coleman & Haussling (1982)), which unfortunately, in turn introduces computational difficulties. It must also be mentioned that till now this method seems to be the only one that has been extended from 2-D to 3-D problems.

It was not until Longuet-Higgins & Cokelet (1976) and Faltinsen (1977) introduced the Euler/Lagrangian method that it seemed to be possible to follow the free surface properly in time. Longuet-Higgins & Cokelet (1976) managed to describe the development of the plunging deep water breaker up to the point where the plunger's jet has been fully developed, which was very promising when regarding it from a numerical ship hydrodynamicist's point of view. Faltinsen (1977) applied a similar method to the forced motion problem of a surface piercing circular cylinder and managed to follow the motion of the fluid for a considerable period of time.

Longuet-Higgins & Cokelet's and Faltinsen's ideas were followed up by Vinje & Brevig (1981a) where the development of the plunging breaker on finite water depth was simulated in time, following the breaker until it's jet hit the wave front.

In the present paper an extension of this method to cover the existence of submerged and surface piercing cylinders is presented and discussed.

First the numerical framework for the space-periodic problem will be presented together with the results from applying this method and secondly a hybrid method that takes into account the incoming wave and the possible diffraction effect from the body will be presented. Some results from use of this method will be presented and the advantages and shortcomings of the method will be discussed. Finally possible improvements will be discussed.

#### SOLUTION OF THE PROBLEM

The mathematical formulation will be given for the 2-D problem of a submerged cylinder under breaking waves. At the end the modifications caused by the existence of a surface piercing body will be indicated. Further more, the solution will be assumed to be periodic in space, which will later be modified by introducing a hybrid method.

The problem is stated as an initial value problem described in mixed Eulerian/Lagrangian formulation: we follow

the motion of marked particles on the free surface referred to a stationary coordinate system. Since the fluid is homogenous, incompressible and the velocity field irrotational we can admit the complex potential:

$$\beta(z, t) = \phi(x, y; t) + i\psi(x, y; t) \quad (1)$$

where  $z = x + iy$ .

$\phi$ , the velocity potential, and  $\psi$ , the stream function both satisfy Laplace's equation and consequently  $\beta$  is analytic in the fluid domain. Hence Cauchy's theorem is valid:

$$\oint_C \frac{\phi + i\psi}{z - z_0} dz = 0 \quad (2)$$

where the contour of integration  $C$  is shown in figure 1 and  $z_0$  is outside the fluid domain. Assuming  $C$  to consist of  $C_\phi$  and  $C_\psi$  where  $\phi$  is given on  $C_\phi$  and  $\psi$  is given on  $C_\psi$  we obtain a Fredholm's integral equation of the second kind:

$$\alpha\psi(x_0, y_0; t) + \operatorname{Re}\left\{\oint_C \frac{\phi + i\psi}{z - z_0} dz\right\} = 0 \quad (3)$$

for  $z_0$  on  $C_\phi$  and

$$\alpha\phi(x_0, y_0; t) + \operatorname{Re}\left\{i\oint_C \frac{\phi + i\psi}{z - z_0} dz\right\} = 0 \quad (4)$$

for  $z_0$  on  $C_\psi$ .

Here  $\alpha$  is the angle between the two tangents of  $C$  at  $z_0$ . When  $z_0$  is on a smooth part of  $C$ ,  $\alpha$  is equal to  $\pi$ .

As will be shown later  $\phi$  is given on the free surface and hence this is part of  $C_\phi$ . On the bottom we assume  $\psi = 0$  and hence this is part of  $C_\psi$ . On the moving cylinder we have  $\psi$  known but for a constant, but examining equation 4 we see that the value of this constant is immaterial since:

$$\oint_{\text{CYL}} \frac{i}{z - z_0} dz = i \oint_{\text{CYL}} \frac{dz}{z - z_0} = 0 \quad (5)$$

when  $z_0$  is outside the cylinder and

$$\operatorname{Re}\left\{\oint_{\text{CYL}} \frac{i}{z - z_0} dz\right\} = \operatorname{Re}\{i2\pi\} = 0 \quad (6)$$

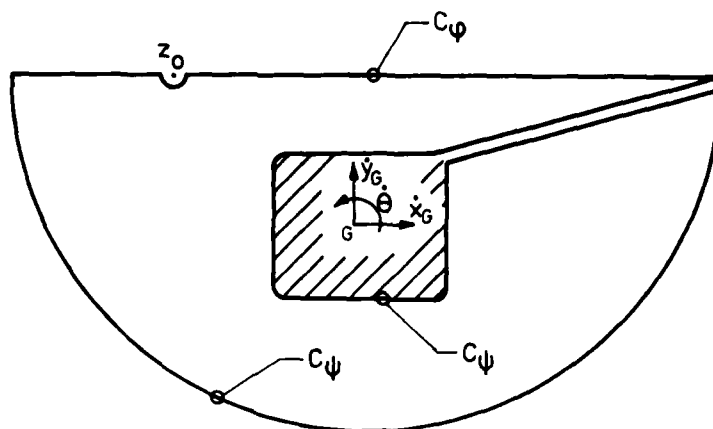


Figure 1 - Definition sketch

when  $z_0$  is inside the cylinder. We therefore do not need to know this constant on the cylinder when solving the problem, after which we can calculate  $\psi$  on the cylinder from equation 3.

For a moving rigid cylinder the kinematic condition on the body reads:

$$\psi(x, y; t) = \dot{x}_G(y - y_G) - \dot{y}_G(x - x_G) - \frac{1}{2}\dot{\theta}^2 R^2 + C \quad (7)$$

where  $(x_G, y_G)$  are the coordinates of the center of gravity of the cylinder and the dot denotes the time derivative,  $\dot{\theta}$  the angular velocity of the body and  $R^2 = (x - x_G)^2 + (y - y_G)^2$ .

When solving the problem equation 7 is introduced into equations 3 and 4 and  $C$  is determined from equation 3 after the problem has been solved.

The free surface kinematic condition is

$$\frac{Dz}{Dt} = u + iv \equiv w^* \quad (8)$$

where  $D/Dt$  is the material derivative, the asterisk denotes complex conjugation and  $w$  is the complex velocity:

$$w(z, t) = u(x, y; t) - iv(x, y; t) = \frac{\partial \beta(z, t)}{\partial z} \quad (9)$$

The dynamic condition on the free surface is given by Bernoulli's equation as:



$$\frac{\partial \phi}{\partial t} = - \frac{1}{2} ww^* - gy - \frac{p_s}{\rho} \quad (10)$$

where  $p_s$  is an arbitrarily applied pressure,  $\rho$  is the density of the fluid and  $g$  is the acceleration of gravity. The material derivative of  $\phi$  is given by:

$$\frac{D\phi}{Dt} = \frac{1}{2} ww^* - gy - \frac{p_s}{\rho} \quad (11)$$

From equations 8 and 11 the position of the free surface and the velocity potential on the free surface can be integrated in time. This in turn makes the free surface part of  $C_\phi$ .

For transient problems like overturning of breaking waves, capsizing of vessels and so on, it seems reasonable to apply periodicity in  $\phi$  and  $\psi$  as the boundary conditions on the vertical boundaries. The validity of this assumption will be discussed more thoroughly later in the paper.

With these boundary conditions introduced ( $\phi + i\psi$ ) is uniquely determined (except possibly for an imaginary constant).

To calculate the force acting on the body  $\partial\phi/\partial t$  has to be calculated. For forced motion this quantity can be calculated by means of f.i. central or backward differences in time. Whilst for problems where the motion of the cylinder is caused by incoming waves, use of backwards differences leads to numerical instability (for the integration schemes chosen). This is probably caused by the estimation of the "added mass term" by means of backwards differences in time. This is easily demonstrated by approximating the equations for the harmonic oscillator:

$$(m - \mu) \ddot{Z} + kZ = 0 \quad (12)$$

by

$$m\ddot{Z}(t) + \frac{\mu}{\Delta t}(\dot{Z}(t) - \dot{Z}(t-\Delta t)) + kZ(t) = 0 \quad (13)$$

which causes the same kind of numerical problems as for our more complicated case, due to the "stiffness" of the differential/difference equation.

This means that for problems where the body-motion is governed by Newton's second law the force acting on the body has to be calculated in the form:

$$F_p = - \sum_j a_{pj} \ddot{\xi}_j + f_p(\dot{\xi}_j, t; \text{geometry}) \quad (14)$$

where  $F_p$  include the forces for three modes of motion for a 2-D cylinder and  $\xi_p$  are the displacements for these modes. This in turn means that  $\partial\phi/\partial t$  along the body has to be expressed in the form:

$$\frac{\partial\phi}{\partial t} = \sum_j \alpha_j \ddot{\xi}_j + \frac{\partial}{\partial t} \phi_0(\dot{\xi}_j, t; \text{geometry}) \quad (15)$$

This is done in the following way: on the body  $\psi$  is given from equation 7, which in turn yields:

$$\frac{\partial\psi}{\partial t} = \sum_j b_j \ddot{\xi}_j + \frac{\partial\psi_0}{\partial t} \quad (16)$$

where the expressions for  $b_j$  and  $\partial\psi_0/\partial t$  are given by Vinje & Brevig (1981b). On the free surface Bernoulli's equation yields  $\partial\phi/\partial t$  directly, on the bottom  $\partial\psi/\partial t = 0$  and on the vertical boundaries periodicity is introduced for  $\partial\phi/\partial t$  and  $\partial\psi/\partial t$ . Since  $(\partial\phi/\partial t + i\partial\psi/\partial t)$  is analytic,  $\partial\phi/\partial t$  and  $\partial\psi/\partial t$  are found on the boundary according to the solution procedure given by equations 2 through 4, solving the four different problems indicated by equations 15 and 16 where the inhomogenous part of  $\partial\phi/\partial t$  on the free surface contributes to  $\partial\phi_0/\partial t$  only.

The expression (equation 15) for  $\partial\phi_0/\partial t$  then leads to equation 14 by integration over the wetted surface of the cylinder, where  $f_p$  gets an additional contribution from the velocity-square term and the static pressure term from Bernoulli's equation.

The generalized forces from equation 14 are now introduced into the equations of motion of the cylinder (where the center of gravity is used as the reference point) yielding:

$$(m_p \delta_{pj} + a_{pj}) \ddot{\xi}_j = f_p(\dot{\xi}_j, t; \text{geometry}) \quad (17)$$

Elimination of  $\ddot{\xi}_j$  from equation 17 then transforms the equation of motion into the standard form:

$$\ddot{\xi}_j = F_j(\dot{\xi}_p, t; \text{geometry}) \quad (18)$$

The problem is solved as an initial value problem, following in time marked particles on the free surface, integrating equations 8 and 11 for each particle. In addition equation 18 has to be integrated. The integration of equations 8, 11 and 18 is done by means of

Hamming's fourth order predictor/corrector method with a Runge-Kutta starting procedure. At each time step equations 3 and 4 have to be solved twice. The solution scheme for this is shown in appendix A.

Results from application of this method have been published earlier. Brevig et al (1981b), (1982) have calculated the motion of and the forces from breaking waves on submerged wave power devices. One example, showing the motion of a freely moving cylinder is given below:

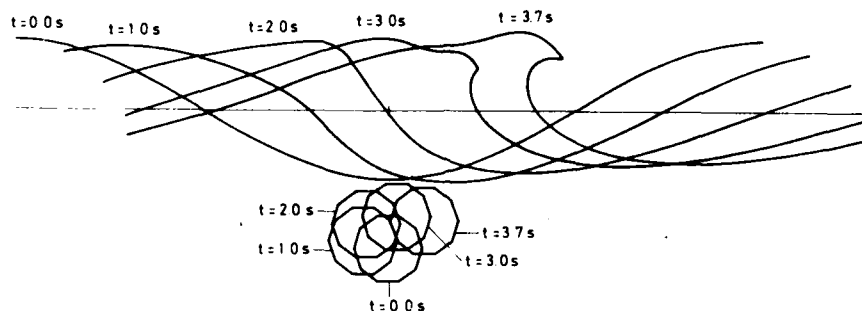


Figure 2 - The motion of a submerged cylinder under a breaking wave (from Brevig et al (1981)).

Vinje & Brevig (1981c) have compared the forces calculated from this method with the forces calculated from the "long wave-length theory" and found that the effect of breaking on the force was small, except when the cylinder was very close to the free surface.

More recently Greenhow & al (1982) have simulated the capsizing of the wave-power device "Salter's Duck" in breaking waves. The results showed good agreement with the experiments done at the University of Edinburgh. This was the case for both the motion of the device and the free surface form. One problem with the surface-piercing body was commented on in this reference, namely the problem with a possible singularity at the intersection between the free surface and the body. This made it necessary to make some assumptions about this contact point. For the details about this the reader is referenced to Greenhow & al (1982). A computer output of these calculations are shown on figure 3.

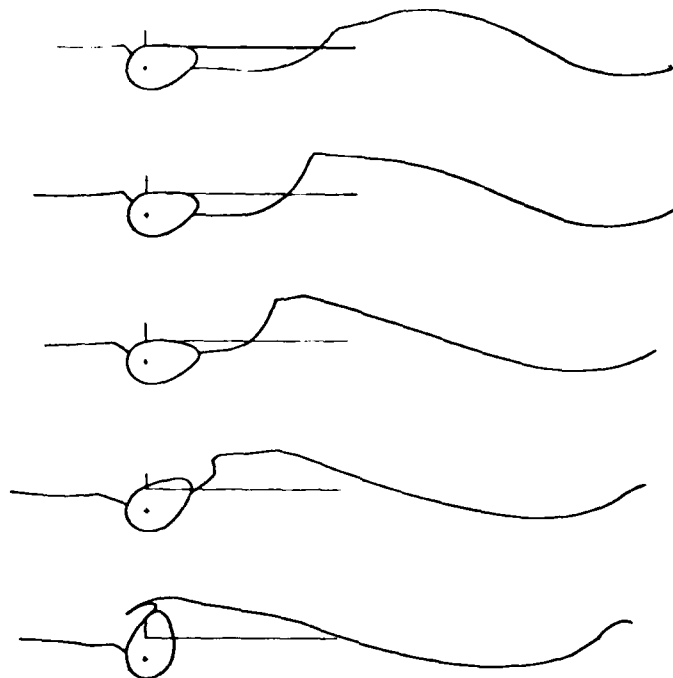


Figure 3 - Capsize of "Salter's Duck" (from Greenhow et al. (1982)).

Although the results of Greenhow & al (1982) are very promising the method still has some shortcomings. One of them is that the hydrodynamic problem is periodic in space, which excludes the possibility of taking properly into account the diffraction effect of the body and the response to waves generated far away from the body. The possibility of reaching a state where the vessel is performing periodic response to periodic waves is also excluded.

To take the above effects properly into account means that the solution in the non-linear "inner domain" should be matched to a non-linear solution in the "outer domain" which contains an incoming wave plus the non-linear diffraction effect (which is not independent of the incoming wave). As far as the authors know, no such "outer" solution is yet found. Not even a perturbation solution to second order is in general "available".

To get around this problem (when regarding the diffraction effect) Baker & al (1982) have introduced artificial energy absorbing boundaries far away from the body. This seems to work reasonably well for forced motion problems, where no incoming wave is present. One might be tempted to try to stretch this a bit further, assuming the

potential to consist of the potential for the incoming waves plus a diffraction problem and introduce the absorbing boundary concept for this added potential. Unfortunately this will violate the non-linear free surface condition in the "inner domain" where it is assumed to be of much importance to take it properly into account.

One is then more or less left with assuming the "outer solution" to satisfy the linear free surface boundary conditions. This, of course, restricts the applicability to problems where the non-linear effects are noticable in the "inner domain" only, as for small amplitude motion of the bow-flare sections or slightly submerged cylinders, simulation of ship motions in breaking waves generated by the transient testing technique or the larger amplitude forced motion problem up to the stage when the waves in the outer domain become "non-linear".

As a first step, the problem with a breaking wave on a sloping beach was simulated, assuming the wave to be generated by imposing a sinusoidal wave at the interface between the "outer" and "inner domains". This, contrary to Baker & al (1981) excludes wave reflection, but allows for an incoming wave. The computer output from a preliminary run is shown on figure 4. Here a long wave was introduced from the left and the calculation was continued until the wave broke. The results seem qualitatively to be in good agreement with what we would expect to happen, even though the results are not checked thoroughly.

It is worth noticing that in this case the particles do not cluster close to the jet's front, as for the deep water breaker, which makes this kind of computations more costly.

The obvious shortcoming of the above approach is that reflection (or diffraction) is totally neglected. This will for ship motion problems lead to unreliable results when trying to reach steady state solutions. One might in this case just as well apply the spacial periodicity assumption. To expect to get a reasonable answer one has to assume the "outer solution" to be capable of absorbing energy from the "inner domain" at the same time as an incoming wave is imposed on the "inner domain". The similarity with the problem leading to the hybrid formulation in linear theory is striking (see f.i. Yeung (1982)), and the matching technique developed in this context might be applied for the present problem as well.

In the linear theory the "outer solution" is assumed to consist of a series of eigensolutions, with coefficients determined from the matching with the "inner solution". In this case the solution in the outer domain can be constructed in different ways, but the basis is the

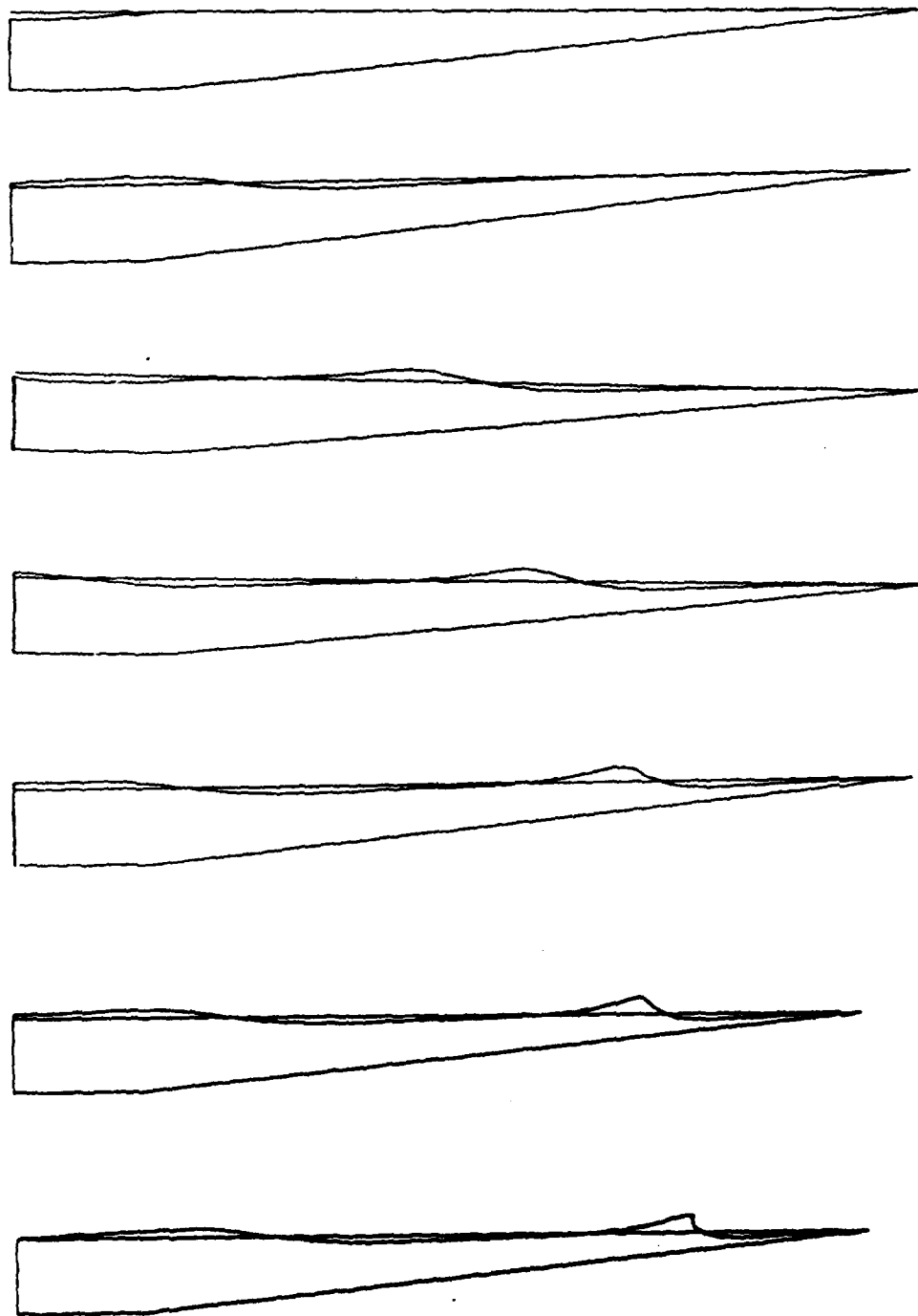


Figure 4 - Wave breaking on a beach

potential of the time-dependent source (see Wehausen & Laitone, (1960) eq. 13.54).

One way of determining the "outer solution" is given by Daoud (1975) who gives the near-bow solution of the wave-making problem in terms of a distribution of time - (or rather space-) dependent sources over the boundary. In the present approach we will apply a much simpler approximation to the linear solution in the "outer domain", namely assuming that it is given by a set of discrete sources and dipoles situated well inside the "inner domain" and below the free surface, which implies that the "outer domain" also is assumed to form the "far field" of the linear solution. Accordingly, the complex potential in the "outer domain" is written:

$$\begin{aligned} \phi_0(x,y,t) + i\psi_0(x,y,t) = & \sum_j \kappa_j(t) G_j(z-\zeta_j, z-\zeta_j^*) \\ & + \sum_j \int_0^t \kappa_j(\tau) H_j(t-\tau, z-\zeta_j^*) d\tau + (\phi_W(x,y,t) + i\psi_W(x,y,t)) \end{aligned} \quad (19)$$

where  $\zeta_j$  is the complex coordinate of the pole/dipole  $j$ .  $z$  is the complex coordinate of the field point and the asterix denotes complex conjugation.  $G_j$  is the complex potential for the impulsive pole/dipole number  $j$ , and  $H_j$  denotes the kernel of the convolution integral in time, which is developed on the basis that  $(\phi_j + i\psi_j) = 0$  along the free surface for  $t = 0$  (See Wehausen & Laitone (1960))  $\kappa_j(t)$  is real and denotes the time dependent pole/dipole strength number  $j$ .  $(\phi_W + i\psi_W)$  is the complex potential of the incoming wave. Equation 19 can be written in the form:

$$\phi_0 + i\psi_0 = \sum_j \kappa_j(t) \cdot G_j + (\phi_0 + i\psi_0) \quad (20)$$

where  $(\phi_0 + i\psi_0)$  consists of the part of  $(\phi_0 + i\psi_0)$  which is in principal known at time  $t$ : the sum of the convolution integrals plus the complex potential of the incoming wave.  $\sum_j \kappa_j G_j$  is unknown and has to be determined by the matching to the "inner domain".

Assuming that  $\psi$  is "known" on the common boundary between the "outer" and "inner domains" from the solution in the "outer domain", the problem in the "inner domain" is formulated as indicated on figure 5 (where  $C$  is undetermined as shown earlier).

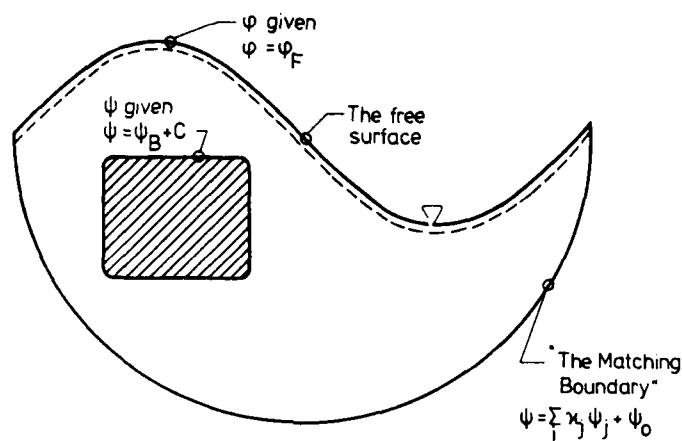


Figure 5 - Formulation of the "inner problem"

This means that the solution in the "inner domain" is found as:

$$\phi_I + i\psi_I = \sum_j \kappa_j (\phi_{Ij} + i\psi_{Ij}) + (\phi_{I0} + i\psi_{I0}) \quad (21)$$

where  $(\phi_{Ij} + i\psi_{Ij})$  and  $(\phi_{I0} + i\psi_{I0})$  are the solutions of the problems defined on figure 6.

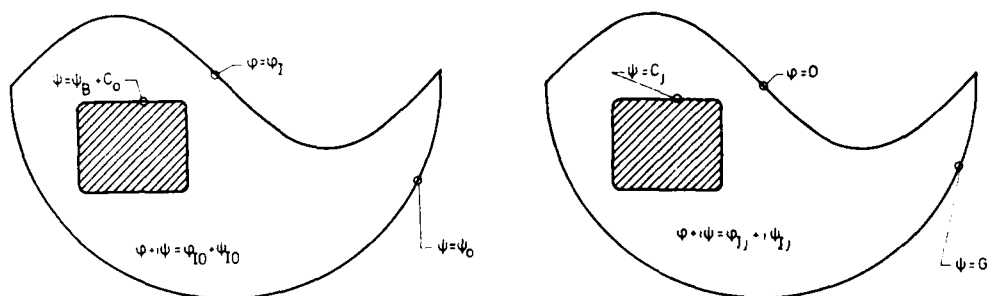


Figure 6 - Formulation of the problems of equation 21.

The matching procedure now requires a (minimum norm) fit of  $\phi_I$  and  $\phi_0$  along the "matching boundary", which in turn yields the following equations for determination of  $\kappa_j$ :



$$\langle (\phi_{Ik} - G_k), (\phi_{Ij} - G_j) \rangle \kappa_j + \langle (\phi_{Ik} - G_k), (\phi_{I0} - \phi_0) \rangle = 0 \quad (22)$$

where  $\langle a, b \rangle$  denotes the "inner product" according to the norm chosen.

The calculation of  $\partial\phi/\partial t$  on the body boundary is in principle performed the same way as for the "periodic" problem, except that the unknown quantities  $(d\kappa_j/dt)$  have to be determined by the matching between the "outer" and "inner" solution at each time step. This implies that the "Laplace-equation-solver" is introduced  $2(j+1)$  times (in addition to 5 times from the body-motion modes) at each predictor (or corrector) point.

#### NUMERICAL RESULTS

First the results will be shown for forced motion of a submerged circular cylinder (as given on figure 7). The cylinder is started impulsively from rest and for  $t \geq 0$  it is given a displacement  $D(t) = A_2 r \sin(\omega t)$ , where  $\sqrt{\omega^2 r/g}$  is chosen as  $\sqrt{0.4\pi} = 1.12$  (the wavelength is  $5r$ ). The corresponding initial free surface condition is  $\phi = 0$  along an undisturbed (i.e. flat) free surface.

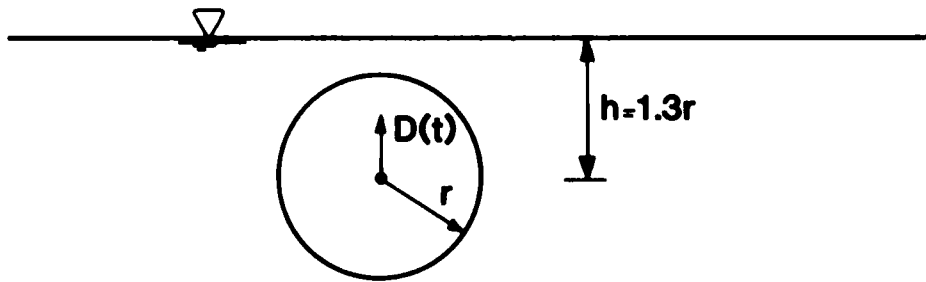


Figure 7 - The initial position of the circular cylinder

In the first example  $A_2$  is taken as 0.15, corresponding to an amplitude of half the initial gap between the top of the cylinder and the free surface. This is a situation where the amplitude of motion is small compared with the

wavelength ( $A_2 r / \lambda = 0.03$ ), reasonably small compared with the diameter of the cylinder ( $A_2 r / 2r = 0.75$ ) and of the same order as the gap ( $A_2 r / (h-r) = 0.5$ ). This means that the waves at infinity are expected to (nearly) satisfy the linearized free surface conditions and that some non-linear effects are expected to appear in the near-field the cylinder.

On figure 8 the elevation of the free surface form is shown at four stages of the development, one period apart.

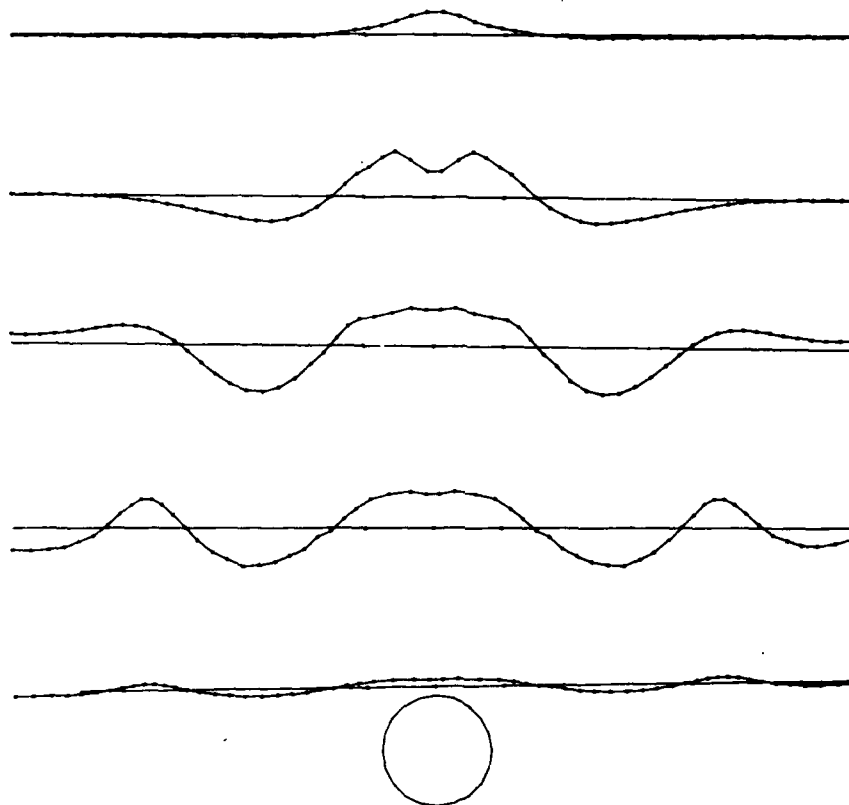


Figure 8 - The development in time of the free surface form.  
 $\Lambda_2 = 0.15$ . The vertical scale is amplified by a factor of 5.

The cylinder has just passed its highest point ( $\omega t = \pi/3 + 2n\pi$ ) and is on its way down with a velocity of 0.5 times the maximum velocity. The vertical scale has been amplified by a factor of 5 compared with the horizontal (except on the

last drawing). On figure 9 the development from  $\omega t = \pi/3 + 4\pi$  to  $\omega t = \pi/3 + 6\pi$  is shown in more details. It is interesting to observe that the outgoing waves show the Stokes' wave characteristics for sharper crests than troughs, indicating a significant nonlinear effect.

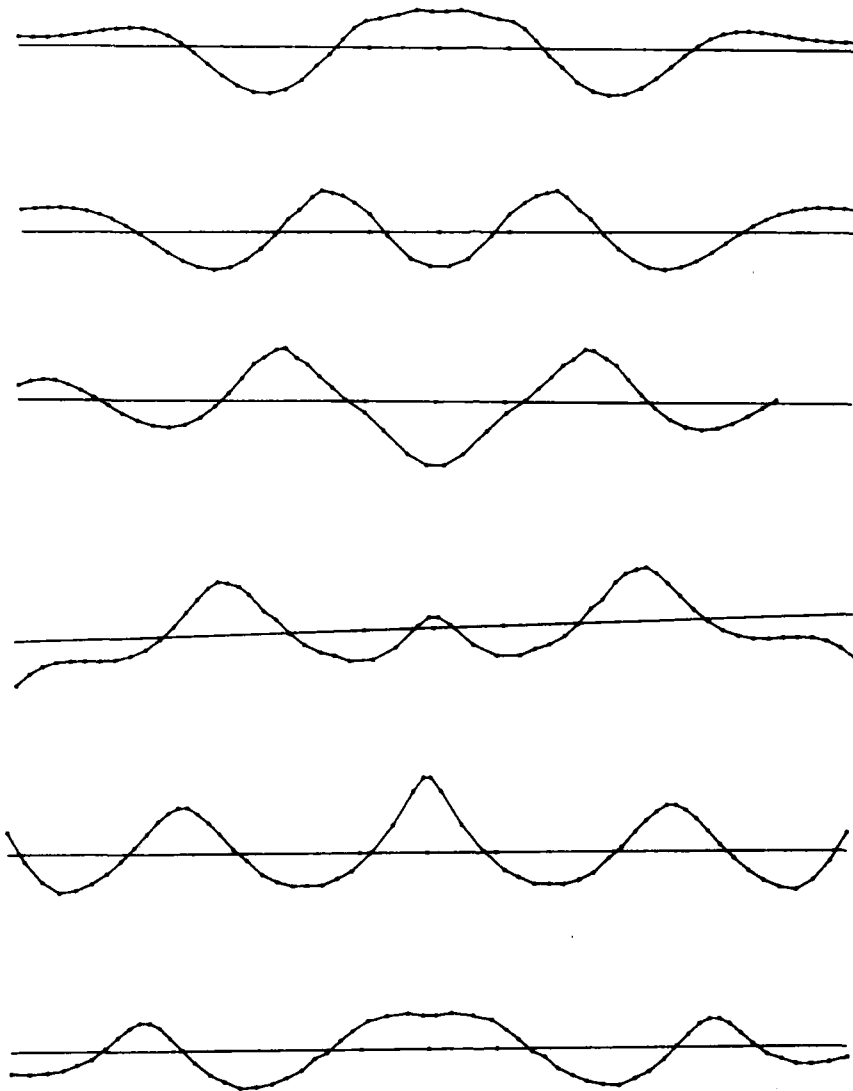


Figure 9 - Detailed development of the free surface form for  $\omega t$  between  $(\pi/3 + 4\pi)$  and  $(\pi/3 + 6\pi)$ .  $A_2 = 0.15$ . The vertical scale is amplified by a factor of 5.

From figure 8 it seems that the fluid motion close to the cylinder becomes periodic after about two oscillations, whilst the "outgoing wave" seems to reach the "matching boundary" after about three periods (which corresponds to the time estimate from the group velocity). After this time a significant asymmetry appeared and the computation of the free surface form became unreliable.

We have not had time yet to investigate this problem properly, but the most probable source for this is, of course, a programming error, and in that case most probably connected to the introduction of the convolution integral in the outer solution which accounts for the outgoing waves in this domain. Another possible source is the formulation of the problem as such, letting a  $C_\psi$ - and a  $C_\phi$ -contour intersect at the free surface. This might very well introduce a weak singularity in the inner solution at this corner point. In the programming we tried to minimize the influence of this by regarding the corner point as a part of  $C_\phi$ , giving the potential from the outer solution at this point and avoid determining anything, not even the position of this point, from the values computed at the point. If this is the source, the problem has to be reformulated completely, giving  $\phi$  on the boundary and determining the additive constant of  $\psi$  from the matching. A third possible source is that the introduction of the matching to the linear solution does not work, at least not for the convolution integral part (we know from Faltinsen (1977) that it works for the impulsive source, which is shown here also). In that case we are in trouble introducing an incoming wave and are left with the costly procedure introduced by Greenhow & al (1982). The asymmetry-problem will be regarded in near future and hopefully the final conclusion will be that the matching technique is applicable for the problems regarded in the introduction.

Since the forces are given from the near-field solution and this seems to become periodic before the problems occur at the boundary, some conclusions about this quantity can be drawn from the computations. On figure 10 the total vertical force on the cylinder is drawn as a function of time. From this sketch it is obvious that the nonlinear effects are more pronounced here than for the wave form. The force seems to have reached a state of periodicity in time after about 2 periods and later shown much sharper troughs than crests. The mean drift force is estimated to be zero, which corresponds well with Ogilvie's (1963) result (figure 7 of the reference.  $\nu a = 1.26$  and  $2\nu h = 3.27$ ).

On figure 10 a sine-curve with frequency  $\omega$  is drawn. Comparison between the force and this sine-curve shows that the force mainly is in phase with the displacement (corresponding to positive added mass in the linear case) and the

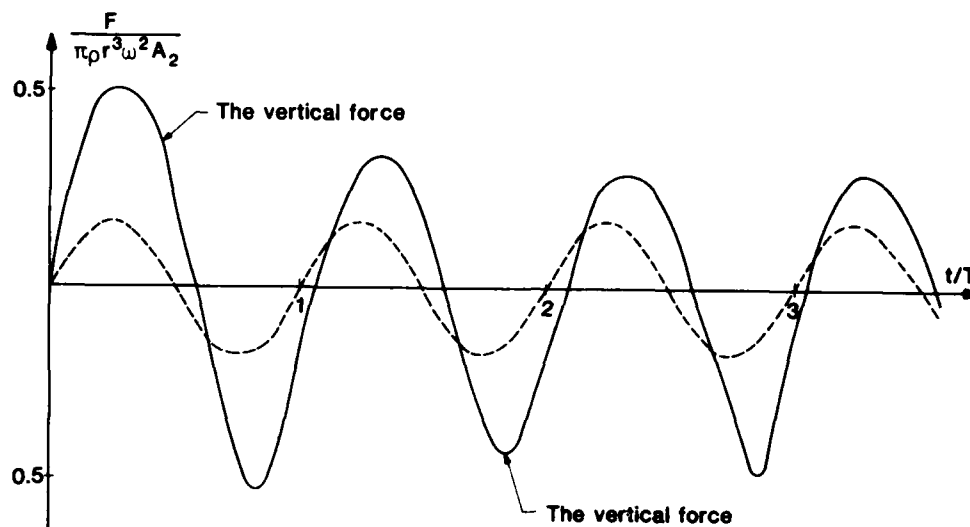


Figure 10 - The vertical force as a function of time.  
 $A_2 = 0.15$ . The time-scale is given in terms of periods of oscillation. The dotted line shows a sinusoidal curve.

phase shift corresponds to a positive damping coefficient for the linear case.

On figure 11 the strength of the vertical dipole is given as a function of time. The deviation from a cosine curve is significant. This deviation can be caused by several effects, but it does probably not reflect the influence of the convolution integral on the matching. The initial value seems to correspond well with the results from matching of the exact solution taken at infinity, yielding the value  $0.877\pi = 2.76$ . Our computed value is 2.83 with the matching taken at the circle with radius  $7.5r = 1.5\lambda$ .

Figure 12 shows  $(-a_{22})$  (from equation 14,  $\xi_2 = y$ ), which is the added mass calculated for  $\phi = 0$  along the actual free surface and with the cylinder situated at its actual position. The wavy form is caused by these two nonlinear effects, partly cancelling each other. For a flat free surface with the cylinder at its actual position,  $a_{22}$  would have been oscillating with an amplitude of about 0.12, whilst the numerical results show an amplitude of about 0.08. The decrease is due to the effect of the free surface elevation above the cylinder being in phase with the displacement of

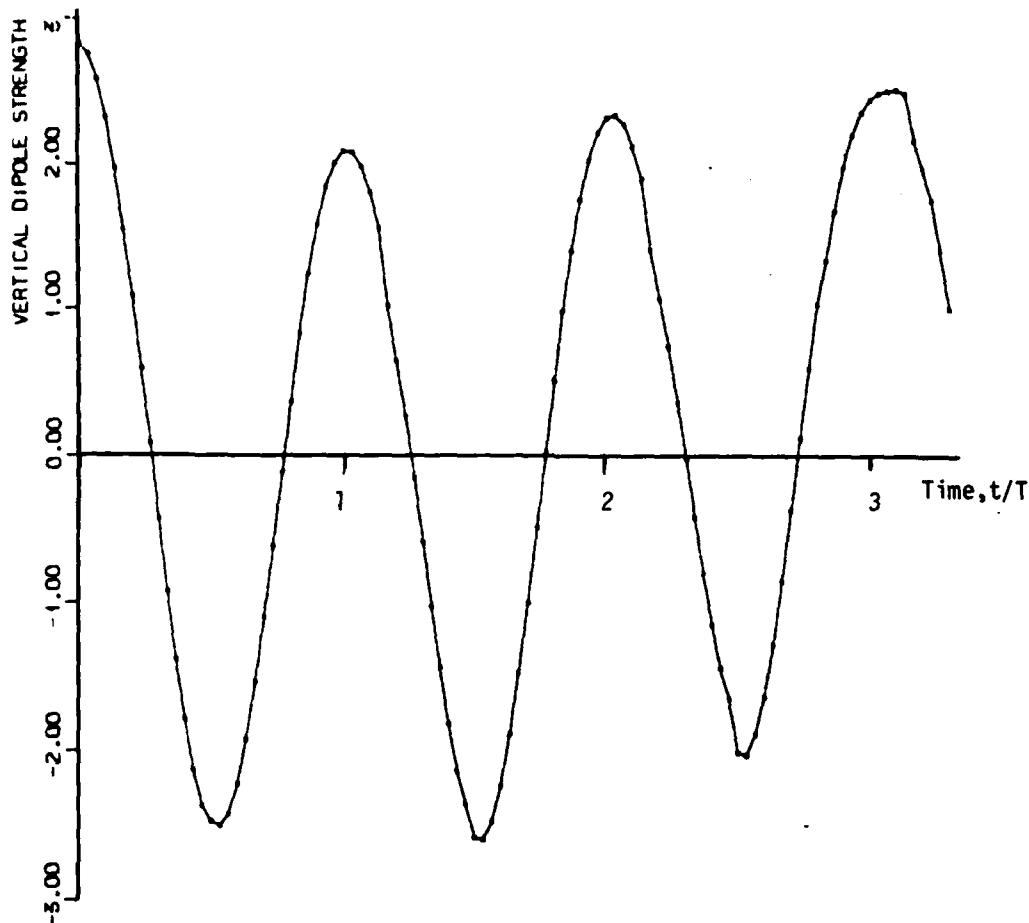


Figure 11 - The strength of the vertical dipole as a function of time.  $T$  is the period of oscillation.

the cylinder.

In the next example the cylinder is oscillated with an amplitude  $A_2 = 0.25$  (or 83% of the initial gap). In this case the nonlinear effects really dominate and the matching does not really come into effect at all. On figure 13 the development of the free surface elevation in time is shown (for slightly less than the first cycle). Here both the cylinder and the free surface elevation are drawn to scale. The figure first shows the cylinder at its maximum elevation during the first cycle, next at its initial position on its way down, then at its lowest position and finally close to the initial position. As seen, a vertical

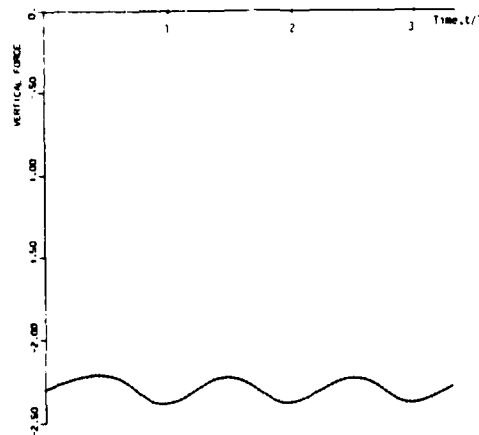


Figure 12 -  $(-a_{22})$  from equation 14.  $(-a_{22})$  becomes  $(-\pi)$  at infinite depth.

jet has developed between the two last stages and continues to move upwards. Shortly after this the computation broke down.

This development is similar to what is reported for standing waves with a large energy input in terms of the initial free surface elevation (see Srokosz (1981)). The element length along the free surface is in the present case so large that the formation of the jet cannot be described in any detail. This would have been interesting to investigate further, but at the moment it mainly serves as an indication that the strong nonlinear effects found for  $A_2 = 0.15$  are real.

The possibility that the formation of the jet is caused by numerical instability is ruled out by the repeatability of the results when decreasing the time step. The physical significance of the results are not confirmed, but experiments to that effect will be brought through in near future.

A numerical experiment with forced motion of a submerged rectangle close to the free surface showed that numerical instability can occur in the present calculations when letting the element length becoming small enough (or the time step too long). This shows to be a removable instability since it disappeared when the time step was shortened. The numerical experiments with the submerged rectangle have not been continued due to computational costs.

Now the results for a fixed cylinder (as shown on figure 7) exposed to incoming, harmonic waves with wavelength  $\lambda = 5r$  will be shown. Brevig & al (1981) and Vinje & Brevig (1981c) have discussed the case with a small cyl-

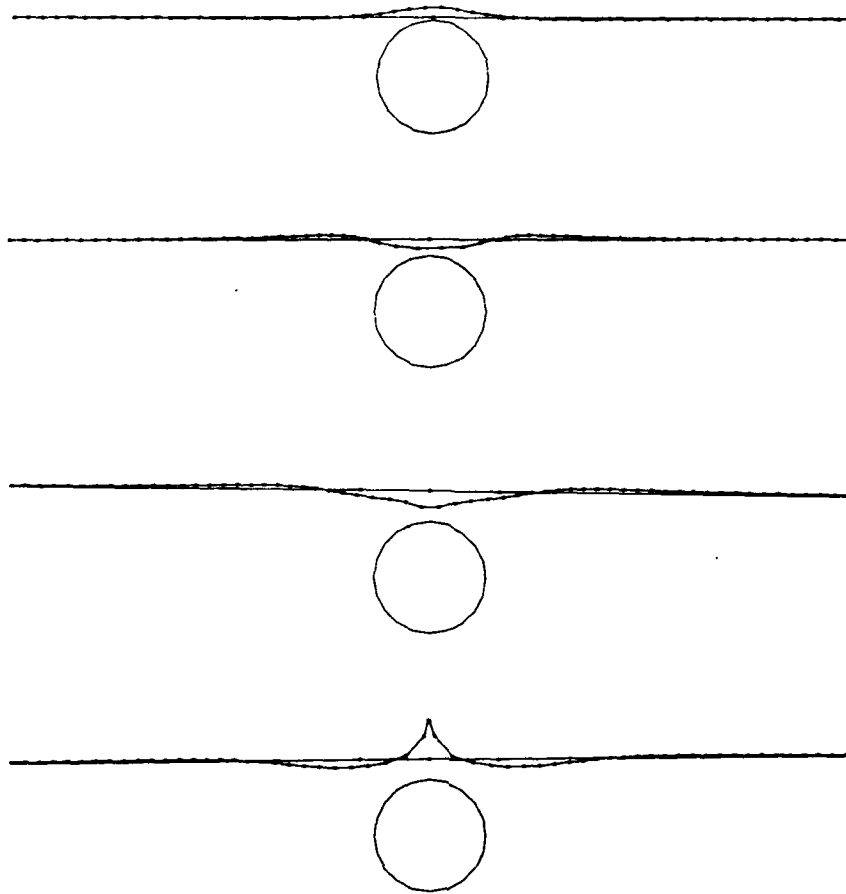


Figure 13 - The development of the free surface form.  
 $A_2 = 0.25$ . Drawn to scale.

inder acted upon by breaking waves (see figure 2). For these calculations the periodicity assumption was applied, which is reasonable for transient problems. The calculations showed that the forces can be estimated fairly well from linear theory if the cylinder is not situated too close to the free surface (i.e. in the wave crest). For the case discussed here the waves will be assumed to be low ( $H/\lambda = 0.008$  and  $0.02$  respectively) and with a fairly low ratio between the amplitude and the gap between the cylinder and the free surface ( $H/2(h-r) = 2/30$  and  $1/3$ ). On the other hand, the cylinder is fairly large compared with the wavelength ( $2r/\lambda = 2/5$ ,  $(h+r)/\lambda \approx 1/2$ ), which might cause certain nonlinear effects. Initially the free surface



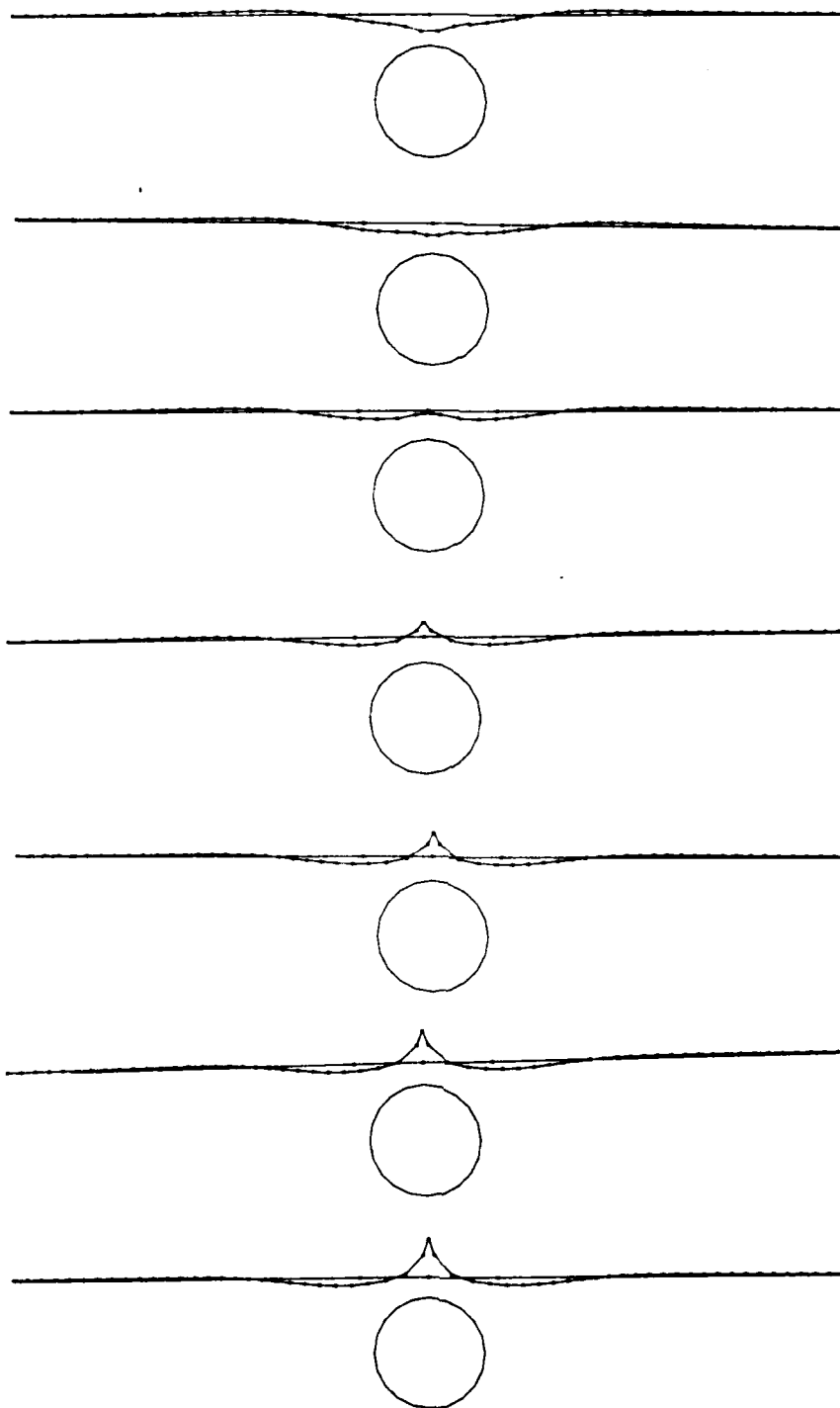


Figure 14 - Detailed development of the free surface form  
for  $\omega t$  between  $3\pi/2$  and  $2\pi$ . Drawn to scale

elevation is sinusoidal with the potential given from linear theory.

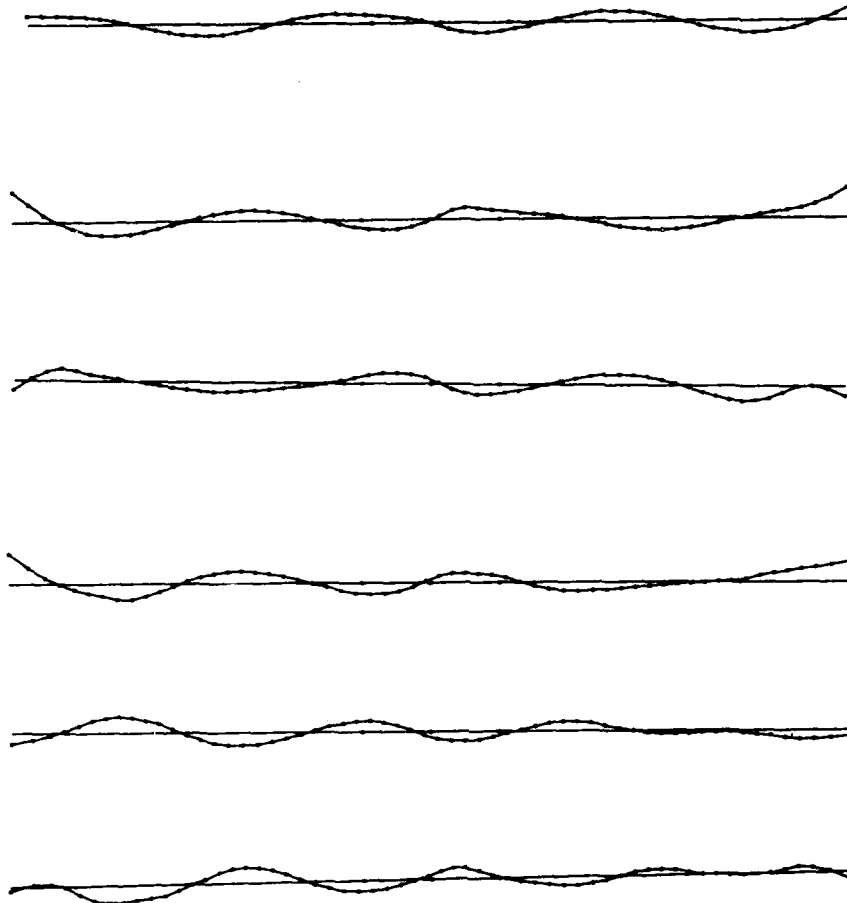


Figure 15 - The development in time of the free surface form.  $H/\lambda = 0.008$ . The vertical scale is amplified by a factor of 10.

On figure 15 the development of the free surface elevation is shown for  $\omega t = n\pi$  ( $n = 1, \dots, 6$ ). This shows that waves are introduced continuously from the left and that the cylinder modifies the waves on the lee side noticeably. What is not that easily seen is that a reflected wave is created from the "matching boundary" on the lee side, penetrating into the "inner domain". This is more easily seen on figure 16. From the experience with the forced motion

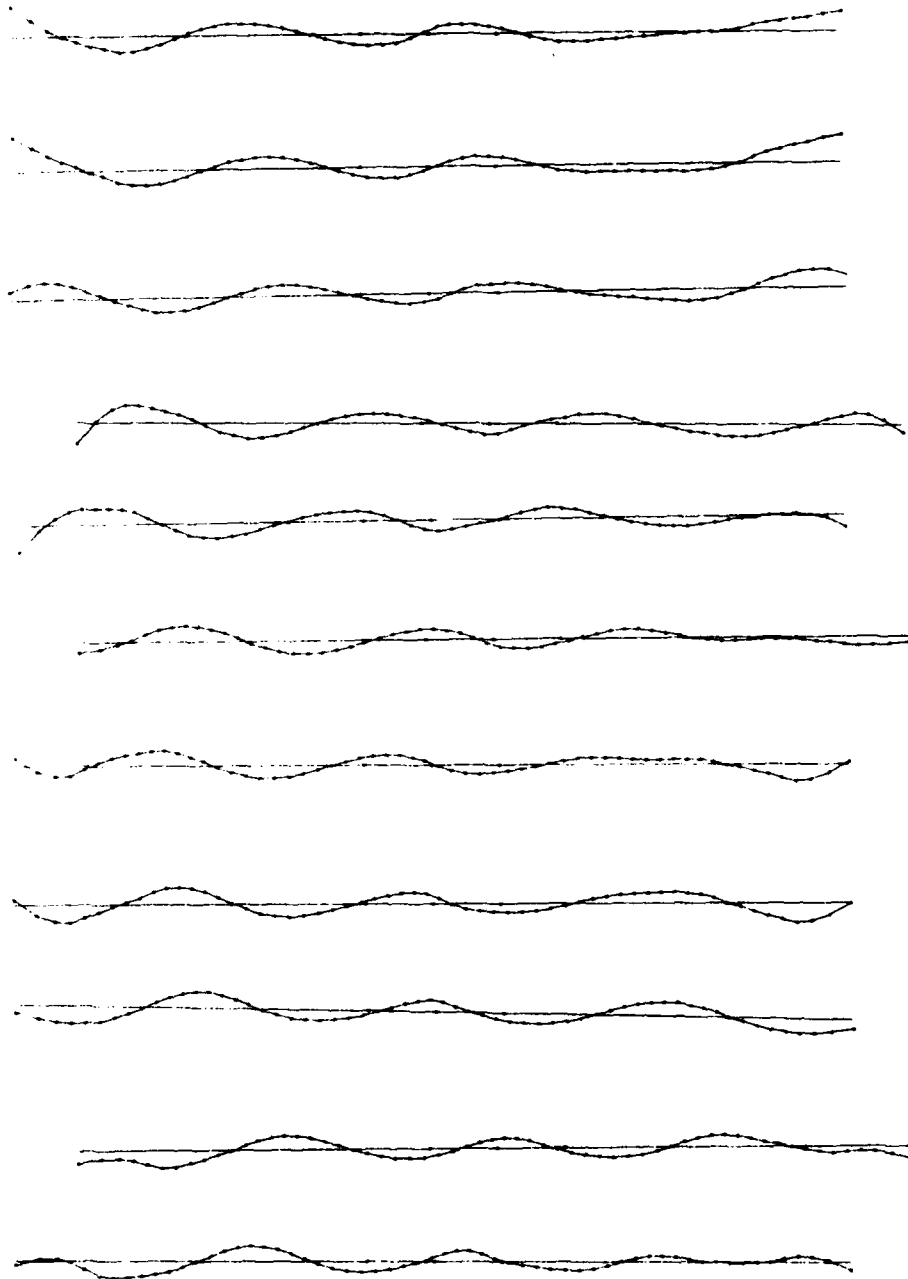


Figure 16 - Detailed development of the free surface form shown on figure 15.

problem one would not expect the matching to work very well with an incoming wave present; Ogilvie (1963) showed that according to linear theory, there would be no reflected waves and that the transmitted wave only shows a phase lag compared with the incoming wave. In the transient development from our initial conditions to this "steady-state"-solution one might expect some reflected waves to be created even from the matching boundaries. In view of the discussion of the forced motion problem we tend to regard it as due to improper matching.

On figure 17 the vertical and horizontal dipole strengths are shown. For the reflected wave to disappear and the transmitted to have the same amplitude as the incoming wave, the vertical and horizontal dipole strengths have to have the same amplitude and be  $90^\circ$  out of phase. Further more: the amplitudes of the dipole strengths have to depend on the incoming wave only, and not on the radius of the cylinder (but on the assumed position of the dipoles). Figure 17 does not show any of these characteristics, and the fact that the horizontal dipole strength dominates the vertical indicates that the cylinder mainly acts as a "wavebreaker". On the other hand, the characteristics indicated from Ogilvie's results are far-field, convolution-integral-effects. Since the convolution integrals are not expected to have any great influence on the solution at this early stage, one cannot expect to find the far-field characteristics present yet.

On figure 18 the horizontal and vertical forces are shown. As for the forced motion problem these quantities seem to reach steady state long before the free surface form and show a periodic behaviour after about 2 cycles. The amplitudes are about equal (horizontal/vertical = 0.93) and both show negligible drift force, which coincides with Ogilvie's results. The vertical force shows slight nonlinear (higher order) effects in its form.

On figure 19 the free surface elevation for an incoming wave of amplitude  $r/10$  is shown. What characterizes this case is that the nonlinear effects seem to dominate close to the cylinder, leading to breaking after about two periods.

On figure 20 a more detailed picture of the breaking is shown. It is interesting to notice that a steep wave is formed on the "upstream" side of the cylinder, and that this reaches its maximum after having passed the top of the cylinder and then decreases before it really breaks.

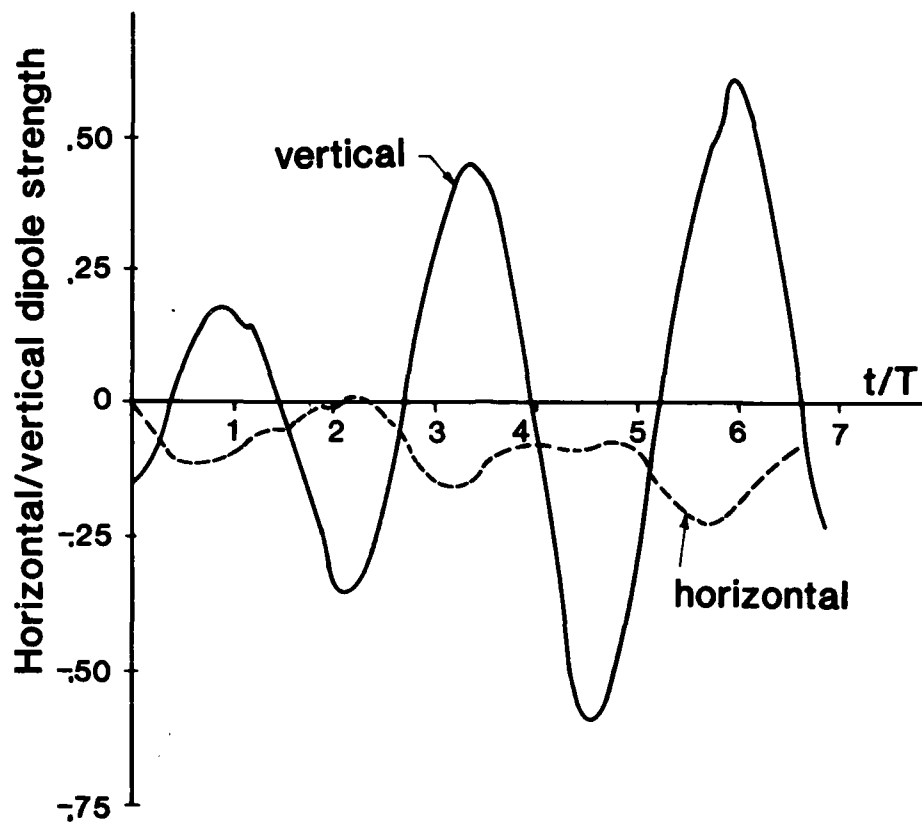


Figure 17 - The horizontal and vertical dipole strength  
 $H/\lambda = 0.008$ .

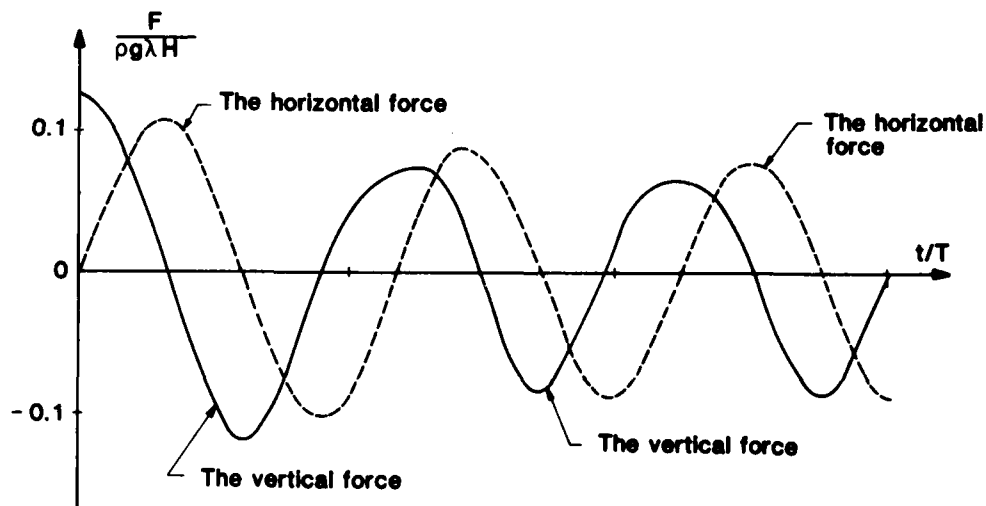


Figure 18 - The horizontal and vertical force.  $F/\lambda = 0.008$

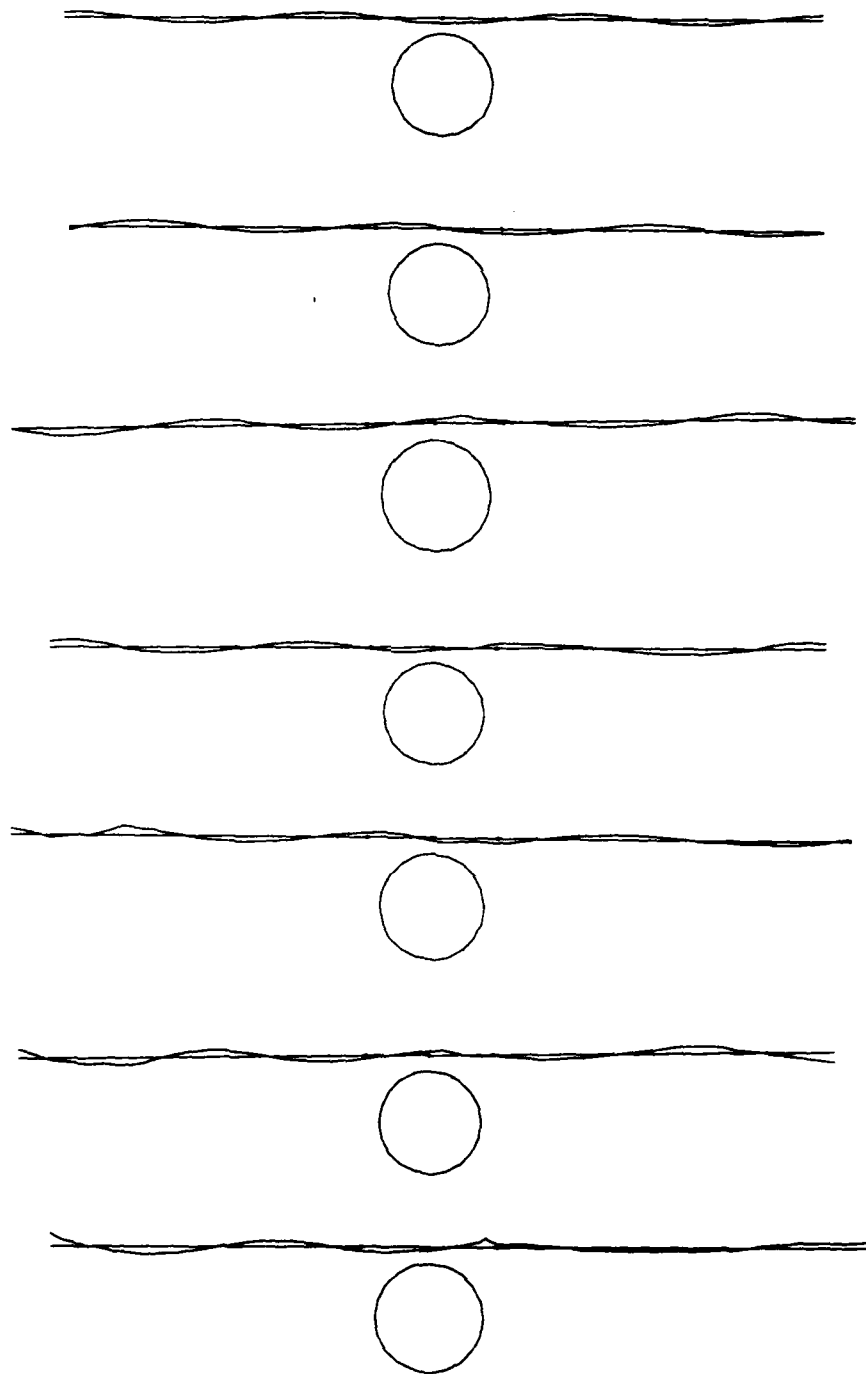


Figure 19 - The development in time of the free surface form  
 $H/\lambda = 0.02$

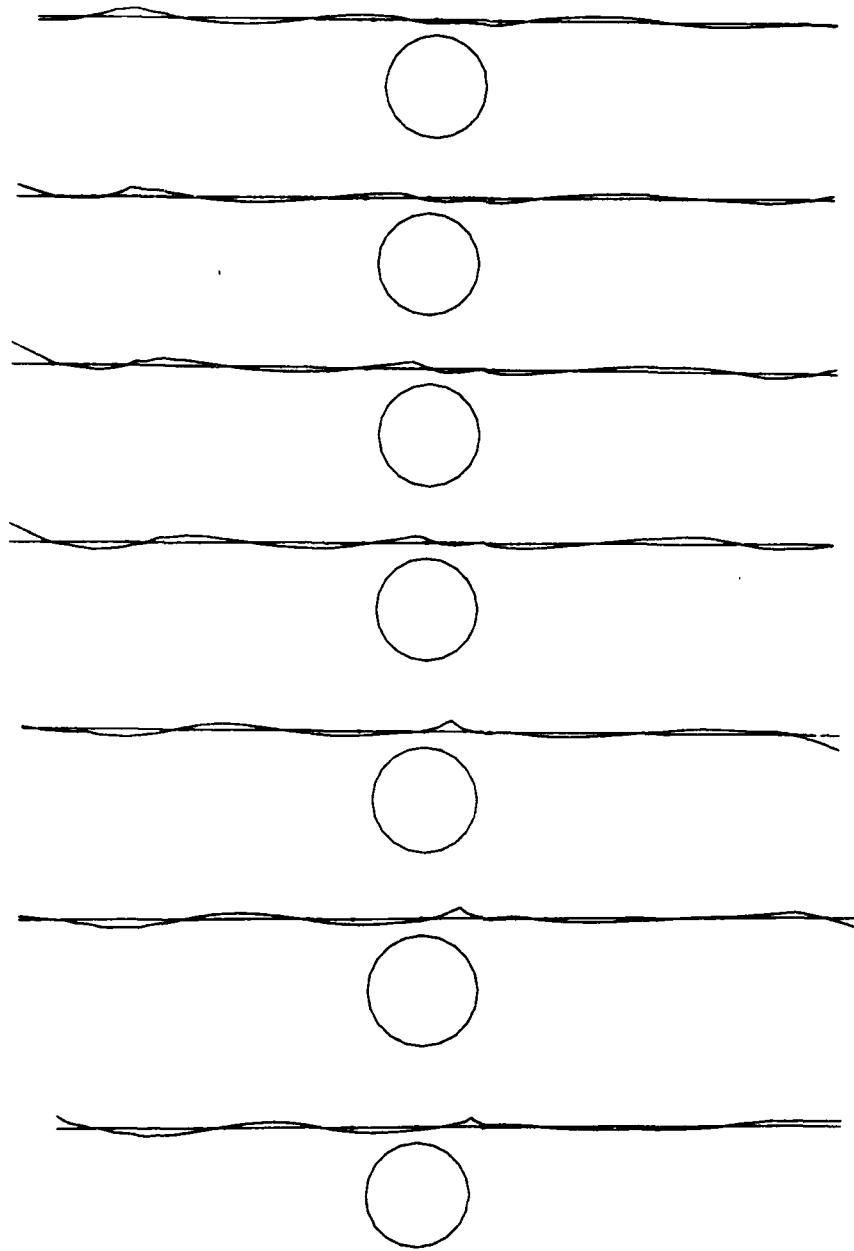


Figure 20 - Detailed development of the free surface form.  
 $H/\lambda = 0.02$ .

## CONCLUSIONS

A time simulation method calculating forces on 2-D submerged bodies is presented. The problem is solved by matching a fully nonlinear inner domain to a linear outer domain. Results are given for fixed circular cylinders in incoming waves, and for circular cylinders in forced heave motions. In both cases the cylinder is close to the free surface.

In the case of a fixed cylinder in incoming waves, the simulated values of the mean horizontal drift forces agree well with Ogilvie's (1963) results. However, in these simulations some problems occurred which we believe are due to the matching. "The impulsive dipole part of the matching" (as successfully also applied by Faltinsen (1977)) seems to work satisfactory, and we therefore expect these problems to be caused by the convolution integral.

The results of the forced motion simulations agreed well with Ogilvie's (1963) results for the vertical drift-forces. Significant nonlinear effects were observed for amplitudes of displacement of order of the gap between the cylinder and the free surface. The same problems occurred as for the fixed cylinder, but at a later stage.

If we are able to solve the problems connected to the present matching procedure satisfactory, we will proceed to extend the method to comply with surface piercing 2-D bodies also. As pointed out by Vinje & Brevig (1981) and Greenhow & al (1982) there are certain problems connected to the intersection point between the body and the free surface that have to be resolved, which makes this problem much more complicated than for the submerged cylinder.

## ACKNOWLEDGEMENT

A large amount of the programming used was developed under the research projects: "Ships in Pough Seas" and "Stability Criteria", sponsored by The Royal Norwegian - Council for Scientific and Industrial Research (NTNF), The Norwegian Fisheries Research Council (NFFP) and the Norwegian Maritime Directorate, and under the project "Non-linear, 3D Hydrodynamic Theory", Sponsored by The Royal Norwegian Council for Scientific and Industrial Research (NTNF) and Det norske Veritas (DnV),



## REFERENCES

- Baker, Meiron & Orszag (1981). Applications of a Generalized Vortex Method to Nonlinear Free Surface Flows, Third Int. Conf. on Numerical Ship Hydrodynamics, Paris, France
- Brevig, Grenhow & Vinje (1981). Extreme Wave Forces on Submerged Cylinders, Second Int. Symp. on Wave & Tidal Energy, Cambridge, England
- Brevig, Greenhow & Vinje (1982). Extreme Wave Forces on Submerged Wave Energy Devices, to be published in Applied Ocean Research
- Coleman & Haussling (1981). Nonlinear Waves Behind an Accelerated Transom Stern, Third Int. Conf. on Numerical Ship Hydrodynamics, Paris, France
- Daoud (1975). Potential Flow Near to a Fine Ship's Bow. Report 177, Dept. of Naval Arch., University of Mich. Ann Arbor, Mich., USA
- Faltinsen (1977). Numerical Solution of Transient Nonlinear Free-Surface Motion Outside or Inside Moving Bodies, Second Int. Conf. on Numerical Ship Hydrodynamics, Berkeley, Calif., USA
- Greenhow, Vinje, Brevig & Taylor (1982). A theoretical and experimental study of the capsize of Salter's duck in extreme waves, J.Fluid Mech. 118
- Longuet-Higgins & Cokelet (1976). The Deformation of Steep Surface Waves on Water. I A Numerical Method of Computation. Proc. Roy. Soc. Lond.A 350
- Nichols & Hirt (1975). Methods for Calculating Multi-Dimensional Transient Free-Surface Flows Past Bodies, First Int. Conf. on Numerical Ship Hydrodynamics, Gaithersburg, Md., USA
- Ogilvie (1963). First- and second-order forces on a cylinder submerged under a free surface, J.Fluid Mech. 16, 3
- Srokosz (1981). Breaking Effects on Standing and Reflected Waves. Int. Symp. on Hydrodynamics in Ocean Engineering, Trondheim, Norway
- Vinje & Brevig (1981a). Numerical Simulation of Breaking Waves, J.Adv. Water Resources, 4 June
- Vinje & Brevig (1981b). Nonlinear Ship Motions. Third Int. Conf. on Numerical Ship Hydrodynamics, Paris, France
- Vinje & Brevig (1981c). Numerical Calculation of Forces from Breaking Waves, Int. Symp. on Hydrodynamics in Ocean Engineering, Trondheim, Norway
- Wehausen & Laitone (1960). Surface Waves, Encyclopedia of Physics, Vol IX, Springer-Verlag, Berlin, Germany
- Yeung (1982) Numerical Methods in Free-Surface Flows. Ann. Rev. Fluid Mech. 1982

## APPENDIX A \_ NUMERICAL SOLUTION

To solve the Cauchy equation for  $\beta$  and  $\partial\beta/\partial t$  we assume a linear variation of these functions in  $z$  between the nodal points on  $C$ . The influence function of the variables at the nodal point  $z$ , is therefore

$$\Lambda_j(z) = \frac{z - z_{j+1}}{z_j - z_{j+1}} \quad \text{for } z \text{ on } C \text{ between } z_j \text{ and } z_{j+1} \quad (\text{A.1})$$

$$\Lambda_j(z) = \frac{z - z_{j-1}}{z_j - z_{j-1}} \quad \text{for } z \text{ on } C \text{ between } z_{j-1} \text{ and } z_j$$

and zero elsewhere on  $C$ .

Introducing this influence function into equation 3 gives the following matrix equation:

$$\oint_C \frac{\phi + i\psi}{z - z_k} dz \approx \sum_j \Gamma_{kj} \beta_j = 0 \quad (\text{A.2})$$

where  $\beta_j = \beta(z_j; t) = \phi(x_j, y_j; t) + i\psi(x_j, y_j; t)$ , and

$$\Gamma_{kj} = \int_{z_{j-1}}^{z_j} \frac{z - z_{j-1}}{z_j - z_{j-1}} \frac{1}{z - z_k} dz + \int_{z_j}^{z_{j+1}} \frac{z - z_{j+1}}{z_j - z_{j+1}} \frac{1}{z - z_k} dz \quad (\text{A.3})$$

$$= \frac{z_k - z_{j-1}}{z_j - z_{j-1}} \ln \frac{z_j - z_k}{z_{j-1} - z_k} + \frac{z_k - z_{j+1}}{z_j - z_{j+1}} \ln \frac{z_{j+1} - z_k}{z_j - z_k}$$

with limiting values applied when  $k = j-1, j$  or  $j+1$ . If

$$\varepsilon = \frac{z_{j-1} - z_j}{z_j - z_k} \quad (\text{A.4})$$

$$\delta = \frac{z_{j+1} - z_j}{z_j - z_k} \quad (\text{A.5})$$

are both small then we can use asymptotic expressions for the logarithms in equation A.3 giving:

$$\Gamma_{kj} = \frac{\delta - \epsilon}{2} \left[ 1 - \frac{\delta + \epsilon}{3} \right] \quad (\text{A.6})$$

Use of the asymptotic expression equation (A.5) when  $(\epsilon, \delta)$  less than 0.2 reduces the cost of running the program by about 40%.

Points around the contour C are labelled consecutively, but points across the branch cut (see figure 1) are considered to be neighbours. When  $z_k$  lies on the submerged body then integration over the branch cut moves us into the next Riemann surface, causing a difference of  $\pm 2\pi i$  in the  $\Gamma$  functions. The program first checks that the difference of the angles included at neighbouring points does not change by more than  $2\pi$  (we stay on the same Riemann surface) and then accommodates the branch cut by adding or subtracting  $2\pi i$  from  $\Gamma_{k,j}$  accordingly.

## Discussion

A. Chwang (University of Iowa)

I would like to ask a question regarding the "matching" between inner and outer solutions. Analytically, it is done relatively simply by equating the inner limit of the outer solution to the outer limit of the inner solution. However, your paper is a numerical one. How do you choose the matching boundary? I suspect that your numerical solution will depend very much on the size of boundary you choose.

A.Y. Odabasi (British Ship Research Association)

We at BSRA are very much interested in the work of Professor Vinje and his colleagues since we are also building up a real-time simulation system for large-amplitude ship motions. The points I would like to raise are as follows:

1. In lateral motions, in particular for large amplitude rolling motion, nonpotential forces and moments make up a larger part of the fluid reactive components, which are not considered in the present work.
2. For surface piercing nonaxisymmetric bodies the instantaneous center of roll does not necessarily pass through the center of gravity owing to the constraint imposed by the presence of a free surface. The result manifests itself in two ways:
  - a. Stream function on the body, i.e., Equation (7), should be written in such a way that  $R$  will be measured from the instantaneous center-of-rotation.
  - b. Additional gyroscopic terms will appear in the governing equations.
3. When the problem is posed as purely two dimensional and potential, the need to split the domain into an inner and an outer region may be avoided. Given the fact that the real and imaginary parts of the complex potential is defined on the domain boundaries, one can obtain an explicit solution by utilizing the results of Keldysh and Sedov after the transformation of the computation domain onto the upper (or lower) half of an auxiliary complex plane. Hence, the problem is reduced to the numerical construction of a conformal mapping function for each time step that will map the boundary of the region onto the real axis.

A. Papanikolaou (University of Berlin)

Referring to the time domain technique used in this paper, I would like to raise a few points:

1. Commenting on a time-domain technique for second-order problems of the type described, one has to worry about the radiation condition at infinity. I do not understand how a fully nonlinear problem is appropriately treated by a linear boundary condition at the "outer" domain. In that respect, perturbation methods, working in the frequency domain, e.g., Ref. 1, have worked more successfully in solving very different second-order problems (forced motions, diffraction, etc.) and surely more efficiently in the computational sense.
2. Referring to Figures 11 and 17, I would like to ask whether a steady-state behavior was expected to occur, and how the numerical results for surface piercing bodies are. In your paper (1981b) you reported on negative horizontal drifting forces of floating cylinders. How is the numerical stability of your results for more difficult, e.g., flared sections (nonvertical entrance at the waterline), if any?
3. The method is based on the theory of analytic functions. How would you proceed in solving the three-dimensional problem of floating ships?

## References

1. A. Papanikolaou and H. Nowacki, "Second Order Theory of Oscillating Cylinders in a Regular Steepwave," Proc. 13th ONR Symposium, Tokyo, 1980.

## Author's Reply

T. Vinje (University of Trondheim)

To A. Papanikolaou

Dr. Papanikolaou raises the question about consistency in the matching of the nonlinear inner solution to a linear outer solution. We do not claim that this matching is consistent, rather, that it is expected to yield a reasonably good solution for nonlinearities localized in the inner domain. I tend to agree with Dr. Papanikolaou's statement that the perturbation method is much better fit to solve a second-order problem than is the present method, especially since a second-order problem is defined according to a perturbation scheme. On the other hand, I do not see how the example shown in Figure 13 of our paper can be solved easily by means of a perturbation scheme.

To the second question: We have not applied the present method to surface-piercing problems. What the discussor refers to is that during the initial stage ( $\sim 1\text{--}\frac{1}{2}$  cycle) of a simulated record the ship was moving against the wave, which probably is caused by nonmatching initial conditions. To conclude that there is a negative mean drift force present, the body has to have a mean acceleration in the negative direction. I am not able to draw that kind of conclusion from the simulated data. As a reply to the third question I will say that Laplace's equation for the three-dimensional problem might be solved by F.I. Green's theorem, the source/sink method, or the finite-element technique.

To A.T. Chwang

The "matching boundary" is chosen as a half-circle connecting the points at the free surface of the inner domain that are furthest away. For the examples that are discussed in the paper, the radius of the semicircle is 7.5 times the radius of the circular cylinder. I suspect that the size of the boundary will influence the solution, depending on the nature of the nonlinearity. For problems where the nonlinearity will penetrate out into the outer domain, the solution will quite surely become erratic after a certain time.

To A.Y. Odabasi

I must only agree with Dr. Odabasi's first statement when regarding large-amplitude rolling motion. For the final stage of capsizing of ships in beam seas, when this is caused by breaking waves, the results of Greenhow et al. (1982) seem to indicate that potential theory is adequate.

To statement 2: I agree that the center of rotation does not necessarily coincide with the center of gravity of the body. This does not mean that the center of gravity cannot be used as the reference point for the rigid body motion; closer to the contrary. For the development of Equation (7), Dr. Odabasi is referred to Vinje & Brevig (1981b) or to the standard textbook on hydrodynamics by Milne-Thomson. Regarding statement 2.b: there cannot be any gyroscopic effects for a strictly two-dimensional problem; the additional terms in the equation of motion are caused by a moving point of reference. The position of this point (the center of rotation) is found from two second-order differential equations equivalent to the ones for determination of the position of the center of gravity.

To his third statement: I have the feeling that the procedure indicated by Dr. Odabasi involves a solution of Laplace's equation in a semi-infinite domain, just like we try to do. I have the feeling that we here are dealing with the fourth principle of conservation: conservation of difficulty.

# Slowly-Varying and Mean Second-Order Wave Forces on Ships and Offshore Structures

R G Standing and N M C Dacunha  
National Maritime Institute, Feltham, Middlesex, UK

## SYNOPSIS

This paper describes the main results of a recently-completed research programme on wave drift forces. Methods for predicting both mean and low-frequency components of the drift force are reviewed. A simple parameter gives some indication of the relative importance of viscous drag and wave diffraction effects. Numerical procedures, based on so-called 'near-field' and 'far-field' expressions for the drift force, are described. Calculated forces on a moored drill-ship, obtained using the NMIWAVE computer program, are compared with simple analytic solutions and with experiment.

Predicted mean forces and first-order response motions agree well with measured values in regular waves and in wave groups. Mean forces in irregular random waves agree slightly less well. Discrepancies are attributed to a mixture of numerical and experimental causes.

The paper also discusses the validity of three different methods for estimating the low-frequency force: the NMIWAVE solution, which calculates the full quadratic transfer function, and two more approximate methods. The main features of these three methods are related to the effects of wave diffraction, and of spatial gradients associated with both the first and second-order wave fields. These in turn are related to three simple parameters. General conclusions based on these parameters are borne out by numerical and experimental data. The importance of the second-order wave is discussed. It is difficult to simulate this component adequately either numerically or experimentally.

## CONTENTS

1. Introduction
2. Physical and Mathematical Processes
3. Mean Forces
  - 3.1 Roles of wave diffraction, inertial and drag loading
  - 3.2 Simple theoretical methods
  - 3.3 Three-dimensional wave diffraction
  - 3.4 Mean wave drift forces by the 'far-field' method
  - 3.5 Mean wave drift forces by the 'near-field' method
4. Slowly-varying Forces
  - 4.1 Roles of wave diffraction, spatial gradient and set-down effects
  - 4.2 Computing procedure
5. Numerical and Experimental Studies
  - 5.1 Mean forces on a moored drill-ship
  - 5.2 Experimental investigations into low-frequency response
  - 5.3 Approximate procedures
  - 5.4 Further implications for experimental or numerical modelling
6. Conclusions

## 1. INTRODUCTION

Wave drift forces and drift motions have recently attracted much research interest. They appear in several different guises and in a wide range of situations. They are clearly involved in the drifting of disabled ships (Dand, 1981), but also in the added resistance of ships advancing through waves (Salvesen, 1974). Moored ships and structures often experience low-frequency drifting motions (Stammers et al., 1977), which can cause severe loads in mooring hawsers, or affect the design of dynamic positioning systems. Low-frequency heave and pitch motions of semisubmersibles (Naess and Børresen, 1978) may have a similar origin.

These forces and motions can arise in several different ways. The underlying causes are often complex, and involve several different types of non-linearity, which are hard to disentangle. The process may involve wind and current loading, variations in mooring stiffness, particularly where both mooring lines and fenders are used (Lean, 1971). The equations of motion may have unstable solutions; this occurs, for example, with ships at single point moorings (Sørheim, 1981) and tethered buoyant platforms (Rainey, 1978). Various non-linear wave forces may also be involved. The present paper discusses this last item. More specifically it discusses various theoretical procedures for predicting the mean and low-frequency components of the second-order wave force.

It is well known that an unmoored ship tends to drift down-wave, and sometimes also changes its heading. Havelock (1940, 1942) developed simple mathematical formulae to predict the wave drift force, and his concepts form the basis of more recent computational procedures. Havelock's formulae predict the mean force. He assumed perfect wave



reflection, as at a plane vertical wall. Later authors (e.g. Maruo, 1960; Longuet-Higgins, 1977) allowed for partial wave transmission, while Newman (1967), Kim and Chou (1973) and others have extended these techniques to calculate mean forces on ship-like forms by means of slender-body and strip theories. Salvesen (1974) incorporated forward speed, so as to predict the added resistance of ships travelling through waves. Faltinsen and Michelsen (1974) extended Newman's theory, so as to calculate mean forces on structures of quite general form, by using linear 3-dimensional wave diffraction theory. They found good agreement between predicted forces and experimental values. This finding was later confirmed by Pinkster (1980) and by the present results.

All the above procedures calculate the mean force from changes in wave momentum far from the structure, and are therefore often classified as 'far-field' methods. Pinkster and van Oortmerssen (1976) employed the alternative 'near-field' approach, calculating second-order forces acting directly on the structure. This approach is computationally more expensive than the corresponding far-field method, but has two great advantages. It gives considerably more insight into the mechanism of wave drift forcing, and can also be used to calculate mean vertical and low-frequency components of the wave force.

The low-frequency force involves a quadratic transfer function describing the force caused by interacting pairs of regular wave trains with different frequencies. Newman (1974) and Pinkster (1974) had earlier proposed an approximate procedure for estimating low-frequency forces, in which the quadratic function is replaced by the mean force acting in regular waves at the mean frequency. This approximate procedure is widely used in design: it is cheap and easy to apply, and the required mean force data are more readily available (from either experiments or theory) than the quadratic function. Rye et al (1975) commented on the sensitivity of the resulting force spectrum to small variations in the mean force function, and there were no clear criteria for judging the accuracy or validity of this method.

Bowers (1976) also proposed an approximate formula, suited to the estimation of surge drifting forces on moored ships, and requiring no diffraction input whatsoever. Again there were no clear criteria for its use.

All the above approaches are based on classical Airy wave theory, which assumes inviscid flow. Huse (1977), Pijfers and Brink (1977) had proposed a mechanism by which drag forces may give rise to drifting of semisubmersibles and similar tubular structures. Criteria for judging the importance of drag and viscous effects were also lacking.

The present paper describes the results of a research programme on wave drift forces, undertaken at the National Maritime Institute so as to:

- a) extend the existing NMIWAVE computer program, which could already calculate first-order wave diffraction forces and responses, in order to predict second-order mean and low-frequency forces, using both the far-field and near-field techniques,
- b) clarify the conditions in which this technique is valid, in particular for the neglect of drag forces,
- c) clarify ranges of validity of the Pinkster/Newman and Bowers approximations.

## 2. PHYSICAL AND MATHEMATICAL PROCESS

Ships moored at jetties or exposed offshore locations are often seen to undergo large-amplitude, long-period drifting motions, which can cause severe loads in mooring lines. Multi-point mooring arrays usually constrain the vessel to make simple surge, sway and perhaps yawing motions, with characteristic periods in the range 30 seconds to several minutes (see, for example, Stammers et al., 1977). These motions may sometimes be excited directly by very long-period swell waves. Little is known about such waves. Conventional waverider buoys cannot detect them, and they are difficult to distinguish from second-order set-down and related effects. The 'linear' process by which these long-period swell waves cause drift motions is essentially the same as that occurring at higher frequencies, and will be discussed no further here.

A wide range of complex non-linear processes can also cause drifting, and are probably of greater significance in most situations. These non-linearities may be divided conveniently into those associated with the response process, and those involved in wave loading. The first process requires no direct excitation at the response frequency: the low-frequency response occurs as either a subharmonic or unstable solution of the equations of motion.

Non-linearities in the wave loading process are perhaps more fundamental, and affect a wider range of design problems. Particular attention is focussed here on the second-order contribution to the wave force. This force has both mean and low-frequency components, causing excitation at frequencies below the range of direct wave action. These components are often known collectively as 'wave drift forces', and arise either through non-linear interactions within the wave field, or through non-linearities in the mechanism by which these waves act on the structure. Forces of the first kind are associated with the second-order wave, and are particularly difficult to calculate. They include effects of set-down (a lowering of the water surface beneath wave groups) and surf beats, which are particularly important at inshore locations (see Bowers, 1980a). Forces of the second kind are the second-order consequences of first-order waves acting on the structure. They can be expressed in terms of products of first-order quantities, and are relatively easy to compute. Both contributions will be discussed in the following sections.

A structure in perfectly regular sinusoidal waves experiences a mean force, but no low-frequency variations. These variations occur in an irregular sea, and are associated with wave grouping. The process can be described in simple mathematical terms. Second-order forces depend on various products of first-order quantities. Two such quantities  $X$  and  $Y$  may be expressed in the form:

$$X = \sum_{n=1}^N X_n a_n \cos (\sigma_n t - \gamma_n - \mu_n)$$

$$Y = \sum_{n=1}^N Y_n a_n \cos (\sigma_n t - \gamma_n - \nu_n)$$

where the surface elevation at the origin of coordinates consists of  $N$  superimposed cosine waves:

$$\zeta = \sum_{n=1}^N a_n \cos (\sigma_n t - \gamma_n) \quad (2.1)$$

Their product

$$XY = \sum_{m=1}^N \sum_{n=1}^N \frac{1}{2} X_m Y_n a_m a_n \{ \cos [(\sigma_m + \sigma_n)t - (\gamma_m + \gamma_n) - (\mu_m + \nu_n)] \\ + \cos [(\sigma_m - \sigma_n)t - (\gamma_m - \gamma_n) - (\mu_m - \nu_n)] \}$$

The first term represents a force at a frequency higher than those in the incident waves, and is of no direct relevance in the present context. The second term represents the wave drift force, which can be expressed more generally in the form

$$F^{(2)} = \sum_{m=1}^N \sum_{n=1}^N T_{mn} a_m a_n \cos [(\sigma_m - \sigma_n)t - (\gamma_m - \gamma_n) - \delta_{mn}] \quad (2.2)$$

where  $T_{mn}$ ,  $\delta_{mn}$  represent the quadratic transfer function and phase of the force relative to the wave group envelope. It is immediately clear that:

- a) the mean force arises from terms with  $m = n$ , and involves no coupling between wave components;
- b) each pair of wave components interacts to produce a force at their difference frequency  $|\sigma_m - \sigma_n|$ ;
- c) the bandwidth and resolution of the second-order force spectrum are identical with those of the first-order wave spectrum. This has important consequences for the simulation of random wave conditions (see section 5.4);
- d) the transfer functions for amplitude  $T_{mn}$  and phase  $\delta_{mn}$  depend on the wave frequencies  $\sigma_m$ ,  $\sigma_n$ , but not on the amplitudes of those wave components, nor on any other components present. Transfer functions computed for pairs of superimposed regular waves ('regular wave groups' or 'beating waves', as shown in figure 1) can therefore be used to predict the force spectrum in an irregular sea. A procedure for calculating  $T_{mn}$ ,  $\delta_{mn}$ , and superimposing forces in irregular seas, will be described in later sections.

The low-frequency forces are themselves of limited interest. They are usually much smaller than wave-frequency forces. They become important, however, when the system has a low natural frequency and the damping is light, by exciting a large resonant response. In these circumstances the mooring force can be many times larger than the low-frequency wave exciting force. The process is illustrated in figure 2. The incident wave spectrum (top left of figure) causes both wave-frequency forces and small low-frequency drift forces (top right). The response characteristic (bottom left) is that of a lightly-damped system with a long natural period. It acts as a band-pass filter, causing an enhanced natural-period response, and an attenuated wave-frequency motion. Low-frequency components thus dominate the response spectrum (bottom

right of figure).

The response process can be described in terms of the equation of motion of a linear system. For each frequency  $\sigma$  of wave forcing the response  $\eta^{(2)}$  satisfies an equation of the form

$$\ddot{\eta}^{(2)} + 2\beta\sigma_0\dot{\eta}^{(2)} + \sigma_0^2\eta^{(2)} = \frac{|F^{(2)}|}{M} \cos(\sigma t - \delta)$$

where  $|F^{(2)}|$  is the amplitude of the wave force,  $M$  the system's inertia,  $\sigma_0$  its natural frequency, and  $\beta$  the damping ratio. The amplitude of the system's response at its natural frequency is  $|F^{(2)}|/2\sigma_0^2\beta M$ , and the corresponding mooring load is  $|F^{(2)}|/2\beta$ . A typical value of  $\beta$  for a moored ship in surge might lie in the range 0.02 to 0.05, so that the maximum mooring force might be 10 to 25 times the maximum wave force at the ship's natural surge frequency. It is worth noting that although the peak amplification factor increases with  $\beta^{-1}$ , the bandwidth of response simultaneously decreases, so that the root mean square response in an irregular sea only varies with  $\beta^{-1/2}$  (see Standing et al., 1982).

It is, therefore, not the non-linear wave forces that are of importance to the designer, but rather the consequential effects of this forcing on dynamic response, mooring loads and fatigue. These effects may be enhanced by non-linearities in the response equations themselves, a process which will not be discussed further here (see van Oortmerssen, 1979).

### 3. MEAN FORCES

#### 3.1 Roles of Wave Diffraction, Inertial and Drag Loading

Two fundamentally different methods are used in offshore design to predict first-order (wave-frequency) loads on structural members. One method is empirical, and the other mathematical, and they have different ranges of validity and use. According to the first method, Morison's (1950) equation represents the wave force as the sum of separate drag and inertial components with appropriate empirical coefficients  $C_d$  and  $C_m$ . This method is most widely used for analysing tubular frameworks. The second, more theoretical, approach is applied to ships and wide-body structures. Hydrodynamic equations describing wave diffraction and radiation by the structure are solved either analytically or numerically. This method usually assumes classical linear wave theory and ideal flow.

It is instructive to compare the physical roles of wave diffraction, inertial and drag loading in the drift force process by reference to these two techniques.

It is convenient to start with a discussion on the mean drift force. The mean force has been studied over many years, both theoretically and experimentally, and is relatively well understood. Criteria and techniques for calculating this component will be discussed before transferring attention to the less well-understood low-frequency component.

Two simple criteria are often used to assess the relative import-

AD-A158 920

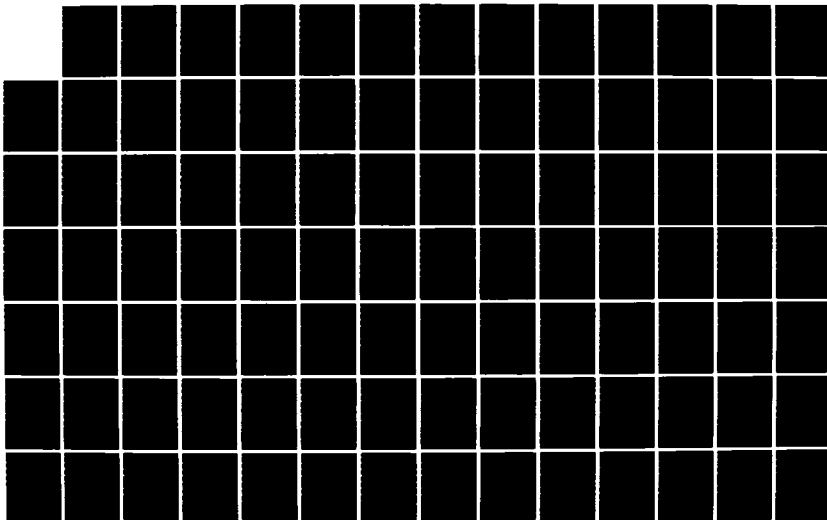
SYMPOSIUM OF NAVAL HYDRODYNAMICS (14TH) HELD AT ANN  
ARBOR MICHIGAN ON AUGUST 23-27 1982(U) OFFICE OF NAVAL  
RESEARCH ARLINGTON VA M P TULIN ET AL. 1982

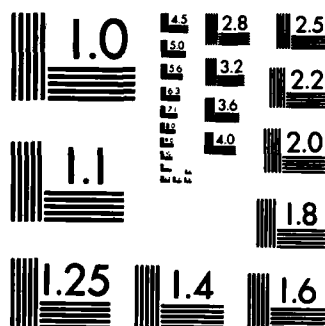
84/13

UNCLASSIFIED

F/G 28/4

NL





MICROCOPY RESOLUTION TEST CHART  
NATIONAL BUREAU OF STANDARDS-1963-A

ance of drag, inertial and diffraction contributions to the first-order wave force:

- a) drag forces are assumed negligible if the ratio  $\delta/D \leq 1$ ,
- b) diffraction effects are assumed negligible if  $D/\lambda \leq 0.2$ ,

where  $\delta$  is the diameter of a typical water particle orbit,  $D$  a typical member diameter, and  $\lambda$  is the wave length. Physical limitations on wave steepness ensure that  $\delta/\lambda$  is small, so that drag and diffraction forces on a member are rarely important simultaneously. The use of linear diffraction theory, based on ideal flow assumptions, may thus be justified.

These simple criteria are based on measured forces and theoretical predictions for a single fixed vertical column, and there are, of course, many exceptions and practical complications when considering more complex and realistic structures. For example well-submerged members are less likely to experience effects of wave diffraction, while dynamic structures may be more susceptible to effects of damping and drag than these simple criteria suggest.

In the same spirit, and with the same note of caution about special cases, some simple criteria will now be sought for describing the relative magnitudes of drag, inertial and diffraction effects on the second-order force.

The role of wave diffraction is fairly clear. Wave diffraction changes the momentum carried by the wave field, and this change implies a mean force acting on the structure. Forces of this kind are associated mainly with short-period waves, with wavelengths typically less than the dimensions of structural members. Longer waves are less affected by the structure, and the mean force is reduced. This is particularly true when the structure is free to respond with the waves, as shown by Faltinsen and Løken (1978).

Drag affects the wave drift force in at least two distinct ways:

- a) on fixed structures, drag forces act between the mean and instantaneous free surfaces, and provide a non-zero mean load,
- b) on responding structures, the amount of hydrodynamic damping affects the phase difference between first-order forces and response motions, particularly near resonance. One component of the drift force involves the product of first-order forcing and response. Huse (1977) attributed observed negative drift forces on a semisubmersible to the phase difference between heave forces and pitch motions.

The inertial term in Morison's equation is associated with a local disturbance in the flow pattern. This disturbance does not affect momentum in the first-order wave field, and so there is no mean drift force. (The structure also disturbs the second-order 'set-down' wave, however, and an inertial-type force results. This force has no mean component, and so discussion will be deferred until the next chapter).

The relative sizes of drag and diffraction contributions can be assessed most simply by calculating wave forces on a fixed vertical column of circular section, as in the first-order example quoted above. The mean force due to conventional drag and inertial loads acting between the mean and instantaneous free surface is

$$\frac{1}{2}\pi \int_0^{2\pi} \left\{ -C_m \rho \frac{\pi D^2}{4} \left( \frac{2\pi^2 H}{T^2} \right) \sin \theta + \frac{1}{2} C_D \rho D \left( \frac{\pi H}{T} \right)^2 \cos \theta \left| \cos \theta \right| \right\} \frac{H}{2} \cos \theta d\theta$$

where the wave is described by linear deep-water theory. The inertial contribution integrates to zero, as noted above. The drag contribution is  $\pi C_D \rho D H^3 / 3T$ .

Havelock (1940) obtained an analytic solution for wave diffraction by a circular column, and Karpinnen (1979) has shown that the mean force may be approximated by the expression  $\rho g D H^2 (\pi D / \lambda)^3 / 3$  when  $D/\lambda$  is small.

Comparing the above two expressions it is seen that diffraction effects dominate the mean force when  $H\lambda^2/D^3 \leq 60$ , and drag effects when this ratio  $\geq 60$ . This result and the corresponding first-order criteria are represented pictorially in figure 3. It is immediately clear that when either drag or diffraction affects the first-order force, the same is true of the mean force. The situation is less clear when both  $\delta/D$  and  $D/\lambda$  are small. Semisubmersible platforms come into this category, particularly in long-period waves. Pinkster (1980) has found good agreement between experiment and theory based on a linear diffraction analysis, while in other cases Pijfers and Brink (1977) and Huse (1977) invoke a drag-force mechanism. Both effects are relevant: diffraction in moderate sea states, and drag forces in large waves and strong currents.

In relating these parameters to practical structures the underlying assumptions must be borne in mind. The appropriate dimension  $D$  is that associated with wave diffraction: this will generally be the width of the member presented to waves at the free surface. Dynamic response may modify or invalidate these criteria, as may submergence of large parts of the structure. These parameters are intended simply to help the designer towards an understanding of wave drift forces, and the reasons why one design procedure may be preferred rather than another.

### 3.2 Simple Theoretical Methods

From this point onwards the theory will be based on classical linear waves and ideal flow assumptions. The drift forces are associated with inertial, diffraction and radiation effects, and all viscous and drag effects are neglected. It is also assumed that no current is present, and that the ship or structure has no forward speed. Cartesian coordinates will be used, as shown in figure 4.

It is convenient to start with a two-dimensional model. Maruo (1960) showed that the mean force on a two-dimensional object in deep water may be expressed as  $\frac{1}{8} \rho g H^2 R^2$ , where  $R$  is the reflection coefficient (ratio of reflected to incident wave height).

Havelock (1940) assumed perfect reflection, as at a rigid vertical wall, so that  $R = 1$ , and showed that the mean longitudinal force acting on a ship may be expressed

$$\frac{1}{8} \rho g H^2 \int_{-B/2}^{B/2} \sin^2 \theta dy$$



where the integral is over the ship's beam  $B$  along the portion of waterline exposed to waves, and  $\theta$  is the angle between the waterline and the wave direction. This formula may be extended straightforwardly to give the transverse force and turning moment. It is widely used in ship design, because of its simplicity, and does in fact represent the mean force fairly well in very short waves. It seriously overestimates the force, however, in long-period waves.

A smaller proportion of the wave energy is reflected, and more transmitted, as the wavelength increases. Vessel response also affects the drift force. Newman's (1967) analytic solution takes account of wave scattering and vessel response, and is also fairly easy to evaluate. It invokes slender-body assumptions to represent flow around a slender ship. The theory assumes that the ship's beam  $B$  is small compared with the wavelength  $\lambda$ .

Figure 5 compares Havelock's short-wave and Newman's long-wave methods with a more accurate numerical procedure based on 3-dimensional diffraction theory, and described in the next section. This figure shows longitudinal and transverse forces on a ship moored at an angle to waves. It is clear that Havelock's method works well in short waves, and is in fact a convenient means of extrapolating numerical results to very high frequencies. Newman's formulae agree rather poorly with diffraction theory over most of the relevant part of the frequency range. This is because it is a long-wave theory, and the drift forces are mainly associated with short and moderate wavelengths. Faltinsen and Løken (1978) reached similar conclusions, and investigated a range of other procedures, including one based on Newman's theory but solving the first-order problem by strip theory rather than slender-body methods. This approach should be valid for moderate and short wavelengths, except in head and following seas. The full three-dimensional approach, described below, should be used for ships or structures of fuller or unusual form, and also for ships in head and following seas.

### 3.3 Three-Dimensional Wave Diffraction

John's (1950) wave diffraction theory describes the scattering of small-amplitude waves by large objects in the sea. NMIWAVE is one of a growing number of computer programs based on John's theory. Programs of this type are used by designers to estimate wave loads on large fixed storage tanks and gravity platforms, and the response motions of large free-floating or moored structures.

Linear wave diffraction theory is based on classical Airy wave and ideal flow assumptions:

- a) the wave height  $H$  is small compared with the water depth and typical body dimensions, so that the hydrodynamic equations may be made linear in  $H$ ;
- b) the response motions of the structure are similarly small, so that the relevant response equations may also be linearised;
- c) the flow is inviscid, incompressible and irrotational, and may therefore be described in terms of a velocity potential  $\phi^{(1)}$ .
- d) It is also assumed that the ship or structure has no mean forward motion relative to the water, and that the water is of uniform depth  $d$ .

The velocity potential in regular waves of frequency  $\sigma$  is expressed as the sum of incident, diffracted and radiated components:

$$\phi^{(1)} = (\phi_i + \phi_s + \sum_{j=1}^J \eta_j \phi_j) e^{-i\sigma t}$$

The diffraction component  $\phi_s$  represents wave scattering by the fixed structure, and components  $\phi_j$  represent wave radiation associated with structural motion  $\eta_j$  in each of its  $J$  degrees of freedom. The hydrodynamic equations are solved for  $\phi_s$  and each  $\phi_j$  separately; forces and moments are then calculated from pressures acting over the structure's surface. Forces associated with wave radiation are converted to added masses and damping coefficients, which are incorporated into the structure's response equations. These equations are then solved for  $\eta_j$ . Standing (1979) gives details of the NMIWAVE program and of a numerical procedure for solving the hydrodynamic equations. The solution is obtained in terms of a distribution of pulsating fluid sources, with density  $f_j(\underline{\xi})$ , over the surface  $S$  of the structure. The velocity potential at the point  $\underline{x}$  is

$$\phi_j(\underline{x}) = \int_{S_0} f_j(\underline{\xi}) G(\underline{x}, \underline{\xi}) dS$$

where the source influence function  $G$  satisfies sea-bed, free-surface and radiation conditions, as well as the Laplace equation in the fluid. The body surface  $S_0$  is divided into a finite number of facets, and equations representing the boundary condition at the centre of every facet are solved simultaneously for every  $f_j$ .

There is a one-to-one correspondence between frequency components of the wave history, forces and response motions. The amplitudes of the force and response at frequency  $\sigma$  are directly proportional to the wave amplitude at the same frequency. Mean and subharmonic forces and motions do not occur.

This linear solution represents the first-order term in a power series expansion of the form:

$$\phi = \epsilon \phi^{(1)} + \epsilon^2 \phi^{(2)} + \epsilon^3 \phi^{(3)} + \dots$$

with associated forcing

$$\underline{F} = \underline{F}^{(0)} + \epsilon \underline{F}^{(1)} + \epsilon^2 \underline{F}^{(2)} + \epsilon^3 \underline{F}^{(3)} + \dots$$

where  $\epsilon$  is a small parameter related to wave steepness, and  $\underline{F}^{(0)}$  represents the (zero-order) hydrostatic force. The problems of calculating mean and low-frequency components of  $\underline{F}^{(2)}$  will now be addressed.

### 3.4 Mean Wave Drift Forces by the 'Far-Field' Method

The mean force can be calculated in either of two different ways. The first, and computationally more straightforward, of these is the so-called 'far-field' method. The mean force is inferred from momentum in the incident, diffracted and radiated wave fields far from the structure. Salvesen (1974) has shown that mean second-order horizontal forces

depend only on the first-order wave field, and not on second-order waves. This fact greatly simplifies the process of calculating these forces.

Newman (1967) has shown that the mean force on the structure in the x-direction may be expressed

$$\bar{F}_x = - \int \int_{S_\infty} [P \cos \theta + \rho U_R (U_R \cos \theta - U_\theta \sin \theta)] R d\theta dz$$

where  $p$  is the first-order hydrodynamic pressure,  $U$  is fluid velocity with radial and tangential components  $U_R$ ,  $U_\theta$ ;  $S_\infty$  is a large cylindrical control surface with radius  $R$ . The bar denotes the mean over a complete wave cycle. Faltinsen and Michelsen (1974) expressed the pressure and velocity components in terms of source densities  $f_j(\underline{\xi})$ , so that

$$\bar{F}_x = \frac{1}{2} \rho s(k) \left[ \frac{\frac{1}{2} \sigma H}{\sinh kd} \sqrt{\frac{2\pi}{k}} q(\psi) \cos \psi \cos \delta - \frac{1}{2} k \int_0^{2\pi} q^2(\theta) \cos \theta d\theta \right]$$

where  $s(k) = \frac{1}{2} \sinh 2kd + kd$ ,  $\delta(\theta)$  and  $q(\theta)$  are defined by

$$q(\theta) e^{i\delta(\theta)} = \frac{2\pi i (v^2 - k^2)}{(k^2 - v^2)d + v} \sqrt{\frac{2}{\pi k}} \int_{S_0} [f_s(\underline{\xi}) + \sum_{j=1}^J \eta_j f_j(\underline{\xi})]$$

$$\cosh k(d+z') \exp [-ik(x' \cos \theta + y' \sin \theta)] dS$$

$\underline{\xi} = (x', y', z')$ ,  $v^2 = \sigma^2/g = k \tanh kd$ . Further details, and similar expressions for the y-component of the force and turning moment, are given by Standing et al. (1981).

### 3.5 Mean Wave Drift Forces by the 'Near-Field' Method

The far-field approach requires little computational effort beyond that required for the first-order solution, but can only describe mean horizontal components of the wave force. Pinkster's (1980) alternative 'near-field' method can predict mean vertical forces as well as the low-frequency components. This method shows more clearly the relationships between the drift force and fundamental physical parameters, such as surface elevation, velocities and pressures. It is, however, more cumbersome to program on the computer, and more demanding in terms of computer time and storage.

Pinkster has shown that the mean and low-frequency forces may be expressed as a sum of six components:

$$\begin{aligned} & -\frac{1}{2} \rho g \int_{L_0} \zeta x^2 \underline{n}'_0 d\ell + \frac{1}{2} \rho \int_{S_0} |\nabla \phi|^2 \underline{n}_0 dS \\ & - \rho \int_{S_0} \left[ \frac{\partial \nabla \phi}{\partial t} \cdot \underline{\eta} \right] \underline{n}_0 dS + R \underline{\tilde{F}} + \underline{W}_1 - \rho \int_{S_0} \frac{\partial \phi^{(2)}}{\partial t} \underline{n}_0 dS \end{aligned} \quad (3.1)$$

where  $L_0$  is the mean waterline, and  $S_0$  the mean underwater surface of the structure;  $\underline{n}_0$  is the normal to  $S_0$  and  $\underline{n}'_0$  is the normal to  $L_0$ ;  $\underline{\xi}$  is the translational motion of the structure at a point on its surface, and the  $3 \times 3$  matrix  $R$  represents a vector cross-product with the first-order rotation of the structure. The force  $\underline{F}$  represents the total first-order fluid force, including both hydrodynamic and hydrostatic components.

$\zeta_r$  is the free surface elevation relative to the structure. All the above ( $\eta$ ,  $R$ ,  $\vec{F}$ ,  $\zeta_r$ ), and the velocity potential  $\phi$ , represent first-order quantities. The fifth and sixth terms will be explained below.

The above terms can be interpreted physically. The first component (called term I in subsequent sections) represents forces acting between the structure's mean waterline and the instantaneous free surface. The second component (II) represents second-order pressures,  $-\frac{1}{2} \rho U^2$ , integrated over the structure's surface. The third component (III) describes the change in the force due to first-order motions of the structure through the first-order pressure field. Term IV represents changes in the direction of the force due to first-order rotations.

Term V was omitted by Pinkster, and is in many cases zero, but represents second-order motions of the structure's centre of buoyancy and waterplane due to first-order response. It contributes to the vertical forces; the heave component is, for example:

$$-\frac{1}{2} \rho g z_c A (\eta_4^2 + \eta_5^2)$$

where  $z_c$  is the z-coordinate of the point at which first-order motions are defined,  $A$  is the structure's waterplane area,  $\eta_4$  and  $\eta_5$  are its first-order roll and pitch response motions.

Term VI represents the effect of the second-order wave, and  $\phi^{(2)}$  is the second-order velocity potential. This term does not contribute to the mean horizontal force for reasons given earlier, though it may make a hydrostatic-type contribution to the vertical force. Term VI will be discussed further in the context of low-frequency forces (sections 4 and 5).

Standing et al (1981) give further details of the numerical process adopted at NMI for evaluating these terms. Once the first-order solution is obtained by John's diffraction method, it is in principle straightforward to substitute first-order quantities into the above expressions for terms I-V, and integrate over appropriate areas of the hull surface and waterline. Results are presented in section 5.

#### 4. SLOWLY-VARYING FORCES

Interest has recently tended to shift from mean drift forces to the less well-understood and less easy-to-compute low-frequency component. This shift has occurred as designers have recognised the underlying causes of low-frequency resonant motions of moored structures, and as computational procedures have advanced. The damping of the system is also important in this context, of course, and is in many ways less well-understood than the loading. The damping problem is mentioned here merely as an aside, and is outside the scope of the present paper.

Because of difficulties in predicting the full quadratic transfer function for the second-order force, various simplified procedures have been devised. Two particular simple methods will be examined because they throw some light on the complex range of parameters involved. Some quantitative comparisons will be made between these methods in section

5.3. There were several reasons for selecting these particular techniques: they are fairly simple to use, the first method is widely used in design, and their assumptions are somewhat complementary.

a) The first such method is that proposed by Pinkster (1974) and Newman (1974). They replaced the quadratic transfer function  $T(\sigma_m, \sigma_n)$  by the mean force acting at the mean wave frequency  $T(\sigma_{mn}, \sigma_{mn})$ , where  $\sigma_{mn} = \frac{1}{2}(\sigma_m + \sigma_n)$ . For this method to be valid they require that

$$|\sigma_m - \sigma_n| \ll \frac{1}{2}(\sigma_m + \sigma_n)$$

where  $\sigma_m, \sigma_n$  are typical frequencies of two wave spectral components.

The underlying assumptions are similar to those of Hsu and Blenkarn (1970), though are more rigorously formulated. Hsu and Blenkarn treated each half-cycle of an irregular wave as part of a regular wave train with the same amplitude and period. The slowly-varying force then emerged as variations in the mean force between successive half-cycles.

The merit of the Newman/Pinkster or Hsu/Blenkarn approach lies in the fact that it is easier to compute (or measure) mean forces in regular waves than slowly-varying forces in irregular seas or regular wave groups. There is now a considerable body of data on mean wave forces, but little reliable information on low-frequency components. This simpler approach allows maximum use to be made of existing data, with minimal computational problems.

b) Bowers (1976) was particularly concerned with low-frequency surge motions of moored ships in short-wave head seas. In such circumstances his neglect of all wave radiation and diffraction effects would appear reasonable. The low-frequency force is defined entirely in terms of properties of the undisturbed incident wave: both first and second-order components. There is no mean force, because there is no mechanism for scattering the waves. Bowers found two distinct force components, both associated with spatial variations along the length of the ship. These variations are in the surface elevation (term I of equation 3.1) and in the second-order 'set-down' wave (term VI). These terms are of opposite sign.

It is immediately clear that the Newman/Pinkster approach represents wave diffraction effects and variations with time, but no spatial gradient effects. Bowers represents local variations in time and space, but neglects wave scattering. Thus the assumptions are somewhat complementary.

The third procedure to be discussed in this paper is the more exact numerical method described in sections 3.5 and 4.2. This method represents all the above effects, though continues to approximate the 'set-down' term, as in Bowers's theory.

#### 4.1 Roles of Wave Diffraction, Spatial Gradient and Set-down Effects

The purpose of this discussion is not to define precise and absolute criteria for applying various prediction techniques in design. The purpose is rather to understand the physical roles of wave diffraction, spatial gradient and set-down effects, and of some of the governing parameters.

It is assumed first that wave diffraction effects may be characterised by means of the mean force acting on a vertical fixed column of diameter  $D$ . Havelock's (1940) analytic expression was evaluated numerically by van Oortmerssen (1971). For present purposes the main features of their mean force (its asymptotic high-frequency behaviour and rapid fall-off at low frequencies) may be reproduced more simply by the formula

$$\frac{1}{2} \rho g D a^2 K(kD)$$

where  $K(kD) = (kD)^3/3$  for  $kD < 1.26$   
 $= 2/3$  for  $kD > 1.26$ ,

and  $\sigma^2 = gk$ . These formulae relate to deep-water regular waves of amplitude  $a$  and frequency  $\sigma$ .

The simplest type of wave form in which slowly-varying forces occur is the regular wave group, consisting of two superimposed regular wave trains with amplitudes  $a_1, a_2$  and frequencies  $\sigma_1, \sigma_2$  (see figure 1). According to Newman's (1974) approximate theory the amplitude of variations in the drift force on this simple column is

$$\rho g D a_1 a_2 K(k_c D) \quad (4.1)$$

where  $k_c$  is the wave number associated with a regular wave of mean frequency  $\sigma_c = \frac{1}{2}(\sigma_1 + \sigma_2)$ :

$$gk_c = \frac{1}{4}(\sigma_1 + \sigma_2)^2$$

Equation 4.1 will be used to characterise wave diffraction effects, and as a measure of force variations predicted by Newman's technique.

Bowers's (1976) formula for the surge force on a ship in head seas contains two terms, both representing spatial gradient effects. The first is associated with variations in the first-order wave field, and more specifically in the surface elevation around the ship's waterline (c.f. term I of equation 3.1). The second term represents the force due to the second-order 'set-down' wave (term VI), and is somewhat analogous to the inertial term in Morison's equation. Standing et al (1982) show how Bowers's formulae may first be extended to deeper water, and secondly simplified when the ship's length  $L$  and beam  $B$  are both small compared with the wave group length:  $|k_1 - k_2|L \ll 1$ . The amplitude of the low-frequency force then has two components

$$\frac{1}{2} \rho g B L a_1 a_2 |k_1 - k_2| \quad (4.2)$$

representing the surface elevation term I, and

$$\frac{1}{2} \rho g B L a_1 a_2 |k_1 - k_2| h f_{12} \quad (4.3)$$

representing term VI, where  $h$  is the ship's draft and

$$f_{12} = \max(1/d, |k_1 - k_2|)$$

Removing a common factor  $\frac{1}{2} \rho g a_1 a_2$  from equations 4.1, 4.2 and 4.3, three simple quantities are left:

$$2DK(k_c D), |k_1 - k_2| BL \text{ and } |k_1 - k_2| BL h f_{12}.$$

It seems reasonable to suppose that these three quantities will characterise the relative importance of (respectively) wave diffraction, gradient terms depending on the first-order wave field, and second-order set-down effects.

There are, of course, difficulties in relating these very simple parameters to realistic structures in irregular seas. The characteristic dimension  $D$  will normally be that associated with wave diffraction: probably the width of the structure presented to waves. The fall-off factor  $(kD)^3/3$  may need to be modified to allow for vessel response or draft. In most cases the relevant difference frequency  $\delta\sigma = |\sigma_1 - \sigma_2|$  will be the natural response frequency of the structure, but it is not always easy to choose an appropriate mean frequency  $\sigma_c$ . This may be near the peak of the wave spectrum, or perhaps at a slightly higher frequency.

Standing et al (1982) draw the following conclusions from sample calculations on a large ship (200000 DWT VLCC), a smaller drill-ship (which will be discussed in greater detail in subsequent sections), and a semisubmersible platform.

(i) In all cases diffraction effects tend to dominate when the structure is large in relation to wavelength (i.e.  $k_c > 1$ ), particularly when the natural frequency of the system is very low. In such conditions the Newman/Pinkster approximate method is likely to be valid.

(ii) Gradient terms of both types become significant when typical member diameters are small compared with the wavelength (i.e. slender tubular members), or when  $L$  is large (i.e. very long ships in head seas), and when the system's natural frequency is fairly high (i.e. a fairly stiff mooring arrangement).

(iii) The second-order set-down wave has a gradient-type effect. It becomes important if the vessel's draft is a substantial part of the water depth, or is more than about  $1/6$  of the relevant wave group length.

(iv) The diffraction parameter decreases very rapidly with both  $k_c$  and  $D$ : it varies in fact with the fourth power of  $D$  and the sixth power of frequency  $\sigma_c$ . This means that the relative importance of diffraction and gradient-type terms can depend very sensitively on structure dimensions and wave spectral content. This is particularly true of semisubmersible-type structures, where it is difficult to decide in advance which of the various effects will dominate in any given sea condition. The second-order wave term may be particularly significant. So too may be viscous drag, particularly in very large waves or strong currents.

(v) Conclusions of Rye et al (1975) may be interpreted in these terms. They compared low-frequency surge spectra for a 'Condrill' platform, calculated by means of the Newman/Pinkster formula, with experiment. They found the response spectra to be highly sensitive to small variations in the force transfer function, and found that Newman's

theory worked best (though, even then, not particularly well) when the wave spectrum contained a substantial amount of short-wave energy.

(vi) The above three simple parameters were also calculated for large and small moored ships. Results suggest that the diffraction process will tend to dominate sway motions rather more than surge, and will be most significant if the ship's natural surge or sway period is long. More exact numerical comparisons will be made in section 5.3 between the Newman/Pinkster, Bowers and more complete theories. These comparisons show that the first-order response of the vessel has an important modifying influence, which is difficult to describe in terms of simple parameters.

#### 4.2 Computing Procedure

Pinkster's (1980) near-field procedure, described in section 3.5, may be used immediately to predict low-frequency forces. There are only two complications: first it is necessary to represent interactions between pairs of waves at different frequencies, and secondly the second-order (set-down) wave has to be approximated in some way.

As regards wave interactions, Pinkster's (1980) approach is followed. Terms  $T_{mn}$ ,  $T_{nm}$  in equation 2.2 may be combined together in various possible ways, but it is convenient to set

$$P_{mn} = \frac{1}{2} (T_{mn} \cos \delta_{mn} + T_{nm} \cos \delta_{nm})$$

$$Q_{mn} = \frac{1}{2} (T_{mn} \sin \delta_{mn} - T_{nm} \sin \delta_{nm})$$

so that  $P_{mn}$ ,  $Q_{mn}$  are symmetric and antisymmetric respectively. Corresponding amplitude and phase functions are defined by

$$F_{mn} = P_{mn}^2 + Q_{mn}^2$$

$$\tan \alpha_{mn} = Q_{mn}/P_{mn}$$

so that  $\alpha_{mn}$  represents the phase of the maximum force relative to the phase of the wave envelope (see figure 1).

Forces in a random irregular sea can be obtained by superposition. If  $S(\sigma)$  is the wave spectral density function, then, following Pinkster (1980), the spectrum of second-order forces can be expressed

$$S_F(\sigma') = 8 \int_0^\infty S(\sigma) S(\sigma' + \sigma) F^2(\sigma, \sigma + \sigma') d\sigma \quad (4.4)$$

where  $F(\sigma_m, \sigma_n) = F_{mn}$  in the above notation. The mean force

$$\bar{F} = 2 \int_0^\infty S(\sigma) F(\sigma, \sigma) d\sigma \quad (4.5)$$

There are several different ways in which the second-order wave contribution might be estimated (term VI of equation 3.1). Lighthill (1979) showed that the complete second-order force can be calculated, without approximation, in terms of an integral of first-order quantities over the free surface. The amount of effort required to evaluate this



integral would be considerable, though less than that required to solve the full second-order problem (see Garrison, 1979; Isaacson, 1981).

Pinkster (1980) approximated the set-down term by treating the second-order wave as a first-order component with a modified phase speed, assuming that the structure was fixed. He thus represented the effect of the structure's added mass, but not second-order wave scattering, nor effects of the structure's first-order response. This method was found to predict forces on a floating cylinder rather poorly: a case for which an exact analytic solution was available.

NMI therefore adopted a rather simpler approximation, which neglects disturbances due to the structure altogether. This approach is analogous to the Froude-Krylov approximation for the first-order force, in which the pressures acting on the structure are those in the ambient wave field. The purpose of this approximation is to indicate quickly and easily whether the set-down term is important. Bowers's (1976) formulae are used, but modified to allow multi-directional waves, and both deep and shallow-water group effects. Full details are given by Standing et al (1982).

Finally second-order motions of the structure are calculated assuming that the response equations are of the usual linear form (see section 2).

## 5. NUMERICAL AND EXPERIMENTAL STUDIES

NMI's new computer programs require various first-order quantities to be evaluated at points on the structure's underwater surface. They rely on the existing NMIWAVE diffraction suite for this purpose. These earlier programs and their validation were discussed in a series of papers, notably that of Standing (1979).

The new second-order programs were validated in four separate ways:

a) against each other. The near and far-field methods provide independent routes by which to calculate the mean drift force. Results from these two programs were found to agree within the limits of numerical accuracy, as will be shown in the next section;

b) against analytic solutions. Comparisons were made with analytic solutions describing the mean force on a vertical fixed circular cylinder, and low-frequency forces on a vertical infinite wall. Good agreement was found, as shown, for example, in figure 6. This figure shows van Oortmerssen's (1971) evaluation of Havelock's (1940) formula, NMIWAVE results for the fixed cylinder, as well as a reworking of Havelock's solution in terms of fluid sources and Faltinsen's (1974) formula given in section 3.4. This last result is labelled 'Havelock/Faltinsen'. Finite depth terms are included in all cases.

c) against numerical data. Similar programs have been developed elsewhere, notably a 'far-field' program described by Faltinsen and Michelsen (1974), and a 'near-field' program developed by Pinkster (1980). NMI's calculations agreed well with Faltinsen's mean forces on a floating caisson, with Pinkster's mean vertical force on a horizontal cylinder, and with Pinkster's mean and low-frequency forces on a simple barge.

Figure 7 shows the separate near-field contributions to the mean force on the barge. It is clear that the waterline integral (term I) dominates but is of opposite sign to all other terms. The net force is sensitive to variations in any of its component parts. Standing et al (1981) recommended that the waterline, required to evaluate term I, should be defined with twice as many points as neighbouring hull-surface facets, in order to minimise numerical inaccuracies. These inaccuracies are associated particularly with the surface-singularity (point source) representation of the hull;

d) against experimental data. Experiments were undertaken in NMI's No. 3 wave tank, specially for the purpose of validating the new drift force programs. Results will be discussed in the following sections.

### 5.1 Mean Forces on a Moored Drill-Ship

A full description of the experiment and its analysis will be found in two reports by Standing et al (1981, 1982). The present paper will concentrate on the results of that investigation, and its implications for design.

The drill-ship was moored by 4 lines attached to its bow and stern. The mountings were strain-gauged, providing a direct measurement of mooring loads. Motions of the vessel were measured in all six degrees of freedom, and the measurement procedure allowed both wave-frequency and low-frequency surge, sway and yaw to be obtained. The initial heading of the vessel was at  $126^\circ$  to the incident wave direction, and its principal dimensions (at full-scale) were:

length ( $L_{pp}$ )	= 94m
beam	= 15.2m
draft	= 5.8m

Comparisons were made first between measured and predicted first-order (wave-frequency) motions of the vessel. Figure 8 shows the response amplitude operators in regular waves. The calculations assume potential flow, except that some (3% critical) viscous roll damping has been added in order to obtain realistic motions at the natural roll period. Agreement between the computed and measured motions is generally good. The theoretical model slightly underpredicts the natural roll period, pitch motions, and heave response at long wave periods.

Figure 9 shows mean drift forces and the turning moment in regular waves, and includes theoretical curves based on both the near and far-field methods. There is good agreement throughout.

Experiments were also performed in regular wave groups (two superimposed regular wave trains). Figure 10 shows two sets of experimental data corresponding to difference frequencies  $\delta\sigma\sqrt{L/g} = 0.26$  and 0.52. The mean frequency  $\sigma_c$  and wave height  $H$  were derived from the measured wave spectrum (see Standing et al, 1981). Measured values in wave groups are compared with the corresponding theoretical curve for regular waves (i.e.  $\delta\sigma = 0.0\text{Hz}$ ). Some differences were to be expected, due to variations in  $\delta\sigma$ , and also to uncertainties in measured values of  $\sigma_c$  and  $H$ .

Figure 11 shows mean forces in irregular random waves. The theore-

tical forces are consistently higher than measured values. It is not entirely clear why this is so, nor which of the two data sets is more reliable. There are, however, several possible indications.

a) The mean force (see equation 4.5) is particularly sensitive to variations in either the wave spectrum  $S(\sigma)$  at high frequencies, or in the transfer function  $F(\sigma, \sigma)$  at low frequencies. Numerical and experimental results are both likely to be inaccurate at these extremes.

b) Experimental results in very short regular waves had already been discarded because of wave generation and measurement difficulties. Reflections from the tank walls and model caused particular problems. The irregular wave spectra inevitably contained these troublesome short-wave components.

c) The theory assumes that the waves superpose linearly. Short waves in the tank were fairly steep, and may have become somewhat non-linear in their behaviour.

The results of this investigation nonetheless encourage confidence in using both types of second-order model to predict mean drift forces. Theory and experiment agree well over a wide range of practical wave frequencies and conditions.

## 5.2 Experimental Investigations into Low-Frequency Response

The drill-ship experiments were also intended to provide low-frequency surge, sway and yaw motions of the vessel, and thus to provide indirect validation of the predicted low-frequency wave forces. Tests in random irregular waves proved hard to interpret. Some clear conclusions, however, have been drawn from experiments in the much simpler regular wave group.

The wave group consists ideally of two superimposed regular wave trains with amplitudes  $a_1$ ,  $a_2$  and frequencies  $\sigma_1$ ,  $\sigma_2$ . A series of experiments were performed, keeping the difference frequency  $\delta\sigma = |\sigma_1 - \sigma_2|$  nominally constant, and varying the mean frequency  $\sigma_c = \frac{1}{2}(\sigma_1 + \sigma_2)$ . This series of experiments was repeated, once with  $\delta\sigma\sqrt{L/g} = 0.26$ , and then with  $\delta\sigma\sqrt{L/g} = 0.52$ . The natural frequencies of the ship in surge and sway lay very close to the first of these two values.

In order to make the model fairly realistic it was thought essential to allow the ship to respond freely at wave frequencies. Substantial low-frequency motions then occurred. It was not possible, therefore, to measure the low-frequency wave force directly, but was necessary to infer it from the vessel's response. The forcing and response are related by means of the ship's total (structural + added) mass, the stiffness of the moorings and the total amount of damping present. Of these the total mass was considered known with most certainty. Comparisons between theory and experiment are therefore made here at the higher of the two values of  $\delta\sigma$ , where the response equations are inertia dominated.

Figure 12, therefore, compares measured and predicted forces when  $\delta\sigma\sqrt{L/g} = 0.52$ . Experimental values were inferred from the measured surge and sway response motions. The solid curve represents the full quadratic transfer function, and the dotted curve represents the Newman/Pinkster approximation, based on mean forces. The experimental values show a slight preference for the full quadratic theory, particularly at

long wave periods (small values of  $\sigma_c$ ). This is in fact where differences between the two theories are most apparent, and where the set-down term becomes particularly important. The set-down component (term VI of equation 3.1 is only approximated in NMI's computer program, and this fact probably explains much of the observed discrepancy between theory and experiment at low values of  $\sigma_c$ . There is another possible source of error: small amounts of spurious high-frequency wave energy may have been present in the tank spectrum, due to reflection from the tank walls and model, wave breaking and non-linear wave interactions. As noted already, drift forces are particularly sensitive to short-wave components of the spectrum.

Bowers (1980b) performed similar experiments on an oscillating water column (OWC) wave energy device. These experiments confirmed the importance of set-down at long wave periods (see also section 5.4). Brendling (1982a) compared Bowers's results with predictions based on the NMIWAVE solution, and reached conclusions similar to those obtained above. Figure 15, for example, shows that theory and experiment agree fairly well at short wave periods, but, as before, theory tends to underpredict the forcing at long wave periods. Errors due to approximating the set-down term may become important in these latter conditions. Note that in figure 15  $L$  is the width of the device, and is 35.5m.

### 5.3 Approximate Procedures

Section 4 outlined two approximate procedures, due to Newman/Pinkster and Bowers, for estimating the low-frequency drift force. Likely ranges of validity were discussed, using simple order-of-magnitude expressions to represent the effects of wave diffraction, spatial gradients and set-down. More precise numerical comparisons will now be made, using results from the NMIWAVE analysis of the moored drill-ship. The results generally bear out the earlier conclusions, though with certain important modifications to account for vessel response.

Figure 13 shows longitudinal and transverse force transfer functions for the moored drill-ship. The quadratic transfer function varies with both the mean wave frequency  $\sigma_c$  and with the difference frequency  $\delta\sigma$ . The earlier figure 12 showed all six components (terms I-VI) of the force combined. Figure 13 now shows separate first-order product (terms I-V) and second-order wave (term VI) components. Terms I-V are calculated exactly, within the limits of numerical accuracy, whereas term VI is only approximated. In the Newman/Pinkster method the full transfer function is replaced by that corresponding to  $\delta\sigma = 0.0$ .

Figure 14 converts these transfer functions into second-order force spectra by means of equation 4.4. Only the surge component is shown. Figure 14 shows results from both approximate methods, as well as the more complete numerical result, in two different sea states:

- (i) an idealised Jonswap narrow-band wave spectrum with significant height  $H_s = 3.42\text{m}$  and mean zero-crossing period  $T_z = 6.14\text{ sec}$ ,
- (ii) a broader-band spectrum, based on the Pierson-Moskowitz formula, but actually as measured in the wave tank, with  $H_s = 3.92\text{m}$  and  $T_z = 7.53\text{ sec}$ .

A number of conclusions have been drawn, as follows:

a) The Newman/Pinkster Method

Confirming earlier conclusions, the Newman/Pinkster approach is more satisfactory for predicting the transverse (sway) component of the force than for the longitudinal (surge) component. The sway force is, however, less well predicted than earlier order-of-magnitude parameters would indicate, and the surge force slightly better predicted. There are two principal reasons, both associated with vessel response, the effects of which are difficult to represent in terms of simple parameters.

Firstly, and as noted earlier, heave, sway and roll motions of the vessel tend to reduce the amount of wave energy reflected in the transverse direction, and thus reduce the mean sway force. Terms excluded from the Newman/Pinkster theory then become relatively more important, and its range of validity is reduced. This method is nonetheless quite satisfactory for predicting sway motions of the drill-ship, the natural frequency of which was around 0.012Hz.

Secondly, terms III and IV, which are both associated with vessel response and make only small contributions to the mean force, make increasingly important contributions to the quadratic force function as  $\delta\sigma$  grows. They tend to cancel other components of the surge force, so that the set-down term VI is relatively more important than the earlier order-of-magnitude parameters suggest.

Figure 14 shows that the Newman/Pinkster method works rather better in the broad-banded Pierson-Moskowitz sea state than in the narrow-band Jonswap spectrum, because the former spectrum contains more short-wave energy. Ranges of validity in these two spectra go up to frequencies of about 0.05 and 0.03Hz respectively. In this example the natural surge frequency of the vessel was around 0.013Hz.

b) The Bowers Method

This approach fails completely at low frequencies, and is therefore inappropriate for predicting mean forces, or for vessels with very elastic moorings. It works fairly well at frequencies above about 0.03Hz in the Jonswap sea state, but seriously overpredicts forces in the same range of the broader-banded Pierson-Moskowitz spectrum. The Bowers method was also found to overpredict forces in a Jonswap spectrum with a longer mean wave period, because it makes no allowance for the vessel's first-order response. The waterline integral (term I), in particular, is calculated using the absolute surface elevation instead of the relative elevation  $\zeta_r$ .

This formula therefore has a restricted range of validity. It is only appropriate for slender ships in surge at fairly stiff moorings. The sea spectrum should be narrow-banded, with waves long enough to remain undiffracted, yet short enough to cause little first-order response.

c) The Set-Down Contribution

There are important differences between both approximate solutions and the full numerical result over certain frequency ranges. In such conditions the full solution is to be preferred, but even here the second-order wave (set-down) contribution is approximated. This contribution is important at long wave periods and short resonance periods,

and may therefore be particularly significant for small stiffly-moored ships in long waves, for tubular structures, or those with much of their volume well-submerged. Important modifying effects of vessel response can, in fact, make the set-down term rather more significant than the earlier simple parameters (section 4) suggest. In such circumstances there will be a considerable degree of uncertainty in computer predictions. Great care also needs to be taken (see section 5.4) if the set-down wave is to be represented correctly in experiments.

Brendling (1982a, 1982b) reached similar conclusions in studies on the OWC wave energy device and on a floating storage platform.

#### 5.4 Further Implications for Experimental or Numerical Modelling

Dacunha et al (1981) drew attention to the need for very long sequences of waves when modelling the effects of wave drift forces and low-frequency response. They examined variations in the mean square response arising through the use of a discrete wave spectral model. They represented the wave spectrum as a series of lines at regularly-spaced frequency intervals. As noted earlier, the spacing between the lines of the second-order force spectrum is the same as that of the original wave spectrum. These lines must be sufficiently close together to define the low-frequency response peak, the width of which is roughly proportional to  $\beta f_0$ , where  $\beta$  is the system's damping ratio and  $f_0$  its natural frequency. Both  $\beta$  and  $f_0$  are typically small for a moored ship in surge, and the spectrum has to be resolved very finely.

Figure 16 shows how the root mean square surge response of a typical model of a moored ship varies with the frequency spacing  $\delta f$ . Estimates vary widely, both above and below the limiting value as  $\delta f \rightarrow 0$ . Dacunha's preliminary study suggests that the frequency spacing should be at most  $\beta f_0$  (or  $0.2f$  if  $\beta > 0.2$ ). This means that there should be more than  $1/\beta$  (or 5) resonant cycles during each test sequence. During that sequence the waves should be random or pseudo-random.

Dacunha's investigation assumed that the phase angle of each wave component was random, and averaged over all possible choices of phase angle. This averaging process greatly simplified the analysis, but removed one possible source of variability. Bowers (1982) avoided this assumption. He measured the surge motions of a moored vessel experimentally, and found that at least 40 resonant cycles were needed in order to obtain a stable rms response. This criterion is comparable with Dacunha's, if it is assumed that the damping ratio  $\beta \approx 0.025$ .

These criteria have to be satisfied regardless of the relative sizes of the second-order wave and first-order-product contributions to the drift force. Further criteria must be satisfied if the second-order wave term is significant. As already noted, there are serious difficulties in computing this term accurately. There are also serious experimental difficulties in modelling the set-down correctly in a wave tank. Bowers (1980a, 1980b) has shown that a long-period free wave may have to be superimposed, in order to remove a spurious component associated with the wave-making process. Bowers (1980b) has shown that this spurious component is significant in precisely the same conditions in which Brendling (1982a) found the theoretical set-down

contribution to be important.

## 6. CONCLUSIONS

(i) Wave diffraction and viscous drag both play important roles in the drift force process. When diffraction effects dominate, mean second-order forces may be calculated directly from first-order wave diffraction theory, using either the so-called 'near-field' or the 'far-field' approach. The theory makes ideal flow assumptions.

(ii) Theoretical predictions of mean forces on a moored drill-ship agreed very well with experimental values, particularly in regular waves and wave groups. Agreement in random irregular seas was slightly less good; several possible reasons are put forward.

(iii) In an irregular sea the drift force has a low-frequency component associated with wave grouping. Force variations depend partly on local changes in quantities which are associated with wave diffraction, and therefore with the mean force. They also depend on spatial gradients, present in both first and second-order wave fields. These three sources of variation (diffraction, spatial gradients associated with first and second-order wave fields) have been characterised by three simple parameters. Order-of-magnitude comparisons between these parameters help to clarify the underlying physical processes. They also suggest when the full NMIWAVE solution may be needed, and when two approximate procedures due to Newman/Pinkster and Bowers might be used.

(iv) These parameters suggest that diffraction effects will tend to dominate when the waves are short in relation to vessel dimensions, and when the natural period of the system is very long. The force associated with diffraction falls off very rapidly as the wavelength increases, and the relative importance of the various terms may be very sensitive to slight variations in wave spectral content. Gradient-type effects become more significant as the wavelength increases, and as the system's natural response period decreases. The second-order wave has a gradient-type effect, and becomes particularly significant if the vessel is deep-drafted.

(v) The low-frequency component of the second-order force can be expressed in terms of a quadratic transfer function relating pairs of frequencies in the underlying wave spectrum. This transfer function may be calculated by the 'near-field' method. Contributions are of two distinct types: terms representing products of first-order quantities, and a term associated with the second-order set-down wave. Components of the first type may be calculated directly from linear wave diffraction theory. The NMIWAVE computer program has been extended for this purpose. It approximates the second-order wave term.

(vi) Experiments on a moored drill-ship in regular wave groups gave confidence in this technique. Experiment and theory agreed well in short-period waves, but relative errors increased in longer waves, as the set-down component became more significant.

(vii) Numerical comparisons were made between the full NMIWAVE solution, the Newman/Pinkster and Bowers approximate methods. The

Newman/Pinkster approach works fairly well in diffraction-dominated conditions (see conclusion (iv) above), and predicted both sway and surge forces on the moored drill-ship quite well. Bowers's method has a restricted range of validity, but may be useful for simple estimates of the surge response of slender ships, provided that the ship's natural surge period is fairly short, and provided the wave spectrum covers a certain narrow band of frequencies. In other circumstances a full numerical solution, based on expressions for the quadratic force function, is to be preferred.

(viii) These comparisons also demonstrate important modifying effects of first-order vessel response. Caution must therefore be exercised when applying the simple parameters discussed above: they do not provide precise criteria, because they take no account of vessel response.

(ix) The set-down contribution may be more significant than these simple parameters suggest, because of cancellation between other components, associated with the vessel's first-order response.

(x) Accurate estimates of rms low-frequency response can only be obtained, either from experiment or numerical simulation, if the wave sequence is random or pseudo-random and extends over many (perhaps 40) natural response cycles. If set-down is important, care must also be taken in experiments to ensure that the second-order wave is correctly represented.

#### ACKNOWLEDGEMENTS

This work was supported by the UK Department of Energy, through both the Offshore Energy Technology Board and the Wave Energy Steering Committee, as part of an overall programme of research into fluid loading of offshore structures. The authors also wish to thank their many colleagues at NMI who assisted with the experiments, with analysing the results and with running computer programs. Thanks are also due to U H Pinto who developed a substantial part of the far-field computer program.

#### SELECTED NOTATION LIST

$A$	waterplane area
$a_n$	amplitude of wave component $n$
$B$	vessel's breadth
$C_d, C_m$	drag and inertia coefficients
$D$	typical member diameter
$d$	water depth
$F_{mn}$	quadratic transfer function for amplitude of low-frequency force
$\bar{F}_x, \bar{F}_y$	mean force components in $x, y$ directions
$ F_x(2) ,  F_y(2) $	amplitudes of low-frequency force in $x$ and $y$ directions
$f_j(\xi)$	source density
$G(\underline{x}, \underline{\xi})$	source influence function
$g$	acceleration due to gravity
$H$	wave height
$h$	vessel's draft
$i$	$= \sqrt{-1}$



$k$	wave number
$k_c$	wave number associated with frequency $\sigma_c$
$L$	vessel's length
$S_o$	vessel's underwater surface in still water
$S(\sigma)$	wave spectral density function
$T$	wave period
$T_{mn}$	quadratic transfer function for low-frequency force
$t$	time
$U$	fluid velocity
$x, y, z$	Cartesian coordinates (figure 4)
$\alpha_{mn}$	phase angle of force relative to wave envelope
$\beta$	damping ratio
$\gamma_n$	phase of wave component $n$
$\delta$	fluid particle orbit diameter
$\delta_{mn}$	force phase angle
$\delta\sigma$	difference frequency $ \sigma_1 - \sigma_2 $
$\varepsilon$	wave steepness parameter
$\varepsilon_n$	phase angle of wave component
$\phi, \phi$	velocity potential
$\eta_j$	response of structure in mode $j$
$ \eta(2) $	amplitude of low-frequency response
$\lambda$	wavelength
$\rho$	water density
$\sigma$	angular frequency of wave component $n$
$\sigma_c$	mean wave frequency $\frac{1}{2}(\sigma_1 + \sigma_2)$
$\zeta$	surface elevation
$\zeta_r$	surface elevation relative to vessel

## REFERENCES

- Brendling W J (1982a). Drift forces on wave energy devices: a comparison of theory and experiment, Nat. Marit. Inst. Rep. R141.
- Brendling W J (1982b). A comparison of two methods for calculating drift forces, Nat. Marit. Inst. Rep. R137.
- Bowers E C (1976). Long-period oscillations of moored ships subject to short-wave seas, Trans. R. Inst. Nav. Archit., London, 118, 181.
- Bowers E C (1980a). Long-period disturbances due to wave groups, Proc. 17th. Int. Conf. Coastal Eng., Sydney.
- Bowers E C (1980b). Second order wave forces on wave power devices, Hydraul. Res. St. Rep. Ex 958.
- Bowers E C and R G Standing (1982). Environmental loading and response. Proc. Conf. Offshore Moorings, Inst. Civ. Eng., London.
- Dacunha N M C, N Hogben and R G Standing (1981). Responses to slowly varying drift forces and their sensitivity to wave spectral modelling: a preliminary assessment, Nat. Marit. Inst. Rep. R101.

- Dand I W (1981). Model studies of freely-drifting and towed disabled tankers, Proc. Symp. Behaviour Disabled Large Tankers, Roy. Inst. Nav. Archit., London.
- Faltinsen O M and F C Michelsen (1974). Motions of large structures in waves at zero Froude number, Proc. Symp. Dyn. Mar. Vehicles Struct. in Waves, Inst. Mech. Eng., London.
- Faltinsen O M and A E Løken (1978). Drift forces and slowly-varying forces on ships and offshore structures in waves, Norw. Marit. Res., 6 (1), 2.
- Garrison C J (1979). The consistent second-order theory of wave/structure interaction, Nav. Postgrad. Sch. Monterey, Rep. NPS-69-79-010.
- Havelock T H (1940). The pressure of water waves on a fixed obstacle, Proc. R. Soc., London, A175, 409.
- Havelock T H (1942). The drifting of a ship among waves, Philos. Mag., 33, 467.
- Hsu F H and K A Blenkarn (1970). Analysis of peak mooring force caused by slow vessel drift oscillation in random seas, Offshore Technol. Conf. paper OTC 1159, Houston.
- Huse E (1977). Wave induced mean force on platforms in direction opposite to wave propagation, Norw. Marit. Res., 5(1), 2.
- Isaacson M de St Q (1981). Steep wave effects on large offshore structures, Offshore Technol. Conf. paper OTC 3955, Houston.
- John F (1950). On the motion of floating bodies, parts I and II, Commun. Pure Appl. Math., 2, 13 and 3, 45.
- Karpinnen T (1979). An approach to computing the second order steady forces on semisubmerged structures, Helsinki Univ. of Technol., Ship Hydrodyn. Lab. Rep. 16.
- Kim C H and F Chou (1973). Prediction of drifting force and moment on an ocean platform floating in oblique waves, Int. Shipbuild. Progr., 20 (230), 388.
- Lean G H (1971). Subharmonic motions of moored ships subjected to wave action, Trans. R. Inst. Nav. Archit., London, 113, 387.
- Lighthill M J (1979). Waves and wave loading, Proc. 2nd. Conf. Behaviour Offshore Struct. (BOSS '79), London, 1, 1.
- Longuet-Higgins M S (1977). The mean forces exerted by waves on floating or submerged bodies, with applications to sand bars and wave power machines, Proc. R. Soc., London, A352, 463.
- Maruo H (1960). The drift of a body floating in waves, J Ship Res., 4 (3), 1.
- Morison J R, M P O'Brien, J W Johnson and S A Schaaf (1950). The force excited by surface waves on piles, Pet. Trans., AIME., 189, 149.

- Naess A and R Børresen (1978). On experimental prediction of low-frequency oscillations of moored structures, Offshore Technol. Conf. paper OTC 2879, Houston.
- Newman J N (1967). The drift force and moment on ships in waves, J Ship Res., 4 (3), 1.
- Newman J N (1974). Second-order slowly-varying forces on vessels in irregular waves, Proc. Symp. Dyn. Mar. Vehicles Struct. in Waves, Inst. Mech. Eng., London, 182.
- Oortmerssen G van (1971). The interaction between a vertical circular cylinder and regular waves, Symp. Offshore Hydrodyn., Wageningen, NSMB publ. 375, chap. XI.
- Oortmerssen G van (1979). Non-linear dynamic mooring problems, NSMB, Wageningen, publ. 617.
- Pijfers J G L and A W Brink (1977). Calculated drift force of two semisubmersible platform types in regular and irregular waves, Offshore Technol. Conf. paper OTC 2977, Houston.
- Pinkster J A (1974). Low frequency phenomena associated with vessels moored at sea, Soc. Pet. Eng., AIME, paper SPE 4837.
- Pinkster J A (1980). Low frequency second order wave exciting forces on floating structures, NSMB, Wageningen, Rep. 650.
- Pinkster J A and G van Oortmerssen (1976). Computation of the first and second order wave forces on bodies oscillating in regular waves, Proc. 2nd Conf. Numer. Ship Hydrodyn., Berkeley, 136.
- Rainey R C T (1978). The dynamics of tethered platforms, Trans. R. Inst. Nav. Archit, London, 120.
- Rye H, S Rynning and H Moshagen (1975). On the slow drift oscillations of moored structures, Offshore Technol. Conf. paper OTC 2366, Houston.
- Salvesen N (1974). Second-order steady-state forces and moments on surface ships in oblique regular waves, Proc. Symp. Dyn. Mar. Vehicles Struct. in Waves, Inst. Mech. Eng., London.
- Sørheim H R (1981). Analysis of motion in single-point mooring systems, Norw. Marit. Res., 9(1), 2.
- Stammers A J, R Brockbank and C J Wennink (1977). Investigation of vessel mooring subject to wave action, Dock and Harbour Auth., 57 (677), 429.
- Standing R G (1979). Use of wave diffraction theory with Morison's equation to compute wave loads and motions of offshore structures, Nat. Marit. Inst. Rep. R74.
- Standing R G, N M C Dacunha and R B Matten (1981). Mean wave drift forces: theory and experiment, Nat. Marit. Inst. Rep. R124.

Standing R G, N M C Dacunha and R B Matten (1982). Slowly-varying  
second-order wave forces: theory and experiment  
Nat. Marit. Inst. Rep. 138.

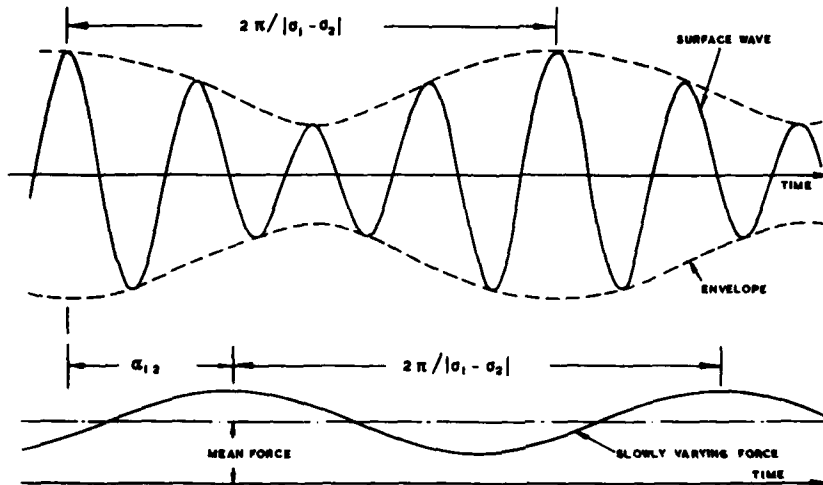


Figure 1. Surface wave elevation and second-order drift force in a regular wave group with component frequencies  $\sigma_1, \sigma_2$ .

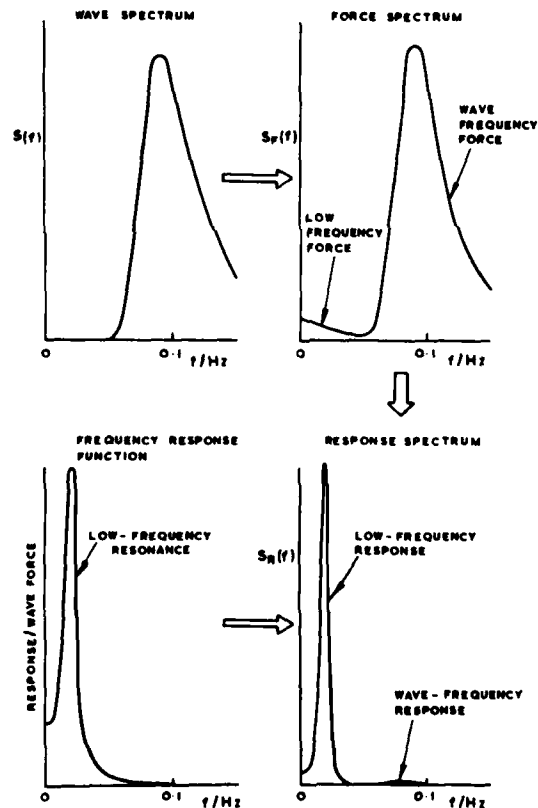


Figure 2. Relationships between the wave, forcing and response spectra for a typical moored structure.

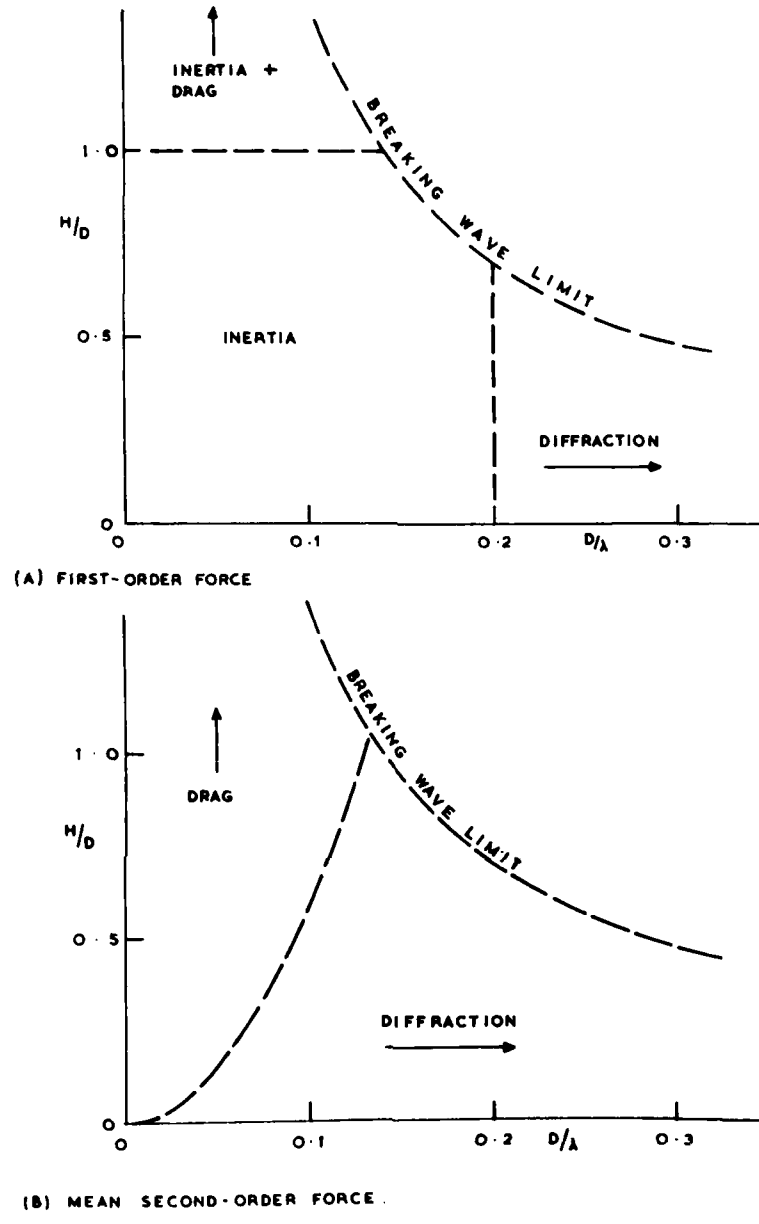


Figure 3.

Approximate force regimes: fixed vertical column in regular waves.

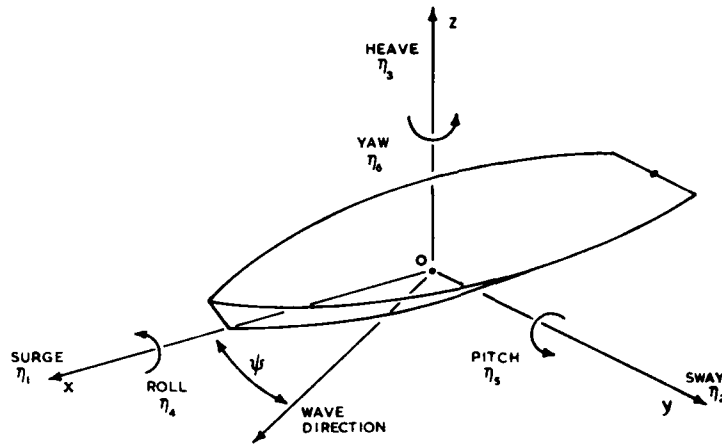


Figure 4. Coordinates and sign convention.

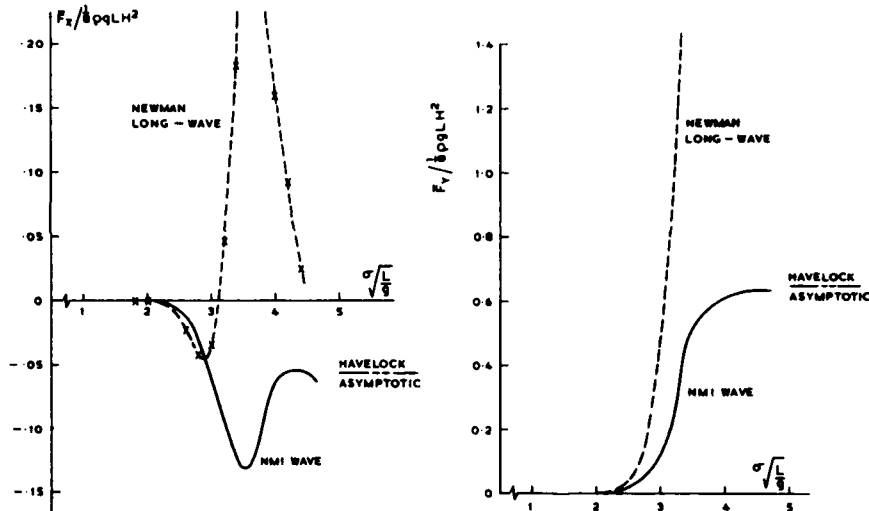


Figure 5. Mean wave drift forces on a drill-ship : comparison between theoretical models.

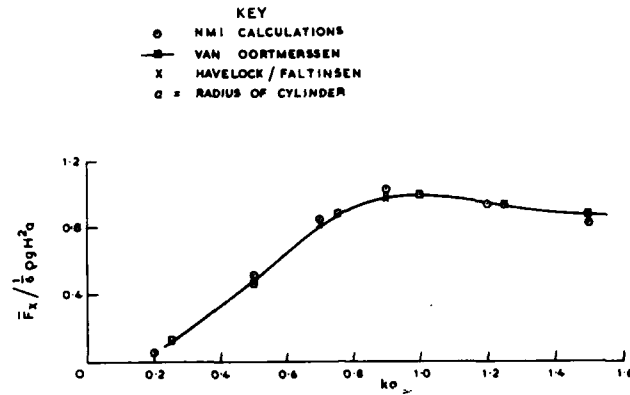


Figure 6. Mean horizontal wave force on a vertical circular cylinder : comparison between analytic and numerical results.

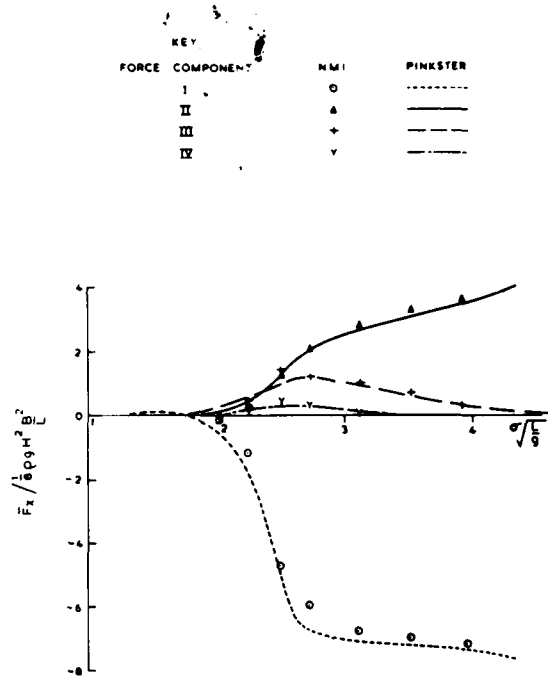


Figure 7. Components of the mean longitudinal force on a barge in regular head seas.



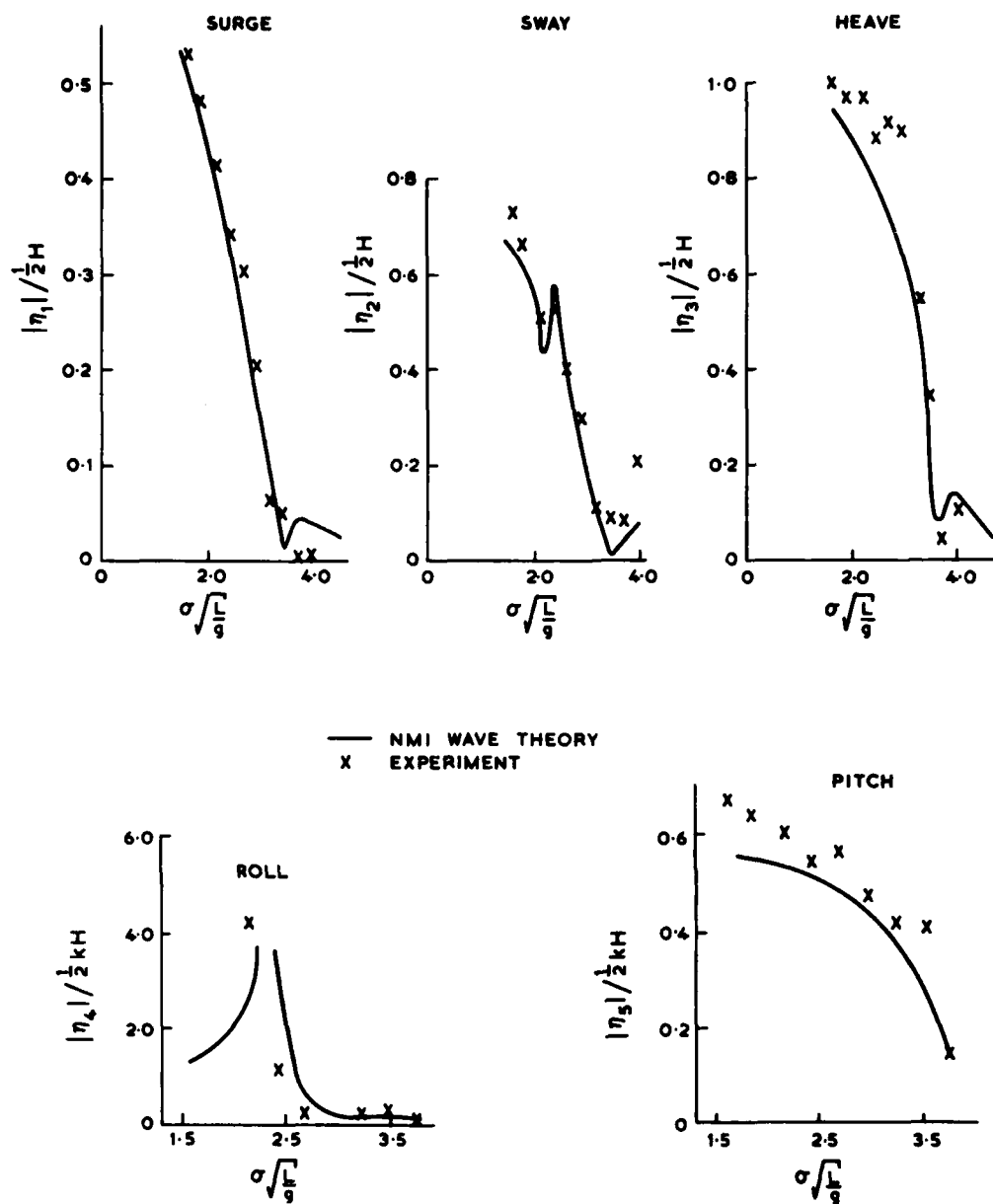


Figure 8. First-order motion amplitudes for a drill-ship in regular waves, heading 126°. Comparison between theory and experiment.

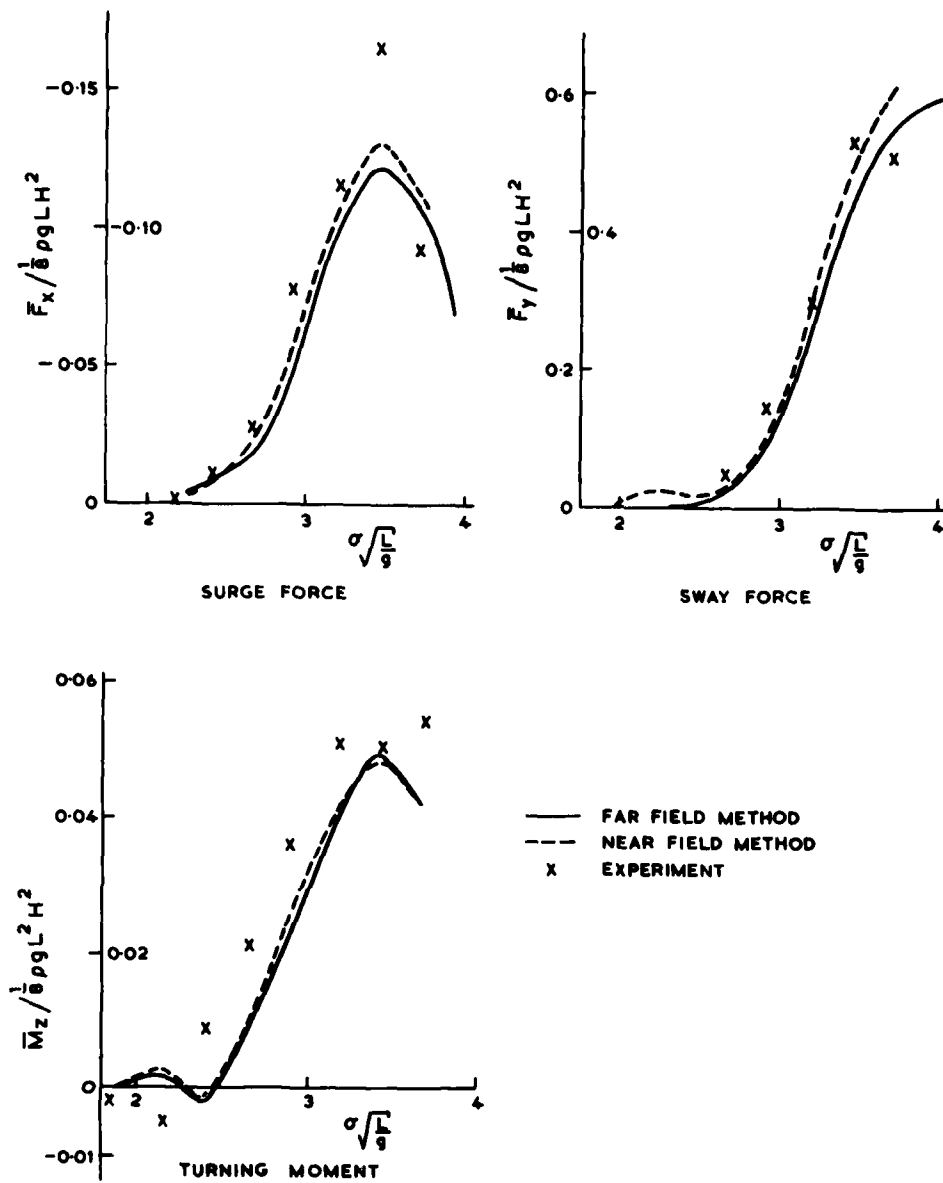


Figure 9. Mean wave forces on a drill-ship in regular waves, heading 126°. Comparison between theory and experiment.

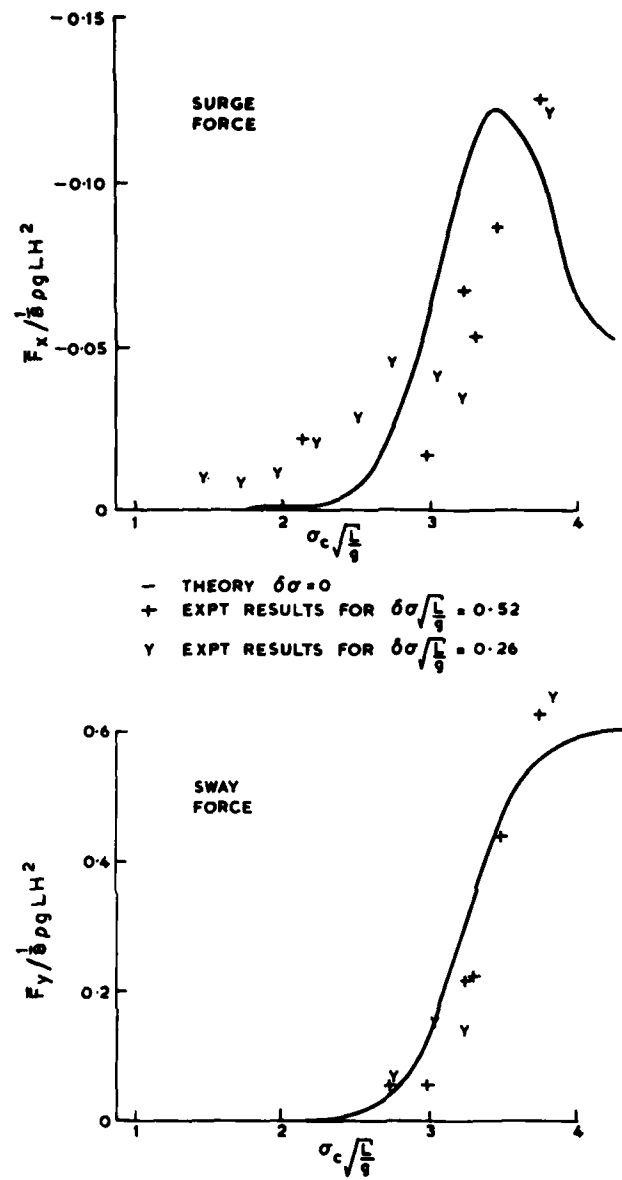


Figure 10. Mean wave forces on a drill-ship in regular wave groups, heading  $126^\circ$ . Comparison between theory and experiment.

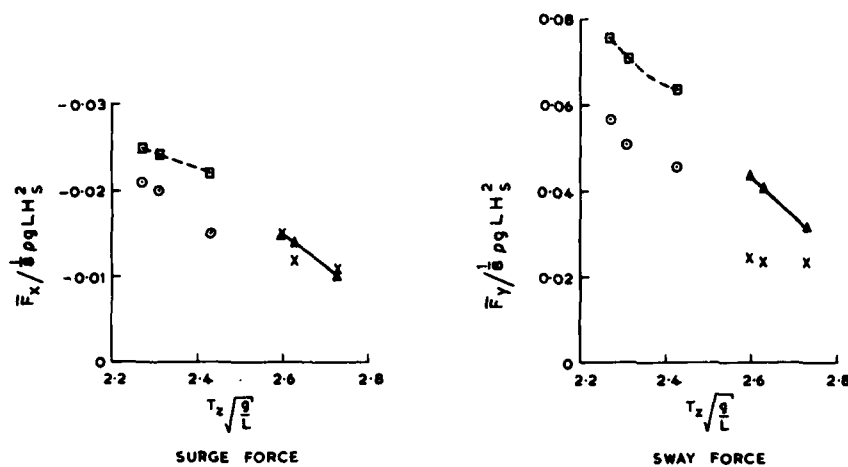


Figure 11. Mean wave forces on a drill-ship in random irregular waves, heading  $126^\circ$ . Comparison between theory and experiment.

- Theory, Pierson-Moskowitz spectrum;  
 —△— theory, Jonswap spectrum;  
 ○ experiment, Pierson-Moskowitz spectrum;  
 × experiment, Jonswap spectrum.

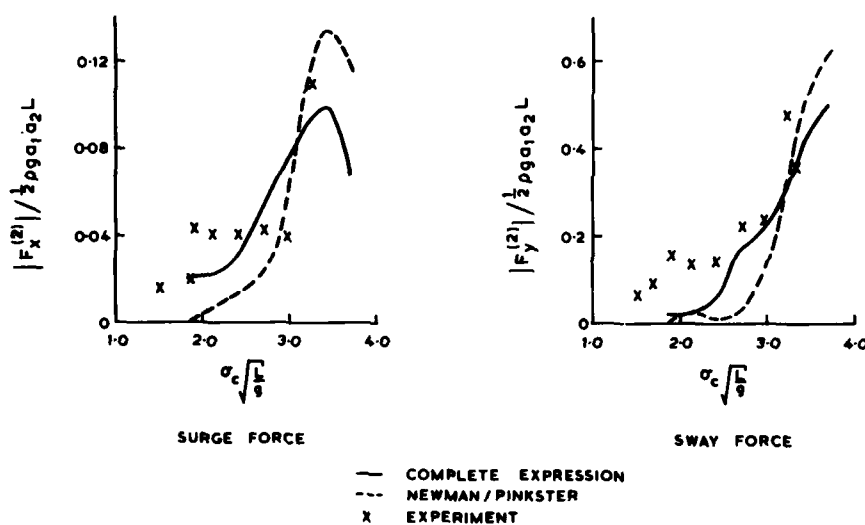


Figure 12. Low-frequency wave forces on a drill-ship in regular wave groups, heading  $126^\circ$ . Comparison between theory and experiment: quadratic transfer functions for force amplitudes when  $\delta\sigma\sqrt{L/g} = 0.52$ .

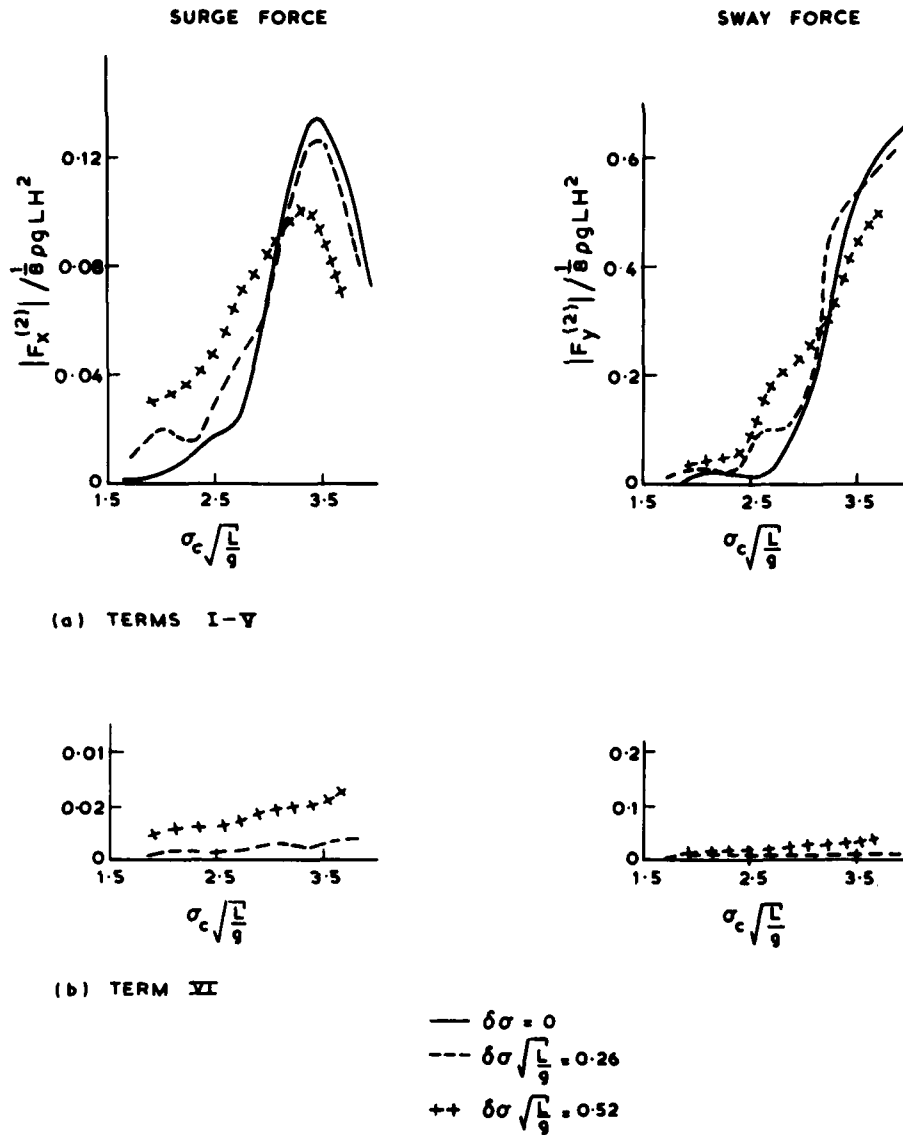


Figure 13. Low-frequency wave forces on a drill ship in regular wave groups, heading  $126^\circ$ . Quadratic transfer functions for force amplitudes. Components I - V and VI are shown separately.

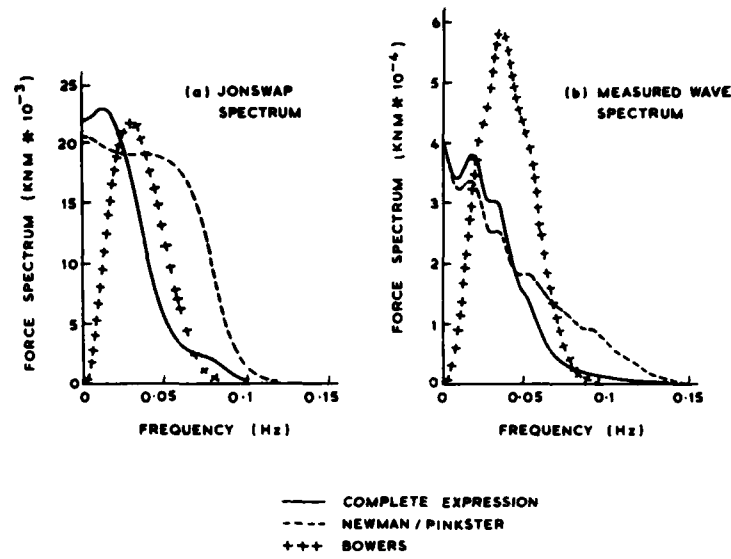


Figure 14. Low-frequency force spectra for a drill-ship in random irregular waves, heading  $126^\circ$ . Comparison between different prediction methods.

- a) Jonswap spectrum,  $H_S = 3.42\text{m}$ ,  $T_Z = 6.14\text{s}$ ;  
 b) measured wave spectrum,  $H_S = 3.92\text{m}$ ,  $T_Z = 7.53\text{s}$ .

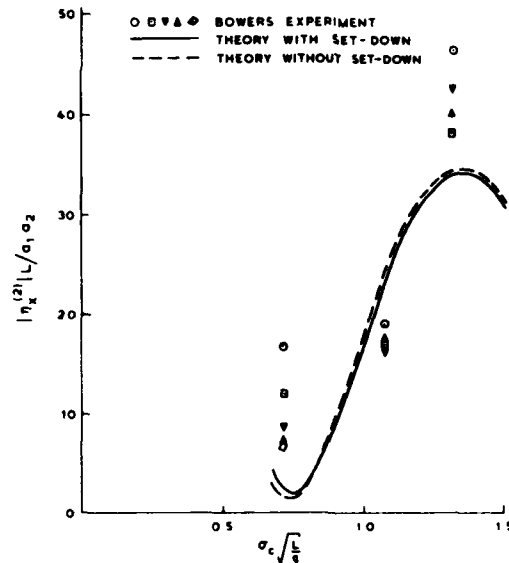


Figure 15. Low-frequency surge response of an oscillating water column wave-energy device. Quadratic transfer function when  $\delta\sigma\sqrt{L/g} = 0.23$ : comparison between theory and experiment.

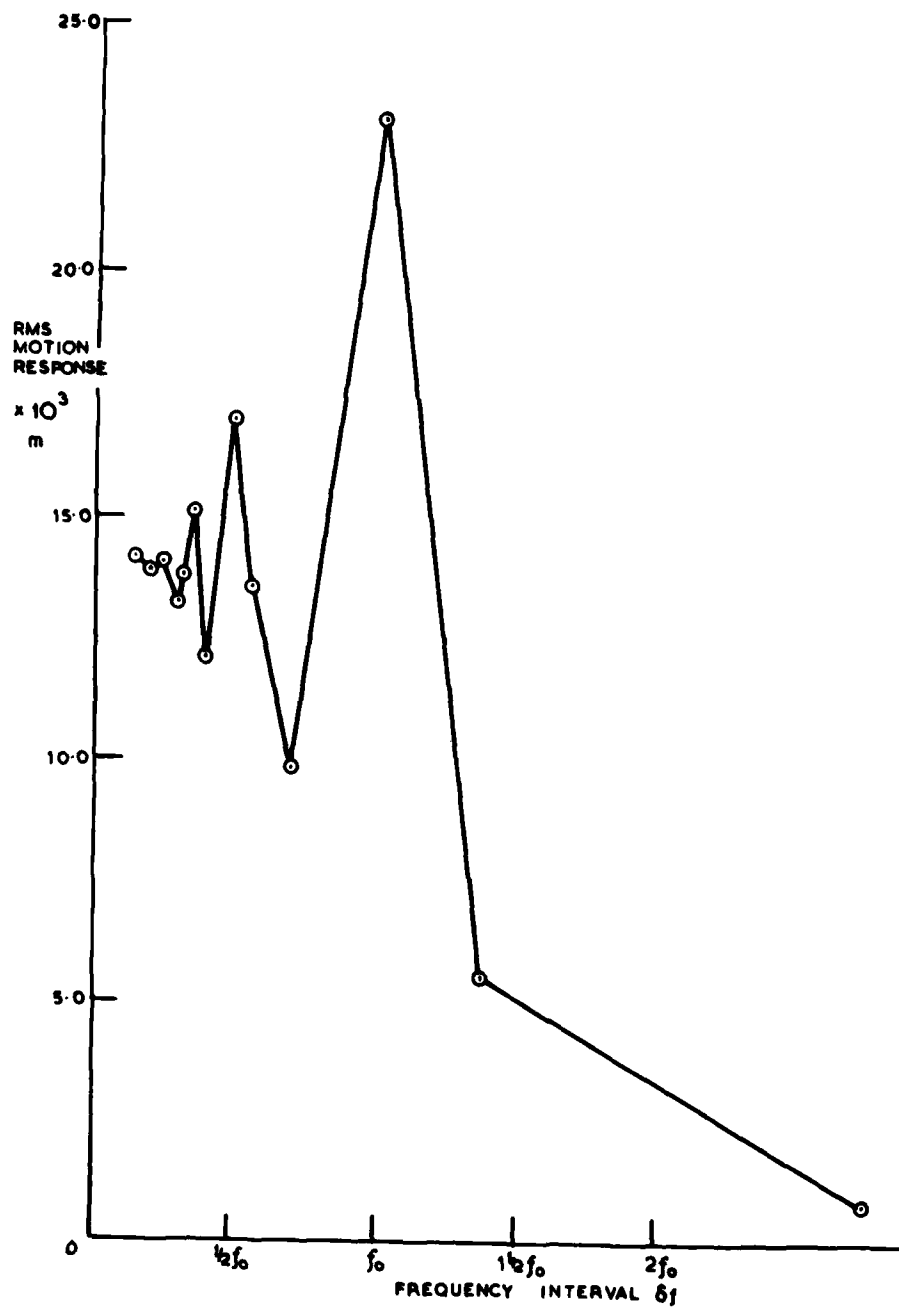


Figure 16. Root mean square surge response of a moored ship : variation with spectral line spacing  $\delta f$ .

## Discussion

A. Papanikolaou (Tech. University of Berlin)

In your paper you are claiming that the presented NMI wave solution includes the full quadratic transfer function, e.g., synopsis. Indeed, you are considering only a part of the full second-order transfer function, especially the part referring to the slowly varying and mean drifting forces in irregular response to regular waves. In the calculation of the slowly varying forces you need some information about the second-order potential, which takes into account the second-order hydrodynamics, e.g., second-order forced motions and couplings, second-order diffraction. I failed to discover what kind of second-order potential you included in your calculation or what the difference is to the approximate method of Pinkster (1980).

## Author's Reply

R.G. Standing (National Maritime Institute)

To A. Papanikolaou

Dr. Papanikolaou has misunderstood our use of the word "full." We have, in fact, included all six terms of Equation 3.1, unlike some other investigators, and, therefore, represent the full theoretical expression. The sixth term is difficult to calculate exactly, however, and we have adopted an approximate "Froude-Krylov" approach, as indicated in Section 4.2. Our approach does not pretend to accuracy, but simply indicates whether the set-down contribution is important, and the likely reliability of our calculations.

Differences between our own and Pinkster's approaches are noted in Section 4.2. Pinkster takes some account of the body's disturbance on the second-order potential by treating the set-down as a quasi-free wave and then solving a conventional diffraction problem. In order to do this he has to adjust  $g$ , the acceleration due to gravity, so as to obtain the correct "dispersion" relationship for set-down. The accuracy of this approach is unclear.



# Experimental Study on Second-Order Forces Acting on Cylindrical Body in Waves

Yusaku Kyojuka

National Defense Academy, Japan

## ABSTRACT

The second-order forces acting on a cylindrical body which oscillates with an arbitrary frequency at a free surface of infinitely deep water are calculated on the basis of the perturbation theory.

The first and second-order boundary value problems are solved by the Boundary Element Method (BEM) which includes both boundaries of the body and the free surfaces. The pressure distribution including the quadratic terms of the Bernoulli equation is evaluated from the solution. The hydrodynamic forces acting on the body are obtained by the integration along the instantaneous wetted contour of the body. Finally, motions of the body in waves are determined by the solution of the equation of the motion up to the second order.

Experiments are carried out for the radiation problems of the heaving and swaying oscillations, and the diffraction problems for a fixed body and a free floating body in steep regular waves.

Those results are discussed in comparison with the numerical calculations.

## NOMENCLATURE

$A$	area of cylinder cross section
$a_i, (i=1,2,3)$	amplitude of forced oscillation in $i$ -mode
$a_w$	wave amplitude
$B=2b$	waterline beam
$a, b, c^{(n)}$ $d^{(n)}, f^{(n)}, h^{(n)}$	body boundary condition, eq.(17)
$C_v$	viscous damping coef. in roll, eq.(75)
$C(t)=C_0+\Delta C(t)$	wetted body contour at time $t$
$C_0$	wetted body contour in a position of equilibrium
$\Delta C(t)$	wetted surface change at time $t$

$Df = -{}_0F_1^{(2)}$	drifting force in sway, eq.(40)
$F_{ij}^{(1)}$	first-order force of j-mode caused by i-mode
${}_kF_{ij}^{(2)}, (k=0,2)$	second-order force of j-mode caused by i-mode oscil. k denotes frequency parameter, eq.(27)
${}_2F_j^{(2)}(i), (i=1,5)$	each component of second order force, eq.(33)
${}_2F_j^{(2)}(i), (i=m,b,f)$	each force due to second-order potential, eq.(59)
$f_{ij}^{(1)}, {}_0f_j^{(2)}, {}_2f_j^{(2)}(i)$	non-dimensional expression for $F_{ij}^{(1)}$ and ${}_kF_j^{(2)}$ , eqs.(70),(71)
$\overline{GM}$	metacentric height from center of gravity
$g$	acceleration of gravity
$H_j^{\pm}(K)$	Kochin function of j-mode, eq.(51)
${}_2h^{(2)}$	second-order body boundary condition due to motions of bi-harmonics, eq.(60)
$h_{ij}^{(2)}$	second-order body boundary condition due to quadra- tic terms of first order motions, eq.(60)
$H_m = {}_0F_3^{(2)}$	steady heeling moment, eq.(42)
$I = M r_G^2$	mass moment of inertia with respect to $\bar{o}$ , eq.(39)
$I_w$	moment of inertia of the waterline, eq.(32)
$K$	wave number
$k$	spring constant of a mooring coil, eq.(41)
$M$	mass of a body per unit length
$\underline{n}$	unit normal vector, positive into the fluid
$\overline{OM}$	metacentric height from coordinate origin
$\underline{o-xy}$	inertial right-handed Cartesian coordinate system
$\overline{o-xy}$	body fixed right-handed Cartesian coordinate system
$p^{(1)}$	first-order hydrodynamic pressure, eqs.(3),(27)
${}_kp^{(2)}$	second-order pressure of frequency parameter k, eqs. (27),(28)
$Q(x)$	second-order inhomogeneous condition on the free surface, eq.(26)
$q(x)$	normalized expression for $Q(x)$ , eq.(60)
$r^{\pm}(t)$	relative wave elevation at time t, eq.(32)
$r_G$	radius of gyration, eq.(39)
$Sf = {}_0F_2^{(2)}$	sinkage force, eq.(42)
$V_n$	normal velocity on body surface, eq.(7)
$x_j^{(n)}$	body motion of j-mode of order n, eq.(13)

$x', y'$	tangential derivative on body, eq.(16)
$(x_G, y_G)$	center of gravity of the body
$(x_B, y_B)$	center of buoyancy of the body
$\varepsilon$	perturbation parameter, $\varepsilon = a_w/b$ or $\varepsilon = a_j/b$
$\rho$	fluid density or radius of curvature of body contour eq.(18)
$\omega$	circular frequency of incident wave and first-order motions
$\lambda$	wave length, eq.(23)
$\eta^{(n)}$	free surface elevation of order n, eq.(10)
$\eta_0^{(n)}$	free surface elevation of incident wave, eq.(24)
$\delta_{ij}^{(n)}, \delta_j^{(n)}$	phase lag between force and incident wave, eqs.(70),(71)
$\alpha_j$	phase lag between motion and incident wave, eqs.(70),(71)
$\phi^{(n)}$	velocity potential of order n, eq.(9)
$\varphi_j^{(1)}, \phi_j^{(1)}$	first order complex potential of j-mode, eqs.(45), (46)
$\varphi_k^{(2)}, (k=m, b, f)$	second-order potential split into each component, eq.(58)
$\phi_S$	source potential placed at the coordinate origin
$\phi_D$	doublet potential placed at the coordinate origin
$\phi_N$	wave free potential, eq.(52)
$\phi_j^R$	radiation potential of unit velocity of j-mode oscillation

## 1. INTRODUCTION

In the field of seakeeping quality of ships in waves, many remarkable achievements have been made on the prediction of the hydrodynamic forces and the ship motions in the past decade. It is evident that the huge and fast computer enables us to calculate the exact hydrodynamic characteristics on the basis of the wave theory. Nowadays, Strip method has become a standard tool and the pure three dimensional calculation has been attempted in the linearized theory.

On the other side, many researchers have attempted to the nonlinear problems. The nonlinear forces are generally thought to be very small compared with the linear forces in this field, and are usually neglected. However, they sometimes play a primary role in the problems such as the drifting force, the slowly drifting oscillation or unstable swaying oscillation of the moored body, the parametric oscillation in

roll and the springing vibration of the ship.

Maruo[1] introduced the well-known formula of the drifting force which enable us to calculate it by the reflected wave amplitude of the linear solution. Ogilvie[2] obtained the hydrodynamic forces on a submerged circular cylinder by the perturbation theory and showed interesting results on the steady forces. However, those steady forces are only a part of the complete second order forces.

Lee[3] and Parisis[4] showed independently the complete solutions of the second order forces on a cylindrical body heaving at the free surface, Lee by the method of multi-pole expansions, Parisis by the method of integral equations. Their formulation seems to have provided the fundamentals of the investigation thereafter.

Potash[5] extended the problem to sway, heave, roll and their coupling oscillations and to arbitrary section of a cylinder by the method of integral equations. Söding[6] showed the formulation for all problems including the diffractions and showed that the second order forces can be obtained by the integration of the functions of the first order potential on both boundaries of the body and the free surfaces. Masumoto[7] extended Lee's method and Papanikolaou[8,9] did Potash's method to all the problems. Kyojuka[10,11] applied the Boundary Element Method which includes both boundaries of the body and the free surfaces to the second order diffraction and radiation problems.

The theory in the investigations mentioned above would be summarized as follows:

- (1) The quadratic terms of the Bernoulli equation are included.
- (2) The boundary condition at the free surface is satisfied in the accuracy of the second order.
- (3) The boundary condition on the body is satisfied at the instantaneous position.
- (4) The forces are obtained by the integration of the fluid pressure at instantaneous position and over the wetted contour.

To solve this nonlinear problem, the perturbation method is applied and the problem is reduced to the linear problems of the same perturbation parameter. Although the theoretical formulations are simple and straightforward, the solution procedure seems to be so complicated as seen in the analysis of Papanikolaou and Nowacki[9]. The potential and its second derivatives must be calculated exactly on the boundaries.

Several researchers derived the approximate solution in the radiation problem. C.H.Kim[13] showed an approximate solution of heaving triangular cylinders by the iteration method from the zero-frequency solution. Yamashita[14] derived an approximate solution neglecting the conditions of (1) and (2) in the heaving oscillation of thin cylinders and showed good agreements up to the third order.

On the other side, there are few reports about experiment on the full second order forces except the drifting force in waves. Tasai and Koterayama[15] presented the experimental results of various cylinders in radiation problem of heaving oscillation and compared them with the calculations of Lee, Parisis and Potash. Yamashita[14] also carried

out the experiments of the same problem up to third order and compared with his theoretical calculations. Kyozyuka[10,11] showed those of the diffraction problem and the radiations of heaving and swaying oscillations. Further, he showed the results of two cylinders which had the same beam/draft ratio and the sectional area, one intersected at right angles at free surface and the other did at a half of right angles[12].

Those experiments would provide valuable information about the validity and the limit of theory, and it is hoped that more experimental studies should be performed in the future.

Recently, Faltinsen[16], Nicholas and Hirt[17], and Vinje and Brevig[18] are attempting to treat the same problem as an initial value one which satisfies the whole conditions rigorously in time-domain. Although those attempts would have the possibility of wide application to the large amplitude problems and the transient phenomena, the larger and faster computer would be needed for the practical use. It can be said without doubt the information of the perturbation theory would be useful to such a simulation in time-domain.

In this paper, the following two points are emphasized under the background mentioned above, that is,

- (1) To propose the practical calculation by the simplification of the numerical procedure
- (2) To discuss the validity of the theory in comparison with the experiments

## 2. MATHEMATICAL FORMULATION

### 2.1 Boundary Conditions

Let us suppose the motions of a floating body in waves as shown in Fig. 1. We employ two coordinate systems,  $o-xy$  be a right-handed coordinate system fixed in space with  $o-y$  vertical downward and  $o-x$  lying in the undisturbed free surface,  $\bar{o}-\bar{x}\bar{y}$  be a system fixed in the body and coincides with  $o-xy$  when the body lies in a position of equilibrium.

Let the displacement of the motion denote  $x_j(t)$ , where subscript  $j=(1,2,3)$  refers to sway, heave and roll motions respectively, then the relation between the two systems is as follows:

$$\begin{aligned} x(t) &= \bar{x} \cos x_3(t) - \bar{y} \sin x_3(t) + x_1(t) \\ y(t) &= \bar{y} \cos x_3(t) + \bar{x} \sin x_3(t) + x_2(t) \end{aligned} \quad (1)$$

Here, we assume the floating body oscillates about its equilibrium position and the drift motion is restrained, that is, the external force cancels out the drifting force acting on it.

We will now assume that the fluid is ideal (inviscid, incompressible) and its motion is irrotational. Hence there exists a velocity poten-

tial  $\Phi(x,y,t)$  satisfying Laplace's equation

$$[L] \quad \nabla^2 \Phi = \Phi_{xx} + \Phi_{yy} = 0. \quad (2)$$

The fluid pressure  $P(x,y,t)$  is determined by Bernoulli's equation

$$P = -\rho\Phi_t - \frac{1}{2}\rho(\nabla\Phi)^2 + \rho gy + P_0, \quad (3)$$

where  $\rho$  is the fluid density,  $g$  the gravitational acceleration constant and  $P_0$  a constant of integration.

On the free surface two boundary conditions must be imposed. If the free surface is described by  $y = \eta(x,t)$ , the kinematic boundary condition is

$$0 = \frac{D}{Dt}(y - \eta(x,t)) = \Phi_y - \Phi_x \eta_x - \eta_t \quad \text{on } y = \eta(x,t), \quad (4)$$

and the dynamic condition is obtained from the Bernoulli's equation on the free surface where the pressure should be atmospheric constant, we choose as  $P = P_0$

$$\eta = \frac{1}{g} \left( \Phi_t + \frac{1}{2} \nabla\Phi\nabla\Phi \right) \quad \text{on } y = \eta(x,t). \quad (5)$$

From these conditions, we obtained the nonlinear free surface boundary condition

$$\begin{aligned} [F] \quad 0 &= \frac{D}{Dt} \left( \Phi_t + \frac{1}{2} \nabla\Phi\nabla\Phi - gy \right) \\ &= \Phi_{tt} - g\Phi_y + 2\nabla\Phi\nabla\Phi_t + \frac{1}{2} \nabla\Phi\nabla(\nabla\Phi\nabla\Phi) \quad \text{on } y = \eta(x,t). \end{aligned} \quad (6)$$

If the body surface is described by  $C(x,y,t) = C_0(\bar{x},\bar{y}) = 0$ , the kinematic boundary condition on it states that the fluid at a point on the body must have the same velocity component in the direction of the normal to the body.

$$\begin{aligned} [H] \quad \Phi_n(x,y,t) &= V_n(x,y,t) \\ &= \frac{\partial x}{\partial n} \frac{\partial x}{\partial t} + \frac{\partial y}{\partial n} \frac{\partial y}{\partial t} \quad \text{on } C(x,y,t) = 0, \end{aligned} \quad (7)$$

where the subscript  $n$  denotes the unit normal on body into the fluid.

If the fluid has a horizontal bottom at  $y = h$ , the kinematic boundary condition is

$$[B] \quad \Phi_y(x,h,t) = 0. \quad (8)$$

If it is infinitely deep, then

$$[B] \quad \lim_{y \rightarrow \infty} \phi_y = 0. \quad (8)'$$

The remaining boundary condition is a radiation condition at infinity, i.e., the waves must be propagating outward at a large distance from the body.

## 2.2 Linearized Problems

The problem formulated above is nonlinear and the boundaries in which the velocity potential is defined change with time. In order to reduce the nonlinear boundary conditions, we assume the potential  $\phi$  can be expanded in a perturbation series in terms of  $\epsilon$  :

$$\phi(x, y, t) = \epsilon \phi^{(1)}(x, y, t) + \epsilon^2 \phi^{(2)}(x, y, t) + O(\epsilon^3), \quad (9)$$

where  $\epsilon$  denotes a small perturbation parameter and may be defined such as the ratio of the incident wave amplitude to the half-beam of the body.

Similarly, the free surface elevation is assumed to be expanded:

$$\eta(x, t) = \epsilon \eta^{(1)}(x, t) + \epsilon^2 \eta^{(2)}(x, t) + O(\epsilon^3). \quad (10)$$

The boundary condition on the free surface can be reduced by expanding  $\phi(x, y, t)$  in Taylor series about  $y=0$  like as:

$$\phi(x, \eta, t) = \epsilon \phi^{(1)}(x, 0, t) + \epsilon^2 \{ \eta^{(1)} \phi_y^{(1)}(x, 0, t) + \phi^{(2)}(x, 0, t) \} + O(\epsilon^3). \quad (11)$$

Then we obtain the first and second order boundary conditions on the free surface as:

$$\begin{aligned} [F] \quad \epsilon : \quad \phi_{tt}^{(1)} - g \phi_y^{(1)} &= 0 \\ \epsilon^2 : \quad \phi_{tt}^{(2)} - g \phi_y^{(2)} &= -2(\phi_x^{(1)} \phi_{xt}^{(1)} + \phi_y^{(1)} \phi_{yt}^{(1)}) \\ &\quad + \phi_t^{(1)} \left( \phi_{yy}^{(1)} - \frac{1}{g} \phi_{tty}^{(1)} \right). \end{aligned} \quad (12)$$

Further, we will assume the body motions are also small as the amplitude of the incident waves and expand as:

$$x_j(t) = \epsilon x_j^{(1)}(t) + \epsilon^2 x_j^{(2)}(t) + O(\epsilon^3) \quad (j=1, 2, 3). \quad (13)$$

Therefore eq. (1) can be reduced as

$$\begin{aligned} x - \bar{x} &= \epsilon (x_1^{(1)} - \bar{y} x_3^{(1)}) + \epsilon^2 (x_1^{(2)} - \bar{y} x_3^{(2)} - \frac{1}{2} \bar{x} x_3^{(1)2}) + O(\epsilon^3) \\ y - \bar{y} &= \epsilon (x_2^{(1)} + \bar{x} x_3^{(1)}) + \epsilon^2 (x_2^{(2)} + \bar{x} x_3^{(2)} - \frac{1}{2} \bar{y} x_3^{(1)2}) + O(\epsilon^3). \end{aligned} \quad (14)$$

Now, we expand both sides of eq.(7) in Taylor series about its mean position

$$\begin{aligned}\phi_n(x,y,t) &= \phi_n^{(1)}(\bar{x}, \bar{y}, t) + (x - \bar{x}) \phi_{xn}^{(1)} + (y - \bar{y}) \phi_{yn}^{(1)} + \phi_n^{(2)}(\bar{x}, \bar{y}, t) + O(\epsilon^3) \\ &= \left( \frac{\partial \bar{x}}{\partial n} - \epsilon \frac{\partial \bar{y}}{\partial n} x_3^{(1)} \right) \{ \epsilon (\dot{x}_1^{(1)} - \bar{y} \dot{x}_3^{(1)}) + \epsilon^2 (\dot{x}_1^{(2)} - \bar{y} \dot{x}_3^{(1)} - \frac{1}{2} \ddot{x}_3^{(1)2}) \} \\ &\quad + \left( \frac{\partial \bar{y}}{\partial n} + \epsilon \frac{\partial \bar{x}}{\partial n} x_3^{(1)} \right) \{ \epsilon (\dot{x}_2^{(1)} + \bar{x} \dot{x}_3^{(1)}) + \epsilon^2 (\dot{x}_2^{(2)} + \bar{x} \dot{x}_3^{(1)} - \frac{1}{2} \ddot{x}_3^{(1)2}) \} + O(\epsilon^3),\end{aligned}\quad (15)$$

where  $\dot{x}_j = \frac{\partial}{\partial t} x_j$  ( $j=1,2,3$ ).

And using the following relations

$$\begin{aligned}\frac{\partial}{\partial n} \bar{x} &= \frac{\partial}{\partial s} \bar{y} \equiv \bar{y}', \\ \frac{\partial}{\partial n} \bar{y} &= -\frac{\partial}{\partial s} \bar{x} \equiv -\bar{x}',\end{aligned}\quad (16)$$

we transform eq.(15) to tangential and normal components of the body surface and obtain the following results[6].

$$\begin{aligned}[H] \quad \epsilon : \quad \phi_n^{(1)} &= f_t^{(1)} \\ \epsilon^2 : \quad \phi_n^{(2)} &= f_t^{(2)} + x_3^{(1)} c_t^{(1)} - x_3^{(1)} \phi_s^{(1)} - f^{(1)} \phi_{nn}^{(1)} - d^{(1)} \phi_{sn}^{(1)}\end{aligned}\quad \text{on } Co(x,y)=0, \quad (17)$$

where

$$\begin{aligned}a &= \bar{x} \bar{x}' + \bar{y} \bar{y}', \quad b = \bar{x} \bar{y}' - \bar{y} \bar{x}', \quad c^{(n)} = \bar{x}' x_1^{(n)} + \bar{y}' x_2^{(n)}, \\ d^{(n)} &= c^{(n)} + b x_3^{(n)}, \quad h^{(n)} = \bar{y}' x_1^{(n)} - \bar{x}' x_2^{(n)}, \quad f^{(n)} = h^{(n)} - a x_3^{(n)}\end{aligned}\quad (n=1,2).$$

And we can use the following relations

$$\begin{aligned}\phi_{nn}^{(1)} &= -\phi_{ss}^{(1)} - \frac{1}{\rho} \phi_n^{(1)} \\ \phi_{sn}^{(1)} &= \phi_{ns}^{(1)} - \frac{1}{\rho} \phi_s^{(1)} \\ 1/\rho &= \bar{x}' \bar{y}'' - \bar{y}' \bar{x}''; \quad \rho: \text{radius of the curvature.}\end{aligned}\quad (18)$$

Neglecting the transient response, we may expand the velocity potential associated with the each harmonic components using the fundamental angular frequency of the incident wave

$$\phi(x,y,t) = \text{Re} \left\{ \sum_{n=1}^{\infty} \sum_{k=1}^{\infty} \epsilon^n \phi_k^{(n)}(x,y) e^{ik\omega t} \right\}. \quad (19)$$

Further we can reduce the combination of  $n$  and  $k$  in eq.(19) as is already proved by Lee[3]

$$\phi(x,y,t) = \text{Re} \{ \epsilon \phi^{(1)} e^{i\omega t} + \epsilon^2 (\phi_0^{(2)} + \phi_2^{(2)} e^{2i\omega t}) \} + O(\epsilon^3), \quad (20)$$

and  $\phi_0^{(2)}$  is also proved to contribute only to the mass transport of the fluid and not contribute to the pressure or the force of the body, then



we will omit hereafter.

The second order incident wave potential is expressed as follows, if the fluid has a horizontal bottom at  $y=h$ ,

$$\begin{aligned}\Phi_0(x, y, t) &= \text{Re}\{\epsilon \varphi_0^{(1)} e^{i\omega t} + \epsilon^2 \varphi_0^{(2)} e^{2i\omega t}\} + O(\epsilon^3), \\ \epsilon \varphi_0^{(1)} &= \frac{ig^a w}{\omega} \frac{\cosh K(y-h)}{\cosh Kh} e^{iKx}, \\ \epsilon^2 \varphi_0^{(2)} &= \frac{i3\omega^a w}{8} \frac{\cosh 2K(y-h)}{\sinh^4 Kh} e^{i2Kx},\end{aligned}\quad (21)$$

where  $a_w$ ; amplitude of the incident wave.

Both  $\varphi_0^{(1)}$  and  $\varphi_0^{(2)}$  satisfies the following dispersion equation

$$\frac{\omega^2}{g} = K \tanh(Kh). \quad (22)$$

If it is infinitely deep, then

$$\begin{aligned}\epsilon \varphi_0^{(1)} &= \frac{ig^a w}{\omega} e^{-Ky+iKx}, \\ \epsilon^2 \varphi_0^{(2)} &= 0, \\ \frac{\omega^2}{g} &= K = 2\pi/\lambda\end{aligned}\quad (23)$$

The free surface elevation in this case is given as

$$\begin{aligned}\eta_0(x, t) &= \text{Re}\{\epsilon \eta_0^{(1)} e^{i\omega t} + \epsilon^2 \eta_0^{(2)} e^{i2\omega t}\} + O(\epsilon^3) \\ \epsilon \eta_0^{(1)} &= -a_w e^{iKx}, \\ \epsilon^2 \eta_0^{(2)} &= -\frac{K a_w^2}{2} e^{i2Kx}.\end{aligned}\quad (24)$$

The first and second order boundary value problems in infinitely deep water are summarized as follows:

#### First order problem

$$\begin{aligned}[L] \quad & \nabla^2 \varphi^{(1)}(x, y) = 0, \\ [F] \quad & \{K + \frac{\partial}{\partial y}\} \varphi^{(1)}(x, 0) = 0, \\ [H] \quad & \varphi_n^{(1)} = i\omega f^{(1)} \quad \text{on } C_0, \\ [B] \quad & \varphi_y^{(1)}(x, \infty) = 0,\end{aligned}\quad (25)$$

$$[R] \quad \left\{ \frac{\partial}{\partial x} \pm iK \right\} \varphi^{(1)}(\pm\infty, y) = 0 ,$$

where  $K = \frac{\omega^2}{g} = 2\pi/\lambda$  ,  $\lambda$  : wave length,

[R] is well-known as Sommerfeld's radiation condition.

Second order problem  $({}_2\varphi^{(2)} \rightarrow \varphi^{(2)})$

$$[L] \quad \nabla^2 \varphi^{(2)}(x, y) = 0 ,$$

$$[F] \quad \left\{ 4K + \frac{\partial}{\partial y} \right\} \varphi^{(2)}(x, 0) = Q(x) ,$$

$$[H] \quad \varphi_n^{(2)} = f_t^{(2)} + \frac{1}{2} (x_3^{(1)} c_t^{(1)} - x_3^{(1)} \varphi_s^{(1)} - f^{(1)} \varphi_{nn}^{(1)} - d^{(1)} \varphi_{sn}^{(1)}) \quad \text{on } C_0 , \quad (26)$$

$$[B] \quad \varphi_y^{(2)}(x, \infty) = 0 ,$$

$$[R] \quad \left\{ \frac{\partial}{\partial x} \pm i4K \right\} \varphi^{(2)}(\pm\infty, y) = 0 ,$$

where  $Q(x) = \frac{i\omega}{2g} \{ 2(\nabla \varphi^{(1)})^2 - \varphi^{(1)}(\varphi_{yy}^{(1)} + K \varphi_y^{(1)}) \}$ .

### 2.3 Pressure, Forces and Moment

Solving the boundary value problem of eqs.(25) and (26), we obtain the distributions of the velocity potential and the pressure.

Let expand the pressure and the hydrodynamic forces in accordance with eq.(20)

$$\begin{aligned} P(x, y, z) &= \text{Re} \{ \varepsilon p^{(1)} e^{i\omega t} + \varepsilon^2 ({}_0p^{(2)} + {}_2p^{(2)} e^{i2\omega t}) \} + O(\varepsilon^3) , \\ F_j(t) &= \text{Re} \{ \varepsilon F_j^{(1)} e^{i\omega t} + \varepsilon^2 ({}_0F_j^{(2)} + {}_2F_j^{(2)} e^{i2\omega t}) \} + O(\varepsilon^3) , \end{aligned} \quad (27)$$

pressure on the body surface are determined by eq.(3)

$$\begin{aligned} p^{(1)} &= -i\rho\omega\varphi^{(1)} + \rho g(x_2^{(1)} + \bar{x}x_3^{(1)}) , \\ {}_0p^{(2)} &= -\frac{1}{4}\rho g y |x_3^{(1)}|^2 - \frac{1}{4}\rho |\nabla \varphi^{(1)}|^2 - \frac{i\rho\omega}{2} \{ (x-\bar{x})\varphi_x^{(1)*} + (y-\bar{y})\varphi_y^{(1)*} \} , \\ {}_2p^{(2)} &= -i2\rho\omega\varphi^{(2)} - \frac{1}{4}\rho g \bar{y} x_3^{(1)2} - \frac{1}{4}\rho (\nabla \varphi^{(1)})^2 - \frac{i\rho\omega}{2} \{ (x-\bar{x})\varphi_x^{(1)} + (y-\bar{y})\varphi_y^{(1)} \} , \end{aligned} \quad (28)$$

where  $\varphi^{(1)*}$  denotes the complex conjugate of  $\varphi^{(1)}$ .

We will calculate the potential distribution and its derivatives on the body surface from the solution of the first order problem as follows:

$$\begin{aligned} (\nabla \varphi^{(1)})^2 &= (\varphi_n^{(1)})^2 + (\varphi_s^{(1)})^2 \\ &= (f_t^{(1)})^2 + (\varphi_s^{(1)})^2 , \\ (x-\bar{x})\varphi_x^{(1)} + (y-\bar{y})\varphi_y^{(1)} &= f^{(1)}\varphi_n^{(1)} + d^{(1)}\varphi_s^{(1)} \end{aligned} \quad (29)$$

$$= f^{(1)} f_t^{(1)} + d^{(1)} \varphi_s^{(1)}.$$

The forces and moment are obtained in the following form by integrating the pressure along the body surface at instantaneous position and wetted contour.

$$F(t) = - \int_{C(t)} (P-P_0) \frac{\partial x_j}{\partial n} (t) ds, \quad (30)$$

where  $C(t)$  denotes the wetted contour;  $C(t) = C_0 + \Delta C(t)$ .

$\Delta C(t)$  may be expanded with the same perturbation series as eq.(10) and we take into account this effect in the hydrodynamic force to the accuracy of the second order and obtain

$$\begin{aligned} \begin{pmatrix} F_1 \\ F_2 \\ F_3 \end{pmatrix} &= \int_{C(t)} (P-P_0) \begin{pmatrix} -y' - x' x_3^{(1)} + \frac{1}{2} y' x_3^{(1)2} \\ x' - y' x_3^{(1)} - \frac{1}{2} x' x_3^{(1)2} \\ a - c^{(1)} - h^{(1)} x_3^{(1)} \end{pmatrix} ds \\ &= \int_{C_0} (P-P_0) \begin{pmatrix} -\bar{y}' - \bar{x}' x_3^{(1)} + \frac{1}{2} \bar{y}' x_3^{(1)2} \\ \bar{x}' - \bar{y}' x_3^{(1)} - \frac{1}{2} \bar{x}' x_3^{(1)2} \\ a - c^{(1)} - h^{(1)} x_3^{(1)} \end{pmatrix} ds + \int_{\Delta C(t)} (P-P_0) \begin{pmatrix} -\bar{y}' \\ \bar{x}' \\ a \end{pmatrix} ds. \quad (29) \end{aligned}$$

Second term of the right hand side of eq.(31) can be calculated by applying Leibniz's rule as

$$\begin{aligned} - \int_{\Delta C(t)} (P-P_0) \frac{\partial x_j}{\partial n} ds &= \int_0^{r^+(t)} (P-P_0) dy' \left[ \frac{1}{y'} \frac{\partial \bar{x}_j}{\partial n} \right]_{(b,0)} \\ &\quad - \int_0^{r^-(t)} (P-P_0) dy' \left[ \frac{1}{y'} \frac{\partial \bar{x}_j}{\partial n} \right]_{(-b,0)}, \quad (32) \end{aligned}$$

where  $r^\pm(t) = \epsilon \{ x_2^{(1)} \pm b x_3^{(1)} - \frac{i\omega}{g} \varphi^{(1)}(\pm b, 0) \} e^{i\omega t}$

= relative wave elevation from  $\bar{y} = 0$ .

Now, we will decompose the second order forces into five terms as

$$F_j^{(2)} = \sum_{n=1}^5 F_j^{(2)}(n),$$

$$F_j^{(2)}(1) = {}_0F_j^{(2)}(1) + {}_2F_j^{(2)}(1)$$

$$= - \int_{C_0} \rho g (\bar{y} + \bar{x} x_3^{(1)} + x_2^{(1)} - \frac{1}{2} x_3^{(1)2} - i\rho\omega \varphi^{(1)}) \frac{\partial x_j}{\partial n} (t) ds,$$

$$\begin{aligned}
F_j^{(2)} &= {}_0F_j^{(2)} + {}_2F_j^{(2)} \\
&= i\rho\omega \int_{Co} \{ (x-\bar{x})\varphi_x^{(1)} + (y-\bar{y})\varphi_y^{(1)} \} \frac{\partial}{\partial n} x_j \, ds, \\
F_j^{(3)} &= {}_0F_j^{(3)} + {}_2F_j^{(3)} \\
&= -\frac{\rho}{2} \int_{Co} (\nabla \varphi^{(1)}) \frac{\partial}{\partial n} \bar{x}_j \, ds, \\
F_j^{(4)} &= {}_0F_j^{(4)} + {}_2F_j^{(4)} \\
&= \frac{\rho g}{2} \left[ (r^+)^2 \left\{ \begin{matrix} -1 \\ x'/y' \\ a/y \end{matrix} \right\}_{(b,0)} - (r^-)^2 \left\{ \begin{matrix} -1 \\ x'/y' \\ a/y \end{matrix} \right\}_{(-b,0)} \right] \quad j = \begin{Bmatrix} 1 \\ 2 \\ 3 \end{Bmatrix}, \\
F_j^{(5)} &= {}_2F_j^{(5)} \\
&= 2i\rho\omega \int_{Co} \varphi^{(2)} \frac{\partial}{\partial n} \bar{x}_j \, ds,
\end{aligned} \tag{33}$$

where  $F_j^{(n)}$  refers to the followings;

- n=1 coupling motion term
- n=2 effect of displacement of the motion
- n=3 quadratic terms of the Bernoulli equation
- n=4 wetted surface change
- n=5 second order potential term.

If the body is symmetric about y-axis, we obtain

$$\frac{1}{\rho} F_j^{(1)} = \left\{ \begin{matrix} 0 \\ -2gbx_2 \\ -g(Iw-Ay_B)x_3 - gAx_1 \end{matrix} \right\}^{(1)} - \int_{Co} \varphi_t^{(1)} \left\{ \begin{matrix} -\bar{y}' \\ \bar{x}' \\ a \end{matrix} \right\} ds, \tag{34}$$

$$\frac{1}{\rho} {}_0F_j^{(1)}(1) = \left\{ \begin{matrix} -\frac{1}{2}\omega^2 Ax_2^{(1)} x_3^{(1)*} \\ -2gbx_2^{(2)} - \frac{1}{4}gAx_3^{(1)} x_3^{(1)*} + \frac{1}{2}x_3^{(1)*} \int_{Co} \varphi_t^{(1)} d\bar{y} \\ -g(Iw-Ay_B)x_3^{(2)} - \frac{1}{2}\omega^2 Ax_1^{(1)} x_2^{(1)*} - \frac{1}{2}x_2^{(1)*} \int_{Co} \varphi_t^{(1)} d\bar{y} \end{matrix} \right\}, \tag{35}$$

$$\frac{1}{\rho} {}_2F_j^{(2)}(2) = \left\{ \begin{matrix} \frac{1}{2}\omega^2 Ax_2^{(1)} x_3^{(1)} \\ -2gbx_2^{(2)} - \frac{1}{4}gA(x_3^{(1)})^2 + \frac{1}{2}x_3^{(1)} \int_{Co} \varphi_t^{(1)} d\bar{y} \\ -g(Iw-Ay_B)x_3^{(2)} - gAx_1^{(2)} - \frac{1}{2}\omega^2 Ax_1^{(1)} x_2^{(1)} - \frac{1}{2}x_2^{(1)} \int_{Co} \varphi_t^{(1)} d\bar{y} \end{matrix} \right\}, \tag{36}$$

where

$I_w = \int_{-b}^b x^2 dx$  : moment of inertia of the waterline with respect to the coordinate origin,

$A = \int_{C_0} \bar{x} d\bar{y} = - \int_{C_0} \bar{y} d\bar{x}$  : sectional area of the body,

$(x_B, y_B) = (0, y_B)$  : coordinate of the center of buoyancy.

The first term in the rolling eqs.(34),(35) and (36) can be written as:

$$\begin{aligned} -g(I_w - Ay_B) &= -gA(I_w/A - y_B) \\ &= -gA \overline{OM} ; \quad \overline{OM} : \text{metacentric height,} \end{aligned}$$

and the following relation is used in eqs.(35) and (36) from the first order equation of the heaving motion[22]

$$-\rho \omega^2 A x_2^{(1)} = -2\rho g b x_2^{(1)} - \rho \int_{C_0} \varphi_t^{(1)} dx . \quad (37)$$

The aforementioned formulation can be simply applied for the radiation problem of j-mode, if we substitute the following equations.

$$\left. \begin{aligned} a_w &= x_j^{(1)} = a_j \\ \varphi_0 &= 0 \end{aligned} \right\} \quad (38)$$

## 2.4 The Equation of the Motion

The inertia forces with respect to the origin o fixed on the body are determined with the consideration of displacements of the motion in eq.(1). Equating them to the pressure forces of eqs.(34) and (35) we obtain the following results.

### First Order

$$\begin{aligned} M(\ddot{x}_1^{(1)} - y_G \ddot{x}_3^{(1)}) &= F_1^{(1)} \\ M \ddot{x}_2^{(1)} &= F_2^{(1)} \\ I \ddot{x}_3^{(1)} + M g y_G x_3^{(1)} - M(y_G \ddot{x}_1^{(1)} + g x_1^{(1)}) &= F_3^{(1)} \end{aligned} \quad (39)$$

where

$M = \rho A$  ; mass of the body per unit length,

$I = \iint \rho(x^2 + y^2) dx dy = M r_G^2$ ; mass moment of inertia of the body with respect to the coordinate origin,

$(x_G, y_G) = (0, y_G)$  ; center of gravity of the body.

The rolling equation in eq.(39) can be written in the usual expression.

$$I\ddot{x}_3^{(1)} + Mg \overline{GM} x_3^{(1)} - My_G \ddot{x}_1^{(1)} = -\rho \int_{C_0} \psi_t^{(1)} a \, ds.$$

#### Quasi-Hydrostatics of the second order

We have assumed the external force which cancels out the drifting force. Let the  $Df$  denote the external force as follows.

$$\begin{aligned} Df &= \sum_{n=1}^4 {}_0F_1^{(2)}(n) \\ 0 &= \sum_{n=1}^4 {}_0F_2^{(2)}(n) \end{aligned} \quad (40)$$

$$Mgy_G \ddot{x}_3^{(2)} = \sum_{n=1}^4 {}_0F_3^{(2)}(n)$$

If the external force are provided by the restoring force of a mooring system, it may be expressed in the form.

$$Df = k_0 x_1^{(2)}, \quad (41)$$

where

$k$  : spring constant of the mooring system,

${}_0x_1^{(2)}$  : drifting displacement in sway.

Further, let us define the sinkage force( $Sf$ ) and the steady heeling moment( $Hm$ ) as follows:

$$\begin{aligned} Sf &= 2\rho g b_0 x_2^{(2)} = \sum_{n=1}^4 {}_0F_2^{(2)}(n) + 2\rho g b_0 x_2^{(2)} \\ Hm &= Mg \overline{GM}_0 x_3^{(2)} = \sum_{n=1}^4 {}_0F_3^{(2)}(n) - Mg y_G \ddot{x}_3^{(2)} \end{aligned} \quad (42)$$

These steady forces may be obtained from the drift displacement of the motion in the free floating problem in waves.

#### Hydrodynamics of the second order

Although the heaving equation is influenced by the first order rolling motion, the swaying and rolling equations are the same as the first order case.

$$M(\ddot{x}_1^{(2)} - y_G \ddot{x}_3^{(2)}) = \sum_{n=1}^5 {}_2F_1^{(2)}(n)$$

$$M[2\ddot{x}_2^{(2)} - \frac{1}{2}y_G\{x_3^{(1)}\ddot{x}_3^{(1)} + (\dot{x}_3^{(1)})^2\}] = \sum_{n=1}^5 2F_2^{(2)}(n) \quad (43)$$

$$I_2\ddot{x}_3^{(2)} + Mgy_G 2x_3^{(2)} - M(y_G 2\ddot{x}_1^{(2)} + g_2 x_1^{(2)}) = \sum_{n=1}^5 2F_3^{(2)}(n)$$

### 3. SOLUTION OF THE PROBLEM

#### 3.1 First Order Problem

The boundary value problems formulated in the preceding chapter can be reduced to the first order theories which have been solved by making use of the methods of multi-pole expansions, Green functions and variational method.

However, in the second order problem there appears inhomogeneous boundary condition on the free surface. This means that we must evaluate the potential and its derivatives to calculate the pressure distribution on it and also evaluate their contribution to the body by integrating over the free surface. These processes may be simplified by applying the Boundary Element Method (BEM) which enable us to deal with the free surface as same as the body surface.

As for the problem treated here, Yeung[19] showed the numerical examples and found its satisfactory accuracy in the two and three dimensional radiation problems. He obtained the solution by integrating all the boundaries around the domain in which the potential satisfies Laplace equation. We will formulate the same problem by a slightly modified approach.

The potential can be expressed in the following form by applying Green's theorem.

$$\varphi(P) = \frac{1}{2\pi} \int_{C+F+B+R^\pm} \left( \frac{\partial \varphi(Q)}{\partial n} - \varphi(Q) \frac{\partial}{\partial n} \right) \log r(P, Q) ds(Q), \quad (44)$$

where  $P=(x, y)$ ,  $Q=(x', y')$  and  $r^2 = (x-x')^2 + (y-y')^2$ ,

$C, F, R^\pm$  and  $B$  denote the each boundaries on the body, free surface, right and left radiation boundaries and bottom of the fluid.

Now, we will decompose the first order potential into the following terms.

$$\varphi^{(1)}(x, y) = \varphi_0^{(1)}(x, y) + \varphi_4^{(1)}(x, y) + \sum_{j=1}^3 x_j^{(1)} \varphi_j^{(1)}(x, y), \quad (45)$$

where subscript  $j=(0, 1, 2, 3, 4)$  refers to the incident wave, sway, heave, roll and diffraction respectively.

Further we will normalize the potentials as

$$\begin{aligned} \varepsilon \varphi_j^{(1)} &= \frac{ig_w}{\omega} \phi_j^{(1)} & \text{for } j=0,4 \\ \varepsilon \varphi_j^{(1)} &= i\omega x_j^{(1)} \phi_j^{(1)} = \frac{ig_w}{\omega} K \frac{x_j^{(1)}}{a_w} \phi_j^{(1)} & \text{for } j=1,2,3 \end{aligned} \quad (46)$$

where  $a_w$  = amplitude of the incident wave  
 $\omega_w$  = angular frequency of the incident wave  
 $g$  = gravitational acceleration  
 $K = \omega^2/g = \text{wave number.}$

Therefore, the total potential is expressed as

$$\varepsilon \varphi^{(1)} = \frac{ig_w}{\omega} \left\{ \phi_0^{(1)} + \phi_4^{(1)} + K \sum_{j=1}^3 \bar{x}_j^{(1)} \phi_j^{(1)} \right\}, \quad \bar{x}_j^{(1)} = x_j^{(1)} / a_w. \quad (47)$$

Surface elevation of the first order is given by

$$\varepsilon \eta^{(1)} = -a_w \left\{ \phi_0^{(1)} + \phi_4^{(1)} + K \sum_{j=1}^3 \bar{x}_j^{(1)} \phi_j^{(1)} \right\}, \quad (48)$$

where  $\phi_0^{(1)} = e^{-Ky+iKx}$ .

The boundary conditions for each subproblems are rewritten as:

$$\begin{aligned} [L] \quad & \nabla^2 \phi_j^{(1)}(x,y) = 0 \\ [F] \quad & \left\{ K + \frac{\partial}{\partial y} \right\} \phi_j^{(1)}(x,0) = 0 \\ [H] \quad & \frac{\partial}{\partial n} \phi_j^{(1)} = \frac{\partial}{\partial n} \bar{x}_j \quad \text{for } j=1,2,3 \\ & \frac{\partial}{\partial n} \phi_j^{(1)} = -\frac{\partial}{\partial n} \phi_0^{(1)} \quad \text{for } j=4 \\ [B] \quad & \frac{\partial}{\partial n} \phi_j^{(1)}(x,\infty) = 0 \\ [R] \quad & \left\{ \frac{\partial}{\partial x} \pm iK \right\} \phi_j^{(1)}(\pm\infty, y) = 0 \end{aligned} \quad (49)$$

For a problem symmetrical with respect to  $\bar{y}$ -axis, let  $\phi_S(x,y)$  be a source potential placed at the origin. Then  $\phi_S(x,y)$  can be expressed by

$$\begin{aligned} \phi_S(P) &= \frac{1}{2\pi} \int_{C+F+R^+ + B} \left( \frac{\partial}{\partial n} \phi_S(Q) - \phi_S(Q) \frac{\partial}{\partial n} \right) \log r(P,Q) ds(Q) \\ &= -\frac{1}{\pi} \oint_0^\infty \frac{e^{-ky} \cos kx}{k-K} dk + ie^{-Ky} \cos Kx, \end{aligned} \quad (50)$$

where  $\oint$  denotes the Cauchy's principal value.



Asymptotic expansions for  $\phi_S$  and  $\phi_j^{(1)}$  are well-known as [20]:

$$\begin{aligned}\phi_S(P) &\rightarrow ie^{-Ky+iKx} & \text{as } x \rightarrow \pm\infty \\ \phi_j^{(1)}(P) &\rightarrow iH_j^\pm(K)e^{-Ky+iKx} & \text{as } x \rightarrow \pm\infty\end{aligned}\quad (51)$$

where  $H_j^\pm(K) = \int_{C_0} \left( \frac{\partial}{\partial n} \phi_j^{(1)} - \phi_j^{(1)} \frac{\partial}{\partial n} \right) e^{-Ky \pm iKx} ds$ ; Kochin function.

Let  $\phi_N(P)$  be a new potential defined as follows:

$$\phi_N(P) = \phi_j^{(1)}(P) - H_j^\pm \phi_S(P), \quad (52)$$

then, at infinity

$$\phi_N(P) \rightarrow 0 \quad \text{as } x \rightarrow \pm\infty.$$

Therefore, we may call this potential a wave-free potential and can express it as:

$$\phi_N(P) = \frac{1}{2\pi} \int_{C+F+R^\pm+B} \left( \frac{\partial}{\partial n} \phi_N(Q) - \phi_N(Q) \frac{\partial}{\partial n} \right) \log r(P,Q) ds(Q). \quad (53)$$

If we take the radiation boundaries  $R^\pm$  far from the body and the problems are restricted in deep water case, the integration on  $R^\pm$  and  $B$  will vanish and we obtain the following equation.

$$\begin{aligned}\phi_N(P) &= \frac{1}{2\pi} \int_{C+F} \left( \frac{\partial}{\partial n} \phi_N(Q) - \phi_N(Q) \frac{\partial}{\partial n} \right) \log r(P,Q) ds(Q) \\ &= \frac{1}{2\pi} \int_{C+F} \left( \frac{\partial}{\partial n} \phi_j^{(1)} - \phi_j^{(1)} \frac{\partial}{\partial n} \right) \log r ds - \frac{1}{2\pi} H_j^\pm(K) \int_{C+F} \left( \frac{\partial}{\partial n} \phi_S - \phi_S \frac{\partial}{\partial n} \right) \log r ds\end{aligned}\quad (54)$$

Thus we obtain the following integral equation making use of the free surface condition and taking into account  $\log r$  becomes singular when  $P$  approaches the boundaries.

$$\begin{aligned}\pi \phi_j^{(1)}(P) + \int_{C+F} \phi_j^{(1)} \frac{\partial}{\partial n} \log r ds + K \int_F \phi_j^{(1)} \log r ds \\ - H_j^\pm(K) \left\{ \pi \phi_S + \int_{C+F} \phi_S \frac{\partial}{\partial n} \log r ds + K \int_F \phi_S \log r ds \right\} = \int_C \frac{\partial}{\partial n} \phi_j^{(1)} \log r ds.\end{aligned}\quad (55)$$

Similary, for anti-symmetry problems let  $\phi_D(x,y)$  be a horizontal doublet potential placed at the origin

$$\begin{aligned}
\phi_D(x,y) &= \frac{1}{2\pi} \int_{C+F+R^{\pm}+B} \left( \frac{\partial}{\partial n} \phi_D - \phi_D \frac{\partial}{\partial n} \right) \log r \, ds \\
&= \frac{1}{\pi} \int_0^\infty \frac{ke^{-ky} \sin kx}{k-K} dk - iKe^{-Ky} \sin Kx, \\
&\rightarrow \pm Ke^{-Ky} \mp iKx \quad \text{as } x \rightarrow \pm\infty.
\end{aligned} \tag{56}$$

Therefore, we introduce the following potential

$$\phi_N(x,y) = \phi_j^{(1)} - \frac{i}{K} H_j^{\pm}(K) \phi_D(x,y), \tag{57}$$

and the same procedure as used in the symmetry problem will be applied.

The similar procedures can be applied to the diffraction problem if the potential is split into two parts, symmetry and anti-symmetry with respect to y-axis.

### 3.2 Second Order Problem

We will decompose the second order potential into three components in the second order boundary value problem of eq.(26), and normalize as

$$\begin{aligned}
\varphi_j^{(2)} &= \varphi_j^{(2)m} + \varphi_j^{(2)b} + \varphi_j^{(2)f} \\
&= \frac{ig_a w}{2\omega} \varphi_m^{(2)} + \frac{ig_a w}{2\omega} (\varphi_b^{(2)} + \varphi_f^{(2)}),
\end{aligned} \tag{58}$$

where  $\varphi_m^{(2)}$ ; second order potential due to the motion of bi-frequency  
 $\varphi_b^{(2)}$ ; due to the second order body surface condition  
 $\varphi_f^{(2)}$ ; due to the second order free surface condition.

Then, the force due to these potentials are also split into each terms as:

$${}_2F_j^{(2)}(5) = {}_2F_j^{(2)}(M) + {}_2F_j^{(2)}(B) + {}_2F_j^{(2)}(F), \tag{59}$$

where  ${}_2F_j^{(2)}(M)$ ; second order force due to the motion of bi-frequency which produces the added-mass and damping forces of  $4K$

${}_2F_j^{(2)}(B)$ ; due to the second order body surface condition

${}_2F_j^{(2)}(F)$ ; due to the second order free surface condition.

Therefore, the boundary value problems for each three potentials are rewritten as:

$$\begin{aligned}
[L] \quad \nabla_i \phi^{(2)} &= 0 \quad (i=m, b, f) \\
[F] \quad \{4K + \frac{\partial}{\partial y}\} (\phi_m^{(2)}, \phi_b^{(2)}, \phi_f^{(2)}) &= (0, 0, q(x)) \quad \text{on } y=0 \\
[H] \quad \frac{\partial}{\partial n} (\phi_m^{(2)}, \phi_b^{(2)}, \phi_f^{(2)}) &= (2h^{(2)}, h_{ij}^{(2)}, 0) \quad \text{on } C_0 \\
[B] \quad \frac{\partial}{\partial y_i} \phi^{(2)}(x, \infty) &= 0, \quad (i=m, b, f) \\
[R] \quad \{\frac{\partial}{\partial x} + i4K\} \phi_i^{(2)}(\pm\infty, y) &= 0, \quad (i=m, b, f)
\end{aligned} \tag{60}$$

where  $q(x) = -2(\nabla\phi^{(1)})^2 + \phi^{(1)}(\phi_{yy}^{(1)} + K\phi_y^{(1)}) = q_c(x) + i q_s(x)$ ,

$$2h^{(2)} = 4Kf^{(2)}/a_w^{(2)},$$

$$h_{ij}^{(2)} = K\bar{x}_3^{(1)}\bar{c}^{(1)} - \bar{x}_3^{(1)}\phi_s^{(1)} - \bar{f}^{(1)}\phi_{nn}^{(1)} - \bar{d}^{(1)}\phi_{sn}^{(1)}.$$

The problems for  $\phi_m^{(2)}$  and  $\phi_b^{(2)}$  are the same as the first order problems in eq.(25), by replacing  $K$  to  $4K$ . The essential difference between the first and second order problems appears in the problems of  $\phi_f^{(2)}$  which must include the boundary condition on the free surface. However, it may be solved easily by applying the BEM described in the preceeding section in the same way as used in the first order problems.

Now, we consider the pressure distribution on the free surface,  $q(x)$ . In the radiation problems of a single mode, we obtain the potential and the pressure distribution from eqs.(47) and (60):

$$\begin{aligned}
\phi_j^{(1)} &= K\bar{x}_j^{(1)}\phi_j^{(1)} \quad (j=1, 2, 3), \\
q_j(x) &= K^2\{-2(\nabla\phi_j^{(1)})^2 + \phi_j^{(1)}(\phi_{jyy}^{(1)} + K\phi_{jy}^{(1)})\}.
\end{aligned}$$

At a large distance from the body, these terms can be expressed in the asymptotic expansions.

$$\left. \begin{aligned} \phi_j^{(1)} &\rightarrow iH_j^{\pm}(K) e^{-Ky \mp iKx} \\ q_j(x) &\rightarrow 0 \end{aligned} \right\} \quad \text{as } x \rightarrow \pm\infty \tag{61}$$

In the case of a symmetric body with respect to  $y$ -axis it can be simply shown by the symmetry relation

$$q_j(x) = q_j(-x). \tag{62}$$

Moreover, we find the following relation for radiations of a single mode oscillation of a symmetric body

$$h_{ij}^{(2)}(x, y) = h_{ij}^{(2)}(-x, y). \tag{63}$$

Therefore, the hydrodynamic forces caused by  $\phi_b^{(2)}$  and  $\phi_f^{(2)}$  always act as vertical forces even in the swaying or rolling oscillations.

Nextly, we consider the incident wave problems, in which the

potential far from the body may be expressed as:

$$\phi^{(1)} = e^{-Ky+iKx} + i(H_4^+ + K \sum_{j=1}^3 \bar{x}_j H_j^+) e^{-Ky-iKx} \text{ as } x \rightarrow \pm\infty.$$

Therefore, we obtain

$$\begin{aligned} q(x) &= -i8K^2(H_4^+ + K \sum_{j=1}^3 \bar{x}_j H_j^+) & \text{as } x \rightarrow +\infty, \\ q(x) &= 0 & \text{as } x \rightarrow -\infty. \end{aligned} \quad (64)$$

The complex constant of the pressure on the free surface of the weather side appears from the standing waves made by the interaction of the incident waves and the reflected waves.

The forces are given in the non-dimensional form.

$$f_j^{(2)}(F) = \frac{F_j^{(2)}}{\rho g a_w^2} = - \int_{Co} \phi \frac{\partial \bar{x}}{\partial n} j ds \quad (j=1,2,3). \quad (65)$$

For the evaluation of this term, we introduce three potentials which satisfy the following boundary conditions.

$$\begin{aligned} [L] \quad \nabla^2 \phi_j^R(x,y) &= 0 \\ [F] \quad \{4K + \frac{\partial}{\partial y}\} \phi_j^R(x,0) &= 0 \\ [H] \quad \frac{\partial}{\partial n} \phi_j^R &= \frac{\partial \bar{x}}{\partial n} j \\ [B] \quad \frac{\partial}{\partial y} \phi_j^R(x,\infty) &= 0 \\ [R] \quad \{\frac{\partial}{\partial x} + i4K\} \phi_j^R(\pm\infty, y) &= 0 \end{aligned} \quad (66)$$

These can be identified as the first order radiation potentials of wave number of  $4K$ . Then, we choose the free surface instead of the body surface for the integral path by applying Green's theorem [6].

$$\begin{aligned} \int_{Co} f \phi \frac{\partial \bar{x}}{\partial n} j ds &= \int_{Co} f \phi^{(2)} \phi_{jn}^R ds \\ &= \int_{Co} f \phi_n^{(2)} \phi_j^R ds + \int_F (f \phi^{(2)} \phi_{jy}^R - f \phi_y^{(2)} \phi_j^R) dx \\ &\quad - \int_{R^\pm} (f \phi^{(2)} \phi_{jx}^R - f \phi_x^{(2)} \phi_j^R) dy \\ &= - \int_F q(x) \phi_j^R dx - \int_{R^\pm} (f \phi^{(2)} \phi_{jx}^R - f \phi_x^{(2)} \phi_j^R) dy. \end{aligned} \quad (67)$$

if we take the  $R^{\pm}$  at infinity, the integral on  $R^{\pm}$  vanishes because of the radiation condition for  $\phi^{(2)}$  and  $\phi_j^R$ . Although the integrand on the free surface of x-positive side never converges as eq.(64), we could solve it as shown in Appendix. However, we could estimate practically it as the mean value of the integral as:

$$\int_{Co} \phi^{(2)} \frac{\partial}{\partial n} \bar{x}_j ds = (\text{mean value of}) \left\{ - \int_F q(x) \phi_j^R dx \right\}. \quad (68)$$

These treatments were pointed out by Söding[6]. Also Kyojuka[10] experienced in the numerical computations the variety of the solutions which strongly depend on the truncation of the free surface in the second order diffraction problems. These difficulties arise from the fact that the reflected waves by the body make a standing waves with the interaction of the incident waves which nondecay and last at infinity in the two dimensional diffraction problems.

In the three dimensional problems, Molin[21] derived the same procedures and obtained the second order wave forces upon fixed axisymmetric bodies without any difficulties.

In this study, the second order forces due to the nonlinear free surface condition are evaluated by eq.(68) making use of the wave-free potential aforementioned. Consequently, they can be obtained by the solutions of the first order problems without solving the second order boundary value problems.

In the radiation problems, the second order forces are obtained by two methods, the one by the direct solution of the second order boundary value problem, and the other by eq.(68). They show good agreement each other.

### 3.3 Numerical Results

The first order potential distribution on the body for a swaying circular cylinder at  $Kb=1.0$  is shown in Fig.2, where the segments on the body(NC) and the free surface(NF) for a half-section are (NCxNF) = (10x25) and (20x60) respectively. These results show good agreement with those of Green function method as shown in the figure. The first order hydrodynamic forces such as the added mass and the damping coefficients are also compared with those of methods by multi-pole expansions and Green functions, and they show satisfactory accuracy in the whole range treated here.

However, it should be noted that some irregularities like irregular frequencies by Green function methods are observed in the present method near the wave numbers

$$KR^{\pm} = n\pi/2, \quad n=1,2,3, \quad (69)$$

where  $R^{\pm}$  = x-coordinate of the radiation boundary.

It might be explained by the eigen solutions of the domain, and it is improved easily by the choice of the radiation boundary between  $R^{\pm}/b = 5.5$  and 9.5 depending on the wave number in this study.

In Fig.3, the potential distribution on the free surface for a

swaying circular cylinder is shown. In the figure, the wave-free potential which excluding the progressing wave term is also shown. The wave-free potential is found to be so monotonous with respect to  $x$  that it may be differentiated numerically with a good accuracy.

The second order boundary conditions on the free surface for a circular cylinder in swaying and heaving oscillations are shown in Fig. 4, and for the diffraction problem of a fixed circular cylinder is shown in Fig. 5. In Fig. 4, the pressure distribution on the free surface seems to approach to zero at a distance of two or three times of the body breadth from the body, while in the diffraction problem it approaches to a complex constant at the weather-side, and does rapidly to zero at the lee-side. Therefore, the hydrodynamic forces due to this condition in eq. (68) seem to strongly depend on the pressure distribution and the radiation potential in the vicinity of the body. The standard computations in this study are performed by the segments of  $(NC \times NF) = (20 \times 60)$ , and the segments on the free surface in the vicinity of the body should be smaller because the boundary condition must be more important there.

In Figs. 6(a) and 6(b), each components of the second order bi-harmonics of a heaving circular cylinder are compared for the real and the imaginary part respectively. Figs. 6(a) and 6(b) show that the force due to the body surface condition is dominant in the real part, while that due to the free surface condition is dominant in the imaginary part.

In Figs. 7(a) and 7(b), the same comparison is made for the diffraction problem of a fixed circular cylinder between two components, the quadratic terms of the velocity in Bernoulli equation and the free surface condition. It is clear that the latter force is dominant as shown in the figures.

The other second order forces are also evaluated for each component and the drifting force shows good agreement with the result of Kim and Dalzell[22]. The other results are presented in Fig. 9 through Fig. 28 together with the experimental results.

All the quantities are non-dimensionalized as follows.

#### Radiation

$$\begin{aligned} x_j(t) &= a_j \cos \omega t, \quad \varepsilon = a_j/b \quad (i=1,2,3) \\ f_{ij}^{(1)} &= |F_{ij}^{(1)}| (\rho g b_i a_i)^{-1} \cos(\omega t + \delta_{ij}^{(1)}), \quad (j=1,2,3) \\ {}_0f_{ij}^{(2)} &= |{}_0F_{ij}^{(2)}| (\frac{1}{2} \rho g a_i^2)^{-1}, \quad {}_2f_{ij}^{(2)} = |{}_2F_{ij}^{(2)}| (\rho g a_i^2)^{-1} \cos(2\omega t + \delta_{ij}^{(2)}) \end{aligned} \quad (70)$$

#### Diffraction

$$\begin{aligned} \eta(t) &= -(a_w \cos \omega t + \frac{K}{2} a_w^2 \cos 2\omega t), \quad \varepsilon = a_w/b \\ \bar{x}_j^{(1)} &= |x_j^{(1)}| (a_w)^{-1} \cos(\omega t + \alpha_j^{(1)}) \quad (j=1,2) \\ \bar{x}_3^{(1)} &= |x_3^{(1)}| (K a_w)^{-1} \cos(\omega t + \alpha_3^{(1)}) \quad (j=3) \end{aligned}$$

$$\begin{aligned}
{}_2\bar{x}_j^{(2)} &= |{}_2x_j^{(2)}| b_j (a_w)^{-2} \cos(2\omega t + \alpha_j^{(2)}) & (j=1,2,3) & (71) \\
f_j^{(1)} &= |F_j^{(1)}| (\rho g b_j a_w)^{-1} \cos(\omega t + \delta_j^{(1)}) & (j=1,2,3) \\
{}_0f_j^{(2)} &= {}_0F_j^{(2)} \left(\frac{1}{2}\rho g a_w^2\right)^{-1} & (j=1,2,3) \\
{}_2f_j^{(2)} &= |{}_2F_j^{(2)}| (\rho g a_w^2)^{-1} \cos(2\omega t + \delta_j^{(2)}) & (j=1,2,3)
\end{aligned}$$

where  $b_j$  denotes as:  $b_1=b_2=b$ ,  $b_3=b^2$  ( $b$ =half-beam at waterline)

#### 4. EXPERIMENTS

All the experiments were carried out at a small tank ( $L \times B \times D = 9 \text{ m} \times 1.2 \text{ m} \times 1.2 \text{ m}$ ) of the Defense Academy.

##### 4.1 Radiation Problem

A model for radiations has 0.3 m length by the limitation of the capacity of the load-cell and its principal dimensions are shown in Table 1. In order to realize the two dimensional condition, narrow waterway of 0.31 m width and 4 m length are constructed in the tank, in which the forced oscillation tests are carried out. A wave absorbing beach is set at both sides of the waterway.

The forces acting on the model are measured by the three component load-cell which are installed on the model, and the progressing waves are also measured by the wave probe at a distance of 1 m from the center line of the model. All the measured records are analyzed numerically by Fourier analysis.

A ball-screw mechanism is used for the forced swaying apparatus which are driven by a D.C. motor controlled by the frequency oscillator and the Scotch-york mechanism for the forced heaving apparatus.

An example of the record of the swaying case is shown in Fig.8. In this case, the second order force is observed directly in the vertical force ( $F_y$ ). In the figure, the horizontal force ( $F_x$ ) contains the high frequency components which seem to be mechanical noises of the apparatus.

As the linear forces have been reported to show good agreement with the calculations by Vugts[23], they are omitted in this paper.

The steady sinkage forces of the semi-submerged circular cylinder in swaying oscillation are shown in Fig.9 and the second order varying forces(bi-harmonics) in the vertical force are shown in Fig.10 together with the calculations.

It should be noted that the phase difference of the second order forces between sine and cosine systems. In this paper, the phases of the forces are defined as follows (downward positive in y-axis)

$$\begin{aligned}
 x_i &= a_i \cos(\omega t) \\
 F_{ij}^{(1)} &= |F_{ij}^{(1)}| \cos(\omega t + \delta_{ij}^{(1)}) \\
 {}_2F_{ij}^{(2)} &= |{}_2F_{ij}^{(2)}| \cos(2\omega t + \delta_{ij}^{(2)})
 \end{aligned} \tag{72}$$

where subscripts  $i, j$  refer to  $i$ -mode oscillation and  $j$ -mode force.

On the other side, Lee et al. define them (upward positive in  $y$ -axis)

$$\begin{aligned}
 x_i &= a_i \sin(\omega t) \\
 F_{ij}^{(1)} &= |F_{ij}^{(1)}| \sin(\omega t + \delta_{ij}^{(1)}(L)) \\
 {}_2F_{ij}^{(2)} &= |{}_2F_{ij}^{(2)}| \sin(2\omega t + \delta_{ij}^{(2)}(L))
 \end{aligned} \tag{73}$$

And the second order phase angles are determined in the range from zero to  $\pi$  in the experiment because they are bi-harmonics.

$$0 \leq \delta_{ij}^{(2)}, \delta_{ij}^{(2)}(L) < \pi$$

Hence, there are the following relations between the two systems.

$$\begin{aligned}
 \delta_{ij}^{(1)} &= \delta_{ij}^{(1)}(L) \\
 \delta_{ij}^{(2)} &= \delta_{ij}^{(2)}(L) - \frac{\pi}{4}, \text{ or } \delta_{ij}^{(2)} = \delta_{ij}^{(2)}(L) + \frac{3}{4}\pi
 \end{aligned} \tag{74}$$

The results show good agreement generally with the calculations. In Fig.10, the bi-harmonics of the experiments become smaller in the range of  $Kb$  exceeding 1.6, while the steady forces show good agreement with the calculation. This might be explained as viscous effects which appear in the high frequency range over  $Kb=1.6$ .

The second order forces do not appear in the horizontal force theoretically, but exist in the experiments. However, the second order horizontal forces appeared in the experiments are so small that we can regard them as zero. Careful experiments must be necessary for achieving precise results when the amplitude of the motion is small.

In Fig.11 and Fig.12, the results of the heaving case are shown together with the present theory. The same experiments are reported by Tasai and Koterayama[15] and Yamashita[14], and the present results of the experiments show good agreement with those. The present theory gives slightly higher value in the bi-harmonics of the second order forces, although the phases of them show good agreement. This difference is not clear, but the theory might give the values of upper limits.

The bi-harmonics components are also small in high frequency range as is the swaying case, which might be interpreted as the viscous effects appearing over the range of  $Kb=1.6$ , because the progressing wave reaches its limit of wave height as shown in Fig.13.



#### 4.2 Diffraction Problem for a fixed body

A model used for the diffraction test has 0.6 m length and its principal dimensions are also shown in Table 1. In this test, the width of the waterway is broadened to 0.61 m, where the wave exciting forces on the fixed model are measured by the three component load-cell. The incident waves are measured in the other side of the waterway, therefore it is possible to measure precisely the phase angles between the waves and the forces. The amplitude of the incident wave is approximately 1.5 cm in the whole range, hence  $a_w/b = 0.15$ .

An example of the experimental records is shown in Fig.14, where nonlinear effects can be observed in the heaving force.

An example of the results of the first order wave exciting force is shown in Fig.15 for the vertical force. The horizontal and vertical forces agree well with the theory for both amplitude and phase angle, while the moments of the excitation with respect to the coordinate origin show slightly lower than the theoretical ones. The cause of this difference might arise from the very small absolute value of the moment and the experimental error.

The results of the second order steady forces are shown in Fig.16 through Fig.18. Although these forces are very small in quantity the results show good agreement with the theory. It is found through both theory and experiments that the vertical force acts as a sinkage force in the whole range, and the steady heeling moment acts to incline the body toward the lee-side. The numerical results for the drifting force coincide with those by Maruo's theory.

The results for the second order bi-harmonics are shown in Fig.19 through Fig.21. The agreement in heaving component is very good in amplitude and phase, while swaying and rolling ones seem to have different tendencies. However, in general experiments are on the same order of the numerical ones.

#### 4.3 Motions of a Free Floating Body in Waves

A model for the free floating experiment and the set-up are the same as used in the diffraction experiments. Motions of a body are measured by the potentiometers on the regular guide and sub-carriage apparatus. The drift force is measured by the elongation of a mooring coil, and the effect of the mooring coil on motions of the body may be neglected because the spring constant of it is very small (20.6 g/cm). Phase differences between the motions and the incident wave should be determined by taking account of the swaying drift of the body.

Main purpose of this experiment is to observe the steady heeling angle of the body in waves, so that the metacentric height (GM) is set to be extremely low as shown in Table 1. In this condition, the body can be easily inclined by a small moment.

An example of the experimental records is shown in Fig.22, where the drifting shifts are observed in swaying and rolling motions.

In Figs.23 to 25, the first order responses of the motion are shown in both amplitude and phase, where the dotted lines in sway and

roll responses designate calculations considering the viscous damping in roll which are described latter. Although some differences between the theory and experiments are found in the phase response especially in the high frequency range, the amplitudes are shown in good agreement with each other. Those differences of the phase might be attributed to the experimental errors due to such as the slowly oscillation of a moored body.

The results of the steady forces are shown in Fig.16 to Fig.18, compared with those of the fixed body. The numerical results for the drifting force in this case also coincide with Maruo's theory. Experiments show good agreement with theory generally. The sinkage force acts as buoyancy in a low frequency range of  $Kb < 0.7$ , while the steady heeling moment always acts to incline the body toward lee-side.

The first order response of the rolling of the body is very abrupt in the direction of the sinkage around the resonance. Such abrupt response can be suppressed by making viscous damping coefficient increase as shown in Fig.17. The viscous damping effects are written in the following equation from the results of the free oscillation test in roll.

$$I \ddot{x}_3^{(n)} + C_v \dot{x}_3^{(n)} + Mg y_G x_3^{(n)} - M(y_G \ddot{x}_1^{(n)} + g x_1^{(n)}) = F_3^{(n)} \quad (n=1,2), \quad (75)$$

where  $C_v = 0.1 \times I = (\text{viscous damping coef.})$ .

The second order motions of bi-harmonics are shown in Figs.26 to 28. It is found in both calculation and experiment that the second order bi-harmonic motions in sway and roll are very small except narrow range of the first order rolling resonance as shown in Figs.26 and 28. The blunt peak in the swaying response is appeared near the range of the first order heaving resonance. On the other hand, there appears three peaks in the calculation of the second order heaving response as shown in Fig.27. The first peak appears near the resonance of the first order rolling motion, which would be suppressed easily by the viscous damping effects in roll as shown in the figure. The second one appears near the resonance of the second order heaving motion, of which wave number is given as one fourth of the first orders. The third one appears near the resonance of the first order heaving motion.

Although experiments give small value at the low frequency range, general tendencies seem to be similar to the calculation.

It would be of interest when two resonances of the first order and second order motions coincide with each other.

## 5. CONCLUSION

The first and second order forces on a cylindrical body in waves are calculated on the basis of the regular perturbation theory along with the previous pursuers.

The second order boundary value problem of the radiations could

be solved without any difficulty, while some considerations should be paid in the diffraction problems. The second order solutions of the diffraction problems strongly depend on the truncation of the free surface condition. However, the forces acting on the body due to these potentials could be obtained reasonably by the mean value of the integrals on the free surface applying Green's theorem. Consequently, the second order forces can be obtained by making use of the first order solutions without solving the second order boundary value problems.

The Boundary Element Method which includes both boundaries of the body and the free surfaces is applied to simplify these procedures, then it enables us to deal with the free surface as same as the body surface. Those numerical results show good agreement with other theories.

Experiments are carried out for not only the radiations of heaving and swaying oscillations but also the diffractions for a fixed and a free floating body in waves. Generally speaking, the present theory shows good agreement with experiments of all the problems, although the second order forces are very small in the extent of the phenomena treated here. The steady heeling angles of a floating body in waves are observed in the experiments as are predicted by the calculation.

Therefore, we conclude that the present theory can be utilized for the purpose of the predictions of the hydrodynamic forces and the ship motions in wave.

The remaining interests should be turned toward the extremely large amplitude problems and the transient problems. It is hoped that further investigations of such problems will be performed in the future.

#### ACKNOWLEDGEMENT

The author wish to express his indebtedness to Prof. M. Bessho, National Defense Academy, for his kindly guidance and encouragement in the course of this study.

#### REFERENCES

1. Maruo, H. (1960). The drift of a body floating on waves, J.Ship Res., Vol.4, No.3, pp.1-10
2. Ogilvie, T.F. (1963). First- and second-order forces on a cylinder submerged under a free surface, J.Fluid Mech., Vol.16, pp.451-472.
3. Lee, C.M. (1966). The second-order theory of heaving cylinders oscillating vertically in a free surface, Report No.NA-66-7., Univ. of California, Berkely.
4. Parissis, G.C. (1966). Second-order potentials and forces for oscillating cylinders on a free surface, MIT-Rept. No.66-10, Dept. of Ocean Eng., MIT.

5. Potash, R.L. (1971). Second-order theory of oscillating cylinders, J. Ship Res., Vol.15, pp.295-304.
6. Söding, H. (1976). Second-order forces on oscillating cylinders in waves, Schiffstechnik, Vol.23, pp.205-209.
7. Masumoto, A. (1978). On the non-linear hydrodynamic forces for oscillating bodies in regular waves, in Japanese, J. Kansai Soc. Naval Arch. Japan, No.172, pp.17-31.
8. Papanikolaou, A. (1978). Potential theory of second order for cylinders oscillating vertically, in German, Schiffstechnik, Vol.25, pp.53-80.
9. Papanikolaou, A. and Nowacki, H. (1980). Second-order theory of oscillating cylinders in a regular steep waves, Proc. of the 13th ONR Symp., pp.303-331.
10. Kyoizuka, Y. (1980). Non-linear hydrodynamic forces acting on two-dimensional bodies (1st report, diffraction problem), in Japanese, J. Soc. Naval Arch. of Japan, Vol.148, pp.49-57.
11. Kyoizuka, Y. (1980). Non-linear hydrodynamic forces acting on two-dimensional bodies (2nd report, radiation problem), in Japanese, J. Soc. Naval Arch. of Japan, Vol.149, pp.47-53.
12. Kyoizuka, Y. (1981). Non-linear hydrodynamic forces acting on two-dimensional bodies (3rd report, effect of the angles of the intersection of the body and the free-surface), in Japanese, J. Soc. Naval Arch. of Japan, Vol.150, pp.257-265.
13. Kim, C.H. (1967). On the influence of nonlinear effects upon hydrodynamic forces in forced heaving oscillations of cylinders, in German, Schiffstechnik, Vol.14, pp.79-91.
14. Yamashita, S. (1977). Calculations of the hydrodynamic forces acting upon thin cylinders oscillating vertically with large amplitude, in Japanese, J. Soc. Naval Arch. of Japan, Vol.141, pp.67-76.
15. Tasai, F. and Koterayama, W. (1976). Nonlinear hydrodynamic forces acting on cylinders heaving on the surface of a fluid, Rept. No. 77, Res. Inst. of Appl. Mech., Kyushu Univ.
16. Faltinsen, O. (1977). Numerical solutions of transient nonlinear free-surface motion outside and inside moving bodies, Proc. 2nd Intl. Conf. on Num. Ship Hydrodyn., pp.347-357.
17. Nicholas, B.D. and Hirt, C.W. (1977). Nonlinear hydrodynamic forces on floating bodies, Proc. 2nd Intl. Conf. on Num. Ship Hydrodyn., pp.382-394.
18. Vinje, T. and Brevig, P. (1981). Nonlinear ship motions, Proc. 3rd Intl. Conf. on Num. Ship Hydrodyn., 4-3.
19. Yeung, R.W. (1973). A singularity-distribution method for free surface flow problems with an oscillating body, Rept. No. NA-73-6, Univ. California, Berkely.
20. Bessho, M. (1967). On the two-dimensional theory of the rolling motion of ships, Mem. Defense Academy of Japan, Vol.7, No.1.
21. Molin, B. (1979). Second-order diffraction loads upon three-dimensional bodies, Appl. Ocean Res., Vol.1, No.4, pp.197-202.
22. Kim, C.H. and Dalzell, J.F. (1981). An analysis of the quadratic frequency response for lateral drifting force and moment, J. Ship Res., Vol.25, No.2, pp.117-129.
23. Vugts, J.H. (1968). The hydrodynamic coefficients for swaying,

heaving and rolling cylinders in a free surface, Int. Shipbuild. Prog., Vol.15, pp.251-276.

### Appendix

Solution for the Problem of a Constant Pressure Distribution on a Free Surface

Let  $\varphi(x,y)$  be a velocity potential which is determined by the following boundary value problem.

$$\begin{aligned} [L] \quad & \nabla^2 \varphi(x,y) = 0 \\ [F] \quad & \left\{ K + \frac{\partial}{\partial y} \right\} \varphi(x,0) = q \quad x_1 \leq x \leq x_2 \\ & \left\{ K + \frac{\partial}{\partial y} \right\} \varphi(x,0) = 0 \quad x < x_1, x_2 < x \\ [B] \quad & \lim_{y \rightarrow \infty} \varphi_y(x,y) = 0 \\ [R] \quad & \left( \frac{\partial}{\partial x} \pm iK \right) \varphi(\pm \infty, y) = 0 \end{aligned} \quad (A.1)$$

where  $q$  is a complex constant.

This solution can be written in the form.

$$\varphi(x,y) = \frac{q}{2\pi} \int_{x_1}^{x_2} \{ \operatorname{Re}[e^{iKz} E_1(iKz)] \mp i\pi e^{iKz} + i\pi \operatorname{Re}[e^{iKz}] \} dx', \quad (A.2)$$

where  $z = (x-x') + iy$ ,

$$E_1(z) = \int_0^\infty \frac{e^{-t}}{t} dt,$$

$\pm$  sign corresponds to the case of  $(x-x') \gtrless 0$ .

If  $x < x_1$  or  $x_2 < x$ , then

$$\varphi(x,y) = L(x,y) + i \frac{q}{K} e^{-Ky} \sin \frac{K}{2}(x_2-x_1) e^{\mp iK(x-\frac{x_1+x_2}{2})}, \quad (A.3)$$

where  $L(x,y) = \frac{q}{2\pi} \int_{x_1}^{x_2} \operatorname{Re}[e^{iKz} E_1(iKz)] dx'$ .

If  $x_1 < x < x_2$ , then

$$\varphi(x,y) = L(x,y) - \frac{q}{K} e^{-Ky} \left[ 1 - \cos K(x - \frac{x_1+x_2}{2}) e^{i\frac{K}{2}(x_2-x_1)} \right]. \quad (A.4)$$

The  $L(x,y)$  can be interpreted as the local disturbance, and is integrable even if  $x_2 \rightarrow \infty$ . However,  $\varphi(x,y)$  strongly depends on the truncation of the pressure distribution by the second term of eqs. (A.3) and (A.4). The  $\varphi(x,y)$  will oscillate periodic depending on  $x_1$  and  $x_2$ .

In the second order diffraction problems, the pressure distribution on the free surface of the weather side rapidly approaches to a complex constant as shown in Fig.5. Therefore, the same consideration should be paid for solving the boundary value problems.

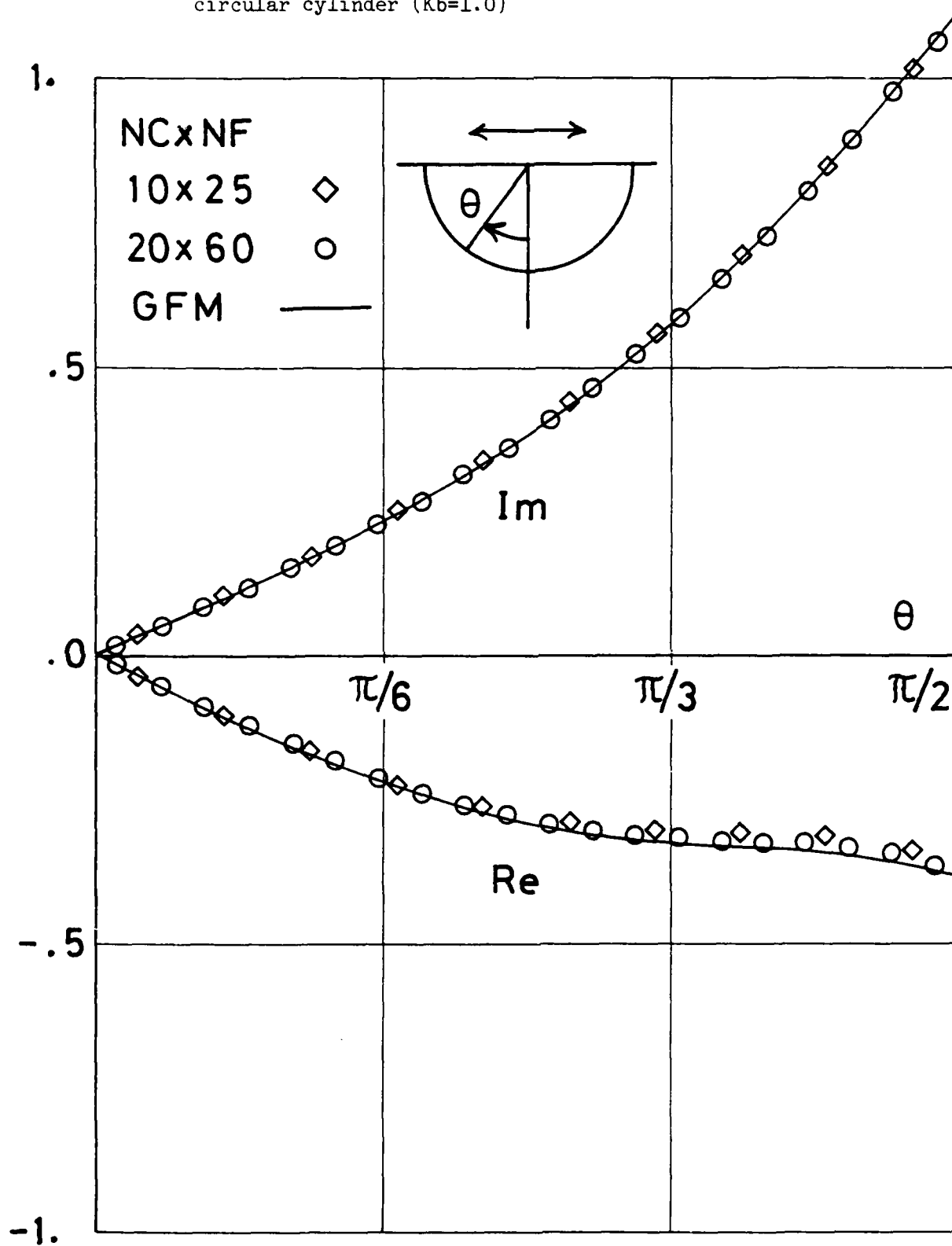
Table 1. Principal dimensions of models

Radiation model (Circular cylinder)	
Half-beam/Draft	1.0
Sectional area coef.	.785
Length (m)	.3
Breadth (m)	.215
Draft (m)	.1075
Displacement (Kg)	5.45
Diffraction model (Lewis-form)	
Half-beam/Draft	1.25
Sectional area coef.	.95
Length (m)	.6
Breadth (m)	.2
Draft (m)	.08
Displacement (Kg)	9.12
Center of gravity : $\overline{OG}/b$	.031
Metacenter height : $\overline{GM}/b$	.080
Radius of gyration : $r_G/b$	1.182
Heave resonance : $Kob(2)$	.75
Roll resonance : $Kob(3)$	.056





Fig. 2 Distribution of the potential on the body for a swaying circular cylinder ( $Kb=1.0$ )



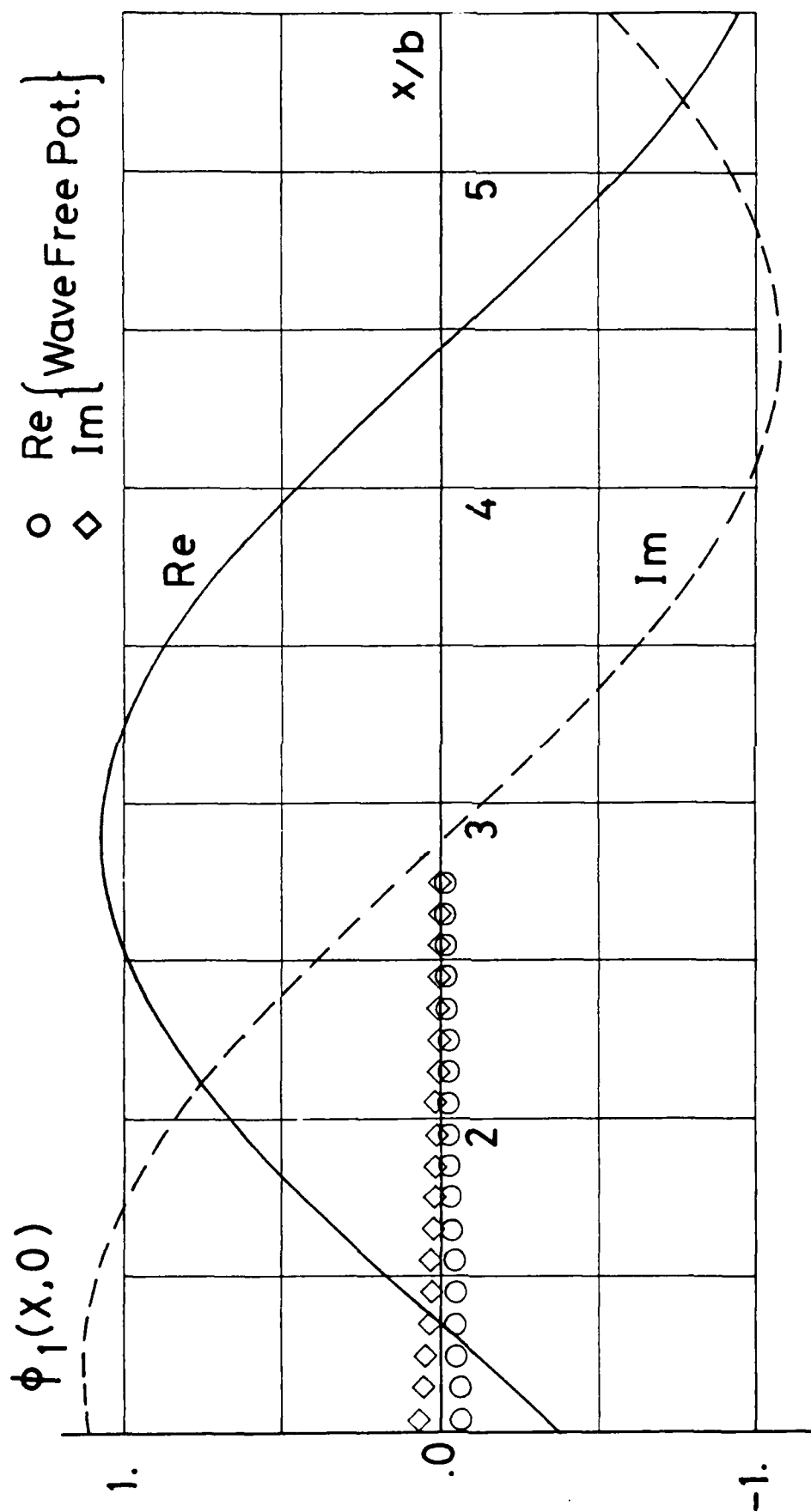


Fig. 3 Distribution of the potential and the wave-free one on the free surface for a swaying circular cylinder ( $Kb=1.0$ )

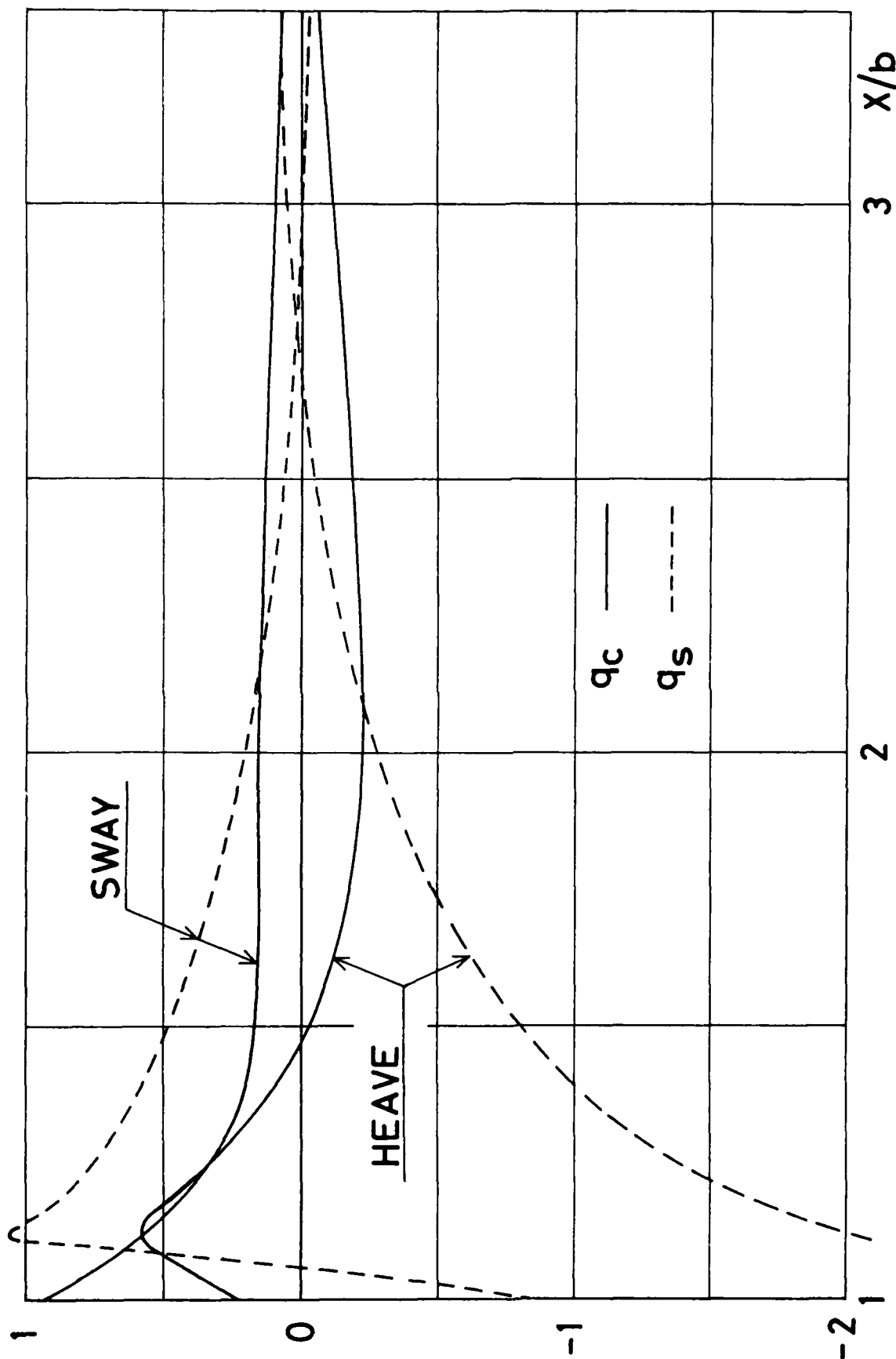


Fig. 4 Pressure distribution on the free surface for a swaying or heaving circular cylinder ( $Kb=1.0$ )

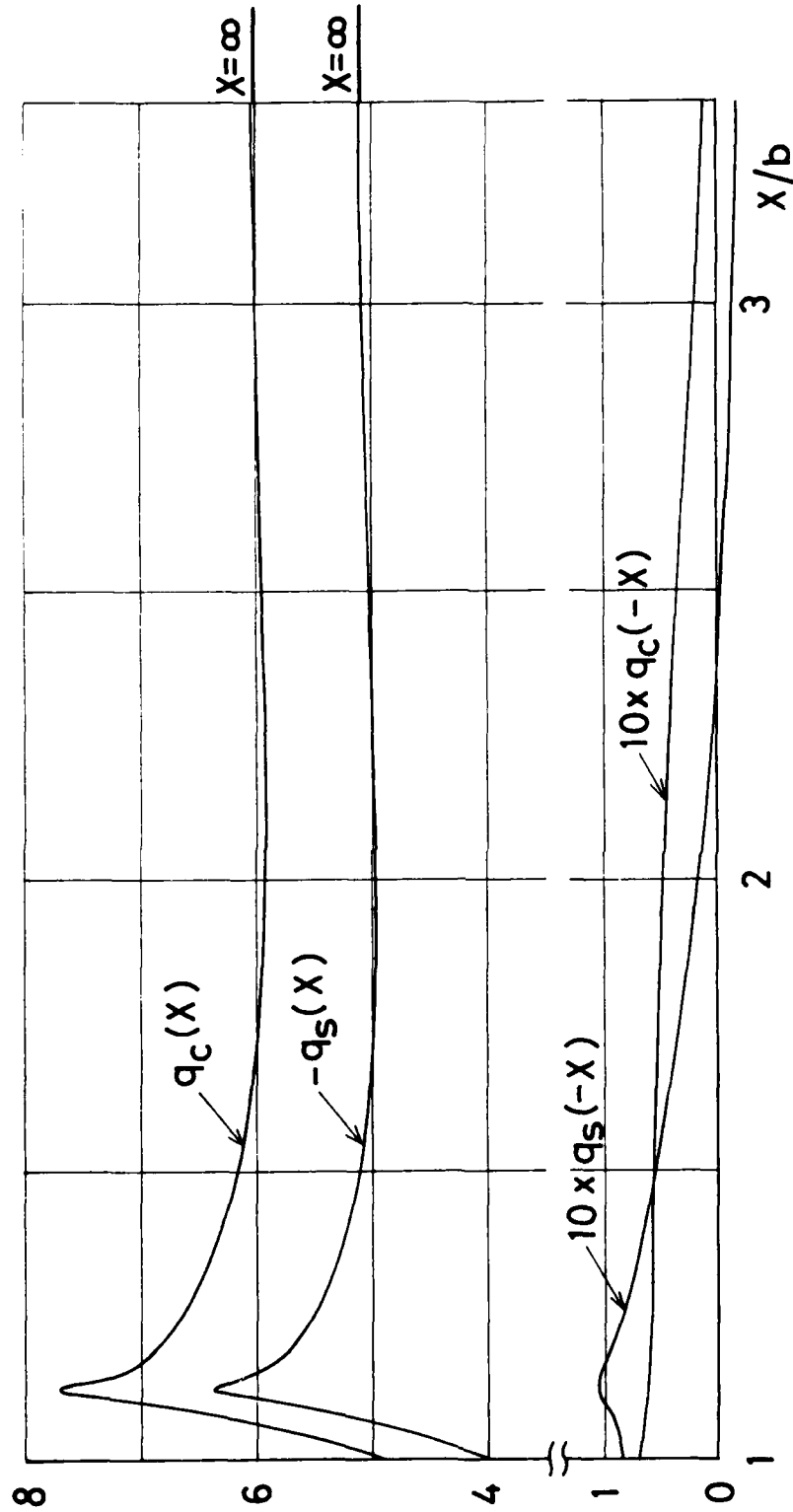


Fig. 5 Pressure distribution on the free surface for a fixed circular cylinder in waves ( $Kb=1.0$ )

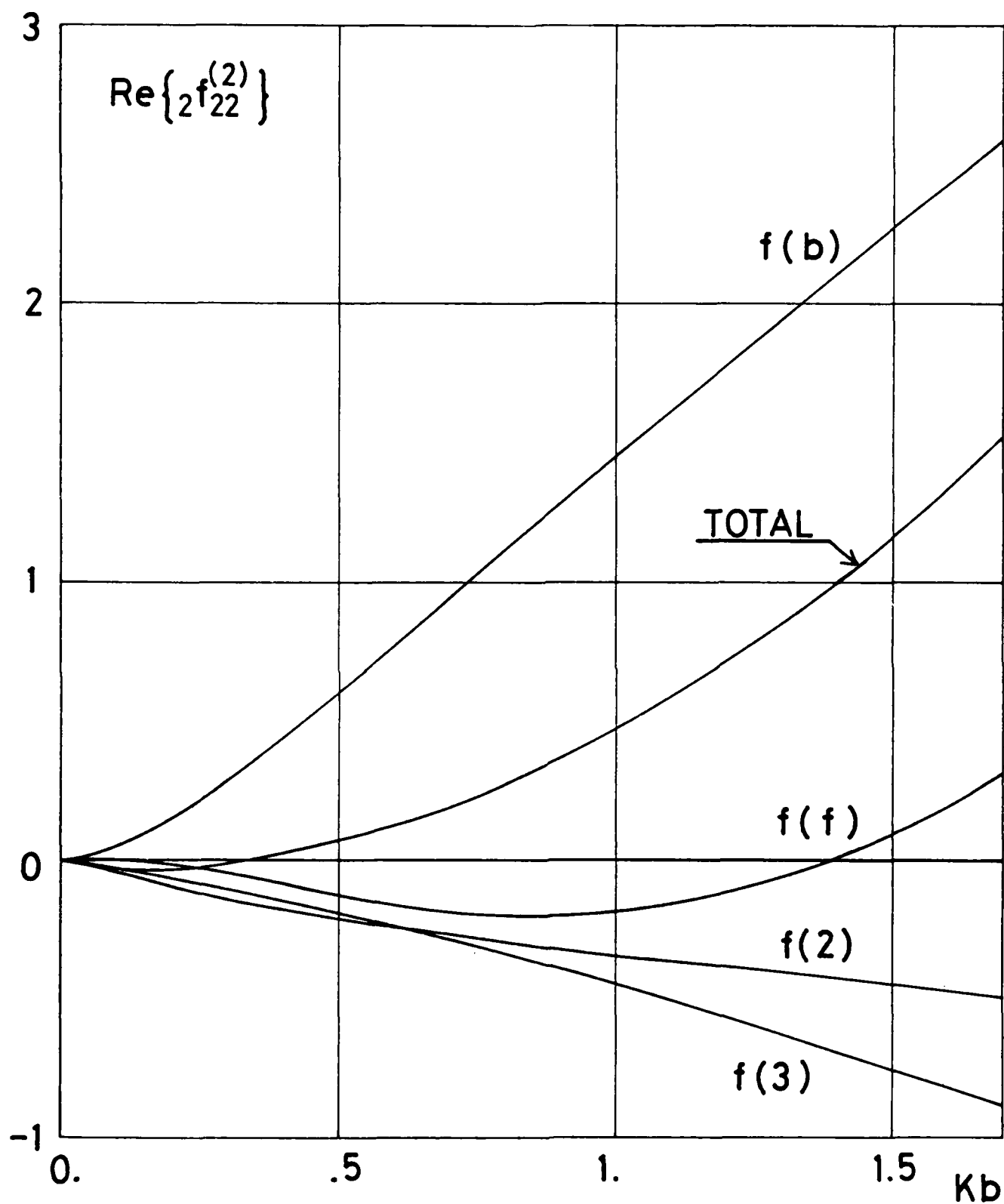


Fig.6(a) Real part of the second order bi-harmonics for a heaving circular cylinder

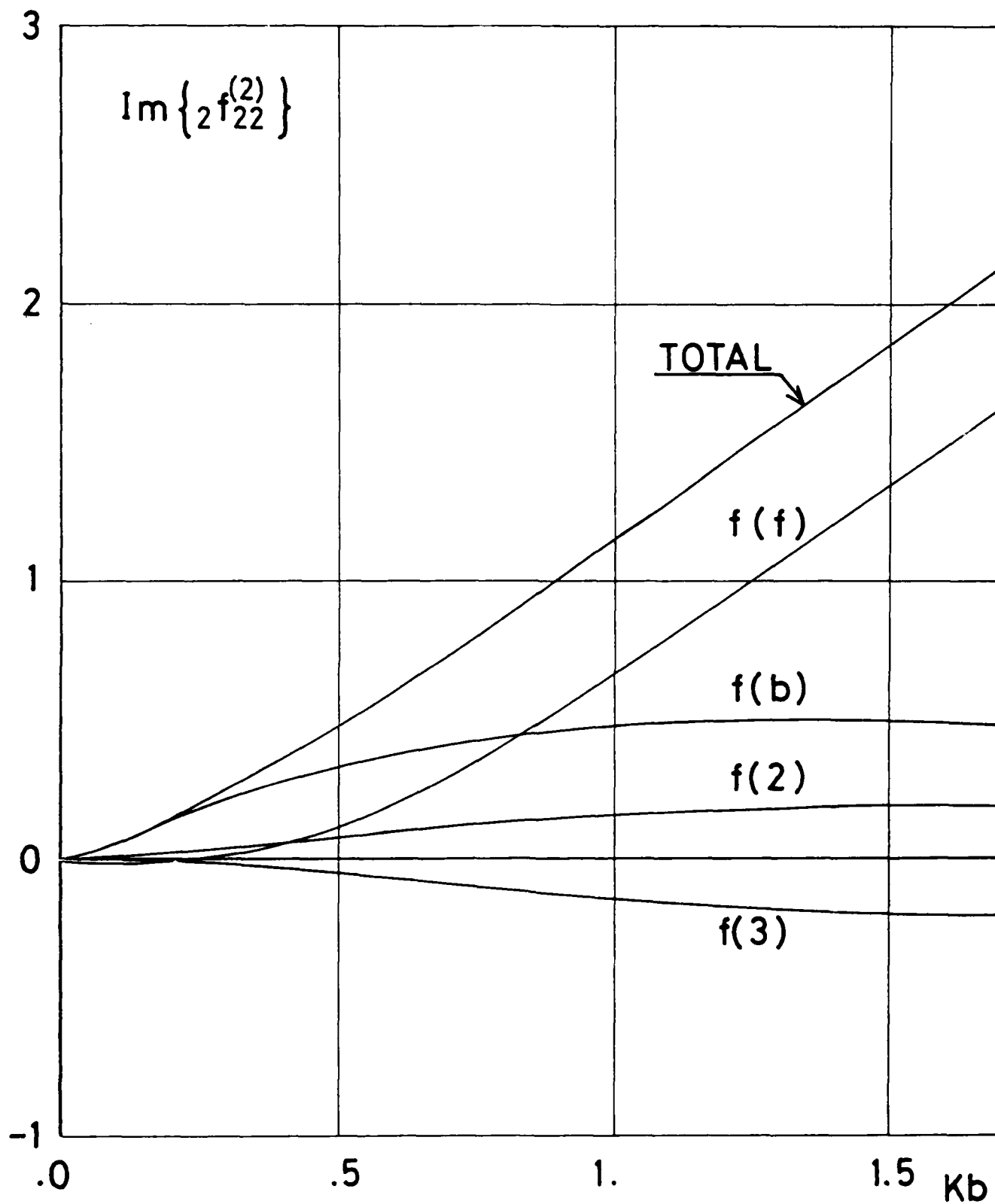


Fig.6(b) Imaginary part of the second order bi-harmonics for a heaving circular cylinder

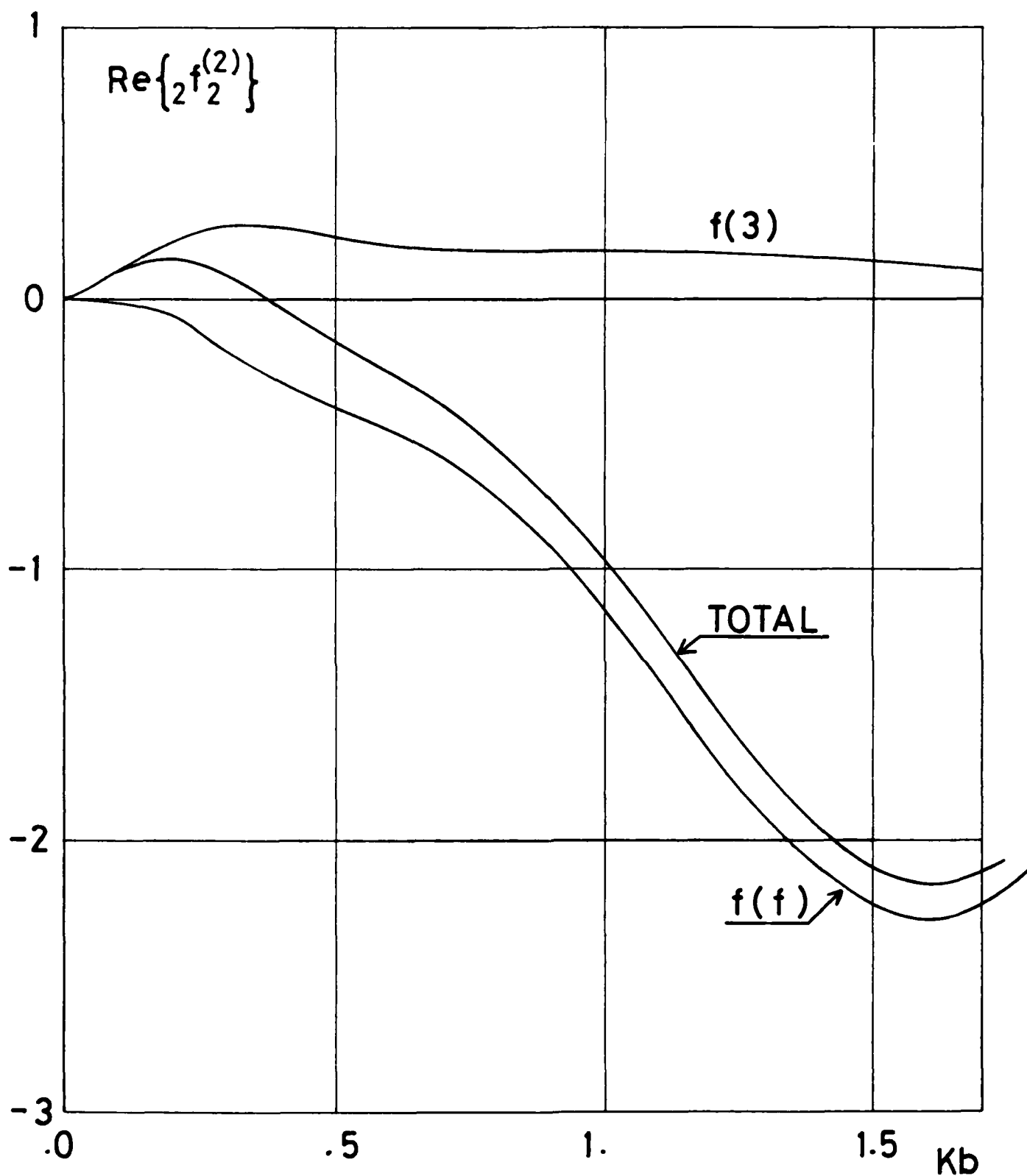


Fig.7(a) Real part of the second order vertical bi-harmonics for a fixed circular cylinder in waves

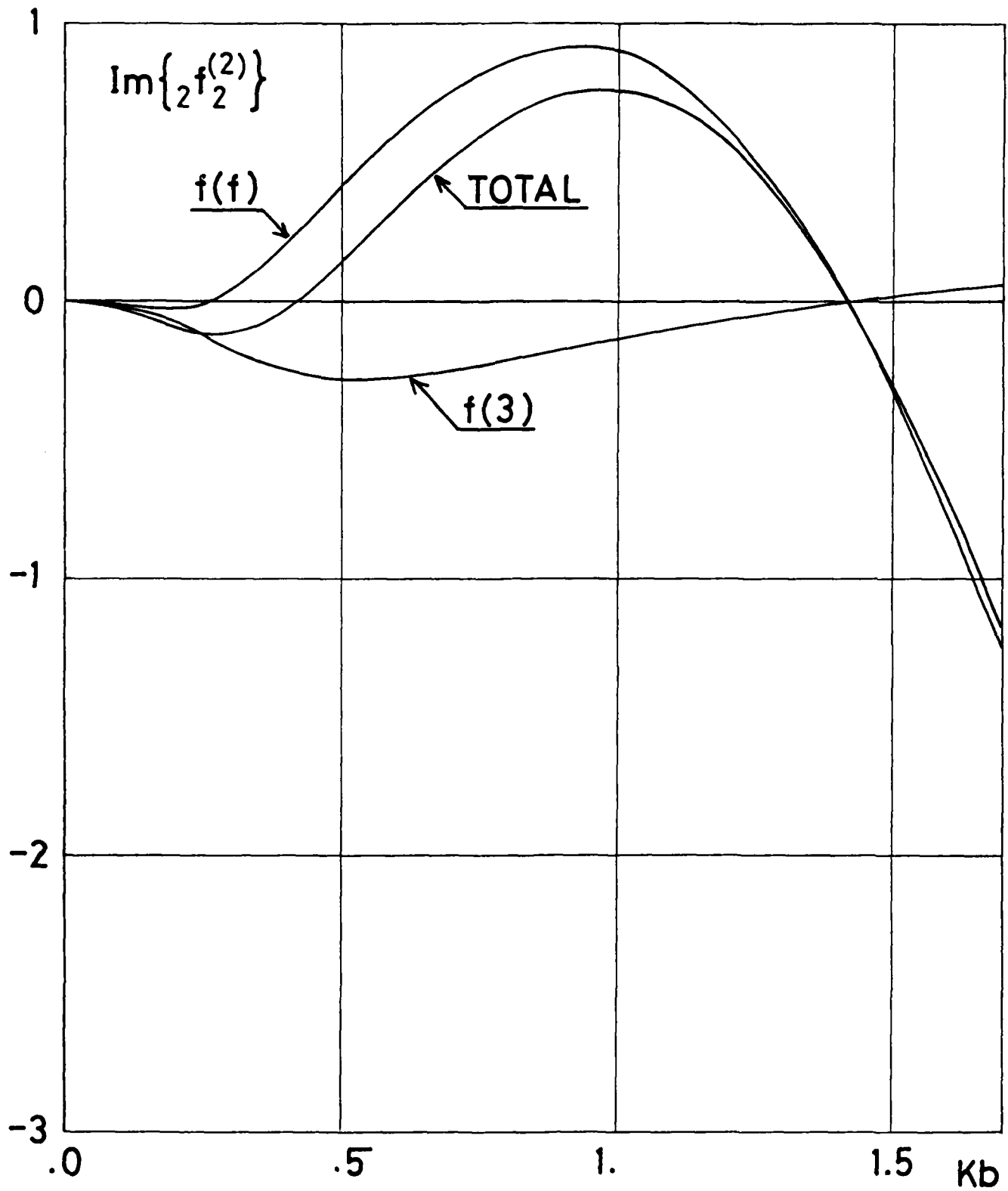


Fig.7(b) Imaginary part of the second order vertical bi-harmonics for a fixed circular cylinder in waves



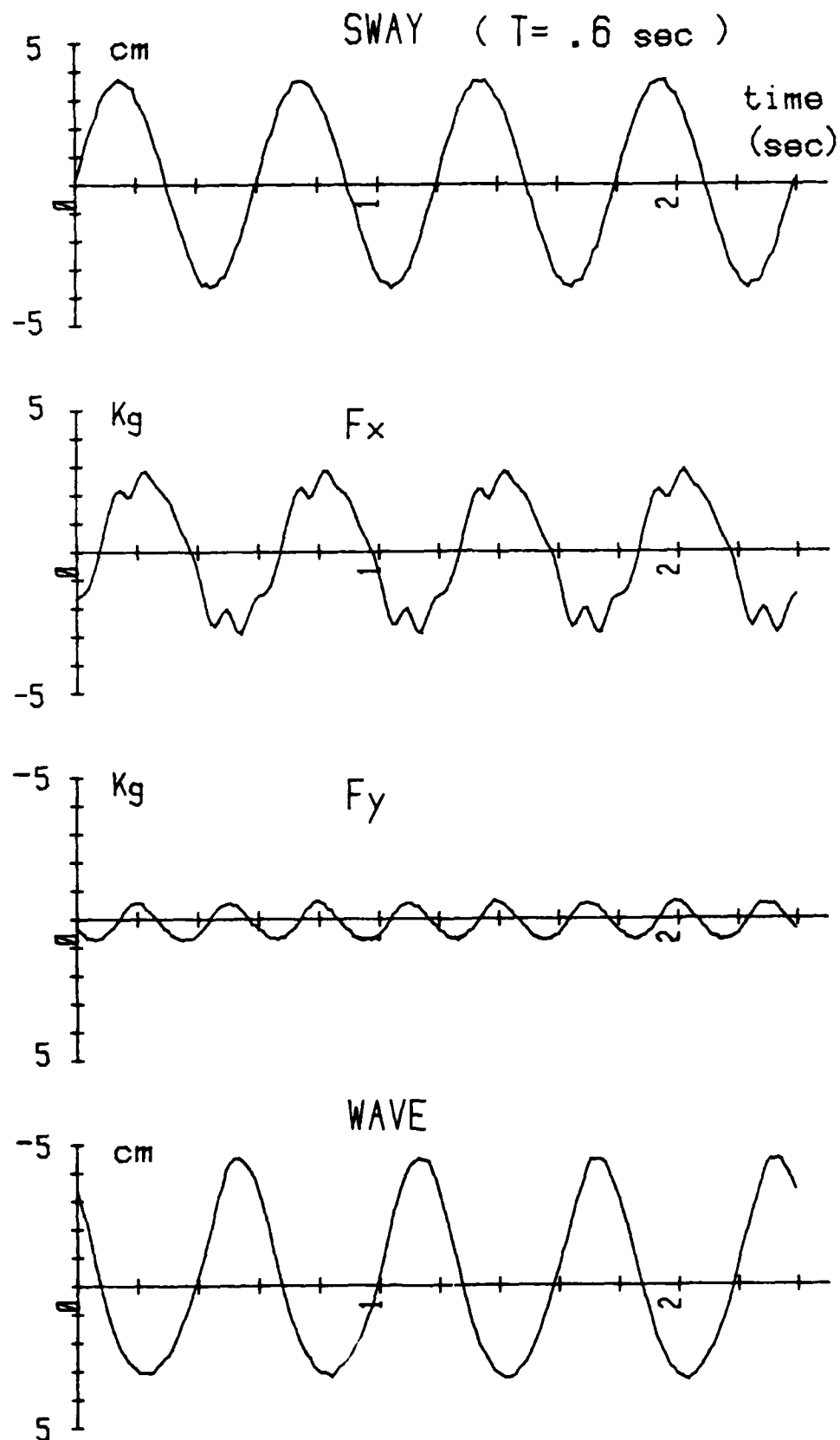


Fig. 8 An example of the experimental records for a swaying circular cylinder

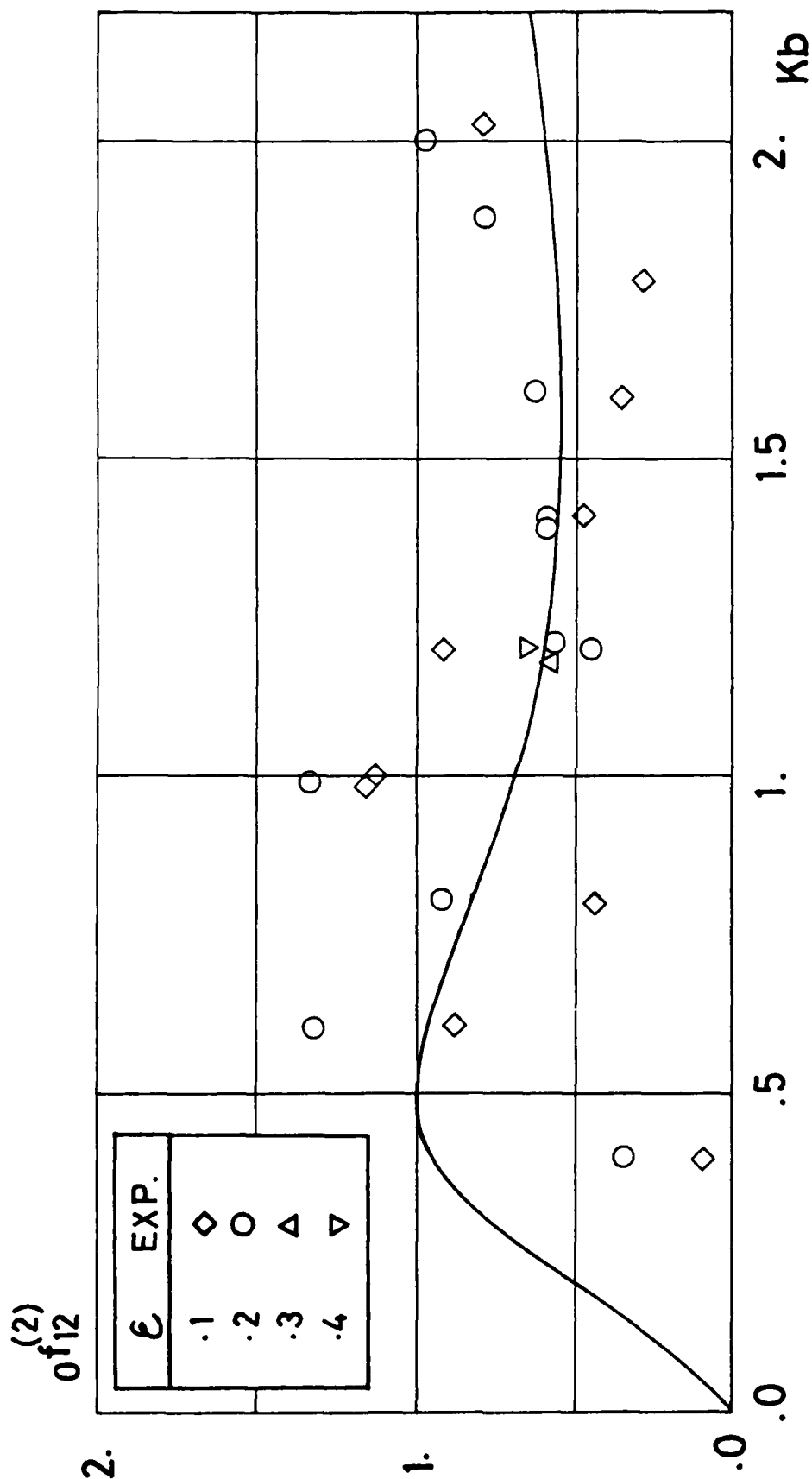


Fig. 9 Second order steady sinkage force of a swaying circular cylinder

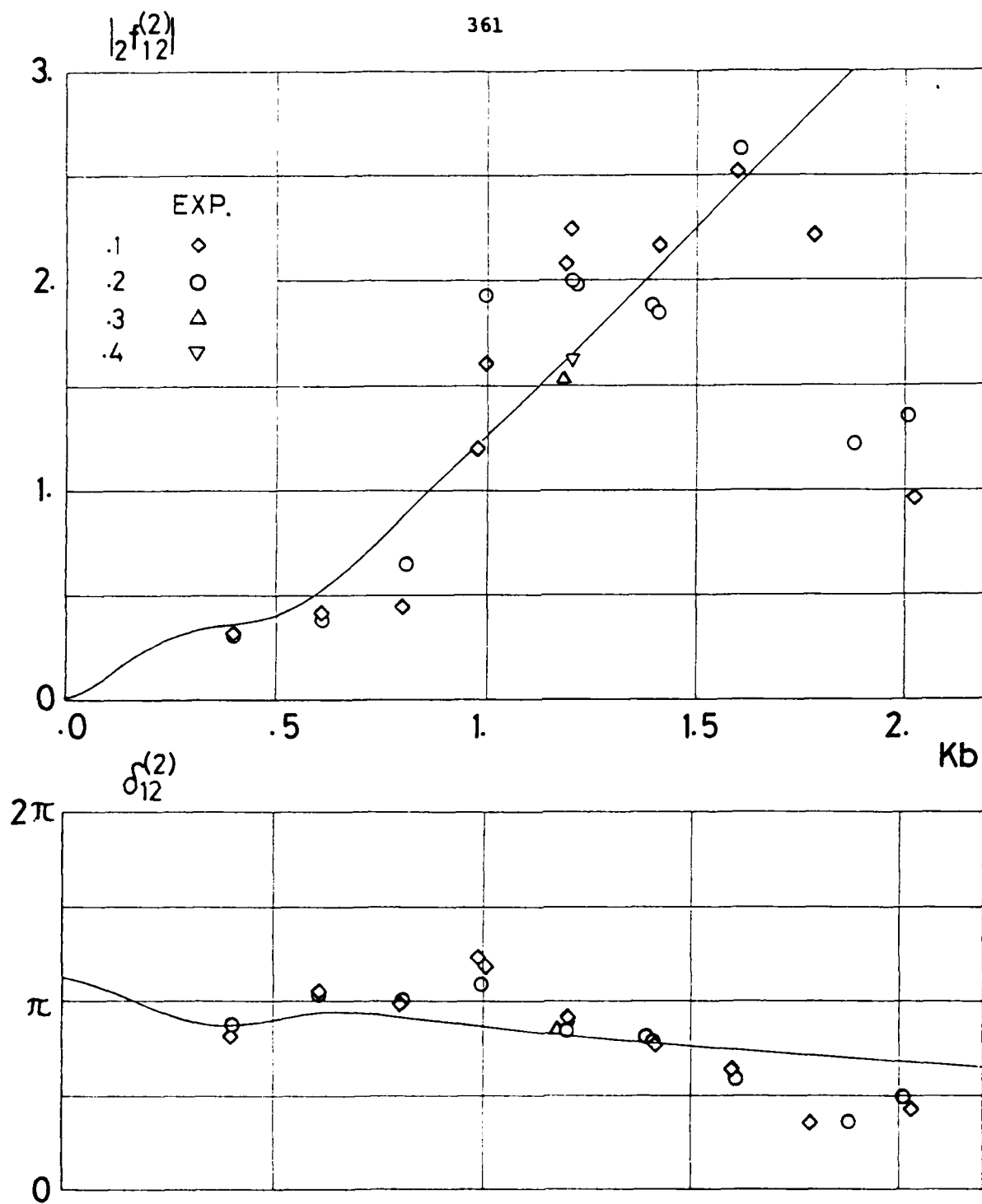


Fig.10 Second order bi-harmonics of a swaying circular cylinder

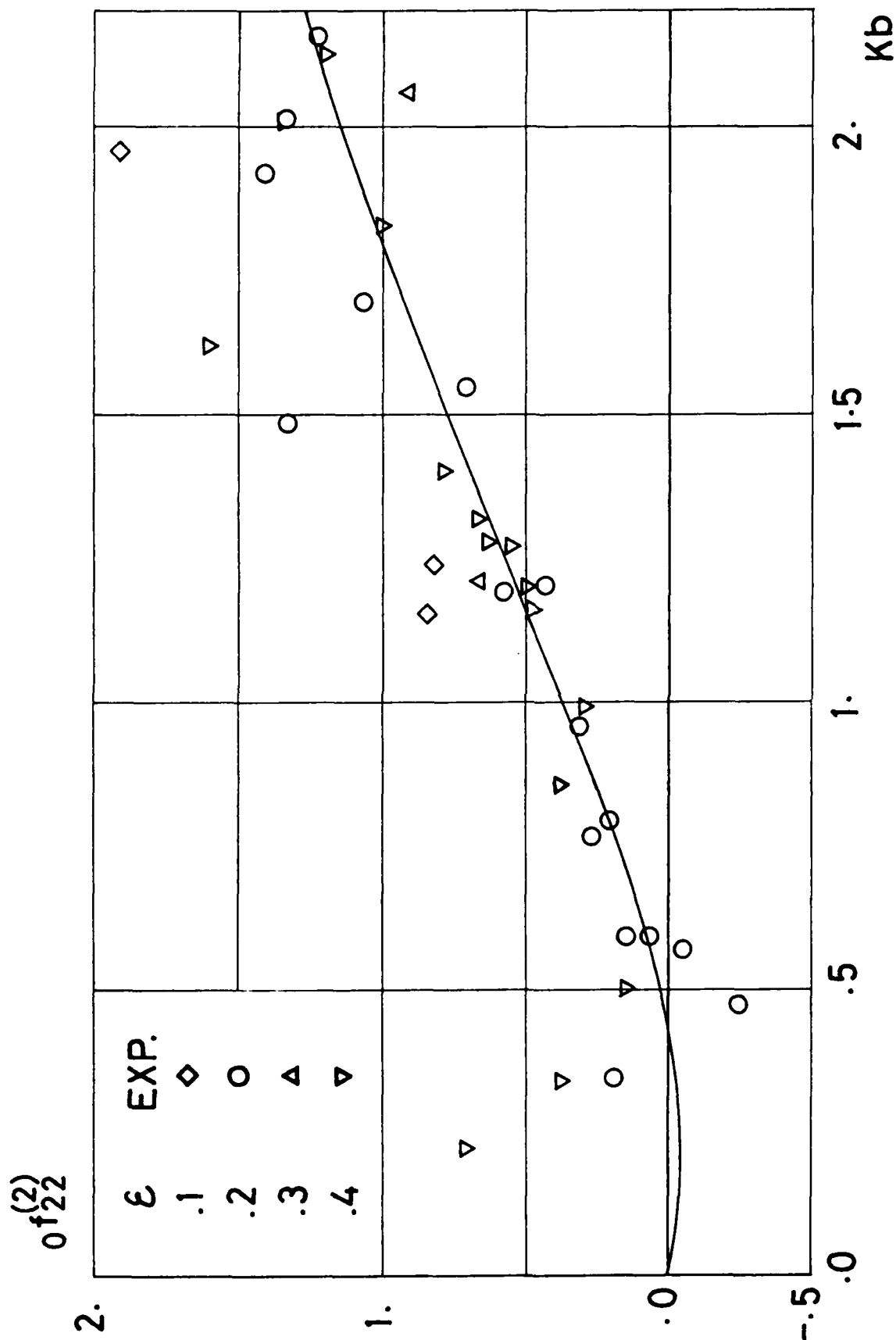


Fig.11 Second order steady sinkage force of a heaving circular cylinder

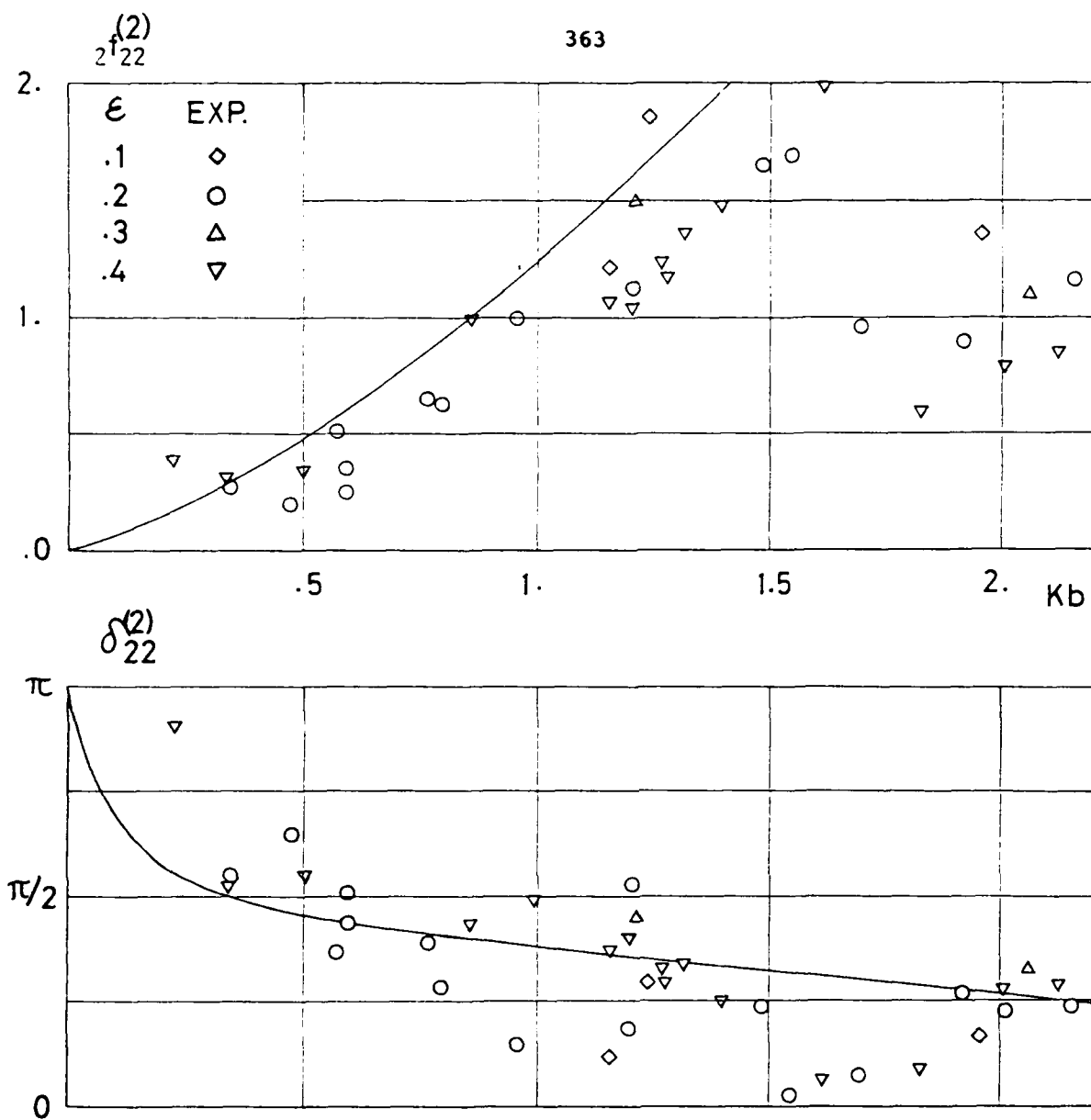


Fig.12 Second order bi-harmonics of a heaving circular cylinder

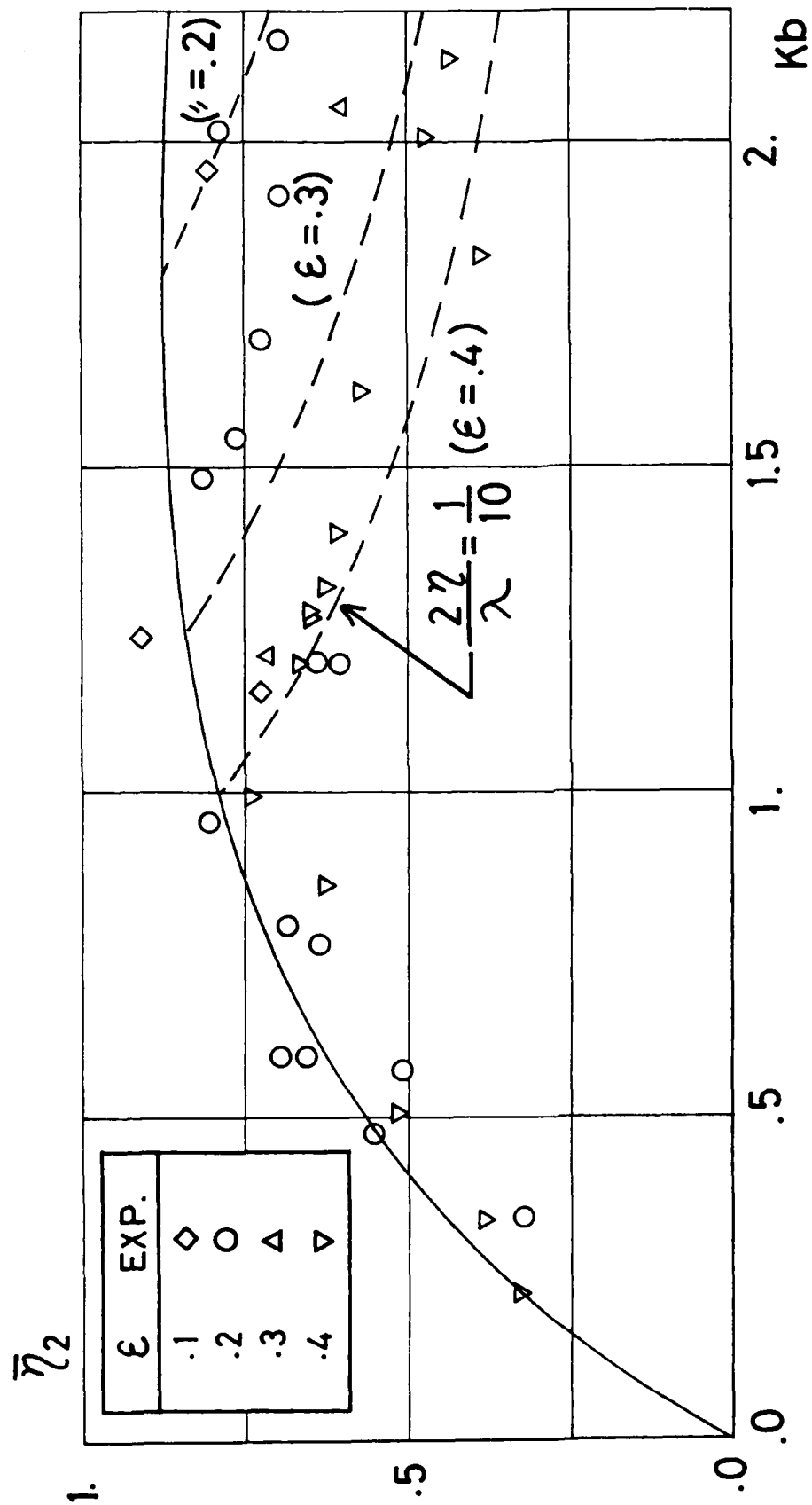


Fig.13 Progressing wave amplitudes of a heaving circular cylinder

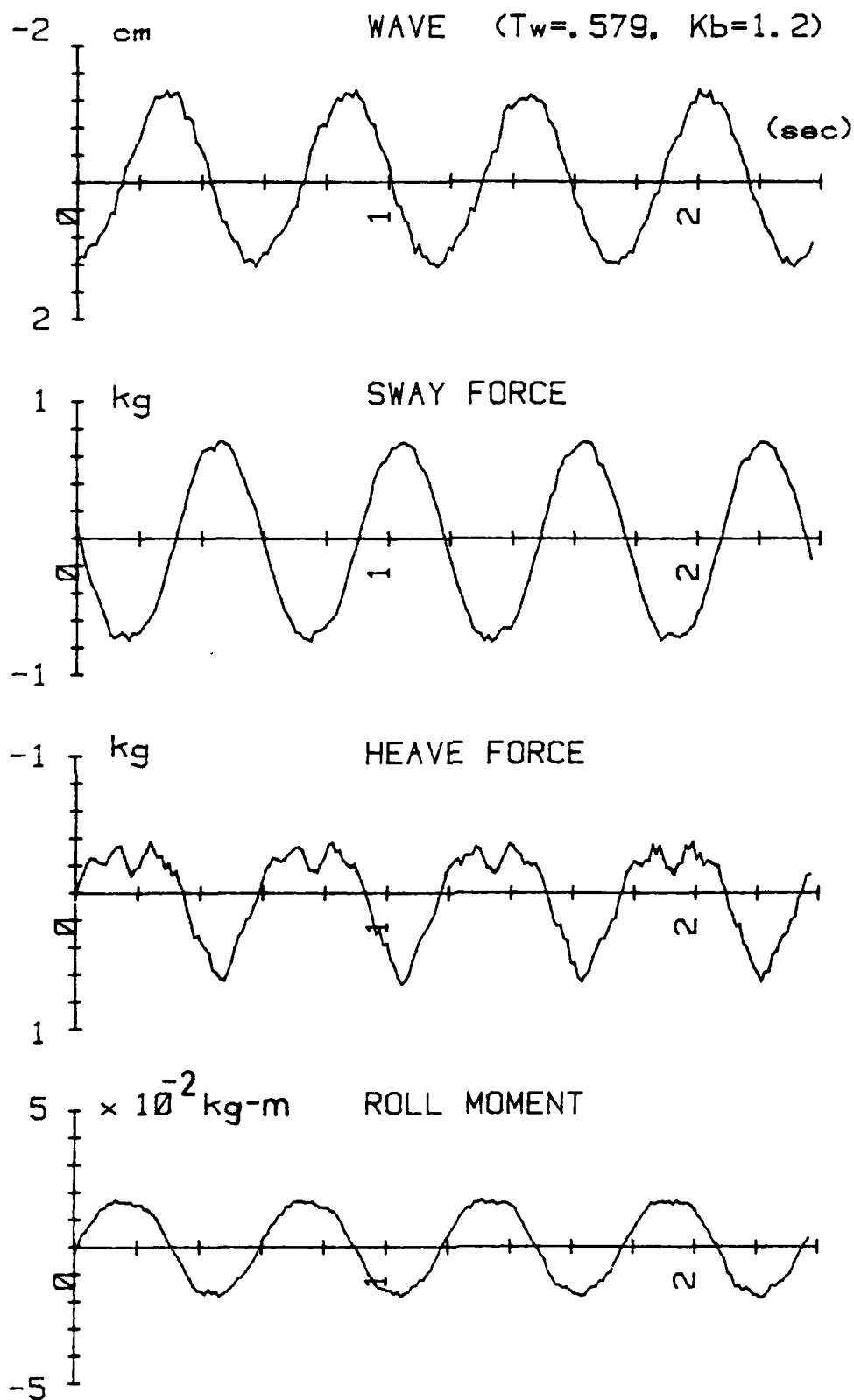


Fig.14 An example of the experimental records for a fixed Lewis-form cylinder in waves

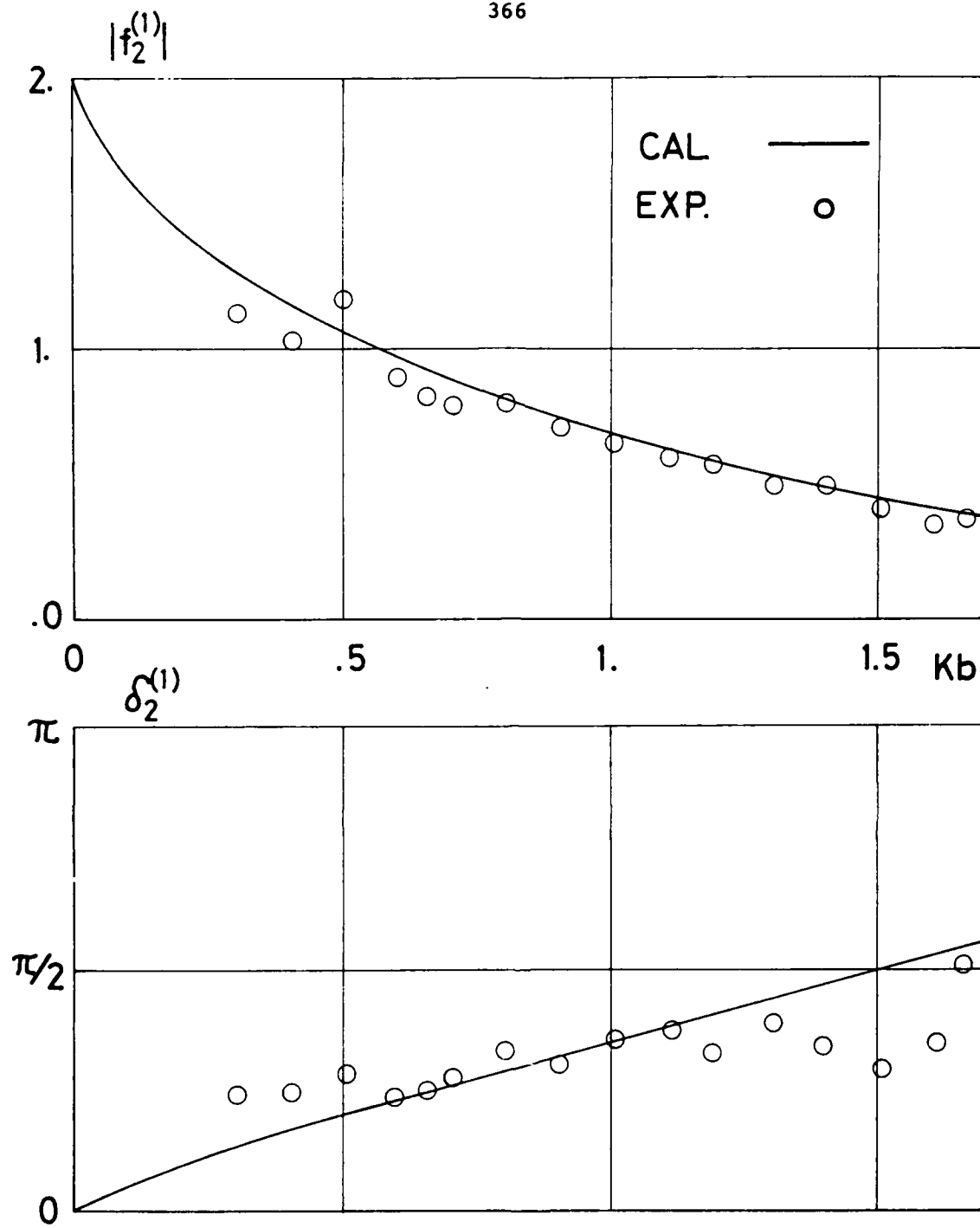


Fig.15 First order vertical wave exciting force of a Lewis-form cylinder in waves



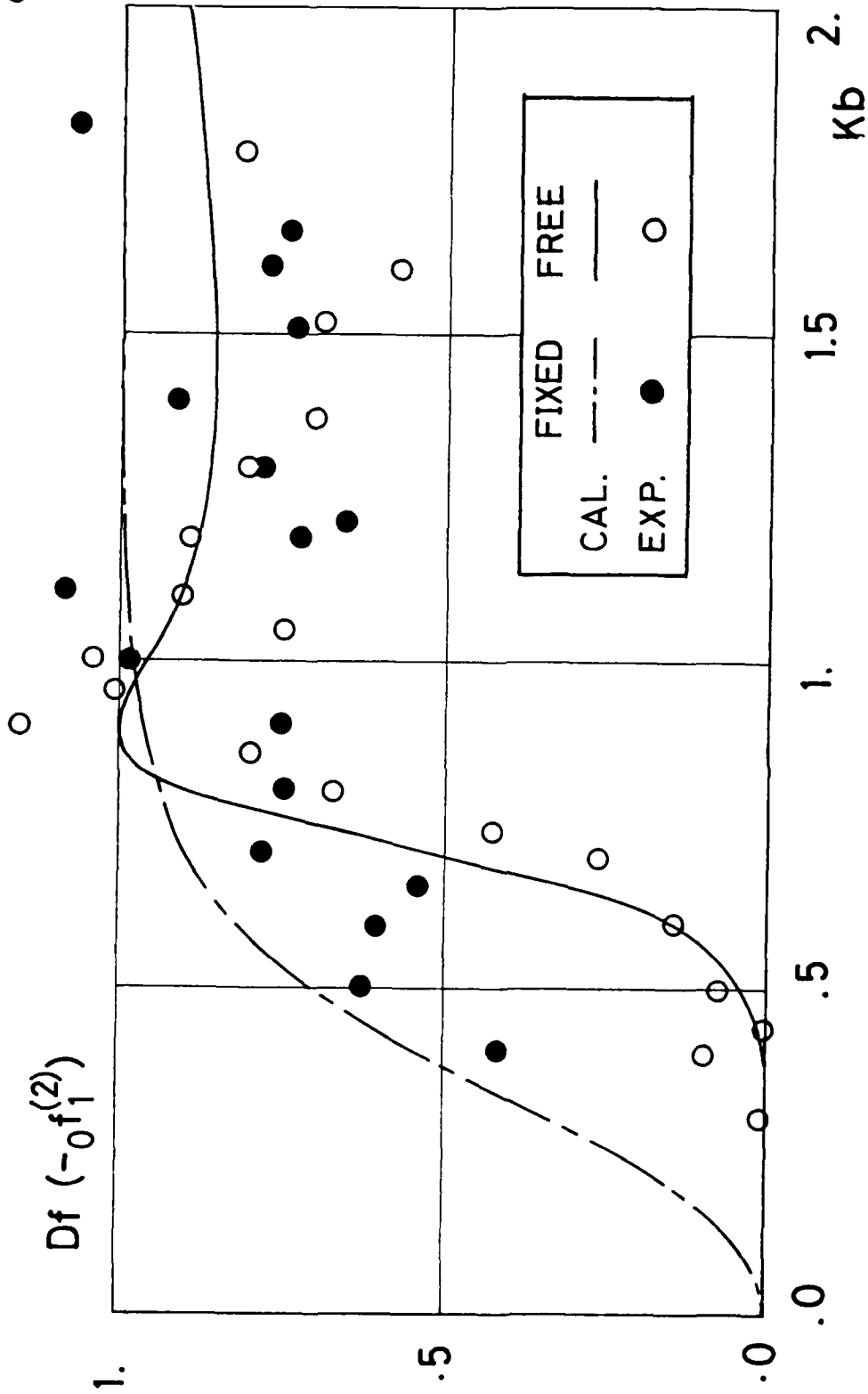


Fig.16 Drifting forces of a fixed and free-floating Lewis-form cylinder in waves

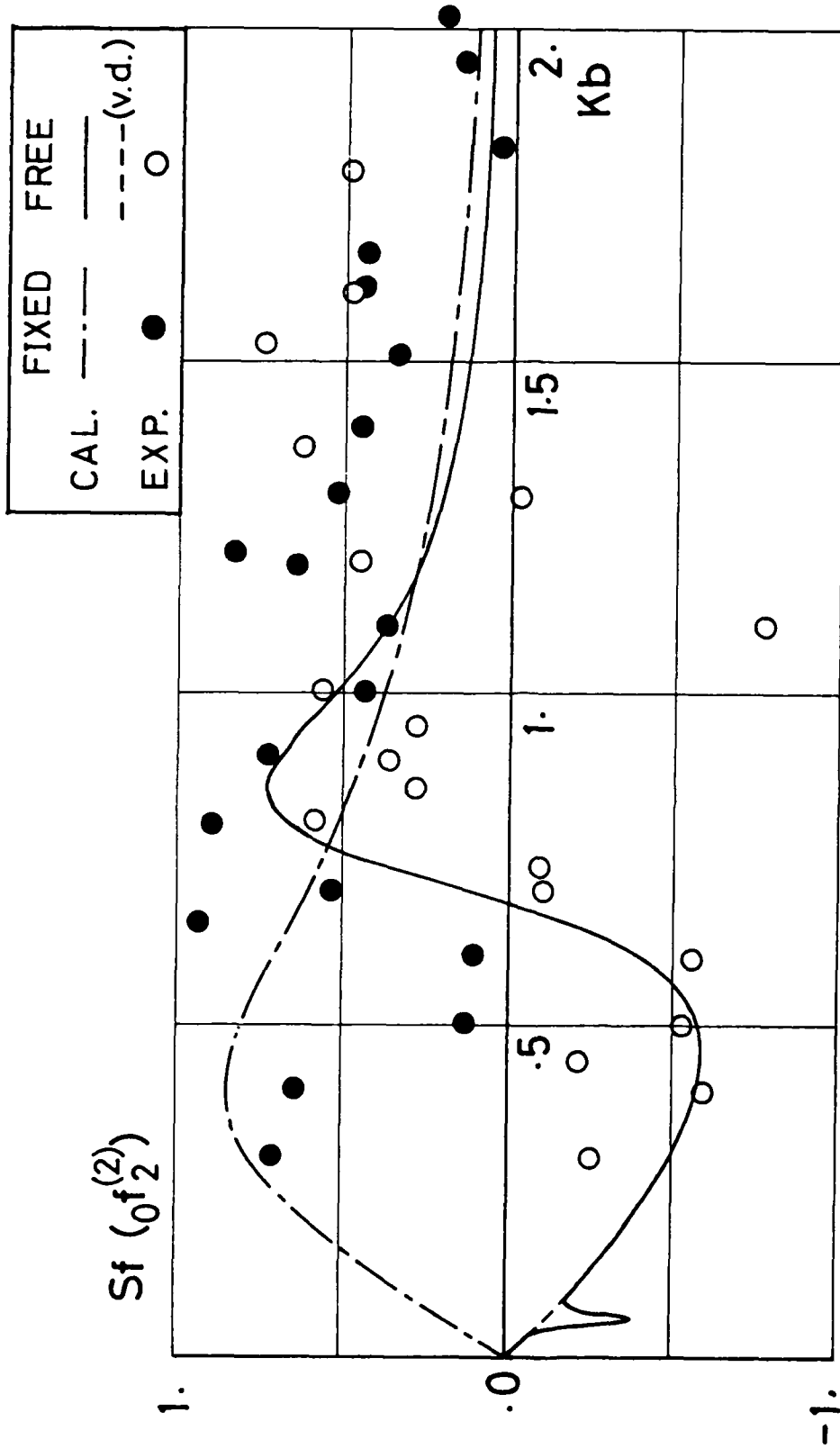


Fig.17 Steady sinkage forces of a fixed and free-floating Lewis-form cylinder in waves

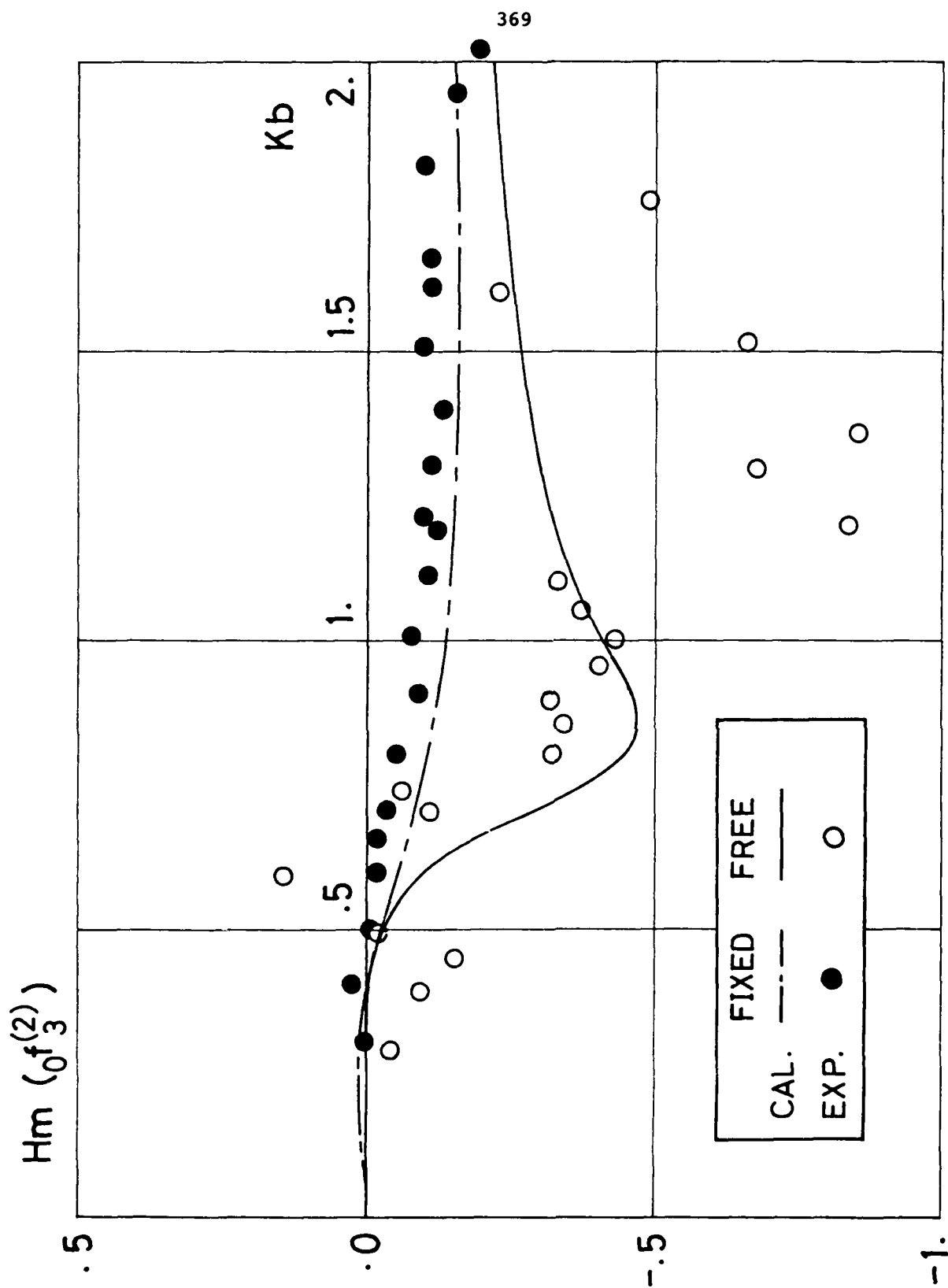


Fig.18 Steady heeling moments of a fixed and free-floating Lewis-form cylinder in waves

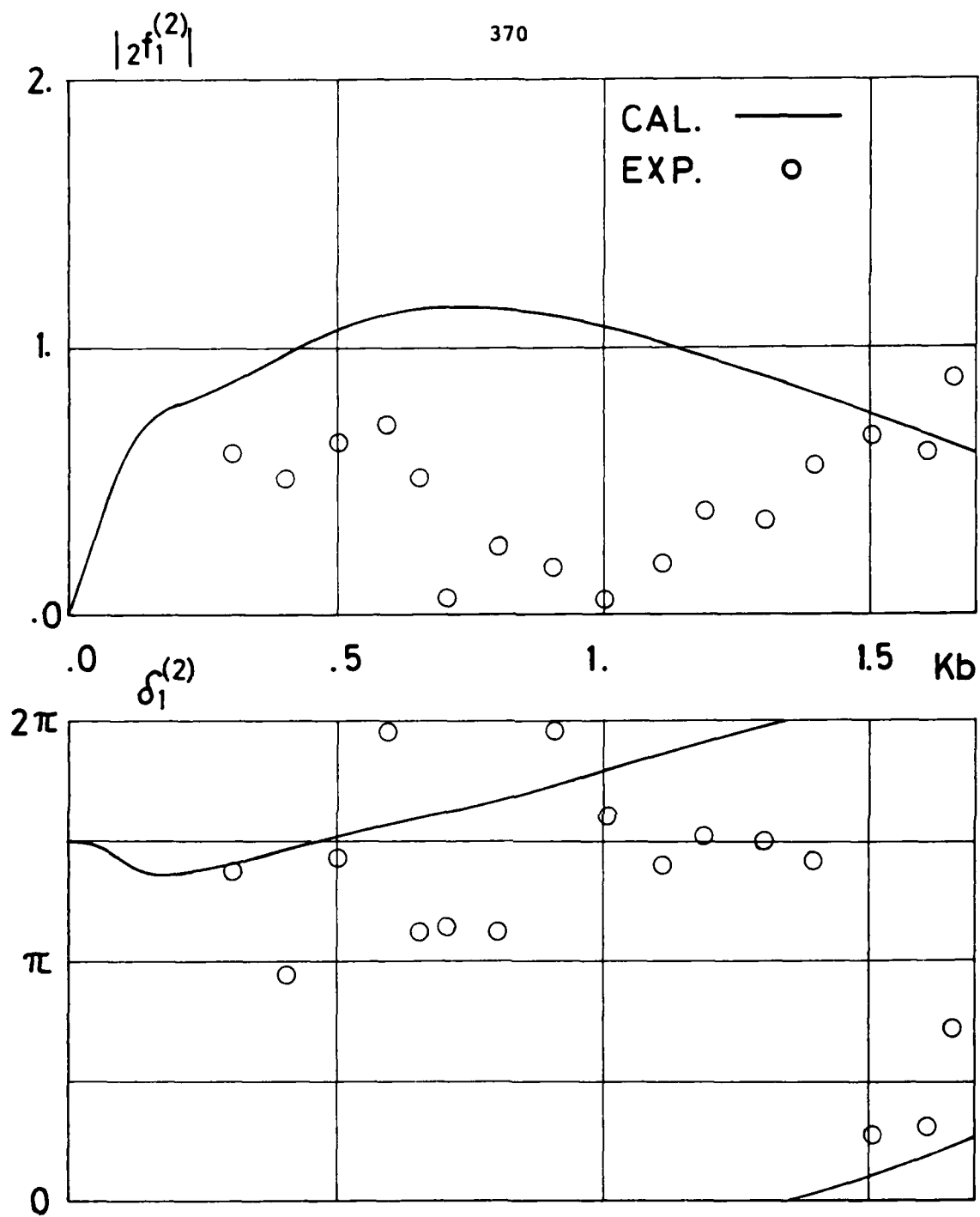


Fig.19 Second order swaying bi-harmonics of a fixed Lewis-form cylinder in waves

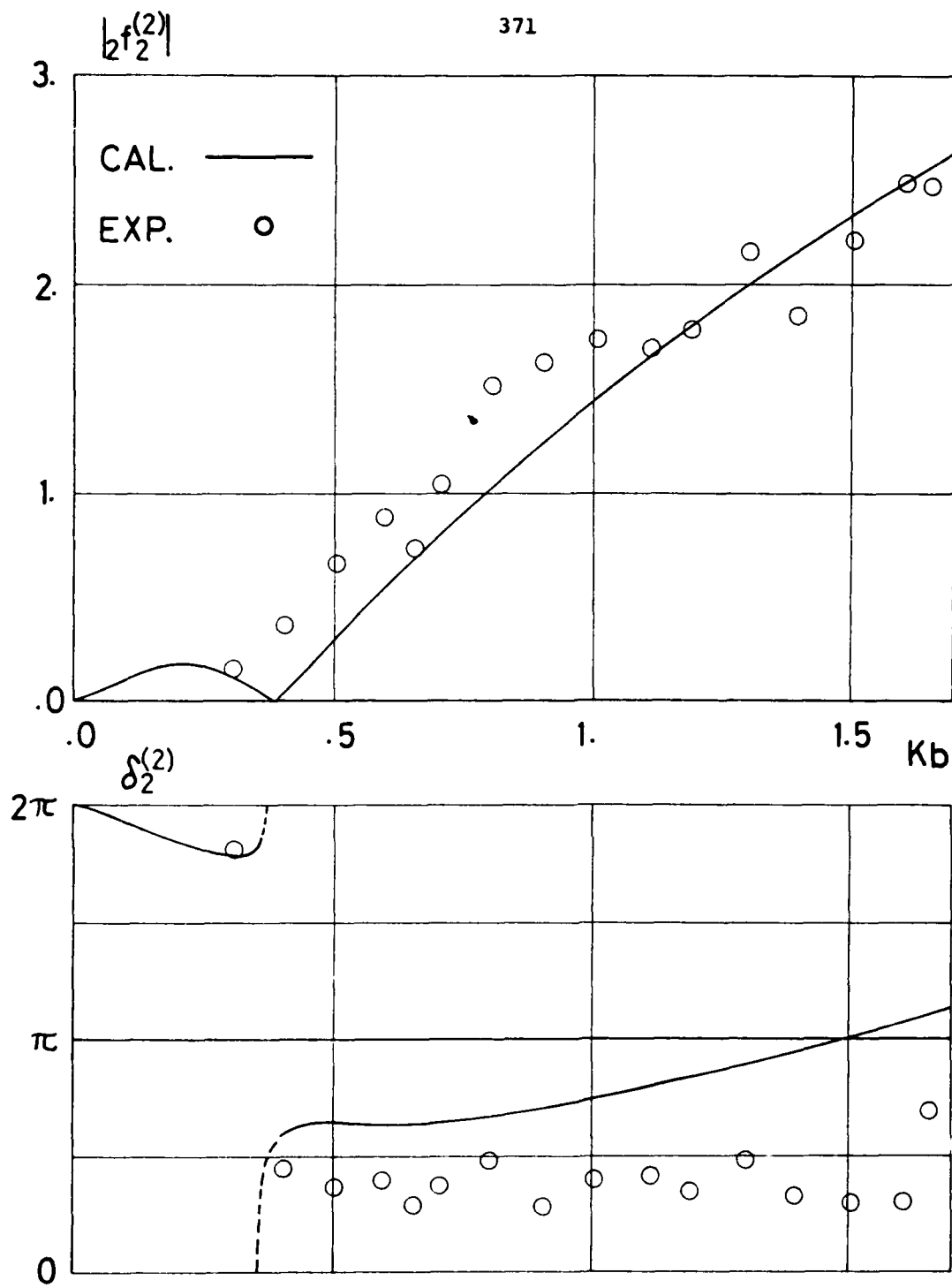


Fig.20 Second order heaving bi-harmonics of a fixed Lewis-form cylinder in waves

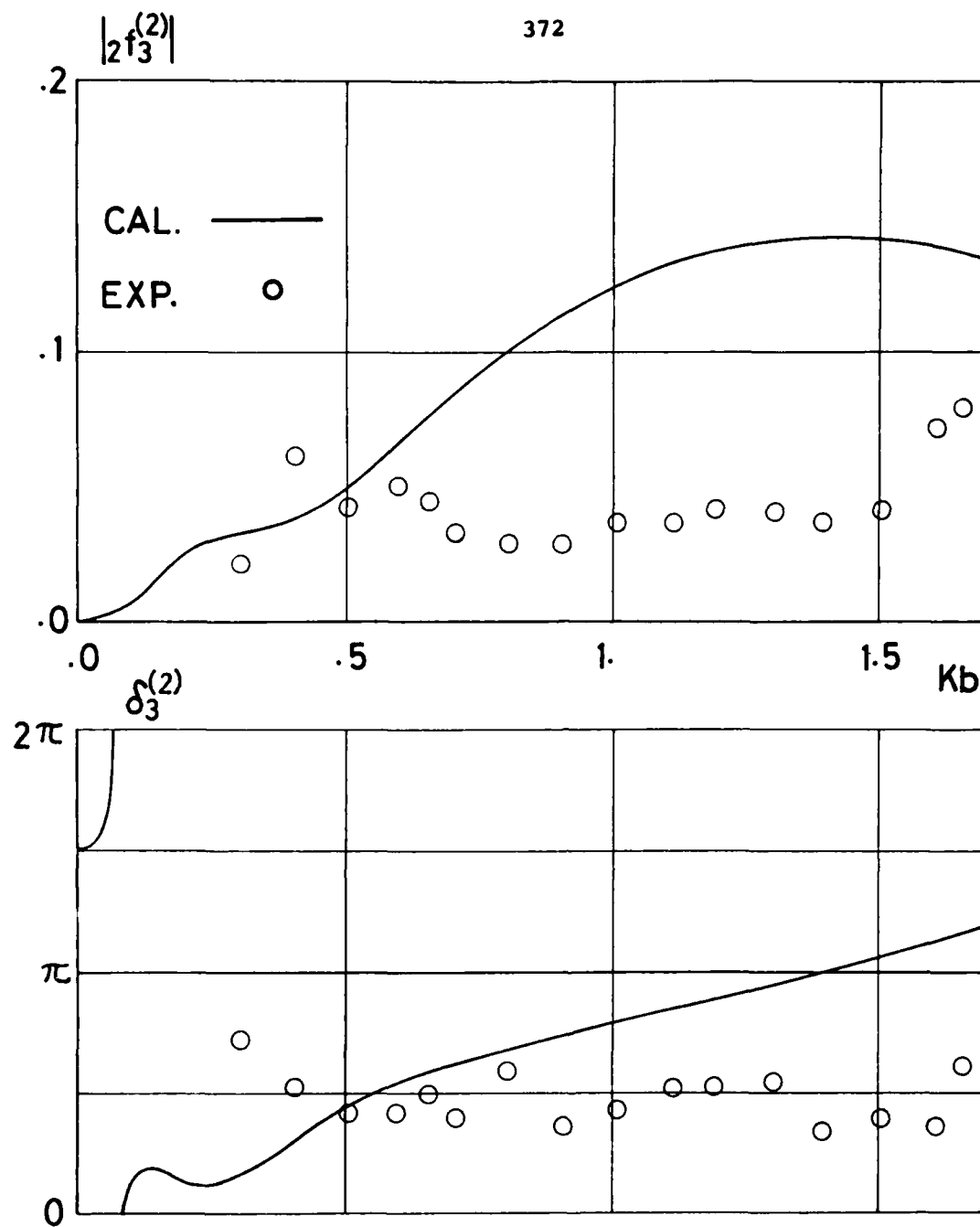


Fig.21 Second order rolling bi-harmonics of a fixed Lewis-form cylinder in waves

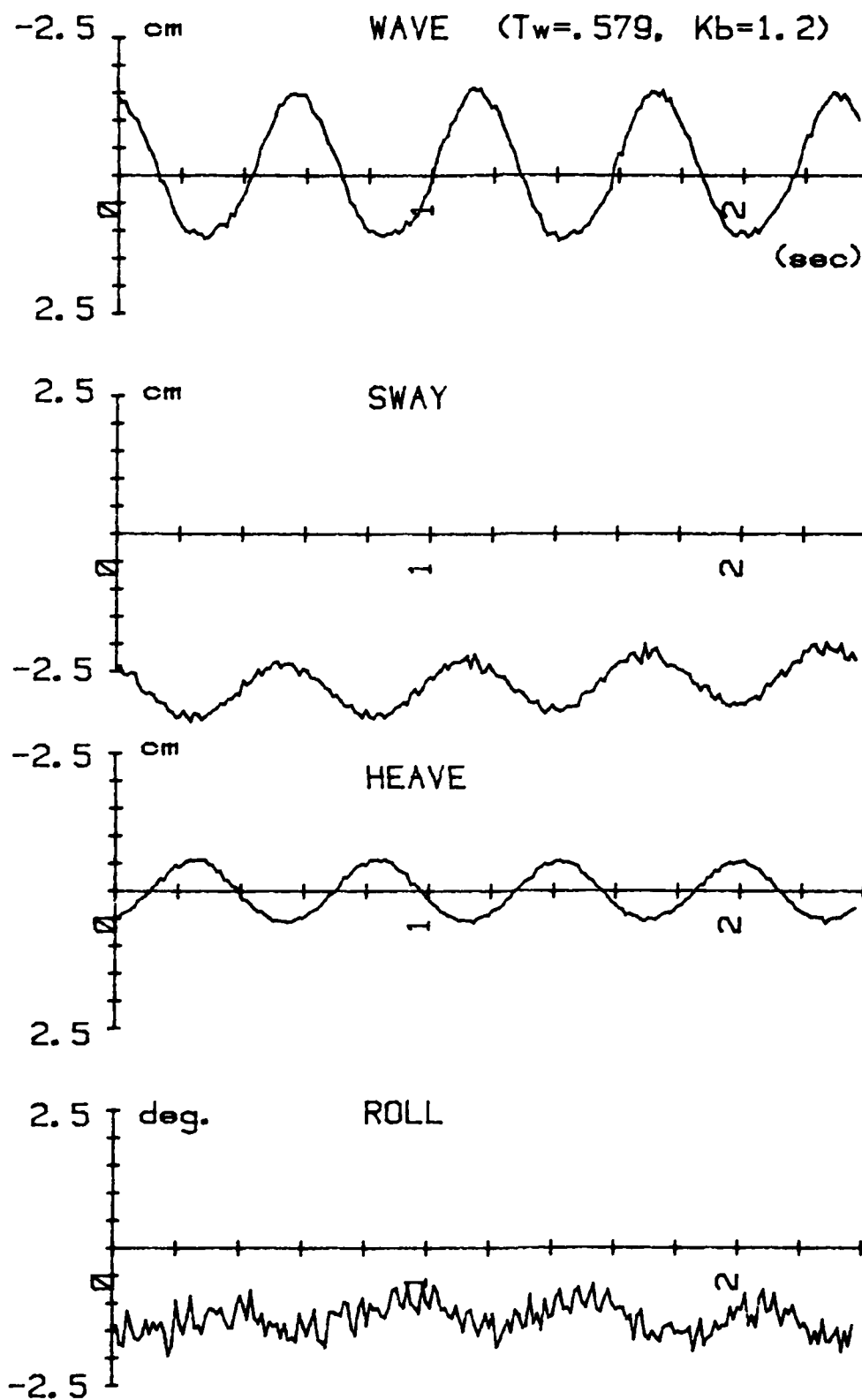


Fig.22 An example of experimental records of motions of a Lewis-form cylinder in waves

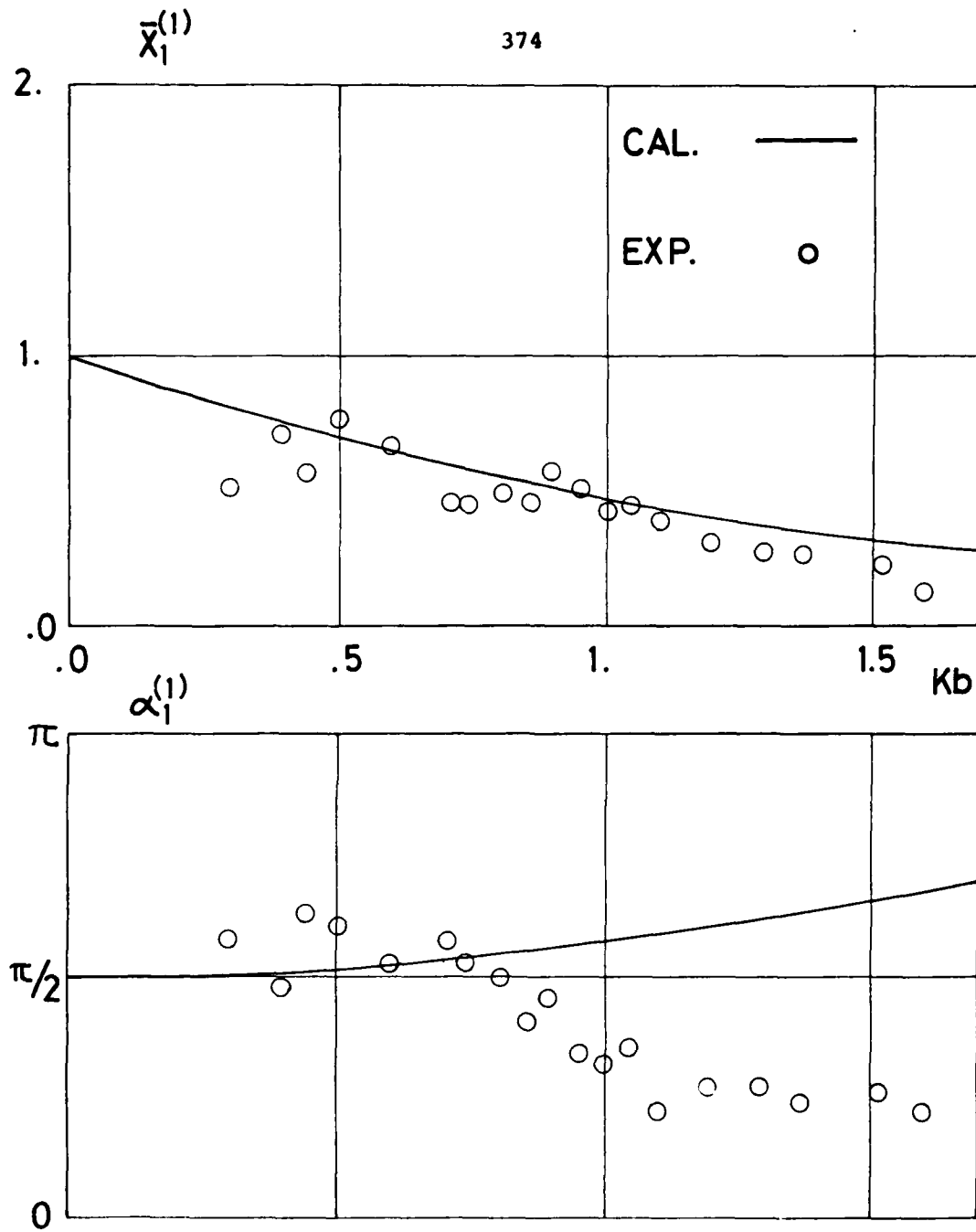


Fig.23 The first order swaying response of a Lewis-form cylinder in waves



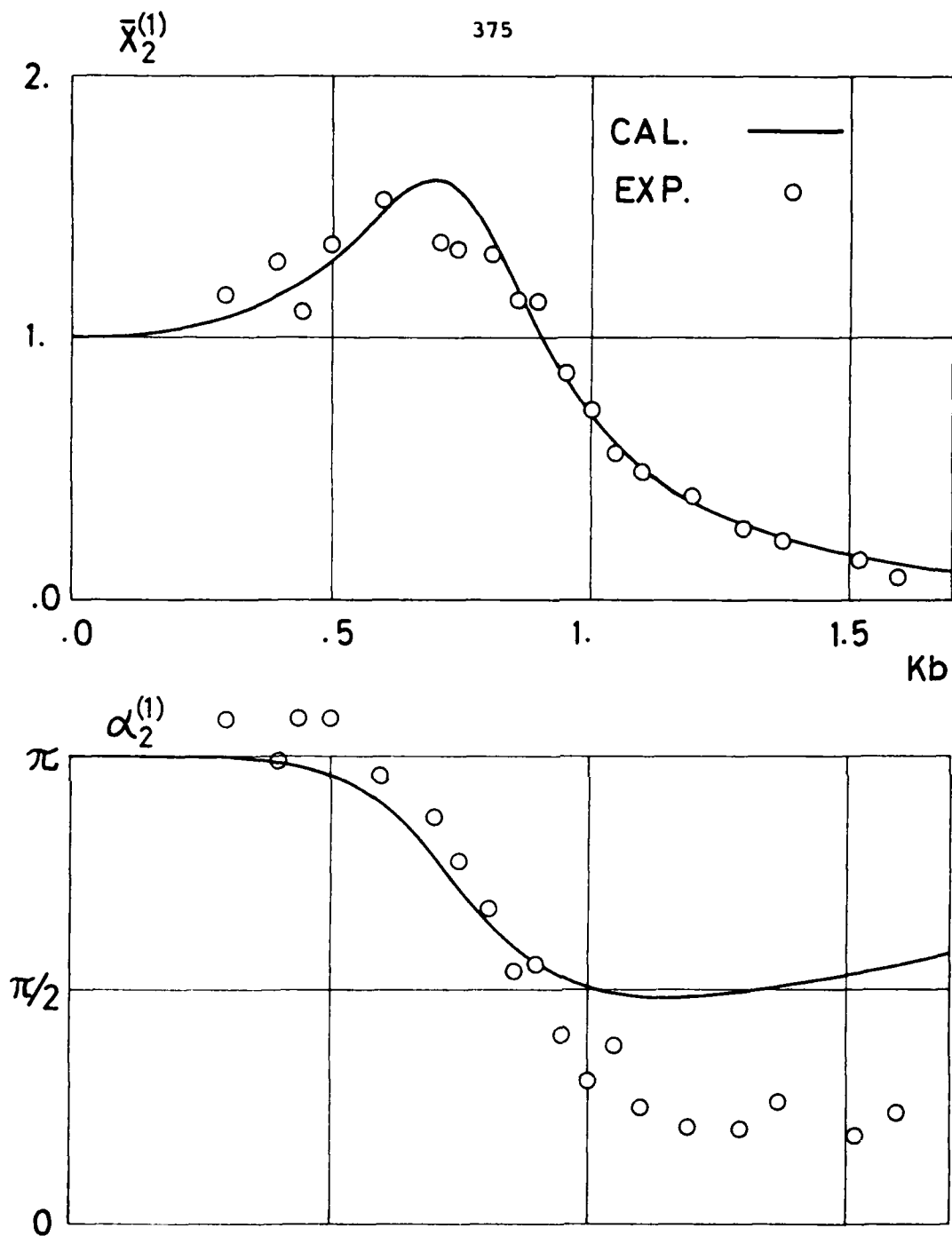


Fig. 24 The first order heaving response of a Lewis-form cylinder in waves

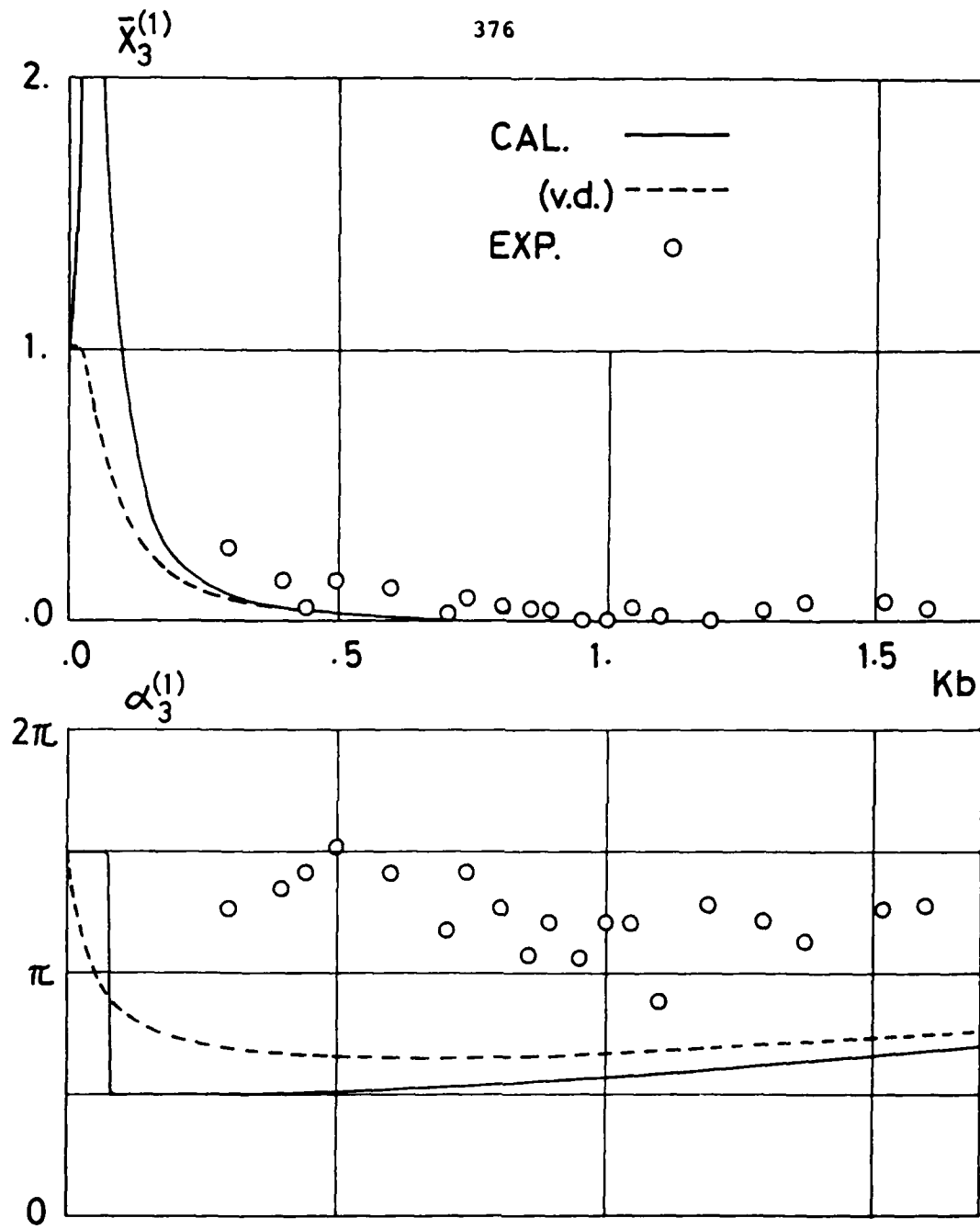


Fig.25 The first order rolling response of a Lewis-form cylinder in waves

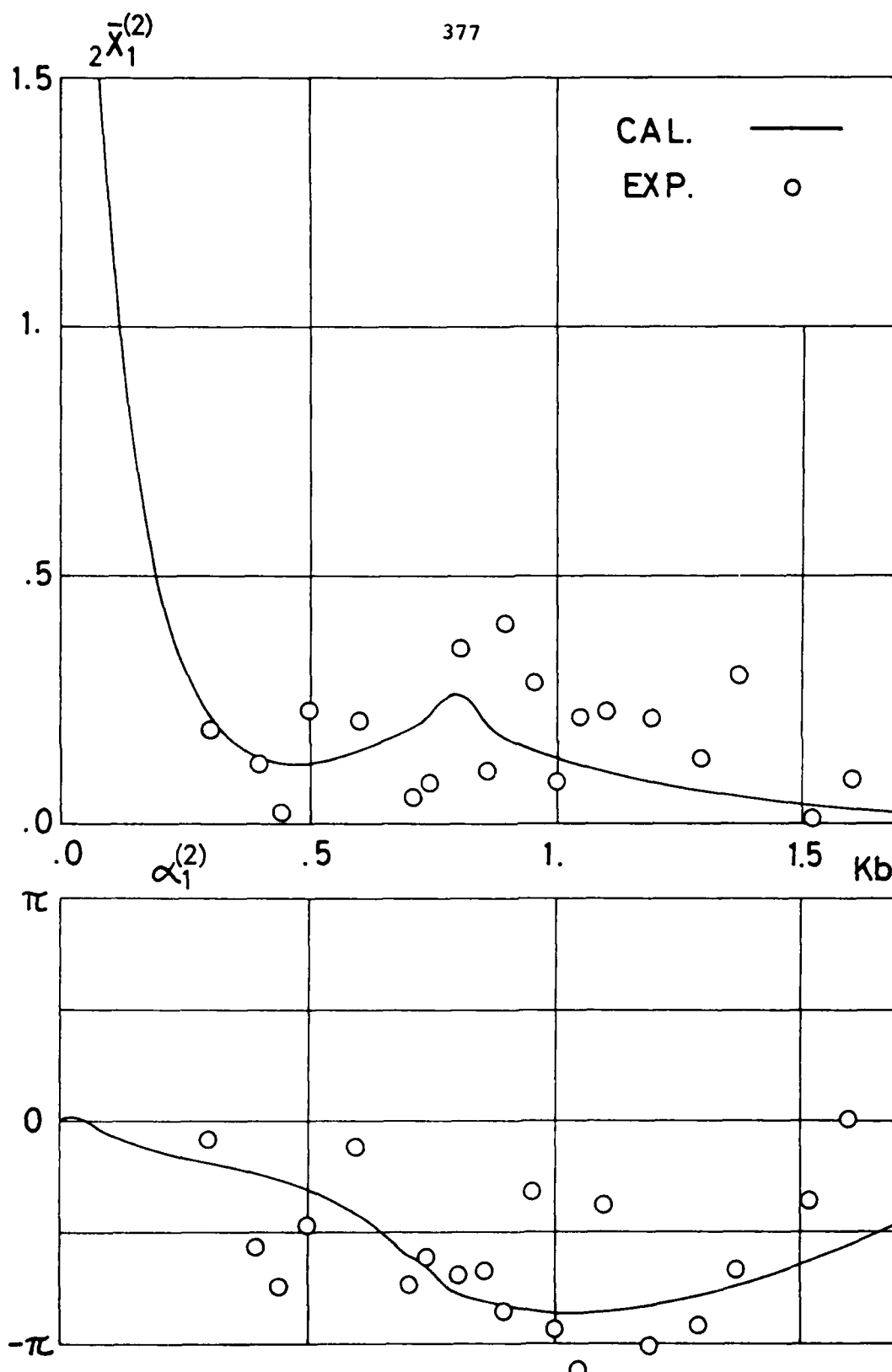


Fig.26 The second order swaying response of a Lewis-form cylinder in waves

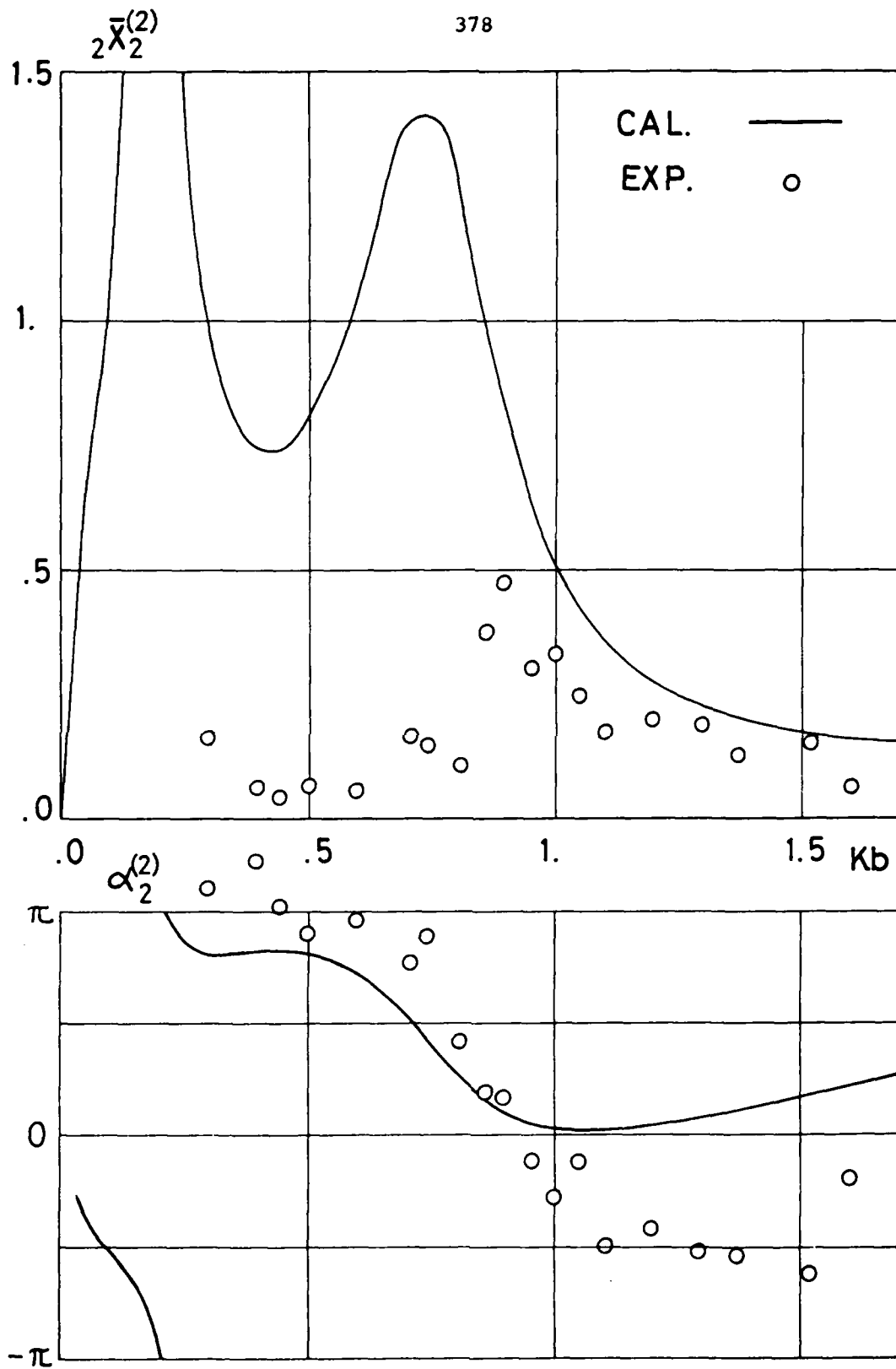


Fig.27 The second order heaving response of a Lewis-form cylinder in waves

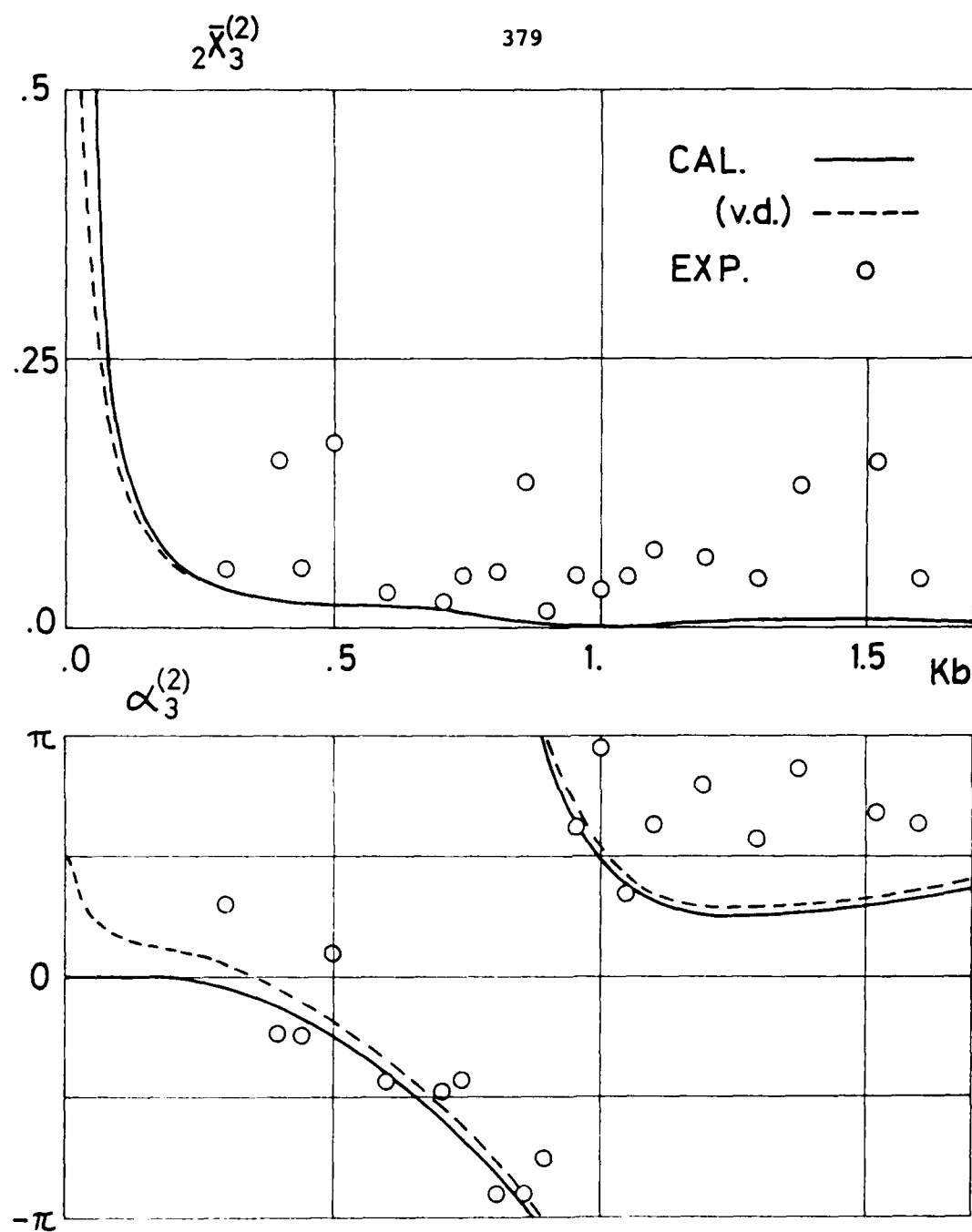


fig.28 The second order rolling response of a Lewis-form cylinder in waves

## Discussion

A.Y. Odabasi (British Ship Research Association)

Owing to the time limitation it was not possible to study the paper adequately and explore the new features of this work. There are, however, two points I would like to raise:

1. Since the models used in the present experiments are quite small, I would like to know whether the author performed checks against well-established data, such as those by Vugts [24]. These experiments clearly demonstrate the amplitude dependence of hydrodynamic derivatives for roll and sway. Given this fact, one would like to know what were the amplitudes in the experiments used for comparison.
2. Although it is customary to use discrete frequencies, i.e.,  $2\omega$ ,  $3\omega$ , etc., to study the higher-order (or nonlinear effects) in a continuous media, such an assumption is not correct and the nonlinearity manifests itself by the existence of frequency deterioration. Therefore, in a more realistic approach, the instantaneous frequency will be allowed to vary, i.e.,  $\omega = \omega(\tau)$ ,  $\tau = \epsilon t$ . Introduction of this variation will produce additional terms in the second-order theory, since

$$\frac{\partial \phi}{\partial t} = (x, y, z) [i\omega + i\epsilon \dot{\omega} + \dots],$$

where  $\dot{\omega} = d\omega/d\tau$ . Furthermore, an additional equation to determine the variation of  $\omega$  with time will also be obtained in the usual manner by the application of the asymptotic technique of Bogoliubov and Mitropolskii.

A. Papanikolaou (Technical University of Berlin)

This is a valuable contribution to the solution of the second-order ship motions problem. I will comment on a few results and ask for the author's opinion:

1. Referring to Figure 16 and similar results by others, it seems that the value of one is not a physical or computational limit of the normalized horizontal drifting force. Maruo's theory, which the author is referring to, does not apply to the situations of resonant study motions nor does it include any finite amplitude effect as the "near-field" method under discussion. Also, the energy of a second-order wave, i.e., to a steep wave in the sense of Stokes, is slightly greater than the corresponding one of a linear wave of equal amplitude and frequency.

AD-A158 920

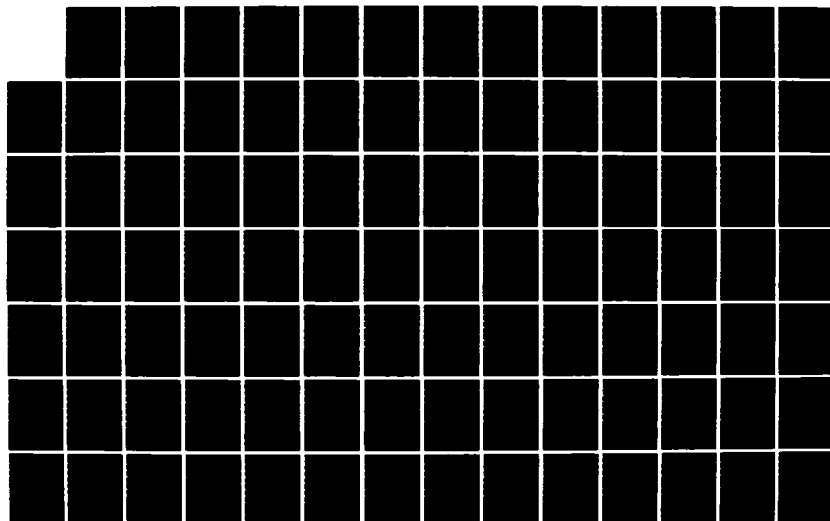
SYMPOSIUM OF NAVAL HYDRODYNAMICS (14TH) HELD AT ANN  
ARBOR MICHIGAN ON AUGUST 23-27 1982(U) OFFICE OF NAVAL  
RESEARCH ARLINGTON VA M P TULIN ET AL. 1982

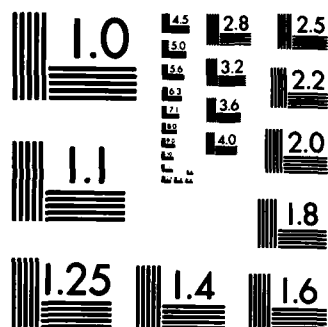
05/13

UNCLASSIFIED

F/G 20/4

NL





MICROCOPY RESOLUTION TEST CHART  
NATIONAL BUREAU OF STANDARDS-1963-A



2. Referring to Figures 27 and 28, the second-order motion calculations are in poor agreement with the experimental results. Viscous damping must be included in the corresponding comments on the value of such comparisons.
3. In my experience (Reference 9), triangular sections are the most sensitive ones to nonlinearities, both hydrostatically and hydrodynamically. What are the experiences of the author with such section forms, if any?

### Author's Reply

Y. Kyojuka (National Defense Academy)

To A. Papanikolaou

The first question is summarized as whether the normalized drifting forces could exceed the value of unity. The author believes that both Maruo's theory and the present results are valid in terms of the second-order theory even in the resonance of the body motion. The steady forces such as drifting force are the second-order forces, but they can be obtained from the first-order solutions. Maruo's theory is derived by changing the integral pass from the body surface to control plains placed far from the body. Therefore, the near- and far-field solutions should coincide with each other. In near-field method, the second force due to the wetted surface change is most dominant in the drifting force, so that we should obtain the potential at the intersection of the body surface and the free-surface precisely.

The drifting force that is discussed by Dr. Papanikolaou seems to be the force the order of which is higher than the second.

The second question is on the discrepancies of the second-order motions between the theory and the experiment. It might be attributed to the viscous damping as the discussor points out. However, I think it necessary to carry out more experiments to clarify it.

In the last question, the discussor refers to the effects named as "wedge effects" by the late Professor Tasai. I also carried out the calculation and the experiment for two cylinders; one is a triangle-like section that intersects the free surface with an angle of  $45^\circ$ , and the other is a Lewis-form section that has the same area coefficient and beam/draft ratio. According to their results, the wedge effects were important for the vertical forces but were negligible for the horizontal forces. More details are shown in Reference 12 of the present paper.

To Y.A. Odabasi

The present experiments were, of course, compared with the existing data such as those of Tasai-Keterayama (Reference 15 of the present paper) and Yamashita (Reference 14 of the present paper). They show good agreement with each other where the hydrodynamic forces are expressed as the summation of Fourier components.

However, the results of Vugts (Reference 23 of the present paper) refer to the amplitude dependency in the added-mass and the damping forces. Such nonlinear effects could be treated in the third-order theory along with the present method.

Vugts also showed some measured records in the diffraction problems. However, they seem to be fairly different from the present records such as Figure 14. Although the models used in the present experiments are quite small, tools for the measurement should be more reliable.

The next suggestion seems very interesting to me.

In the present study, the phenomena are assumed periodic and the quantities are expanded into each Fourier component. Furthermore, the nonlinear forces are mainly caused by the boundary conditions due to the periodic displacements of the body and the free surface, where the perturbation parameter is defined as the ratio of the incident-wave amplitude to the half-beam of the body.

The discussor proposes an application of the asymptotic technique by introducing a new parameter that varies frequency with time. The method of asymptotic expansion is useful for some problems, especially transient phenomena, as a tool of the solution method. However, as the hydrodynamic forces are given as a function of the frequency and the amplitude in general, the problem will be complicated.

# Slender-Body Calculations of Large-Amplitude Ship Motions

Douglas J. Loeser,  
Dick K. Yue,  
and  
Nils Salvesen  
Science Applications, Inc.  
La Jolla, CA and Annapolis, MD

## ABSTRACT

A nonlinear method for the time-domain prediction of the large-amplitude motions of a slender body is presented. The three-dimensional potential-flow problem is approximated by a set of two-dimensional initial value problems for which nonlinear free-surface and "exact" hull boundary conditions are formulated. The free-surface condition is linearized for the implementation of this procedure in a computer code. The resulting large-amplitude two-dimensional initial value problem is solved using a spectral free-surface representation and a distribution of simple sources on the instantaneous wetted hull.

This work is still in progress. Linear damping computations for a submerged ellipsoid with forward speed are presented and compared with linear three-dimensional results and strip theory. Preliminary results for the added mass and damping coefficients for the destroyer Friesland are presented and compared with those of experiments and other theories.

## INTRODUCTION

During the last twenty years it has been demonstrated that linear ship-motion theories can solve many seakeeping problems related to the average performance of ships with good accuracy. However, the linearized approaches cannot be used to forecast some of the more important responses of a ship even in moderate sea conditions. As an example, relative bow motions for an arbitrary heading are predicted poorly by strip theory. In addition, there is information which linear theory cannot provide such as the effect of the above water hull geometry on motions, broaching and the occurrence of green water on the deck.

Recent work by Buckley (1980) and others indicate that significant damage to ship hulls results from episodic waves, single wave

events which cannot be represented by linear wave statistics. There has been much effort expended to characterize these wave events. A non-linear time-domain simulation is the appropriate tool for the study of the ship response to such events.

The non-linear ship motion problem is so complex that there have been few attempts to develop computational methods for solving such fully three-dimensional problems. Salvesen (1982) and Paulling and Wood (1974) developed methods with nonlinear hydrostatic effects for large-amplitude low-frequency motions. Paulling and Wood had some success determining the capsizing of ships due to roll response in following seas. A second order perturbation procedure for predicting nonlinear ship motions and wave induced loads was developed by Jensen and Pedersen (1979).

In this report we present a method for studying finite amplitude ship motions. Using the assumptions that the ship is slender, the wave slopes in the longitudinal direction are small and ignoring any forward radiation of wave disturbances the nonlinear three-dimensional boundary value problem is approximated by a sequence of nonlinear two-dimensional initial value problems. This approach follows that used by Chapman (1976) for a yawed flat plate with forward speed. It has also been applied to the radiation problem by Chapman (1975) and Yeung and Kim (1981), but only for the linear problem.

In principle the nonlinear two-dimensional problem can be solved using techniques such as those of Vinje and Arevig (1981) or Baker et. al. (1981). We choose here, for practical considerations, to linearize the free surface boundary condition but still allow the motion amplitude to be finite. Use of a linearized free surface together with the "exact" hull boundary condition is inconsistent but offers substantial computational simplifications. The important hull geometry effects are still correctly modeled, and the results should in general be valid, especially when the frequency of body motion is relatively low.

The two-dimensional problem is confined to a plane normal to the mean direction of the ship at a fixed location in inertial coordinates. At a time previous to the entrance of the hull the fluid is at rest in the plane. As the ship passes through the plane the hull cross section on which the body boundary condition is applied grows in time to some maximum profile then contracts and disappears as the ship stern exits. The location and local velocity of the boundary are functions of both the hull motions and the rate of change of hull shape in the longitudinal direction.

The free surface wave field in the two-dimensional problem contains the integrated effect of the passage of all previous hull sections. Thus, the effect of forward speed enters the problem through the rate at which the free surface disturbances produced by upstream hull sections are convected down the hull.

In the zero speed limit there is no convection of the wave disturbance down the hull and the slender body approximation reduces identically to strip theory as shown in the Appendix. Thus our method can be viewed as a generalization of strip theory in which the

relative motion between the free surface and hull is treated explicitly. This result is surprising since the assumptions used to obtain the slender body approximation imply that it is valid for long waves and relatively high Froude numbers whereas the strip theory is valid for short waves and low Froude numbers. At low speeds our results should be at least as satisfactory as those from strip theory.

A computer code designed to perform the finite-amplitude time-domain simulation has been written and is in the process of being validated. To date some comparisons with linear computations have been made. These preliminary results are presented. This paper is a progress report on the first steps of a systematic investigation of a promising approach to the complex problem of nonlinear ship motions.

### MATHEMATICAL FORMULATION

The fluid is assumed to be inviscid, incompressible and homogeneous and the flow irrotational. If  $\vec{x} = (x, y, z)$  are cartesian coordinates fixed in space with gravity acting in the negative  $z$  direction and  $t$  denotes time, then the fluid velocity  $\vec{V}(\vec{x}, t)$  can be represented as the gradient of a velocity potential  $\phi(\vec{x}, t)$ . The conditions on  $\phi$  are:

$$\begin{aligned} \nabla^2 \phi &= 0 & z < \eta(x, y, t) \\ -\rho \phi_t - \frac{1}{2} \rho |\nabla \phi|^2 - \rho g z &= p_0 & z = \eta(x, y, t) \\ \eta_t + \eta_x \phi_x + \eta_y \phi_y - \phi_z &= 0 & z = \eta(x, y, t) \\ n_i q_i &= \phi_x n_1 + \phi_y n_2 + \phi_z n_3 & \text{on } S(x, y, z, t) = 0 \end{aligned} \quad (1)$$

and a suitable radiation condition. In the above  $\eta(x, y, t)$  is the free surface elevation,  $p_0$  the atmospheric pressure,  $\rho$  the fluid mass density,  $g$  gravity and  $S(x, y, z, t) = 0$  defines the hull boundary. The generalized unit normal  $n_i$  and velocity  $q_i$  are defined:

$$\begin{aligned} (n_1, n_2, n_3) &= \vec{\nabla} S / |\nabla S| \\ (n_4, n_5, n_6) &= \vec{x}_\ell \times \vec{\nabla} S / |\nabla S| \\ (q_1, q_2, q_3) &= \vec{V}_\ell \\ (q_4, q_5, q_6) &= \vec{\omega}_\ell. \end{aligned} \quad (2)$$

and

Here,  $\vec{V}_\ell$  and  $\vec{\omega}_\ell$  are the velocity and rotation rate of a hull fixed coordinate system denoted by  $\vec{x}_\ell = (x_\ell, y_\ell, z_\ell)$  and located at amidships at the waterline. Positive  $x_\ell$  is forward and  $y_\ell$  is to port. The two systems are related by

$$\vec{x}(t) = \vec{x}_\ell(t) + \int_0^t \vec{v}_\ell(\tau) + \vec{\omega}_\ell(\tau) \times \vec{x}_\ell(\tau) d\tau \quad (3)$$

### Slender Body Approximation

Practical ship shapes are slender, in addition the pitch displacement  $\theta_2$  is generally of the order of  $D/L$ , the draft to length ratio, and the yaw displacement  $\theta_3$  is of the order  $B/L$ , the beam to length ratio, thus

$$n_1 \ll n_2 \text{ or } n_3 \quad (4)$$

We further assume that the longitudinal component of the ambient wave is of the order of  $L$ . It follows that, in the near field, the flow varies an order of magnitude more rapidly in the transverse directions than in the longitudinal direction and that

$$\frac{\partial}{\partial x} \ll \frac{\partial}{\partial y}, \frac{\partial}{\partial z} \quad (5)$$

Applying (5) to equations (1) we obtain:

$$\begin{aligned} \Phi_{yy} + \Phi_{zz} &= 0 & z < \eta(y, t; x) \\ -\rho\Phi_t - \frac{1}{2}\rho(\Phi_y^2 + \Phi_z^2) - \rho g z &= p_0 & z = \eta(y, t; x) \\ \eta_t + \eta_y \Phi_y - \Phi_z &= 0 & z = \eta(y, t; x) \\ q_i n_i = \Phi_y n_2 + \Phi_z n_3 & & \text{on } S(y, z, t; x) = 0 \\ \Phi &\equiv 0 & t < t_0 \end{aligned} \quad (6)$$

where

$$\Phi(y, z, t; x) = \phi(x, y, z, t). \quad (7)$$

The dependence of  $\Phi$  on  $x$  is implicit and occurs only through the hull boundary condition. Thus, the three-dimensional boundary value problem (1) is reduced to a set of initial value problems in two dimensions each fixed at a given  $x$  location in inertial coordinates.

In deriving (6) it is implicitly assumed that disturbances may only propagate downstream. Thus,  $\Phi(t_1)$  is dependent on all  $\Phi(t)$  where  $t < t_1$ , but independent of all  $\Phi(t)$  where  $t > t_1$ . The last condition in (6), in which  $t_0$  is the time the hull first enters the section, is then a consequence of this assumption and the radiation condition.

Physically the problem may be viewed as taking place in a plane normal to the longitudinal axis of the ship, with the hull boundary condition being applied on the instantaneous wetted cross section of the hull. The forward motion of the hull through the plane fixed in  $x$ , the oscillatory motions of the hull and the change in the local

wave height will all influence the section shape on which the body boundary condition must be applied.

In addition to the convection of the free surface disturbances down the hull, the forward speed enters the formulation through the rate of change of the boundary contour in the initial value problem and through the  $n_1 q_1$  term of the hull boundary condition. The time dependence of  $n_1$  can be shown by expressing the vector element in terms of  $\bar{n}_i$ , the elements of the unit normal resolved in hull fixed coordinates:

$$n_1 = \mu_{11} \bar{n}_1 + \mu_{12} \bar{n}_2 + \mu_{13} \bar{n}_3 \quad (8)$$

where  $\mu_{ji}$  is a time dependent tensor made up of the elements of the unit vectors for the hull fixed coordinate system. The tensor elements  $\mu_{12}$  and  $\mu_{13}$  are proportional to the hull yaw and pitch rotations and the last two terms of equation (8) correspond to crossflow velocities induced by the interaction of forward speed and the yaw and pitch of the hull.

The  $\mu_{11} \bar{n}_1$  term is associated with the resistance potential. In the absence of all other motions except forward speed there will still be a non-zero potential similar to that associated with the divergent wave field in a three-dimensional wave resistance problem. Since the  $\phi_{xx}$  in the field equation and  $\phi_x n_x$  in the hull boundary condition are dropped, fluid normally displaced in the x direction due to the motion of the body is restricted to move in the y and z directions.

All of the physical consequences of these assumptions are not known. However, it is clear that forces in the x direction will be poorly modeled and that the transverse waves which may propagate ahead or behind a ship with steady forward speed or oscillating motions will be omitted. The flow near the stagnation points at the ends of the body will also be poorly modeled.

#### Linearizing the Free-Surface Boundary Conditions

While the fully nonlinear initial value problem can in principle be solved using techniques such as those of Vinje and Brevig (1981) and Baker et. al. (1981), we choose here for practical considerations, to linearize the free surface but still allow the motion amplitudes to be finite. After linearizing the free surface, equations (6) become:

$$\begin{aligned} \phi_{yy} + \phi_{zz} &= 0 & z < 0 \\ -\rho \phi_t - \rho g z &= p_0 & z = 0 \\ \eta_t - \phi_z &= 0 & z = 0 \\ q_i n_i &= \phi_y n_2 + \phi_z n_3 & \text{on } S(y, z, t; x) = 0 \end{aligned} \quad (9)$$

$$\phi \equiv 0$$

$$t < t_0$$

The finite-amplitude slender body approximation given in (9) is implemented in a computer code presently under development.

Equations (9) may be further linearized by assuming small motion amplitudes and satisfying the hull boundary condition at its mean position. Chapman (1975) applied this linear formulation to an oscillating flat plate with forward velocity. Yeung and Kim (1981) used a similar approach for conventional hull shapes with forward speed.

At speed, the effect of wave disturbances generated by all previous hull sections are included in the force computation at a given section. In the zero speed limit, there is no relative motion between the hull and the wave field and the small-amplitude motion problem reduces to strip theory (see Appendix). Although the assumption that  $\phi_x \ll \phi_y$  and  $\phi_z$  implies that the Froude number must be high, the slender body approximation should perform at least as well as strip theory at low speeds.

#### Summary of Mathematical Formulation

Three levels of approximation of the nonlinear three-dimensional problem stated in equations (1) have been presented:

- (i) Slender body approximation only, nonlinear free-surface and "exact" hull boundary conditions, eq. (6)
- (ii) Linearized free-surface with "exact" hull boundary condition eq. (9)
- (iii) Infinitesimal motion with hull boundary condition applied at the mean hull location. See Appendix.

Our intention is to eventually solve the nonlinear initial value problem associated with the slender body approximation (i). At the present time we have developed a computer code capable of solving the finite amplitude transient problem (ii). A description of this computational method will be presented here; however, the method is still in the verification stage. Numerical results will be presented only for the linearized case (iii).

Since our primary interest is in solving the nonlinear problem, our approach even in case (iii) differs from the linearized method of Yeung and Kim (1981) in some important ways. Instead of using time-dependent Green's functions for the 2-D transient solutions, we employ a more explicit representation in terms of a combination of a distribution of simple sources on the body and a spectral free-surface representation. Aside from helping in the physical understanding of the problem, this explicit representation is more directly numerical and therefore especially suited to the nonlinear problem. For example models for nonlinear effects such as viscous forces can be included readily in the present framework.



## SOLUTION OF THE INITIAL-VALUE PROBLEM

A spectral method similar to that described by Chapman (1979) is used to solve the finite-amplitude initial value problem (9). To facilitate the computation of the pressure field about the hull and in particular near the free surface, a cubic B-spline representation is used to describe the hull geometry and source strength distribution. The use of B-splines, described in De Boor (1972), makes the regeneration of section shapes at each time step very efficient and produces a smooth source density distribution using relatively few collocation points.

The spectral method uses an integral representation for the free-surface potential and elevation. The body is modeled by a distribution of simple sources on the wetted hull and its negative image. The total potential is given as the sum of the free surface, body and ambient potentials which together satisfy the boundary condition on both the hull and free surface:

$$\Phi = \Phi_A + \Phi_B + \Phi_S \quad (10)$$

where  $\Phi_A$  is the ambient wave potential,  $\Phi_B$  the body potential and  $\Phi_S$  the free surface potential. The sum  $\Phi_B + \Phi_S$  is equivalent to the sum of the radiated plus the diffracted potentials, however, there is not a one to one correspondence between the individual potentials.

At each time step the body source distribution is solved for by satisfying the body boundary condition at evenly spaced points on the section contour. Assuming that the body source distribution is constant over the next time step, the free surface and body position are integrated in time. This process is repeated until the hull passes completely through the section. In the following, the spectral free surface (in the absence of the body), the body representation and the influence of the body on the free surface will be discussed in turn.

## Spectral Free Surface

The free surface potential  $\Phi_S$  and elevation  $\eta$  are represented by the real part of the following integrals

$$\Phi_S(y, z, t) = \int_0^\infty B(k, t) e^{k(z+iy)} dk \quad z < 0 \quad (11)$$

and

$$\eta(y, t) = \int_0^\infty A(k, t) e^{kiy} dk \quad (12)$$

where  $B(k, t)$  and  $A(k, t)$  are complex functions of the wave number  $k$  and time  $t$ . Substituting the above representations into the free-surface conditions (9) the following differential equations are obtained

$$B_t(k, t) = -g A(k, t) \quad (13)$$

and

$$A_t(k, t) = k B(k, t) + D(k, t). \quad (14)$$

Because of the negative image, the body potential is zero on the free surface and does not enter into eq. (13). However, its vertical derivative is non-zero and its contribution to eq. (14) is given by  $D(k, t)$ . The evaluation of  $D$  will be discussed later.

Assuming  $D(k, t)$  constant over one time step the following evolution equations for  $A(k, t)$  and  $B(k, t)$  can be obtained:

$$\begin{aligned} B(k, t+\Delta t) &= B(k, t) \cos \sigma \Delta t - g A(k, t) \frac{\sin \sigma \Delta t}{\sigma} - D(k, t) \frac{(1 - \cos \sigma \Delta t)}{k} \\ A(k, t+\Delta t) &= A(k, t) \cos \sigma \Delta t + k B(k, t) \frac{\sin \sigma \Delta t}{\sigma} + D(k, t) \frac{\sin \sigma \Delta t}{\sigma} \end{aligned} \quad (15)$$

where  $\sigma^2 = kg$ .

The functions  $B(k, t)$  and  $A(k, t)$  are discretized in  $k$ -space, the integrals for  $\phi_S$  and  $\eta$  are evaluated by Filon's method (Abramowitz and Stegun (1972)) and spatial derivatives of  $\phi_S$  and  $\eta$  are computed formally. The time derivative of  $\phi_S$  can be obtained by substituting  $-g A(k, t)$  for  $B_t(k, t)$  in eq. (11).

#### Body Representation

The body potential is represented by a continuous distribution of simple sources over  $C(t)$ , the submerged portion of the section, and its negative image above the free surface:

$$\phi_B(\vec{P}, t) = \frac{1}{2} \int_{C(t)} \gamma(s) \log \frac{\vec{R} \cdot \vec{R}}{(\vec{R}^* \cdot \vec{R}^*)} ds \quad (16)$$

where  $\vec{R}$  is a vector from a point on the section contour to  $\vec{P}$ ,  $\vec{R}^*$  is a vector from the image contour to  $\vec{P}$ ,  $\gamma(s)$  the source density and  $s$  is the arc length along the section. Cubic B-splines are used to represent  $\gamma$  and  $C$  as continuous functions of  $s$ .

From the hull boundary condition (9)  $\phi_B$  must satisfy

$$\frac{\partial \phi_B}{\partial N} = q_i n_i - \frac{\partial}{\partial N} (\phi_S + \phi_A) \quad (17)$$

where  $\vec{N}$  equals  $(n_2, n_3)$ . The source density is obtained by satisfying (17) on a set of points equally spaced along the section.

#### Body Influence on Free Surface

The presence of the body induces a vertical velocity at the free surface which is included in the kinematic boundary condition through  $D(k, t)$  in eq. (15). The complex function  $D(k, t)$  is obtained by expressing  $\partial \phi_B / \partial z$  evaluated at the free surface in integral form

$$\left. \frac{\partial \phi_B}{\partial z} \right|_{z=0} = \text{Re} \left\{ \int_0^\infty D(k, t) e^{kiy} dk \right\}. \quad (18)$$

For a simple source located at  $(y_B, z_B)$  and its negative image

$$\frac{\partial \phi_B(y, 0)}{\partial z} = -2z_B / (z_B^2 + (y - y_B)^2)$$

and

$$D(k, t) = 2 e^{k(z_B - iy_B)}$$

Then integrating over the hull contour

$$D(k, t) = 2 \int_{C(t)} \gamma(s) e^{k(z_B(s) - iy_B(s))} ds \quad (19)$$

#### SOLUTION OF THE EQUATIONS OF MOTION

The equations of motion for the time interval  $t$  to  $t + \Delta t$  may be written in hull fixed coordinates as

$$M_{ij} [q_j(t + \Delta t) - q_j(t)] = \int_t^{t + \Delta t} F_i(\tau) - M_{Hij}(\tau) \dot{q}_j(\tau) d\tau \quad (20)$$

$i, j = 2, 6$

where  $M_{ij}$  is the hull mass matrix,  $M_{Hij}$  the impulse mass matrix and  $F_i$  the total hydrodynamic force with the mass effect removed. To a truncation error of  $\Delta t^2$ , eq. (20) can be written as

$$[M_{ij} + M_{Hij}(t)] (q_j(t + \Delta t) - q_j(t)) = F_i(t) \Delta t \quad (21)$$

from which the updated velocity  $\dot{q}_j(t + \Delta t)$  or the mean acceleration

$$\dot{q}_j(t + \Delta t/2) = (q_j(t + \Delta t) - q_j(t)) / \Delta t$$

can be obtained.

#### Hydrodynamic Impulsive Mass

If the body is given a unit acceleration there will be a force on the body equal to the rate of change of momentum in the surrounding fluid. This force is included in the integration of pressure over the hull surface. Since the force is proportional to the instantaneous acceleration, it must be computed explicitly to permit the formulation and solution of a set of linear equations for the body motion.

At each time step the impulsive mass for the sway, heave and roll modes are computed for each section. The impulse potential  $\psi_i$  must satisfy:

$$\begin{aligned} \frac{\partial^2 \psi_i}{\partial y^2} + \frac{\partial^2 \psi_i}{\partial z^2} &= 0 & z < 0 \\ \psi_i &= 0 & z = 0 \end{aligned} \quad (22)$$

$$\frac{\partial}{\partial N} \psi_i = n_i \quad \text{on } S(y, z, t; x) = 0 \quad i = 2, 4$$

and

$$\psi_i \rightarrow 0 \quad \text{as } y^2 + z^2 \rightarrow \infty$$

The impulse mass for the section  $C(t)$  in mode  $j$  due to a unit acceleration in mode  $i$  is

$$I_{ji}(t; x) = -\rho \int_{C(t; x)} \psi_i n_j ds \quad i, j = 2, 4 \quad (23)$$

$M_{Hij}(t)$  is obtained by integration of  $I_{ji}$  along the hull. The impulse mass computation is performed simultaneously with the calculation of the hull source density distribution with little additional effort. At each time step the submerged hull shape changes and the impulse mass matrix must be recomputed.

#### Force Computation

The total force and moment are computed in hull fixed coordinates as follows

$$F_i = \int_{-L/2}^{L/2} \int_{C(t, x_\ell + Ut)} p(t; x_\ell + Ut) \bar{n}_i ds dx_\ell \quad (24)$$

The Bernoulli equation requires the evaluation of the time derivative of  $\phi_B$  at a fixed point in space. However, since the section shape deforms in time, a convective like derivative is more easily evaluated numerically. The desired quantity can be written in terms of the convective derivative:

$$\frac{\partial \phi_B}{\partial t}(\vec{P}_2, t_2) = \frac{\phi_B(\vec{P}_2, t_2) - \phi_B(\vec{P}_1, t_1)}{\Delta t} - \vec{V}_2 \cdot \vec{\nabla} \phi_B(\vec{P}_2, t_2) \quad (25)$$

where  $\vec{P}_1$  and  $\vec{P}_2$  are points on the section at times  $t_1$  and  $t_2$  respectively and  $\vec{V}_2$  is defined by

$$\vec{V}_2 = (\vec{P}_2 - \vec{P}_1) / \Delta t. \quad (26)$$

The choice of which  $\vec{P}_1$  on the section at time  $t_1$  to align with a particular  $\vec{P}_2$  at time  $t_2$  is arbitrary, however, the approximation is most accurate when  $|\vec{P}_2 - \vec{P}_1|$  is minimized. Substitution of (25) into the second equation in (6) yields the following for the non-linear pressure

$$p(\vec{P}_2, t_2) = -\rho \left[ \frac{\phi_B(\vec{P}_2, t_2) - \phi_B(\vec{P}_1, t_1)}{\Delta t} \right] + \rho \vec{V}_2 \cdot \vec{\nabla} \phi_B(\vec{P}_2, t_2) - \rho \frac{\partial}{\partial t} [\phi_S(\vec{P}_2, t_2) + \phi_A(\vec{P}_2, t_2)] - \frac{\rho}{2} |\vec{\nabla} \phi(\vec{P}_2, t_2)|^2 - \rho g z \quad (27)$$

#### Integration of Body Position

The hull velocity and displacement are obtained by explicit

forward Euler integration. The free surface is integrated analytically from  $t$  to  $t+\Delta t$ , assuming that the hull influence is constant over the interval. These steps are summarized below

1. Set up section geometries
2. Compute section source distributions eq. (17)
3. Compute section impulse mass eq. (23)
4. Sum force and mass over hull eq. (24)
5. Compute body influence on  $\phi_S$  eq. (19)
6. Update  $\phi_S$  eq. (15)
7. Update hull position eq. (20)

To initialize the nonlinear problem for regular incident waves, we first solve the linear motion problem in the frequency domain. The resulting displacements and potentials for the hull and free surface are used to initialize the nonlinear problem.

#### PRELIMINARY RESULTS

At the present time the development of a computer code capable of solving the large-amplitude slender-body problem (ii) has been completed. The code is now being verified and we shall only present results computed with a linearized version of the code. As examples, the damping coefficients for a submerged ellipsoid with forward speed and the added mass and damping coefficients for the Friesland destroyer hull are given here. In linearizing the pressure calculation the  $|\nabla\phi|^2$  term in eq. (27) is dropped, therefore the effect of the resistance potential on these calculations is omitted. When the code validation is complete it will be applied to large-amplitude computations.

The test case of a submerged ellipsoid was chosen because a three-dimensional computation of the damping coefficients [Newman (1961)] showed a strong Froude number dependence which was not modeled by strip theory. Newman's results included the wave resistance potential which had been dropped in the linearized slender-body approximation here. On the other hand, the image of the free surface within the body is included in our slender-body results but is omitted by Newman.

The ellipsoid is defined by

$$\frac{x^2}{a_1^2} + \frac{y^2}{a_2^2} + \frac{z^2}{a_3^2} = 1 \quad a_2/a_3 = 2 \quad a_1/a_2 = 7$$

The centerline of the ellipsoid is at  $z = -2a_2$ . Figures 1-4 are plots of the damping coefficients in heave, pitch, sway and yaw.

In general the Froude number dependence of the three-dimensional computations and that of the slender-body approximation have the same qualitative behavior and are close in numerical value. In the yaw and sway modes the agreement is good and is uniform over both Froude number and frequency ranges. In the heave mode the slender-body approximation predicts a stronger dependence on Froude number than Newman's approach. This difference increases with frequency.

There are two effects which contribute to differences in the pitch damping predictions at low frequencies and  $F_n=0.2$ . First, since the slender-body approximation omits the transverse wave field, it does not model the singular behavior near  $\omega U/g \sim 1/4$  which is modeled by the three-dimensional approach. The critical frequencies for  $F_n=0.2$  and 0.4 are indicated by arrows on the abscissa of Figure 2. Second, both theories predict a qualitative change in the low-frequency behavior near  $F_n=0.2$ , however, the slender body approximation makes the transition earlier. Newman's results for  $F_n=0.1$  have the same general behavior in the low frequency limit as the slender body approximation has for  $F_n=0.2$ .

Our computed off-diagonal damping coefficients for the ellipsoid satisfy the Timman-Newman (1962) relations to within 5% for the given range of frequencies and Froude numbers.

Strip theory predicts the following quadratic dependence on forward speed for the pitch and yaw damping coefficients:

$$\begin{aligned} B_{55} &= B_{55}^0 + \frac{U^2}{\omega^2} B_{33}^0 \\ B_{66} &= B_{66}^0 + \frac{U^2}{\omega^2} B_{22}^0 \end{aligned} \quad (28)$$

where the superscript zero indicates a speed independent term which is the integration of sectional damping coefficients along the hull. Since the sectional damping is positive,  $B_{55}$  and  $B_{66}$  must always increase with increasing Froude number. However, the dependence predicted by the slender-body approximation and Newman is more complex. As the Froude number increases, the damping coefficients above  $\omega^2 a_1/g = 2$  drop significantly while the coefficients below it rise. Strip theory does not have the correct trends in the Froude number dependence and overpredicts the damping coefficients for most of the frequency range. This difference may not be as significant for surface piercing hull forms, for example see figures 5 and 6 in Yeung and Kim (1981).

Figures 5-8 are plots of the added mass and damping coefficients for pitch and heave for the Friesland destroyer hull. These results are preliminary and are presented here to indicate the present level of validation of the basic program.

The spectral free-surface representation allows for direct and efficient evaluation of the instantaneous surface profile. Figures 9 and 10 are plots of the linear free-surface disturbance associated with the oscillatory motion of the Friesland in heave and pitch respectively. The wave field associated with the steady forward speed of the vessel is not shown. In both cases the vertical scale has been amplified for clarity. The surface within the ship waterplane has been assigned a constant height to accentuate the free-surface profile along the hull. In both plots the wave field oscillates in time. The free-surface displacements shown correspond respectively to the instant in time when the maximum vertical heave velocity and nose down pitch rate occur. Wave field plots present a large amount of information in a concise form and facilitate the interpretation of the

results.

Using very conservative computational parameters for the ellipsoid: 30 spline points on each of 29 sections, 12 frequency points were computed in about 6 minutes of CPU time on the SAI DEC-10 computer. A surface piercing body such as the Friesland generates shorter waves and requires a wider representation in the spectral frequency space and more stations along the hull. Using as many as 40 stations, an equivalent calculation for the Friesland took 18 minutes of CPU. These time estimates are very conservative and adequate accuracy can in practice be expected with substantially coarser discretizations.

#### CONCLUDING REMARKS

A method for solving the large-amplitude motion of a slender body moving with forward speed is formulated. By invoking a slender body approximation, the three-dimensional nonlinear problem is reduced to a set of two-dimensional nonlinear initial value problems in the transverse planes. To implement this procedure in a computer code, the free-surface boundary condition is further linearized but the "exact" hull boundary condition is retained. A special numerical approach, utilizing a spectral free-surface representation in conjunction with a cubic B-spline description of the body geometry and the density distribution of simple hull sources, is found to be very effective especially for nonlinear computations. This work is still in progress, however, preliminary linear results indicate that this slender-body approach models important Froude number dependent effects not present in strip theory.

#### ACKNOWLEDGEMENTS

This work was supported by the Office of Naval Research under contract #N00014-80-C-0168.

The authors wish to acknowledge the many fundamental contributions to this paper made by the late Dr. R. B. Chapman through both his published work and private discussions with the authors.

#### REFERENCES

- Abramowitz, M. and I. Stegun (1972). Handbook of Mathematical Functions, National Bureau of Standards, Washington, D.C., p. 890.
- Baker, G. R., D. I. Meiron, and S. A. Orszag (1981). Applications of a generalized vortex method to nonlinear free surface flows, presented at the *3rd International Conference on Numerical Ship Hydrodynamics*, Paris.
- Buckley, W. H. (1980). The applications of half-cycle counting techniques to the analysis of ocean wave data, *19th American Towing Tank Conference*, Ann Arbor, MI.

- Chapman, R. B. (1975). Numerical solution for hydrodynamic forces on a surface-piercing plate oscillating in yaw and sway, *International Conference on Numerical Ship Hydrodynamics*.
- Chapman, R. B. (1976). Free-surface effects for yawed surface-piercing plates, *Journal of Ship Research*, 20, 3.
- Chapman, R. B. (1979). Large amplitude transient motion of two-dimensional floating bodies, *Journal of Ship Research*, 23, 1.
- De Boor, C. (1972). On calculating with B-splines, *Journal of Approximation Theory*, 6, 50-62.
- Jensen, J. J. and P. T. Pedersen (1979). Wave-induced bending moments in ships - a quadratic theory, *Transactions of the Royal Institute of Naval Architects*, 121.
- Newman, J. N. (1961). The damping of an oscillating ellipsoid near a free surface, *Journal of Ship Research*, 5, 3.
- Paulling, J. R. and P. D. Wood (1974). Numerical simulation of large amplitude ship motions in astern seas, *SNAME Technical and Research Symposium*, S-3, Seakeeping 1953-1973, Webb Institute.
- Salvesen, N. (1982). Nonlinear large amplitude low-frequency ship-motions, United States Naval Academy, Division of Engineering and Weapons, Hydromechanics Laboratory Report EW-10-82.
- Salvesen, N., E. O. Tuck, and O. Faltinsen (1970). Ship motions and sea loads, *SNAME Transactions*, New York.
- Smith, W. E. (1966). Equations of motion coefficients for a pitching and heaving destroyer model, Delft Shipbuilding Laboratory, Report No. 154.
- Timman, R. and J. N. Newman (1962). The coupled damping coefficients of symmetric ships, *Journal of Ship Research*, 51, 4.
- Vinje, T. and P. Brevig (1981). Nonlinear ship motions, presented at the 3rd International Conference on Numerical Ship Hydrodynamics, Paris.
- Yeung, R. W. and S. H. Kim (1981). Radiation forces on ships with forward speed, presented at the 3rd International Conference on Numerical Ship Hydrodynamics.

## APPENDIX

### LINEAR MOTION PROBLEM

In the linear motion problem the body boundary condition is applied on the mean location of the hull surface rather than the instantaneous location. All the boundary conditions are linear and the resistance, diffracted and radiated wave potentials can be treated separately. Here we only discuss the radiated wave potential produced by a ship with steady forward speed and oscillating in heave and pitch. The generalization to roll, yaw and sway is straightforward. The  $|\nabla\phi|^2$  term in the pressure calculation eq. (27) is dropped, therefore, the effect of the resistance potential on the added-mass and damping coefficients is omitted.

Consider two cartesian coordinate systems,  $(x_\ell, y_\ell, z_\ell)$  located at



the mean position of the ship center of gravity and  $(x, y, z)$  fixed in space, such that  $x = x_\ell + Ut$ ,  $y = y_\ell$  and  $z = z_\ell$ . The body extends from  $x_\ell = L/2$  to  $x_\ell = -L/2$  and is defined by  $S(x_\ell, y_\ell, z_\ell) = 0$ .

At each  $x$  location there is an initial value problem which defines a two-dimensional velocity potential in inertial coordinates:

$$\begin{aligned}\phi_{yy} + \phi_{zz} &= 0 & z < 0 \\ \phi_{tt} + g \phi_{tz} &= 0 & z = 0 \\ \phi_y N_y + \phi_z N_z &= w e^{-i\omega t} N_z & \text{on } S(x-Ut, y, z) = 0 \\ \phi &\equiv 0 & t < (x - \frac{L}{2})/U\end{aligned}$$

where  $w=1$  for heave,  $w=x_\ell$  for pitch and  $\hat{N} = (N_y, N_z)$ .

The solution to the above initial value problem can be written as a convolution integral of a time dependent impulse response potential  $H(\alpha, \tau)$  which satisfies

$$\begin{aligned}H_{yy} + H_{zz} &= 0 & z < 0 \\ H_{\tau\tau} + g H_{\tau z} &= 0 & z = 0 \\ H_y N_y + H_z N_z &= \delta(\tau - \alpha) N_z & \text{on } S(x-Ut, y, z) = 0 \\ H &\equiv 0 & \tau < \alpha\end{aligned} \tag{A-2}$$

where  $\tau$  is a time like variable.  $H(\alpha, \tau)$  is the potential at time  $\tau$  resulting from an impulsive heave velocity at time  $\tau = \alpha$ . The resulting sectional force at time  $\tau$  is

$$f(\alpha, \tau) = -\rho \int_{S(x-Ut, y, z)} N_z H_\tau(\alpha, \tau) ds \tag{A-3}$$

The total sectional force at  $\tau$  is the integral of the contributions of all upstream (or earlier) sections,

$$G(\tau, t) = e^{-i\omega t} \int_{-U\tau}^{L/2} f(-\frac{\ell}{U}, \tau) e^{i\omega(\frac{\ell}{U} + \tau)} d\ell. \tag{A-4}$$

The heave force and pitch moment are obtained by the integration of  $G(\tau, t)$  along the hull,

$$\begin{aligned}F_{33}(t) &= \int_{-L/2}^{L/2} G(-\frac{x_\ell}{U}, t) dx_\ell \\ &= e^{-i\omega t} \int_{-L/2}^{L/2} dx_\ell e^{-i\frac{\omega x_\ell}{U}} \int_{x_\ell}^{L/2} f(-\frac{\ell}{U}, -\frac{x_\ell}{U}) e^{i\frac{\omega \ell}{U}} d\ell\end{aligned}$$

$$\begin{aligned}
 F_{53}(t) &= - \int_{-L/2}^{L/2} x_\ell G\left(\frac{-x_\ell}{U}, t\right) dx_\ell \\
 &= -e^{i\omega t} \int_{-L/2}^{L/2} x_\ell e^{-i\frac{\omega x_\ell}{U}} \int_{x_\ell}^{L/2} f\left(-\frac{\ell}{U}, \frac{-x_\ell}{U}\right) e^{i\frac{\omega \ell}{U}} d\ell.
 \end{aligned}$$

If we define

$$E(x_\ell) = \int_{x_\ell}^{L/2} f\left(-\frac{\ell}{U}, \frac{-x_\ell}{U}\right) e^{-i\frac{\omega \ell}{U}} d\ell$$

then  $F_{33}$  and  $F_{53}$  are

$$F_{33}(t) = e^{-i\omega t} \int_{-L/2}^{L/2} E(x_\ell) e^{-i\omega x_\ell/U} dx_\ell \quad (A-5)$$

and

$$F_{53}(t) = -e^{-i\omega t} \int_{-L/2}^{L/2} x_\ell E(x_\ell) e^{-i\omega x_\ell/U} dx_\ell,$$

where  $E(x_\ell)$  is the sectional force at  $x_\ell$  due to all upstream hull sections.  $E(x_\ell)$  can be computed directly by solving a complex transient problem for a control plane fixed in space.

If added-mass and damping coefficients are defined as

$$\begin{aligned}
 F_{33}(t) &= (-i\omega A_{33} + B_{33}) e^{-i\omega t} \\
 F_{53}(t) &= (-i\omega A_{53} + B_{53}) e^{-i\omega t}
 \end{aligned} \quad (A-6)$$

then, the real and imaginary parts of the integrals in eqs. (A-5) are proportional to the damping and added-mass coefficients respectively. Similar expressions can be written for the remaining coefficients.

The zero forward speed limit for this approach is the same as that for strip theory. This can be shown by examining  $G(\tau, t)$  defined by eq. (A-4). If the forward speed is zero there are no contributions from upstream sections. All of the contributions come from the previous history of the motion of the particular section at  $x_\ell = x$ . For a steady heave oscillation  $G(\tau, t)$  will equal

$$G(\tau, t) = (-i\omega a_{33} + b_{33}) e^{-i\omega t}$$

where  $a_{33}$  and  $b_{33}$  are the sectional added-mass and damping coefficients. Substitution of these results into the equations for  $F_{33}$  and  $F_{53}$  yields the strip theory results directly.

- STRIP THEORY (SALVESEN et. al. 1970)  
 - - - FULLY THREE DIMENSIONAL LINEAR (NEWMAN 1961)  
 — SLENDER BODY APPROXIMATION

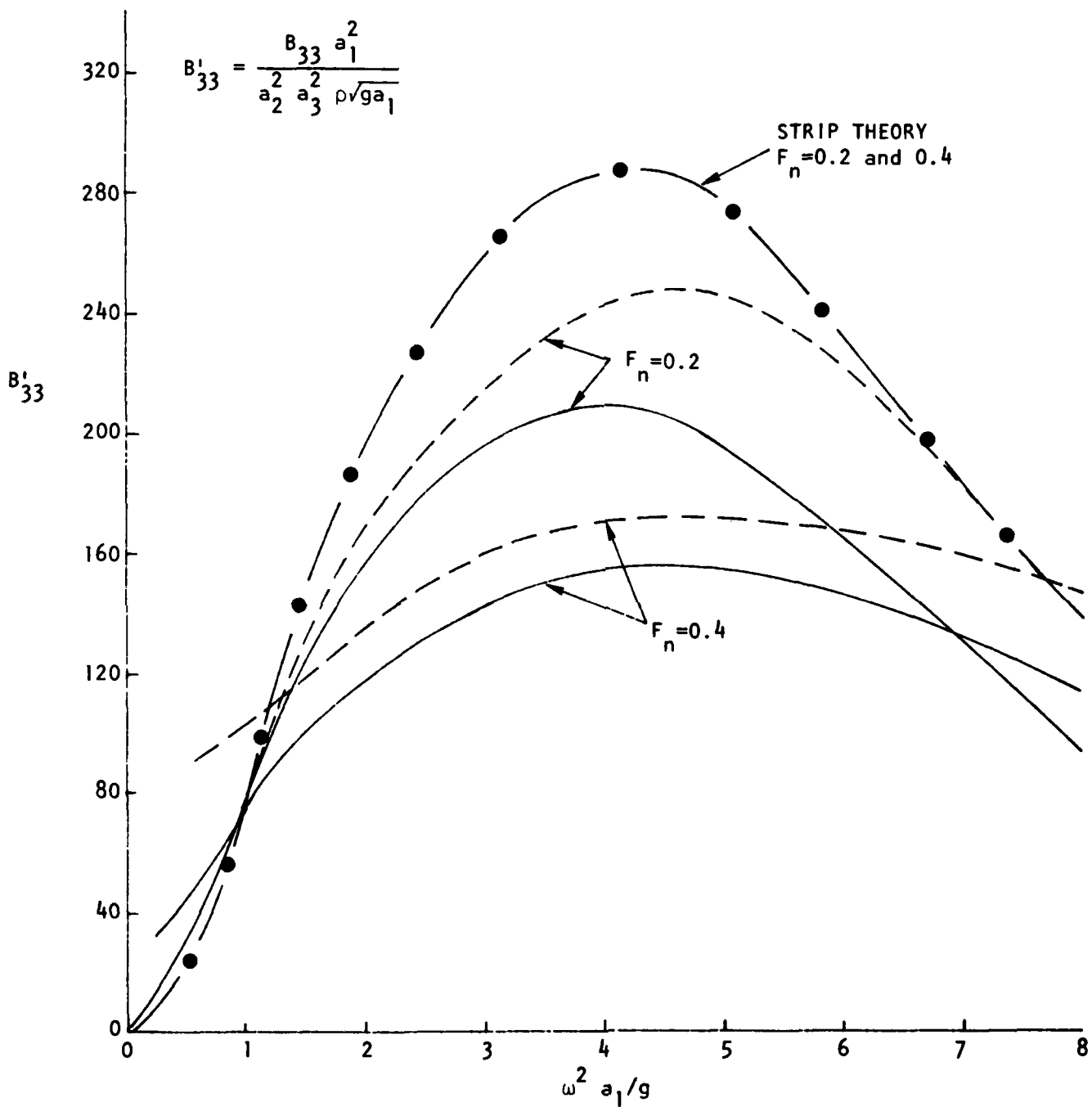


Figure 1. Submerged Ellipsoid - Heave Damping

- STRIP THEORY (SALVESEN et. al. 1970)  
 - - - FULLY THREE DIMENSIONAL LINEAR (NEWMAN 1961)  
 — SLENDER BODY APPROXIMATION

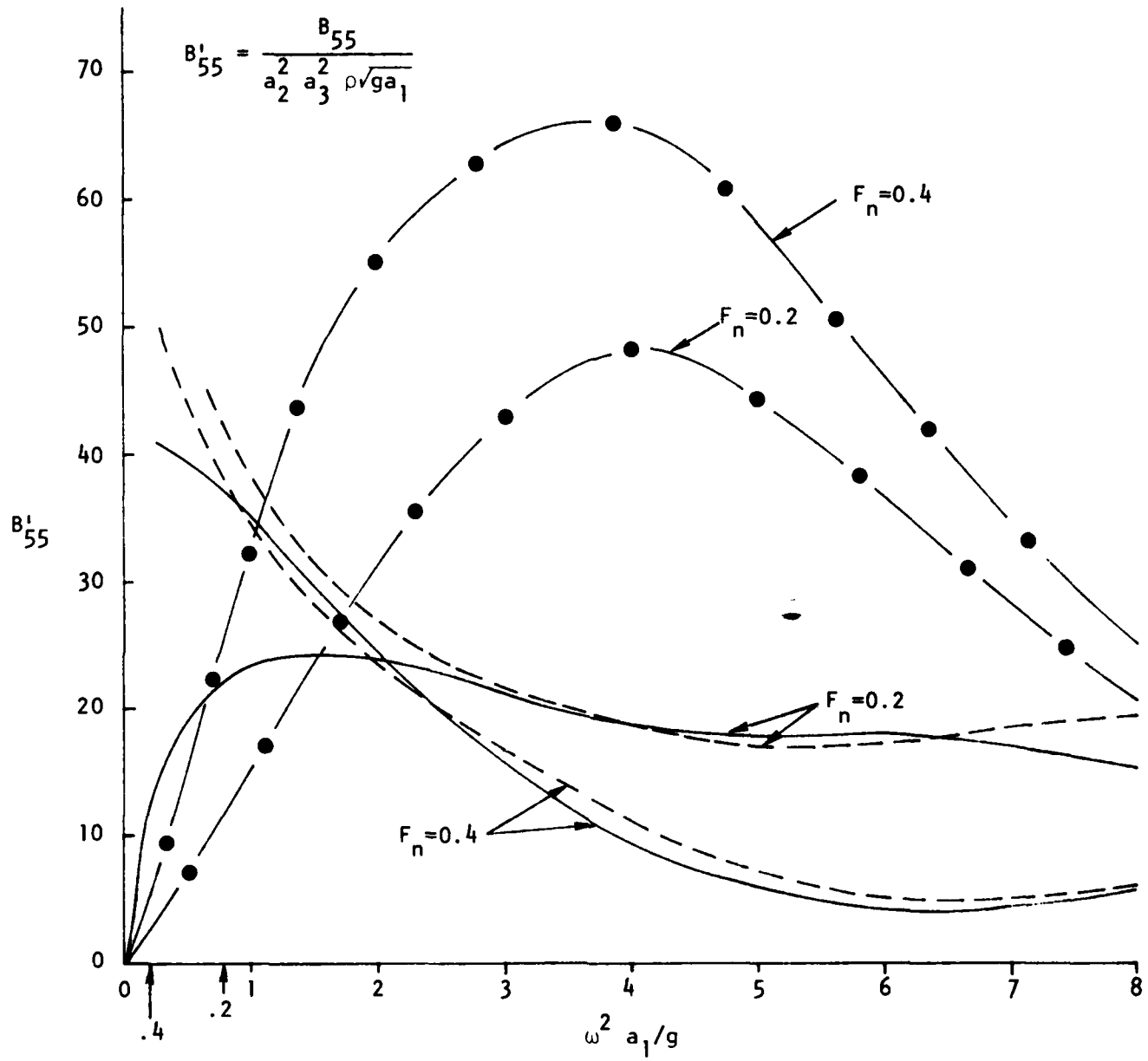


Figure 2. Submerged Ellipsoid - Pitch Damping

- STRIP THEORY (SALVESEN et. al. 1970)  
 - - - FULLY THREE DIMENSIONAL LINEAR (NEWMAN 1961)  
 ——— SLENDER BODY APPROXIMATION

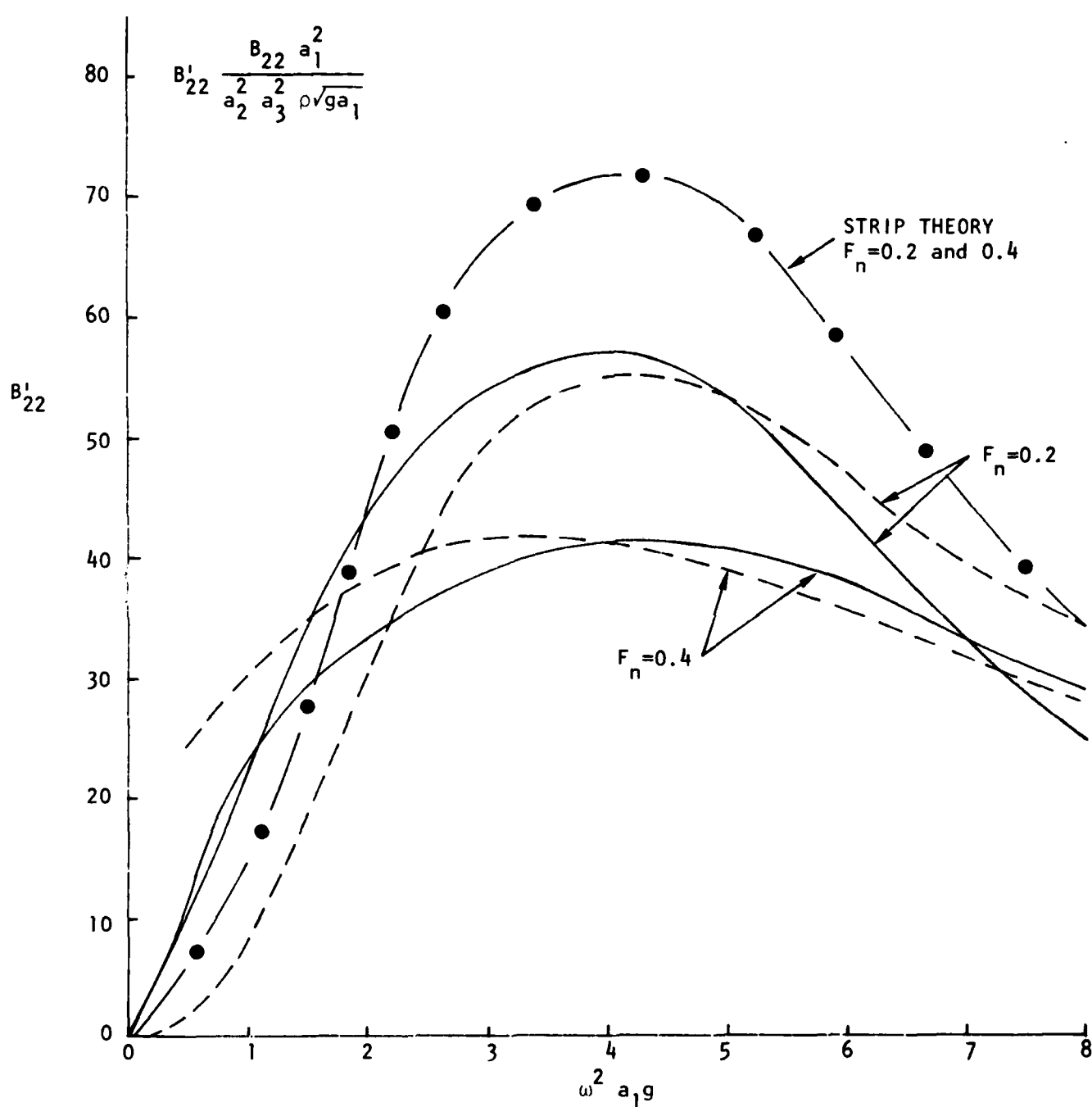


Figure 3. Submerged Ellipsoid - Sway Damping

- STRIP THEORY (SALVESEN et. al. 1970)  
 - - - FULLY THREE DIMENSIONAL LINEAR (NEWMAN 1961)  
 — SLENDER BODY APPROXIMATION

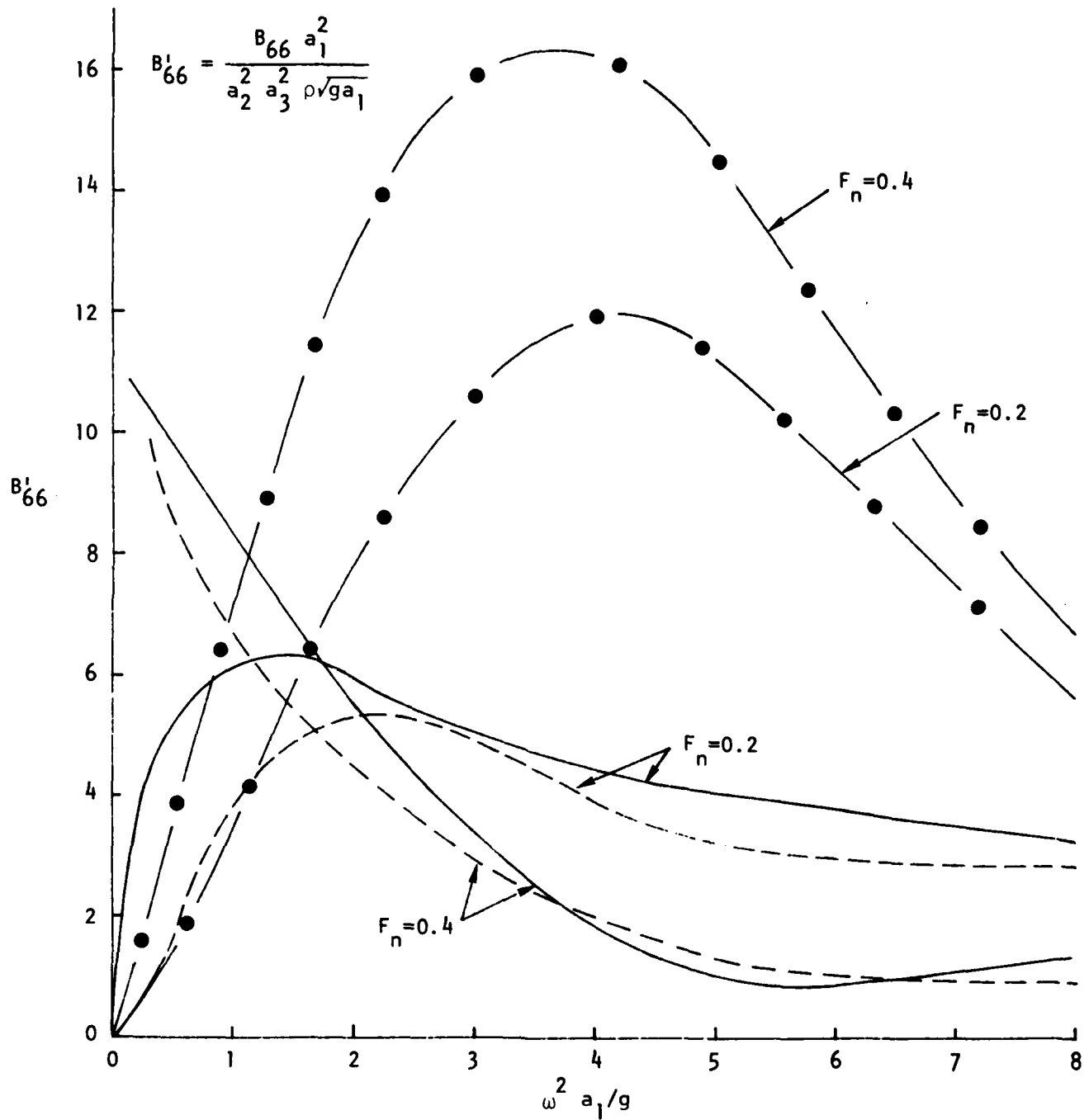


Figure 4. Submerged Ellipsoid - Yaw Damping

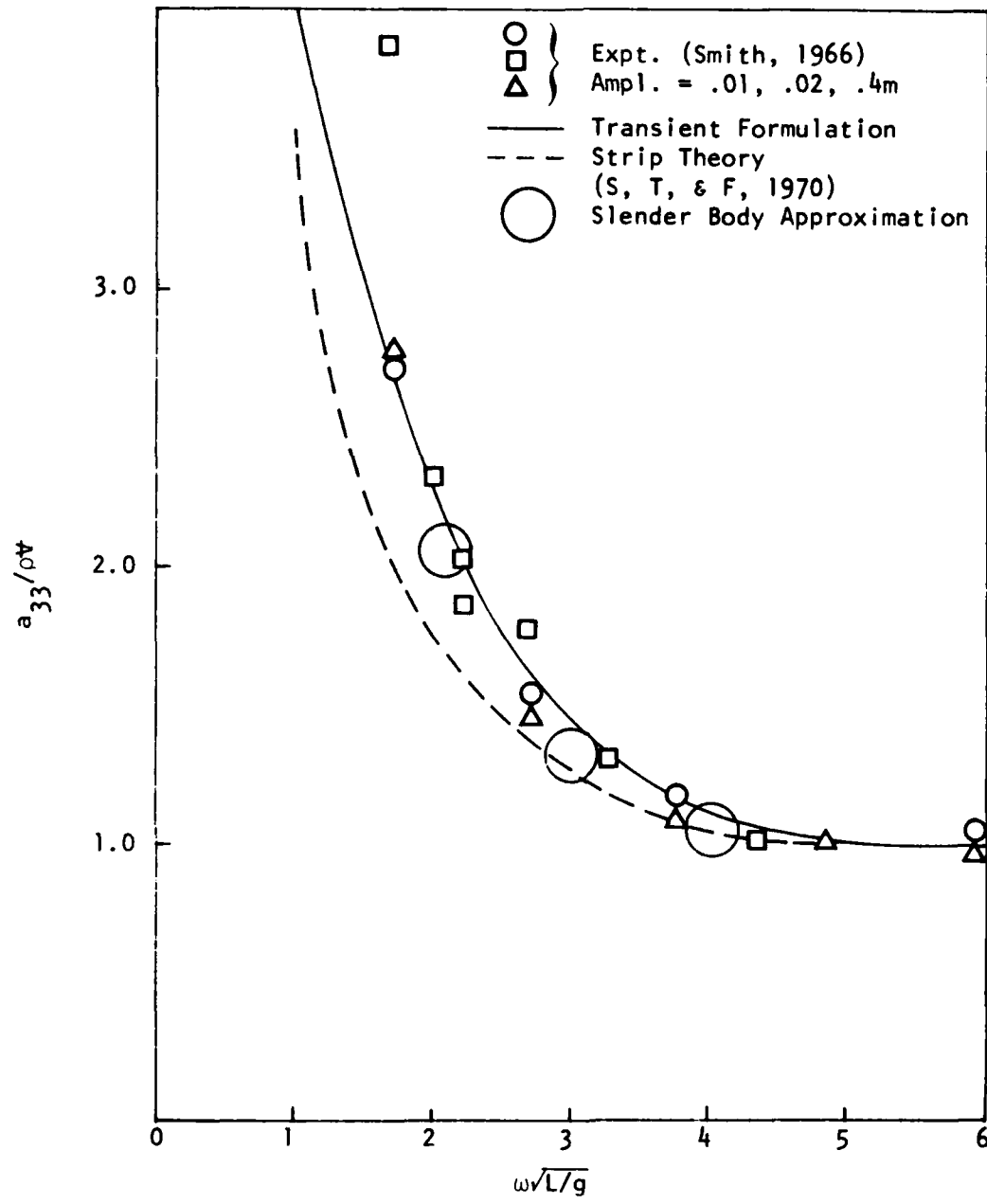


Figure 5. Heave Added Mass

Friesland Destroyer Hull

$$C_B = 0.55, F_n = 0.35$$

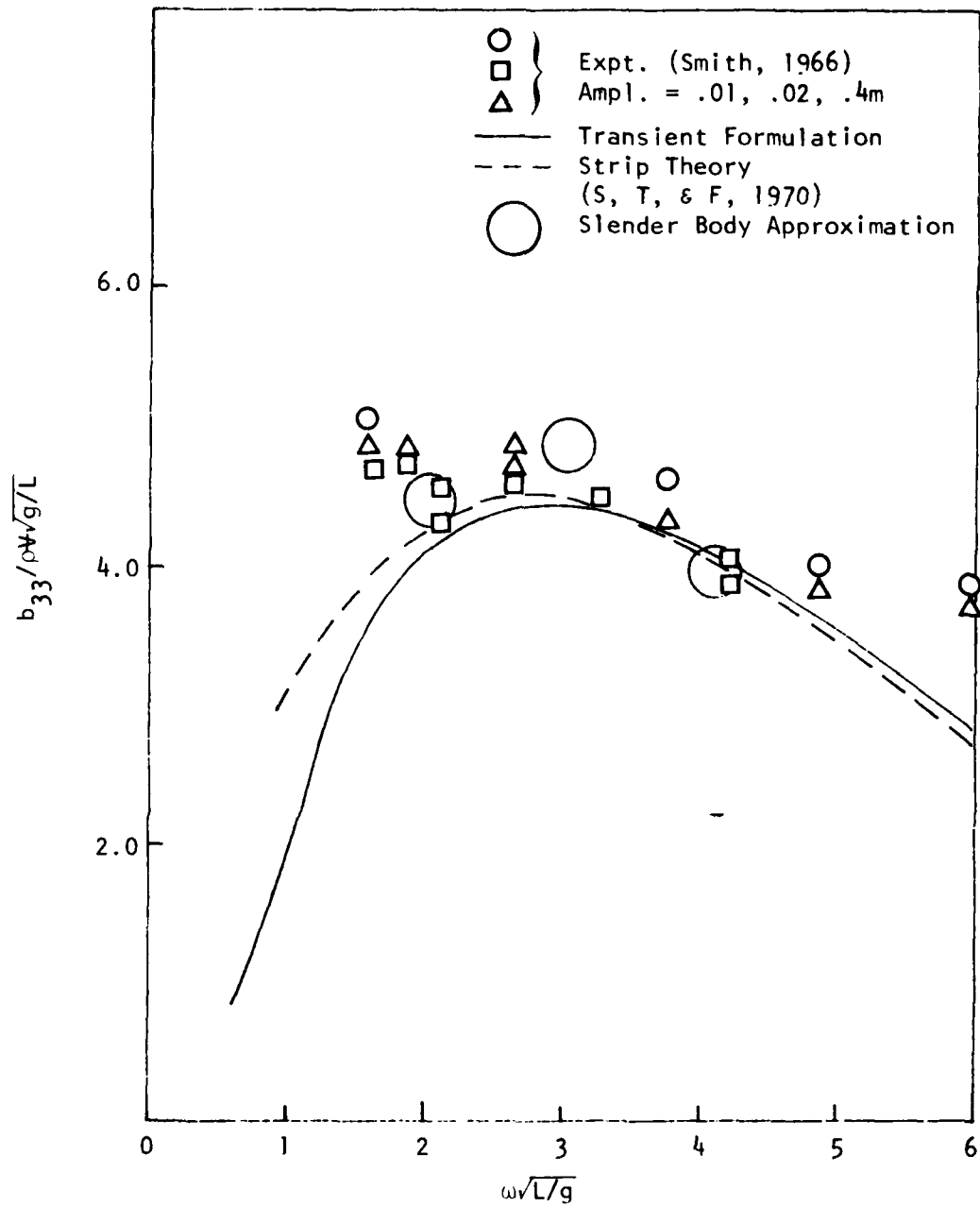


Figure 6. Heave Damping

Friesland Destroyer Hull

$$C_B = 0.55, F_n \approx 0.35$$



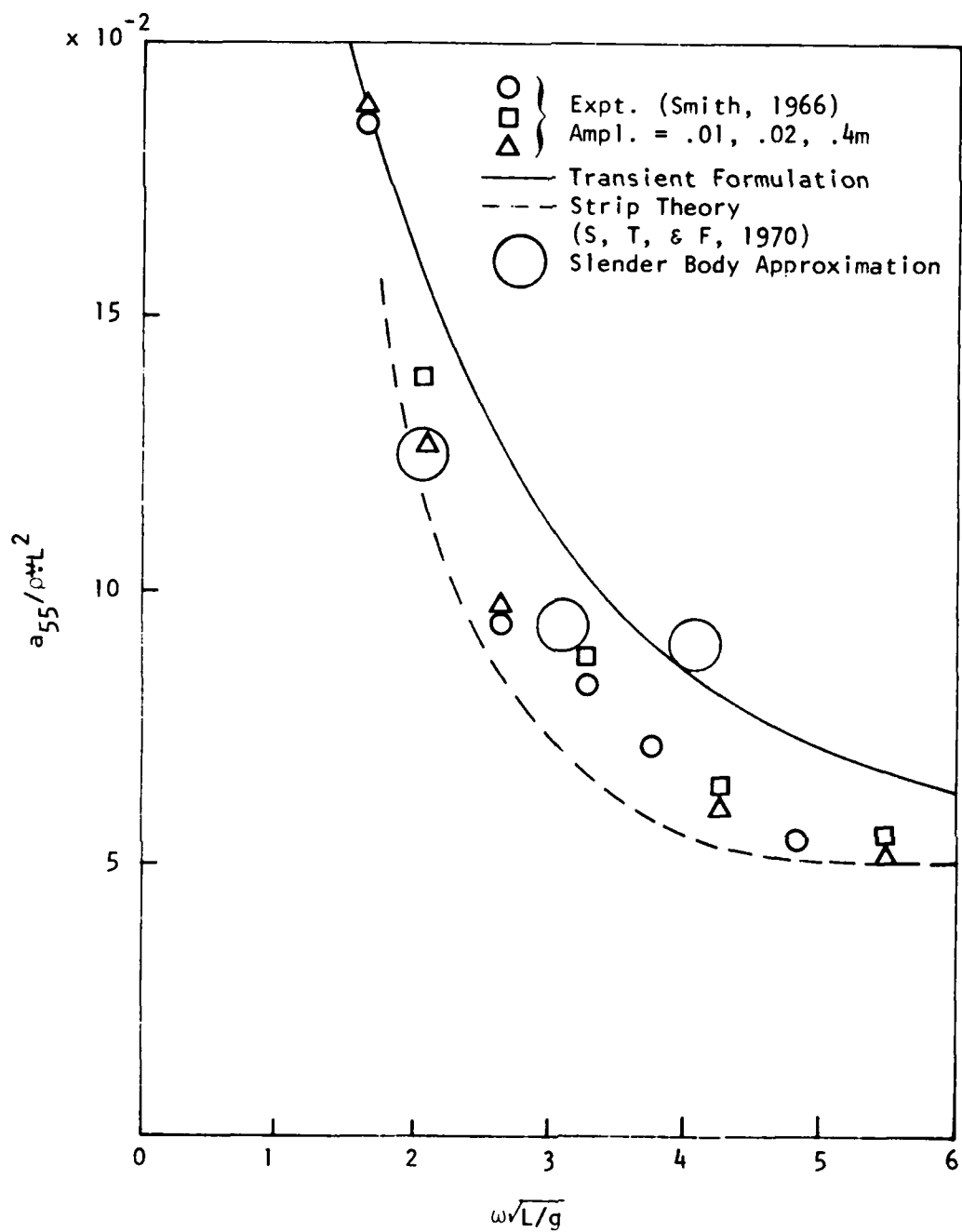


Figure 7. Pitch Added Mass

Friesland Destroyer Hull

$$C_B = 0.55, F_n = 0.35$$

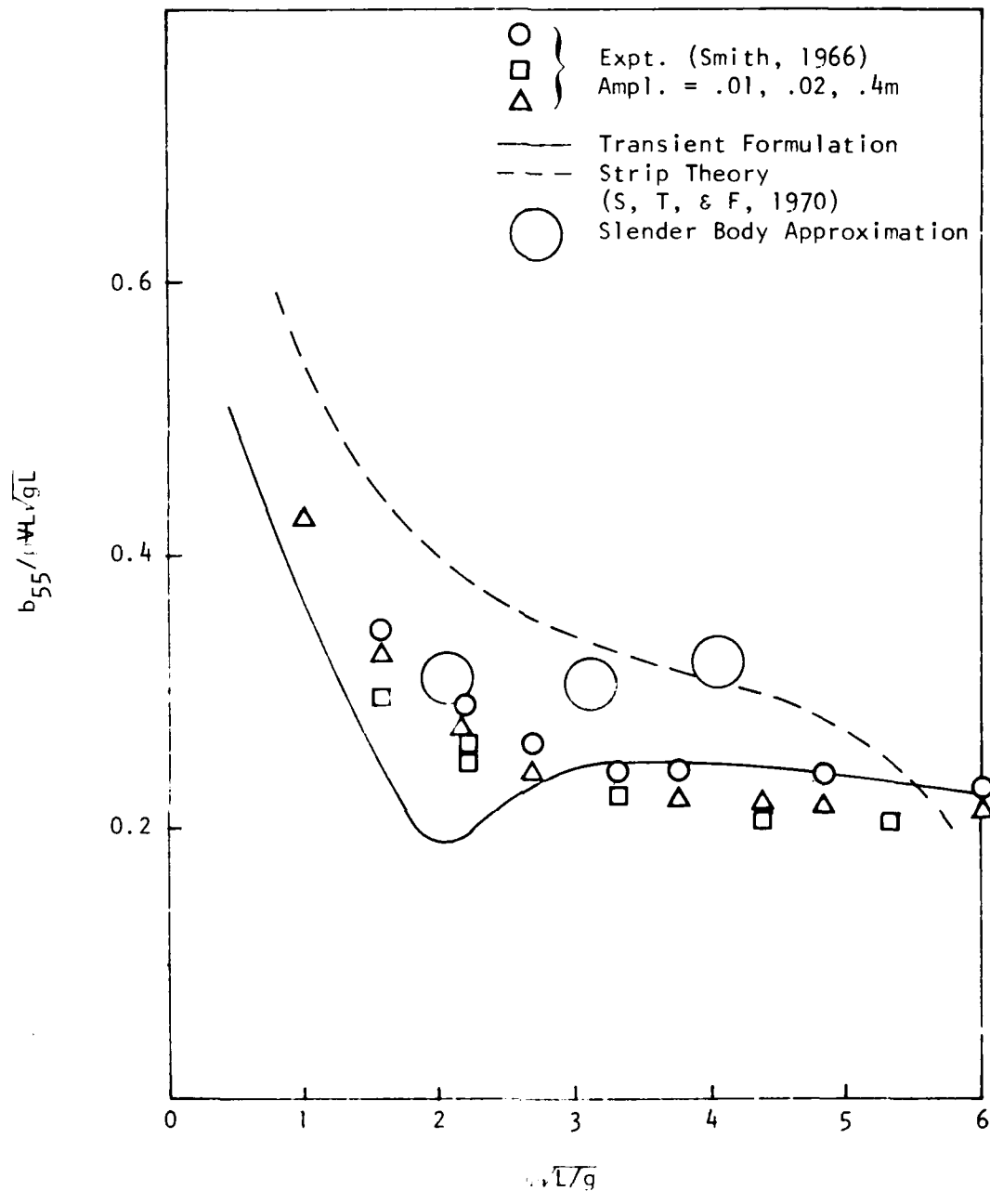


Figure 8 . Pitch Damping

Friesland Destroyer Hull

$$C_B = 0.55, F_n = 0.35$$

Friesland Destroyer Hull

$$C_B = 0.55, F_n = 0.35$$

$$\omega\sqrt{L/g} = 3.0$$

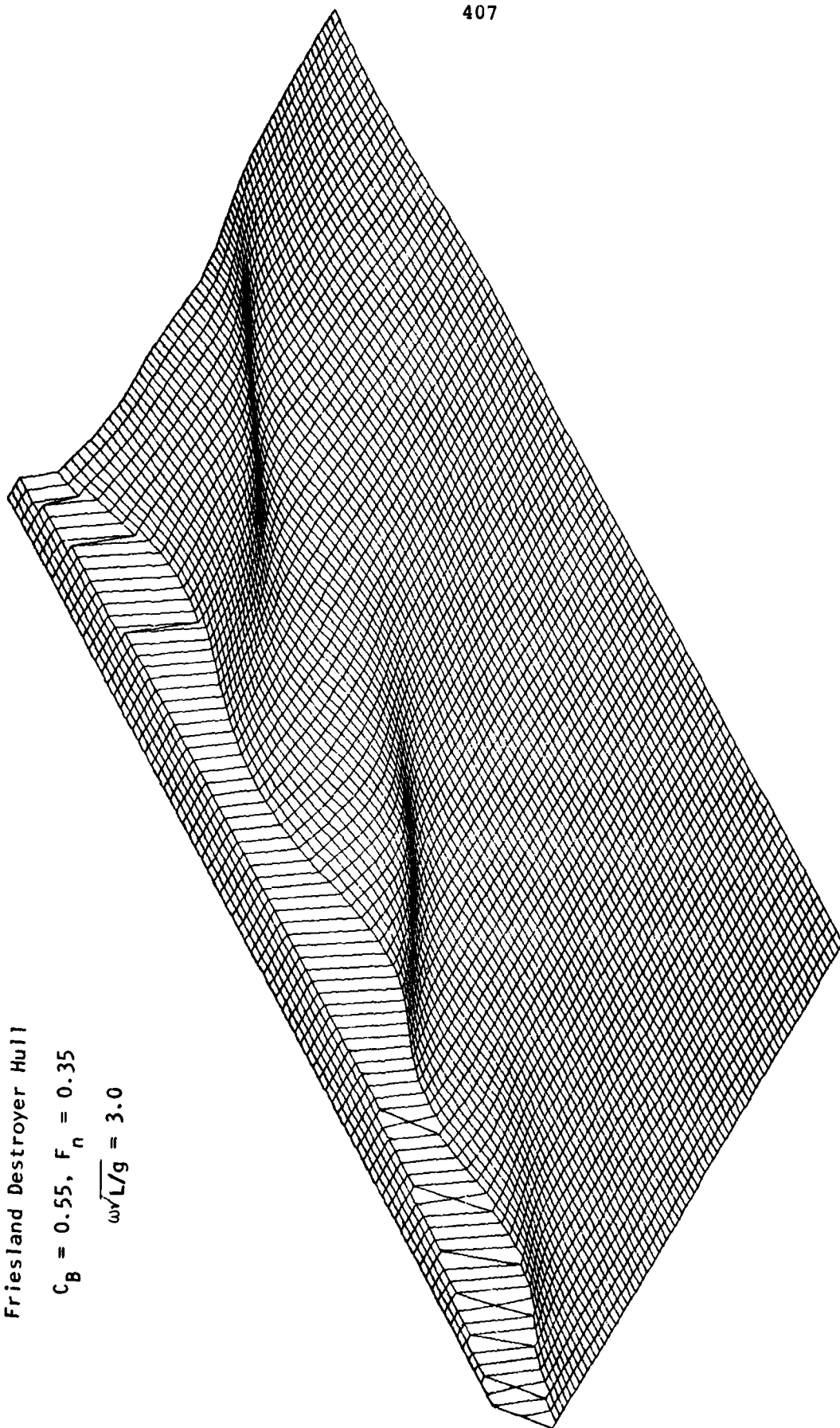


Figure 9. Free Surface Elevation, Unit Heave Motion

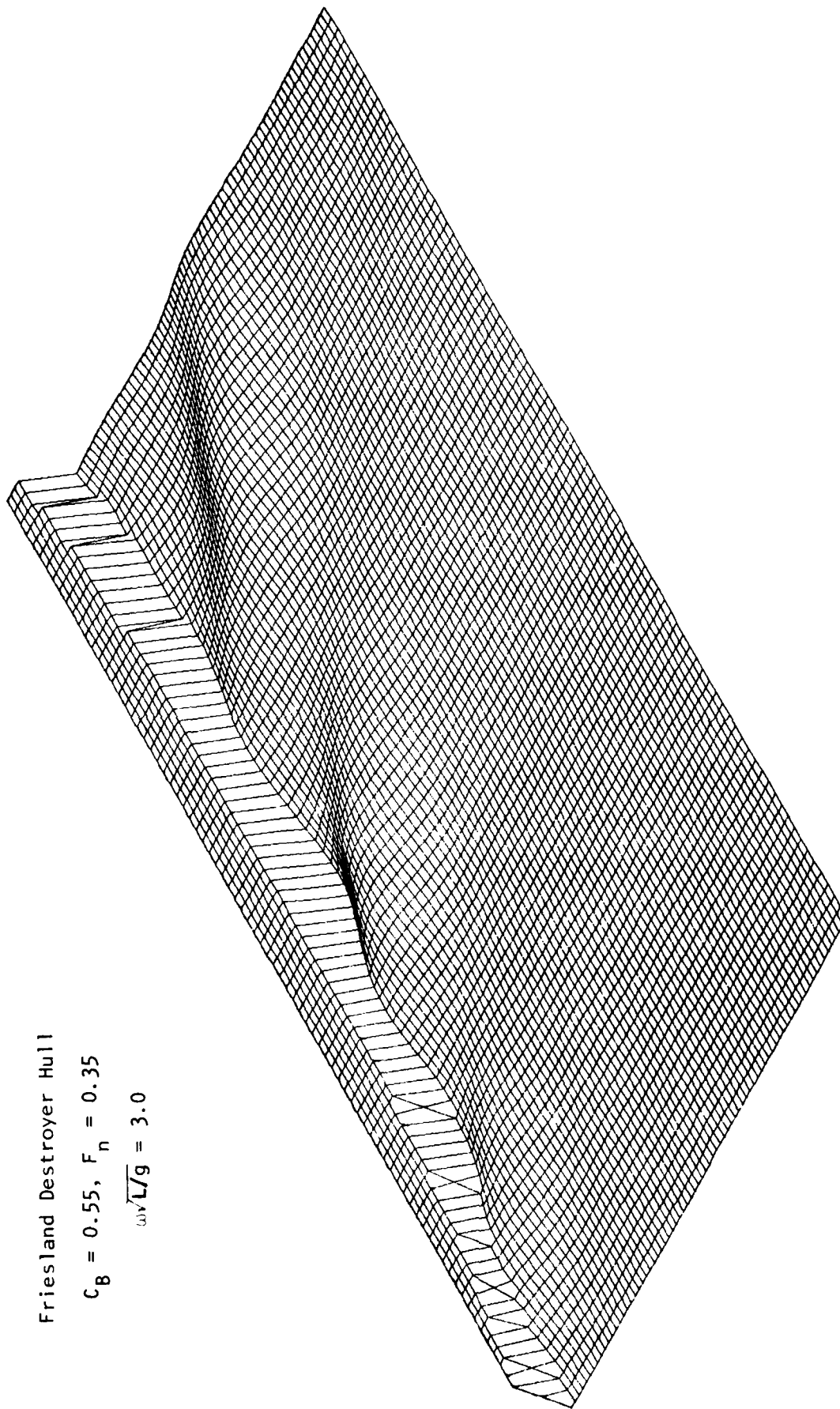


Figure 10. Free Surface Elevation, Unit Pitch Motion

## Discussion

J.N. Newman (MIT)

It appears that with the hull boundary condition linearized, this theory should be essentially the same as that of Yeung and Kim. If that is correct, the numerical results should be identical. It would be helpful to know more precisely how the present work differs from that of Yeung and Kim.

T.F. Ogilvie (MIT)

The authors imply that, by limiting  $\tau = \omega U/g$  to a range  $\tau > \frac{1}{4}$ , they avoid having transverse waves. Of course, they do avoid upstream transverse waves, but there are transverse waves downstream as well, and these are simply lost in the authors' model, as in all mathematical models based on a two-dimensional Laplace equation. Ship length should be much smaller than the shortest transverse-wave wavelength (measured along the shiptrack) for the authors' approach to be valid. They could easily determine how this condition restricts the range of  $\omega$  and  $U$  for which their method may be expected to give realistic results. These restrictions are probably severe:  $U$  should be large, but  $\omega$  should be not large.

A. Papanikolaou (Technical University of Berlin)

What I found interesting was that the time-domain technique supplied started from initial values given by a frequency-domain technique. In that respect, starting from a second-order frequency-domain solution should be more successful. Here, neglecting the nonlinear free-surface boundary condition, especially if all wave systems of a ship advancing in waves are considered, one cannot judge the importance of nonlinearities in ship motions and sea loads. Why did you compare only linear quantities (added mass, damping) to other linear theories (e.g., Newman) and not any nonlinear features?

N. Toki (Mitsubishi Heavy Industries)

I would like to ask the authors' opinion on how to apply their nonlinear simulation method for large-amplitude ship motions to a practical design. The assumption of linear super-position makes many things easy. We can carry out the statistical estimation to get a design value after obtaining a linear amplitude operator or a relatively short time history. However, dealing with nonlinear responses, the situation becomes different.

EXTREME WAVE CONTAINING 1/10000 HIGHEST MEAN WAVE ELEVATION  
SEA SPECTRUM : JONSWAP

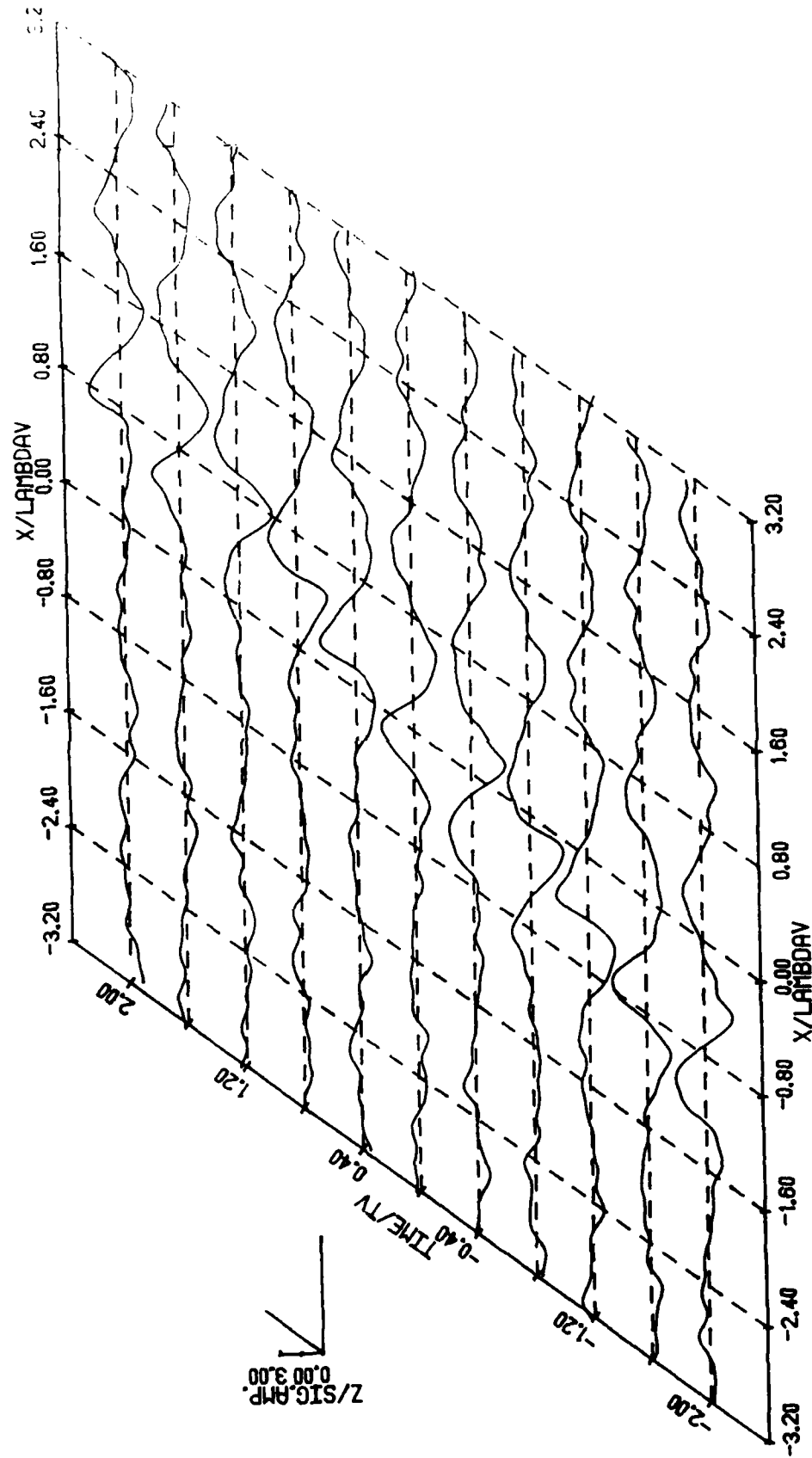


Fig. A

EXTREME WAVE CONTAINING 1/10000 HIGHEST MEAN WAVE ELEVATION  
SEA SPECTRUM : JONSWAP

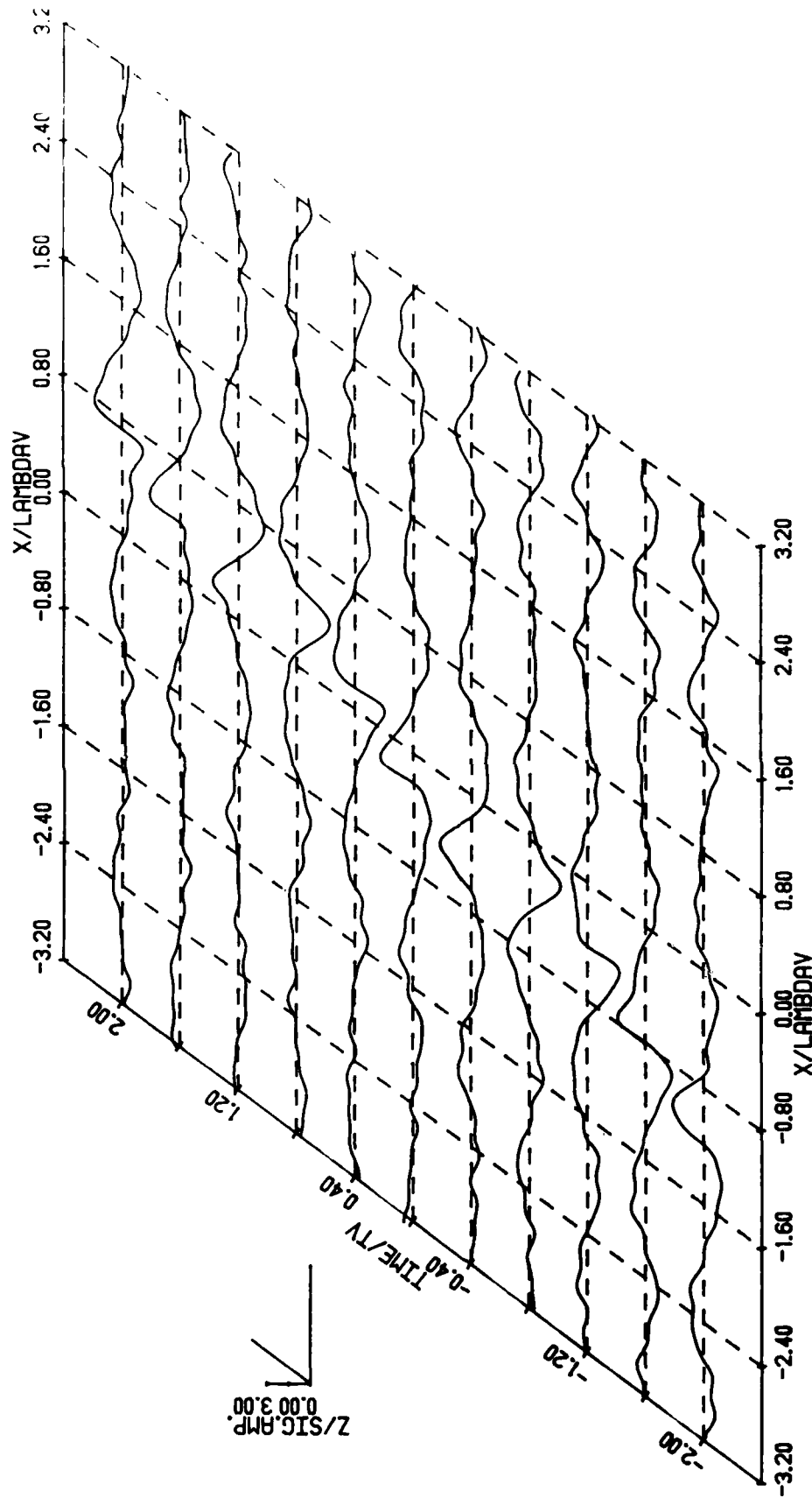


Fig. B

EXTREME WAVE CONTAINING 1/10000 HIGHEST MEAN WAVE ELEVATION  
SEA SPECTRUM : JONSWAP

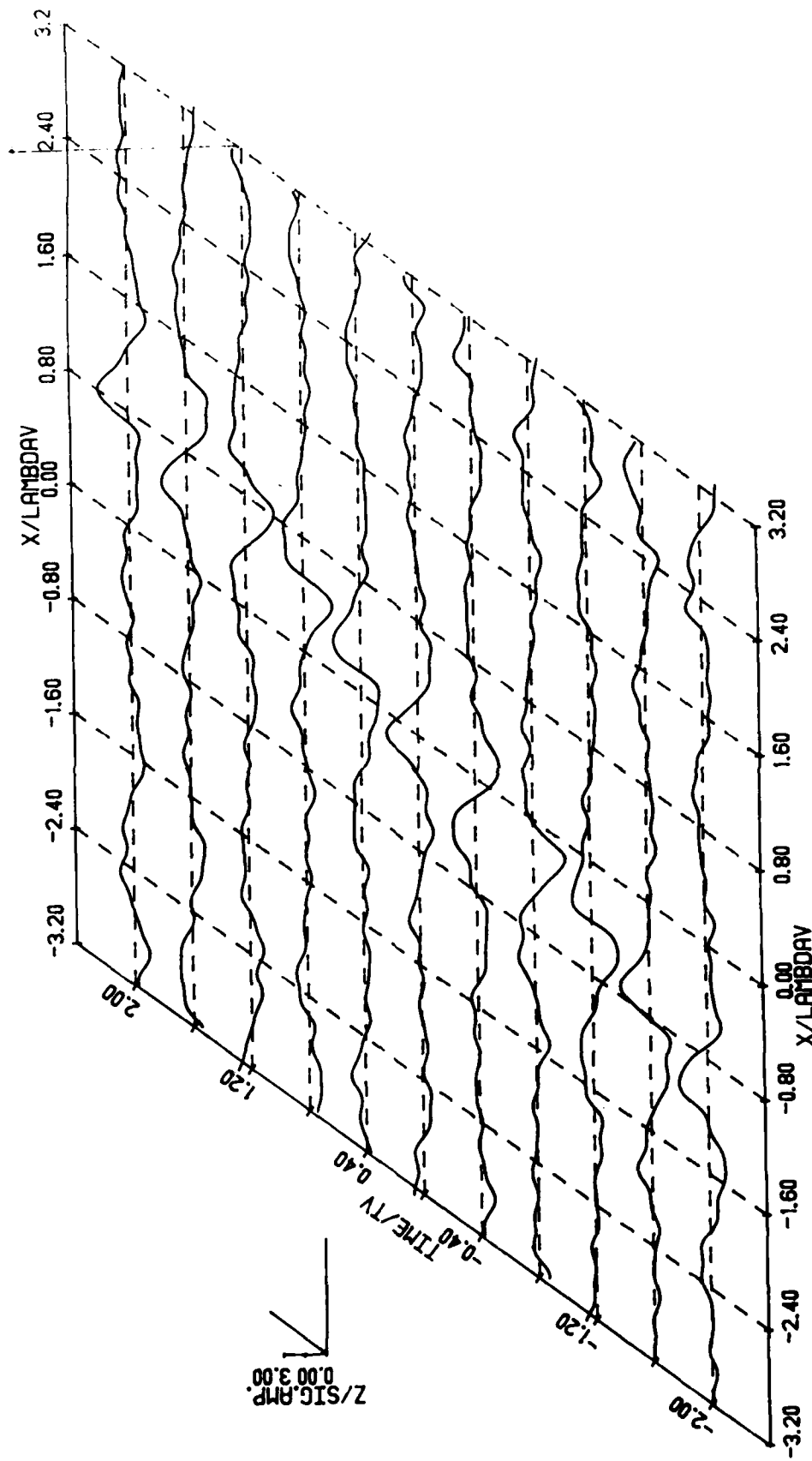


Fig. C



The ways that I think of are:

1. To carry out a long enough simulation to pick up extreme values directly. Or to repeat simulation many times using different incident wave time histories.
2. To finish the statistical consideration at first and obtain a (few) representative time history of the incident wave for a certain extreme condition. And then to carry out a (few) simulation as a deterministic process to obtain design values.

I think the second one is reasonable and more economical. How then can we select the representative? As a first step toward answering this question, I recently surveyed a variety of extreme wave shapes by using an irregular wave model composed of a number of elementary waves. Figures A-C show the wave shapes with respect to space coordinate having the maximum wave elevation close to 1/10,000 highest mean wave elevation at time = 0 and  $x = 0$ . Figure A shows an example having a large value of crest front steepness. Figure B, on the contrary, shows another example having a large value of crest rear steepness and a small value of crest front steepness. The extreme wave shapes have such variety. Figure C shows an example that the present discussor proposes to use as an interim "design irregular wave" having a considerably large value of crest front steepness.

### Author's Reply

D. J. Loeser, N. Salvesen, and D. Yue (Science Applications, Inc.)

As noted by Professor Newman, our slender-body formulation, first used by Chapman (1975, 1976), is indeed similar to that of Yeung and Kim (1981) in the linearized case. As discussed in the paper, our numerical approach is quite different from that of earlier authors. Our linear results for the Friesland are only preliminary; with refinement, they should compare well with Yeung and Kim.

Professor Ogilvie is correct in pointing out that the transverse wave fields are omitted in any approach using only a two-dimensional Laplacian.

Our original assumptions imply that the method is applicable to high Froude numbers and low frequencies. However, since the zero speed limit of our procedure is identical to that of strip theory and the submerged ellipsoid results agree uniformly with those of Newman over the frequency range, it appears that the requirement that  $\partial/\partial x \ll \partial/\partial y$  and  $\partial/\partial z$  may be less restrictive than indicated by the original assumptions. Any final test of the range of applicability of this procedure will be comparisons with experiments and fully three-dimensional calculations.

As commented by Dr. Papanikolaou, the nonlinear code could be initialized using a second-order frequency-domain solution rather than the linear solution. However, the additional complications and cost would probably not be justified.

Our present method using a linearized free surface still allows us to study important large-amplitude features such as the effect of above-water geometry on the ship response. The formulation allows for the systematic extension of the computer code to include a nonlinear free surface. This extension is part of our long-term objective.

The authors agree with Mr. Toki that, since linear superposition cannot be used for nonlinear problems, it is important to choose appropriate inputs to the time-domain simulation to ensure that the results will be useful for practical ship design. This is a difficult problem, and further research in this area is much needed.

*Session IV*

**NONLINEAR FREE-  
SURFACE PROBLEMS AND  
CAVITATION**

# Prediction of Relative Motion of Ships in Waves

Choung M. Lee

Office of Naval Research, Arlington, VA 22207, U.S.A.

John F. O'Dea and William G. Meyers  
David W. Taylor Naval Ship R&D Center  
Bethesda, MD 20084

## ABSTRACT

An analytical method is developed for predicting the vertical motion of a point on a ship relative to the free surface. The method accounts for the deformation of the free surface caused by diffraction and by the waves generated by the motion of the ship. Computed results are compared to experimental results for two hull forms. The phase relations among the incident, diffracted and radiated wave components are found to play a significant role in determining the total free-surface motion. The strip theory used in the present work appears to be inaccurate in predicting correct phase relationships for these components.

## INTRODUCTION

In an assessment of the seakeeping qualities of a ship the deck wetness, bottom slamming, and rudder or propeller emergence are some of the important factors to be taken into account. The occurrence of these events is directly governed by the so-called "relative motion." The relative motion is the measure of the vertical motion of a ship with respect to the undulating free-surface motion.

For instance, if a ship is sailing in a long swell, the vertical motion of any points on the ship would be in unison with the vertical motion of the free surface directly below or above the hull points; hence, the relative motion would be zero. On the other hand, when a large ship is moving in small waves and, therefore, there is practically no motion of the ship but steady forward motion, the relative motion of the ship would be the negative of the wave motion.

Current practice in computing ship relative motion usually neglects interference effects caused by ship-generated waves on the incoming waves. The main reason for neglecting the deformation effect on the oncoming waves has been due to the difficulties involved in its computation. A ship moving in waves creates various wave components which

would interfere with the oncoming waves. These interfering waves are generated by the forward motion, the wave-excited oscillatory motions in six degrees of freedom, and the diffraction by the ship hull. The importance of calculating accurate free-surface motion alongside a ship hull in the relative motion calculation has been well recognized by ship motion researchers because of the clear experimental evidence presented by Cox and Gerzina (1974), Gerzina and Woo (1975), and Bales et al. (1975), showing the discrepancies in the existing theoretical methods. The purpose of the present investigation is to compute the aforementioned individual components of the ship-generated waves and incorporate them into the calculation of relative motions of ships.

To check the validity of the various assumptions made in the theoretical analysis, the calculated results are correlated with model experimental results obtained at the Maneuvering and Seakeeping Basin of DTNSRDC.

The analytical method developed here is based on a two-dimensional approximation within the context of strip theory, which was described in detail by Lee (1982). The main reasons for employing the two-dimensional approximation are first, for its simplicity in incorporating into an existing ship motion computer program which is also based on strip theory given by Salvesen et al. (1970) and second, for checking the validity of the relative motion prediction based entirely on a strip theory. Since there has been no conclusive evidence to demonstrate that ship motion is better predicted by three-dimensional theories than by strip theory, the present investigation, until a reliable other method is developed, is deemed as the necessary first step toward improving the prediction of the relative motions of ships within the present state-of-the-art in ship motion theory.

#### THEORETICAL ANALYSIS

Formulation of the problem is made under the assumption of an ideal fluid, the velocity vector field of which can be represented by the gradient of the velocity potential function  $\Phi$ . It is assumed that the depth of the water is infinite and that no current and wind exist. It is also assumed that the response of a ship to the wave excitation is linear and that the irregular ocean waves can be represented by a linear superposition of various harmonic wave components. Thus, the ship response to the irregular ocean waves can be obtained by determining the frequency response function of the ship to harmonic wave excitations.

The coordinate system to be used in the analysis is a right-handed Cartesian coordinate system which translates on the calm-water plane with the mean speed of the ship. The origin is located on the calm-water plane directly above or below the center of the gravity of the ship at its mean position. The x-axis is directed toward the mean course of the ship, and the z-axis is directed vertically upward, as shown in Figure 1.

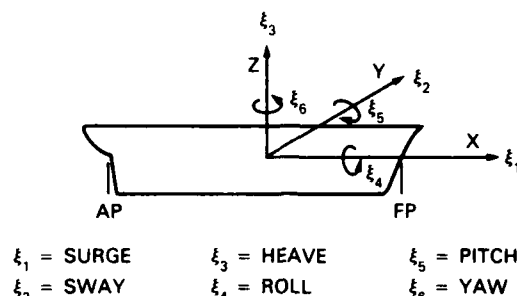
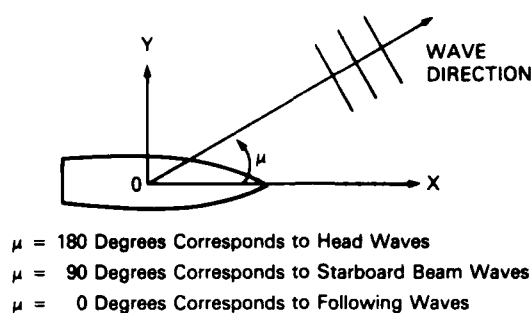


Figure 1 — Description of Coordinate System

Total fluid disturbances generated by the progressive sinusoidal waves of length  $\lambda$ , heading angle  $\mu$ , and amplitude  $\zeta_A$ , with a ship of slender geometry undergoing oscillatory motion at a mean speed  $U$ , can be described, within the linear analysis, by

$$\Phi(x, y, z, t) = -Ux + \phi_s(x, y, z) + \text{Re}[\phi_0(x, y, z)e^{i\omega_e t}] \quad (1)$$

where  $\phi_s$  represents the disturbance of the fluid by the ship at the steady speed  $U$  in calm water;  $\phi_0$  represents the oscillating fluid disturbance generated by the incident wave and the motion of the ship;  $i$ ,  $t$  and  $\omega_e$ , respectively, are the imaginary unit, time, and the wave-encounter frequency which is related to the incident wave frequency  $\omega$  by  $\omega_e = \omega - 2\pi U \cos \mu / \lambda$ , and  $\text{Re}$  means the real part of what follows.

The oscillatory velocity potential  $\phi_0$ , which is given in the form of complex amplitude, can be further decomposed into

$$\phi_0 = \phi_I + \phi_D + \sum_{k=1}^6 \phi_k \bar{\xi}_k \quad (2)$$

where  $\phi_I$  represents the incident-wave potential;  $\phi_D$  the diffraction potential;  $\phi_k$  the radiation wave potential associated with the  $k$ th mode of motion of the ship; and  $\bar{\xi}_k$  the complex amplitude of the

displacement of the ship from its mean position in the direction of the  $k$ th mode of motion.

The incident-wave potential  $\phi_I$  is explicitly given by

$$\phi_I(x, y, z) = i \frac{g \zeta_A}{\omega} e^{-iK(x \cos \mu + y \sin \mu) + Kz} \quad (3)$$

where  $g$  is the gravitational acceleration and  $K = \omega^2/g = 2\pi/\lambda$  is the wave number in deep water. The diffraction potential  $\phi_D$  should satisfy the diffraction principle of water waves, i.e.,

$$\frac{\partial \phi_D}{\partial n} + \frac{\partial \phi_I}{\partial n} = 0 \quad (4)$$

on the ship hull surface  $S_0$  at its mean position where  $\partial/\partial n$  means the normal derivative on  $S_0$  and the normal vector  $\underline{n}$  is into the hull.

The free-surface elevation  $\zeta(x, t)$  can be obtained in terms of  $\phi$  from the Bernoulli equation by

$$\begin{aligned} \zeta(x, y, t) &= -\frac{1}{g} \left( \frac{\partial}{\partial t} - U \frac{\partial}{\partial x} \right) \phi(x, y, 0, t) + O(\phi^2) \\ &= \frac{U}{g} \left[ \phi_{sx}(x, y, 0) + \phi_{0x}(x, y, 0) e^{i\omega_e t} \right] \\ &\quad - i \frac{\omega_e}{g} \phi_0 e^{i\omega_e t} \end{aligned} \quad (5)$$

where the subscript  $x$  means the partial derivative with respect to  $x$  and  $\text{Re}$  is omitted with the understanding that, hereafter, whenever a product involving  $e^{i\omega_e t}$  is present, only the real part of it will be realized.

If  $\zeta$  is decomposed into the steady and oscillatory parts, we can define

$$\zeta = \zeta_s + \zeta_0 e^{i\omega_e t} \quad (6)$$

where

$$\zeta_s(x, y) = \frac{U}{g} \phi_{sx}(x, y, 0) \quad (6a)$$

$$\zeta_0(x, y) = \frac{1}{g} [U \phi_{0x}(x, y, 0) - i\omega_e \phi_0] \quad (6b)$$

If we denote the displacement of the ship from its mean position by  $\xi_k(t)$  where  $k=1,2,\dots,6$ , indicates the surge, sway, heave, roll, pitch and yaw, respectively, we can express the time dependent vertical displacement of a point  $\underline{x} = (x,y,z)$  on the ship,  $\xi_v$ , which is often referred to as "absolute motion," by

$$\xi_v(\underline{x},t) = \xi_3(t) - x\xi_5(t) + y\xi_4(t) \quad (7)$$

for a given initial vertical position  $z$ . Thus, the relative motion  $\xi_R$  at the point  $\underline{x}$  is obtained by

$$\xi_R(\underline{x},t) = \xi_v(\underline{x},t) - \zeta(x,y,t) \quad (8)$$

To determine if a chosen point on the deck will be immersed under the free surface or a point on the ship bottom will be raised above the free surface we can examine whether  $|\xi_R|$  is greater than  $|z+\xi_s-\zeta_s|$  where  $z$  is the vertical coordinate of the point and  $\xi_s$  is the vertical displacement of the point due to sinkage and trim of the ship.

As described in the foregoing, in order to determine the relative motion and the chance of immersion of deck or emergence of ship bottom, we need to know the absolute motion  $\xi_v$ , and the oscillatory and steady free surface elevation,  $\zeta_0$  and  $\zeta_s$ , and the sinkage and trim of the ship. These quantities can be obtained if we can determine the velocity potentials,  $\phi_s$ ,  $\phi_D$ , and  $\phi_k$  for  $k=1,2,\dots,6$ .

#### STEADY EFFECTS

When a ship is advancing in waves, the mean freeboard may be changed by several effects. These include sinkage, trim and wave profile due to forward speed in calm water, plus a possible additional mean shift in these quantities caused by the oscillatory motions of the ship and waves, and its forward speed. Various theoretical methods are available to calculate the steady effects associated with a ship at a constant speed in calm water, ranging from simple thin-ship theory to three-dimensional source panel distribution methods as shown by Bai and McCarthy (1979). From the model experiments conducted in the past, it is well known that the steady wave profile  $\zeta_s$  can be significantly influenced by the sinkage and trim of a ship; however, due to the extreme complexities in the mathematical modelling of the bow-wave phenomenon no existing computational methods have succeeded in correctly predicting the effect of sinkage and trim on  $\zeta_s$ . Since the main focus of the present study is on the prediction of the relative motion  $\xi_R$ , no attempts will be made to improve the prediction of  $\zeta_s$  with more rigorous analysis.

In the present study, an empirical method derived by Bishop and Bales (1978) is used to predict calm water sinkage and trim, and a thin-ship assumption is made to calculate the bow wave profile. The empirical formulas for sinkage  $z_0$ , and trim  $\theta_0$ , are given as quadratic and cubic equations, respectively, which are based on a regression



analysis for a number of destroyer type hulls. The equations may be given in nondimensional form as

$$z_o/L = a_1 \cdot F_n + a_2 \cdot (F_n)^2 \quad (9a)$$

$$\theta_o = b_1 \cdot F_n + b_2 \cdot (F_n)^2 + b_3 \cdot (F_n)^3 \quad (9b)$$

where  $L$  is the length of the ship and  $F_n$  is the Froude number based on ship length. The coefficients have been derived separately for hulls with and without bow domes or bulbous bows, and are given in Table 1.

Table 1 - Coefficients for Predicting Sinkage and Trim in Calm Water

	For Ships With Bulbous Bows	For Ships Without Bulbs
$a_1$	-0.00120	0.00081
$a_2$	-0.01492	-0.02095
$b_1$	-1.137	-0.682
$b_2$	11.793	8.507
$b_3$	-23.779	-17.129

#### STEADY-WAVE POTENTIAL

Assuming that the beam  $B$ , of the ship is much less than the length  $L$ , we use the well-known thin-ship theory first introduced by Michell (for a concise description see Wehausen (1973)) to obtain  $\phi_s$  which is given by

$$\begin{aligned} \phi_s(x, y, z) = & \frac{U}{2\pi} \iint_{S^{(0)}} \frac{f_\xi(\xi, \zeta)}{\sqrt{(x-\xi)^2 + y^2 + (z-\zeta)^2}} d\xi d\zeta \\ & - \frac{U}{2\pi} \iint_{S^{(0)}} \hat{G}_0(x-\xi, y, z+\zeta) f_\xi(\xi, \zeta) d\xi d\zeta \end{aligned} \quad (10)$$

where  $S^{(0)}$  denotes the longitudinal center plane of ship;  $f$  is the half local beam; and the Green function  $\hat{G}_0$  representing a source of unit strength translating in the direction of the positive  $x$ -axis with a constant velocity  $U$  at the depth of  $\zeta$  from the calm water surface is given by

$$\begin{aligned} \hat{G}_0(x-\xi, y, z+\zeta) = & \frac{1}{\sqrt{(x-\xi)^2 + y^2 + (z+\zeta)^2}} + \frac{4g}{\pi U^2} \int_0^{2\pi} d\theta \int_0^\infty dk e^{k(z+\zeta)} \\ & \cdot \frac{\cos[k(x-\xi)\cos\theta]\cos(ky\sin\theta)}{k\cos^2\theta - g/U^2} \\ & + \frac{4g}{U^2} \int_0^{2\pi} d\theta \sec^2\theta e^{\frac{g}{U^2}(z+\zeta)\sec^2\theta} \sin\left[\frac{g}{U^2}(x-\xi)\sec\theta\right] \\ & \cdot \cos\left(\frac{g}{U^2}y\sin\theta\sec^2\theta\right) \end{aligned} \quad (11)$$

in which  $\oint$  means the principal-value integral.

Within the first-order of  $B/L$ , the wave profile along the side of the hull can be obtained from Equations (6a), (10), and (11) by

$$\begin{aligned} \zeta_s(x, 0) = & \frac{U}{g} \phi_{sx}(x, 0, 0) = \text{Re} \left[ -\frac{2i}{\pi^2} \iint_{S^{(0)}} f_\xi d\xi d\zeta \right. \\ & \cdot \left\{ \int_0^{2\pi} d\theta \sec\theta \int_0^\infty e^{kZ'} dk + k_0 \int_0^{2\pi} \sec^3\theta d\theta \oint_0^\infty \frac{e^{kZ'}}{k - k_0 \sec^2\theta} dk \right\} \\ & \left. - \frac{2g}{\pi U^2} \iint_{S^{(0)}} f_\xi d\xi d\zeta \int_0^{2\pi} d\theta \sec^3\theta e^{k_0 \sec^2\theta Z'} \right] \end{aligned} \quad (12)$$

where

$$k_0 = g/U^2 \quad \text{and} \quad Z' = \zeta + i(x-\xi)\cos\theta$$

#### RADIATION AND DIFFRACTION POTENTIALS

In the foregoing section we assumed that the beam of the ship is much smaller than the length. We further assume that the draft  $T$  is also much smaller than the length, and that the longitudinal slope of the ship is much smaller than the transverse slope. In mathematical expressions, the above assumptions correspond to  $B/L$ ,  $D/L$ ,  $n_1 = O(\epsilon)$  for small positive number  $\epsilon$  where  $n_1$  is the  $x$ -component of the unit normal vector  $\underline{n} = (n_1, n_2, n_3)$  on the ship surface. We often call the body which fits the geometric property described above a slender body. In parallel with this slender body geometry, if we assume that the disturbances of the fluid due to the wave diffraction and the oscillatory body motion are  $O(\epsilon)$  in the  $x$ -direction compared to those in the  $y$ - and  $z$ -direction, we can approximate  $\phi_D$  and  $\phi_k$  for  $k=1,2,\dots,6$  by the so-called strip theory. That is, for given  $x$  these potentials can be treated as functions of  $y$  and  $z$  only.

For the radiation potentials  $\phi_k$  for  $k=2, 3$  and  $4$ , the two-dimensional solution for infinitely long horizontal cylinders having ship-like cross sections is well-known [Tasai (1959), Porter (1960), and Frank (1967)]. Then invoking the slender-body assumption, we can determine [Salvesen et al. (1970)] that

$$\phi_5 = - \left( x - \frac{U}{i\omega} \right) \phi_3(y, z; x) \quad (13)$$

$$\phi_6 = \left( x - \frac{U}{i\omega} \right) \phi_2(y, z; x) \quad (14)$$

The diffraction potential  $\phi_D$  is obtained in the same manner as for the radiation potentials  $\phi_2$  and  $\phi_3$  [Lee (1982)] except for imposing the kinematic body-boundary conditions as follows:

$$\frac{\partial \tilde{\phi}_2}{\partial N} = - \omega \zeta_A e^{Kz} [N_2 \sin \mu \cos(Ky \sin \mu)$$

$$+ N_3 \sin(Ky \sin \mu)] = \text{the odd part of}$$

$$\left( - \frac{\partial}{\partial N} \phi_I \right) \text{ with respect to } y \quad (15)$$

$$\frac{\partial \tilde{\phi}_3}{\partial N} = i\omega \zeta_A e^{Kz} [N_2 \sin \mu \sin(Ky \sin \mu)$$

-  $N_3 \cos(Ky \sin \mu)]$  = the even part of

$$\left( - \frac{\partial}{\partial N} \phi_I \right) \quad (16)$$

where the tilda sign is used to differentiate the potentials from  $\phi_2$  and  $\phi_3$  and  $\underline{N} = (n_2, n_3)$  is the unit normal vector in the y-z plane. Then we obtain the solution for  $\phi_D$  by

$$\phi_D = \tilde{\phi}_2 + \tilde{\phi}_3 \quad (17)$$

Strictly speaking,  $\phi_D$  obtained by Equation (17) may only be valid for  $\mu = \pm\pi/2$  (beam waves) or relatively long waves of order of ship length. However, the approximation of Equation (17) is maintained in the present work with the anticipation that it will not significantly degrade our solution for the relative motion.

#### MOTION OF A SHIP

The displacement of a ship from its mean equilibrium position in six degrees of freedom is obtained by solving two sets of linearized coupled equations of motion which are shown below

$$(A_{11} + M)\ddot{\xi}_1 + B_{11}\dot{\xi}_1 + Mz_0\ddot{\xi}_5 = F_1 e^{i\omega_e t} \quad (18a)$$

$$(A_{33} + M)\ddot{\xi}_3 + B_{33}\dot{\xi}_3 + C_{33}\ddot{\xi}_3 + A_{35}\ddot{\xi}_5 + B_{35}\dot{\xi}_5 + C_{35}\xi_5 = F_3 e^{i\omega_e t} \quad (18b)$$

$$Mz_0\ddot{\xi}_1 + A_{53}\ddot{\xi}_3 + B_{53}\dot{\xi}_3 + C_{53}\xi_3 + (A_{55} + I_5)\ddot{\xi}_5 + B_{55}\dot{\xi}_5 + C_{55}\xi_5 = F_5 e^{i\omega_e t} \quad (18c)$$

$$(A_{22} + M)\ddot{\xi}_2 + B_{22}\dot{\xi}_2 + (A_{24} - Mz_0)\ddot{\xi}_4 + B_{24}\dot{\xi}_4 + A_{26}\ddot{\xi}_6 + B_{26}\dot{\xi}_6 = F_2 e^{i\omega_e t} \quad (19a)$$

$$(A_{42} - Mz_0)\ddot{\xi}_2 + B_{42}\dot{\xi}_2 + (A_{44} + I_4)\ddot{\xi}_4 + B_{44}\dot{\xi}_4 + C_{44}\xi_4 + (A_{46} - I_{46})\ddot{\xi}_6 + B_{46}\dot{\xi}_6 = F_4 e^{i\omega_e t} \quad (19b)$$

$$A_{62}\ddot{\xi}_2 + B_{62}\dot{\xi}_2 + (A_{64} - I_{46})\ddot{\xi}_4 + B_{64}\dot{\xi}_4 + (A_{66} + I_6)\ddot{\xi}_6 + B_{66}\dot{\xi}_6 = F_6 e^{i\omega_e t} \quad (19c)$$

In the foregoing equations  $M$  is the mass of the ship;  $I_4$ ,  $I_5$  and  $I_6$  are the mass moment of inertia about the  $x$ -,  $y$ -, and  $z$ -axis, respectively, and  $I_{46} = \iiint_V \rho_m xz \, dv$  where  $\iiint_V dv$  is the ship volume integral,  $\rho_m$  the point mass density;  $C_{ij}$ 's are the hydrostatic restoring coefficients which are given by

$$C_{33} = \rho g \iint_{A_W} dx dy \quad (20a)$$

$$C_{35} = C_{53} = - \rho g \iint_{A_W} x \, dx dy \quad (20b)$$

$$C_{44} = Mg \overline{GM} \quad (20c)$$

$$C_{55} = Mg \overline{GM}_\ell \quad (20d)$$

where  $\iint_{A_W}$  is the integral over the waterplane area and  $\overline{GM}$  and  $\overline{GM}_\ell$  are, respectively, the transverse and longitudinal metacentric heights. The hydrodynamic coefficients  $A_{ij}$ ,  $B_{ij}$  and  $F_i$  represent the added masses, damping coefficients, and wave excitation forces.

According to the strip theory, the expressions for the hydrodynamic coefficients in terms of the radiation potentials  $\phi_k$  can be given by: (see e.g., Lee (1976))\*

$$A_{ik} = \text{Re} \left\{ - \frac{\rho}{\omega_e^2} H_{ik} \right\} \quad (21)$$

\* The difference in the sign from Lee (1976) is due to the change in the harmonic time dependence from  $e^{-i\omega_e t}$  to  $e^{i\omega_e t}$  in the present work.

$$B_{ik} = \text{Im} \left\{ \frac{\rho}{\omega_e} H_{ik} \right\} \quad (22)$$

where, with the notation  $j$  indicating the imaginary unit,

$$H_{ik} = \iint_{S_0} (\phi_{iN}(y, z; x) - 2UN_3\delta_{i5} + 2UN_2\delta_{i6})\phi_k \, ds \quad (23)$$

$$F_i^{(e)} = \rho \iint_{S_0} \left[ -j\omega N_i + \left( \phi_i(y, z; x) - \frac{2U}{j\omega} \phi_3\delta_{i5} + \frac{2U}{j\omega} \phi_2\delta_{i6} \right) \frac{\partial}{\partial N} \right] \phi_i \, ds \quad (24)$$

and  $\delta_{ij}$  is the Kronecker delta.

Since the equations of motion given by (18) and (19) are linear, we can readily set

$$\xi_i = \bar{\xi}_i e^{i\omega_e t} \quad (25)$$

where  $\bar{\xi}_i$  is the complex amplitude of the  $i$ th mode of motion independent of time. Substitution of Equation (25) into Equations (18) and (19) yields two algebraic equations, which can be easily inverted to find the solutions for  $\bar{\xi}_i$  for  $i=1, 2, \dots, 6$ . The amplitude and phase of each mode of motion then can be obtained by

$$\xi_{i0} = |\bar{\xi}_i| \quad (26a)$$

$$\alpha_i = \arctan(\text{Im}\bar{\xi}_i / \text{Re}\bar{\xi}_i) \quad (26b)$$

where  $\alpha_i$  is the phase lead referred to the incident wave crest at the coordinate origin, and  $\text{Im}$  means the imaginary part of what follows.

#### EXPERIMENTAL PROCEDURE

The relative motion experiments were conducted in the Maneuvering and Seakeeping (MASK) Basin at DTNSRDC. This basin is 110 m long by 73 m wide. Pneumatic wavemakers are mounted on two adjacent sides of the basin, and there are sloping beaches on the opposite sides to absorb the waves. The towing carriage is supported from a rotatable

bridge. By proper alignment of the bridge angle and appropriate choice of wavemaker bank, any desired heading of a ship model relative to wave direction can be obtained.

Two ship hull forms were selected for the purpose of validation. The first, designated Ship A, is a modern, high speed container ship. The second, designated Ship B, is a typical Naval combatant hull form. Body plans of the two hulls are shown in Figure 2, and their principal characteristics are shown in Table 2. Ship A has a relatively large bulbous bow and cruiser stern, while Ship B has no bulb but does have a wide transom stern.

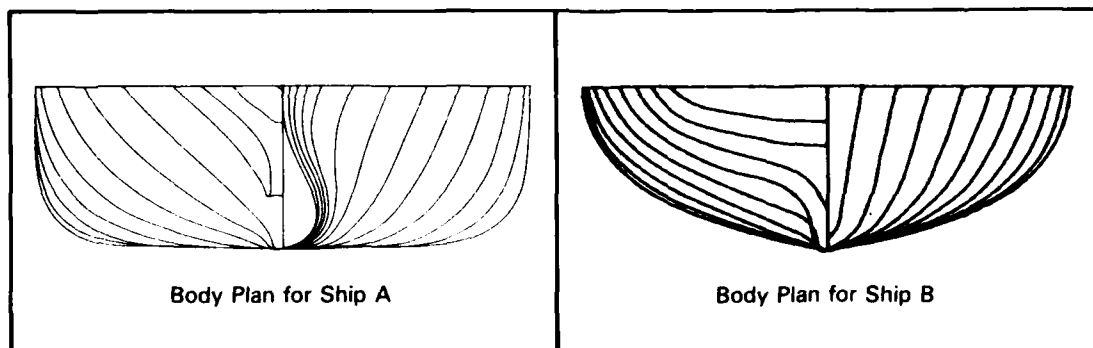


Figure 2 – Body Plans for Ship A and Ship B

Table 2 – Principal Characteristics of Ship A and Ship B

	Ship A	Ship B
LWL	274.3 m	124.4 m
B	32.2 m	13.7 m
T	10.4 m	4.5 m
$C_B$	0.53	0.46
$C_x$	0.94	0.75
$C_P$	0.56	0.61
GMT	1.28 m	1.33 m

The models were attached to the carriage by means of a heave staff. A roll-pitch gimbal was attached to the bottom of the staff, so that the models had three degrees of freedom: heave, roll, and pitch. The models were constrained from surging, swaying or yawing. In addition, experiments on one model (Ship A) were done with the hull rigidly restrained, in order to measure diffraction effects in waves.

Because of varying requirements regarding the placement of instrumentation on each model they had different radii of gyration for pitch and roll. Ship A had a pitch radius of 0.25 times the length, but because of certain heavy instruments on centerline the roll radius was only 0.24 times the beam. On the other hand, Ship B had a more realistic roll radius of 0.38 times the beam, but because of instruments located far forward the pitch radius was forced to a value of 0.27 times length.

All experiments were performed in regular head ( $\mu = 180^\circ$ ) and bow ( $\mu = 225^\circ$ ) waves. All measurements were made electronically and fed to a carriage-mounted digital computer. Rigid body motions were measured by potentiometers mounted to the heave staff. Incident wave elevation was measured by an ultrasonic transducer mounted approximately one-half model length in front of the bow. Relative motions alongside the hulls were measured using resistance-type wave probes. These probes were flush-mounted in the side of the hull in the case of Ship A, but were mounted slightly off the side on short outriggers for Ship B. Ultrasonic transducers could not be used for relative motion measurements near a hull, since the hull side would reflect the sonic pulse and cause spurious measurements.

All data were harmonically analyzed and the first harmonic of the incident wave and all responses were used to calculate linear transfer functions. Mean values were calculated by averaging signals over an integer number of cycles of the first harmonic.

## RESULTS

The presentation and discussion of results may be separated into the kinematic and nonkinematic components of relative motion. The kinematic components are simply the rigid body motions and the incident wave elevation. The vector combination of these components, taking proper account of phase angles, results in the kinematic estimate of relative motion. The additional dynamic components are those due to the diffraction of the incident wave by the presence of the ship plus the radiation of waves due to the oscillation of the ship. Furthermore, there are the mean shifts caused by the steady forward motion of the ship.

The mean sinkage and trim measured in calm water are compared to calculations using Equations (9a) and (9b) in Figure 3. The agreement for sinkage is generally satisfactory for both ships, but is less so for trim. Part of this latter discrepancy is caused by the mean measured trim angles being of the order of magnitude of one-tenth degree, which is near the limit which the instruments can resolve. However,



for the case of Ship A at  $F_n = 0.30$ , an absolute vertical motion transducer was mounted at the stern, which confirmed that there was a slight bow up pitch attitude.

Steady wave profiles are compared in Figure 4. The measured values have been corrected for sinkage and trim. The results are in qualitative agreement with Equation (12) for both ships. However, the shape of the wave profile for Ship A is not well predicted at  $F_n = 0.30$ , possibly because of its bulbous bow (see Figure 2), and the wave profile for Ship B does not rise near the bow at  $F_n = 0.15$ , as predicted by Equation (12).

Predicted and measured rigid body transfer functions are presented in Figures 5 and 6 for Ship A and Ship B, respectively. In these figures, heave has been nondimensionalized by the incident wave amplitude, while pitch and roll have been nondimensionalized by wave slope. Positive heave is defined upward (see Figure 1), while positive pitch is bow down and positive roll is starboard side down. Phase angles are defined as phase leads with respect to maximum wave elevation at the longitudinal center of gravity. Absolute vertical motion near the bow (Station 2 for Ship A and Station 2.5 for Ship B) has been calculated according to Equation (7) using experimental and theoretical heave and pitch transfer functions, and is shown in Figure 7.

The correlation between theory and experiment in head waves for these motions is generally satisfactory for Ship A at the lower speed ( $F_n = 0.10$ ). However, at the higher speed ( $F_n = 0.30$ ) the measured heave does not show the strong resonant peak predicted by strip theory, and pitch magnitudes are also somewhat less than predicted. As a result, the predicted absolute motion in Figure 7 is substantially higher than measured at  $F_n = 0.30$ . In the case of Ship B, the correlation for heave is excellent, but measured pitch is larger than predicted at both speeds. Consequently, the measured absolute motion shown for Ship B in Figure 7 is slightly greater than predicted.

The trends in bow waves ( $\mu = 225^\circ$ ) are similar for pitch and heave. In the case of roll, the correlation between theory and experiment is poor. The magnitude and frequency of the peak are poorly predicted. It is suspected that these results are caused by a combination of inaccurate roll damping estimates, together with the fact that the model tests were conducted with sway and yaw restrained. In any case, as will be shown below, roll has only a minor effect on vertical relative motion at the bow in bow waves. It will have a more important effect in the vicinity of the midship and for beam or stern waves.

The various components of relative motion are discussed in detail below. At low speeds, the previous relative motion theory which only computes kinematic terms appears to give adequate predictions. The consequences of large relative motions are more severe at high speeds, and the dynamic components associated with diffraction and radiation are also larger. Therefore, in the following discussions emphasis is placed on the higher speed case,  $F_n = 0.30$ .

For completeness, all the components of absolute and relative motion for Ship A at one speed and heading are tabulated in the Appendix.

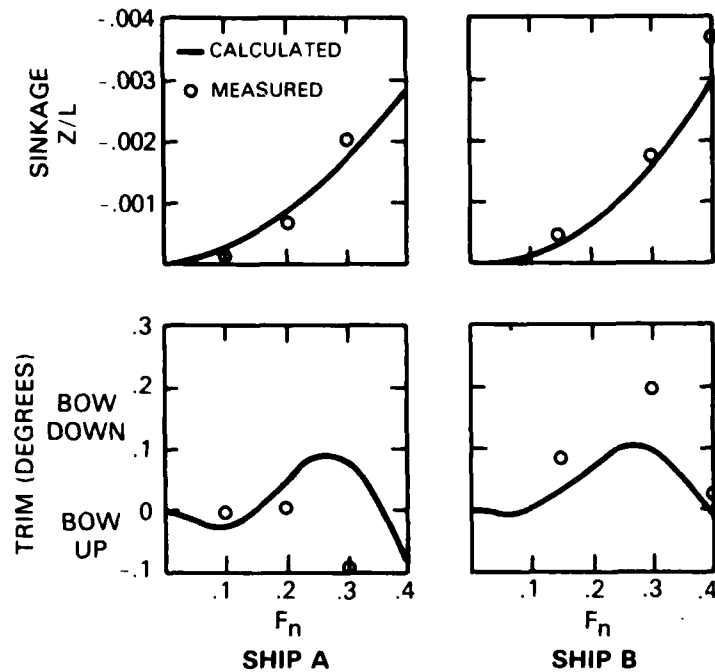


Figure 3 — Comparison of Predicted and Measured Sinkage and Trim in Calm Water

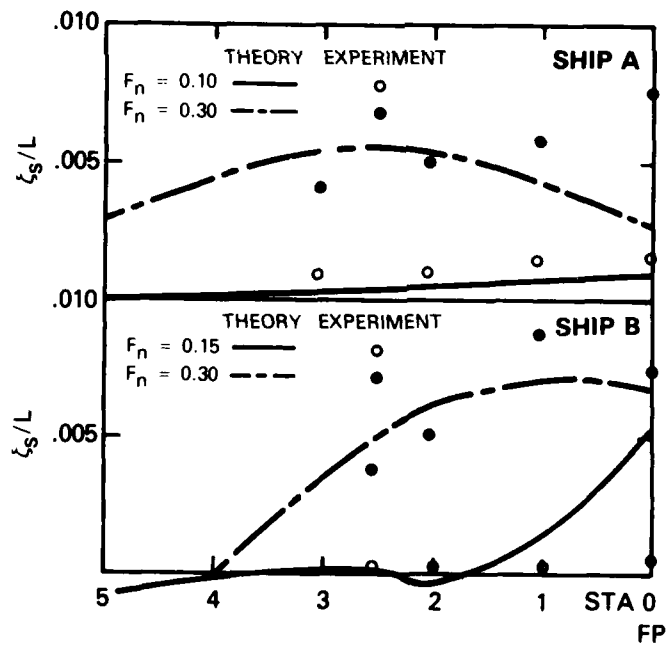


Figure 4 — Comparison of Theoretical and Experimental Bow Wave Profiles in Calm Water

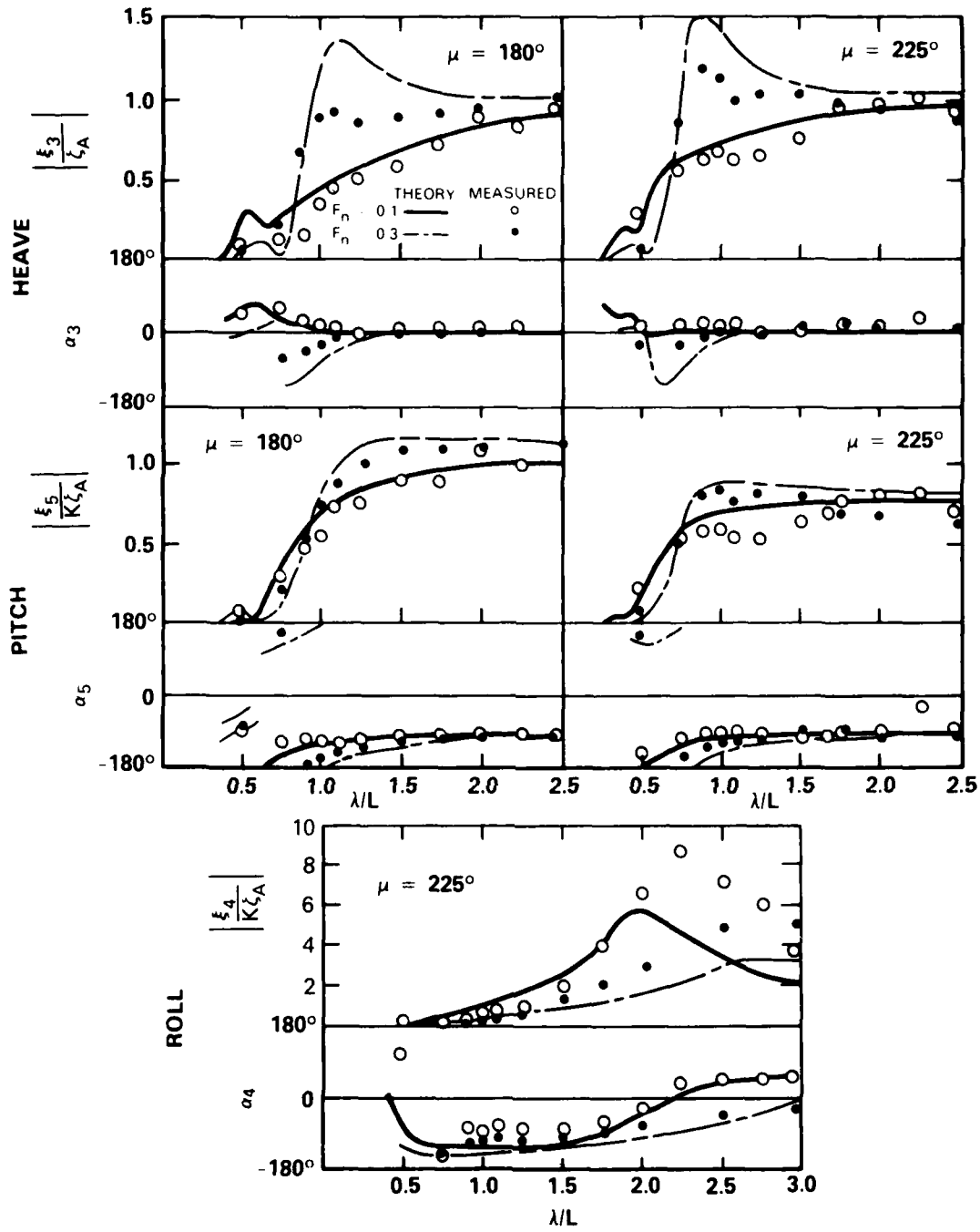


Figure 5 — Theoretical and Experimental Results for Rigid Body Motions for Ship A

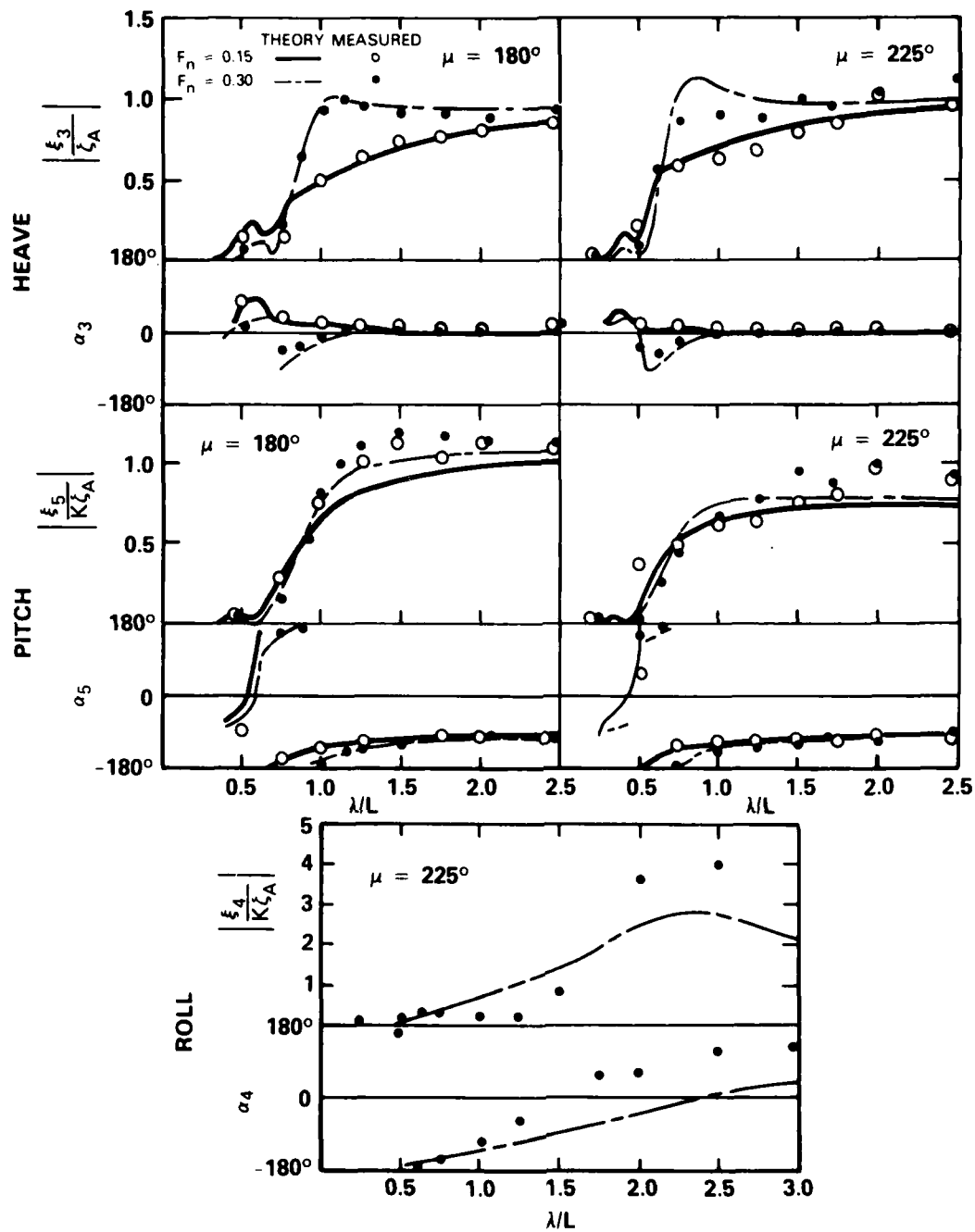


Figure 6 — Theoretical and Experimental Results for Rigid Body Motions for Ship B

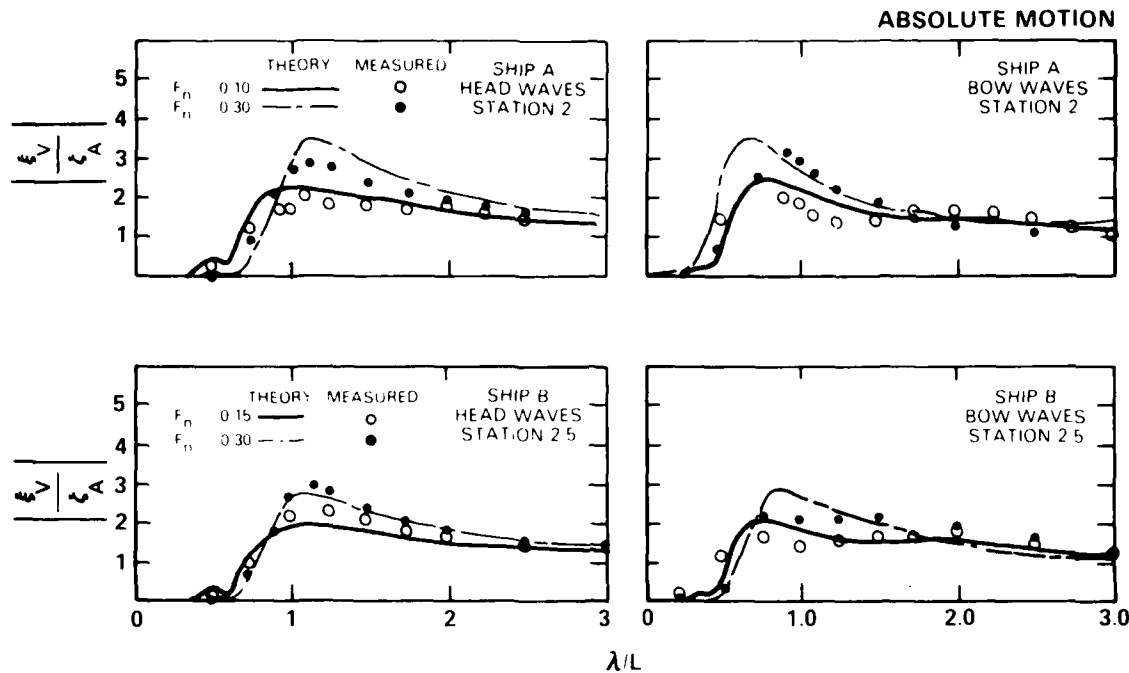


Figure 7 – Theoretical and Experimental Results for Absolute Vertical Motion Near the Bow for Ship A and Ship B in Head and Bow Waves

The components of wave elevation due to motion (radiation component) and diffraction are shown in Figures 8 and 9 for Ship A. In Figure 8, the individual component magnitudes are shown, together with their phase angles while in Figure 9 the predicted components are shown combined, resulting in the total modified wave elevation. The combination of incident plus diffracted wave is shown in Figure 8 for comparison to experimental results for Ship A, since the diffracted component can only be measured in combination with the incident wave in an experiment. As shown, the predicted diffracted wave is only of significant magnitude for short wavelengths in bow waves, and even in this wavelength region in head waves, the diffraction effect is quite small. On the contrary, the measured diffraction effect on Ship A was significant over the entire wavelength range in both head and bow waves. Regarding the phase angles, it is important to note that the phase angles are changing rapidly in the region of  $\lambda/L = 1.0$ , and it is in this region that the relative motion transfer functions reach their peak values. It is also significant that the radiation and diffraction components at long wavelengths have approximately the same magnitude, while their phases are approximately 180 degrees apart. This indicates that these effects will tend to cancel out to make the incident wave remain unmodified at long wavelengths, even though the

individual components may be significant. Finally, it should be noted in Figure 8 that the predicted diffraction component is approximately 90 degrees out of phase from the incident wave at all wavelengths. However, the phase of the measured incident plus diffracted wave was so close to that of the incident wave alone that the diffraction component appears to be in phase with the incident wave, within experimental accuracy. The fact that the measured amplitudes of the incident plus the diffracted waves are greater than those of the incident wave alone implies the closeness of the phases for these two wave components. On this basis of reasoning, the discrepancy between the predicted and measured results of the amplitudes of the incident plus the diffracted waves at long wavelengths shown in Figure 9 on the weather side could be resulting from the erroneous prediction of the phase angles of the diffracted waves by the strip theory employed in this work. As will be shown below, there is also reason to believe that the phase angle of the radiated waves, as predicted by strip theory, also differs from the actual radiated phase angle by approximately 90 degrees.

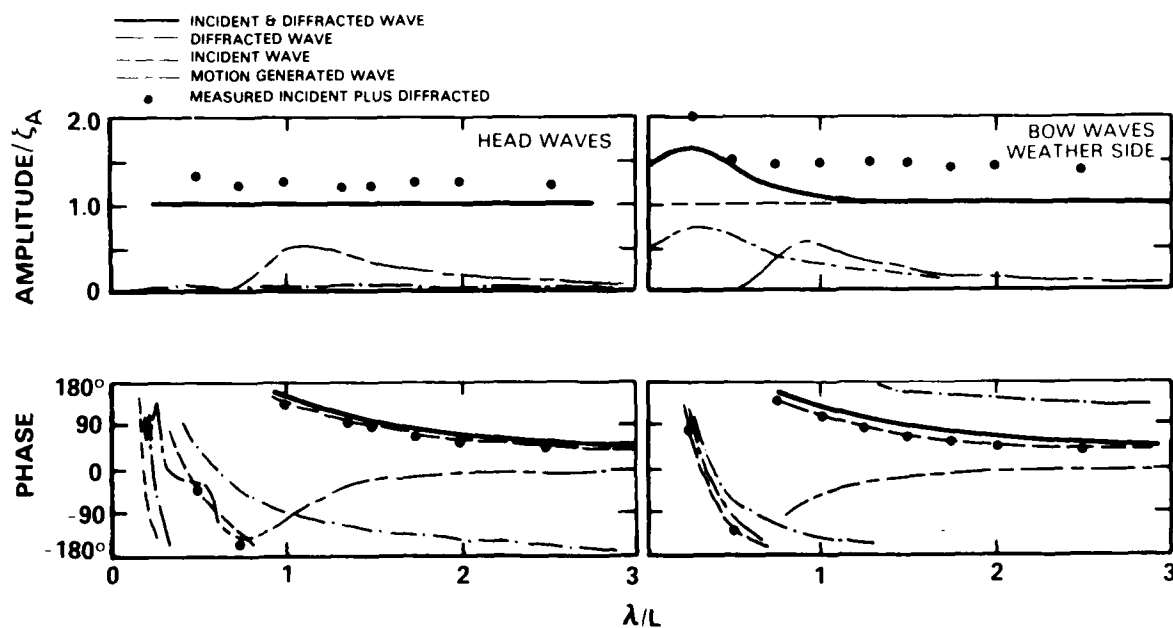


Figure 8 - Wave Amplitudes and Phases Due to Motion and Diffraction at Station 2 on Ship A at  $F_n = 0.30$  for Head and Bow Waves

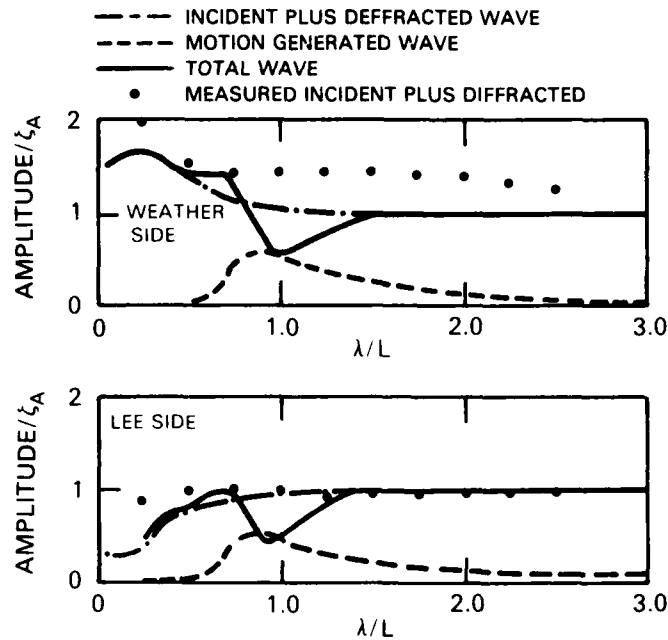


Figure 9 — Amplitudes of Incident Plus Diffracted Waves, Motion Generated Waves and Total Waves at the Weather and Lee Sides at Station 2 of Ship A at  $F_n = 0.30$  for Bow Waves

The relative motion transfer functions of both Ship A and Ship B are shown in Figure 10 for head waves and Figures 11 and 12 for bow waves at two different speeds. The agreement between theory and experiment is somewhat variable, and in general the inclusion of diffraction and radiation effects does not provide a significant improvement. In fact, in some cases the prediction is slightly worse when these effects are added. The difference between the weather and lee sides in bow waves is small, except in short waves where the diffraction component in the new theory predicts a sheltering effect. The effect of roll is only noticed at long wavelengths, where the absolute motion as predicted by Equation (7) shows a slight difference between weather and lee sides.

Careful examination of all the components of relative motion (either predicted or measured) shows that relative motion is strongly affected by both magnitudes and phases of these components. In order to more clearly illustrate these effects, Figures 13-15 are presented in the form of vector diagrams. In these illustrations, the complex amplitude of the various components (motions and waves) are represented as vectors whose magnitude is the absolute value of the quantity and whose phase is as defined in Equation (26b). Phase angles are measured

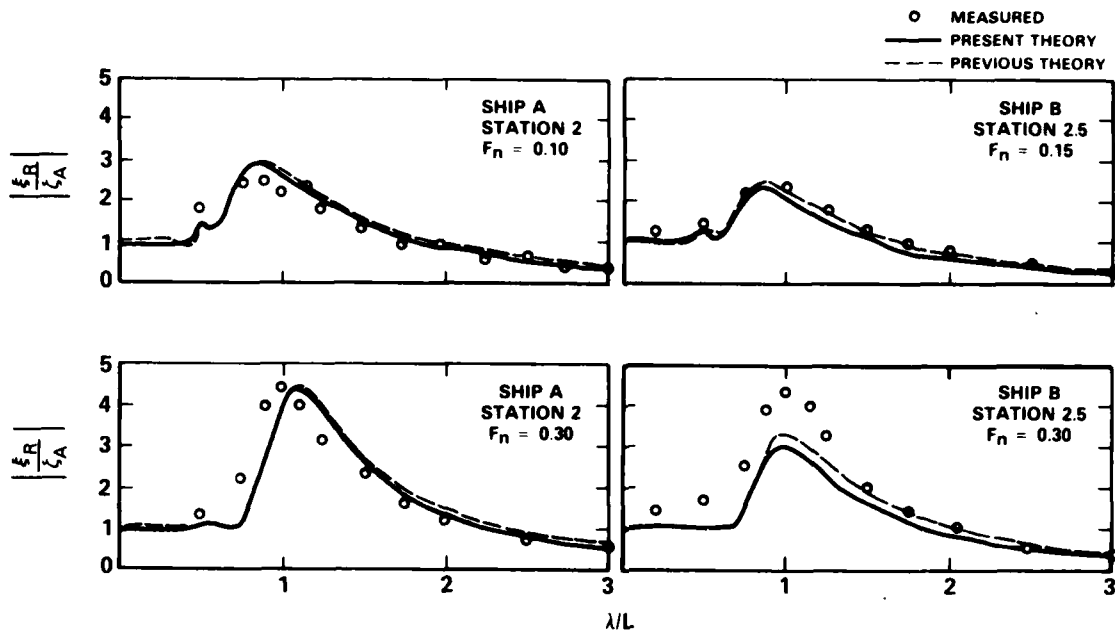


Figure 10 – Theoretical and Experimental Results for Relative Motion Near the Bow for Ship A at  $F_n = 0.10$  and  $0.30$  and for Ship B at  $F_n = 0.15$  and  $0.30$  in Head Waves

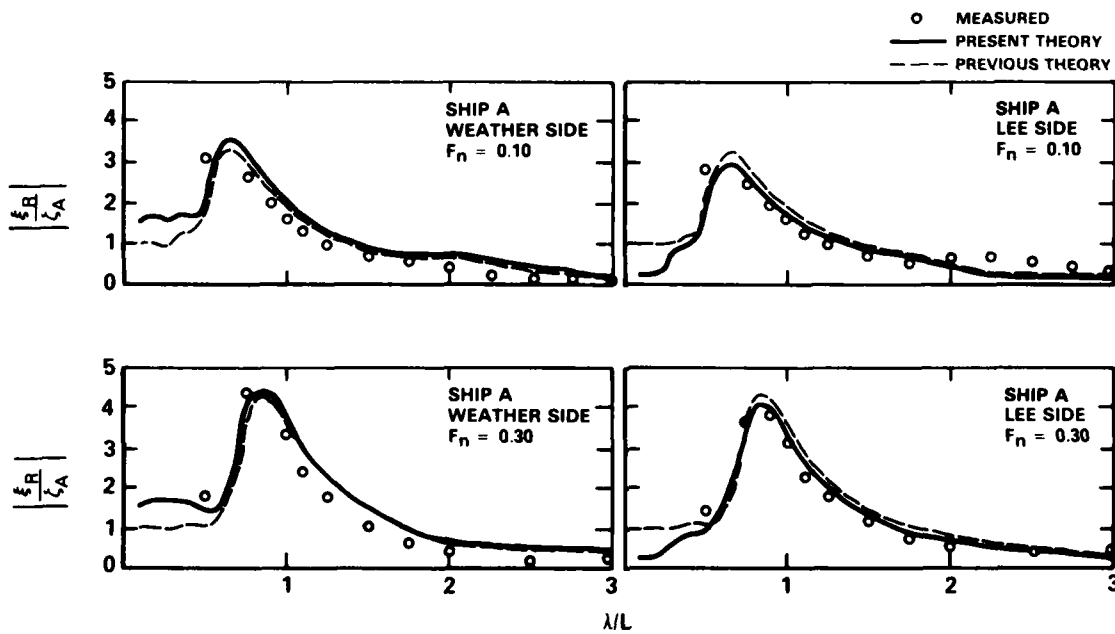


Figure 11 – Theoretical and Experimental Results for Relative Motion on the Weather and Lee Sides at Station 2 for Ship A at  $F_n = 0.10$  and  $0.30$  in Bow Waves.



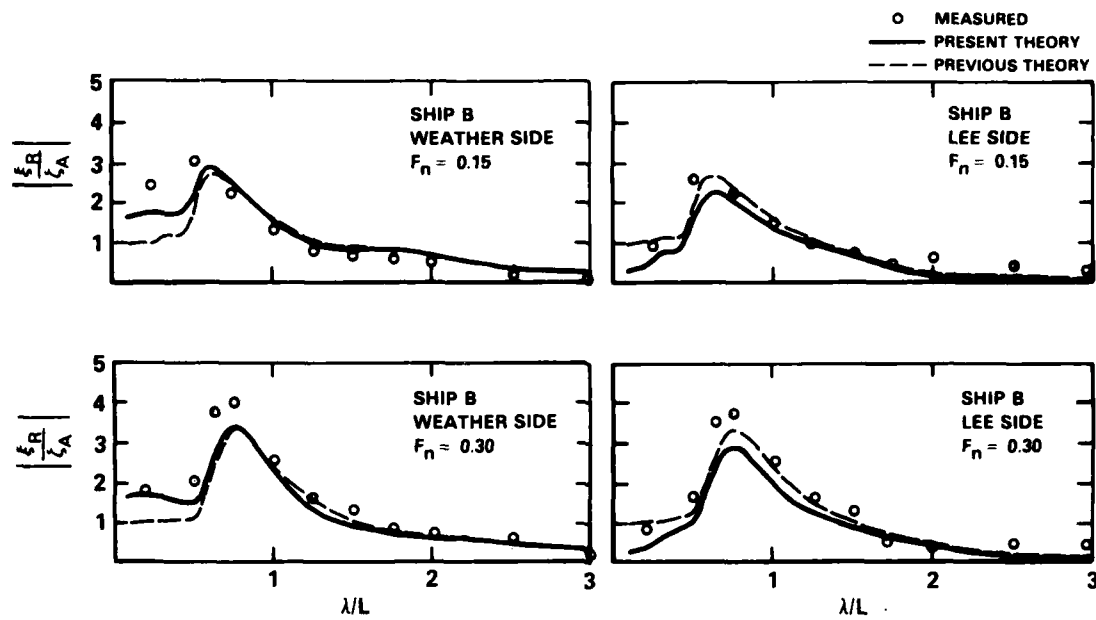


Figure 12 – Theoretical and Experimental Results for Relative Motion on the Weather and Lee Sides at Station 2.5 for Ship B at  $F_n = 0.15$  and  $0.30$  in Bow Waves

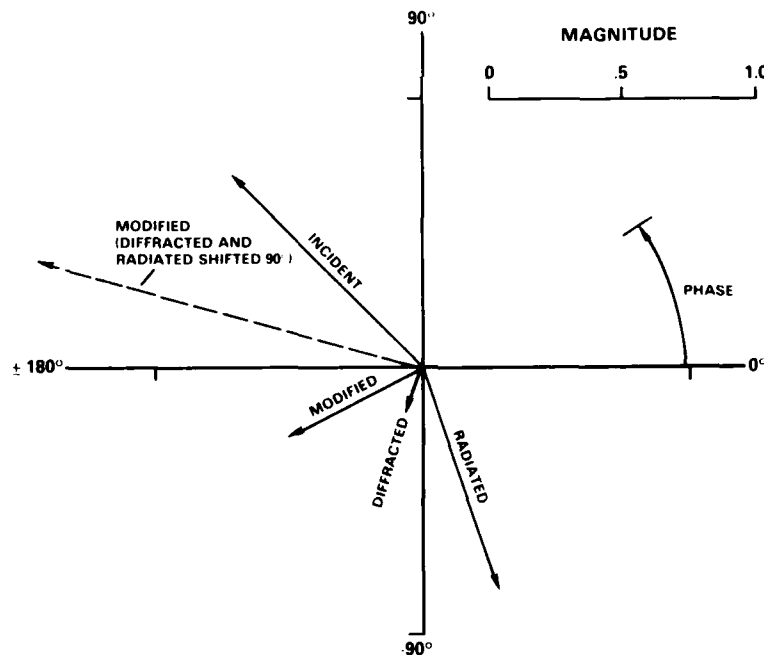


Figure 13 – Vector Diagram of Calculated Wave Components at Station 2.5 On Ship B at  $\lambda/L = 1.0$ ,  $F_n = 0.30$ , Head Waves

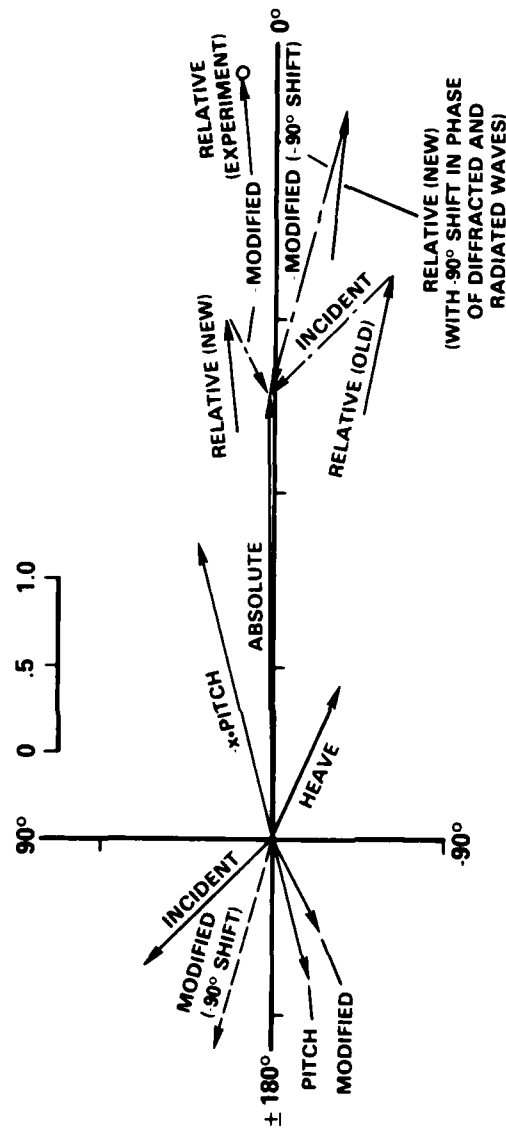


Figure 14 — Vector Diagram of Calculated Components of Relative Motion at Station 2.5 on Ship B at  $\lambda/L = 1.0$ .  
 $F_n = 0.30$ , Head Waves

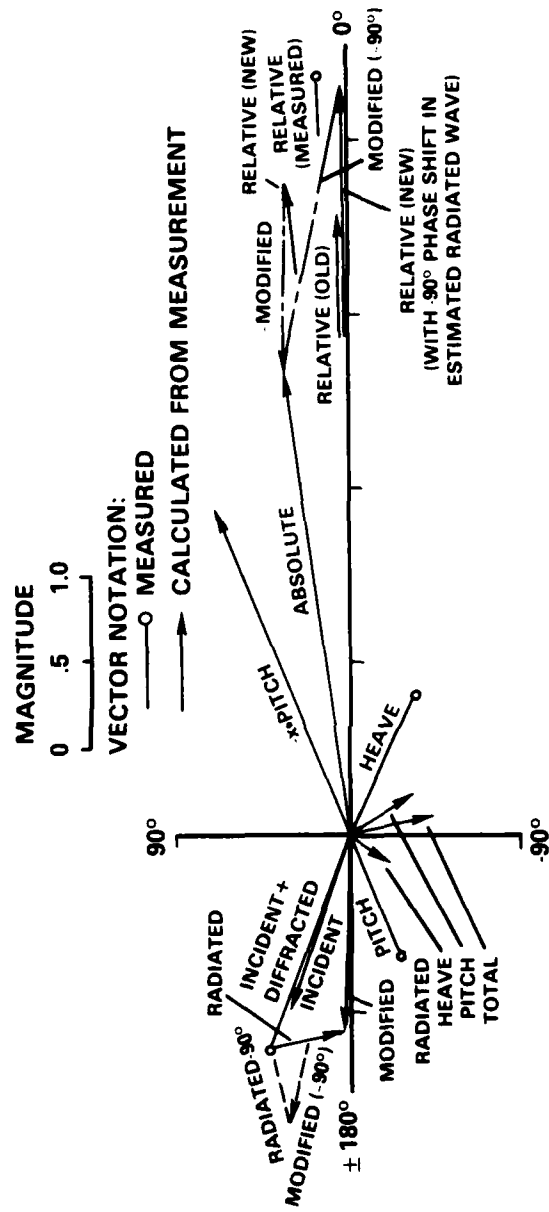


Figure 15 — Vector Diagram of Relative Motion Constructed from Experimentally Measured Components at Station 2 on Ship A at  $\lambda/L = 1.0$   $F_n = 0.30$  in Head Waves

as positive counterclockwise from the real axis, and all amplitudes have been nondimensionalized by the incident wave amplitude.

The various components of calculated oscillatory wave motion at Station 2.5 on Ship B are illustrated as vectors in Figure 13 for one speed and one wavelength. The sum of the incident, radiated (from both heave and pitch) and diffracted waves is defined as the "modified" wave. In addition, the effect on the modified wave of shifting the phases of the radiated and diffracted waves by  $-90$  degrees is shown.

The complete vector construction of relative motion for the same condition is shown in Figure 14. The absolute vertical motion is simply a vector combination of heave and pitch according to Equation (7). The relative motion denoted "old" is the absolute motion with the undisturbed incident wave subtracted. The "new" relative motion includes the predicted radiation and diffraction effects. In other words, it is constructed by subtracting the modified wave from the absolute vertical motion. As can be seen in Figures 10 and 14, the new method shows no improvement over the old, except for the phase angle, when compared to experimentally measured relative motion. However, when the radiated and diffracted phases are shifted by  $-90$  degrees, the agreement is significantly improved. Although not illustrated, a similar result is found at other wavelengths in head seas.

The various components of relative motion illustrated for Ship B in Figures 13 and 14 are based on strip theory calculations of absolute motions, radiated and diffracted waves, since in this particular case the experimentally measured absolute motions agreed closely with the predicted values, and no measurements of the radiated or diffracted components were available. In the case of Ship A, there was considerable discrepancy in the absolute motion at high speed, particularly in the heave motion. Furthermore, experimental measurements of diffraction effects (see Figure 8) were available for this hull form and also differed significantly from the predicted values. Therefore, the complete relative motion was constructed in Figure 15 using measured values of the various components, where available. Since no forced oscillation experiments were done to measure the radiated wave component, this component was determined by combining the radiated wave potentials  $\phi_k$  obtained by the strip theory with experimentally determined complex motion amplitudes  $\bar{\xi}_k$ . The absolute vertical motion at Station 2 was also calculated from the measured motions, rather than being directly measured with a displacement transducer at that station. The calculation of the relative motion by the new method shows slightly better agreement with the measurement than the old method. However, when the estimated radiated wave component is phase shifted  $-90$  degrees, there is excellent agreement in both magnitude and phase.

The results presented above have been for a station near the bow for both ships in head and bow waves. Relative motions near the bow usually affect ship operations the most because of their influence on such phenomena as slamming or deck wetness. However, there may be cases where relative motions further aft along the hull are of concern, particularly where freeboard is small or operations such as replenishment have to be carried out over the side. Figure 16 is presented to

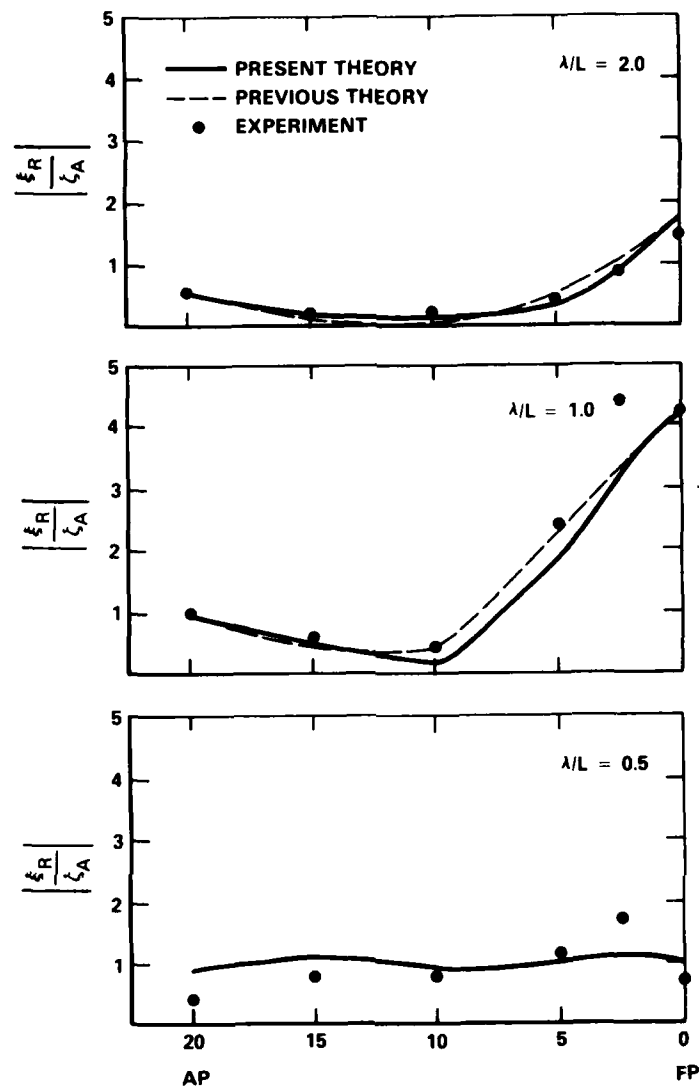


Figure 16 — Theoretical and Experimental Results at Various Stations for Ship B at  $F_n = 0.30$  in Head Waves for  $\lambda/L = 2.0, 1.0$  and  $0.5$

show the relative motion along the full length of Ship B for several values of  $\lambda/L$ . The agreement between prediction and measurement is generally satisfactory except at Station 2.5 at  $\lambda/L = 1.0$  and  $0.5$ . Interestingly, the agreement at the bow (Station 0) is better than at Station 2.5. This is apparently due to the fact that there is little or no radiation or diffraction at this station. The bow of Ship B has a raked stem line and no bulb or dome.

One unexpected phenomenon discovered in the experiments was a shift in the mean values of various quantities when running in waves, as compared to their values in calm water at the same speed. Some of these results are presented in Figures 17 and 18, for Ship A. Mean shifts were detected in heave, pitch and relative motion near the bow. The signal from a vertical absolute motion transducer at the stern was also available and served to independently confirm the heave and pitch mean shifts. As shown in Figure 17, the heave showed a slight rise (or decrease in sinkage) in the wavelength region near  $\lambda/L = 1.0$ , compared to the level in calm water. Similarly, pitch had a small bow up tendency at the same wavelengths. Vertical motion at the stern became more negative (increased sinkage), which is consistent with the bow up pitch shift. The net result of these shifts is that the absolute vertical motion of the forward part of the ship increases in waves, compared to the trim in calm water at the same speed.

The mean value of relative motion at Station 2 becomes less negative in waves (bow is rising relative to local free surface elevation) which is consistent with the direction of mean shift in absolute motion. However, the magnitude of rise in relative motion is less than would be expected from the rise in absolute vertical motion at this station. This implies that there is an absolute rise in the mean free surface near the hull. At Station 0, on the other hand, the mean shift in relative motion is negative at all wavelengths. This means that there is a mean rise in the free surface which is even greater than the mean rise of the bow.

The data in Figures 17 and 18 are a sample of the mean shifts observed. Similar results were found in bow waves, and in the data for Ship B at  $F_n = 0.30$ . Mean shifts were not clearly detectable for either ship at the lower speeds. At present, we know of no analytical prediction method for these mean shifts. It is suspected that they are caused by quadratic interactions between various components of the first order oscillatory potential. In other words, it could be analogous to added resistance or drift forces, except in this case the mean force and moment of interest are the heave and pitch excitation. Since this is still an open question, and we do not have sufficient experimental data to determine whether the shifts vary linearly, quadratically or in some other fashion with wave amplitude, the data of Figures 17 and 18 have simply been made nondimensional with respect to ship length.

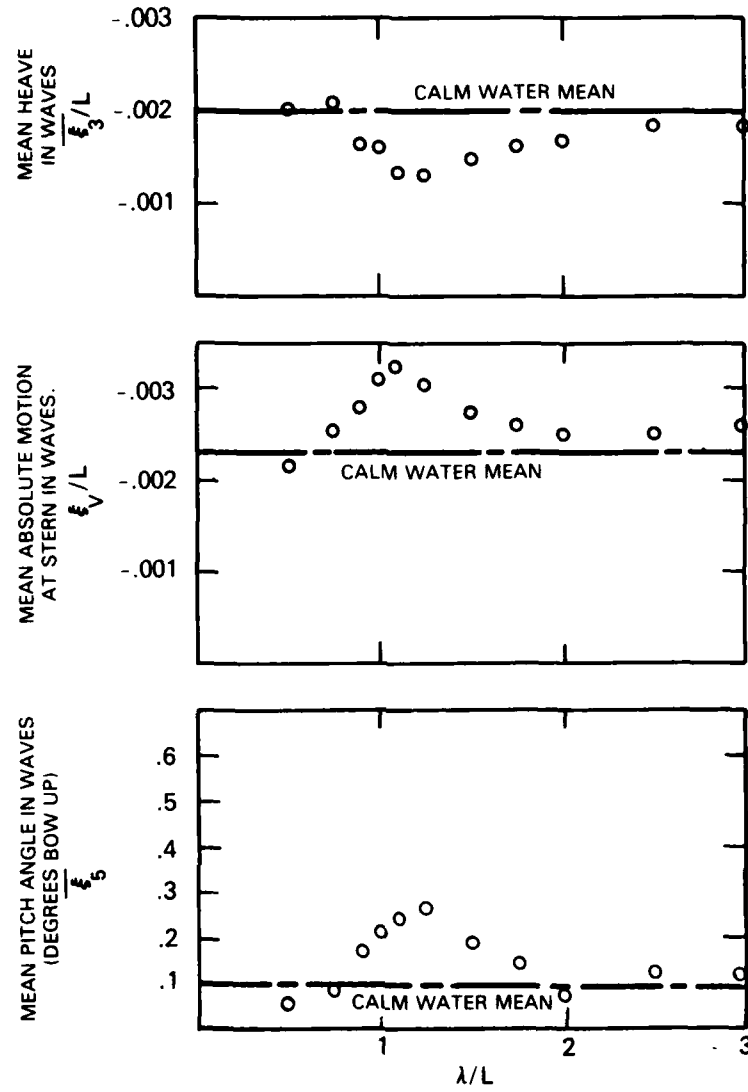


Figure 17 — Change of Mean Values of Rigid Body Motions in Waves for Ship A in Head Seas,  $F_n = 0.30$

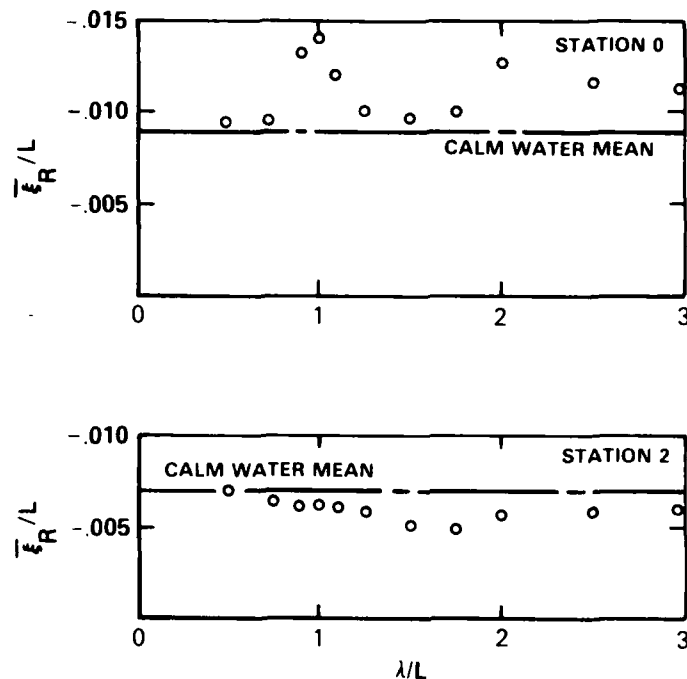


Figure 18 – Change of Mean Value of Relative Motion at Stations 0 and 2 for Ship A in Head Waves,  $F_n = 0.30$

The mean shifts in waves are quite small compared to the static freeboard, as are the shifts due to sinkage, trim and bow wave profile in calm water. However, accurate prediction of these components is ultimately as important as the prediction of transfer functions of the oscillatory components, because the frequency of occurrence of events such as slamming and deck wetness in random seas is a sensitive function of the mean draft or freeboard. For instance, under the assumption of Rayleigh's law of probability distribution the average number of occurrences per hour that a given level  $F$  is exceeded, is given by:

$$\bar{n} = \frac{3600}{2\pi} \left( \frac{\sigma_v}{\sigma_x} \right) e^{-\frac{1}{2} \left( \frac{F}{\sigma_x} \right)^2} \quad (27)$$

where  $\sigma_x$  and  $\sigma_v$  are the standard deviation of relative motion and relative velocity, respectively, and the relative velocity standard deviation is obtained from the second moment of the relative motion spectrum. Thus, the frequency of occurrence is an exponential function of the square of the level to be exceeded (which could be freeboard in



the case of deck wetness or propeller depth in the case of propeller emergence), and even a small change in the mean can have a relatively large effect on the frequency of occurrence.

#### CONCLUDING REMARKS

The computed and measured results reveal no conclusive evidence that inclusion of the diffracted and motion-generated waves, as computed by strip theory, provide much improvement for the computation of relative motions, compared to the old method for which only the kinematic terms are included. However, there is strong evidence from the experimental results that the magnitudes of these terms are significant and that improved prediction of the associated phase angles will noticeably improve the correlation between predictions and experiments. It is also felt that improvements in prediction of the magnitude of the diffraction component must be made.

The deficiencies of strip theory in predicting relative motion may come from several sources. The free surface elevation from Bernoulli's equation (Equation (5)) includes a term proportional to the product of forward speed and the axial derivative of the oscillatory potential. Since in strip theory this term is considered to be of higher order than the time derivative term, it has not been included in the present calculations. However, for an actual hull form which has substantial longitudinal curvatures in the bow and stern regions, this term may be comparable in magnitude to the time derivative term. The nature of the term could also explain why phase angle computations appear to be less satisfactory at higher speeds and in head waves.

In order to accomplish a significant improvement in the prediction of relative motion, it is strongly felt that improved theoretical methods beyond the strip theory and thin-ship theory for free-surface motion as well as body motion including the nonlinear effects should be developed in association with carefully conducted systematic experiments.

#### ACKNOWLEDGEMENTS

The analytical work on ship relative motions was sponsored by the Naval Sea Systems Command under the General Hydromechanics Research (GHR) Program administered by the David W. Taylor Naval Ship Research and Development Center. Experimental work was sponsored under the GHR program, the U.S. Navy Ships, Subs and Boats Exploratory Development Program, and the U.S. Coast Guard Commercial Vessel Safety Program in the Office of Merchant Marine Safety. Much of the experimental work was initiated by the late N.K. Bales and carried out by Harry D. Jones and Richard C. Bishop. Calculations of calm water wave profiles were provided by Dr. Y.S. Hong.

## References

- Bai, K. J., and J. H. McCarthy (Eds.) (Nov. 1979). Proceedings of the Workshop on Ship Wave-Resistance Computations, DTNSRDC.
- Bales, N. K. et al. (Nov. 1975). Validity of a Strip Theory-Linear Superposition Approach to Predicting Probability of Deck Wetness for a Fishing Vessel, DTNSRDC Report SPD-643-01.
- Bishop, R. C., and N. K. Bales (Jan. 1978). A Synthesis of Bow Wave Profile and Change of Level Data for Destroyer-Type Hulls with Application to Computing Minimum Required Freeboards, DTNSRDC Report SPD-811-01.
- Cox, G. G., and D. M. Gerzina (1975). A Comparison of Predicted Experimental Seakeeping Characteristics for Ships With and Without Large Bow Bulbs, Report of the Seakeeping Committee, Appendix 2, Proceedings of the 15th International Towing Tank Conference, Vol. 4.
- Frank, W. (1967). Oscillation of Cylinders in or Below the Free Surface of Deep Fluids, NSRDC Report 2375.
- Gerzina, D. M., and E. L. Woo (Dec. 1975). CVA 68 Relative Motion Investigation, DTNSRDC Report SPD-656-01.
- Hong, Y. S. (June 1977). Numerical Calculation of Second-Order Wave Resistance, Journal of Ship Research 20(2), 94-106.
- Lee, C. M. (1976). Theoretical Prediction of Motion of Small-Water-plane-Area, Twin Hull (SWATH) Ships in Waves, DTNSRDC Report 76-0046 (see Appendix A).
- Lee, C. M. (1982). Computation of Relative Motion of Ships to Waves, DTNSRDC Report 82/019. Also presented at the Third International Conference on Numerical Ship Hydrodynamics, Paris, 1981.
- Porter, W. R. (1960). Pressure Distributions, Added Mass, Damping Coefficients for Cylinders Oscillating in a Free Surface, Inst. Engr. Res., Univ. of Calif., Berkeley, Series 82, Issue No. 16.
- Salvesen, N., O. Faltinsen, and E. O. Tuck (1970). Ship Motion and Sea Loads, SNAME Trans., Vol. 78.
- Tasai, F. (1959). On the Damping Force and Added Mass of Ships Heaving and Pitching, J. Zosen Kiokai 005, 47-56.
- Wehausen, J. V. (1973). The Wave Resistance of Ships, Advances in Applied Mechanics 03.

APPENDIX--AMPLITUDES AND PHASES OF MOTIONS, WAVE COMPONENTS GENERATED BY EACH MOTION, INCIDENT WAVE, DIFFRACTED WAVE, TOTAL MODIFIED WAVE, ABSOLUTE MOTION AND RELATIVE MOTION AT STATION 2 FOR SHIP A AT  $F_n = 0.30$  IN BOW WAVES

Amplitudes and phases of the rigid body motion, together with the wave components generated by the corresponding degree of freedom, are shown. Magnitude and phase of the diffraction and modified waves are also shown. Magnitudes of the wave components and translational motions are nondimensionalized by incident wave amplitude, while those of rotational motions are nondimensionalized by incident wave slope. All phase angles are degrees of lead with respect to maximum wave elevation at the origin.

Table 3 - Amplitudes and Phases of Motions, Wave Components  
Generated by Each Motion, Incident Wave, Diffracted Wave,  
Total Modified Wave, Absolute Motion and Relative  
Motion at Station 2 for Ship A at  $F_n = 0.30$   
in Bow Waves

$\lambda/L$	$\theta^\circ$	SWAY				HEAVE			
		MOTION		WAVE COMPONENT		MOTION		WAVE COMPONENT	
		AMP	PHASE	AMP	PHASE	AMP	PHASE	AMP	PHASE
2.55	.40	.418	82.5	.094	-94.5	1.014	0	.077	-68.3
1.44	.58	.297	89.0	.177	-114.5	1.092	-6	.132	-82.3
1.19	.66	.240	88.3	.198	-125.6	1.222	-4.6	.169	-91.6
1.00	.74	.179	86.8	.187	-136.6	1.442	-19.0	.223	-111.3
.76	.87	.080	82.6	.101	-159.8	.978	-88.5	.174	-170.5
.50	1.18	.018	-57.4	.028	34.9	.081	17.6	.016	-93.2
.23	2.11	.004	64.2	.008	139.7	.010	139.7	.003	54.0

$\lambda/L$	$\theta^\circ$	ROLL				PITCH			
		MOTION		WAVE COMPONENT		MOTION		WAVE COMPONENT	
		AMP	PHASE	AMP	PHASE	AMP	PHASE	AMP	PHASE
2.55	.40	3.096	-60.5	.025	122.4	.786	-98.3	.078	46.4
1.44	.58	.859	-129.9	.033	22.8	.850	-113.2	.219	9.2
1.19	.66	.631	-136.4	.041	4.8	.870	-124.6	.305	-10.1
1.00	.74	.473	-140.3	.046	-9.6	.868	-141.8	.400	-34.7
.76	.89	.260	-141.6	.040	-32.4	.562	164.3	.382	-100.4
.50	1.18	.019	-122.2	.005	-43.4	.031	123.7	.034	-154.8
.23	2.11	.005	68.2	.004	118.7	.002	67.1	.006	168.3

$\lambda/L$	$\theta^\circ$	YAW				TOTAL RADIATED WAVE	
		MOTION		WAVE COMPONENT			
		AMP	PHASE	AMP	PHASE		
2.55	.40	.225	169.3	.026	25.7	.142	-23.0
1.44	.58	.171	-179.1	.217	1.6	.472	-39.3
1.19	.66	.149	-175.1	.312	-7.5	.677	-38.5
1.00	.74	.126	-171.5	.390	-15.5	.861	-51.8
.76	.89	.083	-164.7	.407	-30.9	.614	-85.5
.50	1.18	.021	-140.6	.188	-35.8	.196	-40.9
.23	2.11	.001	-177.3	.028	-94.7	.022	-142.0

$\lambda/L$	$\theta^\circ$	INCIDENT WAVE		DIFFRACTION WAVE		INCIDENT PLUS DIFFRACTION WAVE		TOTAL MODIFIED WAVE	
		AMP	PHASE	AMP	PHASE	AMP	PHASE	AMP	PHASE
2.55	.40	1.000	45.3	.123	148.3	.980	52.3	1.025	44.7
1.44	.58	"	80.6	.219	177.7	.999	93.2	.835	65.6
1.19	.66	"	97.5	.264	-169.7	1.021	112.4	.541	75.0
1.00	.74	"	116.0	.311	-156.5	1.060	133.1	.215	153.0
.76	.89	"	152.3	.410	-131.3	1.166	172.3	1.200	-157.7
.50	1.18	"	-130.6	.636	-72.3	1.416	-109.2	1.500	-102.3
.23	2.11	"	143.6	.714	165.0	1.685	152.5	1.690	153.2

$\lambda/L$	$\theta^\circ$	ABSOLUTE MOTION		PRESENT RELATIVE MOTION		PREVIOUS RELATIVE MOTION	
		AMP	PHASE	AMP	PHASE	AMP	PHASE
2.55	.40	1.143	33.7	.451	8.1	.478	8.2
1.44	.58	2.298	40.7	1.446	27.8	1.637	17.5
1.19	.66	2.840	49.6	2.449	27.2	2.553	13.0
1.00	.74	3.406	17.3	3.063	14.4	3.692	4.8
.76	.89	2.428	-37.8	3.292	-19.4	4.517	-35.0
.50	1.18	1.113	-35.3	1.537	-69.9	1.751	-77.8
.23	2.11	1.074	108.4	1.893	-27.5	2.996	-77.3

## Discussion

J.H. Pattison (Naval Sea Systems Command)

In recent years, various research programs in ship hydrodynamics have provided hull form designers with valuable tools for predicting seakeeping performance.\* Results of the predictions have allowed the designers to choose hull form and appendage parameter values for best seakeeping performance. Even so, the tools are most accurate for predicting absolute motions of the center of gravity of a ship and least accurate for predicting relative motions between points on the ship and the water surface. This limits the accuracy with which deck wetness and damping are predicted. The authors are to be complimented for developing an analytical method for predicting relative motion that includes the effects of the moving ship on the wave field. It is hoped that this methodology can be included in improved tools for the hull form designer in the near future.

The work presented represents a good step toward accurately representing relative motions in that they include both dynamic and steady effects not previously incorporated into the predictive tools. The dynamic effects include wave diffraction and reflection by the ship as well as wave generation by the moving ship. The steady effects include sinkage, trim, and the steady-wave profile caused by the forward movement of the ship. However, to make the problem tractable, the authors chose the linear equations of motion, which limits the applicability to linear ranges of ocean waves and ship responses. For predictions of absolute motion, the limit occurs at Sea State 6, or lower, depending on the size of the ship. It occurs to the discussor that nonlinear effects on relative motion may occur at lower sea states.

Another limitation in the work reported is that only the underwater hull form is considered. Above-water features, such as knuckles and flare, are expected to have significant effects on the predicted relative motion. Also, it is not clear that results obtained in regular waves are directly applicable to irregular waves.

The discussor agrees with the authors that a systematic series of ship model tests are needed to verify and improve the methods for predicting relative motion. Furthermore, the series should include both the underwater hull form and above-water hull form and features. To be useful to the hull form, parameter and feature variations should be kept within reasonable, practical bounds.

\*Meyers, W.G., T.R. Applebee, and A.E. Baitis, "User's Manual for the Standard Ship Motion Program, SMP," DTNSRDC Ship Performance Department Report DTNSRDC/SPD-0936-01 (Sept. 1981).

E.N. Comstock (Naval Sea Systems Command)

The results of this improved predictive method, as presented in Figure 16, raise a question relative to experience we have had in using existing relative motion predictive techniques without radiated or diffracted wave potentials. Specifically, we have observed an appreciable increase in predicted relative motion between stations 10 and 12 for several ships. This phenomenon, which yields a characteristic "W" shape to the relative motion profile, has been observed with regular and irregular waves at various speeds in head and bow seas. This characteristic increase in reactive motion has been observed and confirmed by model tests. Would the authors please comment on whether they have experienced this same effect and their thoughts relative to our experience.

L.J. Doctors (University of New South Wales)

Equation (12) gives the wave profile along the side of the hull on the assumption that the ship is "thin." The two test cases, whose body plans are reproduced in Figure 2 would probably be better described as either "flat" ships or "slender" bodies. Do the authors feel that there would be much error in the results because of their choice of these test cases?

H.T. Wang (Naval Research Laboratory)

I wish to commend the authors for taking a first step toward computing the total wave profile alongside a ship consisting of the incident wave, the wave due to steady forward motion, radiation waves, and the diffraction wave. The authors use thin-ship theory to calculate the steady-wave and slender-body theory to calculate the radiation and diffraction waves. These theories are reasonably accurate over most of the ship. However, in the bow area, where the authors calculate the relative motion, the ship cannot be considered either thin or slender. For example, the term  $\partial f / \partial \xi$ , the longitudinal derivative of the ship half beam,  $\rightarrow \infty$  at the forward perpendicular in the authors' Equation (12) for the steady-wave profile.

I would like to ask how the bow geometry was modeled by the authors and if they made any attempts to make corrections to their theories at the bow area. In particular, did they attempt to make use of the many studies on the bow-wave profile conducted by Professor Ogilvie and his students at the University of Michigan? Or did they try the singularity gap technique, initiated by Professor Landweber, where the singularity distribution does not extend all the way to the blunt edge? The extent of the gap is a function of the geometric properties of the leading edge, principally the radius of curvature.

## Author's Reply

C.M. Lee, J.F. O'Dea, and W.G. Myers (DTNSRDC)

Mr. Pattison raises questions as to whether regular wave results can be directly applied to irregular waves and whether nonlinear techniques including the effect of above-water hull form will be needed. To the extent that linearized absolute motion calculations are valid, we feel that relative motion calculations should be valid also. The sea state limitation depends as much on the size of the ship as on wave height. Some limited experimentation has been done with our Ship A in waves as large as Sea State 7, and there were no serious discrepancies noted in the relative-motion transfer functions, when compared with the regular wave results. However, we do agree that in predicting deck wetness, the statistical extremes rather than just transfer functions are important, and this may very likely require that nonlinear effects be included. Toward that goal, DTNSRDC is at present engaged in a combined analytical and experimental program to determine the effect of above-water bow-shape variations on flare slam loads and deck wetness in very steep waves.

Mr. Comstock has asked about the shape of the relative motion response curve, as a function of axial position on the ship. We calculated the relative motion only at locations for which we had experimental data, so we may have missed details of the shape of this curve. It is certainly possible to have more than one inflection point in the curve along the hull. One way of examining this point is to consider the expression for relative motion in head waves (neglecting radiated and diffracted waves):

$$\xi_R = \xi_3 - \chi \xi_5 - \zeta_A e^{ikx}$$

The magnitude (squared) of this is  $\xi_R \xi_R^*$  where \* denotes the complex conjugate. Taking the derivative of the magnitude squared with respect to  $x$  and setting it equal to zero will provide an equation in  $x$  determining these points of inflection (assuming  $\zeta_A = 1$ ):

$$\begin{aligned} x \left| \xi_5 \right|^2 - \operatorname{Re} \xi_3 \operatorname{Re} \xi_5 - \operatorname{Im} \xi_3 \operatorname{Im} \xi_5 \\ + \cos Kx (\operatorname{Re} \xi_5 - K \operatorname{Im} \xi_3 + Kx \operatorname{Im} \xi_5) + \sin Kx (\operatorname{Im} \xi_5 + K \operatorname{Re} \xi_3 - Kx \operatorname{Re} \xi_5) = 0 \end{aligned}$$

This expression may have several zeros for  $-L/2 < x < L/2$ , depending on the magnitudes and phases of the pitch transfer functions. The characteristic "W" shape curve described by Mr. Comstock would of course have three zeros.

Dr. Doctors asks if we feel that flat-ship or slender-body theory would provide less error than the thin-ship theory we used. We can only reply that the agreement between our theory and experimental measurements does not seem to be inferior to that found using much more complicated computational procedures as shown by Bai and McCarthy,\*\* and the use of any other computational scheme does not seem to be justified at this time.

As to Dr. Wang's question on the validity of applying either slender-body or thin-body assumption at the bow region, our answer is that we have not used the so-called "consistent perturbation expansion" in our work. In regard to the question of the possible singularity caused by the term  $\partial f / \partial \xi$  at a rounded edge stem, it can be simply shown that by taking an integral by parts of Equation (12),  $\partial f / \partial \xi$  can be reduced to  $f$  which vanishes at the stem, and, hence, the appearance of the singularity resulting from the term  $\partial f / \partial \xi$  is actually nonexistent. However, the singularity does appear even at a sharp-edged bow in the second-order approximation as shown by Landweber and Celik at the Ship Wave Resistance Workshop in Japan in 1980. But, Landweber presented the numerical results that showed that the singularity effect on the wave-resistance computation is not serious enough to be concerned with. In our calculation, we have taken twenty stations along the ships, and the numerical integration was performed based on the values of the integrand at these stations with the integrand value at the bow assumed to be zero.

\*\*Bai, Kwang June, and Justin H. McCarthy, Proceedings of Workshop on Ship Wave-Resistance Computations, DTNSRDC, November 1979.

# Relative Motion Components for a Mathematical Form in Regular Waves

Robert F. Beck

Department of Naval Architecture  
and Marine Engineering  
The University of Michigan

## ABSTRACT

The total relative motion in the bow region of a ship is made up of components which result from the incident waves, ship motions, radiated waves, diffracted waves and waves due to steady forward speed. Each of the components has been experimentally and theoretically investigated for a mathematical form in head seas.

Strip theory is used to predict the ship motions and the radiated waves. A slender-body theory is used to predict the diffracted waves. The experiments show that all the components are linearly additive. The agreement between theory and experiment for the total relative motion and the radiated wave components is reasonable. The agreement for the diffracted wave components is poor.

## INTRODUCTION

One of the major detriments to ship operation in a seaway is green water on deck. In small amounts it makes working on deck difficult and may wash overboard small items which are not securely fastened. In excessive amounts severe structural damage can result. Green water will come on deck whenever the relative position of the water surface in the bow region exceeds the freeboard. Since the sea is a random process, the prediction of deck wetness requires a knowledge of both the hydrodynamic and statistical aspects of the problem. In this paper, we shall only examine the hydrodynamic problem. It is presumed that present day statistical techniques and linear system theory are adequate given the proper hydrodynamic information. Assuming linear theory is valid, the required hydrodynamic information is just the relative motion between the bow and the water surface in sinusoidal waves.

The water surface elevation in the bow region is made up of several components. The principal component is the incident wave system. The second is the diffracted waves. Finally, the ship-generated wave system includes both the waves due to steady forward motion and the radiated waves generated by the unsteady ship motions. In linear theory



all the components are additive. To obtain the relative motion between the ship and the water surface, the ship motion must be subtracted from the water surface elevation.

In this paper, the wave amplitude in the bow region of a mathematical model will be examined. The mathematical form was chosen in order to eliminate the unknown effects of bow flare and a bulbous bow. The final results should be a valid comparison between slender-body theory and experiments. Both theoretical and experimental results will be given for the individual components of the wave amplitude and the total relative motion. The discussions are restricted to head seas because the experiments were only conducted in incident waves coming from the bow.

#### THEORETICAL TECHNIQUES

The axis system used throughout this paper is shown in Figure 1. The origin is located in the midship plane at the waterline. The z-axis is positive upward and the x-axis is positive out the bow. In the moving coordinate system, the incident wave potential is given by

$$\phi_0 e^{i\omega_e t} = \frac{iq}{\omega_0} a e^{kz} e^{ikx} e^{i\omega_e t} \quad (1)$$

where  $\phi_0$  = incident wave potential  
 $q$  = acceleration of gravity  
 $a$  = incident wave amplitude  
 $k$  = wave number  
 $= 2\pi/\lambda$   
 $\lambda$  = wavelength  
 $\omega_e$  = frequency of encounter  
 $= \omega_0 + kU_0$   
 $\omega_0$  = absolute wave frequency  
 $U_0$  = forward speed.

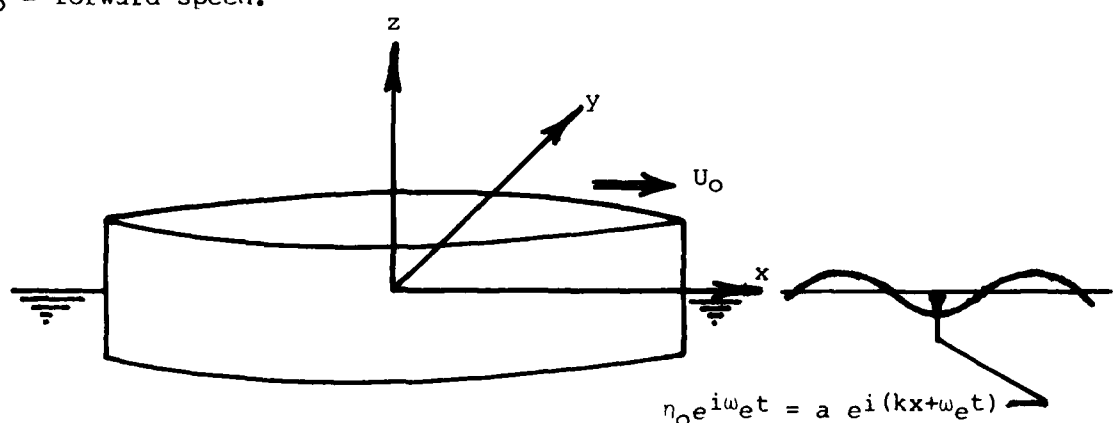


Figure 1. Coordinate System

In the coordinate system moving with the ship, the free surface elevation is given by

$$\eta e^{i\omega_e t} = -\frac{1}{g} \left( \frac{\partial}{\partial t} - U_0 \frac{\partial}{\partial x} \right) \phi e^{i\omega_e t} \Big|_{z=0} \quad (2)$$

where  $\phi$  = perturbation potential.

Thus, the incident wave elevation is given by

$$\eta_0 e^{i\omega_e t} = a e^{i(kx + \omega_e t)}$$

#### Diffracted Wave System

The theory which is used to compute the diffracted wave amplitude is presented in Beck and Troesch (1980). The theory was originally developed by Maruo and Sasaki (1974) and involves the use of the method of matched asymptotic expansions to solve the diffraction problem. In this technique the complete diffraction problem is reduced to a series of problems in the so called inner and outer regions. In the inner region the problem reduces to solving the Helmholtz equation in the cross-flow plane subject to the free surface and body boundary conditions.

In the far field, the ship is represented by a distribution of sources along the x-axis whose density is given by  $\sigma(x) \exp(i\omega_e t + ikx)$ . The value of  $\sigma(x)$  is found by matching with the inner region solution. Maruo and Sasaki (1974) considered the first and second order problems simultaneously so that a Volterra integral equation must be solved to obtain  $\sigma(x)$ .

As shown in Beck and Troesch (1980) the free surface amplitude in the near field due to the incident plus diffracted wave is

$$\frac{\eta_{I+D}}{a} e^{i\omega_e t} = i \frac{\sigma(x) \omega_0}{ga} \frac{1}{\pi B_0(x)} \Psi(y, 0; x) e^{+ikx} e^{i\omega_e t}$$

where  $\Psi(y, 0; x)$  is the value on  $z=0$  of the solution to the two-dimensional, inner-region problem.  $B_0(x)$  is the source strength in the multi-pole expansion of the inner region solution. It is computed as part of the inner region solution and is a function of body shape and frequency.

#### Radiated Wave System

The radiated waves generated by the forced oscillation of the ship are computed using the strip-theory approach of Salvenden, Tuck, and Faltinsen (1970). They define the unsteady perturbation potential due to forced oscillations as

$$\phi_T e^{i\omega_e t} = \sum_{j=1}^6 \zeta_j \phi_j e^{i\omega_e t} \quad (3)$$

where  $\zeta_j$  = amplitude of motion in the  $j^{\text{th}}$  direction  
 $\phi_j$  = potential due to unit motion in the  $j^{\text{th}}$  direction.

Substituting equation (3) into the expression for the free surface elevation (eq. (2)) we find

$$\eta_R e^{i\omega_e t} = -\frac{1}{g} \left( i\omega_e - U_0 \frac{\partial}{\partial x} \right) \sum_{j=1}^6 \zeta_j \phi_j e^{i\omega_e t} \Big|_{z=0} \quad (4)$$

where  $\eta_R$  is the radiated wave amplitude. We will find it convenient to discuss the radiated waves due to each mode of motion separately. Thus we write

$$\eta_R = \sum_{j=1}^6 \eta_j \quad (5)$$

$$\text{where } \eta_j = -\frac{1}{g} \left( i\omega_e - U_0 \frac{\partial}{\partial x} \right) \zeta_j \phi_j \Big|_{z=0}$$

= component of radiated wave system due to the  $j^{\text{th}}$  mode of motion.

Assuming the potential due to steady forward motion and the unsteady perturbation potentials are independent, Salvesen et al show that the  $\phi_j$  potentials can be related to the zero speed potentials as follows:

$$\begin{aligned} \phi_j &= \phi_j^0 \quad j = 1, 2, 3, 4 \\ \phi_5 &= \phi_5^0 + \frac{U_0}{i\omega_e} \phi_3^0 \\ \phi_6 &= \phi_6^0 - \frac{U_0}{i\omega_e} \phi_2^0 \end{aligned} \quad (6)$$

where  $\phi_j^0$  = "zero speed" potential.

The relative motion at any point along the ship length is defined as the free surface elevation at that point minus the vertical ship motion. Thus, we write

$$\rho(x) e^{i\omega_e t} = \eta(x) e^{i\omega_e t} - \xi(x) e^{i\omega_e t} \quad (7)$$

where  $\rho(x)$  = complex relative motion  
 $\eta(x)$  = free surface elevation

$\xi(x)$  = vertical displacement of the ship at the side

$$= \zeta_3 - x\zeta_5 + y\zeta_4$$

The total relative motion due to radiated waves can be separated into its individual components by substituting equation (5) into equation (7) as follows:

$$\rho = \sum_{j=1}^6 \rho_j \quad (8)$$

$$\begin{aligned} \rho_1 &= \eta_1 & \rho_4 &= \eta_4 - y\zeta_4 \\ \rho_2 &= \eta_2 & \rho_5 &= \eta_5 + x\zeta_5 \\ \rho_3 &= \eta_3 - \zeta_3 & \rho_6 &= \eta_6 \end{aligned} \quad (9)$$

In order to compute the radiated wave height we must first evaluate the zero speed potential. At this point in their analysis, Salvesen et al assume the frequency of encounter is sufficiently large that a strip-theory approximation can be used. Thus, the zero-speed potentials may be evaluated by using the two-dimensional potentials for the appropriate section. In this paper, we are only concerned with the radiated waves due to heave and pitch motions. If we define  $\psi_3(x)$  as the two-dimensional potential due to heave motion of the ship cross section at  $x$ , then the zero speed potentials for heave and pitch are

$$\begin{aligned} \phi_3^0 &= \psi_3 \\ \phi_5^0 &= -x\psi_3 \end{aligned} \quad (10)$$

Substituting equation (10) into equations (6) and (5), the final expressions for the radiated wave amplitudes due to heave and pitch are

$$\begin{aligned} \eta_3 &= -\frac{1}{g} \left( i\omega_e \psi_3 - U_0 \frac{\partial \psi_3}{\partial x} \right) \zeta_3 \Big|_{z=0} \\ \eta_5 &= -\frac{1}{g} \left( (2U_0 - i\omega_e x) \psi_3 + \left( U_0 x - \frac{U_0^2}{i\omega_e} \right) \frac{\partial \psi_3}{\partial x} \right) \zeta_5 \Big|_{z=0} \end{aligned} \quad (11)$$

The relative motions due to heave and pitch are found by substituting equations (11) into equations (9).

It should be noted that the strip-theory approach to computing the radiated wave height raises several interesting questions concerning the forward speed effects. First, because of the high frequency assumption, the retention of both terms (one proportional to  $i\omega_e$  and the other  $U_0 \partial/\partial x$ ) in the equation for the wave amplitude (equation 2) is mathematically inconsistent. Secondly, the strip-theory approach

of Salvesen et al has a priori excluded the interaction between the steady forward motion wave system and the unsteady radiated waves. In the final section of this paper, we shall see that the simple strip theory predicts reasonably well the radiated heights.

#### EXPERIMENTAL TECHNIQUES

Experiments were conducted to measure each of the components making up the total free surface elevation in the bow region. The experiments were conducted in the main tank at the University of Michigan's Ship Hydrodynamics Laboratory. The main tank is 360' long by 22' wide with an average depth of 10'. It is fitted with a plunger-type wavemaker at one end and a beach at the other.

The experiments were conducted on a mathematical model which had parabolic waterlines and rectangular section shapes. The bilge radius was approximately 1/2". The model particulars are given in Table 1. The model was constructed of plywood and had a clear varnish finish.

TABLE 1  
Mathematical Model Definition

$L = 12'$	$A_w = 17.454 \text{ ft}^2$	$V = 10.82 \text{ ft}^3$	$L/B = 5.5$
$B = 2.18'$	$C_B = .667$	$k_{yy} = 2.274'$	$R/T = 3.52$
$T = .62'$	$1/2 \text{ entrance angle} = 20.83^\circ$		

#### Parabolic Waterlines

$$\text{Local } \frac{1}{2} \text{ beam} = \frac{12}{11} (1 - (x/6)^2)$$

The model was fitted with 2-wire capacitance wave probes mounted on the side of the model at the fore-perpendicular, and stations 1, 2, 3, 4 and 5. The wires of each probe were .025" in diameter and mounted 1/4" from the side of the model. Several times during a day of testing the probes were statically calibrated. They held their calibration extremely well. In addition, one probe was dynamically calibrated on a special test stand. For the dynamic calibration test, a piece of plywood finished like the model was attached at the appropriate distance from the probe. The dynamic tests verified that over the frequency range of interest the use of the static calibration was acceptable.

During the actual experiments the amplitudes and phase angles were obtained using a carriage mounted data acquisition system. For this particular set of experiments, the analogue signals from the wave probes and motion measuring devices were first digitized. The digitized signals were then properly conditioned using trend removal and the application of a cosine taper window. Finally, a Fast Fourier Transform was used to obtain the amplitude and phase angle of the first harmonic. The data reduction program automatically applied the appropriate calibration constants, non-dimensionalized the data, and corrected the phase angles for the desired axis system.

## EXPERIMENTAL AND THEORETICAL RESULTS

The experimental and theoretical results are shown in Figures 2-40. Figure 2 shows the wave amplitude along the side of the model due to steady forward motion in calm water. The various components of the unsteady relative motions are shown in Figures 3-40. For organizational purposes and to help clarify the results, the plots have been divided into two sections. In this section all the results are plotted versus distance along the ship length for three wavelengths ( $L/\lambda = .8, 1.0, 1.2$ ) and two Froude numbers ( $Fn = .15, .25$ ). In Appendix A the results are plotted versus frequency for each station at which experimental measurements were taken. The graphs based on distance along the ship are cross-plots of the frequency based graphs. Because of the volume of data presented in Appendix A, it is easier to examine the smaller number of cross-plots. Appendix A is presented for the researcher who would like the complete experimental and theoretical results.

In the experiments, some runs for each of the different cases were repeated using a different incident wave height or forced motion amplitude. In all cases the results showed that the linearity assumption was valid. For this reason, in the plots (Figures 17-40) showing the experimental results no differentiation is made between results obtained from the high or low wave amplitude or forced-motion amplitude.

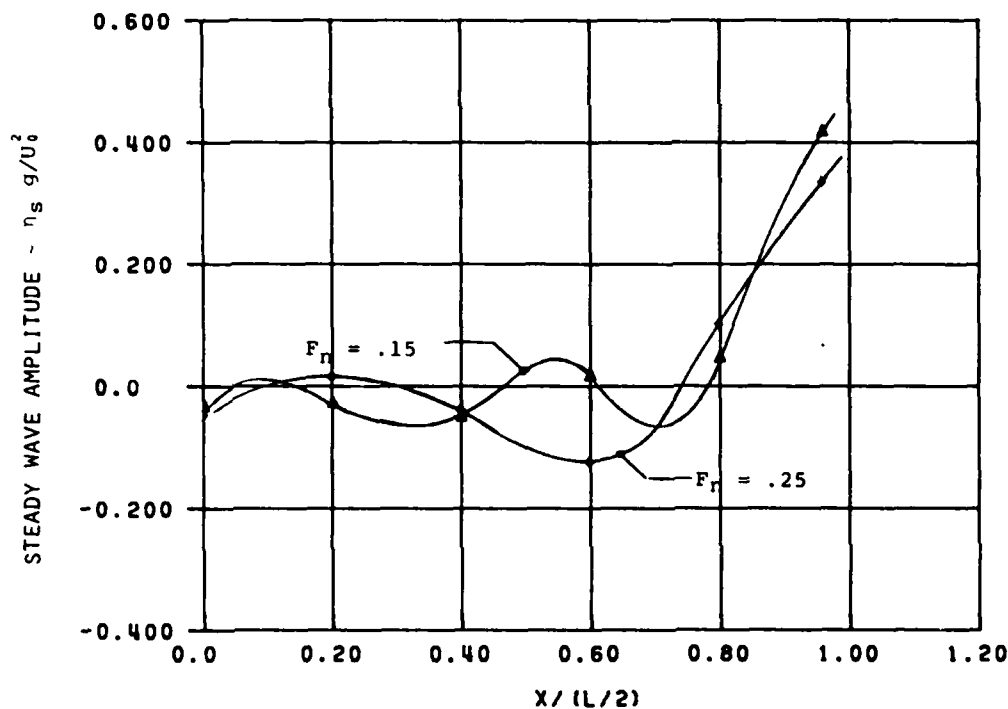


FIGURE 2  
STEADY WAVE AMPLITUDE ALONG SHIP LENGTH

### Relative Motion due to Steady Waves

The first set of experiments measured the steady wave amplitude at the two test Froude numbers of  $Fn = .15$  and  $.25$ . The results are shown in Figure 2. The steady wave amplitude is nondimensionalized as  $\eta_{sg}/U_0^2$ .

It should be noted that the wave amplitude was only measured at stations 0 through 5. Thus, the lines drawn in Figure 2 pass through each experimental point, but in between the stations the graph only approximates the actual wave amplitude.

The steady wave amplitude is not actually used because the unsteady amplitudes were processed by first subtracting out the mean shift; they are presented to give an estimate of the relative magnitudes of the steady and unsteady wave amplitudes.

### Relative Motion due to Forced Heave

Figures 3 and 4 show the amplitudes and phase angles of the relative motion along the model length due to forced heave. The relative motion amplitude is nondimensionalized with respect to the forced heave amplitude. The complete results at each station are presented in Figures 17 to 22 in Appendix A.

As can be seen from the figures, phase angles are almost independent of frequency, distance along the ship and Froude number. The agreement between theory and experiment is very good. On the other hand, the amplitudes are moderately Froude number dependent, and show large frequency dependence near midship. Both the theoretical and experimental results show an increase in the relative motion amplitude as one moves aft from the bow. The magnitude of the relative motion component due to heave is significantly larger than one. Thus, neglecting the radiated wave component in relative motion calculations can lead to significant errors.

Near midship the theoretical predictions are larger than the experimental results. The experiments show the same trends as theory, and the predictions are good in the bow quarter of the ship. The reason for the over prediction near midship is unclear.

It should be noted that the theoretical predictions show an upturn at the bow and a downturn at the stern. These end effects are even more noticeable in the pitch results (Figures 5 and 6). The upturn and downturn are caused by the derivative with respect to  $x$  in the equation for the wave amplitude (Equation 11). They are the result of the strip-theory approximation and do not occur at zero forward speed. Since one does not expect strip theory to be accurate at the ends, it is not surprising that the experimental results do not show a marked upturn. It appears that a three-dimensional theory will have to be developed for the end regions.

### Relative Motion due to Forced Pitch

The longitudinal variation of the relative motion due to forced

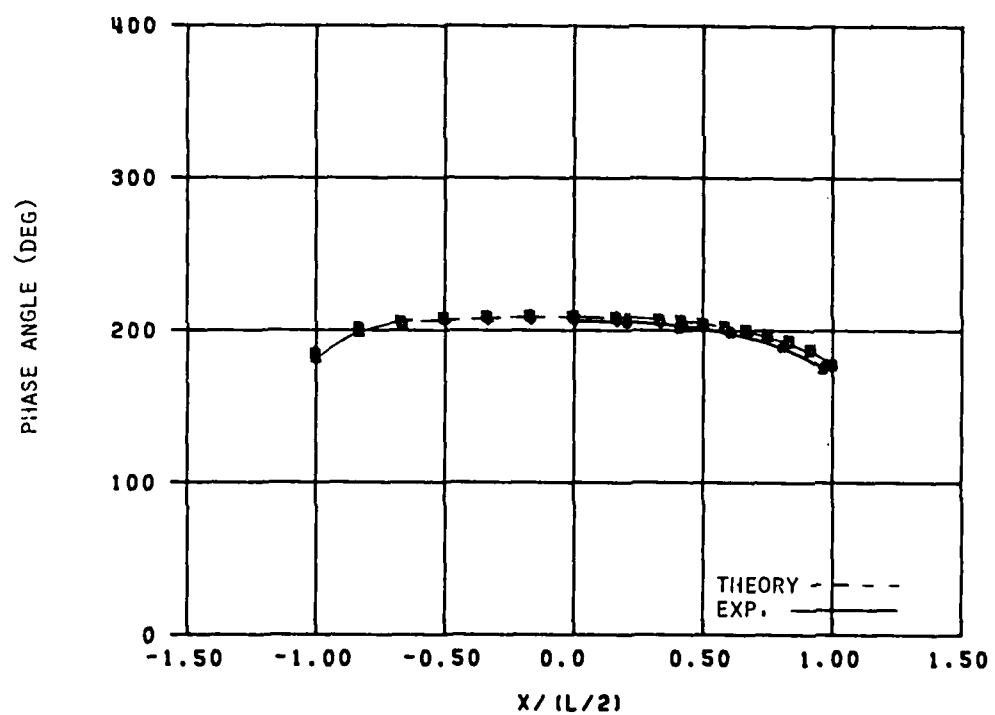
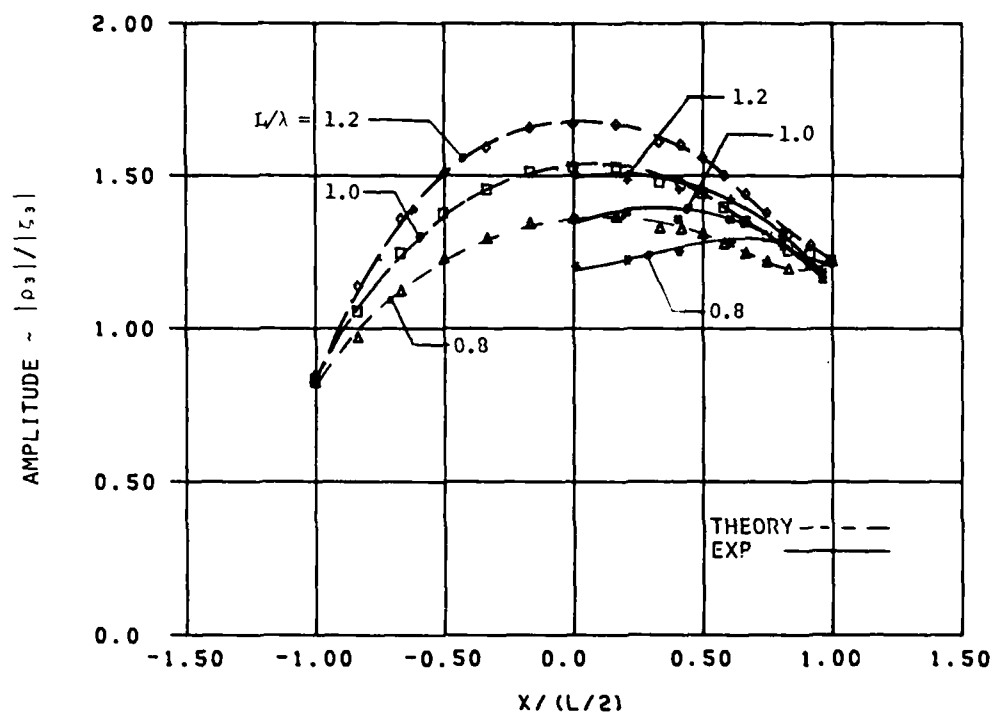


FIGURE 3  
RELATIVE MOTION DUE TO FORCED HEAVE,  $F_n = .15$



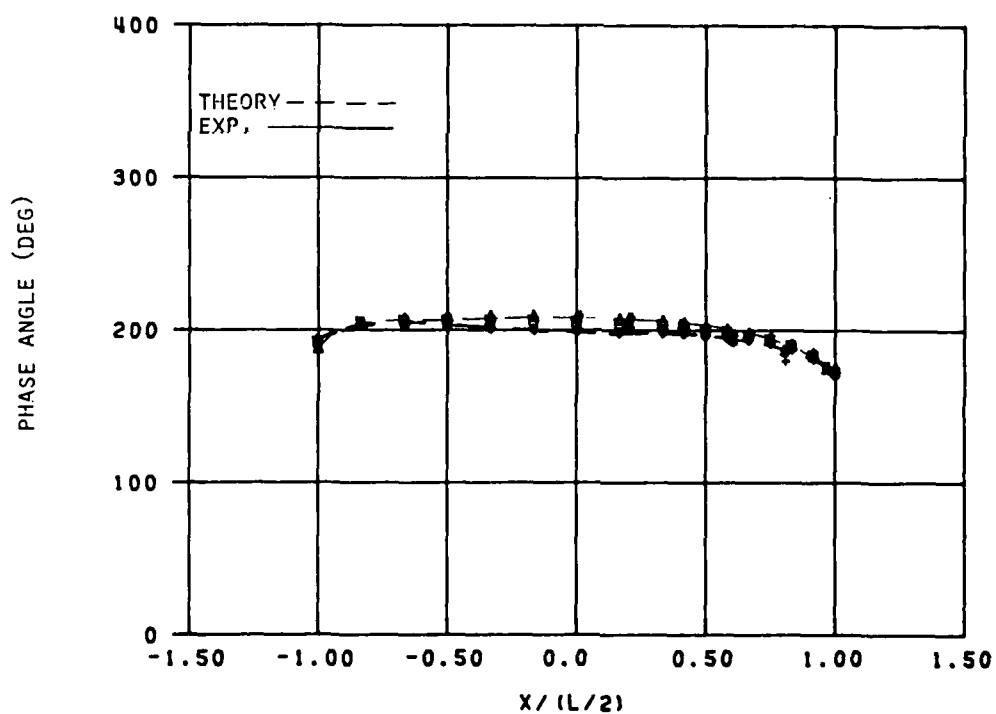
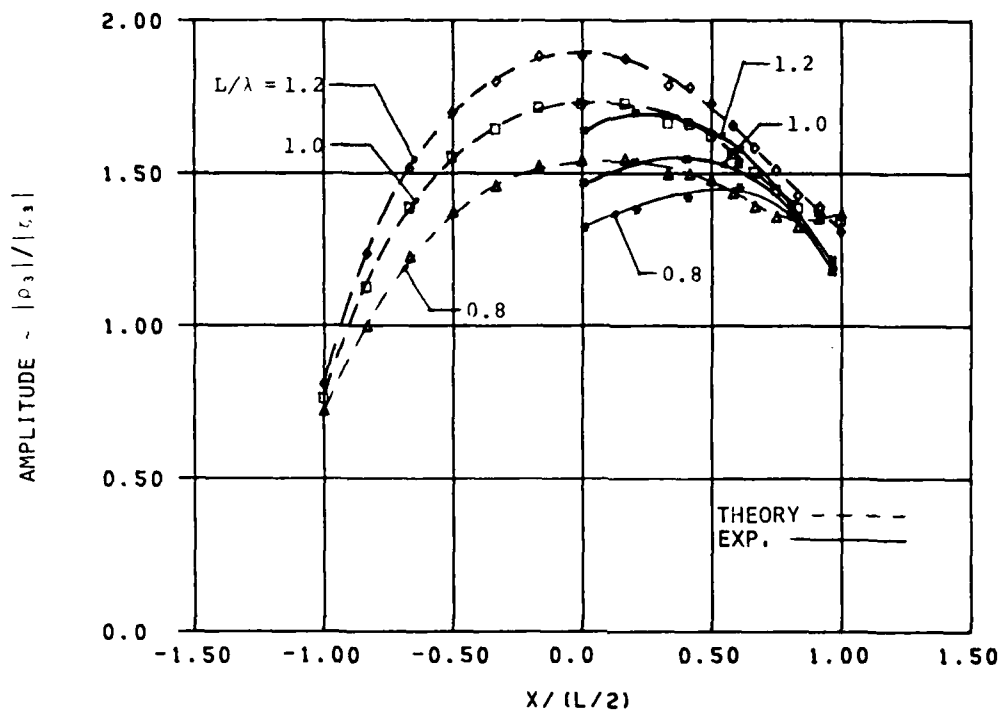


FIGURE 4  
RELATIVE MOTION DUE TO FORCED HEAVE,  $F_n = .25$

pitch is shown in Figures 5 and 6. The variations with frequency for each station are presented in Appendix A. The relative motion amplitudes due to pitch are nondimensionalized by

$$\rho_5^* = \rho_5 / (|\zeta_5|L/2)$$

where  $|\zeta_5|$  is the forced pitch amplitude. The nondimensionalization measures the relative motion in relation to the amplitude of motion at the bow. While it might be more convenient to nondimensionalize with respect to the local vertical motion, this definition breaks down at  $x = 0$ . The straight line in Figures 5 and 6 represent the nondimensional, local vertical amplitude. Thus, by comparing the actual results with the straight lines a measure of the amplitude of the relative motion versus the local vertical amplitude may be obtained.

As can be seen, the theoretical and experimental results agree very well. The trends with longitudinal position, frequency and forward speed are well predicted for both the amplitude and phase. As we previously discussed under the forced heave case, the marked changes in slope at the ends of the theoretical curves are the result of the strip-theory approximation.

#### Relative Motion due to Wave Diffraction

The relative motions produced by the diffraction of sinusoidal incident waves are shown in Figures 7, 8 and 29-34. Because the model is fixed in the diffraction case, the relative motion is given by the sum of the incident plus diffracted wave. In the figures, the relative motion amplitude is nondimensionalized by the incident wave amplitude.

Figures 29-34 show that there was some scatter in the experimentally measured amplitudes. The phase angles show very little scatter. Since the scatter was much less in the forced oscillation tests, it is presumed that the scatter is caused by the noise in the incident waves rather than inaccuracies in the wave probes.

Comparing the theoretical and experimental results, it can be seen that the agreement for the phase angles is very good. In particular, the linear variations of the phase angle with distance along the ship is confirmed by the experiments. It is also obvious that the amplitudes are greatly under estimated by the Maruo-Sasaki theory. In general, the trends of the experimental results with frequency and longitudinal distance are correctly accounted for. It is the absolute magnitude which is too low.

The reasons for the discrepancies between the theoretical and experimental amplitudes is unclear. In previous (cf. Beck and Troesch (1980)) comparisons using the Maruo and Sasaki approach, the agreement for the pressure distribution over the underwater portion of the hull was reasonable. The discrepancies could result from three-dimensional effects, interference effects between the steady and unsteady wave systems, or non-linearities.

The linearity of the results with input amplitude has been experimentally verified by testing at several different amplitudes and com-

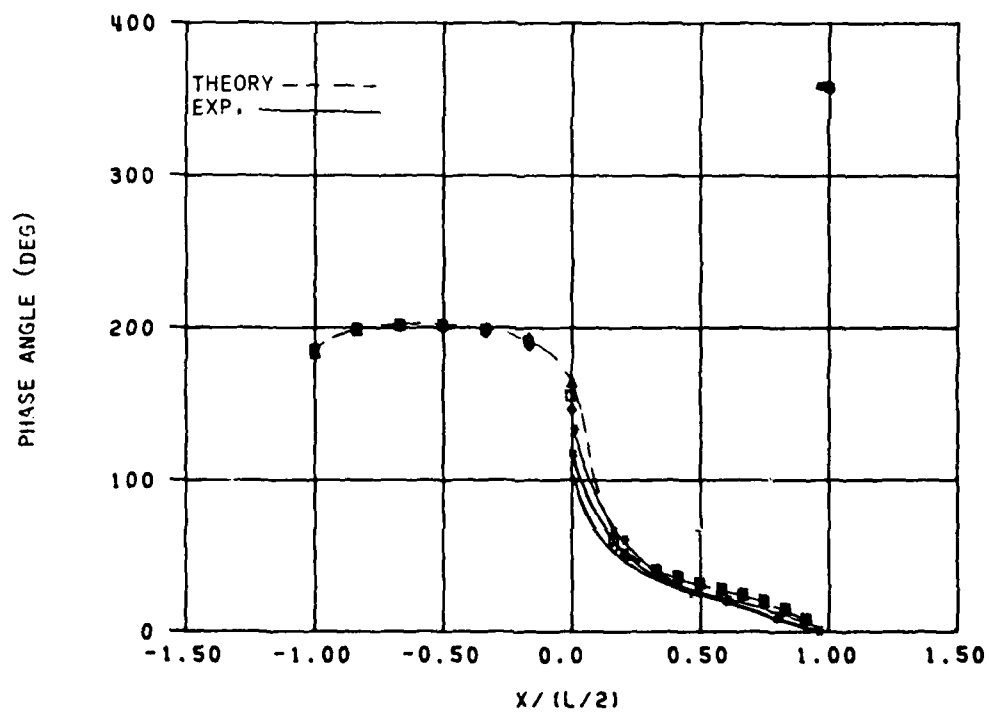
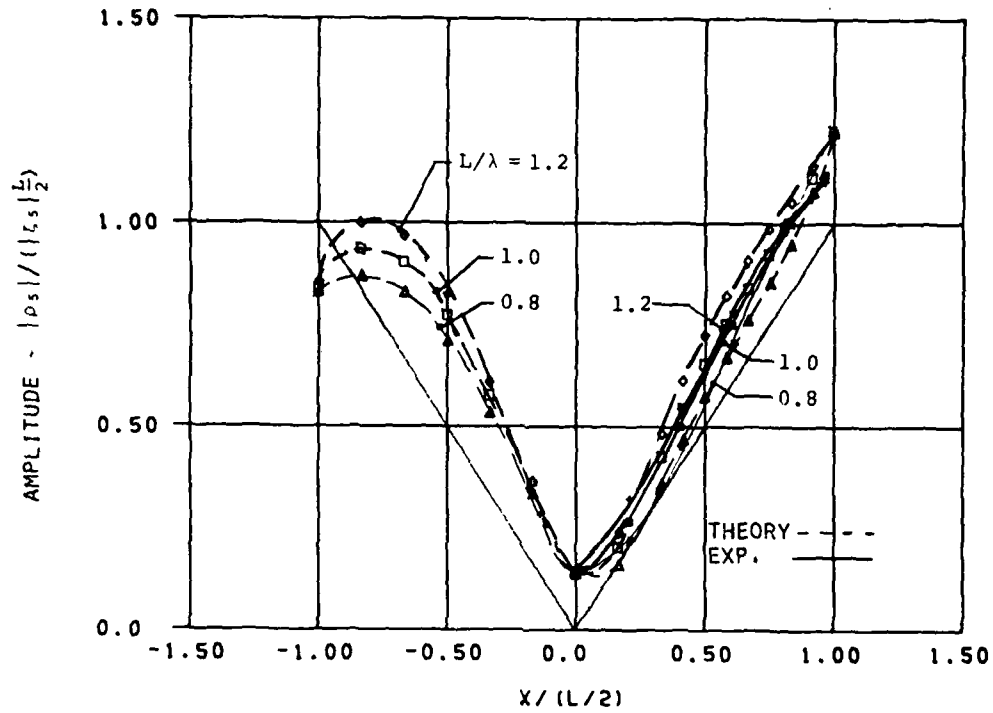


FIGURE 5  
RELATIVE MOTION DUE TO FORCED PITCH,  $F_n = .15$

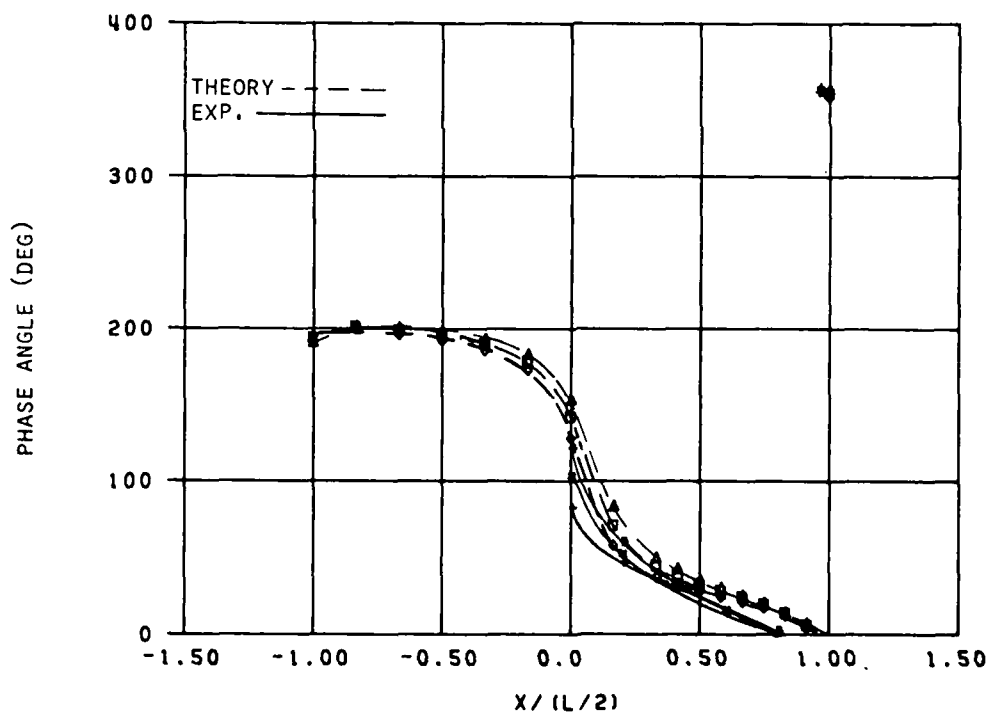
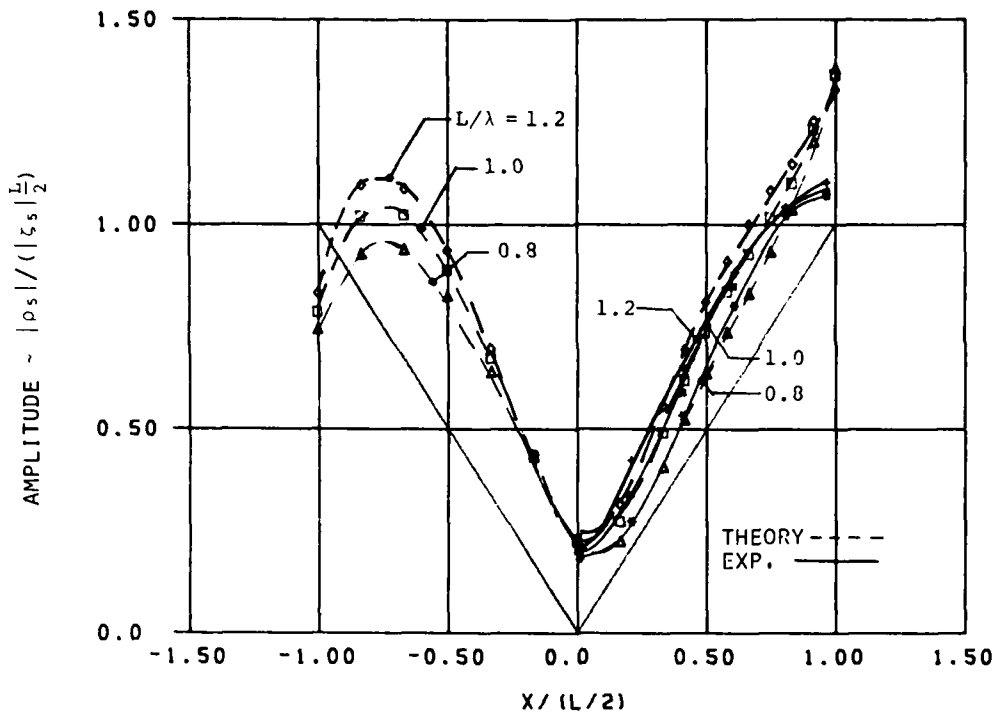


FIGURE 6  
RELATIVE MOTION DUE TO FORCED PITCH,  $F_n = .25$

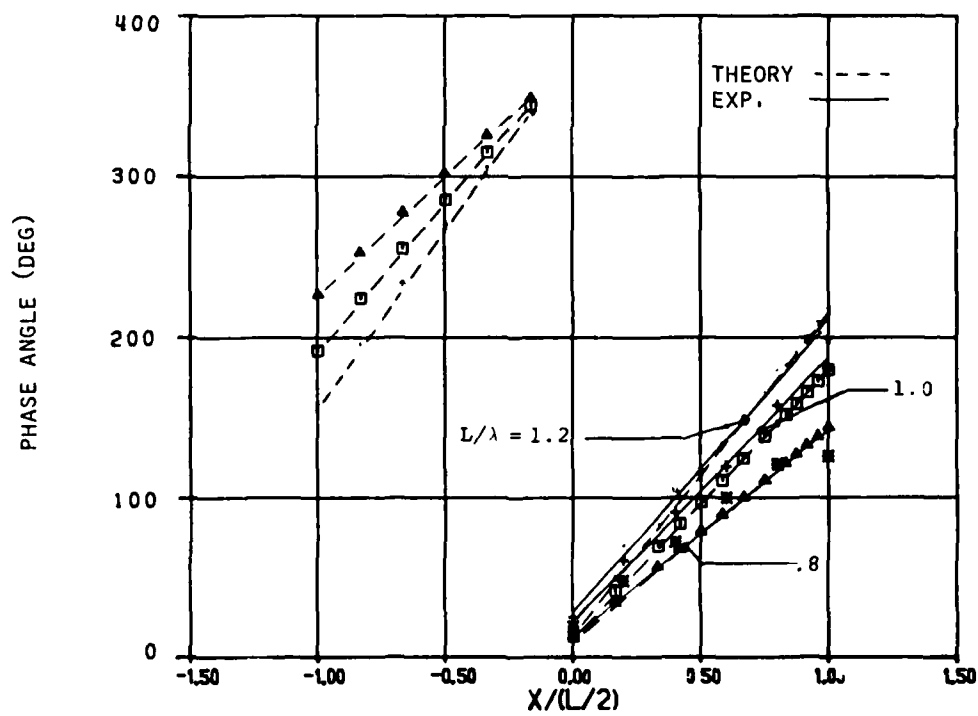
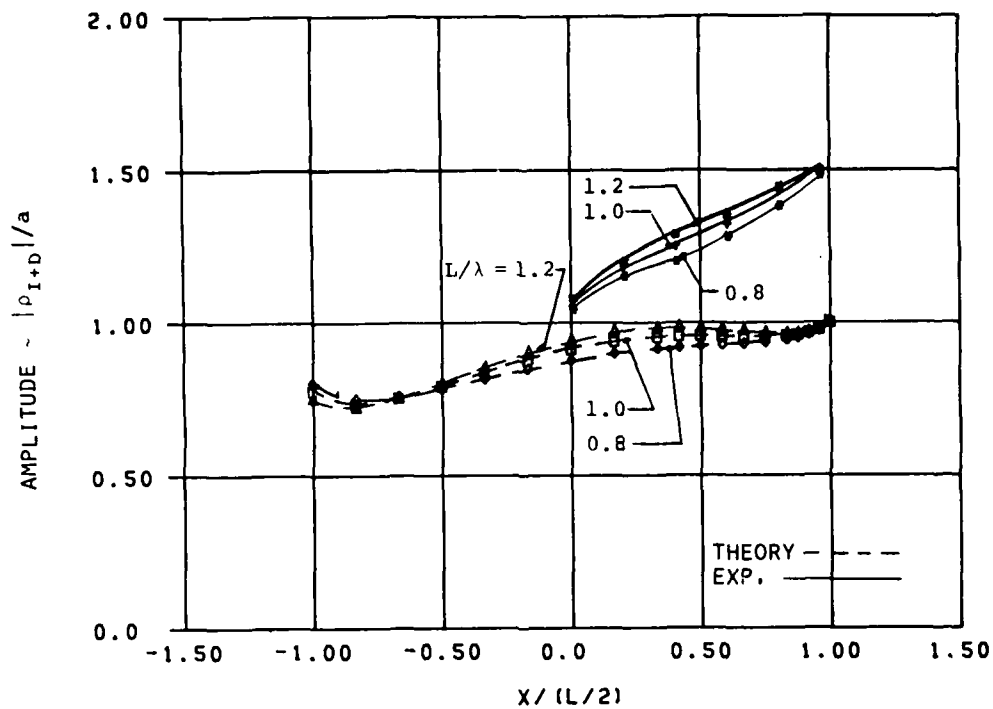


FIGURE 7  
RELATIVE MOTION DUE TO DIFFRACTION,  $F_n = .15$

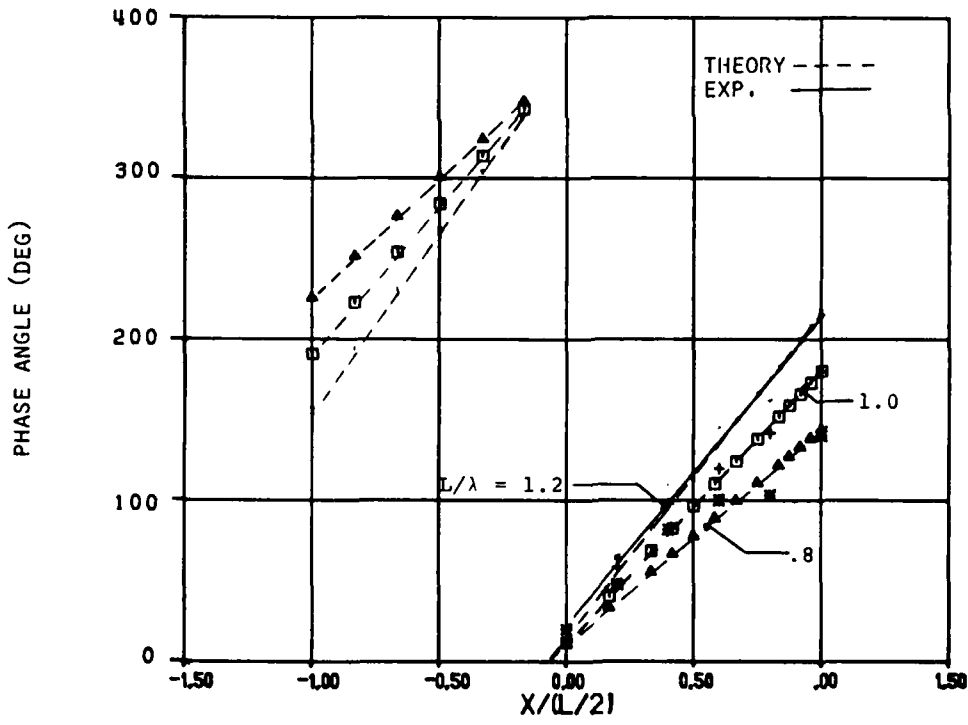
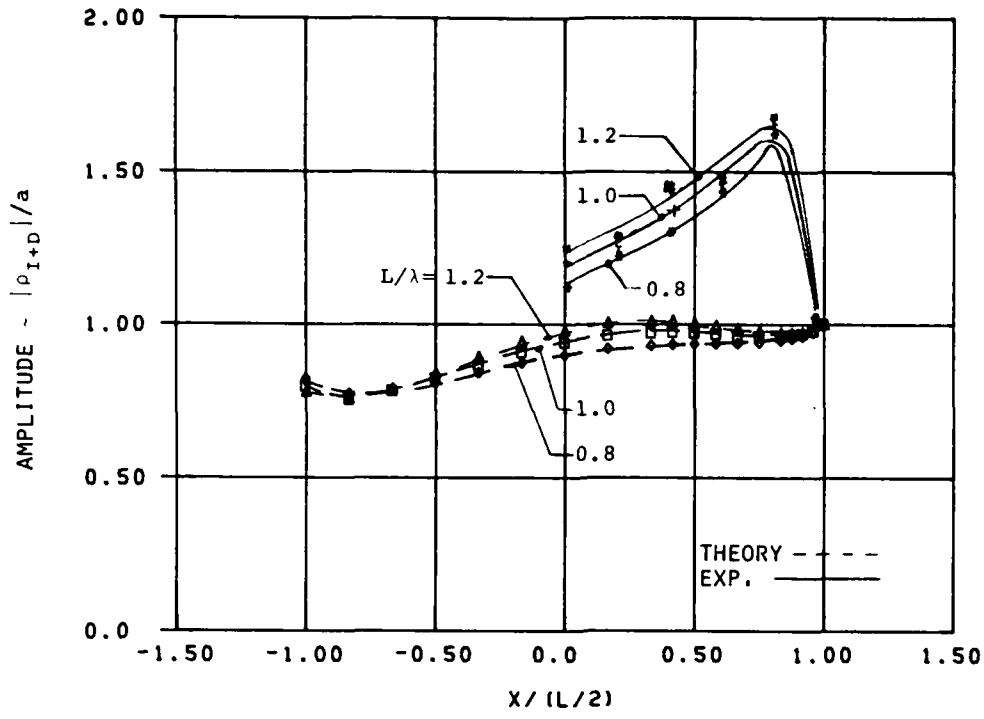


FIGURE 3  
RELATIVE MOTION DUE TO DIFFRACTION,  $F_n = .25$

paring the nondimensional results. In all cases the nondimensional amplitudes agree within experimental accuracy. In the discussion concerning the total relative motion we shall also show that the various components of the wave amplitude in the bow region can be linearly added. Thus, it appears that the effects of non-linearities are small.

It appears that the discrepancies result from a combination of three-dimensional effects and interference between the steady and unsteady wave systems. We are presently trying to ascertain the influence of each of these effects by studying the zero speed problem. The work in progress includes zero speed experiments and numerical calculations using a three-dimensional source panel method. No results are yet available.

It is possible that the bow geometry of the mathematical model has exaggerated the difference between slender-body theory and experiments. The model entrance half-angle of  $20.83^\circ$  is large for a  $C_B = .67$  ship. In addition the model has a flat bottom with a very small bilge radius. On a typical  $C_B = .67$  ship, the bilge in the bow region is slack and the bottom is faired into the sides.

#### Total Relative Motion

The total relative motions for the model free to pitch and heave in head seas are shown in Figures 11-16 and Figures 35-40. The heave and pitch motions are presented in Figures 9 and 10 respectively.

The theoretical predictions were made using a strip-theory program based on the Salvesen, Tuck, Faltinsen (1970) theory and using Lewis forms to compute the two-dimensional added mass and damping. As can be seen the theoretical results over predict both the heave and pitch motions, particularly around resonance. This is apparently due to the under prediction of the damping. The increased damping in the experiments is probably due to the model hull shape. The model was wall-sided with a flat bottom and very little bilge radius; a shape which presumably leads to increased viscous damping. In addition the heave staff added to the damping, but its effects should be small since the heave staff was especially designed to have low friction.

Figures 11-16 show the total relative motion as a function of distance along the ship for three frequencies and two Froude numbers. The results for all frequencies at other stations are presented in Appendix A. Five different cases are plotted as follows:

- i) The solid line is the experimental results. This is a cross-faired curve from the actual experimental data points given in Figures 36-40.
- ii) The dashed line is the strip-theory line. It was obtained from the strip-theory computer program which computes the relative motion by subtracting the vertical motion at any station from the incident wave amplitude at that station. Thus, the strip-theory line disregards the radiated and diffracted wave components.
- iii) The dotted curve results from computing the relative motion by subtracting the experimentally measured vertical motion

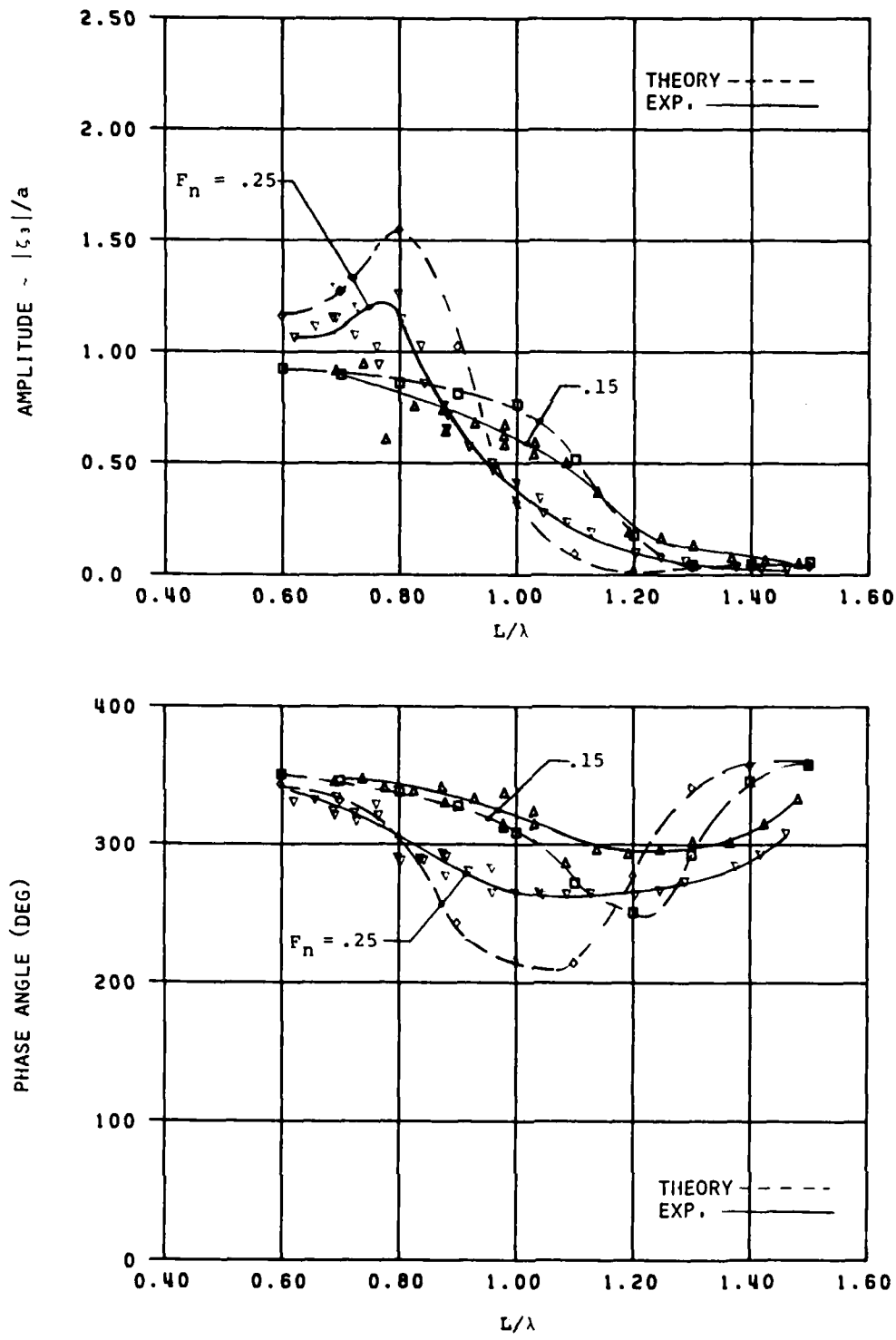


FIGURE 9  
HEAVE MOTION IN HEAD SEAS



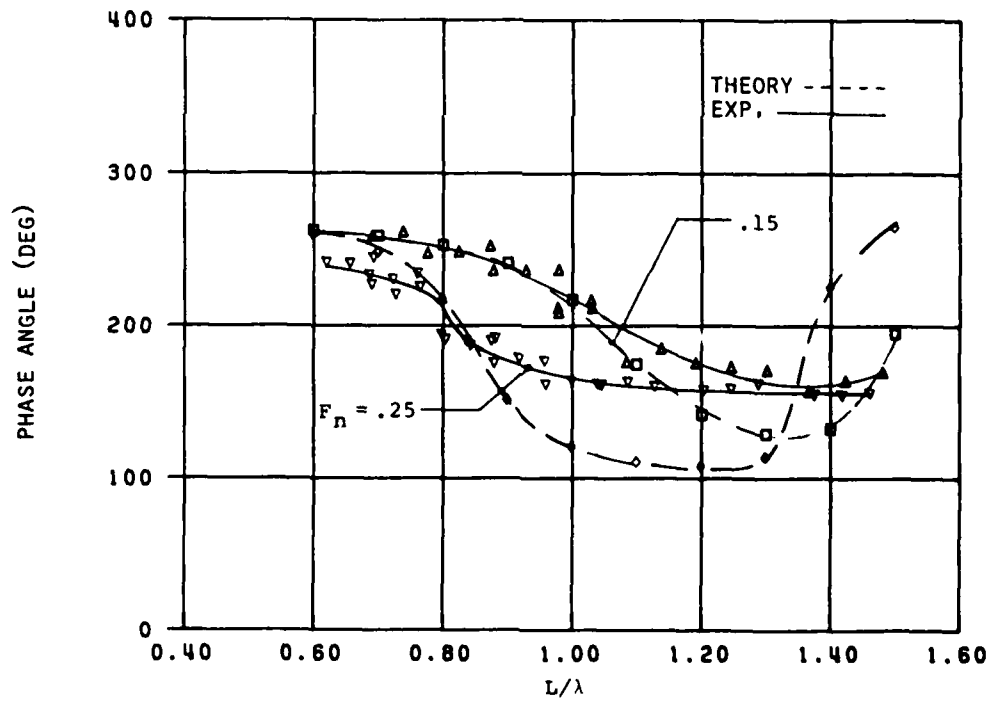
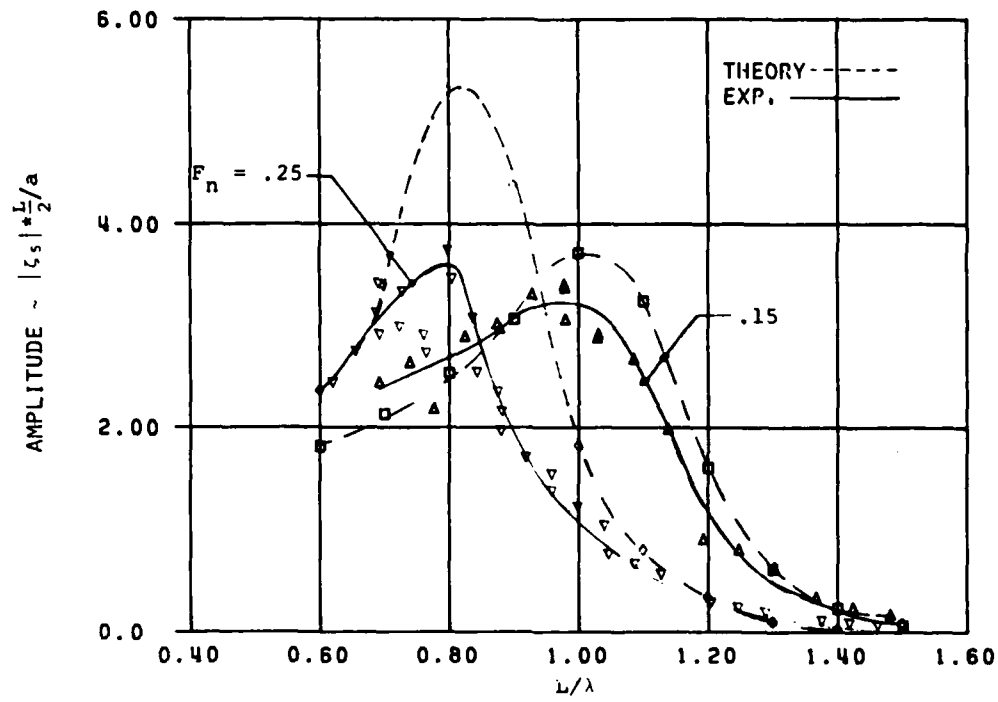
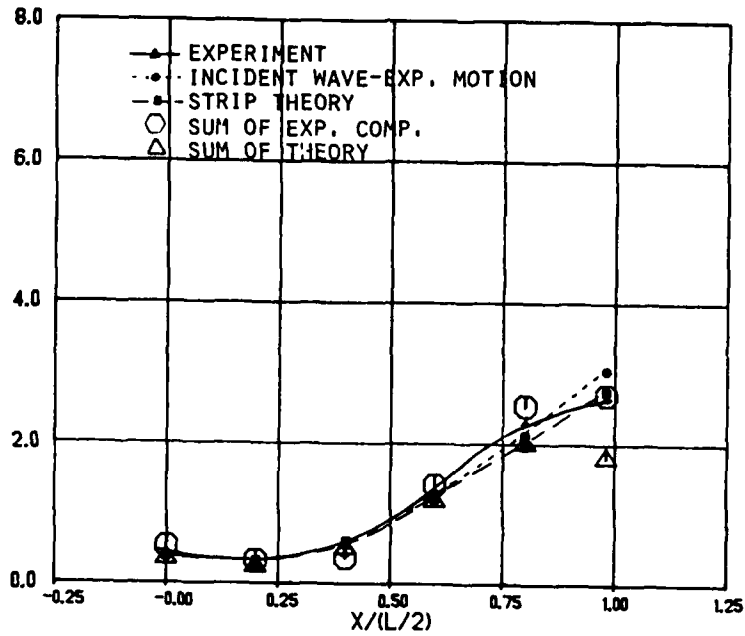


FIGURE 10  
PITCH MOTION IN HEAD SEAS

AMPLITUDE  $\sim |\rho|/a$



PHASE ANGLE (DEG)

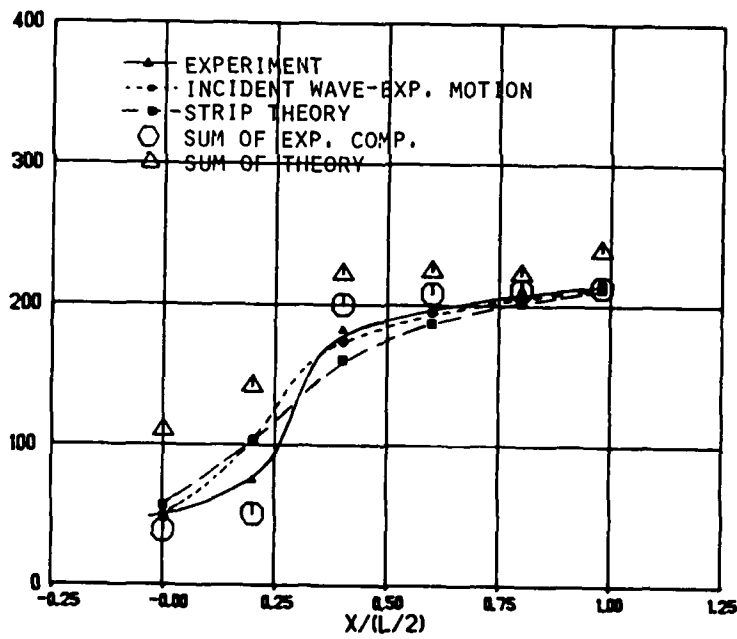
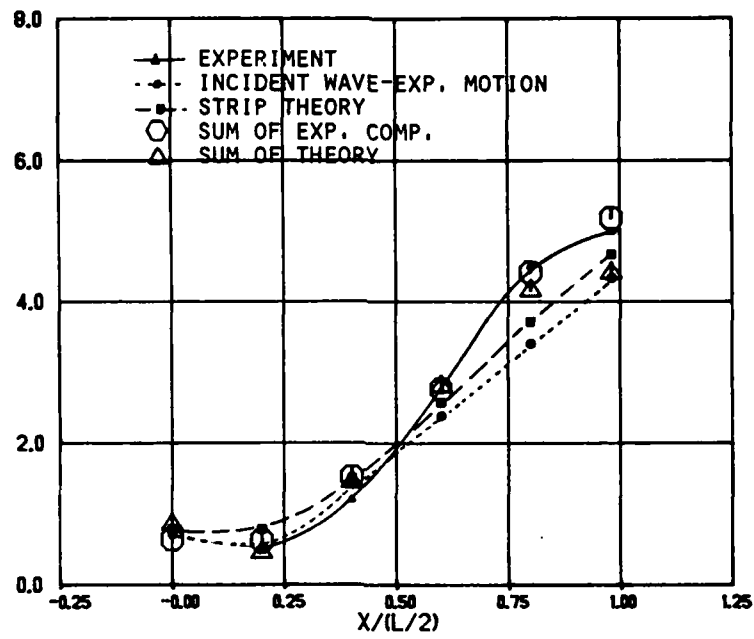


FIGURE 11

TOTAL RELATIVE MOTION IN HEAD SEAS  $L/\lambda = .8$ ,  $F_n = .15$

AMPLITUDE  $\sim |\rho|/a$



PHASE ANGLE (DEG)

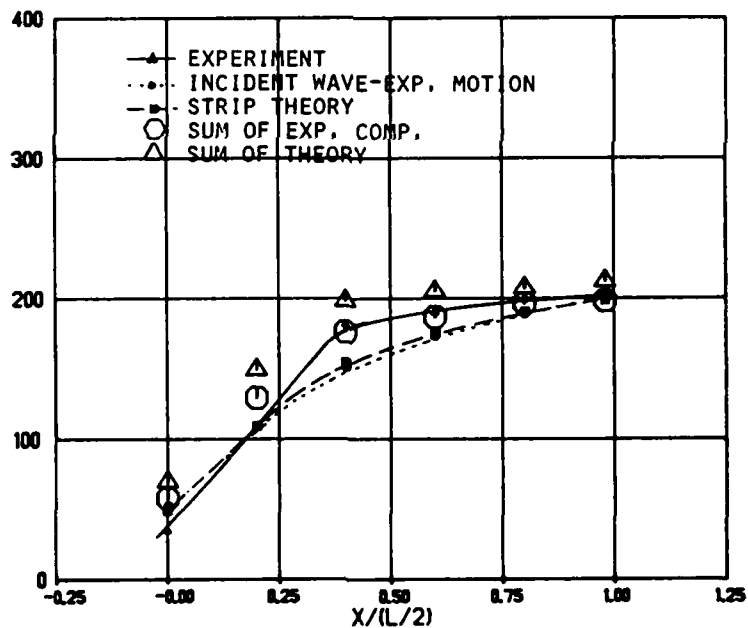


FIGURE 12

TOTAL RELATIVE MOTION IN HEAD SEAS  $L/\lambda = 1.0$ ,  $F_n = .15$

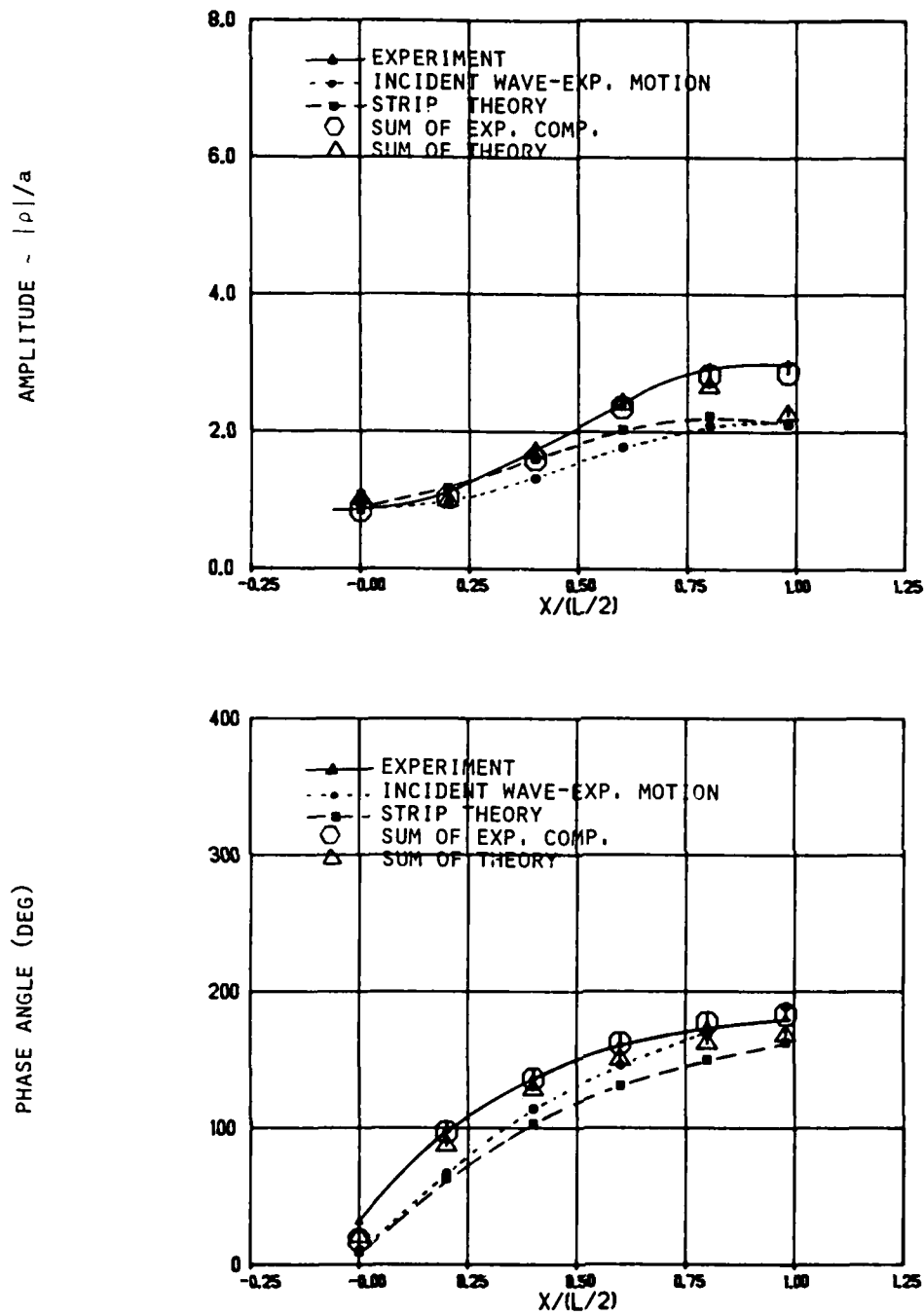
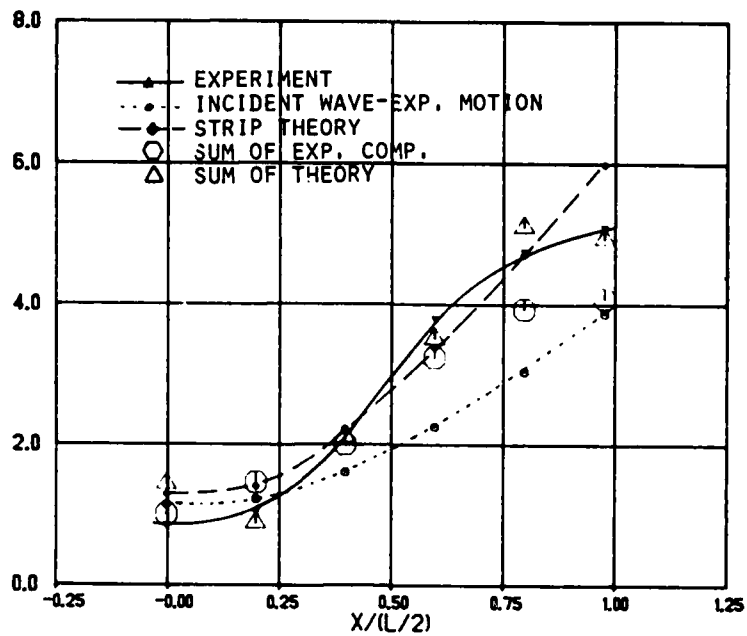


FIGURE 13

TOTAL RELATIVE MOTION IN HEAD SEAS  $L/\lambda = 1.2$ ,  $F_n = .15$

AMPLITUDE -  $|\rho|/a$



PHASE ANGLE (DEG)

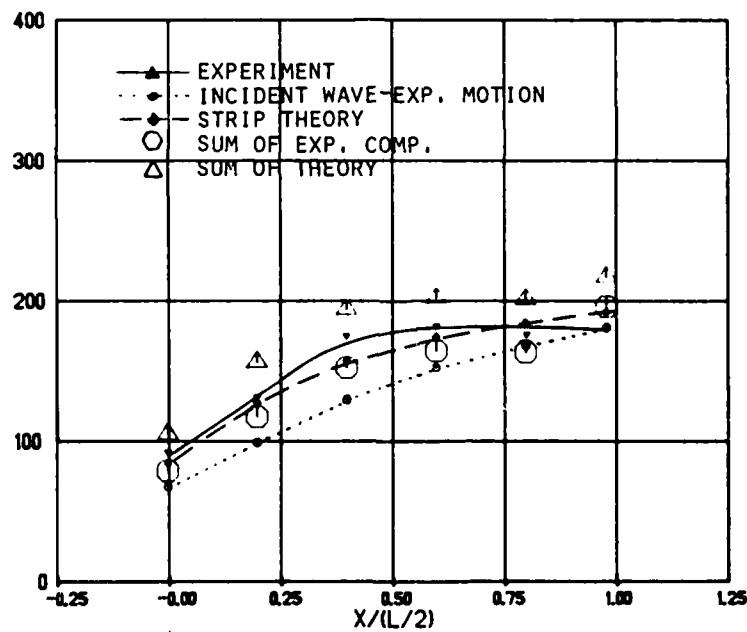
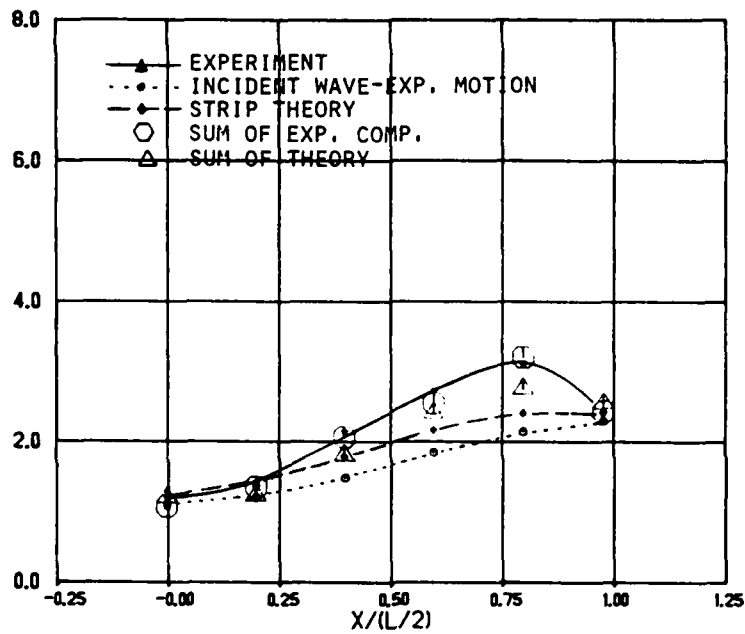


FIGURE 14

TOTAL RELATIVE MOTION IN HEAD SEAS  $L/\lambda = .8$ ,  $F_n = .25$

AMPLITUDE  $\sim |\rho|/a$



PHASE ANGLE (DEG)

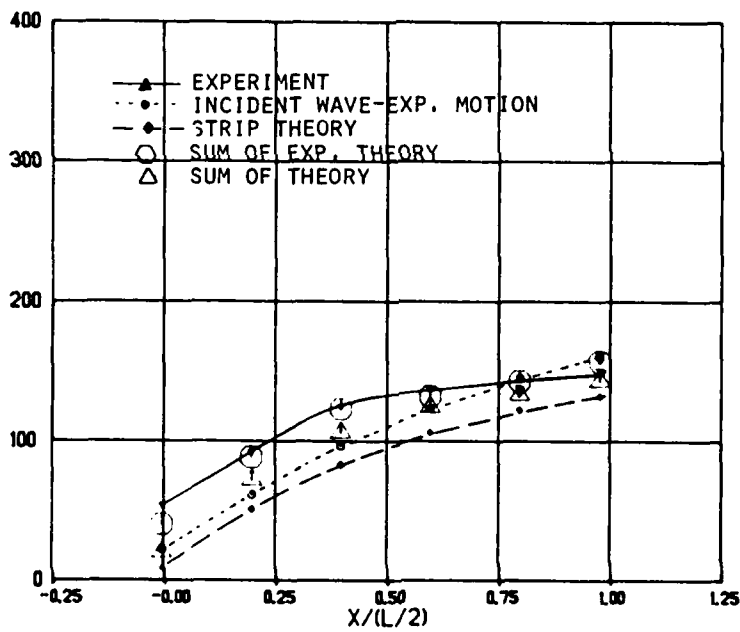
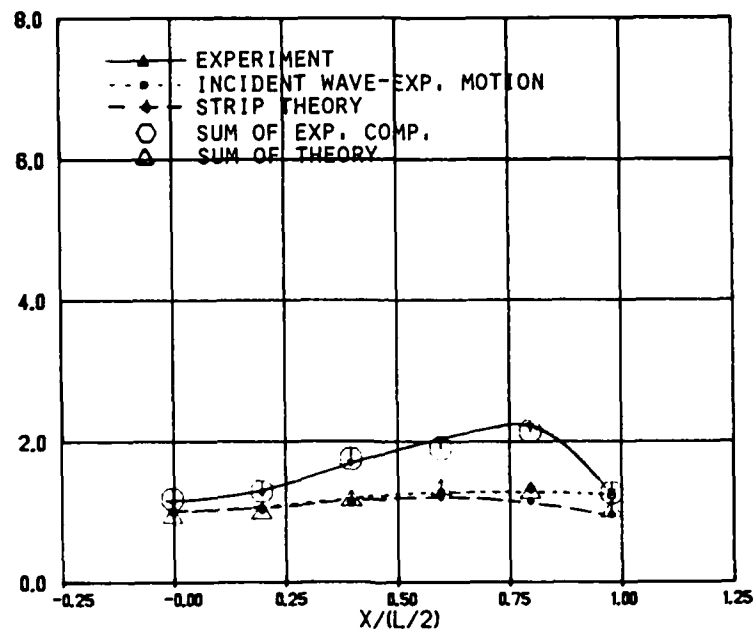


FIGURE 15

TOTAL RELATIVE MOTION IN HEAD SEAS  $L/\lambda = 1.0$ ,  $F_n = .25$

AMPLITUDE -  $|\rho|/a$



PHASE ANGLE (DEG)

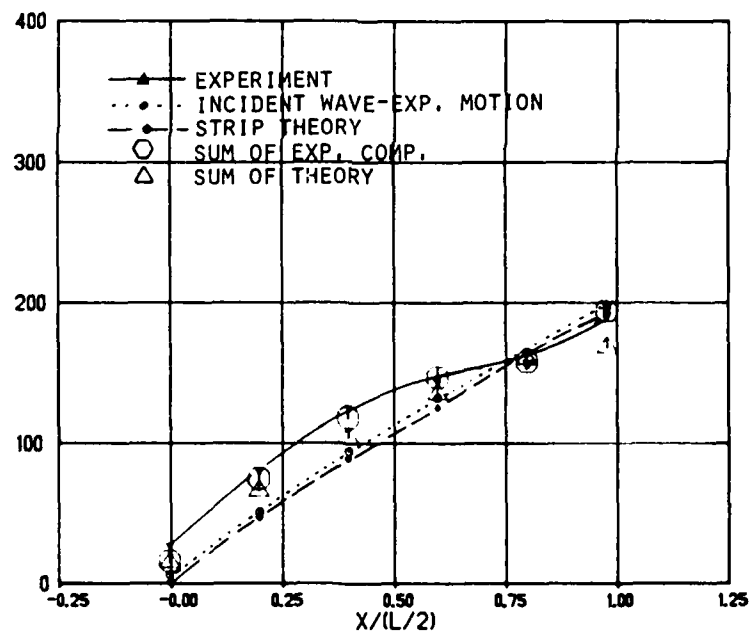


FIGURE 15

TOTAL RELATIVE MOTION IN HEAD SEAS  $L/\lambda = 1.2$ ,  $F_n = .25$

at any station from the incident wave amplitude at that station. This curve is the experimental equivalent to the strip-theory curve.

- iv) The triangles are the sum of the theoretical calculations including the radiated and diffracted wave components. The theoretical heave and pitch motions are given in Figures 9 and 10.
- v) The octagons are the sum of the experimentally measured components.

As expected, the general characteristics of the curves in Figures 11-16 show the relative motion increasing toward the bow. The dip in the relative motion amplitude at the fore-perpendicular, particularly for a  $F_n = .25$ , was unexpected but is consistent with the previously discussed individual components. All the component waves show this dip to some degree. It is most apparent in the diffracted wave component at  $F_n = .25$ .

Examining the octagons and the solid curve we see that linear super-position of the various wave components gives very good agreement with the total experimental results. It thus appears that relative motion in the bow region can be considered a linear process; the total relative motion is linearly proportional to the incident wave amplitude and the various wave components are additive.

A comparison of the solid and dotted curves is an experimental measure of influences of the radiated and diffracted wave components when computing the relative motion. As can be seen, the differences can be significant, particularly at the higher Froude number and in the bow region. In general the relative motion is increased by including the radiated and differential wave components.

The effects of the radiated and diffracted waves in the theoretical relative motion calculations can be measured by comparing the triangles with the dashed line. Again it can be seen that radiated and diffracted wave components tend to increase the relative motion. It appears that the difference between the solid and dotted curve is greater than theoretical predictions. This is to be expected since we have already seen that the theoretical diffracted wave amplitudes are very low.

The agreement between the experimental and the strip-theory curves is reasonable in most cases. However, it should be noted that this agreement is fortitious because the heave and pitch motions are over predicted by theory and the radiated and diffracted wave components are neglected. This may be a possible explanation for why conventional ship-motion programs, which neglect radiation and diffraction wave effects, obtain acceptable values for relative motion. The programs tend to overpredict the ship motion in the region of maximum motion and this overprediction tends to cancel out the neglect of the radiated and diffracted waves.



AD-A158 920

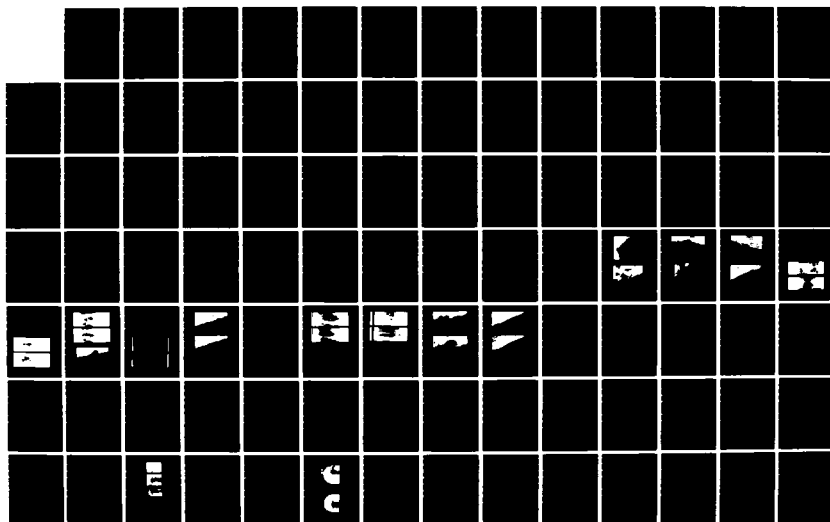
SYMPOSIUM OF NAVAL HYDRODYNAMICS (14TH) HELD AT ANN  
ARBOR MICHIGAN ON AUGUST 23-27 1982(U) OFFICE OF NAVAL  
RESEARCH ARLINGTON VA M P TULIN ET AL. 1982

86/13

UNCLASSIFIED

F/G 20/4

NL





## CONCLUSIONS

To summarize the findings, we can say that:

- The use of a strip approach to compute the radiated waves is reasonable except very near the bow where the derivatives with respect to  $x$  become large. The relative motion amplitude due to pitch and the phase angles for both heave and pitch radiated waves are well predicted. The relative motion amplitude due to heave is slightly overpredicted.
- The linear variation of the diffracted wave phase angle with distance from the bow is well verified by the experiments. The diffracted wave amplitudes are poorly predicted by the Maruo-Sasaki slender-body theory.
- The various unsteady relative motion components are linear functions of the input amplitude. The components can also be added linearly to arrive at the total relative motion.
- The radiated and diffracted waves tend to increase the relative motion 10 to 30% over the simple incident wave minus the local vertical motion calculations.
- At the higher Froude number, the total relative motion is a maximum aft of the fore-perpendicular. The decrease in the total relative motion at the fore-perpendicular appears to be related to forward speed effects.

## ACKNOWLEDGEMENT

This work supported by the Naval Sea Systems Command General Hydromechanics Research Program, administered by the David W. Taylor Naval Ship R&D Center, Contract No. N00014-78-C-0109.

## REFERENCES

- Beck, R.F. and A.W. Troesch (1980). Wave diffraction effects in head seas, International Shipbuilding Progress 27, 306.
- Maruo, H., and N. Sasaki (1974). On the wave pressure on the surface of an elongated body fixed in head seas, J. of the Society of Naval Architects of Japan 136, 34.
- Salvesen, N., E.O., Tuck, and O. Faltinsen (1970). Ship motions and sea loads, Trans. Society of Naval Architects and Marine Engineers 78, 250.

## APPENDIX A

GRAPHS OF RELATIVE MOTION  
COMPONENTS VERSUS FREQUENCY

FIGURES 17-40

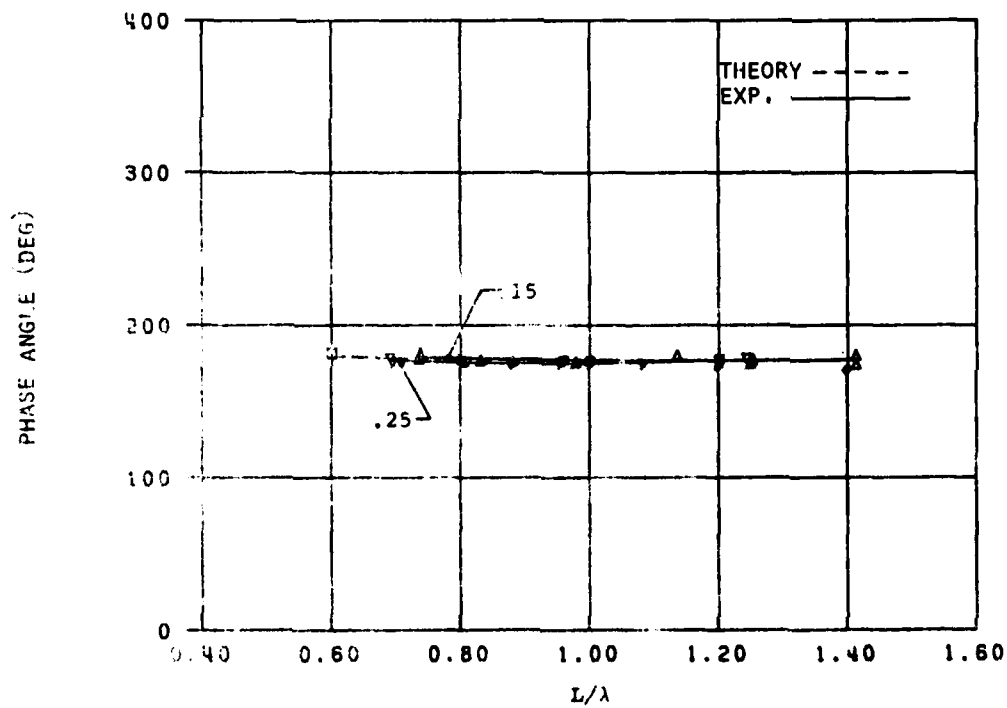
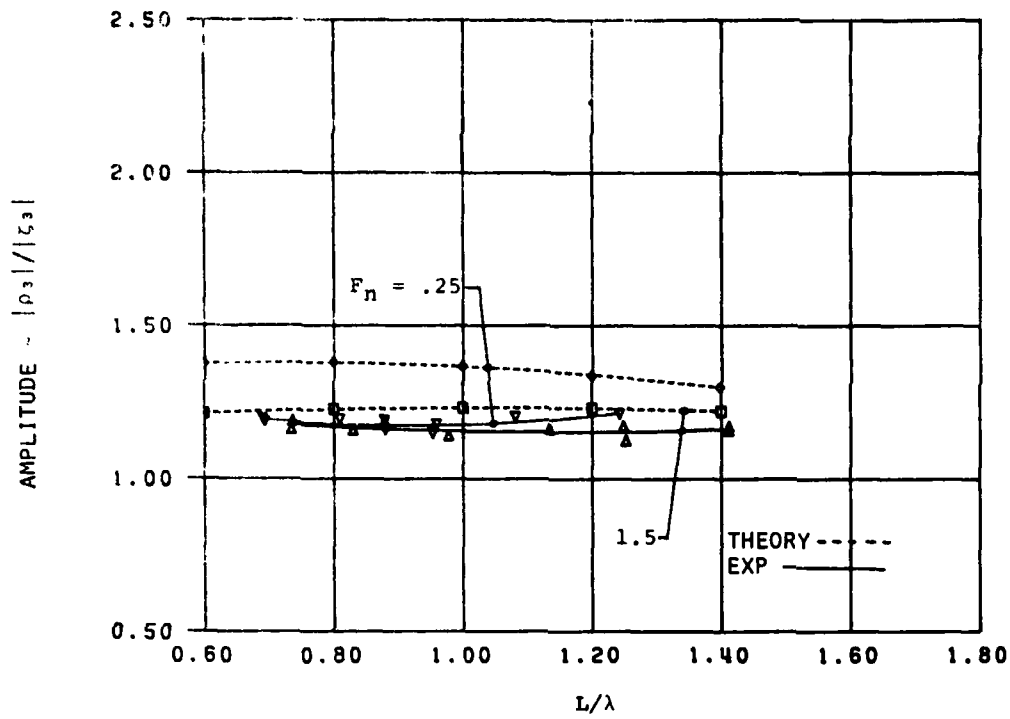


FIGURE 17  
RELATIVE MOTION AT F.P. DUE TO FORCED HEAVE

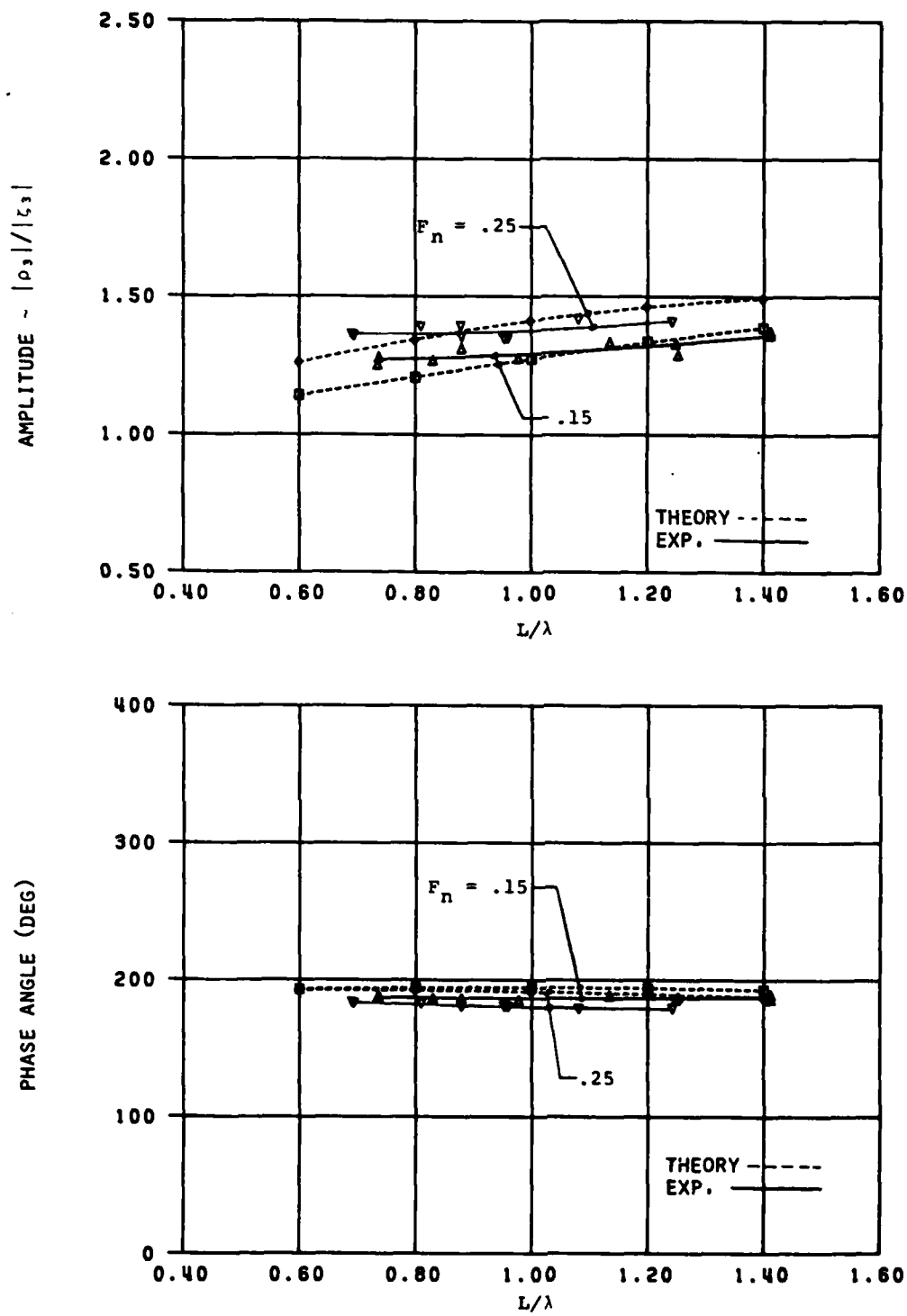


FIGURE 18  
RELATIVE MOTION AT STATION 1 DUE TO FORCED HEAVE

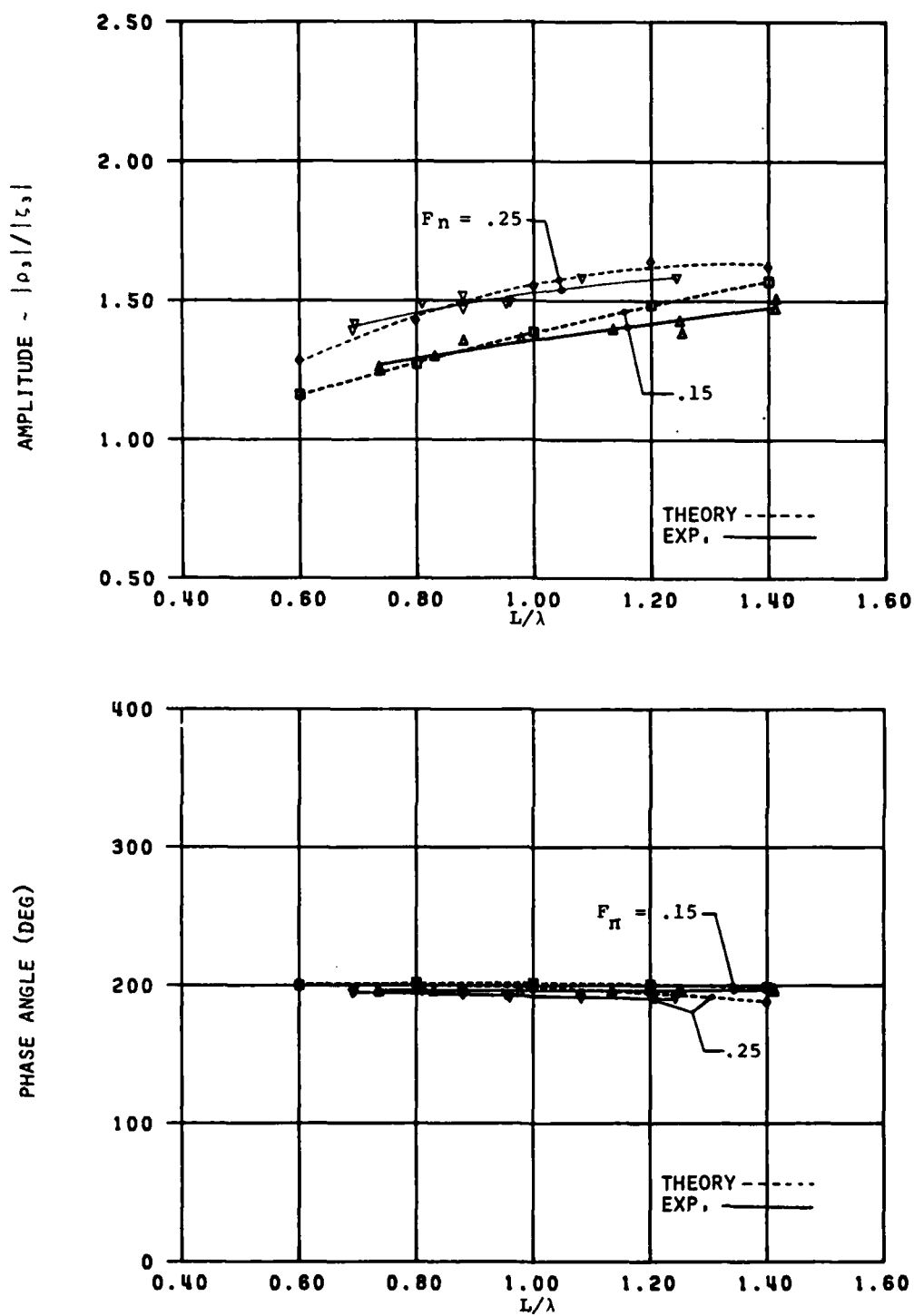


FIGURE 19  
RELATIVE MOTION AT STATION 2 DUE TO FORCED HEAVE

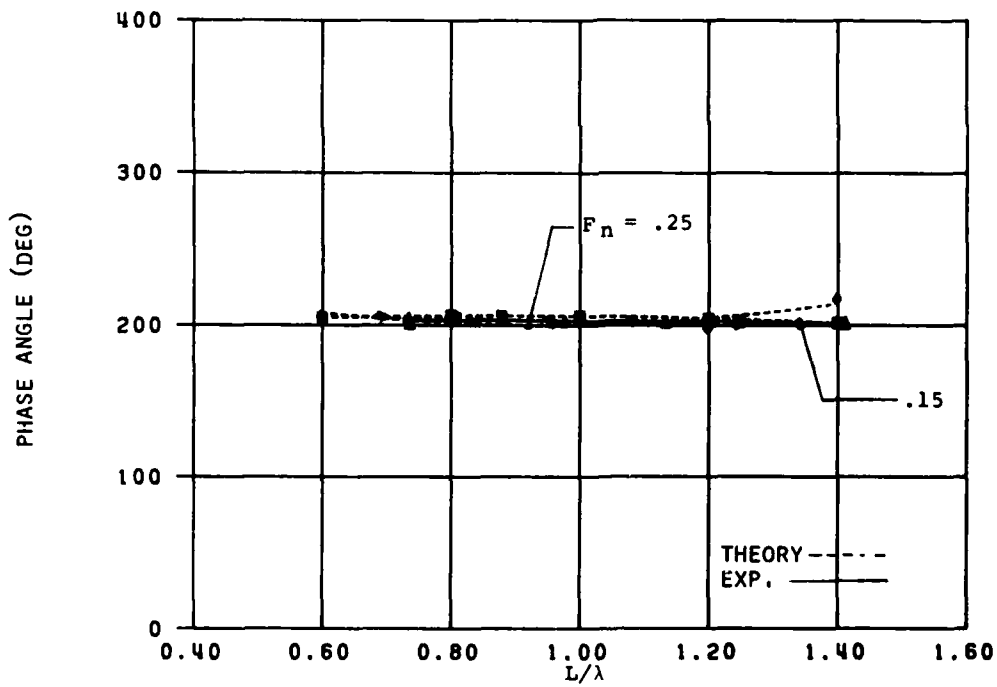
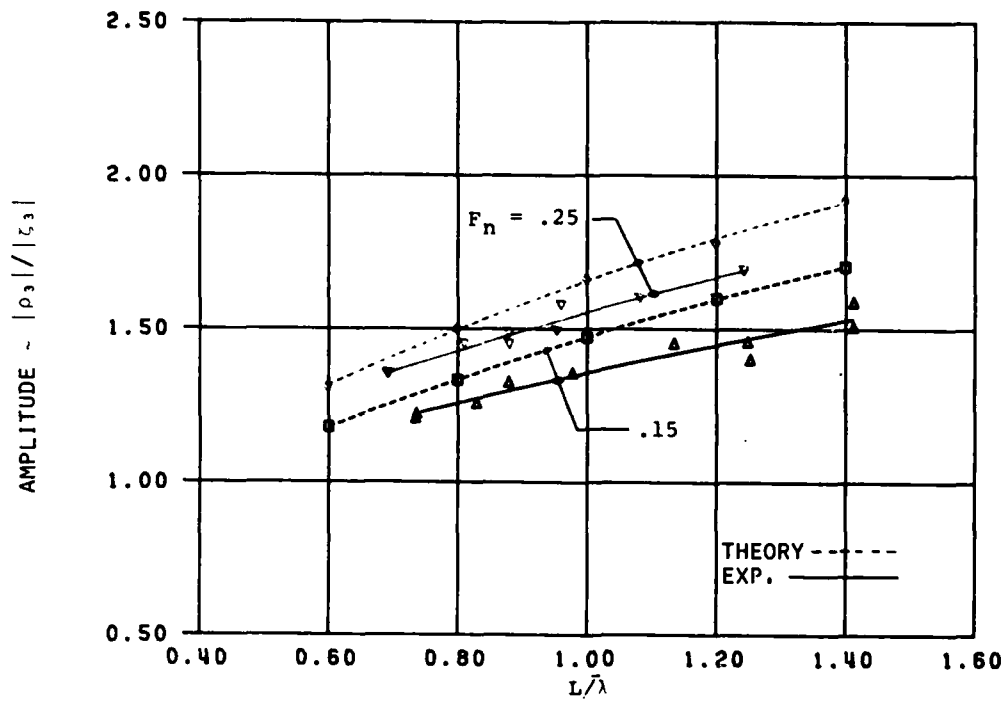


FIGURE 20  
RELATIVE MOTION AT STATION 3 DUE TO FORCED HEAVE



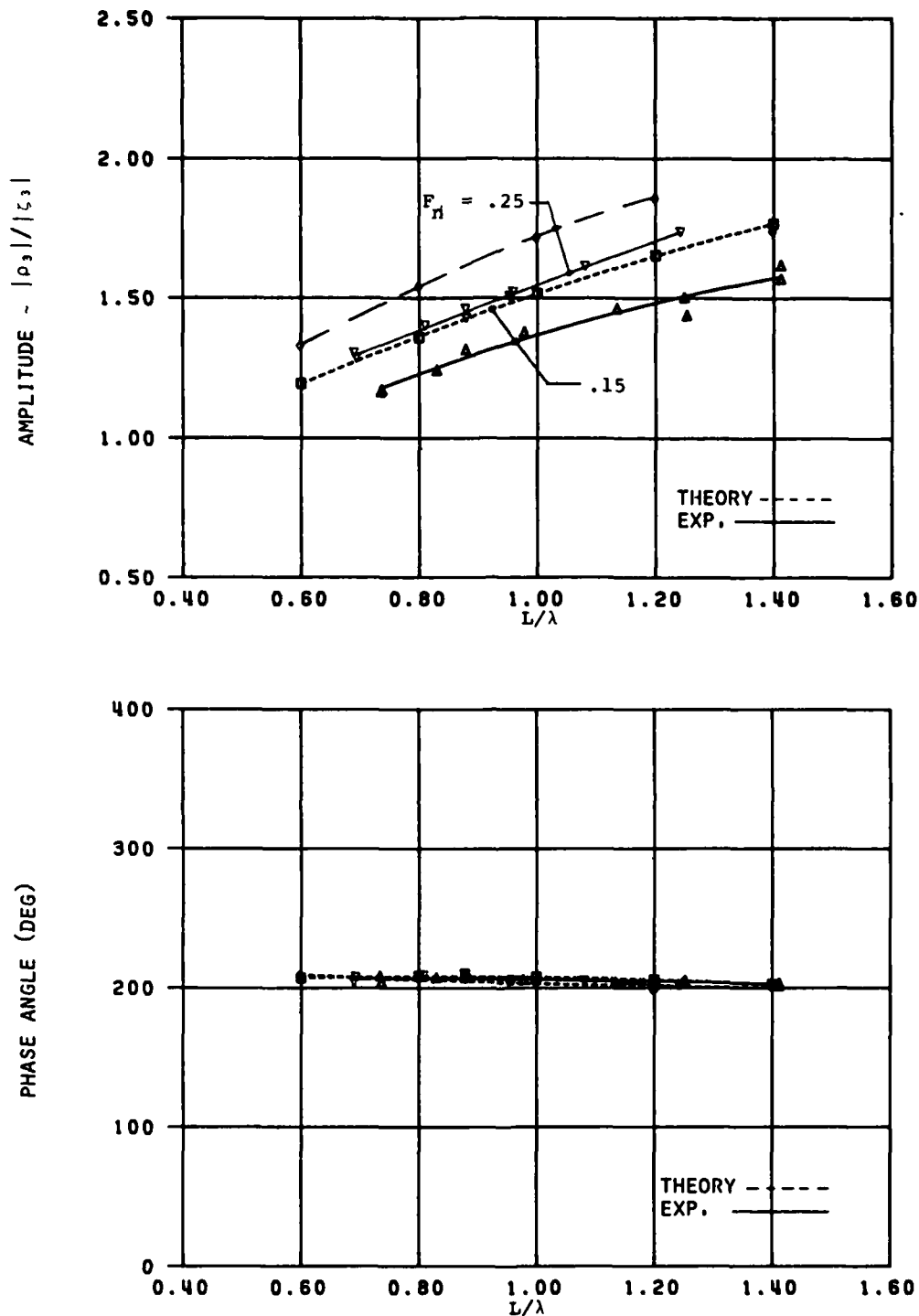


FIGURE 21  
RELATIVE MOTION AT STATION  $1/4$  DUE TO FORCED HEAVE

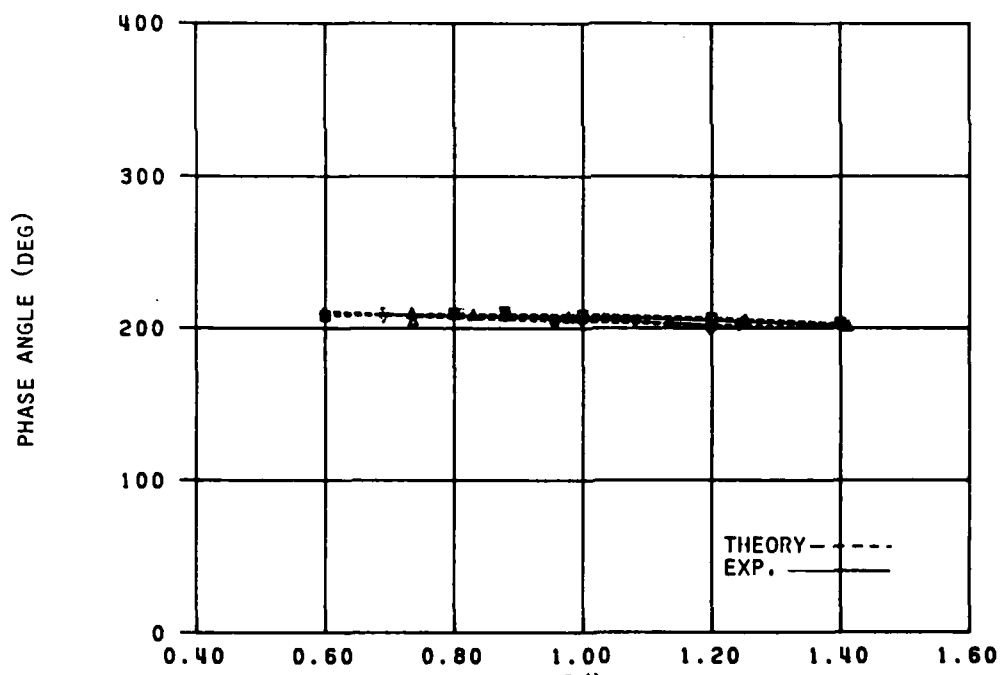
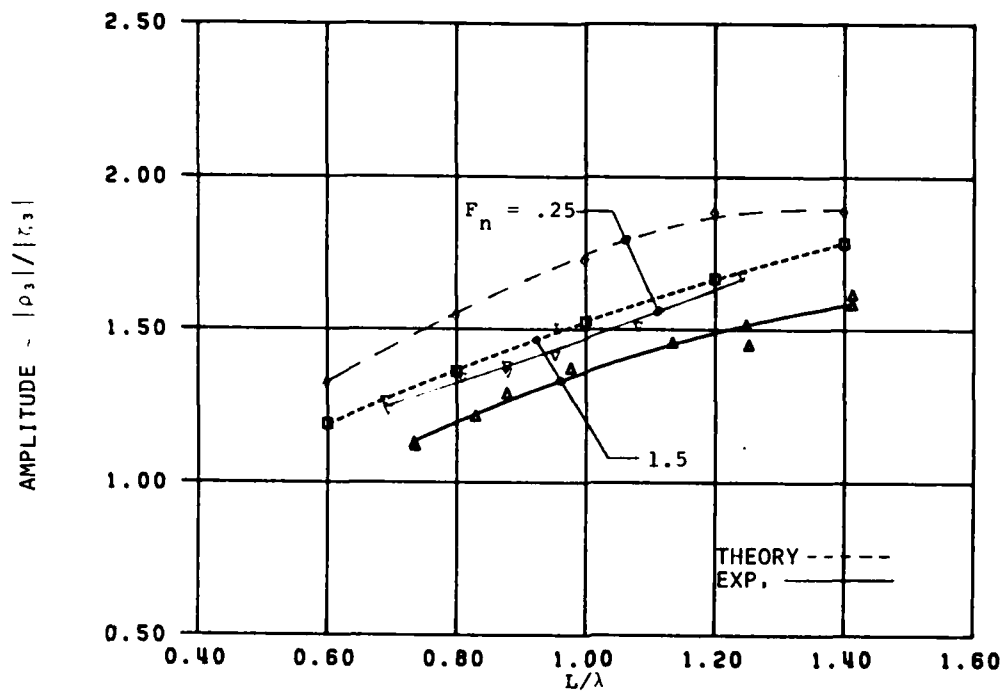


FIGURE 22  
RELATIVE MOTION AT STATION 5 DUE TO FORCED HEAVE

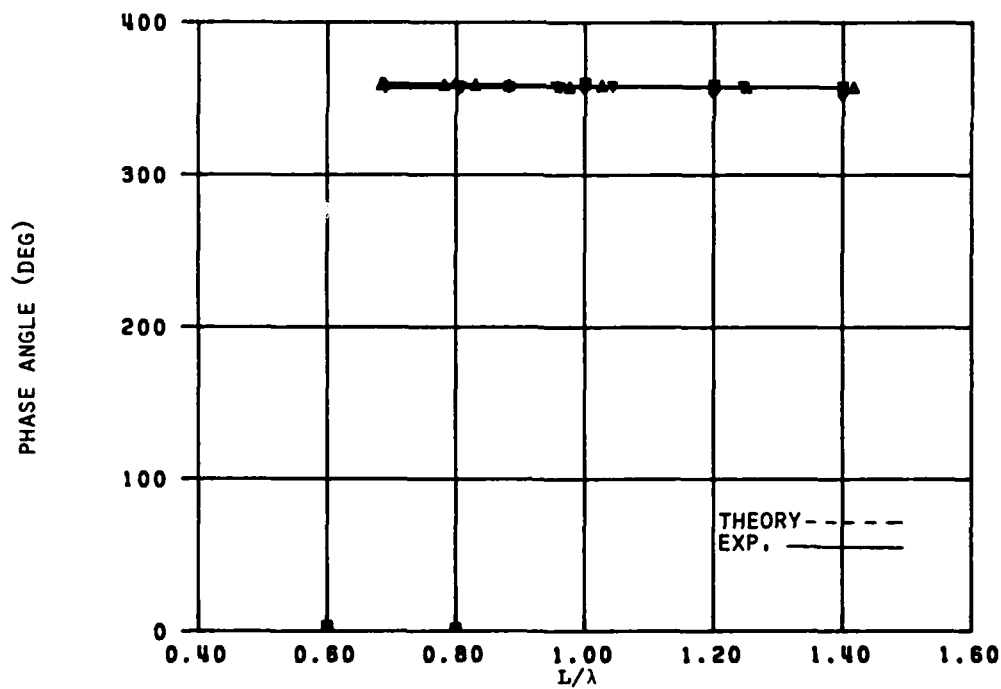
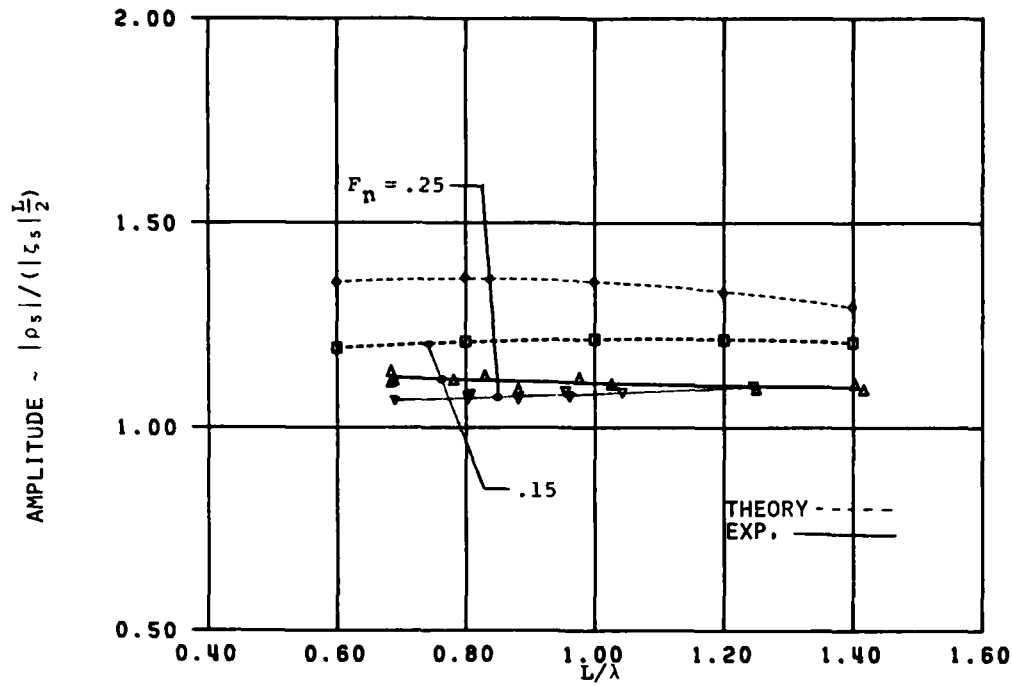


FIGURE 23

RELATIVE MOTION AT F.P. DUE TO FORCED PITCH

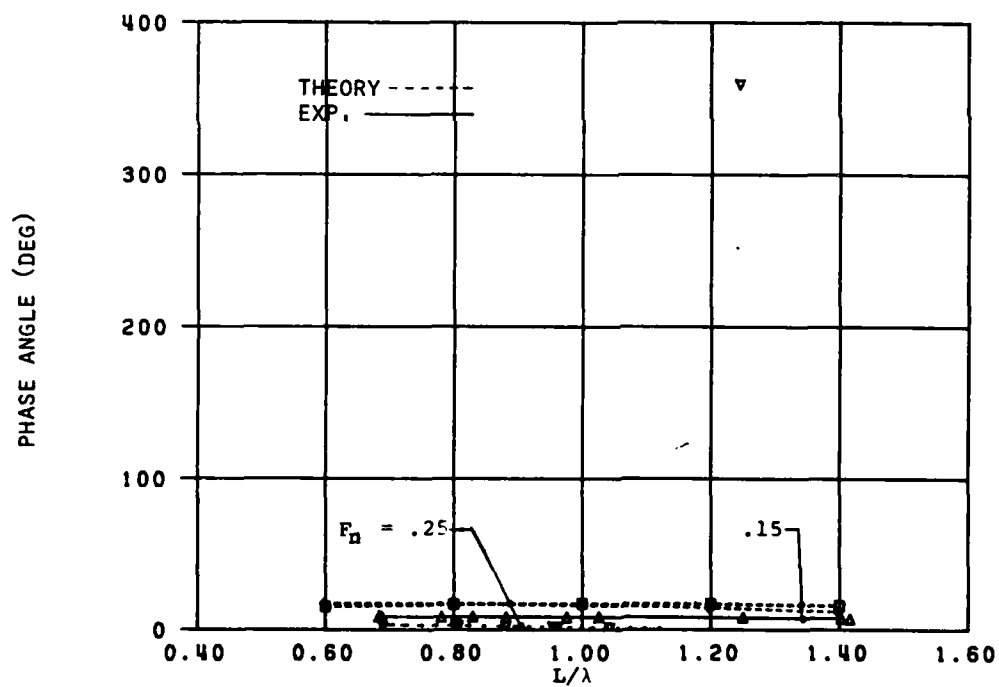
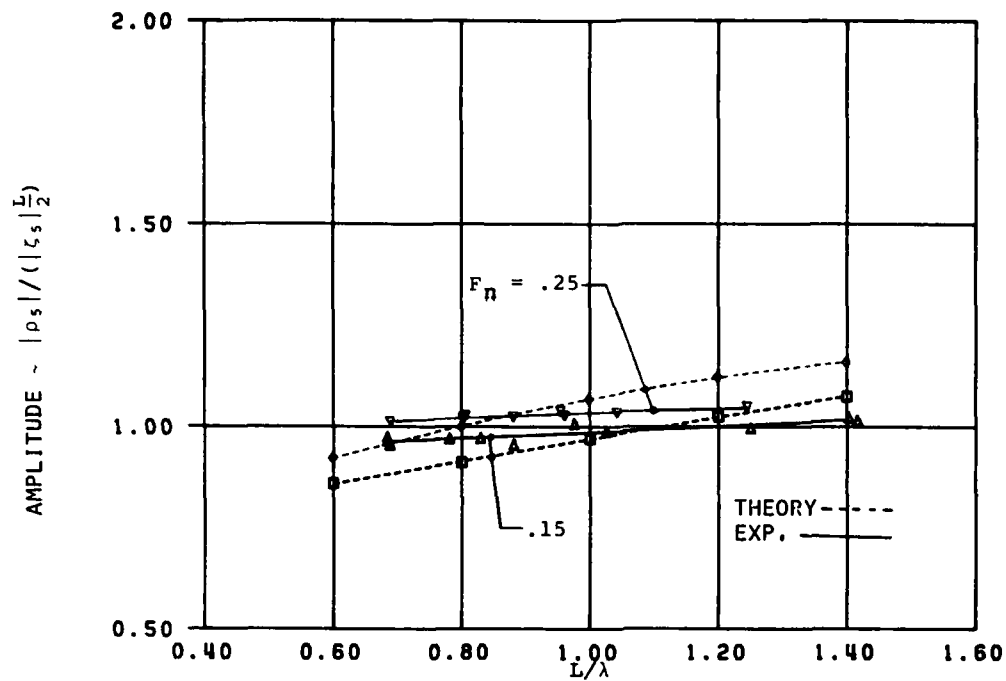


FIGURE 24  
RELATIVE MOTION AT STATION 1 DUE TO FORCED PITCH

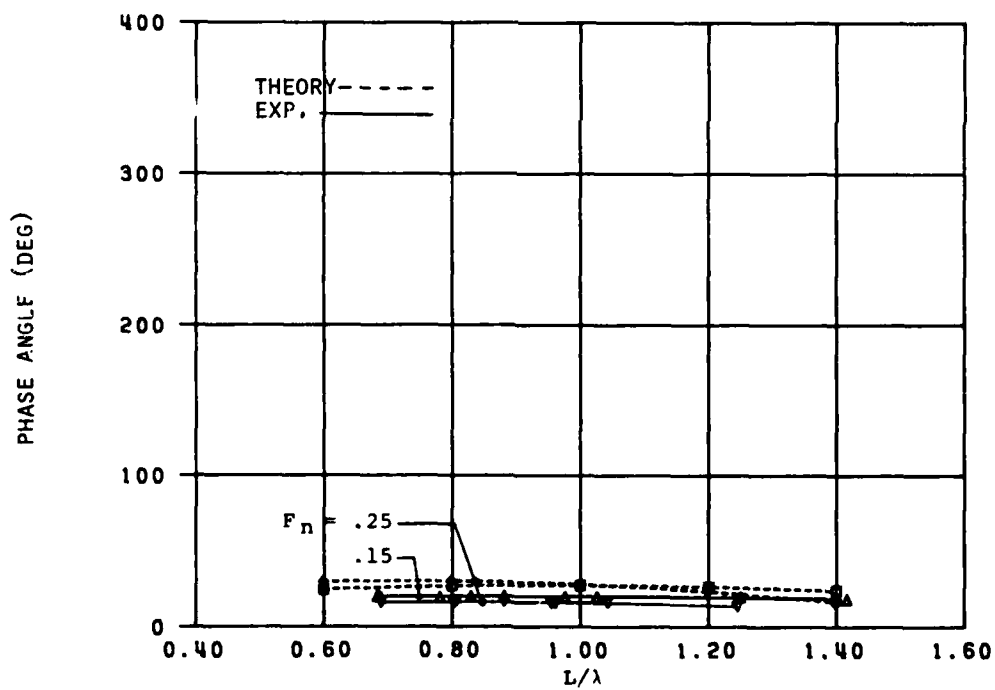
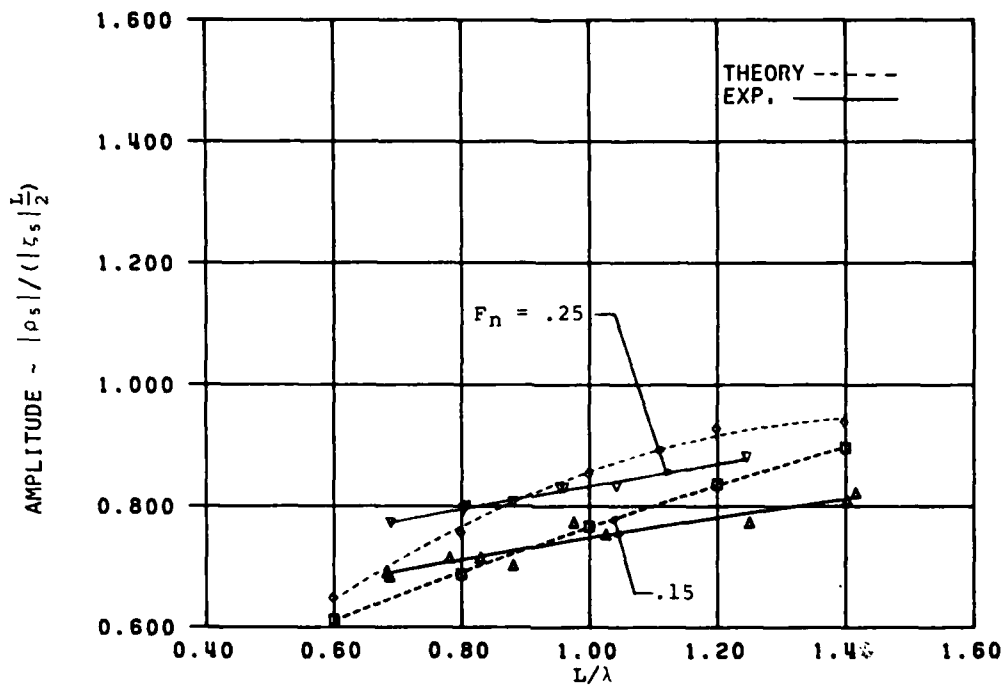


FIGURE 25  
RELATIVE MOTION AT STATION 2 DUE TO FORCED PITCH

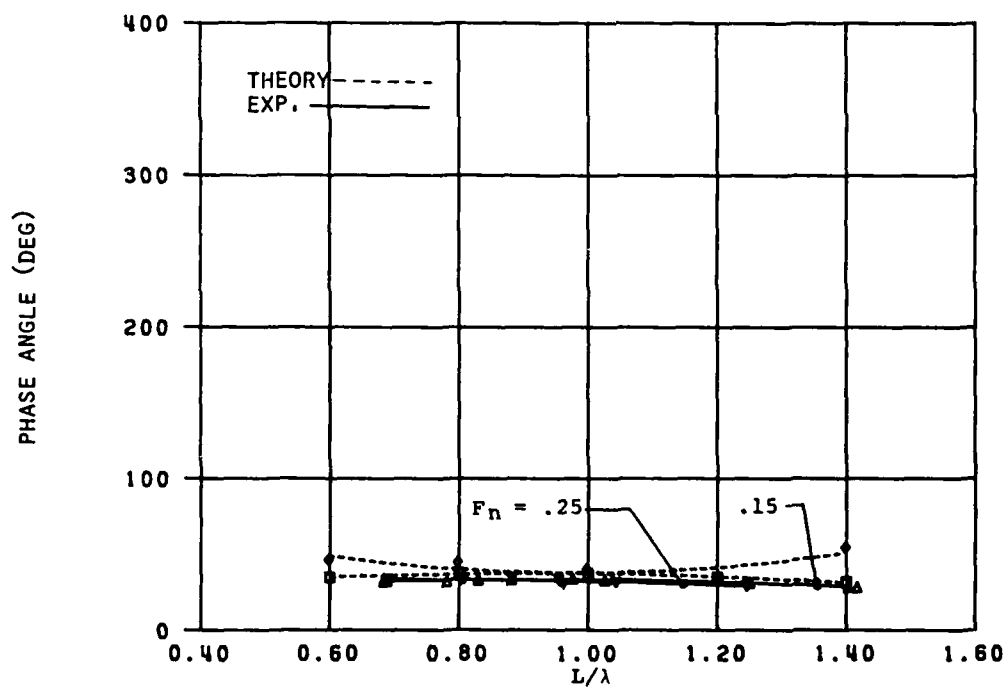
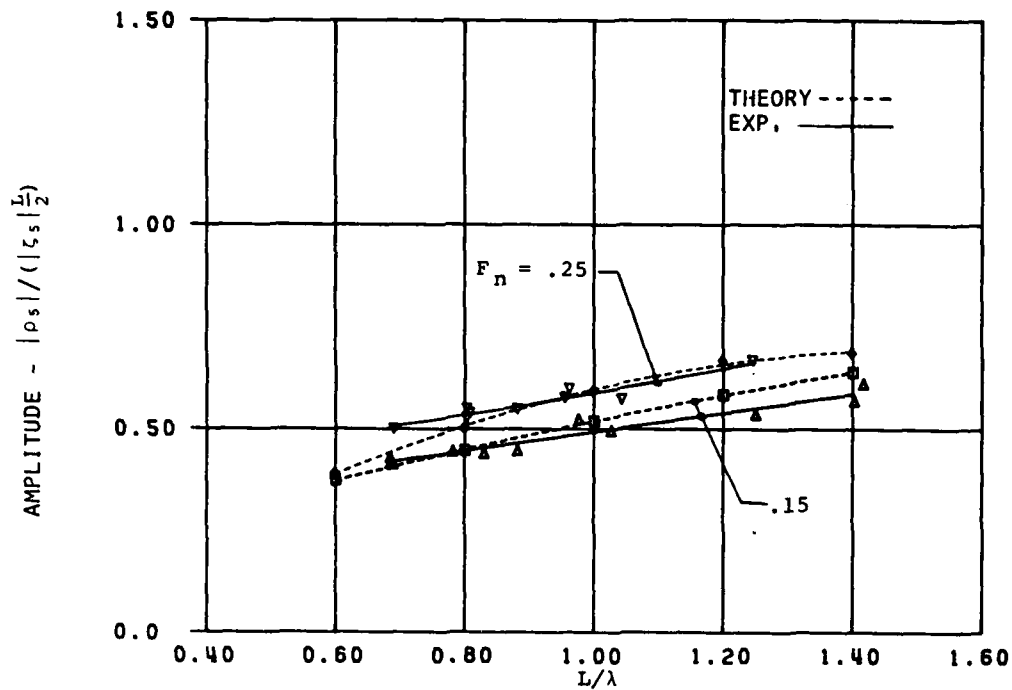


FIGURE 26  
RELATIVE MOTION AT STATION 3 DUE TO FORCED PITCH

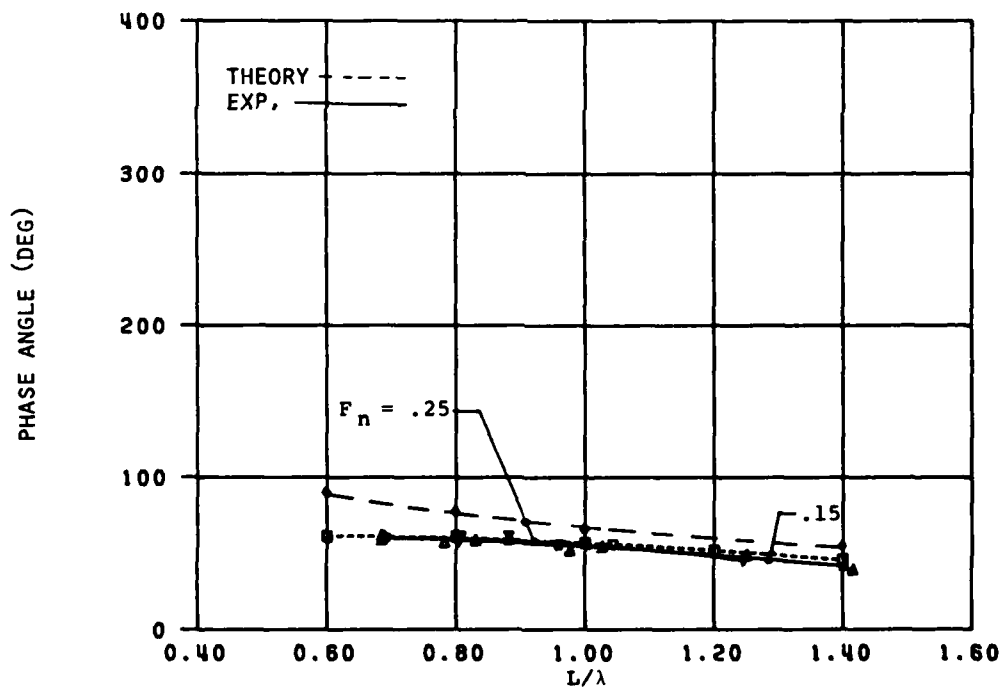
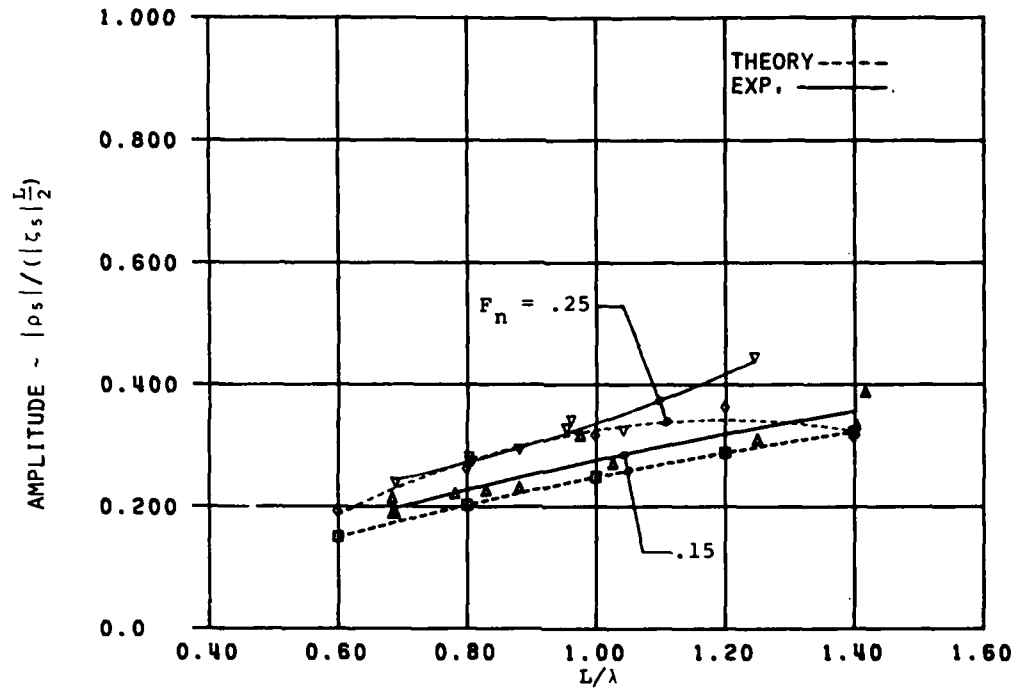


FIGURE 27  
RELATIVE MOTION AT STATION 4 DUE TO FORCED PITCH

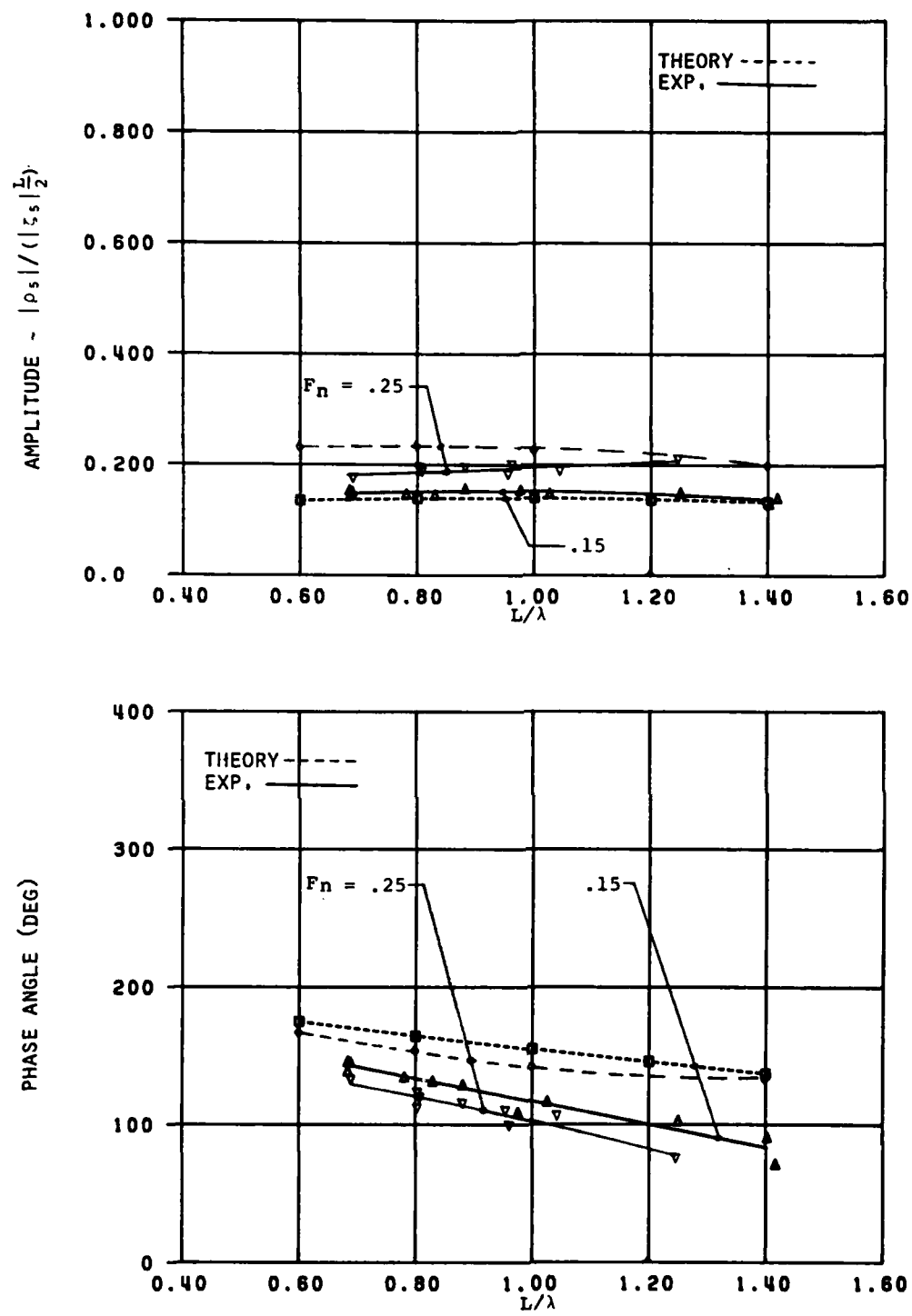


FIGURE 28  
RELATIVE MOTION AT STATION 5 DUE TO FORCED PITCH



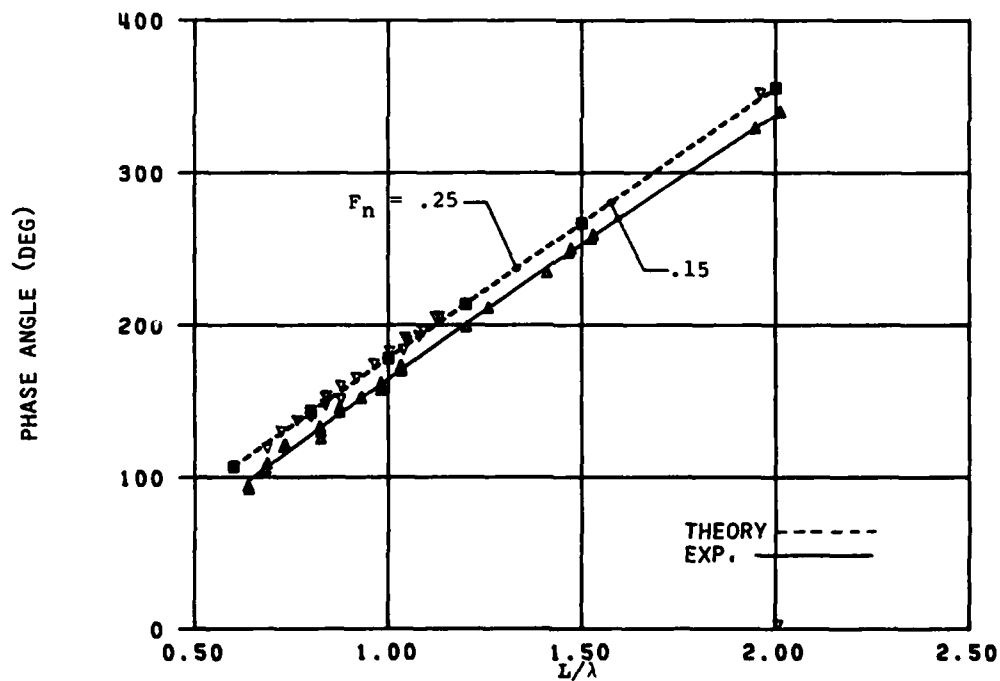
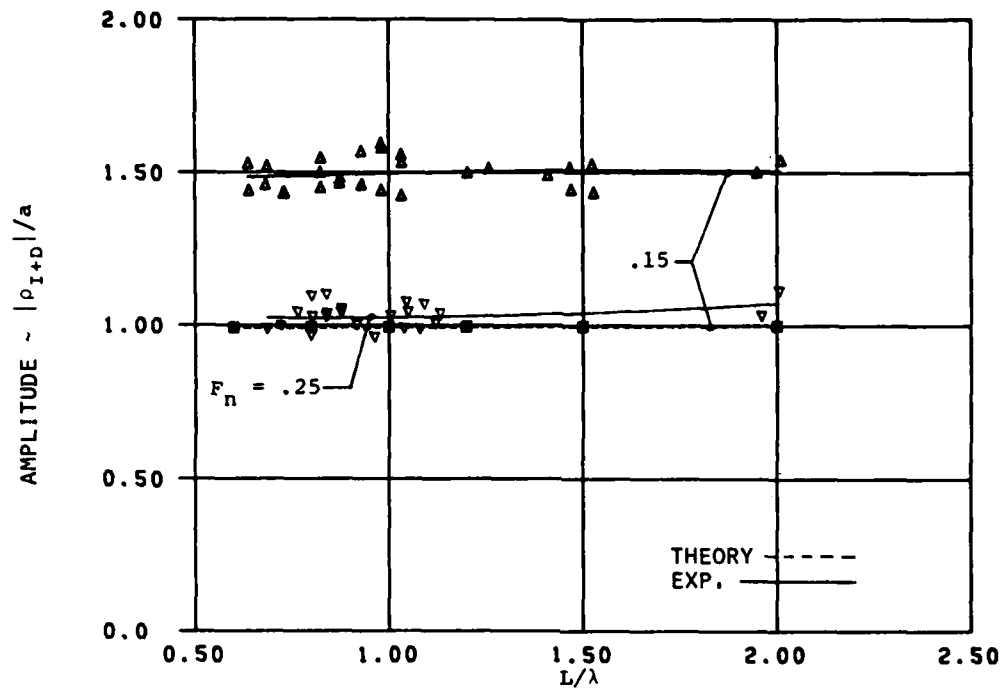


FIGURE 29  
RELATIVE MOTION AT F.P. DUE TO DIFFRACTION

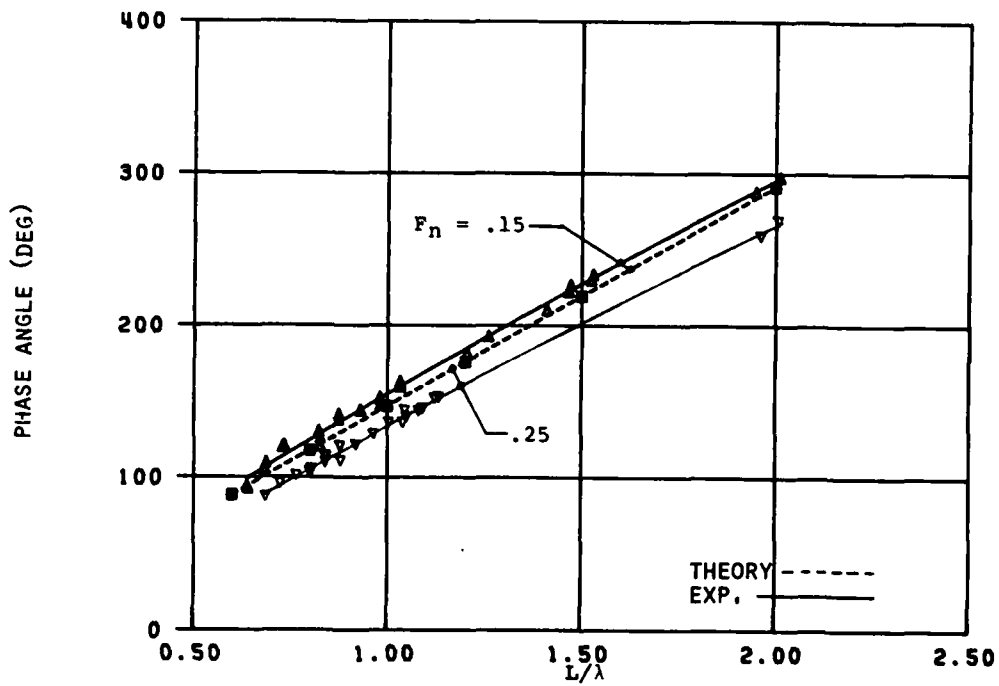
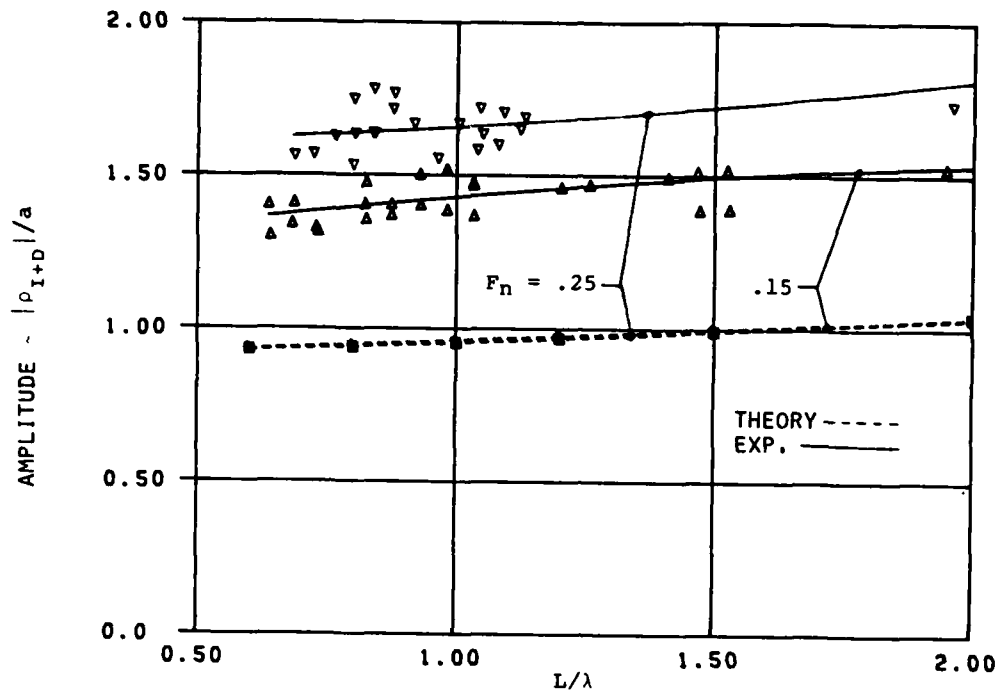


FIGURE 30  
RELATIVE MOTION AT STATION 1 DUE TO DIFFRACTION

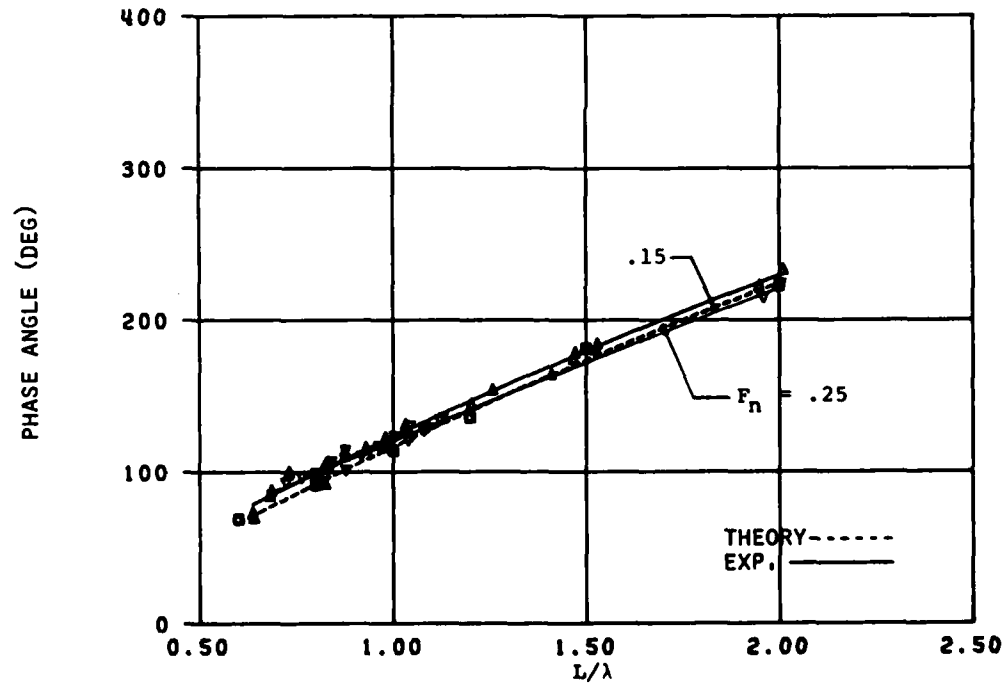
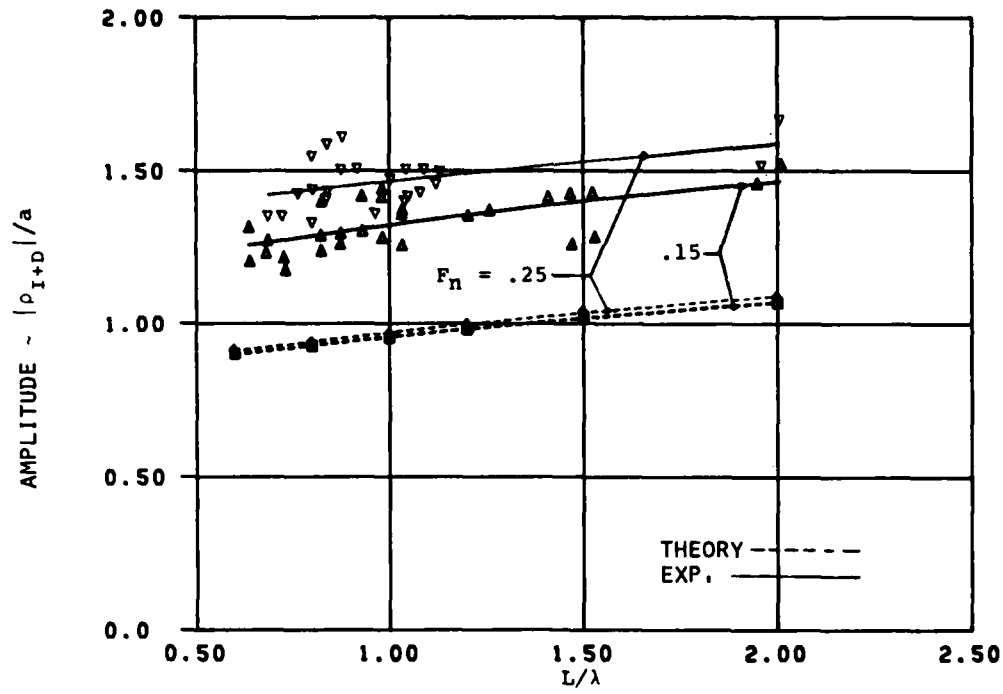


FIGURE 31  
RELATIVE MOTION AT STATION 2 DUE TO DIFFRACTION

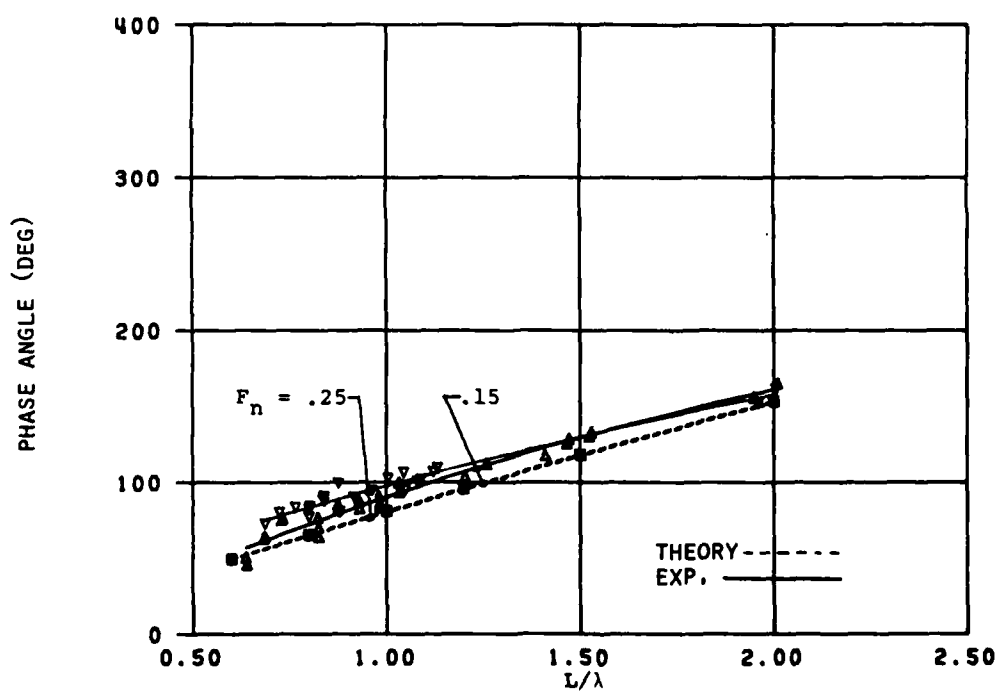
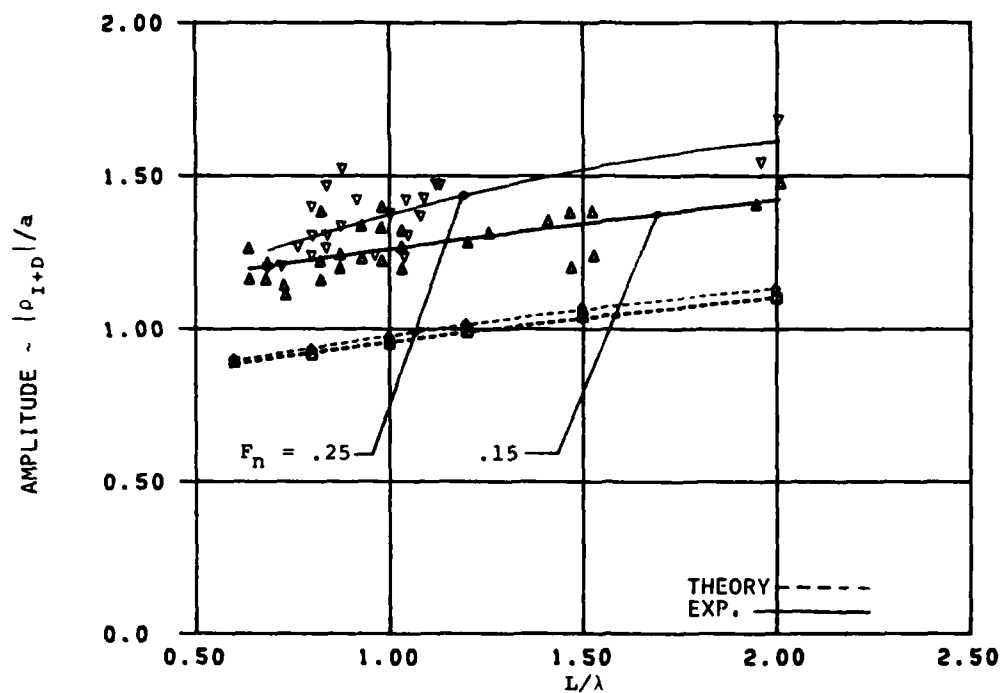


FIGURE 32  
RELATIVE MOTION AT STATION 3 DUE TO DIFFRACTION

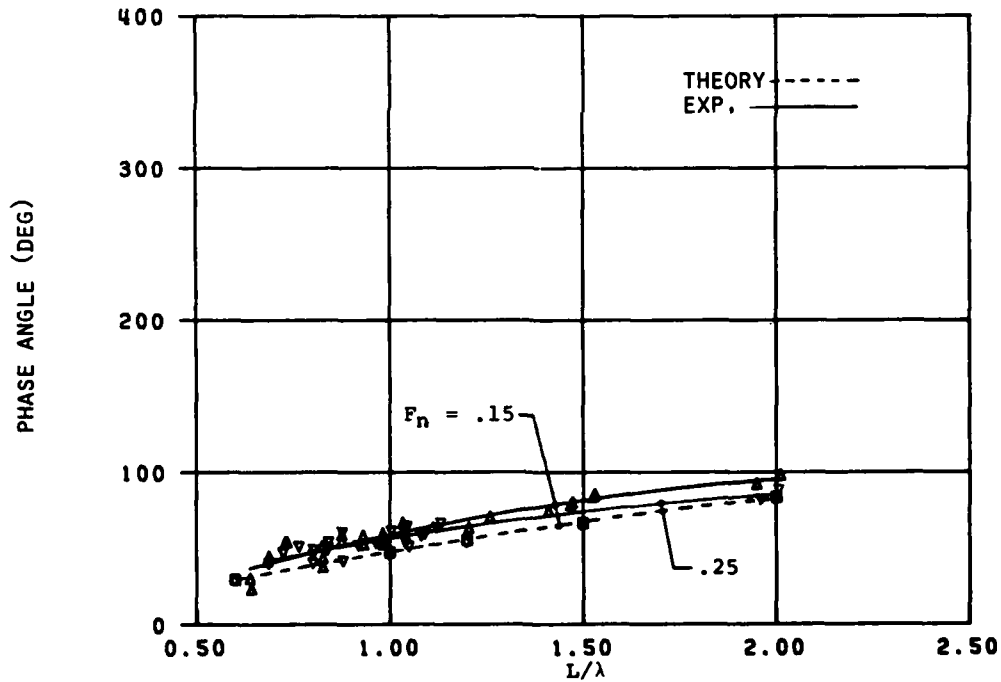
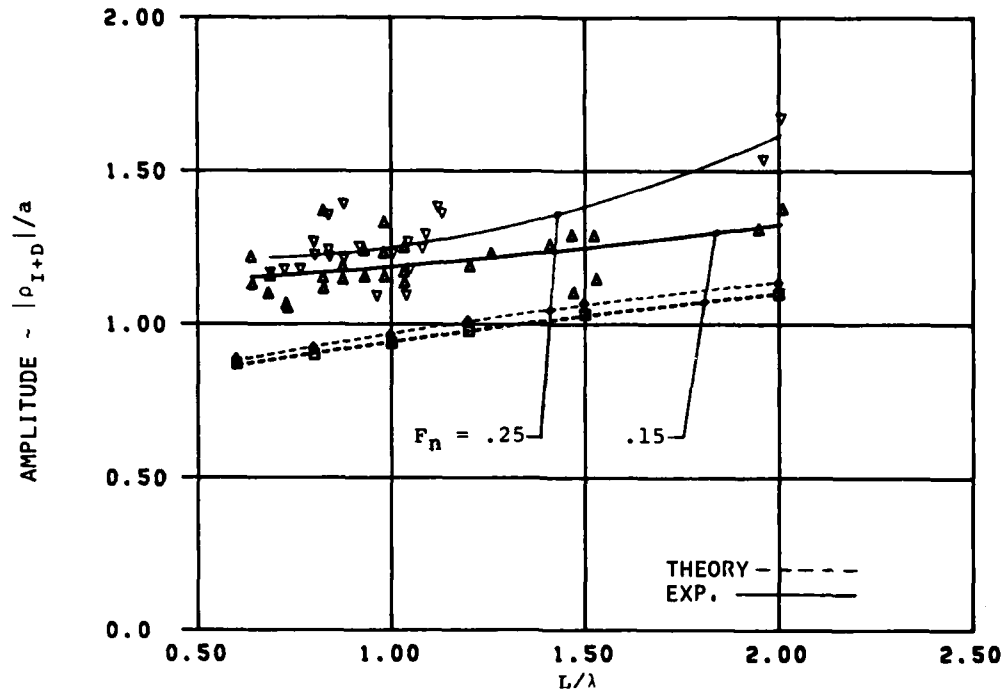


FIGURE 33  
RELATIVE MOTION AT STATION 4 DUE TO DIFFRACTION

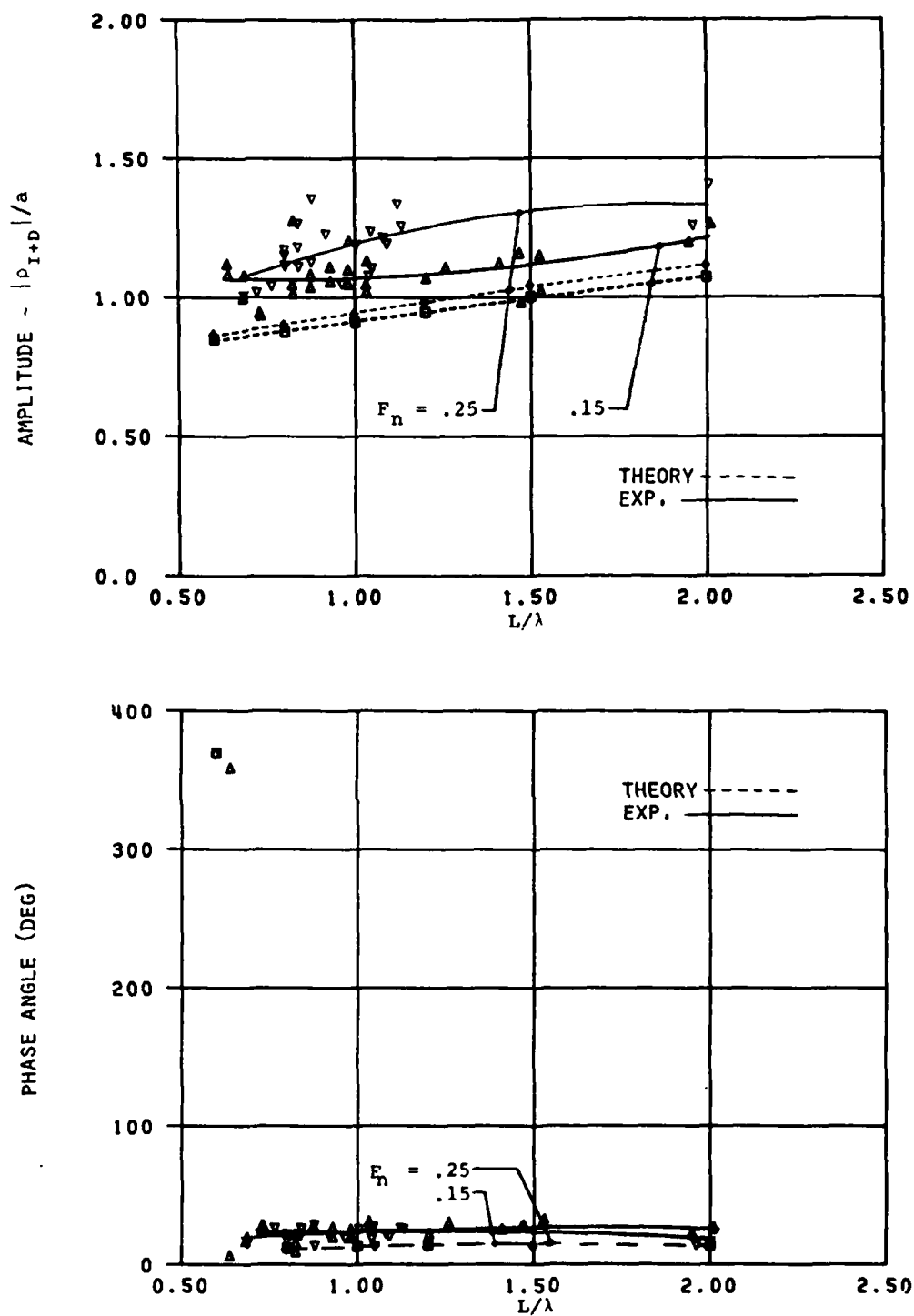


FIGURE 34  
RELATIVE MOTION AT STATION 5 DUE TO DIFFRACTION

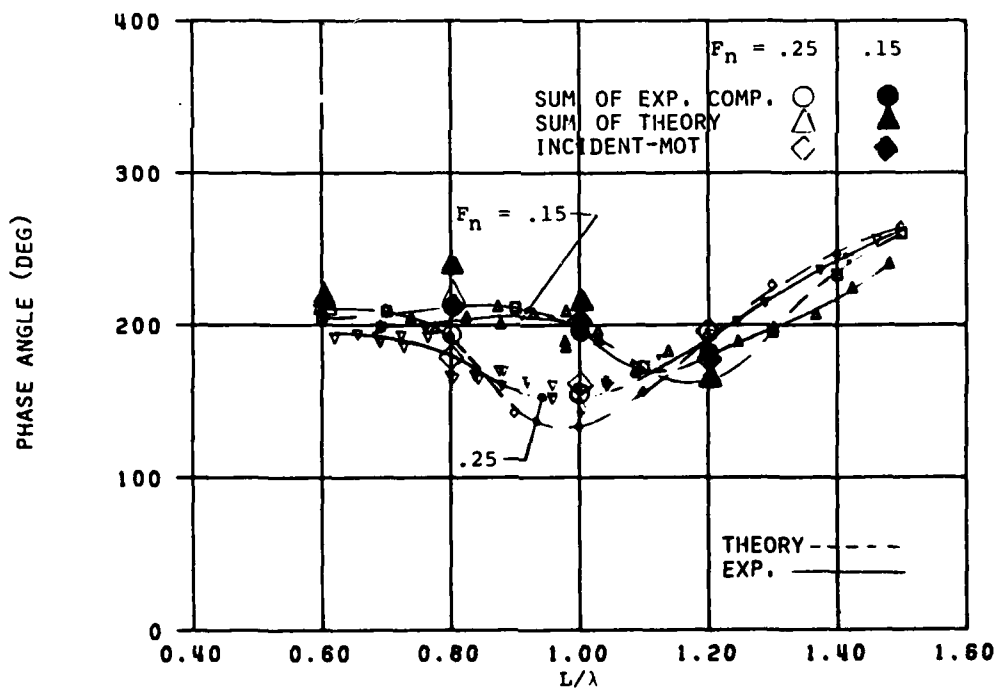
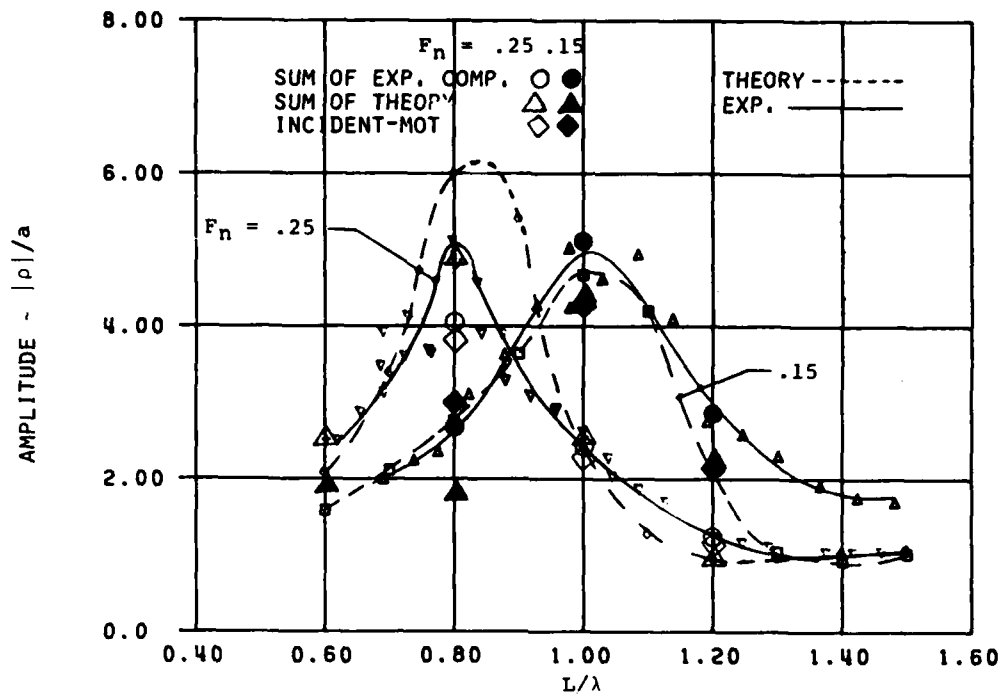


FIGURE 35  
TOTAL RELATIVE MOTION AT F.P.

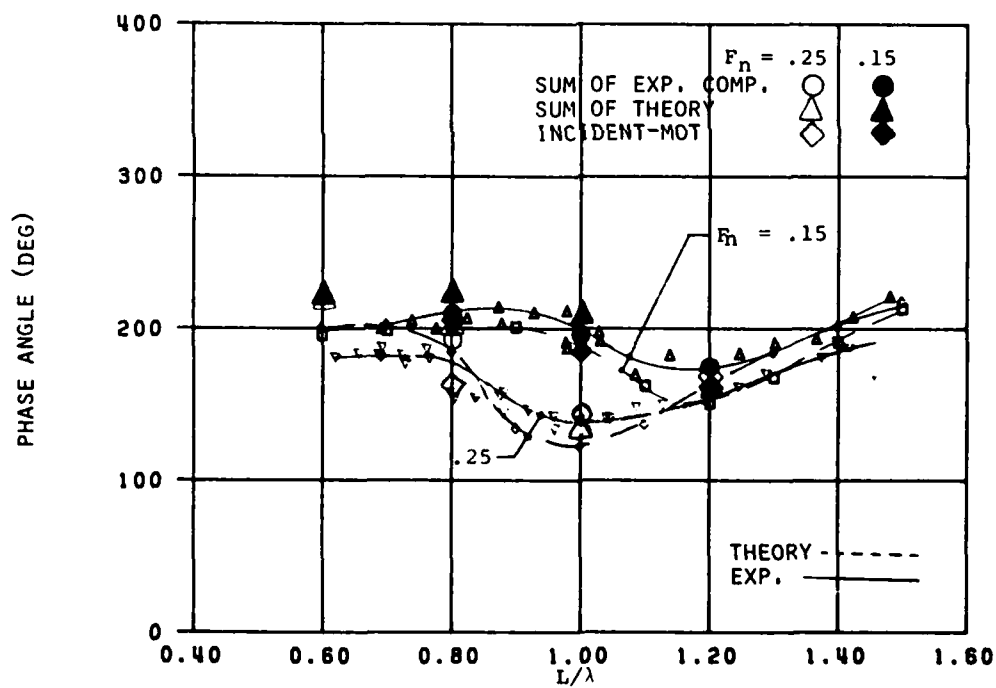
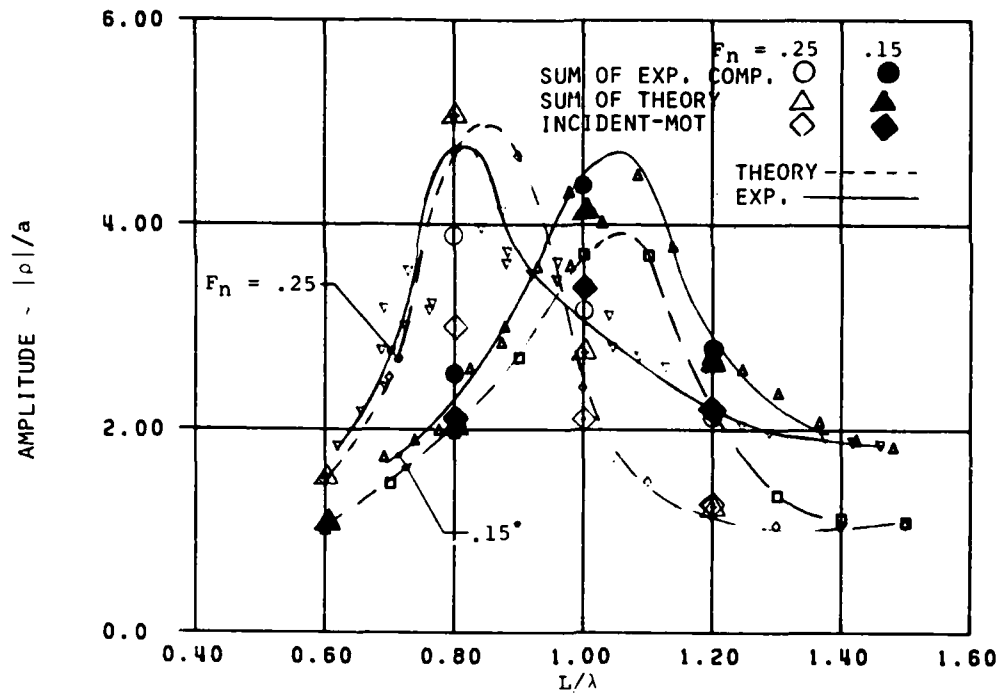


FIGURE 36  
TOTAL RELATIVE MOTION AT STATION 1



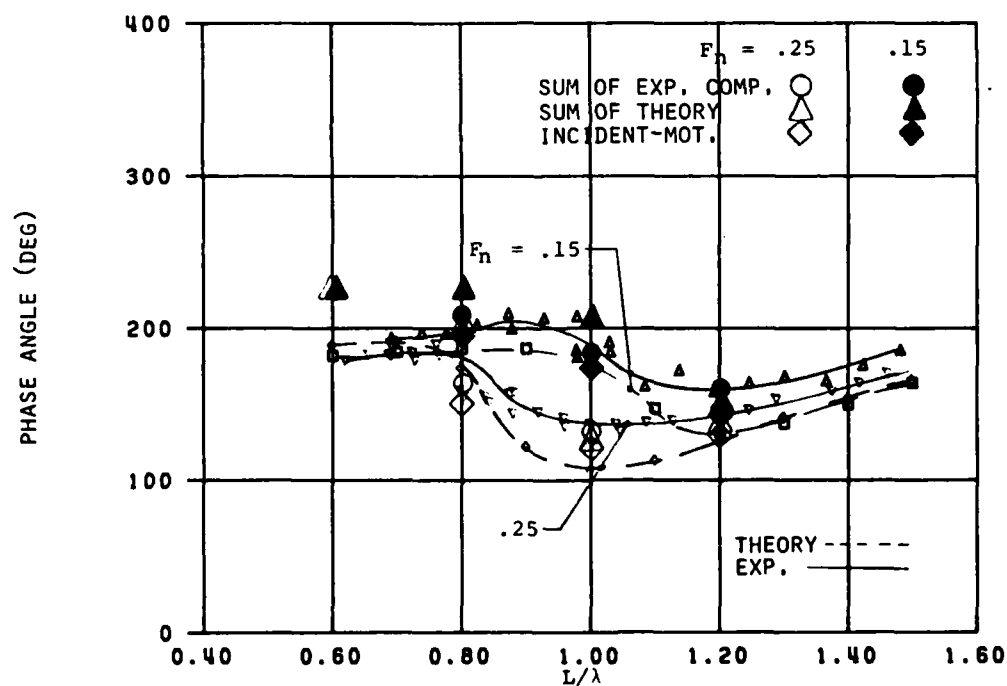
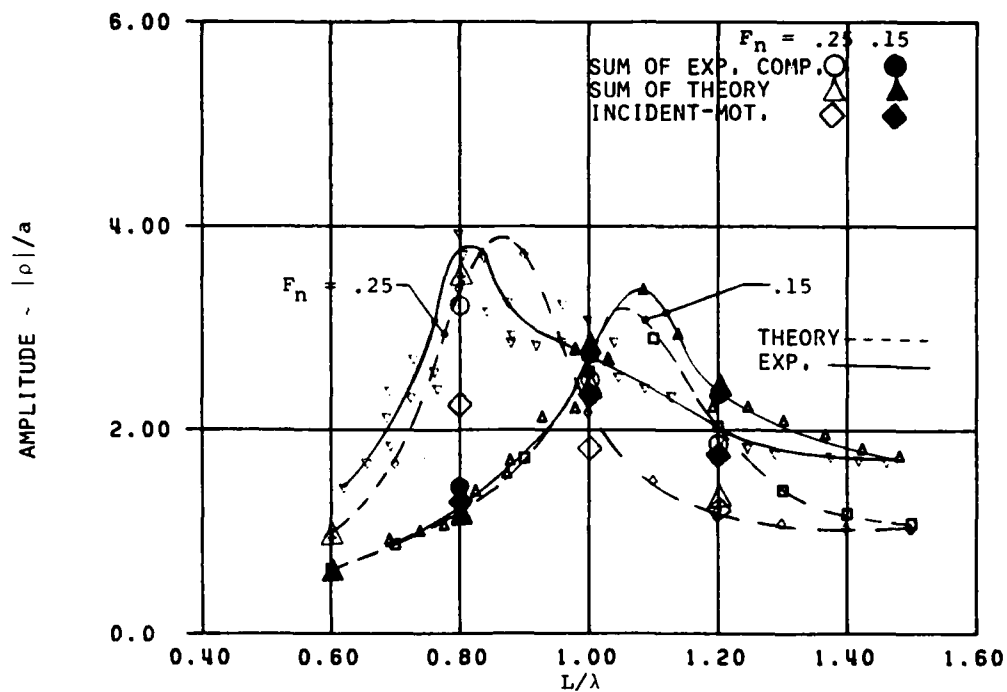


FIGURE 37

TOTAL RELATIVE MOTION AT STATION 2

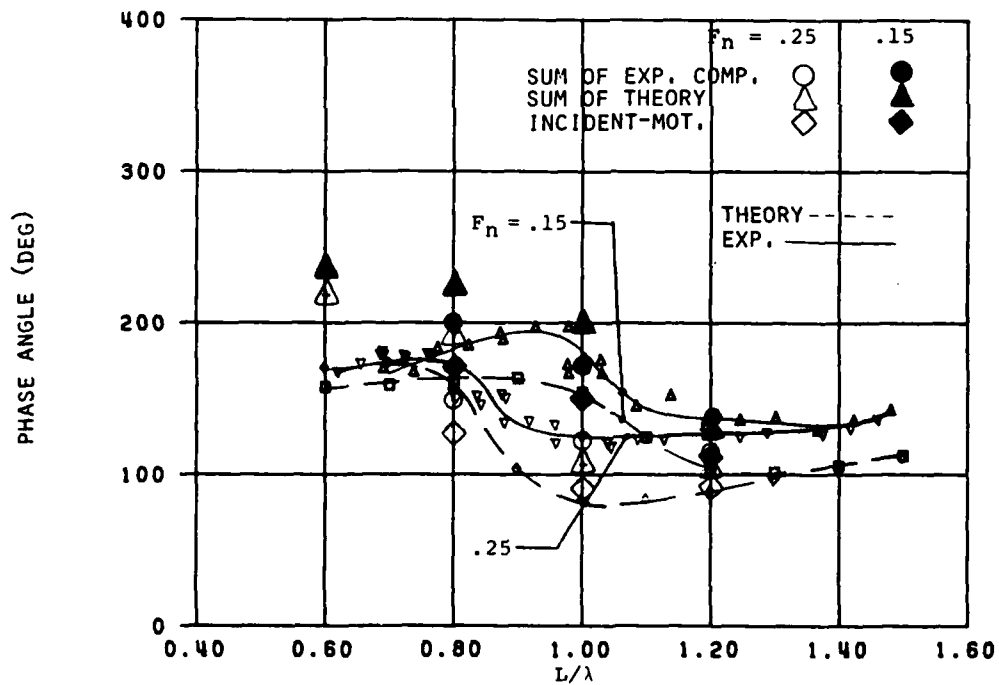
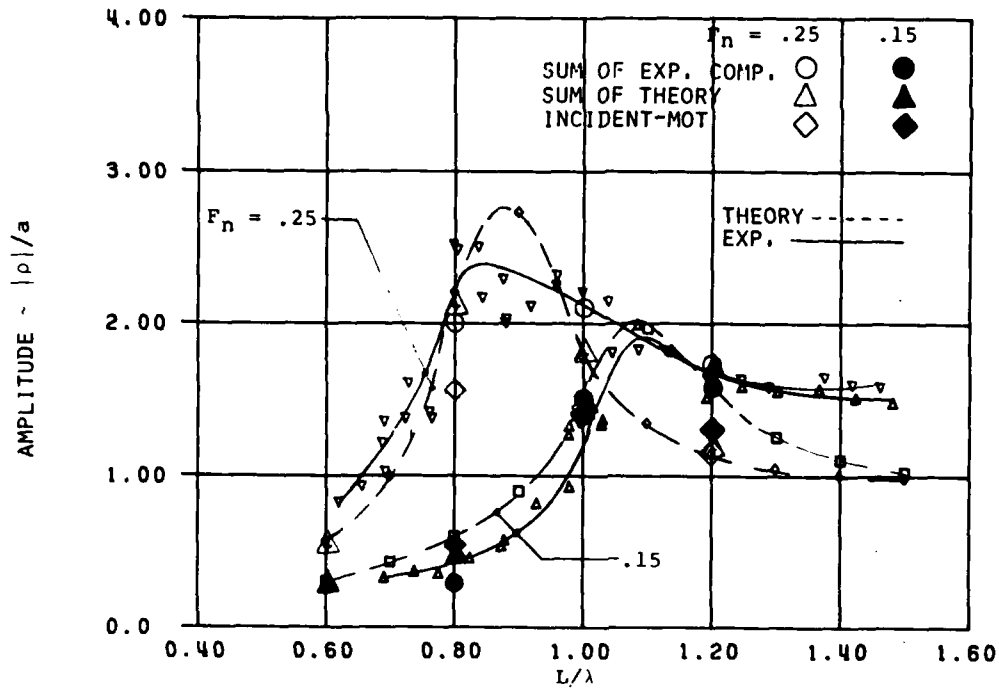


FIGURE 38  
TOTAL RELATIVE MOTION AT STATION 3

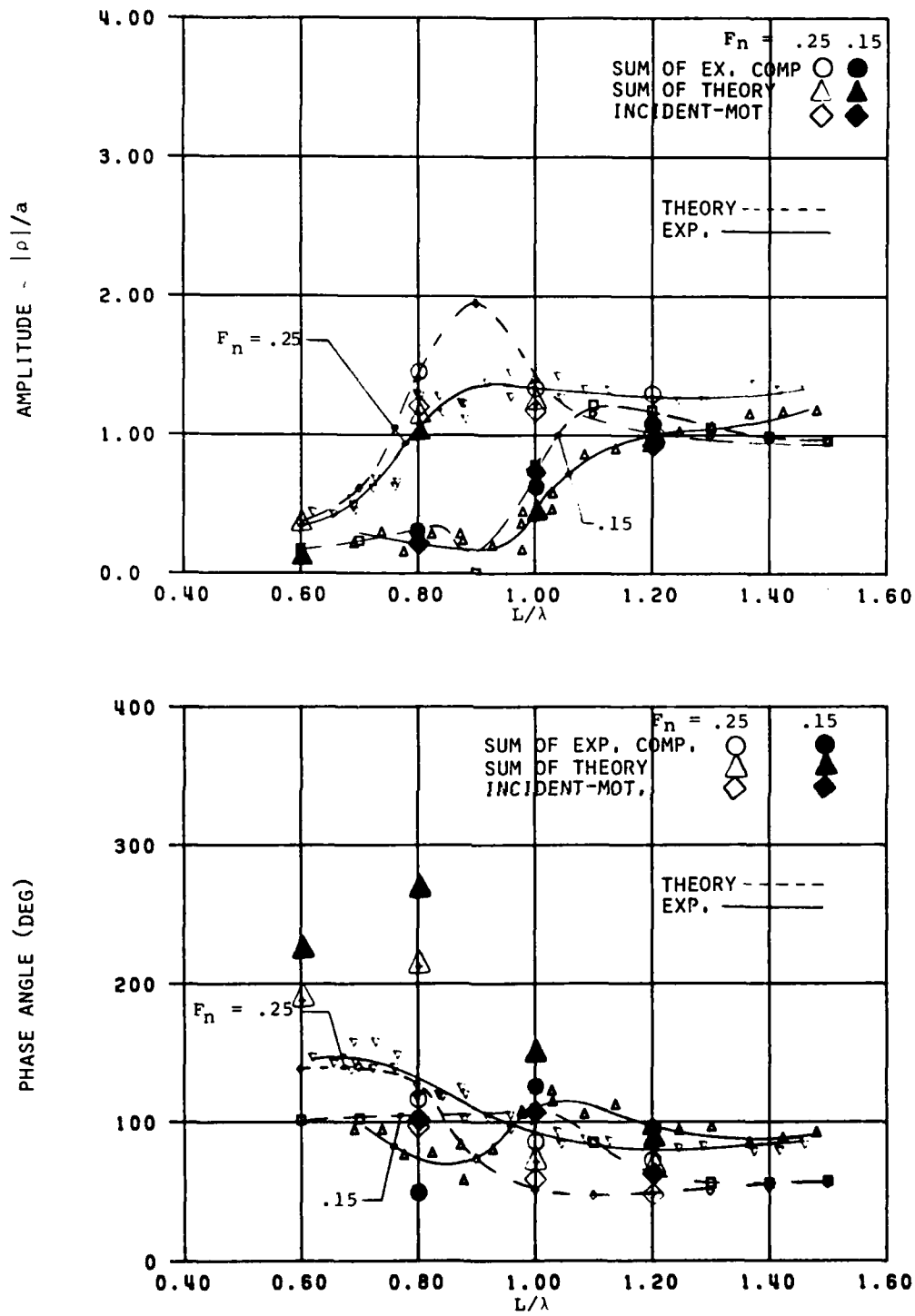


FIGURE 39  
TOTAL RELATIVE MOTION AT STATION 4

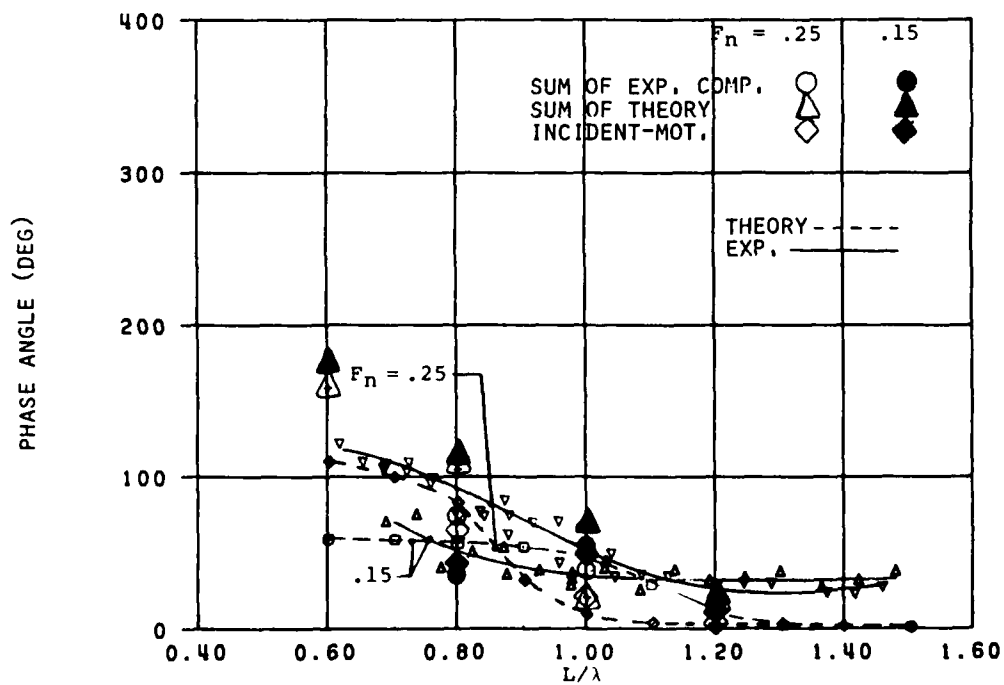
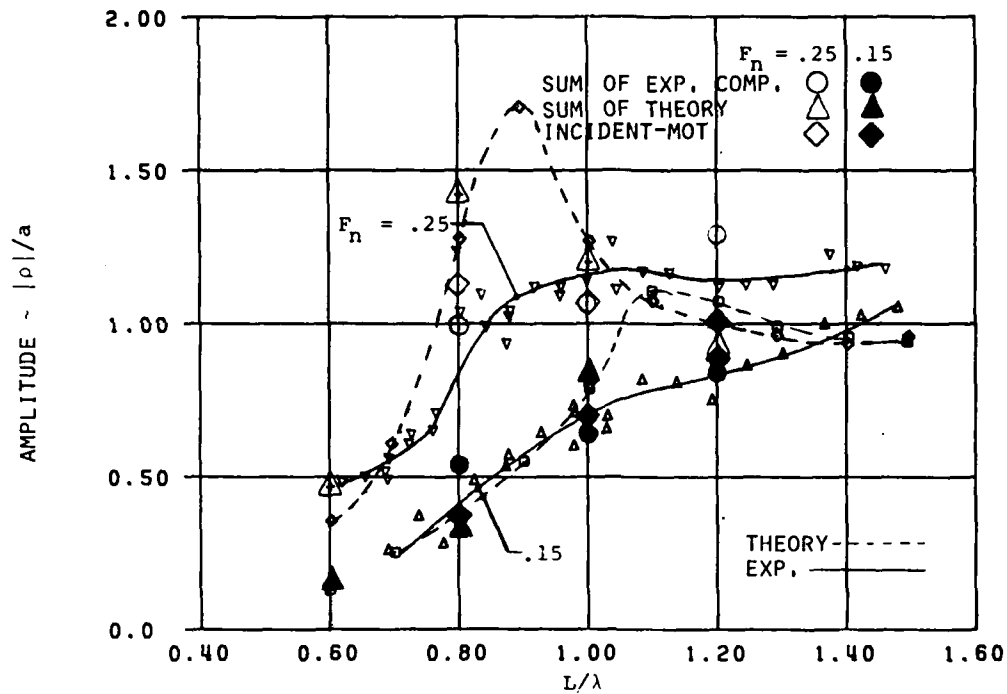


FIGURE 40  
TOTAL RELATIVE MOTION AT STATION 5

## Discussion

L.J. Doctors (University of South Wales)

Will Professor Beck please elaborate on the reasons for choosing a ship model with rectangular sections? It would seem that a model with parabolic sections, for example, would be more suitable for comparison with physical experiments, as flow separation would not then occur.

M. Matsuura and T. Takahashi (Mitsubishi Heavy Industries)

We are very much interested in this paper on the results of a rigorous investigation into the components of relative motion because we have performed relative motion measurements for two ship models and obtained a semiempirical estimation formula based on the strip method by Salvesen, Tuck, and Faltinsen. The tested models are one for a cargo ship ( $C_b = 0.71$ ) and another for a tanker ( $C_b = 0.82$ ). We carried out the measurements of diffraction component and total relative motion. As the result, we obtained empirical coefficients in the following formula:

$$\zeta = \alpha_I \cdot \zeta_I + \alpha_D \cdot \zeta_D + \alpha_R \cdot \zeta_R - \xi$$

where,  $\zeta$  : Total relative motion  
 $\zeta_I$  : Incident wave component  
 $\zeta_D$  : Diffraction wave component  
 $\zeta_R$  : Radiation wave component  
           ( $\zeta_D, \zeta_R$  are calculated by the strip method)  
 $\xi$  : Vertical motion of the point  
 $\alpha_I, \alpha_D, \alpha_R$  : empirical coefficients

The results for ship models are similar to the author's. However, we obtained a larger discrepancy for the diffraction component at the bow near portion than the author's. This is probably because of the effect of flare (especially for a cargo ship), and larger entrance angle (especially for a tanker).

The author did not deal with relative motion near the stern. However, it is also important in relation to propeller racing, etc. By our experiments, it was noticed the incident-wave component is reduced to about a half near the stern.

M. Ohkusu (Kyushu University)

The discrepancy between theoretical prediction and that measured for the wave elevation due to the forced heaving motion around midship, which is given as the difference between 1.0 and the curves in Figures 3 and 4, seems to be surprisingly large, 30 percent. We are convinced of the discrepancy close to the far end of the model considering the theory used is strip theory. In my experience, however, we do not have such a big discrepancy in the radiation wave elevation due to the heaving motion, although at the location half a ship length transversewise away from the hull surface, if we compute the wave elevation with the expression valid in outer region. In this respect I would like to propose that the author try to compute the wave elevation at midship even on the hull surface with the outer region expression for the radiation wave to compare with the measured ones.

### Author's Reply

R.F. Beck (University of Michigan)

To Prof. L. Doctors

The model with rectangular sections was originally chosen to conduct diffraction experiments. As you may know, Stoker gives the analytical solution for the wave diffracted by an infinite draft wedge. We were originally planning to develop an equivalent finite draft wedge solution and compare it with the diffracted waves in the bow region of our model. Subsequently, the test series was greatly expanded but the model had already been constructed. In hindsight, I would have preferred a model with slacker bilges on perhaps even a rounded-type bottom.

To Mr. M. Matsuura

I agree with Mr. Matsuura that relative motion at the stern is important. Unfortunately, the number of channels of data that we could record was limited so that we could not measure the relative motion along the entire length of the ship.

I am interested in hearing that Mr. Matsuura also found large discrepancies between theory and experiment for the diffraction-wave component. Because Mr. Matsuura did not give any values for the coefficients in his formula, my results and his cannot be compared directly.

To Prof. Ohkusu

I thank Professor Ohkusu for his suggestion. I do not know the reason for the large differences between theory and experiment for the heave-radiated wave component near midship. This is one of the results that needs more investigation. Perhaps it is the result of forward speed effects.

# Cavitation Inception Scaling by Roughness and Nuclei Generation

Jan H.J. van der Meulen  
Maritime Research Institute Netherlands

and

Ye Yuan-Pei  
China Ship Scientific Research Center

## ABSTRACT

Scale effects on cavitation inception are mainly caused by viscous and nuclei effects. This paper describes an experimental investigation of artificial means to eliminate these scale effects. The study concerns bubble cavitation inception on a NACA 4412 hydrofoil at an angle of attack of  $2^\circ$ . The tests comprise measurements of the pressure distribution, holographic recordings of (a) the boundary layer flow, (b) cavitation and (c) bubble populations, cavitation inception measurements and photographic recordings of cavitation. Two configurations are tested where bubbles are generated by a cavitating wire ahead of the foil. The influence of artificial roughness is studied for five different configurations. Without the application of roughness, the boundary layer is laminar till a midchord position where transition to turbulence occurs, whereas the type of cavitation observed is travelling bubble or transient spot cavitation. When roughness is applied, early transition to turbulence occurs but this has no effect on the inception or appearance of cavitation. However, when nuclei generation ahead of the foil is applied, or when the roughness elements on the foil are cavitating and thus seeding nuclei, the type of cavitation changes and attached bubble cavitation is observed. Besides, in one case the application of roughness is found to eliminate all scale effects.

## 1. INTRODUCTION

Modelling of cavitation on marine devices is strongly influenced by scale effects. Apart from effects caused by surface imperfections, these scale effects may be classified into nuclei effects and viscous effects. In recent years appreciable progress has been made in deriving prediction methods for the scaling of limited cavitation (Huang and Peterson (1976), Billet and Holl (1981)). Another approach in solving scaling problems is to eliminate scale effects by introducing artificial means in the experimental procedure. Albrecht and Björheden (1975) reported on the use of micro air bubble generators in a free surface cavitation tunnel and attained realistic conditions for the inception and extent

of cavitation on model propellers. Noordzij (1976) introduced electrolysis in the NSMB depressurized towing tank and was able to restore the reproducibility of cavitation patterns on model propellers. The above methods were both aimed at eliminating nuclei effects. A method originally intended to eliminate viscous effects was introduced by Kuiper (1978). The method consists of boundary layer tripping by the application of sand roughness on the leading edge of propeller blades. Visualization of the boundary layer by using a paint technique showed the method to be quite effective in producing a turbulent boundary layer on the propeller blades. Later on, it was observed (Kuiper (1981, 1982a)) that the roughness elements were often cavitating and, apparently, generating nuclei. In this way the application of sand roughness would be able of eliminating both viscous and nuclei effects. Kuiper (1982b) also discussed the risks of applying sand roughness in terms of leading edge pressure distribution effects and cavitation inception effects on the roughness elements proper.

The artificial means mentioned above seem promising tools in eliminating or reducing certain scale effects on cavitation. However, the lack of reliable well-documented full scale cavitation observations complicates the final achievement of "realistic" cavitation patterns on model scale. It is therefore important that the basic mechanisms induced by artificial means are well understood and, if possible, quantified. Studies aimed at these objectives can best be made by using less complicated models such as axisymmetric headforms or hydrofoils. For such models accurate data on the boundary layer flow behaviour and pressure distribution are relatively easy to obtain. A first approach using distributed roughness on a Schiebe headform was made by Billet and Holl (1980). The results showed that it was possible to eliminate scale effects for travelling bubble cavitation by applying distributed roughness. The mechanism involved in this process was not fully understood, but it was suspected that the roughness produced micro-bubbles.

The main objective of the present paper is to provide experimental evidence in explaining some basic mechanisms involved in the application of nuclei generation or leading edge roughness for the scaling of bubble cavitation inception. The tests were made with a NACA 4412 hydrofoil at an angle of attack of  $2^\circ$ . A full description of the viscous flow and cavitation behaviour of this hydrofoil in a wide range of angles of attack was presented in an earlier paper by Van der Meulen (1980) at the 13th ONR Symposium. Additional tests were made to obtain the pressure distribution for the original hydrofoil in the test section environment.

## 2. EXPERIMENTAL METHODS

### Test Facility and Holographic Method

The facility used is the high speed water tunnel of the Netherlands Ship Model Basin. The test section had a 40 mm x 80 mm rectangular cross section with a maximum attainable water speed of 40 m/s. In-line holography was used to obtain detailed information on the cavity type and



boundary layer flow on the hydrofoil and to measure the nuclei (bubble) population. Visualization of the boundary layer was effected by injecting small amounts of a 5 percent sodium chloride solution into the flow through a small hole (dia 0.21 mm) located at the leading edge of the foil. A schematic diagram of the in-line holographic system is shown in Figure 1. A ruby laser ( $\lambda = 694 \text{ nm}$ ) with a 30 mJ single mode pulse duration of 30 ns was used as a light source. Agfa-Gevaert 8E75 HD Holotest plates with a resolution of over 5000 lines/mm were used as a recording medium. In the reconstruction set-up a 2mW HeNe laser ( $\lambda = 633 \text{ nm}$ ) served as a light source. Further details on the application of in-line holography for the visualization of boundary layers and cavitation phenomena on axisymmetric headforms and hydrofoils are given by Van der Meulen (1976, 1978, 1980) and Van der Meulen et al. (1982).

#### Test Models and Configurations

Most tests were made with the original NACA 4412 hydrofoil used in earlier experiments (Van der Meulen (1980)). The chord length of this foil is 70 mm and the span 40 mm. The foil is slightly tapered to enable flow visualization. Thus, the chord length and the maximum foil thickness at the side walls are reduced by 3 percent. In the discussion on the paper by Van der Meulen (1980), questions were raised on possible deviations from the two-dimensionality of the flow caused by the tapering. Therefore, an additional two-dimensional NACA 4412 hydrofoil with a chord length of 70 mm was made and tested. To obtain data on the pressure distribution, a third NACA 4412 hydrofoil, instrumented with pressure taps, was manufactured. This foil is a replica of the original tapered foil. The foils were all made of brass and the foil surfaces were polished. For the original foil the mean roughness height was measured and found to be  $0.18 \mu\text{m}$ .

Several configurations were tested for which either nuclei generation or roughness was applied. These configurations are all related to the original tapered hydrofoil.

Nuclei generation was effected by a cavitating wire spanning the full height of the test section (80 mm) and positioned in the vertical centerplane, ahead of the hydrofoil. Its distance to the leading edge of the foil amounted 22 mm. Some initial tests with a 1 mm dia stainless steel wire were made at a water speed of 8 m/s, but the wire broke within 30 minutes. The use of nylon wires solved this problem. In the final tests two configurations were used: a 1 mm dia nylon wire and a 0.25 mm dia nylon wire. At a water speed of 10 m/s, the maximum deflection of the wires was about 2 mm, whereas at 20 m/s a maximum deflection of about 8 mm was observed.

Five configurations were tested where roughness was applied. In the first configuration a distributed roughness was obtained by spraying a thin layer of paint on the entire foil surface. The mean roughness height was found to be  $0.65 \mu\text{m}$  and the maximum roughness height 3-4  $\mu\text{m}$ . In the second configuration a trip wire with a diameter of 50  $\mu\text{m}$  was glued to the hydrofoil nose. The position of the wire in chordwise direction was  $x/c = 0.015$ . The wire extended over a length of 10 mm in

spanwise direction in the central part of the foil. In the third configuration a trip consisting of sand grain roughness was applied to the hydrofoil nose. The size of the sand grains was  $30\text{ }\mu\text{m}$ , but the total height of the roughness amounted to  $60\text{ }\mu\text{m}$ . The sand roughness covered a length in chordwise direction of  $x/c = 0.0054 - 0.0100$ . The trip extended over a length of  $10\text{ mm}$  in spanwise direction in the central part of the foil. In the fourth configuration  $30\text{ }\mu\text{m}$  sand grain roughness was applied to both the upper and lower part of the hydrofoil nose. The sand roughness covered a length in chordwise direction of  $x/c = 0-0.050$  on the lower part of the nose (pressure side) and  $x/c = 0-0.015$  on the

TABLE 1. Designation of Configurations Tested

Configuration	Description
I	original, tapered hydrofoil
II	two-dimensional hydrofoil
III	1 mm dia wire ahead of foil
IV	0.25 mm dia wire ahead of foil
V	distributed roughness
VI	trip wire
VII	trip of sand roughness
VIII	narrow band of sand roughness
IX	wide band of sand roughness

upper part (suction side). At  $x/c = 0.015$  on the upper part of the nose a rim was observed with a height of  $100\text{ }\mu\text{m}$ . The narrow band of sand roughness extended over a length of  $29\text{ mm}$  in spanwise direction in the central part of the foil. In the fifth configuration  $30\text{ }\mu\text{m}$  sand grain roughness was evenly applied in a rather wide band to both the upper and lower part of the hydrofoil nose. The sand roughness covered a length in chordwise direction of  $x/c = 0-0.036$  on the lower part of the foil and  $x/c = 0-0.072$  on the upper part. The wide band of sand roughness extended over a length of  $32\text{ mm}$  in spanwise direction in the central part of the foil. A survey and designation of all configurations tested (apart from the foil used for the pressure measurements) is given in Table 1.

#### Procedure

The pressure measurements performed with the tapered hydrofoil provided with pressure taps were made at the following angles of attack  $\alpha$ :  $0^\circ$ ,  $2^\circ$ ,  $4^\circ$ ,  $6^\circ$  and  $8^\circ$ . All other tests performed with configurations I through IX were made at  $\alpha = 2^\circ (+ 0.1^\circ)$ . These tests comprised holographic recordings of the boundary layer flow, holographic recordings of cavitation or bubble populations, cavitation inception measurements and photographs of cavitation. The photographs were made with a camera

TABLE 2. Stations and Ordinates of Pressure Orifices

Orifice No.	Station, 100 x/c	Ordinate, 100 y/c
1	6.1	-2.6
2	2.7	3.55
3	7.35	5.7
4	11.9	7.1
5	16.7	8.25
6	21.7	9.0
7	26.1	9.5
8	30.7	9.75

mounted vertically above the hydrofoil, so that its field of view through a plexiglass window in the top of the test section covered the whole length of the hydrofoil and a width of about 28 mm. For each configuration the tunnel was refilled and the water deaerated till a total air content of about 4.6 cm<sup>3</sup>/l was reached (1 cm<sup>3</sup> of air per liter of water at STP corresponds to 1.325 ppm by weight). The water temperature was usually around 20° C. All observations were related to the center part of the hydrofoil, away from the test section walls.

### 3. EXPERIMENTAL RESULTS

#### Pressure Distribution

The pressure measurements were made with a tapered NACA 4412 hydrofoil instrumented with 8 pressure taps. The orifices, each 0.3 mm in diameter, were drilled perpendicularly into the foil surface and are all located in the central plane of symmetry. The locations of the pressure orifices in terms of stations and ordinates in percent of the foil chord c are given in Table 2. The pressure measurements were made at  $\alpha = 0^\circ, 2^\circ, 4^\circ, 6^\circ$  and  $8^\circ$ . The results are expressed in terms of the pressure coefficient  $C_p$ , defined as

$$-C_p = \frac{P_o - P}{\frac{1}{2}\rho V_o^2},$$

where  $P_o$  and  $V_o$  denote the undisturbed static pressure and flow velocity in the test section,  $P$  the static pressure on the foil and  $\rho$  the fluid density. For  $\alpha = 0^\circ, 2^\circ$  and  $4^\circ$  the pressures were measured at  $V_o = 5, 10, 15$  and 20 m/s, whereas for  $\alpha = 6^\circ$  and  $8^\circ$  the measurements were made at  $V_o = 5, 10$  and 15 m/s. All pressures were measured twice. The  $C_p$ -values for  $V_o = 5$  m/s slightly deviated from those at 10, 15 or 20 m/s. Therefore, averaged  $C_p$ -values were only derived from the measurements made at these higher velocities. The maximum deviation thus

TABLE 3. Measured Values of Pressure Coefficient  $-C_p$  for Different Angles of Attack

Orifice No.	0°	2°	4°	6°	8°
1	0.526	0.151	-0.140	-0.395	-0.571
2	0.035	0.544	1.092	1.716	2.407
3	0.459	0.853	1.248	1.681	2.155
4	0.682	1.020	1.355	1.701	2.092
5	0.783	1.085	1.374	1.678	1.990
6	0.819	1.085	1.336	1.594	1.848
7	0.867	1.105	1.335	1.574	1.768
8	0.889	1.105	1.305	1.517	1.673

found within one set of measurements was within 2 percent of  $-C_{p_{min}}$ . Averaged values of  $-C_p$  at each orifice on the hydrofoil and for all angles of attack are tabulated in Table 3. The data are plotted in Figure 2. Also plotted are  $-C_p$ -curves derived from accurate measurements made by Pinkerton (1936) for  $\alpha = 0^\circ, 2^\circ, 4^\circ$  and  $8^\circ$ . These measurements were made with a two-dimensional airfoil with a chord length of 127 mm, provided with 57 pressure orifices, at a Reynolds number of  $3.1 \times 10^6$ . Since the Reynolds number effect is negligible, the differences observed in Figure 2 are mainly caused by blockage effects in the present test section.

It is interesting to estimate the influence of tunnel blockage on the value of  $-C_{p_{min}}$  for small angles of attack. In Table 4  $-C_{p_{min}}$ -values are presented, derived from Pinkerton's measurements and from the present measurements for  $\alpha = 0^\circ, 2^\circ$  and  $4^\circ$ . The ratio  $C_{p_{min1}}/C_{p_{min2}}$  can be approximated by

$$\left[\left(\frac{1}{2}h + \delta\right)/\frac{1}{2}h\right]^2 = 1.464,$$

where  $h$  is the height of the test section (80 mm) and  $\delta$  the maximum thickness of the hydrofoil (8.4 mm). The correction factor originally used by Van der Meulen (1980) is too conservative.

The  $-C_{p_{min}}$ -value to be used in the ultimate comparison with the cavitation inception numbers measured with the configurations I through IX at  $\alpha = 2^\circ$  is 1.105. The approximate location of the minimum pressure is:  $(x/c)_{p_{min}} \approx 0.28$ .

#### Flow Observations

The boundary layer flow behaviour of the original, tapered NACA 4412 hydrofoil at  $\alpha = 2^\circ$  had been studied before by Van der Meulen (1980). Typically, the boundary layer remains laminar till a midchord position for a Reynolds number up to about  $1 \times 10^6$  ( $V_0 = 15$  m/s). Below  $V_0 =$

TABLE 4. Values of  $-C_{P_{min}}$  Derived from Pinkerton (1936) and from Present Measurements

Angle of Attack	$-C_{P_{min1}}$	$-C_{P_{min2}}$	$C_{P_{min1}}/C_{P_{min2}}$
	Present	Pinkerton	
$0^\circ$	0.895	0.61	1.467
$2^\circ$	1.105	0.75	1.473
$4^\circ$	1.375	0.92	1.495

4 m/s, midchord laminar separation was observed followed by transition to turbulence further downstream. The transition data are replotted in Figure 3.

Boundary layer flow visualization studies were also made for the configurations III through IX. For configuration III (1 mm dia wire), the injected sodium chloride solution was unable to follow the surface of the hydrofoil, since it was strongly affected by the outer flow. Apparently, Von Karman vortices generated by the oscillating wire ahead of the foil interfered with the boundary layer on the foil. A photograph showing this interference is presented in Figure 4. The flow direction is from left to right and the flow speed is 8.8 m/s. The photograph seems to represent a vortex pattern perpendicular to the foil surface, just after injection. Also for configuration IV (0.25 mm dia wire) the boundary layer flow in the centerplane of the tunnel was affected by vortices, but the influence was more moderate. In the photograph presented in Figure 5, a vortex perpendicular to the foil surface is clearly visualized at  $x/c = 0.022$ . The flow speed is 3.0 m/s. The main character of the boundary layer is still laminar. In the hologram, transition was found to occur at a midchord position. Since only a part of the sodium chloride was able to follow the foil surface, the exact position of transition could no longer be established. The tendency, however, was that transition occurred much earlier.

Transition data obtained with the configurations V through IX are plotted in Figure 3. For configuration V (distributed roughness) the transition data are not much different from the original data up to  $Re = 7 \times 10^5$  ( $V_0 = 10$  m/s). A detail of the transition region is shown in the photograph of Figure 6. The flow speed is 8.8 m/s. The location of the end of the vortex tongue is at  $x/c = 0.512$ . At speeds in the range 10 - 18 m/s ( $Re = 7 - 12 \times 10^5$ ) transition has moved to an approximate location of  $x/c = 0.2$ . For configuration VI the flow separated at the trip wire and reattached to the surface as a laminar boundary layer up to  $Re = 6 \times 10^5$  ( $V_0 = 8$  m/s). Transition occurred in the reattached boundary layer. At higher speeds ( $V_0 \geq 9$  m/s) transition occurred in the separated layer and the flow reattached to the surface as a turbulent boundary layer. A photograph showing this phenomenon is presented in Figure 7. The flow speed is 10.2 m/s. The trip of sand

roughness (configuration VII) caused transition to occur at the trip for Reynolds numbers above  $4.5 \times 10^5$  ( $V_0 = 6.5$  m/s). For configuration VIII (narrow band of sand roughness) the trip had hardly any effect up to  $Re = 1.5 \times 10^5$  ( $V_0 = 2$  m/s). In this range laminar separation occurred at a midchord position, followed by transition. A photograph showing the final stage of transition is presented in Figure 8. The location of the end of the vortex is at  $x/c = 0.70$ . The flow speed is 2.05 m/s. However, the situation has been drastically changed at  $Re = 2 \times 10^5$  ( $V_0 = 3$  m/s), where transition occurs close behind the roughness zone. A photograph showing this phenomenon is presented in Figure 9. The location where vortices start to grow is at  $x/c = 0.036$ . The flow speed is 4.1 m/s. A more gradual shift of the location of transition was observed for configuration IX (wide band of roughness). Transition at the end of the roughness zone ( $x/c = 0.072$ ) occurred at  $Re = 5.5 \times 10^5$  ( $V_0 = 8$  m/s).

### Bubble Populations

For each configuration, except configuration II, a series of holograms was made for different speeds and different cavitation numbers. The definition of the cavitation number  $\sigma$  is given by

$$\sigma = \frac{P_o - P_v}{\frac{1}{2} \rho V_o^2},$$

where  $P_v$  is the vapour pressure of the liquid. As indicated by Peterson (1972), a parameter which may be of some importance for the bubble population in the test section of a cavitation tunnel is the air content ratio  $\alpha/\alpha_{TS}$ , where  $\alpha$  is the total air content and  $\alpha_{TS}$  the saturated air content referred to test section pressure and temperature. Holographic measurements made in the NSMB large cavitation tunnel at a constant value of  $\alpha = 12.5 \text{ cm}^3/\text{l}$  confirmed Peterson's observations. At  $\alpha/\alpha_{TS} = 0.8$  the number of bubbles/ $\text{cm}^3$  was found to be 0.2, whereas at  $\alpha/\alpha_{TS} = 1.6$  the number of bubbles/ $\text{cm}^3$  was 3.

The holograms made in the high speed water tunnel provided data on nuclei populations. Due to the high quality of the filtering system in the present set-up, and due to the test procedure used, the water in the tunnel did hardly contain detectable particulates. Therefore, only data on bubble populations will be provided. The small value of the total optical pathlength between the bubbles and the holographic plate, and the high resolving power of these plates enabled a discrimination between bubbles and particulates down to a diameter of 5  $\mu\text{m}$ .

The most consistent results were obtained in the wake of the cavitating wires used for the configurations III and IV. Bubble populations were derived from holograms taken at cavitation numbers around 1.19, which happens to be the mean value of the cavitation inception number for configuration IV. In each hologram the location of the analyzed surface, relative to the foil contour, is: 3 - 13 mm behind the nose of the foil and 9 - 13 mm above the chord line. For configuration III bubbles were only counted over a depth of 5.0 mm, which

TABLE 5. Bubble Populations in Wake of 1 mm Dia Wire  
(Configuration III)

Hologram No.	1.2	1.6	1.10	1.14	1.18
Velocity, m/s	7.88	9.82	11.73	14.65	19.52
Cavitation No.	1.16	1.18	1.19	1.19	1.19
$\alpha/\alpha_{TS}$	0.68	0.42	0.30	0.19	0.11
Bubble diameter range, $\mu\text{m}$	Number of bubbles per $\text{cm}^3$				
<10	2476	3482	3477	3611	2021
10-20	1689	1657	1640	1296	331
20-30	889	398	302	66	28
30-40	321	36	25	-	14
40-50	103	6	6	-	-
50-60	62	6	6	-	-
60-70	27	-	-	-	-
>70	-	-	-	-	-
Cumulative	5567	5585	5456	4973	2394

TABLE 6. Bubble Populations in Wake of 0.25 mm Dia Wire  
(Configuration IV)

Hologram No.	3.2	3.5	3.9	3.13	3.17
Velocity, m/s	7.94	9.93	11.74	14.73	19.74
Cavitation No.	1.17	1.17	1.21	1.21	1.19
$\alpha/\alpha_{TS}$	0.59	0.40	0.26	0.16	0.10
Bubble diameter range, $\mu\text{m}$	Number of bubbles per $\text{cm}^3$				
<10	3136	3758	3905	1755	878
10-20	1537	1420	722	284	111
20-30	164	73	-	-	-
>30	-	-	-	-	-
Cumulative	4837	5251	4627	2039	989

covered the width of the wake of the 1.0 mm dia wire. Thus, the total volume analyzed was  $0.154 \text{ cm}^3$ . For configuration IV (0.25 mm dia wire) the wake had a width of 2.6 mm. The total volume analyzed was  $0.081 \text{ cm}^3$ . Because of the extremely high bubble concentrations found in both wakes, these samples are sufficiently large. The results of the bubble population measurements for different velocities are presented in Table 5

(configuration III) and Table 6 (configuration IV).

It is interesting to note that the total number of bubbles per cubic centimeter is almost independent of the condition in the test section with regard to speed, pressure or  $\alpha/\alpha_{TS}$ . In 7 out of 10 holograms the total number of bubbles/cm<sup>3</sup> is of the order of 5000. However, the condition in the test section does have a marked influence on the bubble population. In the absence of bubble generation, the total number of bubbles/cm<sup>3</sup> is at least two orders of magnitude lower than with bubble generation. Besides, all bubbles are smaller than 20  $\mu\text{m}$  and most of them smaller than 10  $\mu\text{m}$ . Some bubble population measurements were made with the original foil (configuration I). The total volume analyzed was 0.154 cm<sup>3</sup>. The results for three different velocities are presented in Table 7.

#### Cavitation Observations and Inception Measurements

Cavitation inception measurements were made for all configurations listed in Table 1. They comprised measurements of the beginning or inception of cavitation, yielding data on the incipient cavitation number  $\sigma_i$ , and measurements of the disappearance or desinence of cavitation, yielding data on the desinent cavitation number  $\sigma_d$ . For reference purposes, two series of inception measurements were made with the original, tapered hydrofoil (configuration I). One series was measured in 1979, the other in 1982. The data are plotted in Figure 10. The speed range covered was 8 - 22 m/s, whereas at  $V_0 = 22$  m/s the water temperature was allowed to increase to about 35° C to obtain higher Reynolds numbers. Also plotted are data from two series of inception measurements made with the two-dimensional hydrofoil (configuration II). These measurements were made in 1981 and 1982. The average values of 52 measurements of the cavitation inception number for both configurations are:

$$\bar{\sigma}_{i,d} \text{ (tapered)} = 0.990$$

and

$$\bar{\sigma}_{i,d} \text{ (2-dim.)} = 0.995.$$

Although the data plotted in Figure 10 show some scatter, the average inception values for both configurations are essentially equal. The results point out that, at least for  $\alpha = 2^\circ$ , the influence on inception, caused by the fact that the tapered foil slightly deviates from a two-dimensional foil, can be neglected.

In the absence of scale effects on inception, the following relation is valid:

$$\sigma_{i,d} = -C_{p_{\min}}$$



TABLE 7. Bubble Populations in Test Section for Original Hydrofoil (Configuration I)

Hologram No.	5.4	5.9	5.13
Velocity, m/s	9.92	11.85	14.73
Cavitation No.	1.20	1.19	1.21
$\alpha/\alpha_{TS}$	0.49	0.35	0.21
Bubble diameter range, $\mu\text{m}$	Number of bubbles per $\text{cm}^3$		
<10	39	6	6
10-20	6	6	6
>20	-	-	-
Cumulative	45	12	12

Since  $-C_{p\min}$  was found to be 1.105, cavitation inception on the tapered foil is subject to moderate scale effects.

Up to a speed of about 15 m/s, the type of cavitation observed on the tapered foil is mainly travelling bubble cavitation. Most of the bubbles are attached to the surface and travel with the main flow. At speeds between 15 and 18 m/s, transient spot and travelling bubble cavitation are both observed. At speeds above 18 m/s, the type of cavitation mainly observed is transient spot cavitation. This is an attached, wedge-shaped type of cavitation for which the location of the wedges is constantly changing. The types of cavitation observed on the two-dimensional hydrofoil were the same as observed on the tapered hydrofoil. Photographs of travelling bubble cavitation ( $V_0 = 7.9$  m/s,  $\sigma = 1.04$ ) and transient spot cavitation ( $V_0 = 19.8$  m/s,  $\sigma = 0.96$ ), observed on the tapered foil, are presented in Figure 11.

Inception data for configurations III and IV are plotted in Figure 12. These data refer to cavitation inception on the foil, in the wake of the wire ahead of the foil. Average inception values are:

$$\bar{\sigma}_{i,d} \text{ (1 mm dia wire)} = 1.24$$

and

$$\bar{\sigma}_{i,d} \text{ (0.25 mm dia wire)} = 1.195.$$

These values are considerably larger than  $-C_{p\min}$ . The abundant supply of nuclei should have been sufficient to eliminate any scale effect. However, the vortices generated by the wires ahead of the foil apparently created additional spots of low pressure on the foil surface, thus enabling premature cavitation. The type of cavitation observed on both

hydrofoils is typically attached bubble cavitation. This type was observed at all speeds. Photographs of attached bubble cavitation for configuration III are presented in Figure 13. These photographs were taken at  $V_0 = 7.9$  m/s ( $\sigma = 1.18$ ) and  $V_0 = 19.6$  m/s ( $\sigma = 1.18$ ). Similar photographs for configuration IV are presented in Figure 14. The conditions are:  $V_0 = 7.9$  m/s ( $\sigma = 1.175$ ) and  $V_0 = 19.7$  m/s ( $\sigma = 1.15$ ). A photograph taken from a hologram, showing an attached cavity for configuration IV, is presented in Figure 15. The flow speed is 14.7 m/s and  $\sigma = 1.205$ . The location of the beginning of the cavity is at  $x/c = 0.182$ .

Inception data for configuration V (distributed roughness) are plotted in Figure 16. Different types of cavitation were observed. At low speeds (8 - 10 m/s) travelling bubble cavitation appeared. At moderate speeds (11 - 14 m/s) travelling bubble and transient spot cavitation appeared, whereas at high speeds (15 m/s and higher) the observed transient spot cavitation was preceded by fixed spot cavitation. In the latter case, the cavities are attached to fixed spots on the foil surface, and the shape resembles a wedge with a small apex angle. The data in Figure 16 refer to either travelling bubble/transient spot cavitation or fixed spot cavitation. The average value of the inception data for travelling bubble/transient spot cavitation is:

$$\bar{\sigma}_{i,d} \text{ (distr. roughness)} = 1.05.$$

The  $\sigma_d$ -values for fixed spot cavitation are considerably larger. Besides, they are well above  $-C_{p_{min}}$ . Photographs of travelling bubble and fixed spot cavitation are presented in Figure 17. The conditions are:  $V_0 = 7.9$  m/s ( $\sigma = 1.01$ ) and  $V_0 = 19.7$  m/s ( $\sigma = 1.11$ ). In Figure 18, a photograph is presented showing the birth of a fixed spot cavity. The photograph refers to a speed of 19.6 m/s and  $\sigma = 1.05$ . At  $x/c = 0.128$  a small cavity with a length of 0.22 mm is observed, apparently attached to a small surface irregularity. The cavity is followed by more isolated cavities, finally leading to a spot cavity with a length of over 10 mm (observed in the hologram). A photograph taken at the same position, but at a lower pressure ( $\sigma = 0.96$ ) is presented in Figure 19.

Inception data for configurations VI and VII are plotted in Figure 20. For configuration VI (trip wire) the type of cavitation observed at inception was the same as observed for configuration I. The average value of the inception data is:

$$\bar{\sigma}_{i,d} \text{ (trip wire)} = 1.025,$$

and thus close to  $\bar{\sigma}_{i,d}$  for configuration I. For configuration VII (trip of sand roughness) inception occurred on the roughness elements up to a speed of 11 m/s. High values of  $\sigma_d$  are found in this speed range. However, above 11 m/s the roughness elements were not (yet) cavitating at inception and the appearance of cavitation was the same as observed for configuration I. The average value of the inception

data in this speed range is:

$$\bar{\sigma}_{i,d} \text{ (trip of sand roughness)} = 1.00$$

and thus essentially equal to  $\bar{\sigma}_{i,d}$  for configuration I.

Finally, inception data were obtained for configurations VIII and IX and the results are shown in Figure 21. For both configurations it was observed (visually and holographically) that at inception a number of minute cavities were attached to the roughness elements. These cavities generated nuclei and the type of cavitation observed at all speeds was attached bubble cavitation. The average values of the inception data for both configurations are:

$$\bar{\sigma}_{i,d} \text{ (narrow band of sand roughness)} = 1.105$$

and

$$\bar{\sigma}_{i,d} \text{ (wide band of sand roughness)} = 1.15.$$

Hence, for configuration VIII we have:  $\bar{\sigma}_{i,d} = -C_{p_{min}}$ , whereas for configuration IX,  $\bar{\sigma}_{i,d}$  is somewhat larger than  $-C_{p_{min}}$ . Photographs of attached bubble cavitation for configurations VIII and IX are shown in Figures 22 and 23 respectively. In Figure 22 the conditions are:  $V_o = 9.9$  m/s ( $\sigma = 1.03$ ) and  $V_o = 19.7$  m/s ( $\sigma = 1.08$ ). In Figure 23 we have:  $V_o = 9.9$  m/s ( $\sigma = 1.06$ ) and  $V_o = 19.7$  m/s ( $\sigma = 1.08$ ). The shape of the cavities could be determined from holographic observations. In Figure 24 a photograph is presented showing attached bubble cavitation on the foil of configuration VIII. The speed is 11.8 m/s and  $\sigma = 1.07$ . The beginning of the first cavity is at  $x/c = 0.212$ . Another photograph showing attached bubble cavitation (configuration VIII) is presented in Figure 25. The speed is 9.9 m/s and  $\sigma = 1.05$ . The beginning of the first cavity is at  $x/c = 0.267$ . The fact that the minute cavities attached to the roughness elements generated nuclei could be detected from the holograms. The fact that these nuclei were actually responsible for attached bubble cavitation was proved by the holographic observation that the plane in which the first cavities appeared coincided with the plane in which a minute cavity was generating nuclei. A photograph showing a minute cavity attached to the roughness and generating such nuclei is presented in Figure 26. The photograph refers to configuration VIII; the speed is 7.9 m/s and  $\sigma = 0.935$ . The end of the cavity is at  $x/c = 0.025$ . The part close to the end of the cavity was further enlarged and a photograph showing this part is presented in Figure 27. The arrows indicate the positions of three nuclei (bubbles) very close to the foil surface. The diameter of these nuclei is roughly 10  $\mu$ m.

## 4. DISCUSSION AND CONCLUSIONS

Most studies on the effect of roughness on boundary layer transition, described in the literature, refer to a flat plate. A distinction is made between the effect of two-dimensional and three-dimensional roughness elements. For single two-dimensional roughness elements, Dryden (1953) found a single functional relation between the transition Reynolds number  $Re_t$  ( $Re_t = V x_t / \nu$ ) and the relative height of the roughness element  $k/\delta_k^*$ , where  $k$  is the roughness height and  $\delta_k^*$  the boundary layer displacement thickness at the position of the element. It means that there is a gradual forward movement of transition when the speed is increased. The trip wire in the present study shows exactly the above behaviour (Figure 3). For three-dimensional roughness elements (spheres), Klebanoff et al. (1955) found a critical roughness Reynolds number  $U_k k / \nu$  to exist, where  $U_k$  is the velocity at the height of the sphere, below which the roughness is essentially without effect, and above which transition is brought to the roughness location. It means that there is a sudden progression of transition to the roughness location when the speed is increased. In the present study the trip of sand roughness and the narrow band of sand roughness show this behaviour (Figure 3).

For configurations VI through IX the critical speeds at which transition occurred at the roughness location itself were found to be: 9, 6.5, 3 and 8 m/s, respectively. Hence, the boundary layer on the foil is essentially turbulent for the full range of speeds (8-20 m/s) for which cavitation observations and inception measurements were made.

Gates and Acosta (1978) and Katz and Acosta (1981) compared various results of nuclei distribution measurements performed in different experimental facilities and in open sea. The nuclei distributions were reduced to the number density distribution function  $N(R)$  and were plotted versus the nuclei radius  $R$ . It was found that the values of  $N(R)$  could differ by several orders of magnitude, but all the data had approximately the same slope. When the present data are plotted in a  $N(R)$ - $R$  diagram, it is found that they also have this slope. The values of  $N(R)$  without bubble generation have the same order of magnitude as those measured by Gates and Acosta (1978) in their low turbulence water tunnel. However, when bubble generation is applied the values of  $N(R)$  are increased by at least two orders of magnitude. According to Lecoffre and Bonnin (1979), bubble cavitation is correctly scaled when the nuclei concentration for the model is  $\lambda^3$  times higher than for the prototype, where  $\lambda$  is the scale ratio. In a qualitative sense it would mean that bubble generation is always necessary in model testing.

Usually, the dimensions of the prototype are at least one order of magnitude larger than those of the model. The same applies to the Reynolds number. It is generally assumed that the prototype environment has no lack of nuclei. Following the nuclei scaling relationship proposed by Lecoffre and Bonnin (1979), the nuclei concentration for the prototype is allowed to be low and thus the previous assumption may easily be confirmed.

Before proceeding with the results of the cavitation tests let us

first consider the question which type of bubble cavitation is to be expected in a full-scale or prototype condition. Unfortunately, full-scale observations of bubble type cavitation are extremely scarce. Rutgersson (1979) reported on some full-scale cavitation observations on a propeller for a torpedo boat. The cavitation pattern was shown to consist of small bubbles. However, the bubble cavitation was preceded by leading edge sheet cavitation and, therefore, can not be regarded as typical for midchord bubble cavitation. Some unpublished observations of midchord blade root cavitation seem to point at an attached type of cavitation and could thus resemble the presently observed attached bubble cavitation.

The trip wire and the trip of sand roughness (for  $V_0$  above 11 m/s) did not cavitate or generate nuclei at the instant of inception. For these configurations it was found that the appearance and inception of cavitation were essentially the same as for the original foil, in spite of the fact that the boundary layer was turbulent. Therefore it is concluded that bubble cavitation is not affected by viscous effects. It means that the mere application of roughness for boundary layer tripping has no effect whatsoever on eliminating scale effects on bubble cavitation.

The generation of nuclei by the wire ahead of the foil or by the roughness on the foil did increase the inception number and changed the appearance of cavitation into attached bubble cavitation. Since this type of cavitation occurred irrespective of the flow speed (or Reynolds number) it is suggested that this type of cavitation may resemble the full-scale appearance. The scale effect on inception experienced by the original foil was more than compensated for by the application of a cavitating wire ahead of the foil. The bubble concentration should have been adequate to eliminate the original scale effect, but the simultaneous generation of vortices caused an additional effect. The original scale effect was effectively eliminated by the application of sand roughness as used for configuration VIII. The essential observation in this case was that very small bubbles were generated by the roughness and that these bubbles travelled with the flow along the foil surface. Apparently, it is less important whether nuclei are generated ahead of the foil or on the foil. It seems essential, however, that a sufficient number of small nuclei can penetrate into the boundary layer on the foil. When bubbles are generated ahead of the foil, the population should be such that the fluid contains a large number of small bubbles since, according to Johnson and Hsieh (1966), large bubbles may be pushed away from the foil surface. The above condition is fully satisfied for the bubble populations obtained with the cavitating wire ahead of the foil.

In conclusion, it is shown that the application of sand roughness can be regarded as an effective means to eliminate all scale effects on bubble cavitation. The method has the advantage of avoiding the complications involved in obtaining a high bubble concentration in the flow ahead of the body. However, the application of sand roughness is rather critical. Configurations VI and VII were without effect, whereas for configuration IX the effect was somewhat too large. The use

of distributed roughness on the entire foil surface had the disadvantage of promoting the occurrence of fixed spot cavitation.

#### ACKNOWLEDGEMENT

This work was partially supported by the Royal Netherlands Navy, and by the Netherlands Department of Economic Affairs.

#### References

- Albrecht, K., and O. Björheden (1975). Cavitation testing of propellers in a free surface tunnel utilizing micro air bubble control, J. Fluids Engng., Trans. A.S.M.E. 97, 523.
- Billet, M.L., and J.W. Holl (1980). The use of distributed roughness for scaling cavitation inception, Proc. 19th ATTC, 971.
- Billet, M.L., and J.W. Holl (1981). Scale effects on various types of limited cavitation, J. Fluids Engng., Trans. A.S.M.E. 103, 405.
- Dryden, H.L. (1953). Review of published data on the effect of roughness on transition from laminar to turbulent flow, J. Aeronautical Sciences 20, 477.
- Gates, E.M., and A.J. Acosta (1978). Some effects of several freestream factors on cavitation inception of axisymmetric bodies, Proc. 12th Symp. on Naval Hydrodynamics, 86.
- Huang, T.T., and F.B. Peterson (1976). Influence of viscous effects on model/full-scale cavitation scaling, J. Ship Research 20, 215.
- Johnson, V.E., and T. Hsieh (1966). The influence of the trajectories of gas nuclei on cavitation inception, Proc. 6th Symp. on Naval Hydrodynamics, 163.
- Katz, J., and A.J. Acosta (1981). Observations of nuclei in cavitating flows, Proc. IUTAM Symp., Applied Scientific Research 38 (1982), 123.
- Klebanoff, P.S., G.B. Schubauer, and K.D. Tidstrom (1955). Measurements of the effect of two-dimensional and three-dimensional roughness elements on boundary-layer transition, J. Aeronautical Sciences 22, 803.
- Kuiper, G. (1978). Scale effects on propeller cavitation inception, Proc. 12th Symp. on Naval Hydrodynamics, 401.
- Kuiper, G. (1981). Cavitation inception on ship propeller models, Ph.D. thesis, Delft.
- Kuiper, G. (1982a). Some experiments with specific types of cavitation on ship propellers, J. Fluids Engng., Trans. A.S.M.E. 104, 105.
- Kuiper, G. (1982b). A comparison between cavitation inception phenomena in a cavitation tunnel and in a depressurized towing tank, RINA Spring Meeting.
- Lecoffre, Y., and J. Bonnin (1979). Cavitation tests and nucleation control, A.S.M.E. Symp. on Cavitation Inception, 141.
- Noordzij, L. (1976). Some experiments on cavitation inception with propellers in the NSMB-depressurized towing tank, Int. Shipbuilding Progress 23, 300.

- Peterson, F.B. (1972). Hydrodynamic cavitation and some considerations of the influence of free gas content, Proc. 9th Symp. on Naval Hydrodynamics, 1131.
- Pinkerton, R.M. (1936). Calculated and measured pressure distributions over the midspan section of the N.A.C.A. 4412 airfoil, NACA Report No. 563.
- Rutgersson, O. (1979). Supercavitating propeller performance; influence of propeller geometry and interaction between propeller, rudder and hull, SSPA Report No. 82.
- Van der Meulen, J.H.J. (1976). A holographic study of cavitation on axisymmetric bodies and the influence of polymer additives, Ph.D. thesis, Enschede.
- Van der Meulen, J.H.J. (1978). A holographic study of the influence of boundary layer and surface characteristics on incipient and developed cavitation on axisymmetric bodies, Proc. 12th Symp. on Naval Hydrodynamics, 433.
- Van der Meulen, J.H.J. (1980). Boundary layer and cavitation studies of NACA 16-012 and NACA 4412 hydrofoils, Proc. 13th Symp. on Naval Hydrodynamics, 195.
- Van der Meulen, J.H.J., H.J. Raterink, and R.L. van Renesse (1982). Visualization of boundary layer flow and cavitation phenomena by in-line holography, Defence Research Group Seminar on Advanced Hydrodynamic Testing Facilities, The Hague.

## LIST OF FIGURES

- Figure 1. Schematic diagram of in-line holographic system for making holograms of cavitation, nuclei population and flow phenomena on hydrofoil.
- Figure 2. Comparison between present and Pinkerton's (1936) measurements of pressure coefficient as a function of distance along chord for NACA 4412 hydrofoil.
- Figure 3. Locations of transition on NACA 4412 hydrofoil as a function of Reynolds number for configurations I, V, VI, VII, VIII and IX at  $\alpha = 2^\circ$ .
- Figure 4. Interference between main flow and injected fluid on nose of foil (configuration III). The flow direction is from left to right ( $V_0 = 9.8$  m/s).
- Figure 5. Interference between main flow and boundary layer on foil (configuration IV). The location of the vortex is at  $x/c = 0.022$  ( $V_0 = 3.0$  m/s).
- Figure 6. Detail of transition region for configuration V. The location of the end of the vortex tongue is at  $x/c = 0.512$  ( $V_0 = 8.8$  m/s).
- Figure 7. Laminar flow separation and transition at trip wire (configuration VI,  $V_0 = 10.2$  m/s).
- Figure 8. Final stage of transition for configuration VIII. The location of the end of the vortex is at  $x/c = 0.70$  ( $V_0 = 2.05$  m/s).
- Figure 9. Transition generated by roughness for configuration VIII. The location of transition is at  $x/c = 0.036$  ( $V_0 = 4.1$  m/s).
- Figure 10. Cavitation inception data for configurations I and II.
- Figure 11. Photographs showing travelling bubble cavitation (top) and transient spot cavitation (bottom) for configuration I. The flow direction is from left to right.  
Top :  $V_0 = 7.9$  m/s;  $\sigma = 1.04$ .  
Bottom:  $V_0 = 19.8$  m/s;  $\sigma = 0.96$ .
- Figure 12. Cavitation inception data for configurations III and IV.
- Figure 13. Photographs showing attached bubble cavitation for configuration III.  
Top :  $V_0 = 7.9$  m/s;  $\sigma = 1.18$ .  
Bottom:  $V_0 = 19.6$  m/s;  $\sigma = 1.18$ .
- Figure 14. Photographs showing attached bubble cavitation for configuration IV.  
Top :  $V_0 = 7.9$  m/s;  $\sigma = 1.175$ .  
Bottom:  $V_0 = 19.7$  m/s;  $\sigma = 1.15$ .
- Figure 15. Attached cavity for configuration IV. The location of the cavity is at  $x/c = 1.182$  ( $V_0 = 14.7$  m/s;  $\sigma = 1.205$ ).
- Figure 16. Cavitation inception data for configuration V.
- Figure 17. Photographs showing travelling bubble cavitation (top) and fixed spot cavitation (bottom) for configuration V.  
Top :  $V_0 = 7.9$  m/s;  $\sigma = 1.01$ .  
Bottom:  $V_0 = 19.7$  m/s;  $\sigma = 1.11$ .
- Figure 18. Birth of a fixed spot cavity for configuration V. The first cavity is at  $x/c = 0.128$  ( $V_0 = 19.6$  m/s;  $\sigma = 1.05$ ).



- Figure 19. Same phenomenon and location as for Figure 18 but at lower pressure ( $V_0 = 19.6$  m/s;  $\sigma = 0.96$ ).
- Figure 20. Cavitation inception data for configurations VI and VII.
- Figure 21. Cavitation inception data for configurations VIII and IX.
- Figure 22. Photographs showing attached bubble cavitation for configuration VIII.  
Top :  $V_0 = 9.9$  m/s;  $\sigma = 1.03$ .  
Bottom:  $V_0 = 19.7$  m/s;  $\sigma = 1.08$ .
- Figure 23. Photographs showing attached bubble cavitation for configuration IX.  
Top :  $V_0 = 9.9$  m/s;  $\sigma = 1.06$ .  
Bottom:  $V_0 = 19.7$  m/s;  $\sigma = 1.08$ .
- Figure 24. Attached bubble cavitation for configuration VIII. The location of the first cavity is at  $x/c = 0.212$  ( $V_0 = 11.8$  m/s;  $\sigma = 1.07$ ).
- Figure 25. Attached bubble cavitation for configuration VIII. The location of the first cavity is at  $x/c = 0.267$  ( $V_0 = 9.9$  m/s;  $\sigma = 1.05$ ).
- Figure 26. Nuclei generation by cavitating roughness for configuration VIII. The end of the cavity is at  $x/c = 0.025$  ( $V_0 = 7.9$  m/s;  $\sigma = 0.935$ ).
- Figure 27. Enlarged part of cavity generating nuclei (taken from Figure 26). The arrows indicate positions of nuclei travelling along foil surface.

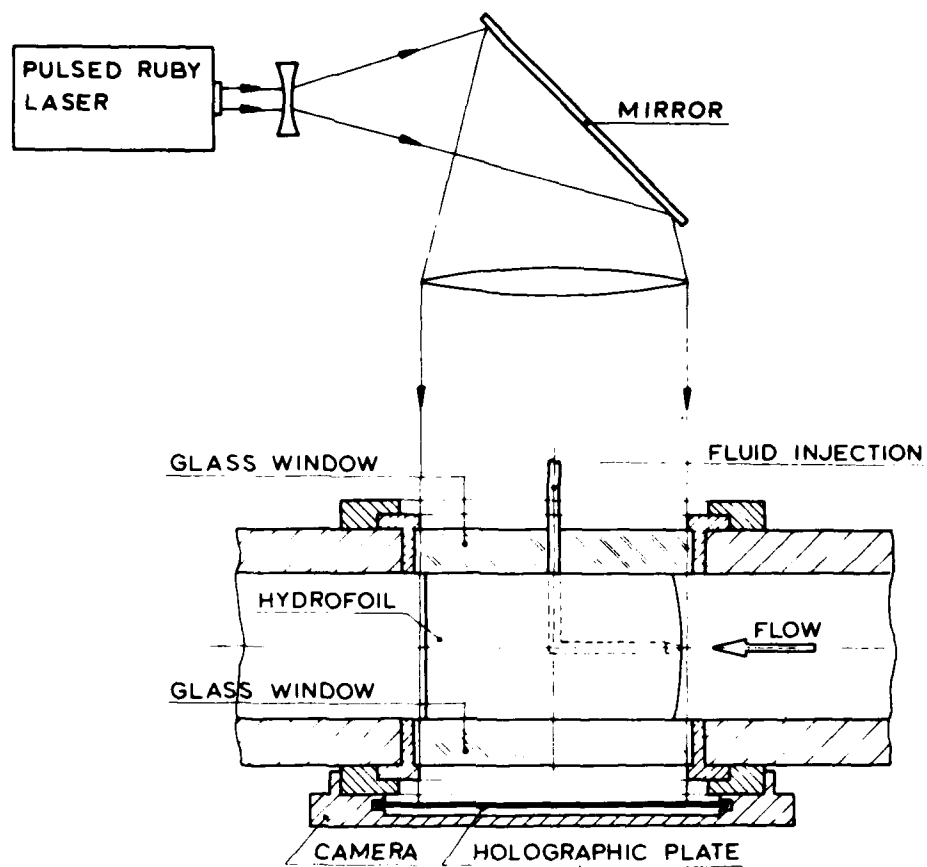


Figure 1

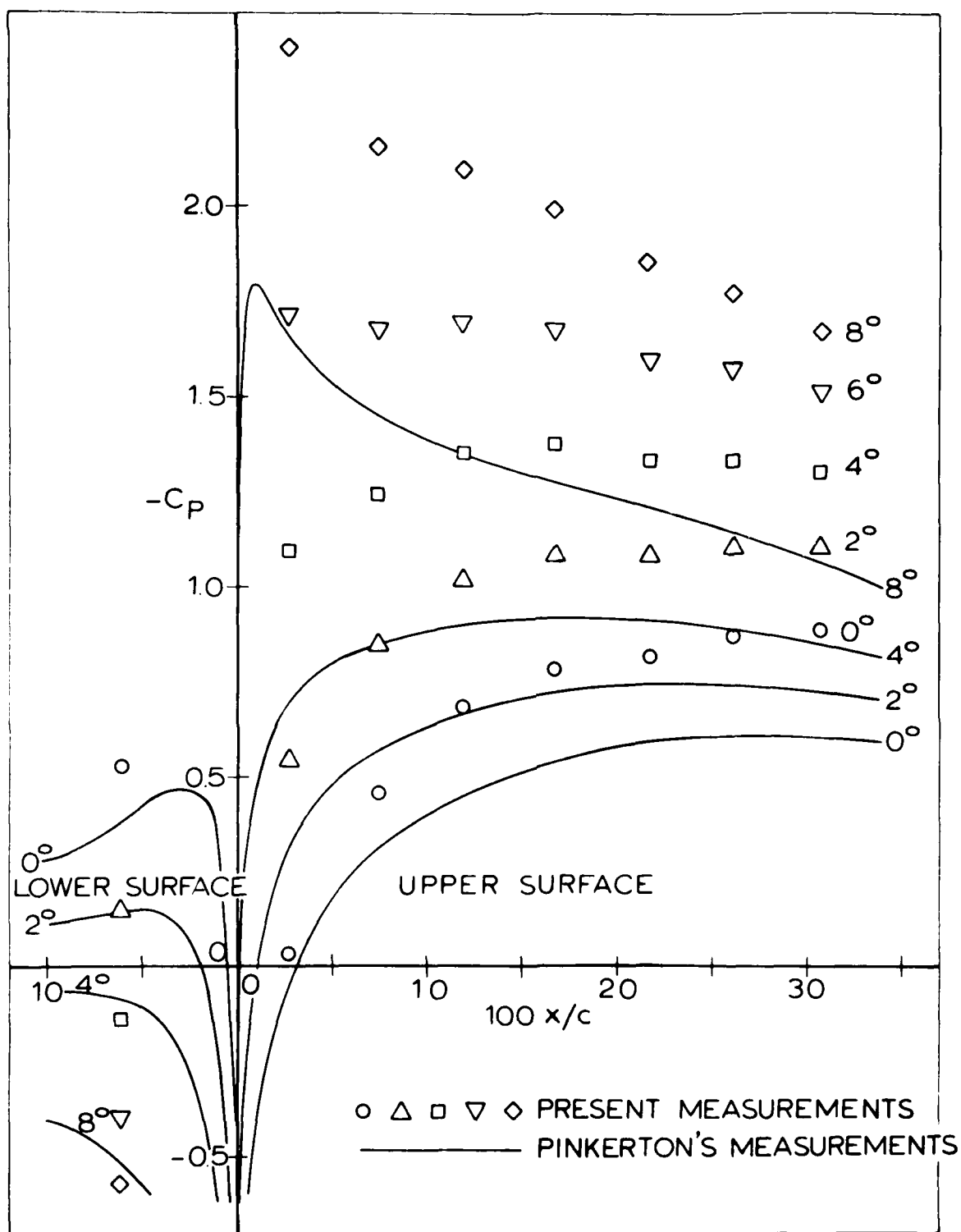


Figure 2

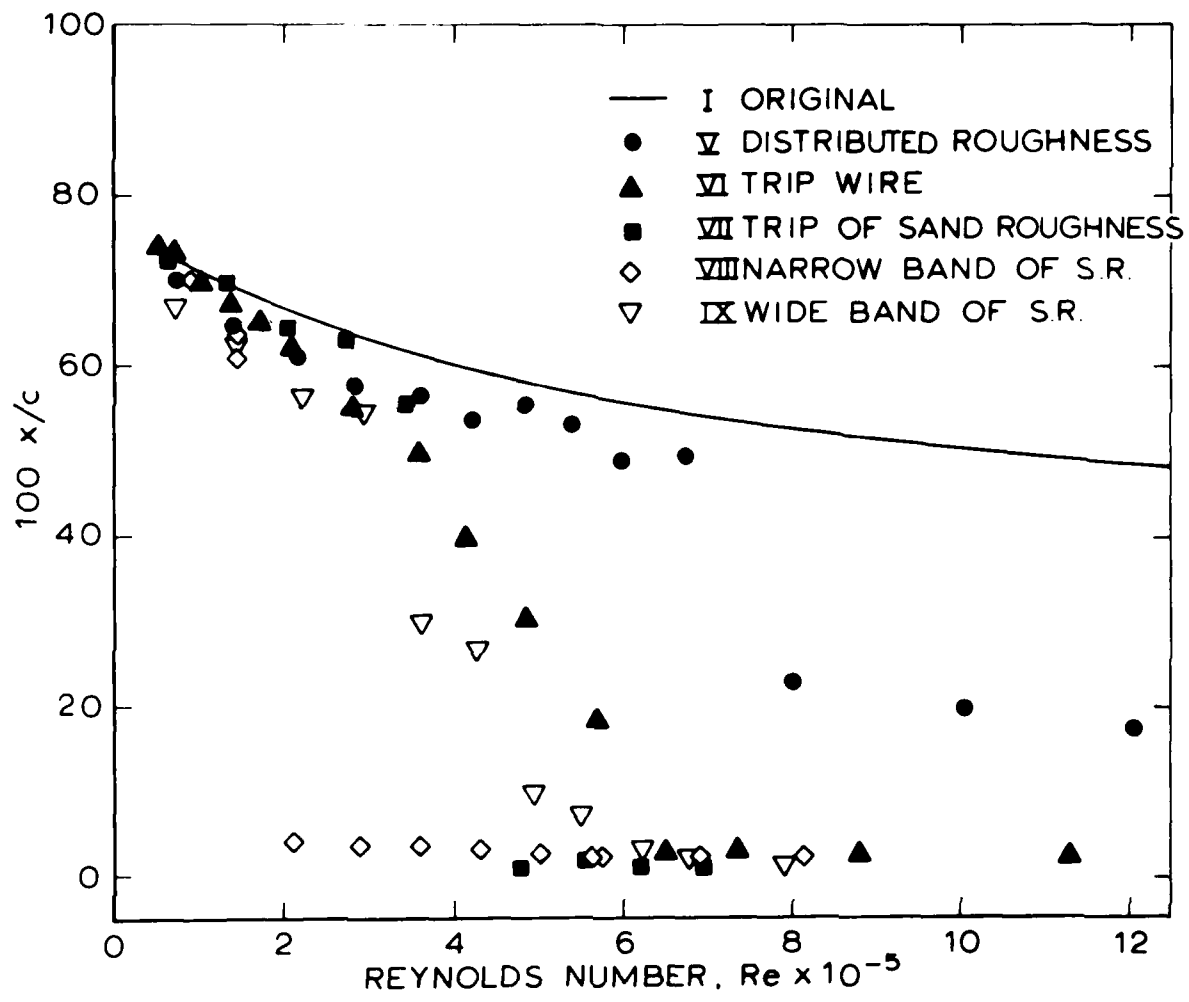


Figure 3

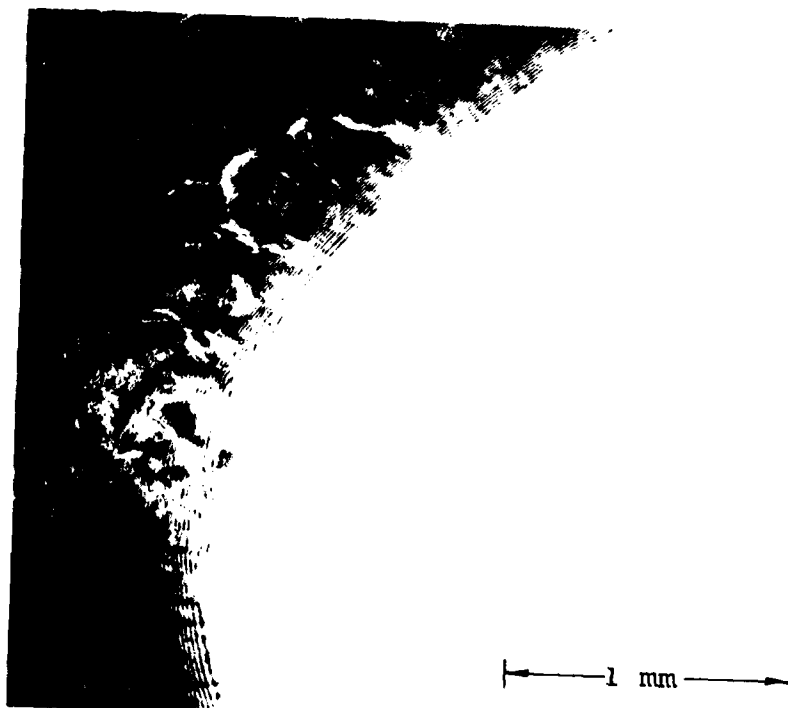


Figure 4

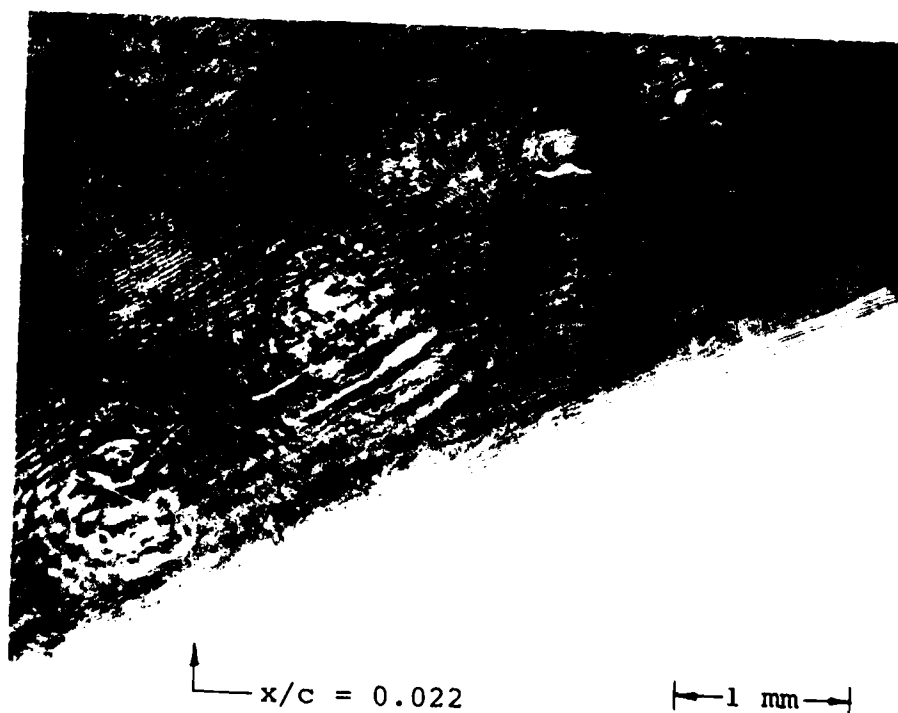


Figure 5

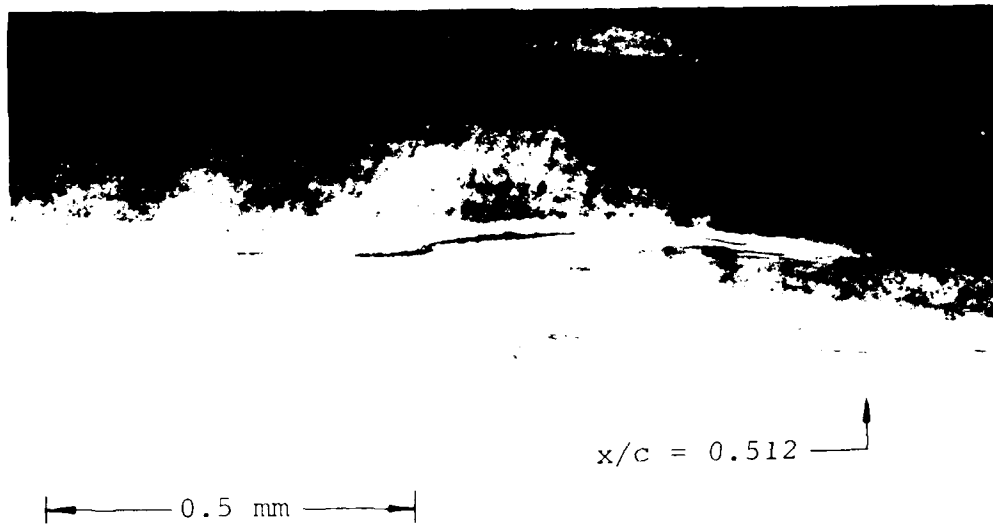


Figure 6

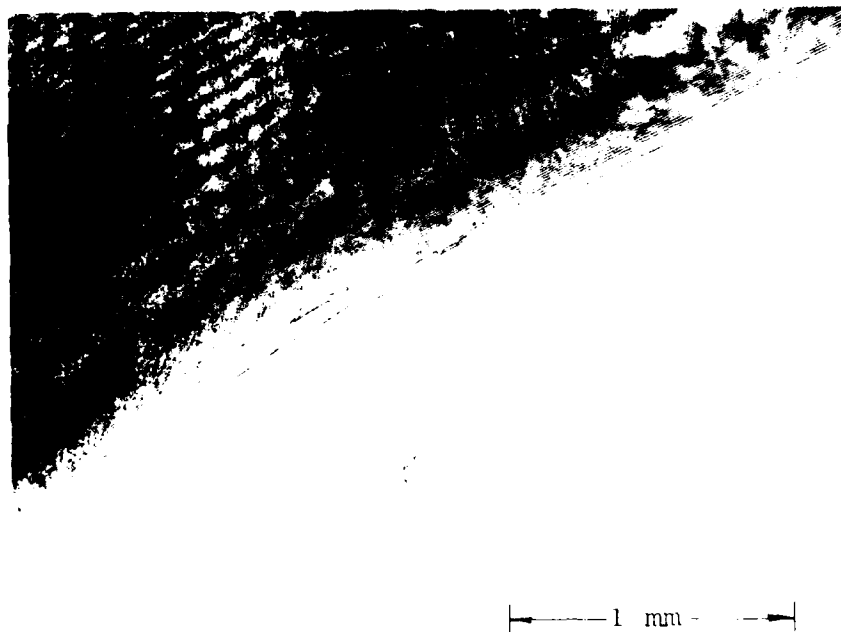


Figure 7

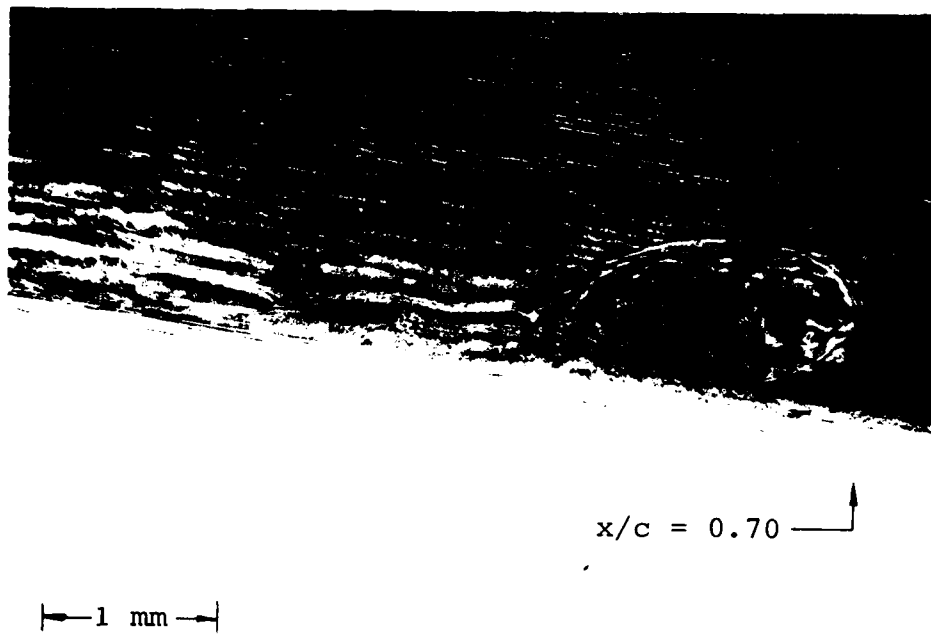


Figure 8

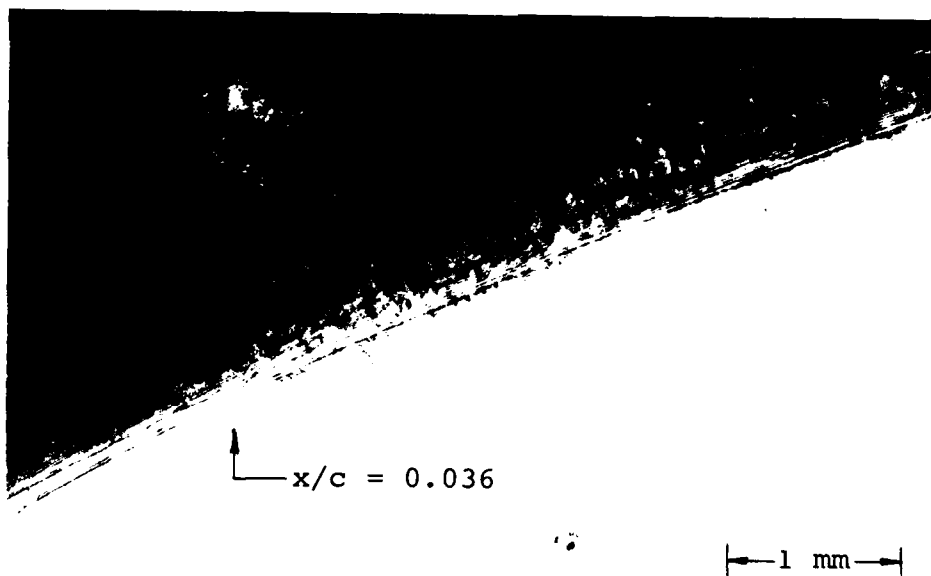


Figure 9

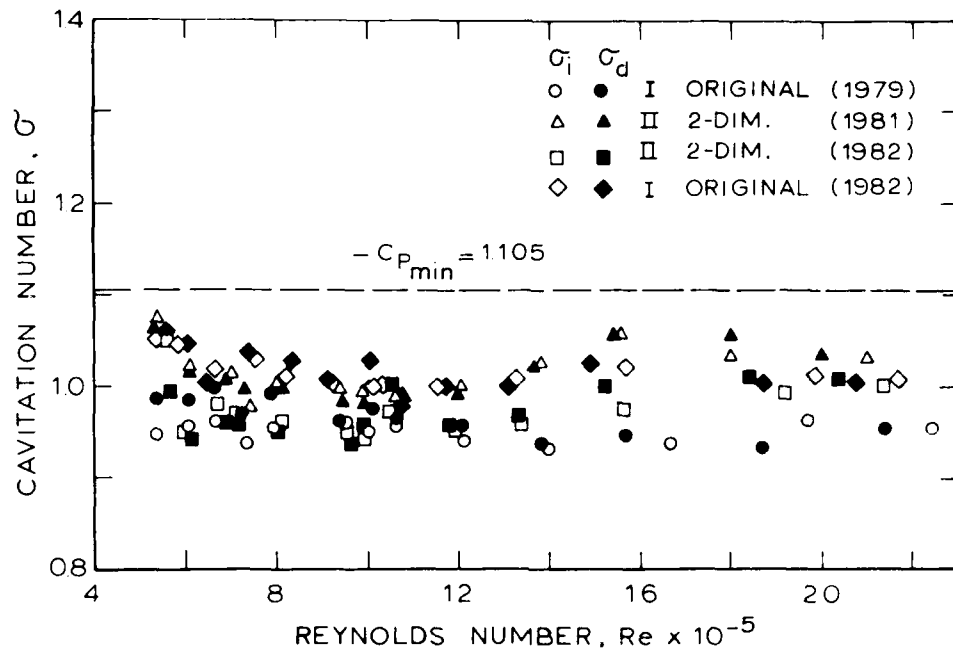


Figure 10

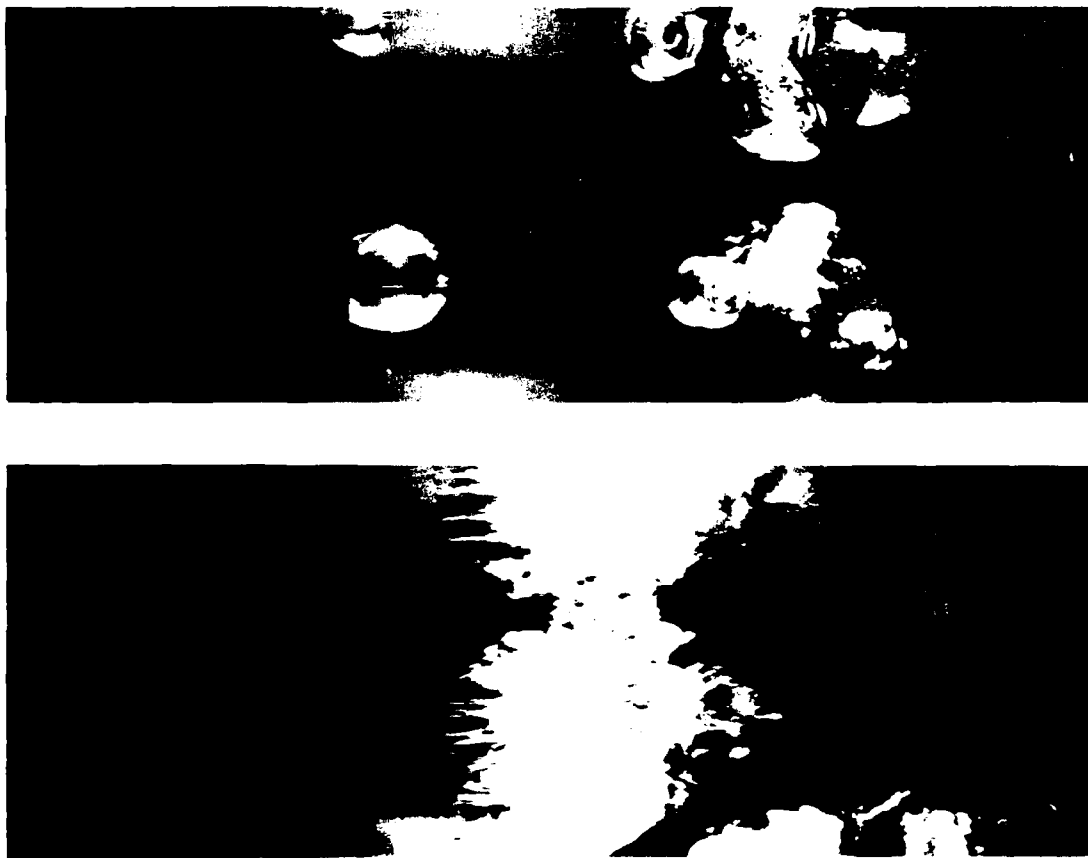


Figure 11



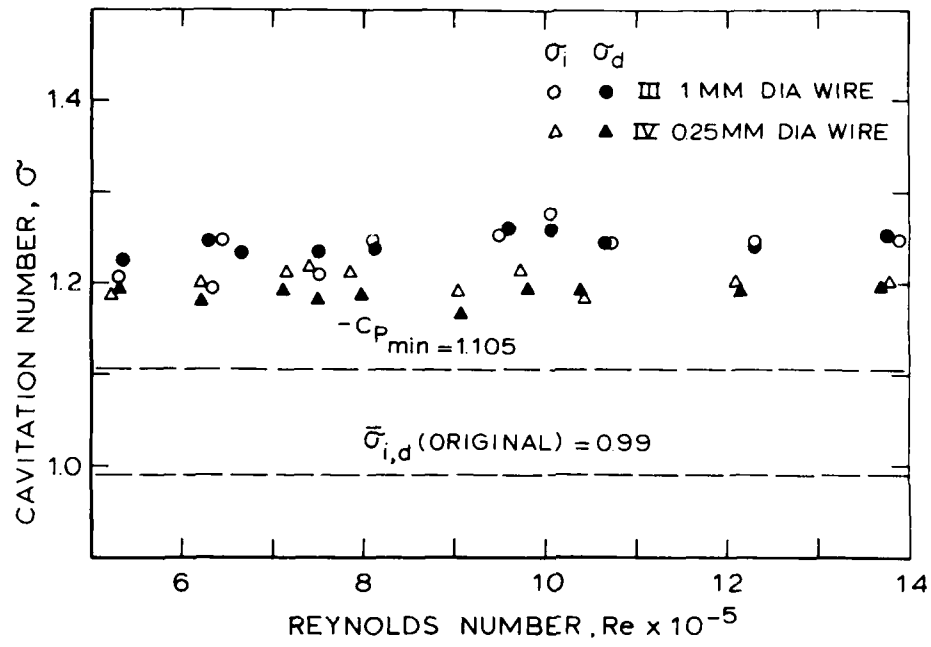


Figure 12

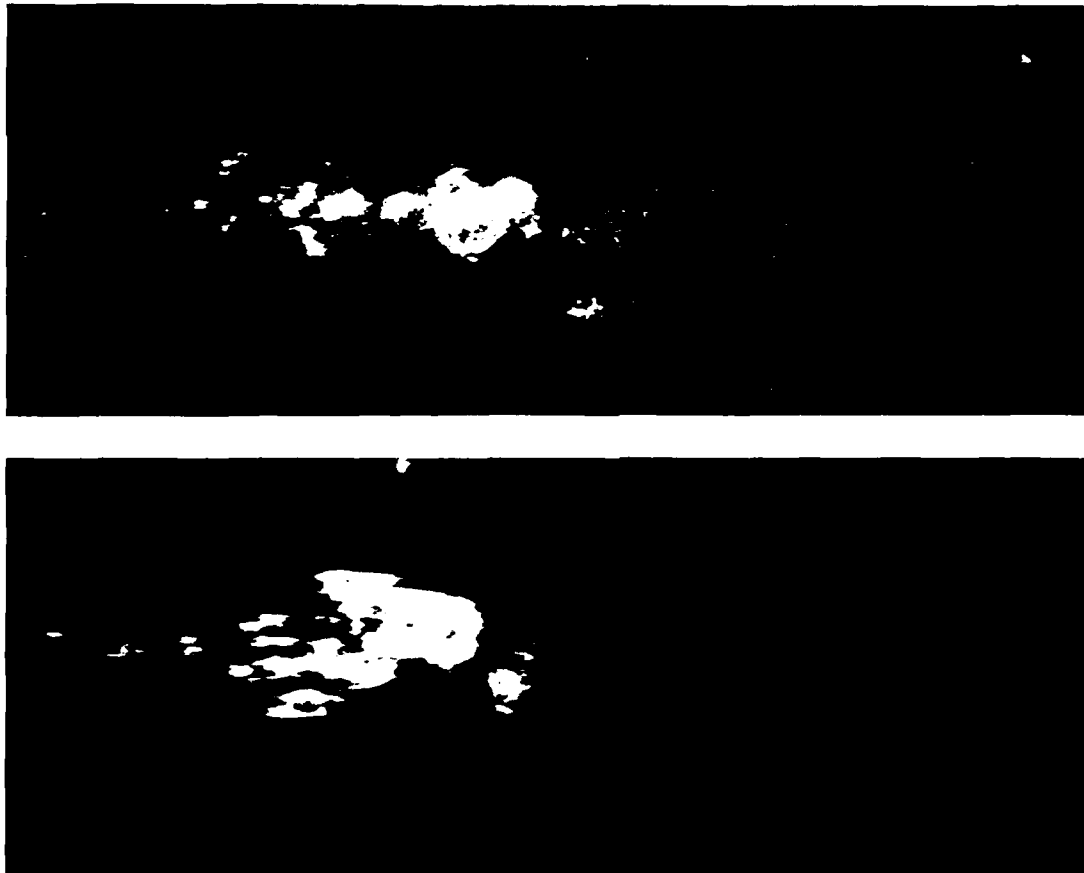


Figure 13

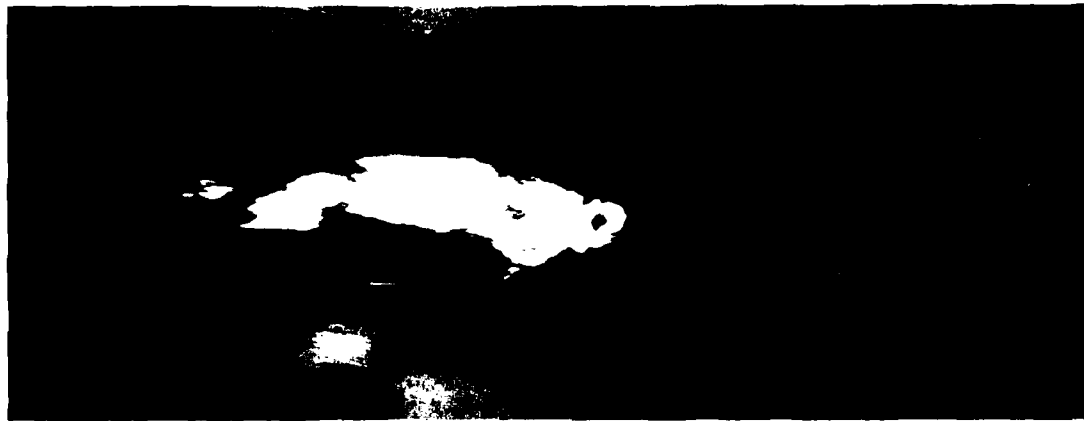
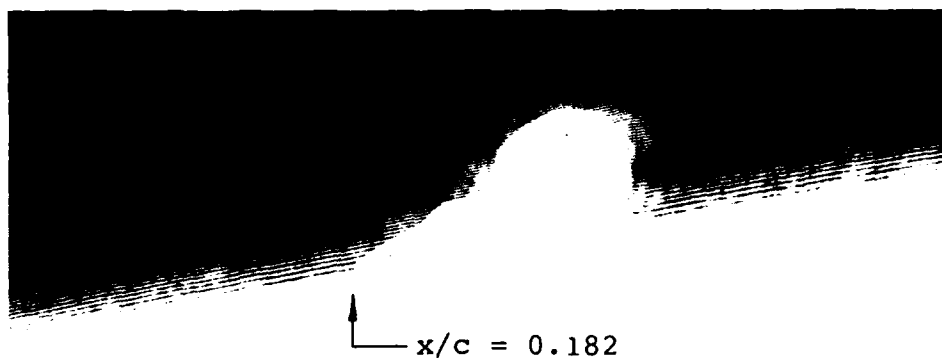


Figure 14



1 mm

Figure 15

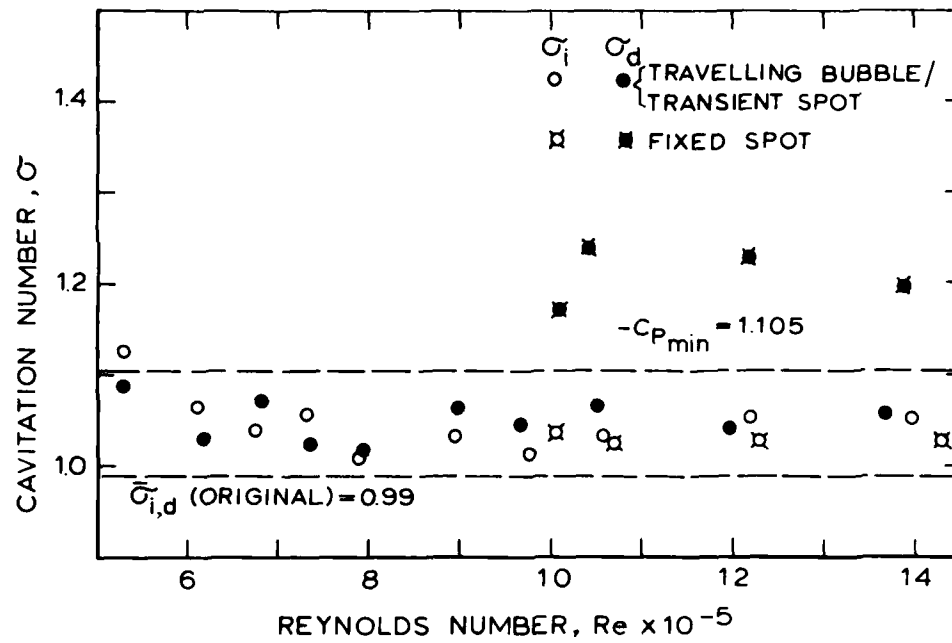


Figure 16



Figure 17

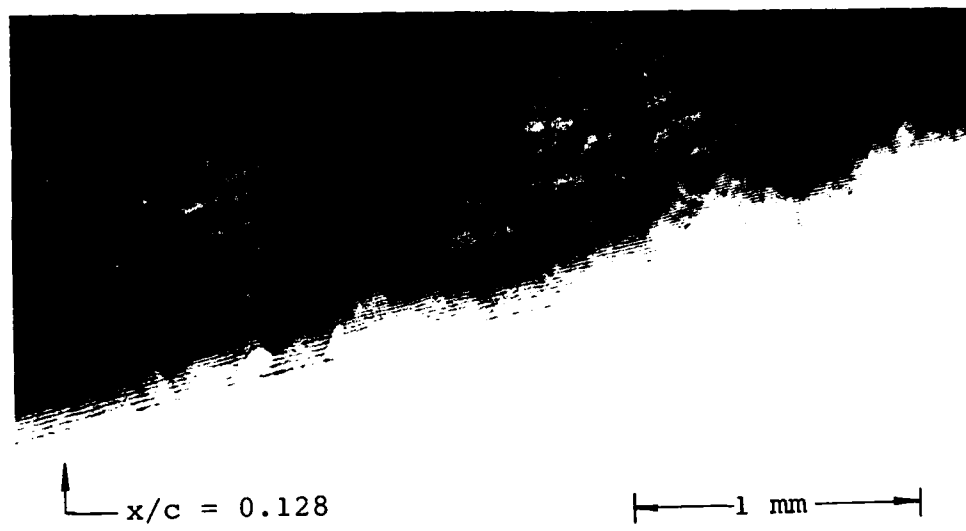


Figure 18

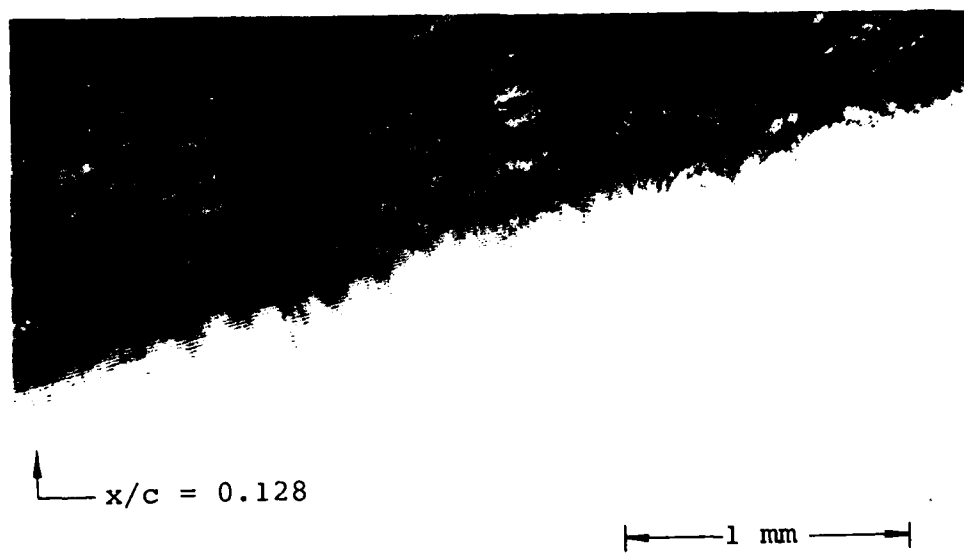


Figure 19

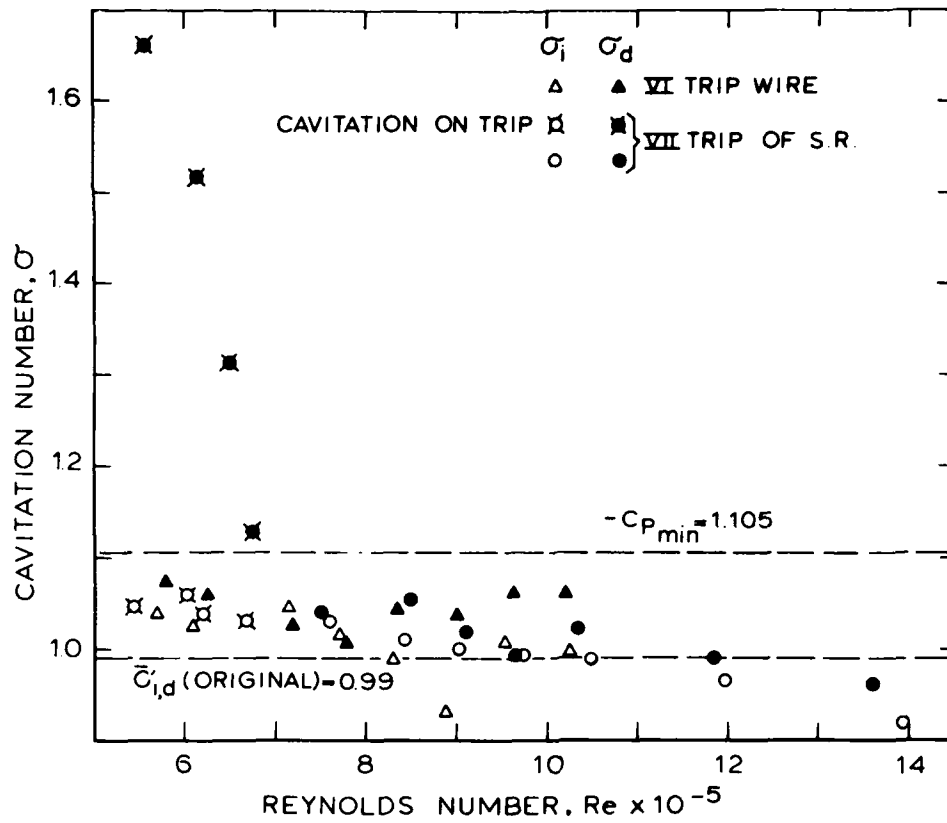


Figure 20

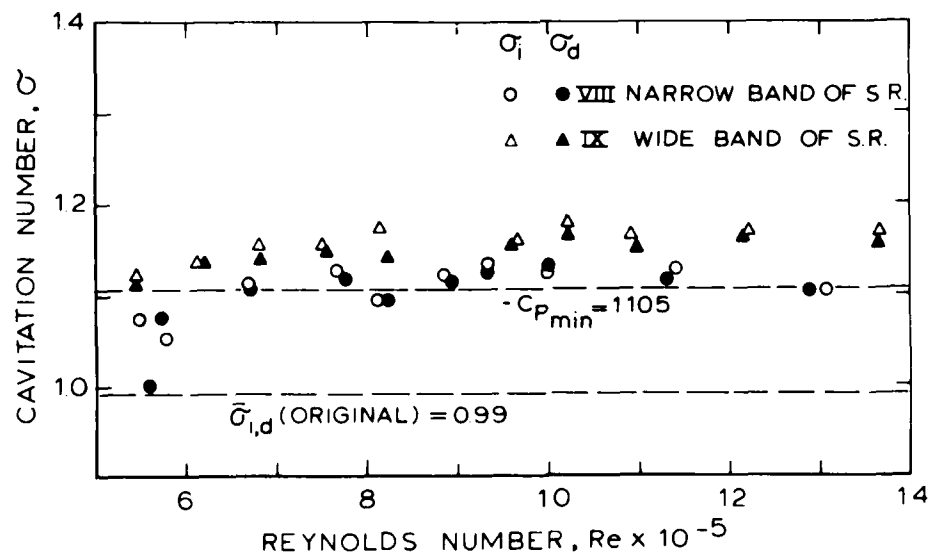


Figure 21



Figure 22

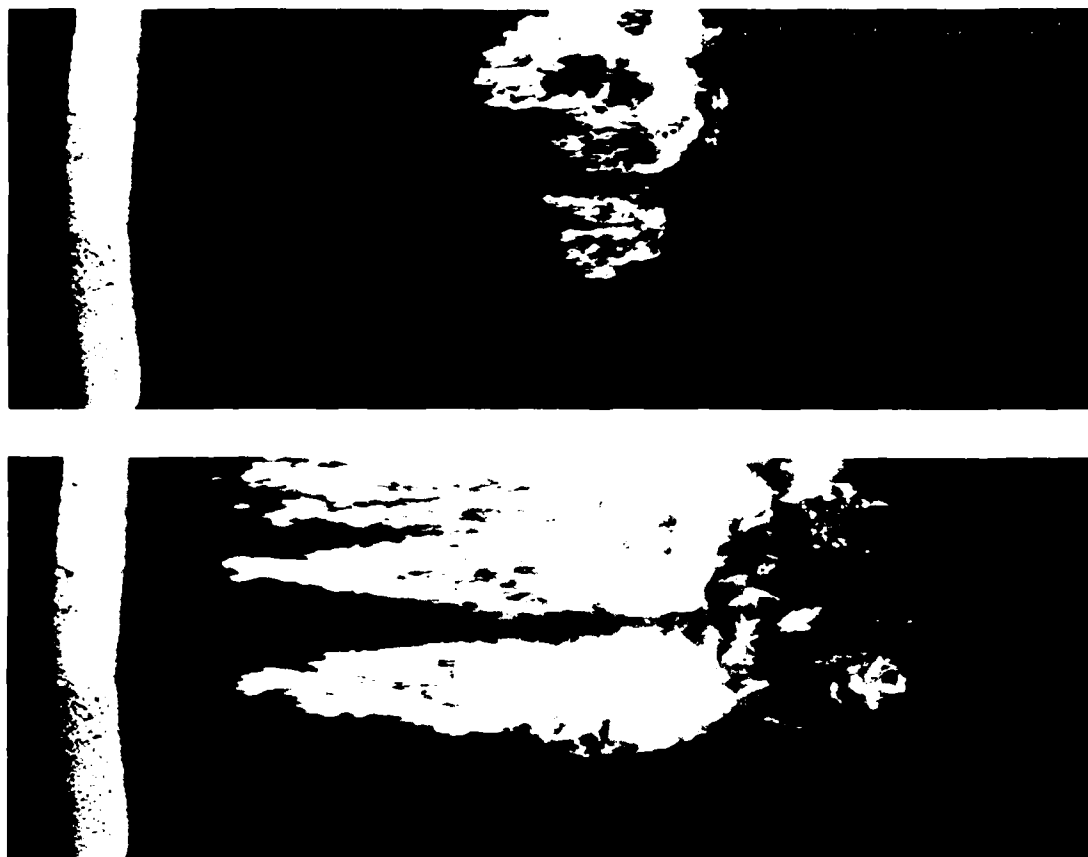


Figure 23

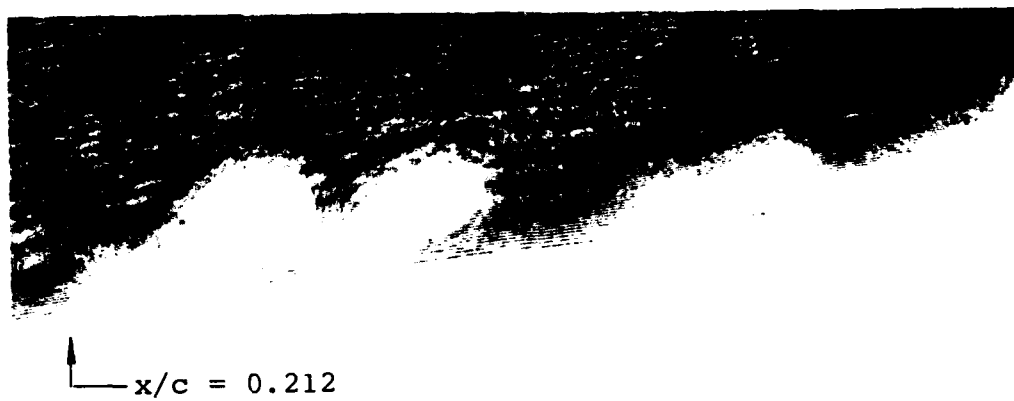


Figure 24

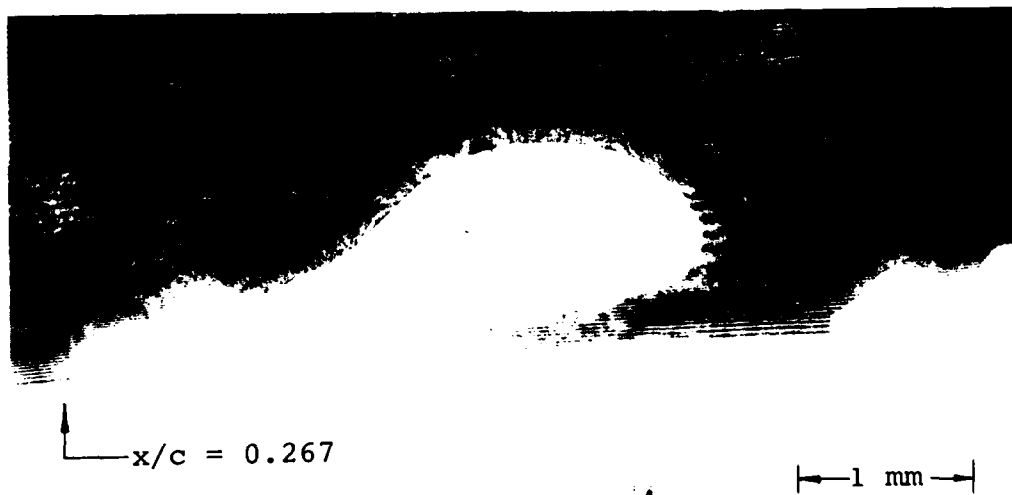


Figure 25



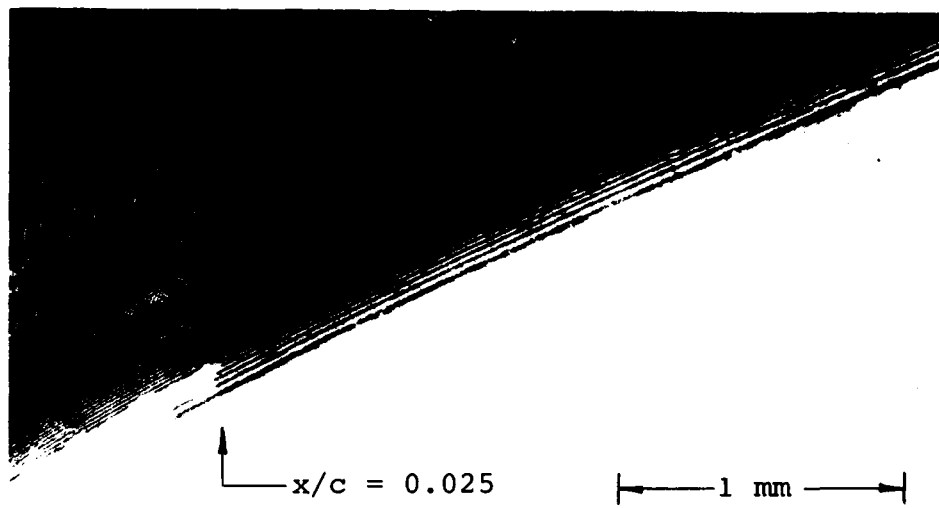


Figure 26

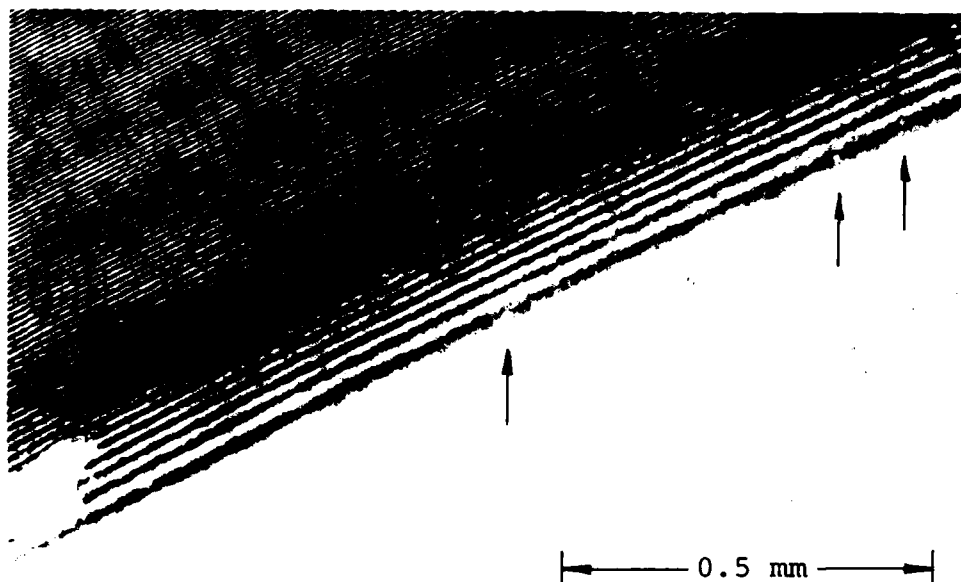


Figure 27

## Discussion

H. Tanibayashi (Mitsubishi Heavy Industries)

As a result of this work, particularly the throwing of light into the microstructure of boundary-layer flow as interacted with nuclei, I learned the effectiveness of the narrow-band sand roughness, which I think deserves application to the propeller experiments. But on looking at the cavity shape in Figure 22 centered around the midspan and not distributed as spots over the span, i.e., lack of two dimensionality, may I ask the authors if there are still some other factors to be considered about spanwise scale (effect) of cavities?

R. Sato (Ishikawajima-Harima Heavy Industries)

The authors must be congratulated for success in taking pictures to prove nuclei generation from sand roughness.

1. In the extension of this discovery, can we also find the growing process of nuclei, if we enlarge only the upstream part of the picture of the attached cavity, for example, in Figure 25?
- 2) I think many microbubbles are scattered in some range along the direction normal to the foil surface at the end of the minute cavity attached to the roughness. Why were only three bubbles very near the surface were shown in Figure 27?

R.L. Waide (Lockheed Missiles & Space Company)

1. The incipient cavitation numbers presented for most of the roughness models (between 40 and 90 percent of the data for each configuration) are greater than the dissonant cavitation number at the same Reynolds number. Most previous test data indicate that incipient conditions are lower than dissonant conditions. Is there any explanation for this new result? Can it be explained by the test procedure that preconditions the nuclei population in the entire tunnel?
2. The three nuclei shown in Figure 27 apparently are in the laminar sublayer of the boundary layer, while the cavitation attached to the roughness elements is as large as the full height of the boundary layer. Since these roughness-generated nuclei are apparently the source of the attached cavitation further downstream, the mechanism for their occurrence in the near-surface layer may be critical to the effectiveness of the roughness in affecting scale effects. If the

nuclei are injected farther from the wall, but still within the boundary layer, attached cavitation may not occur but traveling-bubble-type cavitation would be expected. Do you have an explanation for the apparently selective injection nuclei from the roughness cavitation into the near-surface layer?

V.H. Arakeri (Indian Institute of Science)

The inception observations have been conducted with several configurations, among which the method of leading-edge roughing has been utilized. Is the primary aim of adding leading-edge roughness to stimulate turbulent boundary layer? If so, then the roughness location has to be chosen extremely carefully so that cavitation inception characteristics of the basic profile are not altered. If roughness is located in the critical areas near the minimum pressure point, then the inception characteristics are determined by the combined effects of the profile geometry and roughness. In view of this, it is somewhat surprising that the authors find  $\sigma_i$  values greater than  $-C_{p_{min}}$  values. It would be interesting to know from the authors the reasons behind observed values of  $\sigma_i$  being greater than  $-C_{p_{min}}$  values.

S. Gowing (DTNSRDC)

The demonstration of the independence of traveling bubble cavitation from viscous effects discussed in this paper is significant.

The results of this study seem to vindicate a correlation of the inception index with the nuclei concentration. It might be possible that the index was higher for Configuration III than IV because of the greater number of nuclei, as opposed to the low-pressure fluctuations from the wire vortex shedding. Also, one would expect more nuclei to be generated by Configuration IX than VIII because the larger area of roughness and the inception index are indeed higher for Configuration IX than for VIII. Because the increasing number of nuclei with different configurations do not produce an asymptotic approach of the inception indices to  $-C_{p_{min}}$ , the conclusion of the study might be that the inception index is numerically related to the nuclei concentrations and does not approach  $-C_{p_{min}}$  in the limiting case of "sufficient" nuclei.

T.T. Huang (DTNSRDC)

The cavitation observed in this paper is limited to the traveling-bubble-type cavitation. The occurrence of cavitation events depends on microbubble population. Artificial seeding by electrolysis or roughness has been shown to reduce scale effect on cavitation. Most of your roughness devices were located near the leading edge. A beneficial advantage of using these roughness devices to reduce scale effect on

traveling bubble cavitation had been clearly demonstrated by the authors. Your fundamental finding is a significant contribution to our field of cavitation research.

For attached sheet cavitations near the leading edge of hydrofoils or propellers, most of your roughness devices are difficult to apply. However, distributed roughness with size around  $30\text{ }\mu\text{m}$  had been used at DTNSRDC. These distributed roughnesses were found to eliminate almost all the cavitation-scale effect on headforms and hydrofoils. The attached cavitations were observed around the location of the minimum pressure points, and the values of  $\sigma_i$  were found to be equal to the values of  $-\text{Cp}_{\text{min}}$ .

### Author's Reply

Jan H.J. van der Meulen and Ye Yuan-Pei

We agree with Dr. Tanibayashi's remark on the lack of two-dimensionality observed in the cavitation pattern of Figure 22. In this case the generation of nuclei by the roughness elements was not quite evenly distributed along the span. Another factor that might affect the two dimensionality of the cavitation pattern is the sidewall boundary layer (Jacobs, 1980). To eliminate this influence as much as possible, the present study was concerned with the central part of the hydrofoil only.

With regard to Dr. Sato's questions on the growth of nuclei, in analyzing the relevant hologram we did observe nuclei ahead of the cavity shown in Figure 25. However, to study the actual growth of such nuclei it would be necessary to make a series of holograms at short time intervals, in other words, to use high-speed holocinematography. The application of this technique is described by Lauterborn (1979). Dr. Sato and Mr. Waid both raise questions on the interpretation of Figure 27. In the hologram it was observed that the cavity did not only generate nuclei in the viscous sublayer but also in the outer boundary layer. We agree with Mr. Waid's suggestion that nuclei generated in the viscous sublayer lead to attached bubble cavitation, whereas nuclei generated farther away from the wall lead to traveling-bubble cavitation.

The observation, as pointed out by Mr. Waid, that in a considerable number of cases  $\sigma_i$  was found to be slightly larger than  $\sigma_d$  has, in our opinion, no physical significance. In performing these measurements,  $\sigma_d$  has always been measured first. Human factors involved in attempting to apply the well-known 50-percent criterion for inception may well have caused certain discrepancies.

Dr. Arakeri emphasizes the importance of the roughness location relative to the minimum pressure point. The present study has shown that stimulating a turbulent boundary layer should not be regarded as the primary aim of adding sand roughness in the case of bubble cavitation inception. In the case of sheet cavitation, where the minimum

pressure point is usually located near the leading edge of the foil, the situation is not yet clear. We do not know the reason for the fact that  $\bar{\sigma}_{i,d}$  was found to be somewhat larger than  $-C_{p_{min}}$  for configuration IX. We expected  $\bar{\sigma}_{i,d}$  to be equal to  $-C_{p_{min}}$ . Mr. Gowing suggests that it could be due to having a greater number of nuclei generated by configuration IX than VIII. However, an analysis of the relevant holograms showed that the number of nuclei generated by configuration VIII was actually greater than for configuration IX.

Dr. Huang's finding that distributed roughness was able to eliminate scale effects in the case of attached sheet cavitation deserves full attention. We are anxious to learn more about the detailed test results and the mechanisms involved.

## References

- Jacobs, P.P. (1980). A method of correcting for the effects of the sidewall boundary layer in two-dimensional airfoil testing. Pennsylvania State University Applied Research Laboratory Report No. TM 80-44.
- Lauterborn, W. (1979). Cavitation and coherent optics. Proceedings of First International Conference on Cavitation and Inhomogeneities in Underwater Acoustics, Göttingen, 3.

# The Role of Microbubbles on Cavitation Inception on Head Forms

The Catholic University of America  
Washington, D.C. 20064

S. Gowing and Y.T. Shen

David W. Taylor Naval Ship Research and Development Center  
Bethesda, Maryland 20084

## ABSTRACT

Water tunnel observations of the inception of cavitation on headforms and hydrofoils have shown a wide variation of results obtained at different testing facilities. Free stream microbubbles are known to play a significant role in the cavitation inception process. To quantify the role of these microbubbles, a light scattering instrument was used to measure the microbubble distribution in the three Variable Pressure Water Tunnels at DTNSRDC. At the same time, cavitation observations were made on headforms having different boundary layer characteristics. A new set of parameters based on bubble dynamics is used to parameterize the inception problem. A functional relationship is given that correlates the cavitation inception index with the surface tension parameter and the bubble blowup time parameter. The analysis shows that a general decrease in the cavitation inception index with a reduction in the test velocity is a result of the change in the ratio of the internal gas pressure to the equivalent surface tension pressure of the microbubbles in the fluid. The group effect of the microbubble spectrum on the inception of cavitation is discussed. In general, the parameters show that cavitation of large-scale, high-speed prototype systems is largely independent of the size distribution of the available microbubbles, whereas small scale model systems operating at low speed can cavitate only when a narrow band of microbubble sizes is available.

## NOMENCLATURE

$C$	= diameter of headform or chordlength of hydrofoil
$C_p$	= $(P - P_{wo}) / (\rho U_o^2 / 2)$ , pressure coefficient
$C_{pmin}$	= minimum pressure coefficient on flow boundary
$C_{pc}$	= minimum pressure coefficient inside the vortex core
$C_{ps}$	= minimum pressure coefficient inside laminar separation zone
$N$	= number of microbubbles
$P$	= absolute local pressure
$P_{min}$	= absolute minimum local pressure
$P_{wo}$	= absolute ambient pressure
$P_{woi}$	= absolute ambient pressure at cavitation inception
$\Delta P_{min}$	= $P_{min} - P_{wo}$ , maximum pressure drop
$P_{ao}$	= initial partial pressure of air inside the bubble
$P_{go}$	= total initial gas pressure inside the bubble
$P_{\sigma o}$	= $2\sigma/R_o$ , initial pressure due to surface tension
$P_v$	= vapor pressure of fluid
$R, R_o$	= bubble radius and initial radius
$R_e$	= Reynolds number
$T$	= $t_u/t_b$ , blowup time parameter
$U_o$	= mean flow velocity
$X, Y$	= horizontal and vertical coordinates normalized by $C$ , respectively

- $\Gamma$  =  $\mu(\rho|\Delta P_{\min}|)^{-0.5}/R_o$ , viscous parameter  
 $\Pi, \Pi_i$  =  $P_{wo}/|\Delta P_{\min}|, P_{woi}/|\Delta P_{\min}|$ , bubble cavitation parameters  
 $\psi$  =  $P_{wo}/P_{\sigma o}$ , surface tension parameter  
 $t$  = time  
 $t_u$  =  $C\beta/(1-C_{pmin})^{0.5} U_o$ , characteristic time for the bubble to pass through the low pressure zone.  
 $t_b$  =  $10R_o/U_o (-C_{pmin}/2)^{0.5}$ , characteristic time of blowup  
 $\alpha$  = percent saturation of gas in liquid at standard temperature and pressure  
 $\alpha_o$  = percent saturation of gas under conditions in the test section of water tunnel  
 $\beta$  = percent of C in which  $C_p/C_{pmin} \geq 0.95$   
 $\eta$  =  $R/R_o$ , normalized bubble radius  
 $\mu$  = viscosity of liquid  
 $\rho$  = mass density of liquid  
 $\sigma$  = surface tension of liquid  
 $\sigma_i$  =  $\frac{P_{woi} - P_v}{\frac{1}{2}\rho U_o^2}$ , incipient cavitation index  
 $\tau$  =  $\left(\frac{|\Delta P_{\min}|}{\rho}\right)^{0.5} \cdot \frac{t}{R_o}$ , normalized time



## INTRODUCTION

Most heavily loaded hydrofoils or propellers will develop tip vortex and surface cavitation at high speed. The occurrence of cavitation leads to undesirable changes in hydrodynamic performance, noise generation, and physical damage from vibration and erosion. Therefore, the ability to predict the occurrence of cavitation becomes an important engineering problem. Because of the complexity of physical processes involved with cavitation inception, the prediction of cavitation performance has relied heavily on model experiments and extrapolation of the results to full scale. Unfortunately, the physics involved in the inception process have not been fully understood.

It has often been observed that cavitation takes a variety of forms which may differ from facility to facility with a similar model or even the same model. The famous example is the testing of the ITTC (International Towing Tank Conference) standard headform. Tests on this flat-faced ellipsoidal body were carried out in many different laboratories throughout the world. Measured cavitation inception indices on this single headform ranged dramatically from 0.4 to 1.0 [1]. Even the appearance of the cavitation varied, some forms looking totally dissimilar from one another. These apparently chaotic results were clearly pointed out by Lindgren and Johnson [2] and further discussed by Acosta and Parkin [3].

Parkin and Kermeen were the first to show clearly in their photographs that cavitation on a hemispherical headform [4] was preceded by a region of microbubbles which grew in the boundary layer. Subsequent works by Arakeri [5] and Arakeri and Acosta [6] showed that these microbubbles were associated with a zone of laminar flow separation.

Ripkin and Killen [7], were the first to measure microbubble size distribution and demonstrated the importance of microbubbles for certain types of cavitation. Subsequent work at California Institute of Technology [8], Pennsylvania State University [9,10] and DTNSRDC [11,12] has shown the dependence of traveling bubble cavitation on microbubbles. However, the size range of traveling microbubbles that contributes to the explosive growth and collapse of cavitation is not adequately known.

In order to apply measurements of traveling bubble cavitation to the prediction of full-scale cavitation performance, the size distribution of free bubbles in laboratory testing facilities and in the sea must be measured. Work to characterize the influence of free bubbles on cavitation at sea is currently being undertaken at DTNSRDC. Presently, two optical techniques have been developed for nuclei measurement [13]. The holographic technique produces a hologram of a known volume of water from which the concentrations of different diameter nuclei are counted. The light scattering technique utilizes the light scattered from individual nuclei passing through a light beam to determine their size. The light scattering device developed by Ling was used in this investigation. A brief description of this device is given in Reference [13].

The present paper presents the measured microbubble distributions in the 12, 24, and 36-inch Variable Pressure Water Tunnels at DTNSRDC and their influence on the inception of cavitation on two headforms.

One of the headforms was hemispherical, and under all test conditions experienced laminar separation and a decrease in surface pressures downstream of the minimum pressure location. As will be shown below, when sufficient microbubbles were present, cavitation inception of the traveling bubble type occurred near the minimum pressure location; for reduced microbubble content, cavitation inception of the ring type occurred downstream of the minimum pressure location in the separation region.

The second headform was a blunt cylindrical headform which experienced turbulent separation at its leading edge, and under all test conditions the pressure coefficient distribution on the headform remained essentially unchanged. Cavitation inception for all microbubble populations was of the vortex type. Within the range of test conditions, no direct effect of Reynolds number on the flow regime or the pressure distribution was evidenced.

Although the mechanics of cavitation has fascinated scientists for over a century, two fundamental aspects of the problem still remain unresolved; namely, the mechanics of the inception of cavitation and the mechanics of erosion by cavitation. There is a general lack of proper parameters for defining the inception of cavitation as well as a lack of knowledge concerning the high energy physics associated with the implosive collapse. It is the purpose of this paper to clarify the former problem.

Historically, the inception of cavitation has been linked to the boiling or outgassing phenomenon. Boiling is an evaporative process which is initiated when a liquid is heated or the absolute ambient pressure  $P_{wo}$  is lowered below the vapor pressure of the liquid  $P_v$ . Outgassing is a diffusive process which is initiated when the liquid becomes supersaturated with dissolved gases. Therefore, it is customary to parameterize the cavitation inception by an index defined as

$$\sigma_i = \frac{P_{wo} - P_v}{\rho U_o^2 / 2} \quad (1)$$

where  $U_o$  is the reference ambient flow velocity and  $\rho$  is the mass density of the fluid. The term  $P_{wo} - P_v$  of Equation 1 represents the excess static pressure that prevents evaporation or outgassing, while the denominator  $\rho U_o^2 / 2$  represents the dynamic pressure of the flow system that can produce low pressure for cavitation. For most physical problems involving cavitation over headforms and hydrofoils, however, the inception of cavitation is due to the relatively faster process of direct expansion of the precompressed, noncondensable, microair bubbles that persist in all real fluids [14]. That is, the initial equilibrium gas pressure  $P_{go} = P_{ao} + P_v$  in the microbubbles is responsible for the blowup when the external balancing pressure is reduced, where  $P_{ao}$  is the partial pressure of air in the bubble. More precisely, it is the net internal pressure  $P_{ao} + P_v - P_{so} = P_{wo}$  that is responsible for the fast blowup process, where  $P_{so}$  is the pressure due to the surface tension,  $P_{wo}$  is the ambient pressure and the subscript o indicates the initial

equilibrium condition. Both the evaporative and diffusive processes are considered to be too slow to have a direct contribution to the dynamic processes; they may, however, have a strong influence on the initial size and concentration of bubbles in the fluid system which in turn will affect the cavitation. This is what makes the subject of cavitation inception such a difficult and complex problem. With our present capability to measure the size concentration of microbubbles, we shall discuss the microbubble effect on the inception of cavitation.

From the preceding discussion it is clear that the parameter that influences the potential blowup of microbubbles is  $P_{wo}$  and not  $P_{wo} - P_v$ . Fortunately,  $P_v$  for most physical problems at ambient temperatures and pressures is negligible with respect to  $P_{wo}$ . For example, in the case of water at atmospheric pressure, the ratio of  $P_v/P_{wo}$  is approximately 0.02. However, for certain low speed water tunnel tests  $P_v$  may no longer be small with respect to the low ambient pressure  $P_{wo}$  used in the tunnel. In this case, both evaporative and outgassing processes may become important. It is the lowering of the ambient pressure on the flow boundary by the dynamical flow system  $C_{pmin} (\rho U_o^2/2) = P_{min} - P_{wo} = \Delta P_{min}$  that is responsible for the cavitation process, where  $C_{pmin}$  is the minimum pressure coefficient of the flow system,  $P_{min}$  is the absolute minimum pressure over the flow boundary, and  $\Delta P_{min}$  is the corresponding maximum pressure drop. It will be shown later that a meaningful nondimensional pressure parameter can be expressed in the form

$$\Pi = \frac{P_{wo}}{-C_{pmin} \rho U_o^2/2} = \frac{P_{wo}}{|\Delta P_{min}|} \quad (2)$$

Note that if  $P_v \ll P_{wo}$ , the  $\Pi$  term can be related to the usual cavitation index  $\sigma_i$  as  $\Pi_i = \sigma_i/(-C_{pmin})$ , where the subscript  $i$  indicates the state of incipient cavitation.

Since the inception of cavitation is a problem associated with bubble mechanics, it will be shown that a second major pressure parameter for the problem is the surface tension parameter defined as

$$\psi = P_{wo}/P_{\sigma\sigma}. \quad (3)$$

If this parameter is small ( $\psi < 10$ ), the surface tension effect will strongly inhibit the blowup of microbubbles. The influence of  $\psi$  on cavitation may sometimes have been mistakenly attributed to an apparent dependency of the cavitation inception index on the Reynolds number of the flow.

A third parameter, a characteristic time, can be devised to parameterize the response of the microbubble to the pressure change the bubble experiences as it is convected along the flow boundary. It is defined as the blowup time parameter

$$T = t_u/t_b, \quad (4)$$

where  $t_b$  is the characteristic blowup time of the microbubble and  $t_u$  the

characteristic time for the bubble to traverse the low pressure zone of the flow boundary. It will be shown later that this parameter can be used to relate the dynamic response of the bubbles to the  $\Pi_i$  and  $\psi$  parameters. If  $T$  is very large, the index of cavitation will be insensitive to the model size.

A fourth parameter  $\alpha$  is the percent of saturation of noncondensable gases in the fluid. It will be shown later that this parameter has a significant influence both on the distribution and the mechanics of microbubbles. Another important parameter is the equilibrium condition of the microbubble approaching the headform. Computations by Ling [14] showed that large size bubbles will exhibit oscillatory motion when the bubbles are subjected to a step pressure drop, such as that encountered by bubbles passing through the contraction nozzle of a water tunnel. This initial oscillating motion of the large bubbles will then have a significant effect on the bubble blowup characteristics.

It is clear that the inception of cavitation is too complex a phenomenon to be parameterized by a single  $\sigma_i$  parameter. Thus with proper parameterization many unresolvable problems may now be clarified.

In order to quantify the parametric values for the inception of cavitation, it is necessary to define the state of incipient cavitation. In general, the unstable blowup of microbubbles is considered to be the state of cavitation inception while small stable bubble oscillations are not. A more specific definition becomes a difficult subject. For practicality in the present analysis, we shall define inception of cavitation as the condition in which bubbles blow up to more than 10 times their original equilibrium size and reach a visible size greater than 0.5 mm in diameter. The criterion for blowing up 10 diameters is related to the ability of the bubble to produce a significant collapse pressure. A more customary specification is to define the inception condition by a minimum number of cavitation events per unit time. This is related to the number density of microbubbles and has no direct connection with the mechanics of cavitation. We shall see in the following sections how these parameters and specifications are interrelated.

#### STATEMENT OF THE PROBLEM

It is well known that all real fluids are not absolutely pure, instead they generally contain a significant amount of solid nuclei and noncondensable gas in both free and dissolved states. Hence, it is reasonable to assume that the inception of cavitation should mainly depend on the mechanics of microbubbles, and we shall use it as a base for all subsequent analysis. This paper will be limited to the treatment of microbubbles moving over hydrodynamically smooth boundaries. Cavitation involving substantial evaporative and diffusive processes, and cavitation involving rough surfaces and other special conditions are considered as special problems and not treated in this paper. Individual bubble mechanics will first be treated and then be followed with

the discussion of the effects of groups of microbubbles. The computed results will be compared with the experimental observations in the DTNSRDC water tunnels.

### Governing Equations

The basic equation governing the dynamics of a spherical microbubble can be expressed by the Rayleigh-Plesset equation given as, Ling [14]

$$\eta\ddot{\eta} + \frac{3}{2}\dot{\eta}^2 + 4\Gamma\frac{1}{\eta}\dot{\eta} = \Pi\left[\left(1 + \frac{1}{\psi}\right) \cdot \frac{1}{\eta^{4.2}} - \frac{1}{\psi\eta} - 1\right] + \frac{P(\tau)}{|\Delta P_{\min}|}, \quad (5)$$

where the normalized bubble radius  $\eta$  is defined as  $R/R_o$ ;  $R$  is the radius of the air bubble and subscript  $o$  indicates the initial state;  $\ddot{\eta}$  and  $\dot{\eta}$  are the normalized bubble wall acceleration  $d^2\eta/d\tau^2$  and velocity  $d\eta/d\tau$ , respectively; and the time  $t$  is normalized as

$$\tau = \left(\frac{|\Delta P_{\min}|}{\rho}\right)^{0.5} \frac{t}{R_o}. \quad (6)$$

The normalized viscous parameter is defined as  $\Gamma = \mu(\rho|\Delta P_{\min}|)^{-0.5}/R_o$ , where  $\mu$  is the viscosity of the fluid; and  $P(\tau)$  is the ambient pressure the bubble experiences as a function of the normalized time  $\tau$ . The pressure parameters  $\Pi$  and  $\psi$  are defined by Equations 2 and 3, respectively. Equation 5 can be solved numerically for any combination of the  $\Pi$  and  $\psi$  parameters and the pressure time history  $P(\tau)$  that the microbubble experiences as it is convected along a given flow boundary. Unless the fluid is very viscous compared with water, the  $\Gamma$  parameter does not play a significant role in the present problem.

Equation 5 does not admit a general solution for the inception of cavitation. The  $\Pi_i$  parameter has to be solved by an iterative procedure for each individual case. However, it will be shown later that within a practical range of parametric values a functional relationship among  $\Pi_i$ ,  $\psi$ , and  $T$  parameters can be obtained, see Figure 1. Detailed discussion of this function will be given in the following sections. For the following studies, microbubbles flowing over the flow boundary were assumed to be convected at the speed dictated by the potential flow field with no consideration for the boundary layer effect. Thus, the ambient pressure  $P(\tau)$ , which the bubble experiences as it slides along a given flow boundary, can be obtained directly from the given distribution of pressure coefficient  $C_p$  after proper transformation of the space and time coordinates.

It will be shown later that the  $T$  parameter in Equation 4 can serve as a useful variable relating the bubble mechanics to the external forcing function  $P(\tau)$ . We define the characteristic time  $t_b$  for the microbubble to blow up as the time for it to reach an unstable size of  $\eta > 3$ .

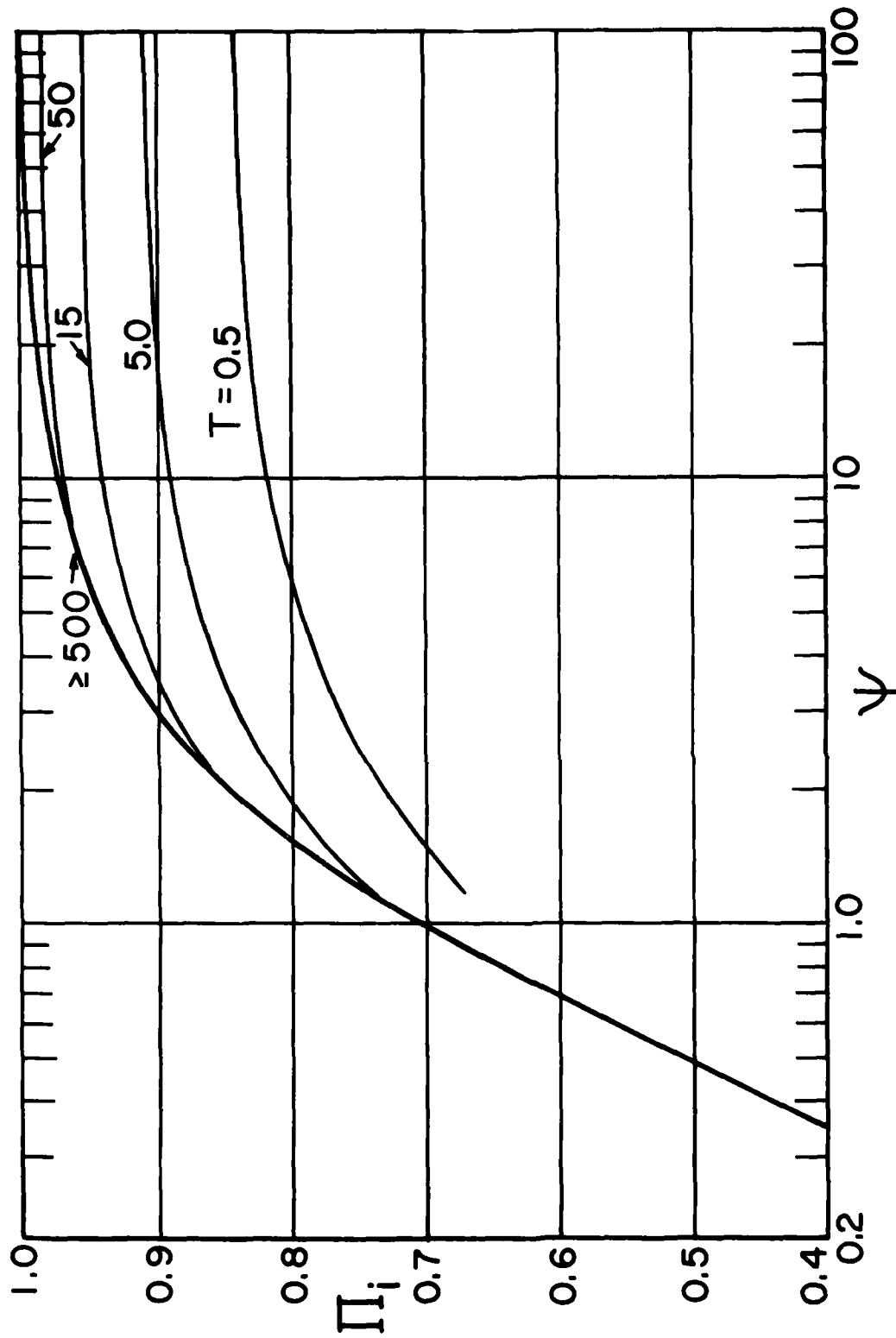


FIGURE 1. Cavitation inception index  $\Pi_i$  as function of  $\psi$  and  $T$  parameters.

For the case of a step change in  $\Delta P_{\min}$  the normalized time  $\tau$  for the bubble to blow up was found to be approximately 10, see Ling [14]. Therefore, from Equation 6 we have  $t_b = 10 R_o (|\Delta P_{\min}|/\rho)^{-0.5} = 10 R_o/U_o (-C_{p\min}/2)^{0.5}$ . We further define a semiempirical characteristic time the bubble is subjected to a low ambient pressure of  $C_p/C_{p\min} \geq 0.95$  as  $t_u = C\beta/(1 - C_{p\min})^{0.5} U_o$ , where  $C$  is the diameter of a headform or the chord length of a hydrofoil,  $\beta$  is the fraction of chord length in which  $C_p/C_{p\min} \geq 0.95$ , and  $(1 - C_{p\min})^{0.5} U_o$  is the effective convecting velocity in the low pressure zone. Therefore, the blowup time parameter  $T$  can be expressed as

$$T = t_u/t_b = \frac{\beta C}{14 R_o (1 - \frac{1}{C_{p\min}})^{0.5}} \quad (7)$$

The numerical solutions from a few headforms and hydrofoils show that for a characteristic time  $T$  greater than 40 the physical size of the model becomes unimportant in dealing with the scale effects of traveling bubble type cavitation inception. This is because there will be sufficient time for the bubble to blow up. Note that the rate of growth required to reach a blowup state for a large bubble is slower than for a smaller bubble as indicated by the functional form of  $\tau$  in Equation 6. Hence, a large bubble may suffer from a lack of time to blow up on a small model. As an example, for a typical hydrofoil with  $C_{p\min} = -1.0$ ,  $\beta = 0.1$ , and  $R_o = 0.001$  cm, a minimum model chord size of  $C$  greater than 8 cm is required in order to achieve  $T$  greater than 40 and hence avoid size scaling effects.

#### TESTING FACILITIES AND EXPERIMENTAL SETUP

Cavitation observations on two different headforms representing different boundary layer characteristics were carried out in the DTNSRDC 12-, 24-, and 36-inch variable-pressure water tunnels.

The 12-inch water tunnel is equipped with an open jet test section. This tunnel has a bypass deaeration system that provides simultaneous water filtration and deaeration to as low as 2% of saturation at standard temperature and pressure (STP). The maximum testing velocity for this tunnel is 7.2 m/s.

Both the 24- and 36-inch water tunnels are equipped to operate either as an open jet or a closed jet testing system. For the present investigation, only the closed jet test sections were used. The 24-inch water tunnel does not have a bypass filtration/deaeration circuit as does the 12-inch water tunnel. Deaeration is accomplished by pulling a vacuum on a free surface inside the tunnel. The minimum attainable air content using this technique is about 25% of saturation at STP. The maximum operating speed is approximately 14 m/s.

The 36-inch water tunnel, unlike the 24-inch and 12-inch tunnels, was used with its bubble resorber in place. The resorber consists of an equivalent of four folded lengths of 24.4m long pipe whose bottom elevation is 35 m below the test section. The long residence time of the bubbles in the resorber combined with the resorber's high hydrostatic pressure are applied to drive the microbubbles into solution. This tunnel is also equipped with a deaerator. The minimum air content achieved is approximately 25% of saturation at STP. The maximum speed of this tunnel is 22 m/s.

A hemispherical headform and a blunt cylindrical headform were selected for the present investigation. All headforms used in the 12- and 24-inch water tunnels were manufactured from brass with the surface highly polished. The hemispheric headform was 7.6 cm in diameter, while the blunt headform diameter was 5.7 cm. Each headform was equipped with 12 piezometric taps for pressure distribution measurements. The headforms used in the 36-inch water tunnel were 10.2 cm in diameter and were made of plastic. No pressure taps were made for these models. The influence of surface materials on cavitation had been studied by Peterson [11]. So long as the headform is smooth, the surface material has no effect on bubble cavitation.

A pitot tube was used for monitoring the mean velocity  $U_0$ . The static tap of this tube provided the reference pressure for the mean flow-field. All pressure taps were connected to a bank of mercury manometers for monitoring the pressures. Alignment of the headform axis with the flow was checked by taking the pressure distribution measurements at different angular locations on the headform. All absolute pressure measurements were referred to the center line of the headform.

The general view of the microbubble detector used in this experiment is shown in Figure 2. It is based on a dark-field, specular-reflection technique to differentiate a solid particle from a microbubble [13]. Water was continuously withdrawn from the high pressure end of the water tunnel, just upstream of the flow contraction section, through a 2-inch plastic pipe to the bubble detector. The water was then returned through the downstream end of the test section. Since the pressure at the bubble detector was different from the pressure in the test section, this pressure difference was noted and a small correction for the measured bubble spectra was made based on the ideal gas law and bubble mechanics.

Measured bubble spectra obtained in the 12-, 24-, and 36-inch water tunnels are shown in Figure 3. The corresponding test conditions are given in Table 1. The influence of these microbubble spectra on cavitation inception will be discussed in the following section.



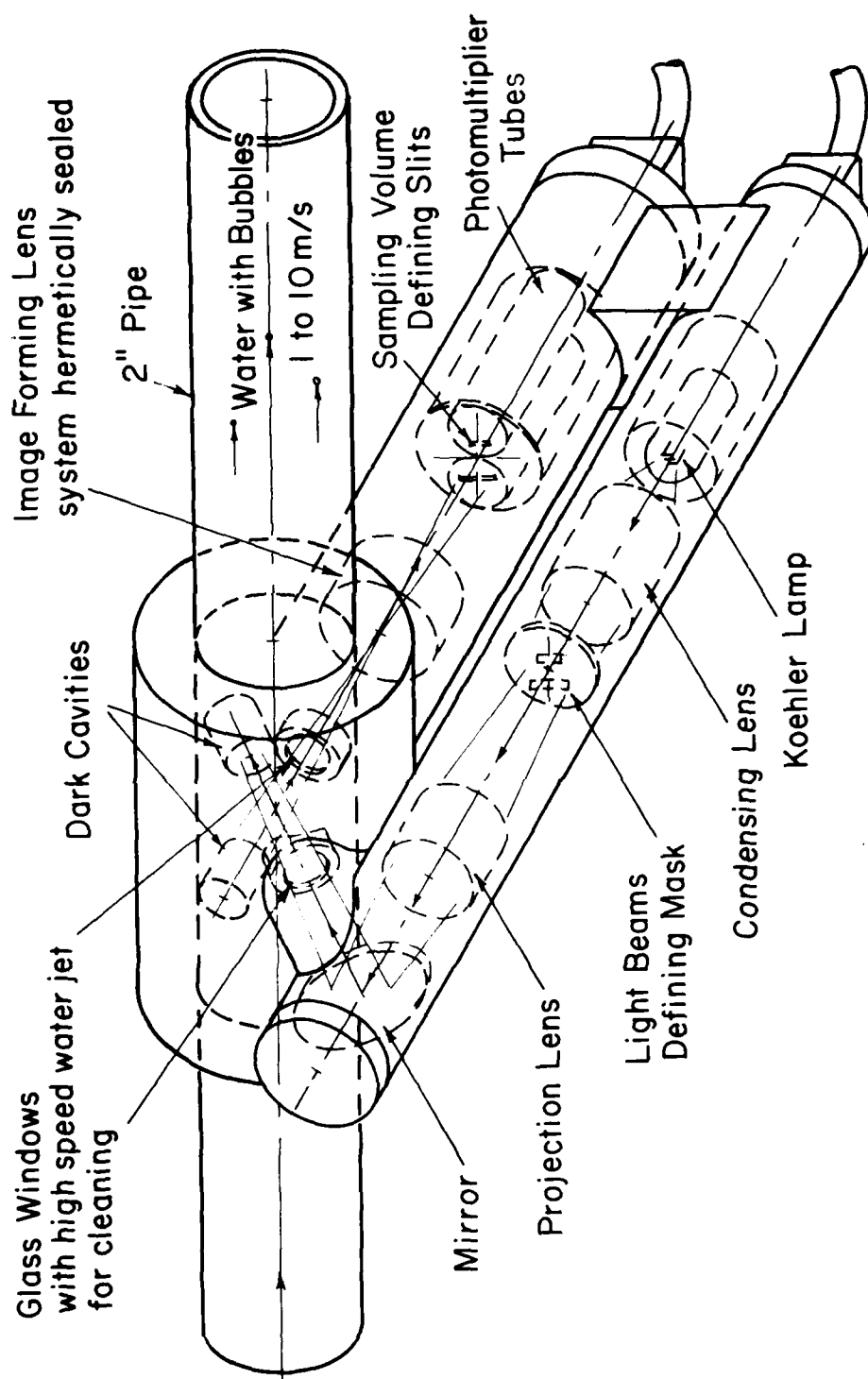


FIGURE 2. General view of microbubble detector. The detector has a sampling cross-sectional area of  $0.30 \text{ cm}^2$  and a sampling volume of  $0.012 \text{ cm}^3$ . It measures bubble size from  $R_0 = 5 \text{ }\mu\text{m}$  to  $200 \text{ }\mu\text{m}$  with a band broadening error of less than 5% for the large bubbles and a counting error less than 1% for a bubble concentration of less than  $10^7 \text{ bubbles/m}^3$ .

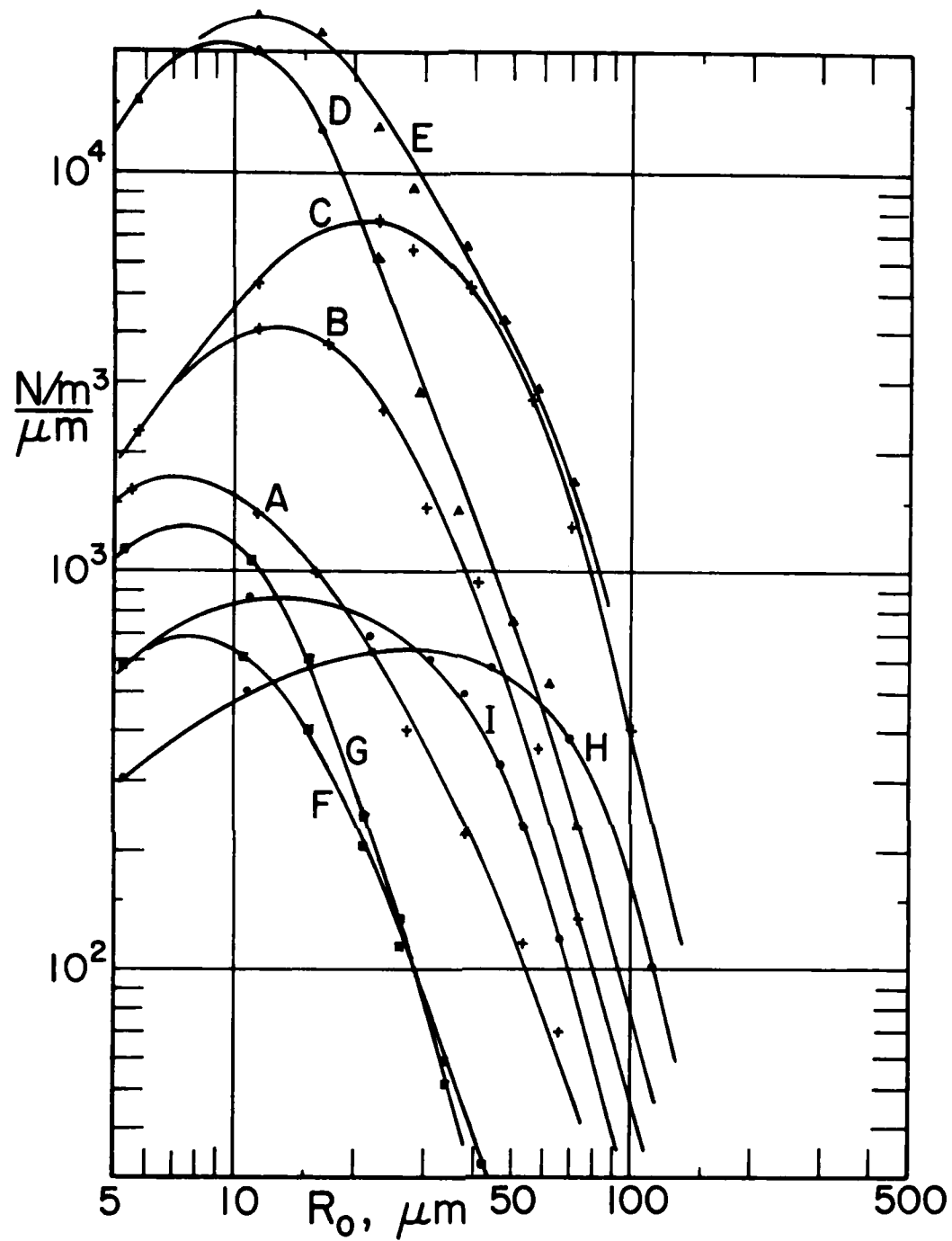


FIGURE 3. Measured bubble spectra. Curves A, B, C, H, and I are from the 12-inch water tunnel; Curves D and E are from the 24-inch tunnel, and Curves F and G are from the 36-inch tunnel. The corresponding water tunnel operating conditions are listed in Table 1.

TABLE 1. Test Parameters

Case	Test Facility	Tunnel Speed (m/s)	Tunnel Pressure at Test Section (atm)
A	12-in WT	7.2	0.17
B	12-in WT	6.8	0.16
C	12-in WT	6.9	0.19
D	24-in WT	13.8	0.68
E	24-in WT	13.6	0.69
F	36-in WT	6.1	0.31
G	36-in WT	21.3	3.76
H	12-in WT	5.6	0.42
I	12-in WT	6.8	0.55

## RESULTS AND DISCUSSION

The usefulness of the dynamic Equation 5 was first tested against data obtained experimentally by Van der Muelen [15], who tested a NACA 4412 hydrofoil section having a chord length of 7 cm. The computed potential flow pressure distribution for the hydrofoil at an attack angle of 0 degrees is shown in Figure 4. For the conditions of the test case, viscous effects are expected to be unimportant in the region of cavitation inception. For a mean flow speed of  $U_0 = 10$  m/s and a cavitation index of  $\sigma_i = 0.68$ , the solution of Equation 5 indicates that this test case corresponds to the critical conditions required for the blowup of a  $R_0 = 10$   $\mu$ m bubble. The corresponding values for the new cavitation inception parameters are  $\Pi_i = 0.86$ ,  $\psi = 2.3$ , and  $T = 57$ . Thus, it may be seen from Figure 1 that, the inception of cavitation is sensitive to changes in the value of the surface tension parameter about  $\psi = 2.3$  and insensitive to changes in  $T$  about  $T = 57$  which implies insensitivity to the size of the model. The relatively large traveling bubbles developed over the hydrofoil as predicted by the theory are shown in the lower part of Figure 4. It was further found that microbubbles in the range of  $10 \mu\text{m} < R_0 < 200 \mu\text{m}$  will all blow up and collapse almost with the same pattern; i.e., growing approximately to the same maximum size and collapsing at the same chord position. This phenomenon has also been reported by Kodama, et al [16]. The patterns of traveling bubble cavitation predicted are essentially the same as those observed experimentally by Van der Meulen [15, Figure 44] for the same flow condition but with a slightly higher  $\sigma_i$  index of 0.70.

Hemispherical Headform

We next study in detail the cavitation inception characteristics of a 7.6 cm diameter hemispherical headform. The computed and the measured pressure distributions for the headform are shown in Figure 5 as the continuous curve and data bars, respectively. Laminar flow separation was found to start at  $X = 0.46$  and reattach at  $X = 0.52$  to  $0.54$  depending on flow speed. The flow separation was measured using an oil paint technique, see Figure 6. The same result of flow separation was observed by Carroll [10].

For this specific problem, the computed results for  $\Pi_i$  are plotted as a function of the dimensional variables  $R_0$ ,  $U_0$ , and  $P_{woi}$  as shown in Figure 7. The nondimensional form of Figure 7 is given in Figure 1. We note that for a given test speed  $U_0$ , only a limited band of microbubble sizes can blow up. In general, smaller values of  $R_0$  are limited by the surface tension parameter  $\psi$ , while the larger values of  $R_0$  are limited by the blowup time parameter  $T$ . As an example, for a test speed of 10 m/s, with  $\Pi_i = 0.88$  or  $P_{woi} = 0.3$  atm, only a narrow band of bubble in the range of  $10 \mu\text{m} < R_0 < 100 \mu\text{m}$  will blow up. As the test speed is increased, the bubble cavitation parameter  $\Pi_i$  tends to approach 1.0 in the limit due to the blowup of small bubbles in the range of 1  $\mu\text{m}$  to

10  $\mu\text{m}$ . This is because of the large increase of  $P_{woi}$  with the increase of  $U_0$ , such that  $\psi = P_{woi}/P_{\sigma 0}$  becomes very large and the  $\Pi_i$  parameter becomes independent of the surface tension effect, see Figure 1. This general increase of  $\Pi_i$  or  $\sigma_i$  with the testing velocity is sometimes referred to as an apparent Reynolds number effect. For bubbles with  $R_0 > 50 \mu\text{m}$ , the reduced value of  $\Pi_i$  is constant and independent of the test velocity at large  $U_0$ . In this case, the T parameters for  $R_0 = 50 \mu\text{m}$  and  $100 \mu\text{m}$  are 7.2 and 3.6, respectively, see Figure 7.

It is important to note that in the range of  $\psi < 10$  where bubble blowing is sensitive to surface tension, with  $\Pi_i$  having a large slope  $d\Pi_i/dU_0$ , the bubble blowup is very distinct; i.e., the bubble blowup or no blowup condition is separated by a very small range of values of  $\Pi_i$  or  $\sigma_i$ . In the range of  $T < 20$  where bubble blowup is sensitive to the T parameter, with  $\Pi_i$  having a small slope  $d\Pi_i/dU_0$ , the blowup characteristic is not sharp; in this case a minimum bubble blowup size of 0.5mm in diameter and  $\eta > 10$  are defined as the state of blowup. We shall use Figure 7 as a basis for interpreting the test results obtained in the 12-, 24-, and 36-inch water tunnels.

As a first example, consider the maximum operating speed of  $U_0 = 7.2 \text{ m/s}$  in the 12-inch water tunnel. The bubble cavitation parameter  $\Pi_i$  was found to be 0.86, with  $P_{woi} = 0.17 \text{ atm}$  and the air content at the test section  $\alpha_0 = 27\%$  of saturation. It is found from Figure 7 that the bubble sizes involved in the blowup at this test condition are in the range of  $20 \mu\text{m} < R_0 < 100 \mu\text{m}$ . The computed locus of the blown up bubble diameter for these bubbles is shown as the dot-dashed curve in Figure 5. This pattern is generally confirmed by high speed photography. The measured bubble spectrum is shown in Figure 3 and marked as curve A. From this spectrum we found that there were approximately  $3 \times 10^4$  bubbles/ $\text{m}^3$  of  $R_0 = 20$  to  $100 \mu\text{m}$  bubbles. Considering that a 2 mm layer of water surrounding the headform was associated with the cavitation process, it may be shown that there will be approximately 100 events of cavitation per second. The inception point was called by visual observation under a strobe light when there was, on the average, one observed blowup event per second. The strobe light flashed for a duration of  $10^{-3} \text{ s}$  and ran at a maximum rate of 20/s. This rate was limited in order for the eyes to retain a frozen image. The blowup lifetime of a bubble was approximately 0.002 of a second. Thus, for a duration of 0.002s per event there would be two observable events per second. This value is about the same order of magnitude as we have observed on the model. In this test, high speed photography also shows occasional glassy sheet cavitation at the zone of laminar separation.

As a second example, we consider the case of a test speed of 6.8 m/s, with the  $\Pi_i$  parameter value increased to 0.89,  $P_{woi} = 0.16 \text{ atm}$  and  $\alpha_0 = 41\%$ . The inception condition was found not to be as sharply defined as in the first case. The measured bubble spectrum is shown as Curve B in Figure 3. There was a large increase in bubble concentration by a factor of 4 larger than in the previous case. This was probably due to cavitation of the tunnel impeller which tended to produce more microbubbles at low values of absolute tunnel pressure. From Figure 7, one notes that only large bubbles in the range of 40 to  $100 \mu\text{m}$  blow up, and the blowup condition was strongly limited by the influence

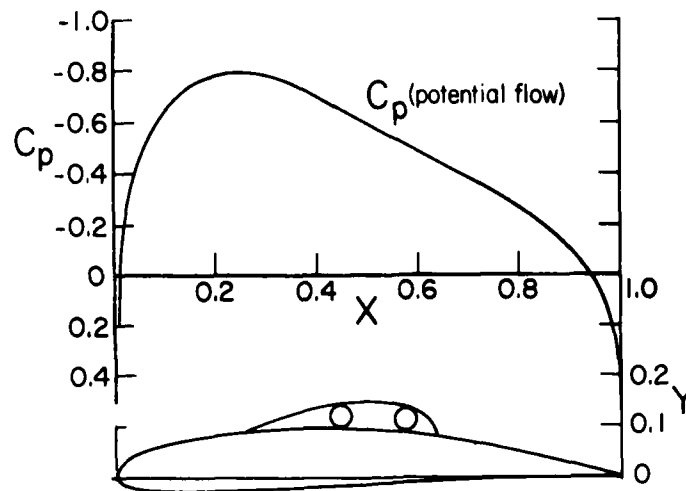


FIGURE 4. Pressure distribution over the top surface of NACA 00-4412 hydrofoil at 0 deg attack angle. Lower curve shows the locus of the bubble diameter for the cavitation inception of a  $R_0 = 10 \mu\text{m}$  bubble with  $U_0 = 10 \text{ m/s}$  and a chord of  $C = 7 \text{ cm}$ .

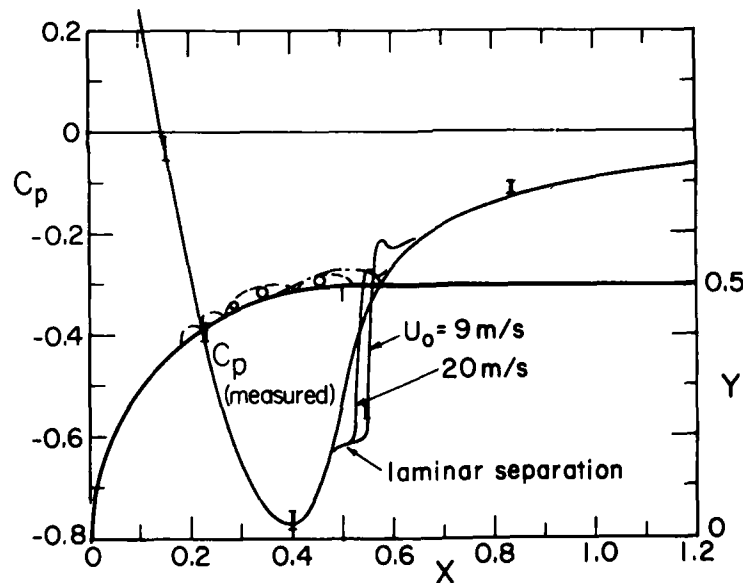


FIGURE 5. Computed and measured pressure distribution over a hemispherical headform for  $Re = 4 \times 10^5$  to  $10^6$ . Locus of bubble diameter for the cavitation of a  $R_0 = 50 \mu\text{m}$  bubble with an initial bubble oscillation of 50% of  $R_0$  and  $\Pi_i = 1.0$  is shown as the dashed curve. The cavitation of a  $R_0 = 10 \mu\text{m}$  with  $\Pi_i = 0.86$  is shown as the dot-dashed curve.

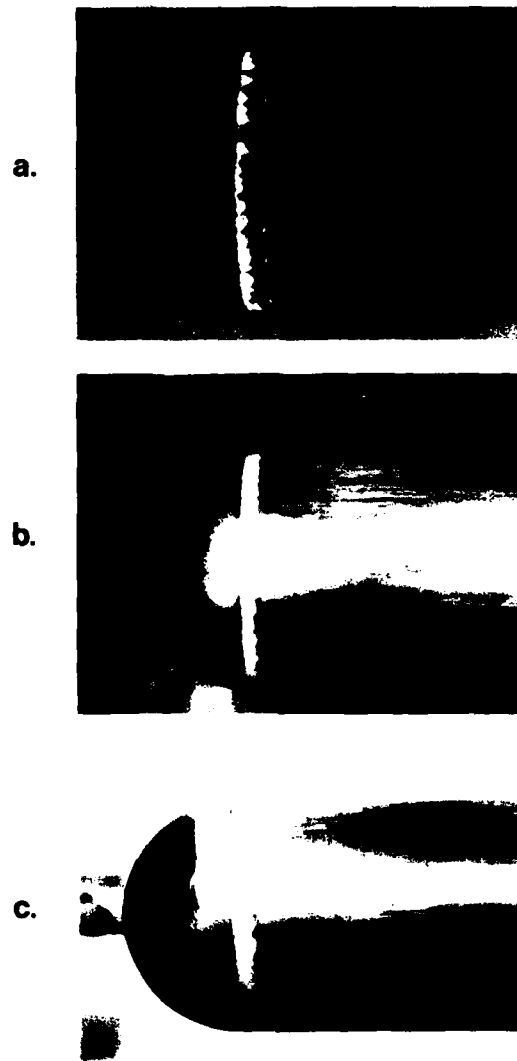


FIGURE 6. Visualization of the laminar flow separation on hemispherical headform using oil paint.

- a. In 12-inch water tunnel with  $Re = 4.6 \times 10^5$
- b. In 24-inch water tunnel with  $Re = 7.5 \times 10^5$
- c. In 36-inch water tunnel with  $Re = 1.7 \times 10^6$

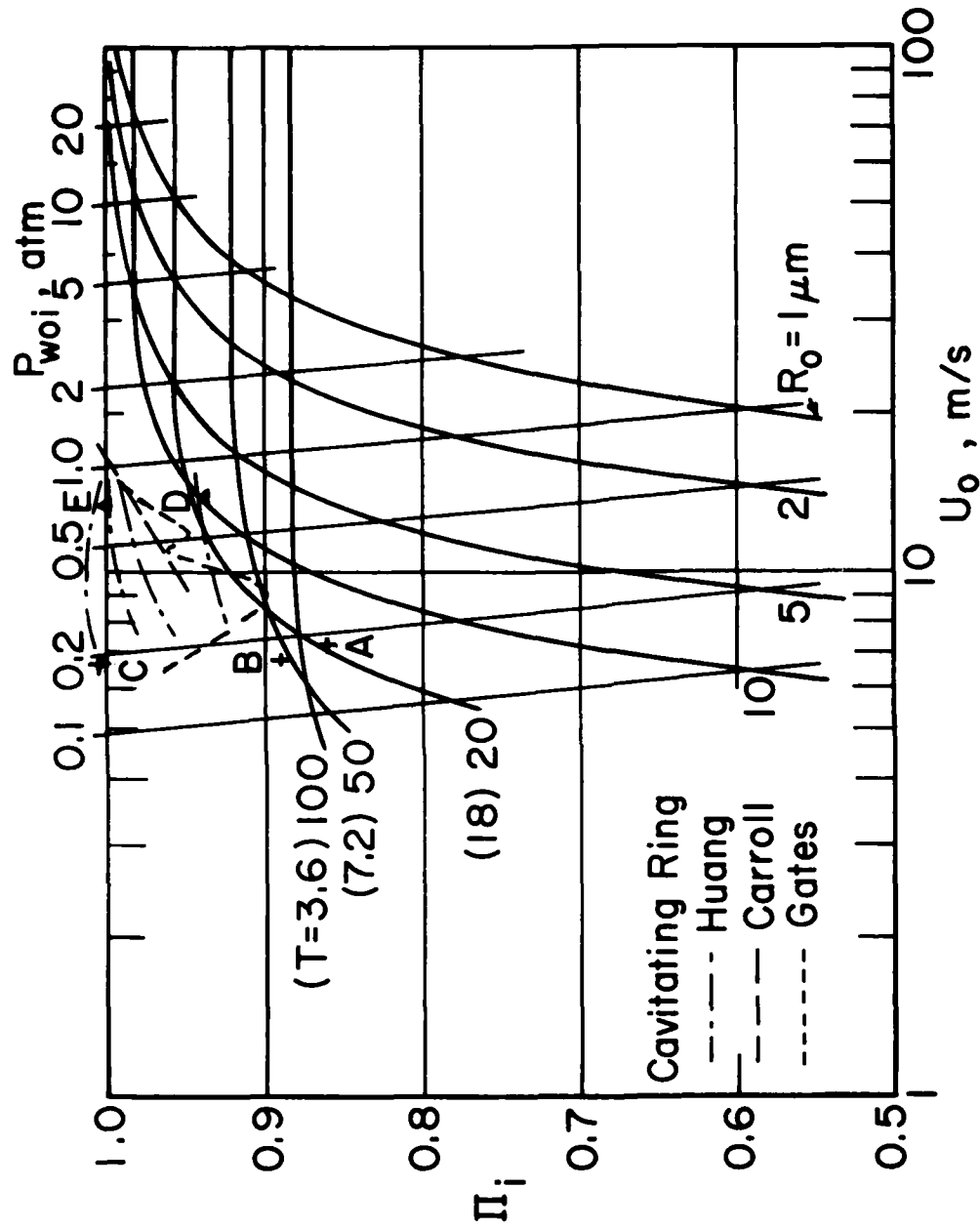


FIGURE 7. Bubble cavitation parameter  $\Pi_i$  as a function of  $U_0$ ,  $R_0$ , and  $P_{woi}$  for a hemispherical headform of 7.6 cm diameter. Alphabetic symbols indicate operating points for the corresponding bubble spectra given in Figure 3.



of the  $T$  parameter. Hence, the condition for cavitation was found not to be distinct, and it could be called over a range of  $\Pi_i$  values. The concentration of bubbles having values of  $R_0$  between 50  $\mu\text{m}$  to 100  $\mu\text{m}$  was found from Curve B of Figure 3 to be  $2 \times 10^4/\text{m}^3$ . Therefore, one could account for calling cavitation inception at a higher value of  $\Pi_i$  than in the preceding case.

As a third example, we consider the case with a test speed of 6.9 m/s and a near saturated air content of  $\alpha_0 = 80\%$ . The measured value of the  $\Pi_i$  parameter was 1.01 with  $P_{woi} = 0.19$  atm. Although the bubble spectra for this case shows a further large increase in the bubble concentration, as indicated by Curve C of Figure 3, it is seen from Figure 7 that no equilibrium bubbles of any size could have blown up under this testing condition. High speed photographs indicate that the cavitating bubbles appeared like regular traveling bubbles, but the cavitation occurs as far forward as  $X = 0.3$  measured from the tip of the headform. This is very far forward of the  $C_{pmin}$  location. The photograph shown in Figure 8 was taken at a  $\Pi$  value slightly lower than that at the inception condition. It is further noted that this photograph was taken after the flow visualization with the thin oil paint in the laminar separation zone still visible on the headform surface. Simulation by Equation 5 of a large  $R_0 = 50$   $\mu\text{m}$  bubble with  $\Pi_i = 1.0$  and an initial oscillation of 50% of its initial size was found to blow up. On the other hand a smaller oscillation will cause no blowup. The locus of the oscillating bubble diameter is shown in Figure 5 as the dashed curve. From Curve B of Figure 3, the concentration of bubbles in the size range  $R_0 = 50$   $\mu\text{m}$  to 100  $\mu\text{m}$  was  $1.5 \times 10^5/\text{m}^3$ . Again there would be enough bubbles to cavitate under this mode and for  $\Pi_i$  to be measured at 1.01.

It is postulated that the initial oscillatory mode of the large bubbles could be caused by the step pressure drop when a bubble moves from the high pressure section of the tunnel into the low-pressure test-section of the tunnel [14]. For this test, the maximum upstream tunnel pressure  $P_{wo}$  was at 0.84 atm and the low pressure in the test section was at 0.19 atm. Hence, the equivalent  $\Pi$  parameter,  $P_{wo}/|\Delta P_{min}| = 1.3$ , could cause large bubbles upstream to continue to oscillate at a frequency of approximately 29 kHz and an amplitude of more than 1.5 times their equilibrium radius at the headform. Smaller bubbles, due to their higher frequency of oscillation and damping, would have no significant oscillation left when they reached the headform. Thus, if the large microbubble concentration is greater than  $10^5/\text{m}^3$ , their nonsteady oscillation mode can also affect the cavitation index. It is noted that the maximum theoretical value of bubble cavitation parameter  $\Pi_i$  is 1.0. However, experimental values of  $\Pi_i$  greater than 1.0 were observed under many test conditions. It is believed that the blowup of large size bubbles due to initial oscillation is the reason for experimental values of  $\Pi_i$  to be greater than 1.0.

The same hemispherical headform was tested in the 24-inch cavitation tunnel. Consider a case with  $U_0 = 13.8$  m/s,  $\Pi_i = 0.94$ ,  $P_{wo} = 0.68$  atm and  $\alpha_0 = 42\%$ . The bubble spectrum for this case is shown as Curve D in Figure 3. Except for the presence of more smaller microbubbles, the general distribution in this case is similar to Curve B for the 12-inch tunnel. This result as expressed by a triangle and D mark in Figure 7,

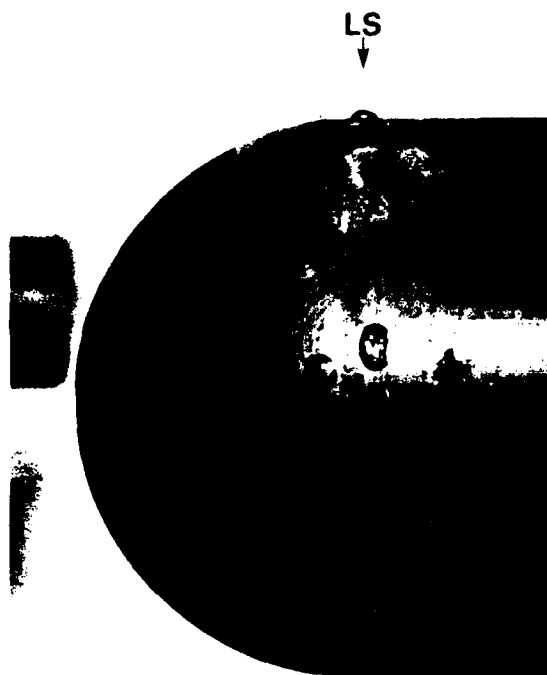


FIGURE 8. Travelling bubble cavitation in 12-inch water tunnel with  $U_0 = 6.9 \text{ m/s}$  and  $\Pi = 1.0$ .



FIGURE 9. Ring and travelling bubble cavitation in 24-inch water tunnel with  $U_0 = 18.8 \text{ m/s}$  and  $\Pi = 0.84$ .

indicates a general increase of the  $\Pi_1$  parameter with the increase of  $U_0$ , when the bubble spectrum remains nearly constant. By lowering the tunnel pressure to 0.61 atm or  $\Pi_1 = 0.84$ , both traveling bubble and ring types of cavitation were observed; see Figure 9. In general, the bubble characteristics of this tunnel at lower test speeds were similar to those of the smaller tunnel, i.e., the concentration of large microbubbles tended to increase greatly at low absolute tunnel operating pressures. The concentration of these large bubbles could cause early inception of cavitation due to undamped bubble oscillations initiated by the tunnel flow contraction; see operating point E in Figure 7. It should be noted that the impellers for the 12- and 24-inch tunnels are located at 4.1 and 5.8 m below the test section, respectively. This fact together with the lack of a bubble resorber in either tunnel may have contributed to the uncontrollable production of large microbubbles in these tunnels.

We next consider similar tests conducted in the large 36-inch cavitation tunnel. This tunnel was equipped with the bubble resorber, and the impeller is located at 8.7 m below the test section. Hence, the measured bubble distributions under a wide range of  $U_0$ ,  $\alpha_0$ , and  $P_{wo}$  showed no tendency to produce extra microbubbles as shown by Curves F and G in Figure 3. Curves F and G are for the conditions of  $U_0 = 6.1$  m/s and 21.3 m/s, with  $\alpha_0 = 94\%$  and 11%, respectively. Bubble concentrations for similar values of  $\alpha_0$  were much less than in the two smaller tunnels not equipped with a bubble resorber. Only ring-type cavitation was observed in the 36-inch water tunnel, which occurred at  $\sigma_1 = 0.62$  or  $\Pi_1 = 0.80$ . The leading edge of the ring coincided with the leading edge of the laminar separation bubble as indicated by the oil paint flow visualization. The cavity appearance was similar to that observed by Arakeri [5,6] and by Katz [17]. The bubble ring cavitation reported by Parkin and Kermean [4] was not observed. Because the concentration of microbubbles in the flow field was so low, no traveling bubble type cavitation was observed in this test facility.

Due to the fact that microbubbles circulating inside the separated flow zone could have very long residence times, they could grow by both the evaporative and diffusion processes until they reached visible sizes. Since these bubbles did not experience the lowest value of  $C_{pmin} = -0.78$  and were subjected only to the minimum separated flow pressure of  $C_{ps} = -0.62$ , see Figure 5, the  $\Pi_1$  parameters for these bubbles in a separated flow should be redefined as

$$\Pi_1 = \frac{P_{woi}}{C_{ps} \cdot \rho U_0^2 / 2} \quad (8)$$

The  $\sigma_1$  data for ring cavitation measured by Huang [20], Carrol [10], and Gates [21] are recomputed in terms of  $\Pi_1$  from Equation 8, and shown in Figure 7. The values of inception parameter  $\Pi_1$  for all cases fall within 0.93 to 1.02. It is in a zone where no equilibrium microbubbles should have blown up. Hence, these bubbles are of the nonequilibrium outgassing type; see Parkin [18,19]. Very similar to ring cavitation is

the so-called spot or patch cavitation. Both ring and patch type cavitation are found to be associated with highly deaerated water where the number of bubbles with  $R_0$  greater than  $10\text{ }\mu\text{m}$  is less than  $10^4/\text{m}^3$ . Thus, due purely to the lack of cavitation events the cavitation index is generally lowered to cause substantial production of the diffusive gas bubbles. The small increase of  $\Pi_1$  with  $U_0$  for these bubbles can also be explained by the effect of the  $\psi$  parameter; see Figure 7.

### Blunt Headform

A distinctive type of cavitation known as vortex type cavitation can be found to develop near the leading edge of hydrofoils when the hydrofoil is at a high angle of attack, see Van der Meulen [15]. High speed photography indicates that this type of cavitation is associated with the line vortices developed through turbulent flow separation. The inception of this type of cavitation can be studied by the use of a blunt cylindrical headform. A 5.7 cm diameter blunt headform was used to study vortex cavitation.\* Tests were first conducted in the 12-inch water tunnel at  $U_0 = 5.6\text{ m/s}$ . The measured pressure distribution along the headform is shown in Figure 10. The value of  $C_{p\text{min}}$  was found to be  $-0.7$ . The inception index  $\sigma_1$  was found to be 2.66, with  $P_{\text{woi}} = 0.42\text{ atm}$  and  $\alpha_0 = 24\%$ . The measured bubble spectrum is shown as Curve H in Figure 3. High speed photography showed that the cavities were in the form of thin cavity lines that appeared like hairs originating near the wall, located approximately at one-half diameter downstream from the leading edge of the headform. The cavity lines streamed away from the wall at an angle of approximately 45 degrees, and terminated at the edge of the separated flow which is one-quarter diameter from the wall; see Figure 10.

By lowering the tunnel pressure, honeycomb-like vortex line patterns became visible. This may be attributed to the self-induced twisting between pairs of vortex lines before the outward-looping vortex lines are stretched into hairlike vortices by the mean shearing velocity field of the separated flow; see Figure 10. With a further lowering of the tunnel pressure, one begins to see the cavitation of individual lines of ring vortices being generated by the separated flow field. We further noted that there was no substantial difference in the characteristics of the cavitation, when the closed solid cylinder was replaced by an open ended pipe section. This indicated that the vortical field of the ring vortices were generated locally in the separated flow zone. Furthermore, the drag coefficient for such a headform is known to be quite independent of the Reynolds number when  $Re$  based on the size of the headform is greater than  $10^4$ . Therefore, we expect that the  $\Pi_1$  parameter should be quite independent of  $Re$  and should be only a function

---

\*The type of vortex cavitation investigated here is not of the same origin as the hub and tip vortex types of cavitation occurring on propellers.

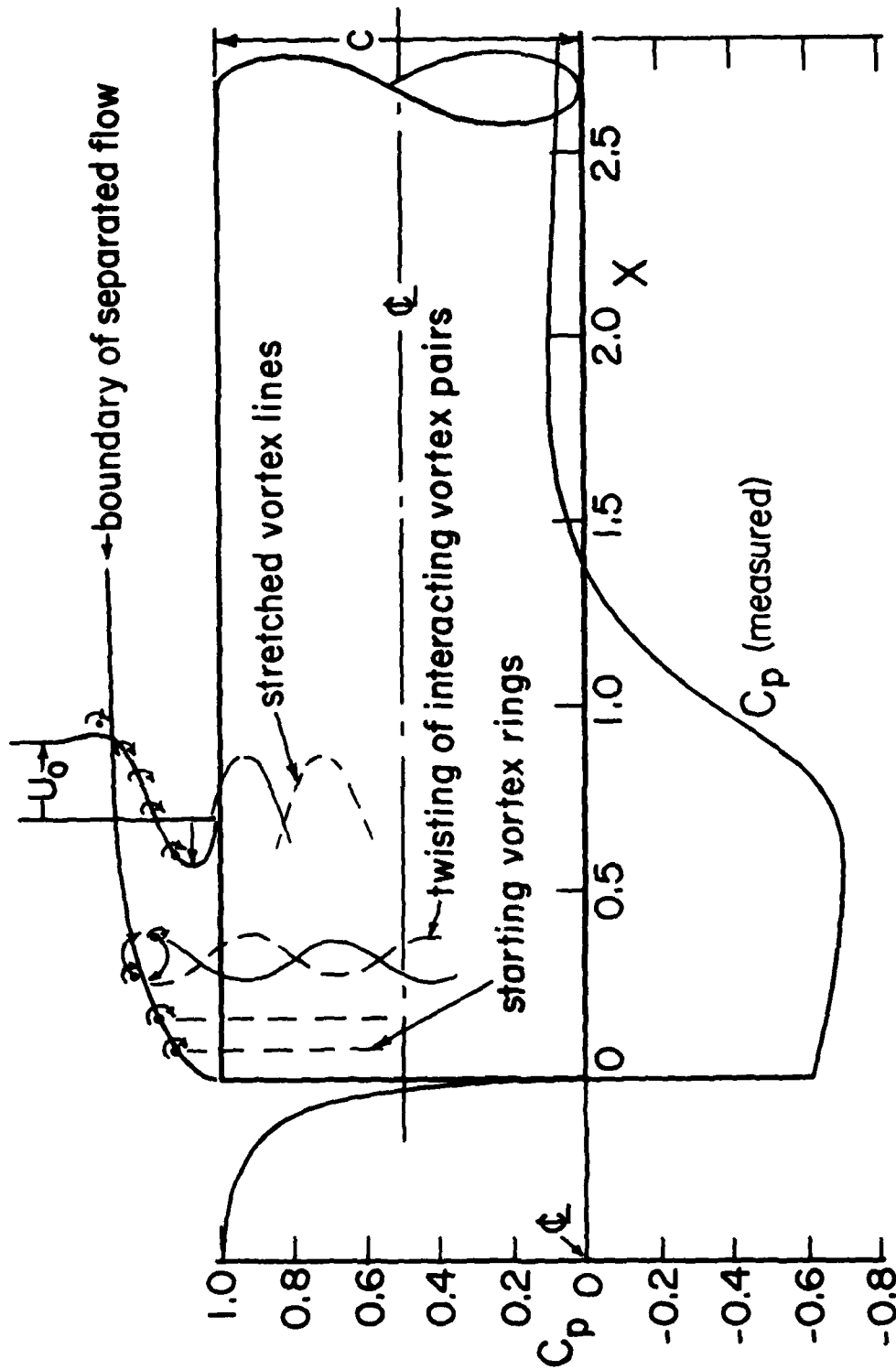


FIGURE 10. Pressure distribution over a blunt cylindrical headform. The upper part of the figure shows the formation of the vortex rings, pairing and twisting of the vortex rings, and the stretching of outward looping vortex lines within the separated flow field.

of the  $\psi$  and  $T$  parameters. Since vortex line cavitation must also start as spherical microbubbles, the condition for incipient cavitation should be the same as for traveling bubbles.

We assumed for this test case that there were sufficient concentrations of large microbubbles which could contribute to a  $\Pi_i$  parameter of 1.0. Although we do not know a priori the net  $\Delta P_{\min}$  of the system, one may assume that  $\Delta P_{\min}$  can be expressed as the sum of the  $C_{p\min}$  of the headform and the minimum pressure  $C_{pc}$  in the core of the line vortices. Since we know that the drag coefficient of this headform is constant for  $Re > 10^4$ , one may assume both  $C_{p\min}$  and  $C_{pc}$  are constant and independent of  $Re$  for the present experiment. The cavitation inception index for the blunt headform can be redefined as

$$\Pi_i = \frac{P_{woi}}{|\Delta P_{\min}|} = \frac{P_{woi}}{-(C_{p\min} + C_{pc})\rho U_o^2/2} \approx \frac{\sigma_i}{-(C_{p\min} + C_{pc})} \quad (9)$$

Hence, taking  $\Pi_i \approx 1.0$  and  $\sigma_i = 2.66$ , we have  $(C_{p\min} + C_{pc}) \approx -2.7$ . Based on this net minimum  $C_p$  value and  $\beta \approx 0.5$ , one may obtain from Equation 5 the functional relationship for  $\Pi_i$  with respect to  $U_o$ ,  $R_o$ , and  $P_{woi}$  as shown in Figure 11. For the  $R_o = 100 \mu\text{m}$  bubbles the  $T$  parameter is 17. We note that this size of bubble is relatively free from the  $T$  parameter effect. With an increase in the test speed  $U_o$  from 5.6 m/s to 6.8 m/s, the measured  $\Pi_i$  parameter was found to reduce to 0.9. This can be explained by the significant reduction of large bubbles as indicated by the bubble spectrum Curve I in Figure 3 in comparison with Curve H. Similar behavior was observed in the 24-inch water tunnel. Depending on the bubble spectrum, the  $\Pi_i$  parameter could vary over a wide range of values from 0.80 to 1.05. Values of the cavitation parameter  $\Pi_i > 1.0$  are possibly due to tunnel induced oscillation of large numbers of large microbubbles.

Data from tests conducted in the large 36-inch water tunnel are plotted as the dashed line in Figure 11. One notes that the observed value of the  $\Pi_i$  parameter increases with test speed in an orderly manner. This can be explained by the fact that the bubble spectrum shown as Curve F in Figure 3 shifted only slightly as the tunnel test pressure was adjusted from 0.3 atm to 3.8 atm. At a test speed of  $U_o = 20$  m/s,  $\Pi_i$  was found to be 0.96, with  $\alpha_o = 6\%$ . Hence, from Figure 11, one notes that all bubbles having radii from  $R_o = 2 \mu\text{m}$  to  $100 \mu\text{m}$  will blow up. From Curve G of Figure 3, we computed that there were  $2 \times 10^4/\text{m}^3$  of these bubbles, which would give approximately 150 cavitation events per second. This would provide few observable events per second under the strobe light illumination. The calling of cavitation inception at  $\Pi_i = 0.96$  was again explainable. From Figure 11, if one assumes that the majority of bubbles had  $R_o = 2 \mu\text{m}$  at a test speed of 20 m/s then when the test speed was reduced to 6.0 m/s, we note from Figure 11 that the  $P_{wo}$  would have to be lowered to 0.3 atm. Hence, the  $2 \mu\text{m}$  bubbles would have expanded to  $5 \mu\text{m}$  with a corresponding  $\Pi_i$  of 0.75, as we have observed experimentally. It is now clear that in order for the cavitation inception index  $\Pi_i$  to behave as

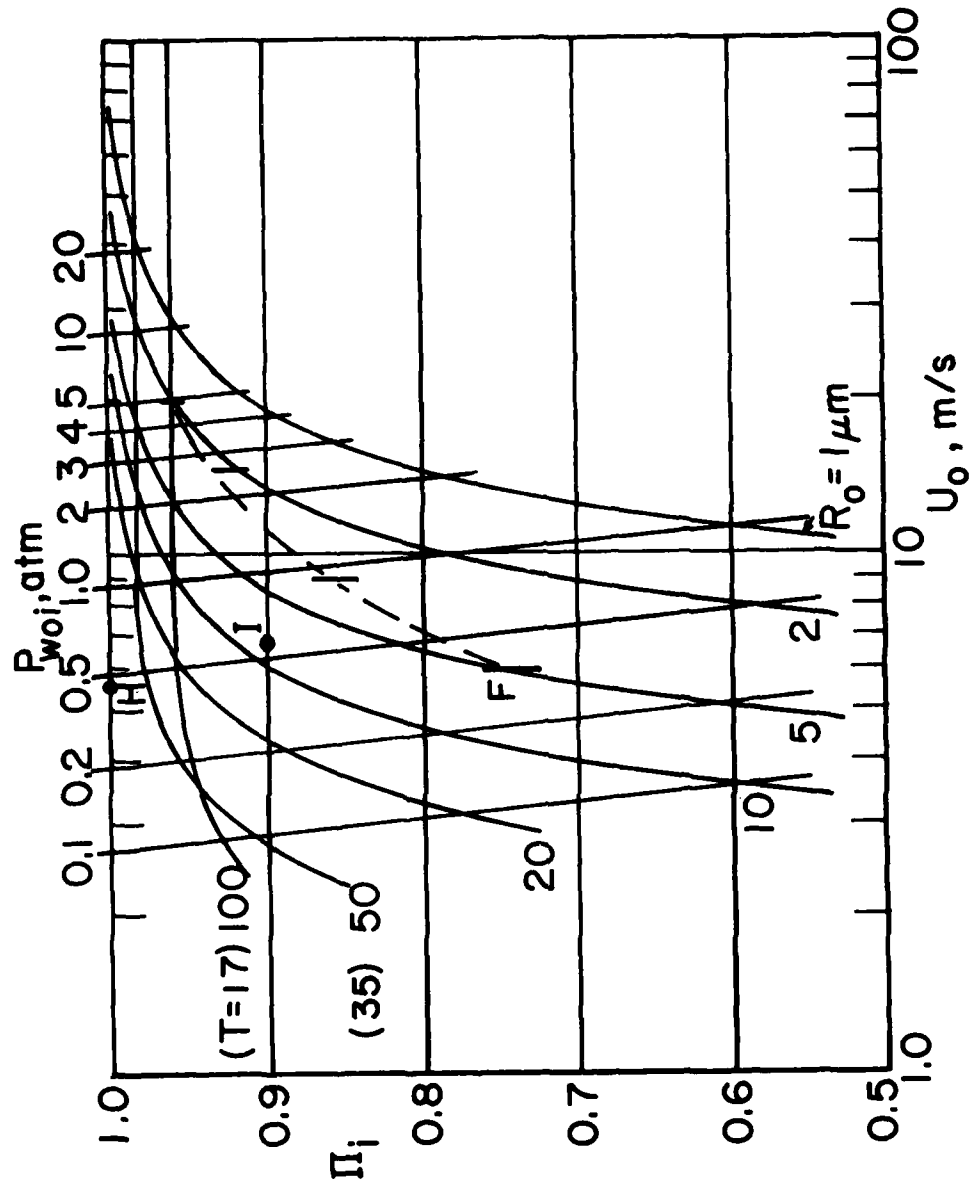


FIGURE 11. Cavitation inception index  $\Pi_i$  as a function of  $U_o$ ,  $R_o$ , and  $P_{woi}$  for a blunt cylindrical headform. Alphabetical symbols indicate operating points for the corresponding bubble spectra given in Figure 3.

analytically predicted, the bubble spectra in the test facility must also behave with no large increase or decrease in the number of microbubbles as the testing parameters are varied. In this respect, the 36-inch water tunnel is superior to the two smaller facilities.

In summary, the value of cavitation parameter  $\Pi_i$  required for microbubbles to blow up is governed by both the surface tension parameter  $\psi$  and the bubble blowup time parameter  $T$ . A functional relationship between  $\Pi_i$ ,  $\psi$ , and  $T$  can be obtained from Equation 5 and is plotted as Figure 1. One notes that for  $\psi < 10$ , the  $\Pi_i$  parameter is dominated by the surface tension effect, and the condition for blowup is very sharp and distinct. In this zone, for  $\psi < 10$ , the effect of surface tension is commonly attributed to an apparent Reynolds number effect. When  $\psi$  is greater than 10, the  $\Pi_i$  parameter becomes independent of  $\psi$  and tends to approach 1.0 in the limit when the  $T$  parameter is greater than 40. The  $T$  parameter effects the  $\Pi_i$  parameter only for large  $\psi$  values; a cutoff effect occurs for the large bubbles, i.e., big bubbles will not blow up due to a lack of reaction time. On the other hand, the  $\psi$  parameter controls the cutoff effect for the smaller bubbles. Thus a small model system operating at a low test velocity is highly selective of a narrow band of bubble sizes for cavitation, while a large prototype is not. A large prototype system operating at a large ambient pressure and velocity can cavitate over the whole band of bubble sizes from  $R_0 = 1 \mu\text{m}$  to  $1 \text{ mm}$  at  $\Pi_i = 1.0$ . Figure 1 can be used for constructing bubble cavitation inception characteristic curves similar to those shown in Figures 7 and 11. For example, consider the case where  $C_{p\text{min}} = -0.78$  for a hemispherical headform,  $\beta = 0.1$  and diameter  $C = 7.6 \text{ cm}$ . To plot the characteristic curve of  $\Pi_i$  versus  $U_0$  and  $P_{\text{woi}}$  for  $R_0 = 50 \mu\text{m}$ , we first find from Equation 7 that  $T = 7.2$ . The equivalent surface tension pressure for  $R_0 = 50 \mu\text{m}$  is  $0.029 \text{ atm}$ . For  $P_{\text{woi}} = 2.0 \text{ atm}$ , we find  $\psi = 2/0.029 = 69$ . From Figure 1, with  $\psi = 69$  and  $T = 7.2$  we find  $\Pi_i = 0.92$ . Finally, from Equation 2 we find the corresponding  $U_0 = (2 P_{\text{woi}} - C_{p\text{min}} \cdot \Pi_i \cdot \rho)^{0.5} = 23.5 \text{ m/s}$ . Proceeding in a similar manner, the characteristic curve as shown in Figure 7 for  $R_0 = 50 \mu\text{m}$  can be constructed. Hence similar characteristic curves for any other headforms or hydrofoils can be constructed from Figure 1.

Under the normal range of ambient temperature, the effects of evaporative and gaseous diffusion on prototype cavitation will be minimal, if the microbubble concentration in the fluid is more than  $10^4/\text{m}^3$ . For microbubble concentrations much less than  $10^4/\text{m}^3$  a reduction of the  $\Pi_i$  value to less than 0.8 is necessary to cause significant cavitation by gaseous diffusion. This is because, like the submicron traveling bubbles, gaseous diffusion bubbles must also overcome strong surface tension forces in their initial growth. In addition, these submicron bubbles require sufficient resident time in the low pressure zone to achieve initial growth by slow evaporative and diffusive processes; for example, within microcracks, behind micro-roughnesses, and in separated laminar flow zones on the flow boundary. Therefore, it is also necessary to know the bubble spectrum of the prototype system before conducting a laboratory simulation.



## CONCLUSIONS AND RECOMMENDATIONS

We have demonstrated that due to different tunnel designs and operating characteristics microbubble concentrations can vary over a wide range. Since cavitation inception is closely related to the blowup of these bubbles, it is strongly affected by microbubble concentration and distribution.

Two different forms of cavitation inception on hemispherical headforms were observed in the DTNSRDC Water Tunnels. The cavitation occurring in the 12- and 24-inch tunnels was the traveling-bubble type. The measured microbubble spectra in both tunnels were found to be very similar. However, due to the existence of the resorber in the 36-inch water tunnel, the measured total bubble population in this facility was an order of magnitude less than those measured in the 12- and 24-inch tunnels. The cavitation observed on the hemispherical headform in the 36-inch water tunnel was of the ring-type located at the zone of laminar separation. The threshold of bubble concentration required to exhibit traveling bubble cavitation versus ring-type cavitation was found approximately to be  $10^4$  bubbles/ $m^3$  for microbubbles having diameters larger than  $10\text{ }\mu m$ .

Cavitation on the blunt cylindrical headform occurred in the core of the vortex lines of the separated flow field. Quantitative estimation of the minimum core pressures of the vortex lines due to the stretching of these vortex elements can be made from the observed cavitation inception.

Irrespective of the sources of microbubbles, the bubble blowup process is governed by three key parameters, the pressure parameter  $\Pi$ , the surface tension parameter  $\psi$ , and the blowup time parameter  $T$ . Based on the mechanics of microbubbles, the apparent dependency of the cavitation inception index on the Reynolds number, sometimes observed in the past, may be explained as an effect of surface tension.

The important effect of the microbubble content on the scaling of cavitation inception is illustrated in the following example. If a prototype hemispherical headform of 1m diameter is operated 15m below the free surface, and the water is known to contain more than  $10^4$  bubbles/ $m^3$  of  $R_0 > 10\text{ }\mu m$  bubbles, it is required to find out which of the three testing facilities and testing conditions will best simulate the prototype system. From Figure 1, we find that for  $R_0 = 10$  to  $100\text{ }\mu m$ , with corresponding  $\psi = 10$  to  $100$  and  $T = 470$  to  $47$ , the average  $\Pi_i = 0.99$  or  $\sigma_i = 0.77$  for the prototype system. If model tests for bubble spectrum B in the 12-inch tunnel and bubble spectrum D in the 24-inch tunnel were used, a respective correction factor of  $1/0.90$  and  $1/0.95$  would have to be applied to the measured indicies in order to obtain the correct inception index for the prototype. Test results for bubble spectrum G in the 36-inch water tunnel would give a  $\Pi_i$  parameter based on the  $C_{pmin}$  of  $0.78$  or  $\sigma_i = 0.61$ , which is 21% lower than the prototype value; because the microbubble population is too small to simulate the conditions for the prototype. At this low microbubble population cavitation is found to occur only at the zone of laminar separation, which

is precluded by turbulent transition on the prototype. However, if bubble spectra similar to spectra B and D, and  $U_0 = 20$  m/s were used in the tunnel, the result would be  $\Pi_i = 0.98$  or  $\sigma_i = 0.77$ , and no correction would be needed. Therefore, it is recommended that both the measurement of microbubble spectra and preconditioning of the microbubble distribution in the testing fluid should be undertaken as part of the general testing procedure. The same is true for field measurements, especially for the bubble concentration, although the bubble spectrum is of less importance.

#### ACKNOWLEDGEMENTS

The work described in this paper was funded under the David W. Taylor Naval Ship Research and Development Center's Independent Research Program, Program Element 61152N, Project Number ZR 000 01. The authors would like to acknowledge the benefit of discussions with M.S. Chang, T.T. Huang and J.H. McCarthy.

AD-A158 920

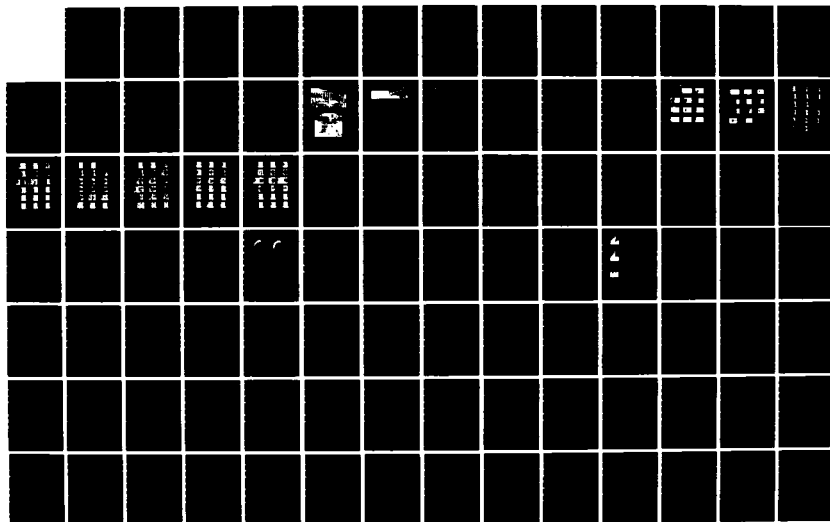
SYMPOSIUM OF NAVAL HYDRODYNAMICS (14TH) HELD AT ANN  
ARBOR MICHIGAN ON AUGUST 23-27 1982(U) OFFICE OF NAVAL  
RESEARCH ARLINGTON VA M P TULIN ET AL. 1982

07/13

UNCLASSIFIED

F/G 20/4

NL





## REFERENCES

1. Gates, E.M. et. al., Cavitation inception and nuclei distributions joint ARL/CIT experiments, California Institute of Technology Report No. E-244.1, (Sept 1979).
2. Lindgren, H. and C.A. Johnsson, Cavitation inception on headforms - ITTC comparative experiments, Publications of the Swedish State Shipbuilding Experimental Tank, No. 48, (1966).
3. Acosta, A.J., and B.R. Parkin, Cavitation inception - a selective review, Journal of Ship Research, Vol. 19, No. 4, pp. 193-205, (1975).
4. Parkin, B.R. and R.W. Kermeen, Inception cavitation and boundary layer interaction on a streamlined body, California Institute of Technology Report E-35-2, (1953).
5. Arakeri, V.H., Viscous effects in inception and development of cavitation on axi-symmetric bodies, Ph.D. Thesis, California Institute of Technology, also Division of Engineering and Applied Science Report E-183-1, (1973).
6. Arakeri, V.H. and A.J. Acosta, Viscous effects in the inception of cavitation on axisymmetric bodies, Journal of Fluid Engineering, American Society of Mechanical Engineers, Vol. 95, Ser. I, No. 4, pp. 519-528, (1973).
7. Ripkin, J.F. and J.M. Killen, A study of the influence of gas nuclei on scale effects and acoustic noise for incipient cavitation in a water tunnel, Technical Paper 27, Ser B, St. Anthony Falls Hydraulic Laboratory, University of Minnesota 1959.
8. Gates, E.M. and A.J. Acosta, Some effects of several freestream factors on cavitation inception on axisymmetric bodies, 12th ONR Symposium on Naval Hydrodynamics, Washington, D.C. (1978).
9. Holl, J.W., Sources of cavitation nuclei, 15th American Towing Tank Conference, Ottawa, (June 1968).
10. Carroll, J.A. Observations of the effects of boundary layer and nuclei on cavitation of axisymmetric bodies, The Pennsylvania State University ARL Report TM 81-60, (Feb. 1981).
11. Peterson, F.B., Hydrodynamic cavitation and some considerations of the influence of free gas content, 9th ONR Symposium on Naval Hydrodynamics, Paris (1972).
12. Peterson, F.B. et. al., Determination of bubble and particulate spectra and number density in a water tunnel with three optical techniques, 14th ITTC, (1975).
13. Gowing, S. and S.C. Ling, Measurements of microbubbles in a water tunnel, 19th ATTC at University of Michigan, (1981).
14. Ling, S.C. Role of Microbubbles on cavitation, Proc. 10th Symposium of the IAHR, Tokyo, pp. 27-37, (1980).
15. Van der Meulen, J.J., Boundary layer and cavitation studies of NACA 16-012 and NACA 4412 hydrofoils, 13th ONR Symposium on Naval Hydrodynamics, Tokyo (1980).

16. Kodama, Y. et. al., The effect of nuclei on the inception of bubble and sheet cavitation on axisymmetric bodies, International Symposium on Cavitation Inception, the ASME Winter Annual Meeting, New York, (Dec 1979).
17. Katz, J., Cavitation inception in separated flows, California Institute of Technology Report E-183-5, (Dec 1981).
18. Parkin, B.R., A possible criterion for cavitation inception on hemispherical headforms, Journal of Fluid Engineering, ASME Vol. 103, pp. 577-582, (Dec 1981).
19. Parkin, B.R., The onset of bubble-ring cavitation on hemispherical headforms, Journal of Fluid Engineering, ASME, Vol. 104, pp. 115-123, (March 1982).
20. Huang, T.T., Cavitation inception observations on six axisymmetric headforms, Journal of Fluid Engineer, ASME, Vol. 103, pp. 273-279, (June 1981).
21. Gates, E.M., The influence of freestream turbulence, freestream nuclei populations and a drag-reducing polymer on cavitation inception on two axisymmetric bodies, CIT Report Eng-183-2, (Apr 1977).

## Discussion

G.L. Chahine (Hydronautics, Inc.)

Professor Ling's effort to synthesize the knowledge on spherical bubble dynamics to answer the practical needs of the engineer concerning scaling effects on cavitation inception is to be recognized. Earlier, more precise and therefore more complex studies attempted to consider the problem\* but have drawn only academic attention. Unfortunately, several oversimplifications in Professor Ling's paper cast in my opinion a serious doubt on the usefulness of the proposed parameters and curves in their present form. I will discuss here only the blow-up time parameter,  $T$ . The author defines the blow-up time,  $t_b$ , as the time that the bubble needs to reach "the unstable size of  $\eta > 3$ ." In reality, the critical value of  $\eta$ , after which the bubble radius is unstable depends on the initial bubble radius. By a simple static equilibrium approach one finds

$$\eta_{cr} = \frac{3}{2} P_{g_0} \frac{R_0}{\sigma}^{\frac{1}{2}}$$

In a dynamical approach, one has to solve Equation (5) when a sudden pressure drop is applied. One finds two types of behaviors depending on the value of  $(P_{wo} - P_v)/|\Delta P_{min}|$ , which is approximately the parameter  $\Pi$  (when  $P_v$  is neglected). Physically, if  $P_{min}$  is above a critical value, the bubble oscillates around an equilibrium value corresponding to  $P_{min}$ . This is not the case of interest here. If  $P_{min}$  is below  $P_{cr}$ , then the bubble expands continuously and rapidly attains an asymptotic behavior easily obtained from the Rayleigh-Plesset equation, for  $\eta \gg 1$ . Not neglecting  $P_v$  one finds

$$\frac{3}{2} \eta^2 = 1 - \frac{P_{wo} - P_v}{|\Delta P_{min}|}$$

Neglecting  $P_v$  this becomes

$$\frac{3}{2} \eta^2 = 1 - \Pi$$

and

$$\eta \approx 1 + \frac{2}{3} (1 - \Pi) t$$

(This can be obtained from Equation (5).) However, there must be a printing error, since at  $t = 0$  one finds  $P(0) = 0$  instead of  $P_{wo}$ .)

These remarks show that to attain a fixed value of  $\eta$ , the blow-up time,  $t_b$ , as defined by Professor Ling, is directly proportional to  $(1 - \Pi)^{-1/2}$ . This makes the parameters  $T$  and  $\Pi$  strongly dependent, and, unless  $\Pi$  is very small compared with 1, Equation (7) is not valid.

\*G.L. Chahine, "Comportement d'une bulle dans un champ de pression sinusoïdale" Journal de Mécanique, Vol. 15, No. 2, 1976.

## Author's Reply

S.C. Ling

To G.L. Chahine

It is clearly stated in the paper that Equation (5) does not admit a general solution for the inception of cavitation. The  $T$  parameter is introduced as an approximate parameter to correlate within a limited range of practical values the general relationship among the basic parameters. The blow-up time  $t_b$  is intended to define a characteristic time for the blow-up of a bubble from  $\eta = 1$  to 3, similar to the definition of the time constant for a first order system (see Reference 14). It is incorrect to relate  $t_b$  functionally to the time for critical blow-up size  $\eta_{cr}$ , or  $\eta \gg 1$ , derived under a static or a step pressure change condition, because we are concerned with the general response of a bubble to a pulsed pressure field normally encountered over a well designed headform or hydrofoil. It should be noted that the expression of  $\eta_{cr}$  derived by Chahine is not generally valid (see Reference 14). Also the expression for  $\eta \gg 1$  by Chahine should be proportional to  $\tau$  and not  $t$ .

In the present paper, the  $T$  parameter does not directly enter into the solution for Equation (5). It is only used to correlate the results from a large number of solutions for different headforms and hydrofoils. The average of these results is represented by Figure 1. Finally, the term  $P(\tau)$  in Equation (5) should be properly redefined as the change in the ambient pressure experienced by the bubble as it traverses along the flow boundary; i.e., for the simplicity of numerical calculation the net ambient pressure experienced by the bubble is expressed as  $P = P_{wo} + P(\tau)$ . For more critical applications, one should obtain solutions directly through Equation (5), while Figure 1 should be sufficient for general application.



*Session V*

**CAVITATION AND  
PROPELLER-RELATED  
PROBLEMS**

# Cavitation Erosion Tests with Oscillating Foil Section

Claus F.L. Kruppa\* and Gero R. Sasse<sup>†</sup>  
Institut für Schiffs- und Meerestechnik  
Technische Universität Berlin

## I. SUMMARY

Cavitation erosion is known to be primarily caused by unsteady flow effects, resulting in transient cavities and cavity break up linked with the phenomenon of cloud cavitation. Unsteady flow effects are largely responsible, for example, for the root erosion often experienced in high-speed inclined-shaft propellers.

In order to evaluate the effect of unsteady flow on cavitation erosion, tests with an oscillating foil were carried out, in the small cavitation tunnel K28 of the Institut für Schiffs- und Meerestechnik. A NACA 16-006 foil, spanning the width of the two-dimensional test section, was forced to oscillate about its quarter-chord position at various reduced frequencies, cavitation numbers, mean angles of attack and pitch amplitudes. For measuring the erosion rate the SSPA stencil ink method was used, in a slightly modified version.

The testing procedure was standardized with regard to application of coating, evaluation of erosion rate and sequence of routine measures to be observed during the tests. For evaluation of the erosion rate a method was developed which is based on measuring the rate of change of light reflected by the foil due to eroded surface areas. The testing technique was refined to an extent that erosion patterns and erosion rates could be reproduced after intervals of several months.

The results of the tests are given in graphical form as erosion rate versus reduced frequency, as a function of cavitation number and mode of oscillation. There is also comprehensive photographic documentation of erosion and cavity flow patterns, accompanied by high-speed film material.

The test results clearly reveal a strong influence of reduced frequency on erosion rate. One also has to draw the conclusion that visual observation of cloud cavitation can not be regarded as sufficiently indicative of erosion. Consequently, erosion tests are required if the danger of rapid erosion is to be predicted.

---

\*Dr.-Ing., Professor of Ship Hydrodynamics

<sup>†</sup>Dipl.-Ing., Scientific Assistant

## II. SCOPE OF TEST PROGRAM

The work on cavitation erosion testing of oscillating foil sections was initiated by repeated experience with cases of severe root erosion in high-speed propellers, operating under inclined-shaft conditions. In some cases the extent of blade erosion in the vicinity of the propeller hub was so extensive, after only a few hours of high speed trials, that the propeller design had to be completely modified. And yet in other comparable cases, hardly any erosion - or even none at all - was experienced.

Propeller model erosion testing was successfully used to predict the probability of rapid full scale erosion, both with regard to location and extent of the erosion zone, and with regard to operating conditions, the latter being characterized by shaft inclination, advance coefficient and cavitation number (Kruppa and Sasse, 1977). In these erosion tests a slightly modified version of the SSPA stencil ink method (Lindgren and Bjärne, 1974) was successfully employed, the SSPA method being probably the most simple and most widely used soft surface technique.

As a result of the inclined-shaft model propeller erosion tests, it was found that for a given propeller model the operating conditions, connected with rapid root erosion, were usually confined to a fairly narrow range of parameter combinations. At the same time it became obvious that rapid blade root erosion was always accompanied by large fluctuations in size of the cavities generated at the leading edge of the root sections, depending on angular blade position. Obviously, these fluctuations are caused by the variations in effective angle of attack, which for propellers in oblique flow reach a maximum at the propeller hub.

Rather than exploring the phenomenon of root erosion in high-speed inclined-shaft propellers, by systematic erosion tests with model propellers, it was decided to make use of an existing facility for the two-dimensional testing of foil sections. This facility had been used for determining the conditions for cavitation onset of oscillating foil sections (Radhi, 1975). It only needed limited modifications for cavitation erosion tests with the existing foils.

Tests of similar nature had been carried out before and were thoroughly reviewed in the Cavitation Committee Reports of the 15th (1978) and 16th ITTC (1981). Among others, the investigations by Ito (1962), Tanibayashi and Chiba (1977), Miyata et al. (1972) as well as Shen and Peterson (1978 and 1980) are concerned with cavitation phenomena on pitching foils. All authors arrive more or less at the conclusion that cloud cavitation can be generated by oscillating foils, as a result of large size leading edge sheet cavities collapsing and finally breaking up into numerous small size cavities. Cloud cavitation was found to occur at reduced frequencies in the vicinity of  $\mu = 0.4$ . Of course, a high noise level and the danger of rapid erosion were expected as unavoidable consequences of cloud cavitation, although no actual measurements of the erosion rate are reported as far as oscillating foil sections are concerned. On the other hand however, the fact that

similar looking cloud cavitation may not be accompanied by the same cavitation erosion intensity has apparently been observed in model propellers (Kurobe and Takie, 1980). No simple explanation can be given for this phenomenon, mainly because of insufficient knowledge of the generation of cloud cavitation and its mechanics in terms of bubble dynamics (Proc. 16th ITTC, 1981).

In this context, the test program described in the following was conceived, from the very beginning, to identify those operating conditions of oscillating foil sections where cloud cavitation is linked with high erosion intensity.

It has been stated in the past that the paint coating method is only suitable to detect the location of erosion susceptibility, but not its intensity. Somewhat in contrast to this opinion, the oscillating foil erosion tests were carried out with the intention to use the paint coating method also for quantitative assessments of erosion intensity, as suggested by Kato et al. (1978) and successfully proven by Georgijewskaja et al. (1981).

### III. EXPERIMENTAL FACILITY

The oscillating foil tests were carried out in the small cavitation tunnel K28 of the Institut für Schiffs- und Meerestechnik at Technische Universität Berlin. The tunnel is usually operated with a free surface test section and has a large degassing tank downstream of the test section (Figure 1). For the oscillating foil tests a closed-throat two-dimensional test section of 70 mm width and 200 mm height (Figure 2) was installed (Radhi, 1975). The associated contraction nozzle had a contraction ratio of 6.2 : 1 which lead to a velocity distribution in the test section with maximum local deviations of less than  $\pm 0.5\%$  of the mean value, outside the wall boundary layer with a thickness of about 5 mm.

The drive motor, transmission and gearbox to generate the sinusoidal pitching motion of the foil sections about the quarter-chord position was modified at several occasions, with the aim to reduce the effect of critical frequencies. The design of the gearbox is such that a pure sinusoidal pitching motion would have been achieved at constant motor speed if the system was fully balanced dynamically. All modifications were measures to reduce the unbalanced masses and finally resulted in a satisfactory sinusoidal foil motion, up to motor speeds of  $f = 20$  Hz.

In order to be able to observe visually and to photograph the flow past the foil sections at predescribed instantaneous foil angles a trigger mechanism for actuating one or more stroboscopic light sources or flash lights was designed and successfully used.

The family of foil sections of the type NACA 16  $a = 0.8$ , available from the earlier cavitation onset tests (Radhi, 1975), had a chord length of  $c = 60$  mm and an effective span equivalent to the test section width ( $b = 70$  mm). Additional 10 mm of span were provided on both sides for support. The foils were made of high tensile stainless steel

classified as X21CrW12 (containing 0.21 % carbon, 12 % chromium and 0.5 % tungsten) and manufactured by a rotating disc grinding machine in which the disc profile was diamond-cut from a scaled-up contour pattern (5 : 1) by special palpating equipment. The accuracy of the finished foil sections was checked by a universal microscope and revealed maximum local deviations in section offsets of not more than  $-7...+15 \mu\text{m}$ .

Originally it was planned to test as many foils of the existing family as possible. However, in view of the actual test duration - quoted below in section IV C - only one foil was investigated so far, i.e. the uncambered foil

NACA 16-006.

With regard to the requirement of two-dimensional flow this was found to be satisfactorily achieved with the existing foil and test section dimensions, at least outside the immediate vicinity of the tunnel walls and as long as measurements of cavitation onset are concerned. As will be shown later, the flow is no longer two-dimensional during the process of collapse of large leading edge cavities when cloud cavitation is generated. For this reason only a 30 mm strip in the centre of the foil is evaluated for erosion, leaving out of consideration the two strips of 20 mm width adjacent to the tunnel walls.

#### IV. TEST PROCEDURES

##### A. Application of Coating

After several years of experience with the SSPA stencil ink method (Kruppa and Sasse, 1977) this type of soft surface technique was used throughout the test program. One obvious advantage of this technique is the strong contrast in color between the coating and the metal surface of the model, rendering this technique suitable for optical methods to assess the erosion rate in terms of eroded area.

Difficulties in applying the coating have been reported in the past (Proc. 15th ITTC, 1978) and were also experienced in the early stages of the oscillating foil program. However, by strictly following a standard routine in preparing the foil for an erosion test these difficulties were completely overcome. In this routine the following steps had to be adhered to:

- Roller system stencil ink S-1 (black) was diluted at a ratio of one part ink to two parts in volume of ethyl alcohol. The diluted ink would never be stored for longer than two weeks. In this way variations in paint composition were avoided.
- Prior to application of the coating the model was thoroughly cleaned with ethyl alcohol.
- The diluted ink had to be carefully stirred before dipping the model into the mixture for about one minute, moving the model slowly but steadily.
- The coating was allowed to dry in air for about 20 minutes with the

leading edge pointing upward, in order to avoid the ink to concentrate locally at the nose of the foil.

- Drying was completed in an oven at a temperature of 50°C for further 20 minutes.
- After application of the coating the erosion test would be carried out within the next two hours.
- Complete removal of the coating after optical evaluation of the erosion rate was easily achieved with the help of ethyl alcohol.

Coating thickness was never actually measured. However, consistency of the results in terms of erosion rate and location was achieved, even if the tests were repeated after several months. Neither a tendency of the coating to peel off or break away in flakes nor brittleness were ever observed. Thus, removal of the coating by cavitation can justifiably be referred to as erosion.

#### B. Evaluation of Erosion Rate

Considerable effort was spent in developing a technique to evaluate quantitatively the erosion rate  $E$ . As a result, a test rig was constructed (Figure 3) which was based on the principle presented schematically in Figure 4. By this technique the degree of diffuse reflection of light off the foil surface is used as a measure for the degree of erosion.

In detail, the test rig consists of a directional white light source. With the help of a number of achromatic doublets, stops etc. a parallel light beam of sufficiently uniform intensity is directed to the foil surface which is mounted in a fixed position in a darkened test chamber. Only a centre strip of the upper foil surface is exposed to the light beam. This strip has a width of 30 mm in the spanwise direction and a length equivalent to the foil chord length of 60 mm. After passing through a system of achromatic doublets and a diaphragm the reflected light is measured in terms of output voltage of a photomultiplier  $V$ .

Due to the convex curvature of the foil surface the degree of diffuse reflection varies with the chordwise position of an eroded surface element of given dimensions  $A$ . In order to calibrate the measuring system for chordwise position of the eroded area, and in order to check on linearity between eroded area and photomultiplier output voltage, a special procedure was adopted. In this procedure the light beam directed towards the uncoated foil was reduced to a narrow strip of 3 mm width in the chordwise direction by an appropriate aperture (Figure 5). By varying the length of the strip in the spanwise direction  $\Delta b$ , areas of different dimensions were exposed to the light beam. By moving the strip in small steps from leading to trailing edge, calibration curves were obtained as shown in Figure 6. If the results were normalized by the area of exposure a correction factor  $C$  for the chordwise position of the erosion zone could be derived (Figure 7).

Whereas the check on linearity between exposed strip area and photomultiplier output voltage was only carried out once, from a principal point of view, the correction factor  $C$  for chordwise position had to be assessed at regular intervals, in particular after

light bulb replacements and associated adjustments of the test rig. For this purpose a standard aperture of  $\Delta b = 30$  mm span and 3 mm width was used.

All tests for the actual evaluation of the erosion rate involved three separate measurements:

- photomultiplier output reading  $V_c$  for the coated foil, with an exposed area of  $A_0 = 30 \times 60 = 1\,800$  mm<sup>2</sup>,
- photomultiplier output reading  $V_e$  for the coated foil after the erosion test, with an exposed area of  $A_0 = 1\,800$  mm<sup>2</sup>,
- photomultiplier output reading  $V_b$  after complete removal of the soft surface coating, with an exposed area of  $A_0 = 1\,800$  mm<sup>2</sup>.

From these measurements the relation

$$E = \frac{\frac{V_e - V_c(1-E)}{C}}{V_b}$$

was used to define the erosion rate

$$E = \frac{A}{A_0} = \frac{V_e - V_c}{CV_b - V_c},$$

where the factor  $C$  had to be estimated from the type of characteristic shown in Figure 7.

For various uncoated surface elements of well-contoured shape, clearly defined area  $A$  and fixed chordwise position  $x$  the formula for the erosion rate was thoroughly checked and found to yield satisfactory results, with maximum deviations of less than  $\pm 1\%$ .

In applying this definition of erosion rate to actual erosion patterns one has to realize that these are not usually well-contoured, that a transition zone may exist between soft surface coating and eroded surface area, that isolated erosion spots may appear, or that the erosion pattern may consist of several larger erosion zones. Consequently, the physical meaning of a set of values of the photomultiplier output readings ( $V_e$ ,  $V_c$ ,  $V_b$ ) and of an estimated position of the erosion zone, in order to derive the correction factor  $C(x)$ , is no longer that of an area ratio, but rather its virtual equivalent, in terms of diffuse reflection of light.

#### C. Routine Testing

In view of the exploratory character of the test program the number of variable parameters was kept to a minimum. The desire to cover a wide enough range of reduced frequencies on one hand, and the limitations in the maximum rotational speed of the drive-gearbox system ( $f \leq 20$  Hz) on the other hand, lead to the selection of a test section velocity of  $V = 6$  ms<sup>-1</sup>, a figure which limited the Reynolds number to

$R_n = 3.6 \times 10^5$  and the reduced frequency to  $\mu \leq 0.63$ . Obviously higher test section velocities would also have permitted a reduction in the standard test duration. Under the prevailing conditions this was finally selected to be  $\Delta t = 30$  min.

If the pitching motion about the quarter-chord position is described by the instantaneous angle of attack

$$\alpha = \alpha_0 + \alpha_1 \sin \omega t,$$

with

$$\omega t = 2\pi f t = \dots,$$

the mean and additional angles of attack were restricted for mechanical reasons to

$$\begin{aligned} -7^\circ &\leq \alpha_0 \leq 7^\circ \\ 0^\circ &\leq \alpha_1 \leq 9^\circ. \end{aligned}$$

For a test section velocity of  $V = 6 \text{ ms}^{-1}$  the lowest cavitation number achievable in the test section was  $\sigma = 0.6$ , if cavitation of the contraction nozzle was to be avoided. This restriction limited the test parameter range even further.

With the restrictions mentioned the only parameters systematically varied were

- the reduced frequency  $\mu = \frac{c \omega}{2V} = \frac{c \tau f}{V}$
- the cavitation number  $\sigma = (p - p_v) / \frac{\rho}{2} V^2$
- the mean angle of attack  $\alpha_0$
- the pitch amplitude in terms of the additional angle of attack  $\alpha_1$ .

In order to guarantee otherwise unchanged test conditions throughout the program the following steps were taken in sequence as a routine:

- Coating of the foil as described in section IV A,
- reading of the photomultiplier output voltage  $V_c$  for the coated foil as described in section IV B,
- mounting of the foil in the test section, setting of tunnel water speed and depressurizing the tunnel for about 20 minutes, with the foil set at  $\alpha = 0^\circ$ ,
- degassing the tunnel for about 20 minutes at low pressure, in order to obtain stabilized test conditions, with regard to dissolved gas content and free gas nuclei, with the foil set at  $\alpha = 0^\circ$  (as a consequence the gas content ratio was always slightly higher than  $\rho_g / \rho_{st} = 1$ , where  $\rho_{st}$  is the gas content of the saturated water



- under ambient conditions in the test section, with regard to pressure and temperature),
- performing of erosion test with a duration of 30 minutes for a given set of parameters,
  - dismantling of the foil immediately after completion of erosion test,
  - reading of the photomultiplier output voltage  $V_e$  for the eroded foil and taking a photograph of the eroded foil,
  - removal of the coating as described in section IV A and taking a photomultiplier output voltage reading  $V_b$  of the uncoated foil,
  - daily filtering of tunnel water for one hour after completion of a days testing.

On the average, not more than two or three erosion tests could be performed during a day. Thus, for the 139 tests documented in this paper about 60 complete testing days were needed. For initial test rig setup and calibration, maintenance and repairs, photography, taking of high-speed film and repeatability checks at least the same amount of time was required.

## V. PRESENTATION OF RESULTS

The results of the erosion tests are presented in graphical form in Figures 8 through 13, in terms of erosion rate  $E$  versus reduced frequency  $\mu$ . In Figures 8 through 11 the cavitation number is systematically increased in the range  $0.6 \leq \sigma \leq 0.9$ , with the pitch amplitude as parameter ( $7^\circ \leq \alpha_1 \leq 9^\circ$  for  $\alpha_0 = 0^\circ$ ). In Figures 12 and 13 the mean angle of attack  $\alpha_0$  is selected to be  $2^\circ$  and  $4^\circ$  for  $\sigma = 0.7$ , with the pitch amplitude as parameter ( $5^\circ \leq \alpha_1 \leq 7^\circ$  and  $3^\circ \leq \alpha_1 \leq 5^\circ$  respectively). Most of the tests which did not lead to visible signs of erosion have not been included in the documentation.

As examples, the erosion patterns were photographed for the curves of maximum erosion rate in Figures 8 and 9 and are presented in Figures 14 and 15. The photographs show the appearance of the centre portion of the upper foil surface as evaluated by the optical method, i.e. of an area of 1 800 mm<sup>2</sup>.

Some representative cavity flow patterns were photographed from above and are presented in Figures 16 through 21. For the test conditions leading to the curve of maximum erosion rate in Figure 8 and to the erosion patterns in Figure 14, the cyclic changes of the cavity flow patterns can be seen from Figure 16, for a reduced frequency of  $\mu = 0.5$ . Under these conditions, the erosion intensity was severe enough to cause erosion starting to develop close to the trailing edge, even during the limited time needed for taking the photographs. This can best be seen at  $\varphi = 210^\circ$ .

For the test conditions leading to the curve of maximum erosion rate in Figure 9 and to the erosion patterns in Figure 15, the cyclic changes of the cavity flow patterns are presented in Figures 17 through 19, for three reduced frequencies ( $\mu = 0.25, 0.425, 0.525$ ). Again in Figure 18 high erosion intensity starts to lead to erosion zones, not only at the half-span position but also close to the tunnel

walls. This type of erosion, starting to develop close to the tunnel walls, is even more pronounced in Figure 19 where no erosion was experienced on the centre strip.

For a reduced pitch amplitude ( $\alpha_1 = 7^\circ$ ) and an increased cavitation number ( $\sigma = 0.9$ ) the cavity flow patterns are presented in Figures 20 and 21 respectively, for a reduced frequency of  $\mu = 0.425$  and a mean angle of attack  $\alpha_0 = 0^\circ$ .

In addition to the photographs taken at discrete foil positions ( $y$ ) the flow conditions of Figures 17 through 21 have also been documented on high-speed film, at a rate of 3 000 frames/s.

## VI. INTERPRETATION OF RESULTS

A number of qualitative conclusions can be drawn straight away from Figures 8 through 13:

- For the limited test section velocity of  $V = 6 \text{ ms}^{-1}$  and the standard test duration of  $\Delta t = 30 \text{ min}$  the maximum instantaneous angle of attack had to be  $\alpha_0 + \alpha_1 \geq 7^\circ$  for signs of erosion to appear.
- At a given reduced frequency  $\mu$  and cavitation number  $\sigma$  the erosion rate  $E$  increases with pitch amplitude  $\alpha_1$ .
- There seems to be a cavitation number  $\sigma$  for which the erosion rate  $E$  becomes a maximum, for fixed values of reduced frequency  $\mu$  and pitch amplitude  $\alpha_1$ .
- There is a marked effect of reduced frequency  $\mu$  on erosion rate  $E$  (e.g. see also Figure 15).
- Maximum erosion occurs at reduced frequencies  $0.3 \leq \mu \leq 0.5$  for  $\alpha_0 = 0$ , shifting to higher reduced frequencies as the mean angle of attack is increased ( $0.4 \leq \mu \leq 0.6$  for  $\alpha_0 = 2^\circ$  and  $0.5 \leq \mu \leq 0.65$  for  $\alpha_0 = 4^\circ$ ).
- If the erosion rate exhibits more than one maximum this is always caused by the presence of more than one erosion zone, each having its maximum intensity at a different reduced frequency.
- No erosion could be detected for pitching motions approaching steady-state conditions ( $\mu \leq 0.2$ ).

From the erosion patterns in Figures 14 and 15 it can be seen that these are by no means two-dimensional, with the exception of those close to the trailing edge in Figure 14 for reduced frequencies  $0.375 \leq \mu \leq 0.525$ . However, there is apparently a symmetry in the erosion patterns with respect to the half-span position.

When interpreting the sequential photographs of the cavity flow patterns in Figures 16 through 21 it should be kept in mind that these have been taken at clearly defined instantaneous foil angles, but of course not during one and the same pitching cycle. Consequently, the extent of deviations from symmetry will not only show up in individual flow patterns but also in the sequential presentation.

Regarding three-dimensional flow effects the following can be deduced from Figures 16 through 21:

- The process of formation of transient leading edge sheet cavities can be classified - within limits - as two-dimensional, as long as the

- downstream end of the cavity does not show signs of breaking up.
- Cavity collapse and break up are highly three-dimensional processes.
  - Evaluating the erosion pattern at the mid-span position is a somewhat arbitrary measure, with the possible consequence that, for larger or smaller geometric aspect ratios, different quantitative results, in terms of erosion rate  $E$ , might have been obtained.

With one exception, all cavity flow patterns in Figures 16 through 21 exhibit fundamentally the same phenomena, i.e.

- cavitation onset in the form of leading edge sheet or bubble cavitation at  $30^\circ \leq \varphi \leq 60^\circ$ ,
- leading edge sheet cavity growth beyond the half-chord point, followed by first signs of cavity collapse at the rear end with the associated loss of transparency,
- formation of cloud cavitation during the process of cavity break up at the rear end,
- sheet cavity detachment from the leading edge,
- cloud cavity collapse and rebound.

This sequence is delayed in phase as the reduced frequency is increased. Although cloud cavitation is generated in all cases it only causes erosion on the centre strip for the test conditions in Figure 18. The two-dimensional erosion pattern for the reduced frequency  $\mu = 0.5$ , shown in Figure 14 and starting to emerge in Figure 16, has been found to result from the bubble cavitation which is generated close to the trailing edge at  $-20^\circ \leq \varphi \leq 30^\circ$ , this being the exception indicated above.

## VII. CONCLUSIONS

The original concept of presenting the test results for a whole family of foil sections was found to be unrealistic, owing to the extremely time consuming test procedure. In spite of this shortcoming however, the erosion test results obtained with the foil NACA 16-006 have clearly demonstrated that there is a pronounced effect of reduced frequency on erosion intensity. By visual detection of cloud cavitation alone these results could not possibly have been predicted in a quantitative way.

Of course, with the limitations in test section velocity ( $V = 6 \text{ ms}^{-1}$ ) and cavitation number ( $\sigma \geq 0.6$ ) erosion was only experienced at fairly large maximum instantaneous angles of attack ( $\alpha_0 + \alpha_1$ ), larger than those occurring in propeller flow. However, it can be assumed that similar results would have been obtained for smaller pitch amplitudes, but at reduced cavitation numbers, if the test section velocity could have been significantly increased.

As to the significance of the test results for prototype conditions there are basically three possible sources of scale effects to which the results at model scale are subjected:

- Cavitation inception may be associated with the phenomenon of laminar separation.
- Whether or not the phenomenon of cloud cavitation, in particular in

terms of its extent and location, is subject to scale effects is still waiting to be resolved.

- Erosion intensity - whatever its definition - and the associated time scale are, of course, strongly dependent on such factors as test velocity, type of soft surface technique etc.

The last of the three scale effect areas is not addressed in the present context and has been discussed elsewhere (Kato et al., 1978).

Thus the question remains as to whether or not the rather small Reynolds number ( $R_n = 3.6 \times 10^5$ ), at which the tests were performed, may significantly affect the flow pattern, the generation of cloud cavitation, its extent and location and finally, as a result of the flow pattern, the erosion intensity. There is, of course, evidence from unsteady airfoil theory that the type of flow occurring in oscillating foil sections is largely governed by inertia forces and thus can be described by potential flow theory. However, this has still to be proven, preferably with the help of geosim tests.

It is therefore planned to pursue the test program in the following directions, hopefully in the near future:

- Erosion tests with a NACA 16-006 foil in the large cavitation tunnel K27 of the Institut für Schiffs- und Meerestechnik for reduced frequencies  $\mu \approx 1.2$  and at a Reynolds number  $R_n = 3 \times 10^6$ ,
- depending on the influence of scale effects, extension of the present test series in the small tunnel K28 with foils of different thickness-chord and camber-chord ratios,
- investigation of the influence of geometric aspect ratio on cavity flow and erosion patterns in two-dimensional test sections of varying width.

#### VIII. REFERENCES

- Proc. 15th ITTC (1978), Vol. 1, Report of Cavitation Committee, Netherlands Ship Model Basin, Wageningen, pp. 297-358
- Proc. 16th ITTC (1981), Vol. 1, Report of Cavitation Committee, Krylov Shipbuilding Research Institute, Leningrad, pp. 377-471
- Georgijewskaja, E.P., M.A. Mawljudow und M. Mehmel (1981). Entwicklung einer Methode zur Vorhersage der Kavitationserosion an Schiffspropellern, Schiffbauforschung 20, 3, pp. 167-175
- Ito, T. (1962). An experimental investigation into the unsteady cavitation of marine propellers, Proc. IAHR Symp. on Cavitation and Hydraulic Machinery, Sendai, pp. 439-459
- Kato, H., T. Maeda, and A. Magaino (1978). Mechanism and scaling of cavitation erosion, 12th Symp. on Naval Hydrodynamics, National Academy of Sciences, Washington, D.C., pp. 452-469
- Kruppa, C., and G. Sasse (1977). Model propeller cavitation erosion tests using soft surface technique, TUB/IST Rep. No. 77/7, Berlin
- Kurobe, Y., and Y. Takie (1980). Propeller erosion test by soft surface method - using stencil ink proposed by Cavitation Committee of the 14th ITTC, Papers of Ship Research Institute, No. 59, Tokyo

- Lindgren, H., and E. Bjärne (1974). Studies of propeller cavitation erosion, Conf. on Cavitation, Inst. of Mech. Eng., Paper No. C 173/74, Edinburgh, pp. 241-251
- Miyata, H., S. Tamiya, and H. Kato (1972). Cavitation on a pitching hydrofoil, Contribution to Report of Cavitation Committee, Proc. 13th ITTC, Berlin/Hamburg
- Radhi, M.H. (1975). Theoretische und experimentelle Untersuchung über den Kavitationseinsatz an schwingenden Tragflügelprofilen, Doctor-Thesis, Technische Universität Berlin (D83)
- Shen, Y., and F. Peterson (1978). Unsteady cavitation on an oscillating hydrofoil, 12th Symp. on Naval Hydrodynamics, National Academy of Sciences, Washington, D.C., pp. 362-384
- Shen, Y., and F. Peterson (1980). The influence of hydrofoil oscillation on boundary layer transition and cavitation noise, 13th Symp. on Naval Hydrodynamics, The Shipbuilding Research Association of Japan, Tokyo, pp. 221-241
- Tanibayashi, H., and N. Chiba (1977). Unsteady cavitation on oscillating hydrofoil, Mitsubishi Technical Bulletin No. 117

## IX. FIGURES

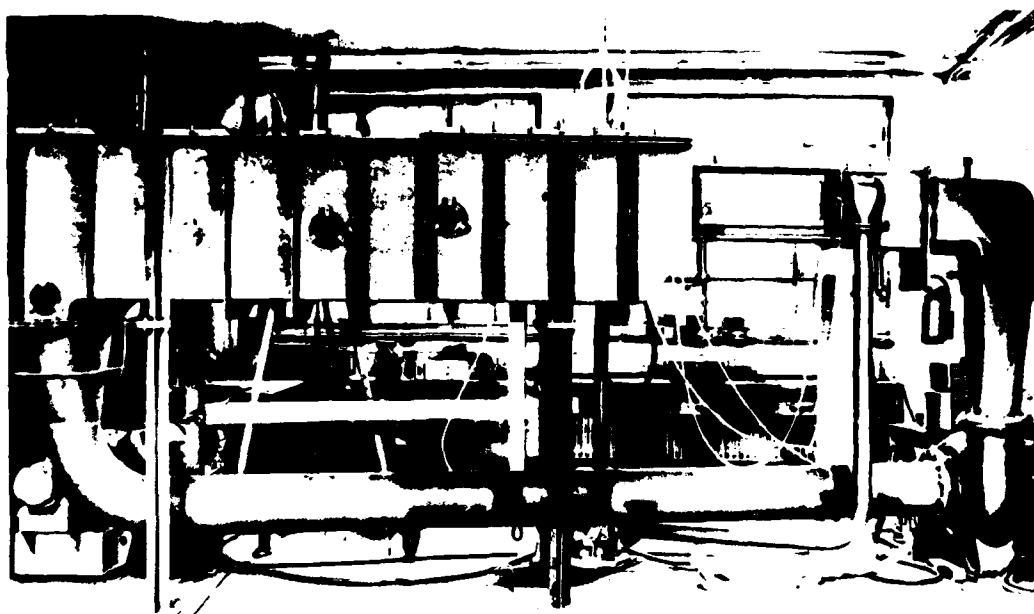


FIGURE 1. Cavitation Tunnel K28

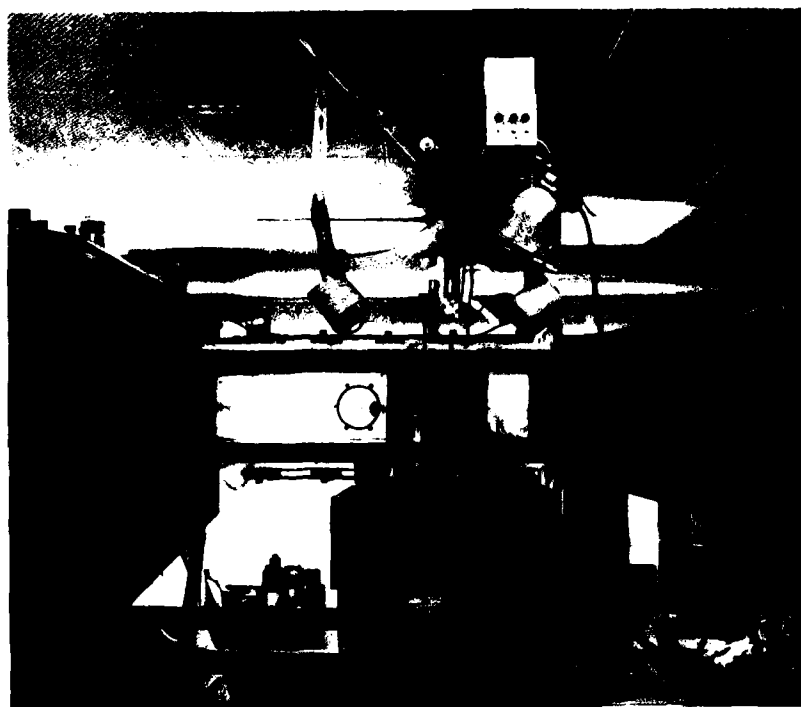


FIGURE 2. Two-dimensional Test Section

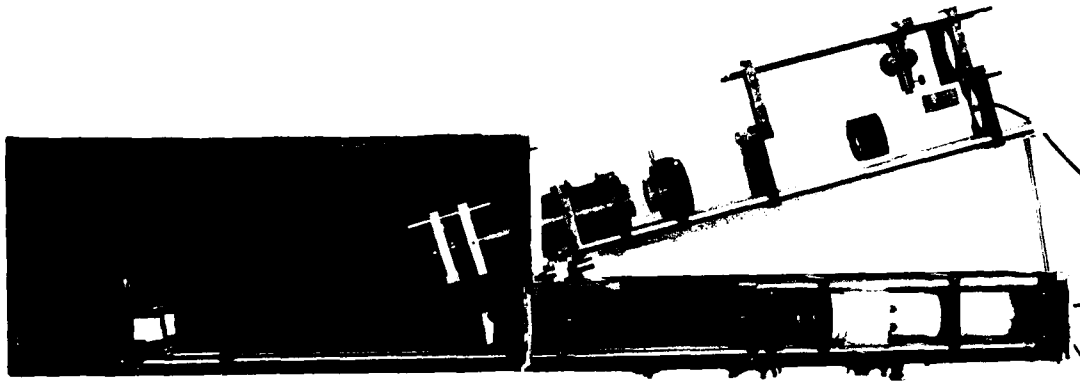


FIGURE 3. Optical Test Rig for Evaluation of Erosion Rate

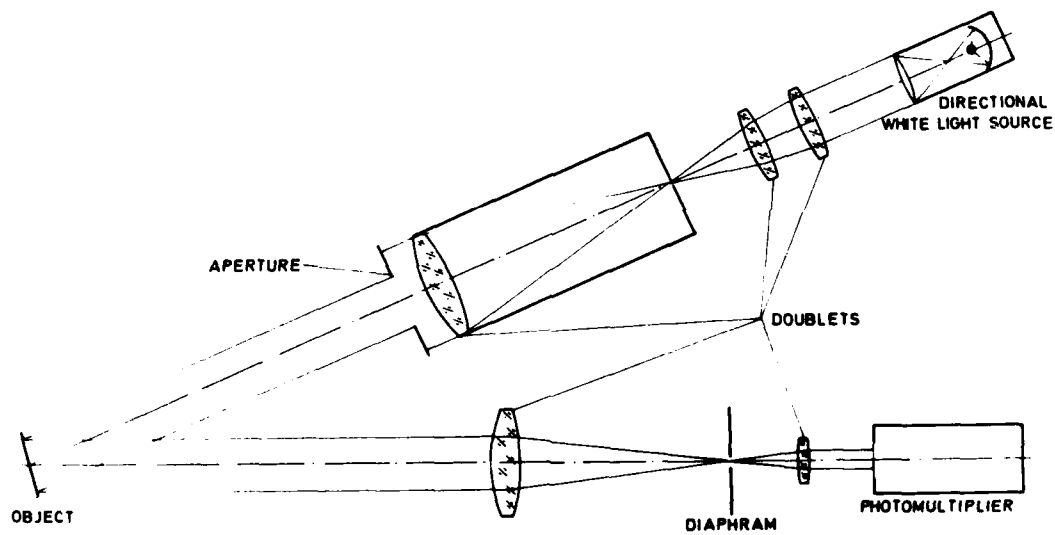


FIGURE 4. Principle of Measuring Diffuse Reflection of Light

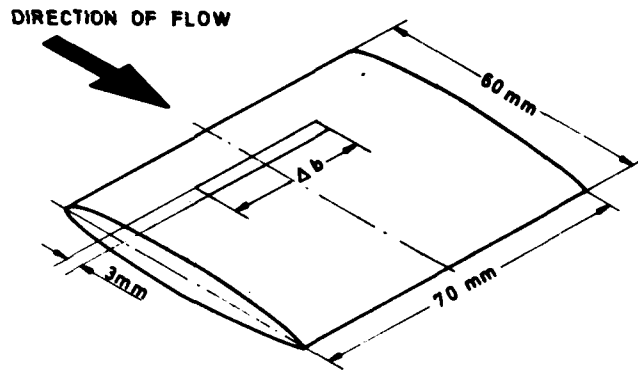


FIGURE 5.  
Strip of Exposure on  
Foil Surface during  
Calibration Test

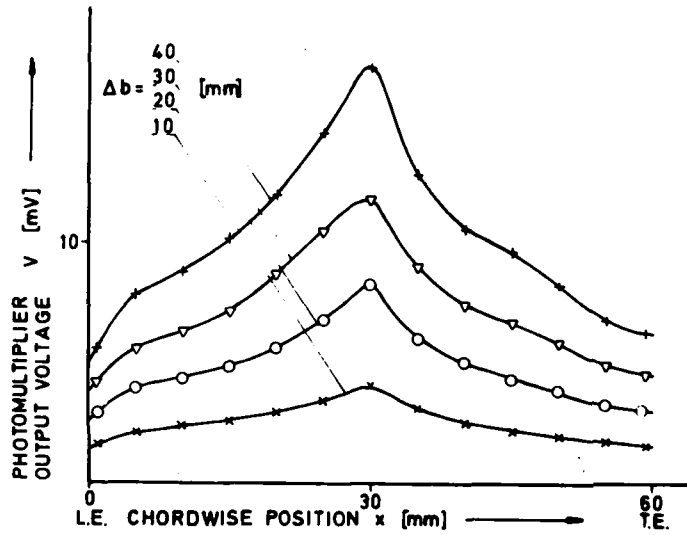


FIGURE 6.  
Calibration Curves

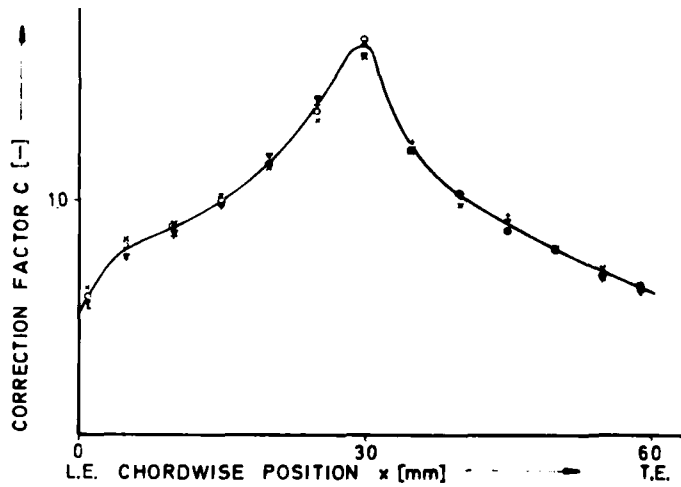


FIGURE 7.  
Correction Factor for  
Chordwise Position of  
Erosion Zone



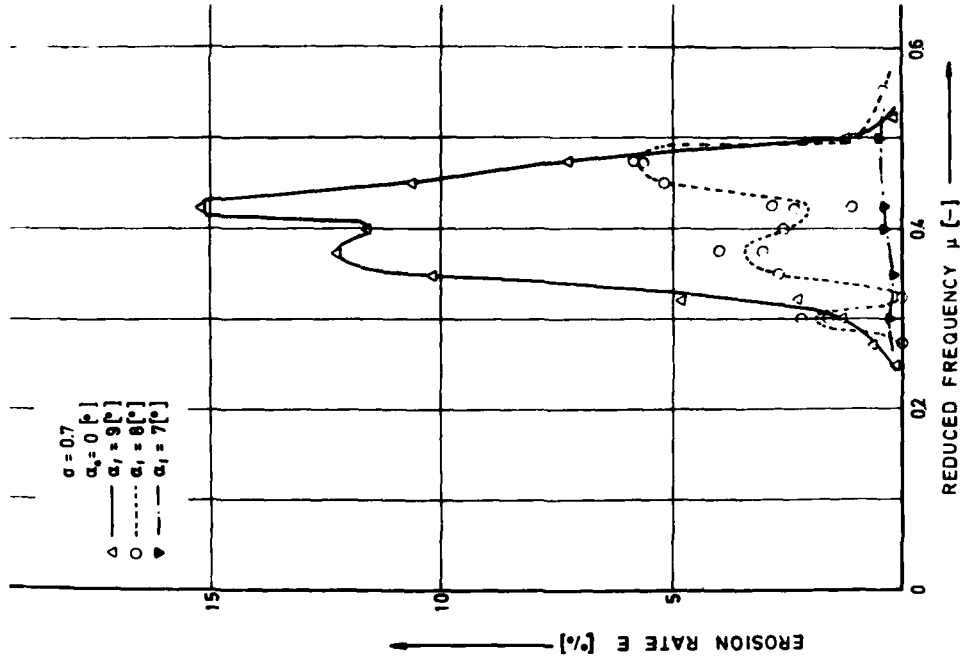


FIGURE 6. Evaluation of 35 Erosion Tests

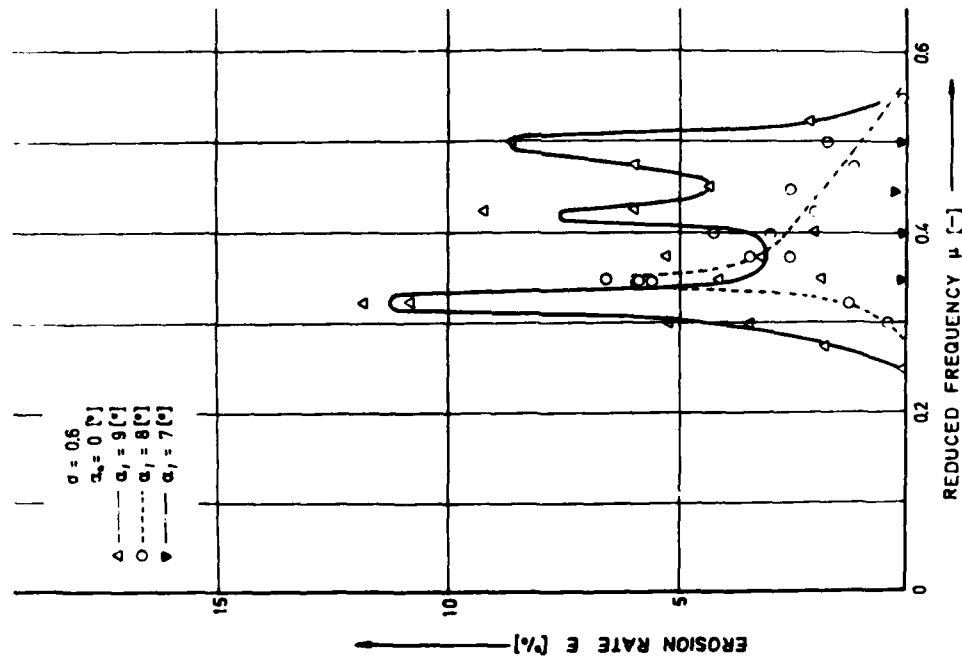


FIGURE 9. Evaluation of 34 Erosion Tests

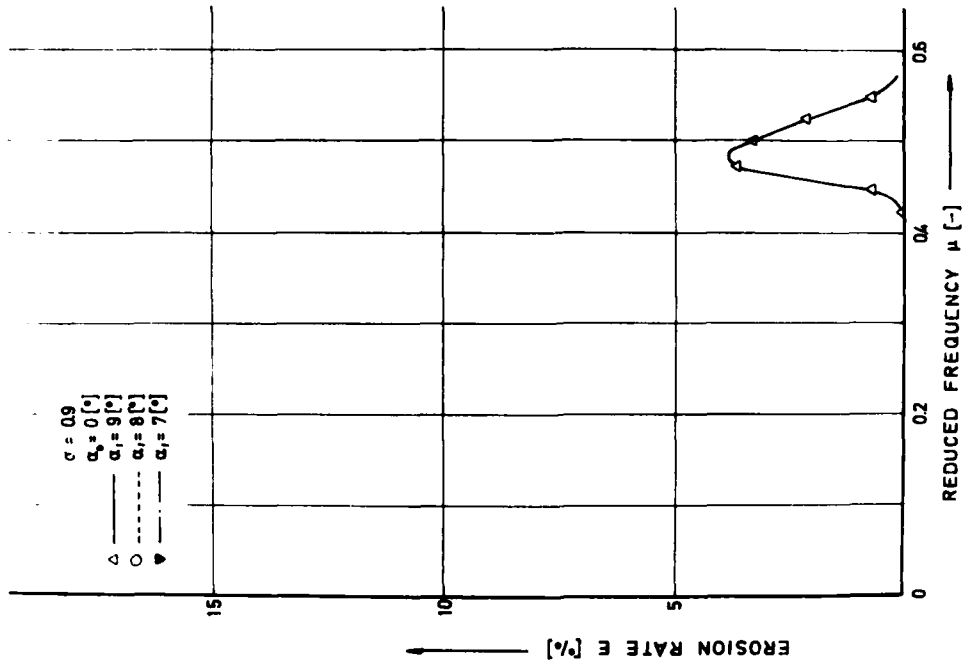


FIGURE 10. Evaluation of 23 Erosion Tests

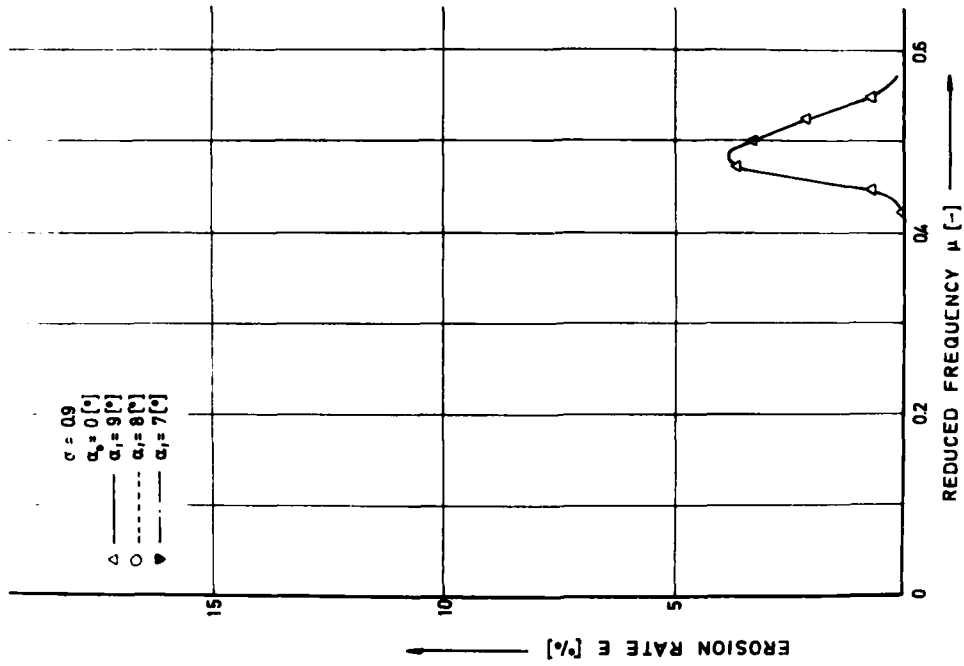


FIGURE 11. Evaluation of 6 Erosion Tests

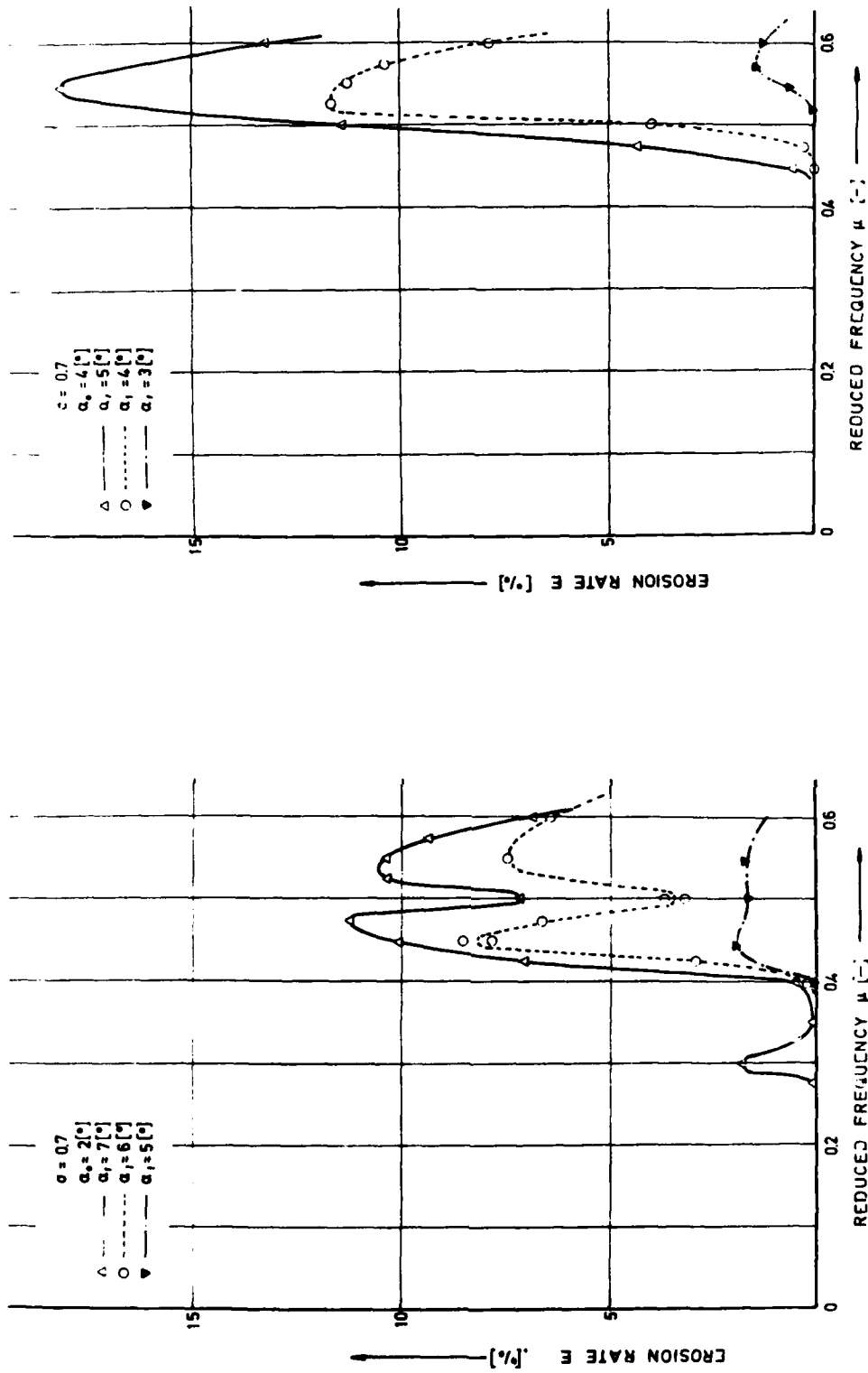


FIGURE 12. Evaluation of 25 Erosion Tests

FIGURE 13. Evaluation of 16 Erosion Tests

← DIRECTION OF FLOW

$$\begin{aligned} \alpha &= 0.6 \\ \alpha_0 &= 0^\circ \\ \alpha_1 &= 9^\circ \end{aligned}$$


 $\mu = 0.275$ 


0.3



0.325



0.35



0.375



0.4



0.425



0.45



0.475



0.5



0.525

FIGURE 14. Erosion Patterns on  
Centre Strip of Foil  
(see Figures 8 and 16)

← DIRECTION OF FLOW

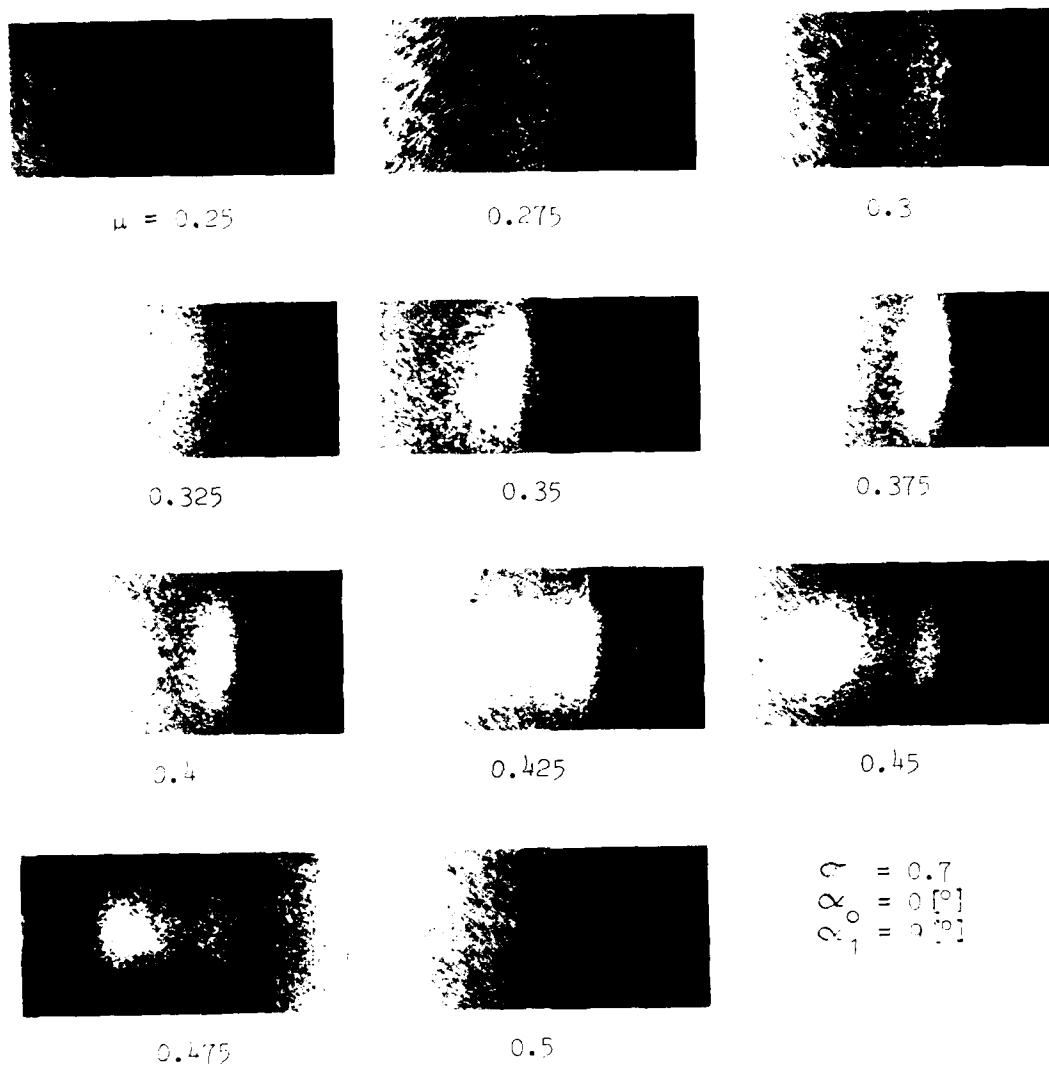
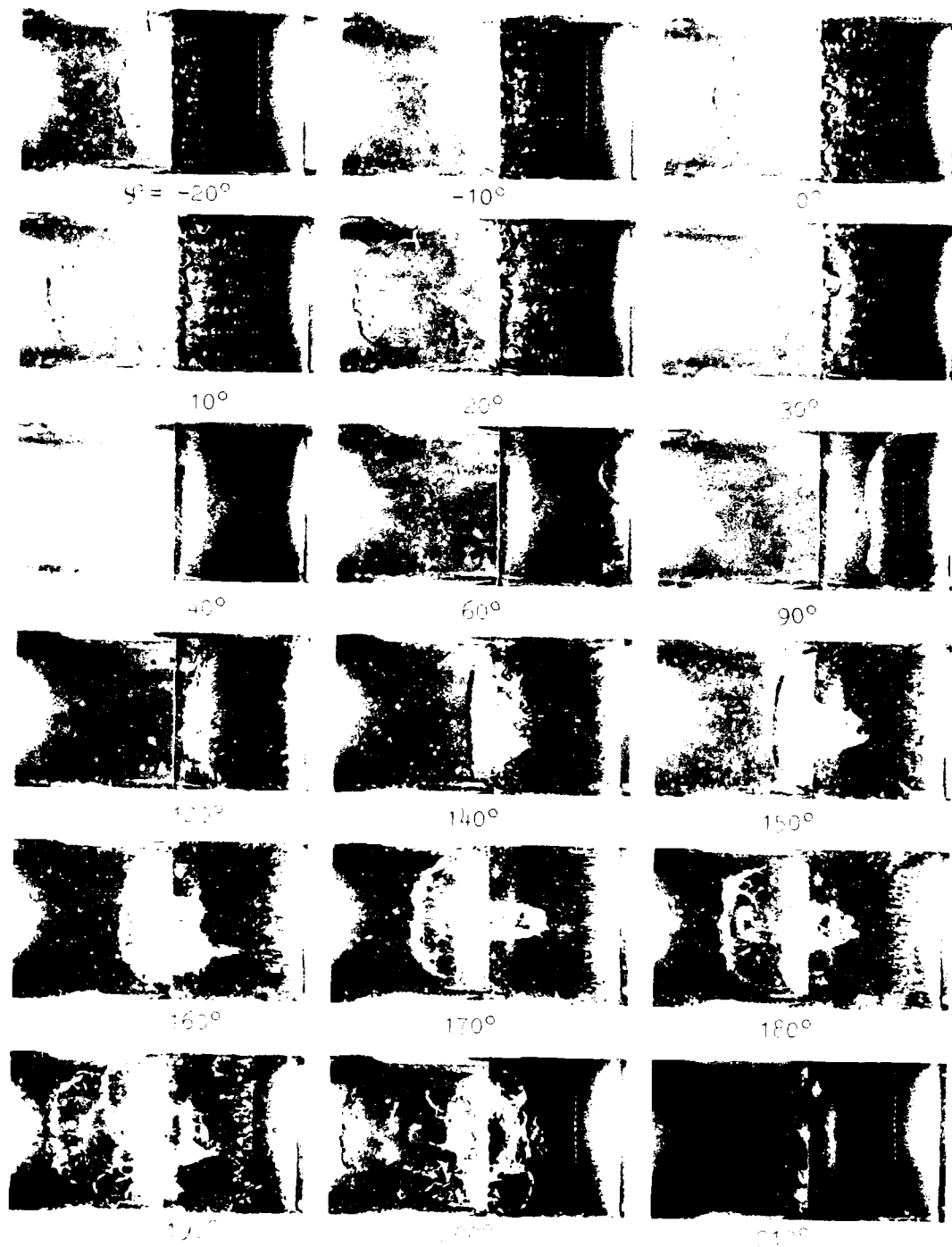
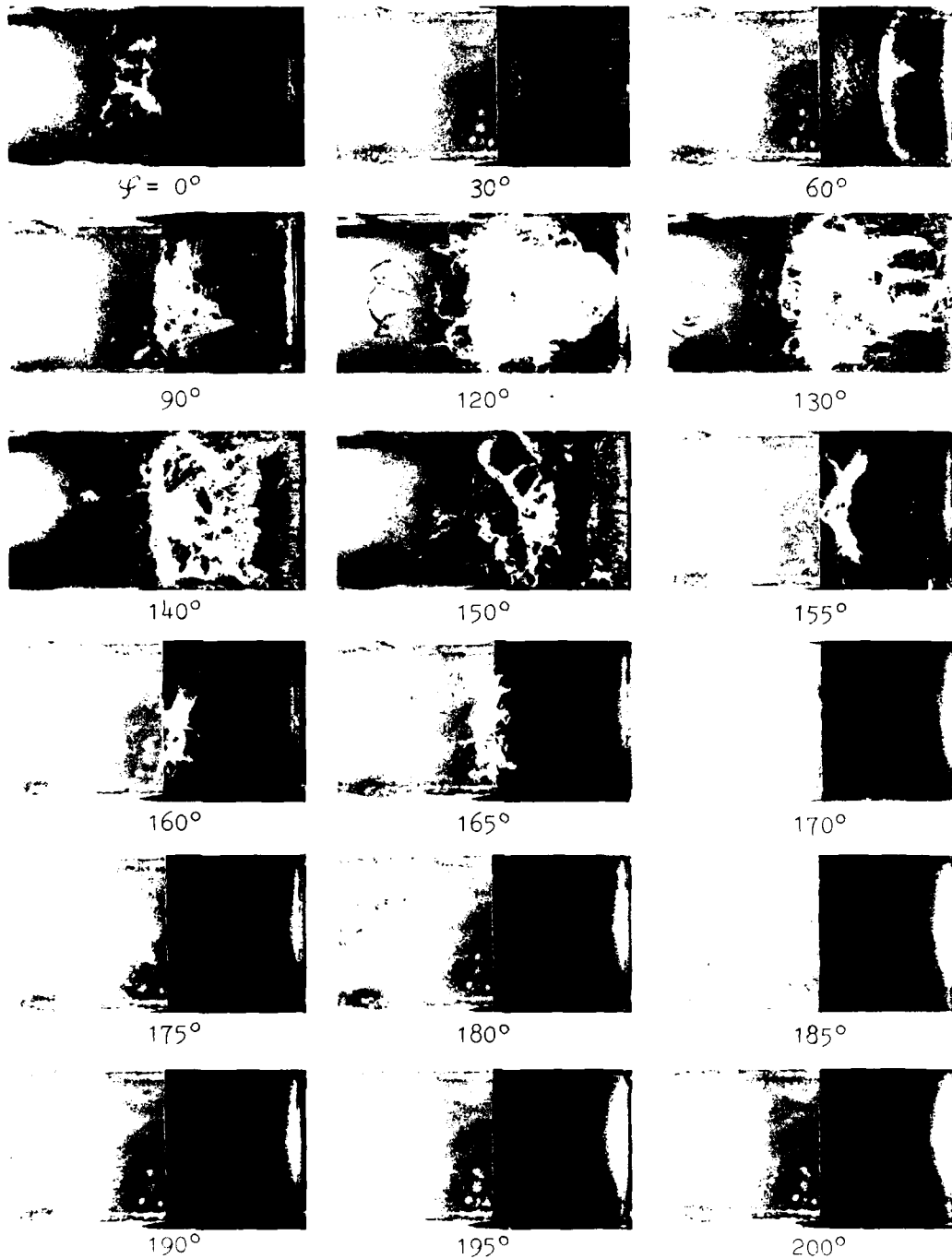


FIGURE 15. Erosion Patterns on  
Centre Strip of Foil  
(see Figures 9 and 17 through 20)



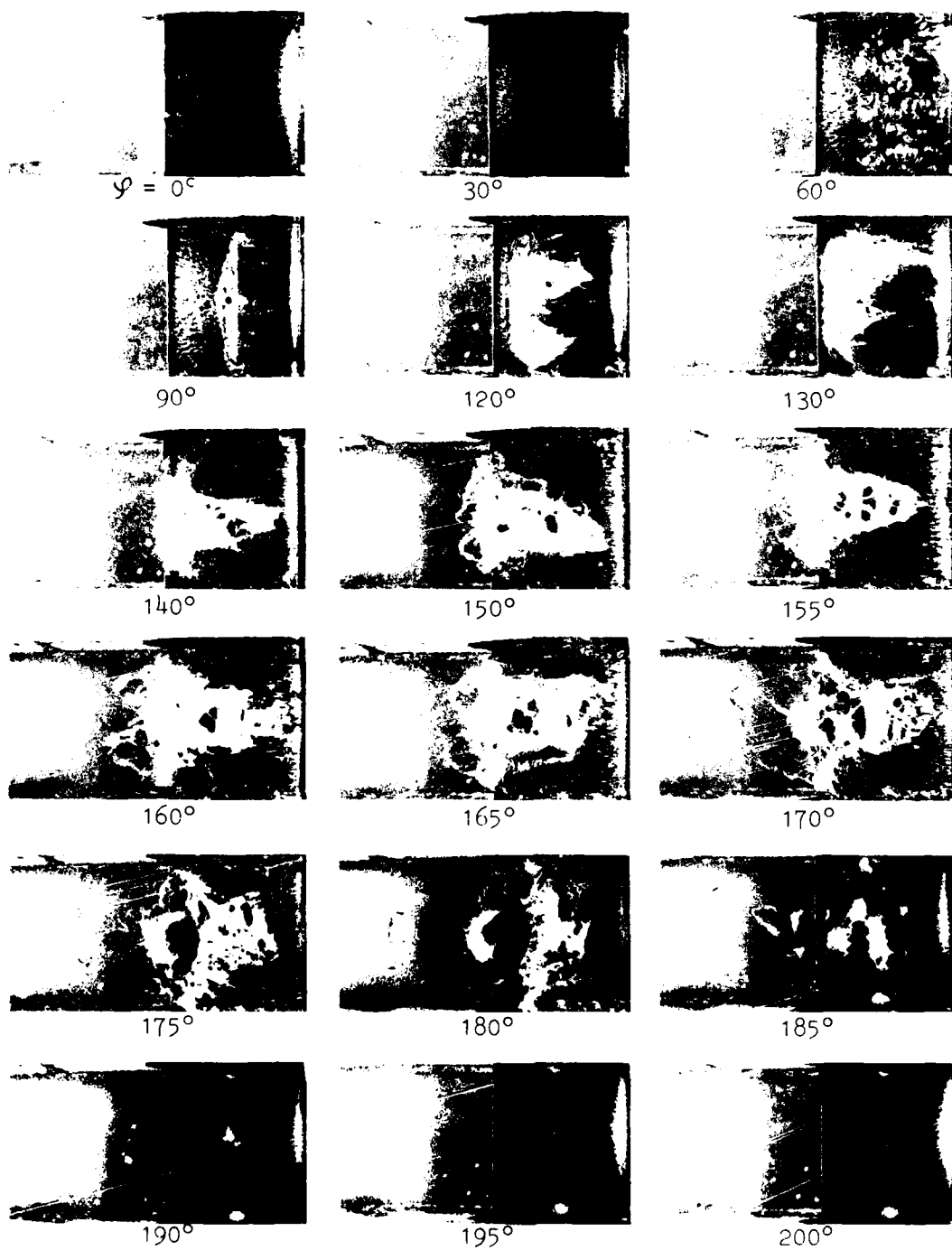
$\sigma = 1.0$   
 $\alpha = 1.0$   
 $\beta = 1.0$   
 $\gamma = 1.0$

FIGURE 1. Evolution of Flow Patterns, Leading to  
a new generation of flow patterns (see Fig. 10)



$Q = 0.7$   
 $\alpha_0 = 0.0^\circ$   
 $\alpha_1 = 9.0^\circ$   
 $\mu = 0.25$

FIGURE 17. Cavity Flow Patterns, leading to no erosion (see Figures 9 and 16)



$\sigma = 0.7$   
 $\alpha_0 = 0[^\circ]$   
 $\alpha_1 = 9[^\circ]$   
 $\mu = 0.425$

FIGURE 18. Cavity Flow Patterns, leading to severe erosion (see Figures 9 and 15)





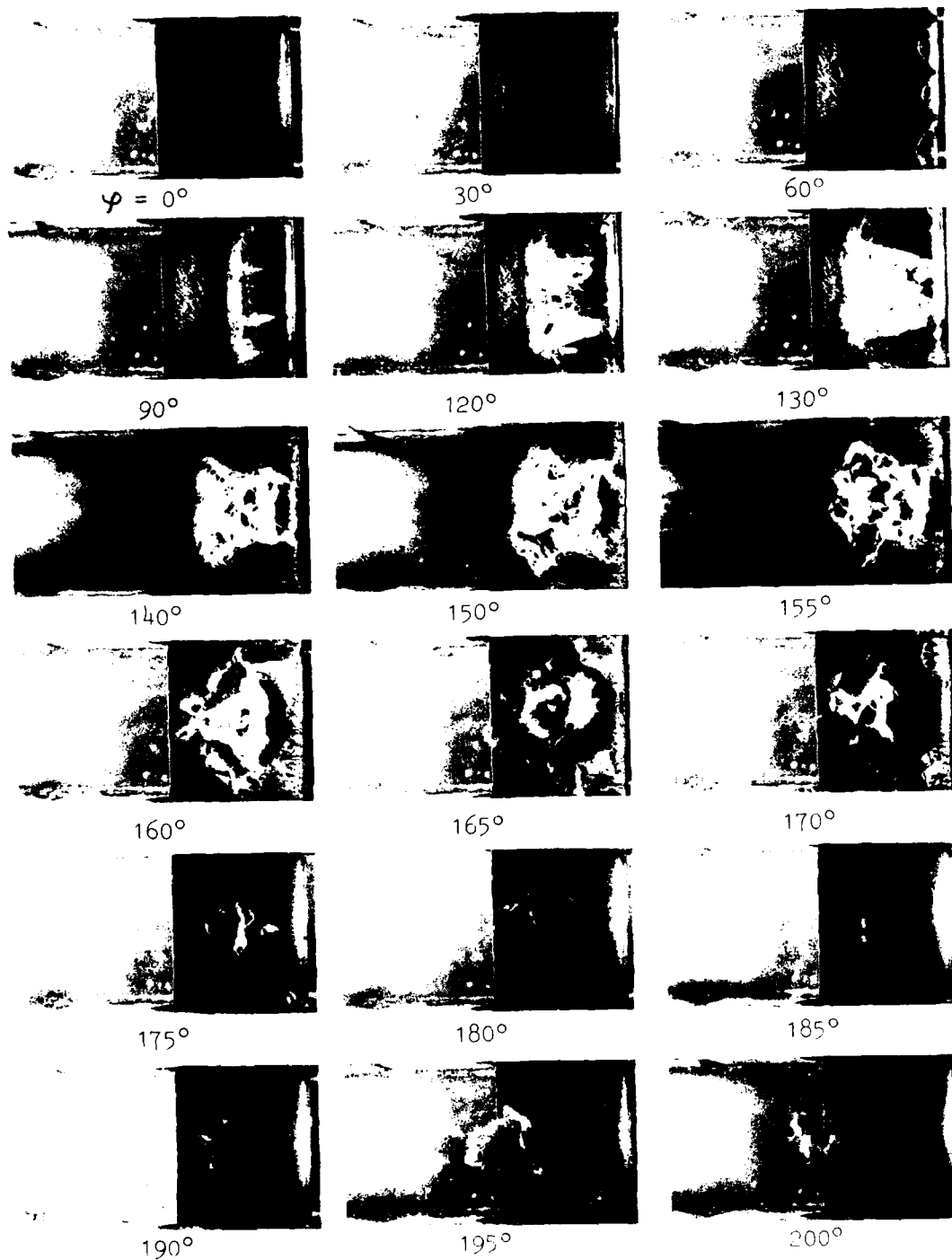
$\alpha = 0.7$   
 $\alpha_0 = 0.5$   
 $\alpha_1 = 0.5$   
 $\mu = 0.525$

FIGURE 19. Cavity Flow Patterns, leading to no erosion on centre strip (see Figure 9)



$\sigma = 0.7$   
 $\alpha_0 = 0 [^\circ]$   
 $\alpha_1 = 7 [^\circ]$   
 $\mu = 0.425$

FIGURE 20. Cavity Flow Patterns, leading to no erosion (see Figure 9)



$\alpha_0 = 0.9$   
 $\alpha_0 = 0[^\circ]$   
 $\alpha_1 = 0[^\circ]$   
 $\mu = 0.425$

FIGURE 21. Cavity Flow Patterns, leading to no erosion (see Figure 11)

## Discussion

N. Chiba (Mitsubishi Heavy Industries)

The bubble cavities can be seen at  $\phi = 0^\circ - 30^\circ$  in Figure 16. Do they have anything to do with erosion patterns?

Erosion is concerned with both material strength and cavity strength. Therefore the test results may be affected by the material of the soft surface. Have you any plan to measure the pressure on the foil directly by a method such as used by the discussor (Chiba, 1975)?

## Reference

Chiba, N., Behavior of Cavity Collapse as Cause of Cavitation Damage of Propeller Blades, ASME Symposium on Cavity Flow, Minneapolis (1975).

H. Kato (University of Tokyo)

If the authors could show how the pressure distribution changed at noncavitating condition, it might be helpful for the understanding of the erosion mechanism.

The discussor also would like to see photographs taken from a side window, because erosion intensity changes markedly if the cloud cavity collapses very close to the surface.

T. Sasajima (Mitsubishi Heavy Industries)

The erosion rate defined by the authors is a parameter of the erosion area caused by the cloud cavitation, the intensity of which is higher than the level of removing the stencil ink. But the discussor thinks it rather difficult to generalize the erosion rate, since both types of erosion near mid-chord and trailing edge are included together, this results in a strange change of the erosion rate with reduced frequency (see Figures 9 and 12). Erosion near trailing is more troublesome, since removal of the material near the trailing edge and bent trailing edge are related to this type of erosion. On the contrary, erosion near mid-chord is not so severe if the material is sound, according to our experiences. Thus it is interesting and informative if the erosion rate is defined for each type of erosion.

As to the erosion near the blade root of a propeller operating in inclined flow condition, extension of erosion depth there is more critical than in the area on the blade surface. Since the erosion rate does not give any information about it, the discussor doubts if the erosion rate is useful in predicting root erosion in full scale.

It is easy to analyze the data in relation to the reduced frequency in the tests with an aerofoil. But it is rather difficult to extend these data to the case of propellers, since occurrence of cloud cavitation is three dimensional and also the definition of the reduced frequency is arbitrary.

E.A. Weitendorf (Hamburg Ship Model Basin)

In supporting Professor Kruppa concerning the question from Mr. Takao Sasajima, it may be mentioned that there is a cooperation between the Institut für Schiffbau in Hamburg and Professor Kruppa's Institute. In a paper<sup>1</sup> from the IfS Hamburg an approximation method is applied in order to treat the coupled integral system for the source-sink and vortex distribution of the unsteady loaded hydrofoil. The comparison of the calculation with the measurements of the authors shows that the cavity extent  $c_e(t)$  is calculated reasonably, the phase between maximal angle of attack and cavity length is well described, and the cavity thickness  $\eta(t)$  attains reasonable values, i.e., maximal thickness for the largest cavity extent. The theory has now been extended to propellers and will be partly presented in a paper<sup>2</sup> at the Schiffbau-Technische Gesellschaft at Berlin in November 1982.

## References

1. Alwaerdt, P., and W. Gleine, Kavitation an instationär belasteten Flügelprofilen, 16. Kolloquium des Sonderforschungsbereiches 98, Hamburg, June 1982.
2. Chao, K.Y., N. Westphal, and P. Alwardt, Berechnung der Druckverteilung, der Kavitationserscheinungen sowie der induzierten Druckschwankungen an der Aussenhaut für Propeller im Nachstrom, Jahrbuch STG, Vol. 76, 1982.

## Author's Reply

Claus Kruppa

Dr. Chiba is asking whether the bubble cavitation visible in Figure 16, for phase angles  $0^\circ < \psi < 30^\circ$ , is in any way related to erosion patterns. This is indeed so. In fact, the only case where erosion was ever found not to be caused by cloud cavitation, but had to be interpreted as a consequence of the occurrence of bubble cavitation, was associated with the flow pattern documented in Figure 16. The corresponding erosion pattern can be seen in Figure 14, close to the trailing edge of the foil. The effect of the soft-surface material strength on erosion is realized, of course. But, at the moment, it is not planned to carry out direct pressure measurements.

In reply to Professor Kato's question it should be mentioned that, for pitching foils, pressure distributions based on theory are available in the literature, at least for thin-foil sections. Unfortunately, very little experimental data exist for foils of finite thickness. In the case of the test program presented it must be stated that the actual foil dimensions were too small for attempting to obtain both erosion patterns and pressure distributions at the same time. For future tests, it is planned to take photographs from side windows as well, because it is realized that the distance of cloud cavity collapse from the surface is an essential indication of the danger of erosion.

Dr. Sasajima realizes that the strangely peaked erosion rate characteristics in Figures 9 and 12 result from two or more erosion zones on the foil surface, each having its maximum at a different reduced frequency, and, as a consequence, he suggests that each erosion zone should be evaluated separately. With the evaluation technique selected in the test program this is, of course, very difficult. In addition, it can be seen from Figures 14 and 15 that erosion zone boundaries are often not well defined. As to the usefulness of the data obtained so far for predicting the danger of root erosion in propellers, it is believed that one still has to go a long way before this problem is solved. The critical remarks with regard to erosion depth, as distinct from the definition of erosion rate used in the paper, are very much appreciated. The same applies to the usefulness of two-dimensional foil tests for predicting propeller flow in general.

Finally, with regard to Dr. Weitendorf's remarks, it should be added that the high-Reynolds-number tests planned for the future will also reveal possible scale effects on cavity dimensions such as maximum length, maximum thickness, and phase angles.

# Comparison of Computational and Experimental Unsteady Sheet Cavitation

Frederick Stern  
Science Applications, Inc., Annapolis, Maryland

## ABSTRACT

A recently developed nonlinear method for predicting unsteady sheet cavitation on marine propellers is partially validated by comparing its results with model and full-scale experimental data. The method employs a dynamical approach in which the form of the instantaneous cavity surface is modeled at each propeller cross section as a semiellipse. Values for the cavity length (major axis), thickness (semiminor axis) and position along the section chord are determined such that the nonlinear cavity surface boundary conditions are satisfied approximately. The pressure on the instantaneous cavity surface is obtained using a two-dimensional, thick-section, unsteady potential flow computer program. Three-dimensional propeller effects are included by correcting the harmonics of the vertical component of the section inflow using the results from an unsteady propeller lifting-line computer program. The vertical component of the section inflow is obtained from the nominal wake modified to represent an effective wake using data for axisymmetric bodies. A review of the computational method is provided.

Comparisons are made with experimental data for two different unsteady cavitation applications: a pitching hydrofoil and the Naval Auxiliary Oiler (AO-177) propeller. For the AO-177 propeller application there is a close agreement between the computational and model-scale experimental results for cavitation inception, duration and extent. The full-scale values are also similar, except the cavitation duration and extent are reduced. A part of this discrepancy is due to scale effects associated with the difference between model and full-scale Reynolds number. Much of the full-scale cavitation behavior observed on the AO-177 propeller is also predicted by the calculations. The maximum cavitation is at the .85 radius; the cavities collapse towards the section trailing edge; and the principal effect of the fins is a reduction in cavity volume and collapse velocity due to a decrease in cavity thickness. For the pitching foil application the computational method yields best results in predicting the cavity dynamics. For fixed cavitation number, mean foil angle and pitch amplitude, the cavity dynamics, such as maximum cavity size and cavity surface behavior, are shown to depend on the ratio of the cavity natural frequency of oscillations for the foil fixed at the maximum pitch amplitude to the foil reduced frequency. The experimental results appear to confirm the computational trends up to the point that experimental data was obtained.

## SECTION 1: INTRODUCTION

The various forms of cavitation which occur on marine propellers are a major problem for both naval and commercial ships. There can be numerous deleterious consequences such as damage to the propeller blades and the hull, radiation of large amplitude pressures causing noise and contributing to the hull surface vibratory excitation and alteration of both steady and unsteady propeller forces. An accurate method for predicting propeller cavitation is needed both by the propeller designer and as a necessary ingredient in procedures for predicting its consequences. In this paper a recently developed nonlinear method for predicting unsteady sheet cavitation on marine propellers (Stern and Vorus, 1982) is partially validated by comparing its results with model and full-scale experimental data. The method employs a dynamical approach which is intended to model the gross features of unsteady sheet cavitation: cavity length, thickness, position and surface behavior including rates of deformation and movement. The method differs significantly in a number of ways from the linear quasi-steady and unsteady propeller cavitation theories. The form of the instantaneous cavity surface is modeled at each propeller cross section as a semiellipse. Values for the cavity length (major axis), thickness (semiminor axis) and position along the section chord are determined such that the nonlinear cavity surface boundary conditions are satisfied approximately. This cavity model does not constrain the leading edge of the cavity to the leading edge of the foil. An interaction between cavity cross sections can be included in a slender body theory sense with a spanwise iterative procedure; however, this was not included in the present applications. The unsteady pressure distribution on the cavity surface and not on the foil surface is used in predicting the cavity's deformation and motion. Also foil thickness is included in the unsteady pressure computation. This eliminates the singularity of the pressure at the foil leading edge that mars thin foil theories. Tulin (1980) has shown that by including foil thickness in his linear steady cavity solution, better agreement is obtained with experiments for foils with thickness.

The conventional quasi-steady theories use Guerst's (1961) or similar two-dimensional linear steady cavity solutions to obtain the sectional cavity characteristics (for example, Noordzig, 1976, and Kaplan, et al., 1979). The cavitation patterns predicted by these theories tend to overpredict the cavity extent and show a phase difference for the volume variation as compared to observations. Chiba, et al. (1980) shows better agreement with observations by including empirical correction factors for the cavity extent and phase in their quasi-steady theory. Yuasa, et al. (1980) and Frydenlund and Persson (1981) depart from the conventional quasi-steady theories by obtaining the sectional cavity characteristics using an adaptation of the numerical (vortex/source lattice) linear steady cavity method of Jiang and Leehey (1977).



In this method cavitation is determined stripwise along the propeller blade in a manner that certain three-dimensional effects can be included. The results reported by Yuasa, et al. and Frydenlund and Persson indicate an improvement over the conventional quasi-steady theories. Lee (1980) presents a numerical (vortex/source lattice) method which uses a linear unsteady cavity solution to obtain the sectional cavity characteristics. A spanwise iterative procedure is used to allow for an interaction between cavity cross sections. Lee's results show better agreement with wake screen experimental data than with full-scale observations.

In this paper comparisons are made with experimental data for two different unsteady cavitation applications: a pitching hydrofoil and the Naval Auxiliary Oiler (AO-177) propeller. In Section 3 results are given for the AO-177 application. There is a close agreement between the computational and model-scale experimental results for cavitation inception, duration and extent. The full-scale values are also similar, except the cavitation duration and extent are reduced. A part of this discrepancy is due to scale effects associated with the difference between model and full-scale Reynolds number. Much of the full-scale cavitation behavior observed on the AO-177 propeller is also predicted by the calculations. The maximum cavitation is at the .85 radius; the cavities collapse towards the section trailing edge; and the principal effect of the fins is a reduction in cavity volume and collapse velocity due to a decrease in cavity thickness. In Section 4 results are given for the pitching foil application. The computational method yields best results in predicting the cavity dynamics. For fixed cavitation number, mean foil angle and pitch amplitude, the cavity dynamics, such as maximum cavity size and cavity surface behavior, are shown to depend on the ratio of the cavity natural frequency of oscillations for the foil fixed at the maximum pitch amplitude to the foil reduced frequency. The experimental results appear to confirm the computational trends up to the point that experimental data was obtained. A review of the computational procedure is provided in Section 2. The reader is referred to Stern and Vorus (1982) and Stern (1980) for more details. The method under consideration is still in the development stage. Possible areas of improvements to the method are discussed in Section 5.

## SECTION 2: COMPUTATIONAL METHOD

The computational method separates the fluid velocity potential boundary value problem for unsteady sheet cavitation on marine propellers into two parts -- a static part and a dynamic part -- which are solved sequentially in a forward time-stepping procedure. The static potential  $\phi_s$  describes the flow around the cavity fixed instantaneously relative to the propeller while the propeller rotates through the non-uniform wake field. The dynamic potential  $\phi_D$  represents the instantaneous reaction of the cavity to the static potential field and thus

predicts the cavity's deformation and motion relative to the blade. For known cavity surfaces  $S_C(t)$  the static potential boundary value problem is solvable by standard methods since the boundary conditions are exclusively kinematic. Therefore, with regard to the dynamic potential boundary value problem the static potential and its derivatives are considered as known at any time. A solution is obtained for the dynamic potential by using the concepts of slender body theory to define near and far field potentials which are matched to form the complete solution. In the far field the cavity is represented by a three-dimensional line distribution of sources. In the near field the cavity is approximated at each cross section as a semiellipse with semimajor axis  $a$  (cavity half-length), semiminor axis  $b$  (cavity thickness) and position  $\ell$  along the section chord. The instantaneous cavity surface is shown schematically in Figure 1.

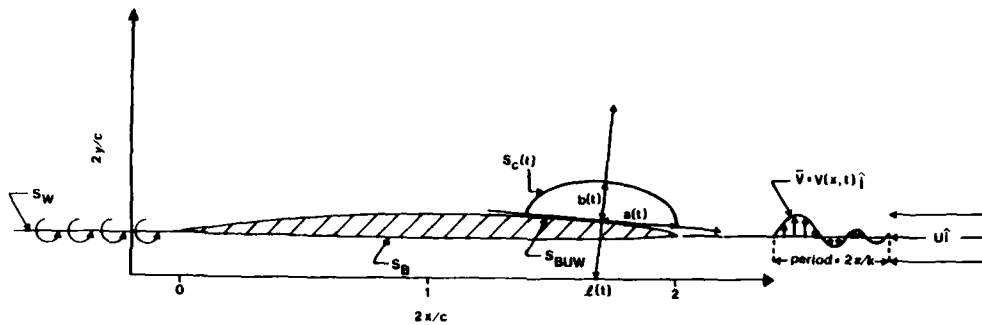


Figure 1. Cavity and Propeller Blade Section Geometry

It can be shown that the dynamic boundary condition on the surface of the cavity can be satisfied in a least square sense by requiring that its Fourier-Cosine coefficients be zero. The first three Fourier-Cosine coefficients provide conditions for determining  $a$ ,  $b$  and  $\ell$ . These conditions yield the cavity equations of motion in the form of three coupled nonlinear second-order ordinary differential equations with time as the independent variable. The cavity equations can be put in the form

$$\begin{aligned}\ddot{a} &= f_1(a, \dot{a}, b, \dot{b}, \ell, R_n, A_r, P_0, P_2) \\ \ddot{b} &= f_2(a, \dot{a}, b, \dot{b}, \ell, R_n, A_r, P_0, P_2) \\ \ddot{\ell} &= f_3(a, b, \dot{b}, \ell, R_n, P_1)\end{aligned}\quad (1)$$

where  $R_n = Uc/\nu$  is the Reynolds number,  $A_r$  is the cavity aspect ratio and

$$P_n = \frac{m}{\pi} \int_0^\pi P \cos n\eta d\eta \quad n = 0, 1, 2 \text{ and } \begin{cases} n = 0, m = 1 \\ n > 0, m = 2 \end{cases} \quad (2)$$

are the first three Fourier-Cosine harmonics of the fluid pressure

$$P = \sigma + C_p \quad (3)$$

evaluated on the instantaneous cavity surface  $S_c(t)$ . In equation (3)  $\sigma$  is the cavitation number

$$\sigma = \frac{p_\infty - p_c}{\frac{1}{2} \rho U^2} \quad (4)$$

where  $p_\infty$  is the ambient pressure,  $p_c$  is the cavity pressure,  $U$  is the steady section speed, and  $\rho$  is the fluid density; and  $C_p$  is the known static potential pressure coefficient. The following terms which are included in the more general form of the cavity equations have been neglected in equation (1) for convenience: the cross product term between the static and dynamic potentials; the slender body theory interaction between cavity cross sections; and the surface tension pressure. The unsteady cavitation prediction results are in the form of response curves ( $a, \dot{a}, b, \dot{b}, \ell, \dot{\ell}$ ) vs. time which are obtained by numerically integrating the cavity equation (1). For fixed  $R_n$  (damping coefficient) and  $A_r$  in equation (1) the cavitation response is controlled by the specification of  $P = P(\vec{x}, t)$ , equation (3). When  $P = P(\vec{x})$  is constant in time the cavity equations have constant solutions,  $(\bar{a}, \bar{b}, \bar{\ell})$ . These constants are determined by the equations such that the first three harmonics of the fluid pressure are zero on the ellipse, that is, the equations fit an ellipse, in a least square sense, to the zero pressure line in the fluid. In earlier work it was shown that the linear response of the cavity about the equilibrium values  $(\bar{a}, \bar{b}, \bar{\ell})$  is damped periodic oscillations. The frequency of the oscillations is referred to as the cavity natural frequency. When  $P = P(\vec{x}, t)$  is not constant in time the cavity equations have unsteady solutions. The character of the unsteady solution depends on the specific form of  $P(\vec{x}, t)$ . In the applications presented in this paper  $P(\vec{x}, t)$  is of the general form

$$P = \text{Re} \sum_{n=0}^N p_n(\vec{x}) e^{i n k t} \quad (5)$$

In equation (5)  $k$  is the section reduced frequency

$$k = \omega c / 2U \quad (6)$$

where  $\omega$  is the excitation frequency and  $c$  is the section chord length. The ratio of a representative value for the cavity natural frequency to the excitation frequency  $k$  will be shown to have an important affect on the unsteady cavitation response.

The integration of the cavity equations requires the determination of the static potential and its derivatives at each time step. It was stated earlier that the static potential boundary value problem can be solved by standard methods. However, it should be recognized that the semielliptical cavity form itself cannot be used in the solution of the static potential problem because it is only an approximation to the

cavity surface. Ostensibly, it provides the necessary information (cavity length, thickness and position) which can be suitably represented in the static potential solution. Presently a thin-cavity approximation is used for the static potential. This procedure distributes sources on the unwetted portion of the foil surface to account for cavity thickness effects in the fully-wetted flow pressure field. The details of this procedure are provided in Appendix A. Further research is needed for determining a more accurate procedure for calculating the static potential.

The fully-wetted flow is calculated using a thick-section unsteady potential flow computer program. The program provides an accurate representation of the fully-wetted flow unsteady pressure field that is sensitive to changes in the section geometry (thickness, camber and angle of attack) and the hull wake section inflow. A description of the theory implemented by this program is provided in Appendix B. For propeller applications, three-dimensional propeller effects are included by correcting the harmonics of the vertical component of the section inflow  $\bar{V}$  using the results from an unsteady propeller lifting-line computer program (Vorus, 1982). This program utilizes Brown's (1964) theory as implemented and extended to skewed propellers by Vorus. In the present application of the method to the AO-177 propeller,  $\bar{V}$  was obtained from the AO-177 nominal wake modified to represent an effective wake using a procedure based on the data presented for axisymmetric bodies by Huang and Groves (1980). This procedure is explained in Appendix C.

### SECTION 3: NAVAL AUXILIARY OILER (AO-177) PROPELLER

The AO-177 experienced excessive vibration/noise during builder's trials in the stern region over the propeller. Erosion and damage were found after the trials on the back side of the propeller blades from the .85 radius to the tip. The damage was most pronounced at the .85 radius. Vibration and propeller viewing trials were conducted to document and determine the probable cause of the problem (Kelly and Jessup, 1981). The results of the trials indicated that violent sheet cavitation collapse was causing the vibration/noise problem. Model-scale experiments were performed to aid in determining a solution to the problem (Bjorne, 1980). Subsequently, flow-modifying fins were installed on the AO-177 for the purpose of reducing the cavitation/noise problem. After the installation special trials were conducted in order to determine the effects of the fins (Koh and Jessup, 1982). Wilson, et al. (1982) provides a detailed account of the AO-177 vibration/noise problem and the fin repair. Also included in Wilson, et al., are results from some other propeller cavitation methods for the AO-177 propeller. Pertinent ship and propeller characteristics are given in Table 1.

Table 1. Pertinent Ship and Propeller Characteristics  
(from Koh and Jessup, 1982)

Ship Characteristics		
Length Overall (LOA), ft (m)	591.5 (180.3)	
Length Between Perpendiculars (LBP), ft (m)	550.0 (167.6)	
Breadth, Molded (Maximum), ft (m)	88.0 (26.8)	
Design Full Load Displacement, tons (metric tons)	27,235 (27,672)	
Design Full Power, shp (kW)	24,000 (17,897)	
Design Shaft RPM	100	
Design Ship Speed, knots	20	
Propeller Characteristics		
Diameter, ft (m)	21.0 (6.4)	
Pitch @ 0.7R, ft (m)	26.25 (8.0)	
Weight, lb. (kg)	69,400 (31,479)	
Number of Propellers	1	
Number of Blades	7	
Expanded Area Ratio	0.771	
Projected Area Ratio	0.590	
Mean Width Ratio (MWR)	0.216	
Blade Thickness Fraction (BTF)	0.067	
Rotation	Right-Hand	

r/R	C/D	P/D	$\theta_s$ (deg)	t/C	$f_M/c$
0.2	0.2070	1.125	0.0	0.2000	0.0490
0.3	0.2456	1.223	2.2	0.1625	0.0444
0.4	0.2722	1.288	7.1	0.1325	0.0367
0.5	0.2817	1.318	13.1	0.1080	0.0314
0.6	0.2684	1.309	20.0	0.0880	0.0300
0.7	0.2320	1.250	27.7	0.0175	0.0295
0.8	0.1815	1.140	34.5	0.0590	0.0281
0.9	0.1180	0.970	40.3	0.0500	0.0263
1.0	0.000	0.722	45.0	0.0450	0.0240

The details of the propeller design and design procedure are given by Valentine and Chase (1976). Valentine and Chase record that a most thorough state-of-the-art design effort was done. Unfortunately, as shown by the actual propeller performance, the cavitation considerations used in the design were inadequate. This points out the need for more advanced methods to insure the success of future designs. Methods like the present one in which cavitation inception, extent and dynamics are considered.

### Computational Results

Calculations were made for the AO-177 both with and without the flow-modifying fins mounted on the hull and for the full load trim condition. Results were obtained at the radial sections,  $r/R = .65, .75, .85$  and  $.95$ . For propeller applications the pressure coefficient  $C_p$  in equation (3) is given by equations (B-6) and (B-8). Also the cavitation number  $\sigma$  in equation (3) is modified to include the change in hydrostatic head due to the blades proximity to the free surface during its rotation

$$\sigma = \sigma_h - \frac{P_c}{\frac{1}{2} \rho U^2} \quad (7)$$

with

$$\sigma_h = \frac{p_a}{\frac{1}{2} \rho U^2} + F_n^{-2} \left[ \bar{h} - \bar{R} \cos(kt - \theta_s) \right] \quad (8)$$

where  $p_a$  is the atmospheric pressure,  $F_n = U/\sqrt{gc}$  is the section Froude number,  $\bar{h} = 2h/c$  is the nondimensional propeller shaft immersion,  $\bar{R} = 2R/c$  is the nondimensional section radius and  $\theta_s$  is the section skew.

The size of the region of negative pressure in the fully-wetted flow pressure field is an indication of the extent of cavitation. The thick-section unsteady potential flow computer program (see Appendix B) can be used to calculate the isobars in the vicinity of the foil surface. The vertical component of the section inflow which can be thought of as an angle of attack variation greatly affects the size of the negative pressure region. Figure 2 shows the nominal, effective and unsteady lifting-line corrected vertical component of the section inflow for the AO-177 without fin wake at the .85 radius. The fully-wetted, unsteady flow isobars calculated using the lifting-line corrected inflow (dotted curve on Figure 2) are shown in Figure 3 for blade angles  $\theta_B = 0^\circ, 20^\circ, 40^\circ, 60^\circ$  and  $80^\circ$ . Also shown in Figure 3 are the fully-wetted, steady flow isobars. Figure 3 shows a substantial region of negative pressure for  $\theta_B = 20^\circ, 40^\circ$  and  $60^\circ$ . This is due to the large angle of attack the section experiences at these blade angles. Next the results from the integration of the cavity equations are presented.

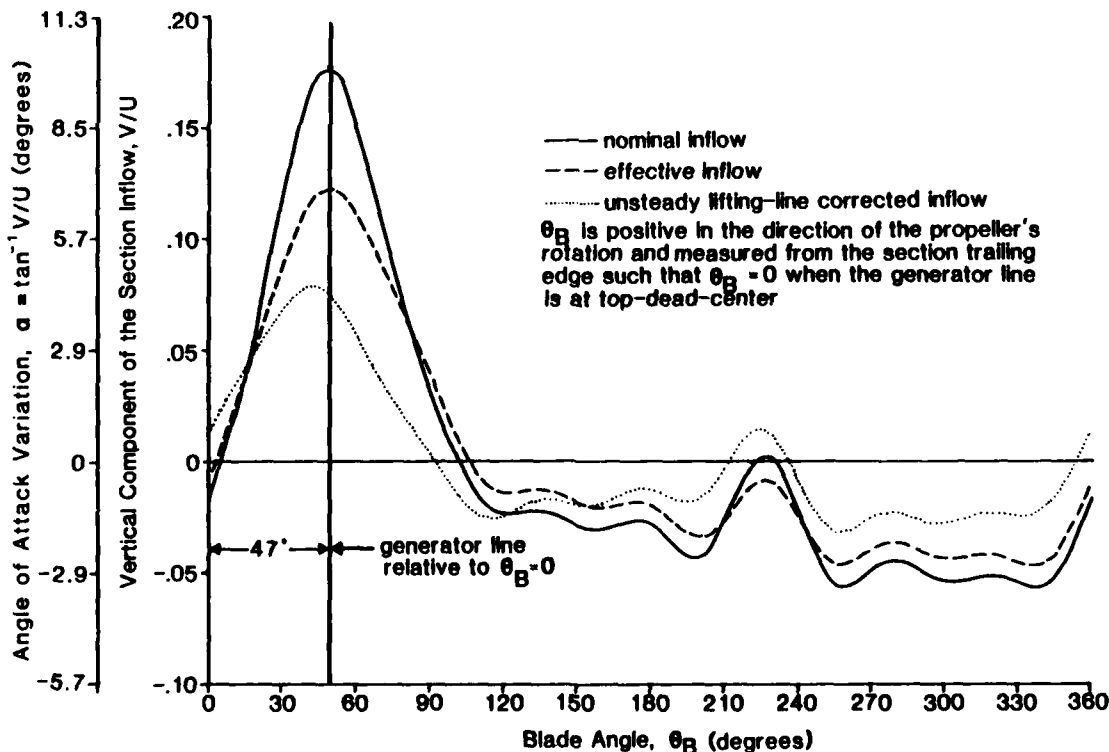


Figure 2. Vertical Component of the Section Inflow for the AO-177 Without Fin Wake at the .85 Radius.

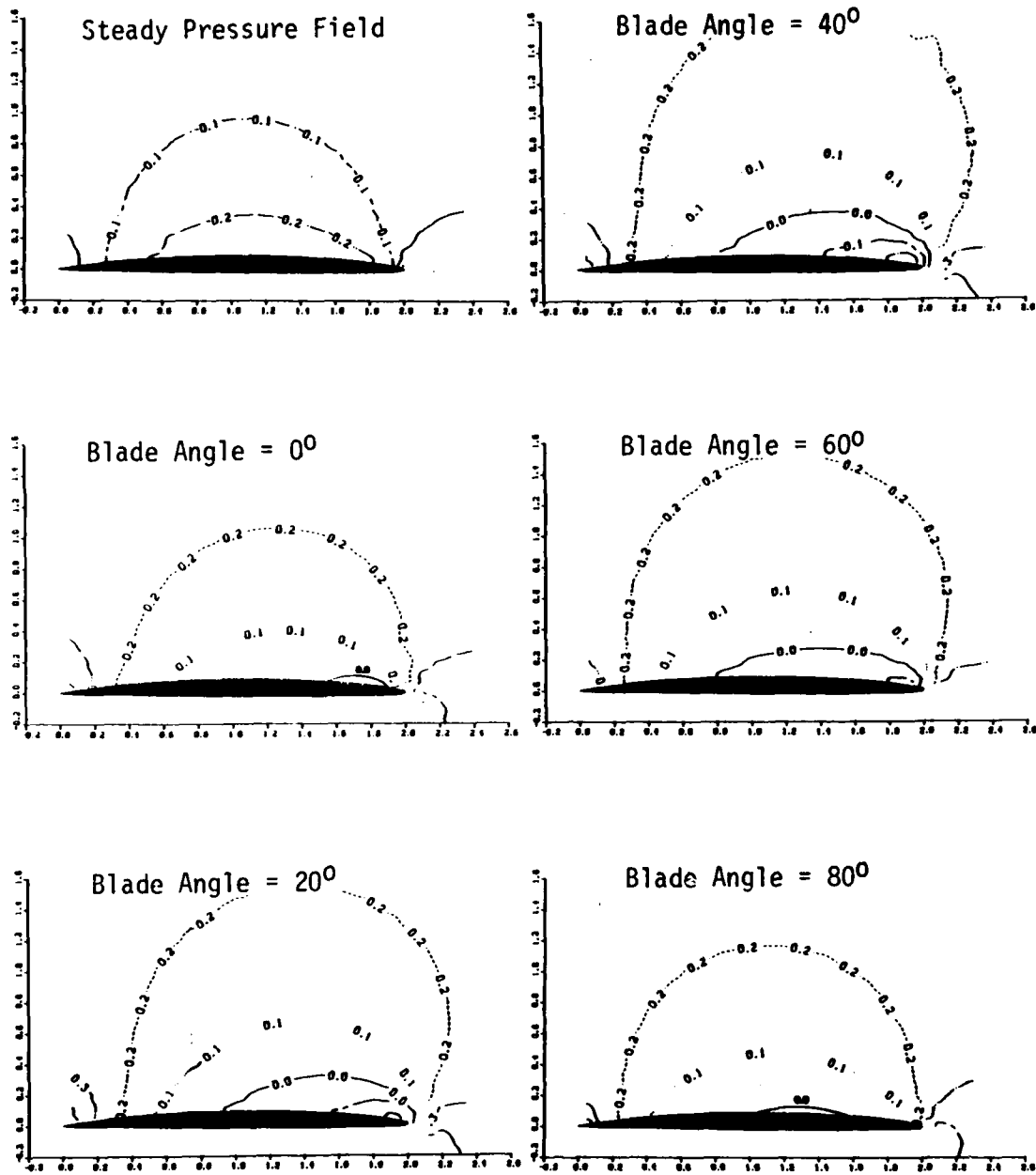


Figure 3. Fully-Wetted Flow Isobars for the A0-177 Without Fin Wake at the .85 Radius.

The radial extent of cavitation during one propeller revolution is shown in Figure 4. From Figure 4 it is seen that the inception angle decreases towards the outer radii. This is primarily due to the effects of skew. Inception occurred when the sections entered the high wake region and for a sufficient angle of attack. The results from the integration of the cavity equations for the .75, .85 and .95 radius are shown in Figures 5 and 6 for the cases with and without the fins, respectively. In Figures 5 and 6 the numbers above each cavity configuration correspond to the blade angular coordinate. The cavity growth phase is shown by the dashed line configurations and the collapse phase by the solid line. The results show extensive cavitation at the .95 and .85 radii. The cavitation initiates at the leading edge and grows to cover most of the section. The cavities are thick. The cavitation at the .75 radius is much less severe. The cavitation also initiates at the leading edge but only grows to cover about half the section and is not nearly as thick as the outer radii. The cavitation calculated at the .65 radius is similar to the .75 radius except the cavities are very thin. The maximum values of cavity length  $l_m$ , cavity thickness  $t_m$  and area  $A_m$  at each section are given in Table 2. The most severe cavitation is predicted at the .85 radius. Figure 4 shows that at the .85 radius the duration of cavitation is greatest. Also, the maximum cavity area is at the .85 radius (see Table 2). At all the radii the cavities collapse towards the section trailing edge. The collapse position  $l_c/c$  moves closer to the trailing edge for the inner radii. This is due to high frequency effects associated with a decrease in the ratio of the cavity natural frequency  $\hat{\omega}_n$  to the section reduced frequency  $k$ . The cavity natural frequency was calculated using the steady section pressure field with the ambient pressure specified to give a cavity about the size of the maximum unsteady cavity predicted at that section. Values for  $l_c/c$ ,  $\hat{\omega}_n$  and  $k$  for each section are given in Table 2. The cavity volume and volume velocity are obtained by integrating the area and area velocity values radially at each blade angle for the duration of the cavitation. These results are shown in Figures 7 and 8.

The results show a 19.26% reduction in the maximum cavity volume due to the flow-modifying fins (see Figure 7). From Table 2 it is seen that this reduction is principally due to a decrease in the cavity thickness. Figure 8 shows that the maximum and minimum cavity volume velocities are also reduced by 22.11% and 12.67%, respectively, due to the fins. The fins effect a small phase shift such that the angle at which the cavity volume is maximum is shifted from  $71^\circ$  to  $75^\circ$  and the collapse angle increases from  $110^\circ$  to  $115^\circ$  (see Figure 7).

#### Comparison with Experimental Data

The model-scale experiments were conducted at the SSPA large water tunnel (Bjorne, 1980). An identical model to that that had been used previously for the nominal wake measurements was used. The model was mounted in the test section with the water surface represented by plywood sheets placed at the design water line. Turbulence stimulating



AO-177 without Flow-Modifying Fins

AO-177 with Flow-Modifying Fins

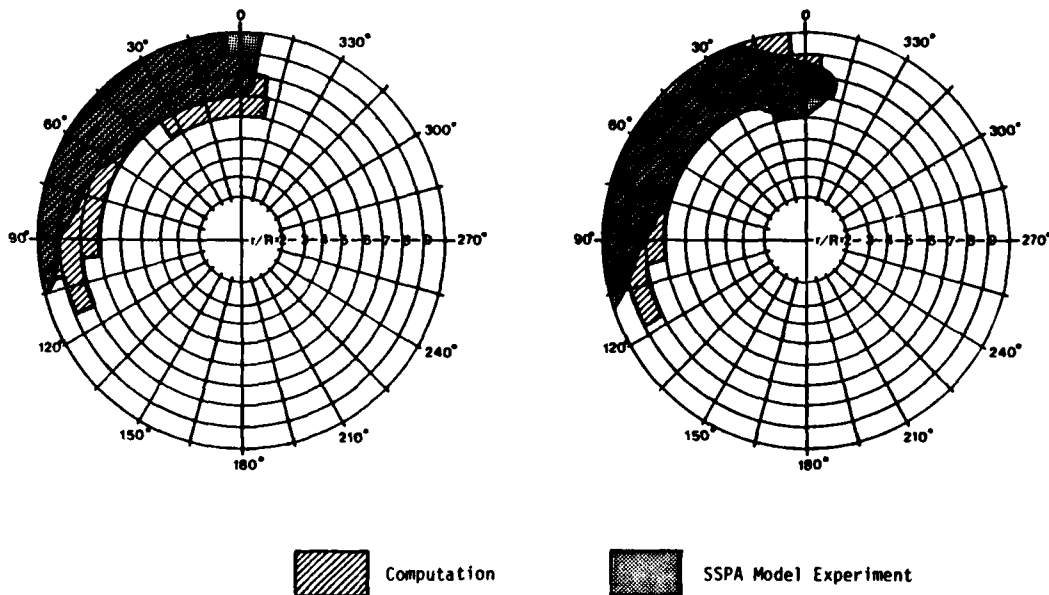


Figure 4. Radial Extent of Cavitation During One Propeller Revolution.

Table 2. Maximum Values of the Predicted Cavity Length, Thickness and Area.

	$k$	$\hat{\omega}_n$	$\hat{\omega}_n/k$		$l_m/c$	$l_m$ (ft)	$t_m/t_s$	$t_m$ (ft)	$A_m$ (ft <sup>2</sup> )	$l_c/c$
.95 Radius	.0815	.1939	2.37	w/o fins	.85	1.45	8.37	.67	.75	.68
				w/ fins	.81	1.37	7.09	.57	.61	.61
				% reduction	5.46		15.26		19.23	
.85 Radius	.1698	.3058	1.80	w/o fins	.73	2.31	3.41	.59	1.0	.36
				w/ fins	.67	2.13	2.96	.51	.85	.29
				% reduction	7.76		13.1		15.26	
.75 Radius	.2619	.3809	1.45	w/o fins	.51	2.25	.9	.25	.42	.33
				w/ fins	.47	2.06	.65	.18	.3	.48
				% reduction	8.4		27.48		29.22	
.65 Radius	.3622	.4321	1.19	w/o fins	.44	2.33	.2	.09	.03	.08

## Nomenclature

$k$  = reduced frequency  
 $\hat{\omega}_n$  = cavity natural frequency  
 $l_m$  = maximum cavity length  
 $t_m$  = maximum cavity thickness

$A_m$  = maximum cavity area  
 $l_c$  = cavity collapse position  
 $c$  = section chord length  
 $t_s$  = section thickness

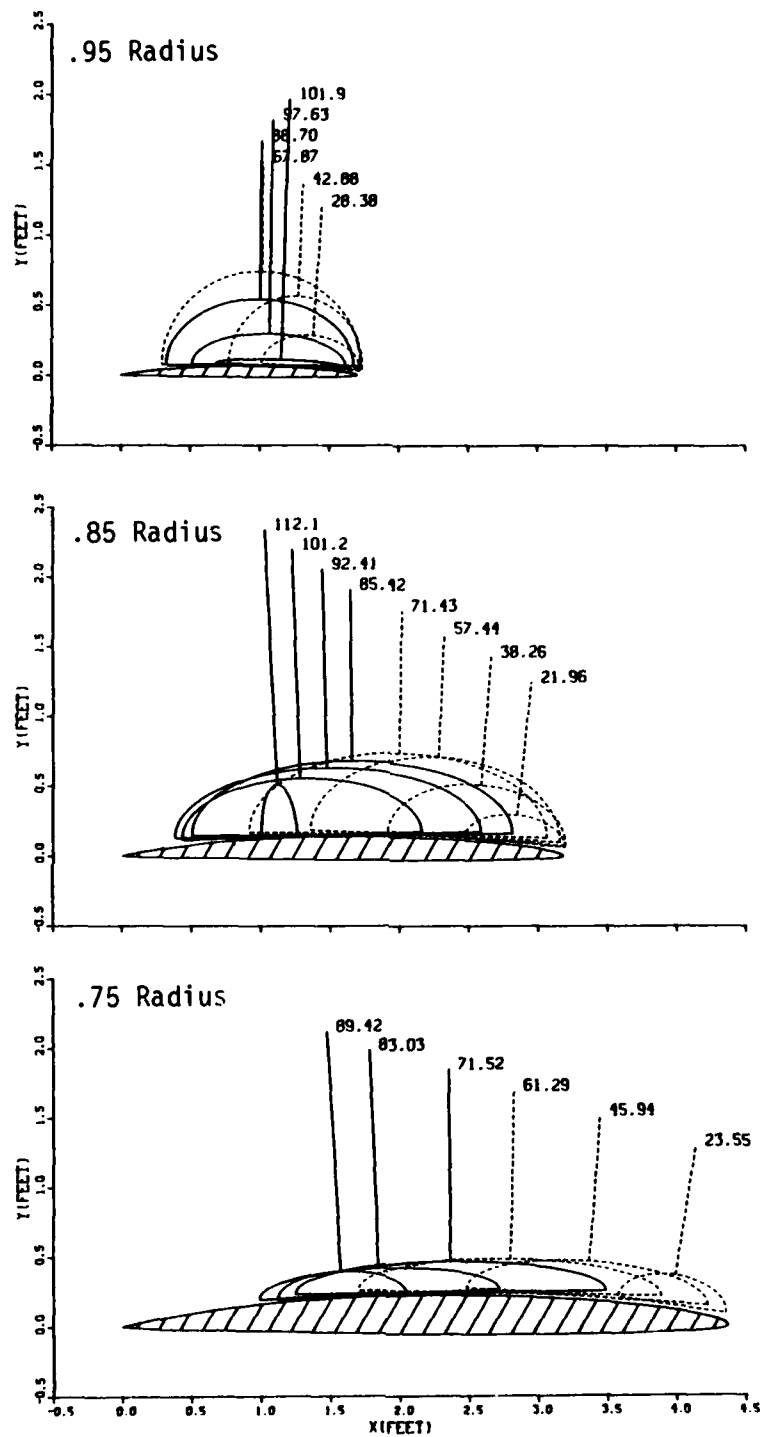


Figure 5. Cavitation Prediction for the A0-177 Propeller at the .75, .85 and .95 Radius for the Without Flow-Modifying Fins Condition.

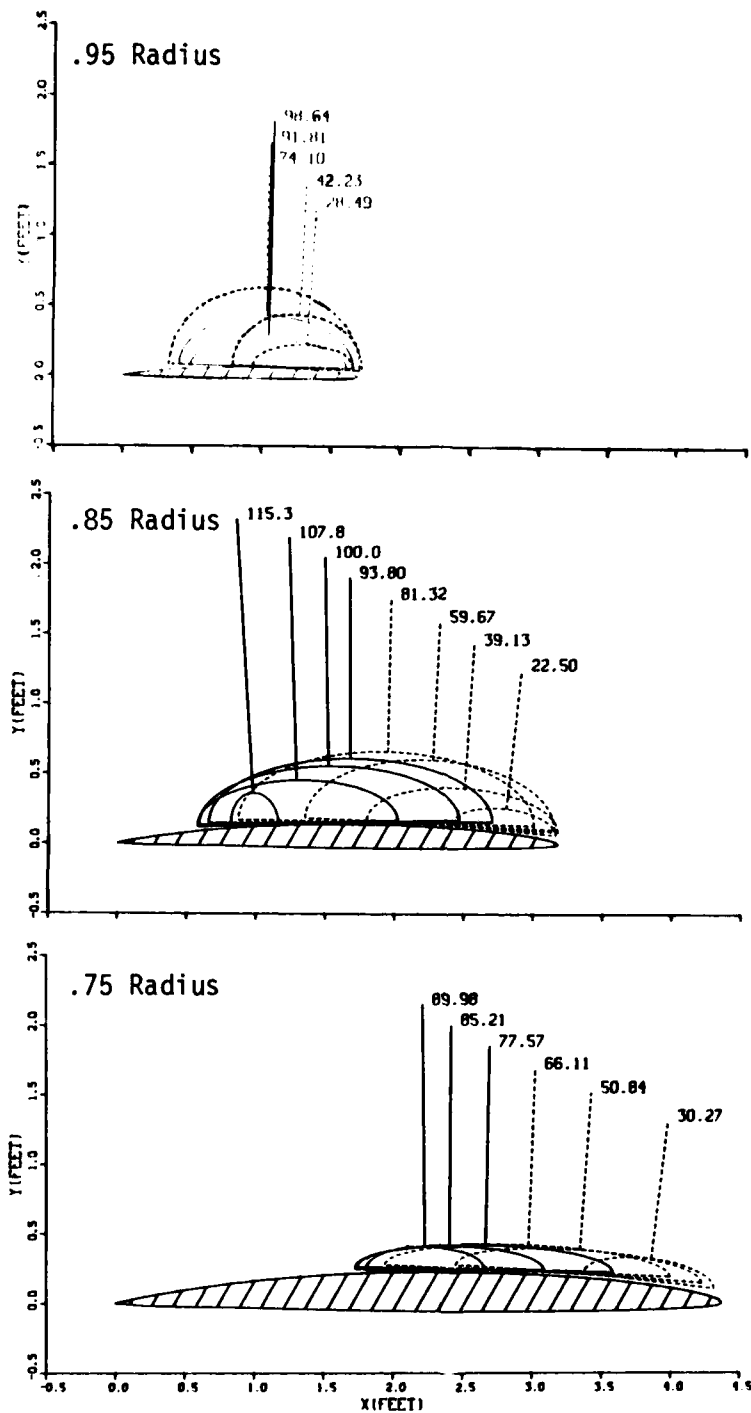


Figure 6. Cavitation Prediction for the A0-177 Propeller at the .75, .85 and .95 Radius for the With Flow-Modifying Fins Condition.

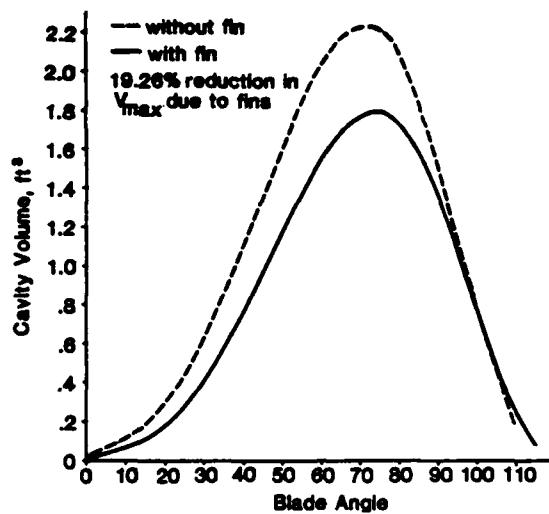


Figure 7. Cavity Volume Prediction for the A0-177 Propeller.

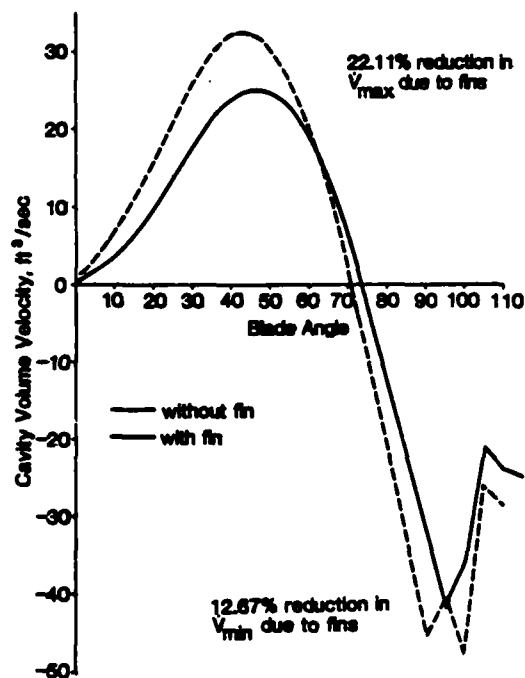


Figure 8. Cavity Volume Velocity Prediction for the A0-177 Propeller.

nets were placed on the model surface in front of the propeller aperture. Experience at SSPA has shown that better correlation between model and full-scale results is obtained with the use of the nets. Apparently, the action of the nets on the model boundary layer reduces the effects of the lack of similarity between the model and full-scale Reynolds number. No new wake survey was conducted on the model with the nets attached. Consequently, the effect of the nets in the calculations could not be determined. The experimental cavitation patterns were determined from visual observations and photographs. Unfortunately, no measurements were made of the cavitation thickness or volume variation. For the full-load trim and without fins condition fairly thick sheet cavitation was reported in the experiments to extend radially from the .6 radius to the tip and at blade angles of  $345^\circ$  to  $105^\circ$ . The sheet cavitation collapsed near the blade trailing edge where it merged into foaming cavitation. When the fin was installed the duration of cavitation was reported to increase from  $105^\circ$  to  $115^\circ$ . Figures 4, 9 and 10 show the experimental results described above. The computational results are also shown on the figures for comparison. Figure 4 shows the radial extent of cavitation during one propeller revolution.

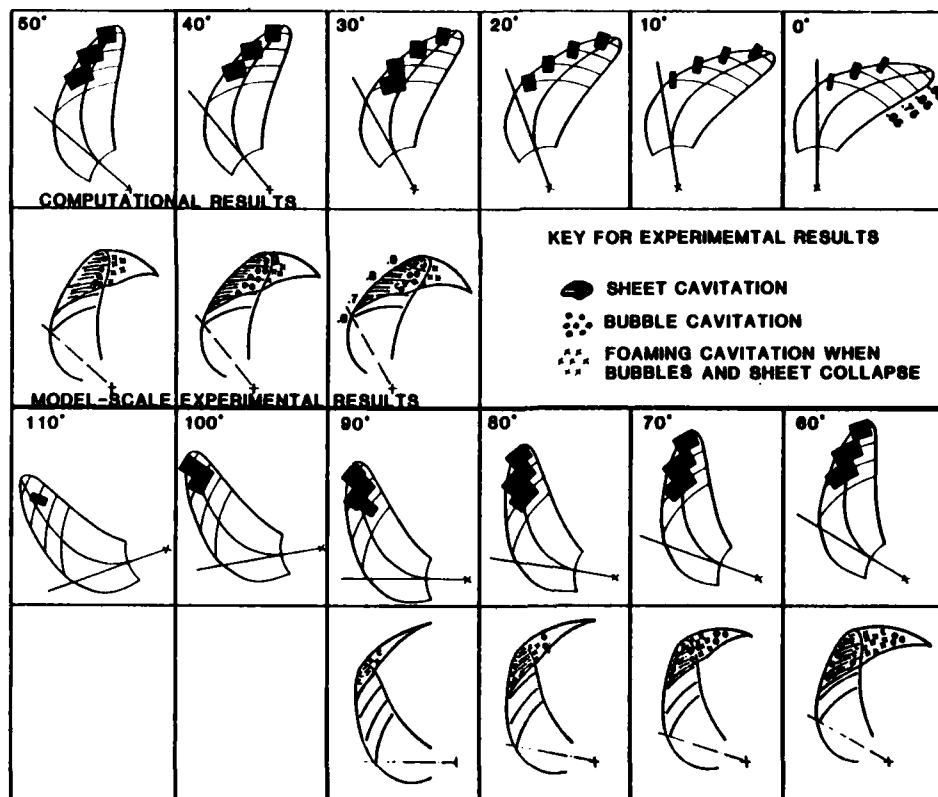


Figure 9. Chordwise Extent of Cavitation at Different Blade Angles for the Without Flow-Modifying Fins Condition.

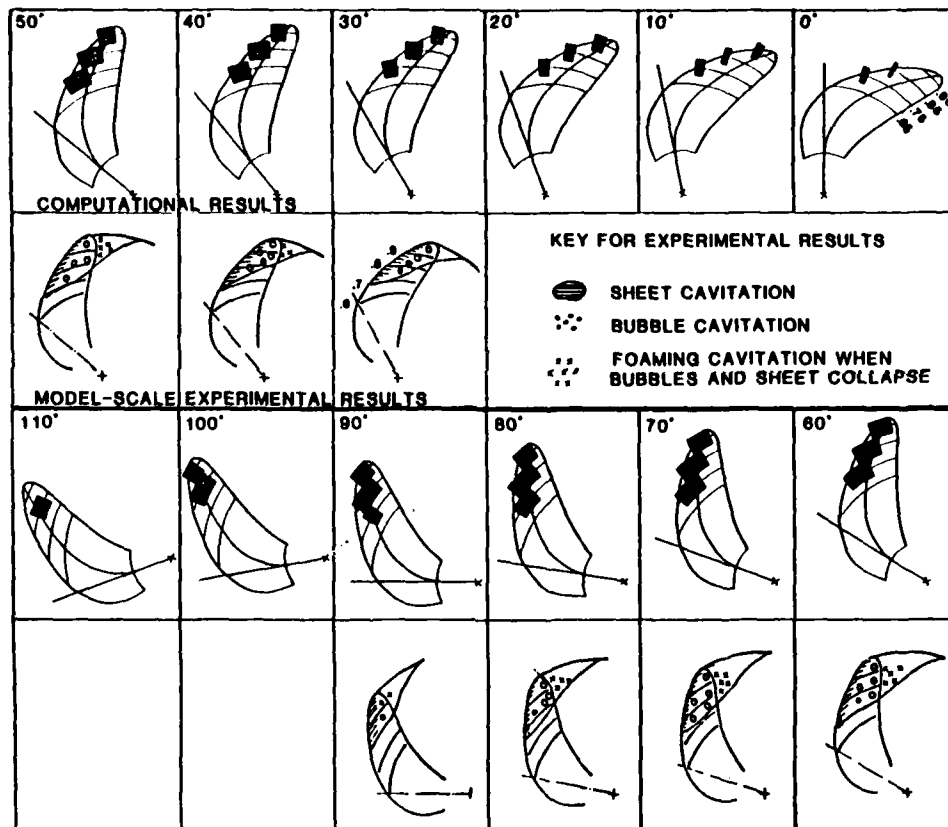


Figure 10. Chordwise Extent of Cavitation at Different Blade Angles for the With Flow-Modifying Fins Condition.

The calculations compare well with the experiments, particularly with regard to the inception angles. The calculations show an increase in the duration of cavitation over the experimental results for the inner radii. It was pointed out earlier that in the calculations one of the effects due to the fins was a small phase shift such that the angle at which the cavity volume was maximum and the collapse angle showed an increase. Figure 4 shows that the experimental results also indicate an increase in the collapse angle due to the fins. Figures 9 and 10 show the chordwise extent of cavitation at different blade angles for the duration of the cavitation. Figure 9 is for the condition without fins, and Figure 10 is for the condition with fins. Here again the computational results compare well with the experimental results.

Full-scale sea trials were conducted on the A0-177 for the purpose of viewing and photographing the propeller cavitation and measuring the vibration/noise. Trials were conducted for both the without (Kelly and Jessup, 1980) and with (Koh and Jessup, 1982) fins conditions. The propeller was exposed using a periscope inserted into tubes installed through the hull plating. Some of the results from the trials are shown in Figure 11. For the full-load without fins condition

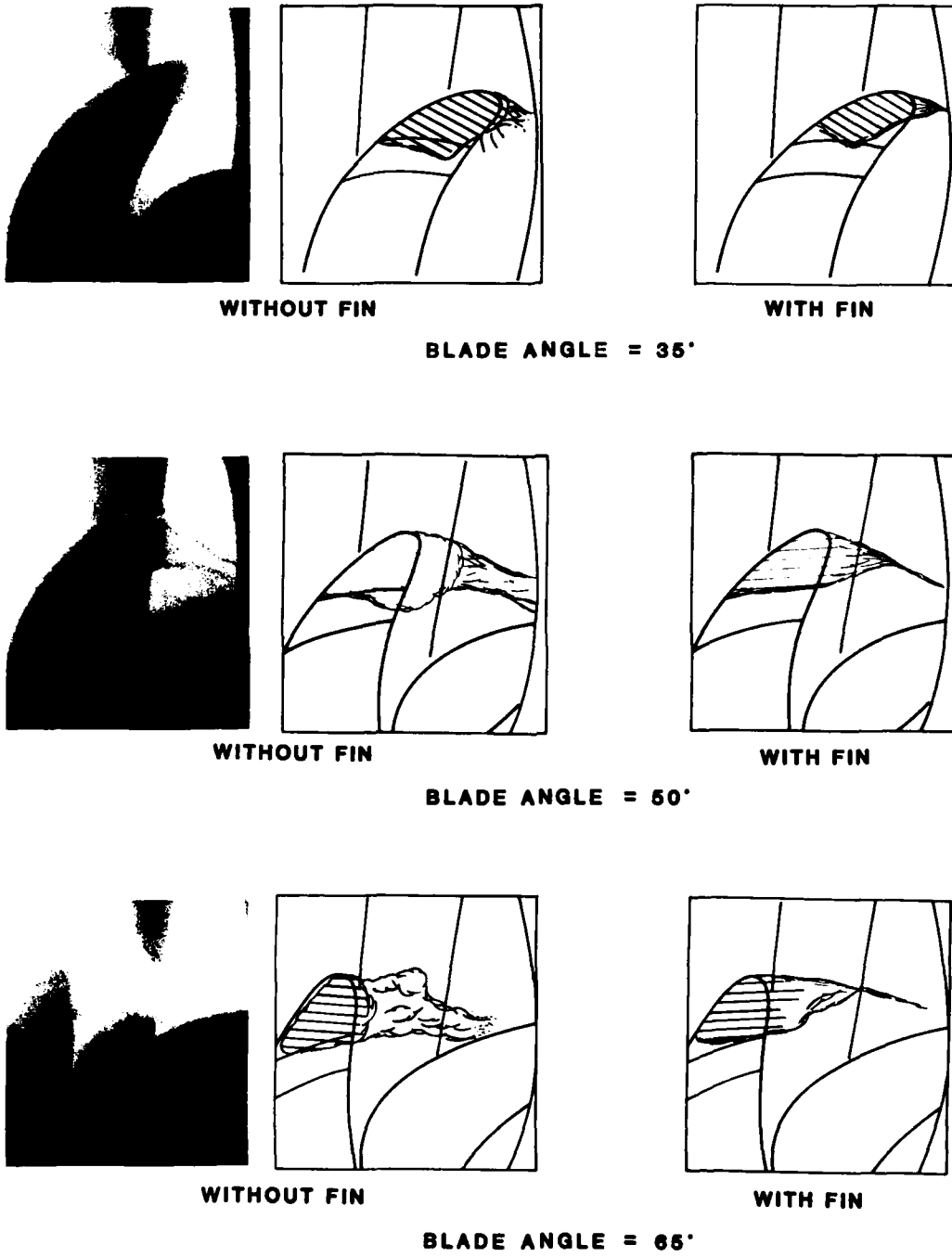


Figure 11. Full-Scale Sea Trial Results for the A0-177 Propeller (from Koh and Jessup, 1982).

sheet cavitation was reported to extend from the .7 radius to the tip and for blade angles of  $20^\circ$  to  $70^\circ$ . Initially, at the  $20^\circ$  blade angle, the chordwise extent was 50% to 70%. At  $35^\circ$  the radial extent is somewhat reduced, the chordwise extent is to the trailing edge and at the tip the cavity begins to sweep off the blade. At  $50^\circ$  the chordwise extent is to beyond the trailing edge where the sheet cavity breaks up into a large thick cloud. The cavity collapse is violent and occurs at a blade angle of approximately  $70^\circ$  near the .85 radius trailing edge. A loud banging noise was heard when the cavity collapsed. For the full-load with fins condition a substantial reduction in cavity volume was observed. The reduction was primarily due to a thinning of the cavity. The radial and chordwise extent of the cavitation was only slightly reduced. The violence of the cavity collapse and the associated noise was also reduced.

Both the model-scale experimental results and the calculations which use model-scale wake data show an increase in the duration and the radial extent of cavitation compared with the full-scale experimental results. This is due in part to scale effects associated with the difference between model and full-scale Reynolds number. The model and full-scale experimental results show cavitation extending over most of the sections' chord with cloud (foaming) cavitation shed from the cavity trailing edge into the propeller wake. The calculations also show cavitation extending over much of the sections' chord. In summary, the calculated cavitation shows many of the trends observed experimentally both for model and full-scale. The inception, amount and duration of cavitation is similar. Both the full-scale observations and the calculations show maximum cavitation at the .85 radius. The trailing edge collapse phenomena is shown in the calculations. The effects of the flow-modifying fins are also correctly reflected in the calculations, that is, a substantial reduction in cavity volume and collapse velocity due to a decrease in cavity thickness.

#### SECTION 4: PITCHING HYDROFOIL

Shen and Peterson (1978 and 1980) conducted experiments at the David W. Taylor Naval Ship Research and Development Center (DTNSRDC) 36-inch water tunnel with a Joukowski hydrofoil of 10.5% thickness and aspect ratio of 3.2. The foil was oscillated in pitching motion about an axis located  $3/4$  of the chord from the trailing edge. The instantaneous foil angle of attack  $\alpha$  was given by

$$\alpha = \alpha_0 + \alpha_1 \sin \omega t \quad (9)$$

where  $\alpha_0$ ,  $\alpha_1$  and  $\omega$  are the mean foil angle, pitch amplitude and circular frequency of the pitch oscillation respectively. The experimental test section, coordinate system and notations used for the computations are shown in Figure 12.



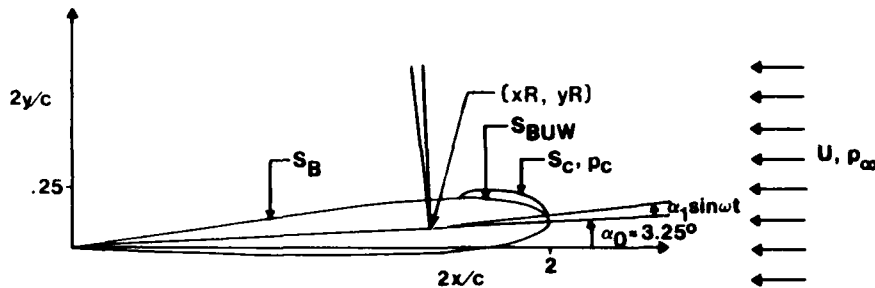


Figure 12. Experimental Test Section.

The most important nondimensional parameters describing this type of flow are the cavitation number  $\sigma$  (equation (4)), the pitch amplitude  $\alpha_1$  and the foil reduced frequency  $k$  (equation (6)). Calculations were made with the cavitation number fixed at one value in order to investigate the effects of the reduced frequency and the pitch amplitude on cavitation inception and the cavity dynamics. Unsteady cavity calculations were made for cavitation number  $\sigma = 1.13$ , mean foil angle  $\alpha_0 = 3.25^\circ$  and for two values of pitch amplitude  $\alpha_1 = .95^\circ$  and  $1.55^\circ$ . Steady cavity calculations were made for two values of foil angle  $\alpha_0 = 4.3^\circ$  and  $\alpha_0 = 4.8^\circ$ . These angles correspond to the maximum foil angles attained for the oscillating foil conditions. The conditions for the calculations were chosen to simulate the experiments. Wherever possible, comparisons are made between the computational and experimental results.

#### Cavitation Inception

Cavitation inception was determined computationally by the condition of the first occurrence of negative pressure on the foil surface  $P < 0$ , where  $P$  is given by equation (3). For the pitching foil application the pressure coefficient  $c_p$  in equation (3) is given by equations (B-6) and (B-7). For steady flow ( $k = 0$ ) inception occurred computationally at a foil angle of  $\alpha_0 = 3.28^\circ$ . The inception location was  $2x/c = 1.97$ . Experimentally, for this same condition, inception occurred at a foil angle of  $3.5^\circ$  and a location of  $2x/c = 1.96$ . This difference is due to the simple scaling law used in the computations for cavitation inception. Consequently, the unsteady inception angles determined computationally were corrected by the difference between the computational and experimental steady inception angles. In Figures 13 and 14 a comparison is made between the unsteady inception angles obtained computationally, experimentally and from Shen and Peterson equation (15). The Shen and Peterson equation is based on unsteady potential theory and the experimental steady inception angles. Figure 13 is for pitch amplitude  $\alpha_1 = .95^\circ$  and Figure 14 is for  $\alpha_1 = 1.55^\circ$ . All three methods demonstrate that for  $k < 2$  there is a delay in inception due to foil oscillation. This delay is seen to increase with pitch amplitude  $\alpha_1$ . The computations and equation (15) from Shen and Peterson both

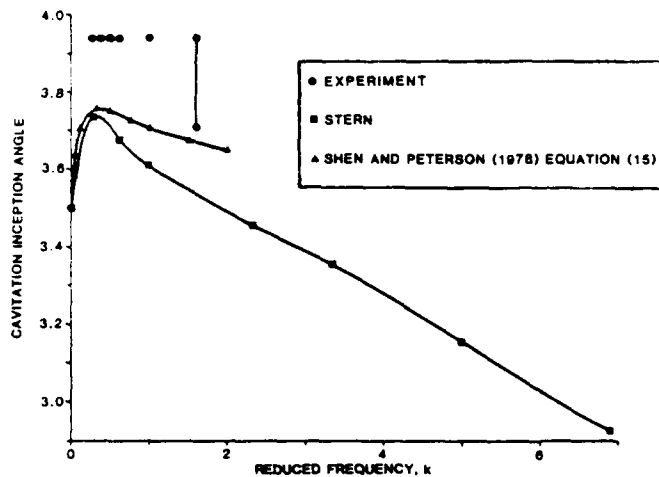


Figure 13. Cavitation Inception Angles for Pitch Amplitude  $\alpha_1 = .95^\circ$ .

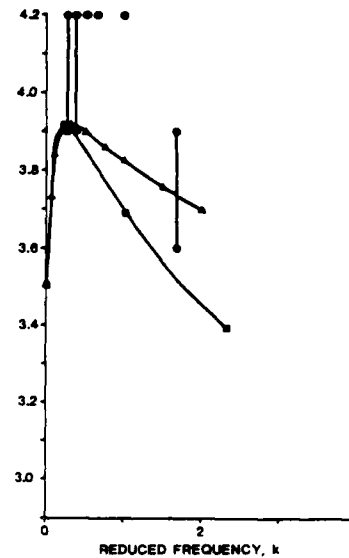


Figure 14. Cavitation Inception Angles for Pitch Amplitude  $\alpha_1 = 1.55^\circ$ .

predict the maximum inception delay to occur at  $k \approx .25$  for both values of  $\alpha_1$ . The experimental results show that for high frequency the amount of cavitation inception delay is reduced. The computational results show that the reduction is substantial and that for  $k > 2$  the unsteady inception angle is actually less than the steady inception angle. This effect is quite pronounced for the  $\alpha_1 = 1.55^\circ$  condition. The experimental results show, in general, larger inception angles than the theories. Shen and Peterson point out that part of the disagreement may be due to the lack of accurate resolution in measuring the foil angles in the experiments. This is the reason that, in some cases, the experimental results are designated as a range of angles instead of a single value.

The inception position was found in the computations to move back from the leading edge towards the trailing edge as the reduced frequency increased. For  $\alpha_1 = .95^\circ$  the inception position moved from  $2x/c = 1.962$  for  $k = .23$  to  $2x/c = 1.89$  for  $k = 6.9$ . This trend was even more pronounced for  $\alpha_1 = 1.55^\circ$ . In fact, for  $\alpha_1 = 1.55^\circ$  and  $k = 6.9$  upper surface inception occurred at a foil angle of  $2.1^\circ$  (before  $\alpha_{min}$ ) and at  $2x/c = .5$ , and lower surface inception occurred at foil angle of  $4.5^\circ$  (before  $\alpha_{max}$ ) and at  $2x/c = 1.95$ . This change in the inception position was not observed in the experiments. Shen and Peterson report that inception occurred at  $2x/c = 1.96$  for all  $k$  investigated ( $.23 < k < 2.3$ ).

## Cavity Dynamics

Steady cavity constant solutions ( $\bar{a}$ ,  $\bar{b}$ ,  $\bar{l}$ ) are obtained by using the cavity equations with estimates of the solutions as initial conditions and large damping (small  $R_n$  in the equations). The cavity equation response is periodic oscillations about the constant solution. Using a  $R_n = 100$ , the constant solution obtained for  $\alpha_0 = 4.3^\circ$  is  $(2\bar{a}/c, 2\bar{b}/c, 2\bar{l}/c) = (.1152, .048, 1.848)$ , and for  $\alpha_0 = 4.8^\circ$  is  $(2\bar{a}/c, 2\bar{b}/c, 2\bar{l}/c) = (.1305, .0612, 1.839)$ . The  $\alpha_0 = 4.3^\circ$  solution is shown by the dashed curve on Figure 15. The nondimensional natural frequency

$$\hat{\omega}_n = \frac{\omega_n c}{2U} \quad (10)$$

obtained for  $\alpha_0 = 4.3^\circ$  is 3.34 and for  $\alpha_0 = 4.8^\circ$  is 3.24. Experimental results were also obtained for  $\alpha_0 = 4.3^\circ$  and with  $R_n = 2.8 \times 10^6$ . For this condition extensive cloud cavitation was observed. Cloud cavitation refers to the condition when an instability in the cavity surface occurs and a portion of the cavity separates, develops the appearance of a cloud and subsequently is shed downstream. The cloud cavity shedding process was reported to be periodic with a frequency of 42 hz.

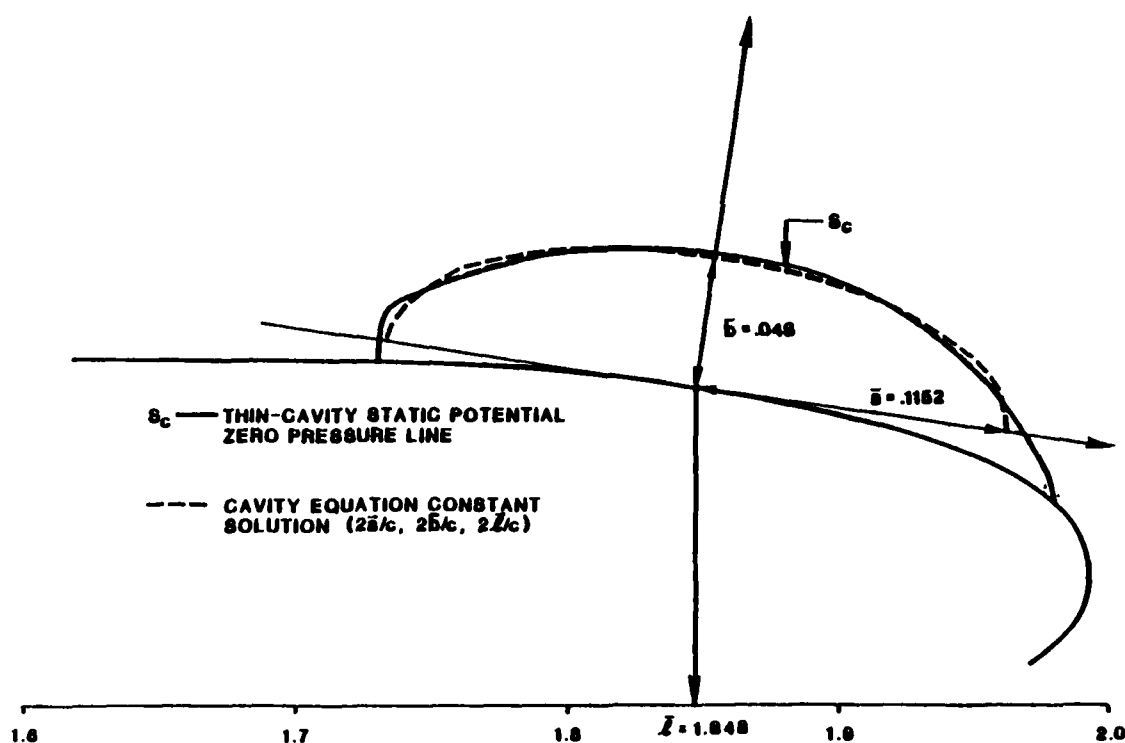
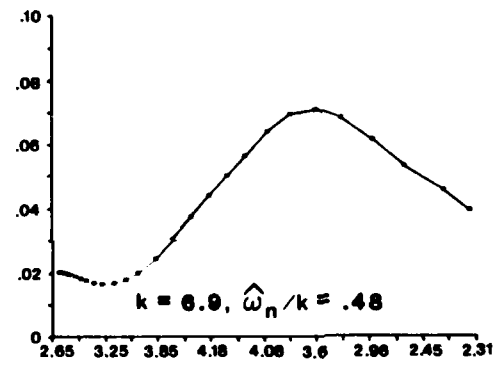
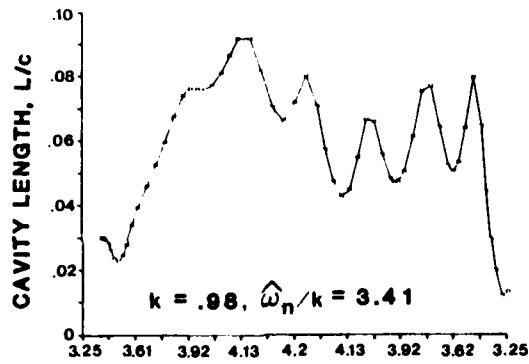
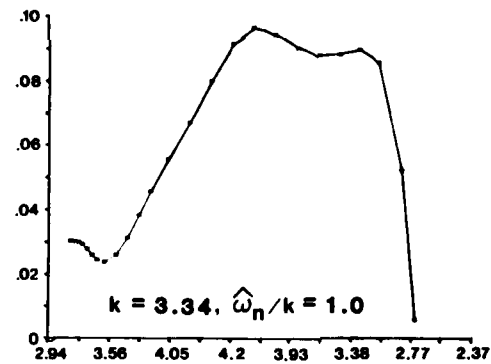
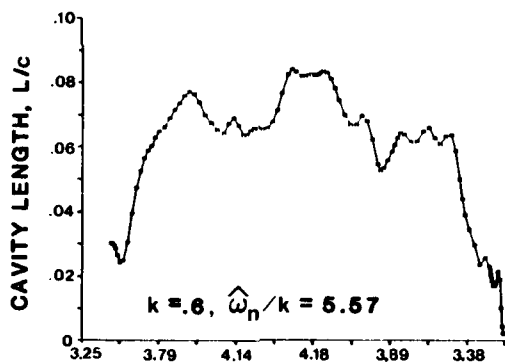
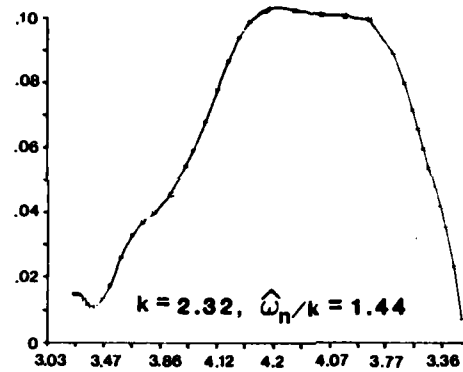
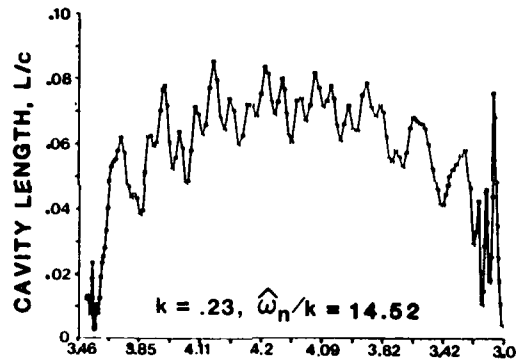


Figure 15. Steady Thin-Cavity Solution for  $\sigma = 1.13$  and  $\alpha_0 = 4.3^\circ$ .

The cavity length reported was  $L_0/c = .39$ . Using the experimental values for the  $R_n = 2.8 \times 10^6$  (light damping) and a small displacement from the constant solution for the initial conditions, the cavity equation response is large amplitude oscillations. The frequency of the oscillations is close to the natural frequency. This type of cavitation behavior suggests an instability of the cavity surface, such as cloud cavitation. This notion is supported by the fact that the natural frequency  $\hat{\omega}_n$  when expressed in equivalent units and for the experimental conditions is 51 hz. This is close to the cloud cavitation shedding frequency of 42 hz observed in the experiments. The value of the computed cavity length for  $\alpha_0 = 4.3^\circ$  is only about 30% of the experimental value for this condition. A part of this discrepancy is due to the approximate nature of the thin-cavity model used for the static potential. However, it is possible that a part of the discrepancy might be due to the imprecision of determining the cavity length by visual observations in the experiments.

Unsteady cavitation computational results were obtained for  $R_n = 2.8 \times 10^6$ ,  $\alpha_1 = .95^\circ$  and six values of reduced frequency,  $k = .23, .6, .98, 2.32, 3.34$  and  $6.9$ . The reduced frequency range,  $0 < k < 7$ , was chosen after consideration of the linear cavity equation system response. The peak amplitude of the linear response depends on the ratio  $\hat{\omega}_n/k$ . For small  $\hat{\omega}_n/k$  small peak amplitudes occur compared to quasi-steady response. For  $\hat{\omega}_n/k \sim 1$  large peak amplitudes occur compared to quasi-steady responses. For large  $\hat{\omega}_n/k$  essentially quasi-steady response occurs. The nondimensional cavity length,  $L/c = 2a/c$ , response for each frequency is shown in Figure 16. For the lower values of reduced frequency ( $k = .23, .6$  and  $.98$ ) the cavity response is seen to be large amplitude oscillations during the cavity life cycle. The oscillatory cavity response at low reduced frequency (large  $\hat{\omega}_n/k$ ) is a result of the fact that the cavity has sufficient time to adjust to the fluid pressure field. For the higher values of reduced frequency ( $k = 2.32, 3.34$  and  $6.9$ ) the cavity response is seen to be a relatively slow, stable growth phase followed by a rapid collapse phase. Results were also obtained for  $R_n = 2.8 \times 10^6$ ,  $\alpha_1 = 1.55^\circ$  and three values of reduced frequency,  $k = .23, .98$  and  $2.32$ . The  $\alpha_1 = 1.55^\circ$  cavity response is similar in character to the  $\alpha_1 = .95^\circ$  response, however, as a result of the larger pitch amplitude, the cavity size is increased. Furthermore, the response velocities were found to be larger than the  $\alpha_1 = .95^\circ$  values resulting in larger amplitude cavity oscillations at the low frequencies ( $k = .23$  and  $.98$ ) and a more rapid collapse phase at the high frequency ( $k = 2.32$ ).

Figure 17 shows a comparison of the computational and experimental maximum cavity length  $L_k/c$  results as a function of reduced frequency. The steady maximum cavity length  $L_0/c$  values are also shown on Figure 17. The computational results underpredict the experimental results. This has been pointed out and discussed previously for the steady cavity solution. The same discussion is also valid for the unsteady cavity solution. Figure 18 shows a comparison of the computational and experimental  $\alpha_1 = .95^\circ$  maximum cavity length results normalized using the steady cavity results. This removes the absolute cavity size without



FOIL ANGLE

FOIL ANGLE

Figure 16. Cavity Length Response for Cavitation Number  $\sigma = 1.13$  and Pitch Amplitude  $\alpha_1 = .95^\circ$ .

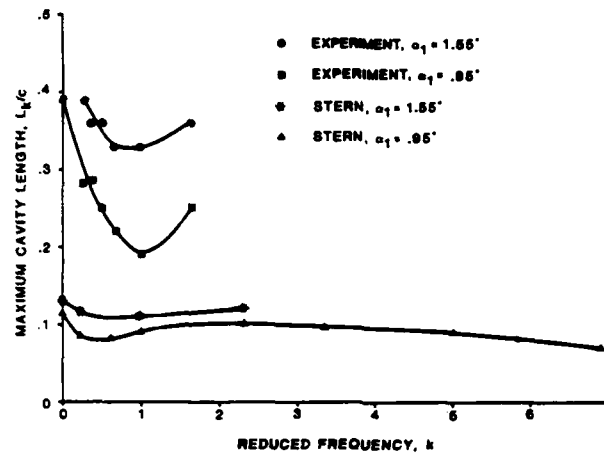


Figure 17. Comparison of Computational and Experimental Maximum Cavity Length.

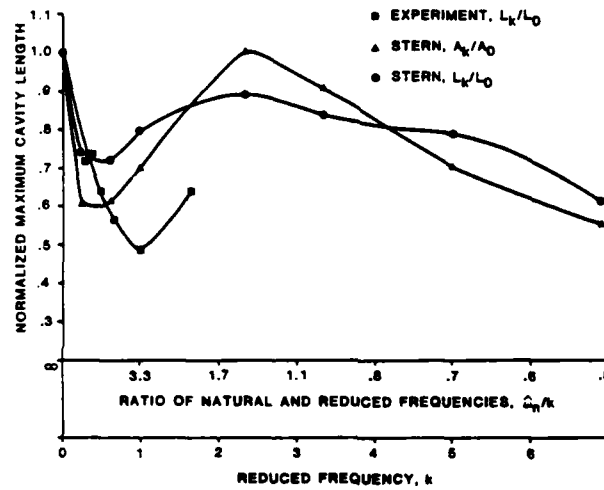


Figure 18. Comparison of Computational and Experimental Normalized Maximum Cavity Length for Pitch Amplitude  $\alpha_1 = .95^\circ$ .

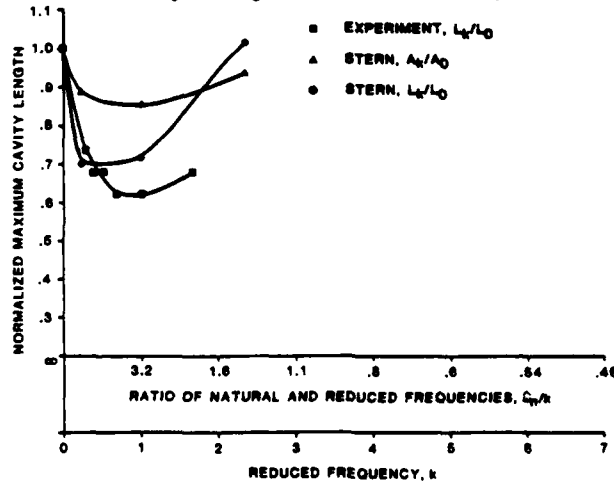


Figure 19. Comparison of Computational and Experimental Normalized Maximum Cavity Length for Pitch Amplitude  $\alpha_1 = 1.55^\circ$ .

effecting the cavity dynamics. The computational cavity area normalized using the steady cavity area is also shown. In Figure 18 both the reduced frequency  $k$  and the ratio  $\hat{\omega}_n/k$  abscissa scales are shown. Figure 18 clearly shows the dependence of the cavity dynamics on the ratio  $\hat{\omega}_n/k$ . It is seen from both the experimental and computational results that there is a minimum cavitation response for a low value of reduced frequency. The computations have a minimum cavitation response for  $k \approx .5$  and the experiments for  $k \approx 1$ . The computations show that as  $k$  increases from the value at the minimum cavitation response, the cavitation response increases reaching a maximum at  $k \approx 2.5$  ( $\hat{\omega}_n/k = 1.3$ ). Then for even higher values of reduced frequency (low  $\hat{\omega}_n/k$ ) the cavitation response decreases again. For  $k = 6.9$  the response is below the  $k = .5$  minimum. The experimental results seem to confirm the computational trends in that they show an increase in cavitation response for  $k$  greater than its value at the minimum cavitation response; however, experimental results were not obtained for  $k > 1.65$ . Figure 19 shows the same comparisons as Figure 18 except for the  $\alpha_1 = 1.55^\circ$  condition. The same cavity dynamic behavior discussed in connection with Figure 18 is found in Figure 19 for the frequency range  $0 \leq k < 2.5$ . The major difference between the figures is the amount of reduction in cavitation response at the minimum. Both the computational and experimental results predict less reduction in response. For the computational results this is due to the larger amplitude cavity oscillations at low frequencies found for  $\alpha_1 = 1.55^\circ$ . If results had been obtained for  $\alpha_1 = 1.55^\circ$  and  $k > 2.5$ , it is not expected that the cavity dynamics would be similar to the  $\alpha_1 = .95^\circ$  results, at least for the high frequency  $k = 6.9$ . Examination of the  $\alpha_1 = 1.55^\circ$  and  $k = 6.9$  unsteady surface foil pressures indicated a large upper surface cavity originating near the foil trailing edge and moving forward to the leading edge. Lower surface leading edge cavitation was also indicated.

Figure 20 shows for the  $\alpha_1 = .95^\circ$  computational results the foil angles when the cavity area and length were maximum and the foil angle at collapse. It is seen that the cavity area and length are maximum when the foil angle is at its maximum  $4.2^\circ$  except for the high reduced frequencies. At the higher reduced frequencies the cavity area and length are maximum at smaller foil angles reached after the foil passes its maximum position. The foil angle at collapse shows a similar trend in that the collapse angle is reduced at the higher reduced frequencies. Figure 21 is similar to Figure 20 except for  $\alpha_1 = 1.55^\circ$ , and it also includes experimental results. The trends are similar to those discussed in connection with Figure 20; however, the experimental results predict larger reductions in foil angles than the computations and at lower values of reduced frequencies. In the computations the cavity position on the foil at the time of the cavity collapse was found in all cases to occur near the foil leading edge. Experimental values for the cavity collapse position were not reported.

Shen and Peterson report that many of the experimental cavities were accompanied by cloud cavitation. For the steady cavity condition ( $k = 0$ ) and for low reduced frequencies the cloud cavitation shedding

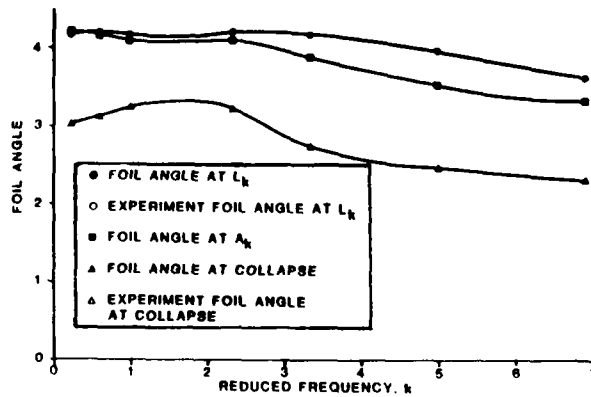


Figure 20. Foil Angles when Cavity Length and Area are Maximum and at Cavity Collapse for Pitch Amplitude  $\alpha_1 = .95^\circ$ .

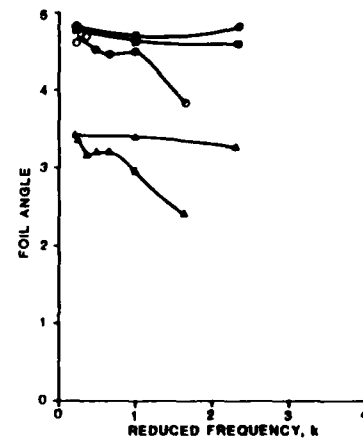


Figure 21. Foil Angles when Cavity Length and Area are Maximum and at Cavity Collapse for Pitch Amplitude  $\alpha_1 = 1.55^\circ$ .

could be very periodic. For the higher reduced frequencies the cavities were reported to be relatively stable up until the final stages of the cloud cavitation collapse. For  $\alpha_1 = .95^\circ$  and at low reduced frequencies ( $k < 1.2$ ) only light cloud cavitation was reported to have been present in the experiments. For this same condition and at the reduced frequency  $k = 1.646$  heavy cloud cavitation was reported. For  $\alpha_1 = 1.55^\circ$  and at all values of reduced frequency heavy cloud cavitation was reported in the experiments. Cavitation noise measurements were also made in the experiments. Cavitation noise was reported to increase with the occurrence and intensity of cloud cavitation. For unsteady cavitation the peak noise occurred near cavitation collapse. When the relative sound power is plotted vs. reduced frequency, Shen and Peterson show the existence of a "noise bucket"; for the steady condition and at low reduced frequencies the noise level is relatively high; for the mid-range reduced frequencies the noise level is minimum; for higher reduced frequencies the noise level increases above the  $k = 0$  value. The differences between the  $\alpha_1 = .95^\circ$  and  $\alpha_1 = 1.55^\circ$  noise response are seen to be at the low and high frequencies, where the  $\alpha_1 = 1.55^\circ$  noise response shows an increase over the  $\alpha_1 = .95^\circ$  values. Results from the computations can be used with standard methods to calculate cavitation noise. These calculations were not made. However, since a measure, in part, of the predicted cavitation noise is the intensity of the response velocities certain qualitative information can be deduced from the results. The computational results appear to contain trends that are similar to the experimental trends concerning cloud cavitation and cavitation noise. The low frequency ( $k = .23$ ) response shows large amplitude oscillations of the cavity surface. The oscillations are particularly intense during the cavity collapse phase. As pointed out earlier, the  $\alpha_1 = 1.55^\circ$  response velocities were larger than the



$\alpha_1 = .95^\circ$  resulting in even larger amplitude oscillation at low frequency. For the medium frequencies ( $k = .6$  and  $.98$ ) where the cavitation response was shown to be minimum, the oscillatory behavior and response velocities are lower than the  $k = .23$  condition. For the resonance frequencies ( $k = 2.32$  and  $3.34$ ) where the cavitation response was shown to be maximum, the oscillatory behavior is not present; however, extremely large velocities are found at collapse. This suggests a different type of cavity instability than was found at low frequencies which is associated with the rapid and violent collapse of the large cavity. For  $\alpha_1 = .95^\circ$  and for the high frequency ( $k = 6.9$ ) where the cavitation response was shown to be reduced, the response velocity was also reduced. For  $\alpha_1 = 1.55^\circ$  and for high frequencies calculations were not made; however, as discussed earlier an examination of the unsteady foil surface pressures for  $k = 6.9$  indicated much more extensive and no longer leading edge cavitation.

The computational results show that for fixed  $\sigma$ ,  $\alpha_1$ , and  $R_n$  the cavitation response such as maximum cavity length and cavity surface behavior (and possibly noise and cloud cavitation) depend on the ratio  $\hat{\omega}_n/k$ . The steady cavitation condition is given by  $\hat{\omega}_n/k = \infty$  ( $k = 0$ ). The cavity equation response is large amplitude oscillations about the equilibrium solution. For  $1 < \hat{\omega}_n/k < \infty$ , the response is quasi-steady; however, the intensity of the oscillations is reduced and for a certain value of  $\hat{\omega}_n/k \approx 7$  a minimum response is obtained. For  $\hat{\omega}_n/k < 1$  the response is no longer oscillatory; the response is a slow stable growth phase followed by a rapid collapse phase. A resonance condition is indicated for  $\hat{\omega}_n/k \approx 1$  in that the response levels are largest. For  $\alpha_1 = .95^\circ$  and  $\hat{\omega}_n/k \ll 1$  the response levels are reduced below the  $\hat{\omega}_n/k \approx 7$  value. For  $\alpha_1 = 1.55^\circ$  and  $\hat{\omega}_n/k \ll 1$  the leading edge cavitation is no longer present and large responses are indicated. The experimental results appear to confirm the computational trends up to the point that experimental data was obtained.

## SECTION 5: CONCLUDING REMARKS

Results from the computational method for cavitation inception, extent, duration and cavity dynamics including surface behavior and collapse position are shown to closely approximate model and full-scale experimental data. Observed trends due to the propeller geometry and ship wake are also correctly reflected in the calculations. The method shows promise towards the development of an engineering tool for predicting unsteady sheet cavitation. At its present state of development, the method contains certain approximations which should be removed in order to further improve the accuracy of the results. An improved method is needed to determine the effects of the cavity on the instantaneous foil/cavity pressure field. The thin-cavity approximation presently used for this is of uncertain accuracy, particularly when the predicted cavities are thick. The mathematical problem which

needs to be solved in order to remove the thin-cavity approximation is equivalent to a nonlinear solution for the flow field of a foil and a fixed (steady) cavity. This problem can be solved numerically using a mixed boundary value problem formulation in conjunction with a free surface adjustment scheme. This solution would also be useful for evaluating the semielliptical form presently used to model the cavity surface. It may be advantageous to use more general forms to model the cavity surface; for example, forms with cusped leading and/or trailing edges. Another component of the computational method which can be improved is the manner in which three-dimensional propeller effects are included. Presently, results from an unsteady propeller lifting-line computer program are used for this. An improvement would be to use results from an unsteady propeller lifting-surface computer program.

#### ACKNOWLEDGMENT

Partial support for this work was provided by Science Applications, Inc. internal research funds. Initial support was provided by the American Bureau of Shipping. I would like to thank Drs. T. Brockett, M. Wilson and Y. Shen and Messrs. R. Boswell and S. Jessup of DTNSRDC for their interest and helpful discussions. I would also like to thank my associates, Drs. N. Salvesen and C. von Kerczek, for their encouragement and technical advice.

#### REFERENCES

- Bjorne, E., "U.S. Navy Oiler, AO-177 Class-Model Tests in SSPA Towing Tank and Cavitation Tunnel No. 2 Design Propeller," Swedish Model Basin (SSPA) Report 2564-1, 2 and 3, October 1980.
- Brown, N.A., "Periodic Propeller Forces in Non-uniform Flow," MIT Report No. 64-7, June 1964.
- Chiba, N., T. Sasajima and T. Hoshino, "Prediction of Propeller-Induced Fluctuating Pressures and Correlation with Full-Scale Data," 13th ONR Symposium on Naval Hydrodynamics, Tokyo, October 1980.
- Frydenlund, O., and B. Persson, "Application of a Discrete Vortex, Source Distribution Model to Propeller Cavitation," Journal of Ship Research, Vol. 25, No. 4, 1981.
- Geurst, J.A., "Linearized Theory of Two-Dimensional Cavity Flows," Thesis, Delft Technical Institute, The Netherlands, 1961.
- Giesing, J.P., "Two-Dimensional Potential Flow Theory for Multiple Bodies in Small-Amplitude Motion," Douglas Aircraft Company, Report No. DAC-67028, 1968.
- Huang, T., and N. Groves, "Effective Wake: Theory and Experiment," 13th ONR Symposium on Naval Hydrodynamics, Tokyo, October 1980.

- Jiang, C., and P. Leehey, "A Numerical Method for Determining Forces and Moments on Supercavitating Hydrofoils of Finite Span," Second International Conference on Numerical Ship Hydrodynamics, Berkeley, 1977.
- Kaplan, P., J. Bentson and J.P. Breslin, "Theoretical Analysis of Propeller Radiated Pressure and Blade Forces due to Cavitation," Symposium on propeller induced ship vibration, Paper No. 10, The Royal Institute of Naval Architects, 1979.
- Kelly, J., and S. Jessup, "Results of Propeller Vibration/Cavitation Investigation on USS Cimarron (AO-177) During Acceptance Trials," DTNSRDC Ship Performance Department Test and Evaluation Report 81/047, May 1981.
- Koh, I., and S. Jessup, "USS Cimarron (AO-177) Fin Survey Trial," DTNSRDC Ship Performance Department Test and Evaluation Report 82/008, February 1982.
- Lee, C., "Prediction of the Transient Cavitation on Marine Propellers by Numerical Lifting-Surface Theory," 13th ONR Symposium on Naval Hydrodynamics, Tokyo, October 1980.
- Noordzij, L., "The Cavitating Propeller and Its Pressure Field; Application of Free Streamline Theory," Symposium on Applied Mathematics dedicated to the late Prof. Dr. R. Timman, Delft, 1978.
- Shen, Y.T., and F.B. Peterson, "Unsteady Cavitation on an Oscillating Hydrofoil," 12th Symposium on Naval Hydrodynamics, Washington, D.C., June 1978.
- Shen, Y.T., and F.B. Peterson, "Influence of Hydrofoil Oscillation on the Boundary Layer Transition and the Cavitation Noise," 13th ONR Symposium on Naval Hydrodynamics, Tokyo, October 1980.
- Stern, F., "A Model for Propeller Sheet Cavitation: The Equations of Motion for Elliptical Cavities in Spatiotemporally Varying Velocity Fields," University of Michigan, Department of Naval Architecture and Marine Engineering Report 221, 1980.
- Stern, F., and W.S. Vorus, "A Nonlinear Method for Predicting Unsteady Sheet Cavitation on Marine Propellers," paper to appear in Journal of Ship Research, 1982.
- Tulin, M.P., and C.C. Hsu, "New Applications of Cavity Flow Theory," 13th ONR Symposium on Naval Hydrodynamics, Tokyo, October 1980.
- Valentine, D., and A. Chase, "Highly Skewed Propeller Design for a Naval Auxiliary Oiler (AO-177)," David Taylor Naval Ship Research & Development Center Report SPD-549-12, September 1976.
- Vorus, W.S., "Unsteady Propeller Lifting-Line Computer Program: PREPROP/PROP III," personal correspondence, 1982.
- Wilson, M., D. McCallum, R. Boswell, B. Bernhard and A. Chase, "Causes and Corrections for Propeller Excited Airborne Noise on a Naval Auxiliary Oiler," to be presented at the SNAME annual meeting, 1982.
- Yuasa, H., N. Ishii, B. Persson, O. Frydenlund and K. Holden, "Practical Applications of the Discrete Vortex Element Method for Calculation of Propeller Induced Excitation Forces," 13th ONR Symposium on Naval Hydrodynamics, Tokyo, October 1980.

## APPENDIX A: THIN-CAVITY APPROXIMATION FOR THE STATIC POTENTIAL

The integration of the cavity equations requires the determination of the static potential and its derivatives at each time step. The boundary value problem for determining the static potential is

$$\nabla^2 \phi_S = 0 \quad \text{in } V \quad (\text{A-1})$$

$$\frac{\partial \phi_S}{\partial n} = \vec{n} \cdot \vec{V}_f(t) \quad \text{on } S_B + S_C(t) \quad (\text{A-2})$$

$$\phi_S = 0 \quad \text{on } S_\infty \text{ (upstream)}. \quad (\text{A-3})$$

In equation (A-2)  $S_B$  is the wetted portion of the foil surface,  $S_C$  is the cavity surface (see Figure 1) and  $\vec{V}_f$  is the inflow velocity for coordinates fixed in the foil. In addition to satisfying conditions (A-1) through (A-3) the static potential must also satisfy a Kutta condition at the foil trailing edge, and proper consideration must be made for the foil wake. The calculations in this paper were made using a thin-cavity approximation for the static potential. For a thin cavity the static potential can be assumed to be a perturbation on the fully-wetted flow,

$$\phi_S = \phi_{fw} + \epsilon \phi_{Sp} \quad (\text{A-4})$$

where  $\epsilon$  is a small parameter related to the cavity thickness. The perturbation potential,  $\phi_{Sp}$ , satisfies the static potential boundary value problem with the kinematic boundary condition, equation (A-2), replaced by

$$\frac{\partial \phi_{Sp}}{\partial n} = V_t n_{cx} + v_n \quad \text{on } S_{BUW} \quad (\text{A-5})$$

$$= 0 \quad \text{on } S_B \quad (\text{A-6})$$

where  $S_{BUW}$  is the unwetted portion of the foil surface (see Figure 1),  $V_t$  is the fully-wetted surface velocity,  $n_{cx}$  is the x component of the cavity normal and  $v_n$  is the normal velocity on the cavity surface. The kinematic conditions, equations (A-5) and (A-6), are obtained from equation (A-2) by expanding (A-2) in a Taylor series about the foil surface and retaining terms of  $O(\epsilon)$ . In order to facilitate the use of the existing fully-wetted flow computer program, condition (A-6) was ignored and in condition (A-5)  $v_n$  was neglected and  $n_{cx}$  was approximated by the x component of the foil normal,  $n_x$ . This simply adds the term  $V_t n_x$  to

the source strengths on the unwetted portion of the foil surface,  $S_{BUW}$ .

## APPENDIX B: THICK-SECTION UNSTEADY POTENTIAL FLOW SOLUTION

The fully-wetted flow potential  $\phi_{fw}$  in equation (A-4) is the solution to the static potential boundary value problem (A-1) through (A-3) with the kinematic boundary condition (A-2) satisfied on the complete foil surface,  $S_B + S_{BUW}$  (see Figure 1). Below  $\phi_{fw}$  is referred to as  $\phi$  and is nondimensionalized as are all variables using the foil semichord  $c/2$  and steady section speed  $U$ . For the pitching foil application the kinematic boundary condition on the surface of the foil is

$$\frac{\partial \phi}{\partial n} = n_x + \alpha_1 \operatorname{Re} \left[ \left[ i n_y + k(-(y-y_R)n_x + (x-x_R)n_y) \right] e^{ikt} \right] \quad (B-1)$$

where  $\alpha_1$  is the pitch amplitude and  $(x_R, y_R)$  is the location of the pitch axis (see Figure 12). In obtaining (B-1) terms of  $O(\alpha_1^2)$  have been neglected. For propeller applications (B-1) is replaced by

$$\frac{\partial \phi}{\partial n} = n_x - n_y \operatorname{Re} \sum_{n=1}^N V_n e^{ink(x+t)} \quad (B-2)$$

where  $V_n$  are the complex amplitudes of the Fourier series expansion of the vertical component of the section inflow  $\vec{V}$  (see Figure 1). Considering (B-1) and (B-2)  $\phi$  is assumed to be of the form

$$\phi = \operatorname{Re} \sum_{n=1}^N \phi_n e^{inkt} \quad (B-3)$$

A solution for  $\phi$  can be obtained from Green's theorem for doubly connected regions

$$\phi = \frac{1}{m\pi} \left[ \int_{S_B + S_{BUW}} \left( \frac{\partial \phi}{\partial n} G - \phi \frac{\partial G}{\partial n} \right) ds - \int_{S_W} \Delta \phi \frac{\partial G}{\partial n} ds \right] \quad (B-4)$$

where  $G = \ln \sqrt{(x-\xi)^2 + (y-\eta)^2}$  is the two-dimensional Green's function  $\Delta \phi$  is the potential jump across the foil trailing wake sheet  $S_W$ , and  $m = 1$  or  $2$  depending on whether  $\phi$  is evaluated on  $S_B$  or a field point respectively. As is depicted in Figure 1,  $S_W$  is constrained to the  $-x$  axis. From the condition of pressure continuity across  $S_W$ ,  $\Delta \phi = \Gamma(x+t)$  where  $\Gamma$  is the foil circulation,

$$\Gamma = \operatorname{Re} \sum_{n=1}^N \Gamma_n e^{inkt} \quad (B-5)$$

The surface values of  $\phi$  in equation (B-4) and the circulation  $\Gamma$  are determined from (B-4) evaluated on  $S_B$  in conjunction with the Kutta condition. The Kutta condition requires that the difference in tangential velocity between the upper and lower surface at the trailing edge is equal to the instantaneous loss in foil circulation  $-d\Gamma/dt$ . Once this is accomplished, field point values for  $\phi$  (or its derivatives) are obtained by direct application of (B-4). The necessary integrations in (B-4) or spatial derivatives of (B-4) can all be performed analytically if  $\phi$  and  $\partial\phi/\partial n$  are assumed constant on line segments representing  $S_B$ . The pressure coefficient,

$$C_p = \text{Re} \sum_{n=0}^N C_{p_n} e^{i n k t} \quad (\text{B-6})$$

is obtained from the Bernoulli equation. In (B-6),  $C_{p_0} = 2\phi_{0x} - \phi_{0x}^2 - \phi_{0y}^2$  and for the pitching foil application,

$$C_{p_1} = 2\alpha_1 \left[ \phi_{1y} - i k \phi_{1x} - \phi_{0x}(y-y_R)k + \phi_{0y}(x-x_R)k + i \phi_{0y} - \phi_{0x}\phi_{1x} - \phi_{0y}\phi_{1y} \right] \quad (\text{B-7})$$

and for propeller applications,

$$C_{p_n} = 2V_n \left[ -i k \phi_n + \phi_{nx} - \phi_{0x}\phi_{nx} - \phi_{0y}\phi_{ny} - \phi_{0y}e^{i n k x} \right] \quad (\text{B-8})$$

In (B-7) terms of  $O(\alpha_1^2)$  and in (B-8) terms of  $O(V_n^2)$  are neglected.

The computer program implementing this theory was validated by comparing its results for unsteady surface pressure on a pitching hydrofoil with the method of Geising (1968) and the experiments of Shen and Peterson (1978). Figure B-1 shows a comparison between the theories and the experiment of unsteady pressure magnitude per radian,  $|C_{p_1}|/\alpha_1$ , for three foil locations,  $2x/c = (1.934, 1.8, 1.5)$ , and for the reduced frequency range,  $0 \leq k \leq 2.5$ . Figure B-1 also shows a comparison for the phase angle. Figure B-1 shows that the theories compare well with the experiments. However, on the average, Geising's results are closer to the results from the experiment for the pressure magnitude. Stern's results show somewhat small pressure magnitudes. In Geising's singularity distribution method the location of the foil trailing wake sheet is determined as part of the solution, where in the present theory it is constrained to the  $-x$  axis. This may account for the differences in their results.

## APPENDIX C: EFFECTIVE WAKE PROCEDURE

The vertical component of the section inflow is given by

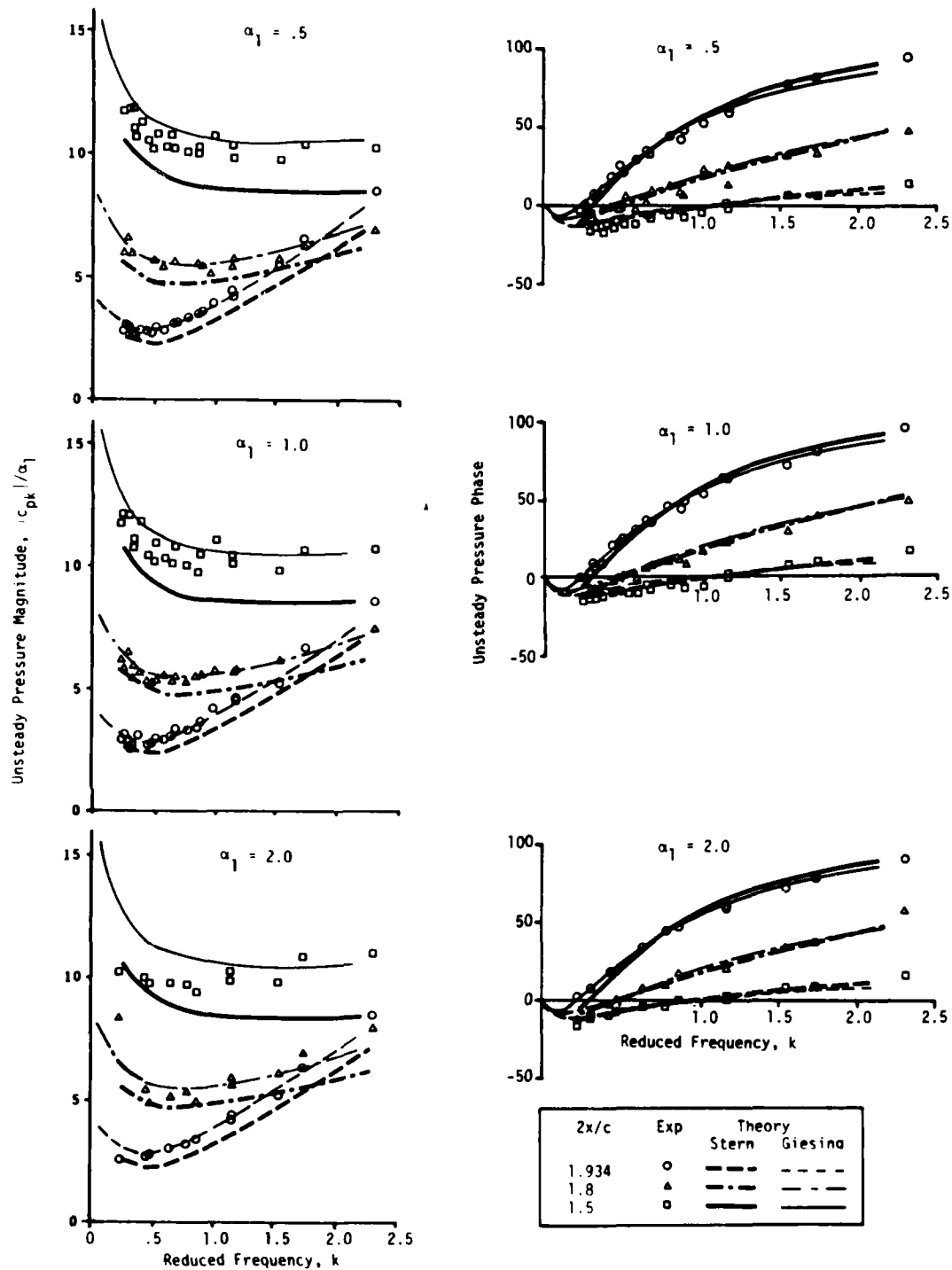


Figure B-1. Fully-Wetted Flow Unsteady Surface Pressure Magnitude and Phase on a Pitching Hydrofoil.

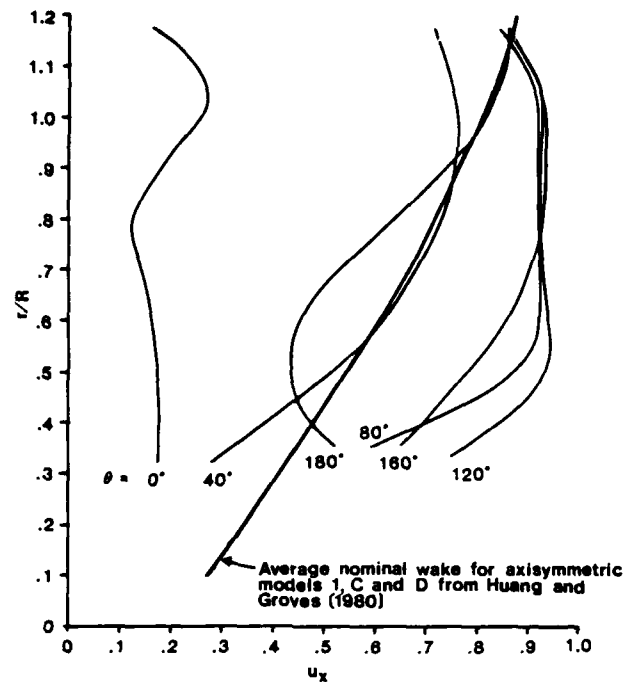


Figure C-1. AO-177 Nominal Without Flow-Modifying Fins Wake Axial Velocity Profiles.

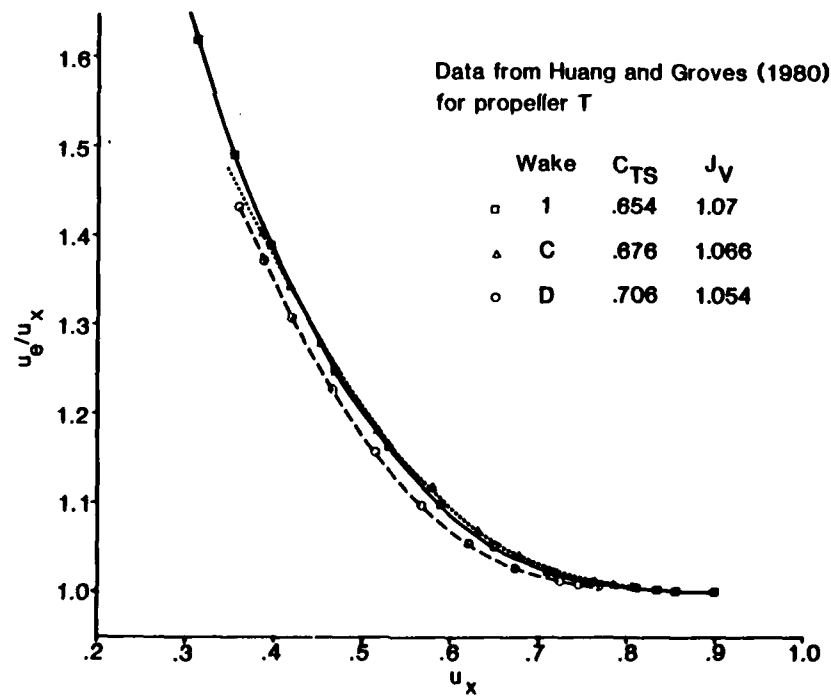


Figure C-2. Ratio of Effective and Nominal Wake Axial Velocities for Three Axisymmetric Bodies.



$$V = V_X \cos\beta_I + V_T \sin\beta_I \quad (C-1)$$

where  $V_X$  and  $V_T$  are the effective (propeller/hull) axial and tangential wake velocities and  $\beta_I$  is the hydrodynamic pitch angle. Experimentally it is difficult to measure an effective wake; consequently, measurements are made without the propeller (nominal wake). The nominal wake tends to overpredict the wake deficit since propeller suction tends to accelerate the flow, particularly in retarded flow regions. Huang and Groves (1980) have shown good agreement between theory and experiments for the effective wake of axisymmetric bodies. Some researchers have constructed effective wakes for ships by applying Huang's theory to nominal ship wakes at blade angle intervals. This procedure is not felt advisable since ship wake profiles do not resemble axisymmetric wake profiles at most blade angles as can be seen from Figure C-1. Figure C-1 shows the A0-177 without fin nominal wake profiles for blade angles from  $0^\circ$  to  $180^\circ$  and an axisymmetric body nominal wake profile. For the calculations made in this paper the nominal wake was modified to represent an effective wake by using data from Huang and Groves rather than applying the theory directly. Figure C-2 shows curves of  $u_e/u_X$  vs.  $u_X$  for three different axisymmetric bodies with propeller loading and speed of advance values near the values for the A0-177.  $u_e$  is the effective wake axial velocity and  $u_X$  is the nominal wake axial velocity, both of which are nondimensionalized using the ship speed. It is seen that the curves are very close. A mean curve from Figure C-2 was used to calculate an effective wake for the A0-177. This was done by multiplying  $V_X$  in equation (C-1) at each blade angle by the factor  $u_e/u_X$  obtained from Figure C-2 for  $u_X = V_X$ . Since the A0-177 had lower nominal wake values than Huang's data, the curve had to be extrapolated. This procedure is only intended as an estimate of the effective wake. It assumes that the effect of the propeller in the ship boundary layer is the same as in an axisymmetric boundary layer for the same wake deficit. The calculation of an effective wake for a propeller/hull is clearly an area of needed research. One possible improvement is to construct ship wake profiles at constant depths where they would resemble two-dimensional profiles and then apply a theory like Huang's. However, the effort would possibly be better spent by scaling the wake using the results from boundary layer calculations for the ship both with and without the propeller. This would also allow for  $R_n$  scaling when making calculations for full scale.

## Discussion

T.T. Huang (DTNSRDC)

Please give a detailed illustration of the differences in your results using nominal and effective wakes as inputs. Are we sure that proper use of effective wake is the only parameter affecting the computed cavitation geometries rather than the models you used? The importance of determining proper effective wake for unsteady propeller theory operated in three-dimensional nonuniform inflow.

R. Sato (Ishikawajima-Harima Heavy Industries)

If we want to calculate the pressure fluctuations on ship the hull, I think it is important to calculate the behavior not only of the cavity on the propeller blades but also of the cavity that appears behind the trailing edge. Is it possible to apply this method to calculate the behavior of this type cavity?

O. Scherer (Hydronautics, Inc.)

Figure 2 indicates a correction to the effective inflow velocity from unsteady lifting-line theory. Could you please explain the nature of this correction?

M.B. Wilson (DTNSRDC)

The author has shown a lot of ingenuity in combining approximations with a nonlinear formulation of the two-dimensional cavity behavior. To a great extent, the ultimate consequences of the various approximations and assumptions have not been addressed directly, but are supposed to be evident in the comparison given with results of experiments in the two examples. One example used by the author deals with features of the cavitating propeller flow on the Naval Auxiliary Oiler AO-177. This single-screw ship encountered problems on its Builders Trials associated with intermittent propeller cavitation, and these problems were subsequently relieved significantly by the installation of a wake-improving fin. The details of this fix are not relevant here, but some caution needs to be exercised with implications conveyed by the author about how the present analysis scheme could be used to analyze the flow problems involved with this particular example.

For the record, it is important to state clearly and accurately what problems the ship actually encountered. The AO-177 did not display excessive levels of vibration in the usual sense of this term.

That is, the hull girder vibration levels were not excessive according to either Navy standards or the ISO recommended levels. This applies to (a) the maximum vertical vibration on main structural members on the ship centerline near the fantail and (b) the maximum horizontal vibration at the top levels of the deckhouse. The principal unsatisfactory feature about this ship was the excessive level of propeller-excited inboard airborne noise, which was found to dominate all other noise sources in most compartments aft of Frame 94. The distinction is important in terms of the frequency content of the exciting pressure pulses. High levels of airborne noise were measured especially in the frequency range of 30 to 250 Hz.

A secondary problem with the AO-177 was the propeller damage. It is somewhat misleading to use the term "erosion damage" in this connection without some qualification. After the Builders Trials, and roughly 40 hours of full-power operation, the propeller blades were found to have patches of burnished and dimpled surface damage that should be termed initial-stage or incubation-zone cavitation damage. This means that there was no material weight loss or gaping ragged holes or pits that are characteristic of what is commonly referred to as erosion damage. Each blade suffered a 6-mm (1/4-inch) lip or bent trailing edge (curled toward the pressure face) between the 0.8R and 0.9R radius that had the appearance of being rolled or beaten over. This early-stage surface distress, typical of cloud cavitation damage, was all concentrated at or very near the trailing edge of each blade.

One has the impression from the present paper that the procedures and results described could somehow have helped avoid the difficulties with the observed AO-177 propeller-wake interaction problems. I think that it may be premature to conclude that the method is accurate enough or that it covers all the physical effects involved. Consider the following observations:

1. It appears to me that neither the predicted history of the chordwise cavity termination position (see Figures 5 and 6) nor the apparent collapse position agrees well enough with the experimental findings (see sketches in Figures 9 and 10). In the cavitation sketches, the cavity termination appears to occur at or beyond the trailing edge of the blade (at the transition between the bubble and cloud [foaming] cavitation regimes). The leading edge of the cloud cavitation would seem also to indicate the location of the breakup of the sheet cavity at or near the trailing edge. Actually, the photographs of the blade cavities (Bjarne, 1980) are needed to show this. The theoretically predicted cavity termination location occurs no farther aft along the blade than about 0.88 chord at the 0.85R radius, and during the collapse phase, the rear end of the cavity moves forward. At this point, the paper gives no indication of what the predicted cavity termination or collapse location and severity have to do with the formation of cloud cavitation or erosion tendency.
2. The cavities predicted seem unrealistically thick (6 inches thick over a 1.5-inch-thick foil section at 0.85R radius).

Perhaps this is a consequence of the semielliptical cavity shape assumed.

3. In order to derive information about the excitation source level that would be important to the actual problem of the AO-177 (excessive airborne noise), it would be necessary to analyze harmonically the cavity volume velocity for its spectral content at the frequencies 3 to 20 times the blade-rate frequency. At least at blade-rate frequency, the results of the paper correctly indicate that the cavity volume velocity could be reduced by the action of the fin. Certainly, some favorable trends are evident. However, further progress with this work should be encouraged in order that the analysis scheme described be useful for troubleshooting actual propeller flows.

### Author's Reply

Fred Stern

In response to Dr. Huang, the representation of the effective wake is certainly not the only parameter affecting the predicted cavitation; however, proper inclusion of propeller suction effects on the nominal wake is important. This can be seen from Figure 2, which shows that the reduction in the wake peak due to the effective wake procedure used (31 percent) is of the same order as that due to the unsteady lifting-line correction (36 percent). The principal effect on the predicted cavitation due to these reductions is a decrease in the cavity thickness. This is indicated from Figure 22, which shows the fully wetted, unsteady-flow zero-pressure lines calculated using both the nominal and effective wake. Figure 22 is for the AO-177 propeller at the .85 radius without-fins condition and for blade angle =  $45^\circ$ .

In response to Dr. Sato, the method allows for free migration of the cavity in response to the fluid pressure field; therefore, it is possible to have cavities shed from the trailing edge into the wake. The fragmentation of the cavity into cloud cavitation is beyond the scope of the method. However, as shown in Section 4, the method does show trends that are similar to experimental trends concerning cloud cavitation.

In response to Mr. Scherer, in the unsteady propeller lifting-line method certain three-dimensional downwash corrections are applied to the harmonics of the vertical component of the two-dimensional section inflow. The propeller blades are modeled by skewed lifting lines. The downwash corrections include the effects due to the bound vortex representing the other blades and the effects due to the trailing radial and streamwise vortices from all the blades. The effects of the bound streamwise vorticity is neglected. Also, interaction effects between the different radial sections on the index blade are neglected. Figure 2 shows the effects of the downwash corrections on the inflow at the .85 radius of the AO-177 propeller. The downwash correction reduces the maximum angle of attack by 36 percent. Although this

seems to be a large reduction, the downwash correction may be conservative. A comparison of the bearing force results from the unsteady lifting-line method with lifting-bearing force results from the unsteady lifting-line method with lifting-surface theories and with experimental data indicate this. If the downwash correction is under-predicted, then the section angle of attack variation would be excessive, implying lower suction pressures resulting in thicker cavities in the present analysis.

I would like to thank Dr. Wilson for setting the record straight with regard to the specifics of the problems encountered by the AO-177. With regard to Dr. Wilson's observations concerning the computational results, I would like to point out that the method is intended to model the gross features of unsteady sheet cavitation: cavity length, thickness, position, and surface behavior, including rates of deformation and movement. With this in mind, I think the results are reasonable; however, improvements are possible, and I agree that the predicted cavities are too thick. This is most likely due to an overestimate of the section angle of attack variation. In response to Dr. Wilson's comments concerning the AO-177 cavity-excited noise problem, the cavity volume velocity (see Figure 8) has been harmonically analyzed (see Figure 23) and the free-space pressures calculated (see Figure 24) for comparison with the experimental data (see Wilson et al., 1982, Figure 39). A value of 2 was used for the reflection coefficient in the free-space pressure calculation. Although the results using this approximate procedure for calculating hull pressures are seen from Figure 24 to be below the model and full-scale experimental results, they do show the same trend as the experiments with regard to the effects of the fins; that is, a reduction in the pressure magnitude except for directly over the tip where the effects of reduced tip clearance offset the reduction due to the fin in the seventh harmonic of the cavity volume velocity,  $V_7$ .

AO-177 .85 Radius

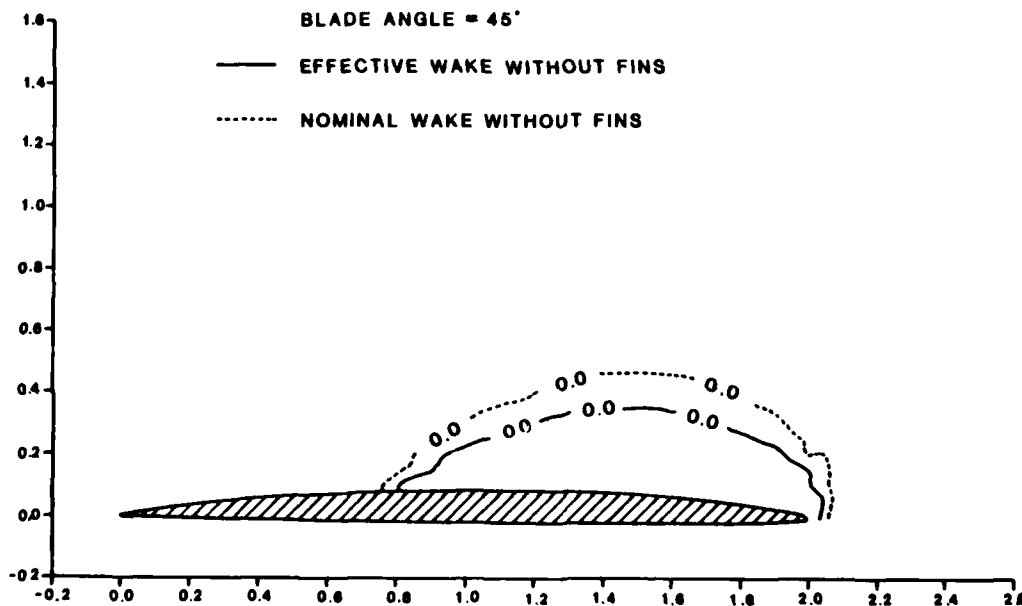


Figure 22. Fully-Wetted Unsteady Flow Zero Pressure Lines Calculated Using Both the Nominal and Effective Wake.

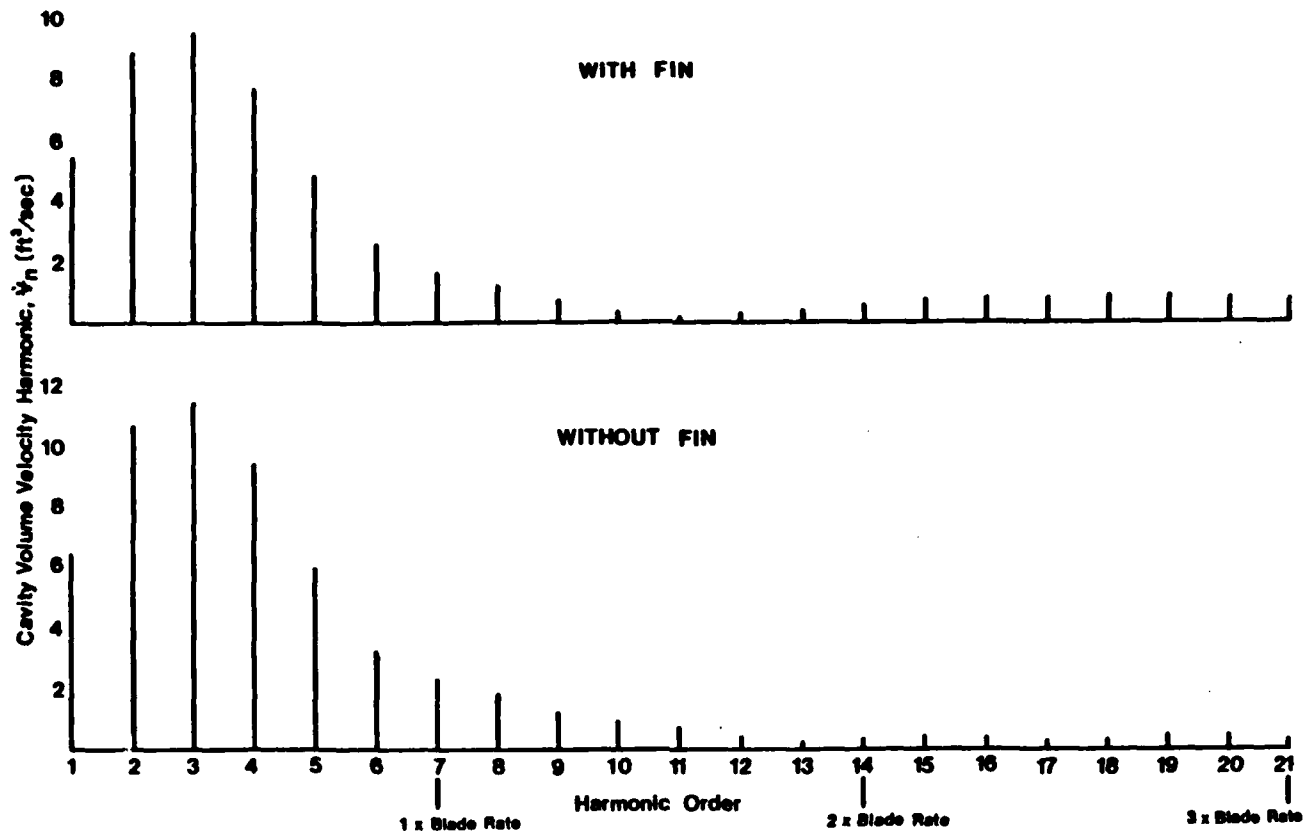


Figure 23. Cavity Volume Velocity Harmonics for the AO-177 Propeller.

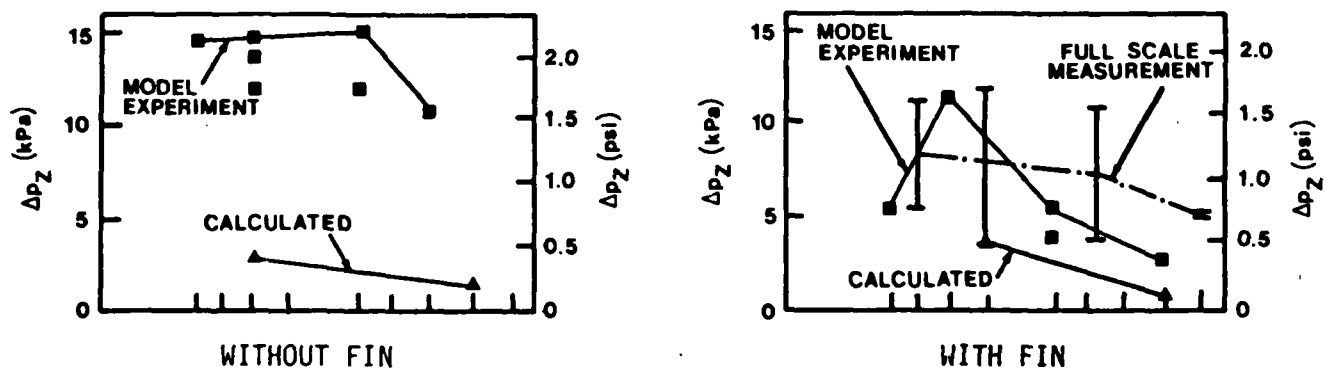


Figure 24. Comparison of Blade Rate Pressure Amplitudes with Experiments.

# Theoretical Treatment of Unsteady Cavitation on Ship Propeller Foils

Hiroshi Isshiki and Mitsunori Murakami  
Hitachi Zosen Corporation  
Osaka, Japan

## ABSTRACT

The propeller surface force due to a cavitating propeller is closely related to the volume variation of the cavity on propeller foils. So, the correct estimation of the propeller surface force requires the correct estimation of the cavity. For the purpose, the unsteady, nonlinear and three-dimensional effects should be introduced into cavity theory. In the present theory, the unsteadiness is theoretically investigated.

The usual "quasi-steady" approach can not take full account of the unsteady effects, that is, the so-called hysteresis effects such as the phase delay of the cavity growth.

In the present paper, the problem of the two-dimensional leading edge cavitation is first discussed, and the theory is then applied to the problem of a ship propeller.

Although the present theory is of approximate nature, the numerical results for the two-dimensional problem may be thought to be, at least qualitatively, correct.

With regard to the propeller problem, the effect on the cavity pattern, the effect on the cavity volume and the effect on the fluctuating pressure on the hull surface are discussed. Through these investigations, some aspects of the hysteresis effects of the unsteady cavity on propeller foils seem to be clarified. The estimation of the cavity pattern, for example, seems to be improved.

The variational principles of the linearized unsteady cavity flow theory are also discussed. Some comments about the exact boundary conditions on the foil surface are also given by using the complex acceleration potential.

## NOMENCLATURE

A sectional area of the cavity on a foil

$c$	chord length of a two-dimensional hydrofoil
$D$	propeller diameter
$C_1$	function of $\dot{V}_c$ and $\ddot{V}_c$
$y = f_U(x), f_L(x)$	equations of the upper and lower surfaces of a two-dimensional hydrofoil
$g(x, t)$	thickness of the cavity
$K_T = T/\rho n^2 D^4$	thrust coefficient
$K_{pt} = p_t/\rho n^2 D^2$	hull fluctuating pressure coefficient (total)
$K_{pn} = p_n/\rho n^2 D^2$	hull fluctuating pressure coefficient (harmonic component of $n$ -th multiple of the rotational frequency)
$l_0, l$	inception and termination points of the cavity
$m = 10 \dot{V}_c/\alpha U c$	unsteadiness parameter
$n$	no. of revolution (r.p.s.) of the propeller
$p_a$	ambient pressure ( $p_a = p_a(t)$ )
$p_v$	vapour pressure in the cavity
$p_t$	hull fluctuating pressure (total)
$p_n$	hull fluctuating pressure (harmonic component of $n$ -th multiple of the rotational frequency)
$t$	time
$T$	propeller thrust
$u, v$	$x$ -, $y$ - components of the fluid velocity
$U$	advance velocity of the hydrofoil
$V_c$	cavity volume
$V_{co}$	steady cavity volume
$(x, y)$	coordinate ( $\rightarrow$ figure 1)
$\alpha$	angle of attack ( $\alpha = \alpha(t)$ )



- $\gamma = \begin{cases} 2 \cos^{-1} \sqrt{\ell/c} & \text{for the partial cavity} \\ 2 \cos^{-1} \sqrt{c/\ell} & \text{for the super cavity} \end{cases}$
- $\delta^*$  cavity end thickness or height of the plate placed at the cavity end (independent of time)
- $\Omega$  fluid region (linearized)
- $\phi$  velocity potential
- $\sigma = (p_a - p_v) / \frac{1}{2} \rho U^2$  cavitation number ( $\sigma = \sigma(t)$ )
- $\sigma^*$  equivalent cavitation number ( $\rightarrow$  equation (19))
- $\sigma_n = (p_a - p_v) / \frac{1}{2} \rho n^2 D^2$
- $\rho$  density of the fluid (constant)
- $\mu^*, \nu^* \dots$  experimental parameters ( $\rightarrow$  equation (16))
- $\lambda, \lambda_0$  camber of the two-dimensional thin parabolic wing

## 1. INTRODUCTION

It is well known that the propeller surface force due to a cavitating propeller is closely related to the volume variation of the cavity on propeller foils. So, in order to get correct estimation of the propeller surface force due to the cavitating propeller, it is most important to estimate the cavity on the propeller foils correctly. For the purpose, the introduction of the unsteady, non linear and three-dimensional effects into cavity theory may be required. In the present paper, the unsteady effects are, among other things, theoretically investigated.

In common practice, the quasi-steady approach is adapted, and unsteady effects are not fully taken into account. The quasi-steady approach can not explain the so-called hysteresis effects such as the phase delay effect which is usually observed in experiment (Chiba et al., 1980; Hoshino, 1980).

In the present paper, the problem of the unsteady cavity on two-dimensional hydrofoils is first discussed (Isschiki and Murakami 1981), and the theory is then applied to the problem on foils of a propeller operating in a ship wake (Isschiki and Murakami, 1982a, 1982b).

The two-dimensional problem is based on the following assumptions:

(1) According to Tulin-Hsu theory (Tulin and Hsu, 1980), the term which expresses dynamic effect is neglected for the pressure on the cavity surface.

(2) The cavity volume is obtained by using a relation based on relationship between cavity length and volume of the steady cavity.

(3) The effect of the trailing vortices due to the lift variation is neglected. But this assumption may not introduce a significant error when the method is applied to a propeller operating in a wake, since the main effects of the trailing vortices is taken into account through the calculation of the equivalent sections by the unsteady lifting surface theory.

A calculation method based on the above mentioned assumptions and linear cavity flow theory is obtained for the leading edge cavitation.

The unsteady cavity on propeller foils behind a ship is then estimated by using the above mentioned two-dimensional theory. For the purpose, a practical method of the calculation is developed by introducing an idea of "effective flat foil". According to the idea, the attack angle-cavitation number ratio of the effective flat foil is calculated by assuming that the quasi-steady cavity length of the effective flat foil should be equal to that of the actual propeller foil section under the same cavitation condition. The quasi-steady cavity length on the actual propeller foil is obtained by a method similar to the Ukon-Kato method (Kato and Ukon, 1979; Ukon, 1979). And, by using the above mentioned attack angle-cavitation number ratio, the unsteady effects are calculated for the effective flat foil.

With regard to the effects of the unsteadiness of the cavity on the propeller foils, the effect on the cavity pattern, the effect on the cavity volume and the effect on fluctuating pressure on the hull surface are studied.

In order to deepen the physical understanding about the unsteady cavity flow, some discussions on the variational principles and the exact boundary conditions on foil and cavity surfaces are also given.

## 2. CALCULATION OF THE TWO-DIMENSIONAL UNSTEADY CAVITATION

### 2.1 Formulation of the Problem

As shown in figure 1, a two-dimensional hydrofoil of the chord length  $c$  is placed in a uniform stream of the velocity  $U$ , and the direction of the flow relative to the foil is  $\alpha(t)$ . The origin of the coordinate system is taken at the leading edge, and the  $x$ - and  $y$ - axes are taken parallel and perpendicular to the line joining the leading and

trailing edges respectively.  $\ell_0$  and  $\ell$  are the inception and termination points of the cavity on the suction side of the foil respectively, and  $\delta^*$  is the cavity end thickness which may be considered to be the height of the plate placed at the cavity end (the efflux  $U\delta^*$  of the fluid from the plate is assumed).  $y=f_L(x)$  and  $f_U(x)$  are the equations of the foil lower and upper surfaces respectively, and  $g(x,t)$  is the thickness of the cavity.  $p_a(t)$  is the ambient pressure, and  $p_y$  is the pressure in the cavity, that is, the vapour pressure of the liquid.

Then equations of the linearized unsteady cavitation are given as follows:

Equation of continuity

$$\frac{\partial u}{\partial x} + \frac{\partial v}{\partial y} = 0 \quad \text{in } \Omega \quad \dots\dots\dots (1)$$

Equation of irrotationality

$$u = \frac{\partial \phi}{\partial x}, \quad v = \frac{\partial \phi}{\partial y} \quad \text{in } \Omega \quad \dots\dots\dots (2)$$

Mechanical condition on the cavity surface ( $\rightarrow$  Appendix A)

$$\frac{u^+}{U} = \left(1 + \frac{\sigma}{2}\right) - \frac{1}{U^2} \frac{\partial \phi^+}{\partial t} \quad \text{on } \ell_0 < x < \ell, \quad y = +0 \quad \dots\dots\dots (3)$$

Kinematical condition on the wetted surface

$$v^+ = U \frac{d}{dx} f_U(x) \quad \text{on } 0 < x < \ell_0, \quad \ell < x < c, \quad y = +0 \quad \dots\dots (4)$$

$$v^- = U \frac{d}{dx} f_L(x) \quad \text{on } 0 < x < c, \quad y = -0 \quad \dots\dots\dots (5)$$

Cavity end condition or the so-called closure condition  
( $\rightarrow$  Appendix B)

$$\oint_{\text{Body}} v dx = U\delta^* + \frac{dV_c}{dt} - \delta^* \frac{d\ell}{dt} \quad \dots\dots\dots (6)$$

Kutta condition

$$u^+ = u^- \quad \text{at } x = c, \quad y = 0 \quad \dots\dots\dots (7)$$

Condition at upstream

$$u \rightarrow U, v \rightarrow U\alpha \quad \text{as } x \rightarrow -\infty \quad \dots\dots\dots (8)$$


---

Kinematical condition on the cavity surface

$$\left(\frac{\partial}{\partial t} + U\frac{\partial}{\partial x}\right) (g + f_U) = v^+ \quad \text{on } \ell_0 < x < \ell, y = +0 \quad \dots\dots\dots (9)$$

Cavity volume

$$V_c = \int_{\ell_0}^{\ell} g dx \quad \dots\dots\dots (10)$$

Mechanical condition of the trailing vortex wake

$$\left(\frac{\partial}{\partial t} + U\frac{\partial}{\partial x}\right) \phi^+ = \left(\frac{\partial}{\partial t} + U\frac{\partial}{\partial x}\right) \phi^- \quad \text{on } c < x, y = 0 \quad \dots\dots\dots (11)$$

Kinematical condition of the trailing vortex wake

$$v^+ = v^- \quad \text{on } c < x, y = 0, \quad \dots\dots\dots (12)$$

where

$t$  : time

$u, v$  :  $x$ -,  $y$ - components of the fluid velocity

$\phi$  : velocity potential

$\sigma(t) = [p_a(t) - p_v]/(\frac{1}{2}\rho U^2)$  : cavitation number

$\rho$  : density of the fluid (constant)

$V_c(t)$  : cavity volume,

and "Body" means the internal boundary surface of the linearized fluid region  $\Omega$  defined by

$$\Omega \equiv \{(x,y) | -\infty < x < \infty, -\infty < y < \infty\} - \{(x,y) | 0 \leq x \leq c, y = 0\} \dots (13)$$

The underlined terms in equations (3), (6), (9) and (11) are the terms which reflect the unsteadiness. In the steady problem, equations (1) through (8) form a closed problem, and equations (9) and (10) are used to obtain the cavity thickness  $g$  and the cavity volume  $V_c$ .

In order to deepen the physical understanding about the unsteady cavity flow, the variational principles equivalent to the above mentioned boundary value problem are shown in Appendix C.

Some discussions about the boundary conditions on the foil and cavity surfaces are given in Appendix D.

According to the Tulin-Hsu Theory (Tulin and Hsu, 1980), if the degree of the unsteadiness is assumed to be small, the second term on the righthand side of equation (3) and the third term on the right hand side of equation (6) may be neglected, that is,

$$\frac{u^+}{U} = (1 + \frac{\sigma}{2}) \quad \text{on } l_0 < x < l, y = +0 \dots (14)$$

$$\oint_{\text{Body}} v dx = U \delta^* + \frac{dV_c}{dt}, \dots (15)$$

However, it must be mentioned that there also exist an unsteady term which originates from the trailing vortices due to the unsteady lift. From the same reason as equation (3) is approximated by equation (14), the trailing vortex terms are also neglected. This assumption may not introduce a significant error when the present theory is applied to a propeller behind a ship, because the unsteady lifting surface calculation to obtain the equivalent sections includes the effect of the trailing vortices due to the unsteady lift.

The cavity volume  $V_c$  should be obtained by integrating equations (9) and (10), but very complex calculation may be required to do this. In the present theory, it is assumed that  $V_c$  is calculated by using the cavity volume - extent relation for the steady cavity, that is,

$$V_c(t) = (1 - \mu^* \frac{\dot{V}_c}{U \cdot c} - \nu^* \frac{\ddot{V}_c}{U^2} - \dots) V_{c0} (l; l_0, \delta^*), \dots (16)$$

where  $V_{c0}$  is the volume of the steady cavity for the given values of  $l$ ,  $l_0$  and  $\delta^*$ , and  $\mu^*$  and  $\nu^*$  are assumed to be parameters determined, for example, by experiments. Equations (9) and (10) are now replaced by equation (16).

Therefore, the above mentioned system of equations, that is, equations (1), (2), (14), (4), (5), (15), (7), (8) and (16) form a closed system. Furthermore, if the value of  $V_c$  is designated, this equation system (excluding equation (16)) is formally identical with a

steady problem for which the thickness of the cavity end is given as  $\delta^* + V_c/U$ . Hence, in the following section, a theory of steady cavity with a given cavity end thickness is used (Geurst, 1959; Geurst, 1960; Geurst and Verbrugh, 1959; Hanaoka, 1965a, 1965b; Hanaoka, 1966; Kato, 1979; Nishiyama and Ota, 1971; Noordzij and Officier, 1977; Tulin and Hsu, 1980; Wade, 1967; Yamasaki and Takahashi, 1979).

## 2.2 Calculation of Unsteady Cavity on a Flat Foil

In the following, the cavity inception point is assumed to be at the leading edge.

The calculation method is explained, at first, for a flat foil.

For the partial cavity, the cavity end condition which gives the relation between the cavity extent and the cavitation number is given as ( $\rightarrow$  Appendix E)

$$Uc \left[ \left( 1 + \sin \frac{\gamma}{2} \right) \cos \frac{\gamma}{2} - \frac{1}{2} \left( \frac{\sigma}{\alpha} \right) \left( 1 - \sin \frac{\gamma}{2} \right) \sin \frac{\gamma}{2} \right] \\ = \frac{2}{\pi} \left( U \frac{\delta^*}{\alpha} + \frac{1}{\alpha} \frac{dV_c}{dt} \right), \dots\dots\dots (17)$$

where

$$\frac{\gamma}{2} = \cos^{-1} \sqrt{\ell/c} \quad 0 \leq \frac{\gamma}{2} \leq \frac{\pi}{2}, \dots\dots\dots (18)$$

The cavity volume  $V_c$  is approximately calculated by using the cavity volume-extent relation of the steady cavity. For this purpose, an equivalent cavitation number  $\sigma^*$  is defined as the cavitation number which gives the same cavity extent  $\ell$  for the steady cavity with the cavity end thickness  $\delta^*$  as that calculated by equations (17) and (18). Hence,  $\sigma^*$  is calculated by

$$Uc \left[ \left( 1 + \sin \frac{\gamma}{2} \right) \cos \frac{\gamma}{2} - \frac{1}{2} \left( \frac{\sigma^*}{\alpha} \right) \left( 1 - \sin \frac{\gamma}{2} \right) \sin \frac{\gamma}{2} \right] = \frac{2}{\pi} U \frac{\delta^*}{\alpha}, \dots (19)$$

The cavity volume is then calculated as

$$\frac{V_c}{\alpha} = -C_1 \frac{\pi c^2}{16} \left[ 2 \left( 1 + \sin \frac{\gamma}{2} \right) \left( 1 - 3 \sin \frac{\gamma}{2} \right) \sin \frac{\gamma}{2} \cos \frac{\gamma}{2} \right. \\ \left. + \frac{1}{2} \left( \frac{\sigma^*}{\alpha} \right) \left( 1 - \sin \frac{\gamma}{2} \right) \left( -1 - 3 \sin \frac{\gamma}{2} + 2 \sin^2 \frac{\gamma}{2} + 6 \sin^3 \frac{\gamma}{2} \right) \right], \dots\dots\dots (20)$$

$C_1$  is a function of  $\dot{V}_c = dV_c/dt$ ,  $\ddot{V}_c = d^2V_c/dt^2$  defined as ( $\rightarrow$  equation (16))

$$C_1 = 1 - \mu^* \frac{\dot{V}_c}{U \cdot c} - \nu^* \frac{\ddot{V}_c}{U^2} - \dots, \dots\dots\dots (21)$$

where  $\mu^*$ ,  $\nu^*$ , ... are considered to be, for example, experimental parameters. The function  $C_1$  is introduced to take account of the unsteadiness of the cavity volume-extent relation, but in the present calculation,  $\mu^*$ ,  $\nu^*$ , ... are assumed to be zero.

For the super cavity, the similar relations are derived as follows:

(a) The cavity end condition

$$Uc \left( \frac{1 + \sin \frac{\gamma}{2}}{\cos^2 \frac{\gamma}{2}} \right) \left[ \cos \frac{\gamma}{2} - \frac{1}{2} \left( \frac{\sigma}{\alpha} \right) \sin \frac{\gamma}{2} \right] = \frac{2}{\pi} \left( U \frac{\delta^*}{\alpha} + \frac{1}{\alpha} \frac{dV_c}{dt} \right), \dots\dots\dots (22)$$

where

$$\frac{\gamma}{2} = \cos^{-1} \sqrt{c/\ell} \quad 0 \leq \frac{\gamma}{2} \leq \frac{\pi}{2}, \dots\dots\dots (23)$$

(b) The formula for the equivalent cavitation number  $\sigma^*$

$$Uc \left( \frac{1 + \sin \frac{\gamma}{2}}{\cos^2 \frac{\gamma}{2}} \right) \left[ \cos \frac{\gamma}{2} - \frac{1}{2} \left( \frac{\sigma^*}{\alpha} \right) \sin \frac{\gamma}{2} \right] = \frac{2}{\pi} U \frac{\delta^*}{\alpha}, \dots\dots\dots (24)$$

(c) The formula for the cavity volume  $V_c$

$$\frac{V_c}{\alpha} = \frac{C_1 \pi c^2}{16(1 - \sin^2 \frac{\gamma}{2})} \left[ 2 \cos \frac{\gamma}{2} (-2 + \sin \frac{\gamma}{2}) + \frac{1}{2} \left( \frac{\sigma^*}{\alpha} \right) (1 + 4 \sin \frac{\gamma}{2} - 2 \sin^2 \frac{\gamma}{2}) \right] \dots\dots\dots (25)$$

In the following, the method and results of the calculation based on the equation (17) through (25) are shown.

(1) Figure 2 shows the relation of  $\ell/c$  and  $\alpha/\sigma$  where  $m$  is the unsteadiness parameter:  $m = 10V_c/(\alpha U c)$ . From this chart, it may be seen that the cavity extent  $\ell$  at the same  $\alpha/\sigma$  is shorter for  $V_c > 0$  than for  $V_c < 0$ . This means that the growth of the cavity is depressed

at the growing stage.

On the other hand, it is well known that physically appropriate solutions can not be obtained in the range  $0.75 < \ell/c < 1.15$ , and the point of  $\ell/c = 0.75$  and  $1.15$  are called the critical points of the partial and super cavities respectively. In order to eliminate this limitation, a proper correction must be introduced in figure 2.

(2) In the present paper, the method illustrated in figure 3 is adopted. Figure 3 shows the relations of  $\ell/c - \alpha/\sigma$ ,  $Vc/(\alpha c^2) - \alpha/\sigma$  and  $Vc/(\alpha c^2) - \ell/c$ . In the figure, the broken line is the theoretical result as shown in figure 2, and the points ( $A_p, B_p, C_p$ ) and ( $A_s, B_s, C_s$ ) are the critical points of the partial and super cavities. On these charts, the linear interpolations between these critical points are shown by the chained lines. The linear interpolation may give a correction method, but in the present paper, a method as shown by the solid lines is adopted.

The details of the method is as follows. In the chart of the  $Vc/(\alpha c^2) - \ell/c$  relation, a line which is tangent to the curves for the partial and super cavities is drawn, and the tangential points are referred to by  $D_p$  and  $D_s$  respectively. The points  $D_p'$  and  $D_s'$  corresponding to the points  $D_p$  and  $D_s$  respectively are found in the chart of the  $\ell/c - \alpha/\sigma$  relation, and three power curves  $D_p'A_M$  and  $A_M D_s'$  are drawn where  $A_M$  is the midpoint of  $\overline{A_p A_s}$ .  $D_p'A_M$  is tangent to the curve for the partial cavity and  $\overline{A_p A_M}$ , and  $A_M D_s'$  to  $\overline{A_M A_s}$  and the curve for super cavity. Furthermore, the  $Vc/(\alpha c^2) - \alpha/\sigma$  relation is also obtained from the  $\ell/c - \alpha/\sigma$  and  $Vc/(\alpha c^2) - \ell/c$  relations. The case when  $m \neq 0$  is also treated in the similar manner.

(3) According to the above mentioned idea, figure 4 is obtained as a correction for figure 2. The following calculations are based on figure 4.

Since the cavity volume  $Vc$  is considered to be the function of the cavity extent  $\ell$ ,  $\ell$  may be considered to be the function of  $Vc$ . If this relation is introduced into the closure conditions (17) or (22), the closure condition may be considered as the ordinary differential equation of the first order for the unknown function  $Vc$ . Actually, the  $Vc/(\alpha c^2) - \ell/c$  relation as shown in figure 3 are used instead of equations (20) and (25), and the  $\ell/c - \alpha/\sigma$  relation as shown in figure 4 instead of equations (17) and (22). The flow of the calculation is illustrated in figure 5.

In the following calculation,  $\alpha/\sigma$  is considered to be a given function of time  $t$ .

(4) Figures 6 and 7 show the results for the case that the extent of the corresponding quasi-steady cavity is smaller than  $0.75c$ . The maximums of  $\alpha/\sigma$  are same for both cases, but the difference is the degree of the unsteadiness. The unsteadiness effect is stronger in figure 7 than in figure 6. From these results, it may be seen that the phase delay occurs because of the unsteadiness, and the maximum of the cavity extent and volume become smaller as the unsteadiness



increases.

If the results in figure 7 are plotted on the chart for the  $\ell/c - \alpha/\sigma$  relation, it may be found that a hysteresis loop is formed as shown in figure 8, and the unsteady cavity extent is shorter than the quasi-steady one at the growing stage, but longer at the decreasing stage.

(5) Figures 9 and 10 show the case when the extent  $\ell_0$  of the quasi-steady cavity satisfies  $0.75 < \max(\ell_0/c) < 1.15$ . The maximums of  $\alpha/\sigma$  are taken equal for both cases, and the results similar to those in figures 6 and 7 are obtained.

(6) Figure 11 shows the case for  $\max(\ell_0/c) > 1.0$ , that is, the super cavity, and the initial value of  $\alpha/\sigma$  is taken as 0.08. Although the variation of  $\alpha/\sigma$  is pretty strong in this case, the maximums of  $\ell$  and  $V_c$  are rather large. This may be related to the adoption of the  $\ell/c - \alpha/\sigma$  relation as shown in figure 4. In this case,  $\alpha/\sigma$  approaches a non-zero value, and it takes fairly long time to recover to the quasi-steady results.

(7) Figure 12 shows the results for the cases when  $\alpha/\sigma$  oscillates. As can be seen from the variation of  $\alpha/\sigma$ , the case (B) is more unsteady than the case (A). They show little difference at the growing stages, but a pretty big difference at the decreasing stages.

(8) The numerical results in the present paper are given for  $\mu^* = \nu^* = 0$  in equation (21). If  $\mu^*$  is taken positive, the cavity volume becomes smaller at the growing stage and, on the other hand, becomes larger at the decreasing stage. The results for  $\mu^* > 0$  and  $\mu^* = 0$  are compared in figure 13. According to the results, the difference of  $V_c$  is small, but the maximum of  $\ell/c$  for  $\mu^* = 0.5$  is attained at the earlier time. This means that  $V_c$  continues to grow even after  $\ell/c$  attains its maximum. This seems to agree with the viewpoint of Dr. Hoshino (Chiba et al., 1980; Hoshino, 1980). If the unsteadiness is introduced into the cavity volume-extent relation, the results are modified as mentioned above. Hence, there is a room for future study about the calculation of the cavity volume. When the present results are plotted on the  $\ell/c - \alpha/\sigma$  chart, a hysteresis loop is obtained as shown in figure 14, and the loop for  $\mu^* = 0.5$  is drawn smoother than that for  $\mu^* = 0$ .

(9) The inception delay can not be evaluated by the present theory. The inception delay itself must be calculated by other theories, and built into the present theory. According to an instruction given by Professor H. Kato of the University of Tokyo, a nuclei is necessary for the cavity inception, and the time delay originated from nuclei density in water causes the cavity inception delay.

As a test, a calculation was conducted by assuming that an inception delay was given. The result is shown in figure 15. In figure 15, it is assumed that a nuclei meets the foil at the time when  $\alpha/\sigma = 0.03$ . The initial value of  $dV_c/dt$  may be calculated as a positive value by using the  $\ell/c - \alpha/\sigma$  relation as shown in figure 4. From figure

15, it is found that, after some time, the result with the inception delay coincides the result without the inception delay.

### 2.3 Effective Flat Foil Method to Calculate the Unsteady Cavity on a Foil

In this section, a practical method of calculation of the unsteady cavitation for a foil is introduced based on the method for a flat foil which is stated in section 2.2.

First, the discussions are made on how to treat practically the unsteady cavity on a thin parabolic foil.

For the partial cavity, the cavity end condition of a thin parabolic wing of camber  $\lambda_0$  as shown in figure 16 is given as

$$Uc \left[ \left(1 + \sin \frac{\gamma}{2}\right) \cos \frac{\gamma}{2} + \frac{1}{\alpha} \left\{ -\frac{\sigma}{2} (1 - \sin \frac{\gamma}{2}) \sin \frac{\gamma}{2} + \frac{2\lambda_0}{c} \sin \frac{\gamma}{2} \cos^3 \frac{\gamma}{2} \right\} \right] = \frac{2}{\pi} \left( U \frac{\delta^*}{\alpha} + \frac{1}{\alpha} \frac{dVc}{dt} \right), \dots\dots\dots (26)$$

where the same notations are used as in the case of a flat foil, and the underlined term reflects the unsteadiness.

Equation (26) is derived by modifying the results by Geurst (Geurst and Verbrugh, 1959). Namely, the cavity end thickness  $\delta^*$  and the unsteady term  $dVc/dt$  are introduced in the same way as in the case of a flat foil ( $\rightarrow$  Appendix E).

Again, the cavity volume  $Vc$  is calculated based on the cavity extent-volume relation for the steady cavity. Namely, an equivalent cavitation number  $\sigma^*$  is calculated by

$$Uc \left[ \left(1 + \sin \frac{\gamma}{2}\right) \cos \frac{\gamma}{2} + \frac{1}{\alpha} \left\{ -\frac{\sigma^*}{2} (1 - \sin \frac{\gamma}{2}) \sin \frac{\gamma}{2} + \frac{2\lambda_0}{c} \sin \frac{\gamma}{2} \cos^3 \frac{\gamma}{2} \right\} \right] = \frac{2}{\pi} U \frac{\delta^*}{\alpha}, \dots\dots\dots (27)$$

The cavity volume is then calculated as

$$\begin{aligned} \frac{Vc}{\alpha} = & -C_1 \frac{\pi c^2}{16} \left[ 2(1 + \sin \frac{\gamma}{2}) (1 - 3\sin \frac{\gamma}{2}) \sin \frac{\gamma}{2} \cos \frac{\gamma}{2} \right. \\ & + \frac{1}{2} \left( \frac{\sigma^*}{\alpha} \right) (1 - \sin \frac{\gamma}{2}) (-1 - 3\sin \frac{\gamma}{2} + 2\sin^2 \frac{\gamma}{2} + 6\sin^3 \frac{\gamma}{2}) \\ & \left. + \frac{\lambda_0}{c \cdot \alpha} (1 - \sin^2 \frac{\gamma}{2}) (1 + \sin \frac{\gamma}{2} - 4\sin^3 \frac{\gamma}{2}) \cos \frac{\gamma}{2} \right], \dots\dots\dots (28) \end{aligned}$$

where  $C_1$  is a function defined by equation (21).

For the super cavity, the relations corresponding to equations

(26), (27) and (28) are derived respectively as follows:

(a) The cavity end condition

$$\frac{Uc}{\cos^2 \frac{\gamma}{2}} \left[ (1 + \sin \frac{\gamma}{2}) \left\{ \cos \frac{\gamma}{2} - \frac{1}{2} \left( \frac{\sigma}{\alpha} \right) \sin \frac{\gamma}{2} \right\} + \frac{1}{2} \left( \frac{\lambda_0}{\alpha} \right) \sin \frac{\gamma}{2} \cos \frac{\gamma}{2} \right] = \frac{2}{\pi} \left( U \frac{\delta^*}{\alpha} + \frac{1}{\alpha} \frac{dVc}{dt} \right) \dots (29)$$

(b) The formula for the equivalent cavitation number  $\sigma^*$

$$\frac{Uc}{\cos^2 \frac{\gamma}{2}} \left[ (1 + \sin \frac{\gamma}{2}) \left\{ \cos \frac{\gamma}{2} - \frac{1}{2} \left( \frac{\sigma^*}{\alpha} \right) \sin \frac{\gamma}{2} \right\} + \frac{1}{2} \left( \frac{\lambda_0}{\alpha} \right) \sin \frac{\gamma}{2} \cos \frac{\gamma}{2} \right] = \frac{2}{\pi} U \frac{\delta^*}{\alpha} \dots (30)$$

(c) The formula for the cavity volume  $Vc$

$$\frac{Vc}{\alpha} = \frac{C_1 \pi c^2}{16 (1 - \sin^2 \frac{\gamma}{2})^2} \left[ 2 \cos \frac{\gamma}{2} (-2 + \sin \frac{\gamma}{2}) + \frac{1}{2} \left( \frac{\sigma^*}{\alpha} \right) (1 + 4 \sin \frac{\gamma}{2} - 2 \sin^2 \frac{\gamma}{2}) - \frac{1}{2} \left( \frac{\lambda_0}{\alpha} \right) (\cos^2 \frac{\gamma}{2} - \sin^2 \frac{\gamma}{2}) (1 - \sin \frac{\gamma}{2}) (\cos \frac{\gamma}{2})^{-1} \right] \dots (31)$$

In the following, the calculated results by using equations (26) through (31) are shown. Furthermore, a practical calculation method is examined for the purpose of applying to a ship propeller in a wake. (In the present paper, the two-dimensional unsteady cavitation theory is applied to the equivalent sections of propeller foils which are calculated by Hanaoka-Koyama's method of the lifting surface theory (Koyama, 1975). Therefore, the equivalent angle of attack, camber and cavitation number change according to the angular position of the blade.

The equivalent sections are, furthermore, approximated by thin parabolic wing sections of camber  $\lambda_0$  as shown in figure 16.)

(1) In figure 17, some results are shown for cambered thin foils. In this case,  $\alpha$  is taken as  $5^\circ$ , and the cavitation number  $\sigma$  is considered to be a function of time. According to these results, as the camber becomes large, both the quasi-steady and unsteady results are found to become large. But the unsteady effects do not seem to be much affected by the camber.

In this case, only the cavitation number  $\sigma$  is subjected to variation, but for equivalent sections of a propeller foil, at which the application of the present theory is aimed, not only  $\sigma$  but also the attack angle  $\alpha$  and camber  $\lambda$  are subjected to variation according to the angular position of the propeller blade.

(2) Figure 18 shows the results for the cambered foil ( $\lambda/c = 0.035$ ). The broken lines show the case when the angle of attack  $\alpha$  is taken constant, that is,  $5^\circ$ , and the cavitation number  $\sigma$  is subjected to

variation. On the other hand, the solid lines show the case when  $\sigma$  is taken constant, that is, 1.09, and  $\alpha$  is subjected to variation. The variation of  $\alpha/\sigma$  is same for both case. In practical situations, both  $\alpha$  and  $\sigma$  are considered to change at the same time. (In the case of the propeller behind a ship,  $\lambda$  is also considered to change.) But from these results, it can be easily confirmed that the  $\alpha$ -constant case and the  $\sigma$ -constant case give almost the same effects each other. (Therefore, in the practical applications to a ship propeller, the calculation may be simplified in such a way that the one of these factors  $\alpha$  and  $\sigma$  is fixed on a mean value while the other is subjected to the effective variation.)

(3) It is natural that the variations of cavitation number, equivalent angle of attack and equivalent camber corresponding to the angular position of the blade should be considered in the unsteady cavity calculation. However, the calculation will then become much complicated. Then, the simplified calculation method, namely, called "effective flat foil method" is introduced.

In figure 19, the unsteady cavity calculation results for a cambered foil of  $\lambda/c = 0.035$  are shown in comparison with those for the effective flat foil.

The concept of the effective flat foil is as follows.  $\alpha/\sigma$  variations represented by a broken line and a solid line are for the cambered foil and the effective flat foil, respectively. The broken line  $\alpha/\sigma$  is given by the operating condition of the propeller. The solid line  $\alpha/\sigma$  is, on the other hand, calculated so that it gives the same quasi-steady cavity length for the flat foil as for the cambered foil. The unsteady cavity length and cavity volume of the effective flat foil are shown with solid lines. On the other hand, those of the cambered foil are shown with broken lines. From these results, it is easily confirmed that the unsteady calculation results for these two foils give good coincidence.

In figure 20, the unsteady cavity calculation results for the cambered foil of  $\lambda/c = 0.020$  are shown together with those for the effective flat foil. Since the camber in this case is smaller than that in figure 19, it is clearly found that the difference between the results for the cambered and effective foils is getting smaller. The effective flat foil method may be sufficiently useful and convenient for numerical calculations of unsteady cavitation on ship propeller foils, since the equivalent camber for actual ship propellers is not so large.

### 3. CALCULATION OF THE UNSTEADY CAVITATION ON SHIP PROPELLER FOILS AND THE HULL FLUCTUATING PRESSURES

#### 3.1 Cavitation Pattern

(1) Figure 21 shows the comparison between theoretical and experimental results of cavity extent on a foil section (0.88 R) of a propeller

behind a ship. The quasi-steady calculation result is expressed by the chained line, and a steady cavity flow theory of a thin parabolic foil is adopted in this case. The unsteady calculation result is obtained by using the quasi-steady calculation result and the effective flat foil method stated in section 2.3. From this figure, it is easily noted that the tendency of the unsteady calculation result becomes much closer to that of the observed result. Namely, the cavity extent shows a depressed growth in the growing stage and, on the contrary, shows a rather rapid decrease in the decreasing stage.

However, in the early part of the growing stage of the cavity, a rather big difference between the unsteady calculation and observed results is recognized. This may be due to the so-called inception delay of the cavity. Though the problem of the inception delay is not treated in the present paper, a little is discussed in section 2.2. For a theoretical treatment of this phenomenon, another point of view may be necessary. The result in which the inception delay is taken into account by applying the same assumptions as stated in section 2.2 is shown for a reference.

Furthermore, it is observed that the depression of the maximum cavity extent is considered to be not so large as expected in the previous section. Namely, in general, in case of a propeller behind a ship, the non-dimensional frequency is not so large.

(2) In figures 22 and 23, the calculated cavitation patterns on a foil of Propeller - (A) behind a ship is compared with the observed patterns. (Propeller - (A) is the test propeller of the cooperative study between the Ship Research Institute of Japan, Kawasaki Heavy Industries, Ltd. and Hitachi Zosen Corporation.) The quasi-steady and unsteady results are compared with the observed ones in figures 22 and 23, respectively. For the quasi-steady calculation in the range of the radial sections between  $0.75 R$  and tip, the cavity flow theory is adopted, and on the contrary, in the other range of the radial sections, the lift equivalent method is adopted following the Ukon-Kato method (Kato and Ukon, 1979; Ukon, 1979). The unsteady calculation in figure 23 is based on the quasi-steady calculation in figure 22 and the concept of the effective flat foil. The unsteady calculation results seem to be in good accordance with the observed ones. The calculated results are much improved in the growing stage, especially in the range from  $-40^\circ$  to  $0^\circ$  of the foil angular position.

It is also observed that the unsteady calculation results in the radial sections between the root of the blade and  $0.75 R$  do not seem to give good coincidence with the observed ones in the decreasing stage, though the unsteady results are improved in comparison with the quasi-steady ones. For this disagreement, a problem is considered to be left in the quasi-steady theory itself. To solve this problem, it seems to be necessary to introduce the effect of the laminar separation point (Taoka et al., 1981) due to the viscosity of fluid, and the non-linearity such as originating from the blade thickness and the leading edge roundness (Tulin and Hsu, 1980; Yamaguchi and Kato, 1981).

Figures 24-25 and 26-27 show the comparison of the cavitation patterns between the calculation and the observation for Propeller - (B).

(Data for Propeller - (B) are offered by Naikai Shipbuilding & Engineering Co., Ltd.) Figures 24-25 and 26-27 are for the ballast and full conditions, respectively. From these figures, the tendency of the improvement obtained by the introduction of the unsteady calculation is similar to that in case of Propeller - (A). Especially, in case of the full condition, the agreement between the theory and experiment is more satisfactory than that for the ballast condition. However, for both of these conditions, the inception delay of the cavity is clearly recognized in the growing stage. As already stated, the inception delay of the cavity can not be treated theoretically at present.

Figures 28 and 29 show the comparison of the cavitation pattern between the calculation and the observation for Propeller - (C). Differing from those mentioned above, these figures show an example which is not in good accordance with the observation even after corrected by using the unsteady theory. An improvement on the cavity extent is surely given in the growing stage. However, it does still give a considerably large difference between the unsteady calculation and the observation in the decreasing stage.

At the angular position of  $30^\circ$ , for example, the observed pattern shows a wavy form. Therefore, for the radial section of  $0.8 R$ , for example, cavity occurs on the two parts on the blade. On the other hand, in the present theory, the cavitation is treated as the two-dimensional leading edge cavitation for every radial section. Hence, the cavitation patterns of the above mentioned type may not be predicted satisfactorily at present. To treat cavitation patterns like this, it may be considered that the three-dimensionality of the cavity should be introduced.

(3) In the following, the observed and calculated cavitation patterns (SR183 Report, 1982) are compared between a conventional propeller and skewed propellers, namely MAU type CP (Conventional Propeller : SR183 MP. No. 1), Forward and Backward Skew type  $45^\circ$  HSP (Highly Skewed Propeller : SR183 MP. No. 2) and Forward and Backward Skew type  $60^\circ$  HSP (Highly Skewed Propeller : SR183 MP. No. 5), respectively.

The quasi-steady and unsteady calculation results for the cavitation patterns on a foil of SR183 MP. No. 1 are compared with the observed results in figures 30 and 31, respectively. Judging from the observed patterns, the unsteadiness effect on the cavitation patterns may not be so large.

For example, a distinct difference is not observed between the cavitation patterns at  $\pm 10^\circ$  of an angular position. Therefore, in this case, it is possible to estimate cavitation pattern to some extent by the quasi-steady theory. The much improvement is not attained by introducing the unsteadiness since the unsteadiness is small in this case. But the moderate improvement in the growing stage of the cavity is confirmed.

Figures 32-33 and 34-35 show the comparisons between the calculated and the observed cavitation patterns for SR183 MP. No. 2 and 5, respectively.

The effect of the skew angles is estimated by a simplified method. This simplified method uses an assumption that the estimations for HSPs

are obtained by shifting the calculated results for the conventional propeller by the corresponding skew angles in every radial section. This is based on the fact that, in case of not extremely large skew angles, pressure distributions in radial sections for HSPs are approximately equal to those shifted from the conventional propeller by the corresponding skew angles (Yamasaki et al., 1981).

It is obvious from these figures that the simplified method can estimate the cavitation patterns on HSPs to some extent.

### 3.2 Cavity Volume

Figure 36 shows a comparison between the calculated and the observed cavity volumes for SR183 MP. No. 1 with respect to the angular position of the blade. It is obviously confirmed from this figure that the unsteady calculation result properly catches the total tendency of the cavity volume variation in comparison with the quasi-steady calculation result. Namely, the unsteady calculation surely gives the depression and the phase delay of the cavity volume expected as the unsteadiness effects.

For the radial distribution of the cavity volume, the tendency of the calculation is, however, considerably different from the measured one as shown in figures 37 through 39. Figures 37, 38 and 39 show the comparisons between the calculated and the measured cavity volume distributions in the radial direction for SR183 MP. No. 1 at the angular position of  $-30^\circ$ ,  $0^\circ$  and  $20^\circ$ , respectively. In these figures, "the quasi-steady  $+20^\circ$ " means the quasi-steady result which is shifted by  $20^\circ$  to include the phase delay effect (chiba et al., 1980). It is confirmed that the actual cavity areas have their maximums near the tip, on the contrary, the calculated ones have their maximums around the radial section of  $0.6R$ .

Bar charts on the left side of these figures show a comparison of the cavity volumes estimated by different methods. From these results, though considerable differences are observed in the radial volume distributions, the unsteady calculation seems to give a relatively good correlation with the measured ones on the whole.

The disagreement in the radial volume distributions should be attributed to the inaccuracy of the quasi-steady theory which forms the basis of the unsteady theory. Consequently, it is absolutely necessary to make efforts to improve the quasi-steady theory, for example, by introducing the non-linearity due to the thickness of a foil and the leading edge roundness, as mentioned before.

### 3.3 Fluctuating Pressure on Hull Surface

The calculation of the fluctuating pressures is based on the method (Yokomachi et al., 1981). Figures 40 through 42 show the results of hull fluctuating pressures with the condition:  $K_T \equiv T/(\rho n^2 D^4) = 0.137$ ,  $\sigma_n \equiv (p_a - p_v)/(\frac{1}{2}\rho n^2 D^2) = 1.649$  (Ukon et al., 1982; SR183 Report,

1982). In the present report, principal purpose is to show the difference between the quasi-steady calculation results and the unsteady ones. Hence, the measured results and the estimated results based on the observed patterns are shown only for a reference. Station 8 corresponds to the point just above the top of the propeller. Propeller rotates clockwise when looking forward, and these figures show the fluctuating pressures in the transverse direction.

Figure 40 shows the result for SR183 MP. No. 1 propeller. In the 1st harmonics, the unsteady results are little different from the quasi-steady ones in magnitude, but it is observed that there exists a qualitative difference. A phase delay is observed for the unsteady results. In the 2nd harmonics, there exist not only the same qualitative difference as the 1st harmonics but also the quantitative difference. Namely, the unsteady results give considerably small values in comparison with the quasi-steady results.

Figures 41 and 42 show the results for SR183 MP. No. 2 and 5 propellers, respectively. Similar tendencies are observed as in the case of SR183 MP. No. 1. The fluctuating pressure decreases clearly as the propeller skew angle increases. The reason for this is considered as follows:

The approximate method of introducing the effect of the skew angle is to shift the calculated cavitation pattern for the conventional propeller by the corresponding skew angle in every radial section. Therefore, if we consider the whole blade, the total amount of cavity volume and its variation may become small at every blade angle.

Figure 43 shows a comparison of the fluctuating pressure components at station 8 with respect to the skew angle.

In the following, the hull fluctuating pressures due to Conventional Propeller - (A) shown in section 3.1 are discussed.

Figures 44 and 45 show the results at a condition:  $K_t = 0.187$ ,  $\sigma_n = 2.06$ . Figures 44 and 45 show the pressure distributions in the transverse and longitudinal directions, respectively. Station 1 refers to the top position of the propeller. The measured data are, again, shown here only for a reference.

It is obviously confirmed from these figures that in the 1st harmonics there exists a qualitative difference, and, in the higher order harmonics, there exist not only qualitative but also quantitative differences between the quasi-steady and unsteady results, in the same way as SR183 MP. No. 1 propeller. Figures 46 and 47 show the results of the same propeller (Propeller - (A)) at the condition:  $K_t = 0.187$ ,  $\sigma_n = 1.55$ . In this case, the cavitation is considered to occur more strongly than in case shown in figures 44 and 45. Hence, the difference between the quasi-steady and unsteady results becomes more evident in the first harmonic. For the higher order harmonics, the tendencies of the difference are similar to those at the above mentioned condition:  $K_t = 0.187$ ,  $\sigma_n = 2.06$ .

Figure 48 shows the comparison of the fluctuating pressures at station 6 with respect to the order of the fluctuating pressure components.



#### 4. CONCLUSIONS

Through a theoretical investigation concerning the unsteady effects on the leading edge cavity on two-dimensional hydrofoils and its application to a cavitating propeller operating behind a ship, the following results are obtained:

- (1) By investigating the unsteady effects on the two-dimensional cavity, the so-called hysteresis effects such as "phase delay", "depression of the growth" and "slow growth and rapid decrease" are clarified. When the unsteadiness is larger, these phenomena become more eminent.
- (2) By introducing an idea of "effective flat foil", a practical method is obtained in order to estimate the unsteady effects on the cavity on foils on a propeller behind a ship. When the unsteadiness is taken into account, the cavity patterns on propeller foils seem to be more realistic.
- (3) The gross tendency of the cavity volume seems to be much improved, but there exists a big difference in this radial distribution between the estimated and experimental values. This is because the accuracy of the quasi-steady estimation which is the basis of the present unsteady estimation is not sufficient.
- (4) With regard to the fluctuating pressure on ship hull, there exists a qualitative and quantitative difference between the quasi-steady and unsteady estimations. The difference is large especially in the higher order components.
- (5) From the above mentioned results, the authors believe that the unsteady effects should not be neglected for the estimation of the cavity on foils of a propeller behind a ship. The unsteady effects may be more important in full scale than in model scale, since the unsteadiness becomes stronger in full scale because of the scale effect of the ship wake.
- (6) In the present method, the estimation of the unsteady effects on the cavity on propeller foils is based on the quasi-steady estimation of the cavity, but the accuracy of the quasi-steady estimation is not sufficient at present. In this respect, it seems to be very important to clarify the nonlinear and three-dimensional effects.
- (7) The variational principles of the linearized unsteady cavity flow theory are derived in order to deepen the physical understanding of the unsteady cavitation.
- (8) Some suggestions are obtained for the exact analytical solution of the linearized unsteady cavity flow by using the complex acceleration potential.

## ACKNOWLEDGMENTS

Professors R. Yamazaki and K. Nakatake of Kyushu University and Professors S. Hatano and M. Nakato of Hiroshima University are deeply appreciated by the authors for their valuable advices and encouragements from the beginning to the end of this study.

The authors are also deeply indebted to Dr. H. Takahashi of the Ship Research Institute of Japan and Professor H. Kato of the University of Tokyo for their useful advices and instructions.

The authors' sincere thanks go to Doctors Y. Ukon and Y. Kodama of the Ship Research Institute of Japan, Mr. S. Yamasaki of Kobe Steel Ltd. and Dr. T. Hoshino of Mitsubishi Heavy Industries for their kind advices and creative discussions.

Mr. S. Uetake and Dr. M. Takagi of Hitachi Zosen Corporation are also appreciated for their supports given to the authors.

The authors have obtained many advices and encouragements from people in the field of ship propellers in Japan. Their favours are highly acknowledged.

Finally, Professor W.H. Isay of the University of Hamburg is highly appreciated for his creative discussions and encouragements. The academic contact between Professor Isay and the authors was really valuable.

## REFERENCES

- Chiba, N., T. Sasajima and T. Hoshino (1980). Prediction of propeller induced fluctuating pressures and correlation with full scale data, 13th Symposium on Naval Hydrodynamics, Tokyo, pp. 89-103.
- Geurst, J.A. (1959). Linearized theory for partially cavitated hydrofoils, Intern. Shipbuilding Progress, Vol. 6, No. 60, pp. 369-384.
- Geurst, J.A. (1960). Linearized theory for fully cavitated hydrofoils, Intern. Shipbuilding Progress, Vol. 7, No. 65, pp. 17-27.
- Geurst, J.A., and P.J. Verbrugh (1959). A note on camber effects of a partially cavitated hydrofoils, Intern. Shipbuilding Progress, Vol. 6, No. 61, pp. 409-414.
- Hanaoka, T. (1965a). Linearized theory of cavity flow past a hydrofoil of arbitrary shape, Journal of the Society of Naval Architects of Japan, No. 117, (in Japanese), pp. 12-19.
- Hanaoka, T. (1965b). Linearized theory of cavity flow past a hydrofoil of arbitrary shape, part 2, a method for the calculation of the characteristics of a hydrofoil, Journal of the Society of Naval Architects of Japan, No. 118, (in Japanese), pp. 1-8.
- Hanaoka, T. (1966). Linearized theory of cavity flow past a hydrofoil of arbitrary shape, part 3, theory for partially cavitated

- hydrofoils, Journal of the Society of Naval Architects of Japan, No. 119, (in Japanese), pp. 18-27.
- Hoshino, T. (1980). Estimation of unsteady cavitation on propeller blades as a base for predicting propeller-induced pressure fluctuations, Journal of the Society of Naval Architects of Japan, No. 148, pp. 33-44.
- Isshiki, H., M. Murakami and A. Kadono (1981). Variational approach in wing theory - on circulation, flexibility and cavitation -, Transactions of The West-Japan Society of Naval Architects, No. 61, pp. 63-80.
- Isshiki, H., and M. Murakami (1981). On a theoretical treatment of unsteady cavitation (1st report), Transactions of the West-Japan Society of Naval Architects, No. 62, pp. 99-120.
- Isshiki, H., and M. Murakami (1982a). On a theoretical treatment of unsteady cavitation (2nd report), Transactions of the West-Japan Society of Naval Architects, No. 63, pp. 51-63.
- Isshiki, H., and M. Murakami (1982b). On a theoretical treatment of unsteady cavitation (3rd report), Transactions of the West-Japan Society of Naval Architects, No. 64.
- Koyama, K. (1975). A numerical method for propeller lifting surface in non-uniform flow and its application, Journal of the Society of Naval Architects of Japan, No. 137, (in Japanese), pp. 78-87.
- Kato, H. (1979). Cavitation, Maki-Shoten, Tokyo, Japan, (in Japanese)
- Kato, H., and Y. Ukon (1979). Chapter 3, prediction of propeller cavitation, symposium on theory of resistance and propulsion for ship design, Journal of the Society of Naval Architects of Japan, (in Japanese), pp. 189-216.
- Kodama, Y. (1980). The growth of an attached cavity on a two-dimensional nonlifting body, Journal of the Society of Naval Architects of Japan, No. 148, (in Japanese), pp. 17-23.
- Lee, C.S. (1980). Prediction of the transient cavitation on marine propellers by numerical lifting-surface theory, 13th Symposium on Naval Hydrodynamics, Tokyo, pp. 41-64.
- Nishiyama, T., and T. Ota (1971). Linearized potential flow models for hydrofoils in supercavitating flows, Journal of Basic Engineering, Transactions of the ASME, pp. 550-564.
- Noordzij, L., and M.J. Officier (1977). The effect of camber on the pressure field of a super cavitating propeller, Intern. Shipbuilding Progress, Vol. 24, No. 273, pp. 115-121.
- Newman, J.N. (1977). Marine hydrodynamics, The MIT Press.
- Tulin, M.P., and C.C. Hsu (1980). New application of cavity flow theory, 13th Symposium on Naval Hydrodynamics, Tokyo, pp. 107-131.
- Taoka, K., H. Kato and H. Yamaguchi (1981). An estimation method of cavity extent on a model propeller considering laminar separation, Journal of the Society of Naval Architects of Japan, No. 150, (in Japanese), pp. 132-139.
- Ukon, Y. (1979). Prediction of cavitation extension on a marine propeller operating in non-uniform flow, Report of the Ship Research Institute, Vol. 16, No. 6, (in Japanese), pp. 83-104.
- Ukon Y., Y. Kurobe, A. Kakugawa and M. Makino (1982). Pressure fluctuations induced by cavity volume on highly skewed propellers for a

- RO/RO ship, Report of the Ship Research Institute, Vol. 19, No. 3, (in Japanese), pp. 1-48.
- Wade, R.B. (1967). Linearized theory of a partially cavitating plano-convex hydrofoil including the effects of camber and thickness, J. Ship. Res., Vol. 11, No. 1, pp. 20-27.
- Yamasaki, S., and M. Takahashi (1979). A source-sink method for the calculation of the characteristics of partially cavitated thick hydrofoils, Journal of the Society of Naval Architects of Japan, No. 146, (in Japanese), pp. 119-125.
- Yuasa, H., and N. Ishii (1980). Practical calculations for prediction of propeller cavitation and propeller induced hull surface pressure, Journal of the Society of Naval Architects of Japan, No. 147, (in Japanese), pp. 62-70.
- Yuasa, H., N. Ishii, B. Persson, O. Frydenlund and K. Holden (1980). Practical applications of the discrete vortex element method for calculation of propeller induced excitation forces, 13th Symposium on Naval Hydrodynamics, Tokyo, pp. 65-88.
- Yamaguchi, H., and H. Kato (1981). A study on a supercavitating hydrofoil with rounded nose, Journal of the Society of Naval Architects of Japan, No. 149, (in Japanese), pp. 80-87.
- Yokomachi, M., H. Tanaka, M. Murakami and H. Isshiki (1981). Prediction method for hull surface force induced by a marine propeller, Journal of the Kansai Society of Naval Architects, Japan, No. 182, pp. 91-102.
- Yamasaki, S., M. Takahashi, M. Oku and M. Ito (1981). Research on highly skewed propeller (1st report: model tests on propulsive performance and cavitation characteristics), Journal of the Society of Naval Architects of Japan, Vol. 149, (in Japanese), pp. 88-99.
- SR 183 (Report of the Research Panel No. 183 of the Shipbuilding Research Association of Japan) (1982). Study on propellers and stern hull forms aiming at reducing the stern vibration and noise, No. 348, (in Japanese).

#### APPENDIX A MECHANICAL CONDITION ON THE CAVITY SURFACE

When  $\alpha$  is a function of time  $t$ , the pressure  $p_{\infty}$  in the upstream is expressed as

$$p_{\infty} = -\rho \alpha(t) U y + P_a(t) \quad \dots \quad (A.1)$$

Equation (A.1) may be easily obtained by substituting  $u = U$  and  $v = \alpha(t)U$  into the Euler equation of motion and integrating it.

By applying the Bernoulli integral, the mechanical condition on the cavity surface may be written as

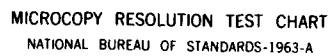
$$P_v + \rho \frac{\partial \phi}{\partial t} + \frac{\rho}{2} (u^2 + v^2) = p_{\infty} + \rho \frac{\partial (Ux + \alpha U y)}{\partial t} + \frac{\rho}{2} (U^2 + \alpha^2 U^2) \quad \dots \quad (A.2)$$

UNCLASSIFIED

SYMPOSIUM OF NAVAL HYDRODYNAMICS (14TH) HELD AT ANN ARBOR MICHIGAN ON AUGUST 23-27 1982(U) OFFICE OF NAVAL RESEARCH ARLINGTON VA M P TULIN ET AL. 1982

NL

F/G 28/4



Then, the substitution of equation (A.1) leads to the linearized mechanical condition on the cavity surface, that is,

$$\sigma(t) \equiv \frac{p_a(t) - p_v}{\frac{1}{2}\rho U^2} = \frac{2}{U^2} \frac{\partial \phi}{\partial t} + 2\left(\frac{u}{U} - 1\right) \dots\dots\dots (A.3)$$

Note: In case of a bubble of the radius R, the term  $\partial \phi / \partial t$  on the righthand side of equation (A.3) becomes

$$\frac{\partial \phi}{\partial t} = -2\dot{R}^2 - R\ddot{R} \quad \text{on the bubble surface.} \dots\dots\dots (A.4)$$

Equation (A.4) suggests that the first terms on the righthand side of equation (A.3) is the order of  $(\omega c/U)^2$ , where c and  $\omega$  is the chord of the foil and frequency of variation, respectively. Hence, if the unsteadiness is small ( $\omega c/U \ll 1$ ), the above mentioned term may be neglected.

## APPENDIX B CAVITY END CONDITION OF THE UNSTEADY CAVITY

By integrating the kinematical conditions (4), (5) and (9) around the foil surface, the following relation is obtained:

$$\begin{aligned} \oint_{\text{Body}} v dx &= \int_0^c U \frac{df_U(x)}{dx} dx - \int_0^c U \frac{df_L(x)}{dx} dx \\ &+ \int_{l_0(t)}^{l(t)} \left( \frac{\partial}{\partial t} + U \frac{\partial}{\partial x} \right) g(x, t) dx \\ &= \int_{l_0(t)}^{l(t)} \left( \frac{\partial}{\partial t} + U \frac{\partial}{\partial x} \right) g(x, t) dx \\ &= \int_{l_0(t)}^{l(t)} \frac{\partial g(x, t)}{\partial t} dx + U \delta^* \dots\dots\dots (B.1) \end{aligned}$$

where  $\delta^*$  is the cavity end thickness.

Then, the substitution of an integral formula:

$$\frac{d}{dt} \int_{l_0(t)}^{l(t)} g(x, t) dx = \int_{l_0(t)}^{l(t)} \frac{\partial g(x, t)}{\partial t} dx + g(l, t) \frac{dl}{dt} \dots\dots (B.2)$$

into equation (B.1) leads to the cavity end condition of the unsteady cavity, that is,

$$\oint_{\text{Body}} v dx = \frac{dV_c}{dt} - \delta^* \frac{dl}{dt} + U \delta^* \dots\dots\dots (B.3)$$

where  $V_c = V_c(t)$  is the cavity volume.

# APPENDIX C VARIATIONAL PRINCIPLES OF THE LINEARIZED CAVITY FLOW (Isshiki et al., 1981)

Let  $(u', v')$  and  $\phi'$  be the perturbation velocity vector and potential respectively, that is,

$$u = U + u', \quad v = \alpha U + v', \quad \dots \dots \dots (C.1)$$

$$\phi = Ux + \alpha Uy + \phi', \quad \dots \dots \dots (C.2)$$

The Kelvin-type variational principle may be given as

$$0 = \delta K [u', v', g; \Gamma]$$

$$\begin{aligned} & \equiv \delta \int_{t_1}^{t_2} dt \left[ \frac{\rho}{2} \iint_{\Omega} (u'^2 + v'^2) dx dy + \int_{l_0}^l (p_v - p_a) g(x, t) dx \right] \\ & + \int_{t_1}^{t_2} dt \int_c^{\infty} \rho \Gamma \left( t - \frac{x-c}{U} \right) \delta v'^- dx \\ & + \rho U \int_{t_1}^{t_2} dt \int_{-\infty}^l u'(x_1, +0, t) dx_1 \delta g(l, t) \dots \dots \dots (C.3) \end{aligned}$$

under

$$\frac{\partial u'}{\partial x} + \frac{\partial v'}{\partial y} = 0 \quad \text{in } \Omega \quad \dots \dots \dots (C.4)$$

$$\begin{aligned} v'^+ &= U \left\{ \frac{d}{dx} f_U(x) - \alpha \right\} + \left( \frac{\partial}{\partial t} + U \frac{\partial}{\partial x} \right) g(x, t) \\ & \text{on } l_0 < x < l, \quad y = +0 \dots \dots \dots (C.5) \end{aligned}$$

$$v'^+ = U \left\{ \frac{d}{dx} f_U(x) - \alpha \right\} \text{ on } 0 < x < l_0, \quad l < x < c, \quad y = +0 \dots (C.6)$$

$$v'^- = U \left\{ \frac{d}{dx} f_L(x) - \alpha \right\} \text{ on } 0 < x < c, \quad y = -0 \dots \dots \dots (C.7)$$

$$v'^+ = v'^- \quad \text{on } c < x, \quad y = 0 \dots \dots \dots (C.8)$$

$$u'^+ = u'^- \quad (\text{Kutta condition}) \dots \dots \dots (C.9)$$

where  $\Gamma = \Gamma(t)$  is the bound vortex on the foil. In the above mentioned



variational principle,  $u'$ ,  $v'$  and  $g$  is subjected to the variations, and  $\Gamma$  should be determined by the Kutta condition (C.9). Furthermore,  $l_0$  and  $l$  are assumed to be given in this case.

If the Lagrangian multiplier  $\phi'$  which has the physical meaning of the velocity potential is used, the Kelvin-type variational principle may be relaxed as

$$\begin{aligned}
 0 = & \delta \int_{t_1}^{t_2} dt \left[ \frac{\rho}{2} \iint_{\Omega} (u'^2 + v'^2) dx dy + \int_{l_0}^l (p_v - p_a) g(x, t) dx \right. \\
 & + \rho \iint_{\Omega} \phi' \left( \frac{\partial u'}{\partial x} + \frac{\partial v'}{\partial y} \right) dx dy \\
 & + \rho \int_0^c \phi'^+ [v'^+ - U \{ \frac{d}{dx} f_U(x) - \alpha \}] dx - \rho \int_{l_0}^l \phi'^+ \left( \frac{\partial}{\partial t} + U \frac{\partial}{\partial x} \right) g(x, t) dx \\
 & - \rho \int_0^c \phi'^- [v'^- - U \{ \frac{d}{dx} f_L(x) - \alpha \}] dx + \rho \int_c^{\infty} \phi'^+ (v'^+ - v'^-) dx \\
 & + \int_{t_1}^{t_2} dx \int_c^{\infty} \rho \Gamma \left( t - \frac{x-c}{U} \right) \delta v'^- dx \\
 & + \rho U \int_{t_1}^{t_2} dx \int_{-\infty}^l u'(x_1, +0, t) dx_1 \delta g(l, t) \dots \dots \dots (C.10)
 \end{aligned}$$

under the Kutta condition (C.9).

From equation (C.10), the natural conditions of the Kelvin-type variational principle are given as

$$u' = \frac{\partial \phi'}{\partial x}, \quad v' = \frac{\partial \phi'}{\partial y} \quad \text{in } \Omega \dots \dots \dots (C.11)$$

$$\begin{aligned}
 p_v - p_a + \rho \left( \frac{\partial}{\partial t} + U \frac{\partial}{\partial x} \right) \phi'^+ = 0 \\
 \text{on } l_0 < x < l, \quad y = +0 \dots \dots \dots (C.12)
 \end{aligned}$$

$$\begin{aligned}
 \phi'^+ - \phi'^- = \Gamma \left( t - \frac{x-c}{U} \right) \\
 \text{on } c < x, \quad y = 0 \dots \dots \dots (C.13)
 \end{aligned}$$

If the irrotationality given by equation (C.11) is constrained in the variational principle (C.10), the Dirichlet-type variational principle may be derived as

$$\begin{aligned}
 0 = & \delta M [\phi', g; \Gamma] \\
 \equiv & \delta \int_{t_1}^{t_2} dt \left[ - \frac{\rho}{2} \iint_{\Omega} \left\{ \left( \frac{\partial \phi'}{\partial x} \right)^2 + \left( \frac{\partial \phi'}{\partial y} \right)^2 \right\} dx dy \right.
 \end{aligned}$$

$$\begin{aligned}
& + \int_{l_0}^l (p_v - p_a) g(x, t) dx - \rho U \int_0^c \phi'^+ \left\{ \frac{d}{dx} f_U(x) - \alpha \right\} dx \\
& + \rho U \int_0^c \phi'^- \left\{ \frac{d}{dx} f_L(x) - \alpha \right\} dx - \rho \int_{l_0}^l \phi'^+ \left( \frac{\partial}{\partial t} + U \frac{\partial}{\partial x} \right) g(x, t) dx \\
& - \rho \int_c^\infty (\phi'^+ - \phi'^-) \left( \frac{\partial \phi'}{\partial y} \right)^- dx + \rho \int_{t_1}^{t_2} dt \int_c^\infty \Gamma \left( t - \frac{x-c}{U} \right) \left( \frac{\partial \delta \phi'}{\partial y} \right)^- dx \\
& + \rho U \int_{t_1}^{t_2} dt \phi'(\ell, +0, t) \delta g(\ell, t) \dots \dots \dots (C.14)
\end{aligned}$$

under the Kutta condition (C.9).

The natural conditions of the Dirichlet-type variational principle are given as

$$\frac{\partial^2 \phi'}{\partial x^2} + \frac{\partial^2 \phi'}{\partial y^2} = 0 \quad \text{in } \Omega \quad \dots \dots \dots (C.15)$$

$$\begin{aligned}
p_v - p_a + \rho \left( \frac{\partial}{\partial t} + U \frac{\partial}{\partial x} \right) \phi'^+ &= 0 \\
&\text{on } l_0 < x < l, y = +0 \quad \dots \dots \dots (C.16)
\end{aligned}$$

$$\begin{aligned}
\frac{\partial \phi'^+}{\partial y} &= U \left\{ \frac{d}{dx} f_U(x) - \alpha \right\} + \left( \frac{\partial}{\partial t} + U \frac{\partial}{\partial x} \right) g(x, t) \\
&\text{on } l_0 < x < l, y = +0 \quad \dots \dots \dots (C.17)
\end{aligned}$$

$$\frac{\partial \phi'^+}{\partial y} = U \left\{ \frac{d}{dx} f_U(x) - \alpha \right\} \quad \text{on } 0 < x < l_0, l < x < c, y = +0 \quad (C.18)$$

$$\frac{\partial \phi'^-}{\partial y} = U \left\{ \frac{d}{dx} f_L(x) - \alpha \right\} \quad \text{on } 0 < x < c, y = -0 \quad \dots \dots \dots (C.19)$$

$$\phi'^+ - \phi'^- = \Gamma \left( t - \frac{x-c}{U} \right) \quad \text{on } c < x, y = 0 \quad \dots \dots \dots (C.20)$$

$$\frac{\partial \phi'^+}{\partial y} = \frac{\partial \phi'^-}{\partial y} \quad \text{on } c < x, y = 0. \quad \dots \dots \dots (C.21)$$

The bound vortex  $\Gamma$  should be determined by the Kutta condition (C.9).

#### APPENDIX D SOME COMMENTS ON THE EXACT BOUNDARY CONDITIONS ON THE FOIL SURFACE

Let  $\psi'(x, y, t)$  be the conjugate harmonics of the perturbation velocity potential  $\phi'(x, y, t)$  (+ equations (C.1) and (C.2)). Then, the

kinematical conditions on the foil and cavity surfaces on the suction side of the foil are given as ( $\rightarrow$  equations (4) and (9))

$$\frac{\partial \psi'^+}{\partial x} = -U \left[ \frac{df_U(x)}{dx} - \alpha \right] \quad \text{on } 0 < x < l_0, \quad l < x < c, \quad y = +0 \quad \dots\dots\dots (D.1)$$

$$\frac{\partial \psi'^+}{\partial x} = -U \left[ \frac{df_U(x)}{dx} - \alpha \right] - \left( \frac{\partial}{\partial t} + U \frac{\partial}{\partial x} \right) g(x, t) \quad \text{on } l_0 < x < l, \quad y = +0 \quad \dots\dots\dots (D.2)$$

By integrating equations (D.1) and (D.2) and operating  $(\partial/\partial t + U \partial/\partial x)$ , the kinematical conditions on the wetted surface on the suction side of the foil may be written as

$$\begin{aligned} \left( \frac{\partial}{\partial t} + U \frac{\partial}{\partial x} \right) \psi'(x, +0, t) &= \frac{d\psi'(0, 0, t)}{dt} \\ &- U \left[ U \frac{df_U(x)}{dx} - \frac{d\alpha}{dt} x - \alpha U \right] \quad \text{on } 0 < x < l_0, \quad y = +0 \quad \dots (D.3) \end{aligned}$$

$$\begin{aligned} \left( \frac{\partial}{\partial t} + U \frac{\partial}{\partial x} \right) \psi'(x, +0, t) &= \frac{d\psi'(0, 0, t)}{dt} \\ &- U \left[ U \frac{df_U(x)}{dx} - \frac{d\alpha}{dt} x - \alpha U \right] \\ &- \frac{d^2 Vc}{dt^2} + \delta \frac{d^2 l}{dt^2} \quad \text{on } l < x < c, \quad y = +0 \quad \dots\dots\dots (D.4) \end{aligned}$$

In the similar way, the kinematical condition on the pressure side is rewritten as

$$\begin{aligned} \left( \frac{\partial}{\partial t} + U \frac{\partial}{\partial x} \right) \psi'(x, -0, t) &= \frac{d\psi'(0, 0, t)}{dt} \\ &- U \left[ U \frac{df_L(x)}{dx} - \frac{d\alpha}{dt} x - \alpha U \right] \quad \text{on } 0 < x < c, \quad y = -0 \quad \dots (D.5) \end{aligned}$$

When a complex variable  $z$  and a complex acceleration potential  $w'$  are defined as

$$z \equiv x + iy \quad \dots\dots\dots (D.6)$$

$$\begin{aligned} w'(z, t) &\equiv \left( \frac{\partial}{\partial t} + U \frac{\partial}{\partial z} \right) (\phi' + i\psi') \\ &= \left( \frac{\partial}{\partial t} + U \frac{\partial}{\partial x} \right) \psi'(x, y, t) + i \left( \frac{\partial}{\partial t} + U \frac{\partial}{\partial x} \right) \psi'(x, y, t), \quad \dots\dots (D.7) \end{aligned}$$

the boundary conditions on the cavity and foil surfaces can be written

as ( $\rightarrow$  equations (D.3), (3), (D.4) and (D.5))

$$\text{Im}[w'] = \frac{d\psi'(0,0,t)}{dt} - U \left[ U \frac{df_U(x)}{dx} - \frac{d\alpha}{dt} x - \alpha U \right] \quad \text{on } 0 < x < \ell_0, y = +0 \quad \text{..... (D.8)}$$

$$\text{Re}[w'] = \frac{U^2}{2} \sigma(t) \quad \text{on } \ell_0 < x < \ell, y = +0 \quad \text{..... (D.9)}$$

$$\begin{aligned} \text{Im}[w'] = \frac{d\psi'(0,0,t)}{dt} - U \left[ U \frac{df_U(x)}{dx} - \frac{d\alpha}{dt} x - \alpha U \right] \\ - \frac{d^2 V_c}{dt^2} + \delta^* \frac{d^2 \ell}{dt^2} \quad \text{on } \ell < x < c, y = +0 \quad \text{..... (D.10)} \end{aligned}$$

$$\begin{aligned} \text{Im}[w'] = \frac{d\psi'(0,0,t)}{dt} - U \left[ U \frac{df_L(x)}{dx} - \frac{d\alpha}{dt} x - \alpha U \right] \\ \text{on } 0 < x < c, y = -0, \quad \text{..... (D.11)} \end{aligned}$$

where  $\text{Re} [ \quad ]$  and  $\text{Im} [ \quad ]$  mean to take the real and imaginary parts of the quantity in the square bracket.

The mechanical and kinematical conditions of the trailing vortex wake given by equations (11) and (12) lead to a following condition for the complex acceleration potential  $w'$ :

$$w'^+ - w'^- = i \left[ - \frac{d^2 V_c}{dt^2} + \delta^* \frac{d^2 \ell}{dt^2} \right] \quad \text{..... (D.12)}$$

The boundary conditions (D.8) through (D.12) may give some suggestions about the exact solution.

#### APPENDIX E CAVITY END CONDITION OF THE STEADY CAVITY OF A FLAT FOIL WITH THE NON-ZERO CAVITY END THICKNESS

The cavity end condition may be written as

$$\oint_{\text{Body}} \frac{v}{U} dx = \left( \delta^* + \frac{1}{U} \frac{dV_c}{dt} \right) \quad \text{..... (E.1)}$$

Introducing a complex function  $w = u - iv$ , then equation (E.1) may be written as

$$\oint_{\text{Body}} \frac{v}{U} dx = \frac{1}{U} \text{Im} \left[ \oint w dz \right] = \frac{1}{U} \text{Im} [2\pi i \{\text{res.} w\}_{z=\infty}], \quad \text{..... (E.2)}$$

where  $z = x + iy$

Using the result of Geurst (Geurst, 1959), the function  $w$  is

obtained as

$$w = U \left[ a_0 + ib_0 + \frac{a_1 + ib_1}{z/(c/2)} + \dots \right], \dots \dots \dots (E.3)$$

where,  $a_n$  and  $b_n$  ( $n = 0, 1, \dots$ ) are real constants defined by Geurst.

Consequently, the cavity end condition is given as

$$\pi c a_1 = \delta^* + \frac{1}{U} \frac{dVc}{dt}, \dots \dots \dots (E.4)$$

where the real constant  $a_1$  is given as

$$a_1 = \sqrt{\sin \frac{\gamma}{2}} \left[ \frac{A}{2} \left\{ \sin \frac{\gamma}{2} \cos \frac{\gamma}{2} \sin \frac{\pi - \gamma}{4} + (1 - \sin^2 \frac{\gamma}{2}) \cos \frac{\pi - \gamma}{4} \right\} \right. \\ \left. + \frac{B}{2} \left\{ (1 + \sin^2 \frac{\gamma}{2}) \sin \frac{\pi - \gamma}{4} + \sin \frac{\gamma}{2} \cos \frac{\gamma}{2} \cos \frac{\pi - \gamma}{4} \right\} \right] \dots \dots \dots (E.5)$$

$$A = \frac{1}{\sqrt{\sin \frac{\gamma}{2}}} \left( \alpha \sin \frac{\pi - \gamma}{4} - \frac{\sigma}{2} \cos \frac{\pi - \gamma}{4} \right) \dots \dots \dots (E.6)$$

$$B = \frac{1}{\sqrt{\sin \frac{\gamma}{2}}} \left( \alpha \cos \frac{\pi - \gamma}{4} + \frac{\sigma}{2} \sin \frac{\pi - \gamma}{4} \right) \dots \dots \dots (E.7)$$

Substituting equations (E.5) through (E.7) into equation (E.4), the closure condition can be written as

$$Uc \left[ (1 + \sin \frac{\gamma}{2}) \cos \frac{\gamma}{2} - \frac{1}{2} \left( \frac{\sigma}{\alpha} \right) (1 - \sin \frac{\gamma}{2}) \sin \frac{\gamma}{2} \right] \\ = \frac{2}{\pi} \left( U \frac{\delta^*}{\alpha} + \frac{1}{\alpha} \frac{dVc}{dt} \right) \dots \dots \dots (E.8)$$

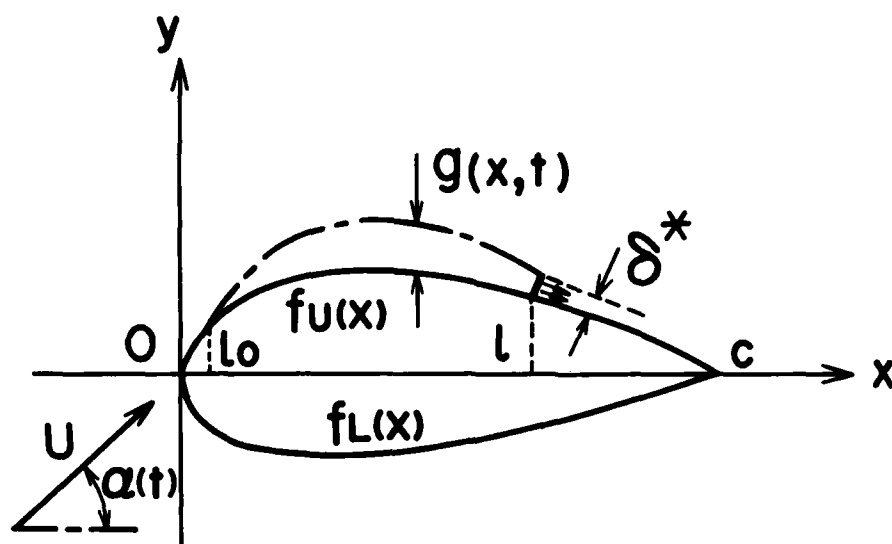


FIGURE 1 Partially cavitating hydrofoil

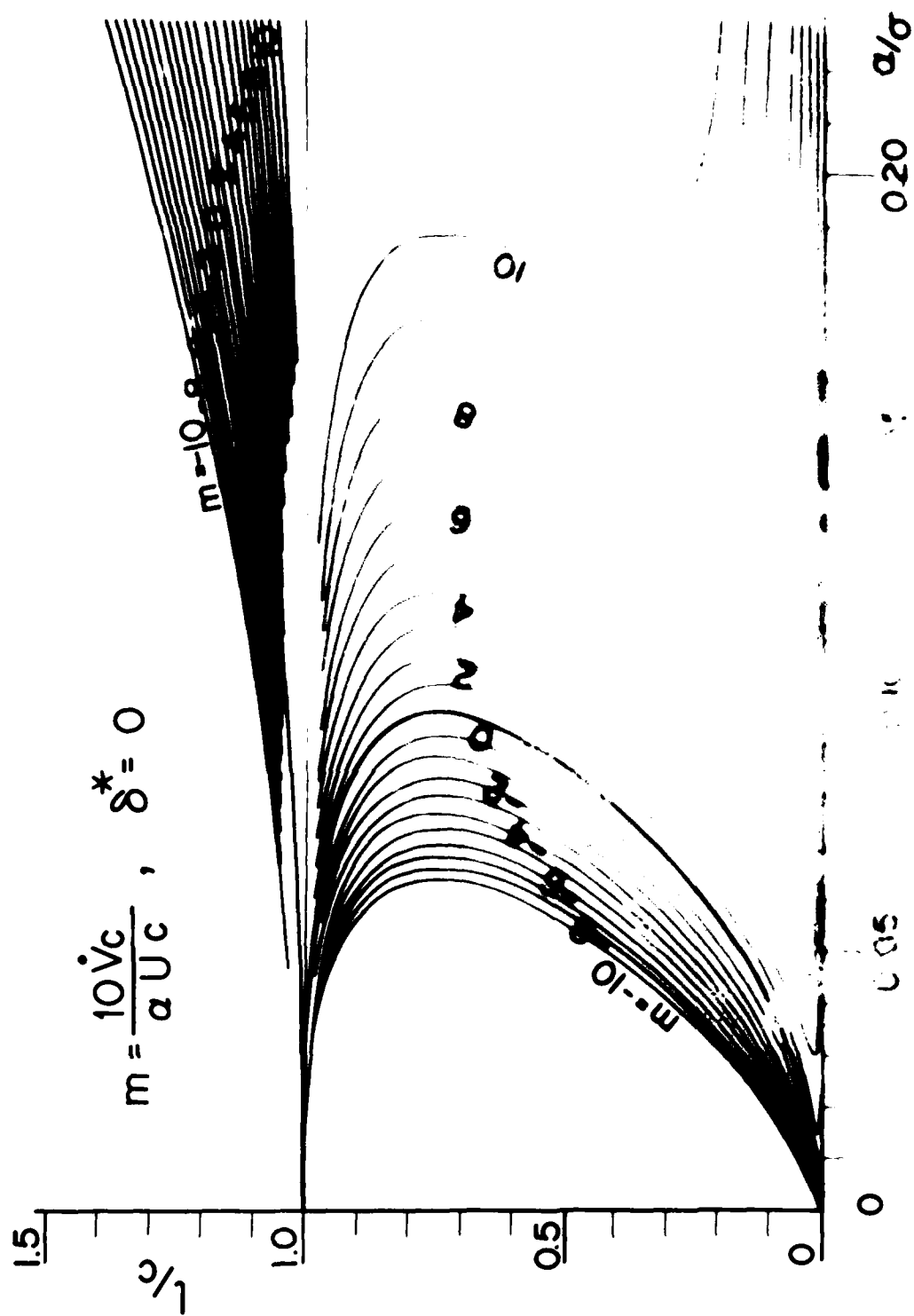


FIGURE 1

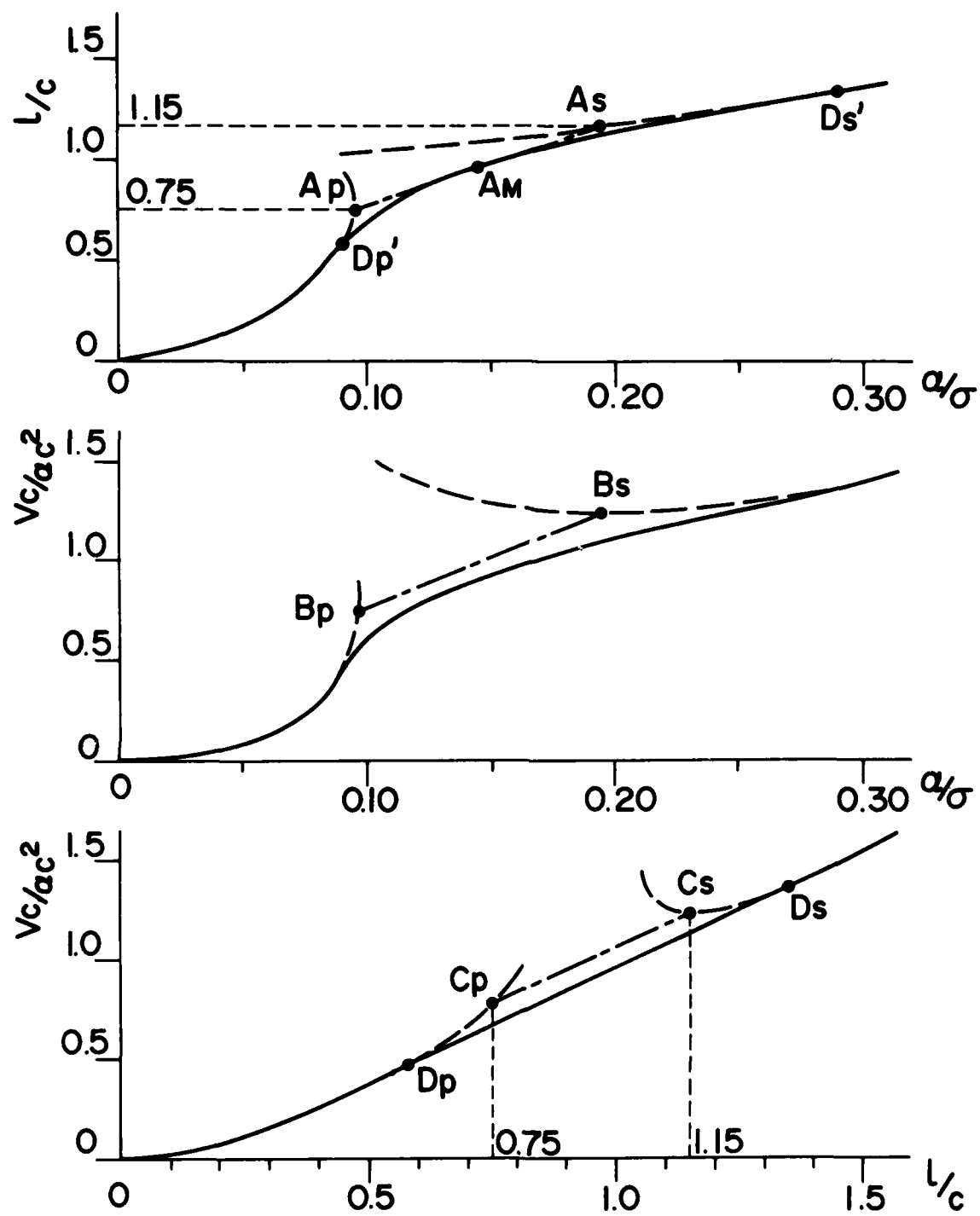


FIGURE 3

Correction method for the cavity volume-extent relation. ( $m = 0$ )



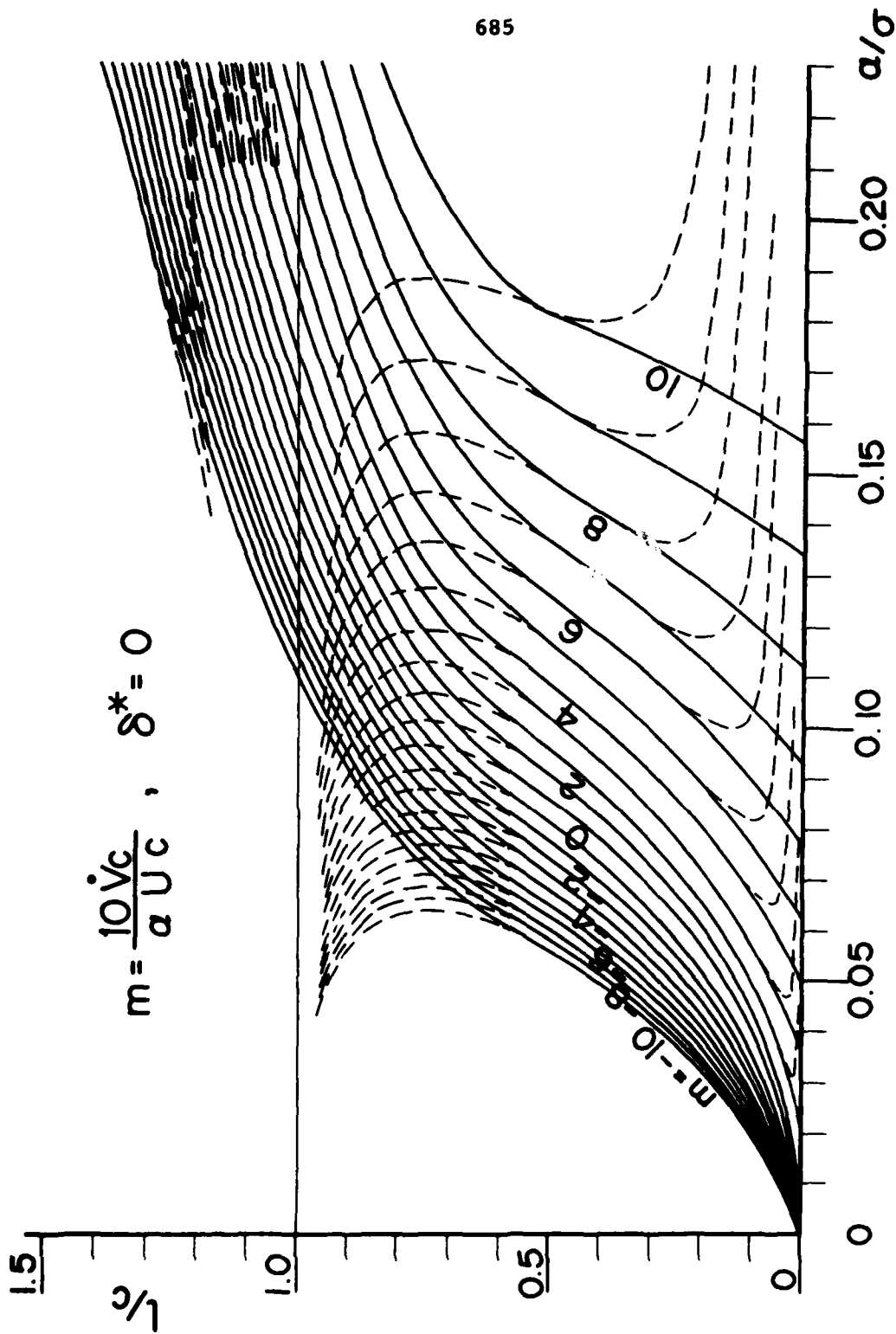


FIGURE 4  $l/c - a/\sigma$  chart of a flat foil with correction.  
( $m$  : unsteadiness parameter)

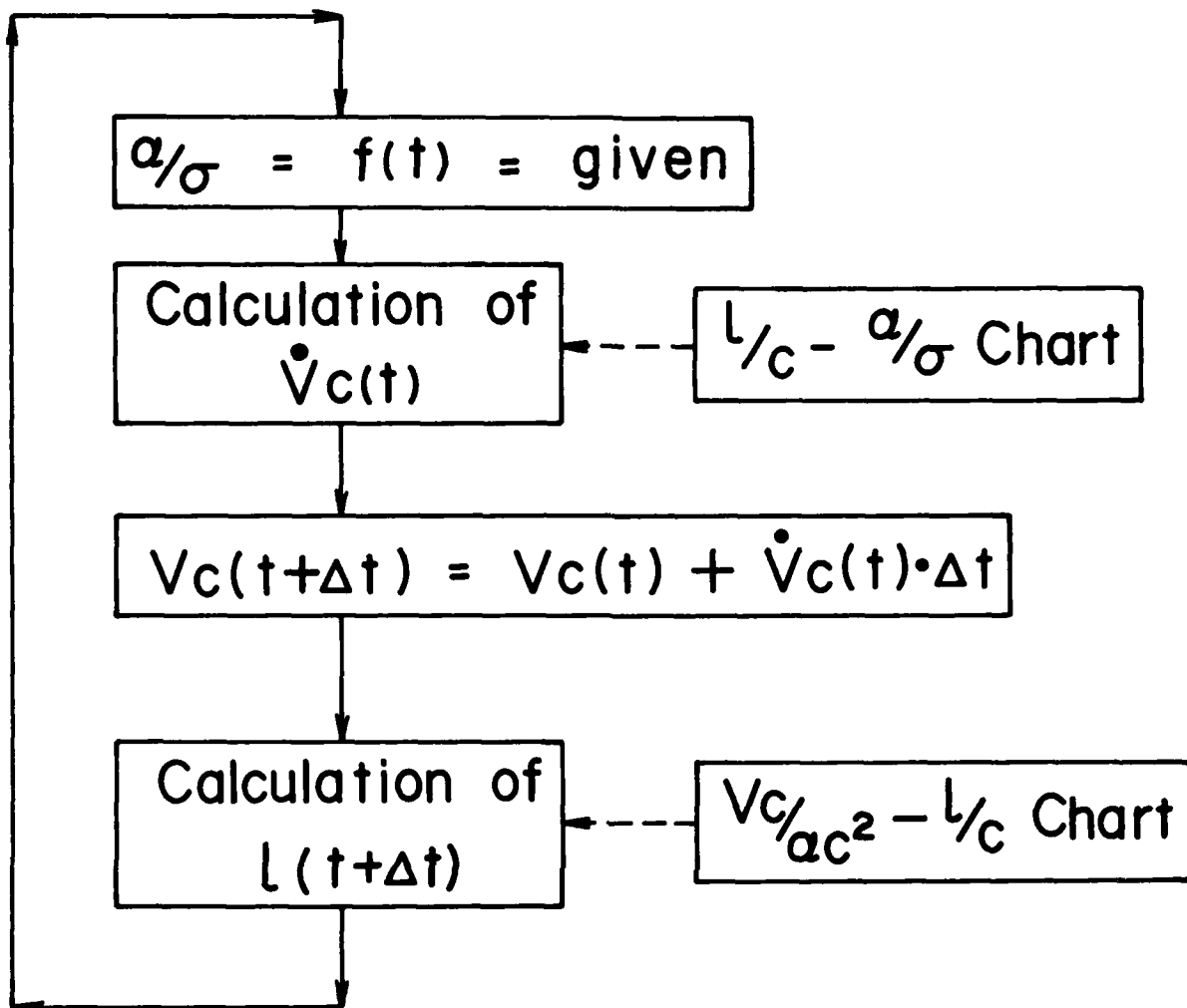


FIGURE 5 Flow chart for calculation of the unsteady cavity.

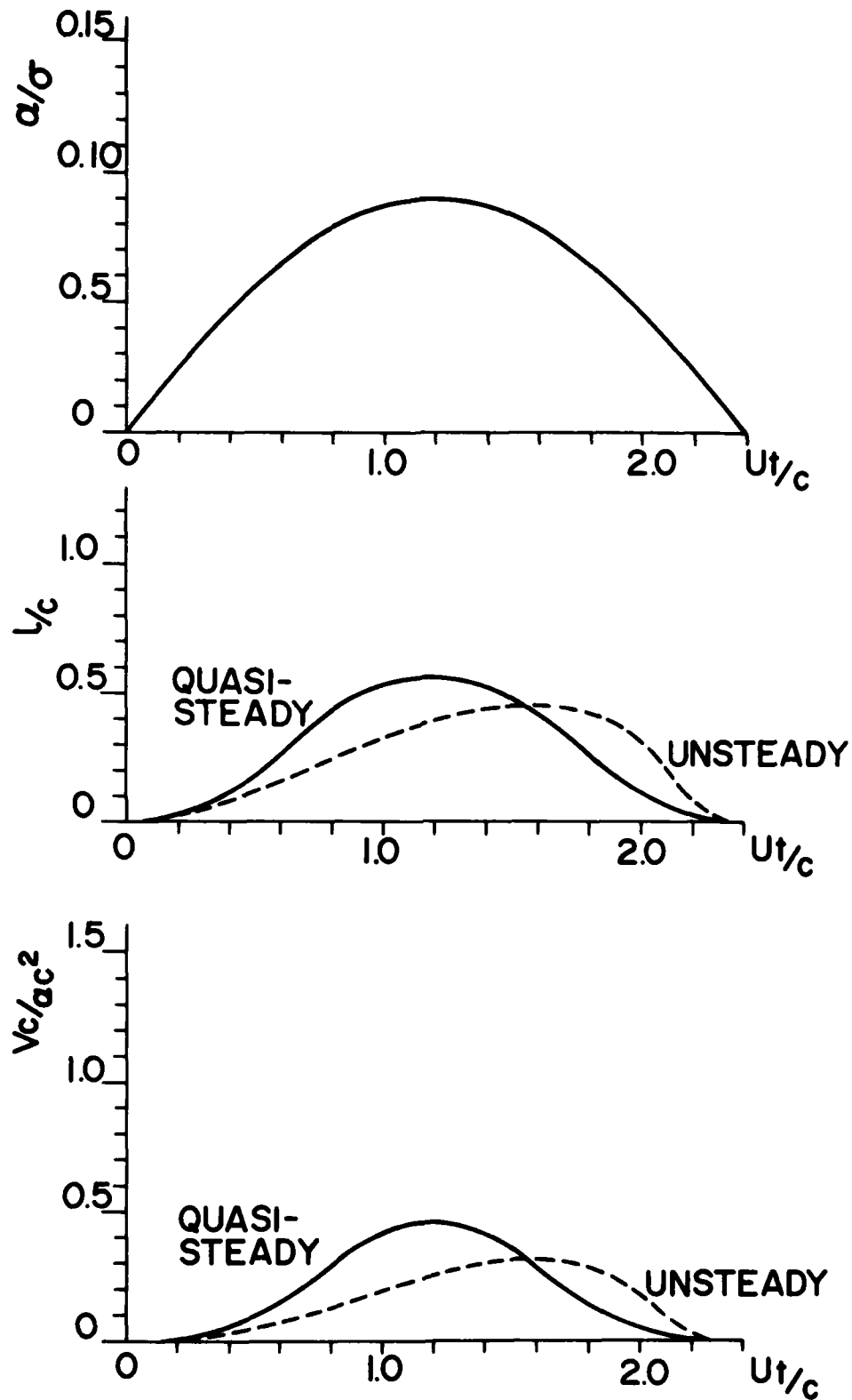


FIGURE 6

Calculated results for an unsteady partial cavity. (weak unsteadiness ;  $\max(l_0/c) < 0.75$  ;  $l_0$  : quasi-steady cavity extent)

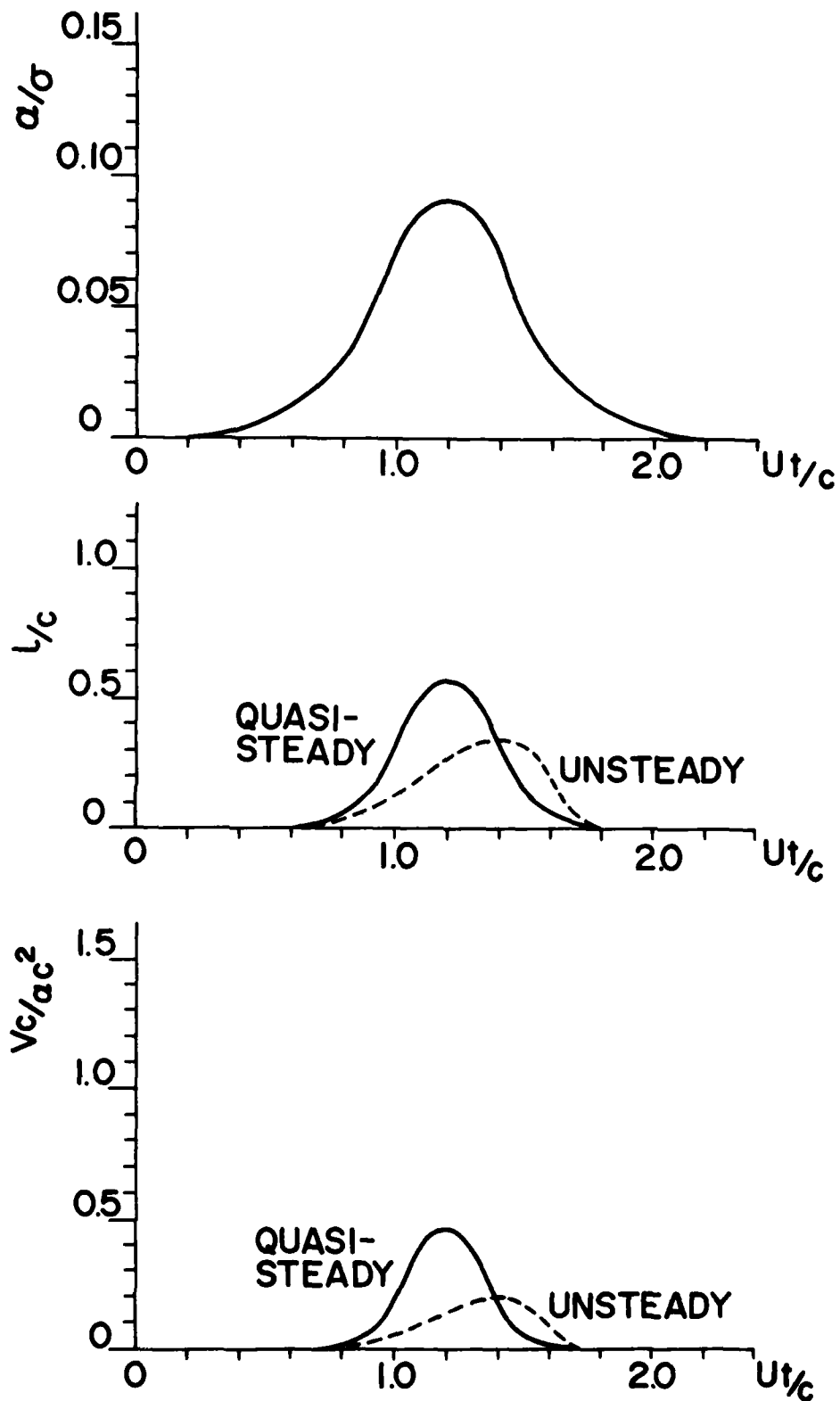


FIGURE 7

Calculated results for an unsteady partial cavity. (strong unsteadiness ;  $\max(l_0/c) < 0.75$  ;  $l_0$  : quasi-steady cavity extent)

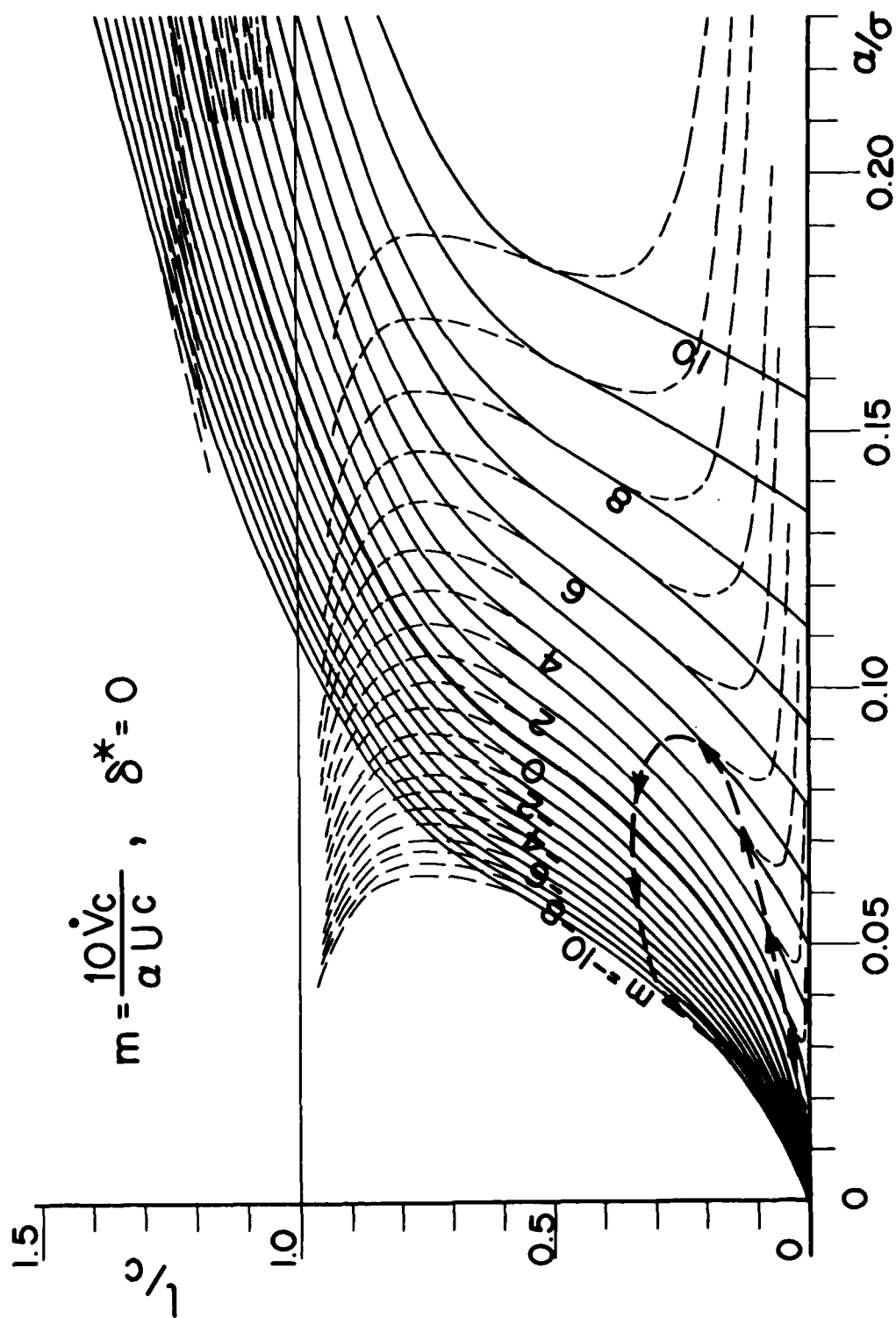


FIGURE 8 Hysteresis loop due to the unsteadiness of the cavity corresponding to figure 7.

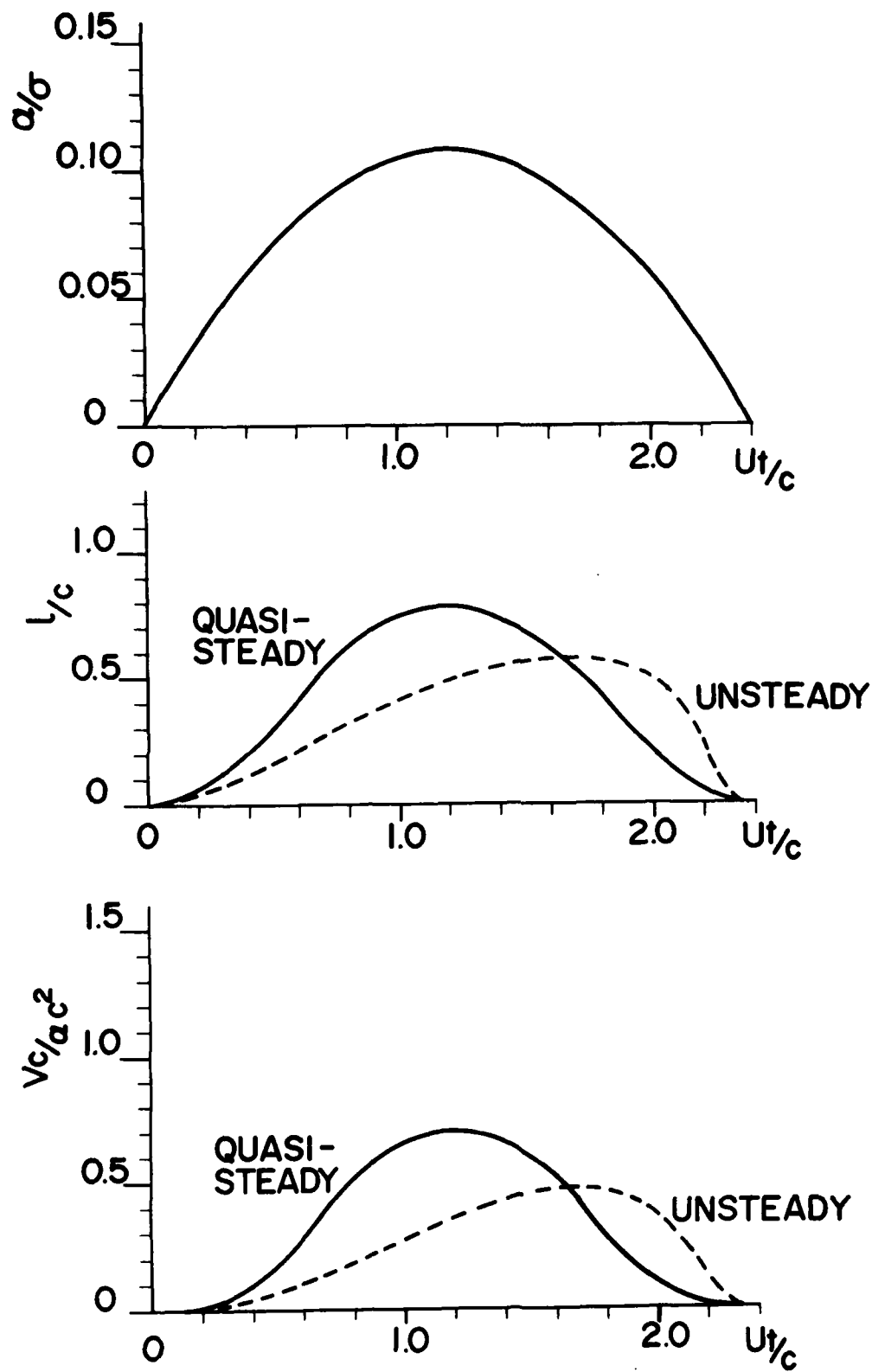


FIGURE 9

Calculated results for an unsteady partial cavity. (weak unsteadiness ;  $0.75 < \max(l_0/c) < 1.0$  ;  $l_0$  : quasi-steady cavity extent)

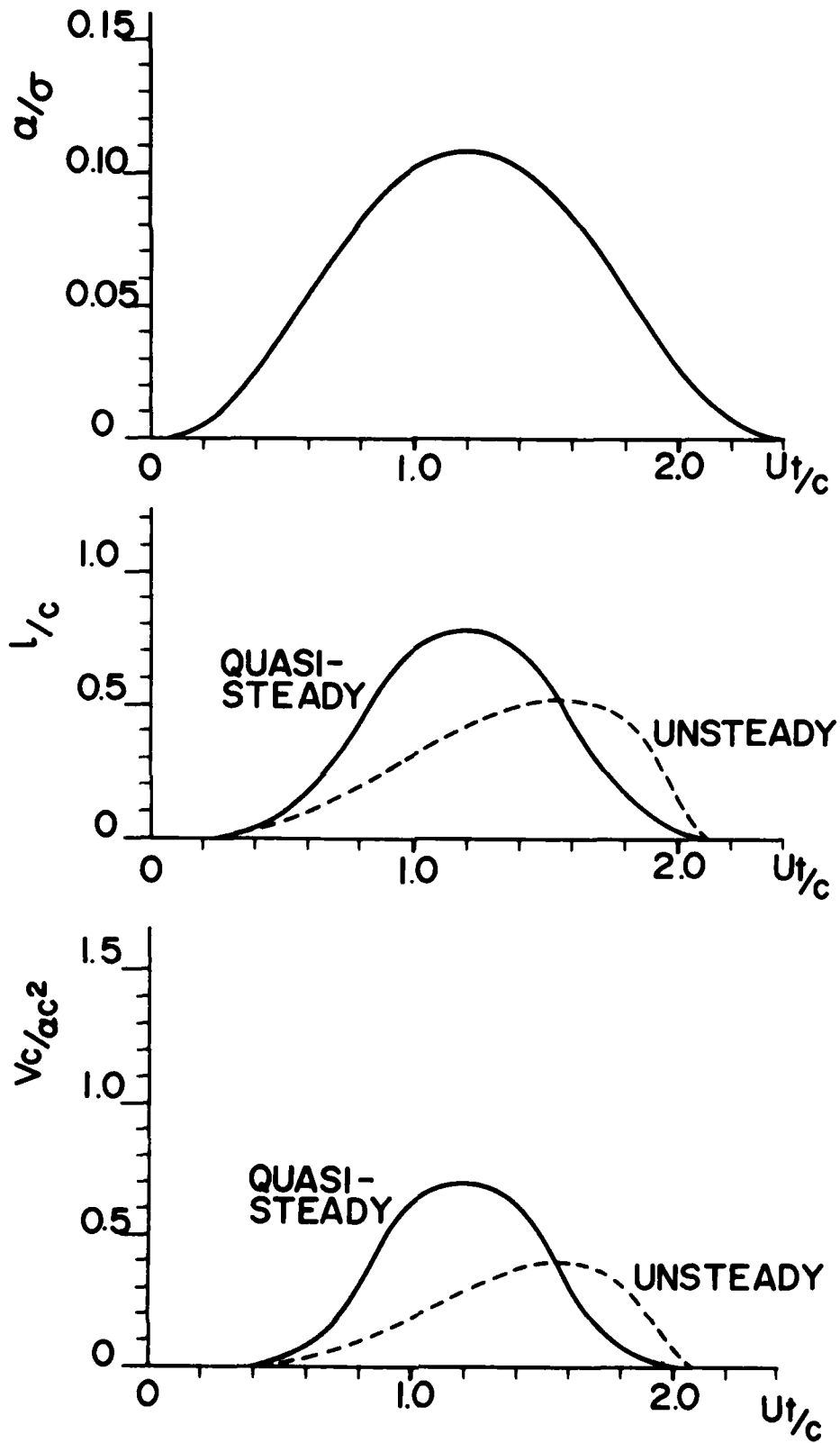


FIGURE 10

Calculated results for an unsteady partial cavity. (strong unsteadiness ;  $0.75 < \max (l_0/c) < 1.0$  ;  $l_0$  : quasi-steady cavity extent)

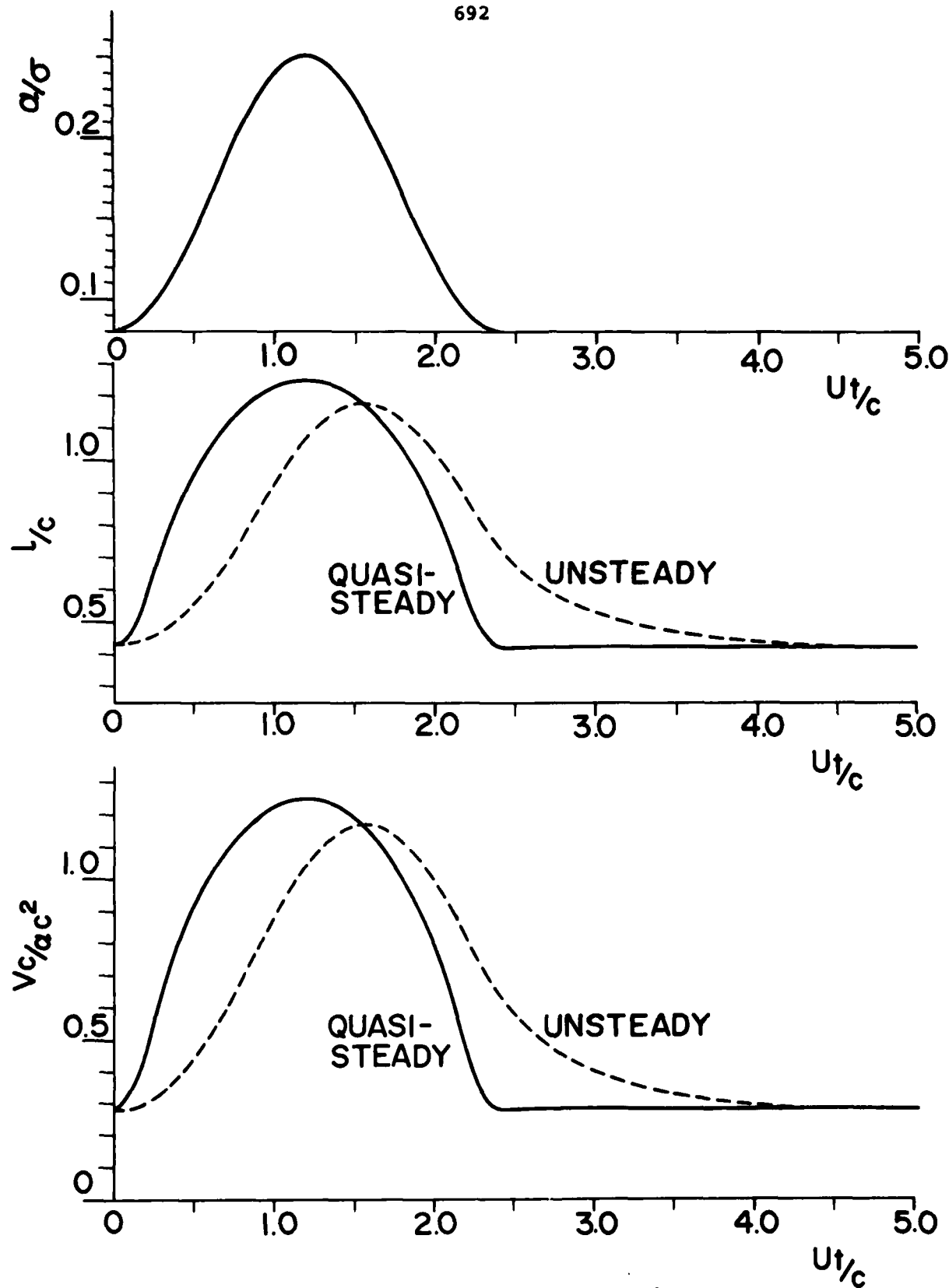


FIGURE 11 Calculated results for an unsteady super cavity. (strong unsteadiness ;  $1.0 < \max(l_0/c)$  ;  $l_0$  : quasi-steady cavity extent)



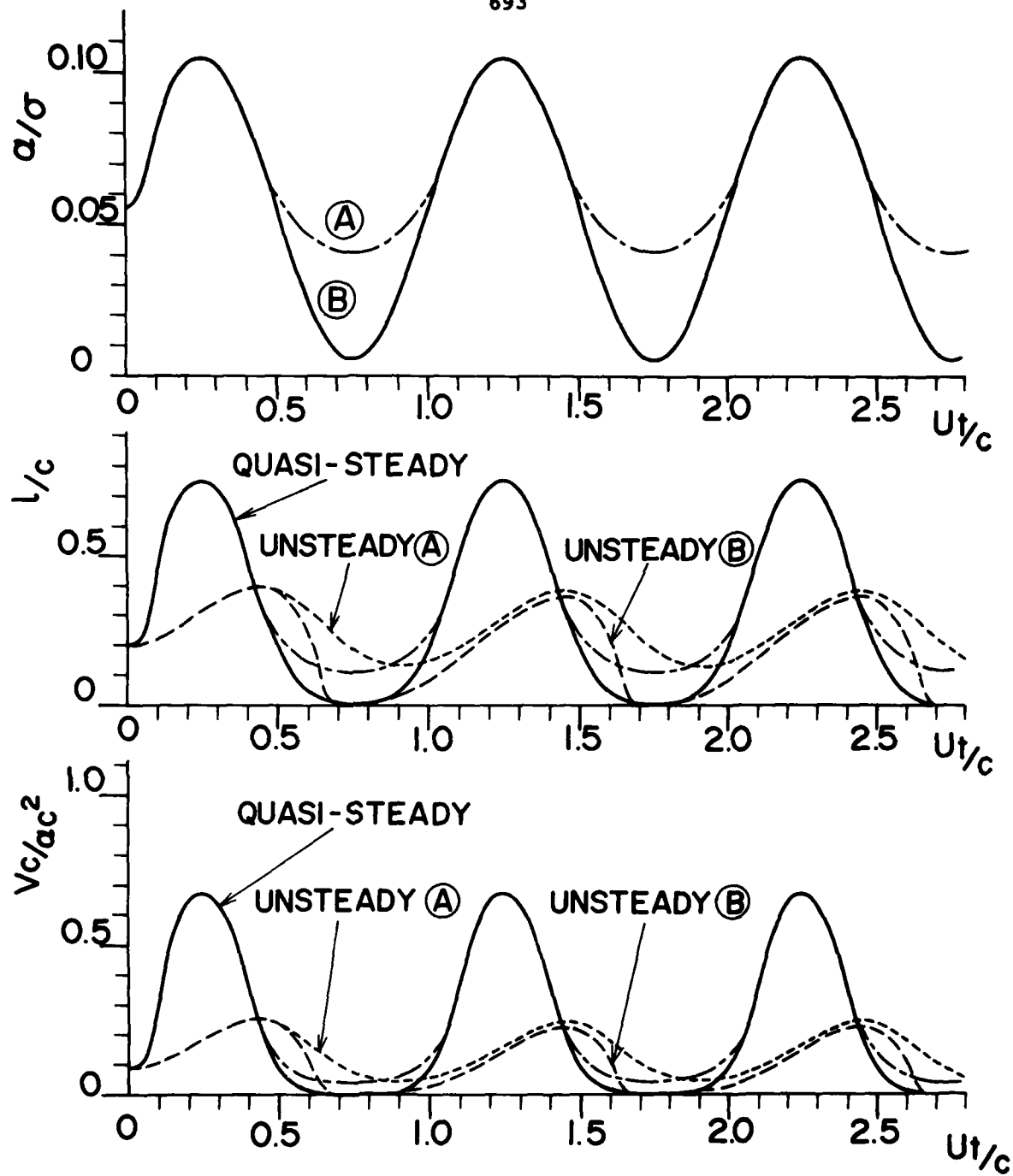


FIGURE 12 Calculated results for an unsteady partial cavities when  $\alpha/\sigma$  oscillates.

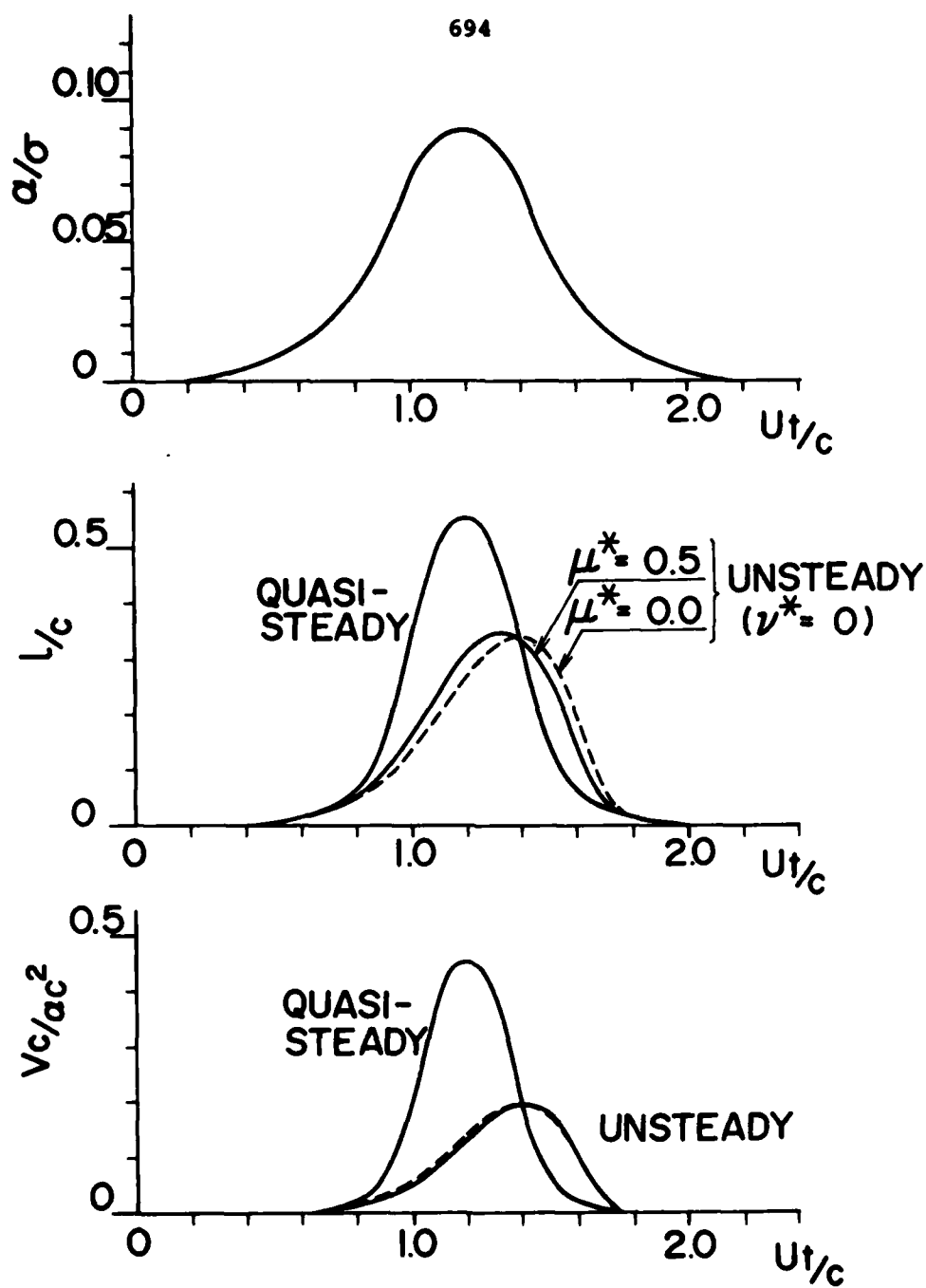


FIGURE 13 Effects of the unsteadiness parameter  $\mu^*$  ( $\rightarrow$  equation (16)) on calculated results for an unsteady partial cavity.

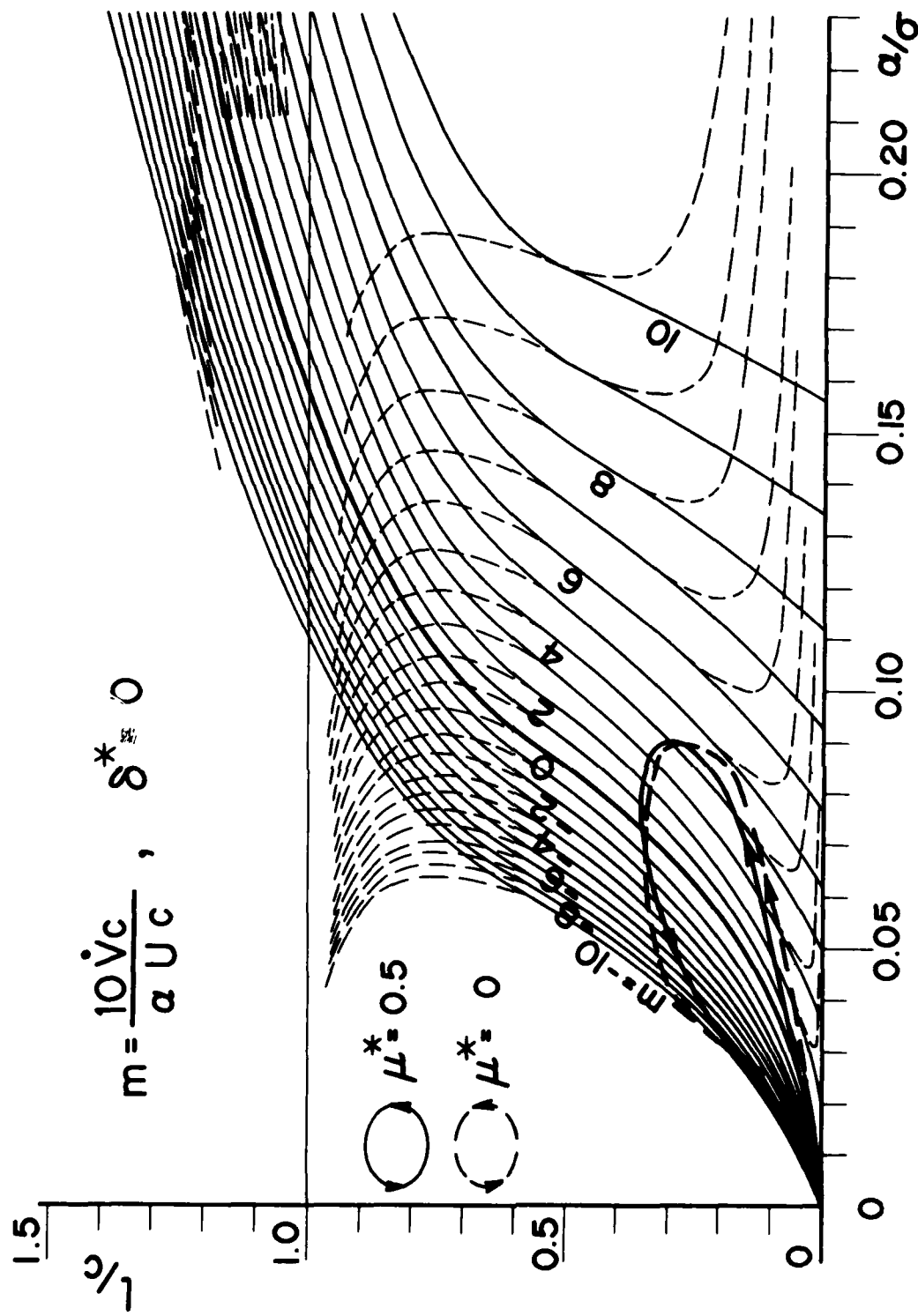


FIGURE 14 Change of the hysteresis loop in the  $l/c - \alpha/\sigma$  chart when  $\mu^* = 0.5$ .

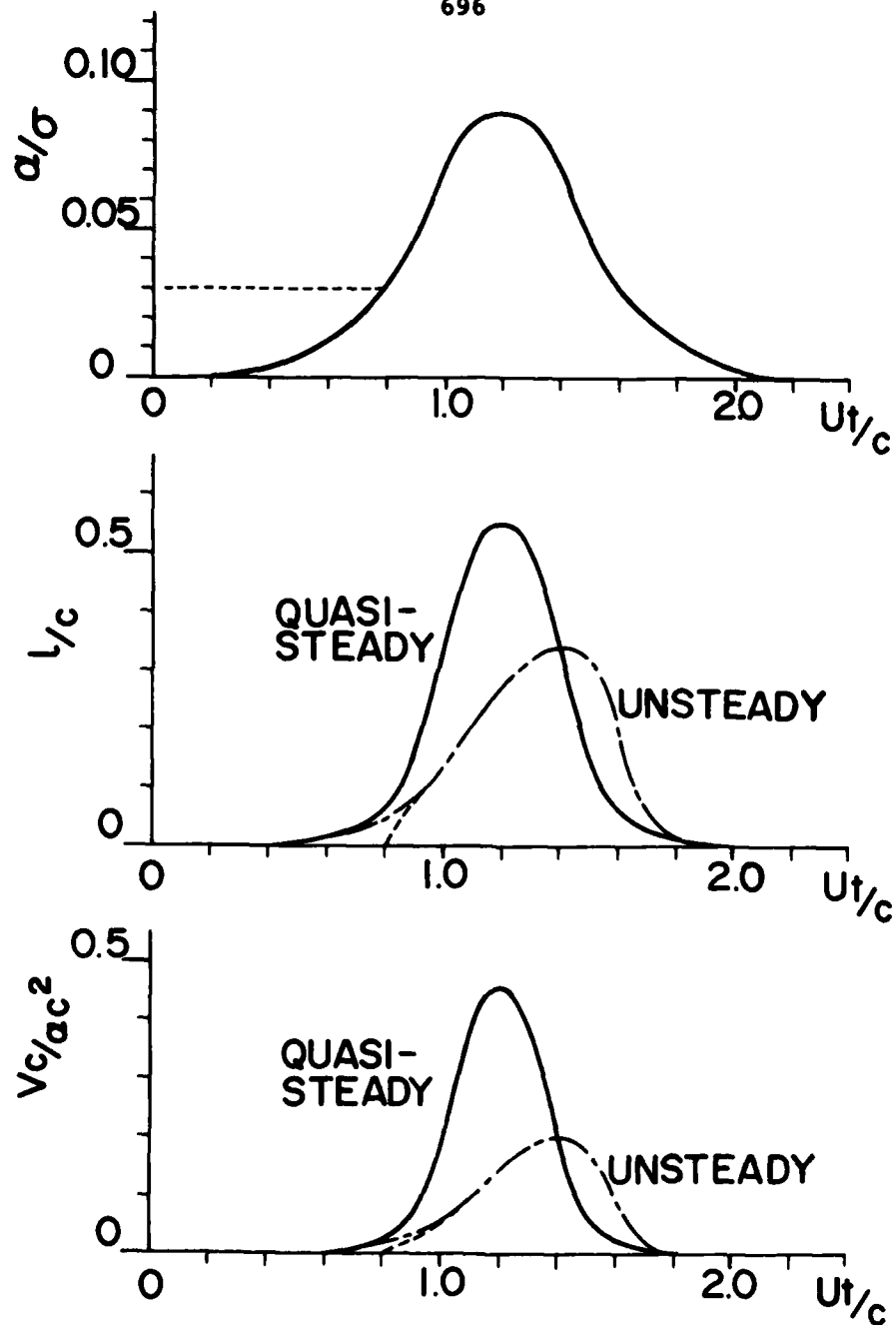


FIGURE 15 Effects of an inception delay on calculated results for an unsteady partial cavity.

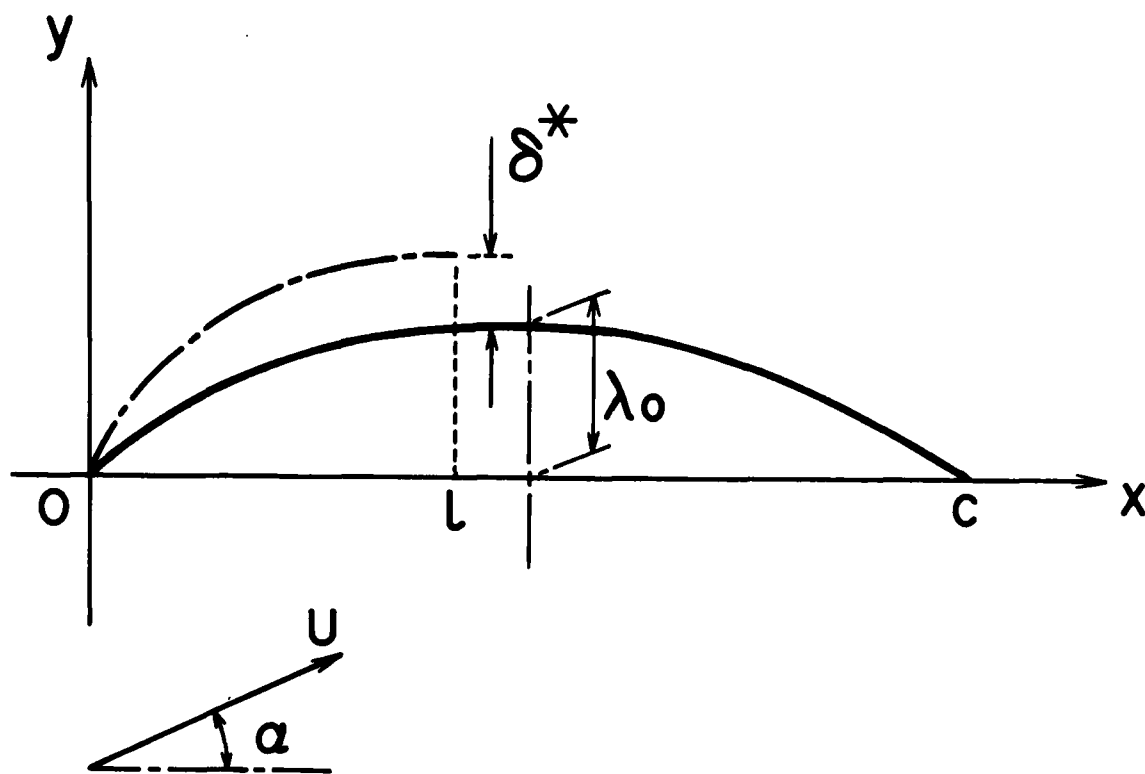


FIGURE 16 Coordinate system for a thin parabolic foil.

## CAMBERED FOIL

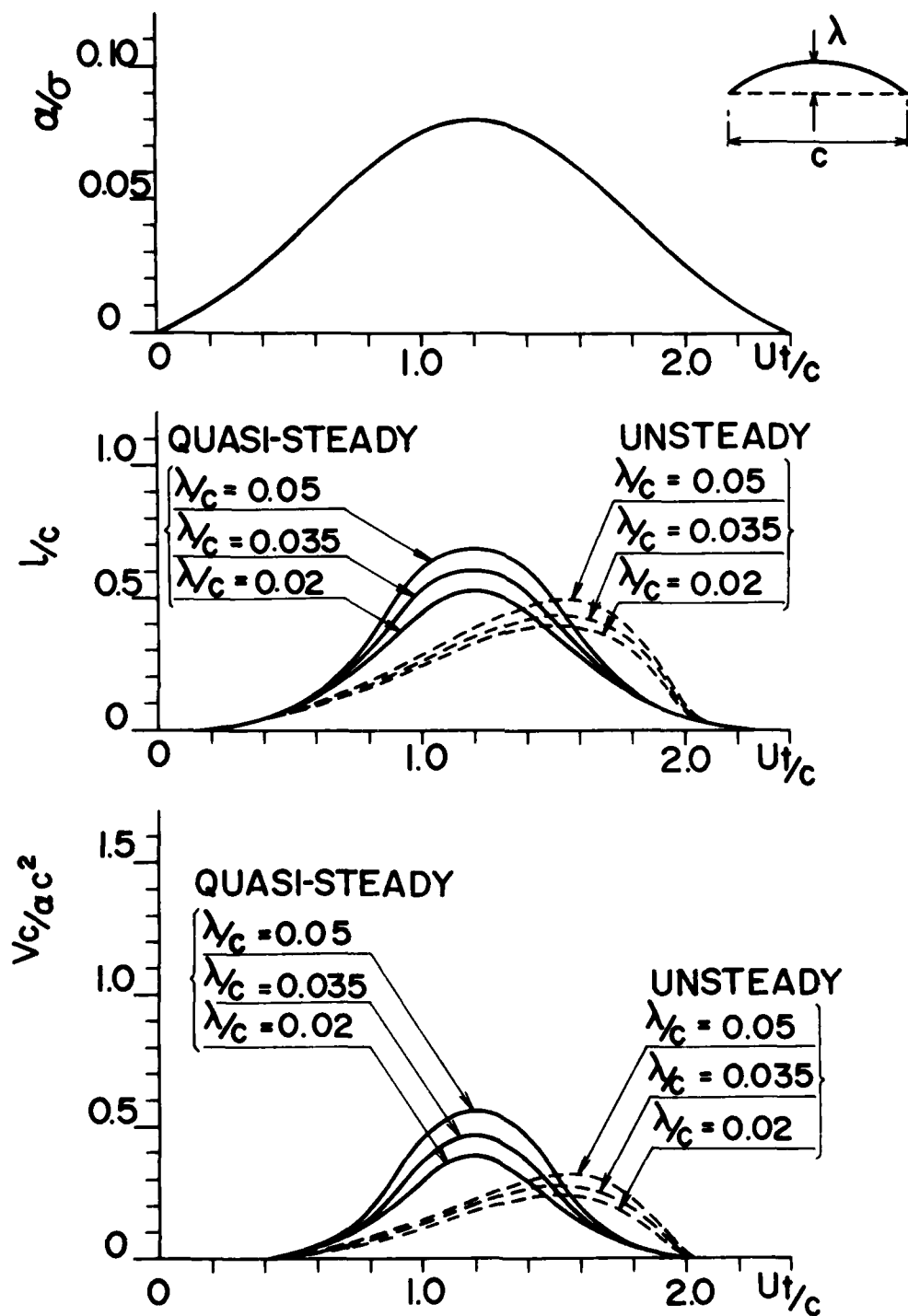


FIGURE 17 Calculated results for unsteady partial cavities on thin cambered foils. ( $\alpha = 5^\circ$ )

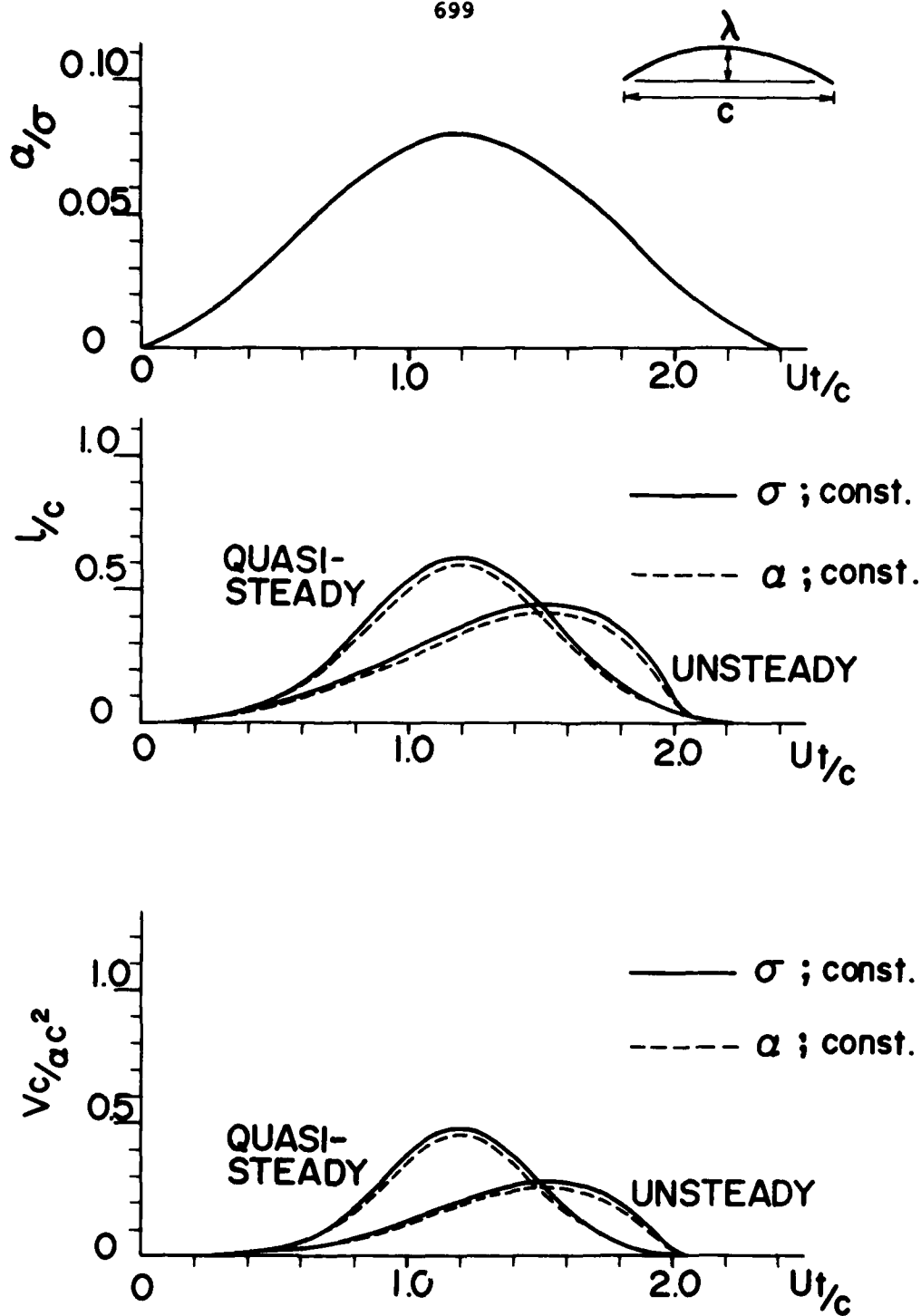


FIGURE 18

Calculated results for an unsteady cavity for a thin cambered foil of  $\lambda/c = 0.035$ . (a comparison between  $\alpha$  - constant case and  $\sigma$  - constant case)

$$\lambda/c = 0.035$$

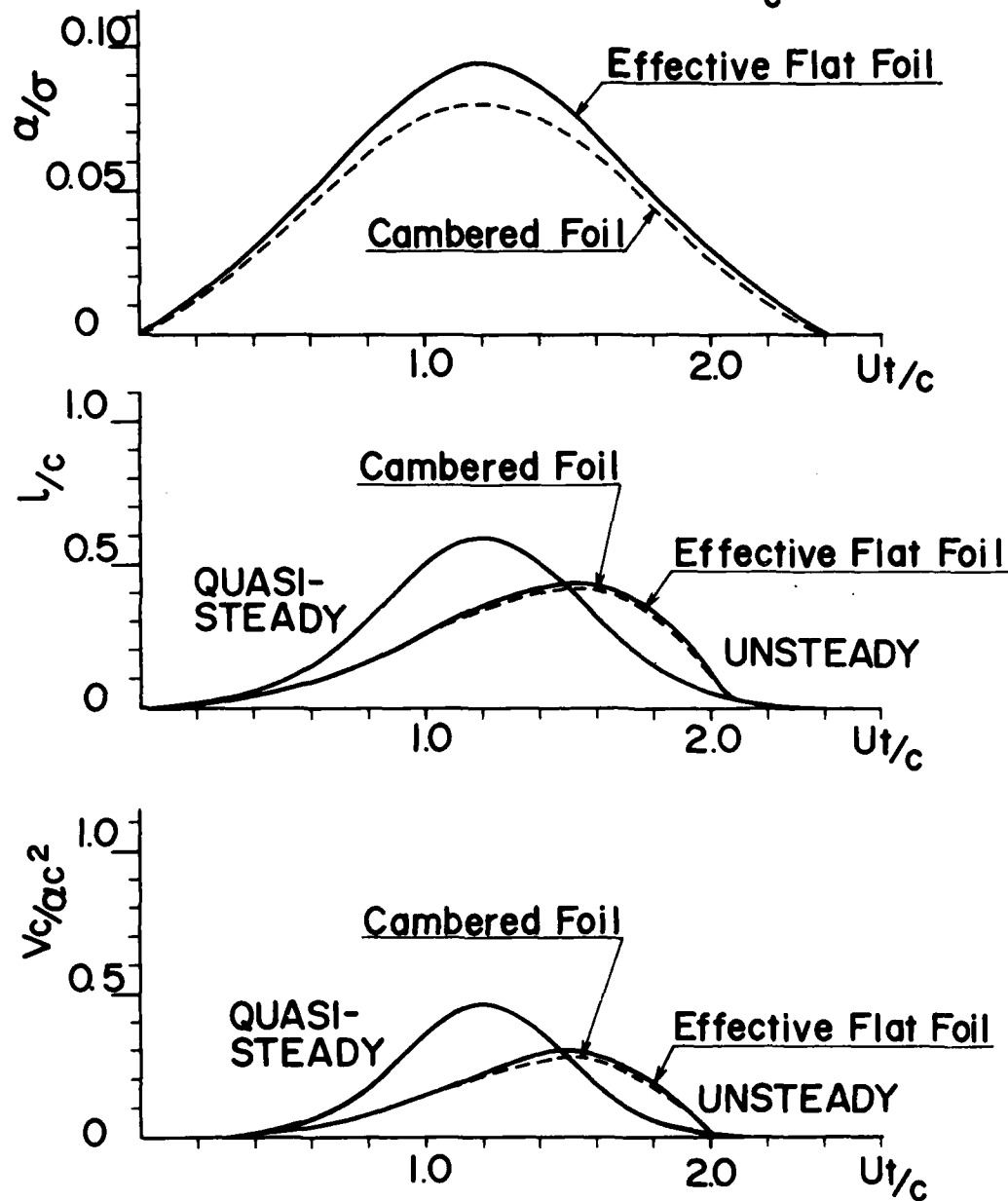
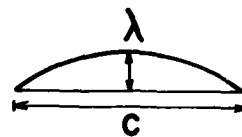


FIGURE 19 Comparison between exact and approximate results for a cambered foil of  $\lambda/c = 0.035$ .



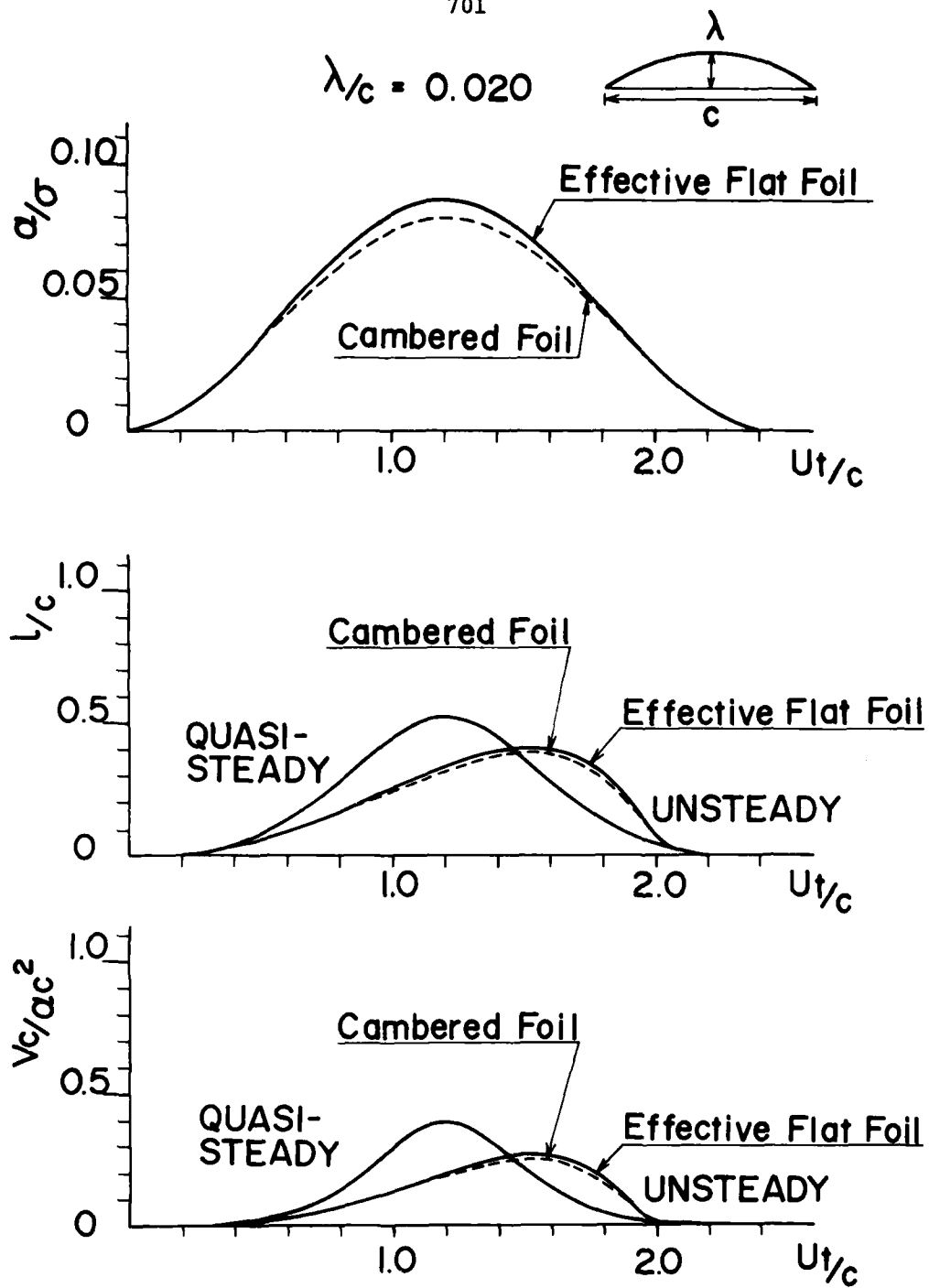


FIGURE 20

Comparison between exact and approximate results for a cambered foil of  $\lambda/c = 0.020$ .

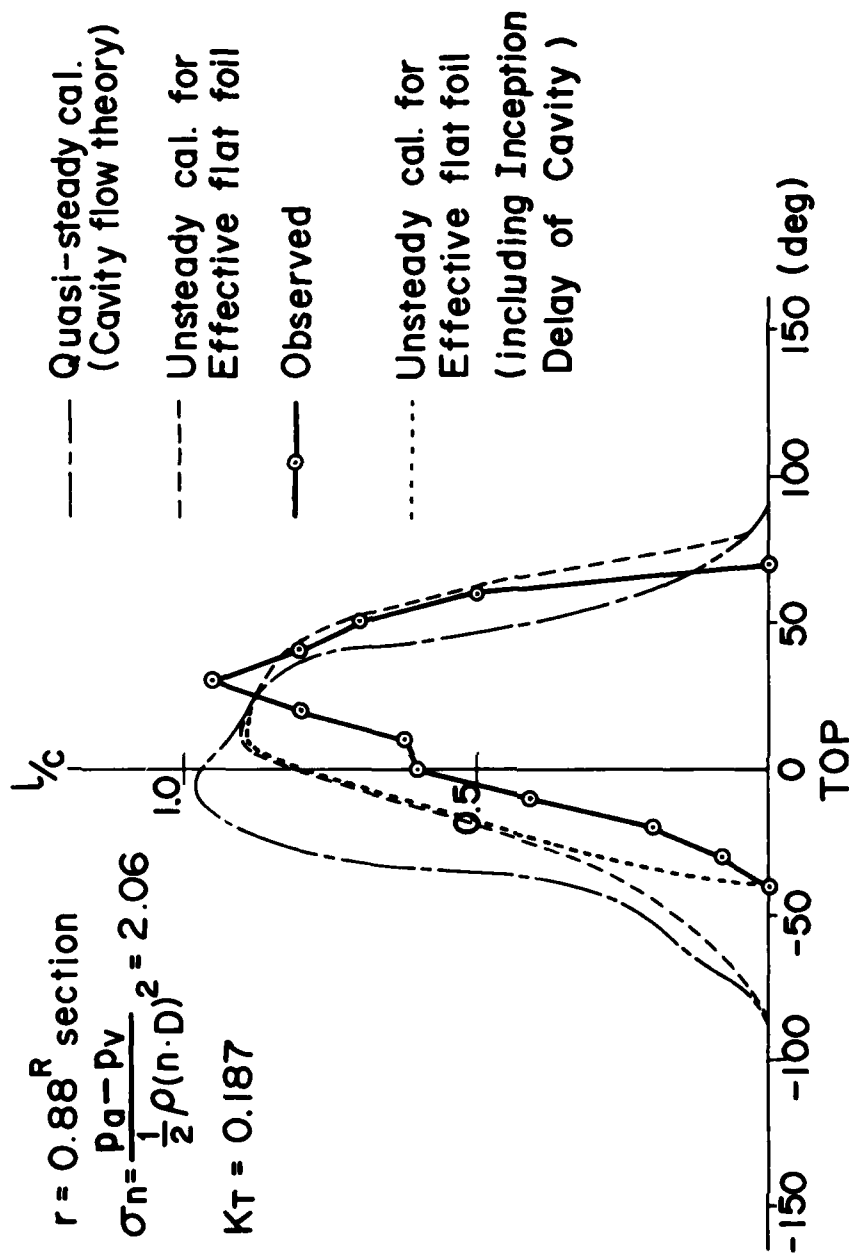


FIGURE 21 Comparison between theoretical and experimental results for cavity extent on a foil section of a propeller behind a ship.

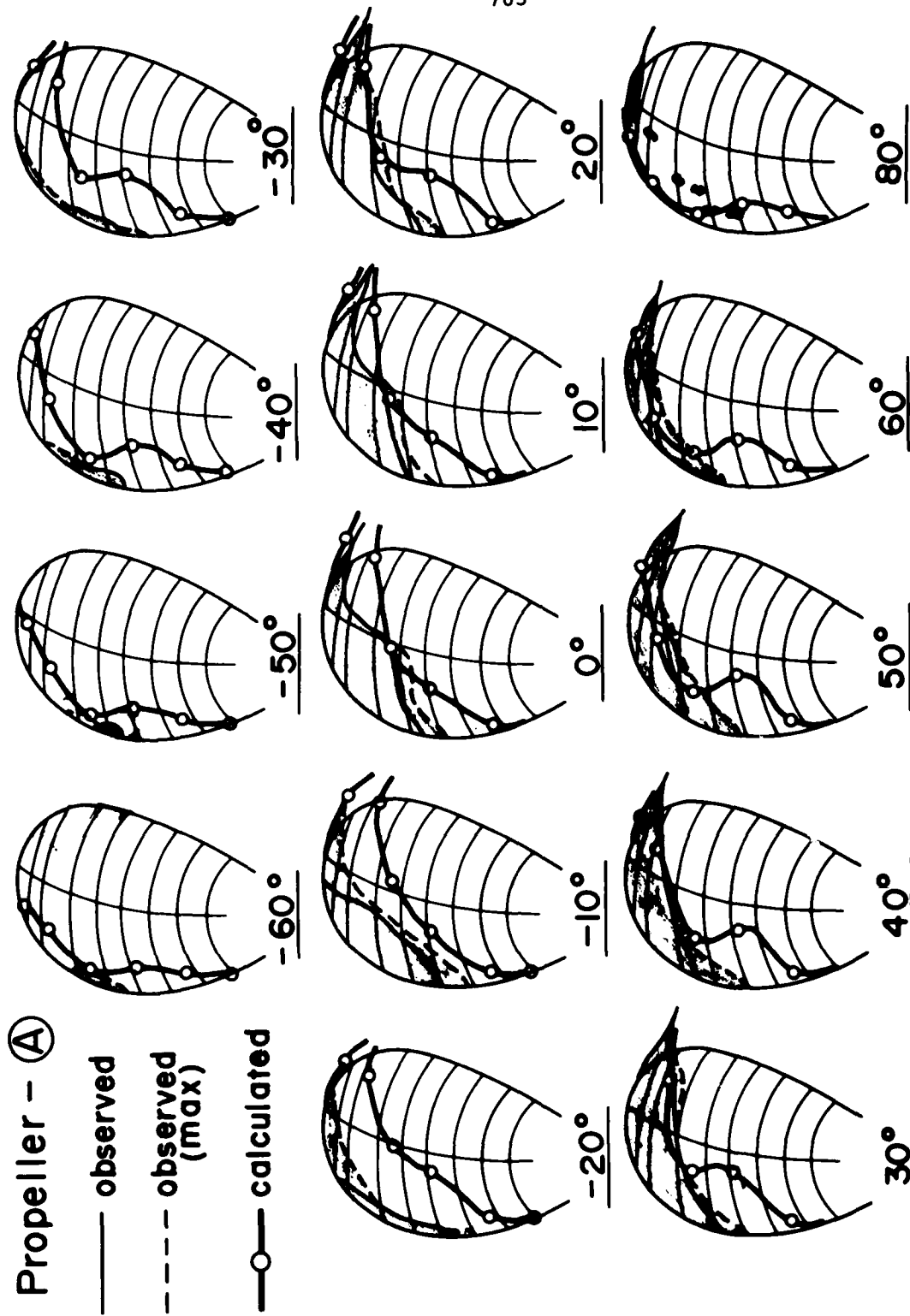


FIGURE 22 Comparison of the cavitation patterns between the quasi-steady calculation and observation.  
 (Propeller - (A);  $K_t = 0.187$ ,  $\sigma_n = 2.060$ )

Propeller - (A)

— observed

--- observed  
(max)

—○— calculated

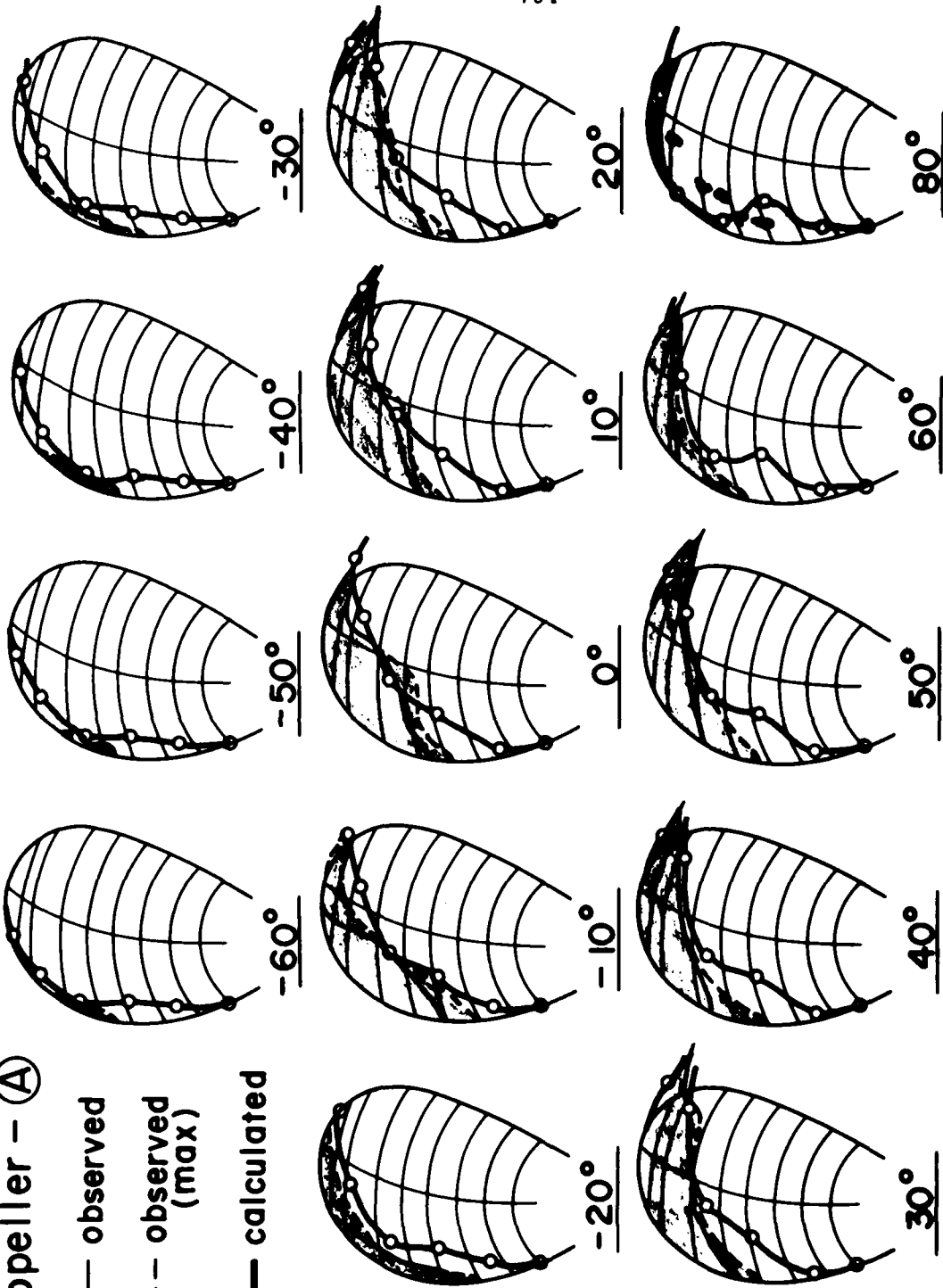


FIGURE 23 Comparison of the cavitation patterns between the unsteady calculation and observation.  
(Propeller - (A);  $K_t = 0.187$ ,  $\sigma_n = 2.060$ )

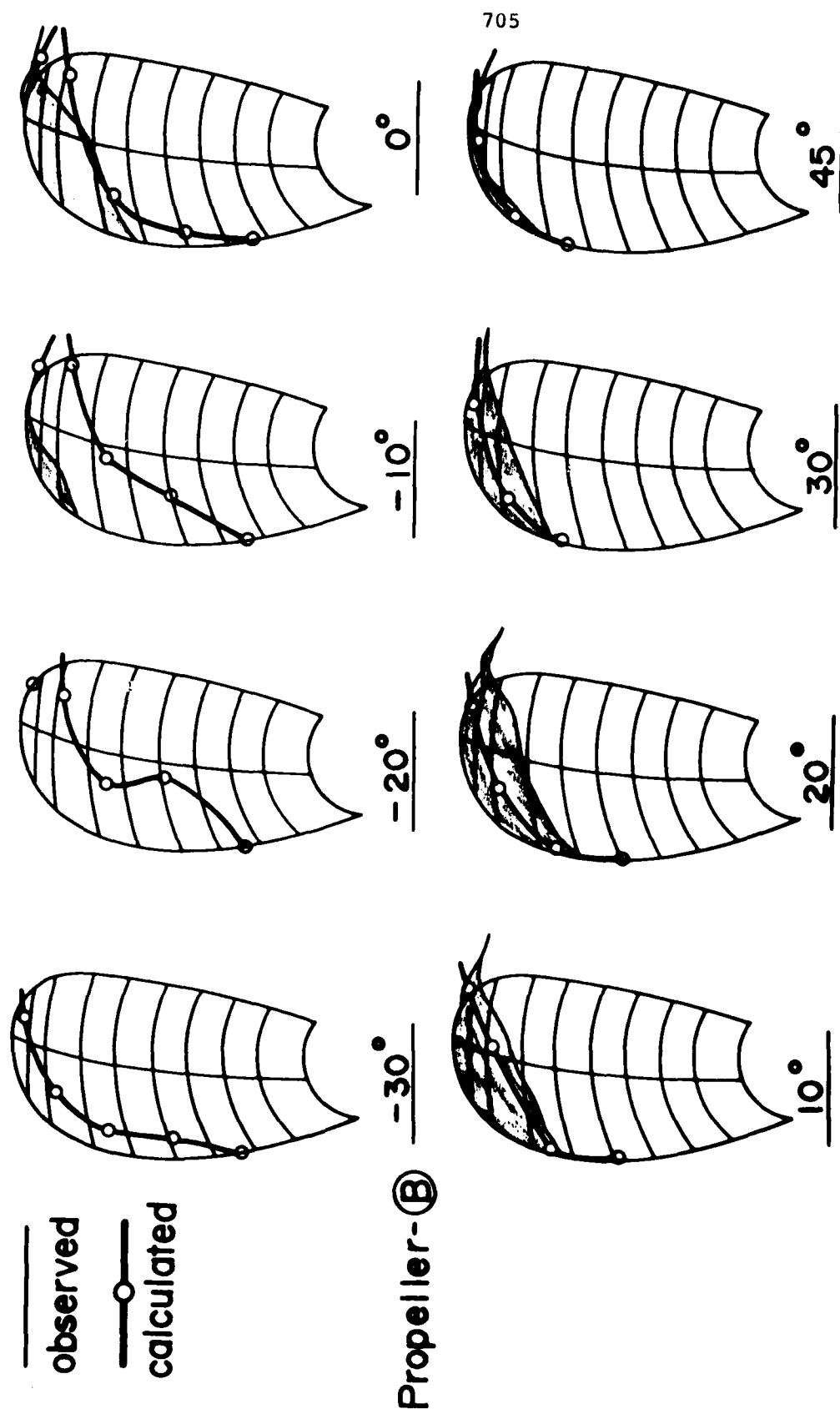


FIGURE 24

Comparison of the cavitation patterns between  
 the quasi-steady calculation and observation.  
 (Propeller - Ⓑ; ballast condition;  $K_t = 0.182$ ,  
 $\sigma_n = 2.033$ )

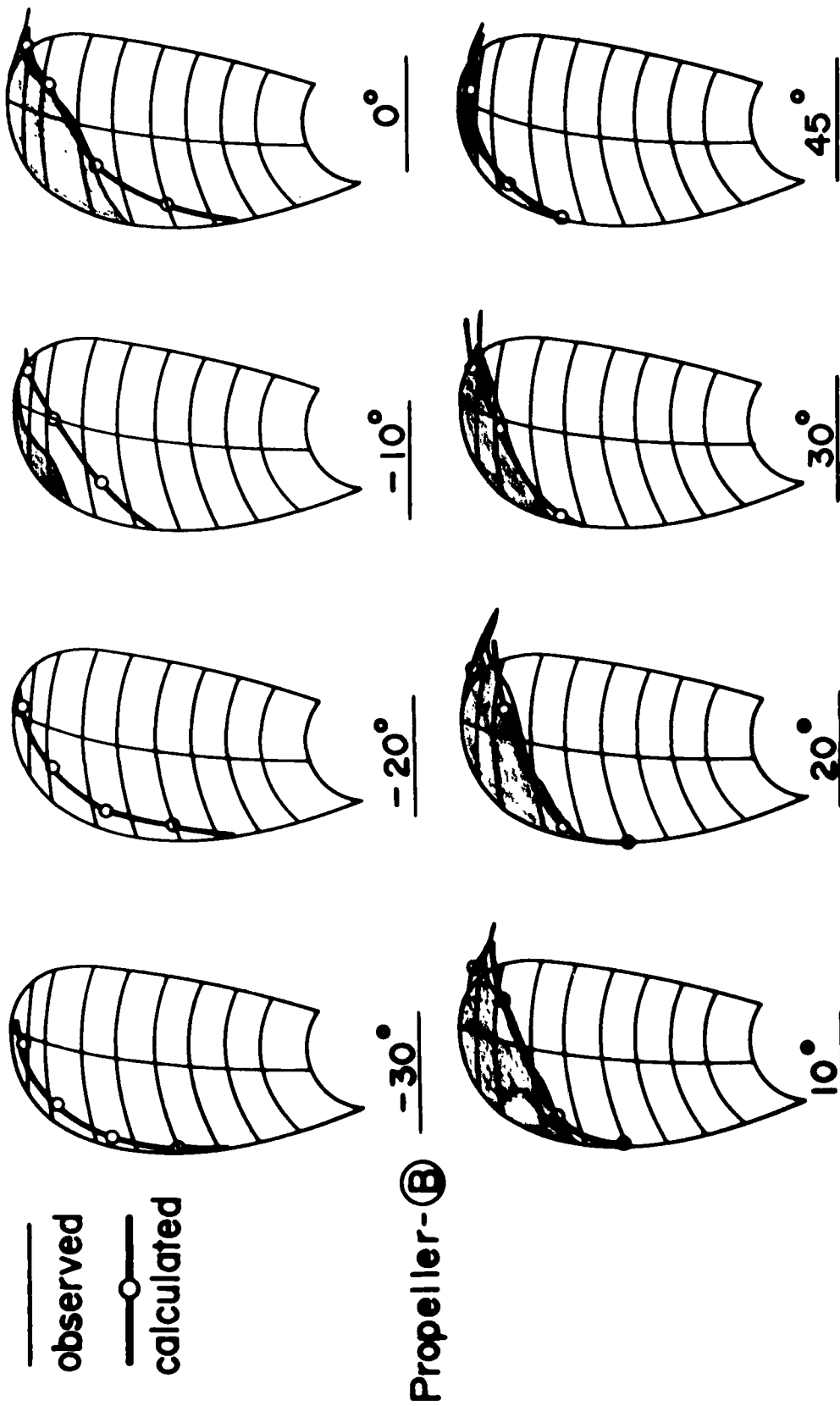


FIGURE 25  
 Comparison of the cavitation patterns between  
 the unsteady calculation and observation.  
 (Propeller - B; ballast condition;  $K_t = 0.182$ ,  
 $\sigma_h = 2.033$ )

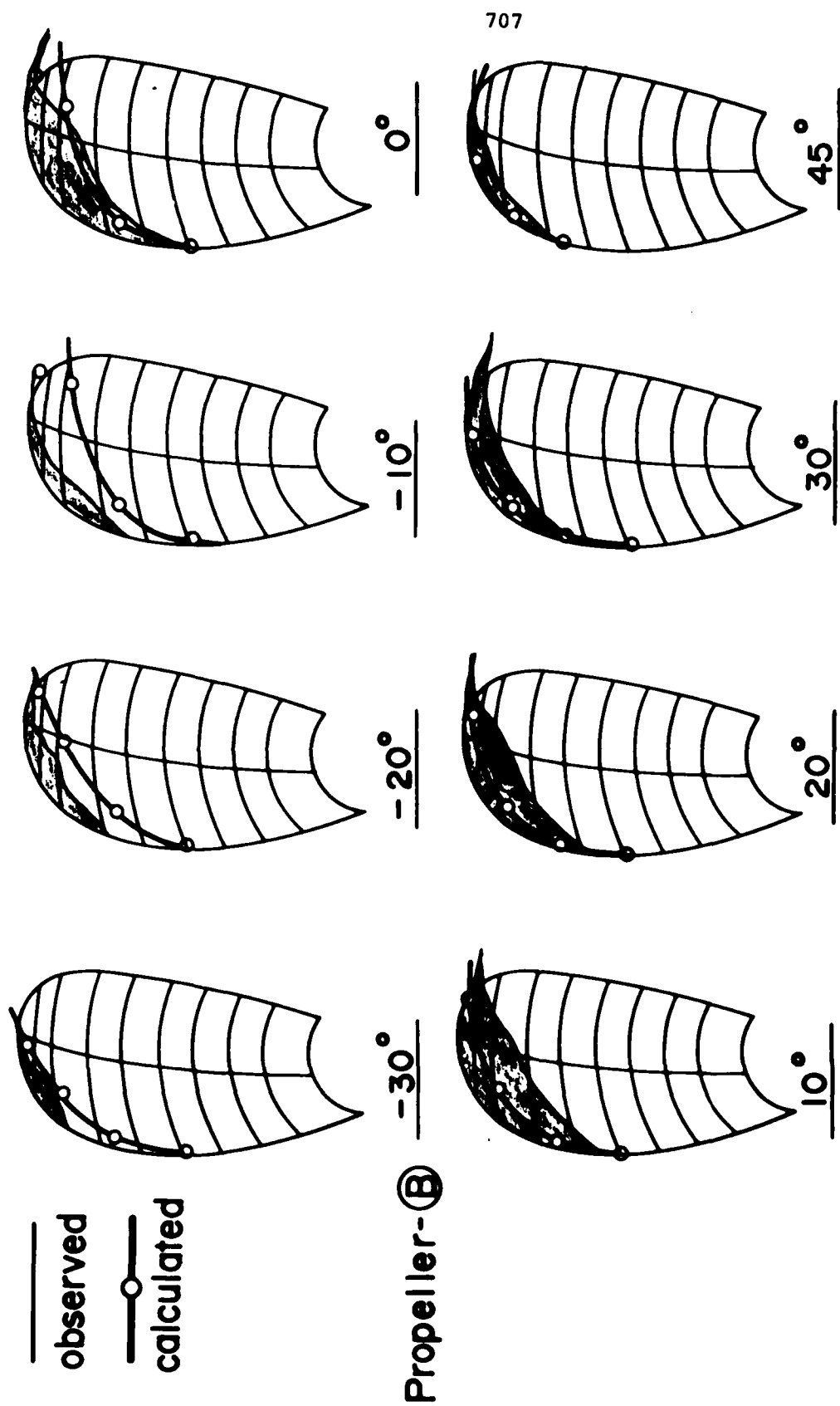


FIGURE 26 Comparison of the cavitation patterns between the quasi-steady calculation and observation. (Propeller - **ⓑ**; full condition ;  $K_t = 0.198$ ,  $\sigma_n = 2.585$ )

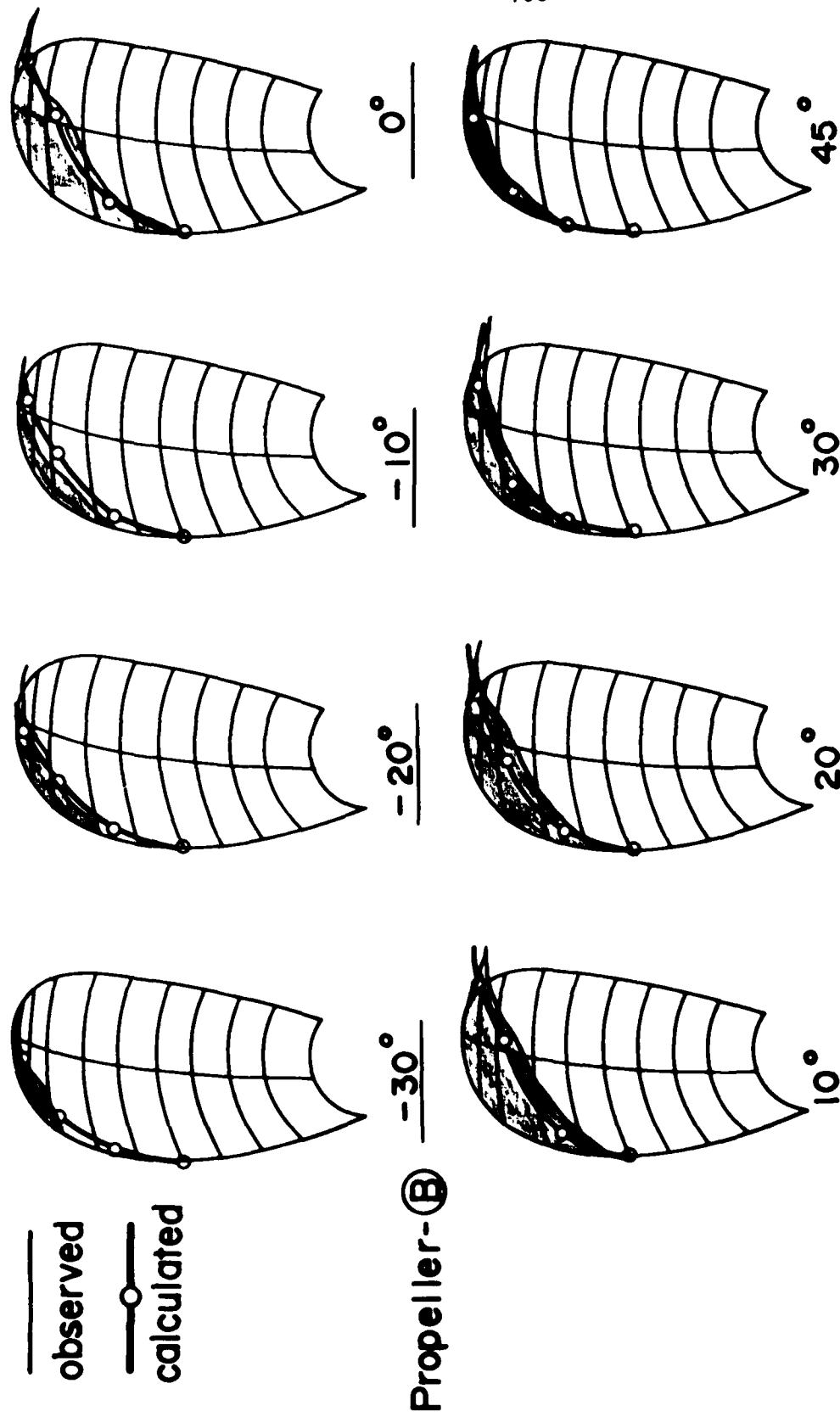


FIGURE 27 Comparison of the cavitation patterns between the unsteady calculation and observation. (Propeller - Ⓑ; full condition;  $K_t = 0.198$ ,  $\sigma_n = 2.585$ )



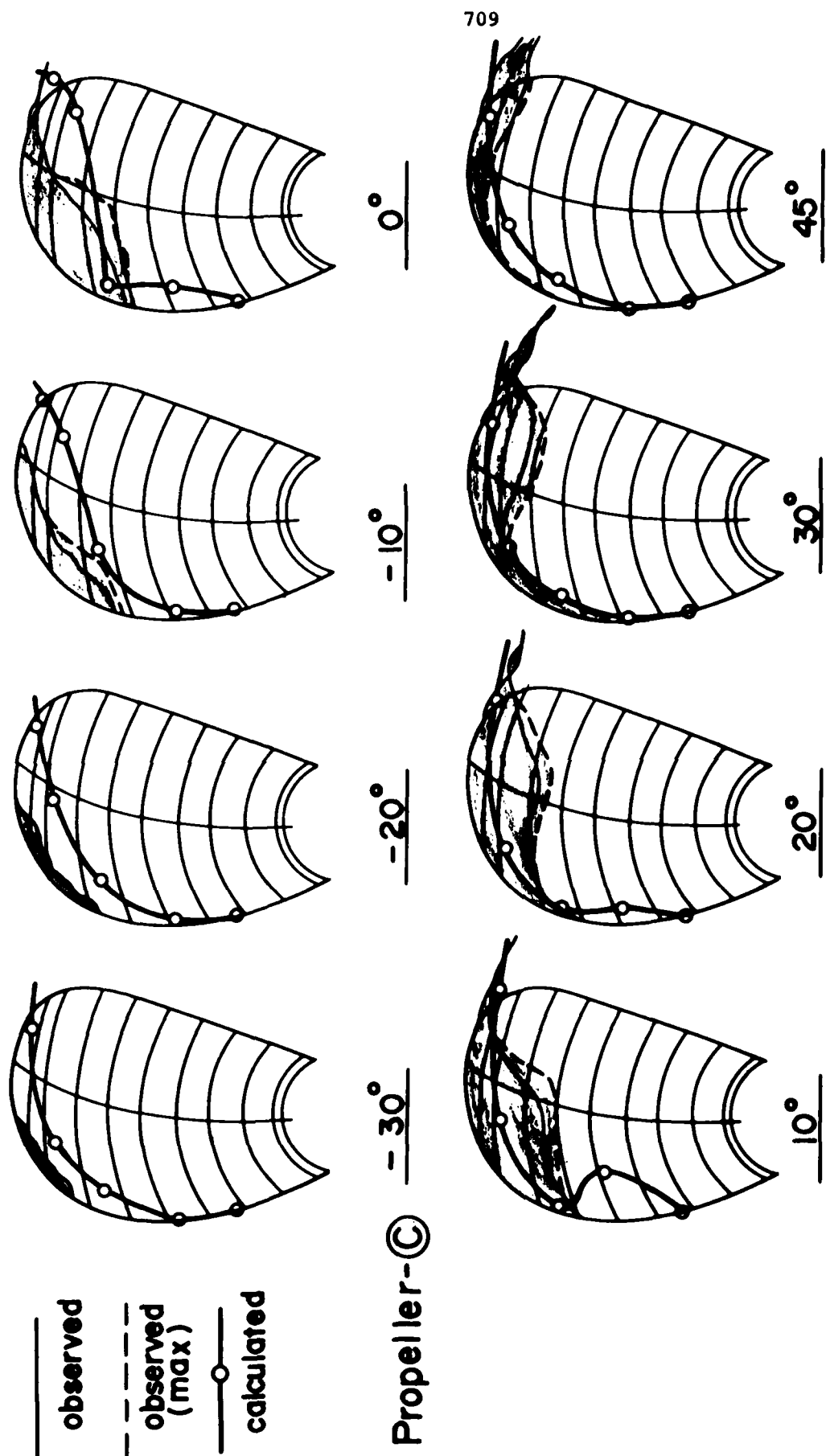


FIGURE 28 Comparison of the cavitation patterns between the quasi-steady calculation and observation. (Propeller - C; ballast condition;  $K_t = 0.189$ ,  $C_{\eta} = 1.645$ )

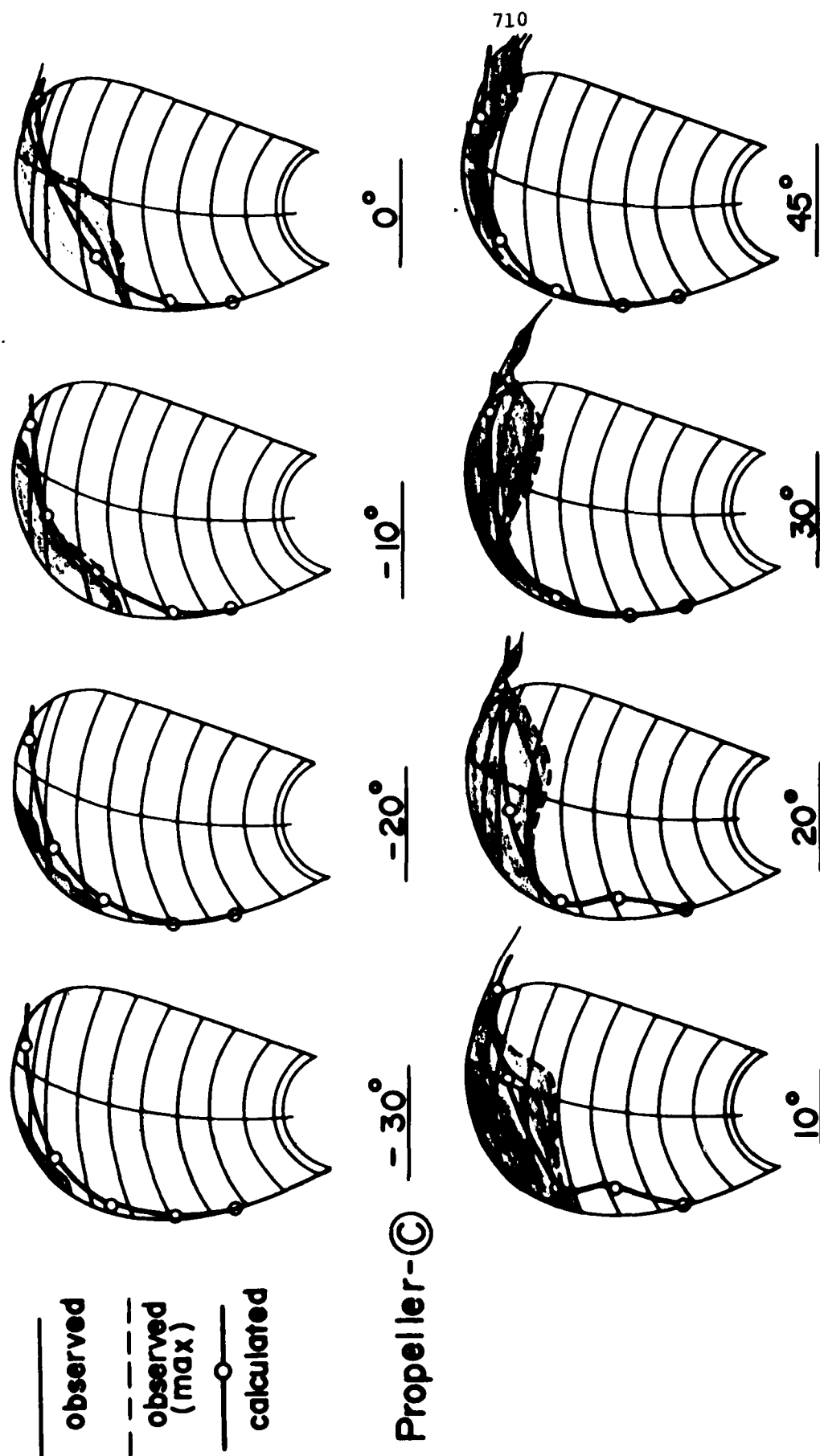


FIGURE 29 Comparison of the cavitation patterns between the unsteady calculation and observation. (Propeller - C; ballast condition;  $K_t = 0.189$ ,  $\sigma_n = 1.645$ )

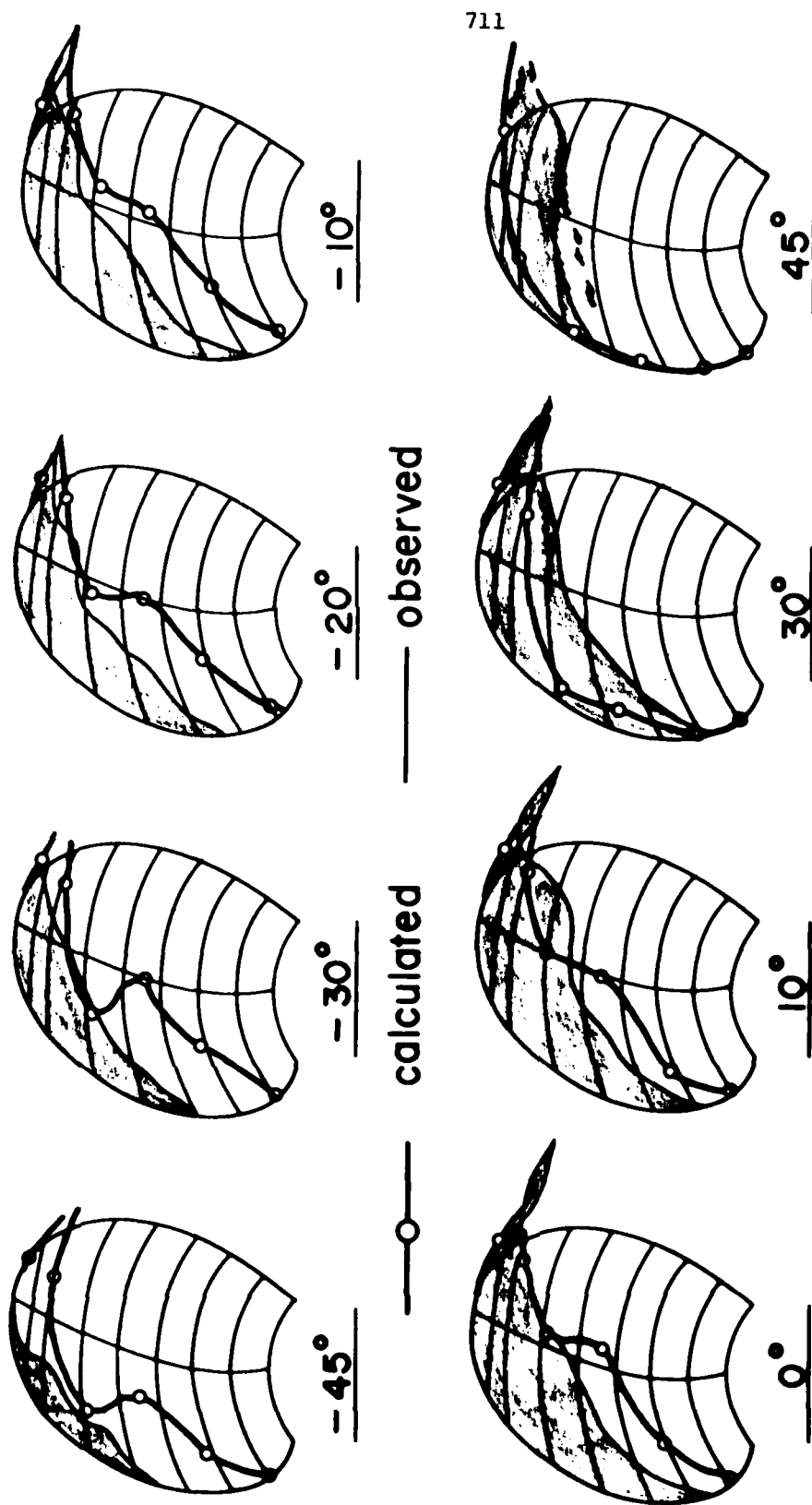


FIGURE 30 Comparison of the cavitation patterns between the quasi-steady calculation and observation. (SR.183, MP.No.1 ;  $K_t = 0.137$ ,  $\sigma_n = 1.649$ )

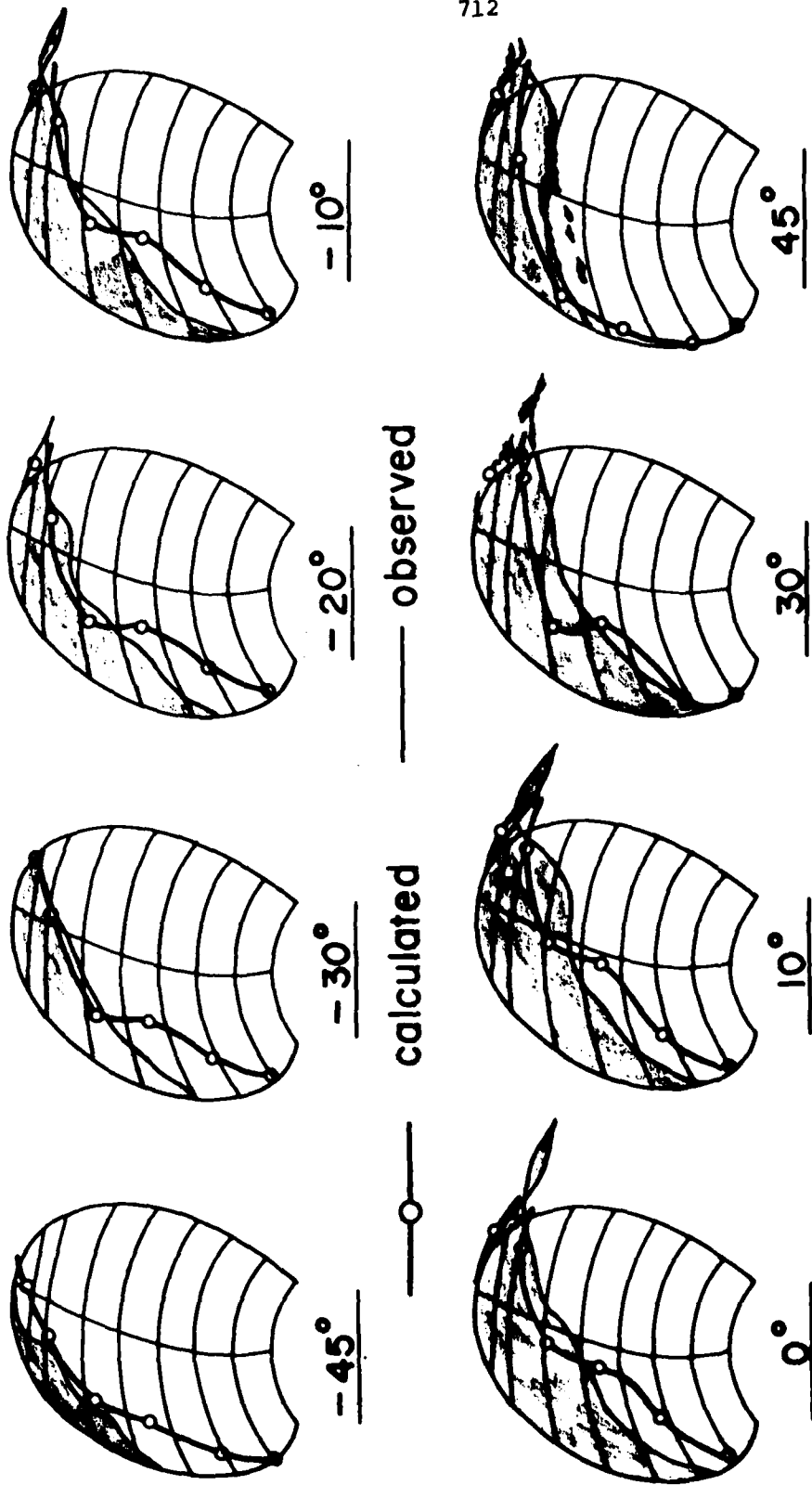


FIGURE 31 Comparison of the cavitation patterns between the unsteady calculation and observation. (SR.183, MP.No.1 ;  $K_t = 0.137$ ,  $C_n = 1.649$ )

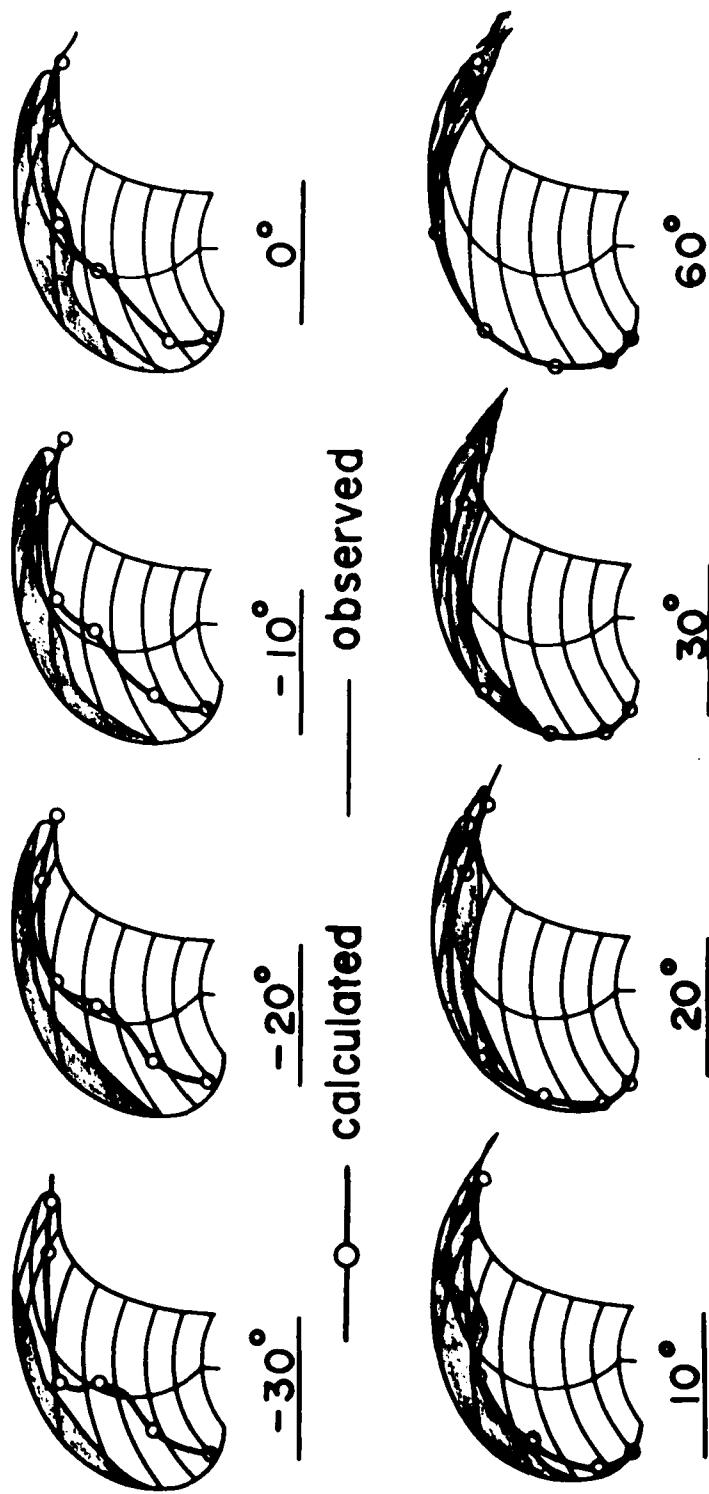


FIGURE 32 Comparison of the cavitation patterns between the quasi-steady calculation and observation.  
(SR.183, MP.No.2 ;  $K_t = 0.137$ ,  $Q_n = 1.649$ )

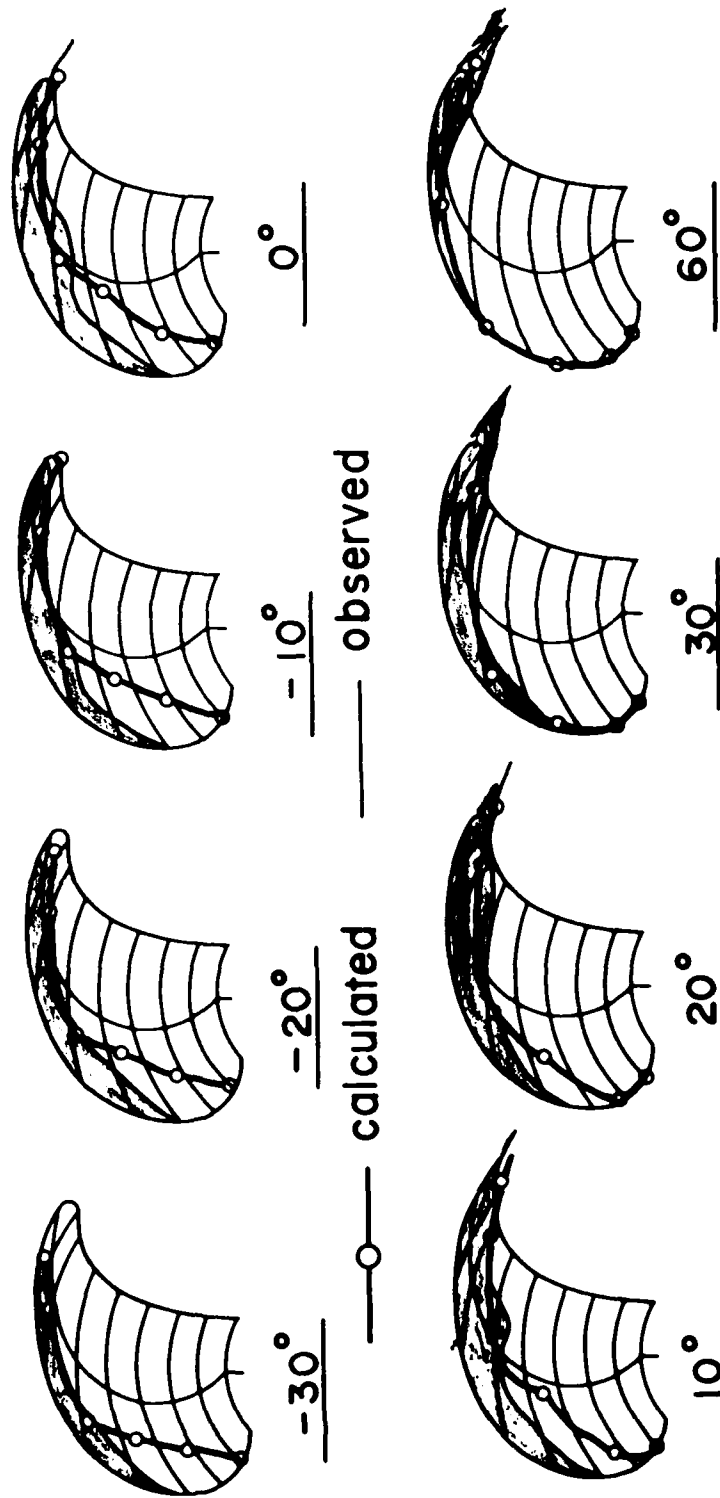


FIGURE 33 Comparison of the cavitation patterns between the unsteady calculation and observation.  
(SR.183, MP.No.2 ;  $K_t = 0.137$ ,  $O_n = 1.649$ )

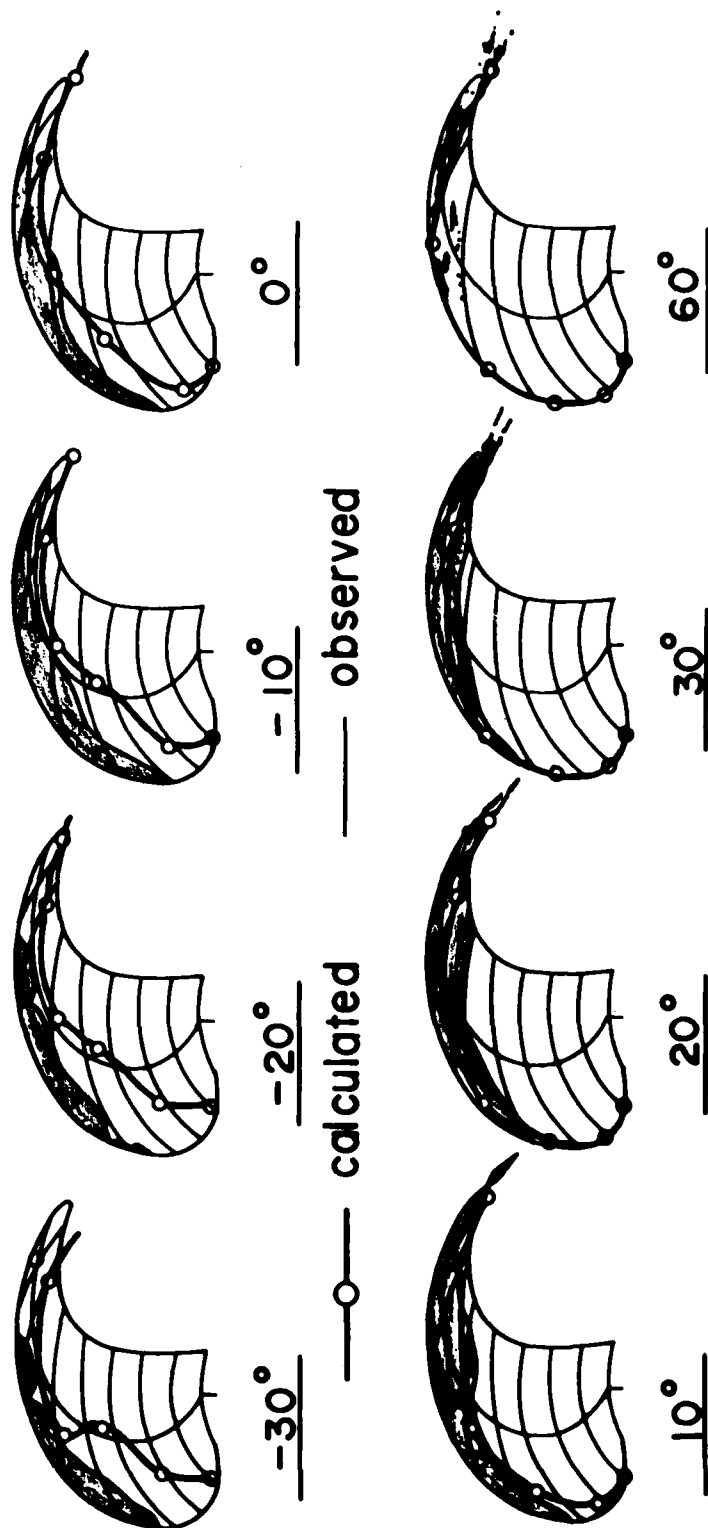


FIGURE 34 Comparison of the cavitation patterns between the quasi-steady calculation and observation. (SR.183, MP.No.5 ;  $Kt = 0.137$ ,  $\sigma_n = 1.649$ )

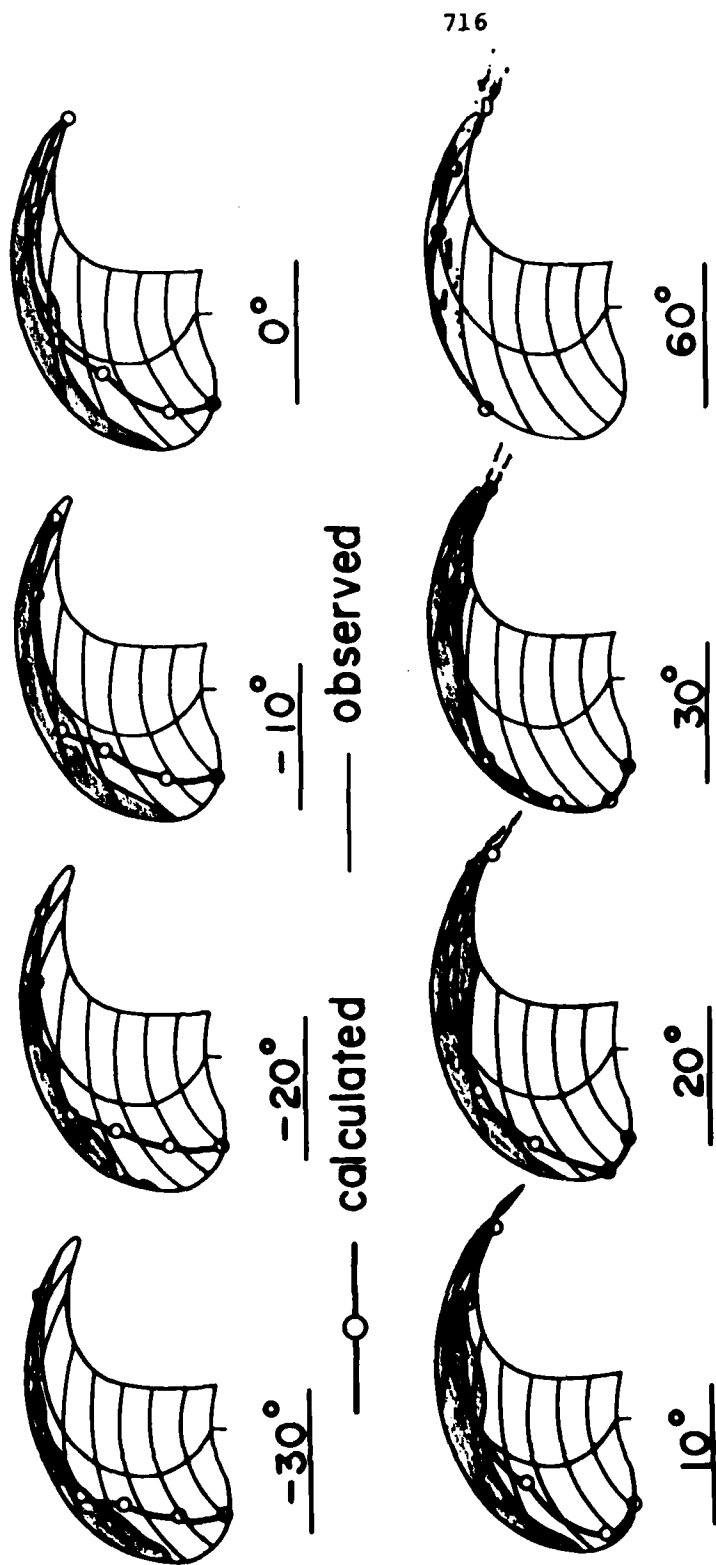


FIGURE 35 Comparison of the cavitation patterns between the unsteady calculation and observation.  
(SR.183, MP.No.5 ;  $K_t = 0.137$ ,  $\sigma_n = 1.649$ )



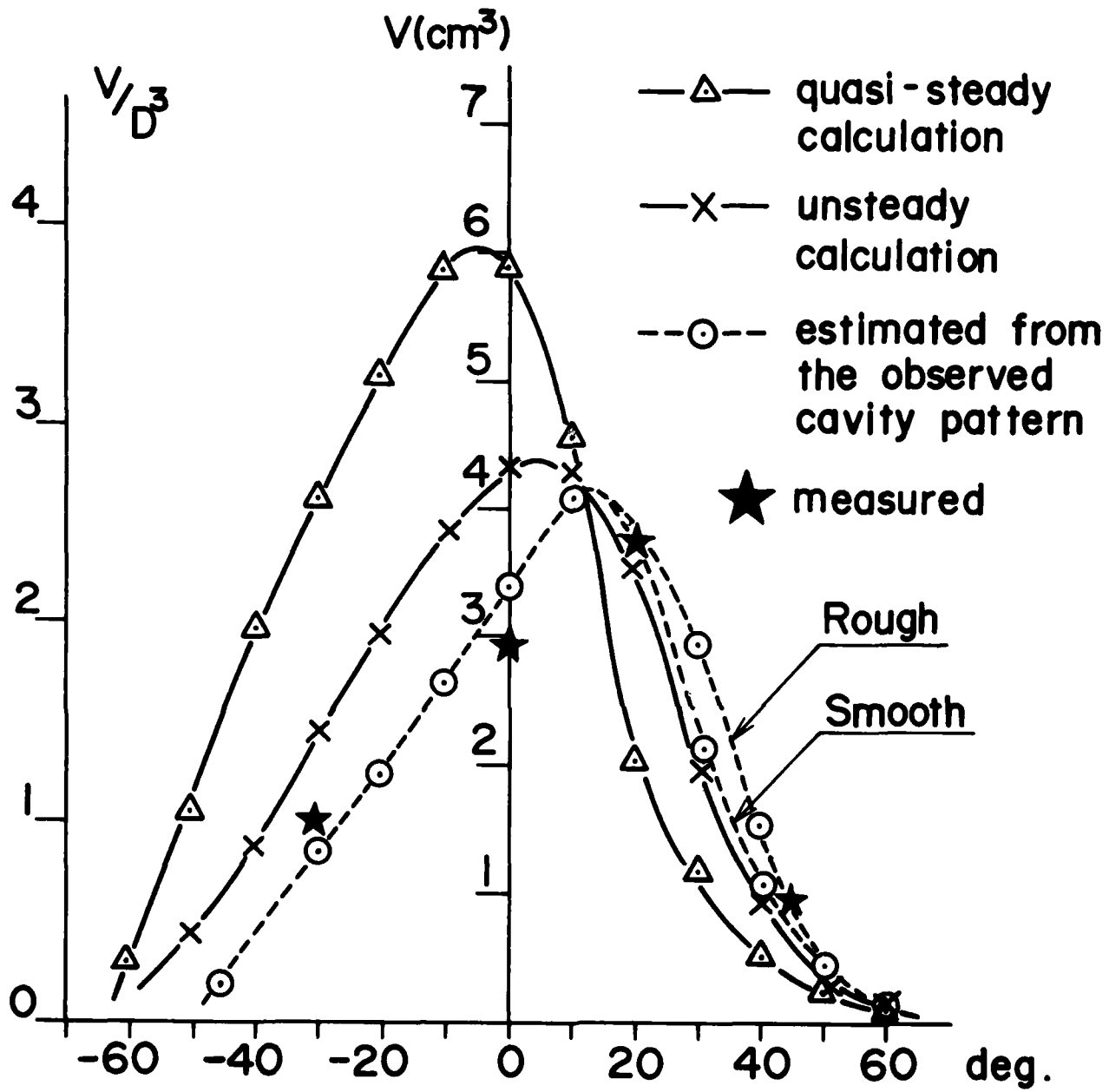


FIGURE 36

Comparison of the cavity volume between the calculations and measurements.  
(SR.183, MP.No.1)

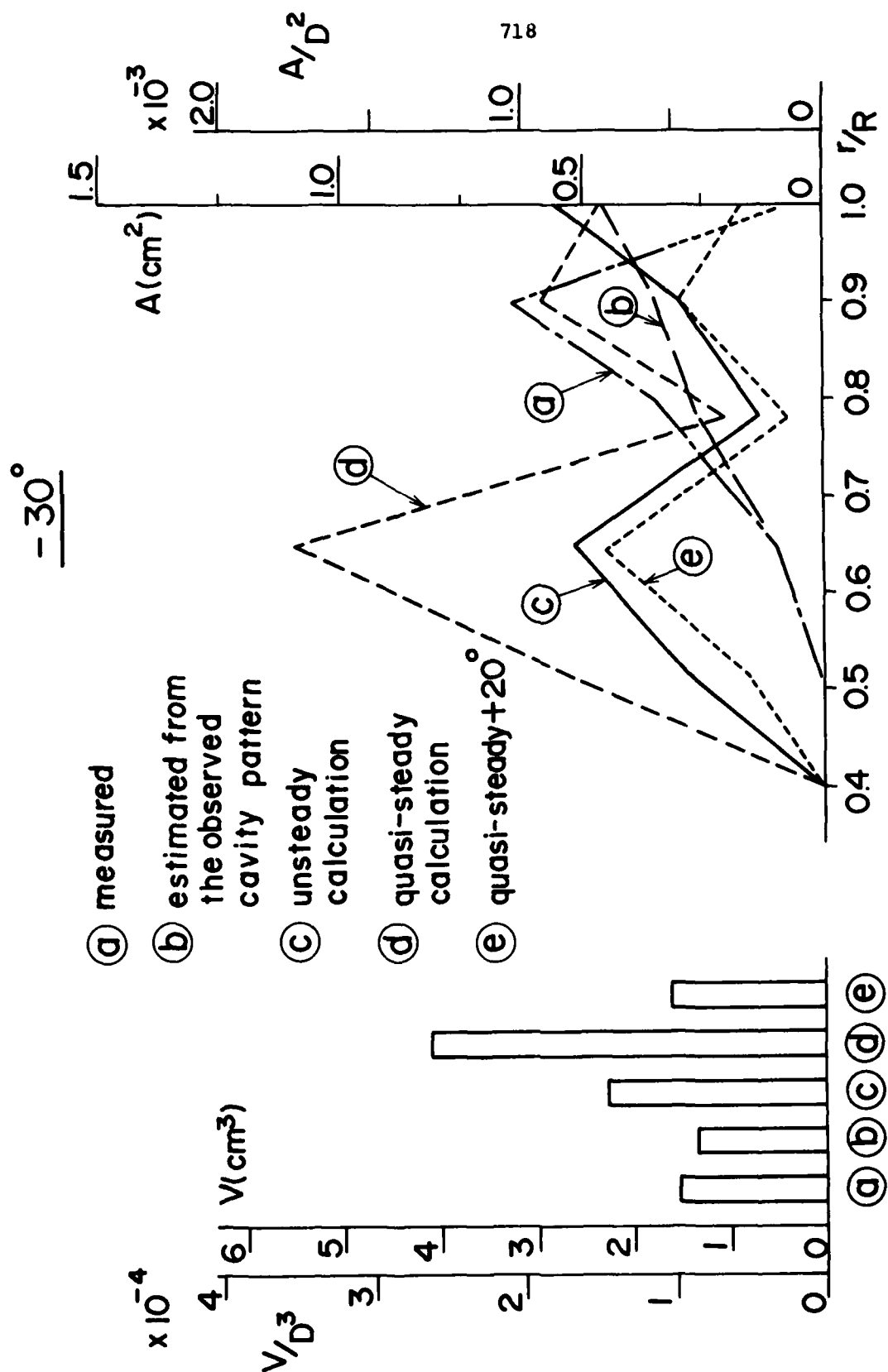
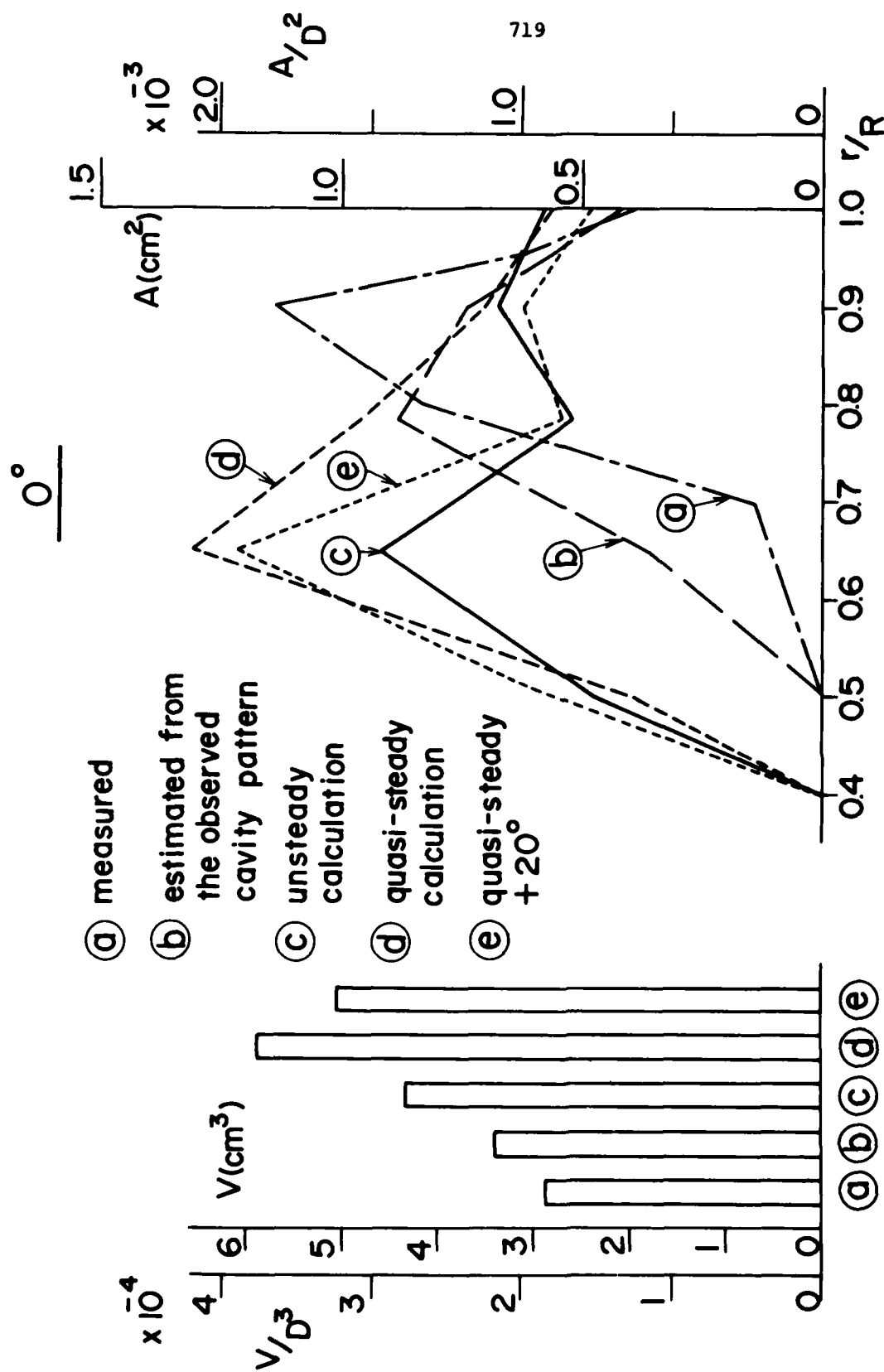


FIGURE 37  
Comparison of the cavity volume distribution in the radial direction between the calculations and measurements. (SR.183, MP.No.1 ; blade angle  $-30^\circ$ )



Comparison of the cavity volume distribution in the radial direction between the calculations and measurements. (SR.183, MP.No.1 ; blade angle  $0^\circ$ )

FIGURE 38

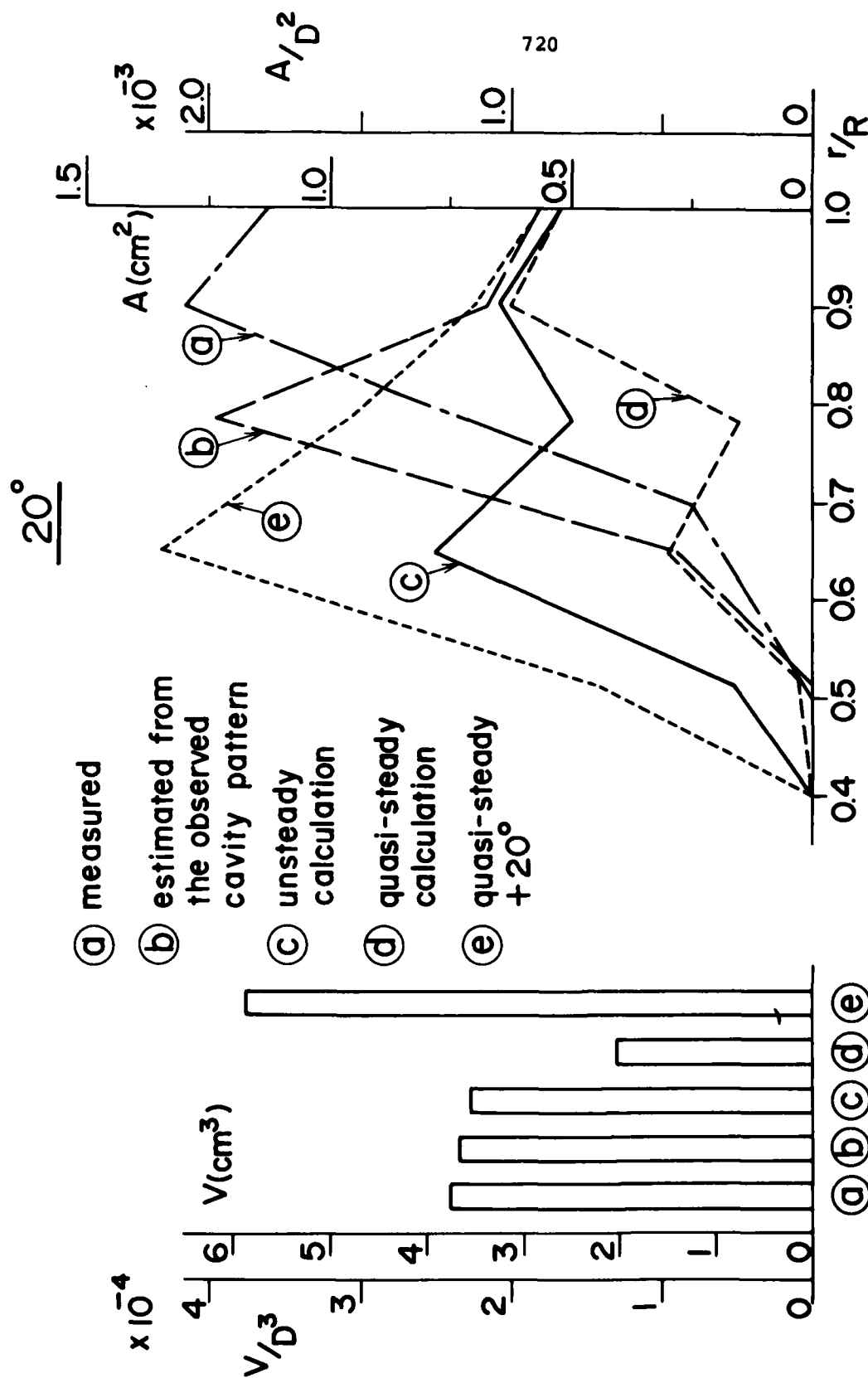


FIGURE 39  
Comparison of the cavity volume distribution in the radial direction between the calculations and measurements. (SR.183, MP.No.1 ; blade angle  $20^\circ$ )

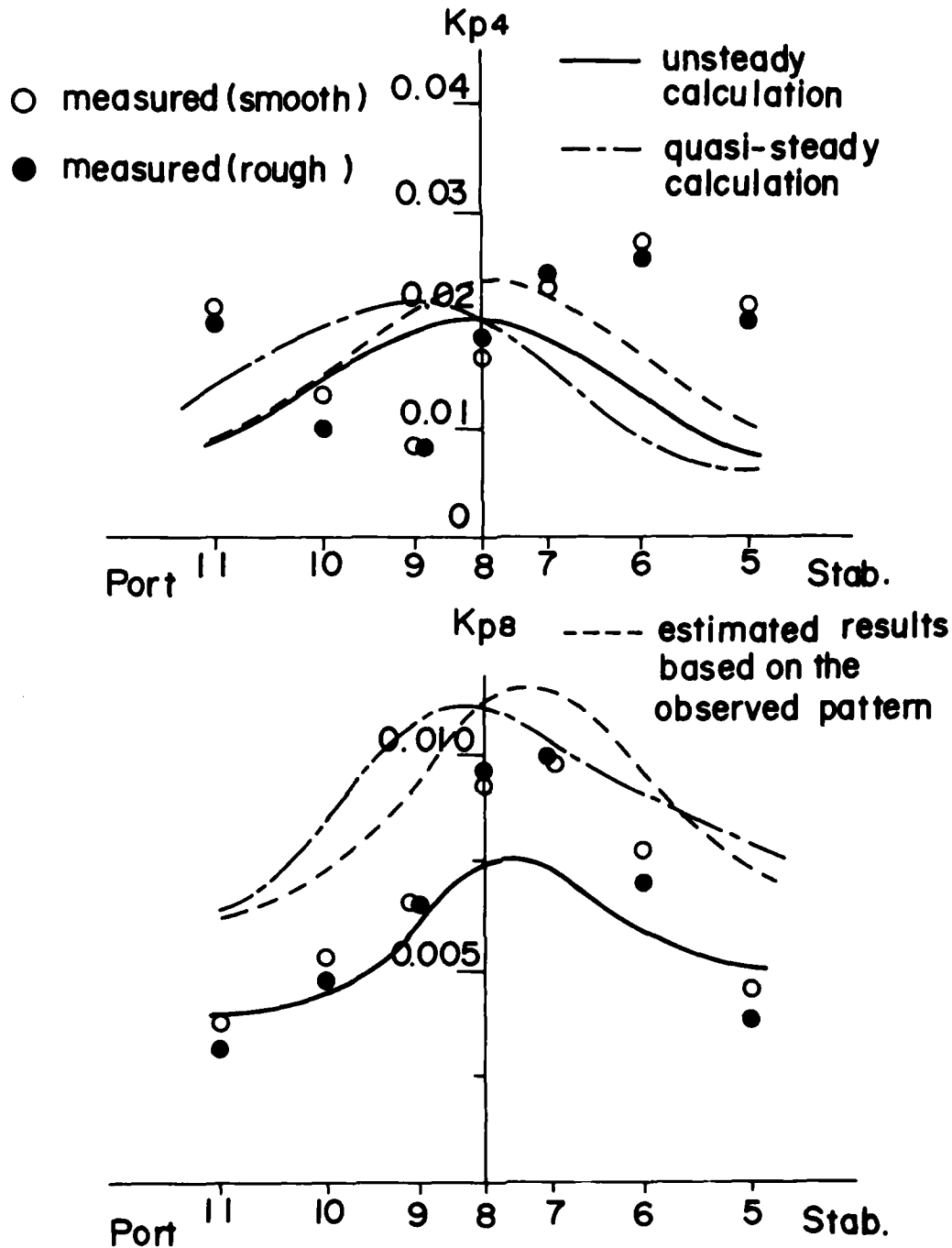


FIGURE 40

Comparison of the fluctuating pressure in the transverse direction between the quasi-steady and unsteady calculations. (SR.183, MP.No.1)

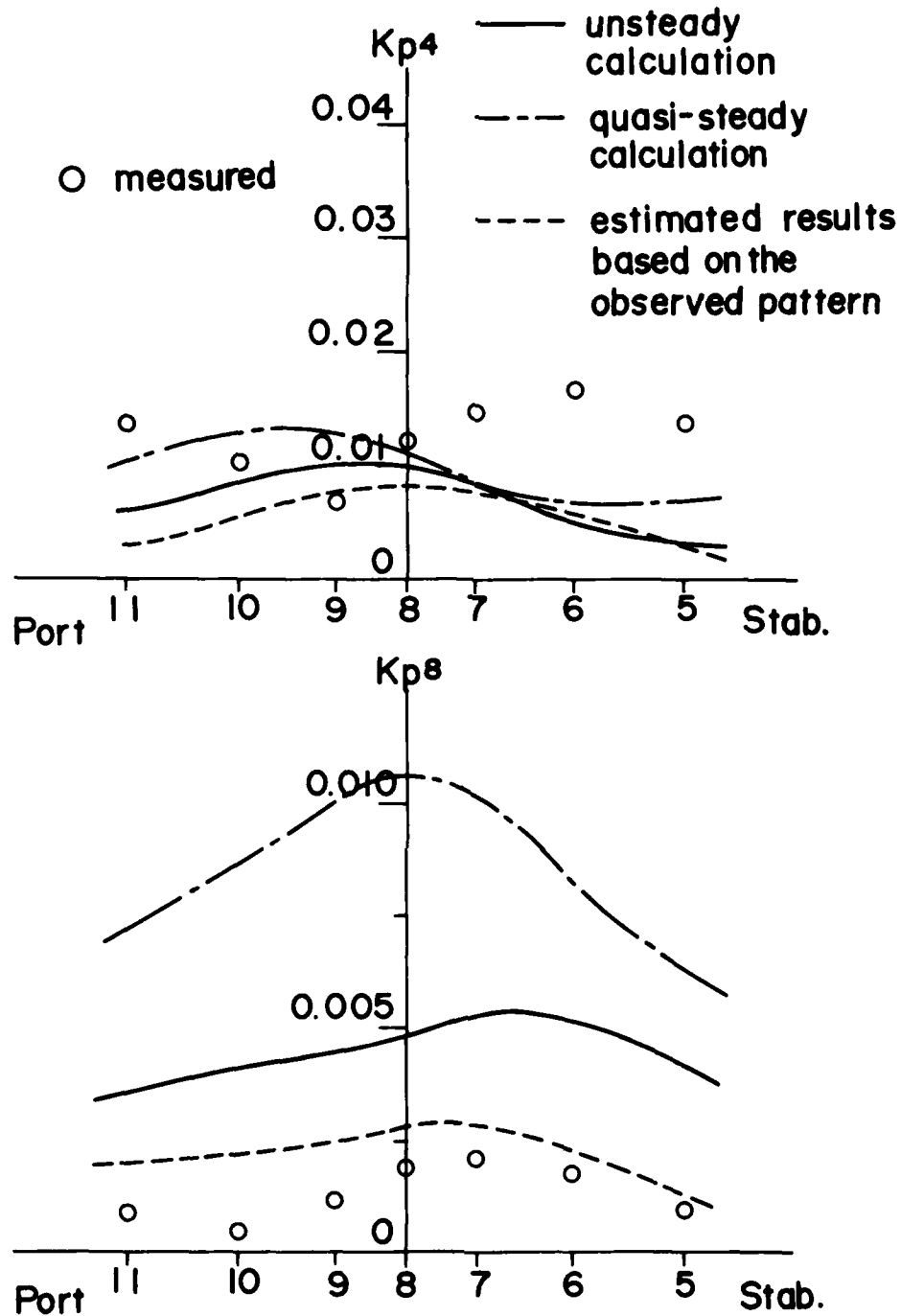


FIGURE 41

Comparison of the fluctuating pressure in the transverse direction between the quasi-steady and unsteady calculations. (SR.183, MP.No.2)

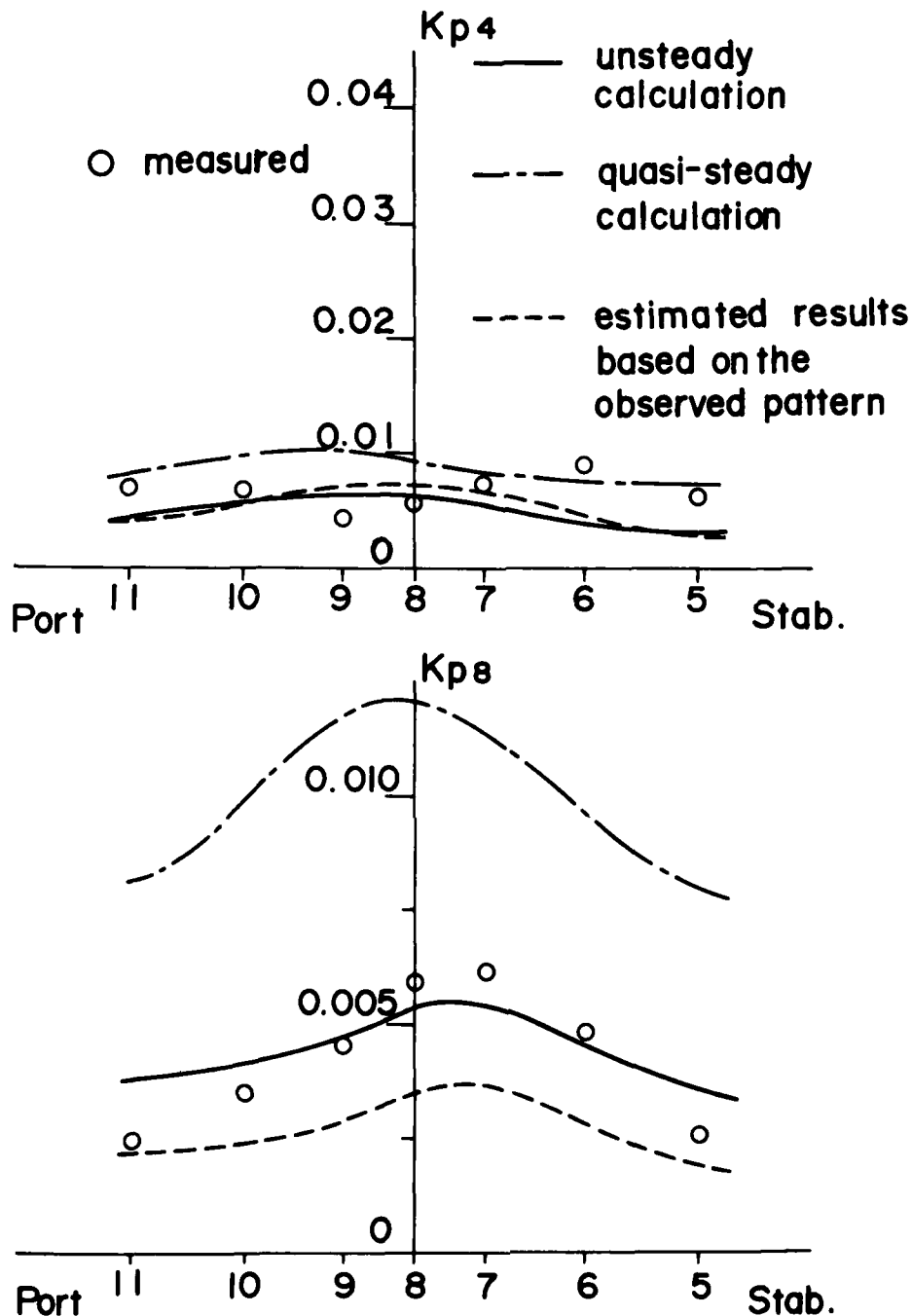


FIGURE 42

Comparison of the fluctuating pressure in the transverse direction between the quasi-steady and unsteady calculations. (SR.183, MP.No.5)

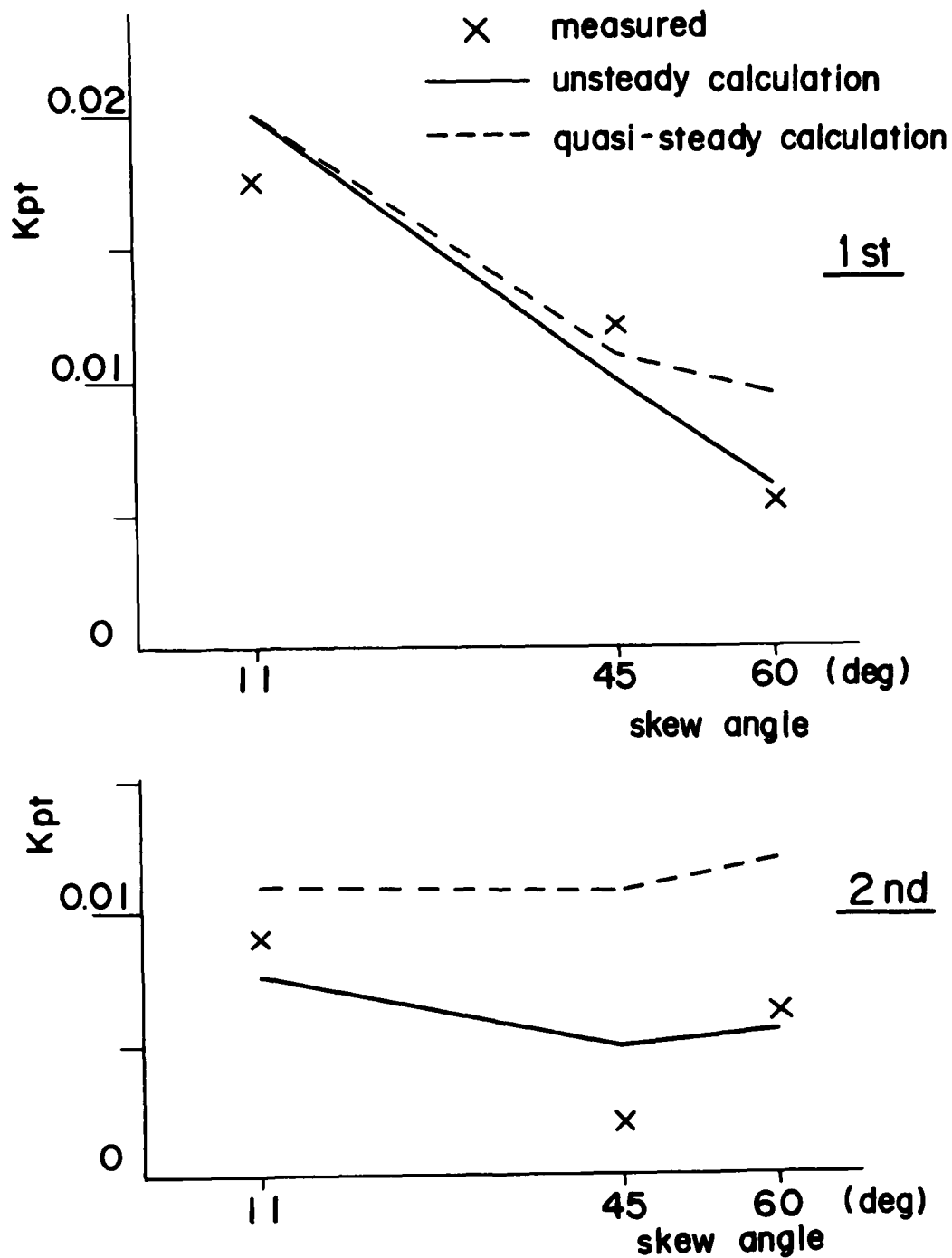


FIGURE 43

Comparison of the effect of the skew angle on the fluctuating pressure between the quasi-steady and unsteady calculations. (SR.183)



$$K_t = 0.187, \quad \sigma_n = 2.06$$

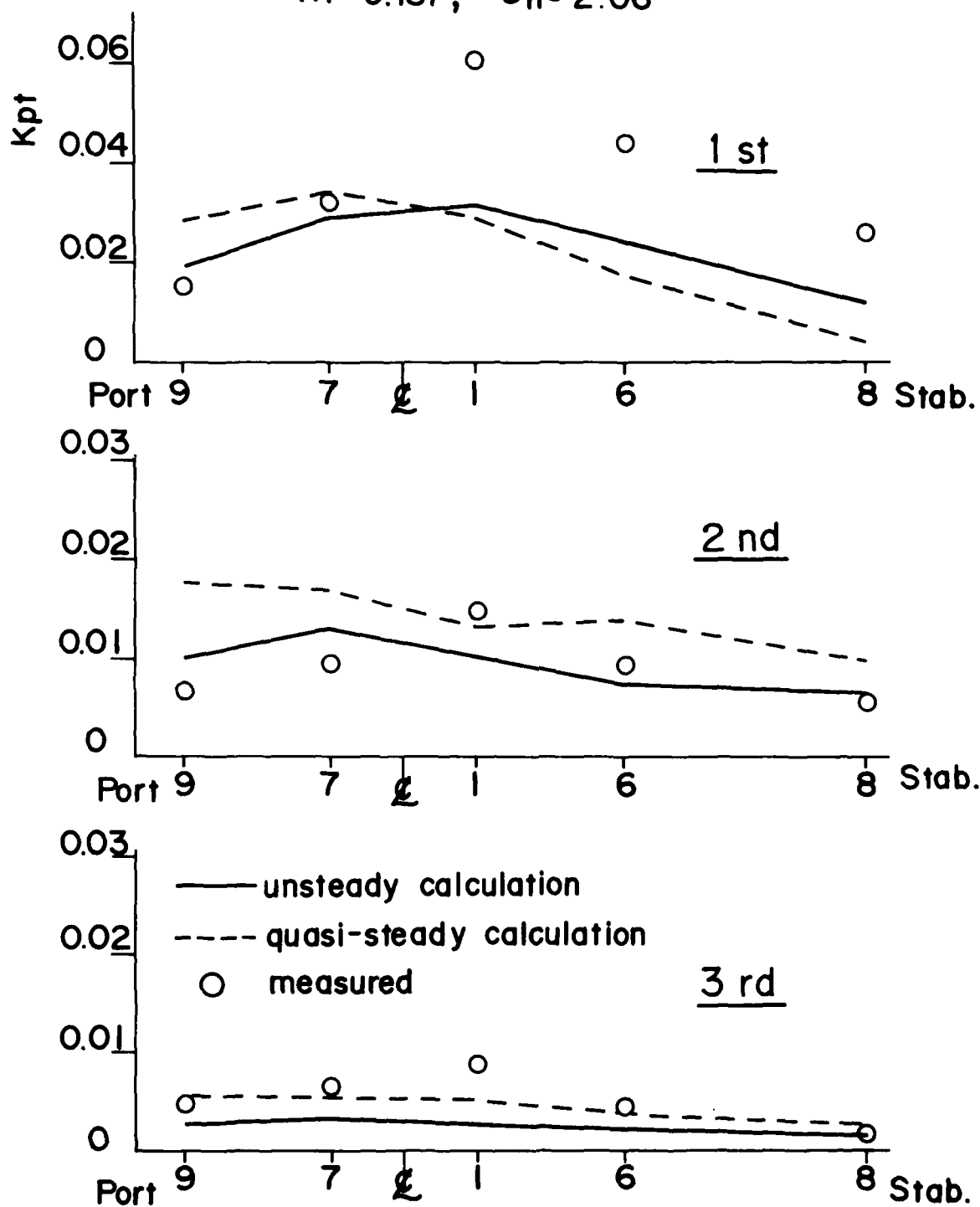


FIGURE 44

Comparison of the fluctuating pressure in the transverse direction between the quasi-steady and unsteady calculations. (Propeller - A)

$$K_t = 0.187, \quad \sigma_n = 2.06$$

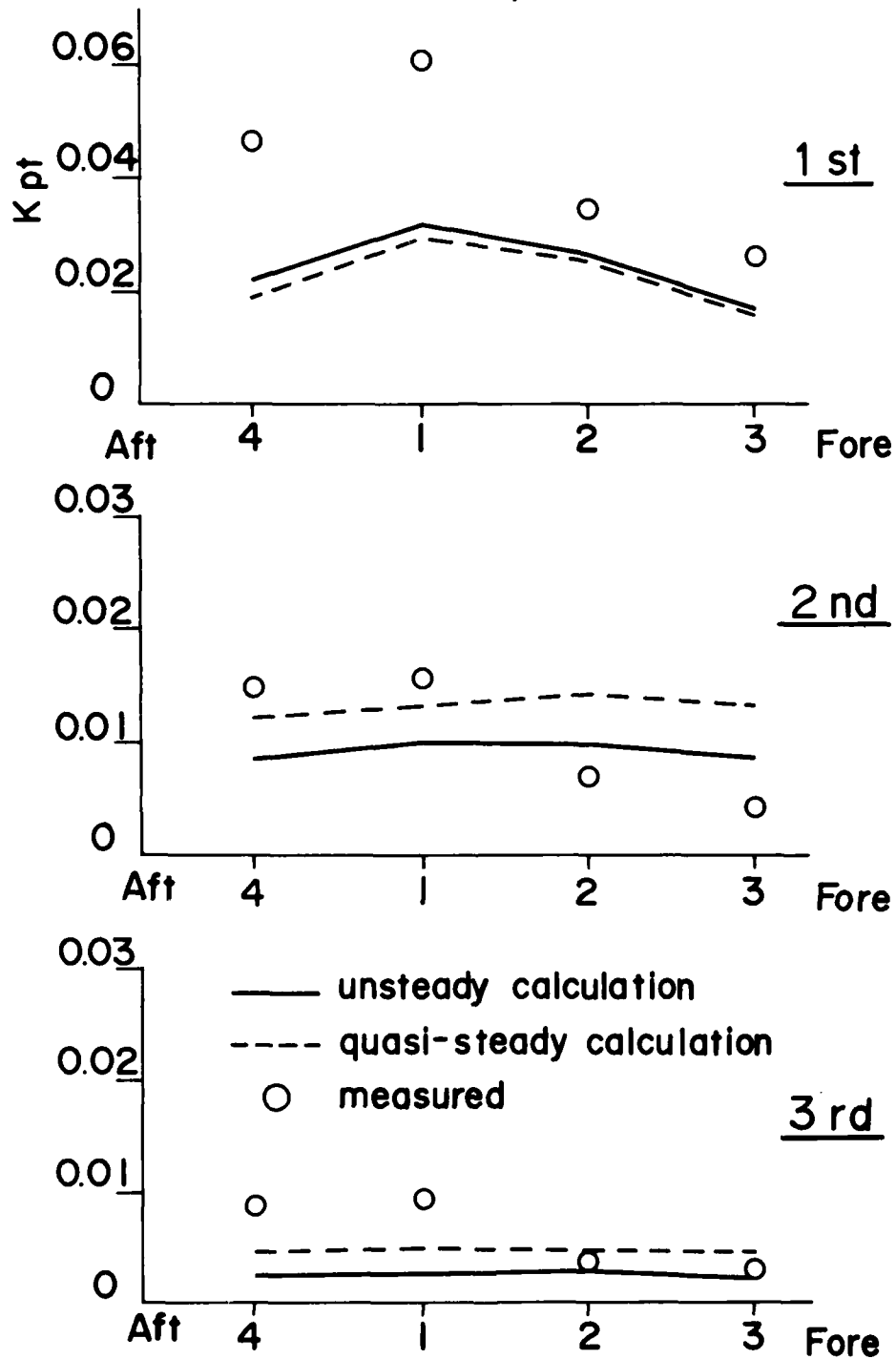


FIGURE 45

Comparison of the fluctuating pressure in the longitudinal direction between the quasi-steady and unsteady calculations. (Propeller - A)

$$K_t = 0.187, \quad \sigma_n = 1.55$$

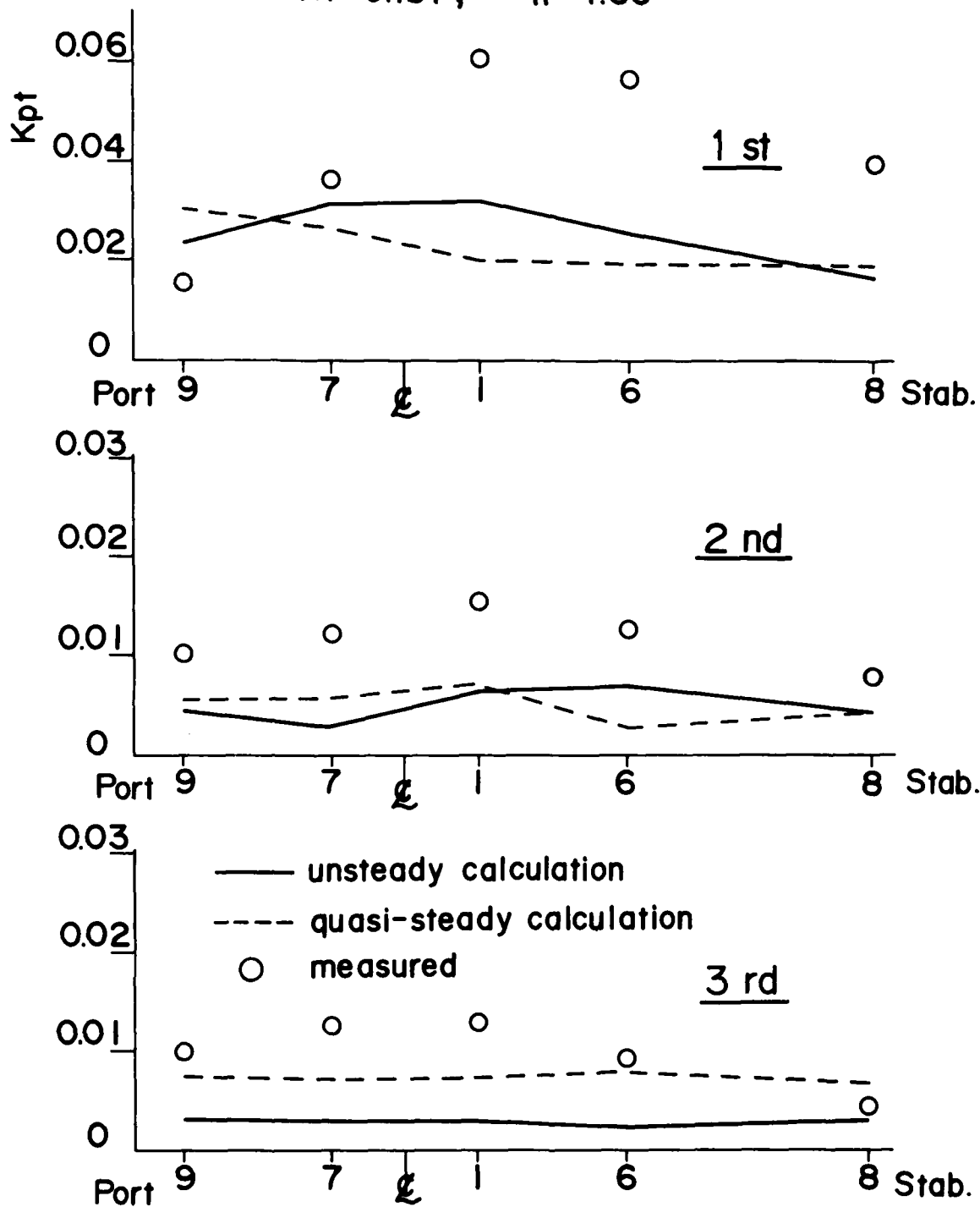


FIGURE 46

Comparison of the fluctuating pressure in the transverse direction between the quasi-steady and unsteady calculations. (Propeller - (A))

$$K_t = 0.187, \quad \sigma_n = 1.55$$

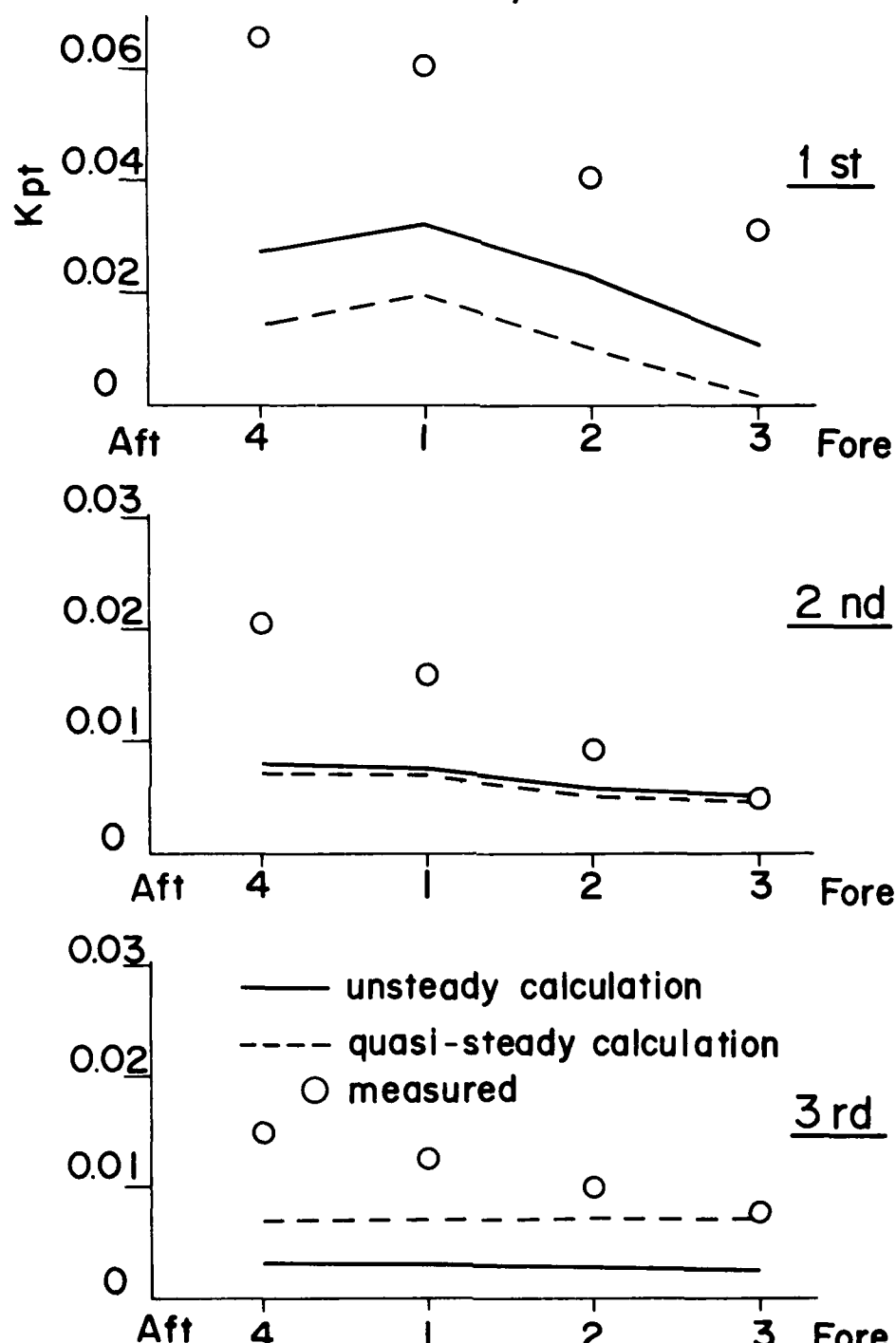


FIGURE 47

Comparison of the fluctuating pressure in the longitudinal direction between the quasi-steady and unsteady calculations. (Propeller - A)

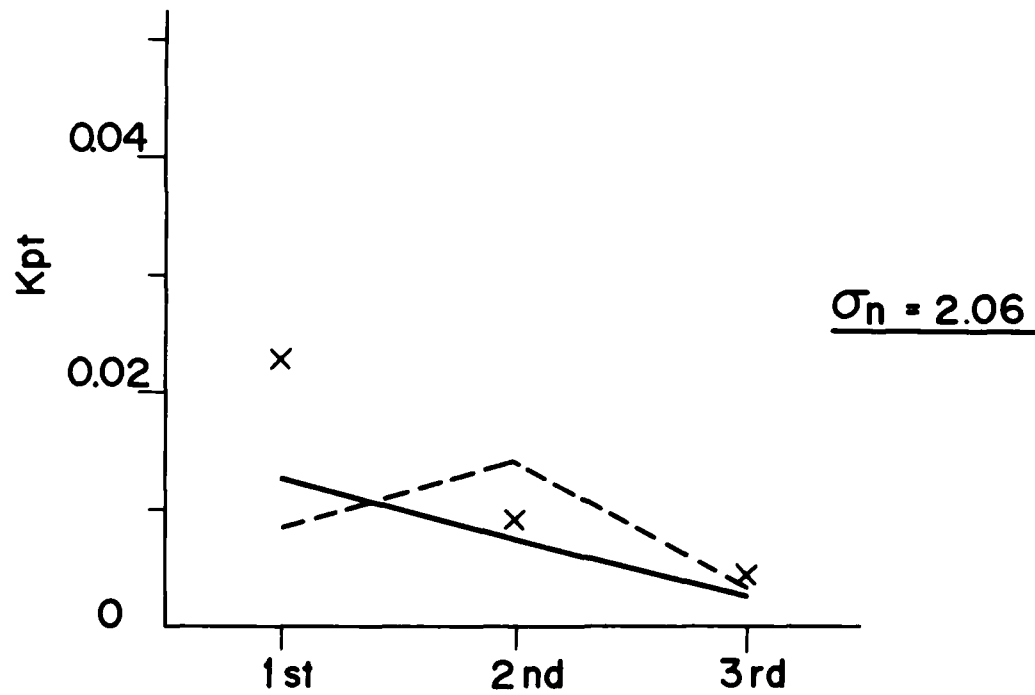
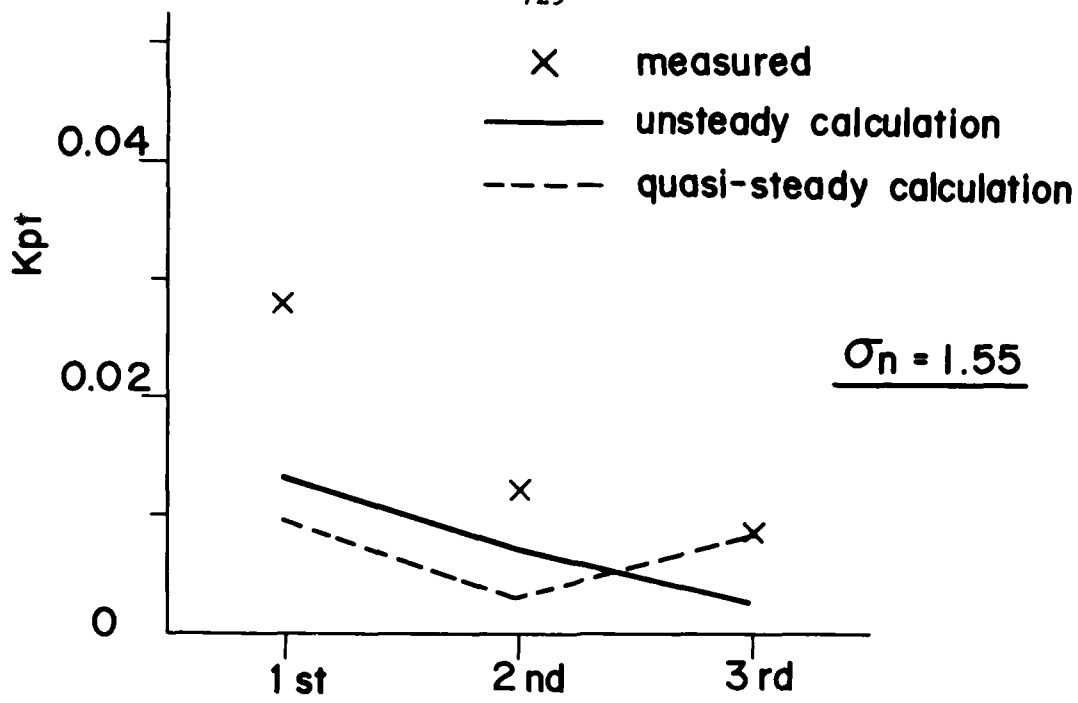


FIGURE 48

Comparison of the different order harmonic components of the fluctuating pressure between the quasi-steady and unsteady calculations. (Propeller -  $\textcircled{A}$ , station - 6)

## Discussion

J. Matusiak (Technical Research Centre of Finland)

This extension of the steady, two-dimensional cavity model resulting in a cavitation history being much closer to the observed on propellers is certainly an interesting and valuable result. I understand that the necessary data for the cavitation extent and volume computation you take from the results of a lifting-surface program. I presume that these results are produced in the form of the time-dependent spanwise distribution of load on a blade. Could you explain, how do you obtain the effective camber and angle of attack of the hydrofoil? Is it done as proposed by Kaplan et al. at the RINA Symposium on Propeller Induced Vibration, 1979, i.e., the camber is related to a steady load component, and the angle of attack includes only nonstationarity of load? If so, does your concept of the effective flat foil neglect the steady component of load when computing the cavitation, or do you calculate the instantaneous angle of attack from the total load?

The disagreement in the radial cavitation volume distributions obtained by the authors should be primarily attributed to the limitations of the two-dimensional approach and not to the inaccuracy of the quasi-steady theory as stated by the authors. The merging of sheet cavitation with the tip vortex cavitation is in my opinion responsible for the high cavitation volume at the blade-tip region. In other words, the cross-flow at the blade tip, not taken into account when applying two-dimensional approach, is the reason for the volume increase of cavitation at this region. It is generally known that the unsteadiness of flow decreases the cross-flow and thus has an opposite effect on the spanwise distribution of cavitation.

## Author's Reply

H. Isshiki (Hitachi Zosen Corporation)

The authors use the unsteady lifting-surface computer program developed by Dr. Koyama of the Ship Research Institute of Japan to calculate loading distributions under noncavitating conditions.

The equivalent foil section at every radial section is obtained by using the above-mentioned chordwise load distribution. Namely, the load distribution is substituted into the integral relation of a two-dimensional steady foil in a uniform flow that is usually understood as an integral equation to obtain the chordwise load distribution (or the vortex distribution) from the given shape of a foil centerplane, which is obtained by solving the above-mentioned integral relation for the given load distribution.

In Japan, this method is widely known as Sugai's Method. Dr. Sugai belongs to the Ship Research Institute of Japan and is an ITTC Propeller Committee member.

Your comment on the importance of the tip vortex is surely agreeable. Some researchers in Japan include the tip-vortex effect on the thickness of the sheet cavity by multiplying the thickness by a correction factor that is determined experimentally.

# The Numerical Prediction of Unsteady Sheet Cavitation on High Aspect Ratio Hydrofoils

Robert J. Van Houten  
Department of Ocean Engineering  
Massachusetts Institute of Technology

## ABSTRACT

The unsteady sheet cavitation of high aspect ratio hydrofoils is a problem of considerable interest in that it provides a simple model of the type of cavitation which can occur on propeller blades operating in a non-uniform ship wake. Its solution is complicated by the fact that the three-dimensionality of the flow field must be considered in computing the lowest order inner solution. The author separates the influence of the three-dimensional flow into two components. One component affects the mass-like resistance of the fluid to changes in the rate of change of local cavity volume. This component is included in the inner solution by proper selection of a source potential. The other component, which must be computed in an iterative manner, is shown to be small when the cavity extent is moderate.

The inner solution is solved in the time domain by direct numerical solution of the integral equations representing the linearized boundary conditions of the flow. Because the cavity length is allowed to vary from zero to several chord lengths, the solution is nonlinear in that a sinusoidal disturbance does not cause a sinusoidal response. Since nonlinear thickness effects cannot readily be incorporated in this theory, the analysis is restricted to foils of zero thickness.

Solutions of the inner problem are presented for a flat-plate foil at various aspect ratios, gust amplitudes, and reduced frequencies. In addition, the convergence of the iterative procedure for computing spanwise interactions is demonstrated.

## NOMENCLATURE

AR	aspect ratio
c	chord
C	constant in source potential



$C_L = \frac{L}{1/2 \rho U_c^2}$	lift coefficient
$C_M = \frac{M}{1/2 \rho U_c^2 l^2}$	moment coefficient
$C_p = \frac{p - p_\infty}{1/2 \rho U^2}$	pressure coefficient
$g_n$	coefficient of expansion of outer potential
$k$	spanwise wave number
$k_r$	reduced wave number of gust
$K_n$	nth order modified Bessel function of second kind
$l$	cavity length
$L$	lift force
$M$	moment about leading edge
$n$	number of discrete vortices along chord
$n_c$	number of sources representing cavity
$p$	pressure
$p_c$	cavity pressure
$p_i$	interaction pressure
$q$	source distribution
$Q$	total source strength
$Q_{i,j}$	strength of ith source at jth time step
$r$	radial coordinate, non-dimensionalized on span
$R$	radial coordinate, non-dimensionalized on chord
$s$	span of hydrofoil
$t$	time
$U$	free stream speed

$v$	vertical gust velocity
$x, y, z$	cartesian coordinates (see Figure 1)
$x_{Q_i}, x_{\Gamma_i}$	positions of $i$ th source, vortex
$\Delta x_{Q_i}, \Delta x_{\Gamma_i}$	length of foil represented by $i$ th source, vortex
$\alpha$	angle of attack
$\alpha_a$	amplitude of gust-induced angle of attack
$\alpha_m$	mean angle of attack
$\gamma$	vorticity distribution; Euler's constant
$\Gamma$	total bound vorticity
$\Gamma_{i,j}$	strength of $i$ th vortex at $j$ th time step
$\Delta t$	length of time step
$\epsilon$	inverse aspect ratio
$\zeta$	dummy spanwise coordinate
$\eta$	camber coordinate
$\theta$	transformed position along chord
$\xi$	dummy streamwise coordinate
$\rho$	fluid density
$\sigma = \frac{p_\infty - p_c}{1/2 \rho U^2}$	cavitation number
$\tau$	cavity thickness
$\phi$	perturbation velocity potential
$\Phi$	total velocity potential
$\chi$	solution vector
$\omega$	frequency of unsteady flow

## INTRODUCTION

The unsteady cavitation of high aspect ratio hydrofoils is a problem which has been studied for many years, but which has yet to yield to a definitive solution. Although early attempts at solving this problem idealized it to one of two dimensions, there exists a fundamental difference between two-dimensional flow and a three-dimensional flow of high aspect ratio, namely the fact that in two-dimensional flow a non-constant growth rate of the cavity volume produces an infinite pressure at infinity. Benjamin (1964) pointed out the fact that the singular behavior at infinity matches with the behavior of a three-dimensional outer potential at small distances from the foil. Benjamin went on to infer that in the solution of the inner problem, one would have to take the time-varying volume velocity to be a completely arbitrary function, imposed by the outer solution. This conclusion ruled out the use of matched asymptotic expansions, and led the way to the use of fully three-dimensional theories to treat the problem. These theories, however, generally treated the supercavitating case only and assumed that variations in cavity length were small compared to the mean cavity length. This simplification allowed the problem to be treated in the frequency domain.

A relatively recent impetus to research in the field of unsteady hydrofoil cavitation was the recognition that marine propellers operating in non-uniform wake fields can experience transient cavitation and cause severe hull vibration. Due to the transient nature of this cavitation, frequency domain solutions could not be applied successfully. Instead, a theory was needed which allowed for significant variations in cavity extent. There have been numerous attempts at formulating such a theory, using a variety of theoretical approaches. Since marine propeller blades are generally of moderate aspect ratio, the three-dimensional nature of the flow must be considered. Some of the approaches used, however, have incorporated some elements of two-dimensional and high aspect ratio theories. As a result, the question of unsteady high aspect ratio hydrofoil cavitation is still a research topic of current interest.

Tulin and Hsu (1977) formulated a theory for steady, "short", leading edge cavitation on two-dimensional foils with thickness, in which the perturbation due to the cavitation was considered to be a small disturbance compared to the steady, non-cavitating flow. This non-cavitating flow was found using non-linear theory and therefore accurately described the behavior of the flow in the leading edge region. Tulin and Hsu showed that the effect of thickness is to reduce significantly the extent of cavitation. This result would presumably not follow from a completely linear model, since in that case the contribution of thickness would be to reduce the pressure everywhere on the suction surface, and thereby increase the extent of cavitation. However, this matter is clouded by the possible role of viscous effects, which may delay the start of sheet cavitation until separation of the laminar boundary layer (Arakeri, 1975), or transition

to a turbulent boundary layer (Kuiper, 1979). This delay of cavitation inception may well cause the cavity to begin in a region where the surface pressure is not badly approximated by linear theory. It is, therefore, quite possible that the effect of thickness on cavitation extent is exaggerated by potential flow theory. In any event, Tulin and Hsu postulated that in those cases where the cavity was of high aspect ratio, their two-dimensional results could be applied to a three-dimensional non-cavitating flow, such as that provided by a propeller lifting surface program.

In 1980, Tulin extended this two-dimensional theory to the unsteady case. By restricting his analysis to thin wings of moderate aspect ratios, where the product of the reduced frequency and the natural log of the aspect ratio is of order one, Tulin concluded that the boundary conditions of the unsteady flow are, to leading order, identical to those of the steady flow, with the exception of the closure condition. In effect, Tulin's conclusion was that under the assumptions he made, added-mass type pressure terms, which are infinite in the two-dimensional limit, are negligible compared with the steady terms at aspect ratios such that  $k_L \ln(AR) = O(1)$ . The role of the unsteady closure condition was seen as causing growing cavities to be thinner than steady cavities of the same length, and collapsing cavities to be thicker, particularly towards the rear.

For the case of a flat-plate hydrofoil Tulin generalized the curve of cavity length versus  $C_L/\sigma$  (Acosta, 1955 and Geurst, 1959) to yield a family of curves, each of which corresponded to a particular growth rate. He went on to derive some general results with regard to unsteady cavitation, such as:

- A) The instability of the upper branch of the cavity length vs  $C_L/\sigma$  curve for flat plate foils. Cavities longer than the equilibrium condition were shown to grow and those shorter were shown to collapse.
- B) In the case of periodic loading,
  - 1) The hysteresis apparent in the trajectory of cavity length versus  $C_L/\sigma$ ,
  - 2) The phase lag between cavity length and lift coefficient,
  - 3) The inverse relationship between maximum cavity length and reduced frequency,
  - 4) The rapidity of cavity collapse compared to cavity growth, and
  - 5) The possibility that part of the cavity will be torn off as the remainder of the cavity collapses toward the leading edge.

Stern (1980) also divided the problem into a three-dimensional outer problem and a more or less two-dimensional inner problem. He, however, included the kinematic effects of the cavity in the outer solution, and satisfied only dynamic boundary conditions in the inner problem. These dynamic boundary conditions included those unsteady terms which Tulin concluded could be neglected. Stern's inner solution

modeled the cavity as a semi-ellipse on a ground plane, whose semi-axes and position were determined by satisfying the dynamic boundary condition in a least-squares sense. He matched his inner solution with that of an assumed outer solution consisting of a three-dimensional line source of varying strength, as was first demonstrated by Benjamin.

Stern obtained solutions to simple flows which demonstrated such observed behavior as:

- A) The pullback of the cavity from the leading edge of the foil, and
- B) The thickening of the cavity at collapse.

Stern also found that in obtaining a steady solution as an initial value problem the cavity would oscillate about an equilibrium condition, and he proposed that these oscillations were physical rather than an artifact of his solution procedure. If this, in fact, is the case, this instability would be intrinsically different from that of Tulin, whereby any oscillations in steady flow would be accompanied by a tearing off of part of the cavity.

Stern (1981) compared results of this theory against the experimental results of Shen and Peterson (1978). The predicted cavity lengths were significantly less than those observed in both steady and unsteady flow. The oscillations which were apparent in simpler flows were once again found in these comparisons. Stern proposed that their presence indicated the occurrence of cloud cavitation, and concurrent cavitation noise.

Peters, Goodman, and Breslin (1980) considered the problem of a high aspect ratio cavitating flat plate foil moving through an unsteady gust. They took the classical approach of expanding the flow quantities in powers of the inverse aspect ratio,  $\epsilon$ . Their conclusions were that the second time derivative of the cavity cross-sectional area was of at least second order in  $\epsilon$ . In reaching this conclusion they made two assumptions which conflict with the work reported here:

- 1) They assume that the lowest order term of the outer velocity potential is of order  $\epsilon$ .
- 2) They imposed a condition on the inner problem that the pressure decay to zero far from the foil, rather than that it be matched to the inner expansion of the outer problem.

Thus Tulin, Stern, and Peters, et al. are in direct disagreement on a very essential question; namely, the influence of aspect ratio on the time-variability of source strength. Tulin finds that for moderate aspect ratio the effect is nil. Peters, et al., find that the influence is quite drastic, and even go so far as to speculate that a propeller blade of high aspect ratio may cause less severe hull vibration than one of lower aspect ratio. Finally, Stern finds that the effect of aspect ratio is important, but not of overriding significance.

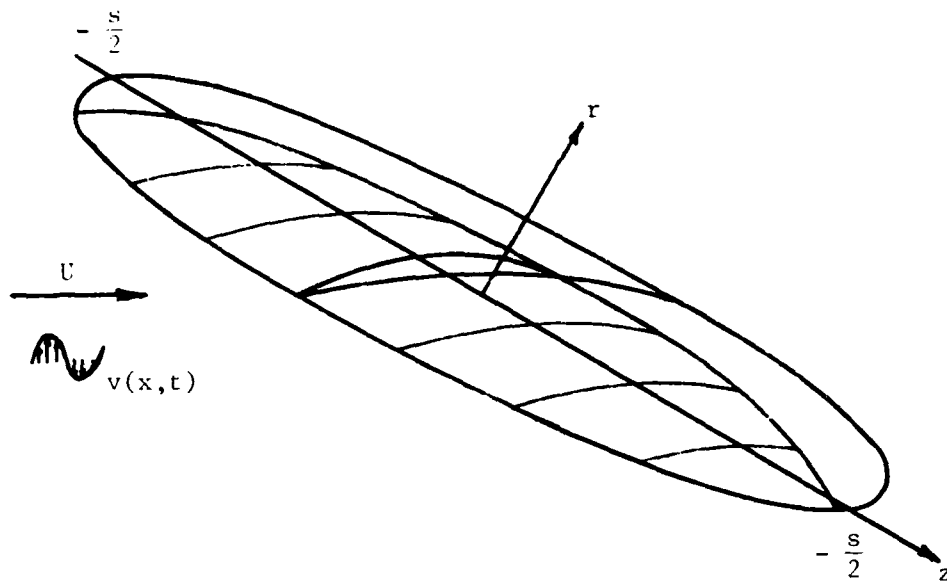
The present author's association with the problem of unsteady hydrofoil cavitation was in developing a two-dimensional unsteady cavity numerical model which was generalized to the case of a propeller operating in a non-uniform wake by Lee (1980). Lee's work was completely three-dimensional, and did not involve any aspect ratio assumption. However, if one matches the two-dimensional inner solution to a three-dimensional outer flow, as was done by Benjamin and later by Stern, the influence of aspect ratio on cavity volume variations can be readily determined by this model. Although the proposed method utilizes matching ideas similar to those of Stern, its treatment of the inner flow is completely different. The dynamic and kinematic boundary conditions are solved simultaneously, rather than sequentially, and no assumptions are made as to the shape of the cavity, other than that it starts at the leading edge of the foil. The proposed method is, however, a linear theory in that the disturbance of the streaming flow due to both foil and cavity is considered small. In this sense it probably does not properly account for foil thickness. However, the possible role of viscous effects makes the true role of thickness poorly understood at present, and it is not clear that a nonlinear, potential flow model such as that used by Tulin or Stern is a real improvement. In any event, the present work is restricted to foils of zero thickness, where these considerations are not relevant.

#### THEORETICAL FORMULATION

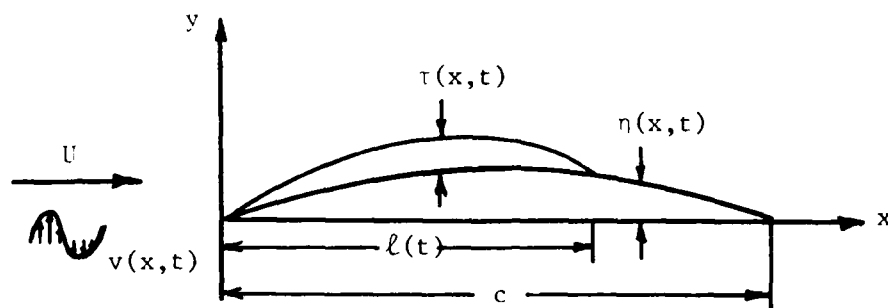
An early attempt at solving unsteady cavity flow problems by numerical lifting surface techniques was by Jiang and Leehey (1977). They primarily addressed the case of unsteady supercavities on three-dimensional hydrofoils, and compared their results with experimental data. Although they also presented two-dimensional results these did not explicitly include the effect of aspect ratio. Although their method allowed large variations of cavity length, and was solved in the time domain, the results they presented were for cases where the variation in cavity length was small compared to the mean cavity length. The work reported here is an extension of the method of Jiang and Leehey to partially cavitating flows where changes in cavity length are of the same order of magnitude as the mean cavity length. Only high aspect ratio foils will be considered, since the three-dimensional extension is straightforward and has been presented in the case of propellers by Lee (1980). The flow situation is sketched in Figure 1.

#### The Inner Solution

The flow is assumed to be inviscid and irrotational, with the exception of a wake of infinitesimal thickness and with the exception of any incident gust. The streaming flow  $U$  is assumed to be constant, and is taken as unity. The chord  $c$  is taken to be of unit length. The forms of unsteadiness which are considered are gust velocities normal to the free stream,  $v(x,t)$  and transverse motions of the foil,



High Aspect Ratio Cavitating Hydrofoil



Section Through Hydrofoil

FIGURE 1

such as pitch and heave. Reduced frequencies  $\frac{U}{2V}$  are assumed to be of order 1. The conditions on the inner solution are the following:

- A) On the cavity surface the pressure must be equal to the cavity pressure, or in non-dimensional terms,

$$C_p = -\sigma(t) \quad (1)$$

where  $C_p$  is the local pressure coefficient and  $\sigma$  is the cavitation number,  $\sigma$  which we have allowed to vary with time. From Bernoulli's equation, we have

$$\phi_t + 1/2 |\nabla \phi|^2 = 1/2(\sigma(t) + 1) \quad (2)$$

where  $\phi(x,y,t)$  is the total velocity potential. Here we have ignored hydrostatic effects.

- B) On the wetted portions of the foil, the flow must be tangent to the foil, or

$$\nabla \phi \cdot \hat{n} + v(x,t)n_j = V_n \quad (3)$$

where  $\hat{n}$  represents the unit normal vector, and  $V_n$  is the component of foil motion in the direction of  $\hat{n}$ .

- C) Kelvin's condition must be satisfied, so the total circulation around the foil and wake must be zero.  
D) A Kutta condition must be satisfied at the trailing edge of the foil, or

$$|\nabla \phi(1,0,t)| < \infty \quad (4)$$

- E) There must be no pressure difference across the wake.  
F) At large radial distances from the foil, the potential must be matched with that of the outer problem.

In order to linearize the problem, the angle of attack,  $\alpha(x,t)$ , and cavitation number,  $\sigma$ , are assumed to be small and the cavity is assumed to be thin. With these assumptions, the perturbation velocities will be small compared to unity. For convenience, the velocity potential can be expressed in terms of a perturbation potential,  $\phi(x,y,t)$ :

$$\phi(x,y,t) = x + \phi(x,y,t) \quad (5)$$

Consistent with these assumptions, the flow can be represented as a



distribution of source strength  $q(x,t)$  over the projection of the cavity on the  $x$  axis, and a distribution of vortex strength  $\gamma(x,t)$  over the projection of the foil and its wake. The perturbation potential can therefore be expressed as:

$$\begin{aligned} \phi(x,y,t) = & \frac{1}{2\pi} \int_0^{\ell(t)} q(\xi) \{ \ell \sqrt{(x-\xi)^2 + y^2} + C \} d\xi + \\ & \frac{1}{2\pi} \int_0^{\infty} \gamma(\xi) \arctan \left( \frac{y}{x-\xi} \right) d\xi - \frac{1}{\rho} \int_0^t p_i(t) dt \end{aligned} \quad (6)$$

Note that in effect an unknown function of time has been added to  $\phi$  in order to match correctly with the outer flow. This function of time has been arbitrarily divided into two parts: One which is proportional to total source strength of the inner flow,  $Q(t)$

$$\frac{C}{2\pi} \int_0^{\ell(t)} q(\xi) d\xi = \frac{CQ(t)}{2\pi} \quad (7)$$

and the remainder, which is expressed in terms of an interaction pressure,  $p_i(t)$ , which is determined by the outer flow. These will be found by matching to the outer solution.

Consistent with the above linearization, the boundary conditions may be imposed on the  $x$  axis rather than the exact foil and cavity surface. The linearized pressure condition becomes:

$$\phi_x(x,0+,t) + \phi_t(x,0+,t) = \sigma(t)/2 \quad (8)$$

In terms of the singularity distributions, this becomes:

$$\begin{aligned} -\frac{\gamma(x,t)}{2} - \frac{1}{2} \frac{\partial}{\partial t} \int_0^x \gamma(\xi,t) d\xi + \frac{1}{2\pi} \int_0^{\ell(t)} \frac{q(\xi,t)}{x-\xi} d\xi \\ + \frac{1}{2\pi} \frac{\partial}{\partial t} \int_0^{\ell(t)} q(\xi,t) \{ \ell |x-\xi| + C \} d\xi = \frac{\sigma(t)}{2} + \frac{p_i(t)}{\rho} \end{aligned} \quad (9)$$

$0 \leq x \leq \ell(t)$

The linearized tangency condition becomes:

$$\frac{\partial \phi}{\partial y} = \frac{\partial \eta}{\partial x} + \frac{\partial \eta}{\partial t} - v(x,t) \quad (10)$$

Here  $\eta(x,t)$  is the camberline of the foil. In terms of the singularity distributions this becomes:

$$-\frac{q(x,t)}{2} + \frac{1}{2\pi} \int_0^x \frac{\gamma(\xi,t)}{x-\xi} d\xi = \frac{\partial \eta}{\partial x} + \frac{\partial \eta}{\partial t} - v(x,t) \quad (11)$$

$$0 \leq x \leq 1$$

Since the cavity is represented solely as a source distribution, the closure of the cavity must be explicitly stated, as  $\tau(\ell) = 0$ , where  $\tau(x)$  represents the thickness of the cavity. This can be written in terms of the source strength by using the relationship:

$$q(x,t) = \tau_x(x,t) + \tau_t(x,t) \quad (12)$$

$\tau(x,t)$  thus satisfies the wave equation, and can be written:

$$\tau(x,t) = \int_0^x q(\xi, t-x+\xi) d\xi \quad (13)$$

so that the closure condition becomes

$$\int_0^{\ell(t)} q(\xi, t-\ell(t)+\xi) d\xi = 0 \quad (14)$$

The closure condition appropriate for steady flow is:

$$\int_0^{\ell} q(\xi,t) d\xi = 0 \quad (15)$$

The Kutta condition requires continuity of vorticity at the trailing edge of the foil. In addition, Kelvin's condition requires that the total vorticity on the foil and in the wake be zero. Vorticity must therefore be shed at the trailing edge as the bound circulation changes with time. In order to satisfy the condition that there be no pressure jump across the wake, the shed vorticity must be convected downstream at the free stream velocity. If the cavity is a supercavity, this wake condition assures the satisfaction of Equation 9 on the lower surface as well as the upper one.

It should be noted that due to the fact that the pressure boundary condition is applied on a variable length  $\ell(t)$ , the problem is inherently nonlinear. The technique used to solve it is to first solve an appropriate steady problem as an initial condition, and then to march out the solution with time.

### The Outer Solution

In order to find the correct values of  $C$  and  $p_i(t)$  in Equation 9, one must match the inner potential to the outer one. Since the critical element of this matching is the potential due to time dependent source strength, only the source-like outer potential will be dealt with. The following analysis follows Benjamin (1964).

The outer perturbation potential due to a cavitating hydrofoil of high aspect ratio (neglecting the bound and trailing vortex systems) can in general be expressed as a harmonic series:

$$\phi_{out}(z, r, t) = \sum_{n=0}^{\infty} \int_{-\infty}^{\infty} e^{ikz \pm in\tau} K_n(kr) g_n(k, t) dk \quad (16)$$

where  $r$  and  $z$  are the radial and spanwise coordinates, respectively, non-dimensionalized on the span. The axially symmetric component is:

$$\phi_{out}(z, r, t) = \int_{-\infty}^{\infty} e^{ikz} K_0(kr) g_0(k, t) dk \quad (17)$$

If the spanwise variations in source strength have a length scale on the order of the span,  $g_0(k)$  will differ significantly from zero only in the region  $k < 2\pi$  or so. In the matching region  $r \ll 1$  and  $kr \ll 1$ , so this potential can be expanded as follows:

$$\phi_{out} = \int_{-\infty}^{\infty} e^{ikz} \left\{ -\ln\left(\frac{1}{2} kr\right) - \gamma + O(r^2) \right\} g_0(k, t) dk \quad (18)$$

where  $\gamma$  is Euler's constant. Letting  $\epsilon$  be the inverse of the aspect ratio, one can relate the inner variable  $R = \sqrt{\frac{x^2}{2} + \frac{y^2}{2}}$  to  $r$  by the relationship  $R = r/\epsilon$ . Furthermore, a new outer potential, expressed in terms of inner variables, is defined as  $\phi_{out}^* = \phi_{out}/\epsilon$ . Substituting these new variables in Equation 18, one gets:

$$\phi_{out}^* = -\frac{1}{\epsilon} \int_{-\infty}^{\infty} e^{ikz} g_0(k, t) \ln(\epsilon R) dk = -\frac{1}{\epsilon} \int_{-\infty}^{\infty} e^{ikz} \left[ \ln \frac{k}{2} + \gamma + O(\epsilon^2) \right] g_0(k, t) dk \quad (19)$$

This potential must be matched with the symmetrical portion of the inner potential at large  $R$ , which is

$$\phi_{inner} = \frac{Q(z, t)}{2\pi} [\ln R + C] - \frac{1}{\rho} \int_0^t p_i(z, t) dt \quad (20)$$

Matching, we get

$$Q(z,t) = -\frac{2\pi}{\epsilon} \int_{-\infty}^{\infty} e^{ikz} g_0(k,t) dk \quad (21)$$

$$C = \ell n \epsilon \quad (22)$$

$$\frac{p_i(z,t)}{\rho} = \frac{1}{\epsilon} \frac{\partial}{\partial t} \int_{-\infty}^{\infty} e^{ikz} [\ell n \frac{k}{2} + \gamma] g_0(k,t) dk \quad (23)$$

or, since

$$g_0(k,t) = -\frac{\epsilon}{4\pi^2} \int_{-\infty}^{\infty} Q(z,t) e^{-ikz} dz \quad (24)$$

$$\frac{p_i(z,t)}{\rho} = -\frac{1}{4\pi^2} \int_{-\infty}^{\infty} \int_{-\infty}^{\infty} Q_t(\zeta,t) e^{-ik(\zeta-z)} [\ell n \frac{k}{2} + \gamma] d\zeta dk \quad (25)$$

#### The Magnitude of the interaction pressure

In Equations 6 and 9, the contribution of the three-dimensional flow was broken down into two components, one of which was proportional to local source strength, and the other of which depended on the solution at other spanwise positions along the foil. The former component can be found as part of the essentially two-dimensional inner solution. This decomposition can be exploited if the remaining term is small compared to the terms obtainable from the two-dimensional solution.

In order that the term in Equation 9 containing  $C$  be of order one in  $\epsilon$ , and thereby balance the other terms, one must have:

$$\frac{C}{2\pi} \frac{dQ}{dt} = O(1) \quad (26)$$

or, since  $C = \ell n \epsilon$ ,

$$Q \sim [\ell n \epsilon]^{-1} \quad \text{and} \quad g_0 \sim \frac{\epsilon}{\ell n \epsilon} \quad (27)$$

This is a fundamentally different result than was obtained by Peters, et al., who assumed that the lowest order of  $g_0$  allowable was of order  $\epsilon$ , and then proved that that term was in fact zero.

Since  $Q \sim [\ell n \epsilon]^{-1}$ ,  $p_i(z,t)/\rho$  is likewise of that order. This is a disappointing result, since it is unlikely that  $\epsilon$  would, in any practical situation, be so small that  $[\ell n \epsilon]^{-1}$  would be

convincingly small. Presumably, this result led Benjamin to his conclusion that the flow is essentially three-dimensional. However, under certain circumstances,  $p_i(z,t)/\rho$  can be shown to be a small quantity compared to other terms in the pressure equation, such as  $\sigma$ .

For simplicity, consider a cavitating flat plate in a harmonic disturbance, where the cavity volume is essentially zero during some portion of the cycle. The total source strength at any time is the time rate of change of the cavity volume. The maximum volume will be on the order of:

$$\text{VOL} \sim \alpha_0 f\left(\frac{\alpha_0}{\sigma}\right) \quad (28)$$

where  $\alpha_0$  is a representative angle of attack. Here the fact that  $\alpha/\sigma$  is a similarity parameter of the flat plate solution has been used. For simplicity, the dependence of  $f$  on the type of the unsteadiness has been suppressed. The total source strength is then of order

$$Q \sim \alpha_0 \omega f\left(\frac{\alpha_0}{\sigma}\right) \quad (29)$$

The time derivative of  $Q$  is of order

$$\dot{Q} \sim \alpha_0 \omega^2 f\left(\frac{\alpha_0}{\sigma}\right) \quad (30)$$

From Equation 25, one finds that likewise

$$\frac{p_i}{\rho} \sim \alpha_0 \omega^2 f\left(\frac{\alpha_0}{\sigma}\right) \quad (31)$$

The ratio of this quantity to  $\sigma$  is

$$\frac{p_i/\rho}{\sigma} \sim \omega^2 \frac{\alpha_0}{\sigma} f\left(\frac{\alpha_0}{\sigma}\right) \quad (32)$$

Since  $p_i/\rho$  acts as a time-dependent change in  $\sigma$ , this ratio can be expressed as

$$\frac{\Delta\sigma}{\sigma} \sim - \frac{\Delta \frac{\alpha_0}{\sigma}}{\frac{\alpha_0}{\sigma}} \sim \omega^2 \frac{\alpha_0}{\sigma} f\left(\frac{\alpha_0}{\sigma}\right) \quad (33)$$

Although the exact form of  $f(\alpha_0/\sigma)$  will depend on the nature of the motion, it will in general be monotonically increasing with  $\alpha_0/\sigma$ . In the case of steady flow, its behavior for small values of  $\alpha_0/\sigma$  was shown by Guerst (1959) to be:

$$f\left(\frac{\alpha_0}{\sigma}\right) \sim 160\pi \left(\frac{\alpha_0}{\sigma}\right)^3 + O\left(\frac{\alpha_0}{\sigma}\right)^4 + \dots \quad (34)$$

If  $f(u_0/\sigma)$  is in general cubic for small  $u_0/\sigma$ , we have

$$\frac{\Delta \frac{u_0}{\sigma}}{\frac{u_0}{\sigma}} \sim \left( \frac{u_0}{\sigma} \right)^4 \quad (35)$$

and the change in the local value of  $u_0/\sigma$  due to the interaction pressure will vary as the fifth power of  $u_0/\sigma$ . Therefore, for sufficiently small values of  $u_0/\sigma$ , the magnitude of the interaction pressure should be fairly small. In fact, since in the steady case partial cavitation occurs for  $u/\sigma$  less than .1 or so, it is not unreasonable to expect that so long as the cavity is shorter than a chord length or so, the interaction pressure  $p_i(z,t)/\rho$  will be small compared to  $\sigma$ .

Note that the smallness of  $p_i(z,t)$  is not equivalent to saying that three-dimensional effects are small. Rather it is equivalent to saying that the influence of the aspect ratio on the inner solution is mainly through the determination of the proper form of the source potential, which has been shown to be, for a source at the origin,

$$\phi_{\text{source}} = \frac{q}{2\pi} \ln r \quad (36)$$

where  $r$  is non-dimensionalized on the span of the foil, rather than the chord.

#### An Iterative Solution Procedure

In those cases where  $p_i(z,t)/\rho$  is expected to be small compared with  $\sigma$ , an iterative procedure suggests itself. The interaction pressure  $p_i(z,t)$  can first be set equal to zero, and the inner solution, and specifically the total source strength  $Q(z,t)$ , found at various spanwise positions. Equation 25 can then be used to find a first approximation to  $p_i(z,t)/\rho$ . This estimate of  $p_i(z,t)/\rho$  can be added to Equation 9 and the inner solution again found. This procedure can be repeated until  $Q(z,t)$  converges to an asymptotic value. The resulting solution is the correct inner solution to zeroth order in  $\epsilon$ .

For a rectangular planform with constant section characteristics,  $Q(t)$  as first calculated will be the same for all sections. In this case, one can compute the value of  $p_i/\rho$  as a function of  $z$  due to unit source strength per unit time per unit length along the span:

$$\frac{p_i(z)}{\rho} = \frac{1}{4\pi} \ln(1 - 4z^2) \quad -\frac{1}{2} < z < \frac{1}{2} \quad (37)$$

This function is sketched in Figure 2. Since its value is zero at  $z=0$ , it can be seen that the initial solution, with  $p_i(z,t) = 0$ , is based on the assumption that the section in question is the mid-span section of a hypothetical rectangular hydrofoil whose flow characteristics are

constant along its span.

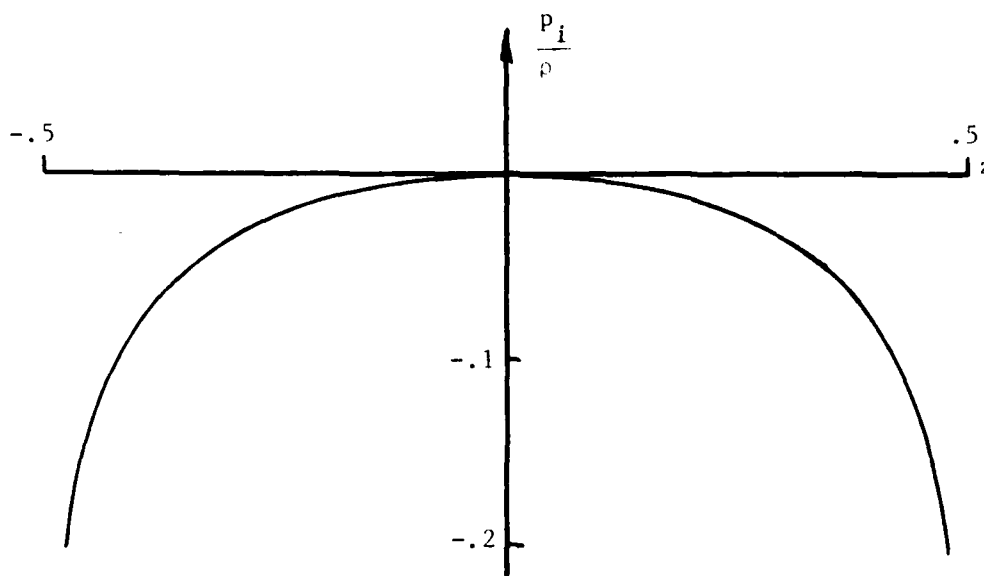


FIGURE 2. Interaction pressure due to unit  $Q_t$  at all spanwise locations

If the planform is other than rectangular, such a simple calculation cannot be made, since the distribution of source strength will not follow the shape of the planform. The tips of the hydrofoil will operate at a different reduced frequency from the rest of the hydrofoil, so the cavitation of the tips will differ from that of the central portion of the hydrofoil.

It is convenient in the case of non-rectangular planforms to take the local chord as unity and to take the value of  $C$  to be the same (in "local" units) for all sections. This results in an extra term being added to  $\frac{p_i(z,t)}{c}$ , so that Equation 25 becomes:

$$\frac{p_i(z,t)}{c} = -\frac{1}{4\pi^2} \int_{-\infty}^{\infty} \int_{-\infty}^{\infty} Q_t(\zeta,t) e^{-ik(\zeta-z)} \left[ \ln \frac{k}{2} + \gamma + \ln \frac{c}{c^*} \right] d\zeta dk \quad (38)$$

where  $c^*$  is the midspan chord.

For reduced frequencies of order unity, James (1975) showed that unsteady downwash corrections to the inner flow are of second order in  $\epsilon$ , so that only the mean downwash need be included to have a solution which is accurate to order  $\epsilon$ . Due to the non-linearity of the inner solution, the complete solution would have to be re-calculated with the mean downwash from the zeroth order solution included.

## NUMERICAL SOLUTION

### Discretization

In order to obtain a numerical solution, the source and vorticity distributions are represented by discrete sources  $Q_i$  and vortices  $\Gamma_i$  on the foil and in the wake. The positions of these singularities are fixed for all time, but the number of sources allowed to be non-zero will vary as the cavity length varies. The advantage of this method is that matrix inversion need be done only once for each discrete cavity length. Since the integral Equations 9 and 11 require the local contribution from one distribution and the Cauchy principal-value integral of the other distribution, the discrete singularities are alternated, and the tangency condition is satisfied at the location of a source,  $x_{Q_i}$ , and the pressure condition satisfied at the location of a vortex,  $x_{\Gamma_i}$ . The portion of the foil whose vorticity is concentrated  $\Gamma_i$  into  $\Gamma_i$  is that which lies between the two adjacent sources, or  $\Delta x_{\Gamma_i} = x_{Q_i} - x_{Q_{i-1}}$ . Similarly, the length of the element whose  $Q_i$  source strength is concentrated in  $Q_i$  is  $\Delta x_{Q_i} = x_{\Gamma_{i+1}} - x_{\Gamma_i}$ .

The time domain is divided into time steps, of length  $\Delta t$ , so that the strength of the discrete sources and vortices are found at specific instants of time. Let  $n$  represent the number of vortices on the foil, and  $n_c$  represent the number of sources over which the cavity extends at  $c_j$  time step  $j$ . Furthermore, let the  $i$ th source and vortex strengths at the  $j$ th time step be represented by  $Q_{i,j}$  and  $\Gamma_{i,j}$ , respectively. If time derivatives are calculated by backwards differencing, Equations 9 and 11 can be approximated as follows:



$$\begin{aligned}
& -\frac{\Gamma_{i,j}}{2\Delta x_{\Gamma_i}} - \frac{1}{2\Delta t} \sum_{k=1}^{i-1} \Gamma_{k,j} + \frac{1}{2\pi} \sum_{k=1}^{n_c} \frac{Q_{k,j}}{x_{\Gamma_i} - x_{Q_k}} + \frac{1}{2\pi\Delta t} \sum_{k=1}^{n_c} Q_{k,j} [\ln|x_{\Gamma_i} - x_{Q_k}| + C] \\
& = \frac{j}{2} - \frac{1}{2\Delta t} \sum_{k=1}^{i-1} \Gamma_{k,j-1} + \frac{1}{2\pi\Delta t} \sum_{k=1}^{n_c} Q_{k,j-1} [\ln|x_{\Gamma_i} - x_{Q_k}| + C] + \frac{p_j}{\rho} \quad (39)
\end{aligned}$$

$$1 \leq i \leq n_c$$

$$\begin{aligned}
& -\frac{Q_{i,j}}{2\Delta x_{Q_i}} + \frac{1}{2\pi} \sum_{k=0}^n \frac{\Gamma_{k,j}}{x_{Q_i} - x_{\Gamma_k}} = \frac{\eta_i - \eta_{i-j}}{\Delta x_{Q_i}} + \frac{\partial \eta_i}{\partial t} - v_{i,j} - \frac{1}{2\pi} \sum_{k=n+1}^{\infty} \frac{\Gamma_{k,j}}{x_{Q_i} - x_{\Gamma_k}} \\
& \quad 0 \leq i \leq n \quad (40)
\end{aligned}$$

Here  $p_j$  represents the interaction pressure at time step  $j$  and  $v_{i,j}$  is the local, instantaneous gust velocity. The integral of vorticity from the leading edge to a pressure collocation point does not include vorticity due to the vortex at the collocation point. This interpretation is consistent with the backward differencing procedure, since the first two terms on the left-hand side of the pressure equation, which represent the jump in pressure across the  $x$ -axis, will be identically zero in the wake when the equation is discretized in this way.

The closure condition as given in Equation 14 is not very convenient for numerical computation. Instead, Equation 12 can be approximated by:

$$\frac{Q_{i,j}}{\Delta x_{Q_i}} = \frac{\tau_{i,j} - \tau_{i-1,j}}{\Delta x_{Q_i}} + \frac{\tau_{i-1,j} - \tau_{i-1,j-1}}{\Delta t} \quad (41)$$

Here  $\tau_{i,j}$  represents the thickness of the cavity at the position of the  $(i+1)$ th vortex, at the  $j$ th time step. Using this difference equation, and the initial condition  $\tau_{0,j} = 0$ , the closure condition  $\tau_{n_c,j} = 0$  can be approximated in terms of the set  $\tau_{i,j-1}$ ,  $i = 0, n_c$ , which are known at time step  $j$ , and the set  $Q_{i,j}$ ,  $i = 1, n_c$ , which are unknown. The result is:

$$\sum_{i=1}^{n_c} Q_{i,j} \prod_{k=i+1}^{n_c} \left(1 - \frac{\Delta x_{Q_k}}{\Delta t}\right) = \sum_{i=1}^{n_c-1} \tau_{i,j-1} \frac{\Delta x_{Q_{i+1}}}{\Delta t} \prod_{i=2}^{n_c} \left(1 - \frac{\Delta x_{Q_k}}{\Delta t}\right) \quad (42)$$

If  $\Delta t = \Delta x / Q_{n_c}$ , Equation 41 becomes simply:

$$Q_{n_c, j} = - \tau_{n_c - 1, j - 1} \quad (43)$$

when the cavity is shrinking, the cavity source strength may be non-zero in elements which lie downstream of the cavity termination at the present time step. The magnitudes of these sources may be obtained from Equation 41 as:

$$Q_{i, j} = - \tau_{i - 1, j - 1} \cdot \left( \frac{\Delta x Q_i}{\Delta t} \right) \quad (44)$$

The Kutta condition is not explicitly imposed on the solution. James (1972) found that for fully wetted, steady flow, with constant spacing of elements over the chord of the foil, and with vortices placed at the quarter chord positions of each element and collocation points placed at the three-quarter chord positions, the Kutta condition was automatically satisfied in the case of parabolic camber lines at an angle of attack. Although no equivalent work has been done in the case of unsteady flows, it is expected that the Kutta condition will at least be approximately satisfied implicitly. In any event, the solution to the problem as posed is unique without the imposition of a Kutta condition.

Kelvin's condition of constant circulation is met by requiring the sum of all the vortices to be zero:

$$\sum_{\text{all } i} \Gamma_{i, j} = 0 \quad (45)$$

For convenience, the time step size can be taken to be equal to the (constant) distance between vortices in the wake, so that a wake vortex is convected exactly one element length in one time step. This means that only the first wake vortex is unknown at each time step, and it can be obtained from Kelvin's theorem as minus the difference between the sum of the bound vortices at that time step and that at the previous time step.

Although the actual value of  $\sigma$  is known, the value which corresponds to a given value of  $n_c$  is unknown, and must be solved for. Since there are  $n$  unknown vortices, and  $n_c$  unknown sources, there are a total of  $n + n_c + 1$  unknowns. If Equation 39 is satisfied at  $n_c$  vortex locations, and Equation 40 is satisfied at  $n$  source locations, and the closure condition (42) is satisfied, there are likewise a total of  $n + n_c + 1$  equations. However, due to the alternate spacing of vortex and source singularities, a pressure or tangency condition cannot be imposed at the singularity closest to the leading edge. A substitute equation has to be found, as will be discussed later.

### Solution Interpolation

Although the actual cavity may end anywhere along the chord or in the wake, the numerical scheme allows the cavity to be ended only at a finite number of different positions. Each position results in a different solution vector. Let  $\chi_k$  and  $\sigma_k$  represent the solution vector and the cavitation number (included in  $\chi_k$ ), which result from the assumption that  $n_c = k$ . To obtain the actual solution vector, the solution is iterated until the  $m$ th source is found, such that  $\sigma_m$  is lower than the actual value of  $\sigma$ , and  $\sigma_{m-1}$  is higher than  $\sigma$ . The actual solution vector is then obtained by first lengthening the solution vector  $\chi_{m-1}$  by the addition of the source strength  $Q_m$ , which was a known quantity in the solution of the case  $n_c = m-1$ , and then averaging  $\chi_m$  and  $\chi_{m-1}$  as follows:

$$\chi = \frac{\sigma_{m-1} - \sigma}{\sigma_{m-1} - \sigma_m} \chi_m + \frac{\sigma - \sigma_m}{\sigma_{m-1} - \sigma_m} \chi_{m-1} \quad (46)$$

For cavities shorter than that length represented by two non-zero source strengths, a similar interpolation is done between the solution for  $n_c = 2$  and the fully wetted solution. Here the interpolation is quadratic in  $1/\sigma$ . This is the behavior of Guerst's (1959) solution for the steady cavitation of a flat plate.

### Singularity Spacing

Jiang and Leehey divided the chord into equal length segments, but with the first two segments further divided in half. A vortex and pressure control point was placed at the quarter chord point of each segment and a source and tangency control point was placed at the three-quarter chord point. The only exception to this rule was implemented at the leading edge, where the positions of the first source and first pressure control point were reversed.

In the present work, a different discretization scheme is used. In order to be able to model small, partial cavities with some precision, a higher density of singularities is desired near the leading edge. Furthermore, in order to improve convergence, the distance between singularities should vary smoothly with position along the axis. Therefore, the transformation  $x = (1 - \cos\theta)$  is used, where  $\theta$  varies from zero to  $\pi/2$  along the chord. The position of the vortices and sources are evenly positioned in  $\theta$ , so that

$$x_{\Gamma_i} = 1 - \cos \frac{(i-1)\pi}{2n} \quad \text{and} \quad x_{Q_i} = 1 - \cos \frac{(i - \frac{1}{2})\pi}{2n} \quad (47)$$

The distance between vortices in the wake is taken to be equal to the distance between the last two vortices on the foil. The sources in the

wake are placed half way between adjacent vortices. The vortex at the trailing edge of the foil represents the vorticity shed during the current time step. The mapping of sources and vortices from  $\theta$  to  $x$  is shown in Figure 3.

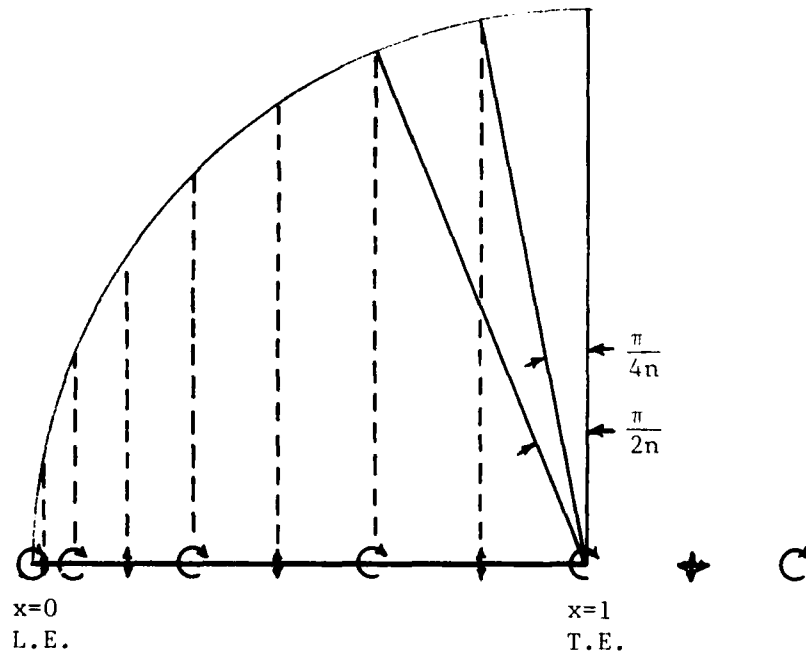


FIGURE 3. Spacing of Discrete Singularities

With this discretization scheme, the pressure Equation 39 cannot be solved at the leading edge vortex. This is the same problem encountered by Jiang and Leehey, leading them to switch the positions of the first source and the first pressure control point. The approach used here is to recognize that the strength of the quarter-root singularity in source strength is the same as that of the quarter root singularity in vorticity. If the number of singularities is large enough, the first source and first vortex will be located in a region where their strength is dominated by the quarter-root singularity, so that the strength of the first source can be related to that of the first vortex, as follows:

$$Q_{1,j} \approx \frac{\int_0^{1-\cos \frac{\pi}{2n}} x^{-1/4} dx}{\int_0^{1-\cos \frac{\pi}{4n}} x^{-1/4} dx} \Gamma_{1,j} \approx 4^{3/4} \Gamma_{1,j} \quad (48)$$

### COMPARISON WITH ANALYTIC RESULTS

#### Steady Flow

In order to determine the accuracy of the above discretization scheme, the steady flow about a partially cavitating flat plate was computed numerically and the results compared with those of Geurst (1959). Equations 39 and 40 reduce in this case to:

$$-\frac{\Gamma_i}{2\Delta x_i} + \frac{1}{2\pi} \sum_{k=1}^n \frac{Q_k}{x_{\Gamma_i} - x_{Q_k}} = \frac{\sigma}{2} \quad (49)$$

$$-\frac{Q_i}{2\Delta x_i} + \frac{1}{2\pi} \sum_{k=0}^n \frac{\Gamma_k}{x_{Q_i} - x_{\Gamma_k}} = -\alpha \quad (50)$$

Here  $\alpha$  is the angle of attack of the foil. The closure condition reduces to:

$$\sum_{i=1}^n Q_i = 0$$

The solution was carried out for  $n_c$  ranging from 2 to  $n$  for various values of  $n$ . Figure 4 shows cavity lengths versus  $\alpha/\sigma$ , where  $\alpha$  is the angle of attack, for a flat plate foil in steady flow. The solid line is Geurst's result. It can be seen that the numerical scheme gives results fairly close to the analytic solution when at least ten elements are used.

The results of the numerical scheme was also compared with the analytic results of Geurst and Verbrugh (1959) for the case of a 2% parabolic camber line. The resulting cavity lengths are shown in Figure 5. Although the agreement with theory is less good than in the case of a flat plate, the results converge toward the exact solution quite rapidly as the number of elements is increased.

The numerical results for a supercavitating flat plate in steady flow were compared with the analytic results of Geurst (1960). These are shown in Figure 6. The agreement is quite good.

#### Unsteady, Fully Wetted Flow

Another check on the numerical scheme was performed by comparing unsteady results at an extremely large value of  $\sigma$  with the known solution for a fully wetted flat plate hydrofoil flying through a gust with a reduced wave number of unity. The amplitude of the lift coefficient was overpredicted by 7% using both 10 and 20 elements. The phase angle was within  $2^\circ$  of the analytic result. The mean lift coefficient was underpredicted by 4 and 2 percent using 10 and 20 elements, respectively.

### RESULTS

#### Inner Solution

The results presented in this section are from the first approximation of an actual three-dimensional flow, wherein the aspect ratio of the foil is used to determine the proper form of the source potential, but where the interaction pressure is taken to be zero.

The type of unsteadiness selected is that of a sinusoidal vertical gust, fixed in the free stream, so that

$$v(x,t) \equiv v(t-x)$$

Before the gust is encountered, at  $t-x = 0$ , the hydrofoil is assumed to have a constant angle of attack equal to the mean angle of attack in the sinusoidal gust. The amplitude of the gust is assumed to increase smoothly during the initial period from zero to the amplitude of the periodic gust which exists after the first period.

$$v(x,t) = \alpha_m + f(t-x) \cdot \alpha_a \sin[2 k_r(t-x)]$$

$$\text{where } f(t-x) = \begin{cases} 0 & t-x < 0 \\ 3\left[\frac{k_r(t-x)}{\pi}\right]^2 - 2\left[\frac{k_r(t-x)}{\pi}\right]^3 & 0 < t-x < \frac{\pi}{k_r} \\ 1 & t-x > \frac{\pi}{k_r} \end{cases}$$

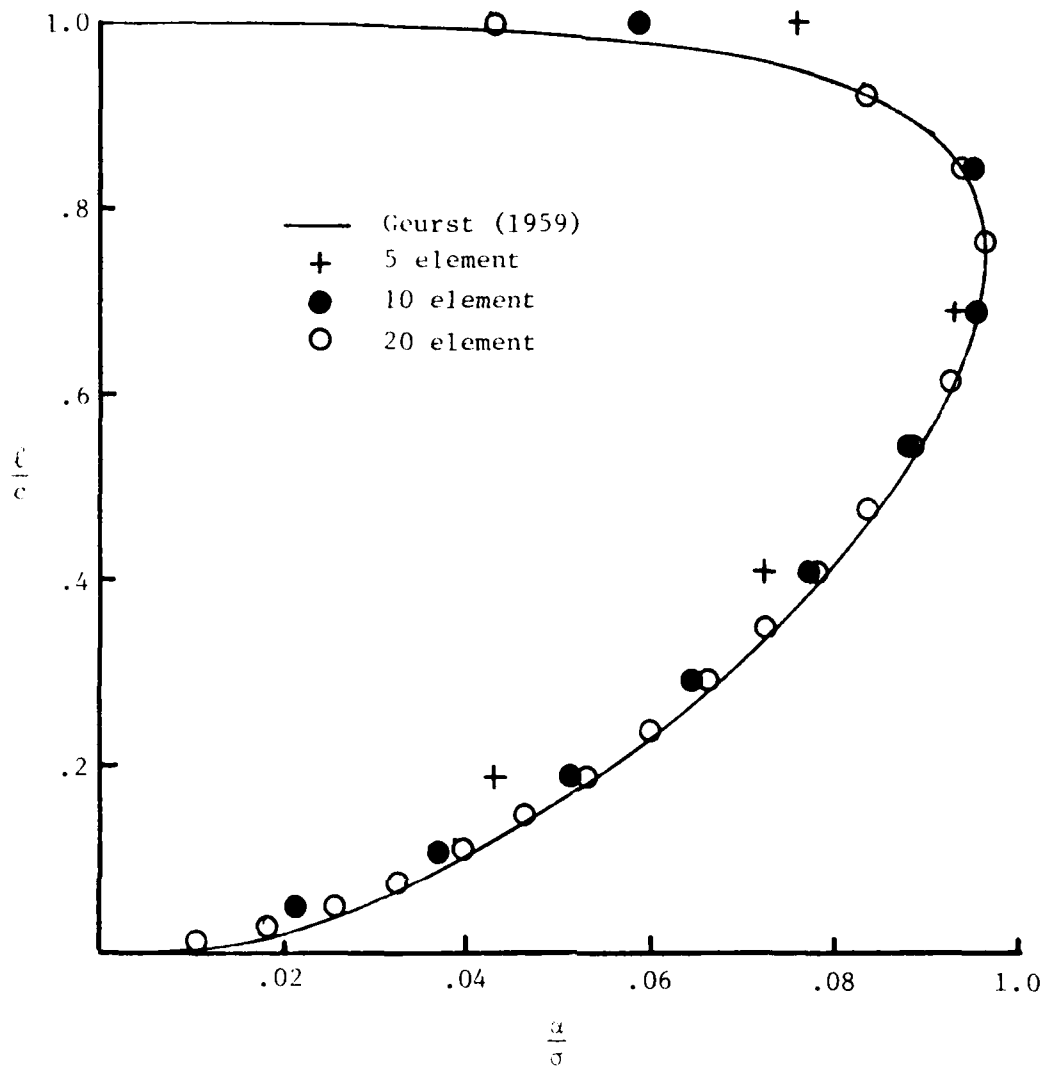


FIGURE 4. Comparison of steady results with theory for partially cavitating flat plate

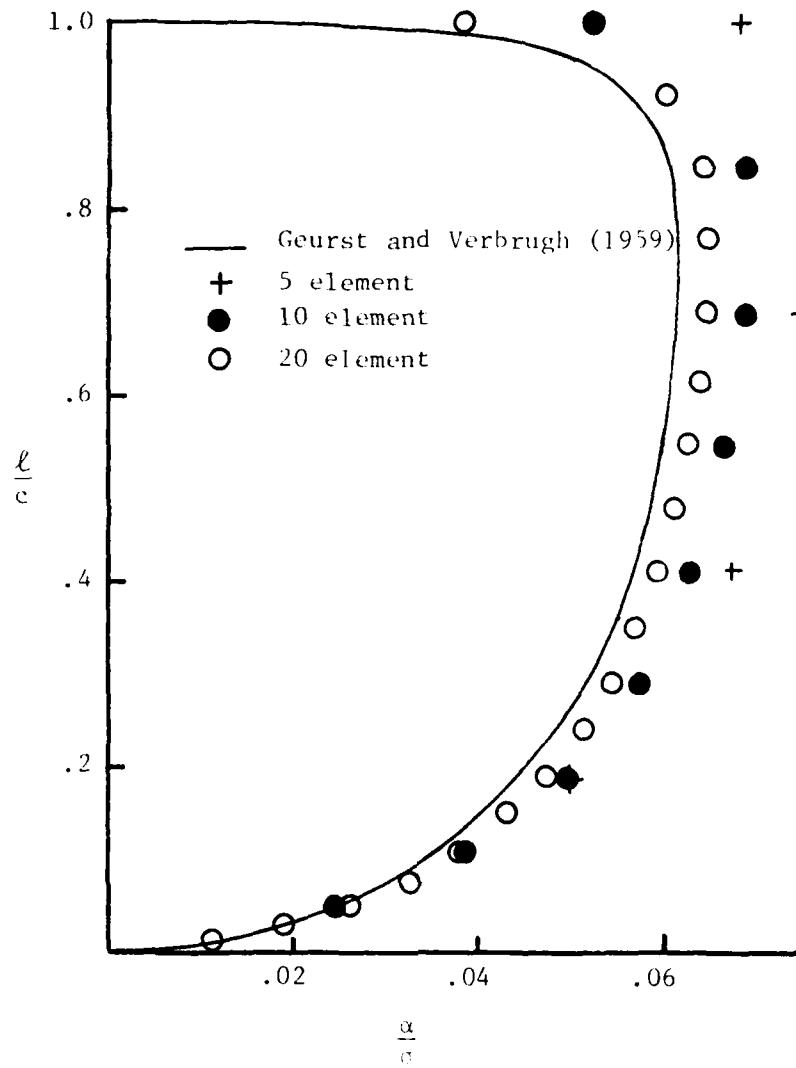


FIGURE 5. Comparison of steady results with theory for 2% parabolic camber,  $1^\circ$  angle of attack



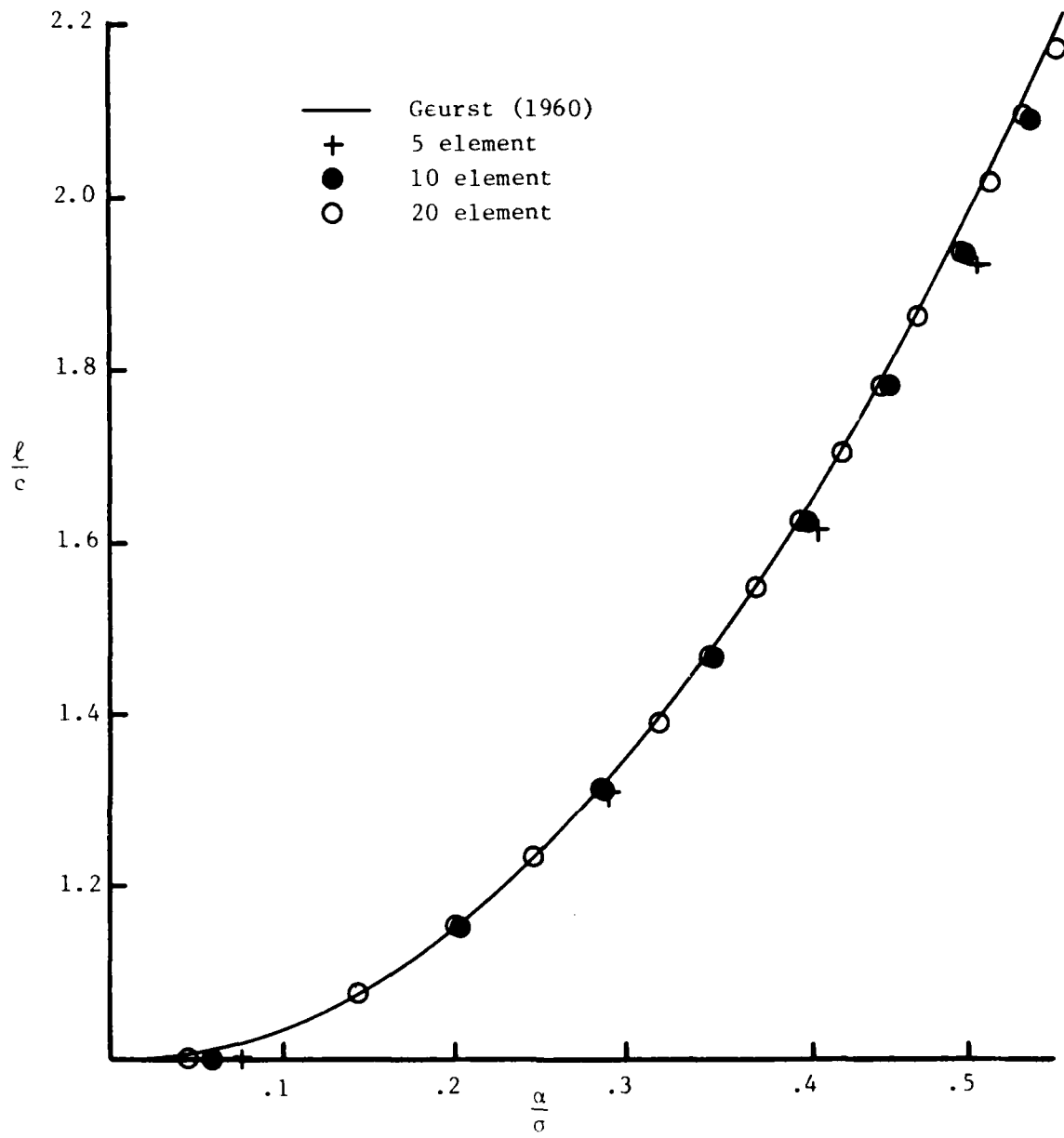


FIGURE 6. Comparison of steady results with theory for supercavitating flat plate

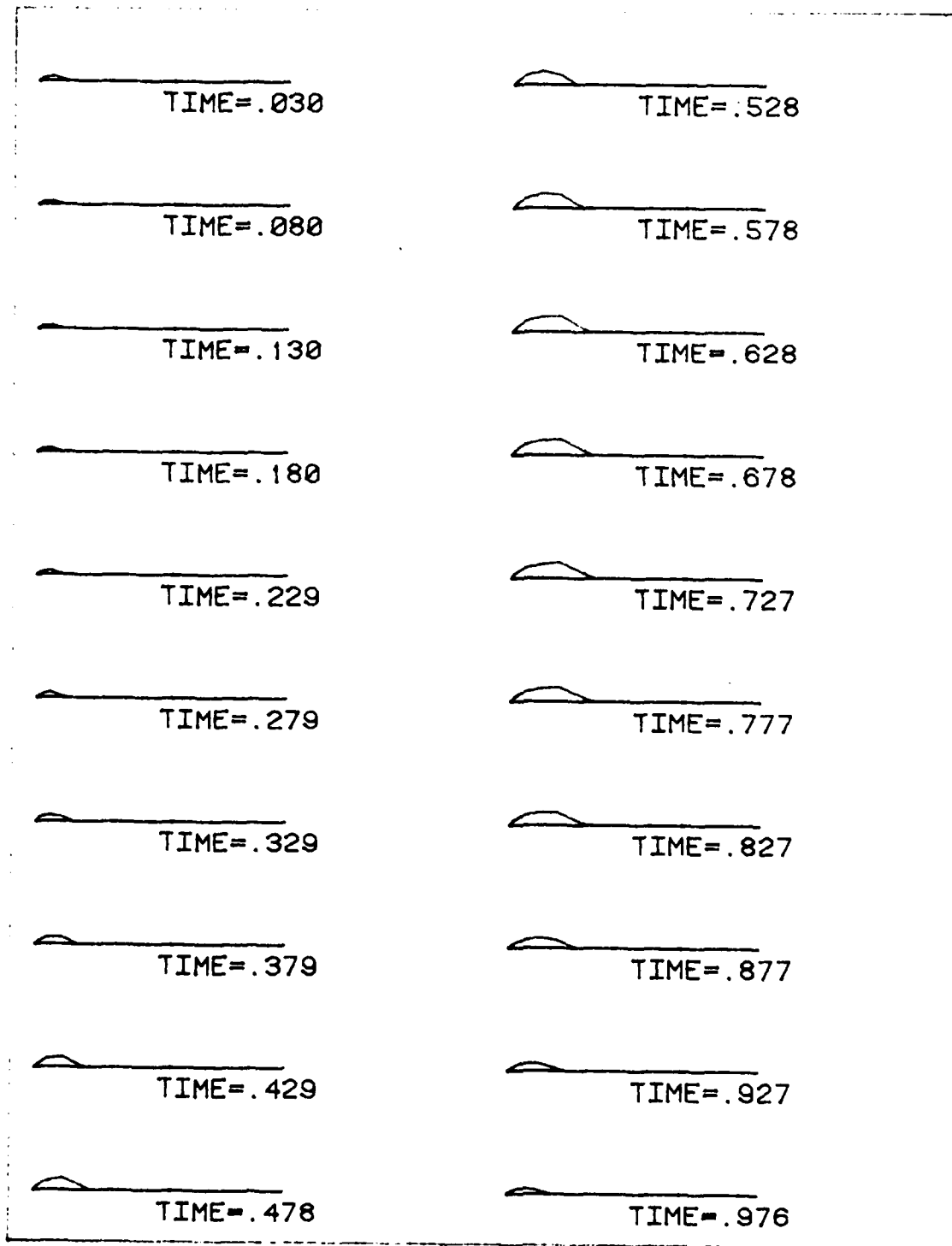


FIGURE 7A. CAVITY PROFILES VS TIME  
VERTICAL GUST,  $\alpha=0-.1$ ,  $\sigma=1.0$ ,  $AR=10$ ,  $K=1$

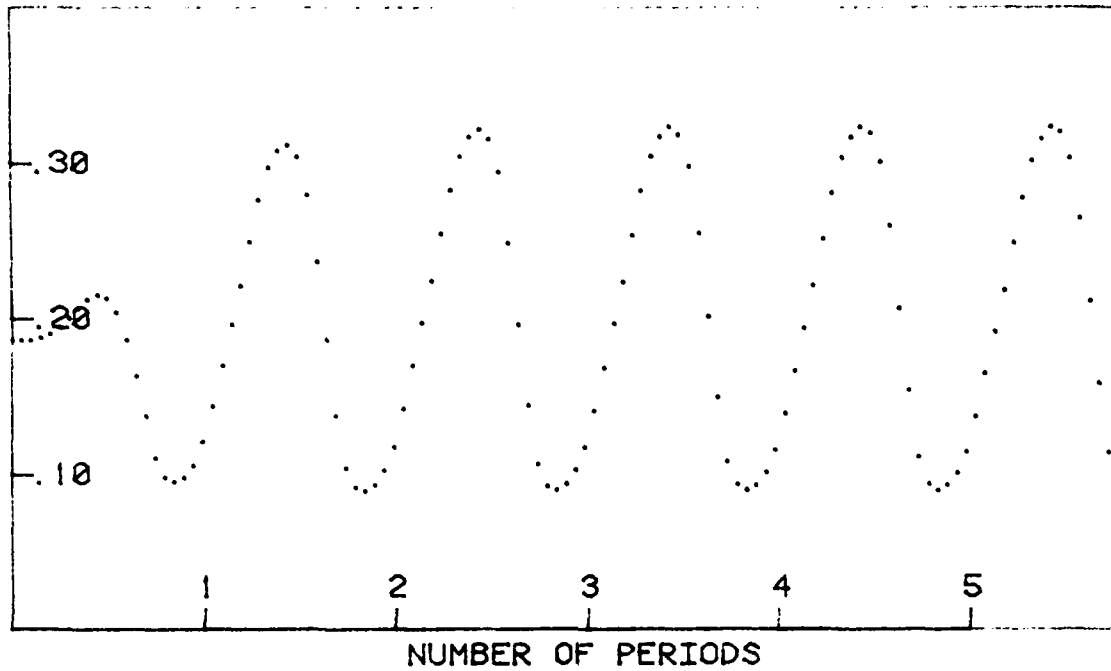


FIGURE 7B. CAVITY LENGTH OVER 5.75 CYCLES  
VERTICAL GUST,  $\alpha=0-.1$ ,  $\sigma=1.0$ ,  $AR=10$ ,  $K=1$

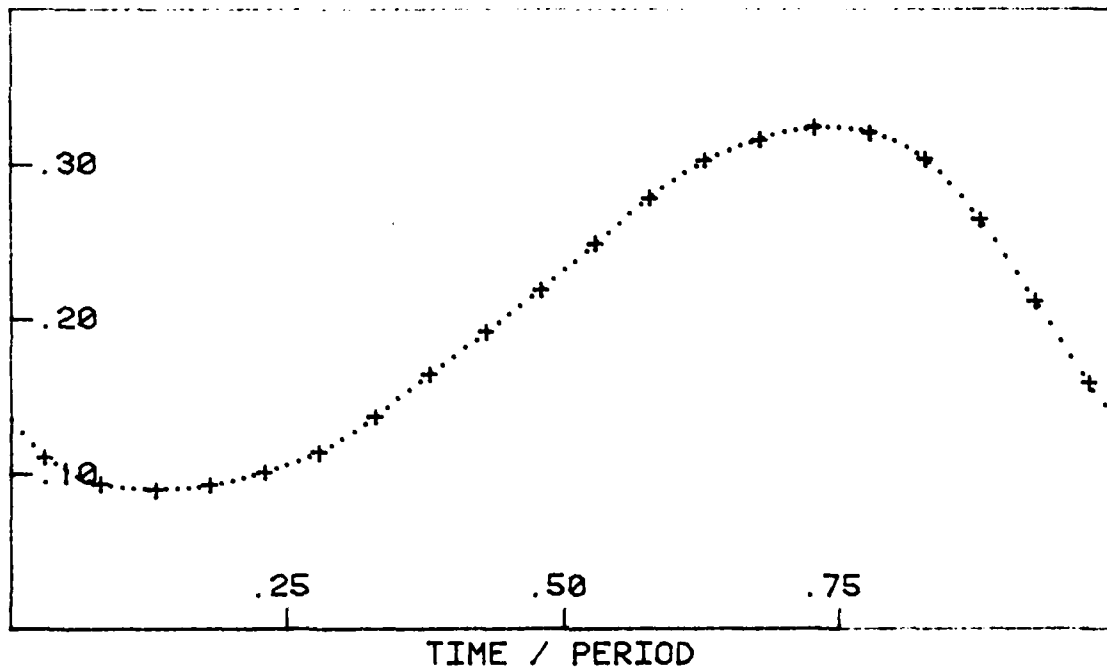


FIGURE 7C. CAVITY LENGTH OVER ONE CYCLE  
VERTICAL GUST,  $\alpha=0-.1$ ,  $\sigma=1.0$ ,  $AR=10$ ,  $K=1$

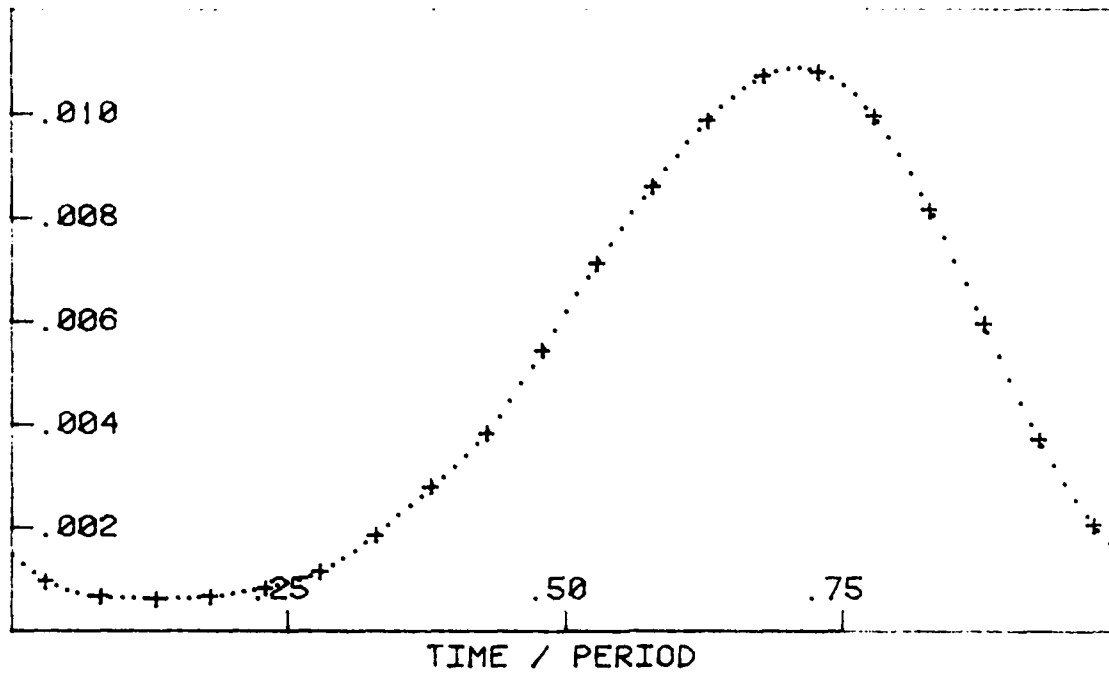


FIGURE 7D. CAVITY VOLUME  
VERTICAL GUST, ALPHA=0-.1, SIGMA=1.0, AR=10, K=1

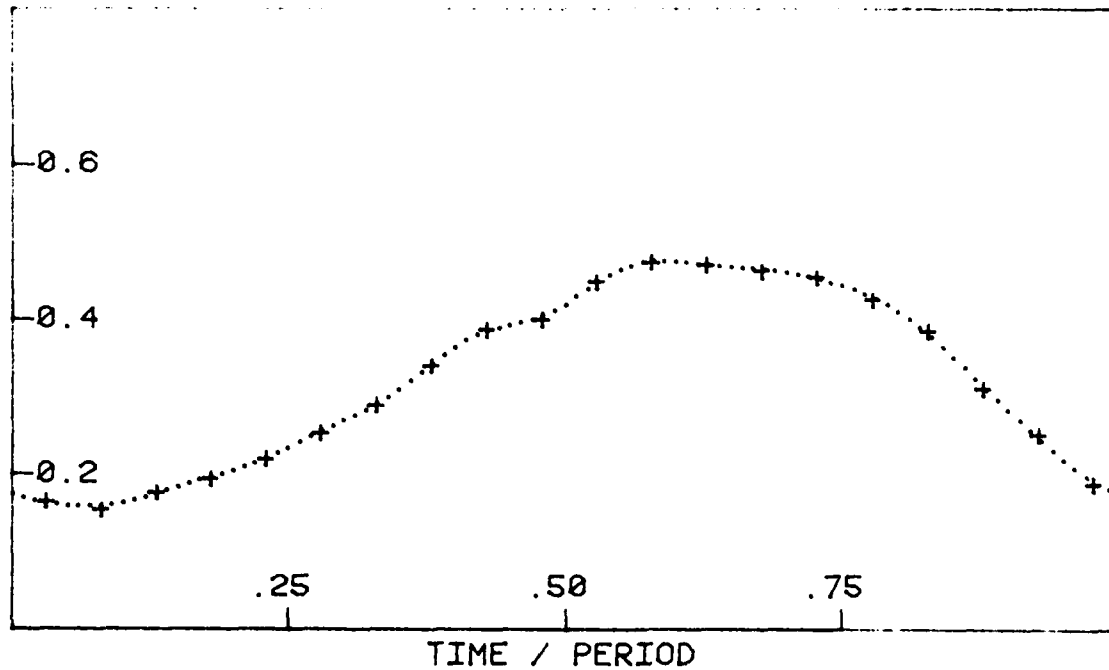


FIGURE 7E. LIFT COEFFICIENT  
VERTICAL GUST, ALPHA=0-.1, SIGMA=1.0, AR=10, K=1

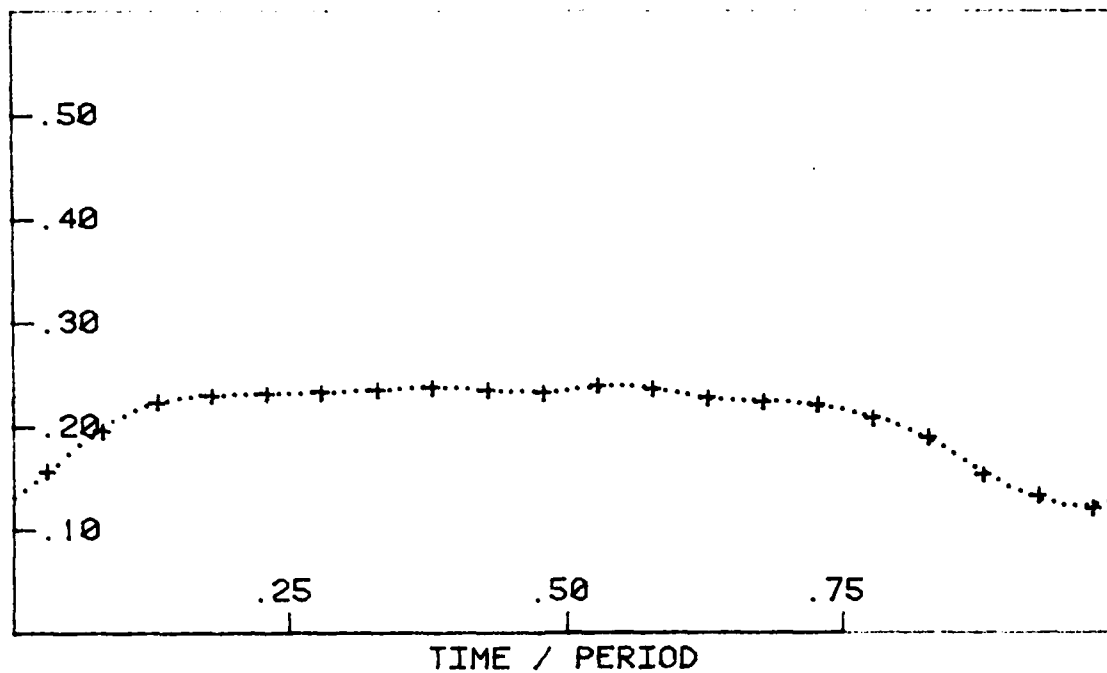


FIGURE 7F. CENTER OF EFFORT (FROM L.E.)  
VERTICAL GUST,  $\alpha=0-.1$ ,  $\sigma=1.0$ ,  $AR=10$ ,  $K=1$

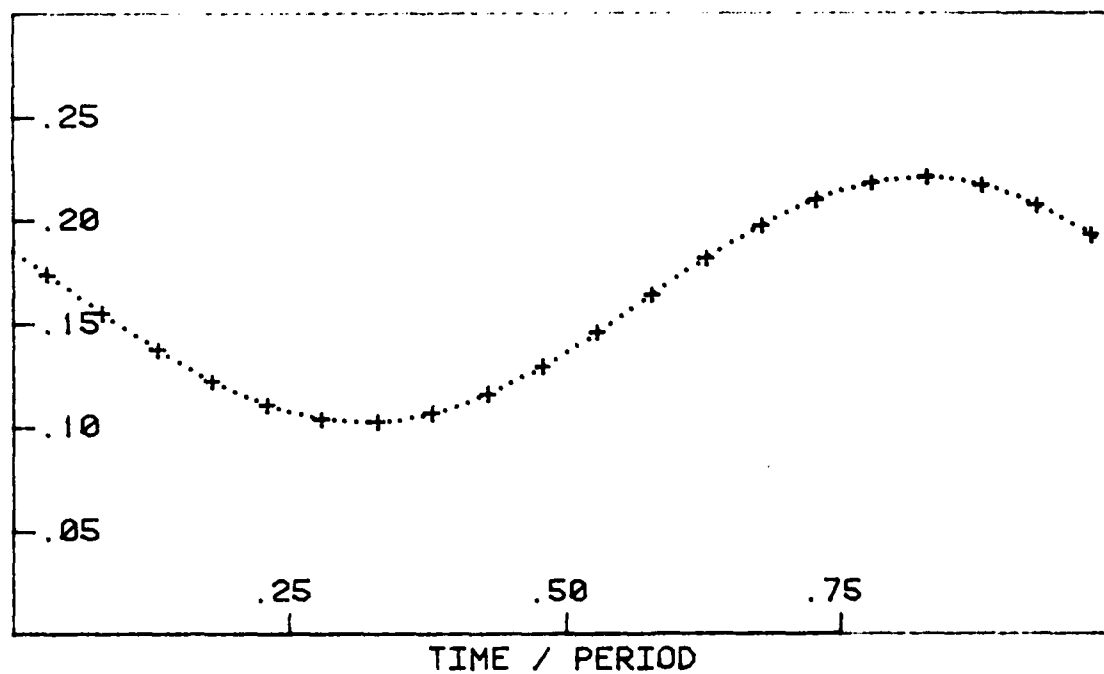


FIGURE 7G. BOUND CIRCULATION  
VERTICAL GUST,  $\alpha=0-.1$ ,  $\sigma=1.0$ ,  $AR=10$ ,  $K=1$

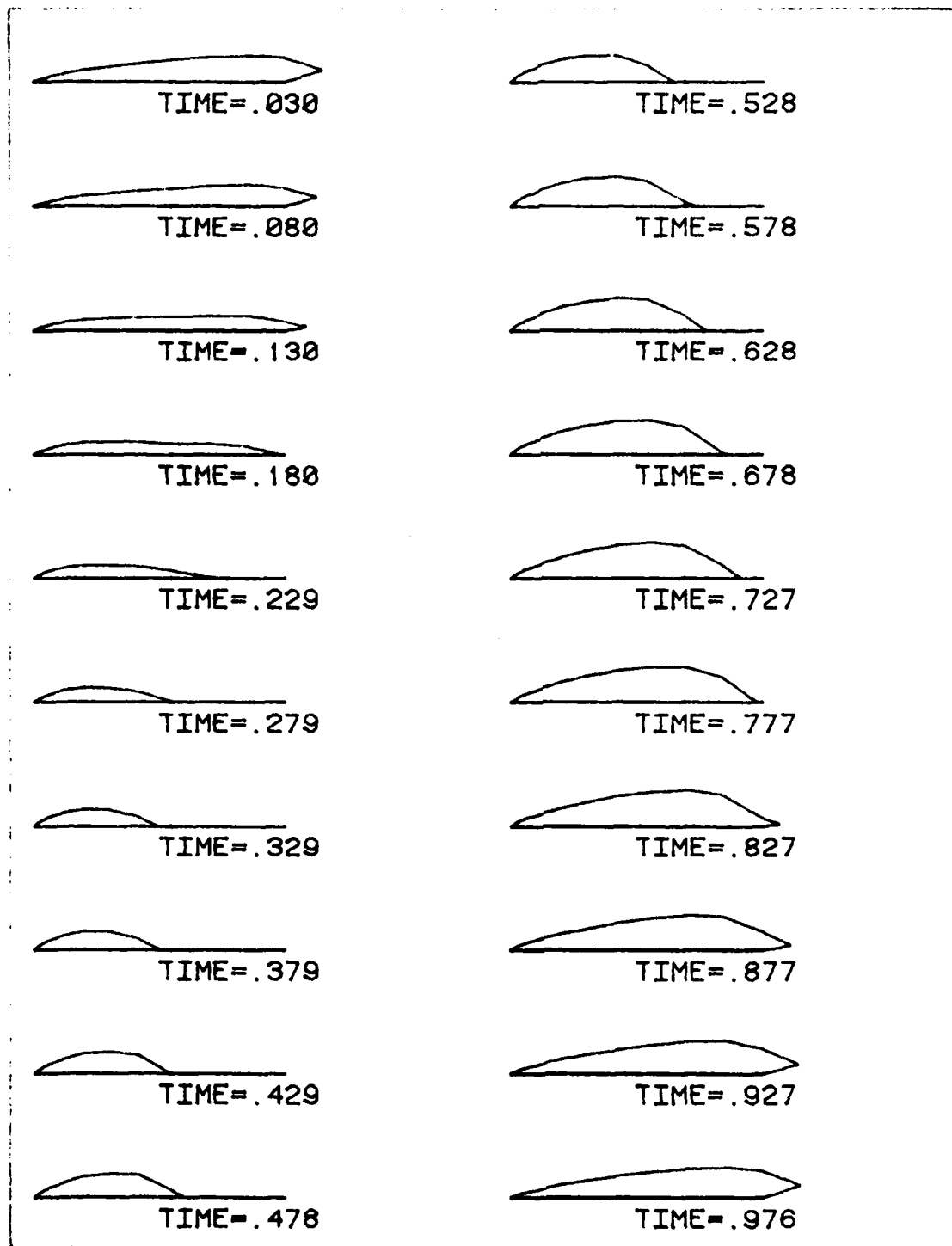
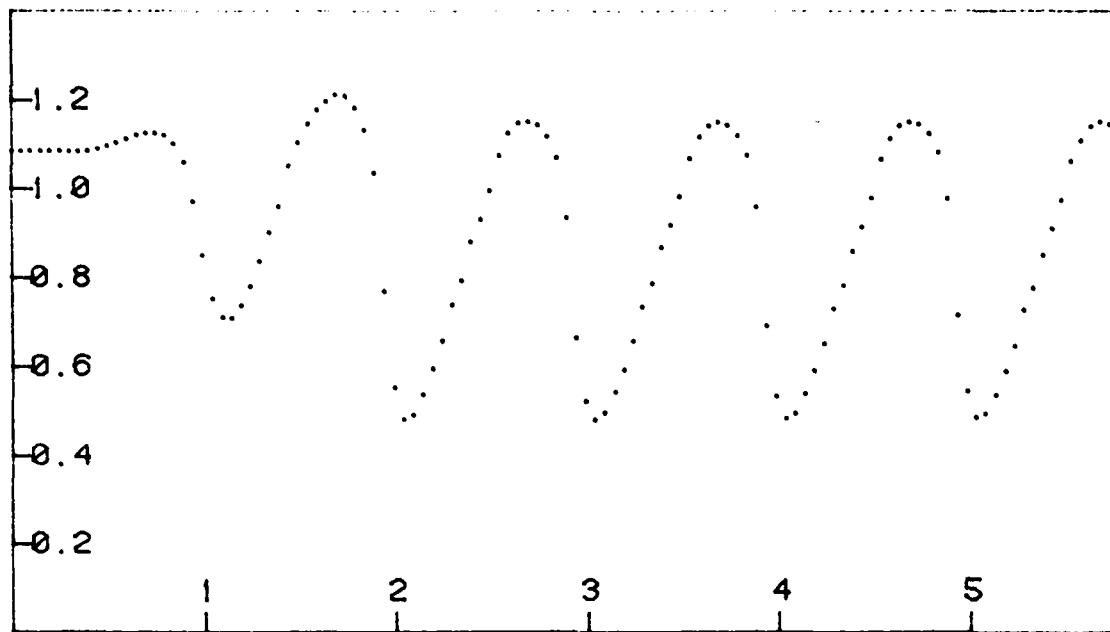
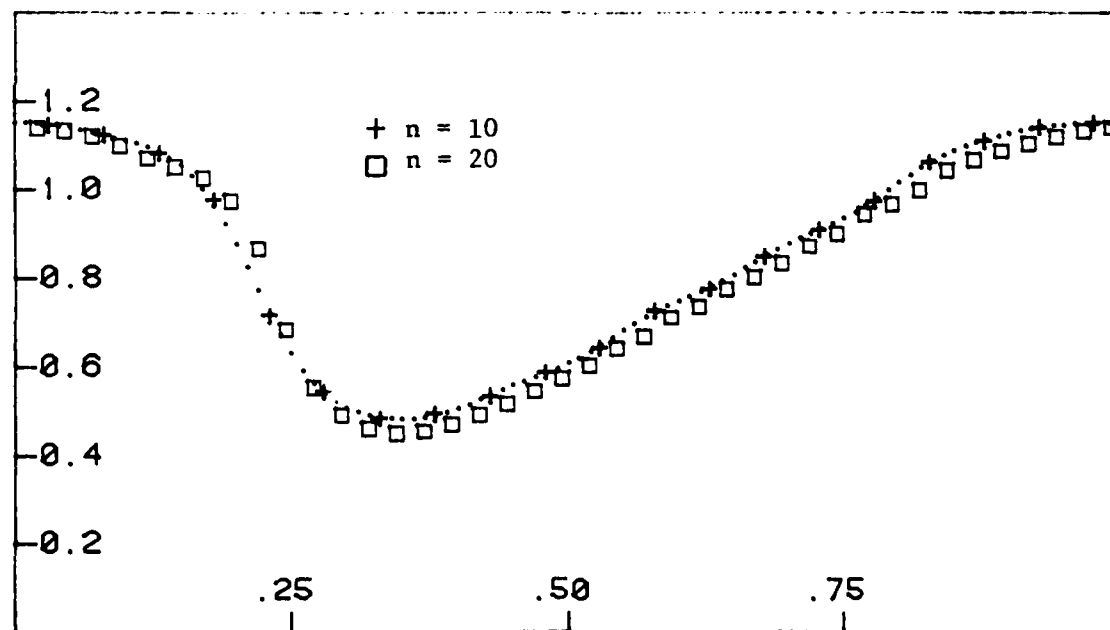


FIGURE 8A. CAVITY PROFILES VS TIME  
VERTICAL GUST,  $\alpha=0-.1$ ,  $\sigma=0.5$ ,  $AR=10$ ,  $K=1$



NUMBER OF PERIODS

FIGURE 8B. CAVITY LENGTH OVER 5.75 CYCLES  
VERTICAL GUST,  $\alpha=0-.1$ ,  $\sigma=0.5$ ,  $AR=10$ ,  $K=1$



TIME / PERIOD

FIGURE 8C. CAVITY LENGTH OVER ONE CYCLE  
VERTICAL GUST,  $\alpha=0-.1$ ,  $\sigma=0.5$ ,  $AR=10$ ,  $K=1$

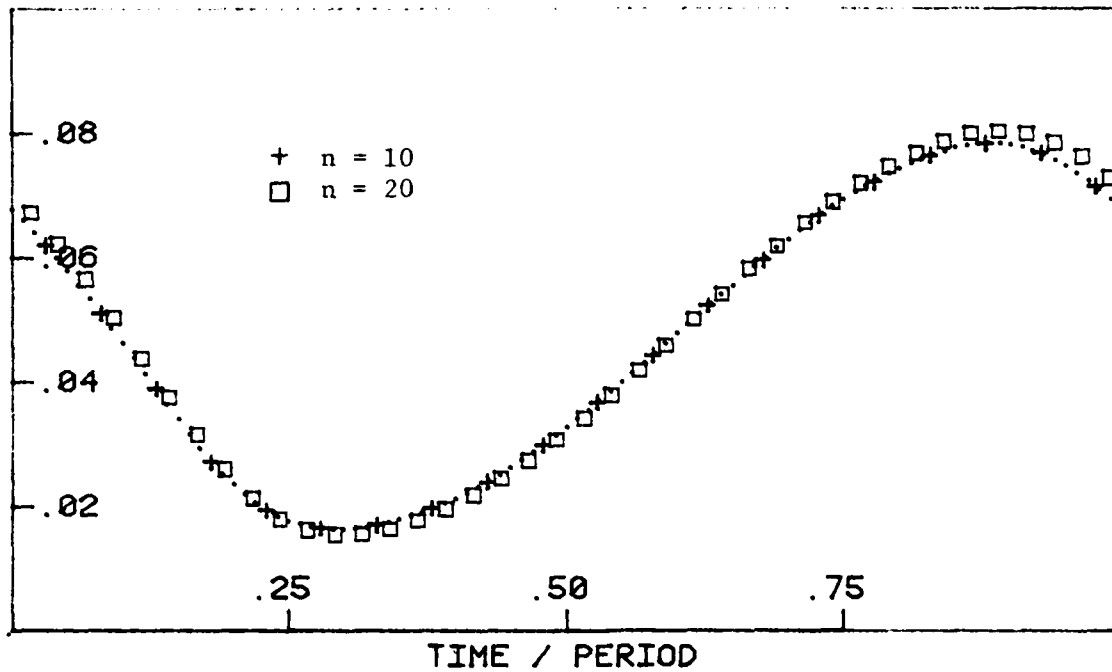


FIGURE 8D. CAVITY VOLUME  
VERTICAL GUST, ALPHA=0-.1, SIGMA=0.5, AR=10, K=1

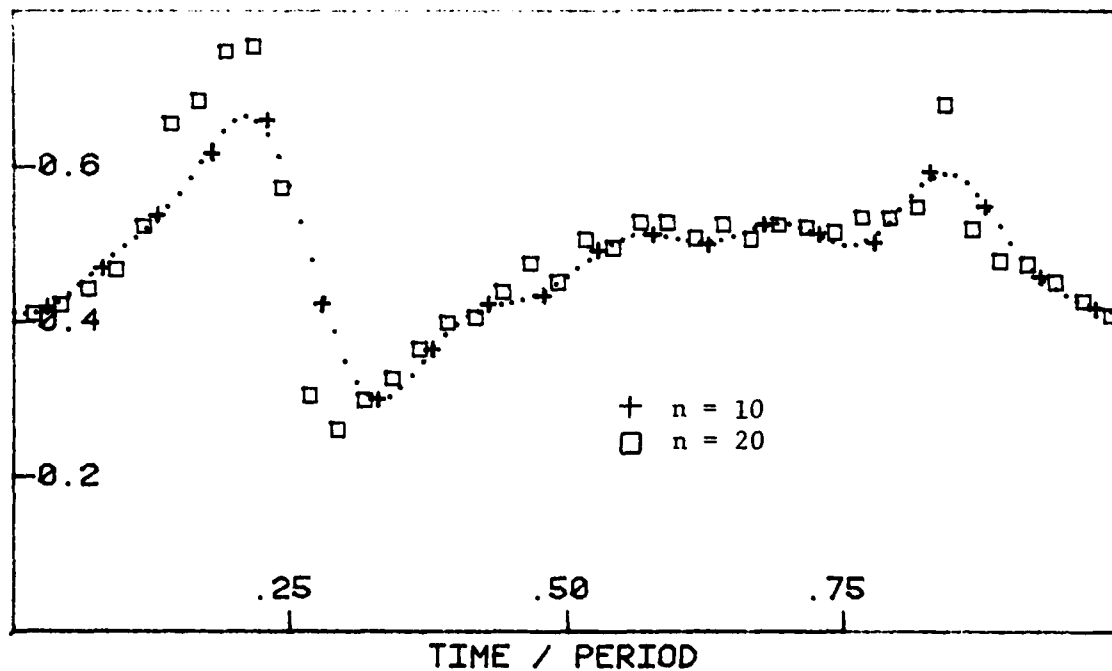


FIGURE 8E. LIFT COEFFICIENT  
VERTICAL GUST, ALPHA=0-.1, SIGMA=0.5, AR=10, K=1



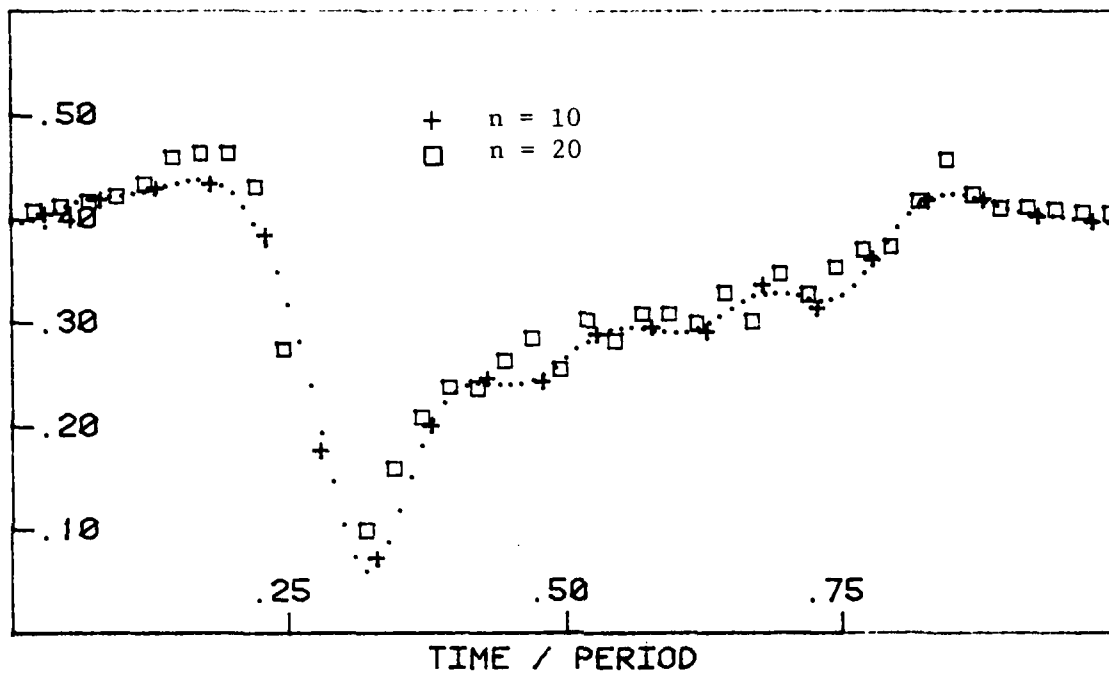


FIGURE 8F. CENTER OF EFFORT (FROM L.E.)  
VERTICAL GUST,  $\alpha=0-.1$ ,  $\sigma=0.5$ ,  $AR=10$ ,  $K=1$

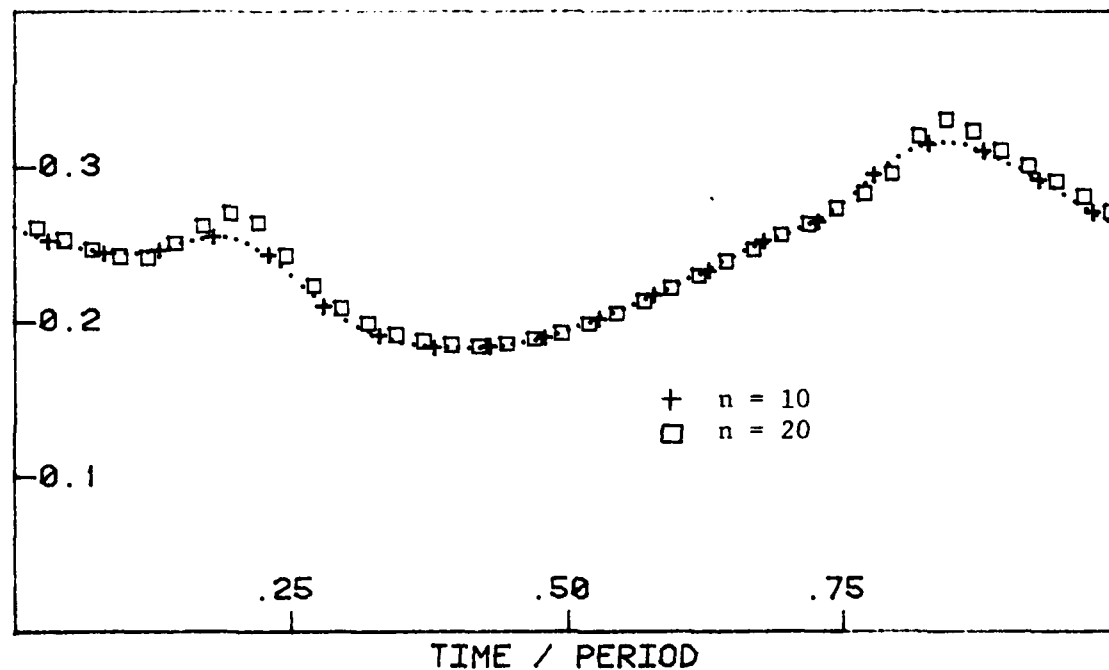


FIGURE 8G. BOUND CIRCULATION  
VERTICAL GUST,  $\alpha=0-.1$ ,  $\sigma=0.5$ ,  $AR=10$ ,  $K=1$

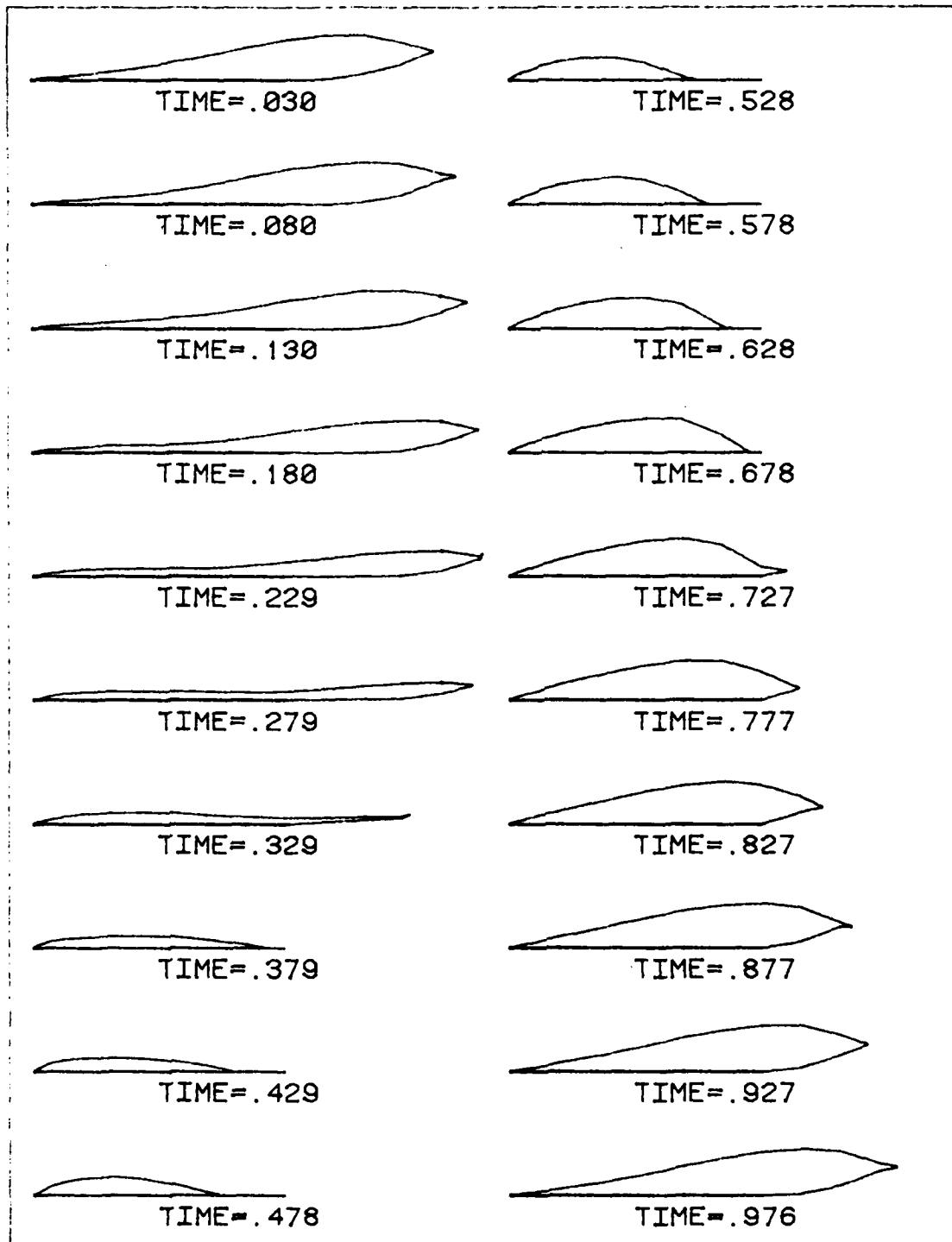


FIGURE 9A. CAVITY PROFILES VS TIME  
VERTICAL GUST,  $\alpha=0-.1$ ,  $\sigma=.25$ ,  $AR=10$ ,  $K=1$

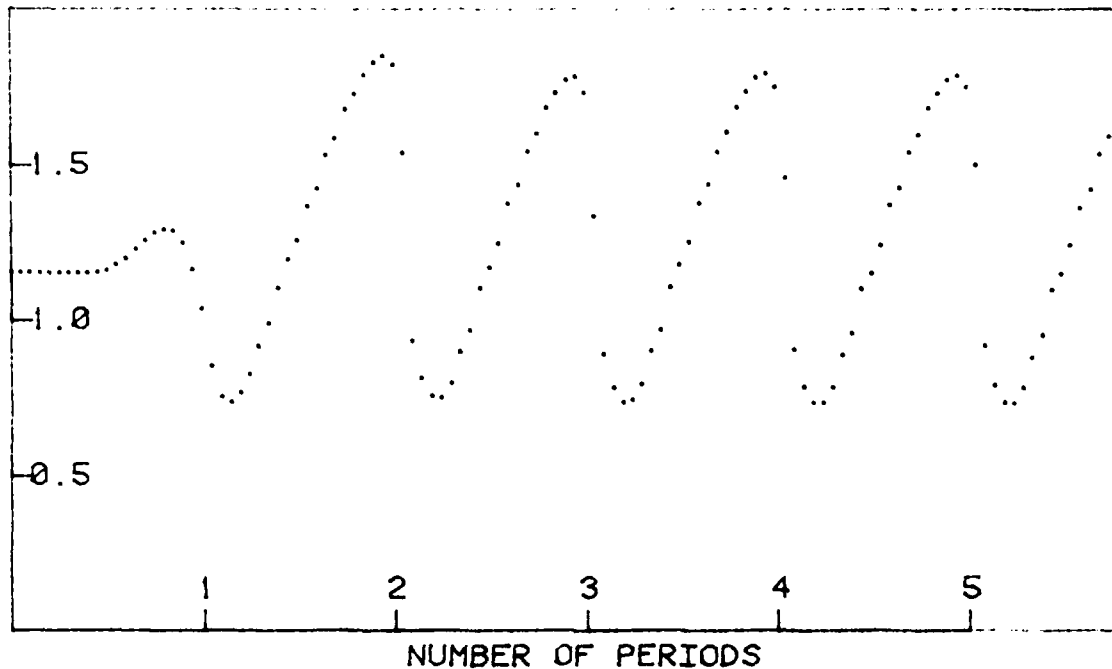


FIGURE 9B. CAVITY LENGTH OVER 5.75 CYCLES  
VERTICAL GUST,  $\alpha=0-.1$ ,  $\sigma=.25$ ,  $AR=10$ ,  $K=1$

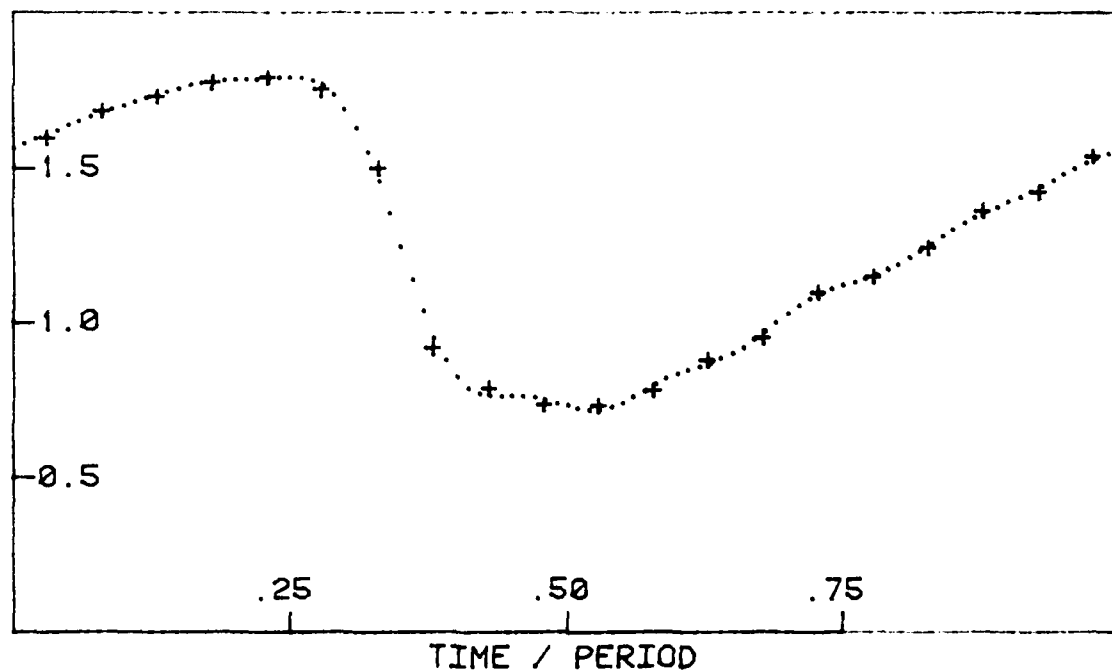


FIGURE 9C. CAVITY LENGTH OVER ONE CYCLE  
VERTICAL GUST,  $\alpha=0-.1$ ,  $\sigma=.25$ ,  $AR=10$ ,  $K=1$

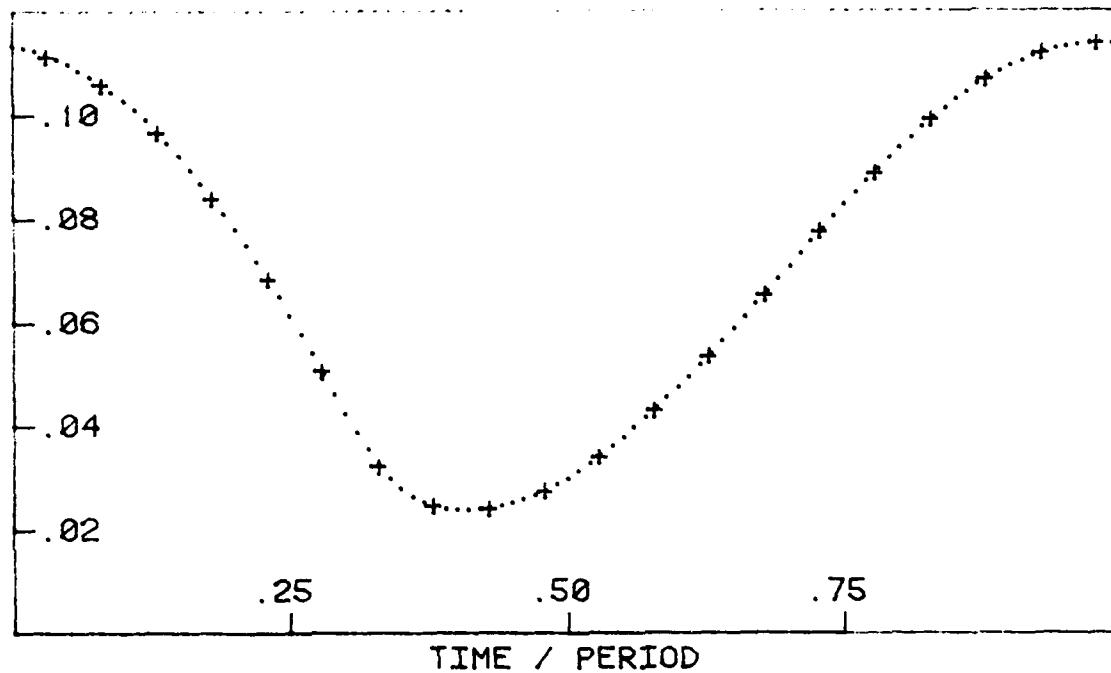


FIGURE 9D. CAVITY VOLUME  
VERTICAL GUST,  $\alpha=0-.1$ ,  $\sigma=.25$ ,  $AR=10$ ,  $K=1$

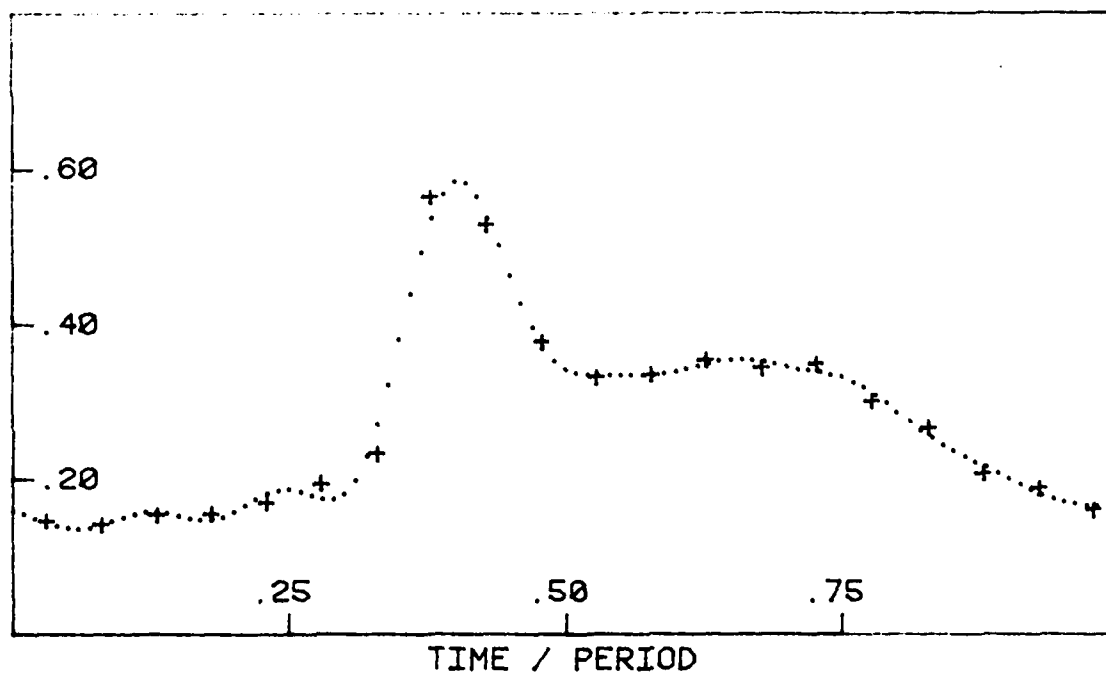


FIGURE 9E. LIFT COEFFICIENT  
VERTICAL GUST,  $\alpha=0-.1$ ,  $\sigma=.25$ ,  $AR=10$ ,  $K=1$

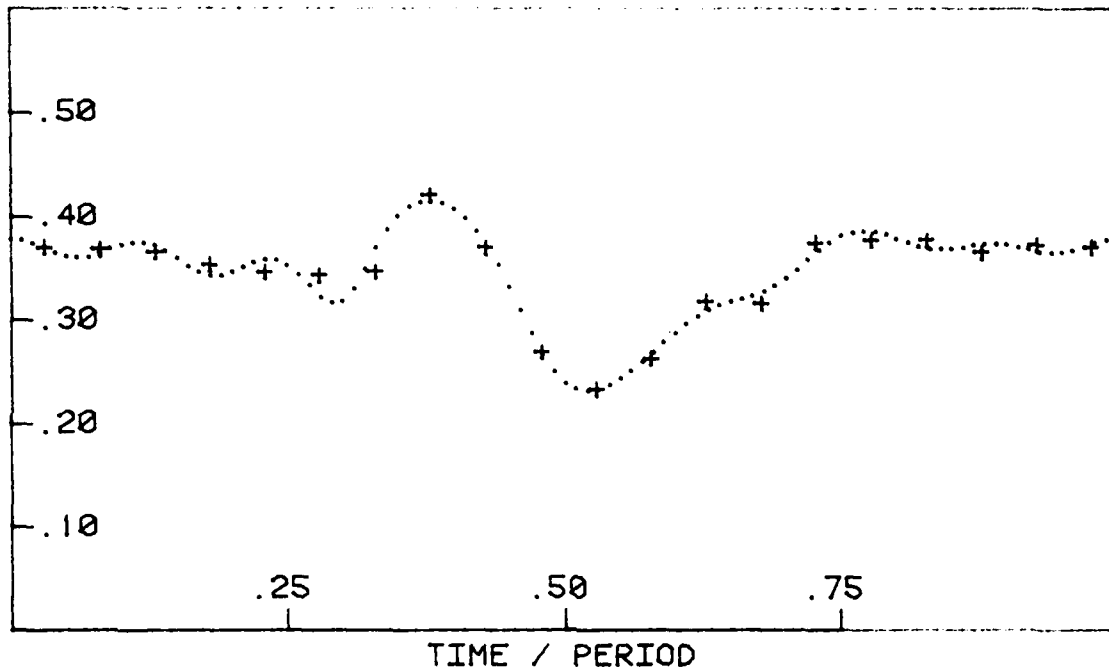


FIGURE 9F. CENTER OF EFFORT (FROM L.E.)  
 VERTICAL GUST,  $\alpha=0-.1$ ,  $\sigma=.25$ ,  $AR=10$ ,  $K=1$

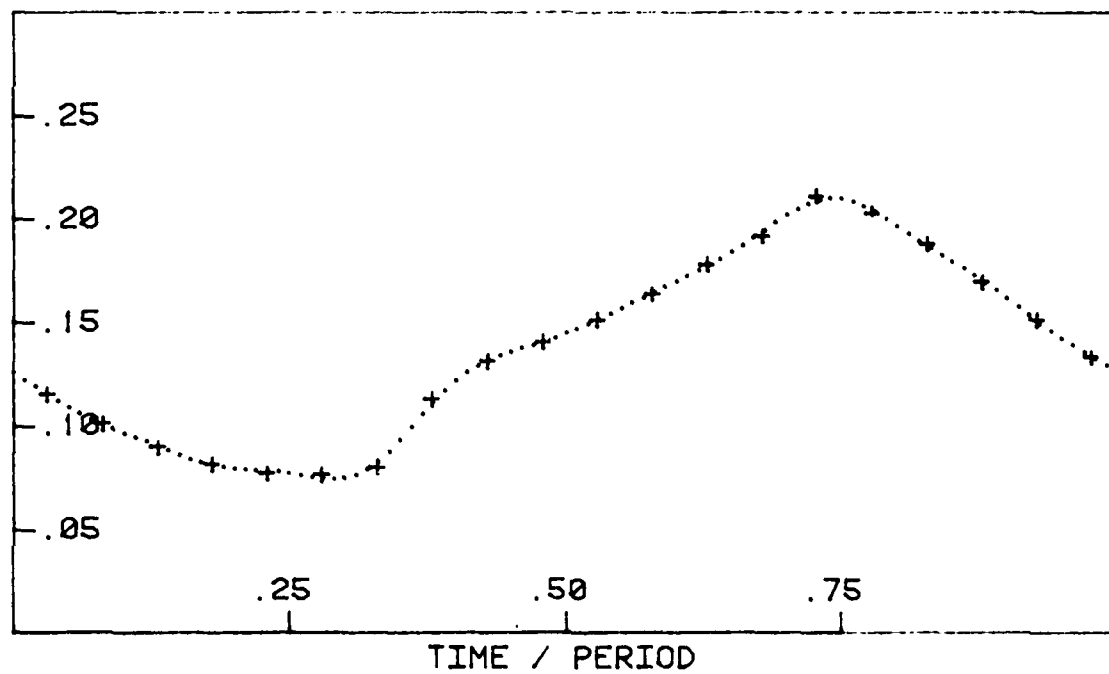


FIGURE 9G. BOUND CIRCULATION  
 VERTICAL GUST,  $\alpha=0-.1$ ,  $\sigma=.25$ ,  $AR=10$ ,  $K=1$

Here  $\alpha_m$  is the mean angle of attack and  $\alpha_a$  is the amplitude of the variations in angle of attack after the first period.  $k_r$  is the traditional reduced frequency of encounter  $\frac{Uc}{2U}$ , which in this case is  $\pi/\lambda$ , where  $\lambda$  is the wavelength of the gust.

Figures 7 through 9 show results for a flat plate of aspect ratio 10 in a gust of reduced frequency  $k_r = 1$ , using 10 elements along the chord. Each figure shows results for a different gust amplitude:

$\frac{\alpha_m}{\sigma} = \frac{\alpha_a}{\sigma} = .05$  in Figure 7,  $.1$  in Figure 8, and  $.2$  in Figure 9. In

order that the cavity profiles be easy to visualize, a value of  $\alpha_a = \alpha_m = .05$  was chosen for all the figures. Since the cavity length for a flat plate depends only on the function  $\alpha(t)/\sigma(t)$ , these figures can be scaled to obtain results at other values of  $\alpha_a$  if  $\alpha_m$  and  $\sigma$  are scaled accordingly. The value of  $\sigma$  corresponding to the plotted results is, in some cases, too large for the linearizing assumptions to hold. For these cases, it is necessary to scale the results to smaller angles of attack to obtain realistic solutions.

Figures 7-9b show the computed cavity length for the entire initial value problem, starting with the initial steady flow. For the cases shown, the solutions quickly approach a periodic response. Figure 7-9a show the cavity profiles during the last cycle of oscillation, beginning and ending at the time of zero gust velocity at the leading edge of the foil. Figures 7-9c, d, e, f and g indicate cavity length, cavity volume, lift coefficient, center of effort (measured from the leading edge), and the bound circulation for the last oscillation cycle. The cross marks indicate the calculated points, and the dotted lines represent the functions reconstructed from the first eight harmonics.

At the higher gust amplitudes shown in Figures 8 and 9, the cavity length has a saw-toothed character, indicating slow growth and quite sudden collapse. This behavior was demonstrated by Tulin (1980) and Stern (1980), and is often observed on propeller blades where the nature of the flow is quite similar to the present examples. Cavity volume is somewhat saw-toothed in character, but less so than cavity length. This is due to the fact that cavity thickness variations tend to be out of phase with cavity length. The cavity tends to thicken, then lengthen, then thin, and then shorten, so that cavity collapse from a volume viewpoint takes place over the periods of thinning and shortening rather than just the latter. This is a somewhat different behavior than was hypothesized by Tulin (1980) on the basis of the form of the unsteady closure condition alone.

The curves of cavity length and volume demonstrate that the cavity trailing edge can move smoothly over the trailing edge of the foil. This is significant in that analytic results for steady cavitation of a flat plate indicate that a maximum of the  $1/\sigma$  vs cavity length curve occurs at the three-quarter chord point, as seen in Figure 4. Tulin (1980) showed that partial cavities longer than three-quarters chord are unstable and therefore not physically

AD-A158 920

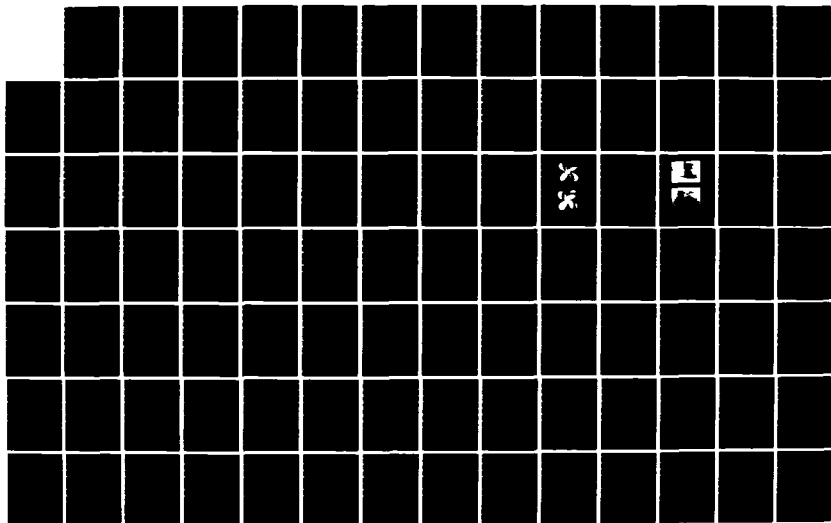
SYMPOSIUM OF NAVAL HYDRODYNAMICS (14TH) HELD AT ANN  
ARBOR MICHIGAN ON AUGUST 23-27 1982(U) OFFICE OF NAVAL  
RESEARCH ARLINGTON VA M P TULIN ET AL. 1982

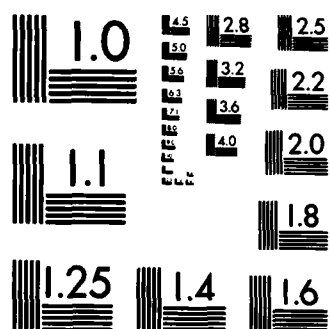
09/13

UNCLASSIFIED

F/G 20/4

NL





MICROCOPY RESOLUTION TEST CHART  
NATIONAL BUREAU OF STANDARDS-1963-A



realizable. It has been supposed that if  $\alpha/\sigma$  were to be slowly increased so that it approaches the maximum value which is associated with partial cavitation, the cavity would become unstable and jump to a supercavity. The present results indicate that an unsteady flow situation would differ significantly from a quasi-steady one, and a sudden jump in cavity length need not occur.

An apparent similarity between the exact solution and the numerical unsteady solution can be seen in the lift coefficient. The steady theory predicts that the lift coefficient becomes infinite when the cavity trailing edge corresponds to the trailing edge of the foil. In the unsteady results there is a peak in the lift coefficient when the cavity trailing edge is in this location. It is particularly large when the cavity is in a collapsing mode. One can also see an augmentation in the circulation strength at this time, although the relative smallness of this effect indicates that the peakiness of the lift coefficient is due primarily to unsteady contributions. The similarity with the steady results is therefore more apparent than real.

Figures 8c, d, e, f, and g also give results obtained using 20 elements over the chord. Due to the fact that the wake element size (and consequently the time step size) is fixed in relation to the foil element size, the twenty element solution has approximately twice the number of time steps than does the ten element solution, which for the case  $k_r = 1$  has approximately twenty time steps per cycle. The differences in the results are always within a few percent, except for the lift coefficient, which exhibits higher and sharper peaks in the twenty element solution. Because the results are so similar, all solutions for  $k_r \leq 1$  were found using ten elements over the chord.

The effect of aspect ratio variations is shown in Figure 10, which shows the variation of cavity volume over one flow cycle for aspect ratios of  $10^0$ ,  $10^1$ ,  $10^2$ , and  $10^3$ . The flow conditions were the same as in Figure 8 above. It can be seen that a factor of 10 in aspect ratio reduces the amplitude of volume variations by approximately 8%, and the phase of these variations by approximately  $20^\circ$ , the low aspect ratio response leading the high aspect ratio response due to the increased "added mass" in the latter configuration. Figure 11 shows the corresponding results for cavity length. Here the major effect of varying the aspect ratio is to change the time of cavity collapse.

Figure 12 shows how the maximum and minimum cavity lengths depend on the wave number of the gust. The flow situations are the same as those shown in Figures 7, 8, and 9, except that the reduced wave number is varied from .5 to 2.0. Ten elements per chord were used for  $k_r = .5$  and 1.0, and twenty elements were used for  $k_r = 1.5$  and 2.0. For the two highest frequencies at the largest gust amplitude a subharmonic response was excited. In these cases, the cavity lengths were averaged over the last two cycles. As expected, the general trend is for the cyclic variation in cavity length to decrease as the frequency increases.

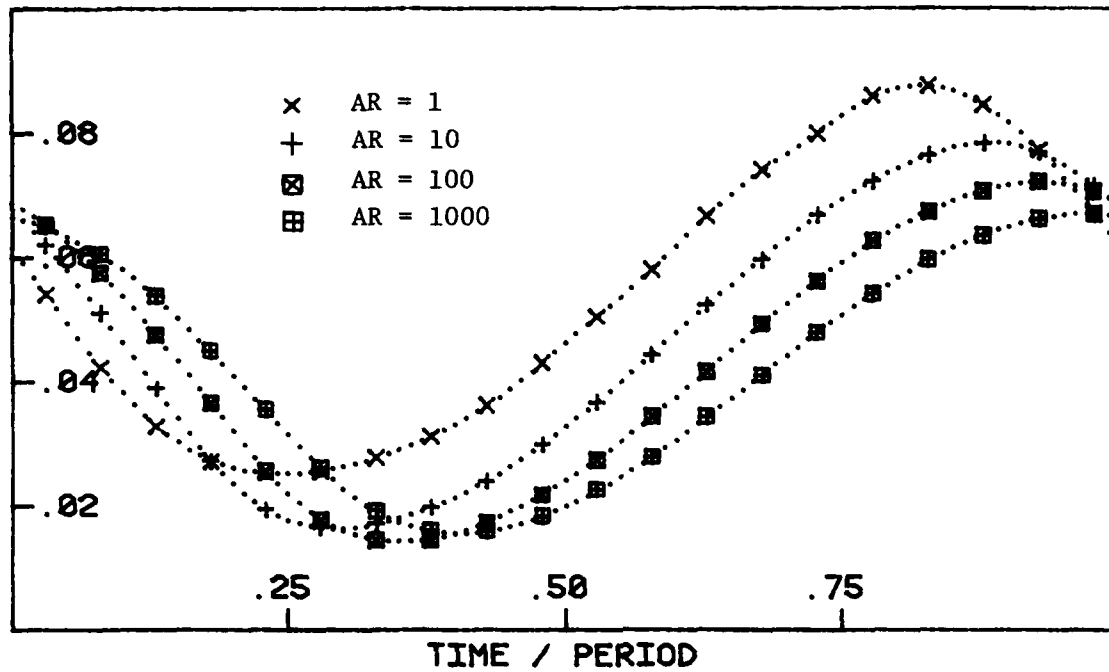


FIGURE 10. Cavity volume vs time for four values of aspect ratio. (Flat plate in gust,  $\alpha = 0-.1$ ,  $\sigma = .5$ ,  $k_r = 1$ )

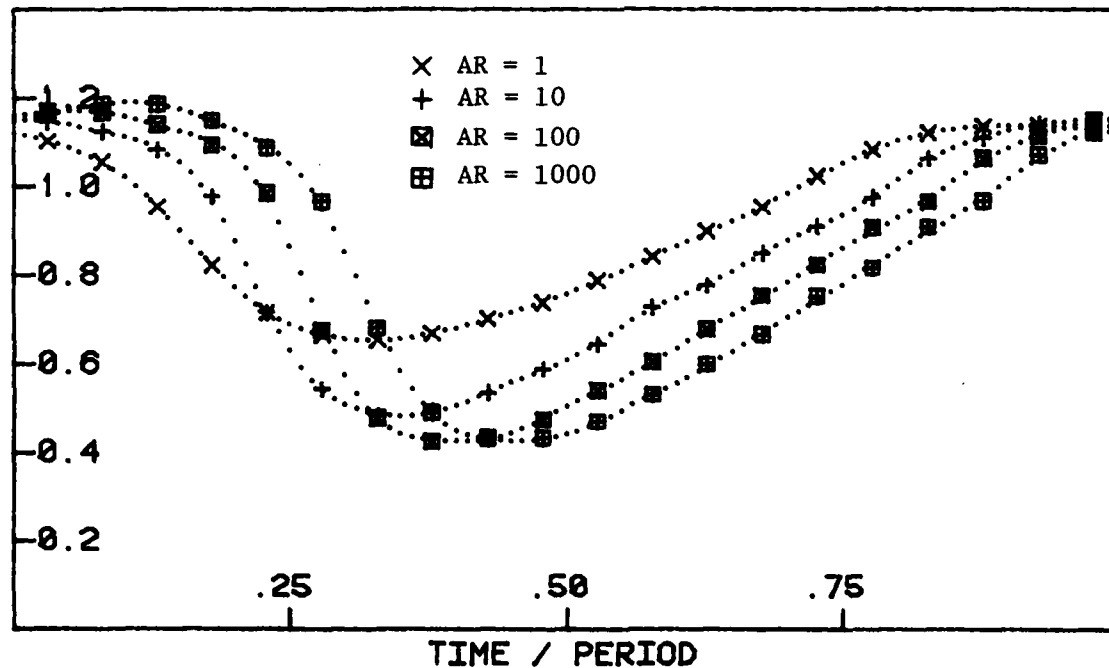


FIGURE 11. Cavity length vs time for four values of aspect ratio. (Flat plate in gust,  $\alpha = 0-.1$ ,  $\sigma = .5$ ,  $k_r = 1$ )

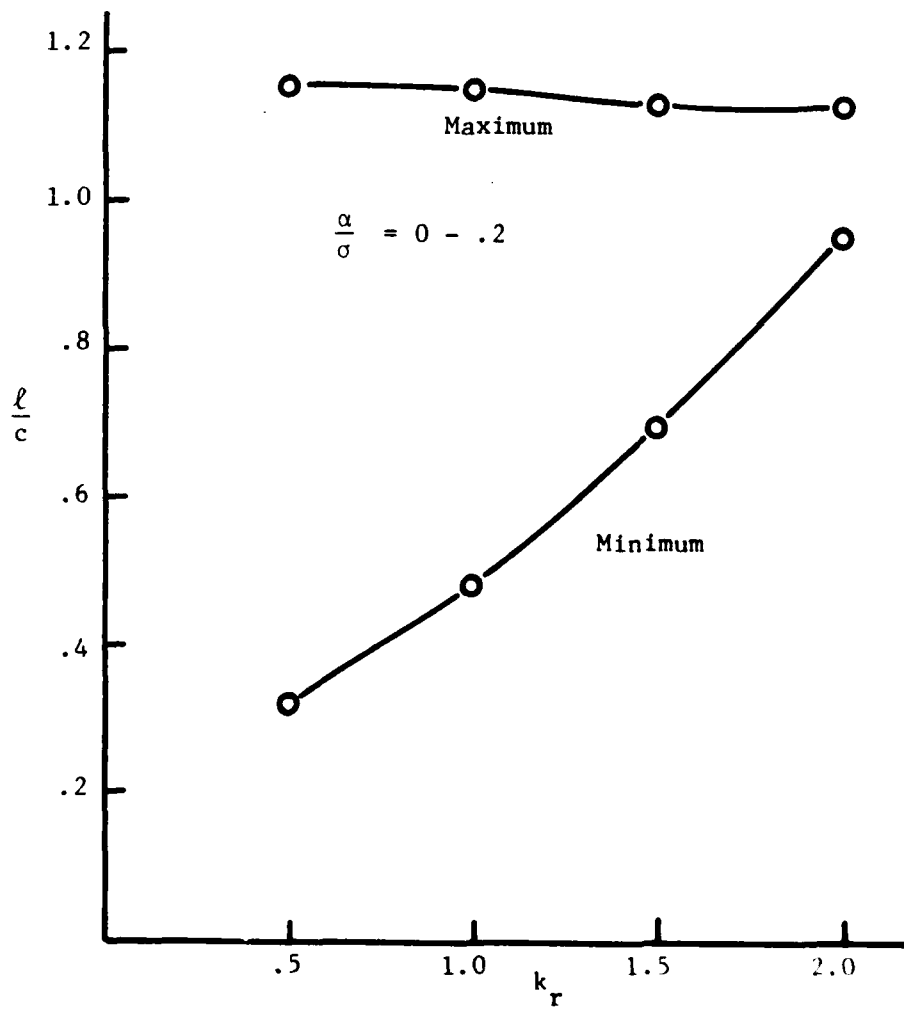
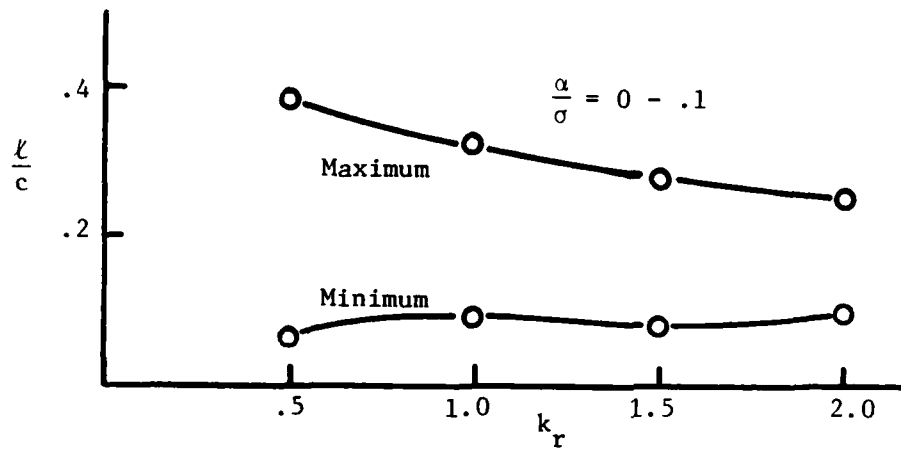
### Iterative Three-Dimensional Solution

In order to test the convergence of the iterative scheme to account for spanwise interactions, it was applied to the case of a flat-plate hydrofoil of symmetrical, elliptical planform with an aspect ratio of 10. The unsteady flow investigated was a vertical gust of  $\alpha_m = .05$  and  $\alpha = .05$ , with a reduced frequency based on midspan chord of unity.<sup>a</sup> The cavitation number  $\sigma$  was .5. Using 10 elements per chord, the inner solution was computed at five equally spaced sections, from  $z=0$  to  $z=.4$ . (The midspan solution is that shown in Figure 8.) Three iterations were performed. After each iteration, the RMS value of the difference between the function  $p_i(t)/\rho$  used in the solution of the inner problem and that computed from the resulting total source strength, using Equation 38, was calculated. This RMS difference was divided by the cavitation number to obtain a measure of the error magnitude at each iteration, which is shown in Table 1. As expected, the RMS interaction pressure is quite small, of the order of 2 to 4 percent of the cavitation number. This indicates that the initial solution, with  $p_i(t) = 0$ , is a good approximation of the actual three-dimensional flow. The calculated error is significantly reduced in each successive iteration, particularly the low frequency components. Table 1 shows the error reduced roughly by a factor of two by each iteration if all harmonics are considered, and by a factor of 7 for the first harmonic alone. The more rapid convergence of the lower harmonics is significant in that these are the ones most effective in causing changes in the inner solution. Table 2 shows the RMS change in computed cavity volume in the second and third iterated solutions.

Figures 13 a-e show, for each of the spanwise positions, the cavity volume variations as computed from the first and third iterations, as well as the sum of the first three harmonics of the computed interaction pressure,  $p_i(t)/\rho$ . Once again, one can see that the initial solution is quite a good approximation of the three-dimensional flow. As might be expected, a positive interaction pressure reduces the cavity volume, and a negative interaction pressure increases the volume, but only after a significant time delay. Comparing Figure 13 with Figure 10, one can see that the effect of the interaction term on the amplitude of the volume variations is the same order of magnitude as the effect of a factor of 10 in aspect ratio, but its effect on the phase of the volume variations is very small. This latter result may be true only for the particular flow situation investigated.

### Computation Time

All computations were performed on an IBM 370/168 computer. A 10-element solution required approximately .1 seconds of CPU time per time step, so that six cycles at a reduced frequency of one required 12 seconds. A 20-element solution required .4 seconds per time step.



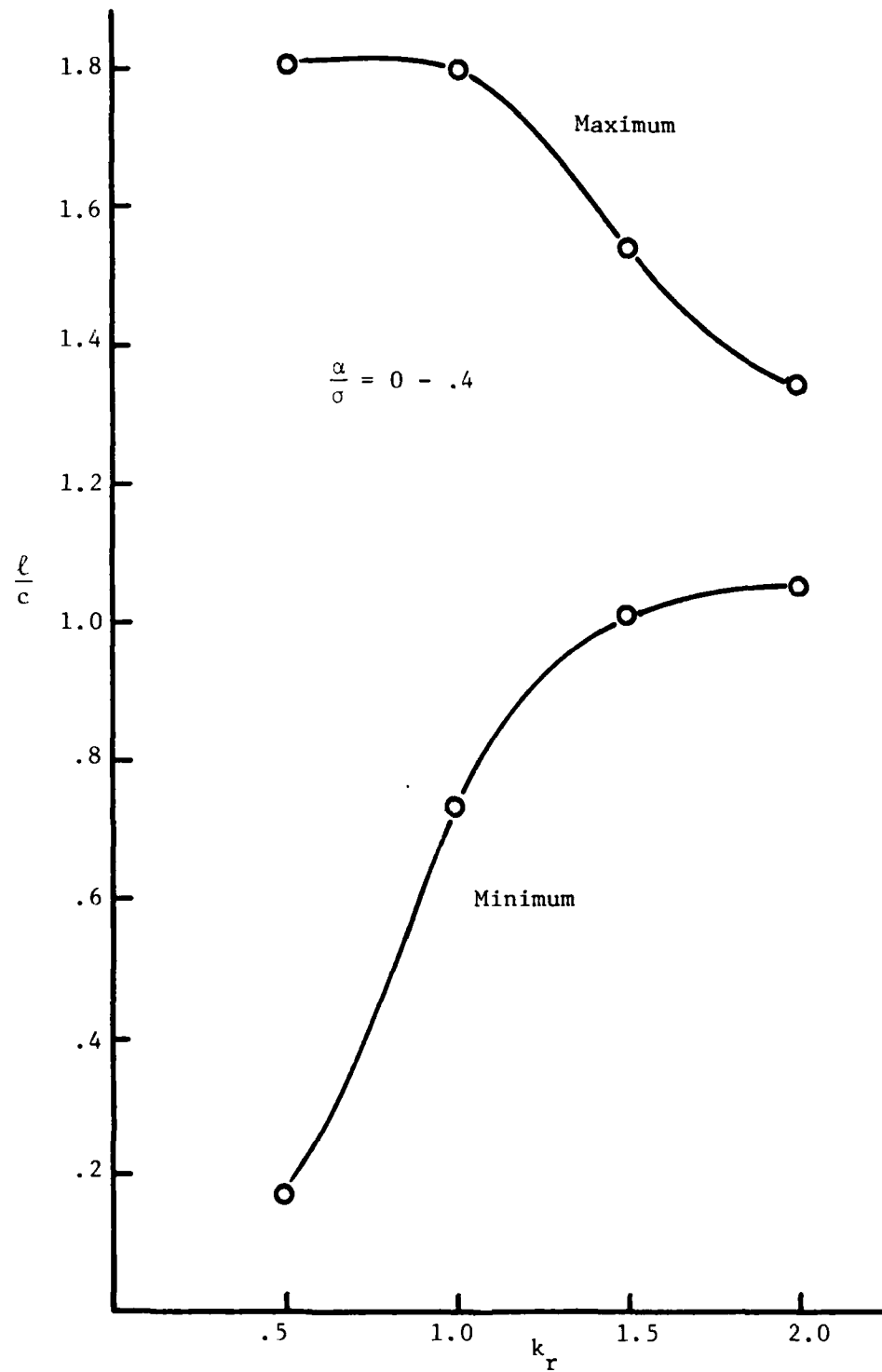


FIGURE 12. Maximum and minimum cavity lengths vs reduced wavenumber for flat plate in gust

## CONCLUSIONS

The method of analysis presented in this paper is a powerful method of solving the problem of unsteady cavitation on high aspect ratio hydrofoils. It allows three-dimensional effects to be incorporated systematically in the inner problem, so that a good first approximation to the flow can be achieved in an essentially two-dimensional solution. By varying the assumed aspect ratio in this inner solution the dependence of cavity volume and length on the aspect ratio of the foil has been demonstrated. This dependence appears to be much weaker than that proposed by Peters, et al. (1980), but it is still significant.

The iterative method proposed here for the determination of the interaction pressure has been shown to converge for a typical hydrofoil of aspect ratio 10. Although it was argued that the iteration scheme should converge in the limit of low values of  $\alpha/\sigma$ , this parameter varied from 0 to .2 in the case investigated. Indeed, the cavity was larger than one chord over a portion of the cycle. This suggests that the iteration procedure is likely to converge for most cases of interest. The relatively small difference between the first approximation to the flow and that obtained after iteration indicates that for many purposes the first approximation of the inner solution should be sufficiently accurate.

The numerical technique proposed here for the solution of the inner problem is simple, and relatively undemanding of computer time. The numerical convergence of the solution to a periodic response in the case of a periodic disturbance has been demonstrated. With the exception of occasional subharmonic responses, the solution is quite stable. It does not exhibit the high frequency oscillations found by Stern (1980). The method has been shown to predict such observed phenomena as slow cavity growth and rapid collapse, and the inability of the cavitation process to respond to high frequency variations in the flow field. It predicts the smooth transition from partial to supercavitation which is observed in the case of propeller blades operating in a non-uniform wake. The predicted behavior of the lift coefficient during this transition is a surprising result which has not previously been encountered.

The major limitations of the present theory are two-fold. Firstly, foil thickness can be included only in a linearized way. The effect of thickness in reducing cavity extent which is predicted by Tulin & Hsu (1977) is a nonlinear effect which cannot easily be incorporated. Viscous effects may have to be considered in determining the true effect of thickness on sheet cavitation.

The second limitation of the present theory is the assumption that the cavity separates from the foil at the leading edge. It is sometimes observed that during cavity collapse part of the cavity tears off and collapses downstream as cloud cavitation. This behavior cannot be predicted by the present theory.

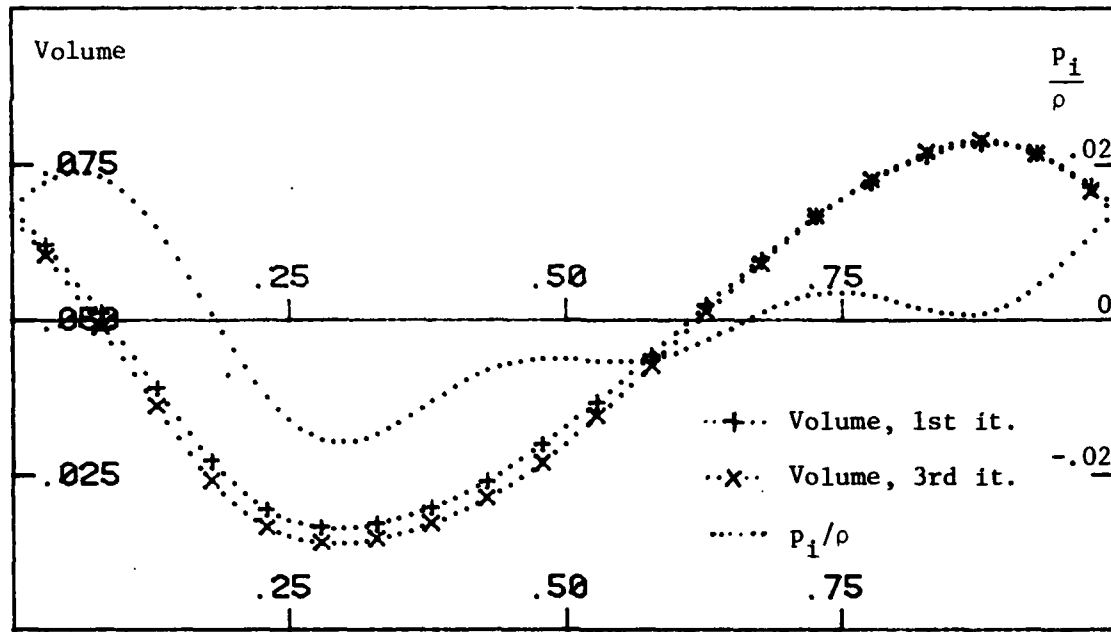


FIGURE 13A. VOLUME AND INTERACTION PRESSURE,  $Z=0$   
VERTICAL GUST,  $\alpha=0-.1$ ,  $\sigma=0.5$ ,  $AR=10$ ,  $K=1$

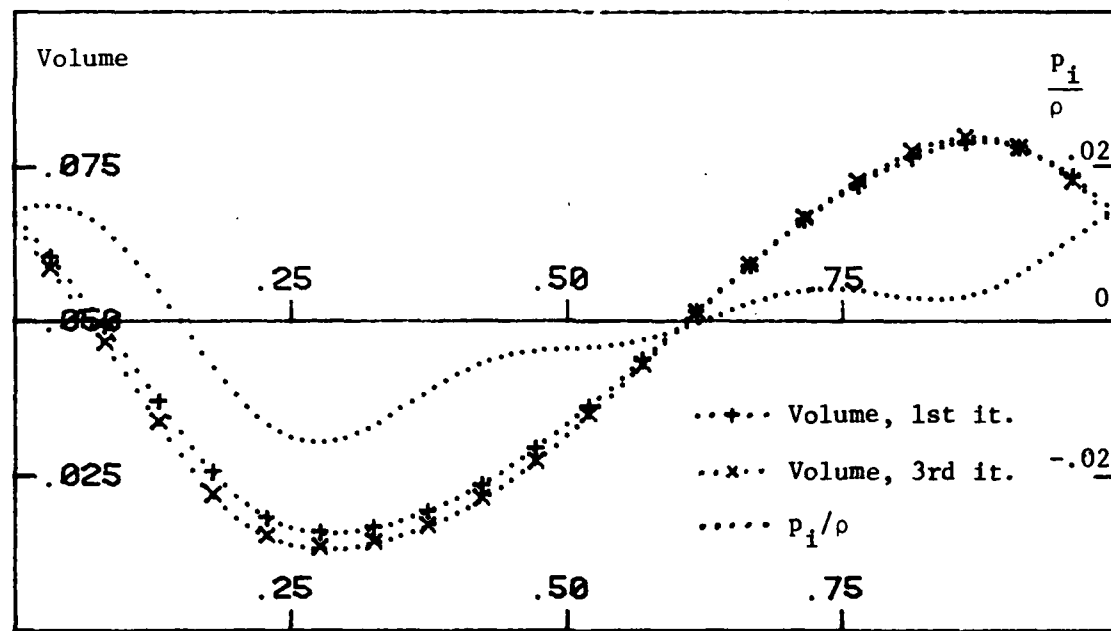


FIGURE 13B. VOLUME AND INTERACTION PRESSURE,  $Z=.1$   
VERTICAL GUST,  $\alpha=0-.1$ ,  $\sigma=0.5$ ,  $AR=10$ ,  $K=1$

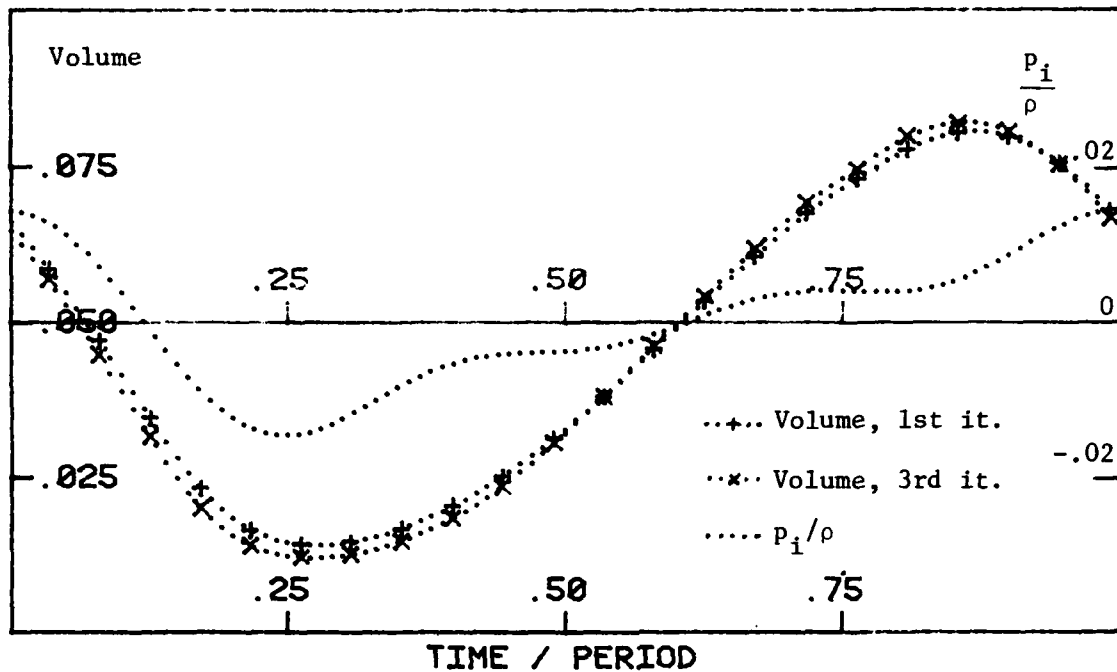


FIGURE 13C. VOLUME AND INTERACTION PRESSURE,  $Z=0.2$   
VERTICAL GUST,  $\alpha=0.1$ ,  $\sigma=0.5$ ,  $AR=10$ ,  $K=1$

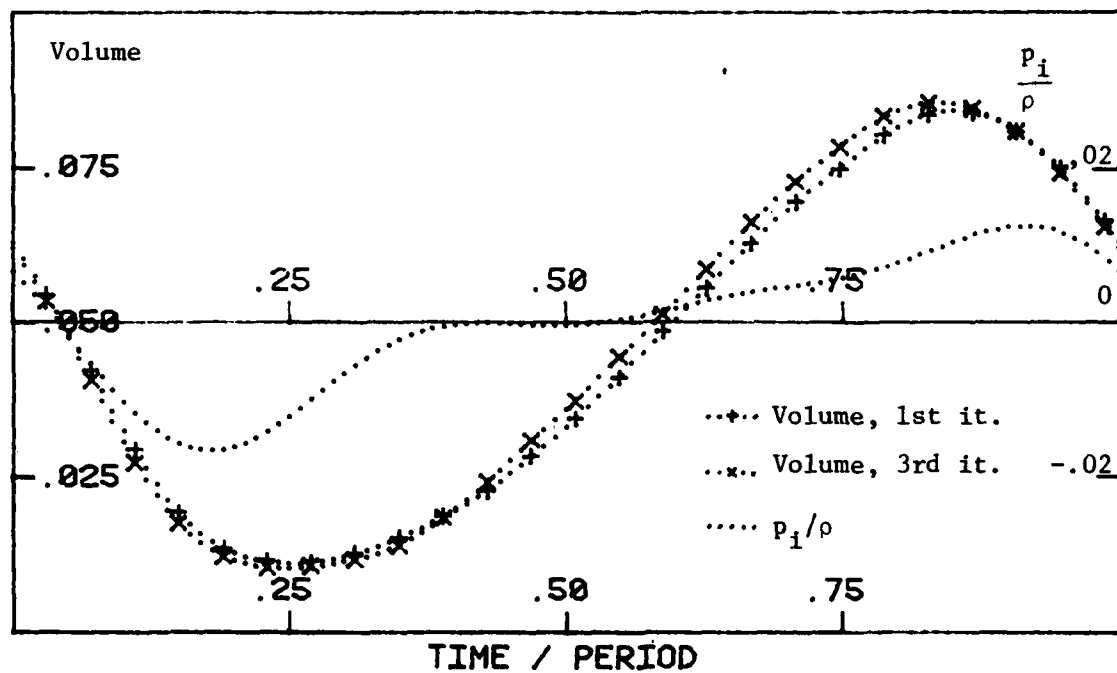


FIGURE 13D VOLUME AND INTERACTION PRESSURE,  $Z=0.3$   
VERTICAL GUST,  $\alpha=0.1$ ,  $\sigma=0.5$ ,  $AR=10$ ,  $K=1$



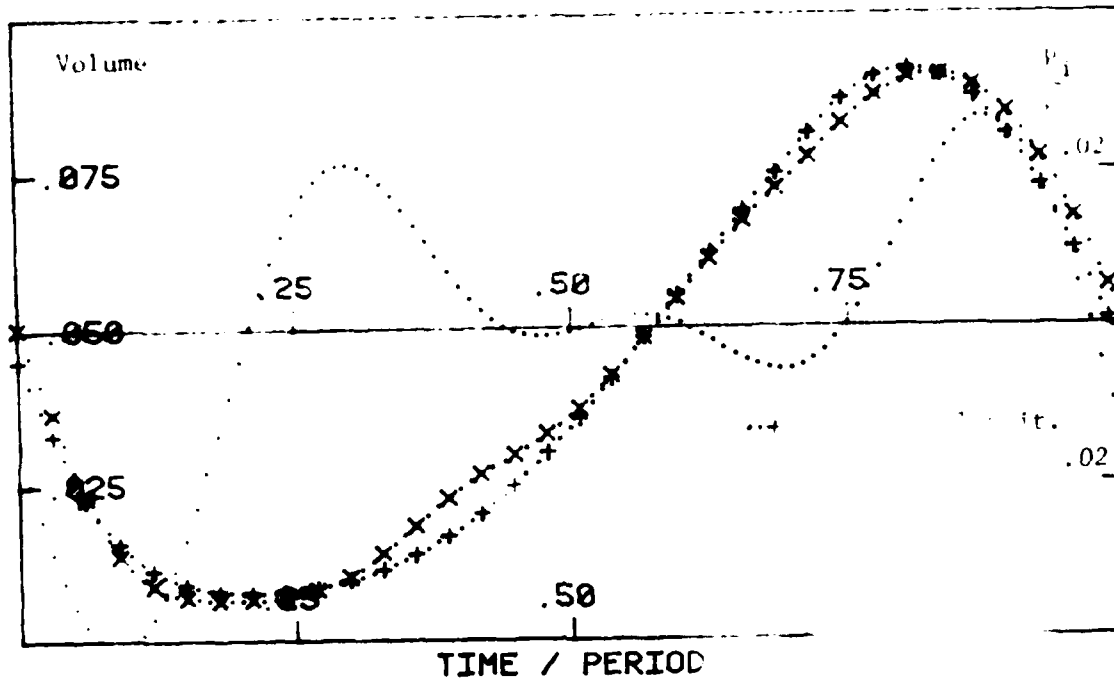


FIGURE 13E. VOLUME AND INTERACTION  
VERTICAL GUST,  $\alpha=0-.1$ ,  $MA=0.5$ ,  $K=1$

TABLE 1. RMS Error in Interaction Pressure  $p_i$ . Non-dimensional. 1 on 3

$z$	Iteration 1	Iteration 2	Iteration 3
		<u>All Harmonics</u>	
0	.0206	.0071	.0040
.1	.0189	.0063	.0022
.2	.0204	.0086	.0053
.3	.0310	.0159	.0113
.4	.0432	.0206	.0181
		<u>First Harmonic only</u>	
0	.0129	.0015	.0003
.1	.0127	.0011	.0001
.2	.0124	.0014	.0003
.3	.0126	.0018	.0008
.4	.0141	.0027	.0010

TABLE 2. RMS Change in Volume

$z$	Iteration 2	Iteration 3
0	.00528	.00125
.1	.00548	.00062
.2	.00497	.00111
.3	.00590	.00211
.4	.00835	.00474

Some extensions to the present theory would be quite simple to incorporate. In Van Houten and Sayre (1982) the theory was modified to account for the presence of air in the cavity. In that work, it was assumed that the mass of cavity air was a constant over the flow cycle. At each time step the solution was iterated until cavity volume and cavity pressure satisfied the ideal gas law. Other extensions that should be quite simple to incorporate are cavity buoyancy effects and pressure side cavitation. This latter extension would be important in studying propeller flows, since face cavitation is generally regarded as a major cause of blade erosion.

A difficulty in evaluating any theory for high aspect ratio hydrofoil cavitation is the fact that due to structural considerations high aspect ratio foils are not used at speeds where cavitation is likely to be experienced. Experimental data is lacking for the same reason. Perhaps the most important extension of the present theory is to planforms of moderate aspect ratio. Three-dimensional lifting surface programs using similar techniques have been developed by Jiang and Leehey (1977) for planar supercavitating foils, and by Lee (1980) for propellers.

#### ACKNOWLEDGEMENTS

This work was supported by the U.S. Maritime Administration, under contract MA-79-SAC-0-0032.

#### REFERENCES

- Acosta, A. J. (1955). A note on partial cavitation of flat plate hydrofoils, Report E-19.9, California Institute of Technology, Hydrodynamics Laboratory.
- Arakeri, V. H. (1975). Viscous effects on the position of cavitation separation from smooth bodies, J. Fluid Mechanics, 68.
- Benjamin, T. B. (1964). Note on the interpretation of two-dimensional theories of growing cavities, J. Fluid Mechanics, 19.
- Geurst, J. A. (1959). Linearized theory for partially cavitating hydrofoils, Int'l. Shipbuilding Progress, 6, No. 60.
- Geurst, J. A. (1960). Linearized theory for fully cavitating hydrofoils, Int'l. Shipbuilding Progress, 7, No. 65.
- Geurst, J. A. and P. J. Verbrugh (1959). A note on camber effects of a partially cavitating hydrofoil, Int'l. Shipbuilding Progress, 6, No. 61.
- James, E. C. (1975). Lifting-line theory for an unsteady wing as a singular perturbation problem, J. Fluid Mechanics, 70.
- James, R. M. (1972). On the remarkable accuracy of the vortex lattice method, Computer Methods in Applied Mechanics and Engrg., 1.
- Jiang, C. W. and P. Leehey (1977). Experimental and theoretical investigation of unsteady supercavitating hydrofoils of finite span, MIT Report 83481-4.

- Kuiper, G. (1979). Some experiments with distinguished types of cavitation on ship propellers, Int'l. Symp. on Cavitation Inception, New York, N.Y.
- Lee, C. S. (1980). Prediction of the transient cavitation on marine propellers by numerical lifting-surface theory, Thirteenth Symp. on Naval Hydrodynamics, Tokyo, Japan.
- Peters, A. S., T. R. Goodman, and J. P. Breslin (1980). A partially cavitating hydrofoil in a gust, Stevens Institute of Technology, Davidson Laboratory, Report SIT-DL-2118.
- Shen, Y. T. and F. B. Peterson (1978). Unsteady cavitation on an oscillating hydrofoil, Twelfth Symp. on Naval Hydrodynamics, Washington, D.C.
- Stern, F. (1980). A model for propeller sheet cavitation: the equations of motion for elliptical cavities in spatiotemporally varying velocity fields, University of Michigan, College of Engineering, Report 221.
- Stern, F. (1981). Comparison of computational and experimental unsteady cavitation on an oscillating hydrofoil, Science Applications, Inc., Report SAI-463-81-238-LJ.
- Tulin, M. P. (1980). An analysis of unsteady sheet cavitation, 19th American Towing Tank Conference.
- Tulin, M. P. and C. C. Hsu (1977). The theory of leading edge cavitation on lifting surfaces with thickness, Symp. on Hydrodynamics of Ship and Offshore Propulsion Systems, Hovik, Norway.
- Van Houten, R. J. and H. C. Sayre (1982). Experimental and theoretical studies of the effect of gas content on unsteady cavity flows, Massachusetts Institute of Technology, Department of Ocean Engineering, Report 82-1.

## Discussion

J.P. Breslin (Stevens Institute of Technology)

Our response to Dr. Van Houten's remarks 1 and 2 on page 6 of the paper is as follows:

If one starts with the author's velocity potential, which we may designate is  $\phi^*$ , then one can find the corresponding acceleration potential  $P^*$ . The boundary problem posed on  $P^*$  can be completely solved by function theoretic methods (as in Reference 1). It then turns out that after cavitation is established, (second-time derivative and cavity area)  $A_{tt}^*$  must be zero in order to satisfy the boundary condition on the upper side of the foil abaft of the cavity and the closure condition.

This result rests on the assumption that the variation of the cavity length  $C^*(t)$  is such that the implicit equation  $\lambda = C^*(\lambda + t - x)$  passes one root  $\lambda_1$ .

After  $\phi^*$  is admitted, the result does not depend on any asymptotic expansion and furthermore holds both for  $P^*$ , which possesses a logarithmic singularity at infinity, and the acceleration potential  $P$  (regular at infinity) of our report (Reference 1).

Thus, we find that the first order approximation that yields  $A_{tt}^* = 0$  is a consequence of enforcing the boundary conditions on the approximate two-dimensional problem rather than a consequence of matching assumed asymptotic expansions.

Van Houten apparently does not find that  $A_{tt}^* = 0$ . This may be due to the fact that the cavity length he discusses does not satisfy the condition arising in the analytical solution, namely, that  $\lambda$  be such that  $\lambda = C^*(\lambda + t - x)$ .

However, his analysis is numerical, and it seems that in the numerical work the boundary condition on the upper side of the foil abaft of the cavity is not strictly enforced. In the text following Equation 43, he states that "... When the cavity is shrinking, the cavity source strength may be nonzero in elements which lie downstream of the cavity termination at the present time step. The magnitudes of these sources may be obtained from Equation 41 as:

$$Q_{i,j} = -\tau_{i-1,j-1} \cdot \left( \frac{\Delta x_{Q_i}}{\Delta t} \right) "$$

In accordance with the boundary conditions, the source strength  $q(\xi) = [\phi_y^*]_{y=0} ([\phi_y^*]$  being the jump in the vertical velocity on  $y = 0$ ) must always be zero abaft the trailing edge of the cavity. This may indeed account for the discrepancy between the behavior of his numerical solution and that of our analytically derived result.

## Reference

1. A.S. Peters, T.R. Goodman, and J.P. Breslin, "A Partially Cavitating Hydrofoil in a Gust," Report SID-DL-80-2118, Davidson Laboratory, Stevens Institute of Technology, November 1980.

## Author's Reply

R.J. Van Houten (MIT)

The source of the discrepancy between the results of Peters, Goodman, and Breslin (1980) and those presented here is not clear. However, it is extremely unlikely that it lies in the use of Equation 44 in assigning source strength to singularities downstream of the current cavity termination. This equation applies only to singularities that were in the cavitating region at the immediately preceeding time step and is a consequence of the discretization scheme used to approximate Equation 12. The magnitude of the error introduced can be systematically reduced by increasing the number of singularities used to represent the foil. Figures 8c through 8g show that for the case  $k_r = 1$  the solution does not change significantly as the number of vortices over the chord is increased from 10 to 20. The discretization error would therefore appear to be small.

*Session VI*

**PROPELLER-  
RELATED PROBLEMS**

# Hydrodynamic Pressure Measurements on a Ship Model Propeller

Guus G.P. Versmissen and Wim van Gent

Maritime Research Institute Netherlands, Wageningen

## ABSTRACT

The results of a feasibility study with regard to the measurements of hydrodynamic pressures on propeller blades in a towing tank are described. Instrumentation, mounting and accuracy problems are carefully treated. An analysis of all error sources, prior to measurements, leads to an estimate of the total error within  $\pm 3$  per cent. This is considered to be satisfactory for the aim of the pressure measurements. Measurements have been carried out on a ship propeller model with a diameter of 0.48 m in uniform flow. In total 40 pressure transducers were mounted, 25 on the suction side and 15 on the pressure side. The transducer type selected was based on strain-gauge techniques. Its small dimensions, diameter 6 mm and thickness 0.6 mm, make it especially suitable to be mounted close to the leading edge. For system calibration the hydrostatic pressure variations, obtained from slow propeller rotation, are used.

The measurement series, for two loading conditions, have been repeated under identical conditions after six months. Checks on the possible error sources give the same estimate of accuracy. The scatter in the experimental results is larger than this estimate. However, for most transducers the scatter is smaller than the maximum, which has been found as a result of an extensive testing of one of the transducers.

The developed method is especially suitable in extensive investigations, when a large number of transducers have to be mounted and many data have to be collected.

## NOMENCLATURE

$C_p$	Pressure coefficient $(p-p_0)/(\frac{1}{2}\rho V^2)$	-
$c$	Chord of propeller section	m
$D$	Propeller diameter	m
$f_{\max}$	Maximum camber	m
$J$	Advance ratio $(U)/(nD)$	-
$K_T$	Thrust coefficient	-
$K_Q$	Torque coefficient	-
$n$	Number of propeller revolutions	$s^{-1}$

P	Pitch	m
p	Pressure	mbar
$p_0$	Static pressure in undisturbed flow	mbar
r	Radius on propeller section	m
R	Outer radius of propeller	m
$t_{\max}$	Maximum thickness	m
U	Axial velocity of propeller	$\text{ms}^{-1}$
V	Undisturbed inflow velocity of a propeller section $V^2 = U^2 + (2\pi nr)^2$	$\text{ms}^{-1}$
x	Chordwise distance from the leading edge of a propeller section	m
y	Ordinate of propeller blade section	m
$\rho$	Specific mass of fluid	$\text{kg m}^{-3}$

## 1. INTRODUCTION

Various calculation programs, based on lifting surface theory are now existing to determine the pressure distribution on propeller blades. To verify the results of these calculations there is a need for comprehensive and accurate sets of measured pressure distributions. A number of attempts have been made. (Mavrudoff (1966), Hoiby (1970), Kato (1977), Takahashi and Oku (1977), Yamasaki (1978), Dohrendorf et al (1978), Takei et al (1979). However, instrumentation problems prevented extensive measurement programs to be carried out with sufficient reliability.

The most important instrumentation problem related to propeller blade pressure measurements, being the mounting of suitable pressure gauges in the blade, can be solved better now by the recent developments in miniature pressure transducers. Takei et al (1979), described measurements, carried out successfully, with 5 pressure gauges on one propeller blade chord. In our case it was thought necessary to measure the pressure distribution over a sufficiently large area of the blade in order to widen the scope of correlation between calculated and measured data.

The work described in this paper has been undertaken to ascertain the feasibility of blade pressure measurements on the complete blade with sufficient accuracy for correlation purposes. First a study of the instrumentation problems has been carried out (choice of pressure transducer, analysis of achievable accuracy, etc.). Next, introductory measurements have been executed on a propeller in open water without cavitation, to assess the reliability and the reproducibility of these measurements.

## 2. THE PROPELLER MODEL

The selection of the propeller to be tested has been based on the following considerations:

- Availability of further characteristics of the propeller on open-water performance, boundary layer and cavitation properties. These



aspects are reported by Kuiper (1981).

- Blade sections are sufficiently thick to allow for mounting pressure transducers close to the leading edge.
- A relatively small pressure gradient near the leading edge is preferred.

The selected propeller was designed to exhibit bubble cavitation. The propeller geometry, given in Figure 1 and Tables 1, has been made as simple as possible: no rake, no skew, an elliptic blade contour and one type of sections over the whole radius.

The propeller has thick, cambered profiles to avoid sheet cavitation and a strongly reduced pitch at the tip to avoid tip vortex cavitation.

The model has been made in bronze with a large diameter (0.48 m). The measured open-water characteristics are given in Figure 2. One blade of the propeller has been prepared to measure pressures at 40 locations. Figure 3 shows the distribution of the measurement locations at both suction side (25 points) and pressure side (15 points).

### 3. DESCRIPTION OF MEASUREMENT SYSTEM

#### 3.1. Pressure transducer

In recent years much progress has been made in the field of miniaturization of pressure transducers. Thin-film and semi-conductor (piezo-resistive) based techniques allow sensitive gauges in very small housings. Two basic configurations of miniature pressure gauges are available nowadays: the cylindrical type with a small circular sensitive area (e.g. 1 mm diameter) but with considerable length (e.g. 12 mm) and the flatline type, which is thin (e.g. 1.2 mm) but has a bigger sensitive area (2 to 4 mm) and an even bigger surface (e.g. 4 x 10 mm). It will be clear that for our purpose a transducer is needed with a very small sensitive area, combined with an extremely small thickness, which up till now is technologically impossible, so some compromise must be made.

Interesting for the future is the very recent development of ultra-thin capacitive pressure gauges (thickness e.g. 80  $\mu\text{m}$ ) which could be simply glued on the blade surface. (Portat et al (1982a, 1982b)). However, as reported, more research is required to make these gauges water resistant.

In the present case a transducer was selected based on ordinary strain-gauge techniques. This gauge (manufacturer KYOWA, type PS-2KA) is an rather small ( $\varnothing$  6 mm) and thin (0.6 mm) device in which a bridge circuit is formed using a foil strain gauge as transducer element. Being a low-cost transducer (price abt. Dfl. 200.--) its use in bigger quantities is possible, while its thickness of 0.6 mm permits mounting in the propeller blade close to the blade's leading edge. In Table 2 the manufacturer's specifications of this gauge are presented. A drawback formed by the relatively low output sensitivity can be met by the use of accurate and stable electronics.

Though the specifications of this gauge are not excellent compared

to bigger transducers, own calibrations and investigations of this gauge in the present application have shown very acceptable results. In its operation area of 0 - 150 mbar the transducer was tested on linearity, hysteresis, and temperature effects. A maximum non-linearity of + 0.75% of the actual measured value has been observed while the other effects accounted for a maximum error of + 1.75% of the actual measured value. Considering the small physical dimensions of this transducer, these characteristics are in every respect acceptable.

One blade of the propeller, described in Section 2, was fitted with 40 gauges. By machining small chambers in the blade, the gauges could be flush mounted. Also the required wiring was countersunk in the blade, see Figure 4.

A special problem was caused by the sensitivity of the transducers for flexure of the blade. Originally the gauges were bonded in the blade by special cement, which caused some influence on the pressure signal by blade flexure. Therefore in the final test set up all gauges were embedded in their chambers with a radial play of abt. 0.5 mm, using parafin wax, which reduced the influence of blade flexure by a factor of abt. 5.

In Figure 3 some data concerning this influence are presented. To simulate the hydrodynamic load on the blade a point force of 50 N has been applied at 0.95R. For 5 transducers the resulting output signals expressed in mbar are given. These crosstalk signals are small compared to the actually measured pressure signals.

To assess any influence of centrifugal load on pressure transducer outputs the propeller was driven in air at 360 rpm. No measurable transducer output was detected.

To smooth the gauges and wiring in the propeller blade, a thin layer of parafin wax was applied on the blade (with a thickness of abt. 30  $\mu$ m). After this treatment virtually no disturbance of the nominal blade sections was recognizable.

### 3.2. Measuring apparatus

During the tests the propeller was driven by a Z-drive which originally was designed for dynamical measurements of fluctuating and weak signals from propeller blade stresses, blade torque of CP propellers ect. Figure 5 shows a schematic of the test arrangement, while Figure 6 shows some photographs of this apparatus. It is capable to measure simultaneously 6 fluctuating or DC signals. The propeller is mounted on a heavy shaft, acting as a flywheel (seismic mass) which rotates in a heavy bronze housing, to keep the resonance frequency of the measurement system as low as possible.

The 6 measurement channels (usually strain gauge bridges) are powered via a 16 channel rotary transformer. The measurement signals are pre-amplified by shaft mounted amplifiers and then connected, via the rotary transformer, to 6 AC - strain gauge conditioners. Electrical calibrations of each channel can be performed by switching a precision resistor in parallel to one arm of the strain gauge bridge, thus simulating a known unbalance of the bridge. Also a rotary encoder is built in to generate 1 and 360 pulses per propeller revolution.

This shaft is driven by an electromotor via a transmission including a transmission ratio of 31 to 26, to prevent possible vibrations from the transmission gear from interfering with blade rate frequencies.

The principal characteristics of the apparatus are:

- 6 measuring channels (strain gauge bridges)
- crosstalk - 60 dB
- signal transmission by low Multi Channel Rotary Transformer
- 6 pre-amplifiers on the propeller shaft
  - gain : adjustable between 10 and 500
  - frequency: 0-5 kHz 100% ampl. 0° phase shift
  - 10 kHz 99% ampl. 5° phase shift
- electrical calibration through switching of precision resistor, + 5 ppm/°C, of known value in parallel to bridge arm
- Rotary Encoder providing 1 and 360 pulses per revolution
- 6 channel AC strain gauge amplifier, carrier frequency 1000 Hz
- propeller submersion adjustable between 200 and 700 mm
- shaft provided with flywheel to enable measurements of fluctuating phenomena at propeller
- mass 210 kg.

An assessment has been made of the overall accuracy of the test set up. In the electronics of the shaft no errors of any importance could be detected, regarding non-linearity, drift etc., while for the AC strain gauge amplifiers an error smaller than  $\pm 0,5\%$  could be measured.

During the measurements the pressure signals were recorded both on magnetic tape and with a digital data acquisition system, with a 12 bit A/D conversion causing neglectable errors.

### 3.3. System calibration

As described under 3.2 the pressure transducers were calibrated, both in air and in water, versus high-precision pressure gauges, to make an assessment of their accuracy. For the actual measurements, however, another procedure has been followed.

Before every test run in the towing tank the 6 at that time connected pressure transducers were calibrated by slowly rotating the propeller shaft (abt. 0.15 rps). The sinusoidal pressure signals, thus obtained could easily be analysed. From the DC levels of these signals the zero pressure levels were derived. The sinusoidal signals were digitally filtered (with a cut-off frequency of 0.25 Hz) where upon the average peak-to-valley values were derived corresponding with the variation in static pressure of the pressure gauges during a revolution. The radial position of the gauges being exactly known, this procedure proved to be very reliable to calibrate the entire measurement set up. This calibration was reproducible with a standard deviation better than 0.4%.

The other test parameters, towing carriage speed and propeller rpm were stabilized by thyristor controllers, allowing a standard deviation of less than 0.5%.

From the error sources as presented in Section 3.2, a good estimation of the total error of the blade pressure measurement seems to be  $\pm 3\%$ , which is mainly produced by errors from the pressure gauges. In view of

the aim of the measurements an maximum error of  $\pm 5\%$  is considered to be satisfactory.

#### 4. RESULTS OF THE MEASUREMENTS

The results of the preliminary investigations justified the execution of a measurement series to further assess the feasibility of measuring blade pressures with the equipment as described above. Measurements have been carried out on the propeller, described in Section 2 in the open-water condition, without cavitation for the following advance coefficients:

$$\begin{aligned} J &= 0.6 \text{ (with } U = 1.74 \text{ ms}^{-1} \text{ and } n = 6.02 \text{ rps)} \\ J &= 0.4 \text{ (with } U = 1.00 \text{ ms}^{-1} \text{ and } n = 5.18 \text{ rps)} \end{aligned}$$

During one test run 6 pressure gauges could be measured and recorded simultaneously. To ascertain the repeatability of successive test runs, pressure gauge No. 14 (located at  $r/R=0.7$ ,  $x/c=0.4$ ) was measured during all test runs.

To assess the reproducibility of these measurements on the long term the complete measurement series was repeated after 6 months.

Table 3 presents a review of the repeatability measurements as carried out with pressure transducer No. 14. Successive tests were carried out with an interval of abt. 1 hour. During this interval the propeller and drive-unit were taken out of the water to connect 5 other transducers to the circuitry. From the table it can be concluded that the reproducibility of the pressure measurements slightly improved from 3.0 and 3.2% in the first series to 2.0 and 2.1% in the second series respectively. This is attributed to a more stable alignment of the mounting frame of the equipment and to a better procedure to stabilize the temperature of the transducers.

Figure 7 shows typical registrations of 2 pressure signals versus time. The sinusoidal pressure fluctuations with a frequency equal to the propeller rotation frequency are clearly perceptible. In this figure 8 seconds of the total analysed signal length of 60 seconds is shown. This figure also gives an impression about the steadiness of the pressure signal.

In tables 4 through 7 the measured average pressure levels are presented together with the related pressure coefficients  $C_p$ . The  $C_p$  values were calculated using the undisturbed inflow velocity of the propeller section:

$$C_p = \frac{p - p_o}{\frac{1}{2} \rho V^2}$$

$$\text{with: } V^2 = U^2 + (2\pi n r)^2$$

Also, accomplished repetition measurements (apart from transducer No. 14) are included in these tables. All information is presented graphically in Figures 8 through 12.

From these figures it can be concluded that in general each

measurement series in itself provides a consistent set of data with a small scattering in the repetition measurements. However, some discrepancies seem to exist between the two measurement series mutually. Especially from the results at the sections  $r/R=0.5 - 0.6 - 0.7$  the propeller seems to have been heavier loaded in the second series of measurements than during the first series. In general this heavier loading occurs both at suction- and pressure side of the blade. No experimental explanation could be found for this phenomenon. Calibrations at low propeller rpm reproduced quite satisfactory (within 0.5%) between both measurement series. Also each measurement series individually reproduced well. Besides no deviations of propeller rpm or axial speed were detected. Between the two measurements all pressure gauges remained in the propeller blade together with their protective layer of wax. After termination of the second measurement series the propeller geometry was checked without finding any changes in the blade contours,

From the observations of transducer No. 14 in all measurements, it can be concluded that the maximum scatter is about  $\Delta C_p = 0.022$ . When the scatter is assumed to be the same for all transducers<sup>p</sup>, the scatter  $\Delta C_p$  at other radii becomes:

$r/R =$	0.4	0.5	0.6	0.7	0.8
$\Delta C_p =$	0.060	0.040	0.029	0.022	0.017

It can be concluded that the differences between the two measurements for most of the transducers fall within this range. The question remains, however, whether the scatter is due to the properties of the transducers or to environmental conditions. The latter possibility is suggested by the sometimes rather systematic differences between both measurements series.

## 5. COMPARISON WITH CALCULATIONS

The experimental results have been compared with theoretical calculations. The computer programmes used are based on linearized propeller theory, in which the effects of camber and thickness of the blade profile are described by separate equations (Van Gent, 1977). Moreover, the effect of camber is primarily a pressure difference between pressure and suction side, i.e. lift; while the effect of thickness is primarily on the pressure level, i.e. mean pressure (arithmetic mean of pressures on both sides).

The computer programme for lift calculation has been developed for prediction of the propeller thrust and torque, Van Gent (1977, 1980). Recently the improved numerical scheme, developed by Vis (1975) has been implemented for standard use. In combination with two-dimensional foil theory it is also in use for cavitation prediction, Kuiper (1981). The calculated open-water characteristics of the investigated propeller compare well with the experimental results:

Advance ratio	$J = 0.4$	$J = 0.6$
$K_T$ calculated	0.197	0.111
measured	0.185	0.110
$K_Q$ calculated	0.0266	0.0170
measured	0.0237	0.0159

The computer programme for calculation of the mean pressure has been developed by Wels (1977).

In Figures 13 through 17 the theoretical and experimental values for lift and mean pressure are collected. The experimental values for both measurements have been averaged at the three chordwise positions  $x/c=0.2 - 0.4 - 0.6$ , where transducers are located on either side of the blade.

The agreement for lift and mean pressure at the lighter loading,  $J=0.6$ , is satisfactory, except for the smallest radius  $r/R=0.4$ . For the higher loading,  $J=0.4$ , the agreement is less, especially for the mean pressure at lower radii.

The most likely reason for the discrepancies has to be found in the restriction of the theoretical models. In both models the induced velocities are approximately normal to the resultant velocities. Especially at the inner radii these components are not necessarily perpendicular. Within the theoretical models used a more accurate derivation is not possible. Effects of heavy loading, slipstream rotation and contraction, can be estimated, however, and introduced as corrections on the resultant velocities. For the lift this has been undertaken by Van Gent (1977); it seems also worthwhile for the mean pressure.

## 6. CONCLUSIONS

- Size and price of modern pressure transducers make it feasible to instrument a model propeller blade with a large number of transducers.
- Mounting of the transducers can be done without problems of blade flexure and allows for a stable calibration.
- Calibration of the transducers is possible by using standard equipment for dynamic measurements on propellers.
- The test program up till now has revealed that in actual measurements the scatter in results is larger than the estimated accuracy. Further investigations are required to find out whether this is due to the properties of the transducers and/or due to environmental conditions in a towing tank beyond control.
- For comparison with theoretical predictions the experimental results are quite satisfactory and appear reliable.
- In theoretical models attention has to be paid to the flow around the inner blade sections. It is speculated that a better estimate of the onset velocity per section will improve the correlation with experimental results.
- The measurement method for propeller blade pressures is suitable for extensive experimental programs, where many data have to be collected. Especially when the operating conditions become more complicated (oblique flow, wake field, cavitation) this may be of decisive importance.

## ACKNOWLEDGEMENT

This work has been carried out as a part of the VOTOMAS project, which is supported by the Royal Netherlands Navy.

## LIST OF REFERENCES

- Dohrendorf, M., K. Kienappel, and R. Voss (1978). Experimentelle und theoretische Bestimmung der Druckverteilung an einem Propeller im simulierten Schiffsnachstrom, Schiffstechnik, Vol. 25.
- Hoiby, O.W. (1970). Three-dimensional effects in propeller theory, Norwegian Ship Model Tank, Publ. No. 105.
- Kato, H. (1977). An experimental study on the pressure fluctuations on a propeller blade in a wake, Proc. Symp. on Hydrodynamics of Ship and Offshore Propulsion Systems, Oslo.
- Kuiper, G. (1981). Cavitation inception on ship propeller models, Doctor's Thesis, Delft Technical University.
- Mavrudoff, M.A. (1965). Measurement of pressure on the blade surface of a non-cavitating propeller model, Proc. 12th I.T.T.C., Tokyo.
- Portat, M., A. Bruere, J.C. Godefroy, and F. Helias (1982). ONERA developed thin film transducers and their applications, Proc. SENSOR 82, Essen.
- Portat, M., M. Dupont, C. Hennion, J. Leiviner, J.P. Le Goff, and C. Crance (1982). Capteur de pression pelliculaires, Proc. DRG-Seminar on Advanced Hydrodynamic Testing Facilities, The Hague.
- Takahashi, M., and M. Oku (1977). The cavitation characteristics of MAU-Type propellers, J. Soc. Nav. Arch., Japan, Vol. 141.
- Takei, Y., K. Kodema, Y. Kurobe (1979). Measurements of pressures on a blade of a propeller model, Ship Research Institute, Tokyo, Paper 55.
- Van Gent, W., (1977). On the use of lifting surface theory for moderately and heavily loaded ship propellers, Netherlands Ship Model Basin, Publ. No. 536.
- Van Gent, W., (1980). Derivation of propeller blade section properties from lifting surface theory, Int. Shipbuilding Progress, Vol. 27.
- Vis, F.C., (1975). De berekening van de drukverdeling over de bladen van een scheepsschroef, Master's Thesis, Twente Technical University.
- Wels, H.C., (1977). Study of thickness effects on the pressure distribution at propeller blades using linearized singularity distributions, Master's Thesis, Delft Technical University.
- Yamasaki, T., (1978). On some tank test results with large model propeller - 0.95 m in diameter, J. Soc. Nav. Arch. Japan, Vol. 144.

r/R	c/D	P/D	(at midchord $f_{\max}/c$ $t_{\max}/c$ )	
.200	.24264	.74411	.02189	.19787
.250	.26176	.80202	.02515	.18202
.300	.27794	.83125	.02797	.16865
.400	.30367	.85937	.03141	.14467
.500	.32352	.86397	.03176	.12102
.600	.33676	.84595	.02882	.09770
.700	.33970	.79503	.02288	.07575
.800	.32352	.70661	.01573	.05681
.850	.30257	.65753	.01196	.04860
.900	.26691	.60937	.00792	.04132
.950	.20367	.55772	.00415	.03610
.975	.14963	.52996	.00245	.03685

Table 1A: Geometry of blade contour of propeller.

r/R	0.200		0.250		0.300		0.400	
x/c	y/c s	y/c p	y/c s	y/c p	y/c s	y/c p	y/c s	y/c p
x 100								
0.0	.08890	.06519	.07679	.05495	.06647	.04623	.04961	.03223
2.5	.11072	.04764	.09734	.03930	.08597	.03219	.06705	.02091
5.0	.12438	.03803	.11037	.03093	.09847	.02486	.07846	.01531
7.5	.13502	.03122	.12059	.02510	.10853	.01987	.08759	.01169
10.0	.14407	.02578	.12933	.02051	.11683	.01601	.09548	.00898
15.0	.15897	.01745	.14379	.01360	.13093	.01030	.10868	.00520
20.0	.17047	.01164	.15502	.00891	.14194	.00657	.11909	.00296
25.0	.17955	.00738	.16392	.00554	.15070	.00396	.12742	.00154
30.0	.18685	.00402	.17108	.00290	.15776	.00194	.13415	.00047
40.0	.19556	.00057	.17969	.00032	.16630	.00011	.14236	.00020
50.0	.19788	.00000	.18202	.00000	.16865	.00000	.14467	.00000
60.0	.19369	.00243	.17797	.00204	.16471	.00170	.14100	.00116
70.0	.18105	.00982	.16575	.00823	.15282	.00688	.12991	.00471
75.0	.17137	.01557	.15639	.01306	.14373	.01093	.12144	.00752
80.0	.15922	.02289	.14467	.01925	.13235	.01615	.11087	.01118
85.0	.14465	.03177	.13062	.02677	.11873	.02250	.09822	.01567
90.0	.12791	.04195	.11447	.03538	.10306	.02978	.08367	.02080
95.0	.10929	.05312	.09650	.04480	.08562	.03771	.06744	.02634
97.5	.09933	.05903	.08687	.04978	.07626	.04189	.05873	.02924
100.0	.08890	.06519	.07679	.05495	.06647	.04623	.04961	.03223

Table 1B: Geometry of blade sections.



r/R	0.500		0.600		0.700		0.800	
x/c								
x 100	y/c s	y/c p	y/c s	y/c p	y/c s	y/c p	y/c s	y/c p
0.0	.03602	.02148	.02596	.01411	.01986	.01012	.01670	.00864
2.5	.05115	.01254	.03847	.00722	.02917	.00527	.02297	.00544
5.0	.06120	.00837	.04687	.00415	.03572	.00295	.02769	.00364
7.5	.06932	.00581	.05369	.00237	.04116	.00152	.03170	.00238
10.0	.07637	.00400	.05964	.00117	.04585	.00061	.03511	.00156
15.0	.08823	.00166	.06969	-.00023	.05370	-.00038	.04081	.00059
20.0	.09765	.00050	.07771	-.00075	.06004	-.00076	.04543	.00005
25.0	.10522	-.00008	.08417	-.00087	.06511	-.00080	.04914	-.00020
30.0	.11134	-.00048	.08939	-.00090	.06918	-.00075	.05204	-.00026
40.0	.11887	-.00039	.09584	-.00044	.07429	-.00037	.05577	-.00021
50.0	.12102	.00000	.09771	.00000	.07576	.00000	.05682	.00000
60.0	.11773	.00075	.09492	.00048	.07357	.00035	.05521	.00035
70.0	.10780	.00306	.08653	.00196	.06702	.00141	.05045	.00133
75.0	.10022	.00492	.08013	.00317	.06201	.00231	.04675	.00220
80.0	.09077	.00738	.07216	.00480	.05570	.00358	.04213	.00335
85.0	.07948	.01042	.06263	.00683	.04814	.00519	.03667	.00472
90.0	.06648	.01388	.05167	.00914	.03959	.00687	.03052	.00615
95.0	.05198	.01759	.03943	.01158	.03010	.00858	.02376	.00757
97.5	.04419	.01951	.03285	.01283	.02505	.00939	.02023	.00818
100.0	.03602	.02148	.02596	.01411	.01986	.01012	.01670	.00864

r/R	0.850		0.900		0.950		0.975	
x/c								
x 100	y/c s	y/c p	y/c s	y/c p	y/x s	y/c p	y/c s	y/c p
0.0	.01607	.00860	.01632	.00916	.01755	.01024	.01984	.01210
2.5	.02094	.00606	.01984	.00718	.01996	.00864	.02193	.01049
5.0	.02476	.00445	.02279	.00570	.02211	.00727	.02387	.00901
7.5	.02805	.00326	.02532	.00455	.02402	.00608	.02561	.00769
10.0	.03087	.00242	.02758	.00360	.02575	.00503	.02722	.00649
15.0	.03556	.00131	.03130	.00226	.02862	.00342	.02990	.00455
20.0	.03934	.00064	.03421	.00141	.03083	.00228	.03200	.00308
25.0	.04238	.00024	.03655	.00081	.03259	.00144	.03366	.00197
30.0	.04472	.00005	.03836	.00042	.03395	.00082	.03492	.00114
40.0	.04775	-.00011	.04067	.00001	.03564	.00012	.03645	.00021
50.0	.04860	.00000	.04132	.00000	.03610	.00000	.03686	.00000
60.0	.04728	.00036	.04028	.00041	.03527	.00050	.03605	.00061
70.0	.04334	.00143	.03715	.00164	.03283	.00195	.03368	.00238
75.0	.04030	.00232	.03474	.00262	.03093	.00309	.03195	.00368
80.0	.03651	.00347	.03178	.00384	.02872	.00440	.02989	.00519
85.0	.03206	.00481	.02836	.00520	.02622	.00582	.02762	.00683
90.0	.02708	.00620	.02459	.00659	.02347	.00732	.02511	.00860
95.0	.02167	.00755	.02048	.00801	.02048	.00890	.02239	.01049
97.5	.01883	.00817	.01832	.00870	.01892	.00968	.02098	.01144
100.0	.01607	.00860	.01632	.00916	.01755	.01024	.01984	.01210

Table 1B: Geometry of blade sections (Continued).

Radius r/R	Suction side Semi-axes		Pressure side Semi-axes	
	a/c	b/c	a/c	b/c
.200	.1432	.0596	.0613	.0365
.250	.1684	.0600	.0586	.0324
.300	.1944	.0604	.0543	.0287
.400	.3061	.0661	.0479	.0228
.500	.9769	.0996	.0451	.0181
.600	15.5087	.3250	.0418	.0140
.700	- 2.5964*	.1019	.0400	.0105
.800	.9360	.0448	.0419	.0079
.850	.2526	.0199	.0429	.0069
.900	.1238	.0118	.0398	.0060
.950	.0599	.0074	.0378	.0056
.975	.0413	.0065	.0386	.0059

Table 1C: Leading-edge ellipses. (\*hyperbola)

Type	: KYOWA, PS-2KA
Range	: 2 bar
Output sensitivity (nominal)	: 0.8 mV/V $\pm$ 25%
Non-linearity	: 1% F.S.
Hysteresis	: 1% F.S.
Bridge voltage- max. allowable	: 3V (AC, DC)
Temperature effects -	
on zero	: 0.2% F.S. /°C
on output	: 0.1% F.S. /°C
Input/output resistance	: 120 $\Omega$ $\pm$ 10%
Natural frequency	: abt. 14 kHz
Allowable operating	
temperature range	: -20 ~ +70°C
Allowable overload	: 150% F.S.
Mass	: 7 gr.
Dimensions	: diameter 6 mm, thickness 0.6 $\pm$ 0.1 mm
Sensitive area	: abt $\varnothing$ 4 mm

Table 2: Specifications of strain-gauge pressure transducer.

1st. measurement series:

J = 0.4			J = 0.6		
Test	Pressure (mbar)	C <sub>p</sub>	Test	Pressure (mbar)	C <sub>p</sub>
1	-40.98	-0.265	1	-49.67	-0.229
2	-39.95	-0.259	2	-49.11	-0.226
3	-40.09	-0.259	3	-48.98	-0.226
4	-39.00	-0.252	4	-49.09	-0.226
5	-39.40	-0.255	5	-47.42	-0.218
6	-37.83	-0.245	6	-47.66	-0.220
7	-38.21	-0.247	7	-50.51	-0.233
8	-41.50	-0.269	8	-52.84	-0.243
Average : -39.62 -0.256			Average : -49.41 -0.228		
Standard deviation: 1.19 0.0078			Standard deviation: 1.60 0.0073		
% : 3.0 3.0			% : 3.24 3.2		

2nd. measurement series:

J = 0.4			J = 0.6		
Test	Pressure (mbar)	C <sub>p</sub>	Test	Pressure (mbar)	C <sub>p</sub>
1	-39.70	-0.257	1	-48.91	-0.225
2	-39.23	-0.254	2	-50.05	-0.231
3	-39.47	-0.255	3	-50.65	-0.233
4	-40.28	-0.261	4	-50.71	-0.234
5	-40.31	-0.261	5	-50.88	-0.234
6	-40.83	-0.264	6	-50.30	-0.232
7	-40.41	-0.262	7	-50.74	-0.234
8	-40.47	-0.262	8	-51.40	-0.237
9	-40.87	-0.265	9	-51.00	-0.235
10	-41.13	-0.266	10	-50.48	-0.233
11	-38.34	-0.248	11	-50.44	-0.232
12			12	-50.78	-0.234
Average : -40.09 -0.260			Average : -50.53 -0.233		
Standard deviation: 0.79 0.0052			Standard deviation: 0.59 0.0028		
% : 1.97 2.0			% : 1.17 1.20		

Table 3: Review of repeatability measurements carried out with pressure transducer 14 located at  $r/R = 0.7$ ,  $x/c = 0.4$ .

Transducer location				1st test		2nd. test	
No.	r/R	x/c	Side	Pressure (mbar)	Cp	Pressure (mbar)	Cp
1	0.4	0.10	Suction	-28.35	-0.527		
6	0.4	0.20	side	-27.83	-0.517		
11	0.4	0.40		-27.64	-0.514		
16	0.4	0.60		-18.60	-0.346		
21	0.4	0.80		- 9.19	-0.171		
2	0.5	0.10		-31.21	-0.384		
7	0.5	0.20		-32.17	-0.396		
12	0.5	0.40		-31.90	-0.392		
17	0.5	0.60		-27.30	-0.336		
22	0.5	0.80		- 8.38	-0.103		
3	0.6	0.10		-38.20	-0.333		
8	0.6	0.20		-38.80	-0.339		
13	0.6	0.40		-34.79	-0.303	-34.68	-0.302
18	0.6	0.60		-33.19	-0.289		
23	0.6	0.80		-15.77	-0.137		
4	0.7	0.083		-28.14	-0.182		
9	0.7	0.20		-33.90	-0.219		
14	0.7	0.40		-39.40	-0.255		
19	0.7	0.60		-35.50	-0.230		
24	0.7	0.80		-18.47	-0.120	-18.21	-0.118
5	0.8	0.10		-44.70	-0.223		
10	0.8	0.20		-36.88	-0.184		
15	0.8	0.40		-38.56	-0.193		
20	0.8	0.60	Suction	-37.14	-0.185		
25	0.8	0.80	side	-22.05	-0.110		
26	0.4	0.20	Pressure	1.89	0.035		
31	0.4	0.40	side	1.79	0.033		
36	0.4	0.60		- 2.33	-0.043		
27	0.5	0.20		3.81	0.047		
32	0.5	0.40		3.84	0.047		
37	0.5	0.60		2.31	0.028		
28	0.6	0.20		4.63	0.040		
33	0.6	0.40		5.47	0.048		
38	0.6	0.60		1.48	0.013		
29	0.7	0.20		7.65	0.050	7.36	0.048
34	0.7	0.40		7.64	0.049	7.55	0.049
39	0.7	0.60		3.91	0.025	3.56	0.023
30	0.8	0.20		5.91	0.030		
35	0.8	0.40	Pressure	4.14	0.021	4.24	0.021
40	0.8	0.60	side	0.73	0.004	0.83	0.004

Table 4: Results of first series of blade pressure measurements average values in uniform flow,  $J = 0.4$ .

Transducer location				1st. test		2nd. test	
No.	r/R	x/c	Side	Pressure (mbar)	Cp	Pressure (mbar)	Cp
1	0.4	0.10	Suction side	-26.75	-0.497		
6	0.4	0.20		-27.54	-0.512		
11	0.4	0.40		-26.96	-0.501		
16	0.4	0.60		-18.61	-0.346		
21	0.4	0.80		- 9.20	-0.171		
2	0.5	0.10		-30.34	-0.373		
7	0.5	0.20		-36.14	-0.445		
12	0.5	0.40		-33.31	-0.410		
17	0.5	0.60		-28.48	-0.350		
22	0.5	0.80		-12.54	-0.154	-11.65	-0.143
3	0.6	0.10		-33.38	-0.291	-35.19	-0.306
8	0.6	0.20		-38.68	-0.337		
13	0.6	0.40		-41.10	-0.358		
18	0.6	0.60		-33.88	-0.295		
23	0.6	0.80		-16.66	-0.145	-15.70	-0.137
4	0.7	0.083		-29.94	-0.194		
9	0.7	0.20		-44.21	-0.286		
14	0.7	0.40		-39.47	-0.255		
19	0.7	0.60		-39.13	-0.253		
24	0.7	0.80		-21.84	-0.141		
4	0.8	0.10	Suction side	-33.88	-0.156		
10	0.8	0.20		-40.78	-0.204		
15	0.8	0.40		-39.09	-0.195		
20	0.8	0.60		-31.63	-0.158		
25	0.8	0.80		-25.08	-0.125	-25.68	-0.126
26	0.4	0.20	Pressure side	- 0.72	-0.013		
31	0.4	0.40		1.29	0.024		
36	0.4	0.60		- 1.57	-0.027		
27	0.5	0.20		4.56	0.056		
32	0.5	0.40		4.42	0.054		
37	0.5	0.60		- 0.20	-0.004	- 0.38	-0.005
28	0.6	0.20		3.35	0.029	3.87	0.034
33	0.6	0.40		1.96	0.017	2.95	0.026
38	0.6	0.60		1.58	0.014	1.96	0.017
29	0.7	0.20		5.75	0.037		
34	0.7	0.40	Pressure Side	5.25	0.034		
39	0.7	0.60		0.10	0.001		
30	0.8	0.20		1.00	0.005	1.58	0.008
35	0.8	0.40		1.82	0.009		
40	0.8	0.60		- 5.92	-0.030		

Table 5: Results of second series of blade pressure measurements  
average values in uniform flow,  $J = 0.4$ .

Transducer location				1st. test		2nd. test	
No.	r/R	x/c	Side	Pressure (mbar)	Cp	Pressure (mbar)	Cp
1	0.4	0.10	Suction	-23.09	-0.285		
6	0.4	0.20	side	-31.38	-0.387		
11	0.4	0.40		-40.12	-0.495		
16	0.4	0.60		-34.62	-0.427		
21	0.4	0.80		-20.33	-0.251		
2	0.5	0.10		-25.14	-0.213		
7	0.5	0.20		-35.23	-0.298		
12	0.5	0.40		-44.74	-0.379		
17	0.5	0.60		-42.61	-0.361		
22	0.5	0.80		-18.64	-0.158		
3	0.6	0.10		-30.41	-0.186		
8	0.6	0.20		-40.00	-0.245		
13	0.6	0.40		-45.92	-0.281		
18	0.6	0.60		-49.56	-0.303		
23	0.6	0.80		-27.41	-0.168		
4	0.7	0.083		- 8.93	-0.041		
9	0.7	0.20		-32.44	-0.149		
14	0.7	0.40		-48.98	-0.226		
19	0.7	0.60		-49.93	-0.230		
24	0.7	0.80		-29.04	-0.134		
5	0.8	0.10		-34.39	-0.123		
10	0.8	0.20		-33.94	-0.122		
15	0.8	0.40		-47.96	-0.172		
20	0.8	0.60	Suction	-51.10	-0.183		
25	0.8	0.80	side	-32.41	-0.116		
26	0.4	0.20	Pressure	-10.79	-0.133		
31	0.4	0.40	side	- 5.34	-0.066		
36	0.4	0.60		- 9.37	-0.116		
27	0.5	0.20		- 9.86	-0.083		
32	0.5	0.40		- 3.39	-0.029		
37	0.5	0.60		- 2.88	-0.024		
28	0.6	0.20		- 9.65	-0.059		
33	0.6	0.40		0.19	0.001		
38	0.6	0.60		- 4.36	-0.027		
29	0.7	0.20		- 7.96	-0.037	-8.38	-0.039
34	0.7	0.40		0.72	0.003	0.92	0.004
39	0.7	0.60		- 1.85	-0.009	-1.97	-0.009
30	0.8	0.20		-12.42	-0.045		
35	0.8	0.40	Pressure	- 5.34	-0.019	-4.72	-0.017
40	0.8	0.60	side	- 5.81	-0.021	-5.87	-0.021

Table 6: Results of first series of blade pressure measurements  
average values in uniform flow,  $J = 0.6$ .

Transducer location				1st. test		2nd. test	
No.	r/R	x/c	Side	Pressure (mbar)	Cp	Pressure (mbar)	Cp
1	0.4	0.10	Suction	-22.27	-0.275		
6	0.4	0.20	side	-31.36	-0.387		
11	0.4	0.40		-38.44	-0.474		
16	0.4	0.60		-33.18	-0.409		
21	0.4	0.80		-18.82	-0.232		
2	0.5	0.10		-23.92	-0.203		
7	0.5	0.20		-39.88	-0.339		
12	0.5	0.40		-45.48	-0.386		
17	0.5	0.60		-44.28	-0.376		
22	0.5	0.80		-23.25	-0.197	-22.52	-0.191
3	0.6	0.10		-25.09	-0.153	-25.75	-0.158
8	0.6	0.20		-42.11	-0.258		
13	0.6	0.40		-55.11	-0.337		
18	0.6	0.60		-51.04	-0.312		
23	0.6	0.80		-28.40	-0.174	-27.42	-0.168
4	0.7	0.083		-13.70	-0.063	-13.58	-0.063
9	0.7	0.20		-46.82	-0.216	-46.86	-0.216
14	0.7	0.40		-50.65	-0.233	-50.71	-0.245
19	0.7	0.60		-52.84	-0.243	-52.61	-0.242
24	0.7	0.80		-33.69	-0.155	-33.52	-0.154
5	0.8	0.10		-15.64	-0.056	-14.99	-0.054
10	0.8	0.20		-38.05	-0.136	-37.85	-0.136
15	0.8	0.40		-47.58	-0.171	-47.29	-0.171
20	0.8	0.60	Suction	-42.61	-0.153	-42.18	-0.151
25	0.8	0.80	side	-35.71	-0.128	-35.43	-0.127
26	0.4	0.20	Pressure	-13.23	-0.163		
31	0.4	0.40	side	- 5.24	-0.065		
36	0.4	0.60		- 6.14	-0.076		
27	0.5	0.20		- 8.42	-0.071		
32	0.5	0.40		- 1.06	-0.009		
37	0.5	0.60		- 6.28	-0.053	- 8.49	-0.072
28	0.6	0.20		-10.97	-0.067	-10.57	-0.065
33	0.6	0.40		- 4.95	-0.030	- 4.26	-0.026
38	0.6	0.60		- 3.66	-0.022	- 2.91	-0.018
29	0.7	0.20		-10.28	-0.047		
34	0.7	0.40		- 1.46	-0.007		
39	0.7	0.60		- 6.38	-0.029		
30	0.8	0.20		-18.95	-0.068	-15.55	-0.056
35	0.8	0.40	Pressure	- 7.51	-0.027		
40	0.8	0.60	Side	-14.53	-0.052		

Table 7: Results of second series of blade pressure measurements  
average values in uniform flow,  $J = 0.6$ .

## LIST OF FIGURES

- Figure 1: Geometry of propeller
- Figure 2: Open-water characteristics of propeller
- Figure 3: Measurement locations on blade
- Figure 4: Instrumented propellers: Suction side (top), pressure side (bottom)
- Figure 5: Test arrangement scheme
- Figure 6: Drive unit for instrumented propeller
- Figure 7: Time registration of typical pressure signal: test run (top), calibration run (bottom)
- Figure 8: Measured pressures at  $r/R=0.4$
- Figure 9: Measured pressures at  $r/R=0.5$
- Figure 10: Measured pressures at  $r/R=0.6$
- Figure 11: Measured pressures at  $r/R=0.7$
- Figure 12: Measured pressures at  $r/R=0.8$
- Figure 13: Lift and mean pressure correlations at  $r/R=0.4$
- Figure 14: Lift and mean pressure correlations at  $r/R=0.5$
- Figure 15: Lift and mean pressure correlations at  $r/R=0.6$
- Figure 16: Lift and mean pressure correlations at  $r/R=0.7$
- Figure 17: Lift and mean pressure correlations at  $r/R=0.8$



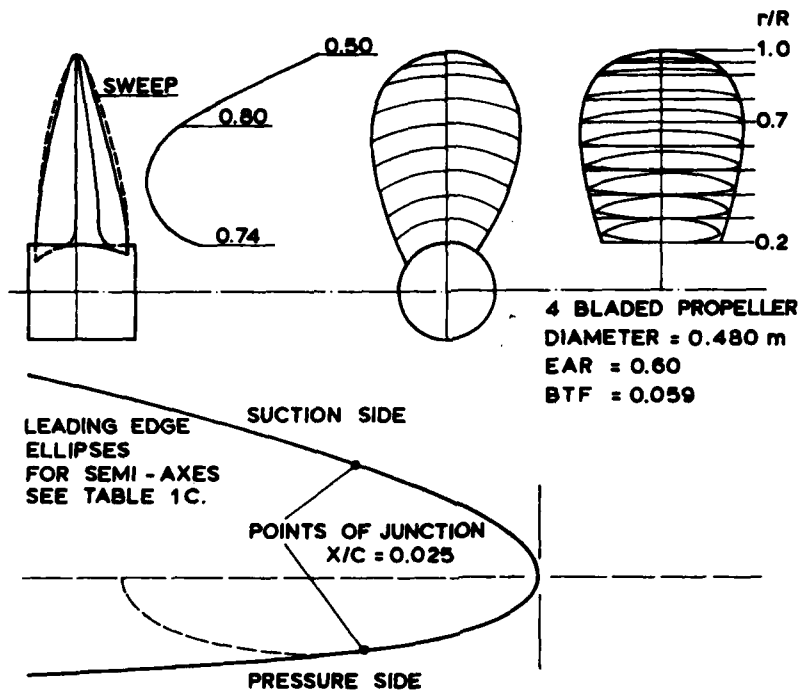


FIGURE 1

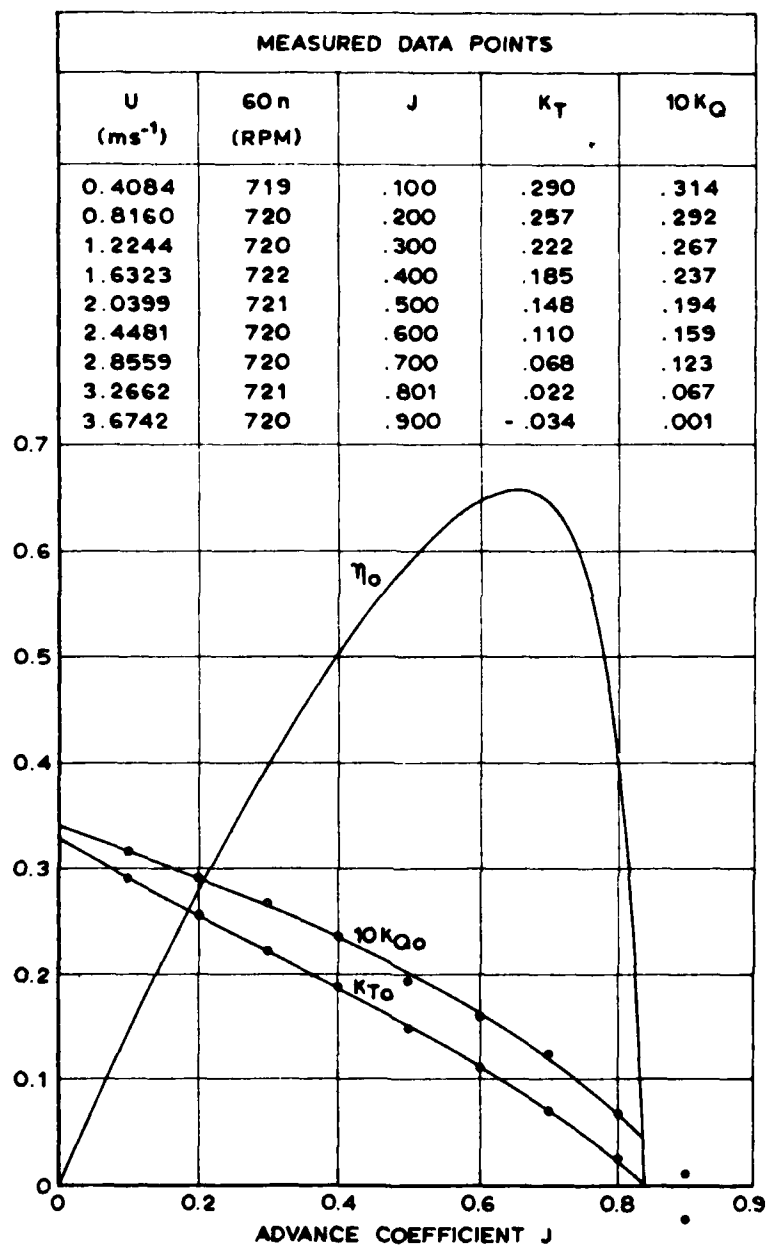


FIGURE 2

INFLUENCE OF FLEXURE BY POINT FORCE					
TRANSDUCER No.	11	4	24	15	14
CROSSTALK (mbar)	0.65	0	0.12	0	0.65

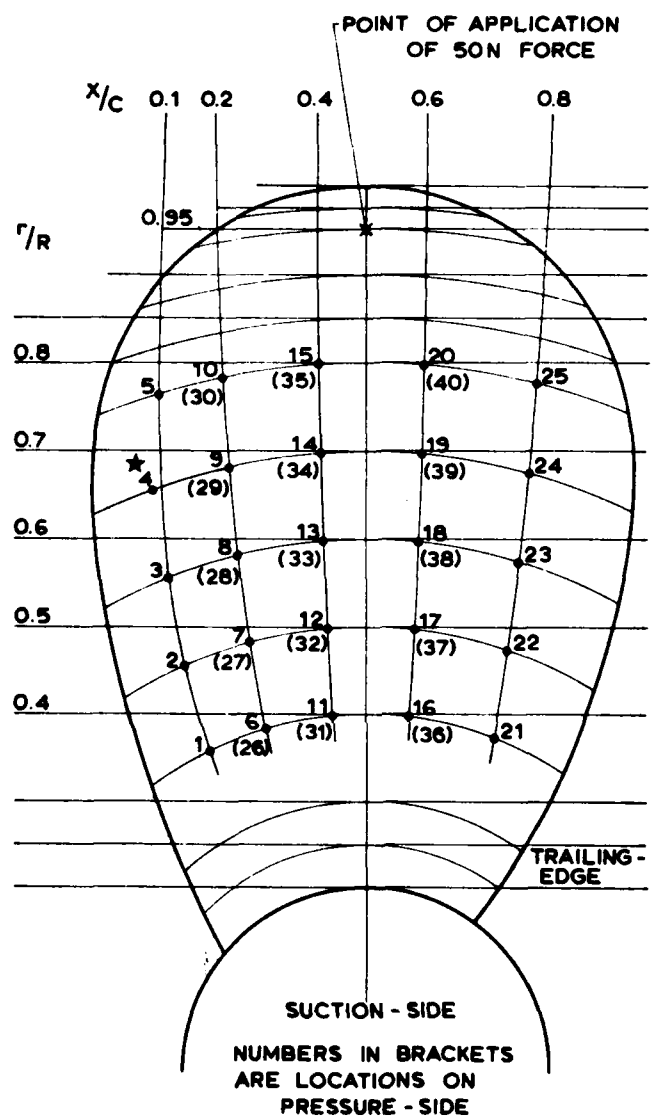


FIGURE 3

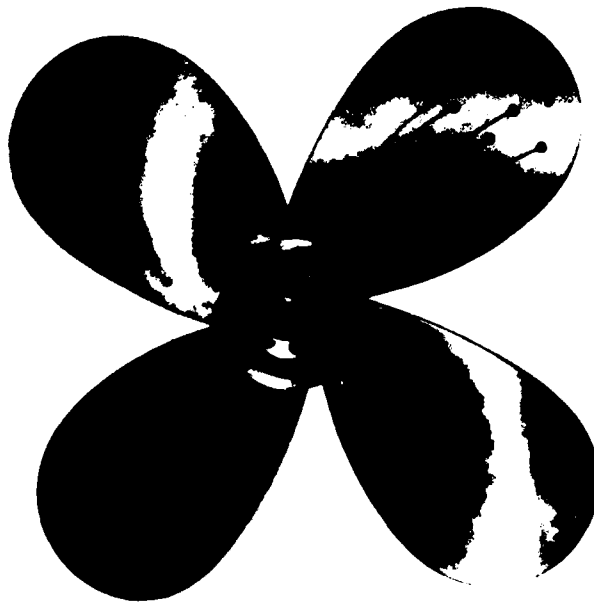
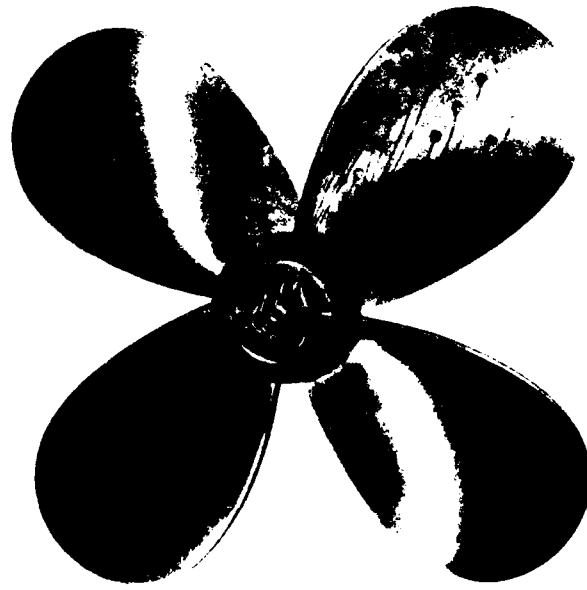


FIGURE 4

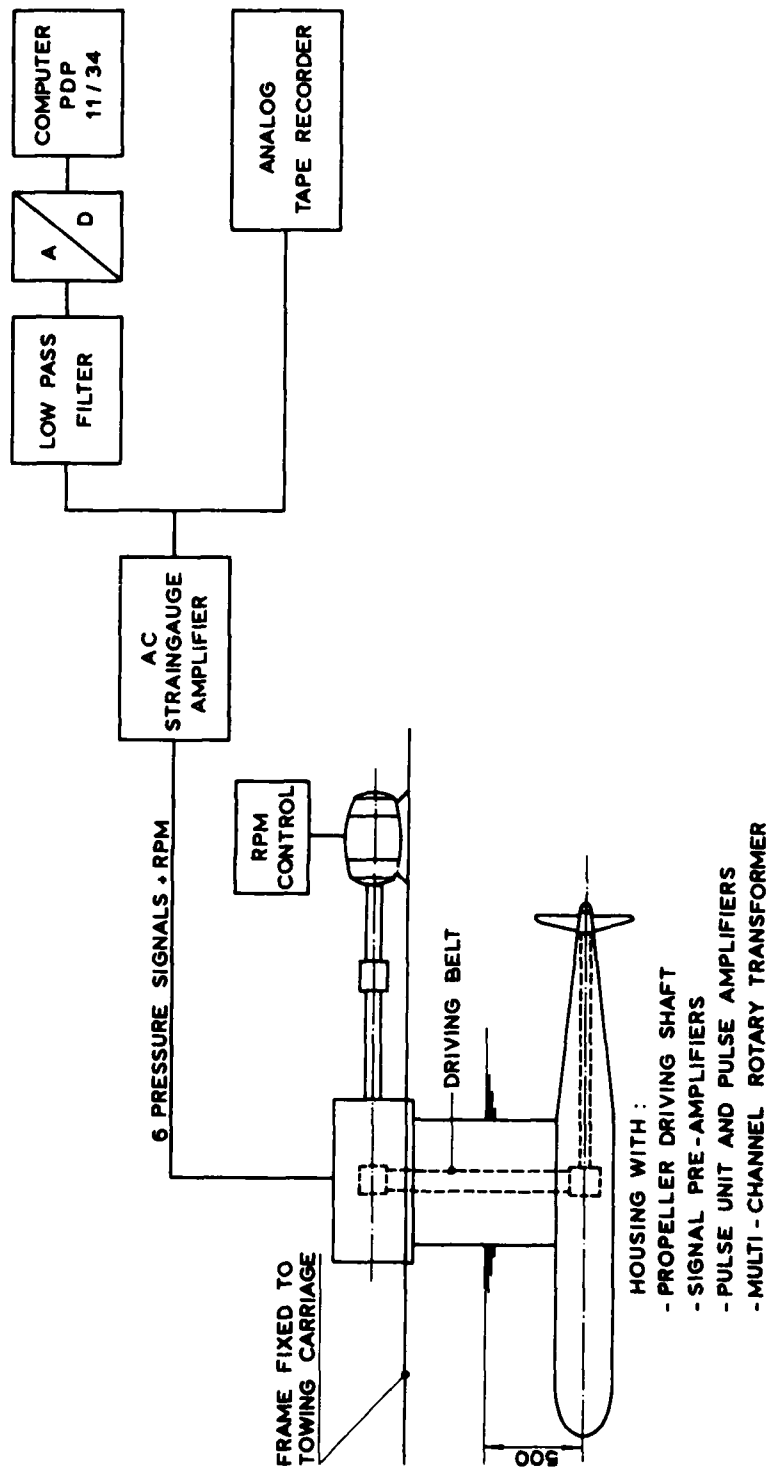


FIGURE 5

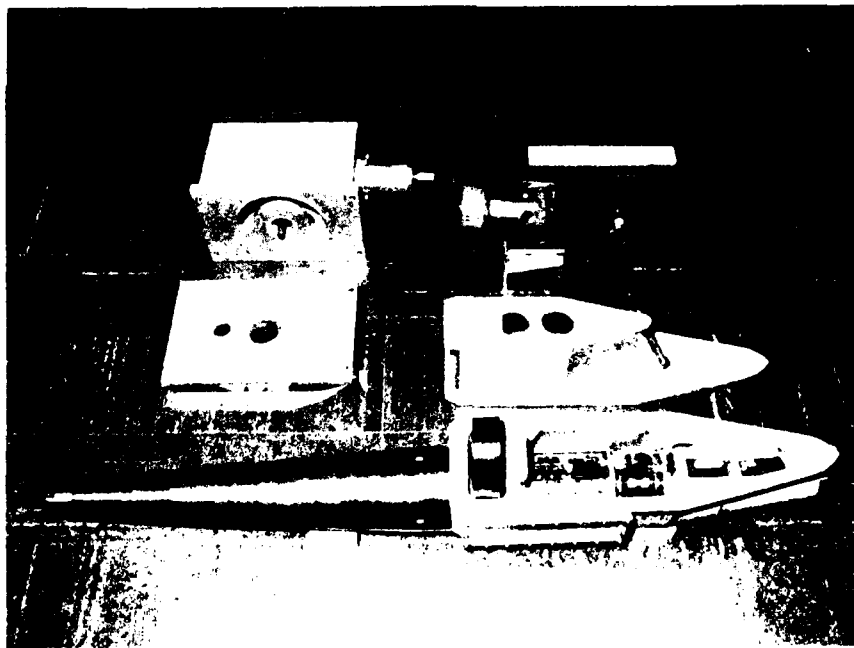
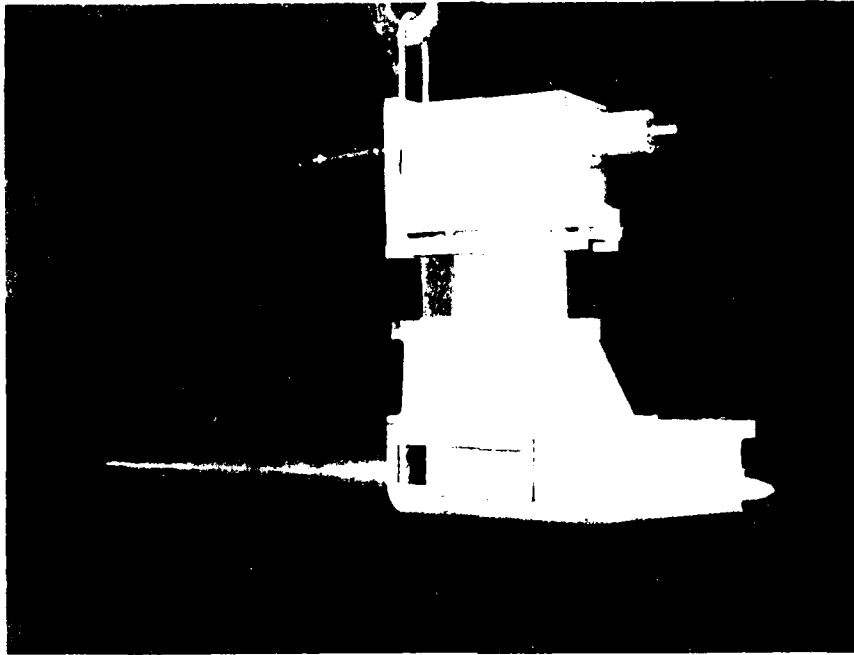


FIGURE 6

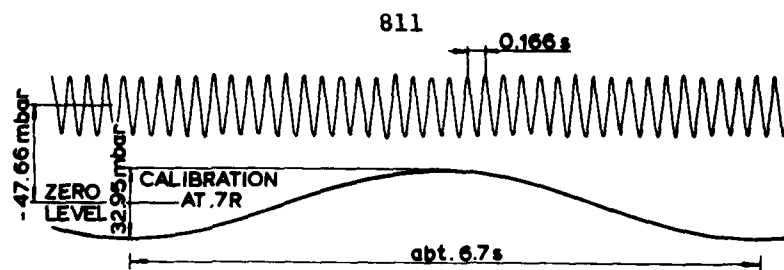


FIGURE 7

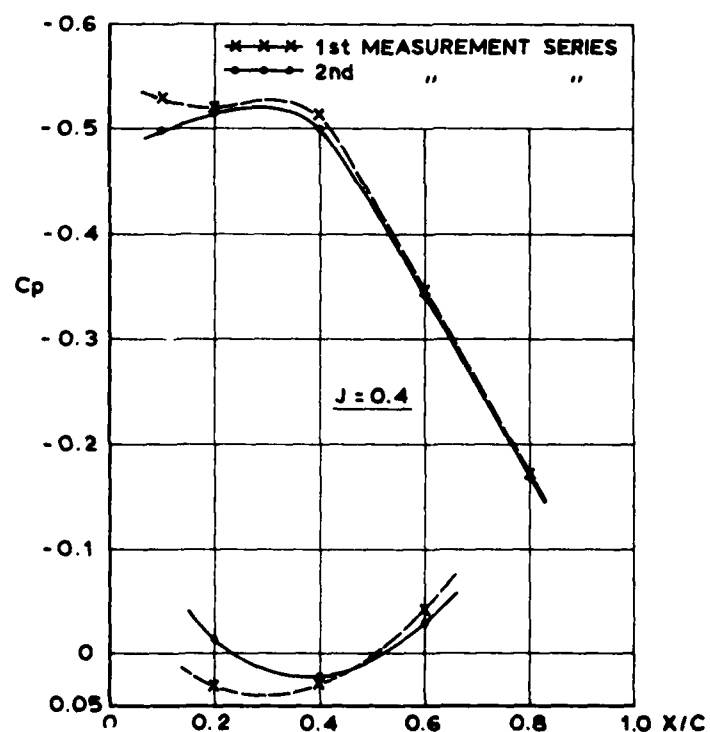
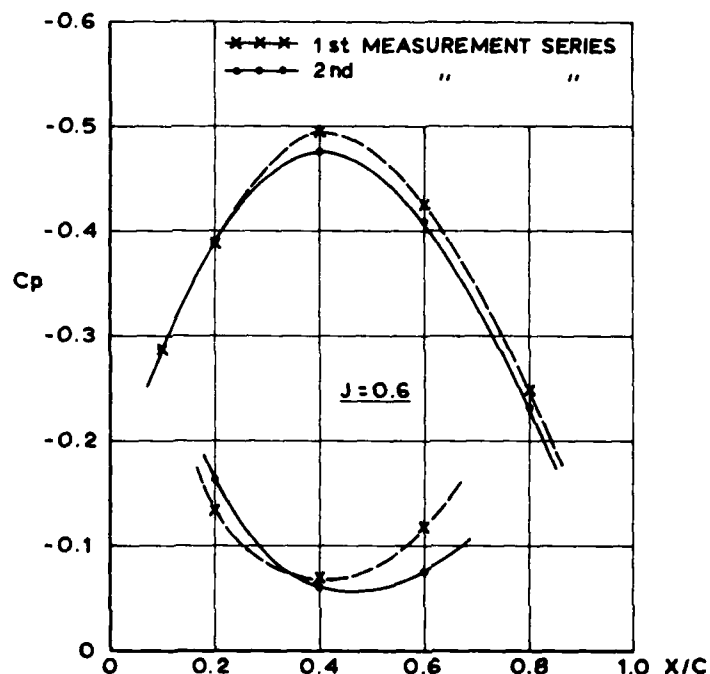


FIGURE 8

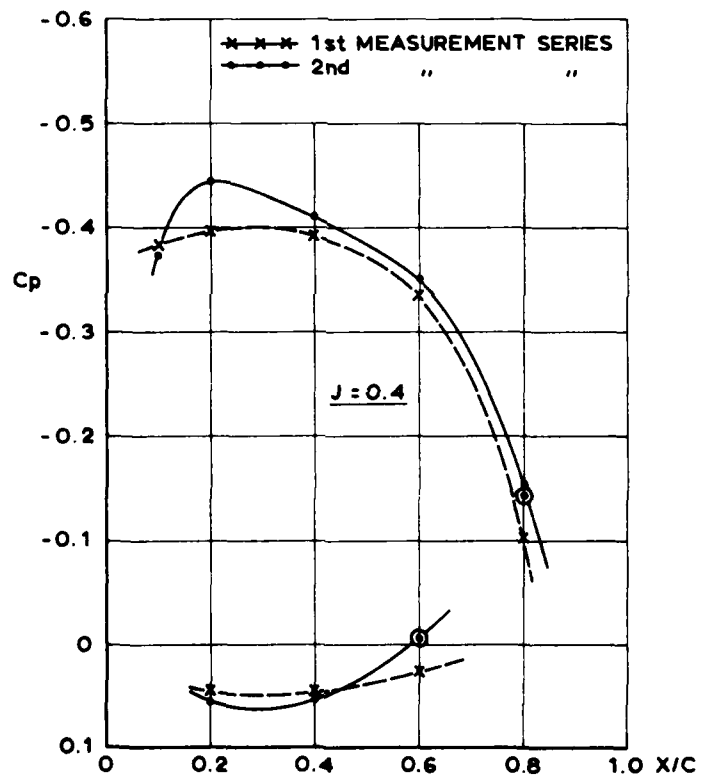
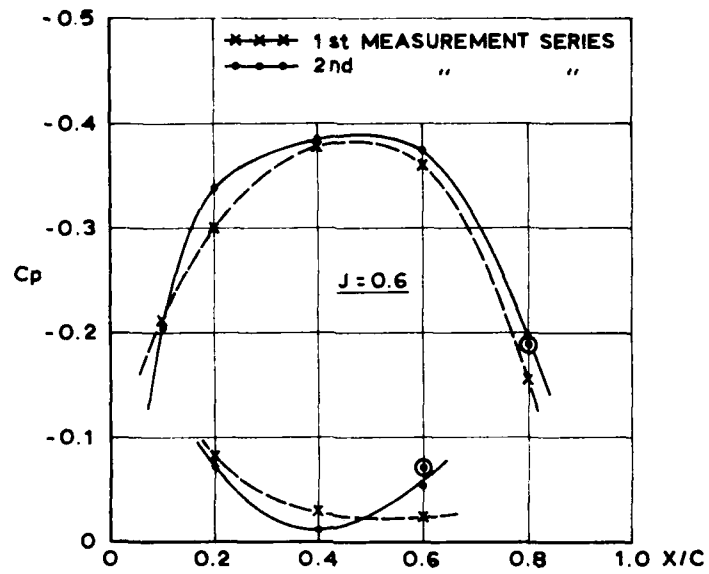


FIGURE 9



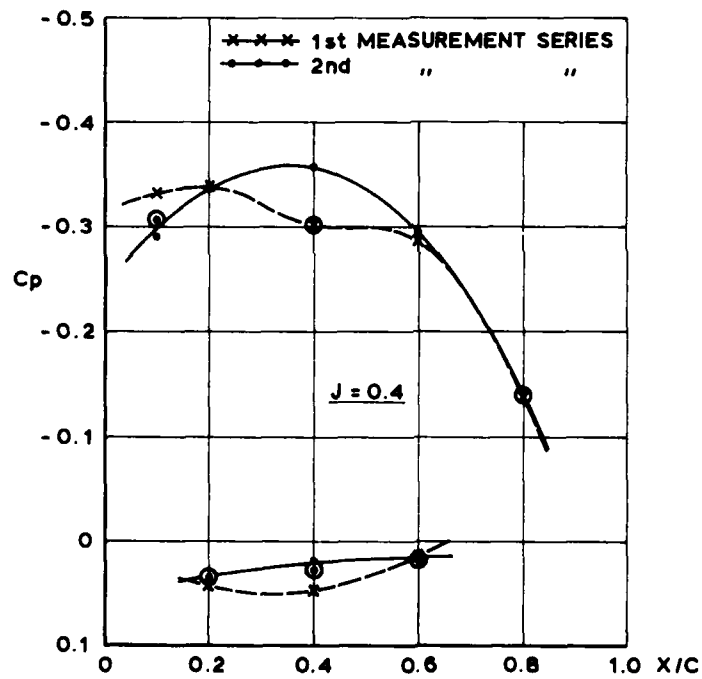
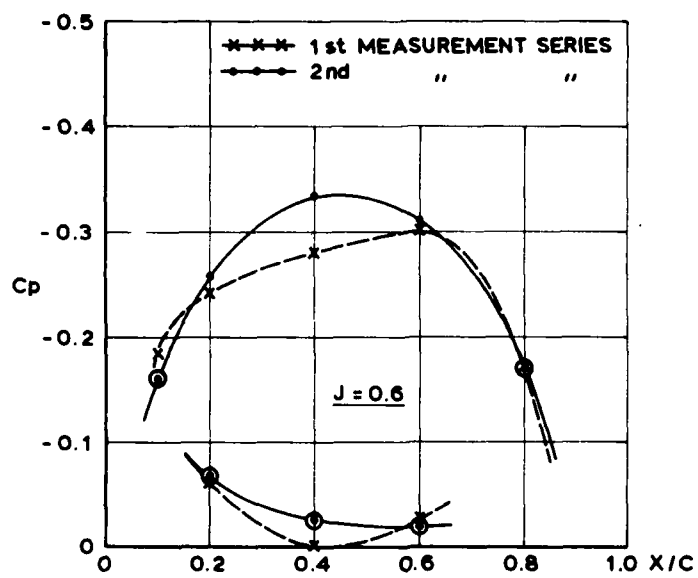


FIGURE 10

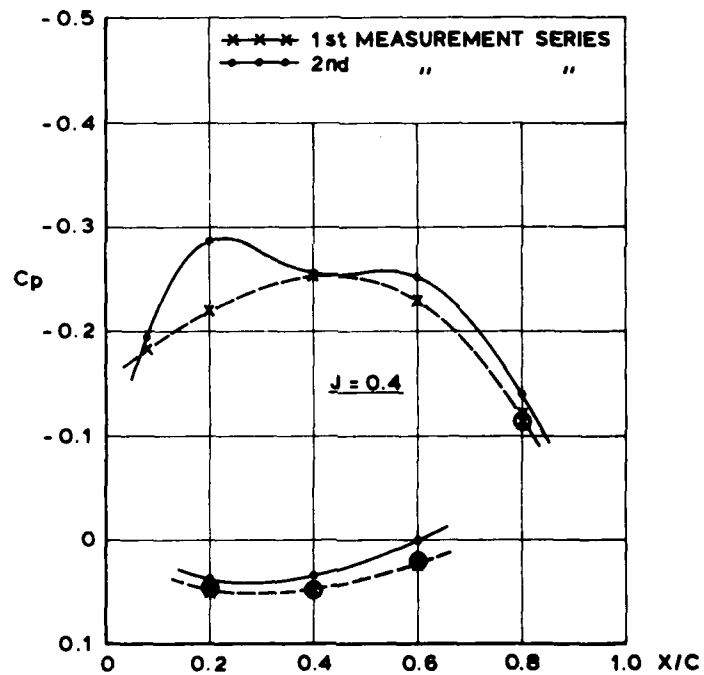
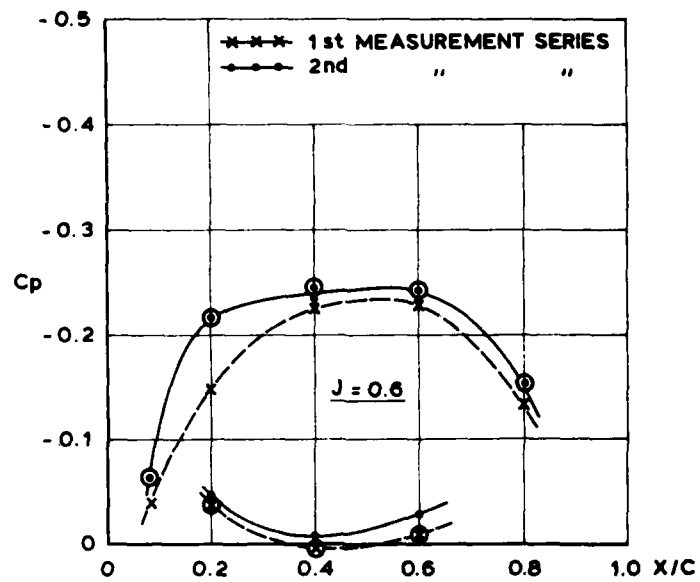


FIGURE 11

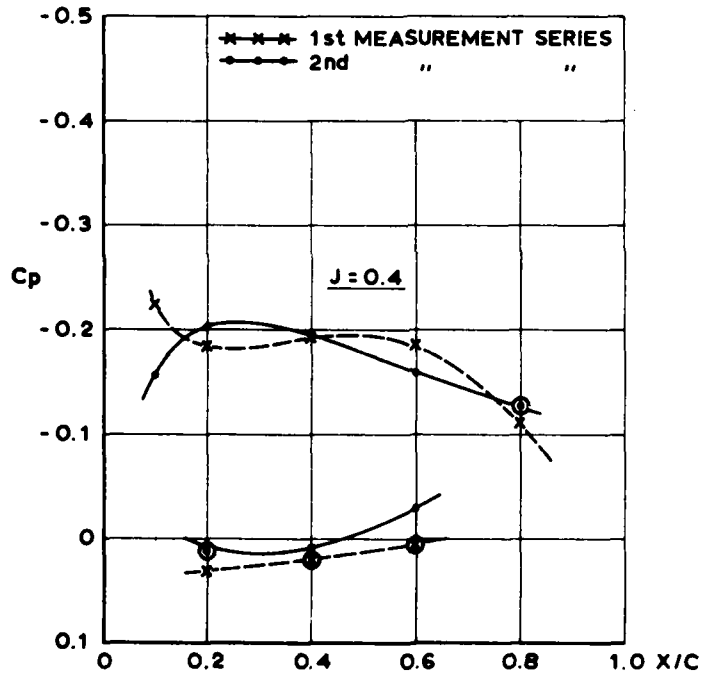
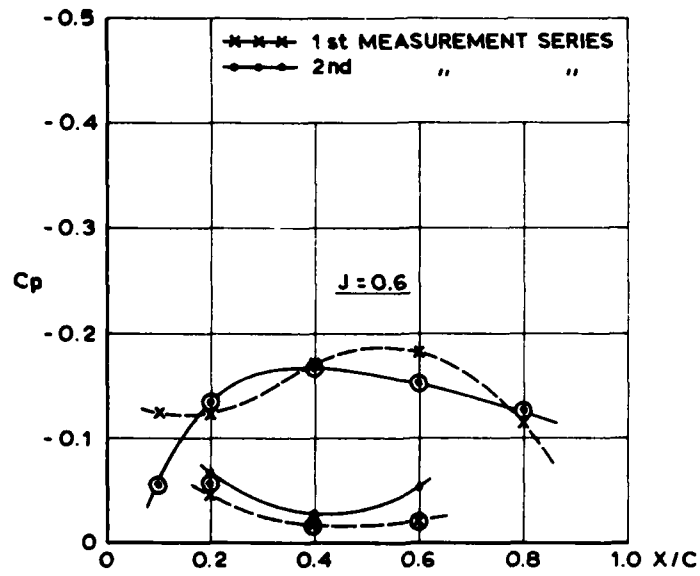


FIGURE 12

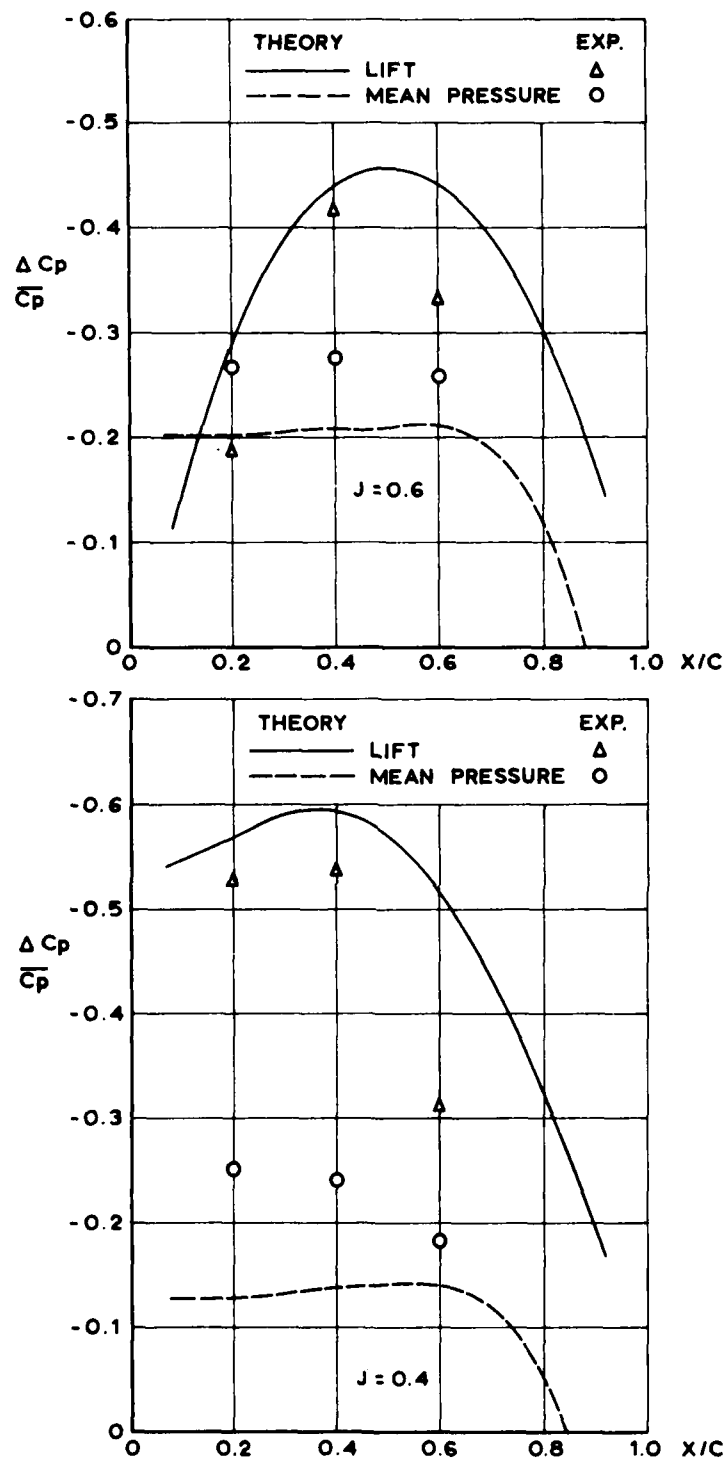


FIGURE 13

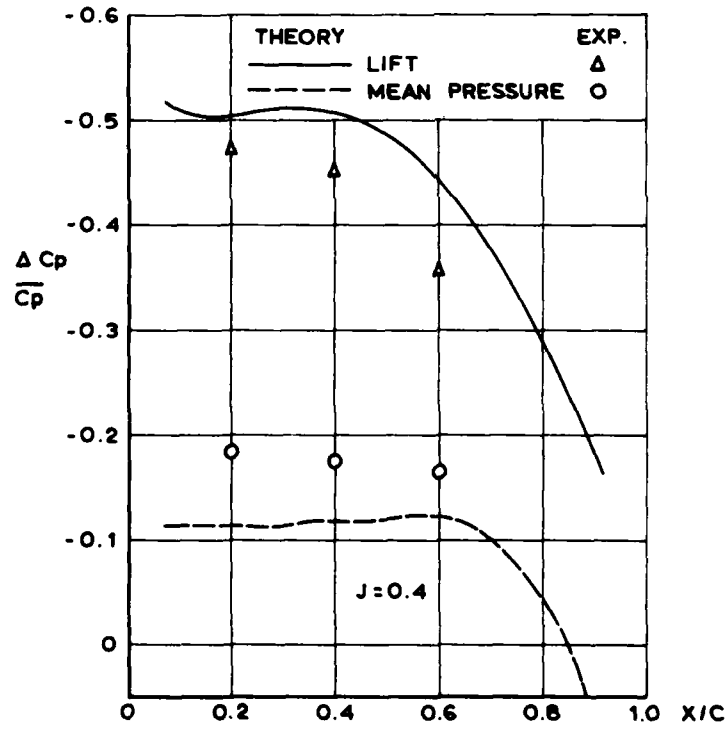
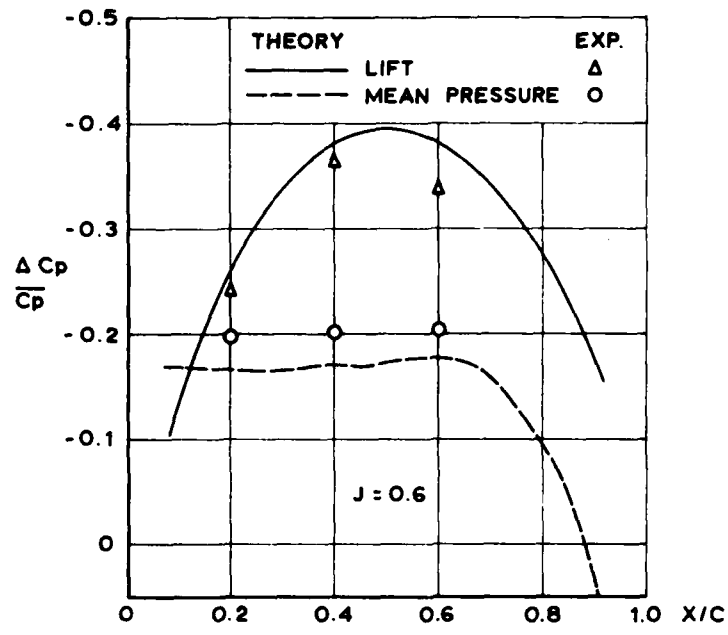


FIGURE 14

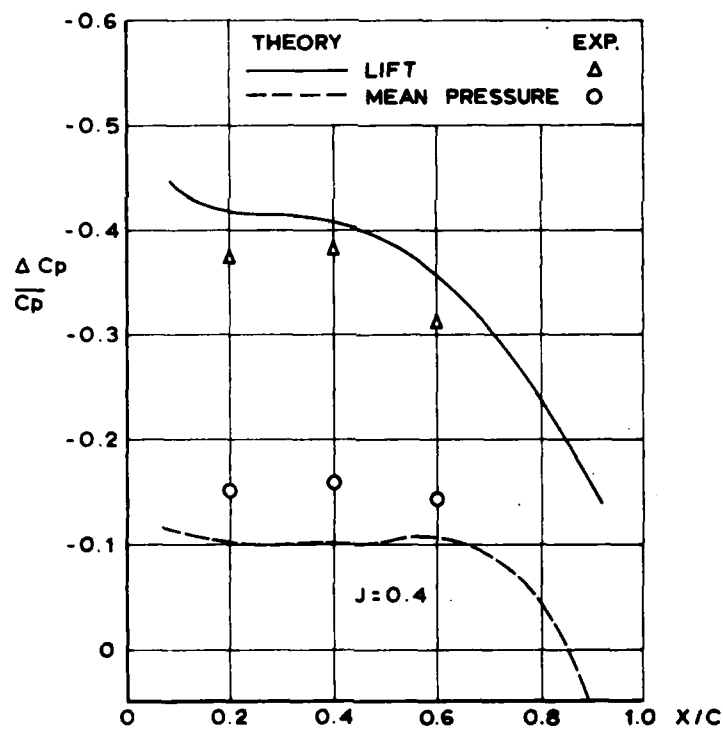
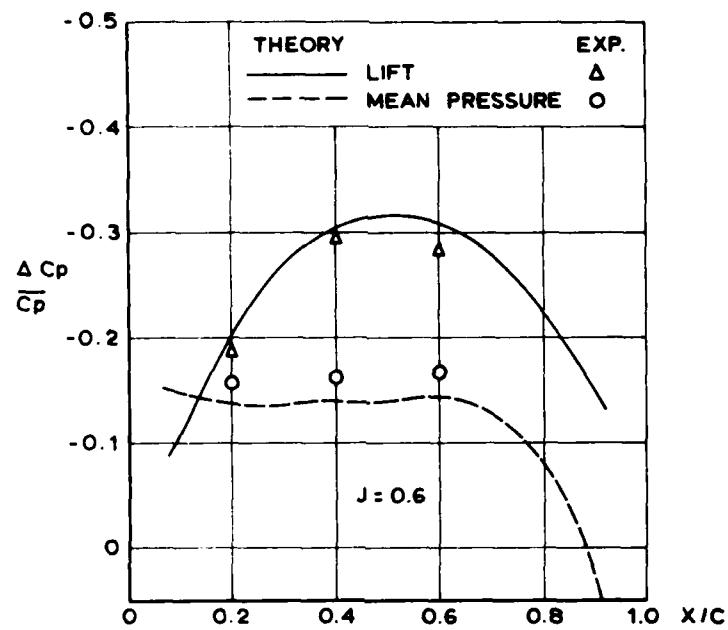


FIGURE 15

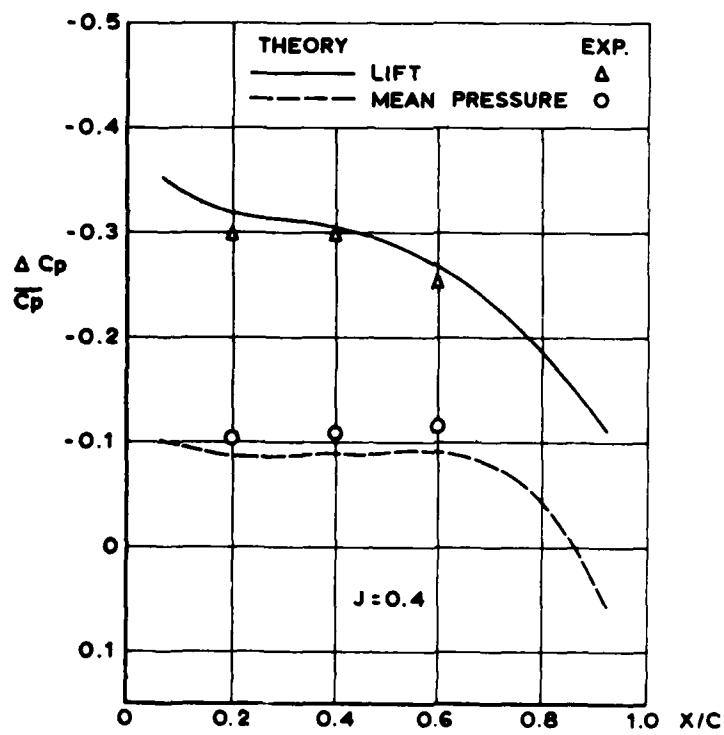
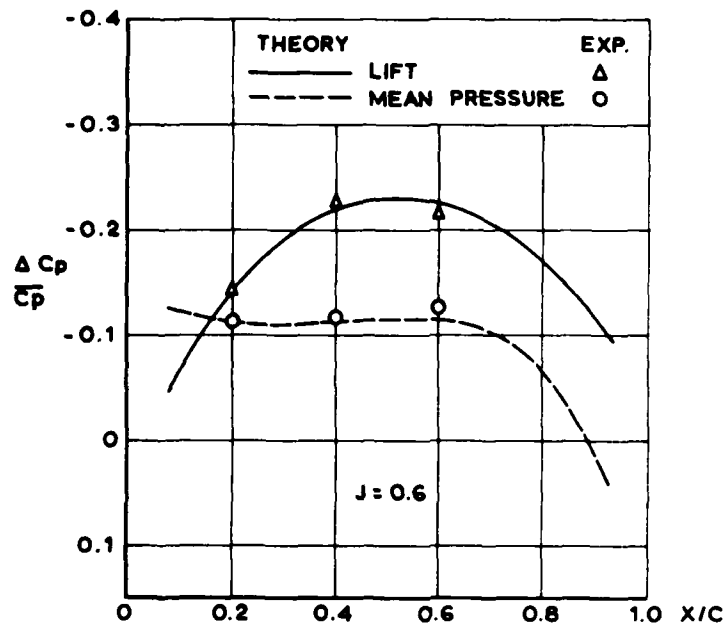


FIGURE 16

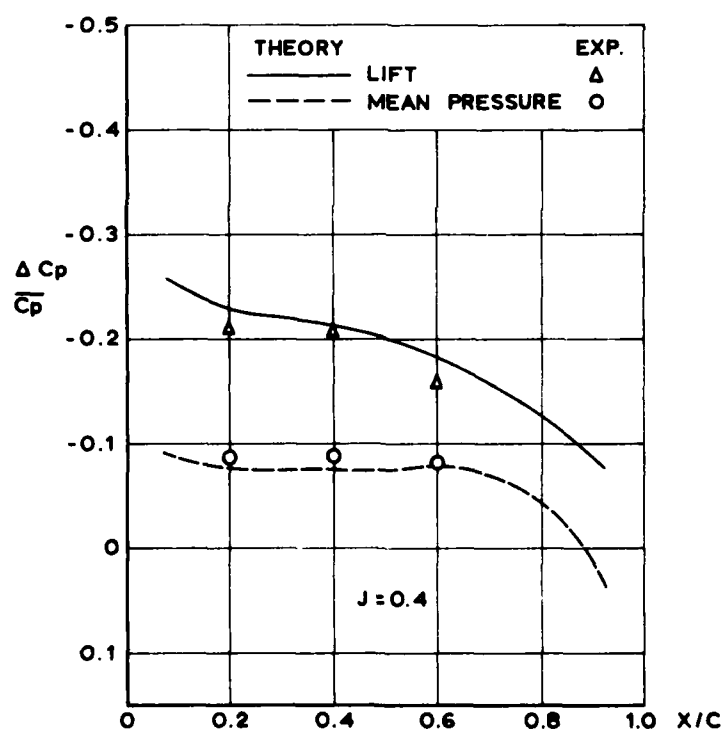
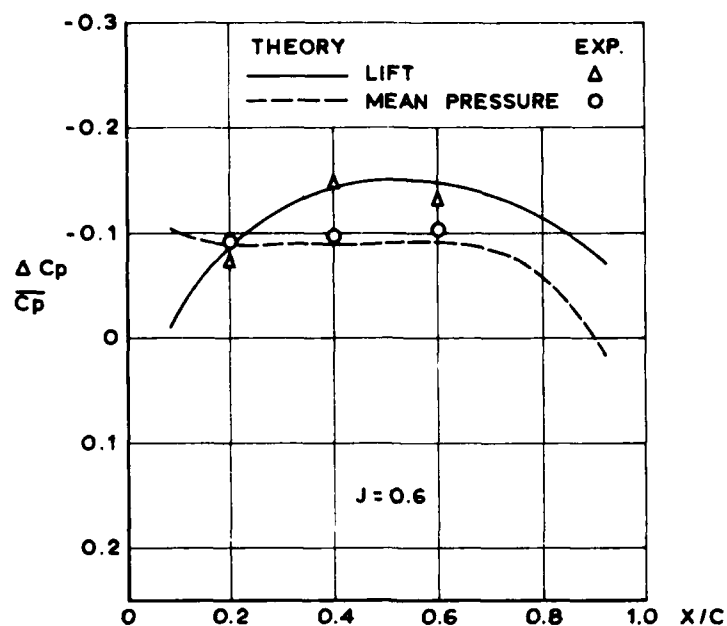


FIGURE 17



## Discussion

S.D. Jessup (DTNSRDC)

I would like to discuss recent work at DTNSRDC to measure propeller-blade pressure distributions. Measurements have been made on two 2-foot-diameter propellers, one of conventional blade shape and one highly skewed. Forty pressure measurements were made on each propeller using individual pressure gauges installed in cavities connected to the blade surface with pressure taps.

Tests were run over ranges of advance coefficient and Reynolds number in uniform and inclined flow. Measured results of steady pressure distributions correlated reasonably well with design predictions in the midspan regions of the conventional propeller. Reynolds number effects were observed at various parts of the blades, some of which were attributed to real flow effects. Some of the problems that we encountered were effects of loading on the pressure of gauge response, centrifugal effects, and smoothness of the surface of the blade where measurements were made.

One possible effect that the authors may have omitted is that of varying wave height above the propeller during towing basin runs. Also, it is recommended to run tests over a range of Reynolds number at constant advance coefficient to determine possible experimental errors. A DTNSRDC report is now available on this work with unlimited distribution.

H. Kato (University of Tokyo)

This is only my quick suggestion: Did you check carefully the surface of wax filled in the play between the foil and pressure pickup? If the surface became convex or concave after the first series of tests, it might be reason for the difference of pressure measurement between two series.

E.A. Weitendorf (Hamburg Ship Model Basin)

Do the authors see any chance to install pressure pickups further toward the leading edge? Otherwise, the possibility for a comparison of calculated and measured pressure distributions in the range of the propeller profile, which is decisive for the cavitation, seems to be rather hopeless.

## Author's Reply

W. van Gent and A.G.P. Versmissen (MARIN)

To S.D. Jessup

It is encouraging to hear of attempts undertaken by others to solve the measurement problems. Some of them differ from ours as the principle is different.

The differences we found between the two measurement series could not be explained by corrections for the wave height; the lift was as well affected as the mean pressure.

Reynolds number variation was avoided by maintaining speed and rpm very strictly constant for each advance constant. But we agree that such a variation may be helpful in tracing the reason for the remaining discrepancies.

To H. Kato

Besides the check on the blade contour after the second measurement series, we also inspected the surface condition after both series. We could not find any difference. But we appreciate Professor Kato's remark and will continue to take care of this possibility.

To E.A. Weitendorf

In the continuation of the project we are installing the transducers at  $x/c = 0.05$  from the leading edge, while in the present case it was  $x/c = 0.10$ .

# Flow Field Computations for Non-Cavitation and Cavitating Propellers

Justin E. Kerwin  
Department of Ocean Engineering  
Massachusetts Institute of Technology

## ABSTRACT

This paper describes two propeller field computation procedures:

- a) The time-varying velocity field of a non-cavitating propeller with steady loading.
- b) The time-varying velocity potential of a propeller with unsteady loading with or without unsteady cavitation.

A variety of sample calculations is given, together with experimental data obtained in the MIT water tunnel using a laser-doppler velocimeter.

## INTRODUCTION

Knowledge of the free-space flow field of a propeller is essential to the understanding of a variety of steady and unsteady hull-propeller interaction problems.

The steady component of the flow field is directly responsible for thrust-deduction, and for the alteration of the nominal wake field. The unsteady component of the flow field gives rise to vibratory hull excitation. A major source of the latter is the presence of intermittent cavitation generated by non-uniform inflow.

Numerical lifting-surface representations of a propeller may be readily adapted to provide flow field information, either in the form of velocities or velocity potentials. Errors due to discretization, which are a major concern in determining velocities on the blades, are fortunately much less of a problem at distant field points.

# FIELD POINT VELOCITIES INDUCED BY A NON-CAVITATING PROPELLER IN STEADY FLOW

## Method of Solution

For a propeller in steady flow, the induced velocity field is independent of time in a coordinate system rotating with the blades. Hence, for any fixed axial and radial position, angular variations in induced velocities in a blade fixed coordinate system are equivalent to time variations in a non-rotating coordinate system advancing with the propeller. Computation of the steady induced velocity at a sequence of angular coordinates then provides the necessary information to construct the time history of velocity at a fixed point. These computations can be readily made given the geometry of the blades and of the trailing vortex wakes and the strengths of the singularity distributions representing propeller loading and thickness.

The present field point velocity computation scheme uses a vortex/source lattice representation of the propeller, and requires as input the results of either the PUF-2 or PSF-2 propeller analysis programs developed at MIT. A description of the former may be found in Kerwin and Lee (1978) and of the latter in Greeley and Kerwin (1982). While the PUF-2 program can accomodate both steady and unsteady non-cavitating propeller flow, its use in the present application is limited to steady flow. The newer PSF-2 program treats only steady non-cavitating propeller flow, but incorporates a more realistic trailing vortex wake representation, and a more accurate lattice arrangement. Since these differences are reflected in their individual lattice coordinates and element strengths, the outputs of either analysis program may be treated with identical logic in the field point program.

In either PUF-2 or PSF-2, the strengths of the individual vortex lattice elements on the blades and in the trailing vortex wake are obtained by imposing a condition of zero net normal velocity at a set of control points on one "key" blade. For efficient computation, a finer grid is used on the key blade, as is evident from the lattice arrangement shown in Figure 1.

However, this is not a desirable feature in performing field point calculations since velocities may be required at points which are close to one of the coarsely represented blades. The assymetry thus introduced will then result in erroneous harmonic content of the angular variation of induced velocity.

This problem can be avoided by calculating the velocity induced by the key blade only, for a sequence of angularly spaced field points covering one complete revolution. The velocity field of a K bladed propeller may then be obtained by summing this result K times, with the record shifted one blade space each time,

$$\begin{aligned}
 v(\theta) &= \sum_{k=1}^K v_1(\theta + \delta_k) \\
 \delta_k &= \frac{2\pi(k-1)}{K} \quad k = 1, 2, \dots, K
 \end{aligned}
 \tag{1}$$

where  $v_1$  and  $v$  denote, respectively, the induced velocity field of one blade and  $K$  blades, and  $\delta_k$  is the angle between blades. This, of course, generates a periodic function whose fundamental is at blade frequency.

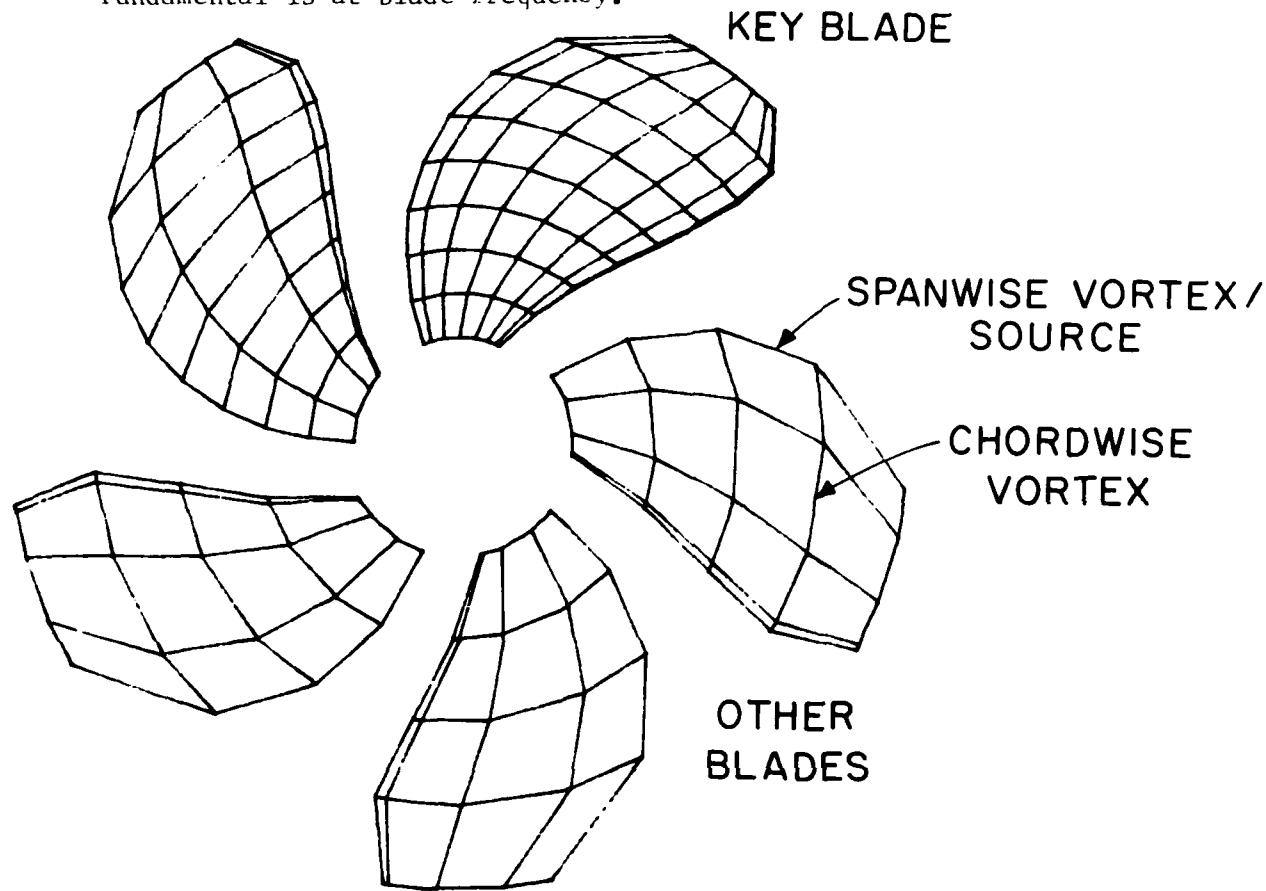


FIGURE 1

Alternatively, one can construct  $v(\theta)$  by summing the blade frequency harmonics of  $v_1(\theta)$  multiplied by the number of blades. The two approaches are equivalent.

If the field point calculation is performed at  $N_R$  equally spaced points over one complete revolution, the angular spacing will be

$$\delta\theta = \frac{2\pi}{N_R} \quad (2)$$

and the number of field points in one blade interval will be  $N_B = N_R/K$ . The maximum number of blade frequency harmonics which can be computed from the tabulated data will be  $N_B/2$ .

The Fourier representation of any component of the induced velocity  $v(\theta)$  may be written as

$$\begin{aligned} v(\theta) &= A_0 + \sum_{n=1}^{N_B/2} A_n \cos(Kn\theta) + \sum_{n=1}^{N_B/2-1} B_n \sin(Kn\theta) \\ &= A_0 + \sum_{n=1}^{N_B/2} C_n \cos(Kn\theta + \phi_n) \end{aligned} \quad (3)$$

where the harmonic phase angle  $\phi_n$  is

$$\phi_n = \tan^{-1} \left( \frac{-B_n}{A_n} \right) \quad (4)$$

and the amplitude  $C_n$  is

$$C_n = \sqrt{A_n^2 + B_n^2} \quad (5)$$

This definition of phase angle is consistent with the complex representation of the function  $v(\theta)$

$$v(\theta) = \operatorname{Re} \left\{ \sum_{n=0}^{\infty} c_n e^{in\theta} \right\} \quad (6)$$

where the real and imaginary parts of the complex coefficients  $c_n$  are

$$\begin{aligned} c_n &= a_n + ib_n = |c_n| e^{i\phi_n} \\ \phi_n &= \tan^{-1}(b_n/a_n) \end{aligned} \quad (7)$$

The real and imaginary parts of  $c_n$  are related to the Fourier coefficients as follows,

$$\begin{aligned} a_n &= A_n \\ b_n &= -B_n \end{aligned} \quad (8)$$

The problem is now reduced to that of finding the velocity induced by one blade of a propeller of given geometry and loading at a specified point in space.

As shown in Figure 2, the discretized version of a blade and its vortex wake consists of three parts, the blade itself, a transition wake in which the vortex sheet contracts and rolls up, and an ultimate wake represented by a single helical tip vortex and a hub vortex. The first two parts are shown to a larger scale in Figure 3. Each singularity element consists of a straight vortex or source segment whose space coordinates and strengths are determined in PUF-2 or PSF-2

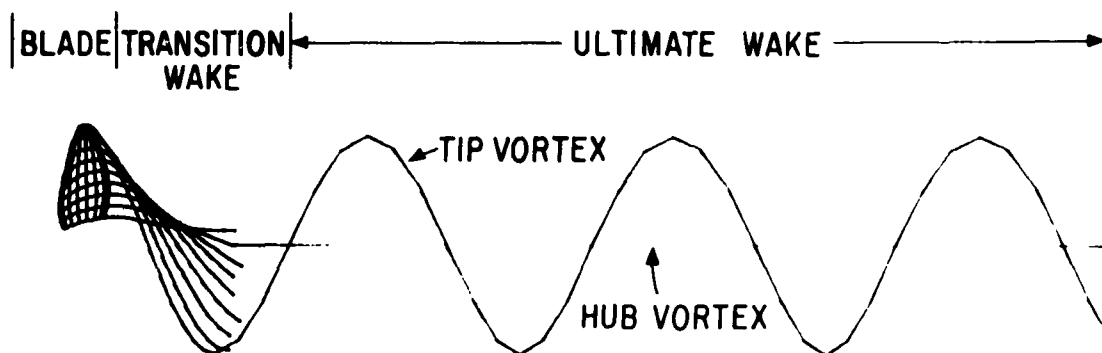


FIGURE 2

The primary singularities consist of the line source strengths  $q_{nm}$  obtained from thin wing theory and the spanwise vortex strengths  $\Gamma_{nm}^{(s)}$  obtained from the normal boundary condition. Here the first index,  $n$ , denotes chordwise position and the second index,  $m$ , denotes spanwise position as illustrated in Figure 3. The remaining singularities, whose strengths follow from consideration of conservation of vorticity, consist of the chordwise vortices  $\Gamma_{nm}^{(c)}$ , the transition wake trailing vortices  $\Gamma_{nm}^{(tw)}$ , the ultimate tip vortex  $\Gamma^{(t)}$  and the ultimate hub vortex  $\Gamma^{(h)}$ . While the transition wake  $n$  and tip vortex elements are given both a streamwise and spanwise subscript, their strengths are independent of streamwise position so that the index in this case only serves to identify the position of the element in question.

The chordwise vortices originating from the outer end of the tip panel require special treatment. These are considered to represent a separated vortex sheet, so that a chordwise vortex leaves the blade surface at the outer end of each spanwise vortex, and proceeds to a collection point a specified distance above the blade at the trailing edge. The elevation of the collection point is loading dependent, thus introducing a non-linear lift contribution which is shown in Kerwin and Lee (1978) and Greeley and Kerwin (1982) to be essential for accurate results at advance coefficients below design.

For the case shown in Figure 3, the advance coefficient corresponds to the design value so that the deviation of the tip chordwise vortex from the blade is not evident, and each of the  $N$  separated

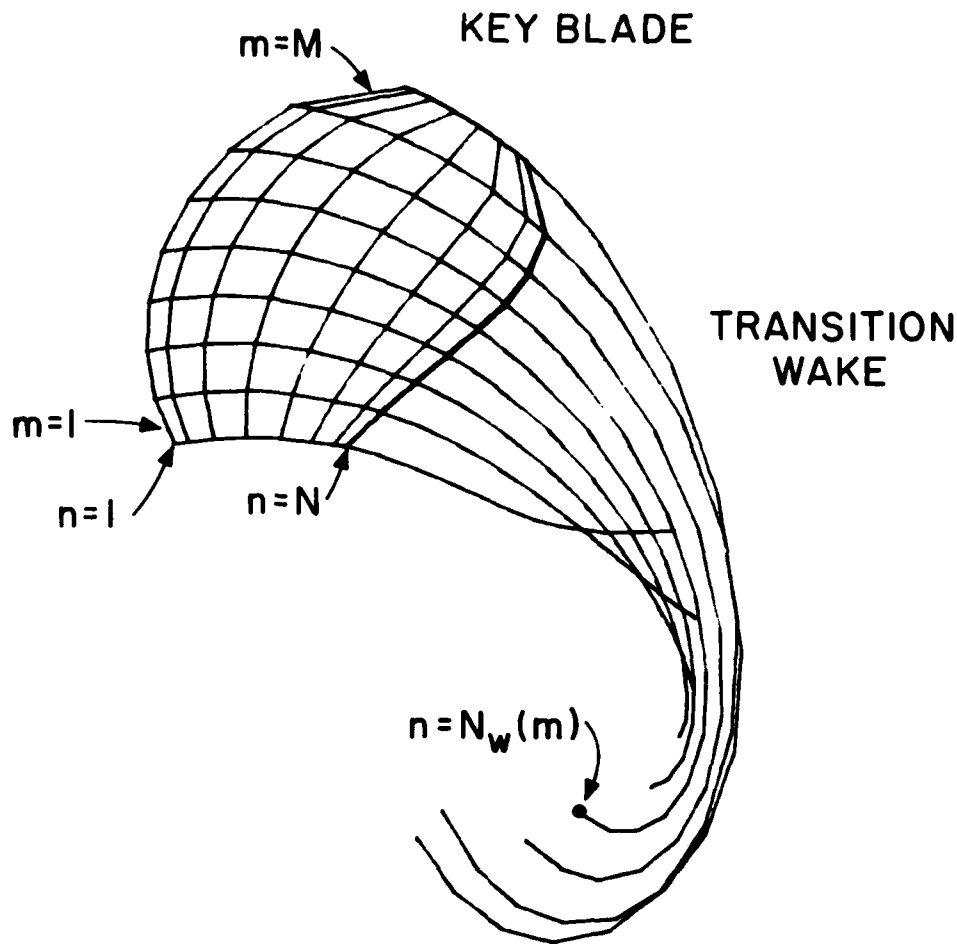


FIGURE 3

vortex lines appear to be coincident.

Induced velocities are then obtained by summation of the product of these singularity strengths with the appropriate velocity influence functions. Let us denote  $\vec{H}_{nm}^v$  and  $\vec{H}_{nm}^q$  as the vector velocity induced at the field point in question by a unit strength line vortex and source, respectively, situated at the position of a lattice element designated symbolically by the particular indices  $n$  and  $m$ . The velocity induced by the spanwise vortices and sources is



$$\vec{v}_s = \sum_{n=1}^N \sum_{m=1}^M \Gamma_{nm}^{(s)} \vec{H}_{nm}^{\Gamma}$$

$$\vec{v}_q = \sum_{n=1}^N \sum_{m=1}^M q_{nm} \vec{H}_{nm}^q \quad (9)$$

where  $N$  is the number of elements over the chord and  $M$  is the number of panels over the span.

The velocity induced by the chordwise vortices, including the separated sheet at the tip is,

$$\vec{v}_c = \sum_{n=1}^{N-1} \sum_{m=1}^M \Gamma_{nm}^{(c)} \vec{H}_{nm}^{\Gamma} + \sum_{n=1}^N \sum_{\ell=1}^{N-n+1} \Gamma_{n\ell}^{(ct)} \vec{H}_{n\ell}^{\Gamma} \quad (10)$$

The  $\ell$  index in the second summation denotes the individual chordwise elements of the vortex shed from the outer end of the  $n$ 'th spanwise vortex. Hence, the chordwise vortex shed from the spanwise vortex closest to the leading edge consists of  $N$  elements, while the one shed from the spanwise vortex closest to the trailing edge consists of a single element connected to the collection point.

The transition wake induces a velocity

$$\vec{v}_{tw} = \sum_{m=1}^{M+1} \sum_{n=1}^{N_{W(m)}-1} \Gamma_{nm}^{tw} \vec{H}_{nm}^{\Gamma} \quad (11)$$

where  $N_{W(m)}$  is the number of points used to describe the path of the trailing vortex shed from the inner extremity of  $\Gamma_{Nm}^s$ . The  $(M+1)$ st transition wake element originates from the collection point of the separated tip vortex.

The ultimate tip vortex induces a velocity

$$\vec{v}_t = \sum_{n=1}^{N_u-1} \Gamma_n^t \vec{H}_n^{\Gamma} \quad (12)$$

where  $N_u$  is the number of points used to form the piecewise linear approximation to the helical ultimate wake. The first point describing the helix coincides with the last point in the tip element of the transition wake.

Finally, the hub vortex, which consists of a single line element extending the same distance downstream as the ultimate tip vortex induces a velocity

$$\vec{v}_h = -\Gamma_1^t \vec{H}_1^{\Gamma} \quad (13)$$

The total induced velocity is then obtained by summing (9) - (13).

#### Steady Field Point Velocity Calculation

Steady field point calculations are shown here for a five bladed propeller operating at a design advance coefficient,  $J$ , of 0.889 in homogeneous flow. This propeller is one of the skew series developed by Boswell (1971) and Nelka (1974), and its vortex lattice representation is shown in Figures 1-3.

Figure 4 shows the results of a field point computation at a radius  $r/R = 0.929$  in a plane situated upstream of the propeller with a longitudinal coordinate  $x/R = -0.25$ . The longitudinal origin is the mid-chord of the root section. However, since this propeller has no mid-chord rake, the section mid-chords at all radii are located in the plane  $x=0$ . The leading edge at  $r/R = 0.929$  is located at  $x/R = -0.082$ . Computations were made at 60 field points over the circumference which results in an angular spacing of 6 degrees. Summation over five blades, from (1) then results in 12 computed values of induced velocity, yielding Fourier coefficients up to the sixth harmonic of blade rate.

The first five harmonic coefficients are tabulated on the left side of the graph. The symbols plotted over the first blade interval are the computed points, while the continuous lines are generated from the resulting Fourier coefficients. The latter are plotted over one complete propeller revolution to provide a better visual impression of the velocity time histories. At this relatively distant field point they appear to be almost sinusoidal, with the second harmonic of blade rate being of the order of ten percent of the fundamental.

The computed value of the mean tangential velocity provides a check on the accuracy of the computational procedure. The mean value must, of course, be zero for any contour which does not cut through the blade or its trailing vortex wake, and this can be seen to be true in this case.

Figure 5 shows a typical result obtained at a point much closer to the leading edge. In this case  $x/R = -0.128$  which corresponds to a distance of  $0.046R$  ahead of the leading edge.

To capture the sharp gradients near the leading edge, 120 points were used, corresponding to three degree spacing. While the maximum number of terms is used in Fourier representation of the velocity, only the first five harmonics are tabulated.

Figure 6 shows the velocities computed just beyond the tip, at  $r/R = 1.05$ . Again, 120 points were used due to the sharp velocity gradients encountered at this small tip clearance.

Finally, Figure 7 shows the results of a velocity computation downstream of the propeller within the transition wake region. Some care must be taken in selecting field point positions at longitudinal positions and radii which intersect either the blade or its trailing vortex wake. The vortex lattice representation of continuous vortex sheets is invalid in the near field except at control points which are

PROPELLER FIELD POINT VELOCITY PROGRAM (FPV-18) RELEASE DATE 6/07/82 RUN DATE 7/19/82 20:19:32 88

AXIAL  
RADIAL  
TANGENTIAL

FIELD POINT POSITION

X=-0.250 R=0.020  
ZERO ANGLE 0.0

AXIAL		
	AMPL	PHASE
0	0.003	0.0
1	0.028	145.1
2	0.003	47.9
3	0.000	18.2
4	0.000	-20.1
5	0.000	-63.4

RADIAL		
	AMPL	PHASE
0	-0.007	0.0
1	0.019	12.5
2	0.003	-45.3
3	0.001	-104.0
4	0.000	-150.0
5	0.000	145.0

TANGENTIAL		
	AMPL	PHASE
0	0.000	0.0
1	0.023	-113.0
2	0.002	153.0
3	0.000	137.1
4	0.000	86.0
5	0.000	27.8

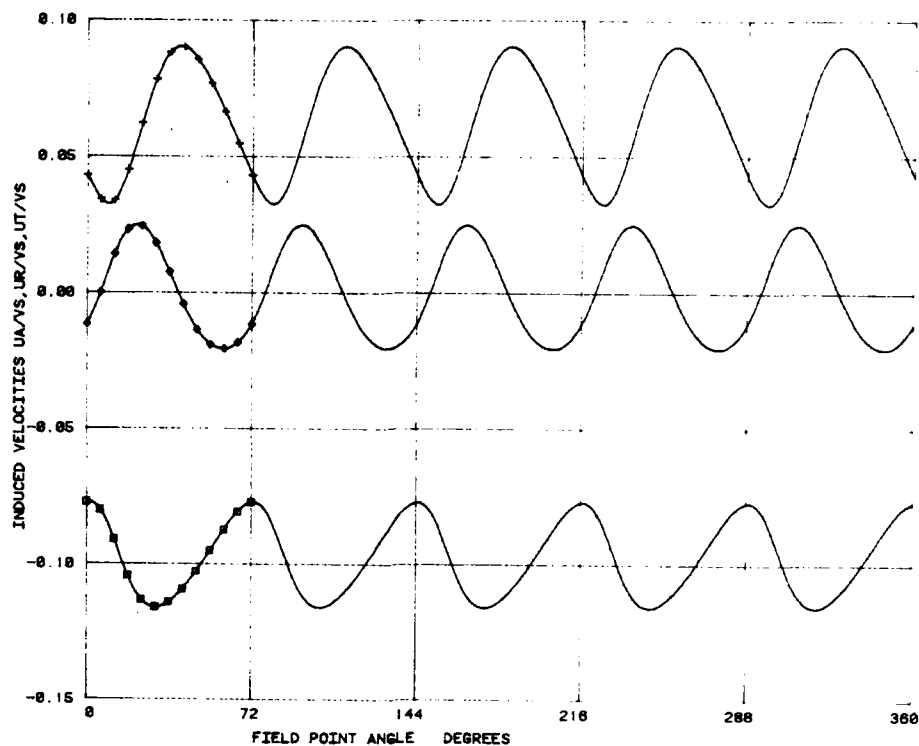


FIGURE 4

PROPELLER FIELD POINT VELOCITY PROGRAM (FPV-18) RELEASE DATE 6/07/82 RUN DATE 7/19/82 20:27:04 88

AXIAL  
RADIAL  
TANGENTIAL

FIELD POINT POSITION

X=-0.128 R=0.020  
ZERO ANGLE 0.0

AXIAL		
	AMPL	PHASE
0	0.005	0.0
1	0.007	125.1
2	0.027	7.5
3	0.010	-81.7
4	0.004	-105.1
5	0.002	110.6

RADIAL		
	AMPL	PHASE
0	-0.141	0.0
1	0.000	-3.7
2	0.021	-87.0
3	0.010	-170.0
4	0.005	105.4
5	0.003	24.0

TANGENTIAL		
	AMPL	PHASE
0	0.000	0.0
1	0.051	-125.0
2	0.010	117.0
3	0.005	30.4
4	0.002	-34.0
5	0.001	-87.1

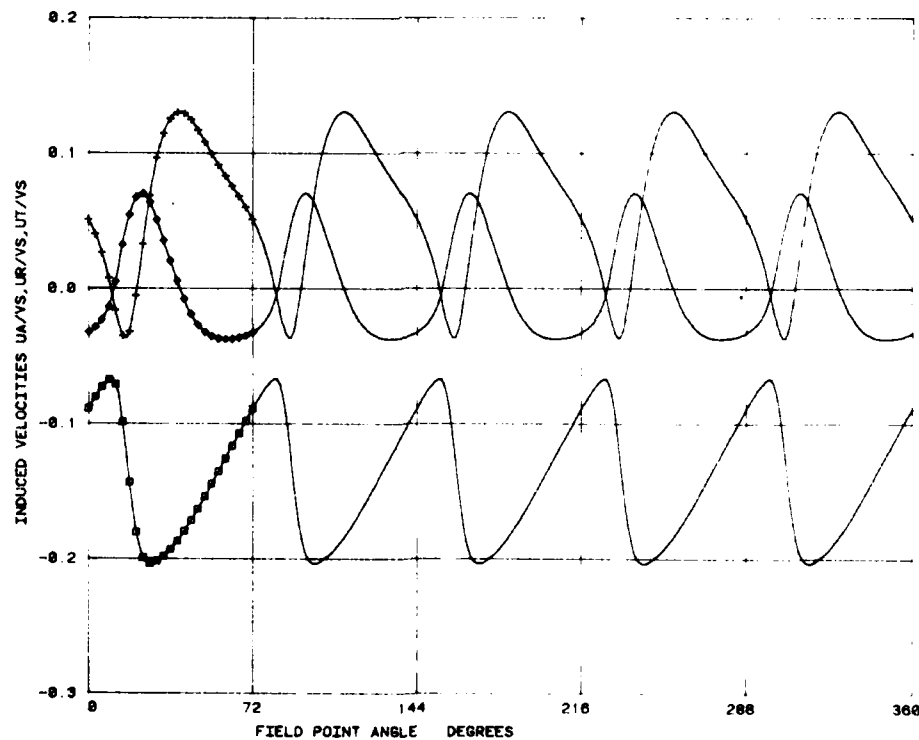


FIGURE 5

PROPELLER FIELD POINT VELOCITY PROGRAM (FPV-10)

RELEASE DATE

6/07/82

RUN DATE

7/19/82 20:35:42.00

AXIAL           + + + + +  
 RADIAL        - - - - -  
 TANGENTIAL   + + + + +

## FIELD POINT POSITION

X= 0.0 R=1.050  
 ZERO ANGLE 0.0

AXIAL		
	AMPL	PHASE
0	-0.020	0.0
1	0.046	-13.6
2	0.016	103.8
3	0.006	-18.8
4	0.002	100.7
5	0.001	-17.0

RADIAL		
	AMPL	PHASE
0	-0.118	0.0
1	0.058	-90.7
2	0.022	80.9
3	0.009	-105.7
4	0.003	69.7
5	0.001	-129.1

TANGENTIAL		
	AMPL	PHASE
0	0.000	0.0
1	0.024	173.7
2	0.010	-9.7
3	0.004	104.0
4	0.002	-20.1
5	0.001	126.1

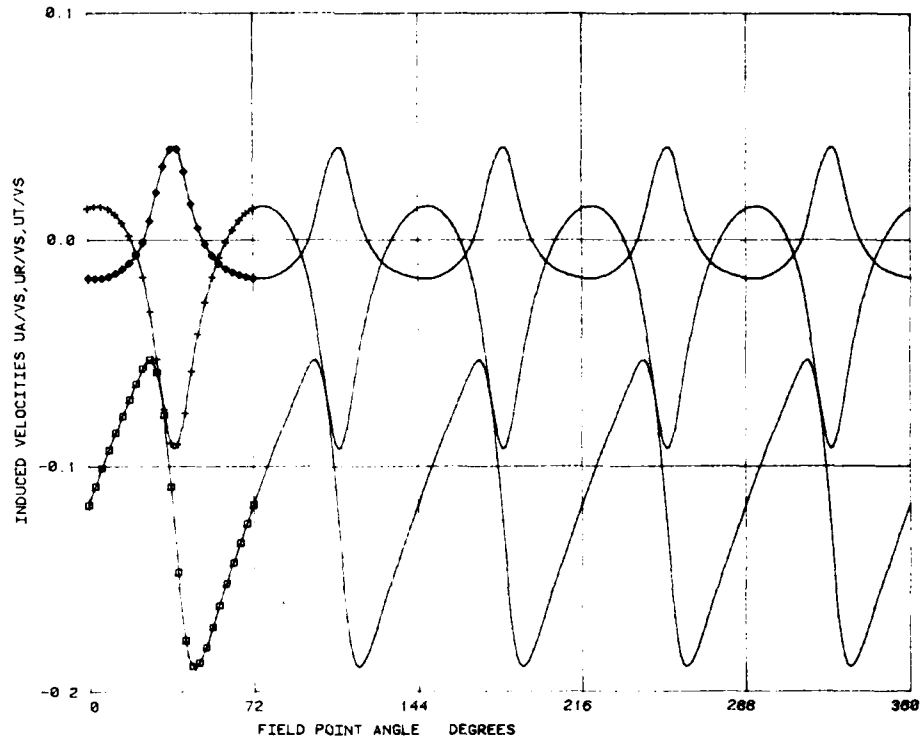


FIGURE 6

PROPELLER FIELD POINT VELOCITY PROGRAM (FPV-10)

RELEASE DATE

6/07/82

RUN DATE

7/19/82 20:46:01.00

AXIAL           + + + + +  
 RADIAL        - - - - -  
 TANGENTIAL   + + + + +

## FIELD POINT POSITION

X= 0.328 R=0.548  
 ZERO ANGLE 48.75

AXIAL		
	AMPL	PHASE
0	0.352	0.0
1	0.036	100.5
2	0.010	25.3
3	0.004	-130.8
4	0.002	50.0
5	0.001	-104.2

RADIAL		
	AMPL	PHASE
0	-0.057	0.0
1	0.029	150.3
2	0.010	-33.9
3	0.005	154.1
4	0.003	-12.0
5	0.002	179.4

TANGENTIAL		
	AMPL	PHASE
0	-0.302	0.0
1	0.032	27.4
2	0.006	-135.0
3	0.003	41.9
4	0.001	-127.6
5	0.001	76.5

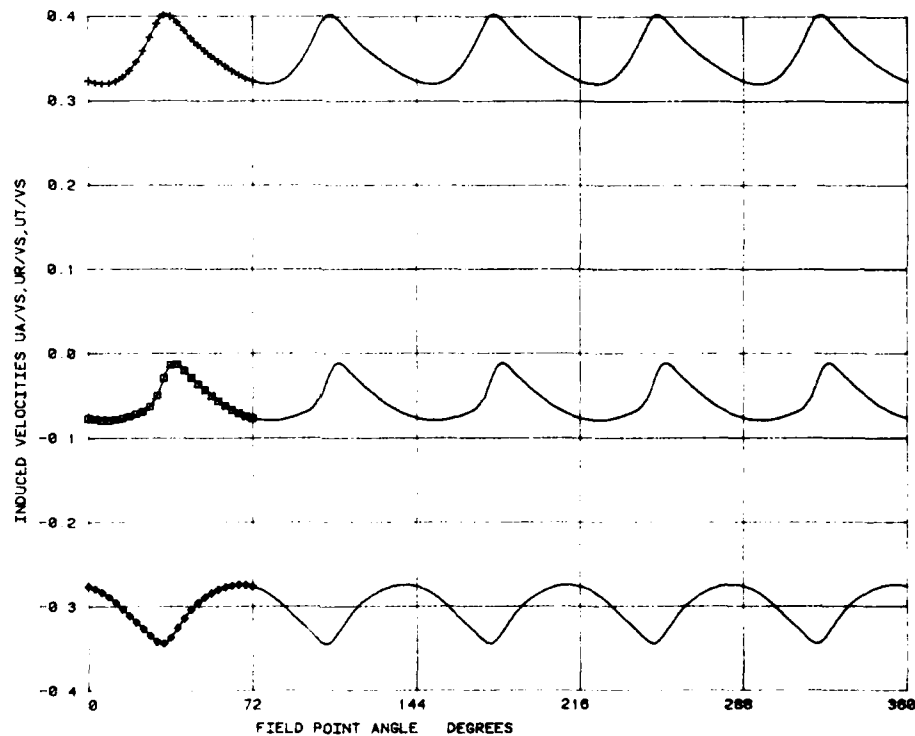


FIGURE 7

properly located. Thus to compute velocities through the transition wake, one specifies the indices of a particular lattice element, and the coordinates of a field point properly centered in this grid are computed. Circumferential spacing at the desired angular increment then proceeds from this point. For convenience in visualization, the angular coordinate is shifted by the amount required to place the vortex sheet in the middle of one blade interval, or 36 degrees in this case.

The mean tangential velocity is not zero in this case, but is related to the total circulation,  $\Gamma$ , around the blade at the lattice element in question,

$$K\Gamma = -2\pi r_w \bar{u}_t \quad (14)$$

where  $r_w$  is the radius of the field point in the transition wake and  $\bar{u}_t$  is the circumferential mean tangential velocity. In this case  $\bar{u}_t/V_s = -0.302$ , so that the non-dimensional circulation should be,

$$G = \frac{\Gamma}{2\pi R V_s} = \frac{1}{K} \left( \frac{r_w}{R} \right) \left( \frac{\bar{u}_t}{V_s} \right) = 0.0331 \quad (15)$$

while the corresponding value of circulation obtained by PSF-2, and used to compute the field point velocities is 0.0328. Thus the computational inconsistency in this case is about one percent.

#### Correlation with Experiments

Direct measurement of propeller induced velocities has become feasible in recent years with the introduction of the laser doppler velocimeter. A complete description of the system installed in the MIT water tunnel, together with experiments and correlation with an earlier version of the field point program is given in Min (1978). In Min's experiments, the signal to noise ratio of the time measurements of velocity was improved by means of an analog signal averager triggered by a magnetic pickup on the propeller shaft. A substantial improvement, both from the point of view of convenience and accuracy resulted from the addition of a laboratory mini-computer with a fast analog-digital conversion capability. This development was reported in Kobayashi (1981), (1982) who addressed the problem of determining sectional drag from velocity field measurements.

A current development in propeller flow field measurement techniques consists of a refinement in the averaging process. A laser doppler velocimeter functions by recording the instantaneous velocity of a random sequence of particles which enter a small measurement volume fixed in space. If the flow field is unsteady in a fixed coordinate frame, the ability to measure a sharp velocity peak is dependent on the presence of a reflecting particle in the measurement volume at the time of the peak. If no particle is present, the

recorded velocity is "frozen" and will therefore correspond to the value present at an earlier time. Single averaging, which is essential to reducing noise, will inevitably round off the velocity peaks due to the accumulation of non-peak velocity measurements.

The most recent refinements consists of modifying the averaging procedure to include only those velocities which correspond to recently observed particles. If the velocity measurement has been frozen for longer than a specified amount, it is not included in the averaging process.

Sample measurements with this system, which is being developed as part of a Master of Science thesis by Schoenberger (1983) are shown in Figures 8 - 11.

In these experiments the 1 foot (.3048 m) diameter propeller model was run at 1200 revolutions per minute with a water velocity set to produce an advance coefficient,  $J$ , of 0.889 after application of the classical closed jet tunnel wall correction, Glauert (1959). All field point velocities were then non-dimensionalized with respect to the corrected tunnel velocity, which in this case was 4.3% less than the measured volumetric flow in the test section. This correction is valid only in the plane of the propeller, but is assumed to be applicable over the range of measurements.

Phase angles were measured relative to a starting pulse generated by the interruption of a small laser beam by the leading edge of each blade. This produced a very sharp, repeatable pulse which is essential for accurate averaging. However, its absolute phase with respect to propeller coordinates was not adjusted precisely, and was considered to have a possible error of 5 to 10 degrees. For purposes of correlation with theory, an adjustment to the experimental phase was made to best fit the computed data. The necessary correction was well within the expected error in all cases.

While the phase agreement in Figures 8 - 11 is therefore irrelevant, the corrections were small enough for the experiments to serve as a check against sign errors in the theory. In Figures 8 - 11, the experimental velocities are shown as continuous lines which are generated by straight lines connecting the approximately 350 points measured during each revolution. The symbols represent the corresponding field point calculations as shown in Figures 4 - 7.

Good agreement is found for all field points outside the slipstream, including points very close to the leading edge. The almost perfect agreement in the very distorted wave forms shown in Figure 9 is particularly encouraging. In the wake region, the experimental traces show a distinct velocity defect associated with blade viscous drag, which has been analysed by Kobayashi (1981). The displacement effect of the velocity defect region influences the potential flow region outside the vortex wake, thus explaining the poorer overall agreement in this case.

The experimentally determined circumferential mean tangential velocity within the slipstream provides an experimental determination of the circulation, as given by (14) and (15). However, as pointed out by Sayre (1980), an error is introduced if the path used to

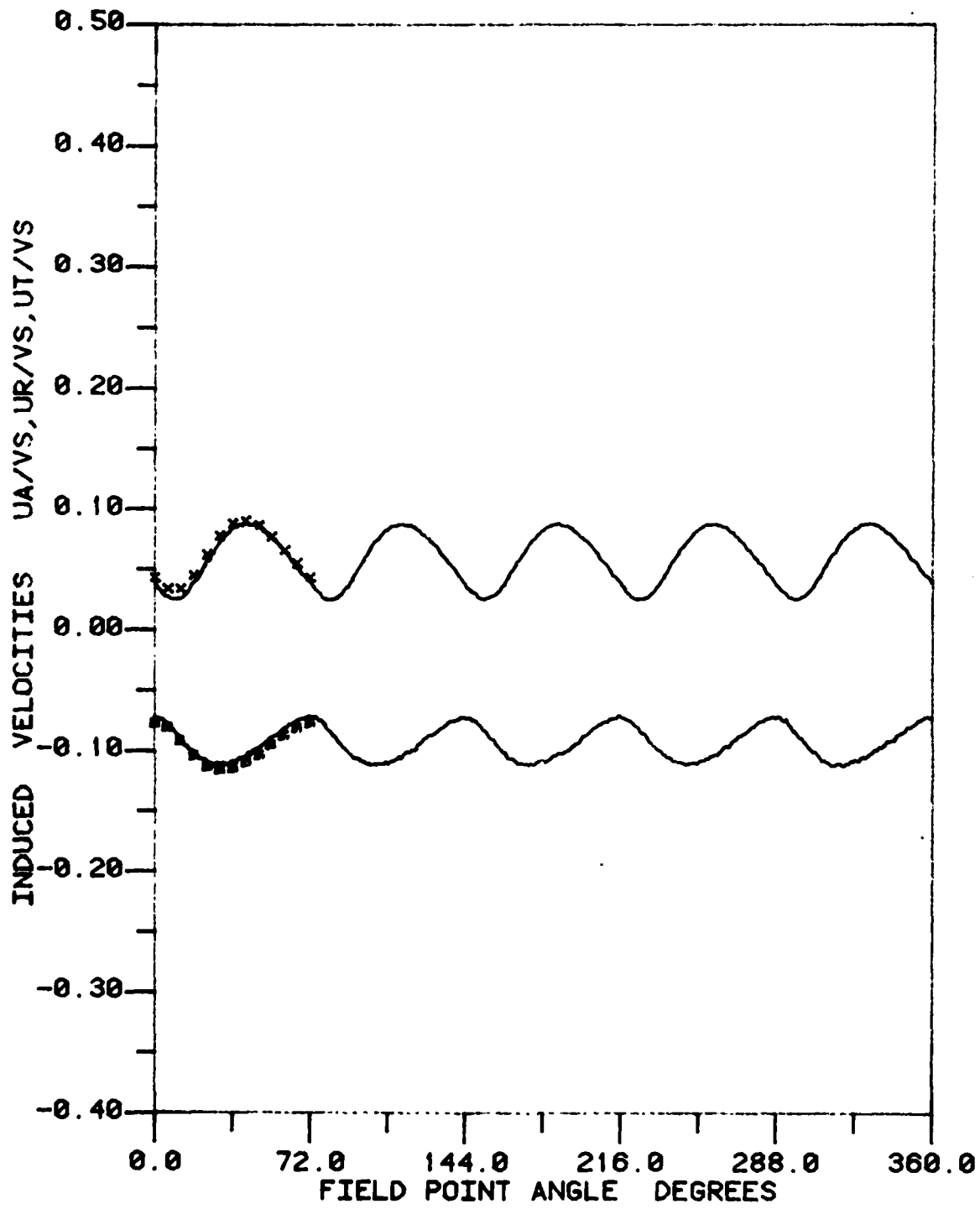


FIGURE 8

N4497

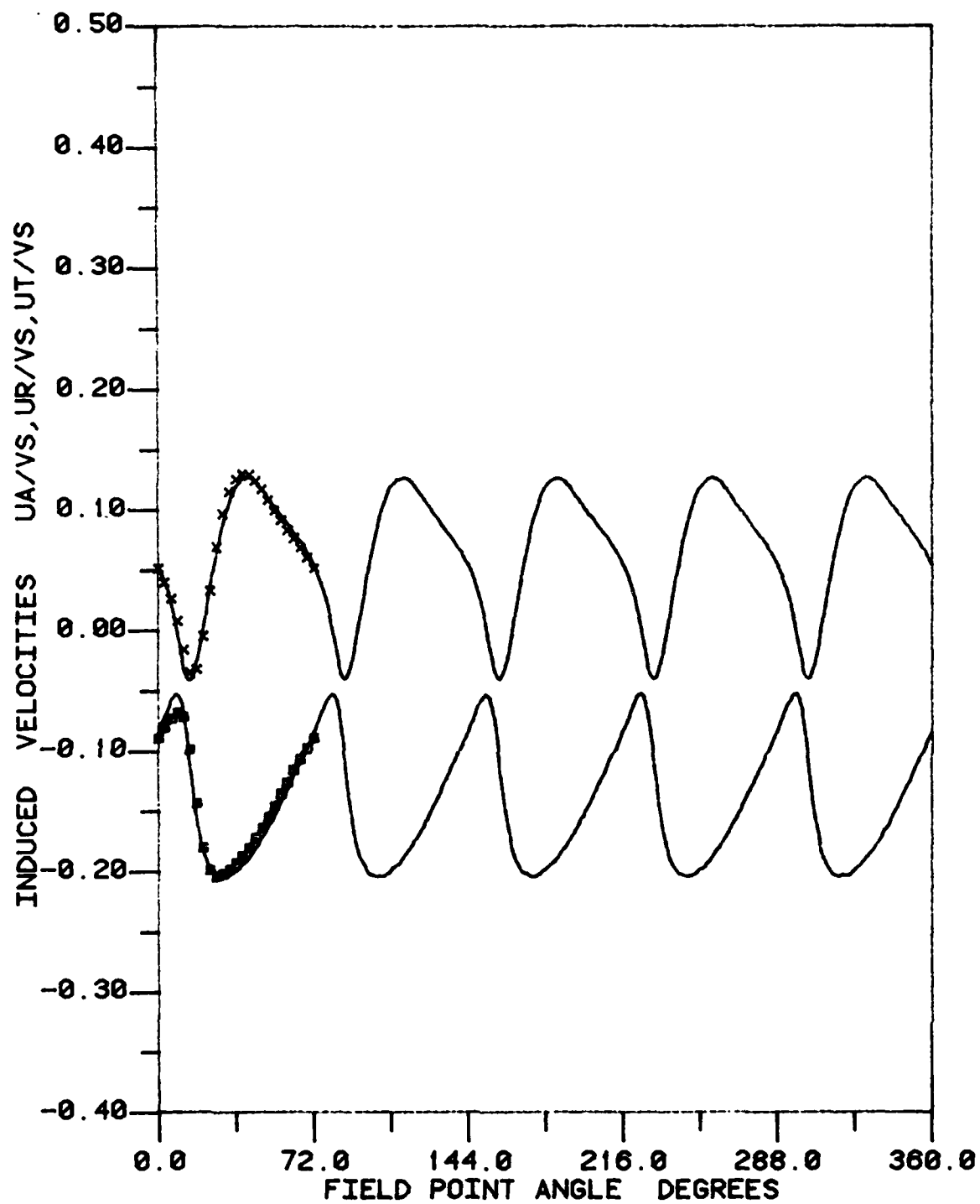


FIGURE 9

N4497



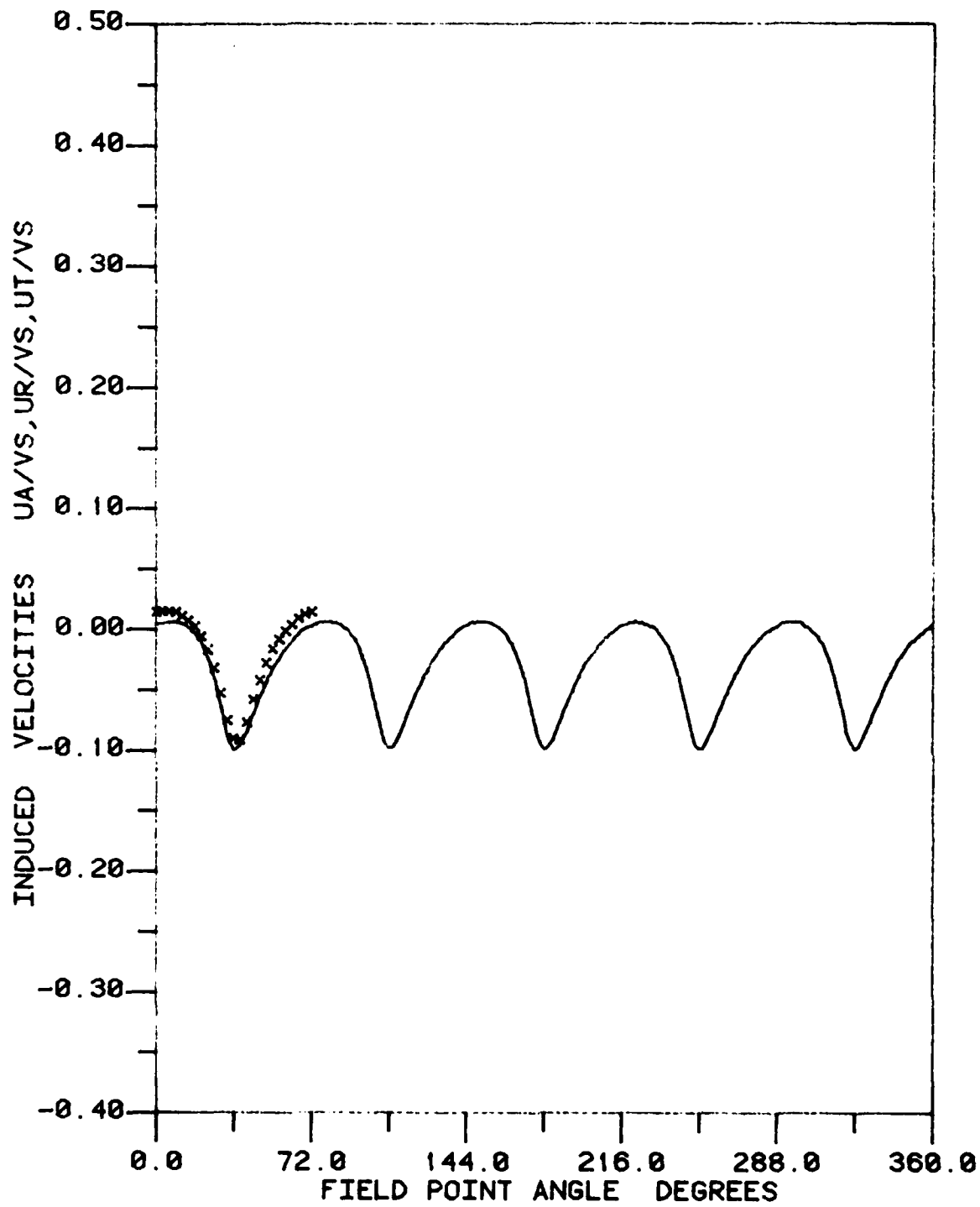


FIGURE 10

N4497

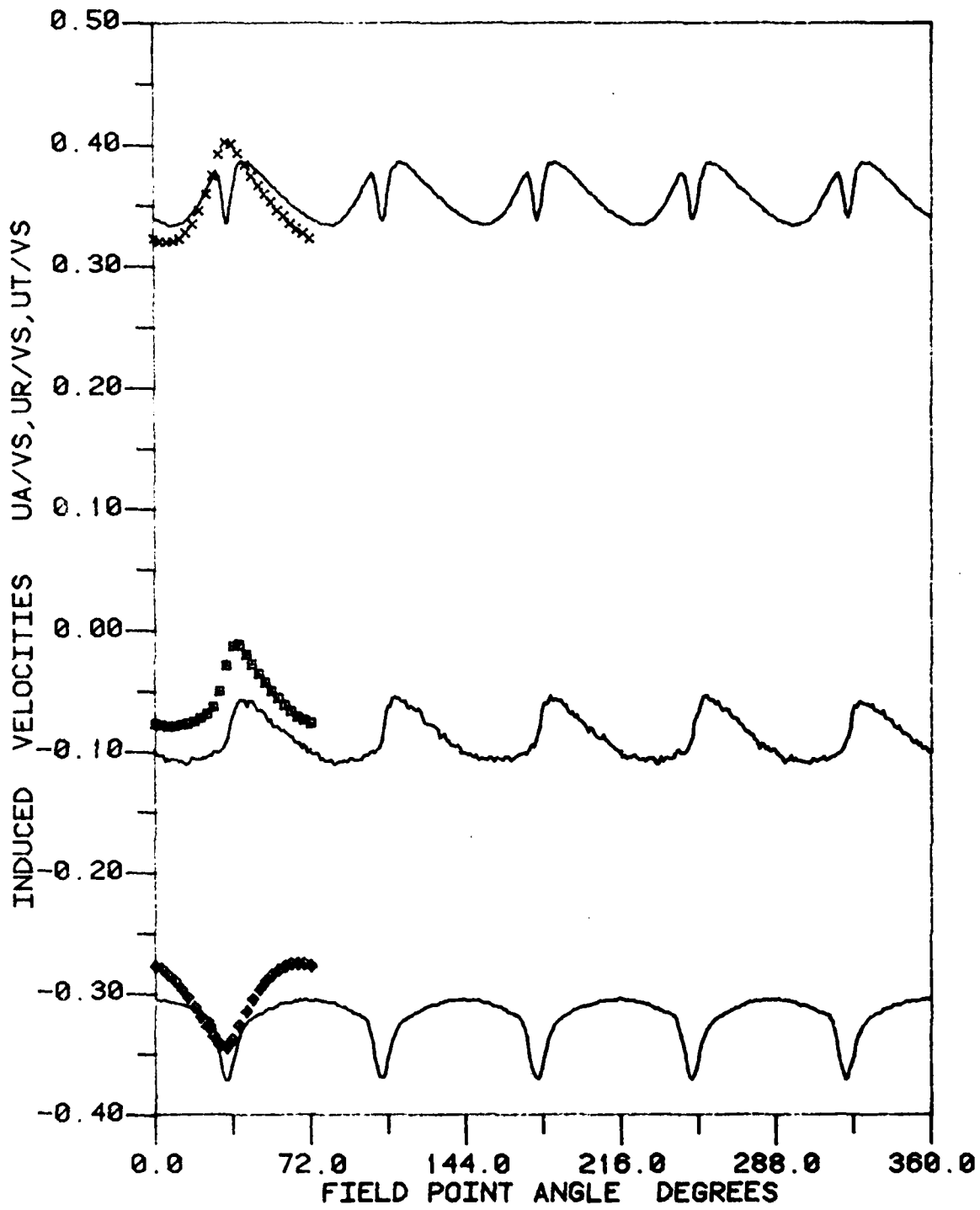


FIGURE 11

N4497

evaluate the circulation does not cross the viscous wake at right angles. This is because the viscous wake contains vorticity which is essentially radial, and thus in the same direction as the bound circulation on the blade. The net wake vorticity contained in a region between two transverse cuts through the wake will be zero only if those cuts are normal to the axis of the wake. Since this is not the case when cutting the wake with a plane normal to the axis of revolution, the tangential component of the viscous vorticity defect contributes to the mean tangential velocity.

The mean tangential velocity derived from the experiment after artistic removal of the viscous wake dents is approximately  $-.32$  as compared with the computed value of  $-.302$ . The measured and computed mean axial components are  $.36$  and  $0.352$  respectively, which agree fairly well. Finally, the measured radial velocity is very similar in form to the calculated results, but its mean value indicates greater flow contraction. This may be due, in part, to the transition wake geometry assumed in PSF-2, but may also be influenced by the absence of a hub in the theory.

## UNSTEADY CAVITATING FLOWS

### Method of Computing the Field Point Potential

We will now consider the more complex problem of a propeller operating in a non-uniform wake field under conditions resulting in unsteady sheet cavitation. The determination of hull exciting forces under these conditions is a topic of great current interest, and methods of solution have been developed by Vorus (1976) and Breslin (1978).

Since the flow is now unsteady, even in a coordinate system rotating with the propeller, the determination of pressures acting either in free space or on the surface of an adjacent body requires a knowledge of the time derivative of the velocity potential. In fact, as shown by Breslin (1982), one only needs the propeller velocity potential, rather than the velocity field itself to determine exciting forces on a body.

If the time history of the singularity distributions representing propeller loading, thickness and cavitation are known, the associated free-space potentials may be readily computed. The determination of these singularity distributions is much more difficult than in the case of steady, non-cavitating flow. A numerical vortex/source lattice procedure for doing this was developed at MIT by C. -S. Lee (1980), and its present version is designated PUF-3. As with PUF-2, the unsteady solution is obtained in discrete time steps of six degrees of propeller rotation. At each time step, the strength of each vortex/source element representing blade loading and thickness, and the strength and extent of the source distribution representing the instantaneous sheet cavity is determined by an iterative solution of non-linear boundary value problem.

Once these discrete singularity strengths are determined, the computation of the free-space potential can proceed in a manner very similar to that described previously for steady non-cavitating flow.

We must first determine the potential of an individual line source and vortex element. This is very easy for the source, where the potential of a three-dimensional point source is simply

$$\phi = \frac{-Q}{4\pi r} \quad (16)$$

where  $Q$  is strength of the source expressed as a volumetric flow, and  $r$  is the distance from the source to the field point. A line vortex is not as simple, since there is no direct analog of Biot-Savart's law for the potential of a three dimensional vortex. However, one can make use of the equivalence between a closed vortex line and a uniform sheet of normal dipoles distributed on a surface bounded by it.

A vortex lattice representation of the propeller and its wake can be readily decomposed into a set of vortex quadrilaterals, which, in turn, can be replaced by normal dipole sheets. Finally, since we are relatively far from the blades, the dipole distribution in each vortex quadrilateral can be replaced by a single point dipole, whose potential is

$$\phi = \frac{\Gamma A(\vec{n} \cdot \vec{r})}{4\pi r^3} \quad (17)$$

where  $\Gamma$  is the strength of the vortex line bounding the quadrilateral element,  $A$  is its area and  $\vec{n}$  is a unit vector normal to the element.

The results of a direct numerical calculation of the velocity field induced by a point dipole, and by a vortex quadrilateral showed that an error of less than one percent can be expected for field points located more than four lattice widths away. This criterion would almost always be met for normal propeller-hull clearances, with a blade lattice consisting of at least ten spanwise and chordwise elements.

Consistent with this approximation, the line sources representing blade and cavity volume may also be represented by point sources with total flux equal to that generated by the equivalent line elements. Hence, equation (16) and (17), summed as before over each of the elements representing the blades and trailing vortex wakes, are all that is required to obtain the potential at a given field point at a sequence of discrete time steps of the propeller.

Two additional complications, however, should be mentioned. First of all, since the propeller loading is unsteady, shed vorticity is introduced into the transition wake. This shed vorticity is assumed to be convected downstream to the roll-up point, but is ignored beyond this point in the ultimate wake. Since the strengths and positions of the discrete shed vortex elements are known, one simply has one additional summation to deal with. The ultimate wake

is represented by concentrated helical tip vortices and a hub vortex, a single point dipole approximation to the "real" dipole sheet connecting these two is obviously inaccurate. Auxiliary helical vortex lines must then be introduced which then divide the wake into quadrilateral elements whose size is small enough to meet the distant field criterion. Numerical experimentation has shown that the introduction of three additional helical lines, producing four elements over the radius, provides sufficient accuracy. Once this auxiliary geometry is determined, the computation of the potential again involves simple summation of the individual dipole contribution given by (17).

For a given field point representing a specified point on a nearby hull surface, one can compute the total potential due to one blade and its wake at sixty times steps during the course of one complete revolution. The contribution of a K bladed propeller is then found by multiplying the blade rate harmonics of the resulting time history by the number of blades. Higher multiples of blade rate may be computed subject to the limitation imposed by the six degree spacing employed in the computation of the propeller singularity distributions, and by interrent inaccuracies in the propeller solution.

#### Sample Calculation of Potentials

Calculations of unsteady loading and cavitation have been made for DTNSRDC propeller 4497 operating in the axial wake field shown in Figure 12. This wake field is representative of a fine form single-screw vessel, and results in propeller cavitation over a relatively narrow extent near the top. Figure 13 shows the computed single bladed non-dimensional cavity source strength as a function of propeller rotation angle for a cavitation number

$$\sigma_n = \frac{P_0 - P_v}{\frac{1}{2} \rho n^2 D^2} = 3.9 \quad (18)$$

at a design volumetric advance coefficient

$$J_A = \frac{V_A}{nD} = 0.889 \quad (19)$$

Figure 14 shows the longitudinal variation in the blade rate amplitude of the potential computed at a set of field points located above the propeller at a radius of  $r/R = 1.4$  and an angular coordinate  $\theta = 0$ . The upper curve is the total potential, including blade loading, thickness and cavity volume. The lower curve includes only the effects of blade loading and thickness.

Table (1) gives the first fifteen harmonics of the normalized potential due to cavitation only at a field point directly above the propeller at a radius  $r/R = 1.4$ . The amplitude of the normalized

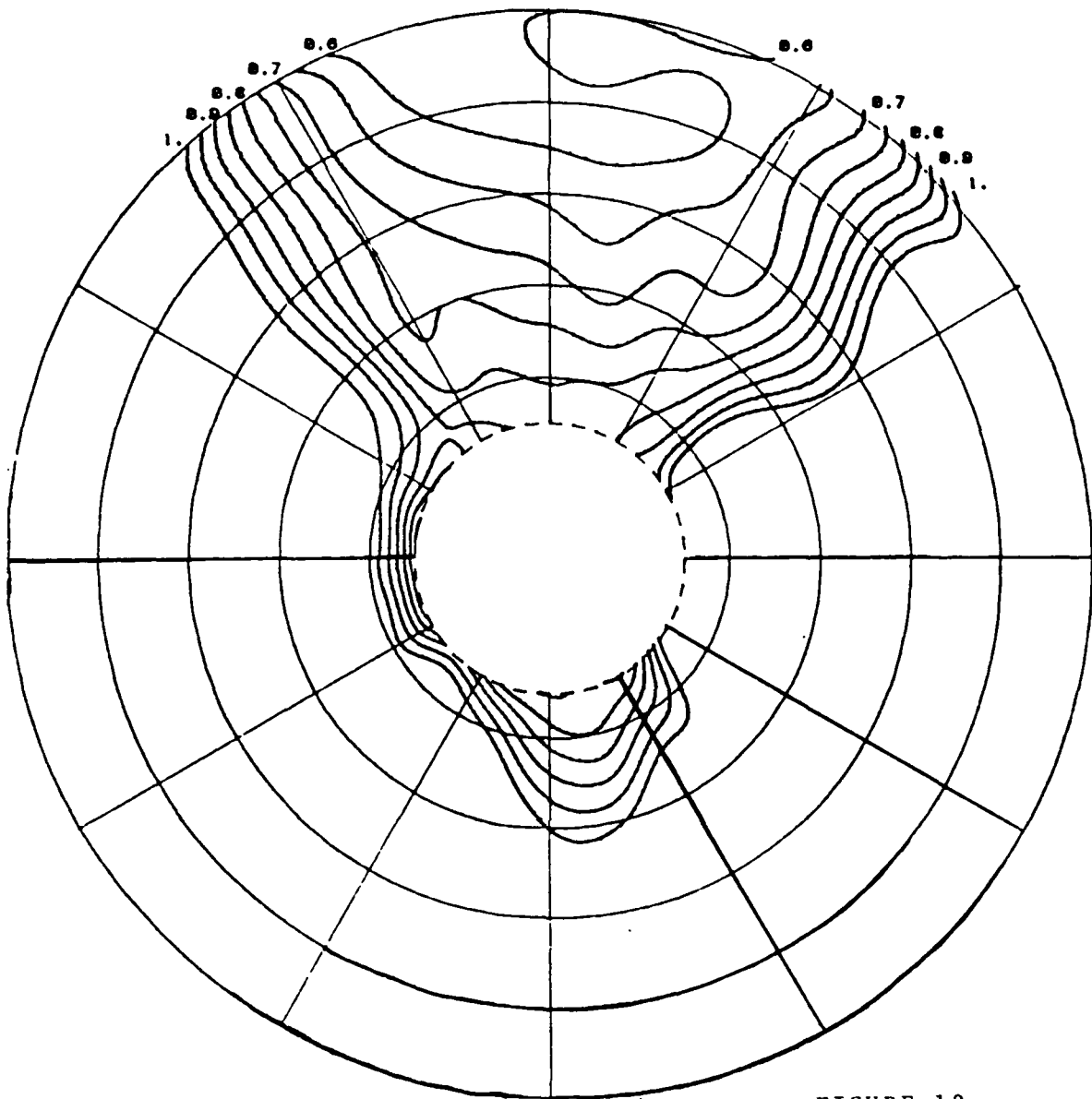


FIGURE 12

potential,  $\phi_N'$ , is defined as follows,

$$\phi_N' = \frac{\phi_N |\vec{r}_f - \vec{r}_c|}{4\pi Q_N} \quad (20)$$

where the subscript  $N$  is the shaft rate harmonic number,  $Q_N$  is the  $N$ 'th harmonic of the total cavity source strength and  $|\vec{r}_f - \vec{r}_c|$  is the magnitude of the distance from a fixed point in space,  $\vec{r}_c$  to the field point. The point  $\vec{r}_c$  may be thought of as an "effective

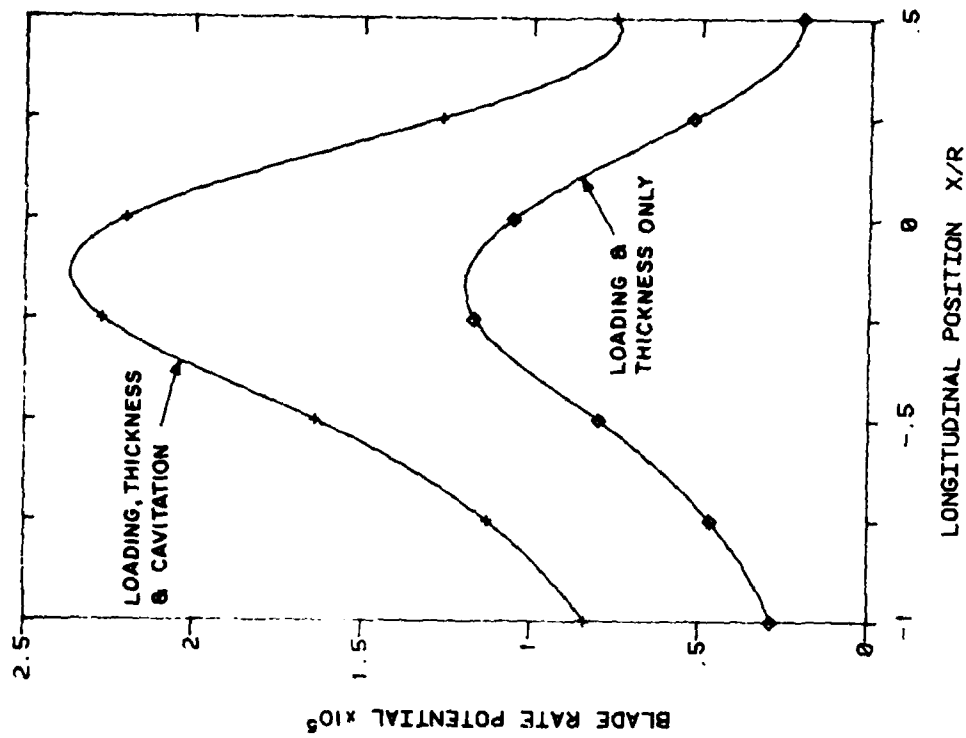


FIGURE 14

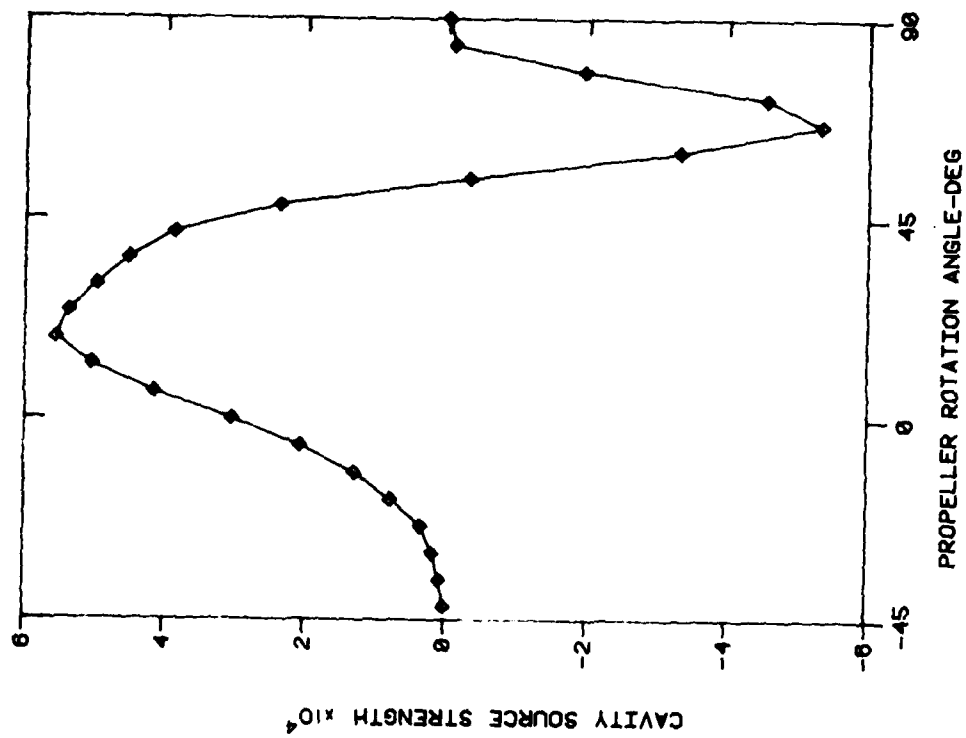


FIGURE 13

cavitation center", and is taken here to be at  $x=0$ ,  $r/R = 0.9$ ,  $\theta=0$ .

The normalized potential is therefore the ratio of the actual potential to the potential that would result if the total space and time dependent cavity volume were concentrated at a fixed point. The normalized phase is simply the phase of the actual potential, as defined in (4), relative to the phase of the corresponding harmonic of  $Q$ .

If the normalized potential is close to unity in amplitude and zero in phase, one can compute cavity induced potentials very simply using a point source approximation. This is not as much of an advantage as one might first think, however. To do this, one needs to have the appropriate harmonics of the time rate of change of cavity volume and this can only be obtained by a detailed calculation of the time history of cavitation extent. Having put this much computational effort into obtaining the cavity volume, one might as well compute the "exact" field point potential!

A far more significant consideration is the validity of experimental procedures for determining cavity volume harmonics. If the cavitation can be modelled as a stationary pulsating source, reciprocal calibration techniques as described, for example, by Whalen, Van Houten and Kerwin (1982), may be used to determine cavity volume experimentally.

TABLE 1

Harmonics of Normalized Field Point Potential  
at  $x = 0$ ,  $r/R = 1.4$ ,  $\theta = 0$ , for DTNSRDC Propeller 4497  
Operating at  $\sigma_n = 3.9$  in Wake Field shown in Figure 13.

Harmonic of Shaft Frequency	Amplitude of Normalized Potential	Relative Phase Angle, Degrees
$\frac{N}{1}$	$\frac{\phi_N}{.656}$	$\frac{\phi_N}{15}$
2	.756	14
3	.821	15
4	.884	18
5	.918	26
6	.856	43
7	.536	57
8	.316	27
9	.409	2
10	.525	-1
11	.608	1
12	.660	5
13	.691	12
14	.668	20
15	.567	23



From Table (1) we can see that the blade rate component of the potential due to cavitation is well represented by a stationary point source, but that twice and three times blade rate would be in error by about a factor of two.

While these results are all based on computations for a five bladed propeller, the time history of cavitation on a single blade would be qualitatively similar for propellers with different numbers of blades with suitably adjusted pitch. Thus, we see that the point source approximation would be reasonable for a 3, 4, 5 or 6 bladed propeller as far as fundamental blade rate is concerned.

These conclusions are valid only for this particular wake field and cavitation number, but are expected to be applicable to other situations in which the angular extent of cavitation is comparable.

#### ACKNOWLEDGEMENTS

The author would like to acknowledge the contributions of David S. Greeley, who wrote the unsteady field point potential program, and Robert S. Schoenberger who carried out the laser velocity measurements.

This research was sponsored by the Office of Naval Research, by the Naval Sea Systems Command General Hydromechanics Research Program, and by the United States Maritime Administration.

#### REFERENCES

- Boswell, R. J. (1971). Design, cavitation performance and open water performance of a series of research skewed propellers, DTNSRDC Report 3339.
- Breslin, J. P. (1978). Propeller-induced hull forces, presented at Seventy-Fifth Diamond Jubilee Symposium, Berlin, West Germany, 21-22 November.
- Breslin, J. P., R. J. Van Houten, J. E. Kerwin, and C. -A. Johnsson. (1982). Theoretical and experimental propeller-induced hull pressures arising from intermittent blade cavitation, loading and thickness, to be presented at SNAME Annual Meeting, November
- Glauert, H. (1959). The elements of aerofoil and airscrew theory, Second Edition, Cambridge at the University Press.
- Greeley, D. S. and J. E. Kerwin. (1982). Numerical methods for propeller design and analysis in steady flow, to be presented at SNAME Annual Meeting, November
- Kerwin, J. E. and C. -S. (1978). Prediction of steady and unsteady marine propeller performance by numerical lifting-surface theory, SNAME Trans., Vol. 86, pp. 218-253.
- Kobayashi, S. (1981). Experimental methods for the prediction of the effect of viscosity on propeller performance, Massachusetts Institute of Technology, Department of Ocean Engineering, Report 81-7.

- Kobayashi, S. (1982). Propeller wake survey by laser-doppler velocimeter, presented at the Int'l. Symp. on Applications of Laser-Doppler Anemometry to Fluid Mechanics, July 5-7, Lisbon, Portugal.
- Lee, C. -S. (1980). Prediction of the transient cavitation on marine propellers by numerical lifting surface theory, 13th Symp. on Naval Hydrodynamics, Tokyo, Japan.
- Min, K. -S. (1978). Numerical and experimental methods for the prediction of field point velocities around propeller blades, Massachusetts Institute of Technology, Department of Ocean Engineering, Report 78-12.
- Nelka, J. J. (1974). Experimental evaluation of a series of skewed propellers with forward rake: open-water performance, cavitation performance, field-point pressures, and unsteady propeller loading, DTNSRDC Report 4113.
- Sayre, H. C. (1980). Laser doppler anemometry and the measurement of loading characteristics of lifting section, New England Section, SNAME, New London, CT.
- Schoenberger, R. (1983). The study of tip vortex roll-up using laser doppler anemometry, Massachusetts Institute of Technology, Department of Ocean Engineering, Master of Science Thesis, (in preparation).
- Vorus, W. S. (1976). Calculation of propeller-induced vibratory hull forces, force distributions, and pressures; free-surface effects, J. Ship Research, 107.
- Whalen, M., J.E. Kerwin, and R.J. Van Houten (1982). Experimental Determination of the Influence of Tip Clearance on Unsteady Propeller Cavitation, Massachusetts Institute of Technology, Department of Ocean Engineering, Report No. 82-6.

FIGURE CAPTIONS

- FIGURE 1. Vortex/source lattice representation of DTNSRDC propeller 4497
- FIGURE 2. Representation of key blade and aligned trailing vortex wake for propeller 4497 operating at design  $J = 0.889$ .
- FIGURE 3. Perspective view of key blade and transition wake showing element indices.
- FIGURE 4. Computed field point velocities for DTNSRDC propeller 4497 at a point upstream.
- FIGURE 5. Computed field point velocities for DTNSRDC propeller 4497 at a point just ahead of the leading edge.
- FIGURE 6. Computed field point velocities for DTNSRDC propeller 4497 at a point close to the tip.
- FIGURE 7. Computed field point velocities for DTNSRDC propeller 4497 at a point inside the transition wake region.
- FIGURE 8. Comparison of laser-doppler velocimeter measurements (solid lines) with computed values (plotted symbols) for the field point shown in Figure 4.
- FIGURE 9. Comparison of laser-doppler velocimeter measurements (solid lines) with computed values (plotted symbols) for the field point shown in Figure 5.
- FIGURE 10. Comparison of laser-doppler velocimeter measurements (solid lines) with computed values (plotted symbols) for the field point shown in Figure 6.
- FIGURE 11. Comparison of laser-doppler velocimeter measurements (solid lines) with computed values (plotted symbols) for the field point shown in Figure 7.

FIGURE 12. Axial wake field used for PUF-3 computation of cavitation and loading time histories. This wake field was measured by a laser-doppler velocimeter in front of DTNSRDC propeller 4497 operating at design thrust. An effective wake was constructed by subtracting from these values the circumferential mean propeller induced velocities calculated by the steady field point program.

FIGURE 13. Variation of total single blade cavity source strength with propeller angular position computed by PUF-3. The source strength is non-dimensionalized by the factor  $2\pi R^2 U_R$ , where  $U_R = [V_S^2 + (0.7R\omega)^2]^{1/2}$ .

FIGURE 14. Variation in amplitude of blade-rate potential with axial position. Positive  $x$  is downstream of the propeller. The potential is non-dimensionalized by the factor  $2\pi R U_R$ .

## Discussion

T. Sasajima (Mitsubishi Heavy Industries)

We understand that the system of discrete vortices and sources, especially configuration of transition wake, is one of the key points of success in the numerical lifting-surface approach of a propeller (Kerwin and Lee, 1978). To understand this model in detail from the viewpoint of flow field, the discussor would appreciate very much if the author could show us the shape and pitch distribution of the slip stream based on this model and also the contribution of each induced velocity component, i.e.,  $\bar{v}_s$ ,  $\bar{v}_q$ ,  $\bar{v}_c$ ,  $\bar{v}_{tw}$ , and  $\bar{v}_n$  to the induced velocity at a point inside the transition wake region, as shown in Figure 7.

E.A. Weitendorf (Hamburg Ship Model Basin)

I would like the author to comment regarding two points:

1. Tip vortex: At the Hamburg Ship Model Basin (HSVA) we found by our laser Doppler velocimeter that distribution of the axial-induced velocities, plotted over the radius in a plane at a distance of 1.2 of the propeller diameter, displays a maximum at the 0.5-0.6 radius. The velocity distribution was by no means constant over the propeller radius. Is, maybe, the disagreement between the calculated and measured results in Figure 11 a reason for the fact that in the calculation a rolled-up tip-vortex is taken into account, whereas in reality the vortex sheet is not yet rolled up?
2. Cavity thickness of skew-back propellers: At the last meeting of the cavitation committee of the ITTC the fact was discussed that there is a strong difference of the cavity thickness between conventional and skew-back propellers. For the latter, the thickness is obviously larger. This fact seems to be connected to the flow behavior around the leading edge. To the knowledge of the discussor there exists no theory that can explain the larger cavity thickness of a skew-back propeller at its leading edge. I would like to know the opinion of the author concerning this problem.

## Author's Reply

Justin E. Kerwin

To Dr. Sasajima

Dr. Sasajima has requested a detailed breakdown of wake geometry and individual contributions to the total induced velocity. Such data are, of course, too voluminous to provide for all the cases shown in the paper. However, I have included in this response a complete tabulation of propeller and wake geometry and of lattice singularity strengths for the propeller computed in Figures 4-7 and a tabulation of a breakdown of induced velocity contributions for the case shown in Figure 5. The latter results are given in 12 degree increments, rather than for 3 degrees. These additional data should serve to document the steady field-point computational procedure. (See Tables 2-6.)

To Dr. Weitendorf

Dr. Weitendorf raises the question of the validity of the assumption of complete roll-up of the tip vortex. We believe that this is an idealization that is valid for computation of velocities near and ahead of the propeller but that is not locally correct. As with the analogous case of a wing, the outer edge of the vortex sheet rolls up into a complex spiral shape that is finite in extent. While the concentrated vortex approximation is not locally valid, it is still far more realistic than the assumption of a helical sheet.

Our laser measurements of axial velocity are in agreement with Dr. Weitendorf's findings, although it is clear that the radial distribution tends to become more uniform with increasing downstream distance. This is evident from Figure 39 from "Numerical and Experimental Methods for the Prediction of Field Point Velocities Around Propeller Blades," by Keh-Sik Min (MIT, Report No. 78-12, June 1978) reproduced here.

The calculations shown in Figure 11 are much closer to the propeller and are in the transition wake region. We believe that the principal discrepancy here is associated with viscous effects.

Dr. Weitendorf also raises the question of the influence of skew on cavity thickness. Our experience to date with the PUF-3 program indicates that skew tends to decrease total cavity volume, which is consistent with experimental findings. There are subtle leading-edge viscous effects associated with skew that may influence cavity thickness, but this effect is not considered in PUF-3.

The author would like to point out an inconsistency in the unsteady cavitating results that was discovered after the presentation of the paper. The extension of the unsteady cavity closure condition as presented in "The Numerical Prediction of Unsteady Sheet Cavitation on High Aspect Ratio Hydrofoils" by R. J. Van Houten, 1982, to PUF-3 contains an error. The integral of total cavity strength over one complete cycle of growth and collapse must be zero, yet this is not the case for

Table 2. Blade Lattice Geometry

N4497								
NBLADE,MM,NN,NPUW:	5	8	8	36				
NSW(M):	14	13	13	12	12	13	13	14
VSR: 1.00000								
-----X(N,M)-----								
-0.1643	-0.1416	-0.0979	-0.0393	0.0257	0.0875	0.1368	0.1636	
-0.1907	-0.1650	-0.1151	-0.0475	0.0279	0.1000	0.1580	0.1897	
-0.2018	-0.1754	-0.1234	-0.0525	0.0272	0.1039	0.1664	0.2004	
-0.1999	-0.1743	-0.1234	-0.0535	0.0254	0.1017	0.1643	0.1984	
-0.1864	-0.1627	-0.1153	-0.0502	0.0234	0.0946	0.1531	0.1851	
-0.1650	-0.1440	-0.1020	-0.0444	0.0206	0.0837	0.1355	0.1638	
-0.1369	-0.1194	-0.0846	-0.0369	0.0171	0.0694	0.1124	0.1358	
-0.1022	-0.0892	-0.0631	-0.0274	0.0129	0.0519	0.0840	0.1015	
-0.0428	-0.0374	-0.0267	-0.0118	0.0051	0.0215	0.0350	0.0424	
-----Y(N,M)-----								
0.2102	0.2154	0.2212	0.2235	0.2209	0.2151	0.2098	0.2066	
0.3008	0.3079	0.3156	0.3172	0.3097	0.2960	0.2831	0.2751	
0.3959	0.4037	0.4110	0.4090	0.3938	0.3697	0.3471	0.3331	
0.4943	0.5012	0.5059	0.4978	0.4727	0.4366	0.4030	0.3826	
0.5946	0.5989	0.5984	0.5821	0.5462	0.4983	0.4542	0.4277	
0.6937	0.6938	0.6856	0.6597	0.6133	0.5554	0.5034	0.4724	
0.7855	0.7802	0.7632	0.7277	0.6735	0.6101	0.5546	0.5220	
0.8590	0.8484	0.8240	0.7829	0.7274	0.6669	0.6155	0.5858	
0.8701	0.8603	0.8414	0.8149	0.7839	0.7533	0.7287	0.7150	
-----Z(N,M)-----								
-0.0761	-0.0598	-0.0324	0.0011	0.0342	0.0609	0.0771	0.0854	
-0.1022	-0.0781	-0.0358	0.0170	0.0706	0.1152	0.1440	0.1588	
-0.1133	-0.0813	-0.0244	0.0474	0.1203	0.1813	0.2216	0.2420	
-0.1078	-0.0686	0.0015	0.0900	0.1802	0.2555	0.3057	0.3310	
-0.0802	-0.0358	0.0444	0.1456	0.2483	0.3342	0.3920	0.4208	
-0.0252	0.0224	0.1081	0.2160	0.3251	0.4163	0.4779	0.5086	
0.0654	0.1124	0.1970	0.3028	0.4096	0.4990	0.5601	0.5906	
0.2015	0.2424	0.3156	0.4070	0.4994	0.5777	0.6322	0.6598	
0.4433	0.4619	0.4955	0.5380	0.5823	0.6214	0.6500	0.6650	

NBLADE = Number of blades

MM = number of lattice intervals over span

NN = number of lattice intervals over chord

NPUW = number of elements in ultimate wake

NSW(M) = number of elements in transition wake at the m'th radius

VSR = ratio of ship speed to reference velocity

X(N,M) = Cartesian coordinates of blade lattice. The n index  
Y(N,M) is chordwise and the m index is spanwise  
Z(N,M)

the example given in Figure 13. A check indicated that this error is not present in the results given by Van Houten.

The error is now being corrected, and this will result in some changes in predicted field-point potentials. However, the results given in this paper are expected to remain qualitatively correct.

-----XTIP(N,M),YTIP(N,M),ZTIP(N,M)-----							
-0.0428	-0.0374	-0.0267	-0.0118	0.0051	0.0215	0.0350	0.0424
-0.0374	-0.0267	-0.0118	0.0051	0.0215	0.0350	0.0424	0.0434
-0.0267	-0.0118	0.0051	0.0215	0.0350	0.0424	0.0434	0.0
-0.0118	0.0051	0.0215	0.0350	0.0424	0.0434	0.0	0.0
0.0051	0.0215	0.0350	0.0424	0.0434	0.0	0.0	0.0
0.0215	0.0350	0.0424	0.0434	0.0	0.0	0.0	0.0
0.0350	0.0424	0.0434	0.0	0.0	0.0	0.0	0.0
0.0424	0.0434	0.0	0.0	0.0	0.0	0.0	0.0
0.0434	0.0	0.0	0.0	0.0	0.0	0.0	0.0
0.8701	0.8603	0.8414	0.8149	0.7839	0.7533	0.7287	0.7150
0.8603	0.8414	0.8149	0.7839	0.7533	0.7287	0.7150	0.7132
0.8414	0.8149	0.7839	0.7533	0.7287	0.7150	0.7132	0.0
0.8149	0.7839	0.7533	0.7287	0.7150	0.7132	0.0	0.0
0.7839	0.7533	0.7287	0.7150	0.7132	0.0	0.0	0.0
0.7533	0.7287	0.7150	0.7132	0.0	0.0	0.0	0.0
0.7287	0.7150	0.7132	0.0	0.0	0.0	0.0	0.0
0.7150	0.7132	0.0	0.0	0.0	0.0	0.0	0.0
0.7132	0.0	0.0	0.0	0.0	0.0	0.0	0.0
0.4433	0.4619	0.4955	0.5380	0.5823	0.6214	0.6500	0.6650
0.4619	0.4955	0.5380	0.5823	0.6214	0.6500	0.6650	0.6669
0.4955	0.5380	0.5823	0.6214	0.6500	0.6650	0.6669	0.0
0.5380	0.5823	0.6214	0.6500	0.6650	0.6669	0.0	0.0
0.5823	0.6214	0.6500	0.6650	0.6669	0.0	0.0	0.0
0.6214	0.6500	0.6650	0.6669	0.0	0.0	0.0	0.0
0.6500	0.6650	0.6669	0.0	0.0	0.0	0.0	0.0
0.6650	0.6669	0.0	0.0	0.0	0.0	0.0	0.0
0.6669	0.0	0.0	0.0	0.0	0.0	0.0	0.0

Table 3. Separated Tip Vortex Geometry

XTIP(N,M)  
YTIP(N,M) = Cartesian coordinates at n chordwise  
ZTIP(N,M) positions of separated vortex originating  
from outboard end of m'th spanwise vortex  
of tip panel.





XU(N)														
1.0570	1.2633	1.4703	1.6775	1.8847	2.0919	2.2992	2.5064	2.7136	2.9208	3.1281	3.3353	3.5425	3.7497	3.9570
4.1642	4.14	4.5786	4.7858	4.9931	5.2003	5.4075	5.6147	5.8220	6.0292	6.2364	6.4436	6.6509	6.8581	7.0653
7.2725	7.4737	7.6870	7.8942	8.1014	8.3086									
YU(N)														
-0.7232	-0.3670	0.0876	0.5187	0.8108	0.8857	0.7232	0.3670	-0.0876	-0.5187	-0.8108	-0.8857	-0.7232	-0.3670	0.0876
-0.5187	0.8108	0.8857	0.7232	0.3670	-0.0876	-0.5187	-0.8108	-0.8857	-0.7232	-0.3670	0.0876	0.5187	0.8108	0.8857
0.7232	0.3670	-0.0876	-0.5187	-0.8108	-0.8857									
ZU(N)														
-0.5187	-0.8108	-0.8857	-0.7232	-0.3670	0.0876	0.5187	0.8108	0.8857	0.7232	0.3670	-0.0876	-0.5187	-0.8108	-0.8857
-0.7232	-0.3670	0.0876	0.5187	0.8108	0.8857	0.7232	0.3670	-0.0876	-0.5187	-0.8108	-0.8857	-0.7232	-0.3670	0.0876
0.5187	0.8108	0.8857	0.7232	0.3670	-0.0876									
GC(N,M)														
-0.000250	-0.002173	-0.004997	-0.008323	-0.011968	-0.015159	-0.015159	-0.015159	-0.015159	-0.015159	-0.015159	-0.015159	-0.015159	-0.015159	-0.015159
-0.000789	-0.001921	-0.003379	-0.005125	-0.006906	-0.008345	-0.008345	-0.008345	-0.008345	-0.008345	-0.008345	-0.008345	-0.008345	-0.008345	-0.008345
-0.000485	-0.001296	-0.002318	-0.003438	-0.004502	-0.005390	-0.005390	-0.005390	-0.005390	-0.005390	-0.005390	-0.005390	-0.005390	-0.005390	-0.005390
-0.000269	-0.000646	-0.001131	-0.001620	-0.002005	-0.002329	-0.002329	-0.002329	-0.002329	-0.002329	-0.002329	-0.002329	-0.002329	-0.002329	-0.002329
-0.000098	-0.000056	-0.000019	-0.000149	-0.000381	-0.000576	-0.000576	-0.000576	-0.000576	-0.000576	-0.000576	-0.000576	-0.000576	-0.000576	-0.000576
0.000082	0.000461	0.001010	0.001686	0.002447	0.003081	0.003081	0.003081	0.003081	0.003081	0.003081	0.003081	0.003081	0.003081	0.003081
0.000185	0.000830	0.001813	0.003017	0.004318	0.005410	0.005410	0.005410	0.005410	0.005410	0.005410	0.005410	0.005410	0.005410	0.005410
0.000038	0.000925	0.002369	0.004340	0.006296	0.007902	0.007902	0.007902	0.007902	0.007902	0.007902	0.007902	0.007902	0.007902	0.007902
0.001587	0.003877	0.006615	0.009314	0.011938	0.014253	0.014253	0.014253	0.014253	0.014253	0.014253	0.014253	0.014253	0.014253	0.014253
GB(N,M)														
0.000250	0.001922	0.002824	0.003326	0.003645	0.003191	0.003191	0.003191	0.003191	0.003191	0.003191	0.003191	0.003191	0.003191	0.003191
0.001039	0.003054	0.004282	0.005072	0.005426	0.004629	0.004629	0.004629	0.004629	0.004629	0.004629	0.004629	0.004629	0.004629	0.004629
0.001524	0.003866	0.005304	0.006192	0.006489	0.005518	0.005518	0.005518	0.005518	0.005518	0.005518	0.005518	0.005518	0.005518	0.005518
0.001794	0.004243	0.005789	0.006681	0.006875	0.005842	0.005842	0.005842	0.005842	0.005842	0.005842	0.005842	0.005842	0.005842	0.005842
0.001892	0.004200	0.005714	0.006551	0.006643	0.005646	0.005646	0.005646	0.005646	0.005646	0.005646	0.005646	0.005646	0.005646	0.005646
0.001810	0.003822	0.005165	0.005874	0.005881	0.005012	0.005012	0.005012	0.005012	0.005012	0.005012	0.005012	0.005012	0.005012	0.005012
0.001624	0.003177	0.004182	0.004670	0.004581	0.003921	0.003921	0.003921	0.003921	0.003921	0.003921	0.003921	0.003921	0.003921	0.003921
0.001587	0.002290	0.002738	0.002699	0.002624	0.002314	0.002314	0.002314	0.002314	0.002314	0.002314	0.002314	0.002314	0.002314	0.002314
SB(N,M)														
0.005808	0.005453	0.003903	0.003903	0.000933	-0.003023	-0.005546	-0.005546	-0.005546	-0.005546	-0.005546	-0.005546	-0.005546	-0.005546	-0.005546
0.005763	0.005372	0.003797	0.003797	0.000897	-0.002903	-0.005373	-0.005373	-0.005373	-0.005373	-0.005373	-0.005373	-0.005373	-0.005373	-0.005373
0.005463	0.005103	0.003613	0.003613	0.000855	-0.002775	-0.005164	-0.005164	-0.005164	-0.005164	-0.005164	-0.005164	-0.005164	-0.005164	-0.005164
0.004831	0.004552	0.003268	0.003268	0.000785	-0.002581	-0.004845	-0.004845	-0.004845	-0.004845	-0.004845	-0.004845	-0.004845	-0.004845	-0.004845
0.003961	0.003774	0.002766	0.002766	0.000681	-0.002287	-0.004353	-0.004353	-0.004353	-0.004353	-0.004353	-0.004353	-0.004353	-0.004353	-0.004353
0.002957	0.002861	0.002159	0.002159	0.000552	-0.001920	-0.003732	-0.003732	-0.003732	-0.003732	-0.003732	-0.003732	-0.003732	-0.003732	-0.003732
0.001935	0.001908	0.001498	0.001498	0.000406	-0.001493	-0.002982	-0.002982	-0.002982	-0.002982	-0.002982	-0.002982	-0.002982	-0.002982	-0.002982
0.000844	0.000867	0.000752	0.000752	0.000242	-0.001067	-0.001986	-0.001986	-0.001986	-0.001986	-0.001986	-0.001986	-0.001986	-0.001986	-0.001986

Table 5. Ultimate tip vortex geometry and singularity strengths

XU(N)

YU(N) = Cartesian coordinates of ultimate tip vortex helix

ZU(N)

GC(N,M) = Strengths of chordwise vortex elements on blade  
(non-dimensionalized by  $2\pi RV_s$ )

GB(N,M) = Strengths of spanwise vortex elements on blade

SB(N,M) = Strengths of spanwise source elements on blade

Table 6. Breakdown of induced velocity  
components in Cartesian coordinates  
for one complete revolution of a single blade

x	y	z	
-0.12800	0.92900	0.00000	-- field point coordinate
0.00477	-0.00473	0.00224	-- ultimate wake
-0.04281	0.02617	-0.00209	-- blade vortices and sources
0.00124	0.00044	-0.00017	-- separated tip vortex
0.01273	0.00383	-0.00635	-- transition wake
-0.02407	0.02571	-0.00637	-- total induced velocity
-0.12800	0.90870	0.19315	
0.00494	-0.00447	0.00146	
-0.10299	0.01614	0.04091	
0.00215	0.00026	-0.00065	Same as above with
0.01465	0.00609	-0.00760	field point incremented
-0.08124	0.01801	0.03413	12 degrees
-0.12800	0.84868	0.37786	
0.00511	-0.00410	0.00081	
-0.05347	-0.14513	0.05297	
0.00724	-0.00557	-0.00627	24 degrees
0.01690	0.00778	-0.01008	
-0.02422	-0.14702	0.03743	
-0.12800	0.75158	0.54605	
0.00528	-0.00364	0.00031	
0.03421	-0.09565	0.01206	
0.01668	-0.03232	-0.03007	36 degrees
0.01947	0.00356	-0.02090	
0.07564	-0.12806	-0.03861	
-0.12800	0.62162	0.69038	
0.00544	-0.00314	-0.00004	
0.04442	-0.03709	-0.01478	
0.00645	-0.01470	-0.01458	48 degrees
0.01826	-0.01653	-0.05386	
0.07456	-0.07145	-0.08326	
-0.12800	0.46450	0.80454	
0.00560	-0.00262	-0.00023	
0.03219	-0.00841	-0.01165	
0.00231	-0.00362	-0.00388	60 degrees
0.01129	-0.01772	-0.06617	
0.05138	-0.03236	-0.08193	

Table 6 (continued)

-0.12800	0.28708	0.88353	72 degrees
0.00575	-0.00212	-0.00026	
0.02307	0.00048	-0.00586	
0.00132	-0.00130	-0.00159	
0.00872	-0.00662	-0.06130	
0.03886	-0.00956	-0.06902	
-0.12800	0.09711	0.92391	84 degrees
0.00589	-0.00166	-0.00016	
0.01708	0.00288	-0.00244	
0.00093	-0.00061	-0.00087	
0.00802	0.00433	-0.05247	
0.03192	0.00494	-0.05593	
-0.12800	-0.09711	0.92391	96 degrees
0.00603	-0.00129	0.00007	
0.01301	0.00326	-0.00044	
0.00073	-0.00032	-0.00056	
0.00758	0.01245	-0.04317	
0.02735	0.01410	-0.04409	
-0.12800	-0.28708	0.88353	108 degrees
0.00614	-0.00097	0.00041	
0.01012	0.00298	0.00078	
0.00061	-0.00019	-0.00040	
0.00711	0.01781	-0.03439	
0.02398	0.01963	-0.03360	
-0.12800	-0.46450	0.80454	120 degrees
0.00624	-0.00074	0.00083	
0.00800	0.00247	0.00152	
0.00052	-0.00011	-0.00030	
0.00660	0.02094	-0.02649	
0.02136	0.02257	-0.02445	
-0.12800	-0.62162	0.69038	132 degrees
0.00629	-0.00058	0.00132	
0.00639	0.00191	0.00197	
0.00047	-0.00006	-0.00024	
0.00611	0.02238	-0.01960	
0.01927	0.02365	-0.01655	

Table 6 (continued)

-0.12800	-0.75158	0.54605	144 degrees
0.00630	-0.00048	0.00188	
0.00513	0.00135	0.00224	
0.00043	-0.00003	-0.00020	
0.00569	0.02253	-0.01372	
0.01755	0.02337	-0.00981	
-0.12800	-0.84868	0.37786	156 degrees
0.00624	-0.00042	0.00249	
0.00411	0.00082	0.00238	
0.00040	-0.00001	-0.00017	
0.00537	0.02173	-0.00882	
0.01612	0.02212	-0.00412	
-0.12800	-0.90870	0.19315	168 degrees
0.00609	-0.00036	0.00316	
0.00326	0.00031	0.00243	
0.00038	0.00001	-0.00015	
0.00518	0.02021	-0.00484	
0.01490	0.02016	0.00060	
-0.12800	-0.92900	0.00000	180 degrees
0.00583	-0.00028	0.00390	
0.00253	-0.00018	0.00241	
0.00036	0.00002	-0.00014	
0.00514	0.01816	-0.00174	
0.01385	0.01773	0.00444	
-0.12800	-0.90870	-0.19315	192 degrees
0.00545	-0.00014	0.00472	
0.00188	-0.00065	0.00232	
0.00035	0.00003	-0.00012	
0.00524	0.01574	0.00055	
0.01292	0.01498	0.00747	
-0.12800	-0.84868	-0.37786	204 degrees
0.00499	0.00002	0.00558	
0.00127	-0.00111	0.00218	
0.00034	0.00004	-0.00011	
0.00545	0.01311	0.00209	
0.01206	0.01205	0.00974	

Table 6 (continued)

-0.12800	-0.75158	-0.54605	
0.00451	0.00014	0.00645	
0.00068	-0.00157	0.00196	216 degrees
0.00034	0.00005	-0.00010	
0.00574	0.01043	0.00297	
0.01127	0.00905	0.01128	

-0.12800	-0.62162	-0.69038	
0.00407	0.00012	0.00724	
0.00009	-0.00203	0.00167	228 degrees
0.00034	0.00006	-0.00010	
0.00604	0.00788	0.00329	
0.01054	0.00602	0.01210	

-0.12800	-0.46450	-0.80454	
0.00375	-0.00011	0.00785	
-0.00054	-0.00250	0.00127	240 degrees
0.00035	0.00007	-0.00009	
0.00632	0.00559	0.00320	
0.00987	0.00305	0.01223	

-0.12800	-0.28708	-0.88353	
0.00358	-0.00058	0.00819	
-0.00124	-0.00295	0.00073	252 degrees
0.00036	0.00008	-0.00009	
0.00655	0.00365	0.00280	
0.00925	0.00019	0.01164	

-0.12800	-0.09711	-0.92391	
0.00353	-0.00125	0.00825	
-0.00204	-0.00336	0.00001	264 degrees
0.00037	0.00009	-0.00009	
0.00677	0.00209	0.00218	
0.00863	-0.00243	0.01035	

-0.12800	0.09711	-0.92391	
0.00358	-0.00202	0.00802	
-0.00301	-0.00368	-0.00097	276 degrees
0.00039	0.00010	-0.00008	
0.00700	0.00091	0.00140	
0.00796	-0.00469	0.00837	

Table 6 (continued)

-0.12800	0.28708	-0.88353	
0.00370	-0.00281	0.00753	
-0.00421	-0.00379	-0.00226	288 degrees
0.00042	0.00012	-0.00008	
0.00728	0.00009	0.00050	
0.00718	-0.00639	0.00568	

-0.12800	0.46450	-0.80454	
0.00385	-0.00352	0.00683	
-0.00578	-0.00351	-0.00396	300 degrees
0.00046	0.00015	-0.00008	
0.00766	-0.00037	-0.00051	
0.00619	-0.00726	0.00227	

-0.12800	0.62162	-0.69038	
0.00403	-0.00411	0.00598	
-0.00792	-0.00247	-0.00611	312 degrees
0.00051	0.00018	-0.00008	
0.00818	-0.00046	-0.00161	
0.00481	-0.00687	-0.00182	

-0.12800	0.75158	-0.54605	
0.00422	-0.00454	0.00504	
-0.01098	-0.00005	-0.00857	324 degrees
0.00059	0.00022	-0.00008	
0.00890	-0.00015	-0.00278	
0.00272	-0.00452	-0.00639	

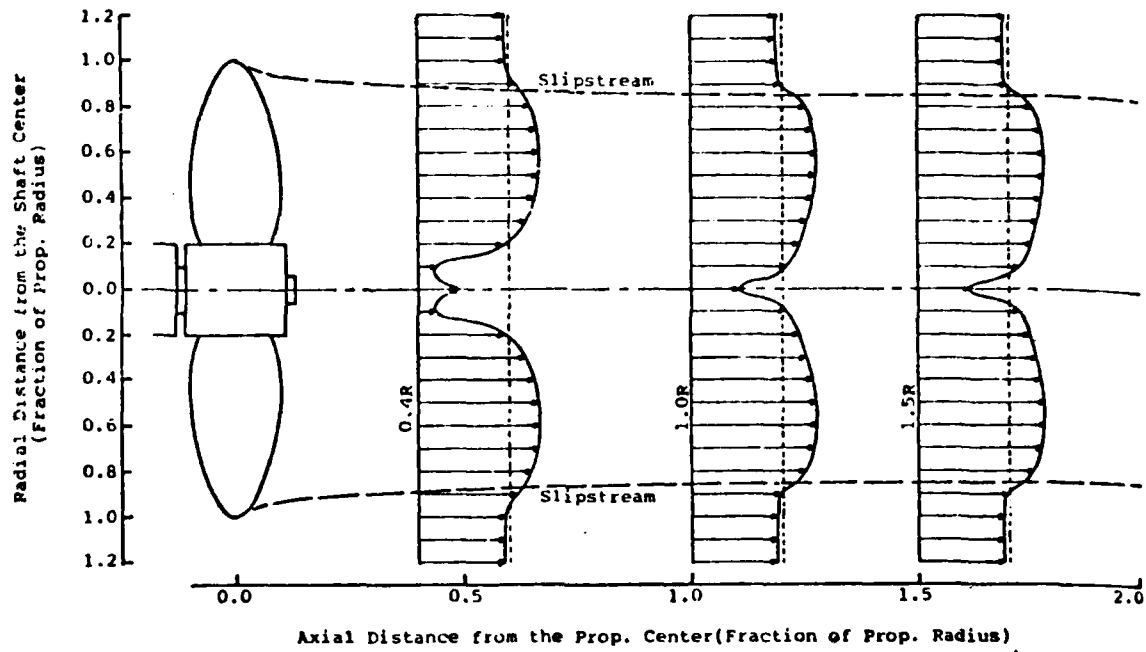
-0.12800	0.84868	-0.37786	
0.00440	-0.00478	0.00407	
-0.01573	0.00474	-0.01075	336 degrees
0.00070	0.00028	-0.00008	
0.00986	0.00064	-0.00399	
-0.00076	0.00087	-0.01075	

-0.12800	0.90870	-0.19315	
0.00459	-0.00484	0.00312	
-0.02413	0.01337	-0.01069	348 degrees
0.00089	0.00036	-0.00009	
0.01112	0.00195	-0.00519	
-0.00754	0.01084	-0.01285	

Fig. 39 NSRDC Prop. 4381(No skew)

## Axial Velocity Distribution behind Propeller

Advance Coeff.(J) = 0.889

Speed of Advance( $V_a$ ) = 13.335 ft/sec



# The Effects of Hull Pitching Motions and Waves on Periodic Propeller Blade Loads

Stuart D. Jessup and Robert J. Boswell  
David W. Taylor Naval Ship Research and Development Center  
Bethesda, Maryland 20084

## ABSTRACT

Fundamental investigations were made of the effects of periodic hull pitching motions and waves on the periodic loads on propeller blades and bearings. These periodic loads were measured during carefully controlled model experiments in which the periodic hull pitching motions, regular waves, and relative phase of the hull pitching to the wave encounter were systematically and independently varied. The periodic blade loads were calculated using trochoidal wave velocity profiles, and representation of the propeller based on a quasi-steady method.

The results of both theory and experiment show significant modulation of the amplitudes of the periodic blade loads with hull pitching motions and wave frequency of encounter. Further, the experiments confirm the theoretical assumption that the individual influences of the wave velocity profile and the induced velocities due to vertical hull motions can be linearly superimposed. The influence of the hull significantly modifies the amount of modulation of the shaft frequency loads due to both the periodic vertical motion of the propeller and the trochoidal wave velocity profile in the absence of the hull. However, trends of shaft frequency loads are well predicted by simple periodic variations of the velocity into the propeller, and a simple quasi-steady representation of the propeller. Trends of the results are shown to be consistent with available full-scale data. Therefore, for engineering purposes, the modulation of blade loads due to waves and hull motions for transom type hulls can be estimated by simple trochoidal wave velocity profiles, quasi-steady propeller theory, and constant multiples derived from the experiments presented in this paper.

## I. INTRODUCTION

The mechanisms by which rough seas and resulting ship motions influence the time-average and periodic loads on propeller blades and propeller shafts and bearings are complex. Factors include the increased time-average propeller loading due to increased hull resistance and the increased periodic loading resulting from the influence of the

free surface and modification of the flow pattern into the propeller disk. This flow pattern is influenced by (1) direct orbital velocities from the ocean waves, (2) relative velocities of the propeller due to ship motions, and (3) modification of the hull wake pattern due to the ship motions in the rough sea.

In general, the rough sea modulates the amplitudes of the periodic loadings on the propeller blades and bearings from the corresponding values in calm water. The periodic loads on individual blades, including modulation by a rough sea, must be considered in the design of the propeller blades from consideration of fatigue. This is especially important for controllable pitch (CP) propellers. Periodic bearing forces, including modulation by a rough sea, are important for consideration of ship vibration, especially in the main propulsion system, noise, and fatigue strength of components of the main propulsion system. Extreme modulation of the periodic thrust in the main propulsion shafting can result in reversals of the thrust on the main thrust bearing which can cause extensive damage.

Procedures for calculating periodic propeller blade and bearing loads in calm water are reasonably well refined. These procedures have been summarized by Boswell et al. (1968, 1981), Breslin (1972), and Schwanecke (1975).

Procedures for calculating the blade and bearing loads in a seaway are much less refined than for steady operation in calm water. Lipis (1975) and Tasaki (1975) review the mechanisms and procedures for predicting the effect of the seaway on periodic bearing forces which, in principle, also apply to unsteady loading on an individual blade. Keil et al. (1972), Watanabe et al. (1973), and Lipis (1975) present data from strain measurements on the blades of full-scale propellers in both calm and rough seas. Gray (1981) presents the modulation of blade rate hull vibration due to ship motion in a seaway.

These existing data and procedures provide valuable information regarding increases in periodic blade and bearing loads due to operation in a seaway. However, they address the overall complex problem in a statistical manner including the net influence of a complex sea state, complex ship responses, and numerous interactions. However, to the authors' knowledge, before the present study there were no experimental measurements of periodic loads on individual propeller blades that demonstrated the influence of waves and ship motions in a controlled environment.

An extensive systematic model experimental program was undertaken to obtain fundamental information on the influences of rough water and ship motions on periodic propeller blade loads on high speed open-shaft transom stern configurations. The experiments were conducted under carefully controlled idealized conditions in which sinusoidal hull pitching motions and regular head waves were independently varied. Experiments with hull pitching were conducted on three hull forms, two of which were reported previously by Boswell et al. (1976a, 1976b, 1978) and Jessup et al. (1977), and the third of which is presented in this paper. Restrained model experiments in waves, including forced sinusoidal pitching of a model in waves, were conducted on only one model, and are presented in the present paper. Experiments were conducted in

calm water with no ship motions, in calm water with forced sinusoidal pitching of the hull, in regular waves with no ship motions, and in regular waves with forced sinusoidal pitching of the hull at the frequency equal to the wave frequency of encounter. The experiments with forced hull pitching in waves were run over a range of relative phases between the hull pitching and the wave encounter. Six components of blade loads were measured during the dynamic conditions simulated.

The modulation of the blade load variation was correlated with predictions calculated from trochoidal wave theory and the periodic vertical motion of the hull. The assumption of superposition of the effects of pitching and waves was evaluated. Trends of modulations of the periodic bearing loads were determined from the modulations of the pertinent harmonics of the single-blade loads.

The objective of these experiments was to obtain accurate systematic experimental data showing the effects of hull pitching and waves on periodic and time-average blade loads under carefully controlled experimental conditions so that the effects of ship motions and waves on periodic and time-average blade loads could be isolated. It is anticipated that these data will serve as a basis for developing procedures for calculating periodic and time-average blade loads for operation in a complex sea state.

In these experiments the model speed and propeller rotational speed were held constant at the values corresponding to operation in calm water with no ship motions. In practice, when a ship operates in rough seas the ship speed and propeller rotational speed at a given delivered power decrease from the corresponding values in calm water due to increased shaft torque resulting from increased resistance of the hull and change in the propulsion coefficients (involuntary speed loss) (Lewis, 1967, Oosterveld, 1978, Day et al., 1977). Furthermore, in rough seas the delivered power is often deliberately reduced from the calm water value (voluntary speed loss) as discussed by Day et al. (1977) and Lloyd and Andrew (1977). Therefore, the difference in blade loads between operation in calm seas and operation in rough seas can be represented as being made up of two major parts:

1. Differences in loads resulting from the difference in ship speed and propeller rotational speed between calm seas and rough seas, and
2. Increases in loads due to the direct influence of waves and ship motions at a given value of ship speed and propeller rotational speed.

The changes in propeller rotational speed, ship speed, and Taylor wake fraction due to operation in rough seas can be estimated experimentally or theoretically using methods or data summarized by Oosterveld (1978), Day et al. (1977), and Lloyd and Andrew (1977). The resulting changes in periodic blade loads can be estimated based on the systematic experimental data or theoretical methods described previously by Boswell et al. (1976a, 1976b, 1978). The experiments described in the present paper provide information on the direct influence of the waves and ship motions on periodic and time-average blade loads.

## II. EXPERIMENTAL TECHNIQUES

### A. Dynamometry

All experiments were conducted using the hull and propeller shown in Figure 1 on Carriage II at the David W. Taylor Naval Ship Research and Development Center (DTNSRDC), using basically the same dynamometry and hardware described by Boswell et al. (1976a, 1976b, 1978). The starboard propeller, on which blade loads were measured, was located in its proper position relative to the model hull but was isolated from the hull and driven from downstream (see Figure 2). This downstream drive system was necessary in order to house instrumentation required to obtain the frequency response characteristics of the system for measuring unsteady loading.

The sensing elements were flexures to which bonded semi-conductor strain-gage bridges were attached. The design of these flexures has been described by Dobay (1971). Three flexures were necessary to measure all six components of force and moment. Flexure 1 measured  $F_x$  and  $M_y$ , Flexure 2 measured  $F_y$  and  $M_x$ , and Flexure 3 measured  $F_z$  and  $M_z$ ; see Figure 3. The flexures were mounted inside a propeller hub specifically designed for these experiments. Only one flexure could be mounted at a time because of space limitations, and this necessitated three duplicate runs for each condition. The flexure calibration procedure was identical to that described by Boswell et al. (1976a, 1976b, 1978).

The port propeller, on which blade loads were not measured, was driven from inside the model hull as would be the case in a self-propulsion experiment. The propeller rotational speed, which could be controlled independently of the starboard propeller, was measured via a toothed gear pickup and recorded on a digital voltmeter. The time-average thrust and torque were measured for selected runs by a transmission dynamometer.

### B. Hull Pitching and Wave Simulation

The downstream body which housed the drive system was modified from the configuration used by Boswell et al. (1976a, 1976b, 1978) so that it could be operated fully submerged. This was necessary in the present experiment because the large shaft angle necessitated deep submergence, and the operation in waves caused an additional disturbance to the water surface. The modifications included a waterproof housing for the drive motor, waterproof electrical cables and connectors, removal of the upper apron which had extended the sides of the boat, and the addition of a nonwaterproof top to the boat. Both the body housing (the drive system was soft mounted to this body) and the model hull were rigidly attached to a pitch-heave oscillator which was driven by a hydraulic cylinder. The pitch-heave oscillator was rigidly mounted on the towing carriage. This arrangement enabled the model hull and the drive system to be dynamically pitched together while maintaining independent support from one another.

For operation in waves, regular head waves were generated by a pneumatic wavemaker (Brownell et al., 1956). The level of the water surface was measured as a function of time by a pulsed ultrasonic probe that was mounted on the carriage; see Figure 4. The output of this probe, which was filtered using a low pass filter to remove the influence of small irregularities in the water surface, yielded the amplitude and frequency of encounter of the wave.

For operation with forced dynamic pitching of the model hull in waves, a servomechanism was used to ensure that the pitching of the model hull maintained the desired phase relative to the wave at the propeller throughout the experimental run. Figure 4 presents a schematic diagram of this servomechanism. In this servomechanism, a servo-control unit subtracts the feedback signal from the hydraulic cylinder,  $e_p$ , from the signal from the wave height probe,  $e_w$ , and sends this difference signal, or servo signal  $e_s$ , to the servo valve. Based on this servo signal,  $e_s$ , the servo valve slightly adjusts the frequency of the hydraulic cylinder so that  $e_s$  seeks the null signal. When  $e_s$  is null,  $e_p$  is in phase with  $e_w$ ; that is, the pitching is in phase with the waves. With this system small corrections to the frequency of the hydraulic cylinder are made continuously to maintain  $e_s$  near the null, and thus to maintain the pitching of the model in phase with the waves. The phase of the wave at the propeller plane was varied relative to the phase of the model pitching by moving the wave height probe used in the servomechanism forward or aft a prescribed distance relative to the plane of the propeller. For example, for setting the phase of the pitching,  $\phi_\psi$ , equal to the phase of the wave at the propeller plane,  $\phi_\zeta$ , the wave height probe was placed in the propeller plane. For setting  $\phi_\zeta - \phi_\psi = 90$  degrees, the wave height probe was placed a three-quarters of a wavelength forward of the propeller plane.

A second wave height probe, which was not used in the servomechanism, remained in the propeller plane for all conditions. The output of this probe was input for the computer and served as a reference for analyzing the blade force and moment data as a function of position in the wave cycle. In all cases, the wave height probes were placed sufficiently far from the model in the transverse plane so that the model did not disturb the water surface at the points at which the water levels were measured.

### C. Experimental Conditions and Procedures

Experiments were conducted at several conditions including steady ahead operation in calm water with no ship motions, simulated periodic pitching of the hull in calm water, operation in regular head waves without pitching of the hull, and operation in regular head waves with periodic pitching of the hull. All conditions were run with the model hull rigidly attached to its support, with no freedom to sink or trim, and with essentially equal rotation on the port and starboard propellers.

The basic condition, which simulates steady ahead self-propulsion in calm water with no ship motions, is defined as Condition 1 in Table 1. The propeller rotational speed, trim and draft at this condition were obtained from model self-propulsion data. No cavitation occurred on the model propeller at any model experimental condition described in this paper.

Runs simulating hull pitching and/or the effect of waves were conducted at the same conditions as the run in calm water with no hull pitching, except that the hull pitch was varied and/or the model was run in waves (Conditions 2 to 6 in Table 1). These experiments were conducted for forced pitching of the model in calm water, for operation in regular head waves without pitching of the restrained model hull, and for forced pitching of the model for operation in regular head waves. For forced pitching in waves, the phase of the wave at the propeller,  $\phi_\zeta$ , was varied relative to the phase of the hull pitching,  $\phi_\psi$ . Three relative phases were evaluated:

1. Wave crest at the propeller plane when the stern of the model hull is pitched up at its maximum value,  $\phi_\zeta - \phi_\psi = 0$  (Condition 4 in Table 1).
2. Wave crest at the propeller plane when the stern of the model hull is pitched down at its maximum value,  $\phi_\zeta - \phi_\psi = 180$  degrees (Condition 5 in Table 1).
3. Wave crest at the propeller planes when the hull pitch is passing through its mean value  $(\psi_{\text{MAX}} - \psi_{\text{MIN}})/2$  from stern down to stern up,  $\phi_\zeta - \phi_\psi = 90$  degrees (Condition 6 in Table 1).

For the unsteady hull-pitch simulation in calm water, the hull-pitch angle  $\psi$  was varied sinusoidally about the calm water equilibrium trim angle ( $\psi_{\text{CW}}$ ) with an amplitude  $\psi_A$  of 1.33 degrees and a frequency  $f_\psi$  of 0.8 hertz,  $f_\psi L_{\text{PP}}/g^{1/2} = 2.63$ . For operation in waves without the hull pitching, the model hull operated in regular head waves with a single amplitude  $\zeta_A$  of 0.118 m (0.39 ft),  $\zeta_A/L_W = 0.019$ ; a wavelength  $L_W$  of 9.20 m (30.20 ft),  $L_W/L_M = 1.62$ ; and a wave velocity  $V_W$  of 3.79 m/s (12.43 ft/s). At the experimental model speed of 3.58 m/s (6.96 knots) the frequency of encounter is 0.8 hertz which is the same as the model pitching frequency. Operation in waves with pitching of the model hull necessitated a reduction in the amplitude of the pitch of the model hull and/or the amplitude of the waves from the aforementioned values in order to prevent flooding of the model hull. The minimum amplitudes of the hull pitch and the waves were 0.67 degree and 75 mm (0.25 ft), respectively (see Table 1). The frequency of the hull pitching and the frequency of encounter of the waves were both 0.8 hertz for all experimental conditions with pitching and waves.

The selected amplitude and frequency of encounter of the waves, and amplitude and frequency of the hull pitching were within the scaled, predicted operating and response characteristics at full scale of an equivalent transom-stern ship.

Air-spin experiments were conducted with all three flexures over a range of rotational speeds in order to isolate the effects of

centrifugal and gravitational loading from hydrodynamic loading. Supplemental experiments were conducted to assess the influence of the downstream dynamometer boat on the flow in the propeller plane. These supplemental experiments consisted of wake surveys in the propeller plane in calm water without the hull pitching (Condition 1 in Table 1) with and without the downstream body. These wake surveys yielded a direct measure of the change in the velocity distribution through the propeller disk attributable to the downstream body.

#### D. Data Acquisition and Analysis

Data were collected, stored, and analyzed on-line using a mini-computer. A computer program was written with options for analyzing each of the two basic types of runs: (1) operation in calm water without hull pitching, and (2) operating with periodic hull pitching and/or operation in regular waves. Data were collected and analyzed in the same manner as described by Boswell et al. (1976a, 1976b, 1978). For a given run, the computer collected force, moment, propeller rotation speed, model speed, hull pitch angle, and wave height at 4-degree increments of propeller angular position over 200 to 300 propeller revolutions.

For operation in calm water without hull pitching, the computer was used to analyze and print the data. The average force and moment signals for each 4-degree angular position were printed along with the average model velocity and propeller rotation speed for the run. The standard deviation of the accumulated data for the run was also calculated for  $V$ ,  $n$ , and the force and moment signals at each position. A harmonic analysis was performed on the force and moment data providing the mean signal and amplitude and phase of the first 16 harmonics of shaft speed.

For runs simulating hull pitching or waves, the force and moment data were selectively analyzed over the range of pitch angles or wave heights measured. Initially, the values of pitch and wave height were averaged over each revolution of a given run. An analysis was used to search through a series of similar runs extracting propeller revolutions of force and moment data corresponding to prescribed values of pitch or wave height with a prescribed slope and tolerance band. Typically, 50 to 200 revolutions were averaged at each value of pitch or wave height. Twenty-six positions in the pitch or wave cycle were selected for analysis.

For runs with pitching in waves, both the pitch angle and the wave height were fed into the computer. The blade loading data could be sorted based on either of these two signals. To check the proper phasing between the two signals, the pitch and wave data were also analyzed in the time domain. For each run, a strip chart record of the pitch angle and wave height variation was printed, along with analysis of the average frequency, amplitude and phase of the two signals. Runs with consistent wave and pitching frequency, amplitude, and phases were selected for blade loading analysis.

Final analysis was conducted after the experimental agenda was repeated for each of the three flexures representing the six components of blade load. Corrections for interactions between the various load components were performed for a representative condition in calm water without hull pitching, as outlined by Boswell et al. (1976a, 1976b, 1978). The resulting load corrections were applied to all other conditions in the experimental agenda. The total loading components were corrected for the centrifugal and gravitational loads to obtain the hydrodynamic loads. Corrections were also made to the mean loads to account for the influence of the dynamometer boat.

#### E. Accuracy

The accuracy of the experiment was generally similar to that described by Boswell et al. (1976a, 1976b, 1978). During the experiments, the on-line analysis averaged data over many revolutions and computed standard deviations of speed  $V$ , rotation speed  $n$ , forces, and moments, assuming a normal distribution in the variation of these quantities. From this, a variation in the measured quantities was calculated with a 95 percent confidence level. Model speed  $V$ , and rotation speed  $n$  varied by  $\pm 0.5$  percent from calculated mean values. For the condition in calm water with no hull pitching, the force and moment signals at each angular position measured, varied by  $\pm 2$  to  $\pm 10$  percent of the calculated average value. Figure 5 shows the measured variation in the raw  $F_x$  signal. Note that the variation in force at each angular position was greatest when the blade was nearest the model hull. The variation of the loading components during the pitching and wave conditions was  $\pm 10$  to  $\pm 20$  percent of the mean values at each angular position. These variations were greater than the still water condition because each run was evaluated over a certain tolerance range in pitch or wave height. It should be noted that the variations from the mean represent the band in which 95 percent of the measured data lie. The accuracy of the mean values calculated will be higher than the variations calculated.

Besides the fluctuation in signals occurring in a given run, the overall accuracy of the data can be represented by the repeatability between different runs. An effort was made to set experimental conditions identically on repeat runs; however, the propeller rotational speed and model velocity were set by hand, so some variation was unavoidable. The variation in the measured experimental conditions and the blade loading data for repeat runs is similar to that documented by Boswell et al. (1978) and Jessup et al. (1977) showing that the variations in the mean forces and moments were  $\pm 4$  percent over all the runs.

As discussed in the section on data acquisition and analysis, for operation with periodic pitching either with or without waves, the data were sorted and analyzed based on instantaneous position in the pitch cycle, and for operation in waves without hull pitching, the data were sorted and analyzed based on instantaneous position of the propeller in the wave cycle. For periodic pitching runs, selection of a propeller revolution at a specified pitch angle  $\psi$  in the pitch cycle necessitated a tolerance of 0.05 degree to  $\pm$ ; however, the average value of  $\psi$  for

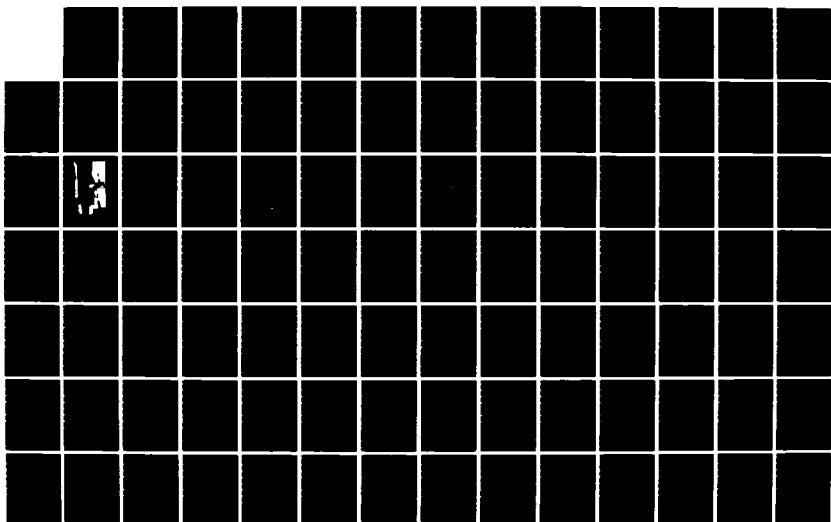


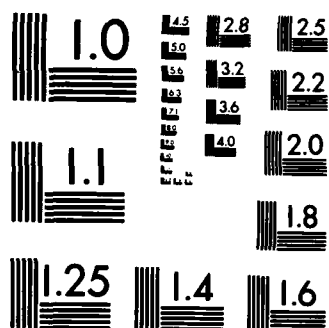
SYMP0SIUM OF NAVAL HYDRODYNAMICS (14TH) HELD AT ANN ARBOR MICHIGAN ON AUGUST 23-27 1982(U) OFFICE OF NAVAL RESEARCH ARLINGTON VA M P TULIN ET AL. 1982

08/13

F/G 20/4

NL





MICROCOPY RESOLUTION TEST CHART  
NATIONAL BUREAU OF STANDARDS-1963-A

which data were presented during the periodic pitching runs was generally within 0.02 degree of the target  $\psi$ . For runs in waves without hull pitching, the selection of a propeller revolution at a specified instantaneous water level within the wave necessitated a tolerance of 5 mm (0.20 in.) of the target water level.

Considering all sources of error including deviations during a run and inaccuracies in setting conditions, the model scale forces and moments presented in this paper are generally considered to be accurate to within (plus or minus) the following variations:

	$\bar{F}$		$F_{MAX}$		$\bar{M}$		$M_{MAX}$	
	N	(1b)	N	(1b)	N-m	(in-1b)	N-m	(in-1b)
Calm water without hull pitching	0.4	(0.1)	0.9	(0.2)	0.02	(0.2)	0.05	(0.4)
Pitching and/or waves	0.9	(0.2)	1.8	(0.4)	0.05	(0.4)	0.09	(0.8)

The values are somewhat more accurate for the runs in calm water without pitching than for runs with pitching and/or waves, because the experimental conditions could be controlled more precisely for runs in calm water without waves and the measured forces and moments were averaged over many more revolutions of the propeller. The time-average values per revolution (based on 90 samples per revolution) are slightly more accurate than the maximum values (based on one sample per revolution) which took into account the variation with blade angular position. Further, the peak values may have been slightly influenced by the dynamic response of the flexures.

### III. DISCUSSION OF EXPERIMENTAL RESULTS

#### A. Loading Components

The basic loading components are shown in Figure 2. For a right-hand propeller, as used in this case, the sign convention follows the conventional right-hand rule with right-hand Cartesian coordinate system.

Each component of loading is represented as a variation of the instantaneous values with blade angular position,  $\theta$ , and as a Fourier series in blade angular position in the following form:

$$F, M(\theta) = (\bar{F}, \bar{M}) + \sum_{n=1}^N (F, M)_n \cos\{n\theta - (\phi_{F, M})_n\} \quad (1)$$

In general, the loads consist of hydrodynamic, centrifugal and gravitational components. However, in this paper, only the hydrodynamic component of blade loading is presented. The results considering total loads showed the same trends as results including only hydrodynamic loads. Centrifugal and gravitational loads were measured to permit the hydrodynamic loads to be determined by subtracting the centrifugal and gravitational loads from the total experimental loads. The centrifugal and gravitational loads were, of course, independent of hull pitching and waves since all conditions were run at the same propeller rotational speed,  $n$ .

#### B. Centrifugal and Gravitational Loads

Centrifugal and gravitational loads were determined from air-spin experiments with each flexure over a range of rotational speed  $n$ . The centrifugal load, which is a time-average load in a coordinate system rotating with the propeller, should vary as  $n^2$ . The time-average experimental data followed this trend. The gravitational load, which is a first harmonic load in a coordinate system rotating with the propeller, should be independent of  $n$ . The first harmonic experimental data followed this trend.

The centrifugal and gravitational loads measured during these experiments agreed with the values determined by Boswell et al. (1981), and the gravitational loads agreed with values deduced from the weights of the blades and associated flexures. Therefore, these results will not be repeated here.

#### C. Influence of Dynamometer Boat

The results of the wake survey with and without the downstream body (dynamometer boat) are presented in Figure 6. Harmonic analysis of these data indicate that the downstream body had only a small effect on the circumferential and radial variations in the flow and only a small effect on the harmonic content of the flow. However, they also indicate that the downstream body reduced the volume mean speed through the propeller disk by approximately 12 percent. These results are, of course, without the propeller in place.

The change in effective speed through the propeller due to the downstream body was deduced from thrust and torque identities between the mean thrust and torque measured during the blade loading experiments and mean thrust and torque measured during the corresponding self-propulsion model-experiment. These results, which include the effect of the propeller, indicate that the downstream body reduced the effective speed through the propeller disk by approximately 14 percent; i.e., without the body,  $(1-w_T) = 1.00$  and  $(1-w_Q) = 1.00$ , whereas, with the body,  $(1-w_T) = 0.86$  and  $(1-w_Q) = 0.85$ . This agrees quite closely with the 12 percent reduction in the volume mean speed due to the downstream body as deduced from the wake surveys at the corresponding conditions.

Based on these results, it was concluded that the downstream body reduced the mean speed into the propeller by 14 percent for all conditions. These reductions are somewhat larger than the 12 and 5 percent reductions obtained by Boswell et al. (1976a, 1976b, 1978), respectively, in which essentially the same dynamometer boat was used behind other model hulls. However, in the earlier experiments the dynamometer boat was not fully submerged.

The downstream body will disturb the location of the shed and trailing vortex sheets from the propeller. This may influence the periodic and time-average propeller blade loads. No correction was made for this effect.

After the effects of centrifugal force were subtracted from the measured loading components as discussed previously, the time-average value per revolution of each hydrodynamic loading component was corrected for the downstream body as follows: From the measured hydrodynamic blade thrust ( $\bar{F}_{xH}$ ) and hydrodynamic blade torque ( $\bar{M}_{xH}$ ), effective advance coefficients based on thrust identity ( $J_T$ ) and torque identity ( $J_Q$ ) were deduced from the open water data (Figure 7). These values were multiplied by (1/0.88) to obtain corrected values of  $J_T$  and  $J_Q$ , i.e., without the downstream body. The corrected values of  $\bar{F}_{xH}$  and  $\bar{M}_{xH}$  were then obtained from the open water data at the corrected advance coefficient  $J_T$  and  $J_Q$ , respectively. It was assumed that the downstream body did not affect the radial centers of thrust  $\bar{F}_{xH}$  and tangential force  $\bar{F}_{yH}$ . Therefore,

$$\bar{M}_{yH} \text{ corrected} = (\bar{F}_{xH} \text{ corrected} / \bar{F}_{xH} \text{ measured}) (\bar{M}_{yH} \text{ measured})$$

$$\bar{F}_{yH} \text{ corrected} = (\bar{M}_{xH} \text{ corrected} / \bar{M}_{xH} \text{ measured}) (\bar{F}_{yH} \text{ measured})$$

No corrections are made to  $F_{zH}$  and  $M_{zH}$  for the effect of the downstream body; however,  $\bar{F}_{zH}$ ,  $\bar{M}_{zH}$  are small for all experimental conditions, as discussed later.

No correction for the effect of the downstream dynamometer boat was made to the measured circumferential variations of the loading components. Calculations made by the methods of Tsakonas et al. (1974) and McCarthy (1961) indicated that the influence of the downstream body alters the peak-to-peak circumferential variation of the loads by no more than 2 percent.

#### D. Operation in Calm Water Without Hull Pitching

For operation in calm water without the hull pitching (Condition 1 in Table 1), Table 2 presents the time-average loads, Figure 8 presents the variation of the  $F_x$  component of hydrodynamic blade loading with blade angular position, and Figure 9 presents the amplitude of the first 25 harmonics of the  $F_x$  component of hydrodynamic blade loading.

Based on the dynamic calibration by Dobay (1971), it was judged that for all loading components the data are valid for the first 10

harmonics. In addition, the wake data show no significant amplitudes for harmonics greater than the tenth. Therefore, all data and analyses except Figures 8 and 9 are based on reconstructed signals using the first 10 harmonics. The symbols shown in Figure 8 indicate unfiltered values determined from the experiment; each represents the average value at the indicated blade angular position for over 200 propeller revolutions. The variation in measured values at a given angular position is discussed in the section on accuracy. The lines on Figure 8 indicate that the variations of the signals with blade angular position are adequately represented by the number of harmonics retained.

The variations of all measured hydrodynamic loading components with blade angular position for simulated propulsion in calm water without hull pitching are shown in Figure 10. The amplitudes and phases of the harmonics of these loading components are presented in Figure 9.

These data show that for hydrodynamic loading the variation of all loading components was predominantly a once-per-revolution variation. The extreme values for all loading components, except  $F_z$  and  $M_z$ , occurred near the angular position of the spindle axis,  $\theta = 114$  and  $270$  degrees; i.e., within 24 degrees of the horizontal. The propeller evaluated has a projected skew angle at the tip of approximately 11 degrees; therefore at the positions of extreme loading the blade tip is within approximately 13 degrees of the horizontal. This suggests that the tangential component of the wake is the primary driving force; see Figure 6. The extreme values of  $F_z$  and  $M_z$  occur within 20 degrees of the extreme values of the other components. The reason for this variation in location of extreme values is not clear; however, it may be partially due to experimental inaccuracy with the  $F_z$ - $M_z$  flexure as discussed by Boswell et al. (1976a, 1976b, 1978). Further the net stresses in the blades are generally less sensitive to the  $F_z$  and  $M_z$  components than they are to the other force and moment components.

The results presented here for circumferential variation of hydrodynamic loads follow trends similar to results presented by Boswell et al. (1976a, 1976b) for a single-screw transom-stern configuration and results presented by Boswell et al. (1978) and Jessup et al. (1977) for a twin-screw transom-stern configuration.

The circumferential variations and first harmonics of all loading components except  $F_z$  and  $M_z$  were substantially larger fractions of their time-average values for the condition evaluated here than they were for the conditions evaluated previously on the models reported by Boswell et al. (1976a, 1976b, 1978). For example,  $(\bar{F}_{xH})_1/\bar{F}_{xH}$  was 0.66 for the present case, 0.40 from Boswell et al. (1976), and 0.42 from Boswell et al. (1978). The differences in the ratios of the circumferential variations of loads to the time-average loads for these three cases arise from many factors including the propeller time-average loading coefficients which are essentially independent of the unsteady loading, the magnitude of the circumferential variation of the wake (primarily the amount of shaft inclination for the three cases under consideration here), and propeller geometry especially the blade width and pitch-diameter ratio. The ratio of the unsteady loading to the time-average loading is useful for evaluating the unsteady loading of a given

propeller over a range of ship and propeller operating conditions; however, this ratio is not a good parameter for comparing the unsteady loadings on different propellers on different ships with different operating conditions. Analytical calculations, not presented here, confirm that the periodic loading components for operation in calm water with no ship motions should be larger fractions of the respective time-average loading components for the propeller-hull combination described in the present paper than for those described by Boswell et al. (1976a, 1976b, 1978).

#### E. Operation in Calm Water with Hull Pitching

Figure 11 shows the variations of peak values per revolution, time-average values per revolution, and first harmonic values of the  $F_x$  and  $M_x$  components of hydrodynamic blade loading with hull pitch angle  $\psi$  (Condition 2 in Table 1). The  $F_y$  and  $M_y$  components showed similar variations as in Figure 11, and the  $F_z$  and  $M_z$  components were found to be relatively independent of hull pitch, and therefore are not shown. Table 4 summarizes the maximum absolute values of the peak loads, first harmonic loads, and time-average load per revolution for operation in calm water with hull pitching.

Figure 11 shows the loading components at the individual pitch angles analyzed. Spline curves were fit through the points shown. An oscillatory behavior is shown in the peak and first harmonic loads at the time when the hull is moving from stern-up to stern-down position. This behavior was believed to be caused by observed slight transverse oscillation of the dynamometer boat probably caused by vortex shedding. This did not occur in the experiments described by Boswell et al. (1976a, 1976b, 1978) because the dynamometer boat was not completely submerged in those experiments as it was in the present experiments. This behavior was believed to have no significance, since the model hull did not oscillate transversely in a similar fashion. Therefore, this oscillation is faired out in the curves shown in Figure 11.

The time-average values per revolution for each of the two loading components remained within 5 percent of their values in calm water without hull pitching throughout the pitch cycle presented. The trends in variations of the time-average values of the various components with position in the pitch cycle are similar. The largest absolute values of the time-average values per revolution of all loading components occurred near the time at which the hull pitch was passing through its equilibrium value from stern-up to stern-down; i.e., near  $(\psi - \psi_{CW}) = 0$ ,  $\dot{\psi} < 0$ .

The maximum absolute values of the peak loads increased by as much as 22 percent relative to the time-average loads in calm water without hull pitching above the corresponding peak loads in calm water without hull pitching. Similarly, the maximum values of the first harmonic loads increased by as much as 13 percent relative to the time-average loads in calm water without hull pitching. The maximum absolute values of both the peak loads and the first harmonic loads for all components

occurred approximately over the angular positions of 145 to 230 degrees in the hull pitch cycle shown in Figure 11. This corresponds to the portion of the cycle in which the hull was passing through its equilibrium value from stern-up to stern-down; i.e., near  $(\psi - \psi_{CW}) = 0$ ,  $\dot{\psi} < 0$ . This is the same portion of the pitch cycle during which the maximum time-average values per revolution occurred; therefore, the maximum increase in the time-average loads per revolution and the maximum increase in the unsteady loads per revolution tend to add (they are in phase relative to the hull pitch) to yield the maximum increase in peak loads. The smallest absolute values of time-average, peak loads, and first harmonic loads occurred near  $\psi - \psi_{CW}$  as the hull passed from the stern-down to the stern-up portion of the cycle; i.e.,  $(\psi - \psi_{CW}) = 0$ ,  $\dot{\psi} > 0$ .

Figure 12 shows the variation of the  $F_x$  component with blade angular position for times in the pitching cycle where the minimum and maximum peak loads occur. The effect of pitching motion is most extreme at blade position angles around 135 degrees, where the maximum blade loading occurs. This explains why the time-average loads and the peak loads occur in phase during the pitching cycle.

The unsteady loads are important from consideration of fatigue of the propeller blades, and of the hub mechanism for controllable pitch (CP) propellers. Since a ship may operate for an extended period in a rough sea, the effect of the ship motions, such as hull pitching, on unsteady blade loads is significant. The difference between the peak load and the time-average load per revolution is a measure of the unsteady loading. With this difference as a measure of the unsteady loading, the results with hull pitching showed that the unsteady hydrodynamic loading for the various components increased by 26 to 38 percent above their corresponding values for  $\psi = \psi_{CW}$  without hull pitching. This indicates that the effect of ship motions can significantly increase the unsteady loading on the blades.

The difference in the unsteady loading with and without the hull pitching is probably due to an additional relative velocity component arising from the motion of the hull during pitching. As the hull passes through  $\psi = \psi_{CW}$  the vertical velocity of the hull (and propeller) is a maximum. As the hull goes from stern-up to stern-down through  $\psi = \psi_{CW}$ , the upward velocity component relative to the propeller plane tends to increase above the values at fixed hull pitch at  $\psi = \psi_{CW}$ . This tends to increase the amplitudes of the first harmonic of the tangential velocity, and thereby increase the unsteady loading (and increase the peak loading). The maximum vertical velocity of the propeller for sinusoidal pitching with  $(\psi_{MAX} - \psi_{CW}) = 1.33$  degrees and frequency = 0.8 hertz is approximately 0.29 m/s (0.96 ft/s). This is equivalent to additional tangential and radial velocity component ratios ( $V_t/V$  and  $V_r/V$ , respectively) of 0.082. For  $\psi$  fixed at  $\psi = \psi_{CW}$ ,  $((V_{t0.7})_1/V) = 0.199$  and  $((V_{r0.7})_1/V = 0.145$  (from a harmonic analysis of the wake survey data). Therefore,



$$\frac{(v_{t0.7})_1 + v_\psi}{(v_{t0.7})_1} = \frac{0.199 + 0.082}{0.199} = 1.41$$

and

$$\frac{(v_{r0.7})_1 + v_\psi}{(v_{r0.7})_1} = \frac{0.145 + 0.082}{0.145} = 1.56$$

These maxima occur at  $\Theta_\psi = 180$  degrees which essentially agrees with the value of  $\Theta_\psi$  at which the maximum loads were measured. The measured increase in unsteady loads arising from hull pitching was somewhat smaller than these calculated increases in tangential and radial velocity component ratios, for example:

$$\frac{F_{x_{MAX},\psi}}{F_{x_{MAX}} - F_x} = \frac{0.89}{0.72} = 1.24$$

Theoretically, the increase in unsteady loading should be approximately proportional to the increases in tangential and radial velocity component ratios; however as shown by Boswell et al. (1981) including calculations in the authors' closure to this paper, the tangential velocity component appears to have a greater influence on periodic blade loads than does the radial velocity component. This simple analysis provides an upper bound to the dynamic pitching load, since the hull boundary above the propeller would tend to reduce the dynamic pitching-induced, upward velocity component relative to the propeller.

Other aspects of the data show the influence of the hull boundary on the upward velocity component relative to the propeller. Figure 13 shows the propeller plane and hull configuration. It is clear that an upward vertical fluid speed relative to the propeller due to pitching would be minimum near the hull centerline corresponding to a blade position angle of 270 degrees. The vertical fluid speed due to pitching would be a maximum at a blade position angle of 90 degrees where it is close to the edge of the hull. Also, some outward turning of the flow would be expected in this region as the hull moves downward into the fluid.

This general character of the flow is represented qualitatively in the effect of pitching on the blade load variation with angular position, shown in Figure 12. As discussed earlier, the effect of pitching is greatest at the outboard blade positions around 100 degrees, where the vertical velocity component due to pitching is greatest. At the inboard positions around 270 degrees, the blade loading is little affected by the pitching motion since the hull boundary restricts the relative vertical velocity. Also shown is a phase shift in the peak

loading between 90 and 135 degrees (also see Figure 11), which may be related to the outward turning of the vertical velocity due to the hull.

Table 3 compares the results presented here for hull pitching in calm water with the same type of results presented by Boswell et al. (1976a, 1976b) for a single-screw transom-stern configuration, and with results presented by Boswell et al. (1978) and Jessup et al. (1977) for a twin-screw transom-stern configuration. The results presented in Table 3 indicate that the experimental results on these three configurations are consistent. The unsteady loads presented in this paper increased by smaller fractions of their values without hull pitching than did the unsteady loads reported by Boswell et al. (1976a, 1976b, 1978); however, this results from the smaller fractional increase in the vertical velocity component relative to the propeller with hull pitching of the present model than with the models reported by Boswell et al. (1976a, 1976b, 1978). The estimated increase in vertical velocity component due to hull pitching was larger than the measured increase in unsteady loading with hull pitching for all three configurations.

Hull pitching was the only one of the six components of ship motions (surge, heave, sway, roll, pitch and yaw) for which blade loads were measured. These experiments showed that hull pitching affects primarily the peak and unsteady blade loading and that this effect appears to be controlled by the ratio of the maximum vertical velocity of the propeller to the ship speed. It appears that the increases in the peak and unsteady blade loading due to the vertical velocity component of the propeller are independent of the type of ship motions producing this vertical velocity. Heave and roll (for propellers off the ship centerline) also produce velocities in the vertical plane of the propeller. Therefore, the effect of heave and roll on the peak and unsteady blade loading can be deduced from the experimental results with hull pitching by calculating the equivalent hull pitching required to produce the same vertical velocity component of the propeller as produced by the specified heave and/or roll.

Surge, sway, and yaw do not significantly alter the flow relative to the propeller in the vertical plane, therefore it is expected that these ship motions would have an insignificant influence on the peak or unsteady blade loading. The primary cause of this unsteady blade load in calm water without ship motions for hulls of the type under consideration here is the upward vertical wake velocity component relative to the propeller plane, therefore any transverse velocity which is small relative to this vertical wake velocity is insignificant when vectorially added to the vertical wake velocity component.

Blade loads were measured for only one pitching frequency. However, any realistic hull pitching frequency is small relative to the propeller rotational frequency; therefore, pitching frequency should not significantly alter the trends of the experimental data. The magnitude of the maximum vertical velocity for a given pitch amplitude is directly proportional to pitching frequency; therefore the peak and unsteady components of blade loading tend to increase as the pitching frequency increases.

Blade loads were measured for only one amplitude of pitching. However, the maximum speed due to pitching is directly proportional to pitching amplitude for a given frequency; therefore, the peak and unsteady blade loading tends to increase as the amplitude of pitching increases. At large amplitudes of pitch the propeller may draw air near the stern-up position. This would tend to unload the blade in the upper portion of the propeller disk so that the unsteady blade loads would increase but the peak loads would not increase. However, this is not the portion of the pitch cycle at which the maximum vertical velocity of the propeller occurs, therefore it appears that maximum steady loads would be controlled by the maximum vertical velocity of the propeller rather than by the air drawing.

Based on these results and those presented by Boswell et al. (1976a, 1976b, 1978), the increase in blade loads due to hull pitching can be estimated for transom stern configurations as follows:

### 1. Time-Average Loads Per Propeller Revolution

Hull pitching increases the maximum time-average loads per revolution by only a small amount over the time-average loads per revolution without hull pitching. This increase can be approximated as follows:

$$\Delta \bar{L}_{MAX,\psi} \approx (\bar{L})(2\psi_A) \approx (\bar{L}_\psi)(\psi_A)$$

where  $\Delta \bar{L}_{MAX,\psi}$  = maximum increase in time-average loads per revolution with hull pitching over the value in calm water

$\bar{L}$  = time-average load in calm water

$\bar{L}_\psi$  = time-average load in waves

$\psi_A$  = amplitude of the variation in hull pitch angle in radians

In practice, this maximum increase in time-average loads per revolution due to pitching is negligible relative to the corresponding increase due to waves, as discussed later.

### 2. Periodic Loads

Hull pitching (in calm water) substantially increases the maximum periodic blade loads over the corresponding periodic loads without hull pitching. The primary controlling parameter is the ratio of the vertical velocity of the propeller resulting from the hull pitching to the ship speed. The maximum periodic loads occur when the velocity of the propeller and stern are maximum downward. This downward velocity of the propeller effectively increases the inclination of the inflow relative to the propeller and thereby increases the periodic loads. Due to the

displacement effect of the hull above the propeller, the vertical speed of the propeller relative to the local fluid particles is only 60 percent or less of the vertical speed of the propeller. Therefore, for ships with high-speed transom sterns with exposed shafts and struts, the maximum periodic blade loads due to hull pitching can be approximated from the corresponding loads without hull pitching as follows:

$$\Delta \tilde{L}_{MAX,\psi} \approx \frac{0.6 V_{\psi}}{V_C} \tilde{L}$$

where  $\Delta \tilde{L}_{MAX,\psi}$  = maximum increase in periodic loads with hull pitching over the values without ship motions

$\tilde{L}$  = periodic blade load without ship motions

$V_C$  = vertical component of spatial average crossflow velocity in propeller plane without ship motions

$V_{\psi}$  = maximum vertical velocity component of the propeller due to the pitching motions

### 3. Peak Loads

The maximum values of the periodic variation of loads with angular position and the time-average loads per angular position occur near the same point in the pitch cycle. Therefore, the increase in peak loads due to hull pitching is approximately the sum of the increases in these components:

$$\Delta L_{PEAK,\psi} \approx \Delta \bar{L}_{MAX,\psi} + \Delta \tilde{L}_{MAX,\psi}$$

The  $nZ-1$ ,  $nZ$ , and  $nZ+1$  harmonics of blade loads directly contribute to the periodic loads on the propeller shaft and bearings. Full scale measurements (Tasaki, 1975) indicate that the amplitudes of periodic bearing loads are modulated by the influences of a rough sea. The maximum amplitudes of these modulated loads at blade rate frequency are commonly more than a factor of two greater than the corresponding amplitudes of the loads measured in a calm sea as discussed by Lipis (1975) and Tasaki (1975). In the present investigation, the influence of hull pitching on periodic bearing loads was investigated by evaluating the influence of pitching on the pertinent harmonics of blade loads.

In the investigations described by Boswell et al. (1976a, 1976b, 1978), no analysis was made of the harmonics of blade loads beyond the dominant first harmonic because of their small amplitudes which were, in many cases, around one percent of the time-average thrust (for forces) and torque (for moments). However, for evaluating the effects of waves and pitching on periodic bearing loads, the variations of these

quantities with wave and pitching parameters are more important than the actual values of the small, pertinent higher harmonics of blade loads.

Figure 14 shows the variations of the first 10 harmonics of the  $F_x$  component of blade loading with location through one pitch cycle. The value of each harmonic amplitude is nondimensionalized on its calm water value. The variations of the amplitudes of the second, third and fourth harmonic are similar in magnitude to the dominant first harmonic of blade loading. These components are the major contributors to the blade loading variation with blade angle, as shown in Figure 9. The amplitudes of the fifth through the eighth harmonics show much larger variations with pitch angle relative to the respective time-average values. This result implies that the relatively small, higher harmonics of blade loading associated with unsteady bearing forces, are very sensitive to relatively small changes in the wake pattern.

#### F. Operation in Waves Without Hull Pitching

Figure 15 presents the variations of the peak values per revolution, time-average values per revolution, and the first harmonic values of the  $F_x$  and  $M_x$  components of hydrodynamic blade loading with wave height for operation in waves without hull pitching (Condition 3 in Table 1). The  $F_y$  and  $M_y$  components showed similar variations as in Figure 15, and the  $F_z$  and  $M_z$  components were found to be relatively independent of wave height. Table 5 summarizes the maximum absolute values of the peak loads, first harmonic loads, and time-average loads per revolution for operation in waves without hull pitching.

The maximum absolute values of the time-average loads per revolution  $\bar{L}_{MAX,\zeta}$  increased by as much as 14 percent above the corresponding time-average loads in calm water without hull pitching  $\bar{L}_{MAX}$ . This is quite different from the corresponding result with hull pitching in calm water where the time-average loads per revolution increased by a maximum of only 5 percent above the corresponding time-average loads in calm water without hull pitching. The variations of the time-average loads per revolution approximately followed the local wave elevation in the propeller plane so that the maximum and minimum time-average loads per revolution occurred at approximately 36 degrees of the wave cycle of encounter before the time at which the wave trough and peak, respectively, were in the propeller plane.

The variations of the time-average loads per revolution with position in the wave are consistent with trends reported by McCarthy et al. (1961). McCarthy et al. measured the low frequency variation of propeller shaft thrust and torque with position in the wave for steady ahead operation in regular head waves without ship motions and without a nearby hull. They did not measure individual blade loads; however, the variations of low frequency shaft thrust and torque are essentially the same as the variations of the time-average values per revolution of blade thrust  $\bar{F}_x$  and blade torque  $\bar{M}_x$ . The results of McCarthy et al. agreed with the results of the present investigation in that the maximum values of the thrust coefficient  $\bar{K}_T$  and torque coefficient  $\bar{K}_Q$

occurred when the trough of the wave was near the propeller plane, and the minimum values of  $\bar{K}_T$  and  $\bar{K}_Q$  occurred when the crest of the wave was near the propeller plane.

The variations of the time-average loads per revolution are also reasonably consistent with trends predicted by a combination of trochoidal wave theory and the quasi-steady propeller theory of McCarthy (1961). According to trochoidal wave theory, the orbital velocities in the head waves vectorially combine with the propeller speed of advance so that speed into the propeller is a maximum when the crest of the wave is in the propeller plane, and the axial velocity component into the propeller is a minimum when the trough of the wave is in the propeller plane. According to simple quasi-steady propeller theory, which should be valid for the low frequency variation of the velocity components in a wave, the maximum and minimum time-average loads per revolution occur when the speed into the propeller plane is minimum and maximum, respectively.

The maximum absolute values in waves of time-average thrust per blade  $\bar{F}_{xH,MAX,\zeta}$  and time-average torque per blade  $\bar{M}_{xH,MAX,\zeta}$ , were compared with values calculated by trochoidal wave theory and quasi-steady propeller theory. In these calculations, the spatial average velocity through the propeller disk under the trough of a trochoidal wave was determined using the formulation of McCarthy et al. (1961). This formulation does not consider any possible effect of the hull on trochoidal wave velocities. This spatial average velocity and the quasi-steady procedures of McCarthy (1961) were used to calculate the values of  $\bar{F}_{xH,MAX,\zeta}$  and  $\bar{M}_{xH,MAX,\zeta}$ . The comparison with experimental results is as follows:

	Experimental	Theoretical
$\bar{F}_{xH,MAX,\zeta} / \bar{F}_{xH}$	1.12	1.14
$\bar{M}_{xH,MAX,\zeta}$	1.09	1.11

This agreement between theory and experiment is considered to be satisfactory and correlates well with the findings of McCarthy et al. (1961) and others as summarized by Tasaki (1975). The small differences between theory and experiment may be due to the influence of the hull on wave velocity distribution. The effect of the hull may account for the discrepancy between theory and experiment of the relative phase between the maximum mean loads and the wave trough. The measured result showed the phase of the maximum load leads the theoretical result by approximately one-eighth of the wavelength.

The maximum absolute values of the peak minus time-average loads per revolution  $\bar{L}_{MAX,\zeta}$  increased by as much as 12 percent of the time-average loads in calm water without hull pitching above the corresponding peak minus time-average loads in calm water without hull pitching,  $\bar{L}_{MAX-L}$  (see Table 4). Similarly, the maximum values of the first

harmonic loads  $(L)_{1MAX}$ , increased as much as 9 percent of the time-average loads in calm water without hull pitching above the corresponding first harmonic loads in calm water without hull pitching,  $(L)_1$ . The variations of the peak minus time-average loads per revolution and the first harmonic loads approximately followed the local wave elevation in the propeller plane so that their maximum absolute values occurred at approximately 45 degrees of the cycle of encounter before the time at which local wave elevation passes through the calm water level from negative to positive ( $\zeta = 0$ ,  $\zeta > 0$ ).

The variations of the peak minus time-average loads per revolution and first harmonic loads are reasonably consistent with trends predicted by trochoidal wave theory. According to computations by McCarthy et al. (1961) using trochoidal wave theory, the longitudinal components of the orbital velocities are essentially independent of location in the propeller disk; therefore, the longitudinal components of orbital velocities do not contribute to the circumferential variations of propeller blade loads. Trochoidal wave theory predicts that the vertical components of the orbital velocities in the head waves reach their maximum values in the upward direction at the position where  $\zeta = 0$  and  $\zeta > 0$ . The wake into the propeller disk for the present hull is predominantly an upward velocity due to the inclination of the propeller shaft relative to the hull (see Figure 6); therefore, at  $\zeta = 0$ ,  $\zeta > 0$  the orbital velocity and the wake velocity vectorially combine to produce the maximum upward velocity relative to the propeller, which is equivalent to the maximum first harmonic of the tangential velocity. The first harmonic of the tangential wake is the primary cause of the unsteady blade loads on the present hull operating in calm water without pitching; therefore, the maximum unsteady loads in trochoidal waves should occur at  $\tau = 0$ ,  $\zeta > 0$ . The measured results show the phase of the maximum unsteady loads leads the predicted result by approximately one-eighth of a wavelength.

The ratio of the maximum variation of blade loading with blade angular position in waves to the corresponding variation of blade loading in calm water should be proportional to the ratio of the maximum vertical velocity in waves to the corresponding vertical velocity in calm water (since the vertical velocity is proportional to the first harmonic of the tangential component of velocity). The temporal maximum upward vertical velocity in the propeller plane (this velocity is essentially constant over the propeller disk) in a trochoidal wave corresponding to Condition 3 in Table 1 was calculated using the formulation of McCarthy et al. (1961) to be 0.235 m/s (0.772 ft/s). This is equivalent to an additional tangential velocity ratio  $V_t/V$  of 0.066. The value of  $(V_{t0.7})_1/V$  for operation in calm water is 0.199 from the wake survey results. Therefore,

$$\frac{(V_{t0.7})_{1MAX}/V}{(V_{t0.7})_1/V} = \frac{0.199 + 0.066}{0.199} = 1.33$$

This maximum ratio, which does not consider the effect of the hull on the vertical component of the trochoidal wave velocities, is predicted to occur when the wave elevation at the propeller plane is increasing through the calm water level, i.e.,  $\zeta = 0$ ,  $\dot{\zeta} > 0$ . The measured increase in the variation of loads with blade angular position for operation in waves was somewhat smaller than this calculated increase in tangential velocity; for example:

$$\tilde{F}_{x_{MAX,\zeta}} / (F_{x_{MAX}} - \bar{F}) = 1.17$$

$$(F_x)_{1MAX,\zeta} / (F_x)_1 = 1.12$$

This simple analysis is believed to provide an upper bound to the increase in variation of loads with blade angular position due to operation in waves, since the hull boundary above the propeller would tend to reduce the vertical component of the trochoidal wave velocity. The corresponding measured increase for other components of blade loading are presented in Table 5.

The maximum absolute values of the peak loads per revolution increased by as much as 22 percent of the time-average loads in calm water without hull pitching above the corresponding peak loads in calm water without hull pitching (see Table 5). This increase in peak loads is made up of the increase in the time-average loads per revolution (up to 14 percent) and the increase in the circumferential variation in loads, or peak minus time-average loads per revolution (up to 12 percent). The increases in the time-average loads per revolution and the increases in circumferential variations of loads are thought to arise from different physical characteristics of the flow as discussed previously; however, the maximum increase in the time-average loads and circumferential variations of loads occur in the same portion of the wave period. Therefore, these two separate increases tend to add almost in phase relative to the wave period so that the maximum increase in peak loads is almost the algebraic sum of the maximum increases in the time-average loads per revolution and the maximum increase in the circumferential variation of loads.

Figure 16 shows the variation of the  $F_x$  component of blade load with angular position for different times during one wave cycle. The variation of the circumferential distribution to waves appears to be more complicated than the corresponding variation due to pitching. This is attributed to the combined effect of the longitudinal and vertical velocities induced by the wave. As in the case of pitching, the greatest magnitude of loading occurs at blade angles around 90 degrees, corresponding to the outboard position of the blades relative to the propeller shaft. Also, the phase angle of the maximum load varies with position relative to the wave, but with the combined effects of mean and unsteady load variations no clear trends are observed. The variation



in first harmonic phase shown in Figure 15 indicates a significant change in vertical flow direction due to the hull.

Blade loads were measured in regular head waves at only one wave amplitude and wavelength. The experiments showed that the increases in both the time-average loads per revolution and the unsteady loads due to waves appears to be controlled by the orbital velocity in a trochoidal wave. It appears that the increase in both the time-average loads per revolution and the unsteady loads are proportional to the orbital velocity. The orbital velocity, and thus the approximate increase in loads, is directly proportional to the wave height and inversely proportional to the square root of the wavelength (Lewis, 1967, McCarthy et al., 1961), neglecting any possible influence of the hull on these trends.

The vertical component of the orbital velocity, which controls the increase in unsteady blade loading due to waves, is independent of the direction of the waves relative to the ship heading. Therefore, the increase in unsteady blade loading due to waves is essentially independent of the relative direction of the waves. The component of the orbital velocity in the direction of the ship velocity, which controls the increase in the time-average loads per revolution due to waves, is proportional to the cosine of  $\mu$ , the angle between the direction of the waves and the ship heading. Therefore, the increase in the time-average loads per revolution is essentially proportional to  $\cos \mu$ , neglecting any possible influence of the hull on these trends.

Based on these results the increases in blade loads due to waves can be estimated for transom-stern configurations as follows:

#### 1. Time-Average Loads Per Revolution

Waves (without ship motions) substantially increase the maximum time-average loads per revolution over the corresponding time-average loads in calm water. The primary controlling parameter is the change in effective advance coefficient due to the longitudinal component of orbital wave velocity. The hull boundary above the propeller does not appear to significantly influence the longitudinal component of orbital wave velocity. Therefore, the maximum increase in time-average loads per propeller revolution due to waves can be adequately predicted by the use of the trochoidal wave theory neglecting the influence of the hull on the waves, and simple quasi-steady propeller theory using the open-water characteristics of the propeller.

#### 2. Periodic Loads

Waves (without ship motions) substantially increase the maximum periodic blade loads over the corresponding periodic loads in calm water. The primary controlling parameter is the ratio of the vertical component of the orbital wave velocity in the propeller plane to the ship speed. The maximum periodic loads occur when the vertical component of the orbital wave velocity in the propeller plane is maximum upward. This upward orbital velocity component effectively increases the inclination of the inflow to the propeller and thereby increases

the periodic loads. Due to the hull boundary above the propeller, the maximum upward orbital velocity into the propeller is only 50 percent or less of the corresponding upward orbital velocity in an unbounded fluid for ships with high-speed transom sterns and exposed shafts and struts. Therefore, for these ships the maximum periodic blade loads due to waves can be approximated from the corresponding loads without waves as follows:

$$\Delta \tilde{L}_{MAX,\zeta} \approx \frac{0.5 V_{\zeta}}{(V_{t0.7})_1} \tilde{L} \approx \frac{0.5 V_{\zeta}}{V_C} \tilde{L}$$

where  $\Delta \tilde{L}_{MAX,\zeta}$  = maximum increase in periodic loads with waves over the values in calm water

$\tilde{L}$  = periodic blade load in calm water

$V_{\zeta}$  = maximum vertical component of the orbital wave velocity in the propeller plane neglecting the influence of the hull

$(V_{t0.7})_1$  = first harmonic of the tangential wake at the 0.7 radius in calm water

$V_C$  = vertical component of spatial average crossflow velocity in propeller plane in calm water

### 3. Peak Loads

The maximum values of the periodic variation of loads with angular position and the time-average loads per angular position occur near the same point in the wave cycle. Therefore, the increase in peak loads due to waves is approximately the sum of the increases in these components:

$$\Delta L_{PEAK,\zeta} \approx \Delta \bar{L}_{MAX,\zeta} + \Delta \tilde{L}_{MAX,\zeta}$$

Figure 17 shows the variations of the higher harmonic amplitudes of the  $F_x$  component of blade load through the wave height cycle. For the case of waves, it appears that the second through fifth harmonic amplitudes show distinct periodic variations up to 50 percent of the calm water values. The sixth through tenth harmonic amplitudes show a more random variation of a lesser extent. This is contrary to the pitching results where less variation occurred over the greater and lesser harmonics and extreme variations occurred in the fifth through eighth harmonics. The large variation in the third, fourth, and fifth harmonic amplitudes of  $F_x$  would lead to significant modulation in the periodic bearing forces produced by the four-bladed model propeller. The large variation in the second through fourth harmonic amplitudes

of  $F_x$ , the amplitudes of which range from 2 to 13 percent of the time-average value, also explain some of the complexity of the wave forms shown in Figure 16. These harmonics have consistent variations in phase angles of up to 45 degrees.

#### G. Operation in Waves With Hull Pitching

As discussed in the section on experimental conditions and procedures, for forced pitching in waves the phase of the wave at the propeller  $\phi_\zeta$  was varied relative to the phase of the hull pitching  $\phi_\psi$ . Three relative phases were evaluated:

- a. Wave crest at the propeller plane when the stern of the model hull is pitched up at its maximum value,  $\phi_\zeta - \phi_\psi = 0$  (Condition 4 in Table 1),
- b. Wave crest at the propeller plane when the stern of the model hull is pitched down at its maximum values,  $\phi_\zeta - \phi_\psi = 180$  degrees (Condition 5 in Table 1), and
- c. Wave crest at the propeller plane when the hull pitch is passing through its mean value  $(\psi_{MAX} - \psi_{MIN})/2$  from stern down to stern up,  $\phi_\zeta - \phi_\psi = 90$  degrees (Condition 6 in Table 1).

Experiments for each of these conditions were conducted at the same model speed, propeller rotation speed, pitching period, wave period of encounter as were the condition in calm water with hull pitching, and in waves without hull pitching, as described in the preceding sections (see Table 1). However, in order to ensure a large influence of the pitching or waves on blade loads while not flooding the model hull, it was necessary to run each of the four pitching conditions with a different pitch amplitude  $\psi_A$ , and each of the four conditions in waves with a different wave amplitude  $\zeta_A$  (see Table 1).

The primary objectives of this portion of the experimental program were:

- a. To determine the validity of linearly superimposing the increase in blade loads due to pitching in calm water, and the increase in blade loads due to waves without hull pitching, to obtain the net increase in blade loads due to hull pitching in waves,
- b. To determine the influence of the phase of the hull pitch relative to the phase of the wave ( $\phi_\zeta - \phi_\psi$ ) on the maximum absolute values of the peak, unsteady and time-average blade loads, and
- c. To determine the values of ( $\phi_\zeta - \phi_\psi$ ) which result in the largest values of peak, unsteady and time-average blade loads for different relative values of pitching amplitude  $\psi_A$  and nondimensional wave amplitude,  $\zeta_A/L_{pp}$ .

Therefore, the experimental results will be discussed and interpreted from the viewpoint of these three objectives.

In order to determine the validity of linearly superimposing the increase in blade loads due to the pitching only and the increase in blade loads due to waves only, the experimental results with hull pitching in calm water and the experimental results in waves without hull pitching were linearly combined to simulate the blade loads for the

three experimental conditions with hull pitching in waves. The linear superposition accounts for the phase differences between the hull pitching and the waves, and for the differences in amplitudes of pitching and waves for the various experimental conditions. It is assumed in this linear superposition that the increases in loading due to hull pitching and waves are directly proportional to the amplitude of the hull pitching and the amplitude of the waves, respectively.

From the experiments in calm water with hull pitching (Condition 2 in Table 1) the increase in loading due to a unit pitch amplitude is:

$$\Delta \bar{L}_{\psi}(t_{\psi})/\psi_A = (L_{\psi}(t_{\psi}) - \bar{L})/\psi_A$$

$$\Delta \tilde{L}_{\psi}(t_{\psi})/\psi_A = (\tilde{L}_{\psi}(t_{\psi}) - (L_{MAX} - \bar{L}))/\psi_A$$

From the experiments in waves without hull pitching (Condition 3 in Table 1) the increase in loading due to a unit wave amplitude is:

$$\Delta \bar{L}_{\zeta}(t_{\zeta})/\zeta_A = (L_{\zeta}(t_{\zeta}) - \bar{L})/\zeta_A$$

$$\Delta \tilde{L}_{\zeta}(t_{\zeta})/\zeta_A = (\tilde{L}_{\zeta}(t_{\zeta}) - (L_{MAX} - \bar{L}))/\zeta_A$$

Linearly superimposing the above increases in loading due to pitching only and due to waves only, the predicted loads with pitching amplitude  $\psi_A^*$ , wave amplitude  $\zeta_A^*$ , and with the wave leading the pitch by  $(\phi_{\zeta} - \phi_{\psi})T_E/2\pi$  seconds is

$$\bar{L}_{\psi,\zeta}(t_{\psi}) = \Delta \bar{L}_{\psi}(t_{\psi})\psi_A^* + \Delta \bar{L}_{\zeta}((t_{\zeta} + (\phi_{\zeta} - \phi_{\psi})T_E/2\pi)\zeta_A^* + \bar{L}$$

$$\tilde{L}_{\psi,\zeta}(t_{\psi}) = \Delta \tilde{L}_{\psi}(t_{\psi})\psi_A^* + \Delta \tilde{L}_{\zeta}((t_{\zeta} + (\phi_{\zeta} - \phi_{\psi})T_E/2\pi)\zeta_A^* + (L_{MAX} - \bar{L}))$$

$$L_{PEAK,\psi,\zeta}(t_{\psi}) = \bar{L}_{\psi,\zeta} + \tilde{L}_{\psi,\zeta}(t_{\psi})$$

Figure 18 compares  $F_x$  component loads calculated by this linear superposition procedure with loads measured in waves with hull pitching for the three conditions run,  $\phi_{\zeta} - \phi_{\psi} = 0$ ,  $\phi_{\zeta} - \phi_{\psi} = 180$ ,  $\phi_{\zeta} - \phi_{\psi} = 90$  degrees. Figure 18 shows that the linear superposition gives a reasonably good estimate of both the magnitudes and the variations with position in the pitch and wave cycles of the peak loads, unsteady loads, and time-average loads per revolution. For most conditions the values based on linear superposition are slightly larger than the measured results.

Therefore, it is concluded that linear superposition of the separate increases in blade loads due to pitching and waves gives a good, or slightly conservative, estimate of net increase in blade loads due to operation in waves with hull pitching.

In order to evaluate the relative importance of the amplitude of hull pitching, the amplitude of the waves, and the phase difference between the hull pitch and the wave at the propeller, the experimental results with hull pitching in calm water and the experimental results in waves without hull pitching are linearly combined as described previously to simulate blade loads for the following values of  $\psi_A$ , and  $\zeta_A/L_{pp}$ :

$\psi_A = 1.0$  degrees,  $\zeta_A/L_{pp} = 0.01$  - representing calm to moderate sea conditions

$\psi_A = 2.0$  degrees,  $\zeta_A/L_{pp} = 0.03$  - representing moderate to rough sea conditions

Figure 19 presents the maximum values of the  $F_x$  component time-average loads per revolution, peak loads per revolution, and the peak minus time-average loads per revolution calculated by linear superposition for the selected values of pitch amplitude and wave amplitude over the complete range of the relative phase between the pitch and the wave. Only the  $F_x$  component is shown since the pertinent trends are basically the same for the  $F_x$ ,  $M_y$ ,  $M_x$ , and  $F_y$  components. The abscissa of these curves,  $\phi_\zeta - \phi_\psi$ , is the phase angle by which the pitch lags the wave at the propeller relative to the frequency of encounter or the pitching frequency.

The results shown in Figure 19 indicate that for given amplitudes of waves and pitching the maximum values of the time-average loads per revolution, peak loads, and unsteady loads (peak loads minus time-average loads per revolution) vary substantially depending on the difference in phase between the hull pitch and the wave at the propeller,  $\phi_\zeta - \phi_\psi$ . The peak loads are more sensitive to this difference in phase than are the unsteady loads which, in turn, are more sensitive than the time-average loads per revolution. The time-average loads, peak loads, and periodic loads are near their respective largest values in the region where  $-30$  degrees  $< (\phi_\zeta - \phi_\psi) < 120$  degrees; i.e., where the crest of wave reaches the propeller between 120 degrees before and 30 degrees after the maximum stern-up position in the pitch cycle. Over this region of  $\phi_\zeta - \phi_\psi$  the maximum increase in loads due to pitching in calm water and the maximum increase in loads due to waves without hull pitching add almost algebraically, i.e., there is very little cancellation due to phase differences between these increases. The values of the maximum peak loads and maximum unsteady loads reach their smallest values near  $\phi_\zeta - \phi_\psi = 240$  degrees. These trends hold true for the  $F_x$ ,  $M_y$ ,  $F_y$  and  $M_x$  components for all combinations of amplitudes of hull pitching and amplitude of waves which were evaluated.

In summary, the experiments with hull pitching in regular head waves with pitching frequency equal to the wave frequency of encounter showed the following:

a. For given amplitudes of waves and pitching the maximum values of the time-average loads per revolution, peak loads, and the periodic variation of loads with angular position vary substantially depending upon the difference in phase between the hull pitch and the wave at the propeller. The time-average loads, peak loads, and periodic loads are near their respective greatest values for any difference in phase whereby the crest of the wave reaches the propeller between 0.3 and -0.1 of the period of encounter before the maximum stern-up position.

b. Linear superposition of the increases in blade loads due to pitching in calm water and due to waves without hull pitching, taking into account the phase between the waves and the pitching, gives a satisfactory, or slightly conservative, estimate of the net increase in blade loads due to operation in waves with hull pitching. For engineering calculations, it is recommended that the absolute values of the maximum increases in time-average, peak, and periodic loads due to the separate influences of waves and hull pitching be added without regard to the relative phase between the wave and the hull pitching.

#### IV. DISCUSSION

The results presented in this paper showing the effects of hull pitching and waves on the dominant once per propeller revolution variation of loads provide extensive insight to the flow patterns in the propeller plane under these conditions. These data and insights should form a basis for developing and validating a computational procedure for predicting blade loads under these conditions.

The experimental results presented here are applicable to only high speed transom stern configurations. The influences of the hull boundary of more complex stern geometries, such as for full stern cargo ships, are more complex. Experiments of the type described in this paper would serve as a valuable guide for validating any computational procedure applied to cargo ships.

The prediction of the modulation of bearing loads due to waves and pitching cannot be performed using the simple procedures described in this paper. More elaborate models of the interaction between the propeller wake and the waves and pitching influences may capture the fundamental nature of the modulation of the bearing loads.

All results presented in this paper are in the absence of cavitation. It is anticipated that if cavitation were sufficiently extensive to influence blade loads it would reduce the maximum time-average and periodic loads. Therefore, it is judged that neglecting cavitation results in a conservative estimate of maximum loads.

## V. SUMMARY AND CONCLUSIONS

Fundamental investigations were made of the effects of periodic hull pitching motions and waves on the periodic loads on propeller blades and bearings. These periodic loads were measured during carefully controlled model experiments on a twin-screw, transom-stern hull. The objective of these experiments was to obtain systematic accurate experimental data showing the effects of hull pitching and waves on periodic and time-average blade and bearing loads under carefully controlled experimental conditions so that the effects of ship motions and waves on periodic and time-average blade and bearing loads could be isolated. The experiments were conducted under steady ahead operation in calm water with no ship motions, in calm water with forced sinusoidal pitching of the hull, in regular waves with no ship motions, and in regular waves with forced sinusoidal pitching of the hull at a frequency equal to the wave frequency of encounter over a range of phases between the pitching motion and wave encounter. An error analysis indicates that the experimental results are sufficiently accurate to support the conclusions drawn. The periodic blade loads were calculated using trochoidal wave velocity profiles, and a representation of the propeller based on a quasi-steady method.

The experimental results show the following:

- a. The amplitudes of the periodic blade loads are significantly modulated hull pitching motions and wave encounter.
- b. The time-average blade loads per propeller revolution vary significantly with wave encounter but only slightly with hull pitching motion.
- c. The peak blade loads per revolution vary significantly with hull pitching motions and wave encounter.
- d. The individual influences of the wave velocity profile and the induced velocities due to vertical hull motions can be linearly superimposed for transom stern configurations.

The results show that the hull significantly alters the amount of modulation of the shaft frequency loads due to both the periodic vertical motion of the propeller and the trochoidal wave velocity profile in the absence of the hull. However, trends of shaft frequency loads are well predicted by simple periodic variations of the velocity into the propeller, and a simple quasi-steady representation of the propeller. The quasi-steady representation of the propeller is sufficient for this application because the frequencies of encounter of the waves and of the hull pitching motions are low relative to the propeller rotational speed; i.e., the reduced frequency is low. Therefore, for engineering purposes, the modulation can be estimated by simple trochoidal wave velocity profiles, quasi-steady propeller theory, and constant multiples derived from the experiments presented in this paper.

The experimental results show that the first eight shaft rate harmonics of blade loads are modulated and increased by hull pitching motions and waves relative to the respective values in calm water without hull pitching. Comparable modulations and increases in bearing loads

are anticipated, where the number of blades determines the pertinent harmonics of blade loading. However, the data are not sufficient to quantify the modulations of bearing loads due to hull pitching and waves nor to provide guidance for predicting these modulations.

Trends of the results for both blade loads and bearing loads are consistent with available full-scale data.

## VI. ACKNOWLEDGMENTS

The authors are indebted to many members of the staff of the David W. Taylor Naval Ship Research and Development Center. Special appreciation is extended to Messrs. Michael Jeffers, Benjamin Wisler, and Douglas Dahmer for development of the on-line data analysis system, assembling the servomechanism for accurately controlling the model pitching relative to the waves, assisting in running the experiments, and analyzing data.

## VII. REFERENCES

- Boswell, R. J., and M. L. Miller (1968). Unsteady Propeller Loading - Measurement, Correlation with Theory, and Parametric Study, NSRDC Rept 2625.
- Boswell, R. J., J. J. Nelka, and S. B. Denny (1976). Experimental Determination of Mean and Unsteady Loads on a Model CP Propeller Blade for Various Simulated Modes of Ship Operation, Eleventh Symposium on Naval Hydrodynamics, Mechanical Engineering Publications Limited, London and New York, pp. 789-834.
- Boswell, R. J., J. J. Nelka, and S. B. Denny (1976). Experimental Unsteady and Mean Loads on a CP Propeller Blade on the FF-1088 for Simulated Modes of Operation, DTNSRDC Rept 76-0125, DTIC ADA 034804.
- Boswell, R. J., S. D. Jessup, and J. J. Nelka (1978). Experimental Time Average and Unsteady Loads on the Blades of a CP Propeller Behind a Model of the DD-963 Class Destroyer, Propellers '78 Symposium, The Society of Naval Architects and Marine Engineers Publication S-6, pp. 7/1-7/28.
- Boswell, R. J., S. D. Jessup, and K. H. Kim (1981). Periodic Blade Loads on Propellers in Tangential and Longitudinal Wakes, Propellers '81 Symposium, The Society of Naval Architects and Marine Engineers Publication S-8, also DTNSRDC Rept 81/054.
- Brandau, J. H. (1968). Static and Dynamic Calibration of Propeller Model Fluctuating Force Balances, DTMB Rept 2350, also Technologia Naval, 1, pp. 48-74.



- Breslin, J. P. (1972). Propeller Excitation Theory, Proc. 13th International Towing Tank Conference, Report of the Propeller Committee, App. 2c, 2, pp. 527-540.
- Brownell, W. F., W. L. Asling, and W. Marks (1956). A 51-Foot Pneumatic Wave-maker and a Wave Absorber, DTMB Rept 1054.
- Day, W. G., A. M. Reed, and W.-C. Lin (1977). Experimental and Prediction Techniques for Estimating Added Power Requirements in a Seaway, Proc. 18th American Towing Tank Conference, U.S. Naval Academy, Annapolis, Maryland, I, pp. 121-141.
- Dobay, G. F. (1971). Time-Dependent Blade-Load Measurements on a Screw-Propeller, Presented at the 16th American Towing Tank Conference, Instituto De Pesquisas Technologicas, Marinhas Do Brasil.
- Gray, L. M. (1981). Investigation into Modeling and Measurement of Propeller Cavitation Source Strength at Blade Rate on Merchant Vessels, Propellers '81 Symposium, The Society of Naval Architects and Marine Engineers Publication S-8, pp. 165-180.
- Jessup, S. D., R. J. Boswell, and J. J. Nelka (1977). Experimental Unsteady and Time Average Loads on the Blades of the CP Propeller on a Model of the DD-963 Class Destroyer for Simulated Modes of Operation, DTNSRDC Rept 77-0110, DTIC ADA-048385.
- Keil, H. G., J. J. Blaurock, and E. A. Weitendorf (1972). Stresses in the Blades of a Cargo Ship Propeller, J. of Hydronautics, 6, 1, pp. 2-7.
- Lewis, E. V. (1967). Motion of Ships in Waves, Chapter IX, Principles of Naval Architecture, Edited by J. P. Comstock, The Society of Naval Architects and Marine Engineers, pp. 607-717.
- Lipis, B. V. (1975). Hydrodynamics of a Screw Propeller with Motions of the Vessel (in Russian: Gidrodinamika Grebnogo Vinta pri Kachke Sudna), Publishing House Sudostroyeniye, Leningrad.
- Lloyd, A. R. J. M., and R. N. Andrew (1977). Criteria of Ship Speed in Rough Weather, Proc. 18th American Towing Tank Conference, U.S. Naval Academy, Annapolis, Maryland, II, pp. 541-564.
- McCarthy, J. H. (1961). On the Calculation of Thrust and Torque Fluctuations of Propellers in Nonuniform Wake Flow, DTMB Rept 1533.
- McCarthy, J. H., W. H. Norley, and G. L. Ober (1961). The Performance of a Fully Submerged Propeller in Regular Waves, DTMB Rept 1440.
- Oosterveld, M. W. C. (editor) (1978). Report of the Seakeeping Committee, 15th International Towing Tank Conference, The Netherlands Ship Model Basin, Wageningen, pp. 55-114.
- Schwanecke, H. (1975). Comparative Calculations on Unsteady Propeller Blade Forces, Proc. 14th International Towing Tank Conference, Report of the Propeller Committee, App 4, 3, pp. 357-397.
- Tasaki, R. (1975). Propulsion Factors and Fluctuating Propeller Loads in Waves, Proc. 14th International Towing Tank Conference, Report of Seakeeping Committee, App 7, 4, pp. 224-236.
- Tsakonas, S., W. R. Jacobs, and M. R. Ali (1974). An Exact Linear Lifting Surface Theory for Marine Propeller in a Nonuniform Flow Field, J. of Ship Research, 17, 4, pp. 196-207.
- Watanabe, K., N. Heida, T. Sasajima, and T. Matsuo (1973). Propeller Stress Measurements on the Container Ship HKONE MARU, Shipbuilding Research Association of Japan, 3, 3, pp. 41-51.

## NOTATION

$c$	Chord length
$D$	Propeller diameter
$(F)_n$	$n$ th harmonic amplitude of $F$
$F_{x,y,z}$	Force components on blade in $x,y,z$ directions
$J_Q$	Effective advance coefficient based on torque identity
$J_T$	Effective advance coefficient based on thrust identity
$K_Q$	Torque coefficient, $Q/(\rho n^2 D^5)$
$K_T$	Thrust coefficient, $T/(\rho n^2 D^4)$
$L$	Any of the measured components of blade loading
$L_{pp}$	Length between perpendiculars
$L_W$	Wavelength
$(M)_n$	$n$ th harmonic amplitude of $M$
$M_{x,y,z}$	Moment components about $x,y,z$ axes from loading on one blade
$n$	Propeller revolutions per unit time
$R$	Radius of propeller
$r$	Radial coordinate from propeller axis
$T_E$	Period of encounter of waves
$T_\psi$	Period of pitching
$t$	Time
$t(r)$	Maximum thickness of propeller blade section
$V$	Model speed or ship speed
$V_A$	Propeller speed of advance
$V_C$	Vertical component of the spatial average crossflow velocity in propeller plane in calm water without ship motions
$V_r(r, \theta_W)$	Radial component of wake velocity at propeller plane, positive towards hub
$V_t(r, \theta_W)$	Tangential component of wake velocity at propeller plane, positive counterclockwise looking upstream for starboard propeller (right-hand rotation), positive clockwise looking upstream for port propeller (left-hand rotation)
$(V_t)_n$	$n$ th harmonic amplitude of $V_t$
$V_W$	Wave velocity
$V_x(r, \theta_W)$	Longitudinal component of wake velocity at propeller plane, positive forward
$V_\psi$	Maximum vertical velocity component of propeller resulting from hull pitching motions
$w_Q$	Taylor wake fraction determined from torque identity
$w_T$	Taylor wake fraction determined from thrust identity
$w_{VM}$	Wake fraction determined from volume mean longitudinal velocity component through propeller disk determined from a wake survey, $(V - V_{VM})/V$
$x,y,z$	Coordinate axes rotating with propeller; see Figure 2
$Z$	Number of blades
$\zeta$	Instantaneous wave elevation, positive upward from undisturbed surface
$\zeta_A$	Wave amplitude

$\theta_\zeta$	Angular variable in cycle of wave encounter, $2\pi t/T_E$ ; $\theta_\zeta = 0$ when $\zeta = 0$ , $\zeta > 0$
$\theta_\psi$	Angular variable in cycle of hull pitching, $2\pi t/T_\psi$ ; $\theta_\psi = 0$ when $\psi = 0$ , $\psi > 0$
$\theta$	Angular coordinate used to define location of blade and variation of loads measured from vertical upward; positive clockwise looking upstream for starboard propeller (right-hand rotation), positive counterclockwise looking upstream for port propeller (left-hand rotation), $\theta = -\theta_W$
$\theta_W$	Angular coordinate of wake velocity measured from upward vertical; positive counterclockwise looking upstream for starboard propeller (right-hand rotation), positive clockwise looking upstream for port propeller (left-hand rotation), $\theta_W = -\theta$
$\mu$	Angle between the direction of the waves and the ship centerline
$\rho$	Mass density of water
$\phi_\zeta$	Phase of wave at the propeller plane based on sine series, $\zeta(t) = \zeta_A \sin(\theta_\zeta + \phi_\zeta)$
$\phi_\psi$	Phase of hull pitch based on sine series, $\psi(t) = \psi_A \sin(\theta_\psi + \phi_\psi)$
$\phi(r)$	Pitch angle of propeller blade section, $\tan^{-1}(P/(2\pi r))$
$(\phi_{F,M})_n$	$n$ th harmonic phase angles of F,M based on a cosine series, $(\bar{F}, \bar{M}) = (\bar{F}, \bar{M}) + \sum_{n=1}^N (F, M)_n \cos(n\theta - (\phi_{F,M})_n)$
$\psi$	Pitch of hull, positive stern up
$\psi_A$	Amplitude of hull pitch angle

## Subscripts:

CW	Value in calm water
Exp	Experimental value
H	Arising from hydrodynamic loading
h	Value at hub radius
M	Model value
MAX	Maximum value
MIN	Minimum value
p	Port propeller
PEAK	Peak value including variation of both time-average value per revolution and variation with blade angular position
s	Starboard propeller
x,y,z	Component in x,y,z direction
0.7	Value at $r = 0.7R$
$\zeta$	Value for operation in waves
$\psi$	Value for operation with hull pitching motion

## Superscripts:

—	Time-average value per revolution
~	Unsteady value, peak value per revolution minus time-average value per revolution
.	Rate of change with time

	MODEL
LENGTH ON WATERLINE	6.10m (20.0 ft)
LENGTH BETWEEN PERPENDICULARS	5.70m (18.7 ft)
LENGTH BETWEEN PERPENDICULARS	5.70m (18.7 ft)
BEAM (MAXIMUM)	0.81m (2.66 ft)
DRAFT (MEAN)	0.21m (0.68 ft)
DISPLACEMENT	0.46 TONNES (0.46 TONS)
WETTED SURFACE	3.17m <sup>2</sup> (50.2 ft <sup>2</sup> )

APPENDAGES: SHAFTS, V-STRUTS, CENTERLINE SKEG,  
STABILIZER

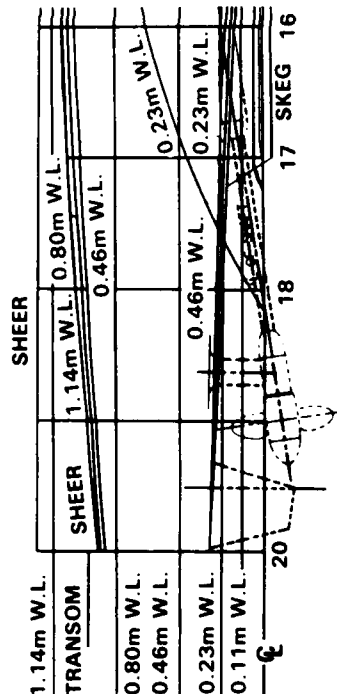
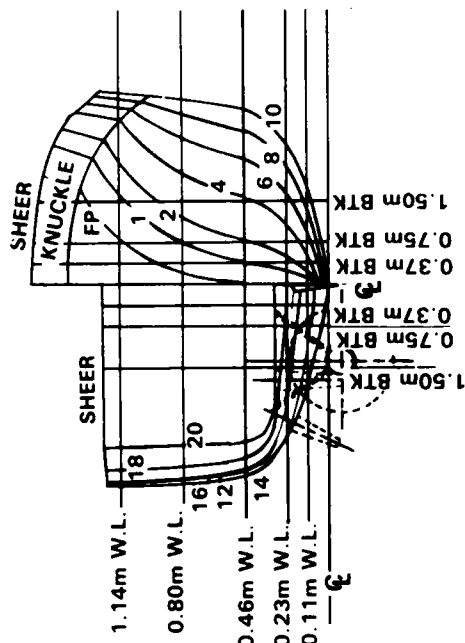


Figure 1a - Profile Lines and Body Plan

Figure 1 - Hull and Propeller Geometry

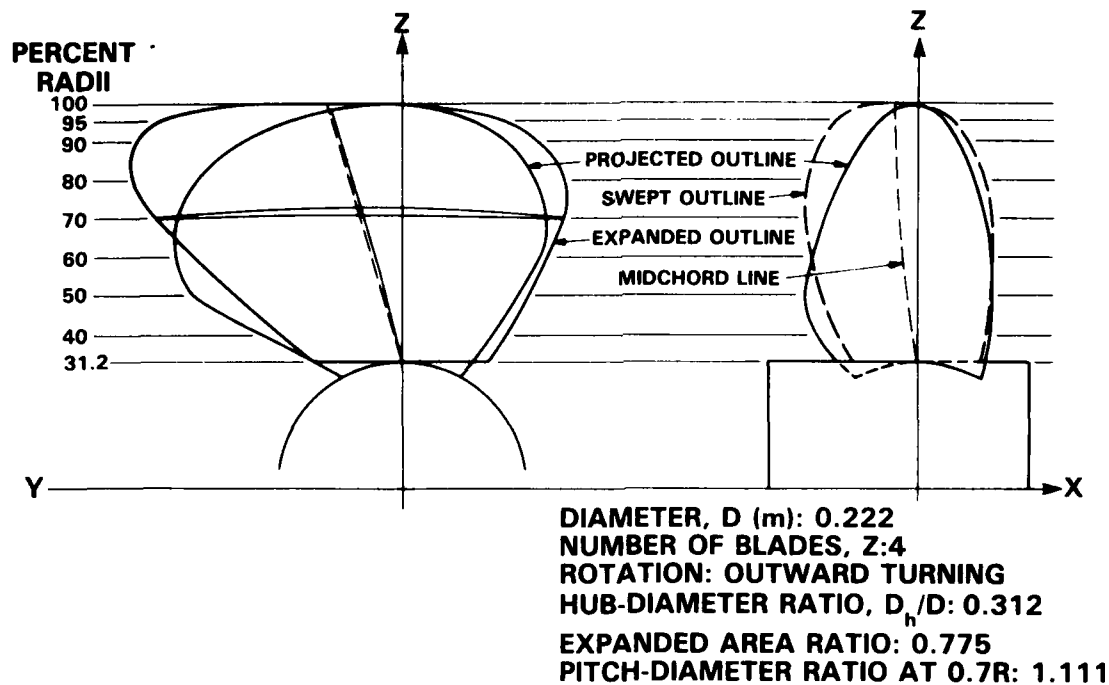


Figure 1b - Schematic Drawing of Propellers

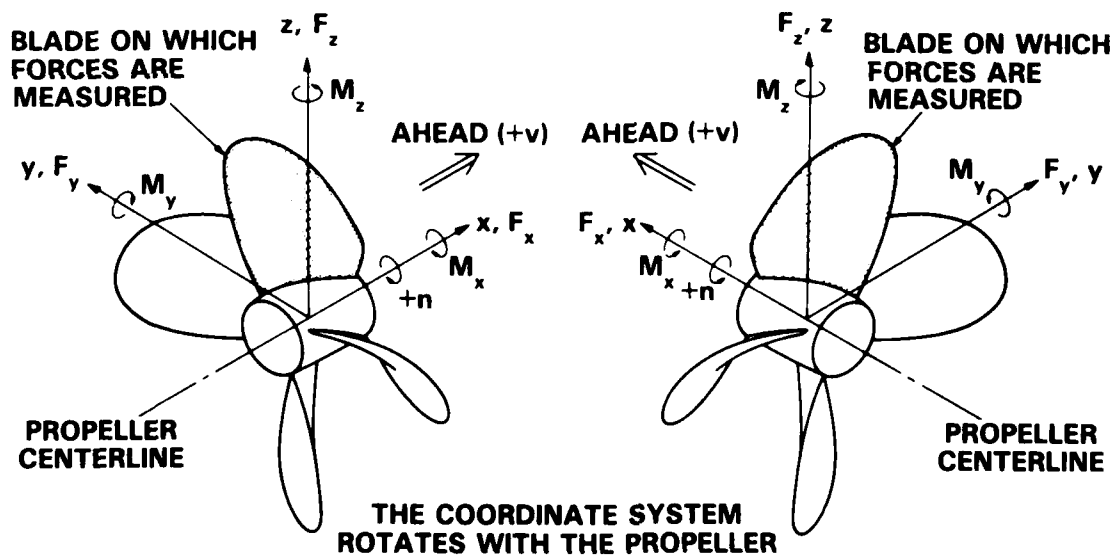


Figure 2 - Components of Blade Loading

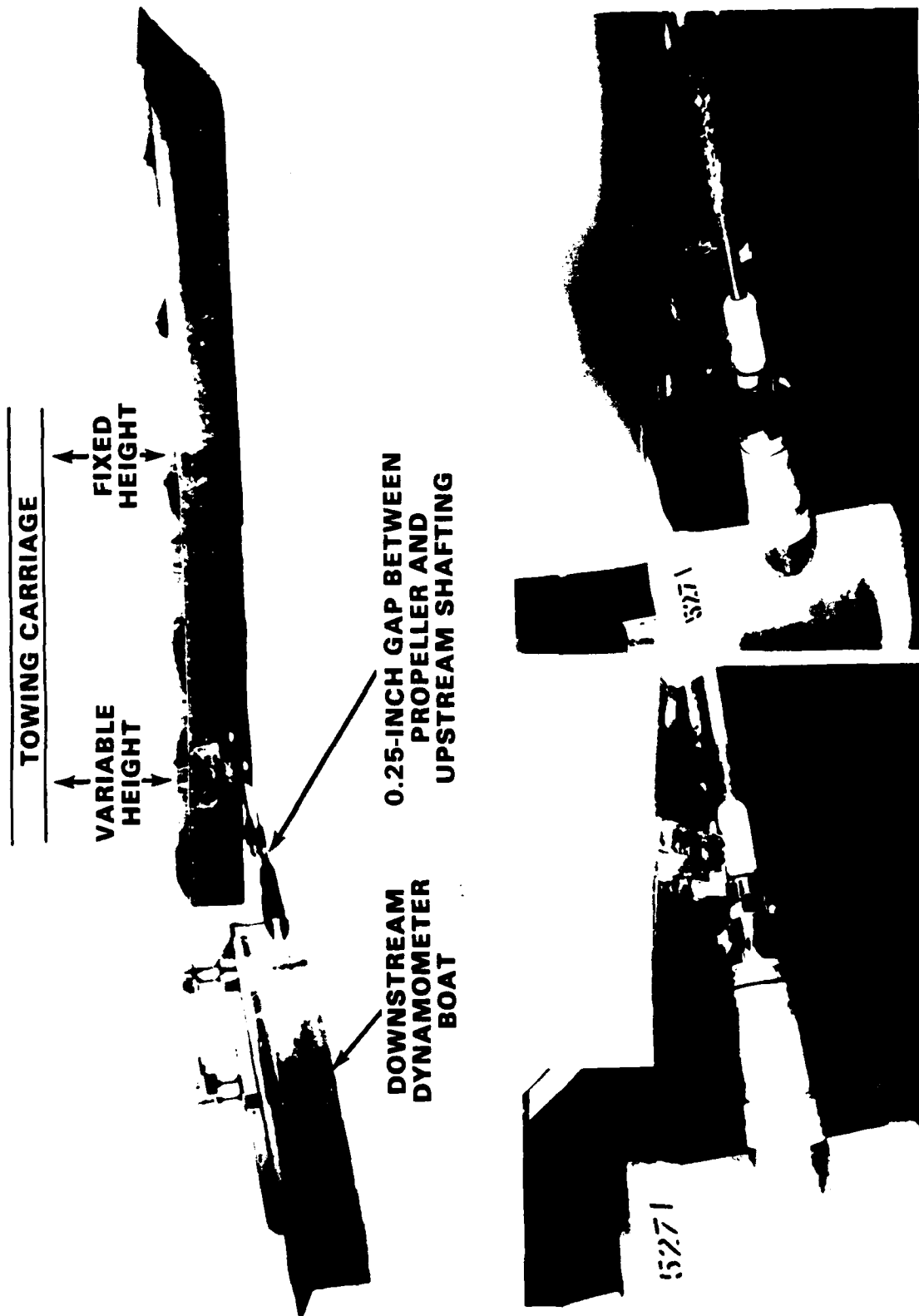


Figure 3 - Hull and Dynamometer Boat

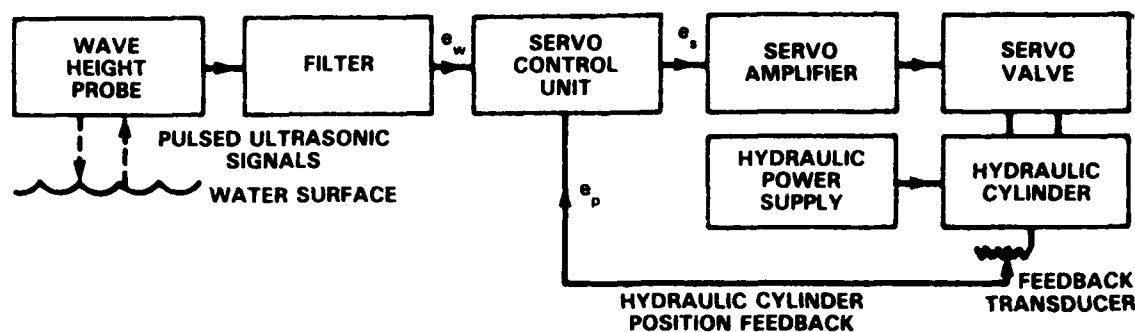


Figure 4 - Block Diagram of SERVOMECHANISM for Pitching Model at Specified Phase Relative to Waves

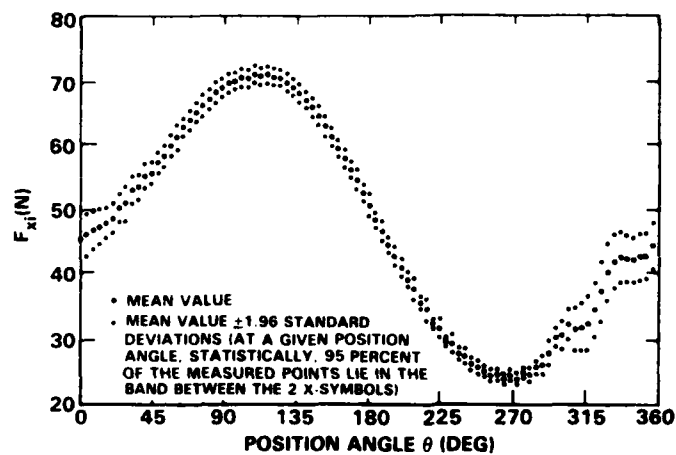


Figure 5 - Experimental Data Showing Plus and Minus 1.96 Standard Deviations on Measured Values of  $F_x$

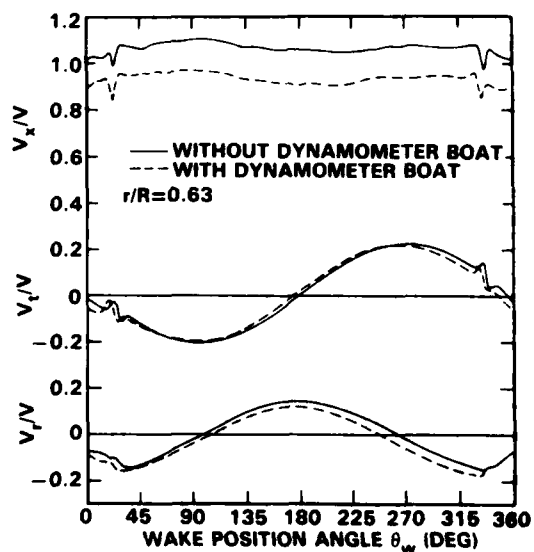


Figure 6a -  $r/R = 0.63$

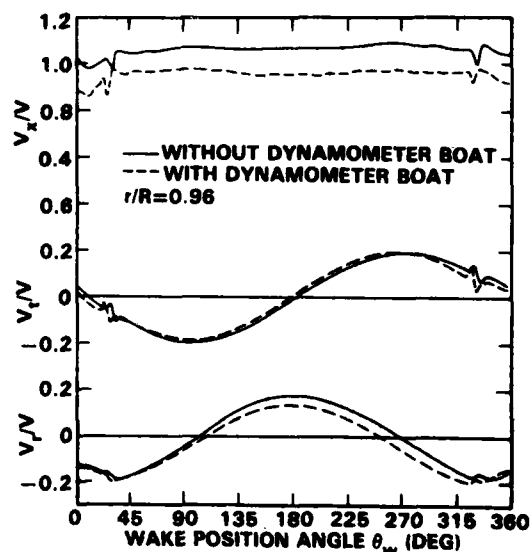


Figure 6b -  $r/R = 0.96$

Figure 6 - Distribution of Wake in Propeller Plane

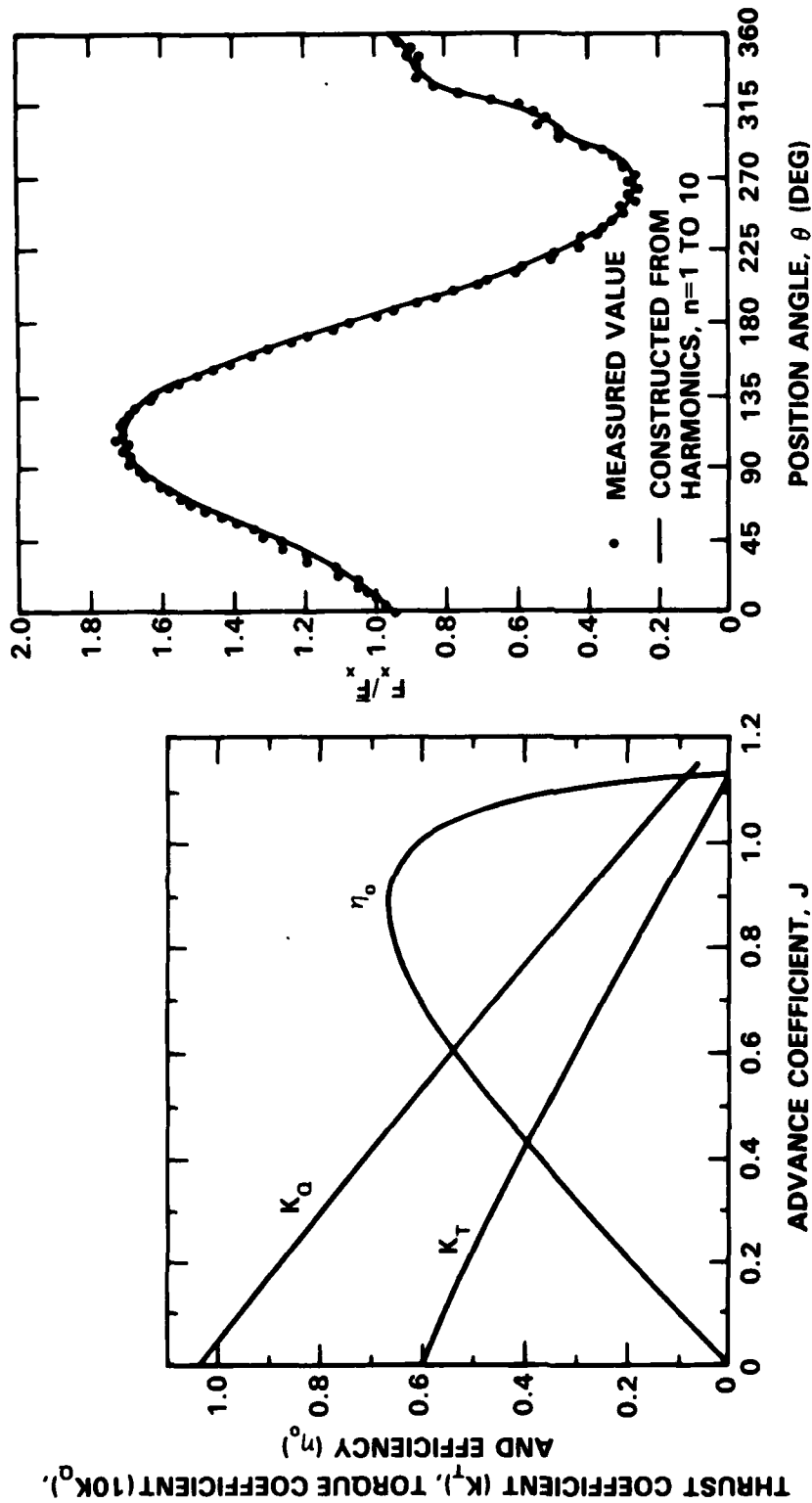


Figure 7 - Open-Water Characteristics of DTNSRDC Model Propellers 4710 and 4711

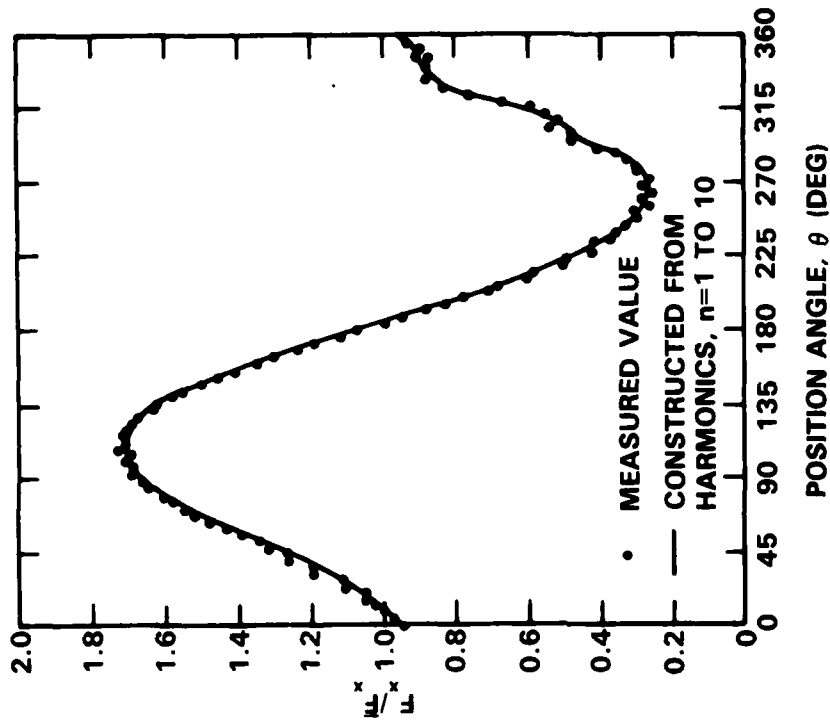


Figure 8 - Influence of Extraneous Signals on measured Loads



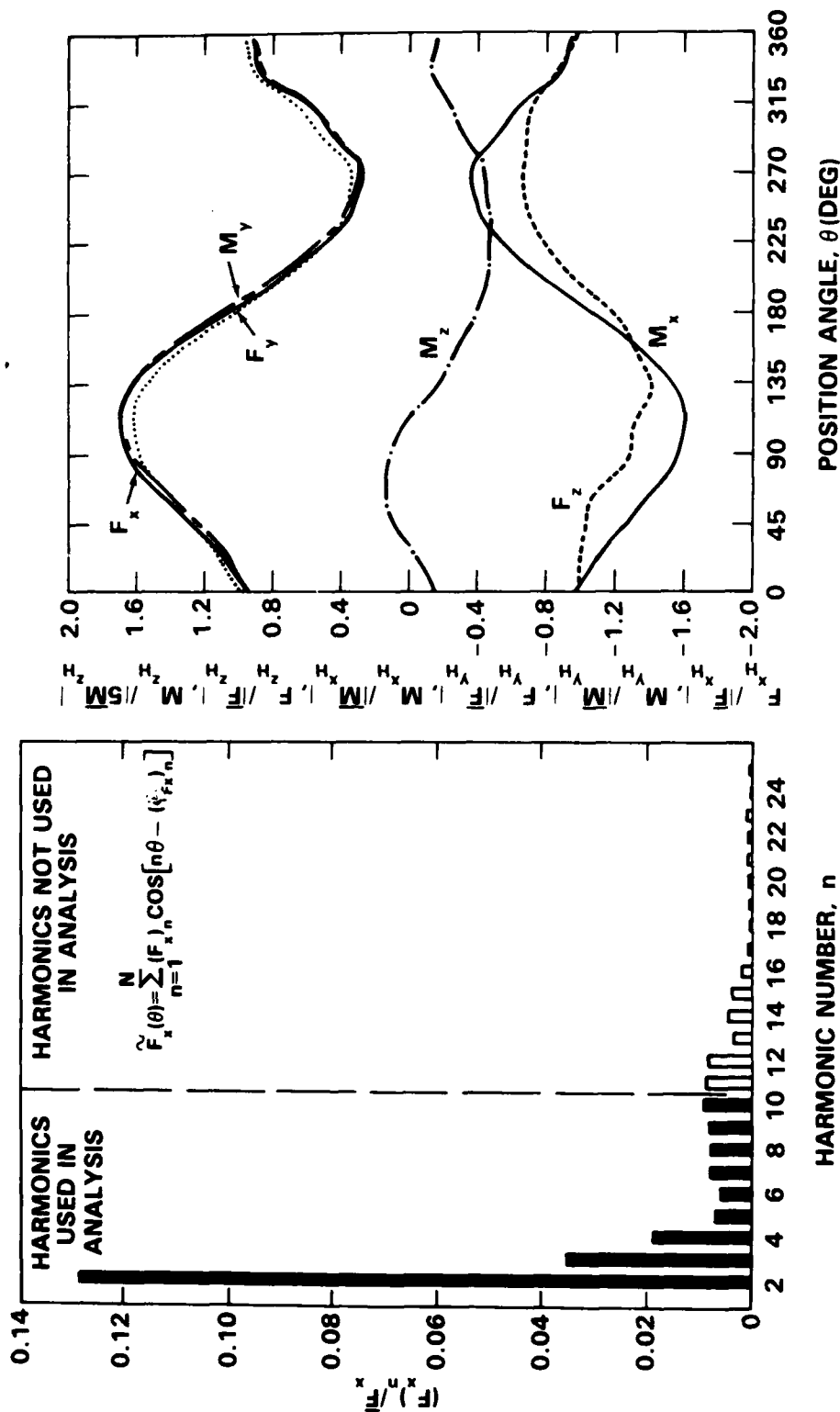


Figure 9 - Experimental Data Showing Extraneous Higher Harmonics

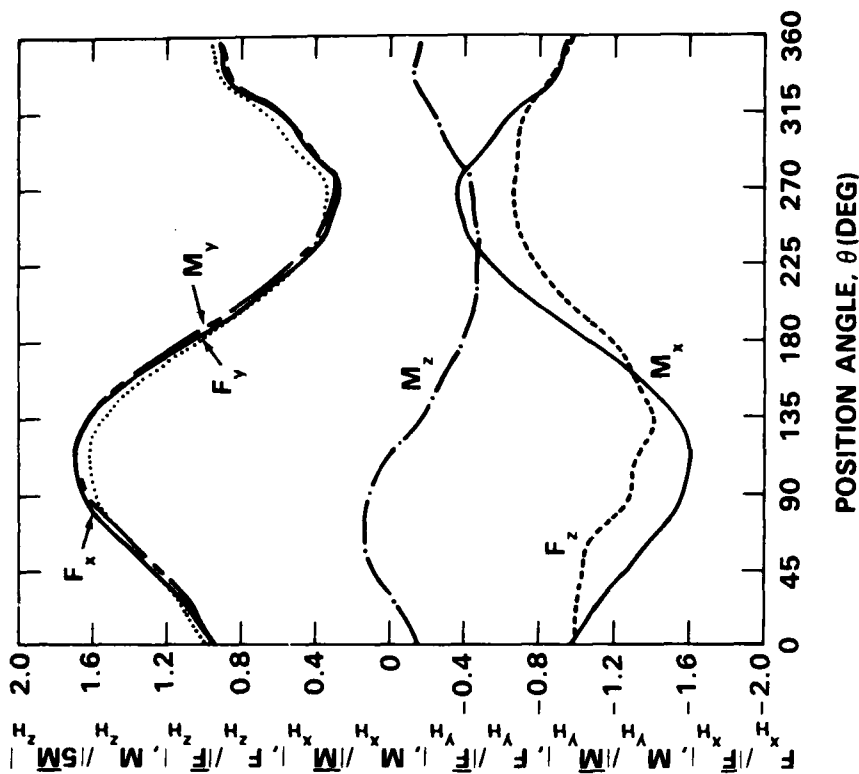


Figure 10 - Variation of Experimental Hydrodynamic Loads with Angular Position for Simulated Propulsion in Calm Water without Hull Pitching

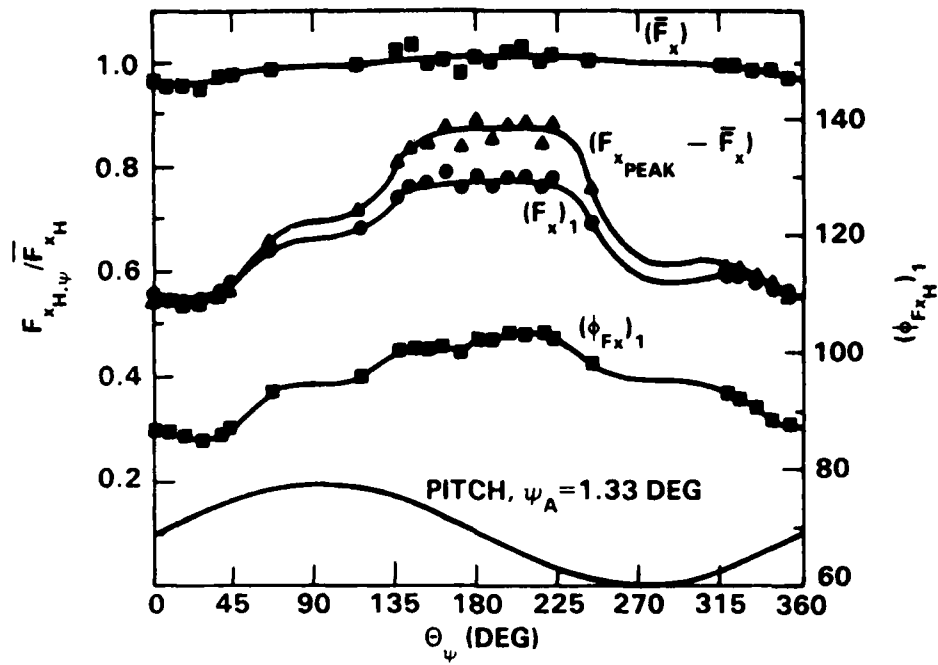
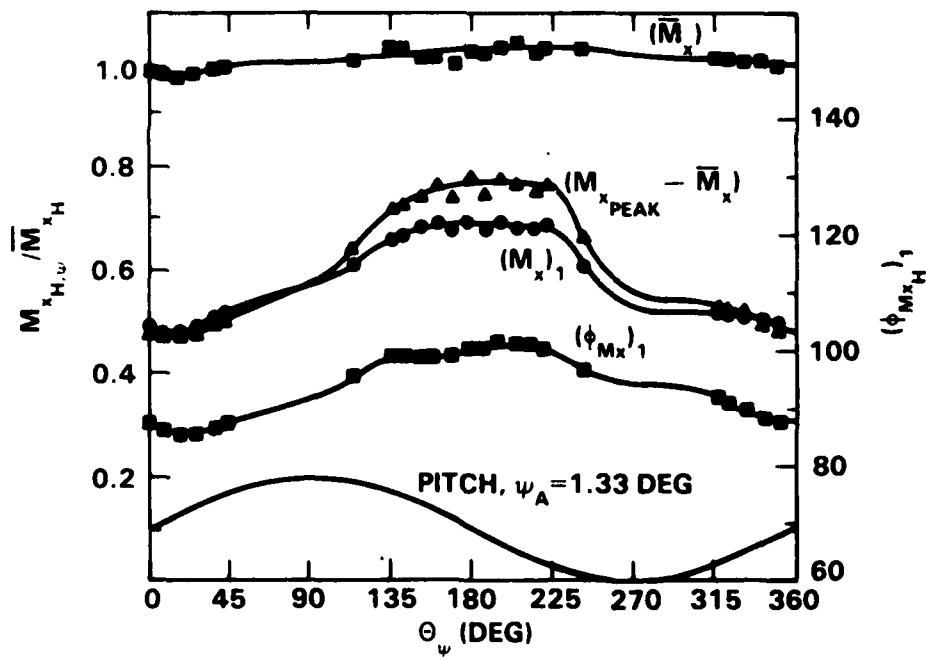
Figure 11a -  $F_x$  ComponentFigure 11b -  $M_x$  Component

Figure 11 - Variations of Hydrodynamic Loads with Hull Pitch Cycle for Operation in Calm Water

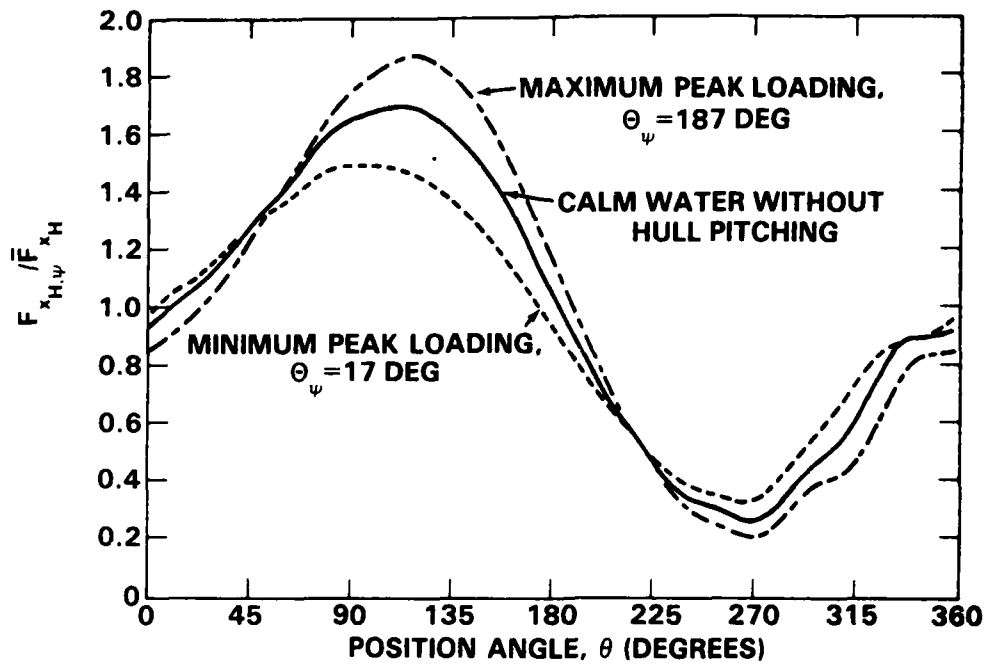


Figure 12 - Variation of  $F_x$  with Blade Angular Position for Hull Pitching in Calm Water Showing Portions of the Hull Pitch Cycle with Extremes of Peak Loading

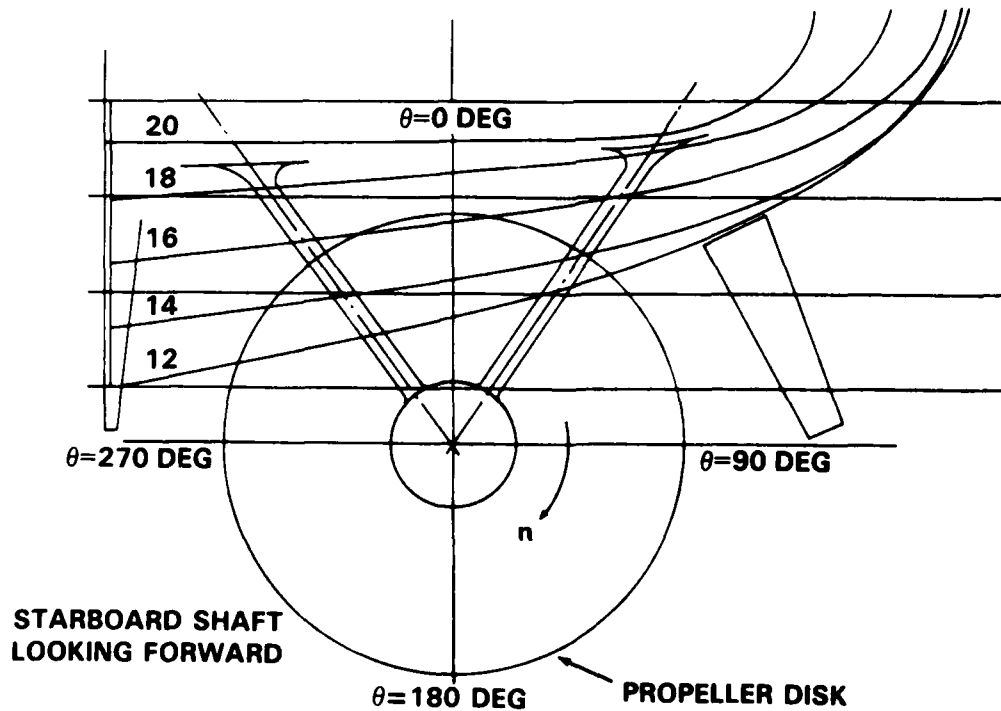
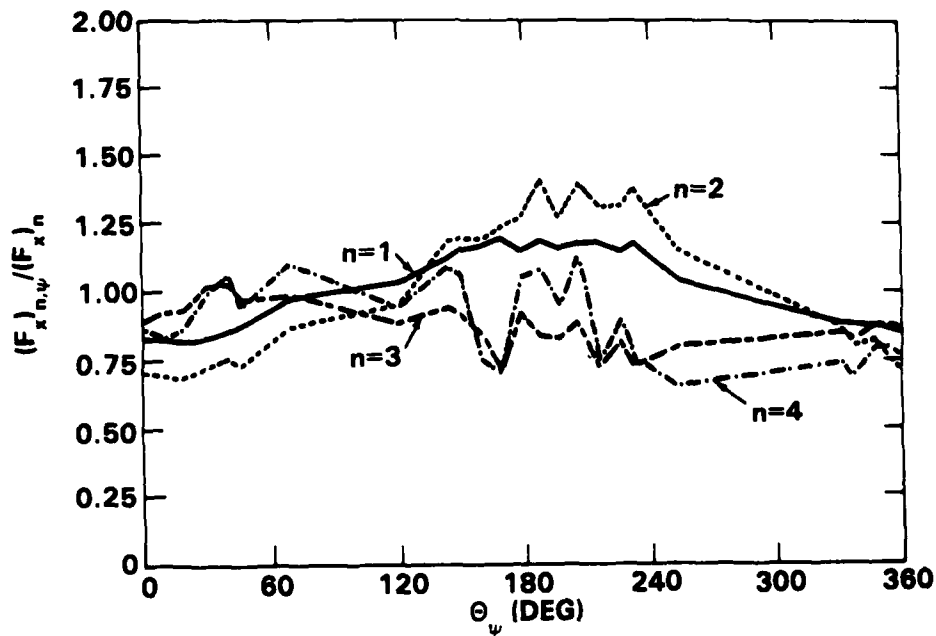
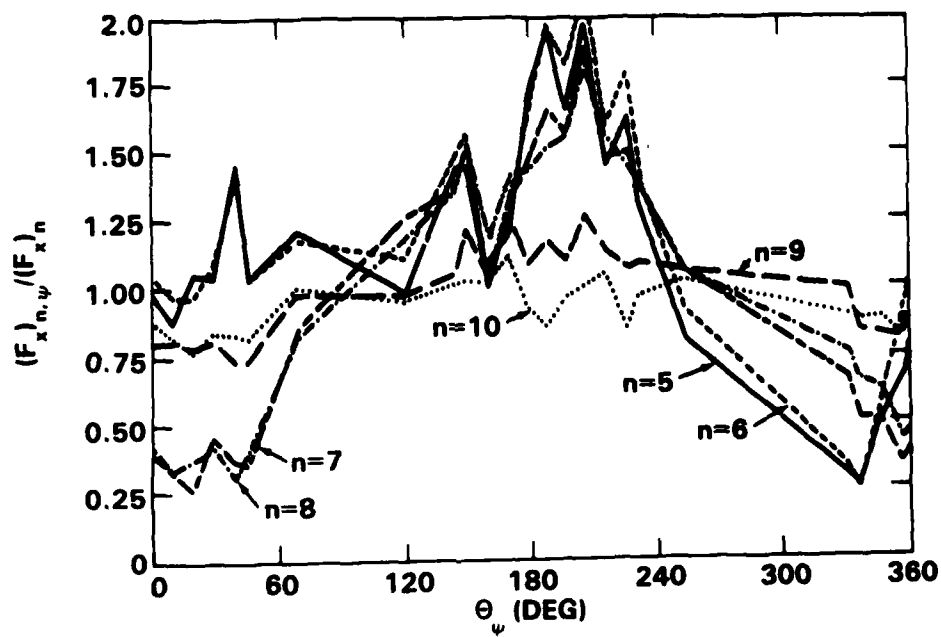


Figure 13 - Afterbody of Hull Showing Propeller Disk

Figure 14a - Harmonics  $n = 1$  to  $n = 4$ Figure 14b - Harmonics  $n = 5$  to  $n = 10$ Figure 14 - Variations of the Harmonic Amplitudes of  $F_x$   
During the Hull Pitch Cycle in Calm Water

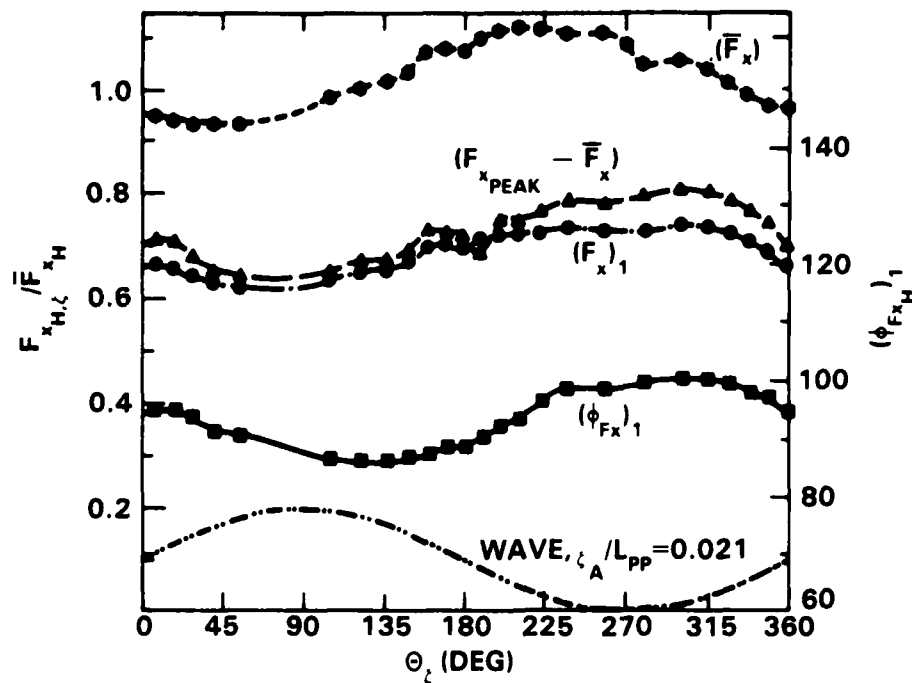
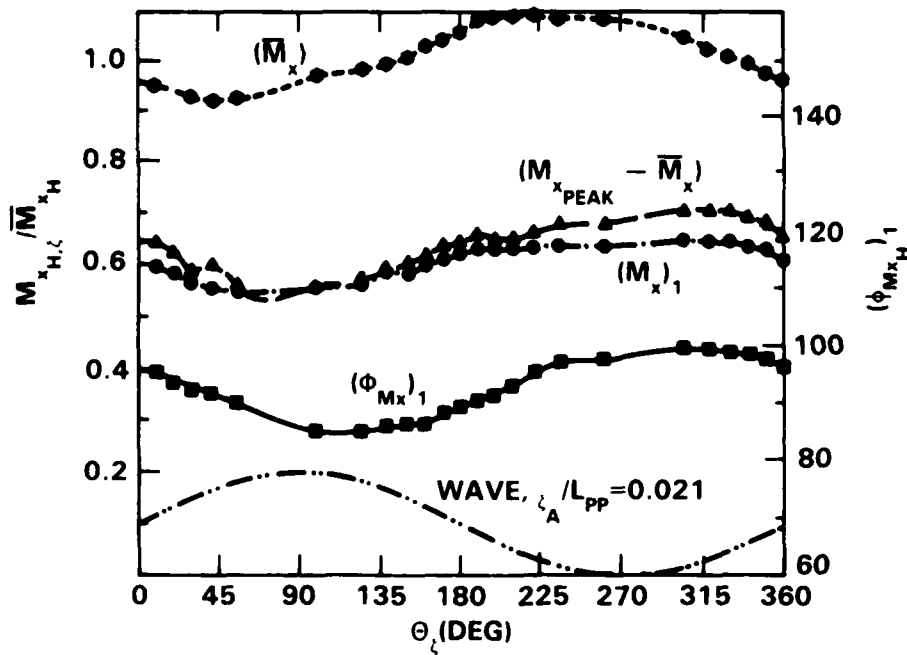
Figure 15a -  $F_x$  ComponentFigure 15b -  $M_x$  Component

Figure 15 - Variations of Hydrodynamic Loads with Location in Wave Cycle for Operation Without Hull Pitching

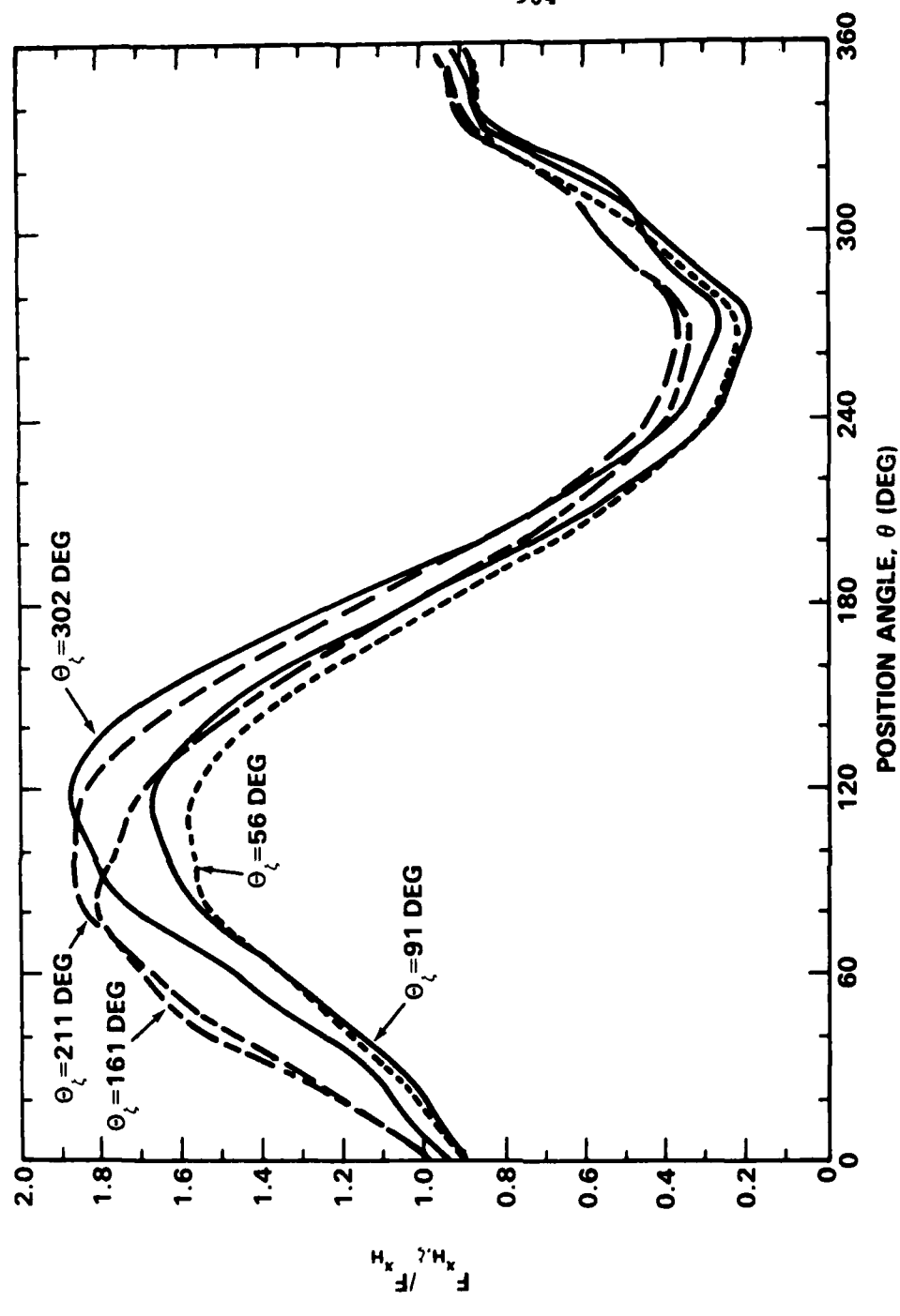
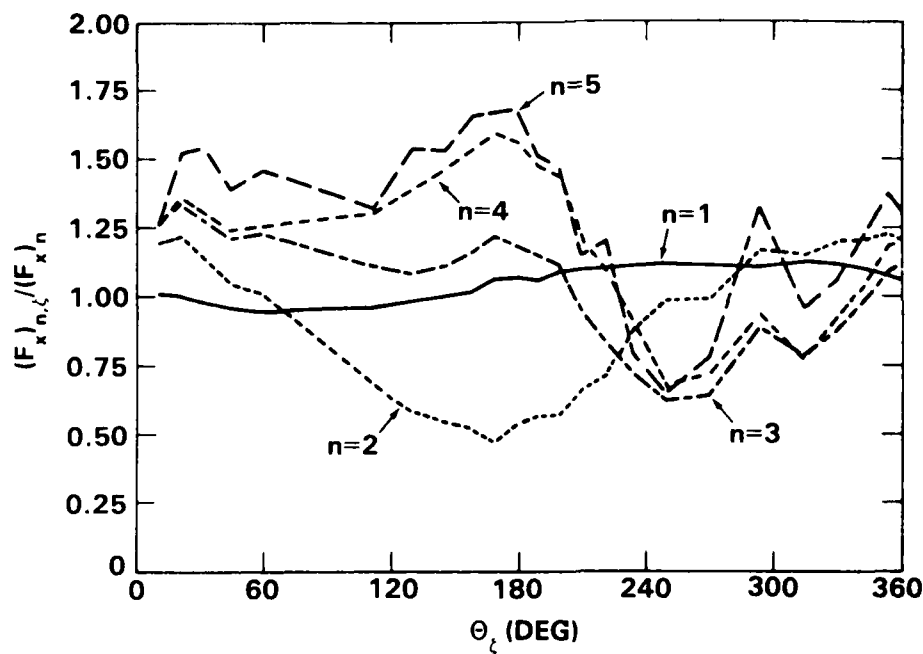
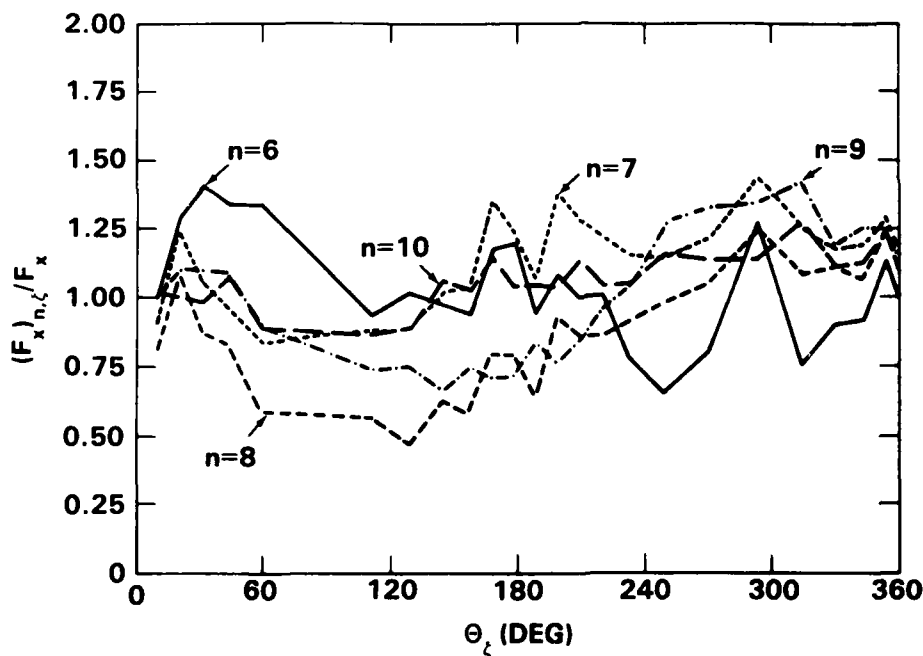


Figure 16 - Variation of  $F_x$  with Blade Angular Position for Operation in Waves Without Hull Pitching Showing Selected Locations in Wave Cycle Illustrating Extremes of Variation in Loading

Figure 17a - Harmonics  $n = 1$  to  $n = 5$ Figure 17b - Harmonics  $n = 6$  to  $n = 10$ Figure 17 - Variations of Harmonic Amplitudes of  $F_x$  During Wave Cycle Without Hull Pitching

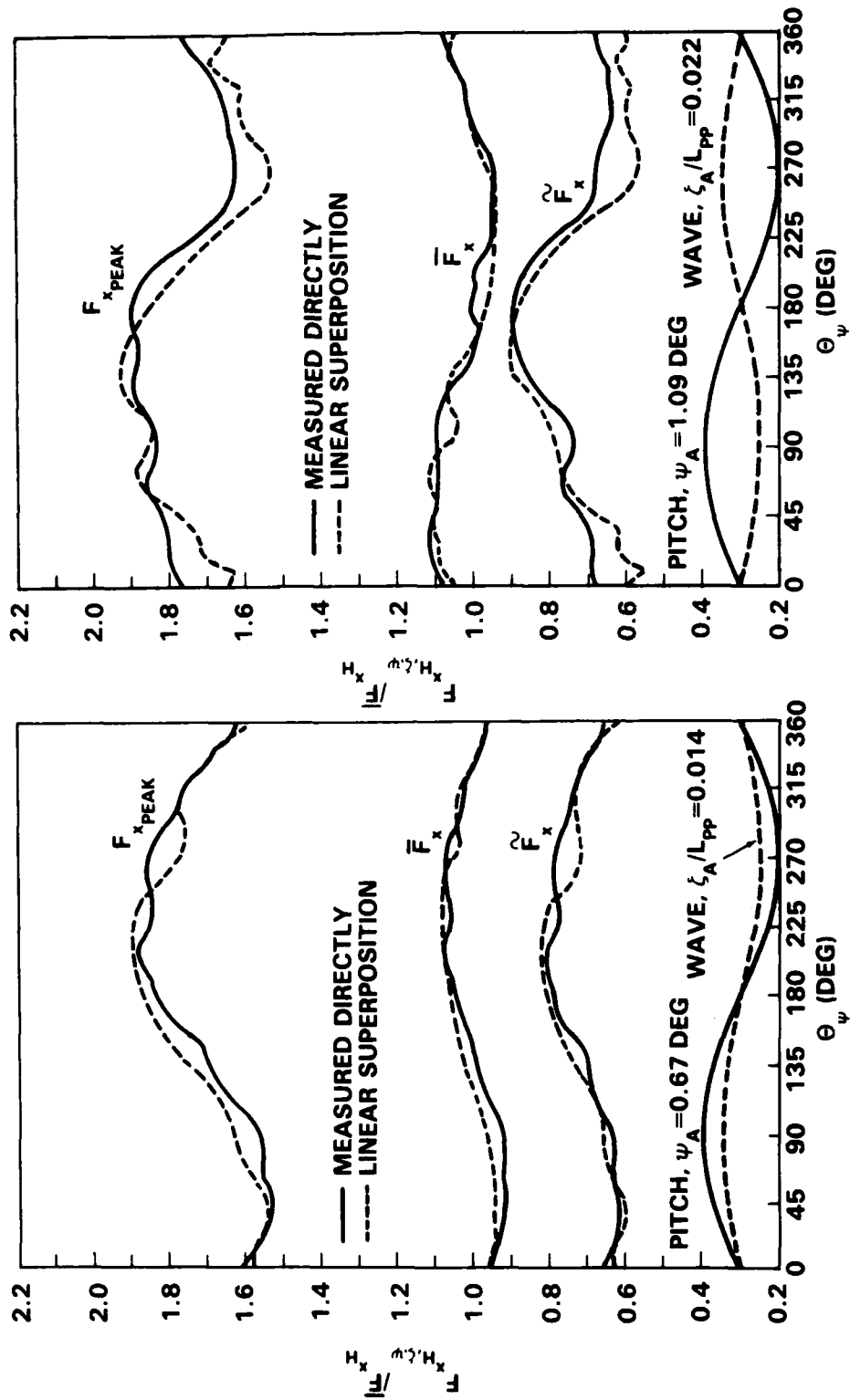
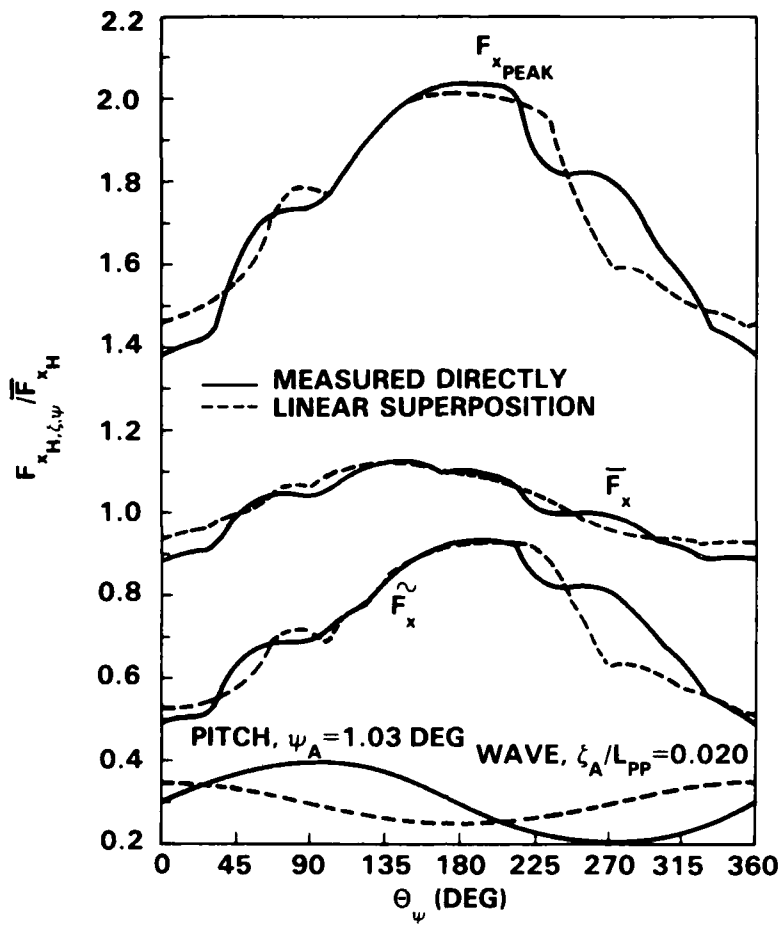
Figure 18a -  $\Phi_\zeta - \Phi_\psi = 0$ Figure 18b -  $\Phi_\zeta - \Phi_\psi = 180$ 

Figure 18 - Comparison of Hydrodynamic Blade Loads for Operation in Waves with Hull Pitching with Values Obtained from Linear Superposition of Increases due to Pitching Only and Increases Due to Waves Only



Figure 18c -  $\Phi_\xi - \Phi_\psi$  90 degrees

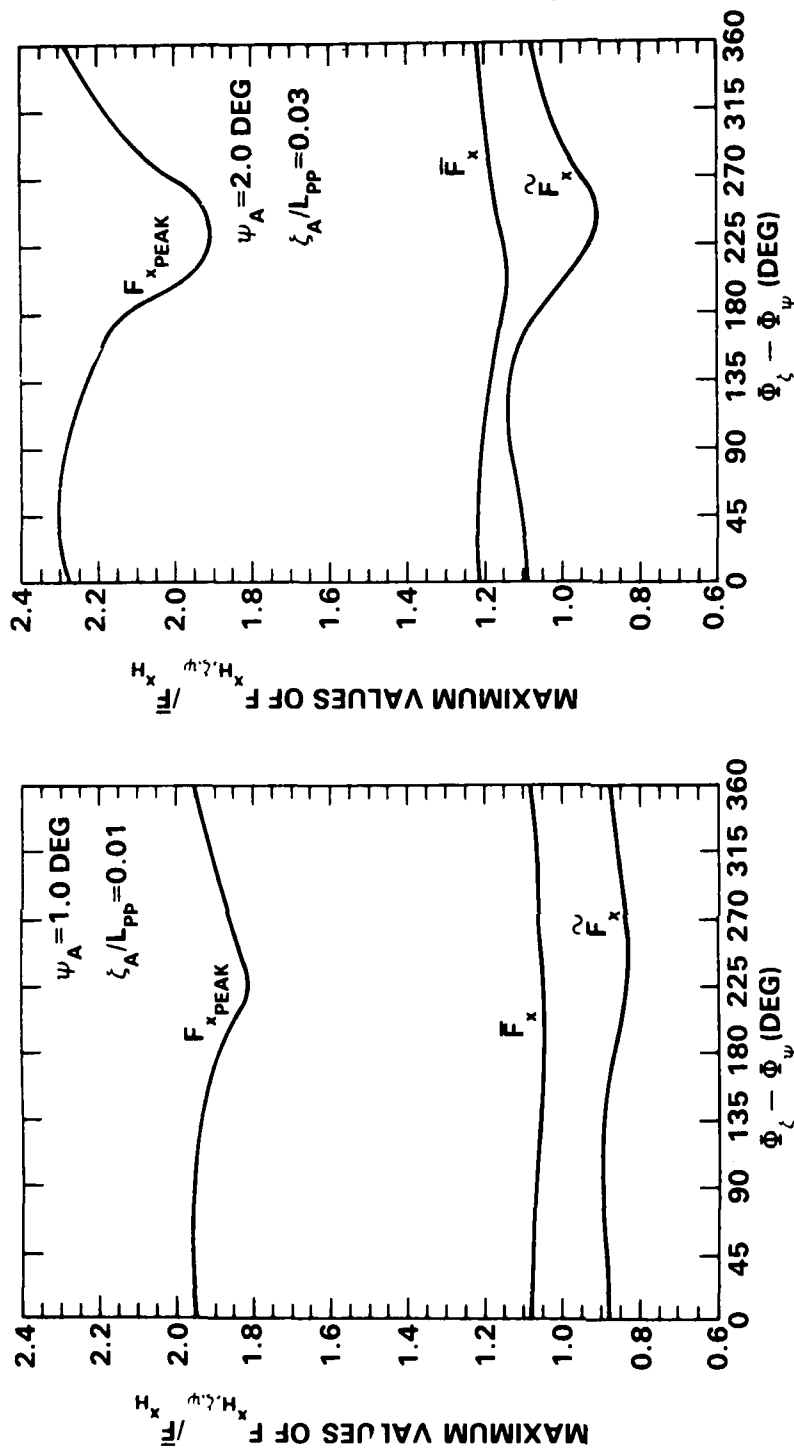
Figure 19a -  $\psi_A = 1.0$  deg,  $\zeta_A/L_{PP} = 0.01$ Figure 19b -  $\psi_A = 2.0$  deg,  $\zeta_A/L_{PP} = 0.03$ 

Figure 19- Maximum Absolute Values of Blade Loads for Various Values of  $\psi_A$ ,  $\zeta_A/L_{PP}$  and  $\Phi_\zeta - \Phi_\psi$  Derived from Linear Superposition of Increases due to Pitching Only and Increases due to Waves Only

Table 1 - Experimental Conditions

FOR ALL EXPERIMENTS:  $V_M = 3.58$  m/s (6.96 knots) $n_M = 18.80$  rps $J_V = 0.86$  $(1 - w_T) = 1.00^*$  $J_T = 0.86^*$ 

+		$\psi_A$ (DEG)	$f_\psi$ ( $H_z$ )	$f_\psi \sqrt{\frac{L_{PP}}{g}}$	$\zeta_A/L_{PP}$	$f_\zeta$ ( $H_z$ )	$L_W/L_{PP}$	$\phi_\zeta - \phi_\psi$
1	Calm Water without Hull Pitching	0	NA	NA	0	NA	NA	NA
2	Hull Pitching in Calm Water	1.33	0.80	2.63	0	NA	NA	NA
3	Waves without Hull Pitching	0	NA	NA	0.021	0.80	1.62	NA
4	Hull Pitching in Waves	0.67	0.80	2.63	0.014	0.80	1.62	0
5	Hull Pitching in Waves	1.09	0.80	2.63	0.022	0.80	1.62	180
6	Hull Pitching in Waves	1.03	0.80	2.63	0.020	0.80	1.62	90

\* Effective value without dynamometer boat

+ Number of Condition

Table 2 - Time-Average Hydrodynamic Loads for Operation in Calm Water without Hull Pitching\*

$\bar{F}_x$	32.64 N +	7.338 LB ++	$\bar{K}_{Fx}$	0.0383 ++
$\bar{M}_y$	2.463 N-m +	21.801 IN-LB ++	$\bar{K}_{My}$	0.0130 ++
$\bar{F}_y$	19.92 N +	4.480 LB ++	$\bar{K}_{Fy}$	0.0234 ++
$\bar{M}_x$	- 1.549 N-m +	- 13.712 IN-LB ++	$\bar{K}_{Mx}$	-0.0082 ++
$\bar{F}_z$	- 25.47 N	- 5.725 LB	$\bar{K}_{Fz}$	- 0.0299
$\bar{M}_z$	- 0.194 N-m	- 1.719 IN-LB	$\bar{K}_{Mz}$	- 0.0010

\* Condition 1 in Table 1

+ Effective value without dynamometer boat

++ Corrected for influence of dynamometer boat

Table 3 - Comparison of Measured  $F_x$  with Other Transom-Stern Configurations for Operation in Calm Water with Hull Pitching

MODEL HULL	PRESENT MODEL TWIN-SCREW	SINGLE SCREW	TWIN-SCREW
Reference	—	Boswell et al (1976a, 1976b)	Jessup et al (1977) Boswell et al (1978)
Amplitude of Pitching, $\psi_A$ (deg)	1.33	2.00	1.85
Period of Pitching $T_\psi$ (sec)	1.25	1.25	1.25
Model speed, $V_M$ (m/sec)	3.58	3.33	3.25
Maximum pitching velocity of propeller, $V_\psi/V_M$	0.082	0.145*	0.133
$(V_{10.7})_1/V$	0.199	0.156	0.123
$[(V_{10.7})_1 + V_\psi]/(V_{10.7})_1$	1.41	1.93*	2.08
$\tilde{F}_{x_{MAX,\psi}}/F_x$	0.89	0.59	0.60
$(F_{x_{MAX}} - F_x)/F_x$	0.72	0.38	0.42
$\tilde{F}_{x_{MAX,\psi}}/(F_{x_{MAX}} - F_x)$	1.24	1.55	1.43
$[\tilde{F}_{x_{MAX,\psi}} - (\tilde{F}_{x_{MAX}} - F_x)]/F_x$	0.17	0.21	0.18
$\tilde{F}_{x_{MAX,\psi}}/\tilde{F}_x$	1.03	1.03	1.10
$F_{x_{MAX}}/F_{x\psi}$	1.03	1.02	1.05
$\tilde{F}_{x_{MAX,\psi}}/(\tilde{F}_{x_{MAX}} - \tilde{F}_x) - 1$	0.59	0.59	0.40
$[(V_{10.7})_1 + V_\psi]/(V_{10.7})_1 - 1$			

The subscript  $\psi$  refers to operation in calm water with hull pitching, whereas absence of the subscript  $\psi$  refers to operation in calm water without hull pitching.

The subscript MAX with superscript — indicates the maximum absolute value of the time-average load per revolution.

The subscript MAX with no superscript indicates the maximum absolute value of the peak load per revolution.

The subscript MAX with superscript  $\sim$  indicates the maximum absolute value of the peak minus time-average load per revolution.

\* A numerical error was found in the values presented by Boswell et al (1976a, 1976b). This error has been corrected in the values presented in this Table.

Table 4 - Summary of Maximum Values of Hydrodynamic Loads for Operation in Calm Water with Hull Pitching

LOADING COMPONENT	$F_{x_H}$	$M_{y_H}$	$F_{y_H}$	$M_{x_H}$
$\bar{L}_{MAX,\psi}/\bar{L}$	1.03	1.04	1.04	1.05
$L_{MAX,\psi}/\bar{L}$	1.91	1.92	1.84	1.82
$L_{MAX}/\bar{L}$	1.71	1.70	1.62	1.61
$(L_{MAX,\psi} - \bar{L})/(L_{MAX} - \bar{L})$	1.28	1.31	1.35	1.34
$(L_{MAX,\psi} - L_{MAX})/\bar{L}$	0.20	0.22	0.22	0.21
$L_{MAX,\psi}/L_{MAX}$	1.12	1.13	1.14	1.13
$L_{MAX,\psi}/\bar{L}$	0.89	0.88	0.80	0.78
$\tilde{L}_{MAX,\psi}/(L_{MAX} - \bar{L})$	1.25	1.26	1.29	1.28
$(\tilde{L}_{MAX,\psi} - (L_{MAX} - \bar{L}))/\bar{L}$	0.18	0.18	0.18	0.17
$(L)_1 MAX,\psi/\bar{L}$	0.79	0.77	0.73	0.69
$(L)_1/\bar{L}$	0.66	0.64	0.59	0.59
$(L)_1 MAX,\psi/(L)_1$	1.20	1.20	1.24	1.17
$((L)_1 MAX,\psi - (L)_1)/\bar{L}$	0.12	0.12	0.13	0.10
$\bar{L}$ (N OR N-m)	32.65	2.46	19.93	1.55

$L$  refers to any one of the indicated loading components; i.e.,  $F_x$ ,  $M_y$ ,  $F_y$ ,  $M_x$ .

The subscript  $\psi$  refers to operation in calm water with hull pitching (Condition 2 in Table 1), whereas the absence of the subscript  $\psi$  refers to operation in calm water without hull pitching (Condition 1 in Table 1).

The subscript MAX with superscript  $-$  indicates the maximum absolute value of the time-average load per revolution.

The subscript MAX with no superscript indicates the maximum absolute value of the peak load per revolution.

The subscript MAX with superscript  $\sim$  indicates the maximum absolute value of the peak minus time-average load per revolution.

The subscript 1MAX indicates the maximum value of the first harmonic load per revolution.

Table 5 - Summary of Maximum Values of Hydrodynamic Loads for Operation in Waves without the Hull Pitching

LOADING COMPONENT	$F_{x_H}$	$M_{y_H}$	$F_{y_H}$	$M_{x_H}$
$L_{MAX,\zeta}/\bar{L}$	1.12	1.14	1.08	1.09
$L_{MAX,\zeta}/\bar{L}$	1.90	1.92	1.77	1.77
$L_{MAX}/\bar{L}$	1.71	1.70	1.62	1.61
$(L_{MAX,\zeta} - \bar{L})/(L_{MAX} - \bar{L})$	1.27	1.31	1.24	1.26
$(L_{MAX,\zeta} - L_{MAX})/\bar{L}$	0.19	0.22	0.15	0.16
$L_{MAX,\zeta}/L_{MAX}$	1.11	1.13	1.09	1.10
$L_{MAX,\zeta}/\bar{L}$	0.81	0.82	0.72	0.70
$\tilde{L}_{MAX,\zeta}/(L_{MAX} - \bar{L})$	1.14	1.17	1.16	1.15
$(\tilde{L}_{MAX,\zeta} - (L_{MAX} - \bar{L}))/\bar{L}$	0.10	0.12	0.10	0.09
$(L)_{1MAX,\zeta}/\bar{L}$	0.74	0.73	0.67	0.65
$(L)_1/\bar{L}$	0.66	0.64	0.59	0.59
$(L)_{1MAX,\zeta}/(L)_1$	1.12	1.14	1.14	1.10
$((L)_{1MAX,\zeta} - (L)_1)/\bar{L}$	0.08	0.09	0.08	0.06
$\bar{L}$ (N OR N-m)	32.65	2.46	19.93	1.55

$L$  refers to any one of the indicated loading components; i.e.,  $F_x$ ,  $M_y$ ,  $F_y$ ,  $M_x$ .

The subscript  $\zeta$  refers to operation in waves without hull pitching (Condition 3 in Table 1), whereas the absence of the subscript refers to operation in calm water without hull pitching (Condition 1 in Table 1).

The subscript MAX with superscript  $-$  indicates the maximum absolute value of the time-average load per revolution.

The subscript MAX with no superscript indicates the maximum absolute value of the peak load per revolution.

The subscript MAX with superscript  $\sim$  indicates the maximum absolute value of the peak minus time-average load per revolution.

The subscript 1MAX indicates the maximum value of the first harmonic load per revolution.

## Discussion

J.P. Breslin (Stevens Institute of Technology)

This experimental study reveals important modulations of shaft forces. I think that it would be important to examine a single-screw configuration in the same fashion. For such cases the basic blade-frequency force measurements in calm water without hull-motions wave revealed modulations in amplitude by factors as much as 3 presumably due to large-scale variations in wake flows across the propeller disk emanating perhaps from boundary-layer intermittancy. Would the authors comment on this aspect for this twin-screw configuration.

J.N. Newman (MIT)

This work provides a welcome opportunity for discussions between specialists in seakeeping and propulsion. A few obvious thoughts from the former viewpoint relate to the possible frequency dependence of these results. While the reduced frequency of the propeller blades is small, one may expect the oscillatory inflow to depend on the frequency of pitching and/or incident wavelength. Thus I would expect the quoted 50 percent reduction factor for the hull effect on pitching inflow to be dependent to some extent on the frequency. Similarly, the "Froude-Kriloff philosophy," where the horizontal component of orbital velocity is not affected by the hull, should be modified in short wavelengths owing to hull diffraction effects.

## Author's Reply

Stuart D. Jessup and Robert J. Boswell

Professor Breslin expressed interest in the modulation of periodic blade rate (shaft) forces in calm water without hull pitching and cited an example of a single-screw ship experiencing blade frequency modulations of as much as a factor of 3 in calm water without hull motions.

This effect was not investigated in experiments described in the present paper, and, unfortunately, the original raw experimental data no longer exist. However, the statistical variation of the data for operation in calm water without hull pitching show that at a given blade angular position 95 percent of the thrust data fall within a bandwidth of  $\pm 5$  percent of the time-average thrust (see Figures 5 and 8 of the paper). The blade-rate harmonic of thrust based on the statistical average of the data is approximately 2 percent of the time-average

thrust (see Figure 9 of the paper). Based on these statistical variations, it is possible, but appears unlikely, that the blade rate harmonic of thrust varied by as much as a factor of 3 for operation in calm water without hull pitching.

In the paper it was concluded that the relatively small, higher harmonic blade load amplitudes were very sensitive to the small changes in the wake pattern. This effect could lead to large modulations of the relatively small, blade-frequency shaft loads in calm water without hull motions. For transom stern ships in calm water without hull motions, periodic wake inflow could be caused by oscillatory flow about the shaft and struts. For these configurations the propeller generally operates outside the hull boundary layer, so it would not be significantly affected by hull boundary-layer intermittency. For single-screw merchant ships, the propeller is not outside the hull boundary layer, so significant influences of the hull boundary-layer intermittency would be expected.

Professor Newman discussed the possibility of a dependence of the blade-load modulations on frequency. He expects that the modulated inflow to the propeller would be dependent on the frequency of encounter of the waves or hull pitching frequency. The authors agree that this dependence may exist; however, the experiments described in the paper were conducted at only one representative frequency for the hull configuration under consideration. For design purposes this is probably sufficient.



# Analytical Prediction of Pressures and Forces on a Ship Hull Due to Cavitating Propellers

Paul Kaplan, James Bentson and Moshe Benatar  
Hydromechanics, Inc.

## ABSTRACT

An existing technique for determining free space pressures generated by a cavitating propeller operating in a ship is used as the basic input for determining the pressure distribution on various ship sections. The procedure involves establishing a boundary value problem on the ship section and the free surface, with appropriate conformal mapping operations that allow conversion of the problem to a more simplified boundary, viz. a flat plate and its adjacent free surface which represents the boundary for the lower half-plane. The integral equation for solution of this problem to determine the pressure is established and solved analytically, with evaluation carried out by means of digital computation in terms of the various physical parameters and those obtained from the mapping procedure.

The solution provides the pressure distribution at different sections on the hull, from which the total forces are then determined via integration with this strip theory approach. In addition the effects of different mode shapes of hull vibration are incorporated in order to obtain generalized forces for determining hull vibration responses. Illustrations of results are given for a representative naval auxiliary vessel.

The effect of different section shapes and dimensions in establishing body solid boundary factors (relative to the free space pressure) is also demonstrated. An extension of the basic analysis is applied to the problem of a ship section with adjacent rigid boundaries on the free surface similar to the case of particular cavitation tunnel test facilities, thereby providing a method of evaluating boundary effects of laboratory test facilities relative to full scale flow conditions.

## INTRODUCTION

During the past 25 years extensive studies have been carried out, both theoretically and experimentally, relating to the bearing forces acting on a propeller in a ship wake as well as determining the free

space hydrodynamic pressure generated by such a propeller in that operating mode. While most of these studies were initially concerned with propellers for which cavitation was not present, the occurrence of cavitation on the propeller has led to free space pressures that are an order of magnitude larger than those associated with the non-cavitating propeller. The occurrence of cavitation is usually present in a limited angular region about the upright (i.e. 12 o'clock) position of the propeller blade as it encounters a wake field that varies significantly in that region. This large pressure due to cavitation results from the rapid growth and collapse of the cavity volume which begins in the region of the blade tips.

In view of the importance of this effect of cavitation which leads to these high pressures, and the interest by designers in various propeller modifications that could result in reduced tip clearance and changes in the local hull shape in proximity to the propeller, it is important to have a method that could predict the magnitude of the pressures as well as the forces acting on the ship hull due to the effects of the cavitation that may occur on the propellers under those conditions. Some work has been previously published (Kaplan et al, 1979) that allows determination of the vibratory hydrodynamic pressures arising from propeller cavitation, and that work has demonstrated a fair degree of success in prediction and correlation with a number of experimental measurements (both model and full scale). This particular tool can be used as a basic element to determine the extent of possible vibratory problems associated with design variations of propeller-hull form configurations for different applications.

The method of (Kaplan et al, 1979) is primarily concerned with determining the basic free space pressures associated with the occurrence of cavitation. What is important for further practical utility would be a method that allowed accurate determination of the pressure distribution on various sections of a ship hull due to these cavitating propellers. The usual procedure has been to multiply the free space pressure by a factor of 2, reflecting the influence of a large flat boundary. Since all ship sections do not necessarily have such a characteristic, an appropriate analysis should be made to determine the proper pressure distribution on a ship section.

In addition to the determination of pressure per se, it is recognized that any vibration analysis would require determining the total forces acting on the ship hull due to the propeller-induced pressures. There are a number of different ways in which this can be done at present, either by solution of a diffraction problem as in the work of (Breslin and Eng, 1965) or by use of the reciprocity relations derived by (Vorus, 1974). Another possibility would be to integrate the pressure distribution along each section, if that information is available. Regardless of which way is considered for determining the force by any of the methods discussed above, an extensive degree of analysis and/or computation is necessary in order to determine the total forces with the present state-of-the-art.

The present paper describes a technique for determining the pressure distribution at various ship sections as a function of the

ship section geometry, using information on the free space pressure field due to a cavitating propeller in a wake. Another element of this work is a simple determination of the total force on different ship sections, from which the entire vibratory force can be evaluated. A description of the procedures that are used to obtain all of these results is given in the following sections of this paper.

#### FREE SPACE PRESSURES, INCLUDING CAVITATION EFFECTS

Since the present work applies and extends the procedures developed by (Kaplan et al, 1979), some of the basic concepts used in that particular study are described here. The procedure in (Kaplan et al, 1979) initially makes use of an existing computer program and analysis (Tsakonas et al, 1976, 1977) developed at Davidson Laboratory to predict the blade forces acting on a non-cavitating propeller operating in a ship wake. The information on the radial distribution of blade forces from (Tsakonas et al, 1976) is used to establish values of local camber and angle of attack distributions along the propeller span. These quantities, which establish local propeller blade section inflow velocity, cavitation index, etc., are used to evaluate the cavitation quantities appropriate to a particular propeller and wake at each propeller section of interest by use of a two-dimensional quasi-steady model of cavity flow (Geurst and Verbrugh, 1959). The cavitation quantities of interest in this case are the section force coefficients ( $C_L$ ,  $C_m$ , etc.) and the local cavity area for each section, which are found for conditions appropriate to partial cavitating flow ( $\ell/c < 1$ , where  $\ell$  = cavity length and  $c$  = chord length), supercavitating flow ( $\ell/c > 1$ ), and the important "transition" range between these two cavitation regions.

With the basic cavitation properties described above, the analysis of (Kaplan et al, 1979) establishes a general representation of the velocity potential and hydrodynamic pressure field associated with a time-varying cavity on a propeller blade. The expressions contain terms associated with the effect of changing thickness and loading of the propeller, as well as the important source-like contribution associated with the changing volume of the cavity on the propeller (obtained in terms of the distribution of cavity sectional area along the span of each propeller blade). The total free space pressure at any point is then found by the sum of the terms corresponding to the cavitation effect (cavity source effect and loading) as well as the effects of the non-cavitating propeller found from (Tsakonas et al, 1977). In most practical cases the non-cavitating propeller contribution is essentially negligible in comparison with the contributions arising from cavitation.

The expression for the field pressure due to the cavity effect on the propeller is given in terms of variables related to the coordinate system shown in Figure 1, and is given by

$$p_c = \frac{\rho f \Omega}{4\pi} \int_{r_c(\theta)}^{r_o} \left\{ \frac{1}{R^3} \frac{\partial A_c}{\partial \theta} \left[ \bar{U}x - \Omega r_p \left( 1 + \frac{1}{2r} \frac{\partial \ell}{\partial \theta} \right) \cdot \sin \left[ \theta + \sigma_s - \phi - \frac{(c-\ell)}{2r} \right] \right] \right. \\ \left. + \frac{\Omega}{R} \frac{\partial^2 A_c}{\partial c^2} \right\} dr \quad (1)$$

In this expression  $R$  is the distance from any blade element to the field point;  $\bar{U}$  is the mean axial velocity averaged over the propeller disc;  $r$  is the radial coordinate along the propeller blade;  $A_c$  is the cavity area;  $\Omega$  is the propeller angular velocity;  $\sigma_s$  is the skew angle of the blade. The radiated field pressure due to the cavity can be seen to contain sources with strength proportional to  $\partial^2 A_c / \partial t^2$  and dipoles (axial and transverse) with strength proportional to  $\partial A_c / \partial t$ , together with a dependence on the cavity length and its variation with time.

The field pressure due to the change in loading arising from cavitation is expressed by

$$p_i = - \frac{1}{4\pi} \int_{r_c}^{r_o} \frac{\partial}{\partial n} \left( \frac{1}{R} \right) \Delta L_{cav}(r,t) dr \quad (2)$$

where the integration is carried out over the cavitated region on the blade. The quantity  $\Delta L_{cav}$  is the change in lift of each radial section of the propeller blade due to cavitation, and the operation  $\partial/\partial n$  represents the normal derivative relative to the helicoidal surface. The various operations to obtain the lift due to cavitation, the angle of attack, force coefficients, cavity characteristics, etc. used in the evaluation of Eqns. (1) and (2) are described by (Kaplan et al, 1979).

The values of pressure due to cavity geometry variations (from Eqn. (1)) and pressure due to load changes due to cavitation (from Eqn. (2)) are added together to produce the total pressure due to cavitation for a single blade. This is evaluated as a function of time (or blade angle) during a single propeller rotation, and the resulting time history is then Fourier analyzed in terms of the shaft rate and higher harmonics. With proper allowance for relative blade phasing the total effect for the entire propeller is obtained by summing all the harmonic components, which results in final output pressure at the propeller blade rate and its harmonics.

The results obtained by this method (Kaplan et al, 1979) showed good agreement for measured point pressures on a ship hull, for both model and full scale conditions. The model test results were obtained in European research establishment water tunnels using simulated wakes and dummy stern regions, while full scale data was obtained from direct measurements at sea. In view of the good agreement with measurements exhibited by (Kaplan et al, 1979), which includes

the important higher harmonics of blade rate, the basic theory used there appears to be a valid representation of the important effects occurring due to propeller blade cavitation.

#### METHOD OF ANALYSIS - PRESSURE DISTRIBUTION ON SHIP SECTIONS

With knowledge of the free space pressure due to the propeller it is necessary to determine the effect of different ship sections on the actual pressures experienced on the ship hull boundary, i.e. the effect of the ship hull in changing the magnitude of the incident free space pressure. The basic method of analysis used here assumes that a strip theory method is applicable, with the effect of the ship hull section determined by means of a two-dimensional analysis. This procedure is considered to be applicable to the present case since the rate of spatial decay of the pressure field is primarily due to the changing volume of the cavity, which acts as a source whose rate of spatial variation is much smaller than that due to loading variations that has been the primary influence for non-cavitated propellers.

The effect of the ship hull section is evaluated by assuming that the sections can be represented in terms of a multi-parameter conformal mapping that generalizes the Lewis form method (Lewis, 1929) for ship sections. In the present case the incident flow field is that due to the free space pressure field of the propeller, which is evaluated in the plane of the ship section of interest. The method of formulating the boundary value problem appropriate to this type of approach is given below.

#### Boundary Value Problem

The boundary value problem is established in terms of the pressure as the dependent variable, with the pressure determined by a linear operation on the velocity potential, i.e.

$$p = -\rho_f \left( \frac{\partial}{\partial t} + \bar{U} \frac{\partial}{\partial x} \right) \phi \quad (3)$$

where  $\phi$  = the velocity potential and the pressure is expressed with respect to atmospheric pressure as a reference. On that basis the boundary value problem for any ship section is expressed as shown in Figure 2, where the pressure is assumed to be zero on the free surface due to the high frequencies associated with propeller vibratory effects. The requirement that the normal derivative of the pressure is zero on the section boundary follows from the requirement that  $\partial\phi/\partial n = 0$  on that boundary; since pressure is defined in terms of linear differentiation operations on the potential, this boundary relationship then follows.

The problem can be simplified further by decomposing the pressure field into a sum of contributions due to the incident flow field  $p_p$  due to the propeller free space pressure,  $p_i$  due to the image with respect to the free surface, and the additional pressure  $p'$  repre-

senting the effects of the ship section

$$p = p_p + p_i + p' \quad (4)$$

The image pressure is selected so that  $p_p + p_i = 0$  on the free surface. This is easily accomplished using the representation in Eqns. (1) and (2) (Kaplan et al, 1979) with a simple change in the definition of the distance  $R$  for the image terms. The resulting boundary value problem on the free surface and on the ship section boundary is given in Figure 2 in terms of values of the pressure  $p'$ , i.e.

$$p' = 0 \quad , \text{ on free surface} \quad (5)$$

and

$$\frac{\partial p'}{\partial n} = - \left( \frac{\partial p_p}{\partial n} + \frac{\partial p_i}{\partial n} \right), \text{ on the section boundary} \quad (6)$$

The normal derivative of the propeller free space pressure and its image are known functions determined from the properties of the pressure field due to the cavitating propeller, which can be determined from the work of (Kaplan et al, 1979).

This boundary value problem can be put into a simpler form by means of conformal transformations from a ship section to a unit radius semicircle and from there to a flat plate. In this manner the various boundary values of the pressure and its derivatives are also transformed in such a way that the problem complexity is reduced and the boundary is simplified.

Introducing the complex potential  $W$ , whose real part is taken as the pressure, the complex derivative of  $W$  in the physical body plane defined by  $Z = y + iz$  is given by

$$\frac{dW}{dZ} = \frac{\partial p}{\partial y} - i \frac{\partial p}{\partial z} \quad (7)$$

The flow in the body plane is then transformed to the circle plane ( $\zeta$ - plane) by means of a conformal mapping defined by

$$Z = a_1 \left[ \zeta + \sum_{n=1}^{\infty} a_{n+1} \zeta^{(-2n+1)} \right] \quad (8)$$

The mapping function from the body plane to the circle plane defined by Eqn. (8) requires  $a_{n+1}$  to be found in order to relate the coordinates in the body plane to points along the semicircle. The coefficient  $a_1$  is selected as a normalizing factor so that the transformation goes from the body to a semicircle of unit radius.

The complex pressure gradient determined from the complex potential  $W$  is then transformed into the circle plane by means of the operation

$$\frac{dW}{d\zeta} = \frac{dW}{dZ} \frac{dZ}{d\zeta} \quad (9)$$

With  $\zeta = \xi + i\eta = e^{-i\phi}$  on the unit circle, Eqn. (9) then becomes

$$\frac{dW}{d\zeta} = \frac{\partial p}{\partial \xi} - i \frac{\partial p}{\partial \eta} = a_1 \left( \frac{\partial p}{\partial y} - i \frac{\partial p}{\partial z} \right) \left[ 1 - \sum_{n=1}^{\infty} (2n-1) a_{n+1} e^{i2n\phi} \right] \quad (10)$$

which leads to

$$\frac{\partial p}{\partial \xi} = a_1 \frac{\partial p}{\partial y} \left[ 1 - \sum_{n=1}^{\infty} (2n-1) a_{n+1} \cos 2n\phi \right] - a_1 \frac{\partial p}{\partial z} \sum_{n=1}^{\infty} (2n-1) a_{n+1} \sin 2n\phi \quad (11)$$

and

$$\frac{\partial p}{\partial \eta} = a_1 \frac{\partial p}{\partial z} \left[ 1 - \sum_{n=1}^{\infty} (2n-1) a_{n+1} \cos 2n\phi \right] + a_1 \frac{\partial p}{\partial y} \sum_{n=1}^{\infty} (2n-1) a_{n+1} \sin 2n\phi \quad (12)$$

As shown in Figure 3, the mapping then proceeds from the unit semicircle to a flat plate ( $\omega$ -plane) by means of the transformation

$$\omega = \frac{1}{2} \left( \zeta + \frac{1}{\zeta} \right) \quad (13)$$

where  $\omega = \alpha + i\beta$ . The pressure gradient relations are then

$$\frac{dW}{d\omega} = \frac{\partial p}{\partial \alpha} - i \frac{\partial p}{\partial \beta} = \frac{dW}{d\zeta} \frac{d\zeta}{d\omega} \quad (14)$$

where

$$\frac{d\zeta}{d\omega} = 1 \pm \frac{\omega}{\sqrt{\omega^2 - 1}} \quad (15)$$

Since in conformal mapping procedures the normal to the surface is preserved, the pressure gradient  $\partial p / \partial \beta$  normal to the flat plate corresponds to the transformed value of the normal derivative of the pressure on the original body section. For the lower surface of the flat plate, which corresponds to the body section boundary, this leads to

$$\frac{\partial p}{\partial \beta} = \frac{\partial p}{\partial \eta} - \frac{\partial p}{\partial \xi} \frac{\alpha}{\sqrt{1-\alpha^2}} \quad (16)$$

The boundary value problem is then shown in Figure 3 as a mixed boundary value problem for the pressure  $p'$  along the entire real axis of the  $\omega$ -plane. All that is needed for establishing the values of the normal derivative along the plate boundary are the values of the  $a_n$  quantities in the transformation to the circle plane given by Eqn. (8). Those values are found by a method based upon a least squares-sequential iterative procedure (von Kerczek and Tuck, 1969) for which a computer program was established. The program considered 7 values of the  $a_{n+1}$  coefficients (plus the value of  $a_1$ ) for proper representation of ship sections of practical interest.

## INTEGRAL EQUATION - FORMULATION AND SOLUTION

The boundary value problem on the flat plate plane ( $w$ -plane) can be solved by establishing an integral equation by the use of Green's theorem. The Green's function is selected as

$$G(u, v; \alpha, \beta) = \ln \sqrt{(u-\alpha)^2 + (v-\beta)^2} - \ln \sqrt{(u-\alpha)^2 + (v+\beta)^2} \quad (17)$$

for which

$$G(u, 0; \alpha, \beta) = 0 \quad (18)$$

$$G_v(u, 0; \alpha, \beta) = \frac{-2\beta}{(u-\alpha)^2 + \beta^2} \quad (19)$$

Applying Green's theorem to a contour along the real axis with a large circular arc in the lower half-plane and small arcs about the points  $-1$ , and on the limit as the small arcs  $\rightarrow 0$  and the radius of the large circle  $\rightarrow \infty$ , this leads to

$$\begin{aligned} p'(\alpha, \beta) &= \frac{1}{2\pi} \int_{\text{real axis}} (G p'_v - p' G_v) du \\ &= \frac{1}{2\pi} \int_{-1}^1 p'(u, 0) \frac{\partial}{\partial \beta} \ln \left[ (u-\alpha)^2 + \beta^2 \right] du \end{aligned} \quad (20)$$

which is the Poisson formula for the half plane.

Since  $p'_\beta$  is known on the plate, differentiate with respect to  $\beta$  leading to

$$\begin{aligned} p'_\beta(\alpha, \beta) &= \frac{1}{2\pi} \int_{-1}^1 p'(u, 0) \frac{\partial^2}{\partial \beta^2} \ln \left[ (u-\alpha)^2 + \beta^2 \right] du \\ &= -\frac{1}{2\pi} \frac{\partial^2}{\partial \alpha^2} \int_{-1}^1 p'(u) \ln \left[ (u-\alpha)^2 + \beta^2 \right] du \end{aligned} \quad (21)$$

by means of the Laplace equation. Integrating both sides with respect to  $\alpha$  (from  $-1$  up to  $\alpha$ ), and letting  $\beta \rightarrow 0$  while taking appropriate limits and values, leads to

$$c + \int_{-1}^{\alpha} f(s) ds = \frac{1}{\pi} \int_{-1}^1 \frac{p'(u)}{u-\alpha} du \quad (22)$$

where  $f(\alpha)$  is the known value of  $p'_\beta$  along the flat plate. As discussed previously that value is found at any ship section from knowledge of the propeller and free surface image pressure gradients and the mapping coefficients (multiparameter transformation from  $Z$  to  $\zeta$ -planes), with the basic expressions shown in Eqns. (11), (12) and



(16).

The singular integral equation in Eqn. (22) is essentially the same as that in (Kaplan and Sargent, 1972) and the solution is also similar. With the requirement of the solution being bounded at both ends ( $\pm 1$ ), it is given by

$$p'(\alpha) = -\frac{1}{\pi} \sqrt{1-\alpha^2} \int_{-1}^1 \frac{\int_{-1}^u f(s) ds}{\sqrt{1-u^2} (u-\alpha)} du \quad (23)$$

as indicated by the methods in (Muskhelishvili, 1963).

The solution in Eqn. (23) is evaluated by defining new variables, i.e.  $u = \cos \theta$ ,  $\alpha = \cos \theta_0$ , and it is assumed that the integral  $\int_{-1}^u f(s) ds$  can be expanded into a Fourier series form in terms of cosines, viz.

$$\int_{-1}^u f(s) ds = \sum_{n=1}^{\infty} A_n \cos n\theta \quad (24)$$

Substituting the new variables and the Fourier expression of Eqn. (24) leads to

$$p'(\alpha) = -\sum_{n=1}^{\infty} A_n \sin n\theta_0 \quad (25)$$

where  $\theta_0 = \cos^{-1} \alpha$ , by use of the Glauert integrals of airfoil theory (Glauert, 1937).

The pressure distribution along the ship section boundary of interest is found by adding the contribution from Eqn. (25) together with the free space pressure of the cavitating propeller as well as its free surface image. The computational procedure considers the separate sine and cosine harmonic terms at blade rate and higher harmonics from each constituent term, adding all contributions to each oscillatory function and then determining the resulting amplitude and phase of the final total pressure signal on the boundary.

The pressure distribution is determined at points along the section boundary that correspond to points that are equally spaced in the unit circle in the  $\zeta$ -plane, i.e. equally spaced angles. This procedure assists in the determination of the Fourier cosine coefficients in the expansion of Eqn. (24). The location of the points on the section in the  $Z$ -plane is readily determined by use of Eqn. (8), which establishes the locations at which the pressures and pressure gradients from the cavitating propeller and its free surface image are to be calculated.

The total lateral and vertical force on each section are determined by integrating the pressure along the boundary, with appropriate account of directions, separate sine and cosine components for each harmonic of blade rate, etc. With knowledge of the sectional forces obtained in this manner the total forces are obtained by integrating the section forces along the length of the hull, which is the con-

ventional procedure employed in strip theory analyses. Devoting the local sectional forces as  $F'_Z(x)$  and  $F'_Y(x)$  for the vertical and lateral forces, the total vertical and lateral forces on the ship due to the pressures arising from a cavitating propeller are represented by

$$F_Z = \int F'_Z(x) dx, \quad F_Y = \int F'_Y(x) dx \quad (26)$$

The integrations in Eqn. (26) extend over a length region for which appreciable pressures and forces exist on the ship, which is determined either computationally, or by establishing a cut-off level, or arbitrarily to some location such as up to midships at which the pressures and forces will generally be negligible. When considering the force information to determine forced vibratory response of a ship, by use of a modal method of analysis as an example (McGoldrick, 1960), the total force integral is weighted by a modal weighting function, viz. the normal mode shape  $X_i(x)$  for the  $i^{\text{th}}$  normal mode. The generalized modal force is then represented by

$$F_{Z_i} = \int F'_Z(x) X_i(x) dx \quad (27)$$

as a typical example, with appropriate consideration of the particular blade rate harmonic force values being used in such expressions. The use of a strip theory approach, with modal weighting from response analysis, has been used in various ship dynamic problems such as slamming response analysis (Kaplan and Sargent, 1972) and has proven to be a useful method for response predictions.

#### APPLICATION AND DISCUSSION OF RESULTS

In order to illustrate the nature of the results obtained from the preceding analysis, some representative calculations are carried out. The basic computational procedures that are necessary for the case of a cavitating propeller for a particular ship are described in block diagram form in Figures 4 and 5. The procedure in Figure 4 represents the various steps associated with the calculation of the pressure field arising from a particular propeller in a specified wake field, as described by (Kaplan et al, 1979). The diagram in Figure 5 essentially describes the procedures developed in the present paper.

The particular case illustrated here considers the auxiliary naval vessel designated as AO-177, which is a single screw tanker vessel. The propeller has 7 blades, with 45 deg. skew angle, with a 21 ft. diameter. This ship has been studied in a number of special investigations, with consideration of the occurrence of cavitation on the propeller blades due to the particular ship wake, e.g. (Bentson and Kaplan, 1981 a,b). Model tests have been carried out by David Taylor Naval Ship Research and Development Center for the basic ship to measure its wake field, as well as for the case where special flow-modifying fins were installed on the ship, with that data provided as

input information that is used for the present calculations.

For the present purpose the particular wake, propeller design, etc. of the AO-177 is used only as a means of illustrating the nature of results for representative ship sections when using the present analysis. The various representative ship sections used for illustrating the present results are not necessarily those of the AO-177, although the flow field from which the propeller cavitation disturbing flows arise does correspond to that particular ship. The first case illustrated is that of a flat plate with a width of 60 ft. which is located in the free surface, where that section is assumed to be located at a distance of 5 ft. aft of the propeller plane (i.e.  $x=5$  ft.). The wake field is that corresponding to the AO-177 fitted with the fins.

Calculations were made to determine the free space pressure along this flat plate section, as well as using the methods of the present analysis to determine the actual pressure inclusive of all other flows that would satisfy the boundary conditions of the present problem. An important feature of the results is not necessarily the pressures per se, but the ratio of the pressure along the plate to that of the free space pressure at each point along the plate. The results of this computation are shown in Figure 6 illustrating the ratio of the pressure on the plate to the local free space pressure. Two curves are shown here in order to illustrate the accuracy of the results as a function of the number of points along the plate that are taken as input information for the integral equations. The differences due to the different number of points are more predominant in the region of the larger pressures, although the extent of such differences is not very significant. It can be seen by examination of Figure 6 that the pressure on the plate increases to a value of the order of 2.6 times the local free space pressure, with the values of the pressure falling off to zero at the ends of the plate as expected. The average pressure for this distribution was found by means of integration, and was found to be 1.94 as is also illustrated in Figure 6, with that value being close to the usual assumed value of the factor of 2 that is applied to free space pressures when determining pressure effects along a boundary.

While the results in Figure 6 are informative, that only illustrates information appropriate to a particular special case. Other results are described below which have different numerical values and provide a different interpretation for the effect of the interaction of a representative ship section and the incident flow from a cavitating propeller. Another case considers a flat plate section of 21.6 ft. width which is located in the free surface at the same position (i.e.  $x=5$  ft.) in the wake due to the AO-177 with fins. The ratio of the pressure to the local free space pressure due to the propeller along this plate is shown in Figure 7. It can be seen that this ratio has a maximum value of just under 1.4, with that maximum occurring near the plate center but slightly to port. This result illustrates the nature of the influence of the size of the plate relative to the disturbing flow field and/or the propeller.

Another application of the analysis considers an actual ship section taken from the AO-177, with that section being the profile corresponding to Station 19.5 on that vessel as illustrated in Figure 8. This section is essentially a shallow V-wedge shape, with the total lateral extent equal to 21.6 ft. Assuming that this particular section is located at the position corresponding to  $x=5$  ft. relative to the propeller, and with the wake the same as that of the AO-177 fitted with fins (the same case as for Figures 6 and 7), the ratio of the pressure to the free space pressure along this section is shown in Figure 9. In that situation the ratio reaches a maximum value of 2.0, with that maximum occurring somewhat to the starboard of the middle of the section. This result, when contrasted with that in Figure 7, illustrates the effects of the actual section shape as well as the influence of the proximity of the center of the wedge region relative to the propeller tip.

Another illustration considers the same section corresponding to Station 19.5 of the AO-177, with the propeller operating in the basic wake of that ship without any flow-modifying fins. The section is assumed to be located 6 ft. forward of the propeller plane ( $x=-6$  ft) and the results for the ratio of the pressure along the plate to that of the local free space pressure due to the propeller are shown in Figure 10. In that case the maximum value of this particular pressure ratio is 1.4, occurring somewhat to port of the center of the section.

All of the above results illustrate the effect of the size of the section as well as its shape in regard to determining the magnitude of the pressures along different ship sections. The so-called boundary factor that accounts for the influence of the body section results in an increase in the value of the free space pressure to some factor that ranges both above and below the number 2, with the particular maximum value dependent upon the nature of the lateral size extent of the section, the shape of the section, the nature of the distribution of the free space pressure, etc. In addition the requirement that the pressure goes to zero at the ends of the section at the free surface is also a significant aspect of the present analysis that will affect the magnitude of the pressure distribution acting on various ship sections. All of these features influence the resulting pressure distribution values, indicating the basic complexity of determining the pressures on different ship sections and reducing the significance of the use of simplified factors for prediction of propeller-induced pressures and forces.

#### EFFECT OF RIGID FREE SURFACE CONDITIONS

In the preceding analysis the mathematical problem was formulated with the boundary condition corresponding to  $p=0$  on the free surface. This particular boundary condition applies to the physical conditions corresponding to high frequencies, which is generally appropriate for the case of propeller-induced unsteady flows. There has been some previous analysis which considered the effects of different boundary

conditions on the free surface (Vorus, 1976), where that analysis was applied to noncavitating propellers and was concerned with the total force as well as the local force on a strip section of a semi-infinite flat plate.

Aside from the basic interest in the influence of the free surface boundary condition, the consideration of a rigid wall free surface condition is important because it is representative of the flow conditions associated with model test procedures for ships in specialized water tunnel facilities that simulate full scale operation. In that case the free surface region is covered by rigid plates whose extent laterally can generally be represented by employing the boundary conditions of a rigid wall out to  $-\infty$ . On that basis the boundary condition for the pressure would correspond to  $\partial p / \partial n = 0$  for the free surface as well as on the ship section boundary.

This problem can be analyzed by methods similar to that used for the case with a free surface boundary condition corresponding to  $p=0$  by introducing a special image flow that results in satisfying the condition  $\partial p / \partial z = 0$  on the free surface. This particular image is essentially the negative of the previous free surface image used for the earlier boundary condition, so that the total pressure can be represented by the expression

$$p = p_p + p_r + p' \quad (28)$$

where  $p_r$  = the pressure induced by the rigid wall image ( $p_r = -p_i$ , as defined previously). The resulting boundary value problem on the ship section and the free surface is given by

$$\frac{\partial p'}{\partial n} = 0, \text{ on the free surface} \quad (29)$$

$$\frac{\partial p'}{\partial n} = -\left( \frac{\partial p_p}{\partial n} + \frac{\partial p_r}{\partial n} \right), \text{ on the section boundary} \quad (30)$$

where the required normal derivatives can be found from the cavitating propeller and the appropriate image.

By carrying out the same mapping procedures to the  $\zeta$  and  $\omega$ -planes, the resulting boundary value problem in the  $\omega$ -plane is shown in Figure 11. This boundary value problem can be solved by the use of Green's theorem, with the Green's function selected as

$$G(u, v; \alpha, \beta) = \ln \sqrt{(u-\alpha)^2 + (v-\beta)^2} + \ln \sqrt{(u-\alpha)^2 + (v+\beta)^2} \quad (31)$$

for which

$$G(u, 0; \alpha, \beta) = 2 \ln \sqrt{(u-\alpha)^2 + \beta^2} \quad (32)$$

$$G_v(u, 0; \alpha, \beta) = 0 \quad (33)$$

By applying Green's theorem to the same type contour as was done previously, the basic solution for the pressure is given in terms of the values of the derivative  $p'_\beta$  on the plate, which is represented by the function  $g(\alpha)$ , in the form

$$p'(\alpha) = \frac{1}{\pi} \int_{-1}^1 g(u) \ln|u-\alpha| du \quad (34)$$

The value of  $g(\alpha)$  is determined from the same basic relations as in Eqn. (16) applied to the combined pressure values found from the propeller and the rigid wall image. With the expression for the value of  $p'$  on the flat plate given above by Eqn. (34), this value is then transformed back to the appropriate points along the actual ship section boundary in the body plane. To this value is added the pressure values arising from the propeller and the rigid wall image, resulting in the total pressure distribution as defined by Eqn. (28).

The above procedure describes the method for determining the pressure distribution on the ship section when considering a rigid wall free surface boundary condition rather than the conditions that are appropriate to the real physical case in full scale. Numerical evaluation for particular cases (which is not done here) will provide information on the pressure distribution appropriate to both sets of boundary conditions on the free surface, so that comparisons can then be made between the different results that arise from each set of conditions. In that way it is possible to evaluate the influence of the boundary effects applied in laboratory test facilities that do not employ an actual free surface, so that the influence of these boundary effects can be determined relative to what would be present for full scale flow conditions.

#### CONCLUSION

The method of analysis described herein provides a technique for determining the pressure distribution along different ship sections due to a cavitating propeller, with appropriate account of the effects of the free surface boundary condition and the influence of the body shape. The major results are presented for the case wherein the free surface boundary condition corresponding to zero pressure is imposed, with the resulting pressure distribution illustrating the manner in which the pressure reduces toward zero at the intersection of the section with the free surface. The figures illustrating the results demonstrate the difference between a more precise method of solution and the simplified methods that are usually applied in engineering practice.

As a result of the analysis presented here, a straightforward procedure is then available for determining pressure distributions, local forces at various sections of a ship, and also the total force due to the disturbing flows arising from a cavitating propeller, including a procedure for modal weighting for use in vibratory analysis. The analytical tool described here is recommended for further practical applications to various problems of interest involving propeller-excited vibrations.

The analysis in the case of a rigid wall free surface boundary condition provides an entirely different type of solution that describes the pressure distribution under such a boundary condition.

Since that type of boundary condition corresponds to the physical characteristics associated with particular types of model test facilities used for determining propeller vibratory pressures on ship hull sections, the analysis shown herein provides a means of representing the effects due to an imposed propeller pressure field. Comparisons can be made between the results predicted with the rigid wall boundary condition vis-a-vis those from the zero pressure free surface condition as a means of illustrating the effects of model test facility boundary influence on measured pressures on ship hulls obtained from tests in such facilities.

It is recommended that extended calculations be carried out by these different approaches in order to provide guidance that will assist in interpreting the relation of model test values to the actual full scale pressures on ships with cavitating propellers. In view of the present use of such test facilities for predicting propeller-induced vibratory pressures and their associated effects, as well as possible new facilities being built with the same basic testing concept, such an investigation has practical importance.

#### REFERENCES

- Bentson, J. and P. Kaplan (1981). Prediction of the propeller excited Fluctuating pressures and hull surface forces acting on the AO-177 fleet oiler, Hydromechanics, Inc. Rpt. No. 81-24.
- Bentson, J. and P. Kaplan (1981). Prediction of the propeller excited fluctuating pressures and hull surface forces acting on the AO-177 fleet oiler equipped with flow-improving fins, Hydromechanics, Inc. Rpt. No. 81-36.
- Breslin, J. and K. Eng (1965). A method for computing propeller-induced vibratory forces on ships, Stevens Inst. of Tech., (also DTMB Rpt. 2002, Aug. 1965).
- Geurst, J. A. and P.J. Verbrugh (1959). A note on camber effects of a partially cavitated hydrofoil, Intl. Shipbuilding Prog., Vol. 6, No. 61.
- Glauert, H. (1937). Elements of Aerofoil and Airscrew Theory, Cambridge Univ. Press, Cambridge, Eng., p. 92.
- Kaplan, P. and T.P.Sargent (1972). Further studies of computer simulation of slamming and other wave-induced vibratory structural loadings on ships in waves, Ship Structure Comm. Rpt. SSC-231.
- Kaplan, P., J. Bentson, and J.P.Breslin (1979). Theoretical Analysis of propeller radiated pressure and blade forces due to cavitation, Symp. on Propeller Induced Ship Vibration, RINA, London, England.
- Lewis, F.M. (1929). The inertia of the water surrounding a vibrating ship, Trans. SNAME, Vol. 37.
- McGoldrick, R.T. (1960). Ship vibration, DTMB Rpt. No. 1451.
- Tsakonas, S., W.R.Jacobs and M.R. Ali (1976). Documentation of

- a computer program for the pressure distribution, forces and moments on ship propellers in hull wakes, Davidson Lab. Rpt. SIT-DL 1863 (in four vols.).
- Tsakonas, S., W.R.Jacobs and M.R.Ali (1977). Documentation for the pressure field generated by a propeller in a variable inflow, Davidson Lab.Rpt. SIT-DL-77-1910 (in two vols.).
- von Kerczek, C. and E.O.Tuck (1969). The representation of ship hulls by conformal mapping functions, J. of Ship Research, Vol. 13, No. 4.
- Vorus, W.S. (1974). A method for analyzing the propeller-induced vibratory forces acting on the surface of a ship stern, Trans. SNAME, Vol. 18.
- Vorus, W.S. (1976). Calculation of propeller-induced vibratory hull forces, force distributions, and pressures; free-surface effects, J. of Ship Research, Vol. 20, No. 2.



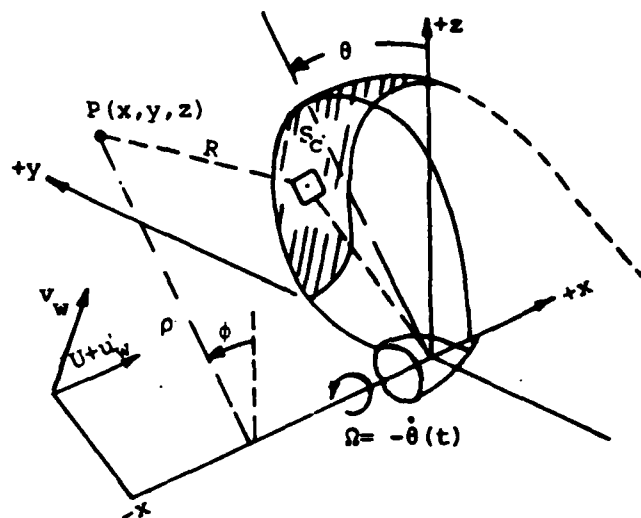


Figure 1 Coordinate definition

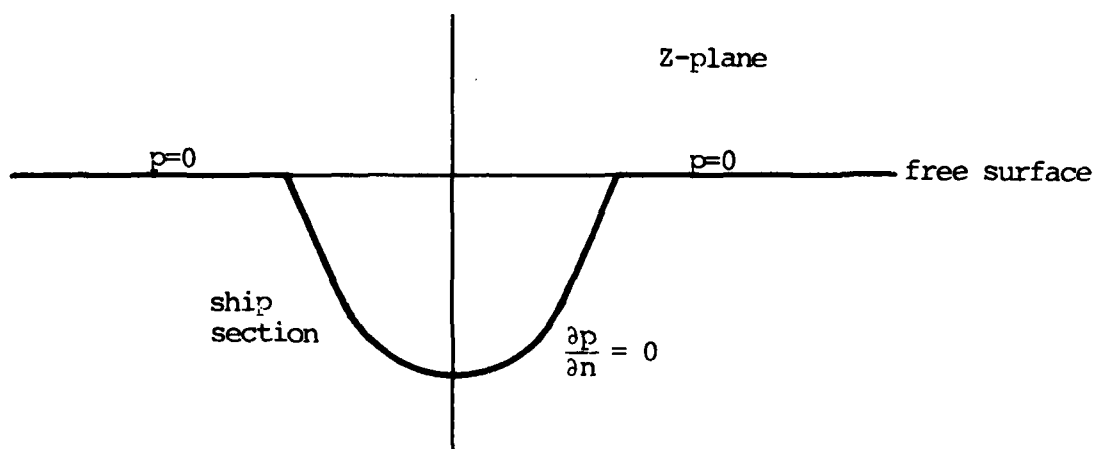


Figure 2 Boundary value problem in physical plane

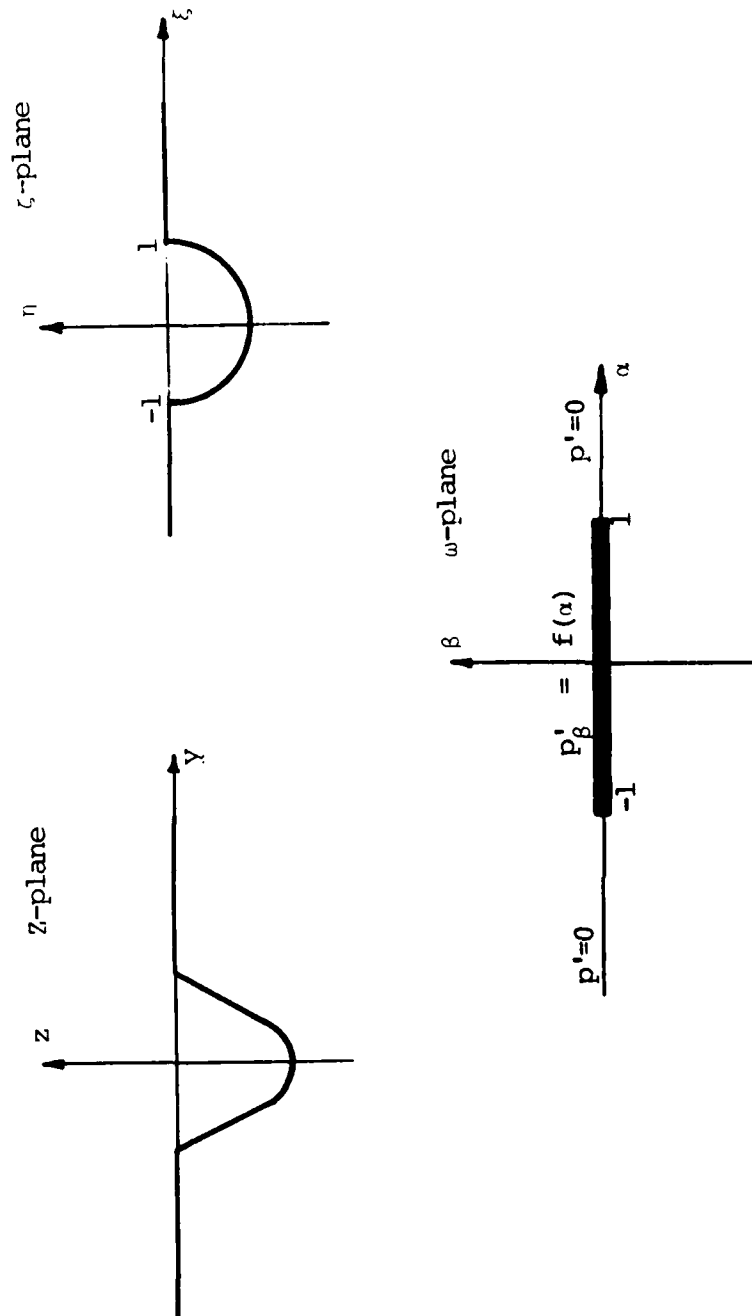


Figure 3 Conformal mappings and mixed boundary value problem

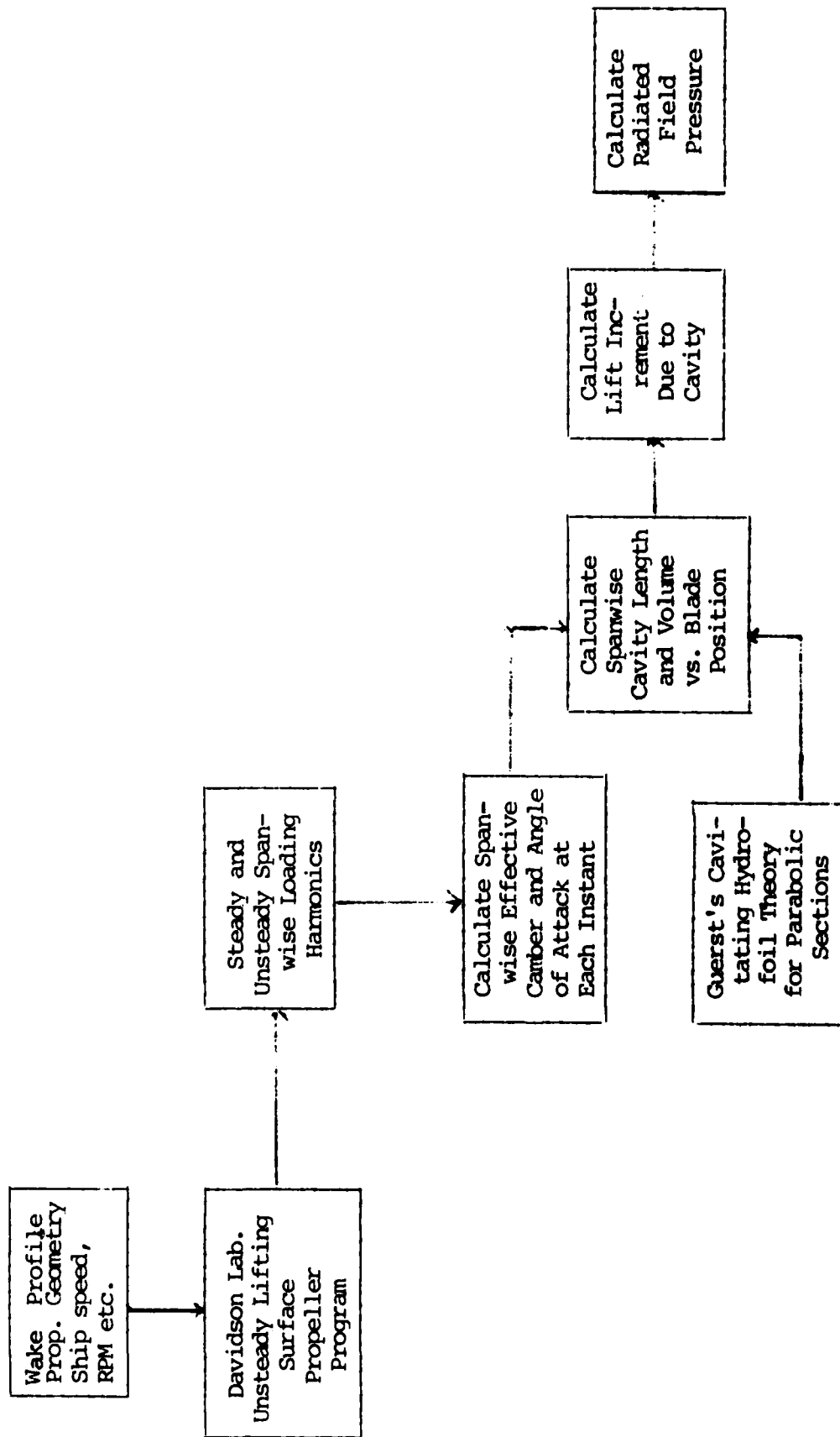


Figure 4 Computational procedure for cavitation program

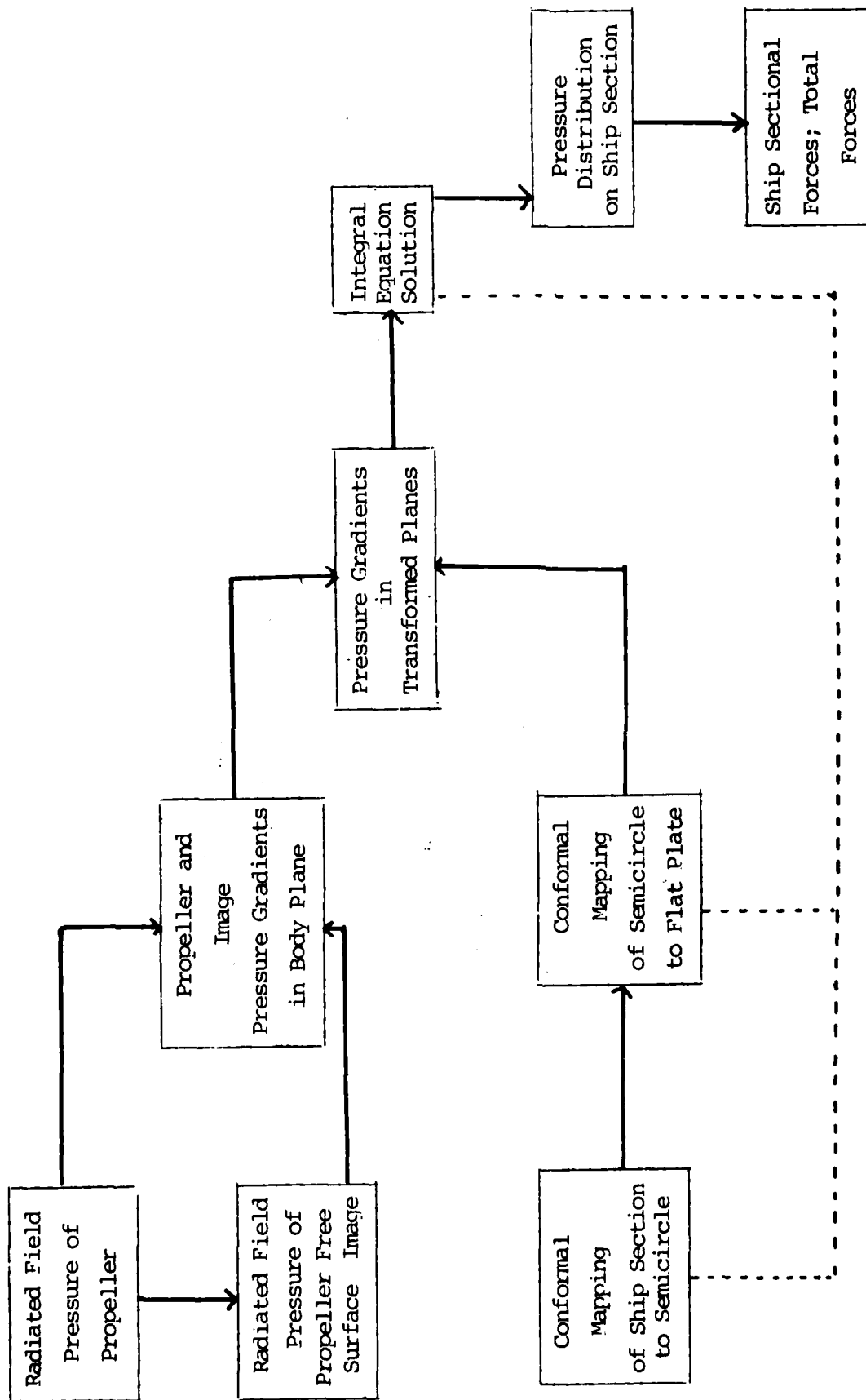


Figure 5 Computational procedure for determining pressure distribution and forces

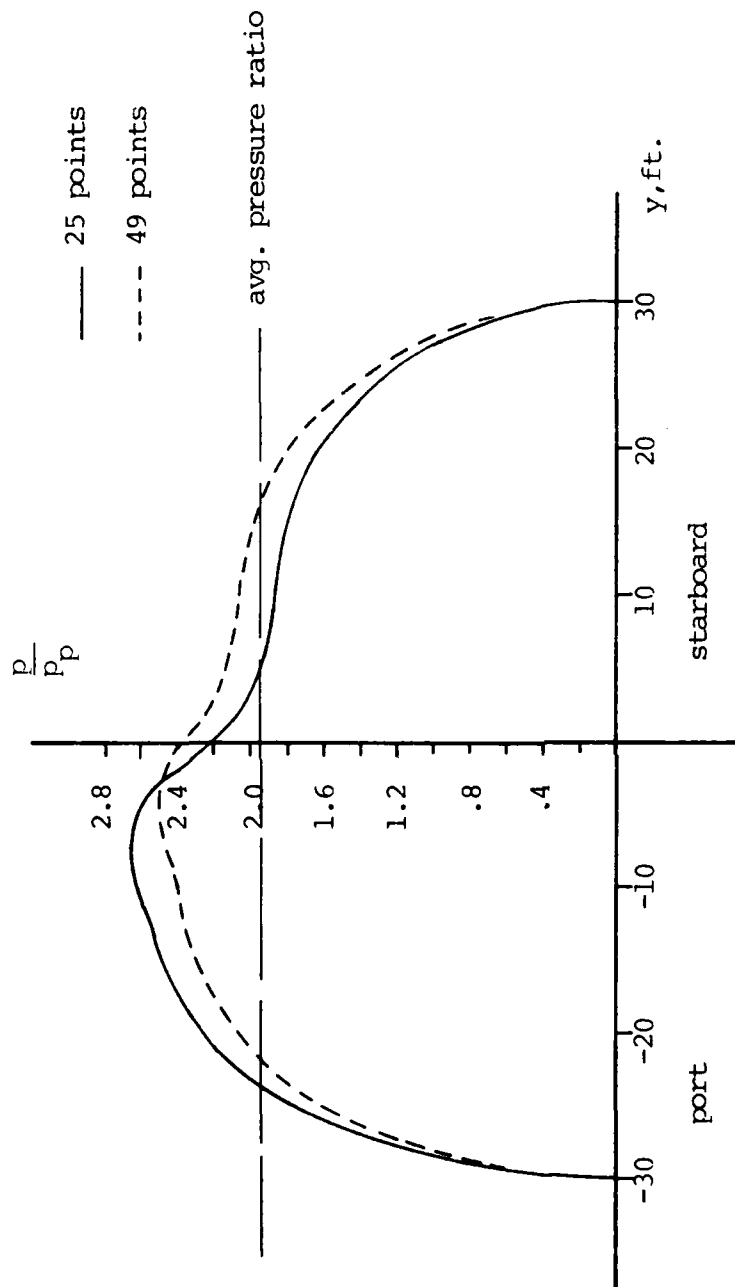


Figure 6 Variation of pressure relative to local propeller free space pressure on 60 ft. width flat plate, flow field due to AO-177 propeller in wake with fins,  $x=5$  ft. location

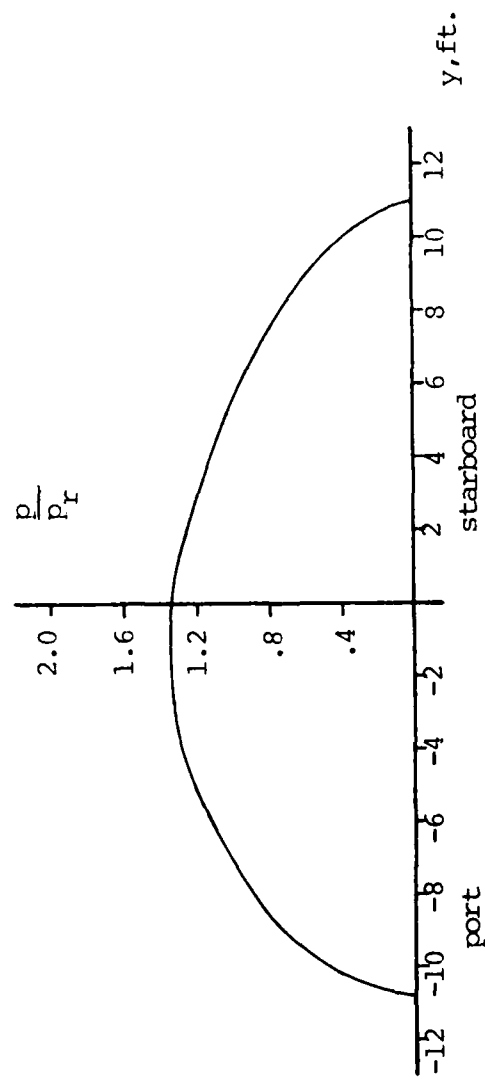


Figure 7 Variation of pressure relative to local propeller free space pressure on 21.6 ft. width plate plate, flow field due to AO-177 propeller in wake with fins,  $x=5$  ft. location

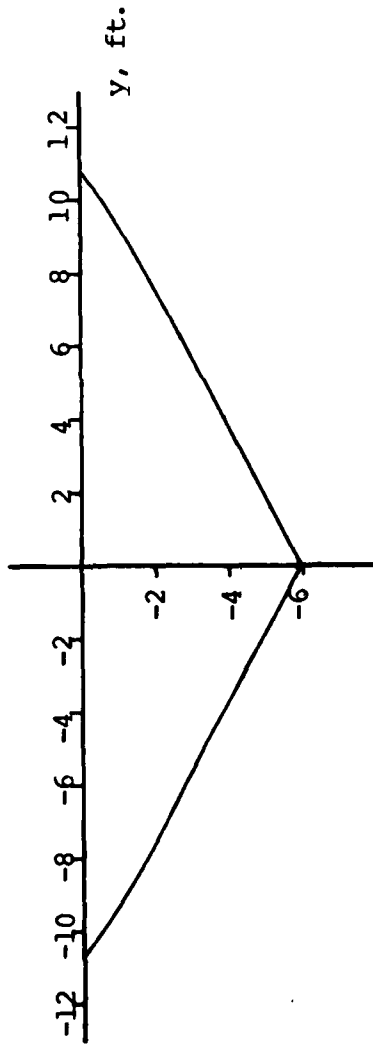


Figure 8 Section shape of AO-177 at Station 19.5

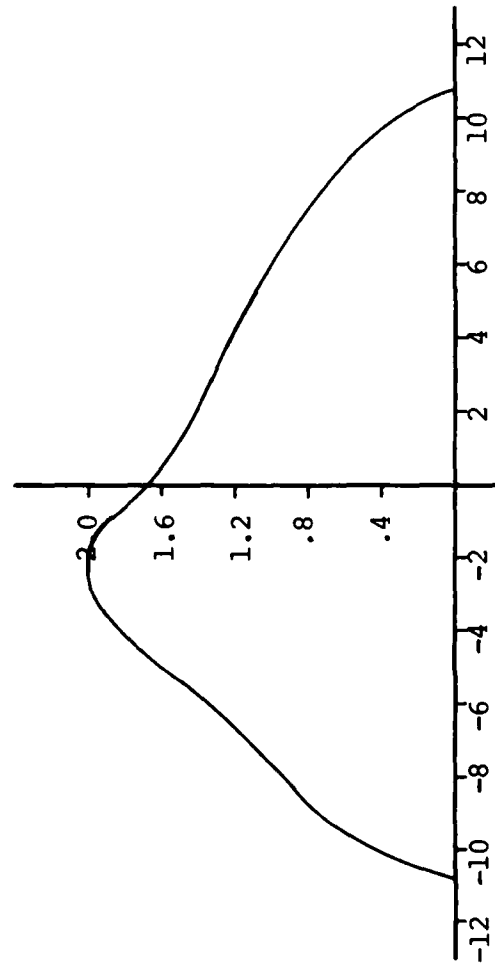


Figure 9 Variation of pressure relative to local propeller free space pressure along ship section corresponding to AO-177 Station 19.5, flow field due to AO-177 propeller in wake with fins,  $x=5$  ft. location

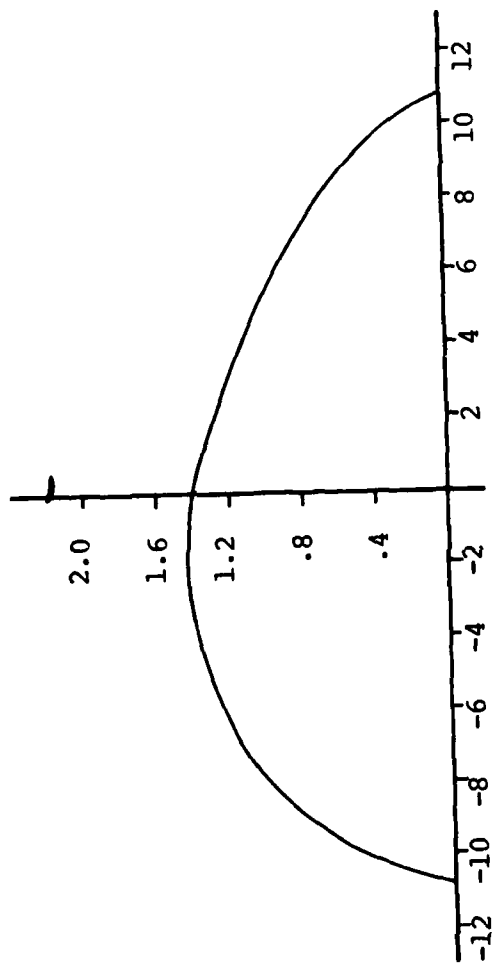


Figure 10 Variation of pressure relative to local propeller free space pressure along ship section corresponding to AO-177 Station 19.5, flow field due to AO-177 propeller in ship wake,  $x = -6$  ft. location

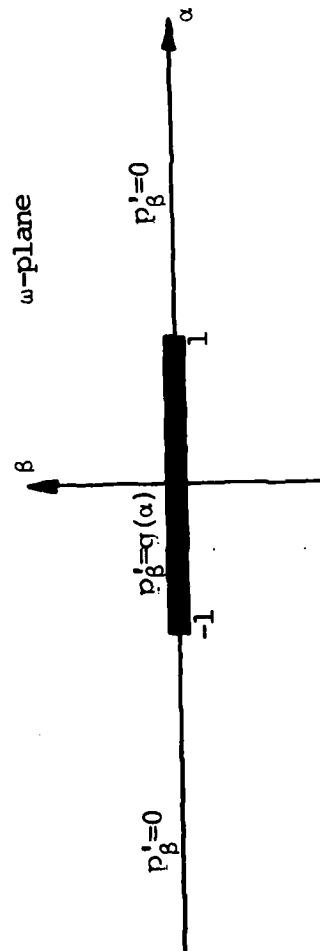


Figure 11 Boundary value problem in transformed  $w$ -plane for free surface rigid wall condition



## Discussion

T. Sasajima (Mitsubishi Heavy Industries)

This paper describes the calculation method of a surface force acting on the ship hull induced by a propeller operating in wake.

As to the solid boundary factor, Hoshino (1979) calculated the pressure fluctuation induced on a solid wall by a pulsating spherical bubble, which moves along the solid wall, as shown in Figure A. Since it can be said that the pulsating spherical bubble is a good first-order approximation of the unsteady cavitation near the blade tip, the solid boundary factor nearly equal to 2 obtained from the Figure A has been used in the calculation of the pressure fluctuation in the ship hull at this stage of calculation. The authors' calculation of pressure fluctuation on the flat plate shows the same results (see their Figure 6).

It is interesting to point out that the effect of the size of the ship bottom is relatively larger if we compare their Figures 6 and 7. Thus these results imply the importance of the design of the ship bottom above the propeller. Since the results of the calculation are limited, further calculation changing bottom shape of the ship and tip clearance will be highly appreciated from the practical application point of view.

## Reference

Hoshino, T., Pressure Fluctuation Induced by a Spherical Bubble Moving with Varying Radius, The Western-Japan Society of Naval Architects, No. 58 (1979).

J.P. Breslin (Stevens Institute of Technology)

This paper advances a strip theory procedure for the calculation of the pressures and sectional forces induced on ship hulls by the action of the normal derivative of the pressure field of a cavitating propeller and its image in the water surface. Strip theory is applicable to incident flows and body geometries that vary slowly with the longitudinal coordinate. First, the geometry of many ships changes rapidly in the longitudinal coordinate in the vicinity of the propeller. Second, and more significant, the incident pressure field of the propeller in the presence of the free surface decays rapidly with distance from the propeller. The slowest decay is exhibited by the component arising from the second derivative of the  $q_n^{\text{th}}$  harmonic of the cavity volume, which varies as  $1/x^2$  with  $x$  in multiples of the propeller radius (which is small compared to ship dimensions). There are many other components, which are significant in the near field,

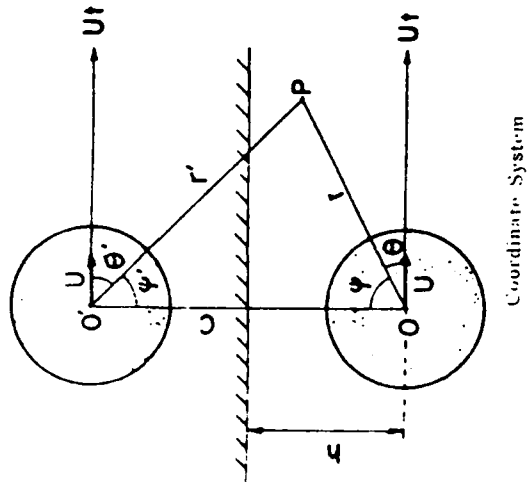
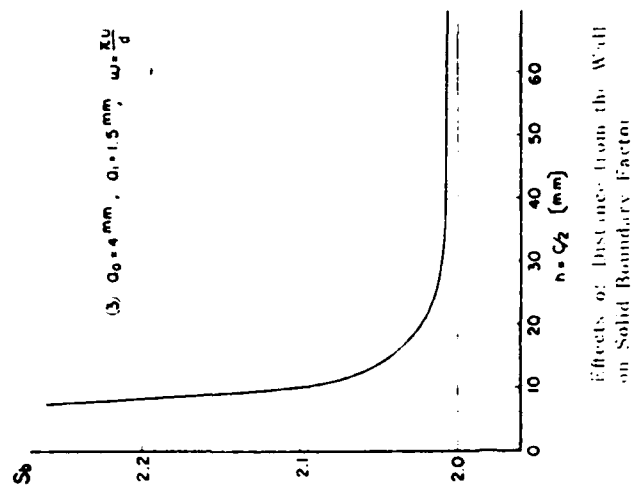


Fig. A

that decay more rapidly. It is, therefore, questionable that strip theory can give realistic results.

It would seem mandatory that the authors justify their assumption of strip theory by comparisons with measurements. As this has not been done, the applicability of this procedure remains to be proven.

Some measure of the effectiveness of strip theory in application to propeller-generated hull excitations may be gleaned by considering simple geometries. First, consider a circular cylinder of infinite length in the presence of an intermittently cavitating propeller. At field points beyond about one diameter, the cavitating blade appears to act as a pulsating point source located at the axis whose strength is the time derivative of the cavity volume at the axis. The geometry of this configuration is shown in Figure 1.

The total potential of the cylinder and the source is found to be

$$\phi_c - \frac{M}{4\pi R} = -\frac{M(t)}{4\pi^2 a} \sum_{m=0}^{\infty} \epsilon_m \sum_{n=-\infty}^{\infty} \int_{-\infty}^{\infty} \frac{dk}{|k|} A_{m,n} e^{ikx} \cos(n\alpha - m\theta)$$

where

$$A_{m,n} = \frac{I_m(|k|s) K_{m+n}(|k|h)}{K_n'(|k|a)}$$

and the I's and K's are the modified Bessel functions of the first and second kind.

Only the term  $m = 0$  represents the stationary pulsating source and only  $n = 1$  can contribute to the force density on the cylinder. The ratio of the vertical force density from the three-dimensional solution to that from strip theory (in which the normal flow at each section is imposed parametrically) is, for the source on the axis, ( $x = 0$ ):

$$\frac{|Z_3'|}{|Z_2'|} = \frac{\int_0^{\infty} \frac{d\lambda}{\lambda} \frac{K_1(h'\lambda) \cos x'\lambda}{K_1'(\lambda)}}{\int_0^{\infty} d\lambda [I_1(\lambda) + \lambda I_1'(\lambda)] K_1(h'\lambda) \cos x'\lambda} \quad (1)$$

where  $h' = h/a$ , the interaxial distance/cylinder radius

$x' = x/a$ , the station location from the propeller in fraction of cylinder radius.

Evaluation of Equation (1) for  $h' = 1.375$  (corresponding to a tip clearance of 0.25 propeller diameter and a cylinder of radius equal to 4 propeller radii) yields the variation with  $x'$  shown in Figure 2. Here it is seen that, in the interval  $|x'| < 0.7$ , the three-dimensional force density is less than that from strip theory and that for  $|x'| > 0.7$  the three-dimensional result is in excess of that from

strip theory, rising to a maximum ratio of 1.65. We see a considerable difference between three-dimensional and strip theories.

Asymptotic analysis for large  $x'$  yields the ultimate ratio to be

$$\frac{|Z'_3|}{|Z'_2|} \rightarrow 1 + \left(\frac{a}{h}\right)^2 = 1.529 \text{ (in this case)} \quad (2)$$

to which the computed curve appears to be descending. Another check on the calculations is provided by the fact that the total force on the cylinder is the same by three-dimensional or strip theory. This can be shown directly or from global considerations. Integration of numerical values of the numerator and the denominator showed agreement to within 2 percent. The result for the force at frequency  $qn$  is for an  $n$ -bladed propeller:

$$(Z_3)_{qn} = (Z_2)_{qn} = \frac{-n\pi a^2}{h} (qn\omega)^2 R_e(V_{qn} e^{iqn\theta}) \quad (3)$$

where  $V_{qn}$  is the complex amplitude of the  $qn^{\text{th}}$  harmonic of the cavity volume. It is seen that the force (for constant  $V_{qn}$ ) decays slowly with tip clearance  $\tau$  as  $h$  in propeller radii is  $(1 + a + \tau)$ . (In practice,  $V_{qn}$  will depend on tip clearance because of the changing flow in the hull boundary layer.) The force given by Equation (3) applies to a cylinder floating half submerged in the water surface.

A corresponding calculation of the force density on a flat plate of infinite  $x$ -wise extent and of finite width  $2b$  beset by the flow from a source located on the propeller axis, as shown in Figure 3, involves the solution of an integral equation:

$$\frac{|\xi|}{\pi} \int_{-b}^b \frac{K_1(|\xi||y-\eta|)}{|y-\eta|} \mu(\xi, \eta) d\eta = 2\hat{w}_s(\xi, y) \quad (4)$$

where  $K_1$  is the modified Bessel function of the second kind,  $\mu$  is a "dipole" density,  $\hat{w}_s$  is the  $x$ -wise Fourier integral transform of the vertical velocity due to the source on the plate and  $\xi$  the transform variable. The equation reduces to the airfoil integral equation for  $\xi = 0$ . The equation, when converted to an equation of the second kind, is inverted by computer.

Results for the ratio of the force densities  $Z'_3/Z'_2$  are shown in Figures 4 and 5. Here, in contrast to the cylinder, the three-dimensional densities are larger for small  $x$  and less for large  $x$  than the strip values. Again, the force on the plate is the same and, hence, the density ratios must act as they do with  $x$ . The results are, therefore, artifacts of the doubly infinite  $x$ -wise extent of these simple forms.

More realistic forms are afforded by slender spheroids. The Neumann potential of a spheroid in the presence of an offset source as

depicted in Figure 6 can be written down by analogy to the solution of the Dirichlet Green's function given in Reference 1. The ratio of the vertical force densities is given by

$$\frac{|Z'_3|}{|Z'_2|} = \frac{\frac{r(x)}{2c} \sum_{n=1}^{\infty} \frac{(2n+1)}{n(n+1)} P_n^1(\eta) P_n^1(\eta_0) Q_n^1(\xi_0)/Q_n^1(\xi_1) (1-\xi_1^2)}{\sqrt{r(x)/h} \{ (\frac{r}{h} - Z) Q_{-1/2} + (1 - \frac{rZ}{h}) Q_{1/2} \} / 4\pi (Z^2 - 1)}$$

where  $P_n^m$ ,  $Q_n^m$  are the associated Legendre functions

$Q_{n/2}$  are the associated Legendre functions of the second kind of half-integer order and of argument  $Z$

$$Z = \frac{x^2 + r^2(x) + h^2}{2hr(x)}; \quad r(x), \text{ the spheroid local radius}$$

$c$  the semi-interfocal length;  $\xi_0$ ,  $\eta_0$  the source location

$\xi_1$  defines the spheroid ( $\xi_1 < \xi_0$ )

Evaluation for a spheroid of 6:1 length/diameter with a source on the axis of the propeller below the after focus at a distance  $h = 3.12$  propeller radii (a propeller disk having a local tip clearance of 0.25 diameter) yields the values shown on Figure 7. Here we see that, for  $x < 1.75$  radius  $Z'_3/Z'_2$  is less than unity, and beyond this distance the force density ratio rises to a maximum of 1.42. Again, the total force by either process may be close, but the local force variations are considerably different in the region of significance. It is also interesting to note that our calculations show that the three-dimensional force density falls only to about one tenth of its maximum value at 5 diameters forward of the propeller on this body, which has a length of 30.77 propeller diameters. Hence, more than one sixth of the body is sensibly loaded by cavitation-induced pressures (and that, indeed, one should account for phase shift due to the speed of sound in water at blade frequencies at such distances).

Those who espouse the procedure of multiplying the incident pressure field by 2.0 to allow for the reflecting effect of the body may be interested in the ratios of the three-dimensional densities to those due to twice that induced by the source alone. The force density due to the source alone is

$$\frac{|Z'_0|}{|\rho \dot{M}|} = \frac{1}{2} \sqrt{\frac{r(x)}{h}} Q_{1/2} \left( \frac{x^2 + h^2 + r^2(x)}{2hr(x)} \right)$$

The ratios are given in Table 1.

TABLE 1

x	$ z_3'/2z_0' $
0	0.188
1	0.204
2	0.240
4	0.291
6	0.242
10	0.232

This comparison clearly suggests that the expedient of doubling free-space pressures grossly overestimates the force densities for curvilinear bodies.

The authors show pressure ratios in their Figure 6 on a flat plate (doubly infinite in length because of their two-dimensional theory) that are in excess of 2.0. This is an artifact of the infinite extent of the plate, as similar results have been found by the discussor for locations close to the propeller, whereas at distance the ratios are always less than 2.0 (also as implied by my Figures 4 and 5). In a discussion of a paper by Reed et al.,<sup>2</sup> I have shown that, for a flat surface in the water plane of finite longitudinal and transverse extent, as is provided by a disk, the pressure on the boundary is less than twice the incident pressure field and approaches that limit monotonically from below as the disk radius is increased. Hence, the authors' results are artifacts of their strip theory!

The effects resulting from lack of modeling of the water surface in water tunnel facilities are indeed significant when the draft is reduced in way of the propeller. Calculations made on behalf of the Swedish Maritime Research Centre (SSPA) have shown that corrections should be made to propeller-induced hull pressures to account for the replacement of the water surface by a wood cover. Indeed, the SSPA subsequently devised empirical corrections for cases in which propeller submergence is sufficiently small to warrant them. As the new facility being planned by the U.S. Navy embodies this lack of scaling of the water surface, I have been urging that calculated correction factors should be determined from our three-dimensional procedure.

At Davidson Laboratory, we have developed a three-dimensional procedure in which the hull is represented by an array of normal dipole panels. The effects on hull pressures of the free or rigid surface condition on the locus of the water surface are directly secured. The authors do us a rank disservice by citing only our first effort made way back in 1965. To correct its gross omission, I cite seven references to publications of DL work on hull forces and pressures that have demonstrated good agreement with model measurements for non-cavitating conditions.<sup>3-9</sup> A forthcoming paper to be presented at the SNAME Annual Meeting in November 1982 provides good to excellent correlations with pressure measurements made in the SSPA water tunnel when account is taken of the effect of the boundary condition imposed in that facility.

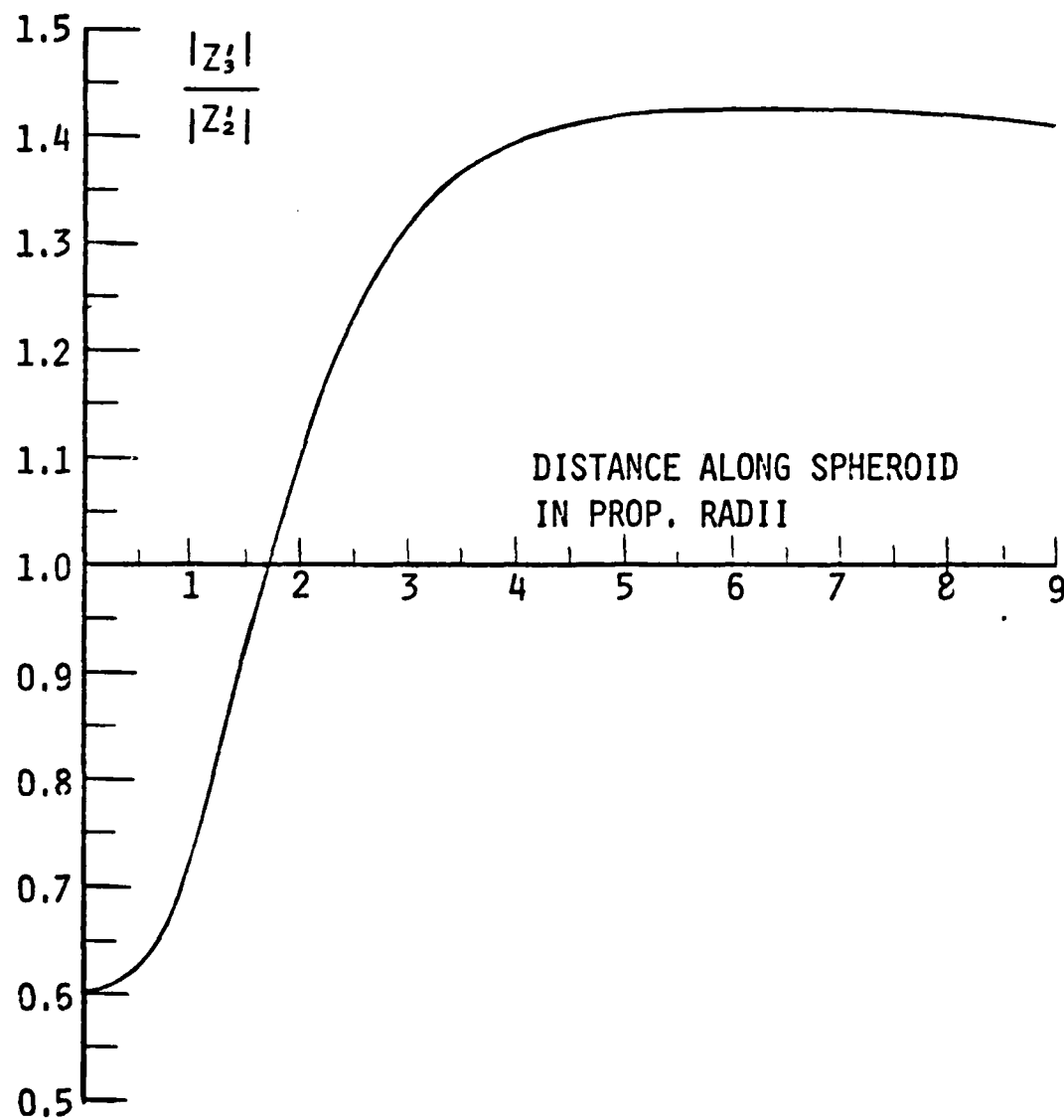


FIGURE 7. VARIATION OF THE RATIO OF PROPELLER-CAVITATION-INDUCED THREE-DIMENSIONAL VERTICAL FORCE DENSITY TO THAT FROM STRIP THEORY ALONG A 6:1 SPHEROID FORWARD OF THE PROPELLER

Having made these points, I commend the authors for an ingenious development that can be used for estimates of propeller-induced excitations. Indeed, in view of the uncertainty of our knowledge of ship wakes, many may be content to use this less complicated procedure.

#### ACKNOWLEDGMENTS

I wish to acknowledge the extensive programming and analytical efforts of colleagues Dr. T. Glenn McKee and Dr. T. R. Goodman.

#### References

1. Morse, P.M., and H. Feshbach, Methods of Theoretical Physics, McGraw-Hill, 1953, Vol. II, p. 1291.
2. Breslin, J.P., Discussion of "Effects of Hull and Propeller Design Change on the Vibration of a Lakes Freighter," by E. Reed and J. Norton, Trans. SNAME 1981, Vol. 89, p. 436.
3. Breslin, J.P., "Propeller-Induced Hull Forces," Schiffstechnik, Band 26, Heft 4, November 1979 (presented at Diamond Jubilee Symposium, VSWS, Berlin, November 1978).
4. Breslin, J.P., "Review of Theoretical and Experimental Procedures for Prediction of Ship-Propeller-Induced Excitations," IAHR/IUTAM Symposium on Practical Experiences with Flow-Induced Vibrations, University of Karlsruhe, Germany, September 1979.
5. Breslin, J.P., S. Tsakonas, and D. Valentine, "A Method for Predicting Effects of Propeller-Hull Configurations on Vibratory Excitation of Ships," DL Tech Note SIT-DL-79-7-893, May 1979 (prepared for IAHR/IUTAM Symposium, Karlsruhe).
6. Breslin, J.P., S. Tsakonas, and D. Valentine, "Vibratory Propeller Forces on Arbitrary Hulls," Soc. Civil Engineers, Engineering Mechs. Div. Specialty Conf., University of Texas, 1979.
7. Tsakonas, S., and D. Valentine, "A Theoretical Procedure for Calculating Propeller-Induced Hull Forces," Davidson Laboratory Report SIT-DL-79-9-1979, September 1980.
8. Tsakonas, S., J.P. Breslin, and J. Teeters, "Correlation of Theoretical Predictions of Propeller-Induced Hull Pressures with Available Data," Davidson Laboratory Report SIT-DL-80-9-2130, November 1980.
9. Breslin, J.P., "Propeller-Induced Hull Pressures and Forces," Third International Conf. on Numerical Ship Hydrodynamics, Paris, June 1981.

C-A. Johnsson (Swedish Maritime Research Centre SSPA)

Representing a laboratory possessing what is referred to in the paper as "specialized water tunnel facilities that simulate full-scale operation" I would like to comment on the practical consequences of this interesting paper.



First, one remark concerning the boundary conditions. The main part of the paper is devoted to establishing a relation between the propeller-induced pressure amplitudes on a ship-like section placed in a water surface and the corresponding free-space amplitudes and some results of these calculations are given. In the last part of the paper the authors discuss how the corresponding relations could be established when replacing the free surface by a rigid wall indicating that this case is the proper representation of a ship model in a cavitation tunnel without a free surface.

This may be true for most tunnels of this kind but does not apply to the large tunnel at SSPA. In this tunnel the model is submerged in water, the thickness of the water layer above the water line being 850 mm which, for most models, corresponds to more than twice the draught of the model. Thus the free surface is replaced by a water-wood-water transition and results of experiments with the propeller replaced by a loudspeaker or hydrophone indicate that the reflection of the wall is very small, although somewhat frequency dependent. Accordingly, this arrangement would be best represented in the calculations by a ship submerged below a flat plate, a case which could be expected to be somewhat closer to the free surface case than the one discussed in the paper.

Turning to the diagrams of the paper I would like to ask the authors if they can explain why the results of Figures 7 and 10 are almost identical in spite of the fact that they were obtained for different shapes of the ship section, different flow fields for the propeller and entirely different positions relative to the propeller. On the other hand, the results of Figures 7 and 9 differ appreciably, the only differences in input data for the two cases being different shape of the ship sections.

Finally, I can mention that we have noticed, at our model-full scale comparisons, an increasing effect of the lack of a free surface in the tunnel when the interest was changed from large tankers, for which full scale results are normally available at fully loaded draught, to container and Ro-Ro-ships, ferries, etc. The latter types of ships have in general smaller draught than a tanker and the influence of the free surface is amplified by the fact that most of the full scale measurements of pressure amplitudes are made in ballast condition for these ships.

In order to explore the effect of the free surface several investigations were started, one being to carry out the loudspeaker tests referred to above, another to give a contract to Dr. Breslin to carry out some theoretical calculations.

A third way of identifying this effect was to make a careful analysis of the model-full scale comparisons available. The kind of results obtained so far from the last type of work is illustrated by the diagram of Figure 1, which will be discussed below.

As the height of the stern wave is important for this effect, the Froude number has to be considered, if the nominal water line should be used as the basis for the analysis. Accordingly, different plots of the ratio amplitude full scale/amplitude model scale were made for different Froude numbers, the one shown in Figure 1 applying to

$0,15 \leq F_{nL} \leq 0,20$ . The horizontal axis shows the immersion of the transducer relative to the water line at zero speed, normalized with the length of the ship. Similar diagrams are available for other ranges of Froude number and for blade frequency, as well as twice blade frequency amplitudes. The correction factors read in these diagrams are at present applied when predicting the full-scale excitation amplitudes to be used for estimation of the vibration levels.

A lot more could be said about the advantages and disadvantages of not having a free water surface at the model tests but, summarizing our experiences so far, we have found that, much because of the presence of the stern wave, the influence on the amplitudes of blade frequency and its first multiples is not large for the majority of projects tested, considering the general accuracy of the measurements of this kind.

### Author's Reply

Paul Kaplan, James Bentson, and Moshe Benatar

Since the paper by Hoshino is something with which we are not familiar the discussion by Mr. Sasajima is certainly appreciated. and we can only make a short statement in response. That particular analysis makes use of the solid boundary factor equal to 2, which has been used in almost all of the work discussed in the past. It is because people have only used such a factor for a solid boundary that we felt it necessary to provide the results in our paper, which shows the importance of the influence of the free-surface boundary condition. Only in the case of a very large flat plate does the boundary factor equal 2, and as shown in our paper the factor approaches zero at the ends.

We do appreciate the fact that Mr. Sasajima has recognized the differences in the boundary factors due to both the size of the ship bottom as well as its shape characteristics. Our results are only illustrative for these effects, and certainly further calculations would be useful for specific practical applications. Such results have to await the opportunity to apply them to specific cases, using the procedure described in our paper.

Dr. Breslin's comments are wide-ranging and require an extensive effort for response. Since it is not possible to check the details of the complicated mathematical forms that he presents in his discussion, we can only respond in general and hope that we may have an opportunity to examine the results of his analysis in more detail when a completely published version is available. As far as the capability of strip theory is concerned, we considered the disturbance to be that due to a source alone, where the pressure field decays in an inverse linear fashion with distance from the propeller. When considering the presence of the image that decay is certainly much faster, but the presence of the image is only applied in the course of our analysis in order to simplify the form of the boundary conditions and the solution

of the integral equation. This particular issue can be argued further, but it is perhaps only a matter of what point of view is adopted initially when viewing the problem.

It does not seem possible that the assumption of strip theory can be justified simply by means of comparison with measurements, since two different effects are present simultaneously. It is necessary to represent properly the free-space pressure field of a cavitation propeller and then also account for the influence of the ship boundary surface. This would be the case when considering an actual ship model in a test facility with a free surface present. Since adequate experiments of this nature are not really available at present, it still remains difficult to prove the utility of strip theory per se by this means. Perhaps a set of simplified experiments in an appropriate test facility for a flat-plate surface in the presence of a simple source disturbance could be used for that purpose, but even then it is an overcomplicated approach relative to the real practical problem to which our analysis is directed.

Since our analysis deals with pressures, any comparisons made in Dr. Breslin's discussion cannot be directly applied since he uses integrated sectional force values for simplified bodies. As mentioned earlier, the mathematical results in the form of integrals of Bessel function quantities do not allow us to determine the nature of the procedures used in arriving at such results and the extent of their validity. However, we do appreciate the fact that the analysis by Dr. Breslin shows that the total force on various bodies is the same by use of either three-dimensional analysis or by means of strip theory. Since the vibratory response of any vessel subject to oscillatory-type disturbances from a propeller is generally dependent on the total force, and since that is the major problem of engineering interest to which the present analysis is directed, it appears that our approach is certainly useful for that case.

The information in Table 1 that Dr. Breslin presents also supports our conclusion that the free-space pressures should not be multiplied by a factor of 2 when accounting for the presence of a ship hull section. No direct comparison can be made between our results and those of Dr. Breslin since he is using force densities, applying the results to only a simple source, the geometry is different, etc.

We do not believe that our results for the pressure ratios are necessarily artifacts of strip theory due to the general complexity of the pressure field associated with a cavitation propeller. The fact that even the ratios shown in Dr. Breslin's presentation extend both above and below 1, depending on the location along the body, is an indication of the general complexity of arriving at guidelines for the behavior of the pressure distribution due to this type of propeller.

We do appreciate the point of view expressed by Dr. Breslin that different corrections should be made to propeller-induced hull pressures in accordance to whether a free surface or a rigid surface is present in a test facility. The prospective appearance of a paper at the SNAME meeting (November 1982) as well as a possible future publication that provides a detailed description of the methods used by Dr. Breslin are certainly items that we would hope to examine in order to

determine the basis for the conclusions presented in his discussion. We also thank him for the fact that he does recognize that the method we presented can be used for estimates of propeller-induced excitation effects, which was the basic intent of the procedure that we have presented in this paper.

The discussion by Mr. Johnsson is appreciated, especially in view of his experience with a specialized water-tunnel test facility. The points made in his discussion regarding the results shown in Figures 7, 9, and 10 are well taken. The similarity of certain results, even though they are obtained for different flow fields, different positions, different section shapes, etc. does illustrate the fact that only a theoretical approach could provide such results. In most cases the shape of the curves would tend to be similar since they go to zero at the ends and exhibit a peak somewhere near the center, with the shape of the distribution of pressure ratio being almost elliptical. However, since the results are given in the form of ratios, the actual pressure distributions themselves would be very different in magnitude (and possibly shape also) since the free-space pressures for the cases in Figures 7 and 10 are different. The differences in the results for Figures 7 and 9 are primarily due to the effect of the shape of the section, and that is consistent with our expectation that the flow around different shapes would produce different pressure distributions.

The importance of the effect of the lack of a free surface in the SSPA water tunnel is most evident for vessels that have smaller draft, which would then be closer to naval ships. The fact that there are differences between full-scale results and those obtained in the water tunnel can possibly be ascribed to the effect of the boundary conditions, which has been separately mentioned within the discussion by Dr. Breslin. We cannot tell from Figure 1 of Mr. Johnsson's discussion whether the main effect illustrated there is due to the influence of the free surface and the boundary conditions used in the water tunnel, or whether the effect is due to accounting for the height of the stern wave.

There does not appear to be any definitive conclusion of what the major effects are for any particular type of model test facility. Almost all laboratory facilities still need some type of correction in order to predict full-scale values, with the correction based on hydrodynamic flow principles as well as empirical comparisons with full-scale values. We hope that more detailed comparisons between theory and experiment, as well as between model and full-scale results, will allow a useful resolution of the major factors influencing the flow about ship-hull sections associated with cavitation propellers.

We do appreciate the comments made by the discussors and hope that we have satisfied them with our responses. The particular problem areas discussed in our paper still remain of significant importance and interest in naval hydrodynamics, and we are pleased that our work has made some contribution toward a more complete understanding of these phenomena.

*Session VII*

# VISCOUS FLUID PROBLEMS

# A Streamline Curvature Method for Computing the Flow Near Ship Sterns

Lars Larsson and Lars-Erik Johansson

Swedish Maritime Research Centre SSPA, Göteborg, Sweden

## ABSTRACT

The SSPA - ITTC Workshop on Ship Boundary Layers, held at SSPA in June 1980, clearly showed that none of the ordinary first order boundary layer methods was capable of computing the flow near the ship stern. One main reason for this seems to be the fact that the normal curvature of the surface is neglected. A very severe effect of this approximation is that the co-ordinate system does not fit into the space outside the hull, which means that the continuity of the flow is not maintained as the boundary layer develops downstream. Assuming that this is the essential deficiency of the common methods, a generalization has been made of the 2-D and axisymmetric streamline curvature methods previously developed at SSPA. In this approach, the flow equations are solved along the streamlines inside the boundary layer, and, since only the longitudinal velocity component is non-zero in this system, the equations become very simple. However, the location of the streamlines, and thus of the co-ordinate system, is unknown beforehand and must be part of the solution. In the paper the development of the new method is described. As a pilot case, the boundary layer developing on a flat plate, and disturbed by an obstacle, is investigated. Thereafter the method is applied to the two test cases of the Boundary Layer Workshop.

## LIST OF SYMBOLS

$a$	radius of cylinder
$f, g$	velocity similarity functions, see (17) - (19)
$\vec{G}$	pressure gradient vector
$i, j, k$	indices, see figure 3
$K_{12}, K_{13}$	normal and geodesic curvature resp., of streamlines
$l_m$	mixing length
$p$	static pressure
$p_0$	total head
$r, \phi$	polar coordinates, see figure 7
$s, t$	non-orthogonal coordinates in the grid, see figure 10
$s_1, s_2, s_3$	stress terms of the Reynolds equations
$U_\infty$	undisturbed velocity (in the X-direction)
$U_p, W_p$	potential flow velocities in the X and Z directions
$U_{rp}, U_{\phi p}$	potential flow velocities in the r and $\phi$ directions
$u, v, w$	velocity components in the x, y, z coordinate system
$u_e$	velocity at the edge of the viscous region
$u_l, u_c$	velocities along and across the reference direction
$u_\tau$	friction velocity ( $\sqrt{\tau_w/\rho}$ )
$X, Y, Z$	global Cartesian coordinates, see figure 4
$x, y, z$	local Cartesian coordinates, see figure 3
$y_D$	modified distance from the wall, see figure 10
$y_D^+$	$y^+$ at the junction between the two velocity laws (18), (19)
$y^+$	$y_D u_\tau / \nu$
$\alpha, \gamma$	angles, see figure 7
$\alpha, \beta, \gamma$	direction cosines in the X, Y, Z system.
$\beta$	crossflow angle
$\beta_w$	cross flow angle at the wall
$\delta$	thickness of the viscous region (boundary layer)
$\epsilon$	eddy viscosity, see (23)
$\eta$	$y_D / \delta$
$\phi, \Omega$	angles, see figure 11
$\nu, \mu$	viscosity, kinematic and dynamic, resp.
$\rho$	density
$\overline{\rho u v}, \overline{\rho v w}$ , etc.	Reynolds stresses
$\sigma$	$\dot{V}/2\pi$ , where $\dot{V}$ is the volume flux
$\tau_w$	shear stress at the wall
$\tau_{xy}, \tau_{zy}$	shear stresses

## INTRODUCTION

In recent years, considerable achievements have been made in the computation of the flow around ship hulls. Thus, in the 1970's the growing capacity of the computers made possible a strong development of calculation methods for viscous as well as inviscid flows. Although the basic theories are much older, not until now have methods which may become useful for practical purposes started to appear. A good indication of the state of the art was given in the two workshops organized in cooperation with the ITTC Resistance Committee by DTNSRDC in 1979 (Bai and McCarthy, 1980) and by SSPA in 1980 (Larsson, 1981). While potential flow calculations were the subject of the former meeting, ship boundary layer computations were presented at the latter. It turned out, that the best of the potential flow methods were able to predict the wave resistance with fair accuracy, and reasonable results were obtained for most of the boundary layer methods over the main part of the hull. However, one weakness was definitely revealed: none of the first order boundary layer methods could predict the flow near the stern of either of the two test cases considered (one cargo liner, the SSPA Mod 720, and one tanker, named the HSVA tanker). The methods incorporating higher order effects seemed to produce more reasonable results and, at least for two of them, the excessive girthwise variations found in most results were reduced to a reasonable level. Quantitatively the results were not very good, though.

At SSPA, a research program for developing calculation methods for ship stern flows has been under way for about five years. Unfortunately, none of the methods were ready at the time of the workshop, where the two SSPA entries were of the first order type. Not very long thereafter, however, the first SSPA method of higher order was presented at the Thirteenth Symposium on Naval Hydrodynamics, see Larsson and Chang (1980). In that work an extension of the first order method developed by Larsson (1974a) was applied to a mathematical hull form for which wave resistance calculations with and without the displacement thickness were also carried out. Quite good results were obtained for this hull.

The higher order method had however some weak points. Thus, gradients of surface curvatures were required, which made it difficult to apply the method to real ships. Further, it turned out that the fully 3-D solution produced considerably less accurate results than the small cross-flow approximation, a somewhat disturbing fact. The further development of this method was therefore postponed.

Recently, the development has proceeded in two directions. In cooperation with Chalmers University of Technology quite a complex method of the partially parabolic type, using an analytical body fitted coordinate system, is being developed. This will become very expensive and its full development will require another two to three years of work. There is, however, an urgent need for a simple method, good enough for distinguishing between various alternatives at an early stage in the ship design process. Ideally, it should be easy to apply, and the cost should not be too high, if several alternatives are to be evaluated. On the other hand, it might not be necessary to ask for



results, as accurate as the ones expected from the method of the partially parabolic type.

In the present paper the development of a method which might satisfy the above requirements will be described. It should be pointed out at once, that there is still some work to be done before the full potential of the method can be exploited, but the results obtained already are quite interesting.

#### FEATURES TO INCORPORATE IN THE NEW METHOD

The task of producing a stern flow method, which works as well, or better, than the more established ones, but at a lower cost, might seem presumptuous. However, it should be borne in mind, that practically all methods which have been used for computing the viscous flow around the hull have been designed to work all the way from bow to stern, or at least in the entire region, where the flow is of the same type (i.e. laminar or turbulent). This is probably not the best way to proceed, since different approximations may be made in the viscous flow region near the stern and in the boundary layer further forward.

In the boundary layer area, essentially three different types of approximations are used, one for the pressure, one for the stresses and one for the coordinate system. The pressure is assumed constant across the boundary layer and equal to the one computed in the potential flow on the surface. Most stresses are neglected; only the two shear stresses in the plane of the surface are retained. The metrics, finally, in the curvilinear coordinate system needed for ship flow calculations are also assumed constant across the boundary layer.

In principle, none of these approximations should be made for the flow near the stern, where the thickness of the viscous region approaches the local radius of curvature of the surface. However, since the momentum loss due to shear stresses is almost exclusively concentrated to the boundary layer part, turbulence modelling might play a much less important role near the stern.

It is conceivable that the major weakness of all first order boundary layer methods when applied to the stern flow is the neglect of variation in the metrics with  $y$ . This means that the normals to the surface are parallel to one another, i.e. the surface is assumed to be flat. On a ship model the transverse curvature may well be so large that the normals intersect within the boundary layer. Neglecting this effect means essentially that the continuity of the flow is not maintained. The flow may escape in an uncontrolled manner when the computation proceeds downstream.

Figures 1 and 2 support the above findings. In Figure 1 the magnitude of the terms in the longitudinal boundary layer integral equation is shown. The calculations were carried out for the SSPA model 720 using Larsson's integral method (Larsson, 1974a), and the results are given along a streamline, which is on the bilge at mid-ship and at mid-girth at both ends. It appears, that the skin friction term (1) is by far the largest on the forebody, but drops to zero near the stern. It is, however, counteracted by some other terms near the

start of the calculation, so the increase in momentum thickness, term (5), is not very high initially. At  $X = 0$  it has reached a fairly constant level. The magnitude of the term (2) is quite interesting. This represents the influence of the longitudinal pressure gradient, so important in 2-D flows. It can be seen here that it has a very small effect on the results. The terms (3) and (4), on the other hand, greatly influence the solution. (3) represents the effect of convergence-divergence of the potential flow at the edge of the boundary layer, while (4) is a measure of the convergence-divergence due to cross flow. Terms of this type, directly related to the continuity, therefore determine the increase in momentum thickness near the stern. It may of course be argued, that the figure is based on computations which may not be very accurate in this region, but the results correspond quite well with measurements at  $X = 0.5$  (25 % LBP from AP, see Figure 4) and reasonably well at  $X = 0.7$ , so the trends near the stern should be all right.

Further evidence of the small influence of the shear stresses in the stern region is given in figure 2, based on recent measurements at SSPA (Löfdahl, 1982). Profiles of the  $\rho u v$  shear stress are given at four locations along a streamline close to the one of figure 1. It appears that the stress is appreciable only very close to the wall, while in the major part of the boundary layer the stress is much smaller than the one in the flat plate boundary layer, shown as reference. Particularly the y-wise gradients, which appear in the momentum equations, are much reduced.

The third type of boundary layer approximation related to the pressure, should not be made near the stern. Thus the pressure variation across the viscous region should be considered, as well as the interaction between this region and the potential flow.

Summing the requested features of the new method, unlike an ordinary boundary layer method, it should consider correctly the continuity and the pressure variation including interaction. Turbulence modelling is not too critical.

#### BASIC PRINCIPLES OF THE NEW METHOD

A possible way of satisfying the requirements put forward would be to extend to 3-D the streamline curvature method, developed for 2-D and axisymmetric cases by Dyne (1980, 1978). This method has shown excellent performance when applied to wing sections and axisymmetric bodies, but its extension to 3-D is by no means straight forward, since the lateral displacement of the streamlines causes considerable difficulties. This is however the approach chosen, and the basics of the method may be described as follows.

The Reynolds equations in Cartesian coordinates for turbulent, incompressible, steady mean flow may be written

$$\rho \left( u \frac{\partial u}{\partial x} + v \frac{\partial u}{\partial y} + w \frac{\partial u}{\partial z} \right) = - \frac{\partial p}{\partial x} + \mu \nabla^2 u - \rho \left[ \frac{\partial \overline{u'^2}}{\partial x} + \frac{\partial \overline{u'v'}}{\partial y} + \frac{\partial \overline{u'w'}}{\partial z} \right] \quad (1a)$$

$$\rho \left( u \frac{\partial v}{\partial x} + v \frac{\partial v}{\partial y} + w \frac{\partial v}{\partial z} \right) = - \frac{\partial p}{\partial y} + \mu \nabla^2 v - \rho \left[ \frac{\partial \overline{u'v'}}{\partial x} + \frac{\partial \overline{v'^2}}{\partial y} + \frac{\partial \overline{v'w'}}{\partial z} \right] \quad (1b)$$

$$\rho \left( u \frac{\partial w}{\partial x} + v \frac{\partial w}{\partial y} + w \frac{\partial w}{\partial z} \right) = - \frac{\partial p}{\partial z} + \mu \nabla^2 w - \rho \left[ \frac{\partial \overline{u'w'}}{\partial x} + \frac{\partial \overline{v'w'}}{\partial y} + \frac{\partial \overline{w'^2}}{\partial z} \right] \quad (1c)$$

where  $\nabla^2$  is the Laplace operator and the other symbols are given in the List of Symbols.

Assume that the x-axis is locally directed in the mean flow direction. Such a system is shown in figure 3, where it appears that the z-axis is also along a stream surface (to be defined) and the y-axis is at right angle to it. For a fluid element at the origin, v and w are zero, although their gradients are not. If the exact form of the stress terms is left for later discussion the equations for this element are

$$\begin{aligned} \rho u \frac{\partial u}{\partial x} &= - \frac{\partial p}{\partial x} + s_1 \\ \rho u \frac{\partial v}{\partial x} &= - \frac{\partial p}{\partial y} + s_2 \\ \rho u \frac{\partial w}{\partial x} &= - \frac{\partial p}{\partial z} + s_3 \end{aligned} \quad (2)$$

where  $s_1, s_2, s_3$  are the stress terms. By definition, the normal curvature  $K_{12}$  of a streamline may be expressed as

$$K_{12} = \frac{\partial(v/u)}{\partial x} = \frac{1}{u^2} \left( u \frac{\partial v}{\partial x} - v \frac{\partial u}{\partial x} \right) = \frac{1}{u^2} \left( u \frac{\partial v}{\partial x} \right) \quad (3)$$

since v is zero. A corresponding relation holds for the lateral curvature of the streamline,  $K_{13}$ . The equations may then be written

$$\frac{\partial p_0}{\partial x} = s_1 \quad (4a)$$

$$\rho u^2 K_{12} = - \frac{\partial p}{\partial y} + s_2 \quad (4b)$$

$$\rho u^2 K_{13} = - \frac{\partial p}{\partial z} + s_3 \quad (4c)$$

where  $p_0$  is the total head

$$p_0 = p + \frac{1}{2} \rho u^2 \quad (5)$$

The total head loss along a streamline is thus determined by the

action of the stresses (gradients), and the normal and lateral curvatures of the streamline are determined by the pressure gradients in the corresponding directions, and the stresses. These equations are to be solved in connection with a suitable form of the continuity equation.

Obviously, the simplifications obtained in this streamline coordinate system are considerable. The disadvantage is that the location and orientation of the coordinate system are not known beforehand, but must be part of the solution. It is thus necessary to introduce a global coordinate system,  $X, Y, Z$ , defined in figure 4.

The solution of the problem may be explained with reference to figure 5, where a simplified flow chart is given. (See also figure 3.)

1. Give initial data (velocities and stresses) for the streamlines at an initial plane  $X = X_1$ , and an estimated pressure distribution on the surface. (From a potential flow solution, possibly modified, as explained later.)
2. Assume a pressure distribution outside the surface (for instance  $p = \text{const}$  along a normal).
3. Compute the necessary stress gradients in the plane ( $x$ -gradients will hardly be used) and determine  $s_1, s_2, s_3$ . All streamlines.
4. Compute the lateral pressure gradient  $\partial p / \partial z$  and the curvature  $K_{13}$  from (4c). All streamlines.
5. Use the known direction and location of each streamline in the known  $X$ -plane, and the computed curvature  $K_{13}$  of the streamline to obtain a first approximation in the next plane (at  $y = \text{const}$ ). One "layer" ( $j = \text{const}$ ) at a time.
6. Let the streamlines four by four ( $j-1, k, j-1, k+1, j, k+1, j, k$ ) define corners in a streamtube and compute for each streamline the velocity at the new plane, knowing the pressure and the viscous losses  $s$  during the step. Compute the average velocity in the stream tube and move the outermost two streamlines ( $j, k+1, j, k$ ) of each tube outwards in such a way that the continuity is maintained within the tube, see figure 6. When one layer is computed return to 5.
7. After tracing the streamlines all the way back, compute the normal curvature  $K_{12}$  for each streamline at all  $X = X_1$  using the known location in the  $X, Y, Z$ , system. Use (4b) to obtain the normal pressure gradient.
8. Integrate the pressure gradient from the outermost stream surface inwards to get a new pressure at all grid points in the entire region. (Points 7 and 8 are not carried out until point 9 has been performed at least once.)
9. Use the outermost stream surface (defined by the outermost row of streamlines) to define a body shape and recompute the potential flow to obtain the pressure at this surface.

In this scheme it has been assumed that the Reynolds stresses can be computed from local conditions, but transport equation for turbulent

quantities may readily be introduced if necessary. Since the same simplifications are obtained for such equations as for (4) it should not be too difficult to introduce them.

Comparing the features of the method with the ones requested, it is seen that it should be very well suited for the purposes. In particular, the continuity of the flow is maintained exactly (within the numerical approximation). Further, the cost may be kept low, since the solution is essentially one-dimensional; the streamlines are traced one by one from  $X_i$  to  $X_{i+1}$ .

So far, the method has only been developed to point 6, so the pressure corrections of points 7-9 are not included in the results presented. Nevertheless, as will become evident, they seem quite reasonable.

### THE PILOT CASES

Although the procedure outlined is in theory quite simple, difficulties could be foreseen in its practical implementation. Accurate streamline tracing in space, for instance, might present problems, particularly if the lines meet or curl. Therefore, the simplest possible 3-D boundary layer flow, namely the boundary layer on a flat plate, intersected perpendicularly by a line source, was used as a pilot case. To simplify the problem as much as possible, shear stresses and pressure variation across the boundary layer were neglected. A computer program was written for this test, and it may briefly be explained with reference to figure 7.

The velocities in the potential flow are ( $\sigma$  is the source strength)

$$U_p = U_\infty + \frac{\sigma}{r} \cos\phi \quad (6a)$$

$$W_p = \frac{\sigma}{r} \sin\phi \quad (6b)$$

and the pressure, from the Bernoulli equation

$$p = p_\infty - \frac{1}{2}\rho\left[\left(\frac{\sigma}{r}\right)^2 + 2U_\infty \frac{\sigma}{r} \cos\phi\right] \quad (7)$$

Differentiation with respect to  $r$  and  $\phi$  yields the components of the pressure gradient vector  $\vec{G}$ , whose angle,  $\alpha$ , to the radius vector becomes

$$\alpha = \tan^{-1} \left[ \frac{\sin\phi}{\frac{\sigma}{U_\infty r} + \cos\phi} \right] \quad (8)$$

Its magnitude is

$$G = \frac{\rho\sigma}{r^2} \left[ \left(\frac{\sigma}{r}\right)^2 + 2 \frac{\sigma U_\infty}{r} \cos\phi + U_\infty^2 \right]^{\frac{1}{2}} \quad (9)$$

Neglecting shear stresses, (4c) yields

$$\rho u^2 K_{13} = - \frac{\partial F}{\partial z} \quad (10)$$

If the streamline direction,  $x$ , is at an angle  $\gamma$  to the  $X$ -axis, the normal,  $z$ , is at an angle  $\gamma + \pi/2$  to this axis and at an angle  $\gamma + \pi/2 - \phi - \alpha$  to the pressure gradient  $\vec{G}$ . Thus

$$\frac{\partial p}{\partial z} = G \cos(\gamma + \frac{\pi}{2} - \phi - \alpha) \quad (11)$$

But

$$K_{13} = \frac{\partial \gamma}{\partial x} = \frac{\partial \gamma}{\partial X} \cdot \cos \gamma \quad (12)$$

so, using (10), (11) and (12)

$$\frac{\partial \gamma}{\partial X} = - \frac{G}{\rho u^2} \frac{\cos(\gamma + \pi/2 - \phi - \alpha)}{\cos \gamma} \quad (13)$$

Now, if a rectangular grid is put at  $X = X_1$  and all grid points are considered starting points for streamlines, the direction of all lines at a new  $X$  station may be computed. In the program the integration is carried out using the Runge-Kutta method, which is thereafter applied once more to the equation

$$\frac{dZ}{dX} = \tan \gamma \quad (14)$$

to get the  $Z$  coordinate at the new station. In the starting grid the velocity is assumed to vary according to the  $1/7$ -th power law and the pressure is computed from (7).

Having marched one step the velocity is obtained from (4a), again assuming zero shear stress and constant pressure across the boundary layer. The streamlines close to the surface must however be considered separately, since the no-slip condition violates the assumption of constant total head. Therefore, the velocity at the innermost 10 lines is computed from a power law, whose exponent is computed so as to yield a smooth junction at the 11th line.

Knowing the velocity, stream tubes according to point 6 above are formed, and the exit area is enlarged in the  $Y$ -direction so that the initial volume flux can be maintained. Since adjacent streamtubes generally have different displacements, the average is taken at the common boundary.

In this manner all streamlines were traced downstream, until separation occurred, i.e. the streamlines close to the surface merged into an envelope. No particular problems were encountered, but the grid turned quite distorted downstream. The expected features, such as the more rapid turning of the inner streamlines occurred, but since no experiments for this case were known to us at that time\* no quantitative evaluations could be made. An example of the results is given in

---

\* The first part of this work was carried out in 1978. One year later measurements for the line source case were reported by Krogstad (1979).

figure 8.

To enable some quantitative comparisons, a change was made to the original potential flow. Equations (6a, b) were replaced by

$$U_{rp} = U_{\infty} \cos\phi \left(1 - \frac{a^2}{r^2}\right) \quad (15a)$$

$$U_{\phi p} = -U_{\infty} \sin\phi \left(1 + \frac{a^2}{r^2}\right) \quad (15b)$$

corresponding to a circular cylinder with the radius  $a$ . This case has been experimentally investigated by East & Hoxey (1969).

Using the measured initial data the calculations were carried downstream until separation. This occurred considerably further downstream in the measurements, but as can be seen from figure 9 the correspondence between the measured and computed momentum thickness (at least at the symmetry line, where it was evaluated) is surprisingly good, despite the neglect of the shear stresses. This is due to the fact that this case is strongly dominated by pressure forces, which are indeed considered in the method.

The experiences from the pilot cases were considered so promising that it was decided to start the development of a method for ship stern flow.

#### DETAILS OF THE STERN FLOW METHOD

The general principles of a method of this kind were explained in the points 1-9 above and in figure 5. If proper account is taken of the Reynolds stresses, a full solution of the Reynolds equations might be accomplished in this way.

In the present work two types of simplifications have been introduced.

1. Since the Reynolds stresses seem to play a very limited role near the stern, only the largest ones, considered in ordinary boundary layer methods, i.e.  $\rho u v$  and  $\rho v w$  are taken into account.
2. The scheme 1-9 is interrupted after point 6, so there is no iterative updating of the pressure. This approximation will be removed in future work.

The details of the method may conveniently be explained following the scheme 1-6.

#### A. Input

All calculations presented here have been started at  $X = 0.5$ , using 18 grid points (streamlines) circumferentially and 12 in the normal direction. The velocity distributions along the eighteen normals are computed from analytical formulae to yield smooth initial data. Input parameters are the friction velocity,  $u_{\tau}$ , the boundary layer thickness,  $\delta$ , and the wall cross flow angle,  $\beta_w$ . Since the purpose of the present calculations is to test the method, measured input parameters

are used. In further applications the data should be taken from boundary layer calculations upstream.

The longitudinal velocity,  $u_1$ , is computed from a formula combining smoothly the linear part of the velocity profile with the wall-wake law. ( $y_D$  is the distance from the surface.)

$$\frac{u_1}{u_e} = 1 - (1 - f \frac{u_1}{u_e})g \quad (16)$$

where

$$g = 1 - \eta^2(3 - 2\eta); \quad \eta = \frac{y_D}{\delta} \quad (17)$$

$$f = \frac{y^+}{\sqrt{1 + Cy^{+2}}} \quad \text{for } y^+ \leq y_D' \quad (18)$$

$$f = 2.39 \ln y^+ + 5.45 \quad \text{for } y^+ > y_D' \quad (19)$$

$$y^+ = \frac{u_\tau y_D}{\nu} \quad (20)$$

$C$  and  $y_D'$  are chosen so as to yield a smooth distribution of  $u_1$  and  $\partial u_1 / \partial y_D$  at the junction.

Alternatively, the 1/7th power law may be used for the longitudinal flow

$$\frac{u_1}{u_e} = \eta^{1/7}$$

The cross flow is obtained from Mager's formula

$$\frac{u_c}{u_e} = \frac{u_1}{u_e} (1 - \eta)^2 \tan \beta_w \quad (21)$$

and as reference direction ( $\beta = 0$ ) the potential flow direction on the surface is used.

Also in case of the pressure on the surface, measured data are used as input when comparing the results with measurements. Some examples from theoretical pressure distributions are however also given.

## B. The Pressure Outside the Surface

Since the pressure iteration procedure is not applied here an assumption has to be made for the pressure outside the surface. Some improvement of the ordinary boundary layer assumption is obtained if the pressure is assumed constant across each layer of stream tubes, i.e. in principle at right angles to the stream surfaces. This simplification is adopted at present, and it will, in the future, be used as the first approximation of the pressure iteration.



### C. Stresses and Stress Gradients

The simple mixing length model is used for the shear stresses, i.e.

$$\tau_{xy} = \rho(\nu + \epsilon) \frac{\partial u}{\partial y} \quad (22a)$$

$$\tau_{zy} = \rho(\nu + \epsilon) \frac{\partial w}{\partial y} \quad (22b)$$

where the eddy viscosity,  $\epsilon$ , is computed from

$$\epsilon = l_m^2 \left| \frac{\partial u}{\partial y} \right| \quad (23)$$

and the mixing length,  $l_m$ , from

$$l_m = 0.085\delta \tanh \left( 4.82 \frac{y_D}{\delta} \right) \quad (24)$$

according to Michel et al (1968). This function is similar to the more commonly used ramp function but produces a smoother distribution of the shear stress.

Close to the wall,  $l_m$  is multiplied by the van Driest damping factor

$$F = 1 - \exp\left(-\frac{y^+}{26}\right) \quad (25)$$

To be able to obtain  $y^+$ ,  $u_\tau$  is needed. This is computed after each step from the innermost points, starting with the one closest to the surface. By matching  $u/u_e$  to the equations (16), (19) a value of  $u_\tau$  may be found. If this yields an  $y^+$  which is larger than  $y_D'$  it is kept. Otherwise the next point for  $k = \text{const}$  is tested, etc. Having found  $u_\tau$ , the velocity for all points for which  $y^+ < y_D'$  is adjusted to follow (16), (18).

At the initial station the grid is generated at right angles to the surface so the definition of  $y_D$  is straightforward. At all other stations, however, the grid is distorted, so the computation of  $y_D$  is not that simple. In accordance with the assumption for the pressure,  $y_D$  is computed along lines which are at right angles to the stream surfaces, see figure 10, (each layer is considered as a boundary layer). The fact that the normal to the surface is not in the plane  $X = \text{const}$  is thus neglected when computing  $l_m$ .

In fact, neither  $y$  nor  $z$  are in the  $X = \text{const}$  plane. The direction cosines of the  $\hat{x}$ ,  $\hat{y}$ ,  $\hat{z}$  unit vectors in the  $X$ ,  $Y$ ,  $Z$  system are obtained as follows.

$\hat{x} = (\alpha_x, \beta_x, \gamma_x)$  is computed by upstream differencing between the points  $(i-1, j, k)$  and  $(i, j, k)$ . To obtain  $\hat{y}$ , a unit vector  $\hat{t}$  is introduced along the intersection between the stream surface and the plane  $X = \text{const}$ , see figure 10. This is found from central differencing between the points  $(i, j, k-1)$ ;  $(i, j, k)$  and  $(i, j, k+1)$ . (The other

direction in the grid corresponds to a unit vector  $\hat{s}$ , computed from the points  $(i, j-1, k)$ ,  $(i, j, k)$  and  $(i, j+1, k)$ . At the boundaries one-sided differences are used.  $\hat{y}$  is found from the relation

$$\hat{y} = \frac{\hat{x} \times \hat{t}}{|\hat{x} \times \hat{t}|} \quad (26)$$

and  $\hat{z}$  from

$$\hat{z} = \hat{x} \times \hat{y} \quad (27)$$

When computing y-derivatives of velocities and shear stresses, derivatives in X are neglected.  $\partial/\partial y$  may then be obtained from

$$\frac{\partial}{\partial y} = \beta_y \frac{\partial}{\partial Y} + \gamma_y \frac{\partial}{\partial Z} \quad (28)$$

where  $\partial/\partial Y$  and  $\partial/\partial Z$  are found from the relations

$$\frac{\partial}{\partial Y} = \frac{\gamma_s \frac{\partial}{\partial t} - \gamma_t \frac{\partial}{\partial s}}{\beta_t \gamma_s - \beta_s \gamma_t} \quad (29a)$$

$$\frac{\partial}{\partial Z} = \frac{\beta_s \frac{\partial}{\partial t} - \beta_t \frac{\partial}{\partial s}}{\beta_s \gamma_t - \beta_t \gamma_s} \quad (29b)$$

and the derivatives with respect to  $t$  and  $s$  are obtained from differences between the points mentioned above.

Having computed the shear stresses from (21a, b) the stress terms of (4a, c) may be evaluated. Since the boundary layer assumption is employed for the stresses, derivatives with respect to  $x$  and  $z$  may be neglected in comparison with the ones with respect to  $y$ . The terms  $s_1$ ,  $s_3$  thus become

$$s_1 = \frac{\partial \tau_{xy}}{\partial y} \quad (30a)$$

$$s_3 = \frac{\partial \tau_{zy}}{\partial y} \quad (30b)$$

#### D. The Lateral Pressure Gradient and the Geodesic Curvature of the Streamlines

To obtain a derivative with respect to  $z$ , derivatives with respect to  $x$  and  $t$  may be employed

$$\frac{\partial}{\partial z} = \frac{1}{\frac{dz}{dt}} \left[ \frac{\partial}{\partial t} - \frac{\partial}{\partial x} \cdot \frac{dx}{dt} \right] \quad (31)$$

AD-A158 920

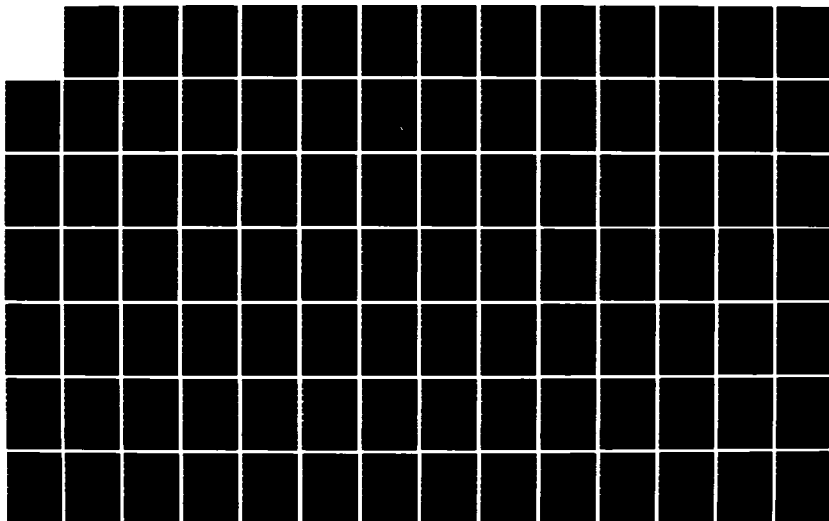
SYMPOSIUM OF NAVAL HYDRODYNAMICS (14TH) HELD AT ANN  
ARBOR MICHIGAN ON AUGUST 23-27 1982(U) OFFICE OF NAVAL  
RESEARCH ARLINGTON VA M P TULIN ET AL. 1982

11/13

UNCLASSIFIED

F/G 20/4

NL





where

$$\frac{dx}{dt} = \hat{x} \cdot \hat{t} \quad \text{and} \quad \frac{dz}{dt} = \hat{z} \cdot \hat{t} \quad (32)$$

Since the pressure at all grid points may be obtained according to section F,  $\partial p / \partial z$  can be computed from (31). It is now possible to get the geodesic curvature of the streamlines at  $X = X_i$  using (4c) where all quantities but  $K_{13}$  are known.

E. The step from  $X = X_i$  to  $X = X_{i+1}$

The step is carried out in the  $x, z$ -plane, see figure 11, between the intersections with the planes  $X = X_i$  and  $X = X_{i+1}$  and the new location in the  $X, Y, Z$ , system may be expressed by

$$\vec{X}_{i+1} = \vec{X}_i + \Delta x \cdot \hat{x} + \Delta t \cdot \hat{t} \quad (33)$$

where  $\vec{X} = (X, Y, Z)$

$\Delta t$  may be found from the sine theorem, see figure 11

$$\Delta t = z_{i+1} \frac{\sin(\pi/2 + \phi)}{\sin(\pi/2 - \phi - \Omega)} = z_{i+1} \frac{\cos \phi}{\cos(\phi + \Omega)} \quad (35)$$

and  $\Delta x$  is simply

$$\Delta x = \frac{\Delta X}{\alpha_x} \quad (36)$$

It remains to determine  $\Omega$ ,  $\phi$  and  $z_{i+1}$

$$\Omega = \cos^{-1}(\hat{t} \cdot \hat{z}) \quad (37)$$

$$\phi = \tan^{-1} \left( \frac{dz}{dx} \right)_{i+1} \quad (38)$$

$z_{i+1}$  and  $(dz/dx)_{i+1}$  may be obtained by series expansion about  $x=x_i=0$ . Since by definition  $y_{i-1}$  and  $y_i = 0$ , there is obtained

$$z_{i+1} = \frac{d^2 z}{dx^2} \Delta x^2 + \mathcal{O}(\Delta x^4) \quad (39)$$

$$\left(\frac{dz}{dx}\right)_{i+1} = \frac{3}{2} \cdot \frac{d^2 z}{dx^2} \Delta x + \mathcal{O}(\Delta x^2) \quad (40)$$

where the second derivative may be found from

$$K_{13} = \frac{\frac{d^2 z}{dx^2}}{\left[1 + \left(\frac{dz}{dx}\right)^2\right]^{3/2}} = \frac{d^2 z}{dx^2} + \mathcal{O}(\Delta x^2) \quad (41)$$

#### F. Continuity

After the step, the change in total head,  $p$ , is computed from (4a), knowing the shear stress term  $s_1$ . Since the<sup>0</sup> pressure  $p$  may be found according to section B, the new velocity is taken from (5). When one layer of streamlines has been marched forward the lines are used four by four to define corners in the stream tubes and the average longitudinal (X-wise) velocity is computed. Since the volume flux,  $\bar{V}$ , is known from the start of the steps, the required new area can be found. As explained in figure 6, the two outer stream lines ( $j,k$  and  $j,k+1$ ) are moved so as to create the exact area. Now, this must be done without displacement sideways, i.e. in the  $z$ -direction, because otherwise the lateral curvature will be changed.

Several attempts were made to find a good solution to this problem. A straightforward way would be to start at the lower symmetry line ( $k=1$ ), assuming a boundary condition, for instance constant thickness of the first streamtube. Since adjacent tubes must have a common outer corner, ( $j,k$ ) to yield a smooth stream surface, only one of the corners ( $j, k+1$ ) could be moved, in the second stream tube to get the required area. This corner being determined, the next tube could be computed, etc. Unfortunately, this method turned unstable, and after some other attempts a two-step procedure was adopted.

This procedure may be described with reference to figure 12, which explains how the location of point ( $j,k$ ) is found. First, normals are computed through the filled circles, representing the location of the streamlines after the step. The base points of the normals are connected by straight lines, with which the dotted lines are parallel. The locations of the dotted lines are determined so as to yield the correct areas. A first approximation of the location of the streamlines has now been obtained (open circles). However, as appears from the figure,

there is a gap between the stream tubes. The point  $(j,k, a \text{ cross})$  is therefore, in the second step, computed to give a common corner with the total area of the two stream tubes unchanged.

The formulae for this procedure follow from simple 2-D geometry but are rather lengthy. They will not be given here.

#### G. Special features

When testing the computer program two difficulties were encountered. As found in the pilot tests, the grid got quite distorted downstream, so problems arose when trying to satisfy the continuity of the very skewed stream tubes. The other problem was linked to the assumption of constant pressure in the  $y_D$ -direction. Since streamlines are traced downstream, the computation is bound to meet with problems if separation is encountered, i.e. if the streamlines merge into an envelope. An ordinary finite difference method might not be so sensitive, since the grid is usually independent of the solution, at least in the  $z$ -direction, so all quantities will be smoothed by the coarseness of the grid. Now due to the pressure assumption, there is a feed-back missing between the streamline convergence and the pressure. In a real flow, if the streamlines in some way would be forced to converge rapidly, continuity would require a large normal velocity, i.e. a large upward bend of the streamlines. This, in turn would create a large normal pressure gradient towards the surface, where the pressure would be increased. The streamlines would then be moved apart, and the convergence reduced. Since this link is missing, separation will be predicted too early.

To overcome these difficulties, a procedure for creating a new grid was developed. The program thus continuously tests the distortion of the stream tubes and the convergence (divergence). If certain limits are exceeded a new grid is generated after the step. In this grid the stream surfaces ( $j = \text{const}$ ) are kept, but the stream tubes between the surfaces are rearranged more uniformly. Linear interpolation around the girth, i.e. in the  $t$  direction, is used for all quantities, when generating the new grid. It should be mentioned, that it is the thickness of each layer of stream tubes which is interpolated, not the  $Y, Z$  coordinates. In this way large smoothing is avoided.

#### H. Boundary conditions

The no-slip condition is applied on the surface, and, as mentioned above, for streamlines below  $y^+ \leq y_D^+ (=33)$  the wall function (16), (18) is used.

At the edge of the computed region the total head will continuously drop. Since no new streamlines are introduced into the computations as they proceed downstream, part of the viscous region will be missed. This is not a very serious problem, though, since the velocity drop is only a few per cent.

At the lateral boundaries the streamlines are forced to stay in the symmetry planes.

## RESULTS

The two cases used for testing the method were the ones of the SSPA-ITTC Ship Boundary Layer Workshop (Larsson 1981), namely the SSPA Mod 720 cargo liner model, tested by Larsson (1974b), and the HSVA tanker model tested by Hoffman (1976) and Wieghardt and Kux (1980). Extensive sets of data are available for both.

## A. The SSPA Model 720

The calculations were started at  $X = 0.5$ , i.e. 25% LBP from the AP, using  $u_T/u_e$ ,  $\delta^+$  and  $\beta$  from 7 measured velocity profiles, distributed around the girth. The data were interpolated to 18 girth-wise locations, where the input was given. 12 grid points were used in the normal direction, located at 0, 5, 10, 16, 25(10)85, 100 per cent of the boundary layer thickness. Some reduction of the measured cross-flow angles were made to make the analytical cross-flow profiles more similar to the measured ones. (The measured cross-flow was large only very close to the surface). The Reynolds number  $R_{nL}$  was  $5 \cdot 10^6$ .

A separate program, using spline approximation was run to interpolate the measured pressures and the coordinates of the hull to 18 points per section of interest,  $X = 0.5(0.025)0.7(0.01)0.94$ .

In the figures 13-17, computed isowakes are compared with measurements. The latter have been interpolated by hand from the velocity profiles given by Larsson (1974b) and the former are direct computer plots of the output from the program. Linear interpolation has been used to get the isowakes.

In general, there is good correspondence between the calculations and the measurements. The thickness and the shape of the viscous region is well predicted all the way back and the velocity distribution inside the region is realistic, except close to the surface at the aftermost stations. In the keel region, the measurements indicate a low speed area which is not found in the calculations. A possible explanation for this is that the convergence of the flow has been reduced too much by the new grids. Note that the isowakes have been made dimensionless by the undisturbed velocity,  $U_\infty$ , not by the edge velocity  $u_e$ , as in the Boundary Layer Workshop. That is why the velocities are larger than unity at stations  $X = 0.5$  and  $0.6$ .

It might also be of interest to see the shape of the grid at some stations. In the figures 18 and 19 computer plots of the grid at  $X = 0.5$  and  $X = 0.9$  respectively, are given. As mentioned, the stream surfaces ( $j = \text{const}$ ) are the same in the two plots, while the lateral divisions have been changed.

Another point of interest is the influence of the shear stresses. What would be the result if these were removed, i.e. if the method were purely inviscid? Since this is very easily accomplished in the present method by putting the terms  $s_1$  and  $s_2$  equal to zero, a separate



run was made. The result may be seen in figure 20, which gives the isowakes at  $X = 0.9$ . Note that the 0.95-line is now complete. The thickness of the region is reduced somewhat, but not very much, so the importance of the viscous terms is not very great, although the stresses are considerably larger in the computations than in the measurements close to the stern.

#### B. The HSVA tanker model

The calculations for the HSVA model ( $R_{nL} = 6.8 \cdot 10^6$ ) started at the same station,  $X = 0.5$ . It was first attempted to use the same type of input as for the SSPA model, but the resulting velocity profiles from equations (16) - (20) corresponded very badly with the measured ones. This is due to the fact that the measured skin friction is unusually large (which yields a large  $u_T/u$ ). A much better fit to the measured initial velocities was obtained using the 1/7-th power law, so this was adopted. In this case, the grid points were located at 7, 13, 19, 25(10)85 and 100 per cent of the boundary layer thickness.

In figure 21, the computed isowakes at  $X = 0.9$  are compared with the very detailed measurements by Wieghardt and Kux (1980). Unfortunately, there is some difference between the shape of the sections in the computations as compared with the measurements. In particular, the depth of the measured model is slightly smaller. This does not seem to influence the results, however, since the correspondence between calculations and measurements is again quite encouraging. The only major difference is near the surface on the keel, when the accuracy is low also on the SSPA model.

#### C. The pressure distribution

All comparisons so far have been made for results based on the measured pressure distribution. To test the computer program at this stage, such an approach is justified. However, in the final computational procedure it is of course necessary to start from theoretical calculations both for the pressure and for the initial data.

Tests with the purely theoretical pressure on the surface did not work too well, so an ad hoc adjustment was made. The major difference between the theoretical and the experimental pressures seem to be that the latter is more even, girthwise, near the stern. Since the convergence (divergence) depends on the second derivative of the girthwise pressure distribution this effect must be important. It was therefore decided to assume a constant pressure,  $c_p = 0.1$  at  $X = 0.9$  and to let the adjusted  $c_p$  vary linearly with  $X$  between the theoretical one and 0.1. The adjustment started from zero at  $X = 0.5$ .

In figures 22 and 23 the computed results at  $X = 0.9$  are shown. Obviously the adjustment works quite well for the SSPA model and reasonably well for the HSVA model. In any case this approach might be taken as a start of the iteration process of the full, iterative procedure.

## CONCLUSIONS

It has been suggested that the major effect to take into account when computing stern flows is the rearranging of the momentum loss from the boundary layer further forward. This rearranging is due to flow convergence (divergence), which must therefore be computed accurately. On the other hand, turbulence modeling might not be too important in the stern region.

Some preliminary evidence for these assumptions have first been given in the paper. Thereafter, a method based on the assumptions has been presented. Although considerably more work is needed to fully develop the procedure, already at this stage, the presented results must be considered most encouraging.

## ACKNOWLEDGEMENTS

The authors owe great thanks to Dr Gilbert Dyne, SSPA, for providing the original ideas for this work, and for many interesting discussions during its completion. Special thanks are also extended to Miss Eira Samuelsson, who spent many late nights, trying to translate our vague instructions into the FORTRAN language.

The work was sponsored by the Swedish Board for Technical Development, Contract No 81-4313.

## References

- Bai, K. J. and J. H. Mc Carthy (1980). Proceedings of the workshop on Ship wave-resistance computations, David W. Taylor Naval Ship Research and Development Center.
- Dyne, G. (1978). A streamline curvature method for calculating the viscous flow around bodies of revolution, in Proceedings of the International symposium on ship viscous resistance, L. Larsson, ed., SSPA, pp 6:1-6:22.
- Dyne, G. (1980). A streamline curvature method for the calculation of the boundary layer and wake of two-dimensional symmetrical airfoils, SSPA Report 2466-1.
- East, L. F. and R. P. Hoxey (1969). Low-speed three-dimensional turbulent boundary layer data. Parts I and II, Aeronautical Research Council, Reports and Memoranda No 3653.
- Hoffmann, H. P. (1976). Untersuchung der 3-dimensionalen, turbulenten Grenzschicht an einem Schiffsdoppelmodell im Windkanal, Institut für Schiffbau, Bericht Nr 343.
- Krogstad, P. Å. (1979). Investigation of a three-dimensional turbulent boundary layer driven by simple two-dimensional potential flow, Dissertation, Norwegian Institute of Technology.
- Michel, R., C., Quémard and R. Durant (1968). Hypothesis on the mixing length and application to the calculation of turbulent boundary layers, in Proceedings of the computation of turbulent boundary layers - 1968 AFOSR-IFP - Stanford conference, Volume 1, pp 195-212 A.

- Larsson, L. (1974a). Boundary layers of ships. Part IV. Calculation of the turbulent boundary layer on a ship model, SSPA Report No 47
- Larsson, L. (1974b). Boundary layers of ships. Part III. An experimental investigation of the turbulent boundary layer on a ship model, SSPA Report No 46.
- Larsson, L. (1981). Proceedings of the SSPA-ITTC workshop on ship boundary layers 1980, SSPA Publication No 90.
- Larsson, L. and M. S. Chang (1980). Numerical viscous and wave resistance calculations including interaction, in Proceedings of the Thirteenth Symposium on Naval Hydrodynamics, T. Inui, ed., The Shipbuilding Research Association of Japan, pp 707-728.
- Löfdahl, L. (1982). Measurements of the Reynolds stress tensor in the thick three-dimensional boundary layer near the stern of a ship model, SSPA Report No 61.
- Löfdahl, L. and L. Larsson (1982). Measurements of Reynolds stress profiles in the stern region of a ship model, Paper presented at the IUTAM Symposium on three-dimensional turbulent boundary layers in Berlin, March 1982.
- Wieghardt, K. and J. Kux (1980). Nomineller Nachstrom auf Grund von Windkanalversuchen, Jahrbuch der Schiffbautechnischen Gesellschaft, 74 Band, pp 303-318.

$$\frac{c_{12}}{2} - \frac{\nu}{u_*} \frac{\partial u_*}{\partial s} (2 + H_{12}) - K_{21} (r_{11} - r_{21}) - \frac{\partial' u}{\partial r_1} - \frac{\partial'' u}{\partial s} = 0.$$

(1)
(2)
(3)
(4)
(5)

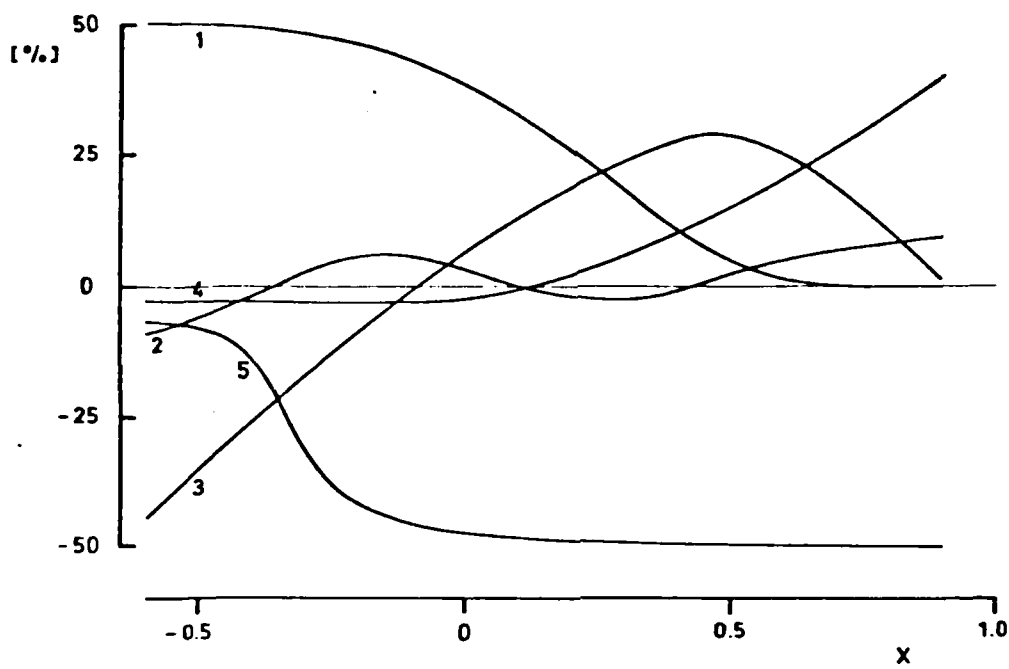


FIGURE 1. Distribution of terms in the longitudinal momentum integral equation along a streamline.

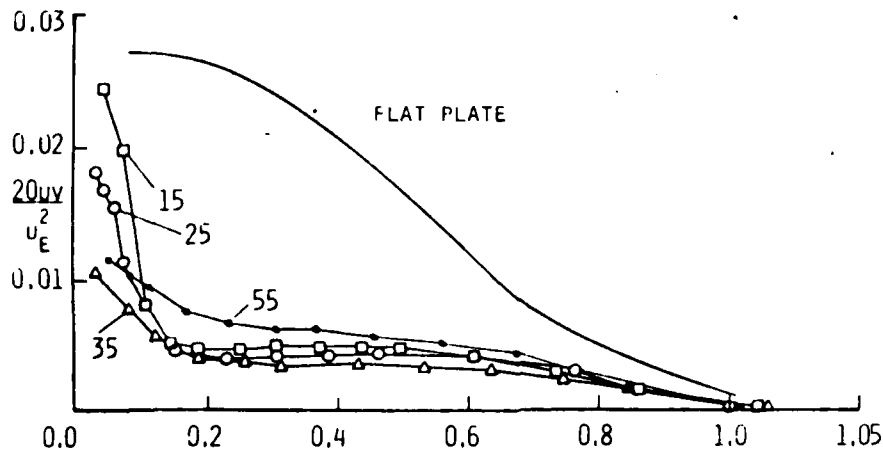


FIGURE 2. Four profiles of  $puv$  measured on the SSPA Mod 710, compared with the flat plate profile. From Löfdahl (1982) and Löfdahl & Larsson (1982).

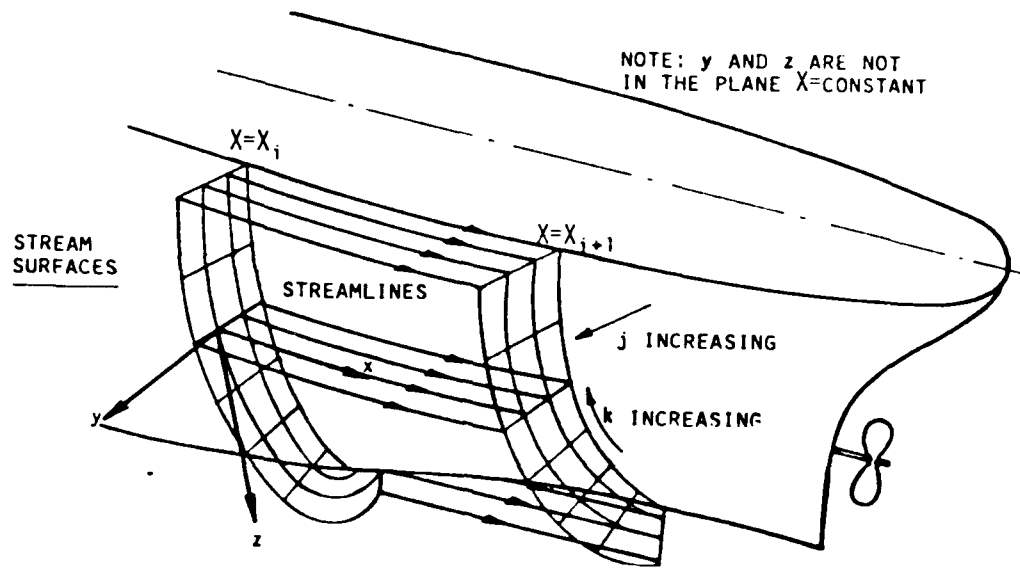


FIGURE 3. The  $x, y, z$ , coordinate system and the grid.

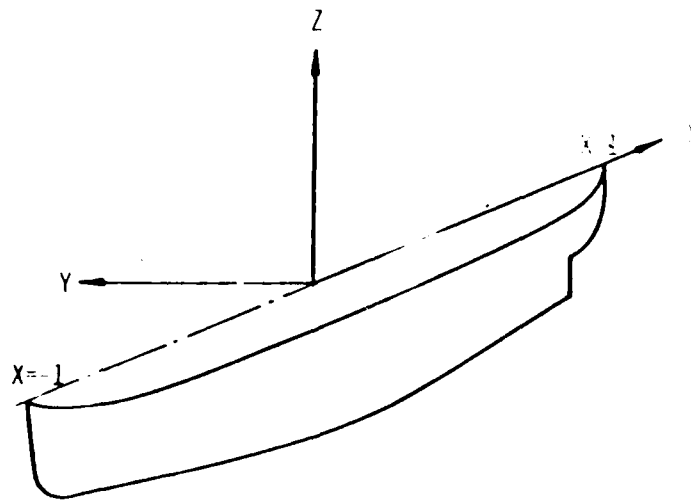


FIGURE 4. The  $X, Y, Z$ , coordinate system.

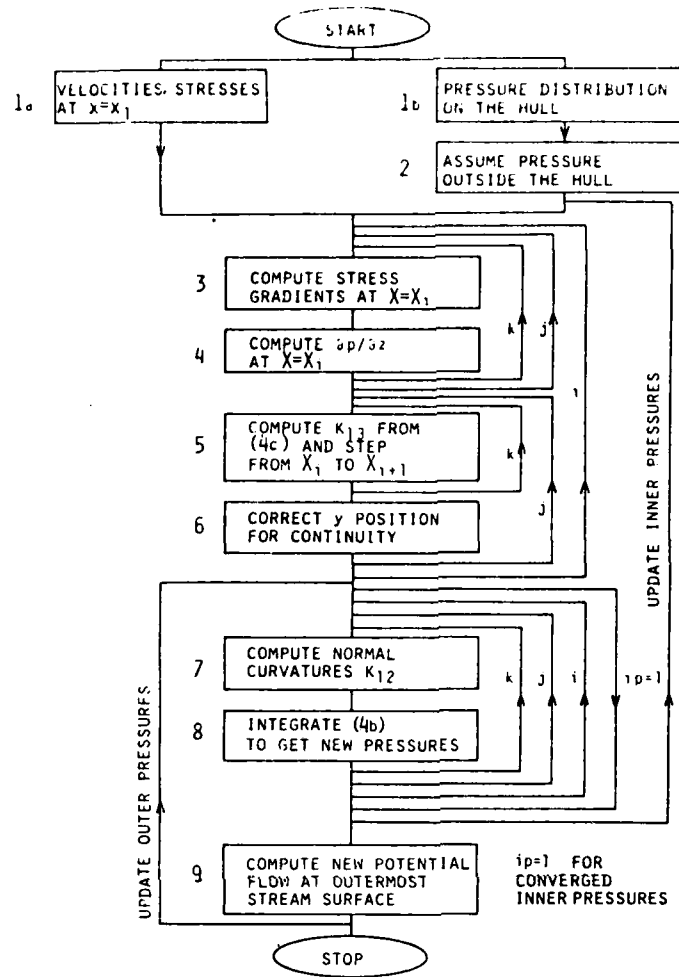


FIGURE 5. Flow chart for complete 3-D streamline curvature method (schematic).

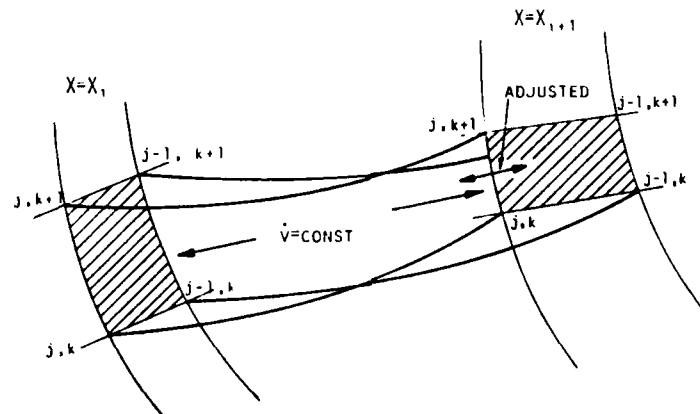


FIGURE 6. A stream tube.

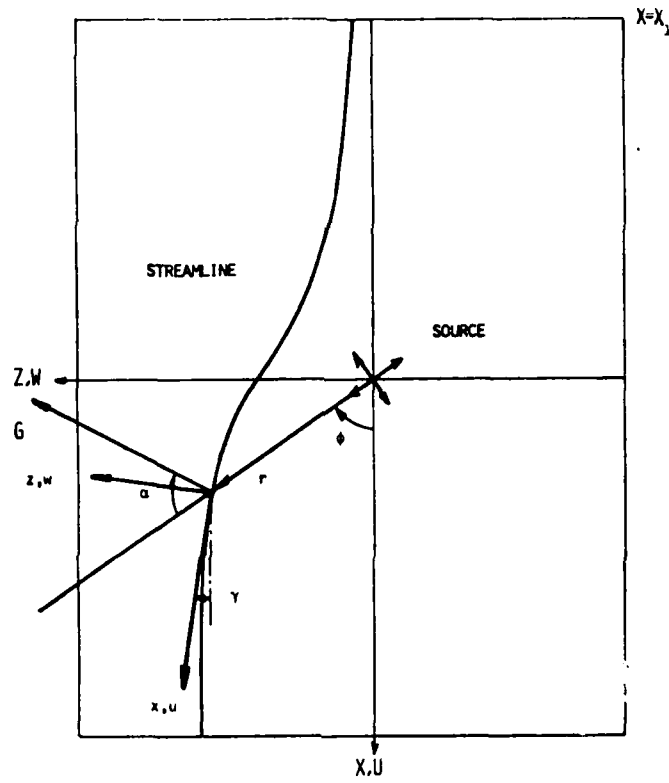


FIGURE 7. The first pilot case.

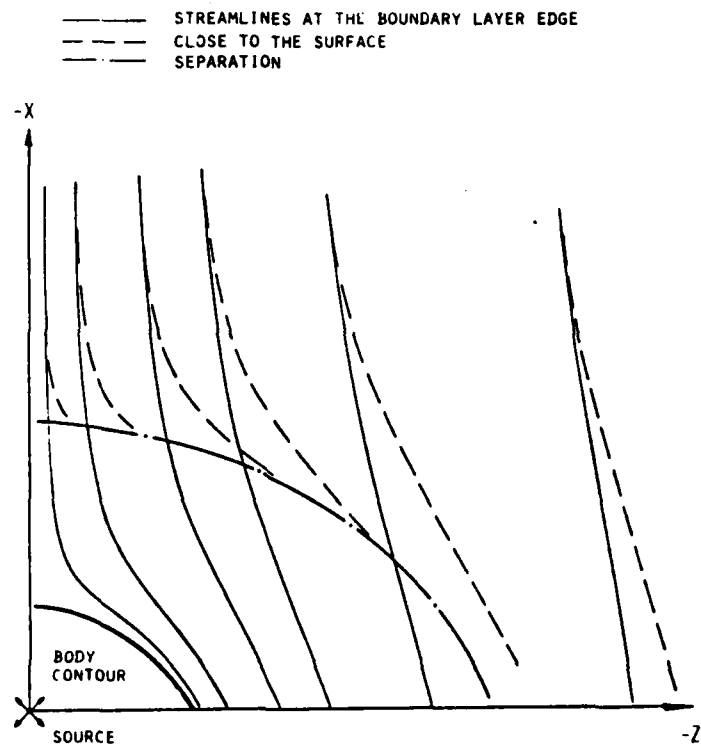


FIGURE 8. Results from the first pilot case.

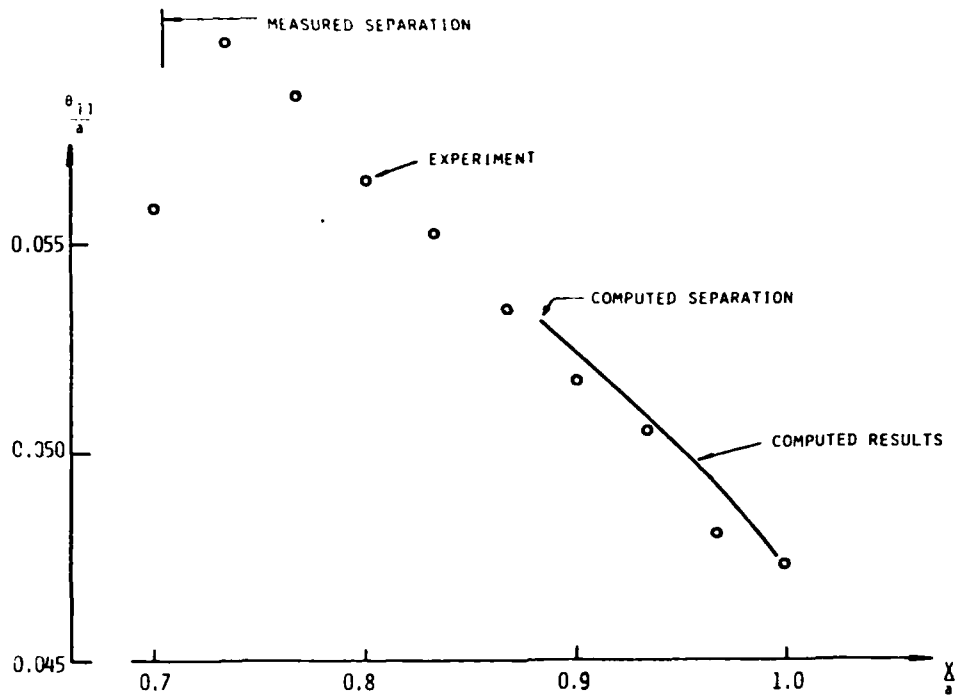


FIGURE 9. Momentum thickness at the centreline for the second pilot case.

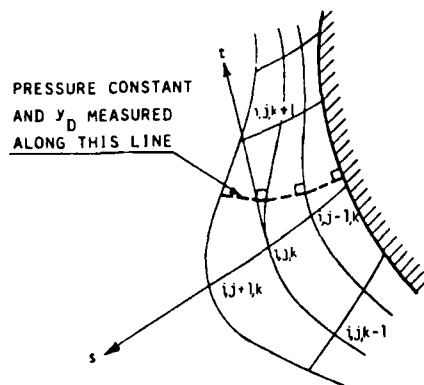


FIGURE 10. Definition of the line along which  $y_D$  is measured and  $p = \text{const.}$



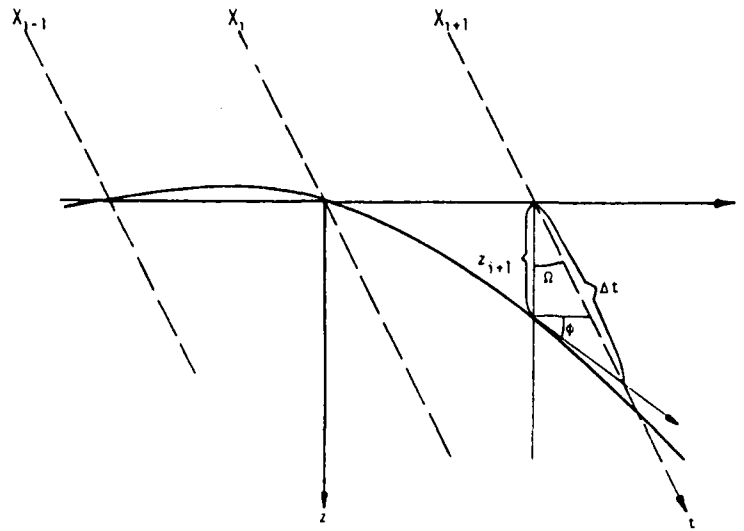


FIGURE 11. The step from  $X = X_i$  to  $X = X_{i+1}$

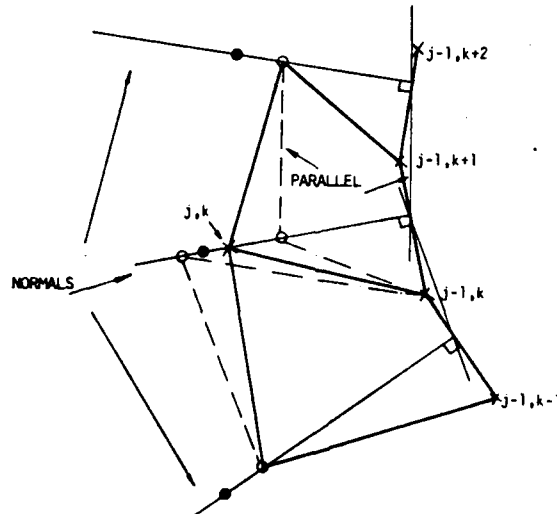
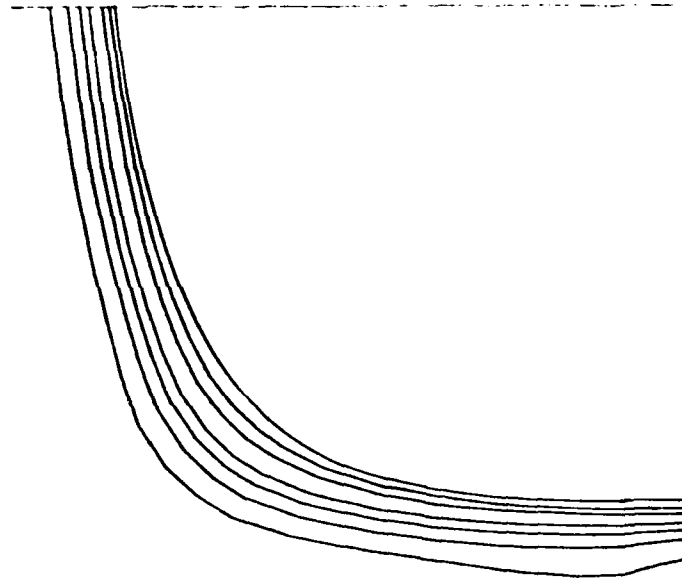
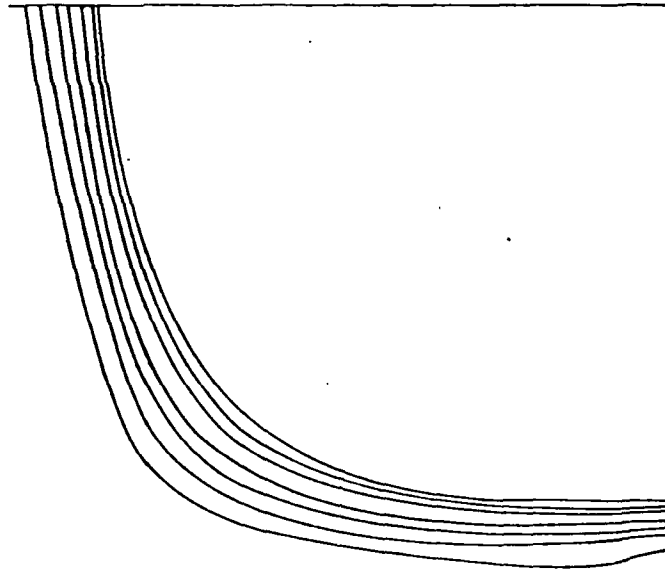


FIGURE 12. The normal displacement of the streamlines.  $X = \text{const}$  plane.

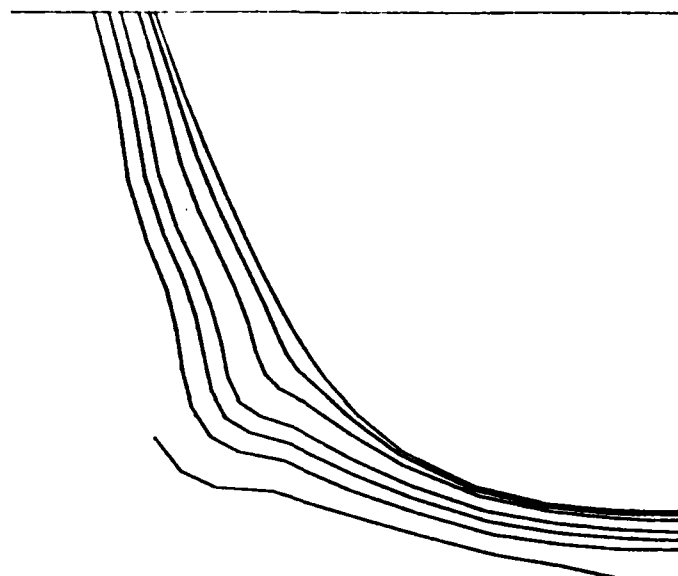


a. calculated

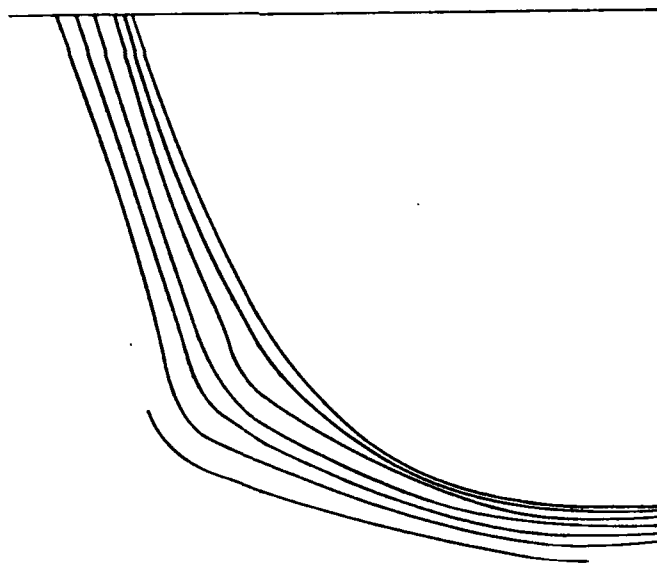


b. measured

FIGURE 13. Isowakes at  $X = 0.5$ . ( $u/U_\infty = 0.7, 0.8, 0.9, 0.95, 1.0, 1.05$ )  
SSPA model.

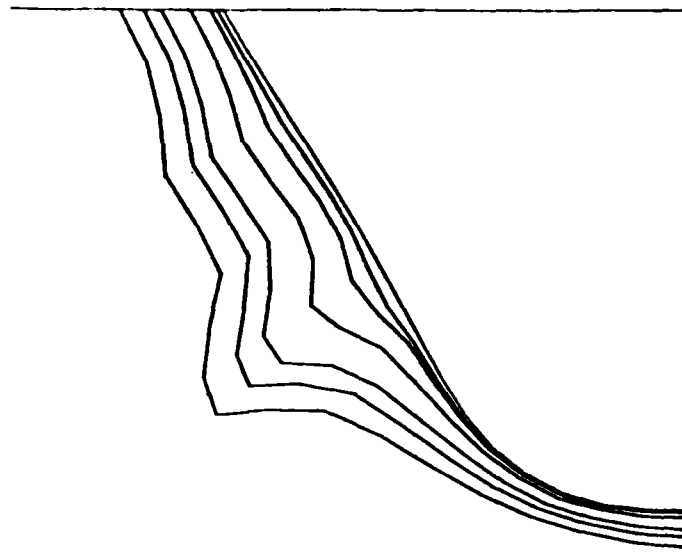


a. calculated

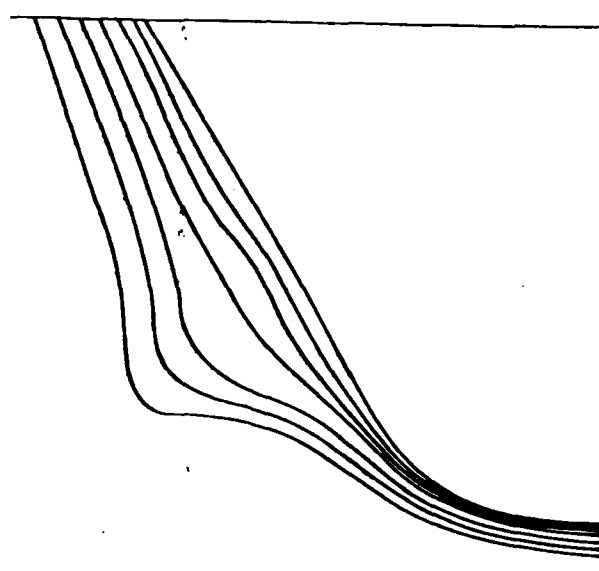


b. measured

FIGURE 14. Isowakes at  $X = 0.6$ . ( $u/U_\infty = 0.7, 0.8, 0.9, 0.95, 1.0, 1.05$ ) SSPA model.

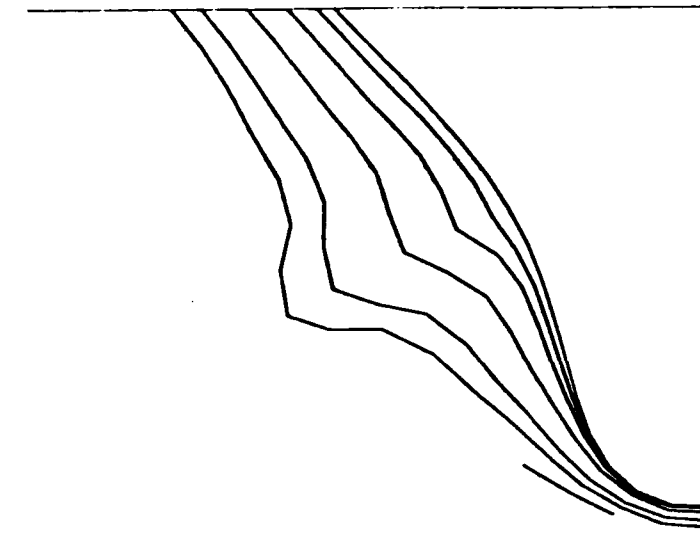


a. calculated

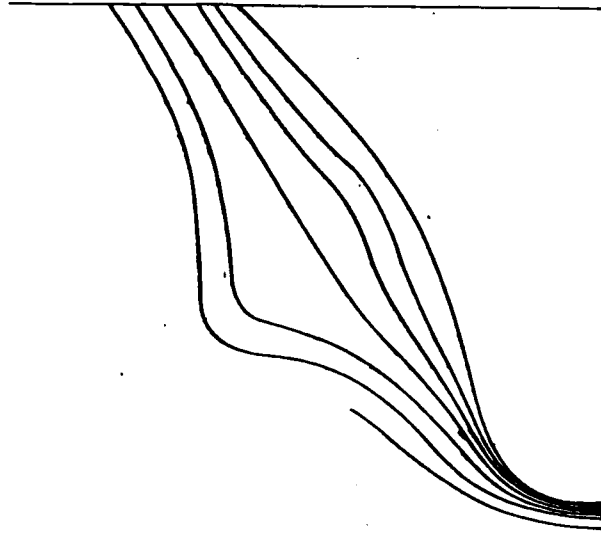


b. measured

FIGURE 15. Isowakes at  $X = 0.7$ . ( $u/U_\infty = 0.6, 0.7, 0.8, 0.9, 0.95, 1.0$ ) SSPA model.

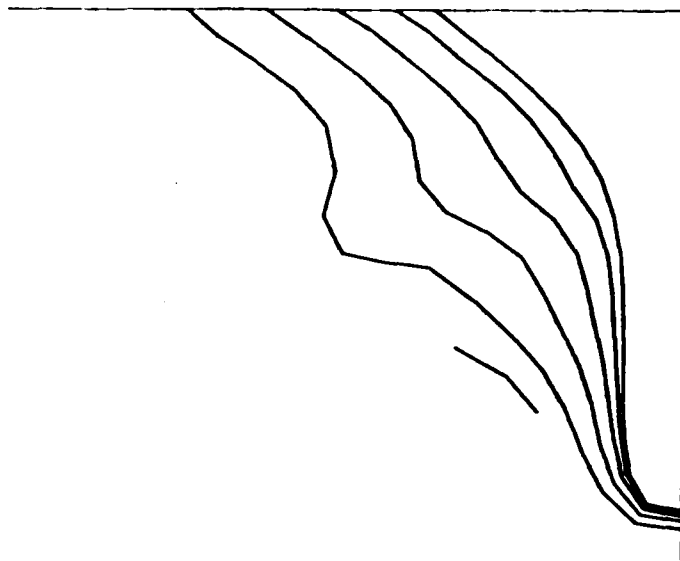


a. calculated

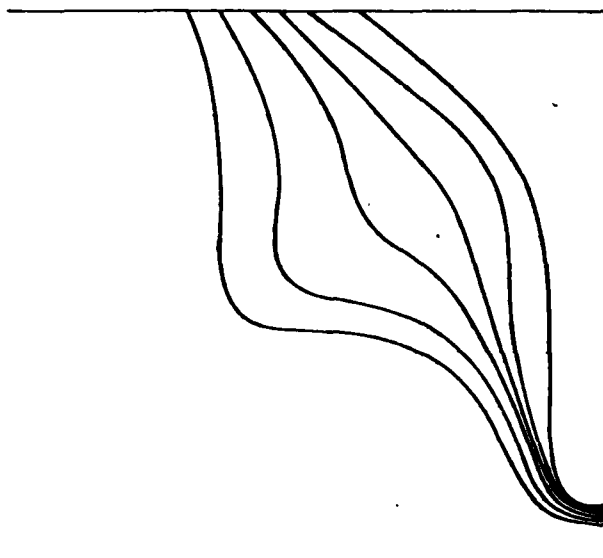


b. measured

FIGURE 16. Isowakes at  $X = 0.8$ . ( $u/U_\infty = 0.6, 0.7, 0.8, 0.9, 0.95, 1.0$ ) SSPA model.



a. calculated



b. measured

FIGURE 17. Isowakes at  $X = 0.9$ . ( $u/U_\infty = 0.6, 0.7, 0.8, 0.9, 0.95$ )  
SSPA model

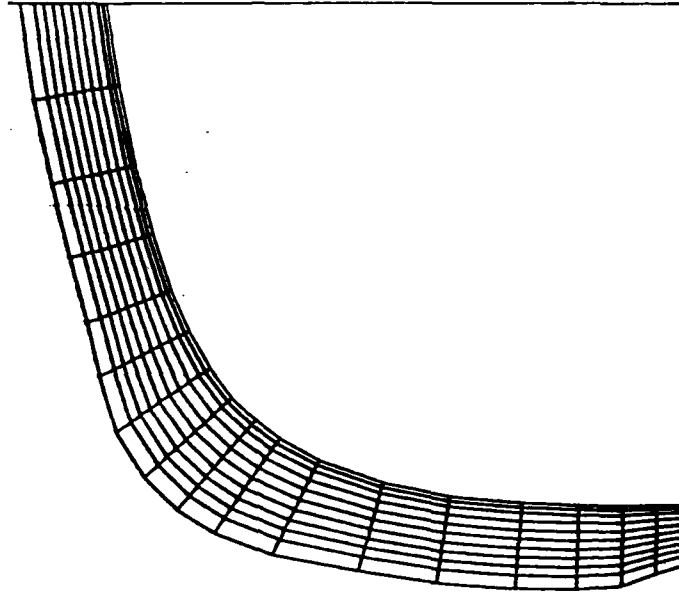


FIGURE 18. Computational grid at  $X = 0.5$ .  
SSPA model.

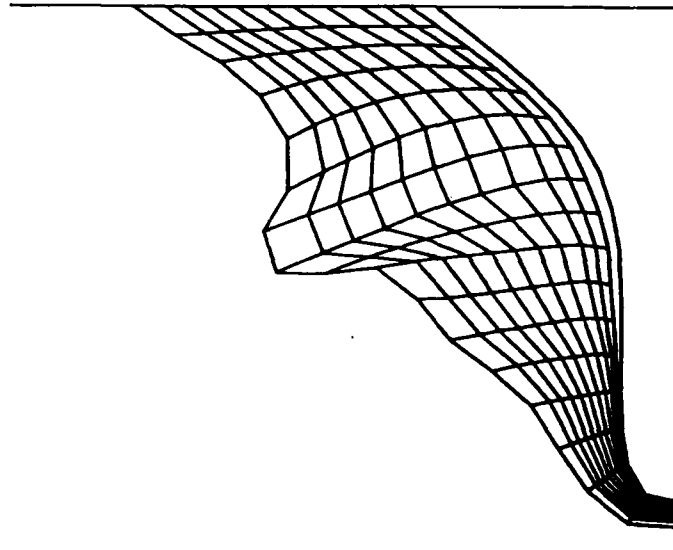


FIGURE 19. Computational grid at  $X = 0.9$ .  
SSPA model.

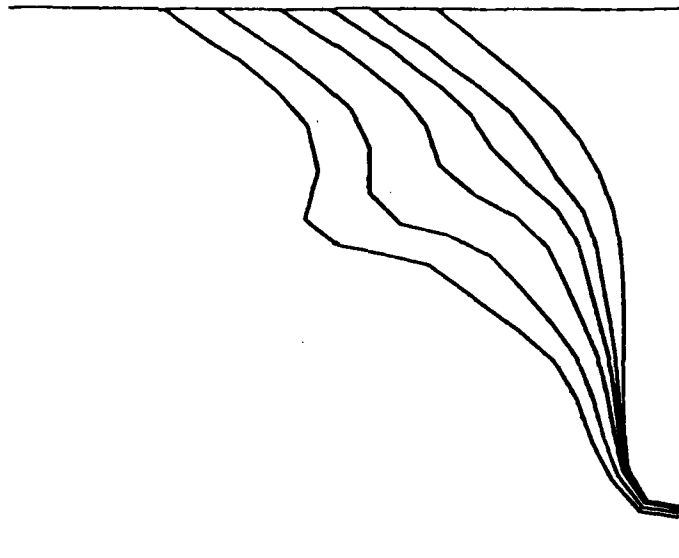
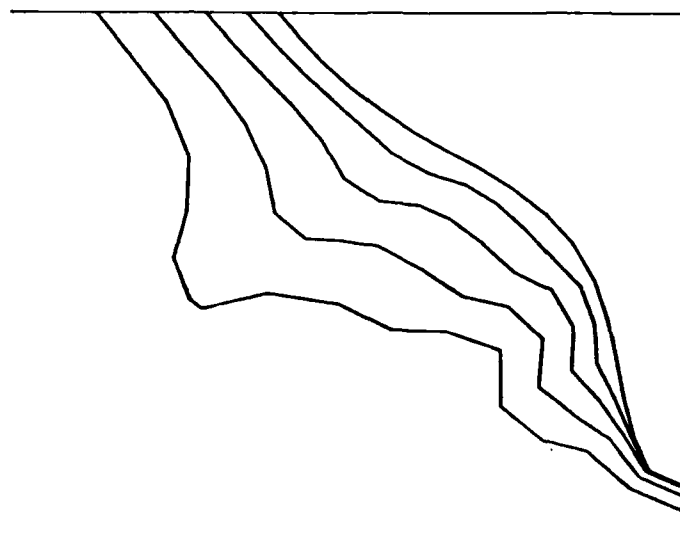
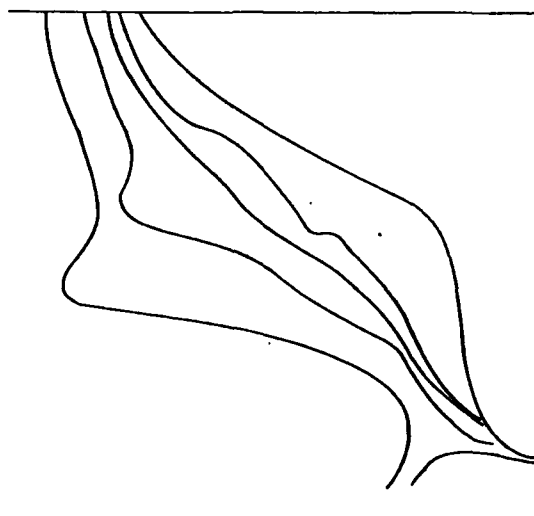


FIGURE 20. Calculated inviscid isowakes at  $X = 0.9$ . ( $u/U_\infty = 0.6, 0.7, 0.8, 0.9, 0.95$ ) SSPA model





a. calculated



b. measured

FIGURE 21. Isowakes at  $X = 0.9$ . ( $u/U_\infty = 0.6, 0.7, 0.8, 0.9$ )  
HSVA model

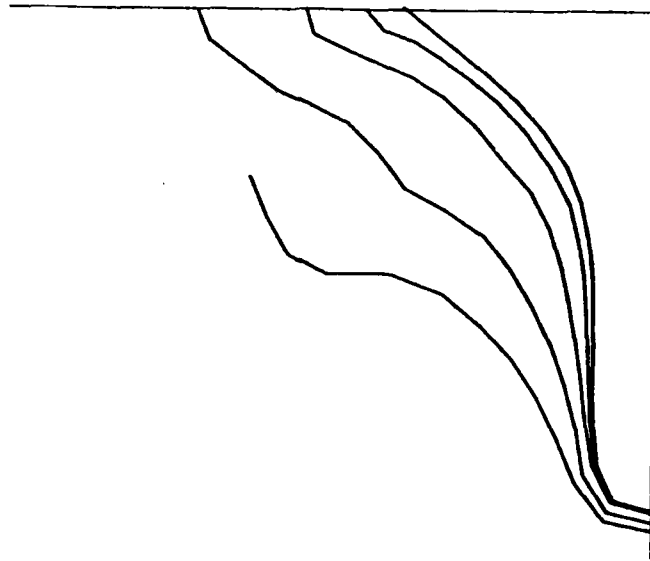


FIGURE 22. Calculated isowakes at  $X = 0.9$ . Modified, theoretical pressure. ( $u/U_\infty = 0.6, 0.7, 0.8, 0.9$ ) SSPA model.

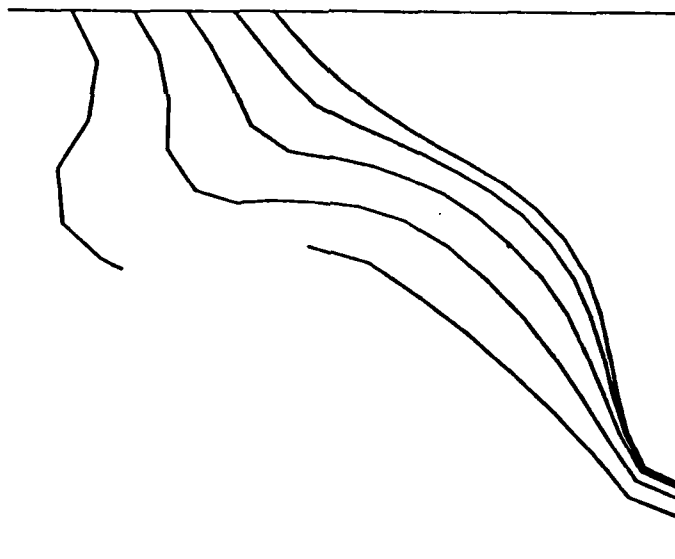


FIGURE 23. Calculated isowakes at  $X = 0.9$ . Modified, theoretical pressure. ( $u/U_\infty = 0.6, 0.7, 0.8, 0.9$ ) HSVA model.

## Discussion

T. Nagamatsu (Mitsubishi Heavy Industries)

Predicting the flow field near the ship stern is one of the most difficult and important problems for us.

The authors indicated by computations that the shear stresses do not play an important role in the stern region. The discussor has also obtained the same results by an experiment (Nagamatsu, 1980). The inertia and pressure terms of the Navier-Stokes equation were calculated from the measured velocity and pressure field, and the summation of them was found to be nearly equal to zero in the outer half of the boundary layer (see Figure 1). This implies that the shear stresses seem to be small.

It is well known that the bilge vortex exists in the stern flow and affects significantly the iso-wake contour curves at the plane of propeller as shown in Figure 2. Therefore the flow prediction taking the bilge vortex into account is important. I would be grateful if the authors would comment on this point.

## References

Nagamatsu, T., Flow Measurements Near the Stern of a Model of a Full Form Ship, *Theoretical and Applied Mechanics*, Vol. 30 (1980).

V.C. Patel (University of Iowa)

It is apparent from the results presented by the authors that the method being developed holds considerable promise. The success of the method is presumably due to the use of the law of the wall to treat the region of large gradients near the surface and the careful explicit solution of the equation of continuity, two of the features that also became evident from my review of the existing experimental evidence on thick boundary layers.

I would like to point out one interesting difference between the experimental and calculated iso-wake lines of the authors' Figures 15-17. In the region of the maximum boundary-layer thickness, the measured iso-wakes close to the hull have a pronounced dip toward the surface. I believe that this is associated with the local divergence and would also explain the measured bulge in the iso-wakes on both sides. A somewhat similar situation exists in the HSVa model data shown in their Figure 21. The failure of the method to reproduce these features appears to indicate that the method does not accurately calculate the local rates of change of streamline curvature. This may, in turn, be due to the assumed pressure field and stress gradients. Would the authors expect the solutions to improve when viscous-inviscid interaction is taken into account, or is the problem a numerical one?

Fig. 1

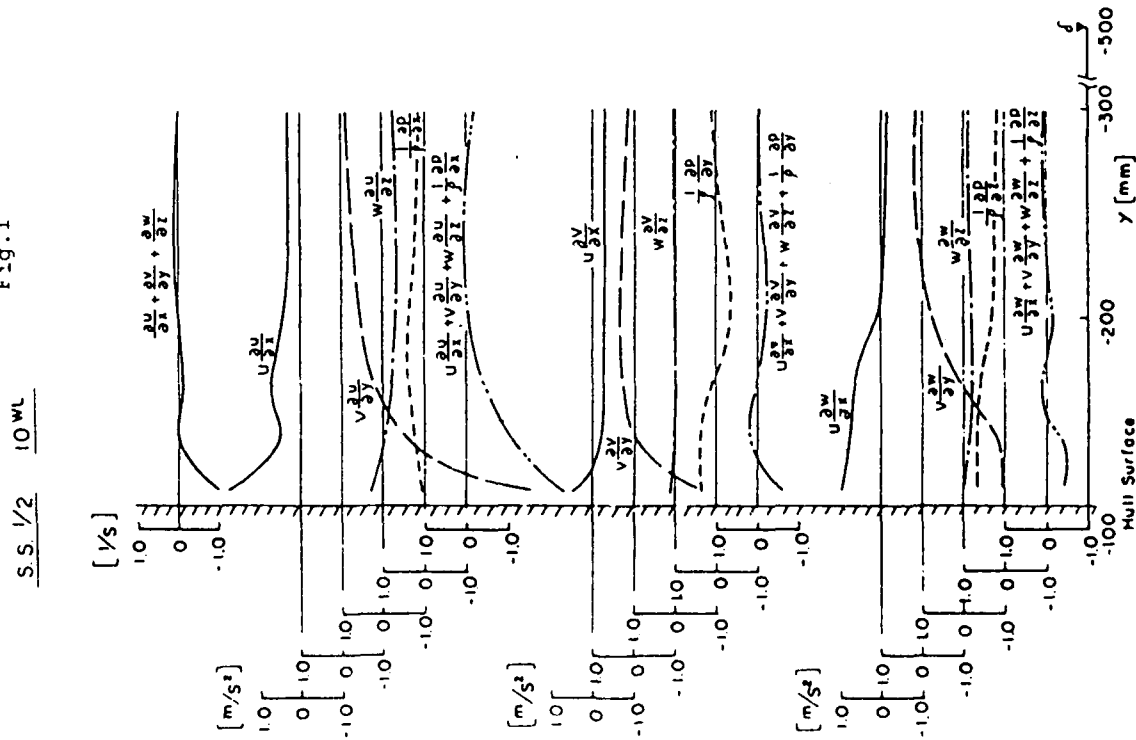
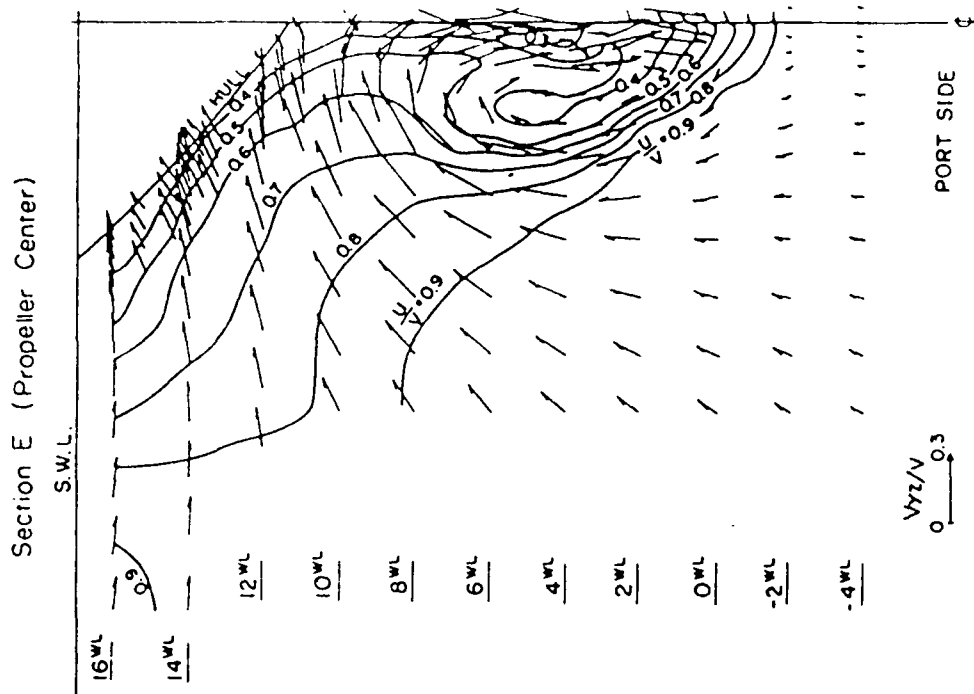


Fig. 2



K. Mori (Hiroshima University)

The determination of streamlines is essentially important in the present method. This is because all the solutions depend on them. The method proposed in the present paper does not give exact streamlines. They should be determined to satisfy the streamline equation.

The discussor understands that the present computation is not the final one. But he would raise an objection to the assumption of the constant pressure in the lateral direction. Though the lines along which the pressure is assumed constant are not always the same as those used in the ordinary boundary-layer calculation, the scheme is no more than the boundary-layer approximation, if his understanding is correct. The main reason for the success to continue the calculation close to the stern without any breakdown is the use of the measured pressure distribution. (There must be discontinuity in pressure at the edge of the boundary layer.)

Y.A. Odabasi (British Ship Research Association)

This paper, by using the information available to the authors, attempts to design a computational scheme for the computation of the flow near ships sterns. Since a similar study has been continuing at BSRA since 1974, I fully appreciate and agree with the main objectives of the authors, i.e., the aim of stern boundary layer and near-wake calculations is not so much to replace the need for scaled model tests but to identify good and bad flow features both to assess a given hull design and to assist in the design of more favorable hull form. A scheme developed for this purpose at BSRA is demonstrated in the authors' Figure 24. Since, however, our data included detailed wind-tunnel boundary-layer measurements of three hull forms (up to and including triple velocity correlation terms) including near wakes as well as the corresponding total in flow-velocity measurements on full-scale ships at the propeller plane, the assumptions adopted in our computational scheme differ considerably from those adopted in the present paper. Below, some of these differences are highlighted with the aid of experimental data and computed results.

1. Computational Grid The choice of a computational grid, to a certain extent, is arbitrary except for some broad guidance that one of the coordinates is aligned with the mainstream (and hence the marching direction) and one of the other coordinates should be aligned with the normal to allow for certain simplifications to be made. Therefore, to specify one coordinate system being superior to the other is not correct. Here the main problem is related more to the accurate representation of the hull form and the usual mesh representation, and the associated planar panels in the computation potential flow create larger sources of error than any other possible error resulting from a variety of choices that are available within the broad guidelines given

above. For this reason a B-spline surface patch system (named B-SURF) is being used at BSRA, which provides all the necessary surface information needed both in the potential flow and boundary-layer/near-wake computations, including metric coefficients. The use of curved normals is desirable and were adopted at BSRA (Odabasi and Saylan, 1980), since the beginning in the interactive scheme by setting both the hull surface and the external matching surfaces as constant coordinate surfaces, i.e.,  $n = 0$  and  $n = 1$  surfaces.

2. Effect of Longitudinal Pressure Gradient The authors state that contrary to two-dimensional boundary layers, the longitudinal pressure gradient does not play a significant role in stern boundary-layer development. In our experience, this assumption is not justified and is a result of the implicit assumptions employed in the method of Larsson (1974). The authors' Figures 25 to 28 display the role of the longitudinal pressure gradient in the development of the momentum thickness by using Gadd's integral method (1978). To qualify this statement, the following information may be useful.

In a computational scheme the influence of hull form on the boundary-layer development by affecting the external flow is felt in two ways:

- a. Convergence and divergence of the external streamlines as a result of continuity,
- b. Formation of streamwise and crossflow pressure gradients.

As will be discussed in the following parts, the role of the pressure gradient is, by no means, less than the former. This, however, will not be felt within the method proposed in the paper owing to the neglect of certain terms. They are:

- a. The assumption used in the velocity profiles near the wall region, i.e., Equations (16) to (21), is valid only for equilibrium boundary layer; a change in the pressure gradients will only be felt in a very indirect and inaccurate manner. A more detailed study, cf. McDonald (1969), Townsend (1976), and Van den Berg (1976), clearly links the flow in the near-boundary region to the pressure gradients, which is of paramount importance in the prediction of stern flow.
- b. If one carries out a dimensional analysis similar to the one carried out by Kader and Yaglom (1978), it can be shown that the boundary layer contains a pressure-gradient length scale,  $\delta_p = u_t^2/\alpha$ ,  $\alpha = (1/\rho)\partial_p/\partial_s$ , and, by the use of this length scale, flow properties can be predicted or matched in a better manner.
- c. Formation of near wake to a large extent depends on the relative location of the weak singularity, i.e., shear separation, and the maximum adverse pressure gradients. If the former precedes the latter, a severe flow retar-

dation results, whereas if they are close to each other a weak or strong vortex forms depending on the relative location and the rate of acceleration, as shown in the authors' Figure 29 (cf. Odabasi, 1980). Recently, this process has been used in the design of the stern region of a Ro-Ro, and model tests conducted in both SSPA and NHL proved the validity of this concept, i.e., paint tests showed a smudged region near the location of shear separation whereas tuft tests proved smooth flow resulting in low wake nonuniformities in all three tested draught conditions.

3. Role of Turbulence Terms Based on limited data, the authors state that turbulent shear-stress terms, and, hence turbulence, are not important and the choice of a turbulence model is, therefore, trivial. Their Figure 30 gives a comparison of the measured turbulence production terms at  $x/L = 0.875$  and  $0.9675$ . While one may justify the assumption for the profiles given for  $x/L = 0.875$ , the measured data further downstream refute this argument. The situation is not too different in the near wake as shown in their Figure 31, where shear reversal regions are also identified with the accompanying bursts of turbulent production.

Since there is a simple way to demonstrate the role of turbulence this will be used in this discussion. In a tuft flow visualization the presence of turbulence is demonstrated by the fluctuations of the tufts, since turbulence production terms are mean-square values of the fluctuating velocity components. As the observation of even, wild, fluctuations of tufts near the stern is a common observation, this proves the presence and the role of turbulence-related terms, since an ideal rotational flow would produce no tuft fluctuation.

Accepting that turbulence-related terms play an important role, modeling of turbulence also gains importance. Since, however, this subject will be raised in the discussion of other papers of this symposium I shall be content with stating that the isotropic eddy viscosity assumption is the least appropriate to choose.

In conclusion, I would like to suggest that the authors reconsider their assumptions as they do not agree with the experimental data.

## References

- Gadd, G.E. (1978), A Simple Calculation Method for Assessing the Quality of the Viscous Flow Near a Ship's Stern, Int. Symposium on Ship Viscous Resistance, SSPA, Goteborg.
- Kader, B.A., and A.M. Yaglom (1978), Turbulence in the Region of Applicability of the "Half-Power Law" for a Decelerating Boundary Layer, Sov. Phys. Dokl., Vol. 23, No. 10, p. 718.
- McDonald, H. (1969), The Effect of Pressure Gradient on the Law of the Wall in Turbulent Flow, J. Fluid Mech., Vol. 35, No. 2, p. 311.

- Odabasi, A.Y. (1980), A Contribution to the Calculation of Flow Around the Aft-Ends of Ships, Int. Shipbldg. Progress, Vol. 20, p. 316.
- Odabasi, A.Y., and O. Saylan (1980), GEMAK--A Method for Calculating the Flow Around Aft-End of Ships, 13th Symp. on Naval Hydrodynamics, Tokyo.
- Townsend, A.A. (1976), The Structure of Turbulent Shear Flow, Cambridge University Press, Cambridge, 2nd Ed.
- Van Den Berg, B. (1976), Investigations of Three-Dimensional Incompressible Turbulent Boundary Layers, National Aerospace Laboratory, NLR, Netherlands, Report NLR TR 76001U.

### Author's Reply

L. Larsson

To T. Nagamatsu

Our statement that the shear stresses are not very important near the stern, except close to the surface, is based on direct shear-stress measurements by Lofdahl (1982). Since such data are extremely rare, we are most satisfied to learn that Mr. Nagamatsu has reached the same conclusion by determining the stresses in an indirect way.

We agree that bilge vortices may be quite important for the flow pattern near the stern, but, at present, our method is not able to compute vortical flows since, in that case, the normal pressure gradient must be taken into account. Furthermore, the stream tubes and the grid would become quite distorted in such flows, so new grids must be generated frequently. It would probably be necessary to carry out a two-dimensional interpolation when generating the new grid. In the present version of the method, one-dimensional interpolation is carried out along the stream surfaces, which are kept unchanged downstream. Both modifications to the present procedure will be considered in future work.

To V.C. Patel

We share Professor Patel's opinion that the pronounced dip of the iso-wakes close to the surface in the region of maximum boundary-layer thickness is due to local flow divergence. This feature is not realized in the computation, and the most likely reason for this is the unintentional smoothing that occurs when generating the new grids. Thus, it seems to be a numerical problem, which will be further investigated.



To K. Mori

Professor Mori is quite right in pointing out that an important reason why the calculations can be carried all the way back without problems is the use of the measured pressure distribution. However, it is not true that the method, even in its present form, is equivalent to the ordinary boundary-layer approach. The main difference is that the continuity of the flow is maintained exactly (within the numerical approximation), while in boundary-layer methods the lateral curvature of the surface, which is neglected, may cause appreciable errors. As appears from the paper, we claim that this source of error is the most important one in the boundary-layer approximation.

To Y.A. Odabasi

Dr. Odabasi raises several important questions in his discussion. Our replies are as follows:

1. Computational Grid The most important feature of the present method is the orientation of the coordinate system, with the x-axis along the local streamline. The entire procedure is based on this orientation. We do not claim, however, that this is the only possible system. In fact, virtually all other methods would require a body-fitted coordinate system, and this can be designed in many, equally good ways. What is important is that the system really fits to the body and the space around it. In the ordinary boundary-layer approach, the system does not fit into the space (the metrics are independent of y). This is a serious disadvantage of the ordinary boundary-layer methods.
2. Effect of Longitudinal Pressure Gradient The discussor claims that our conclusion as to the magnitude of the convergence terms, relative to the magnitude of the longitudinal pressure gradient term, in the momentum integral equations, is due to some implicit assumption in Larsson's integral method. It would have been interesting to know what assumption the discussor had in mind. We recommend that the discussor use the measured quantities found in Larsson (1974b) for computing the various terms. Since the results from the computations agree very well with measurements, except close to the stern, there is no way the orders of magnitude of the terms could be changed by such an exercise. We would also like to give one striking example of the importance of the divergence of the flow. In our Figure 32 a line plan for the SSPA model 720 is shown. Eight potential flow streamlines are drawn on the surface. At the after part of the keel the flow is divergent. Streamline 2 diverges from streamline 1 (at the plane of symmetry). Our Figure 33 shows that along streamline 1 (1) the pressure increases, (2) the skin friction is high, and (3) the momentum thickness is strongly reduced. In spite of the

fact that both the pressure and the skin friction cooperate to increase the momentum thickness, the strong divergence makes it decrease rapidly.

It should also be pointed out that the longitudinal pressure gradient is indeed considered in our method. Only inside  $y^+ = 33$ , i.e., in the viscous sublayer and the buffer region, are similarity functions used when marching the solution downstream. The wall law is only used when generating the initial velocity profile.

3. Role of Turbulence Terms Our statement that the turbulence terms play a relatively minor role in the thick boundary layer, except close to the surface, is based on the very detailed measurements of twenty turbulence profiles in the stern region of the SSPA model 720, carried out by Lofdahl (1982). These are, to our knowledge, the only data from such measurements that are available in the open literature. We were, however, also guided by axisymmetric results obtained by Patel, Nakayama, and Damian (1974) when developing the method. After writing the paper, we were pleased to notice that Nagamatsu has reached the same conclusion indirectly from mean-flow measurements on a full ship form (see his discussion above), that Hatano and Hotta have unpublished data for the Wigley hull supporting this assumption, and that Grooves, Belt, and Huang in their very recent measurements on an elliptic body also found very small Reynolds stresses near the stern. The latter three sets of data are discussed in the paper by Patel at this symposium. If the discussor has data that contradict the findings of these five experiments, we would be most interested in seeing a full report on the work.

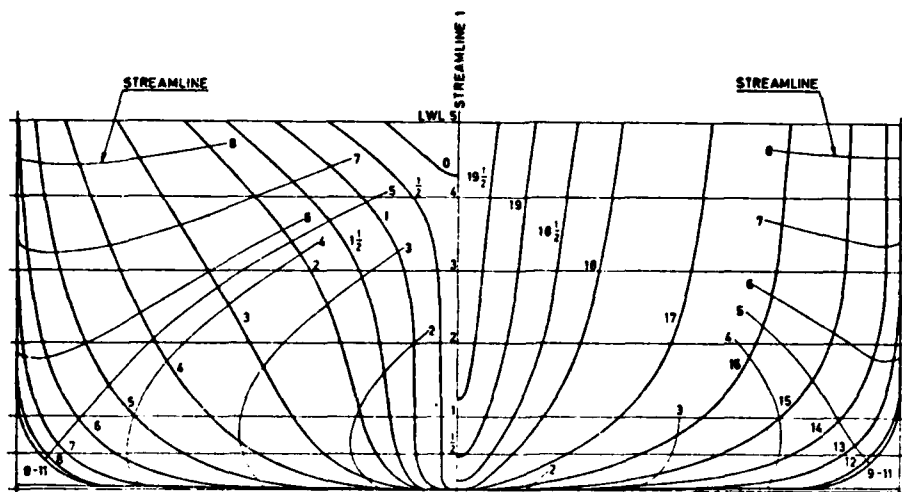


Fig 32. SSPA Model 720 with computed potential flow streamlines.

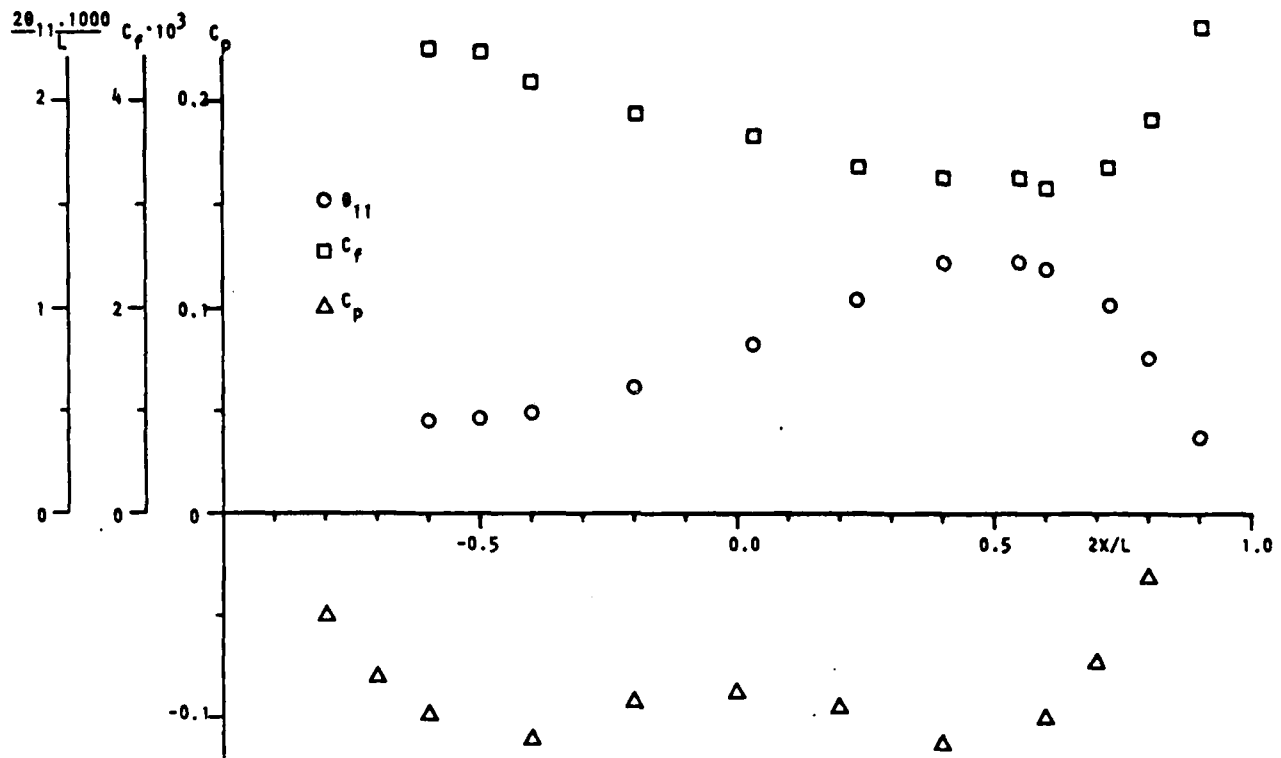


Fig 33. Measured momentum thickness, skin friction and pressure coefficient along streamline No1, SSPA Model 720.

### References

- Patel, V.C., A. Nakayama, and R. Damian, "Measurements in the Thick Axisymmetric Turbulent Boundary Layer Near the Tail of a Body of Revolution," *Journal of Fluid Mechanics*, Vol. 63, pp. 345-362.

# Some Aspects of Thick Three-Dimensional Boundary Layers

by

V.C. Patel

Iowa Institute of Hydraulic Research  
The University of Iowa  
Iowa City, Iowa 52242

## ABSTRACT

Available experimental information on thick three-dimensional turbulent boundary layers on bodies of revolution and ship forms is reviewed in order to identify general features which may be used to develop suitable approximations and solution procedures. It is shown that the primary mechanism responsible for the thickening of the boundary layer is streamline convergence, and that prolonged convergence of the external flow leads to divergence close to the surface. Thick boundary layers are accompanied by viscous-inviscid interactions and cross-stream gradients of velocity and stresses which cannot be neglected a priori as in the first-order thin boundary-layer theory. Experiments also indicate the absence of flow reversal in the direction of motion. These features are incorporated in the so-called partially-parabolic equations whose complexity is intermediate between the exact Reynolds equations and the first-order boundary-layer equations. A form suitable for ship sterns is suggested. The available turbulence measurements indicate a two-layer structure of thick boundary layers: a thin near-wall layer whose properties are similar to those of thin boundary layers and a much larger outer layer in which the stresses and stress gradients are small and the flow may be assumed to be rotational but inviscid. The importance of the various general features observed in thick boundary layers is discussed with reference to the development of suitable flow models and calculation methods.

## I. INTRODUCTION

Several methods are now available for the solution of the classical first-order boundary-layer equations for the flow past arbitrary three-dimensional bodies. These equations are obtained from the Navier Stokes or Reynolds equations under the assumption that the boundary layer is thin in comparison with some characteristic length(s) of the body. The most important aspects of the approximations are that the pressure is assumed to remain constant across the boundary layer and stress gradients in directions parallel to the surface are negligible in comparison with those normal to the surface. The former uncouples the boundary-layer equations from those of the external inviscid flow,

while the latter implies that the transport of momentum and energy by viscous and turbulent stresses occurs predominantly in the direction normal to the wall. Together, the approximations make the equations parabolic or hyperbolic, and conventional marching techniques can be used for their numerical solution.

This paper is concerned with a class of flows which, for one reason or another, do not satisfy all of the underlying approximations of thin boundary-layer theory. For lack of a more precise term, we shall refer to them as thick boundary layers. In this paper, we shall discuss the occurrence and origin of such thick boundary layers, the characteristics which have been observed experimentally and the equations required for their description, and then review the requirements of calculation methods which address the important features of such flows on ship hulls.

## II. ORIGIN OF THICK BOUNDARY LAYERS

It is well known that, in two-dimensional flow, the boundary-layer equations breakdown in the neighborhood of separation. Separation is usually preceded by a short region of rapidly thickening boundary layer and, even in the absence of turbulence, the local flow does not satisfy the usual boundary-layer approximations. In general, however, separation is not a requisite for the occurrence of thick boundary layers. This is well illustrated by the axisymmetric boundary layer over the tail of a body of revolution (Fig. 1). Even in the absence of separation, the boundary layer continues to thicken as the body radius diminishes and leads to a wake whose diameter is of the order of the maximum diameter of the body.

This particular flow has been explored rather extensively in recent years (Patel et al., 1974; Patel and Lee, 1977; Huang et al., 1979, 1980). It is useful to briefly review the main results for this relatively simple case in order to identify the similarities and differences in the more general three-dimensional case.

Experiments indicate that the thickening of the boundary layer is accompanied by increasing normal component of velocity and variation of pressure across the boundary layer, implying a coupling between the boundary layer and the external flow, and therefore viscous-inviscid interaction. Together, these observations suggest that first-order boundary-layer equations cannot be used. In addition, it is found that all Reynolds stresses are considerably smaller than those in a thin boundary layer.

The experimental information has provided an impetus to the development of calculation methods (Nakayama et al., 1976; Geller,

1979; Dietz, 1980; Dyne, 1978; Huang et al. 1976; Hoffman, 1980) which use more general thick boundary-layer equations with varying degrees of sophistication and couple their solutions in an iterative manner with those of the external flow, either directly at the edge of the boundary layer or indirectly through a displacement thickness or an equivalent source distribution. In general, only the turbulent stress responsible for momentum transport normal to the wall is retained in the equations, and its observed decrease is accounted for in a turbulence model by means of direct or indirect corrections for surface curvatures or by empirical correlations for simple eddy-viscosity and mixing-length distributions.

There is of course a natural tendency to assume that the various features observed in axisymmetric flow apply in the more complex three-dimensional case and that the methods found suitable for the former could be used in the latter. Unfortunately, the differences are not small enough to guarantee the success of such an approach.

The principal reason for the growth of a thick boundary layer in the axisymmetric case is the convergence of the streamlines in planes parallel to the surface. The equation of continuity then demands an increasing normal velocity, streamline curvature normal to the surface and hence static pressure variation across a thickening boundary layer. Thus, the development of the flow is controlled by a simple kinematical requirement stemming from the diminishing cross-sectional area of the body. Fig. 1 shows that the fluid in the thin upstream boundary layer comes to occupy a much larger area near the tail of the body, and entrainment of the external fluid into the boundary layer plays a much smaller role than in a thin boundary layer. The streamline convergence and the body geometry are related through the parameter

$$K_{31} = \frac{1}{h_3 h_1} \frac{\partial h_3}{\partial x} = \frac{1}{r_0} \frac{dr_0}{dx},$$

negative values indicating convergence.

In three-dimensional flows, the streamlines within and exterior to the boundary layer are curved in planes parallel to the surface, in addition to being convergent or divergent. In streamline coordinates, where  $x$  and  $z$  are directed along and normal to the streamlines in planes parallel to the surface, the curvature and divergence indicators are  $K_{13}$  and  $K_{31}$ , respectively. Here again, the primary agent for the development of a thick boundary layer is streamline convergence. This is illustrated by three examples involving different geometries.

Figure 2 shows the geometry and the potential-flow (without boundary-layer corrections) streamlines of the ship model SSPA 720 investigated by Larsson (1974) and later by Lofdahl (1982). The mean-flow data from the earlier experiments were utilized as one of the two test cases at the SSPA-ITTC Ship Boundary Layer Workshop (Larsson, 1981). The evolution of the thick stern boundary layer is illustrated in Fig. 3. It is obvious that the boundary layer remains thin along the keel along which there is strong streamline divergence, and the region of most rapid, almost explosive, growth coincides with the strong convergence of the external streamlines from both sides along streamline 5. Although the actual streamlines outside the boundary layer will be different from the potential-flow streamlines used here as a frame of reference, it is seen that the streamline convergence is responsible for packing the boundary layer fluid into an area whose girthwise dimension decreases while the normal dimension increases rapidly. In fact, the detailed velocity measurements indicate that the crossflow angle in the boundary layer along streamline 5 is everywhere less than 3 degrees except at the last section, where it is 5 degrees. Also, the prolonged convergence of the external streamlines leads to a divergent flow in a region close to the surface. Thus, the boundary layer development along this streamline resembles that along a plane of symmetry into which flow converges from both sides (often referred to, rather confusingly, as a line of detachment) and, as we shall see later, offers an opportunity to examine, in detail, some of the interesting characteristics of thick boundary layers.

As an aside, Fig. 3 points out the danger of extending measurement techniques of thin boundary layers to thick boundary layers: due to the concave transverse curvature of the hull at section 1, the measurement of velocity profiles along the local surface normals led to the duplication of data in the triangular region over streamlines 2 to 7 and a paucity of data over a large part of the stern flow. Secondly, it should be noted that the data of Larsson are used here since they are particularly well documented, although similar measurements have been made elsewhere on other hulls (see, for example, Hoffmann, 1976; Wieghardt, 1982; Hatano et al. 1978; Hatano and Hotta, 1982; Nagamatsu, 1980).

The second example is shown in Fig. 4. These are the recent measurements of Groves, Belt and Huang (1982) on an elongated body of 3:1 elliptic cross section. The boundary layer over the rear 15 percent of the model length thickens rapidly as in the axisymmetric case, but the rates of growth along the minor ( $\theta = 0^\circ$ ) and major ( $\theta = 90^\circ$ ) axes are quite different. The velocity profiles indicated crossflow angles within the boundary layer to be less than 5 degrees everywhere. Here again the differential rates of thickening may be attributed to the different rates of convergence of the potential-flow streamlines in planes parallel to the

surface. The divergence of streamlines along  $\theta = 0^\circ$  is responsible for the relatively thin boundary layer, while flow convergence into the  $\theta = 90^\circ$  plane of symmetry leads to the much rapid growth in thickness. The boundary-layer development along the latter indeed resembles that along streamline 5 in the previous example.

The final example is the boundary layer on a body of revolution at incidence. Fig. 5 shows some aspects of the measurements of Ramaprian, Patel and Choi (1981) on a combination hemisphere semi-spheroid body at an incidence of 15 degrees. The potential-flow streamlines diverge out of the windward plane ( $\theta = 0^\circ$ ) and converge into the leeward plane ( $\theta = 180^\circ$ ), resulting in a gradual thickening of the boundary layer over the leeward side. The prolonged convergence into the leeside plane of symmetry eventually leads to a divergence of the streamlines close to the surface and, further downstream, the region of maximum boundary layer thickness coincides roughly with the line of circumferential flow reversal into which the surface streamlines from the windward and leeward sides converge.

The foregoing examples indicate that the primary mechanism responsible for the development of thick boundary layers, both in the axisymmetric as well as the general three-dimensional cases, is the convergence of the external-flow streamlines in planes parallel to the surface. This convergence is, of course, brought about by the body geometry but it cannot be predicted by potential-flow theory alone since the external inviscid flow is modified very dramatically once the boundary layer becomes thick. In short, the problem is one of a strong interaction between the viscous and inviscid flows. The level of this interaction is well illustrated in Fig. 6 by the surface pressure measurements on the body of revolution. It is seen that the actual pressure distribution, and hence the pressure field around the body, is very different from that calculated by potential-flow methods, and that the greatest differences are observed on the leeside where the boundary layer thickness is largest.

An important common characteristic of all the thick boundary-layer examples presented here is the absence of separation. Although the detailed measurements (see, for example, Wieghardt, 1982) indicate the generation of longitudinal vorticity and the development of a weak vortical motion in the thickening boundary layer, there is no hint of a free-vortex type of separation such as that observed on long slender bodies at large angles of attack. Perhaps the matter is one of semantics but, insofar as ship hulls are concerned, it is safe to say that the vortical motion is weak and diffused, and there is no detachment of the vortex from the surface except in the wake itself. Furthermore, there is no evidence of a singular or closed separation which requires longitudinal flow reversal.



Finally, it remains to provide a working definition of a thick boundary layer. In this regard, we may use the experience in simpler flow geometries. In two-dimensional boundary layers, longitudinal surface curvature influences the turbulence when  $\kappa\delta = K_{12}\delta \sim 0.01$ , well before curvature has to be taken into account explicitly in the momentum equations. On the other hand, experiments on axisymmetric bodies indicate that thick boundary-layer effects, in the turbulence as well as the mean flow, are observed when  $\delta/r = K_{32}\delta \sim 1$ . Here we have used the usual notation for the longitudinal ( $K_{12}$ ) and transverse ( $K_{32}$ ) surface curvatures. The above values serve as guidelines for three-dimensional flows.

### III. LIMITATIONS OF FIRST-ORDER BOUNDARY-LAYER THEORY

For simplicity, we consider the equations of motion in Cartesian co-ordinates for a three-dimensional incompressible flow. The exact equations of continuity and momentum of the mean flow are, respectively,

$$\begin{aligned}
 & \frac{\partial U}{\partial x} + \frac{\partial V}{\partial y} + \frac{\partial W}{\partial z} = 0 \\
 & \frac{U}{1} \frac{\partial U}{\partial x} + \frac{V}{1} \frac{\partial U}{\partial y} + \frac{W}{1} \frac{\partial U}{\partial z} + \frac{\partial}{\partial x} \left( \frac{P}{\rho} + \overline{uu} \right) + \frac{\partial}{\partial y} (\overline{uv}) + \frac{\partial}{\partial z} (\overline{uw}) - \nu \left\{ \frac{\partial^2 U}{\partial x^2} + \frac{\partial^2 U}{\partial y^2} + \frac{\partial^2 U}{\partial z^2} \right\} = 0 \\
 & \frac{U}{\epsilon} \frac{\partial V}{\partial x} + \frac{V}{\epsilon} \frac{\partial V}{\partial y} + \frac{W}{\epsilon} \frac{\partial V}{\partial z} + \frac{\partial}{\partial x} (\overline{uv}) + \frac{\partial}{\partial y} \left( \frac{P}{\rho} + \overline{vv} \right) + \frac{\partial}{\partial z} (\overline{vw}) - \nu \left\{ \frac{\partial^2 V}{\partial x^2} + \frac{\partial^2 V}{\partial y^2} + \frac{\partial^2 V}{\partial z^2} \right\} = 0 \\
 & \frac{U}{1} \frac{\partial W}{\partial x} + \frac{V}{1} \frac{\partial W}{\partial y} + \frac{W}{1} \frac{\partial W}{\partial z} + \frac{\partial}{\partial x} (\overline{uw}) + \frac{\partial}{\partial y} (\overline{vw}) + \frac{\partial}{\partial z} \left( \frac{P}{\rho} + \overline{ww} \right) - \nu \left\{ \frac{\partial^2 W}{\partial x^2} + \frac{\partial^2 W}{\partial y^2} + \frac{\partial^2 W}{\partial z^2} \right\} = 0
 \end{aligned} \tag{1}$$

(U,V,W) are mean velocities in the (x,y,z) directions, respectively, and the barred quantities are the Reynolds stresses. Let x be the predominant direction of flow.

The thin boundary-layer equations are derived from the above by considering high Reynolds-number flow on a surface  $y = 0$ . The influence of viscosity and turbulence is then confined to a boundary layer of thickness  $\delta$ , which is much smaller than a

characteristic length of flow development,  $L$ , which may be measured along a reference streamline from the origin of the boundary layer. In the usual boundary-layer approximations it is then assumed that

$$\frac{\delta}{L} = \epsilon \ll 1, \quad v \sim O(\epsilon^2)$$

$$u, w \sim O(1), \quad V \sim O(\epsilon)$$

$$\frac{\partial}{\partial x}, \frac{\partial}{\partial z} \sim O(1), \quad \frac{\partial}{\partial y} \sim O(\epsilon^{-1}) \quad \text{etc.}$$

$$\overline{u_i u_j} \sim O(\epsilon)$$

the last of these being supported only by experimental evidence. The orders of magnitude of the various terms are then as shown below the equations. If terms of  $O(\epsilon)$  and smaller are neglected, we obtain the first-order boundary layer equations. From the third equation, the pressure variation across the boundary layer is due only to the normal-velocity fluctuations and the total change in pressure from  $y = 0$  to  $y = \delta$  is of  $O(\epsilon)$ .

If terms of  $O(\epsilon)$  are retained, in addition to those of  $O(1)$ , we obtain what are often called the "second-order" boundary-layer equations (Nash and Patel, 1972). These may be useful in the determination of the errors involved in first-order boundary-layer theory, but should not be confused with the equations required for THICK boundary layers.

From the examples cited in the previous section it is obvious that not all of the above approximations are applicable in thick boundary layers. In fact, it is observed that when thin boundary-layer equations are used to continue the solutions in the region of thick boundary layers, the results indicate, without exception, a much more rapid boundary layer growth and, in some instances, premature separation. This is well illustrated by all the calculations presented at the SSPA-ITTC Workshop (Larsson, 1981) on ship hulls, those of Groves, Belt and Huang (1982) on the elliptic cross-section body and of Patel and Baek (1982), Hayashita (1982) and others on bodies of revolution at incidence.

#### IV. THICK BOUNDARY-LAYER EQUATIONS

The departures from thin boundary-layer behavior do not necessarily imply that all of the simplifications of boundary-layer theory must be abandoned and recourse had to the original Navier-Stokes or Reynolds equations. In fact, there are many other commonly observed flows which exhibit features similar to those of thick boundary layers. For example, the boundary layer along a

corner (wing-body junction), developing flows in square and rectangular ducts, and three-dimensional wall jets share the same common features, namely viscous-inviscid interaction and lateral or cross-stream gradients which are not negligible. For such flows, a consistent set of equations may be obtained by assuming that

$$\frac{\partial}{\partial x} \sim 0(1); \quad \frac{\partial}{\partial z}, \frac{\partial}{\partial y} \sim 0(\epsilon^{-1})$$

The equation of continuity then suggests

$$U \sim 0(1); \quad V, W \sim 0(\epsilon)$$

and, if the largest viscous and turbulence terms are to be  $0(1)$ ,  $v \sim 0(\epsilon^2)$  and  $u_i u_j \sim 0(\epsilon)$ . Then the orders of magnitude of the terms in the momentum equations are as indicated below.

$$\begin{aligned} & \underbrace{U \frac{\partial U}{\partial x}}_1 + \underbrace{V \frac{\partial U}{\partial y}}_1 + \underbrace{W \frac{\partial U}{\partial z}}_1 + \underbrace{\frac{\partial}{\partial x} \left( \frac{p}{\rho} + \overline{uu} \right)}_{\epsilon} + \underbrace{\frac{\partial}{\partial y} (\overline{uv})}_1 + \underbrace{\frac{\partial}{\partial z} (\overline{uw})}_1 - \underbrace{\nu \left\{ \frac{\partial^2 U}{\partial x^2} + \frac{\partial^2 U}{\partial y^2} + \frac{\partial^2 U}{\partial z^2} \right\}}_{\epsilon^2 (1, \epsilon^{-2}, \epsilon^{-2})} = 0 \\ & \underbrace{U \frac{\partial V}{\partial x}}_{\epsilon} + \underbrace{V \frac{\partial V}{\partial y}}_{\epsilon} + \underbrace{W \frac{\partial V}{\partial z}}_{\epsilon} + \underbrace{\frac{\partial}{\partial x} (\overline{uv})}_{\epsilon} + \underbrace{\frac{\partial}{\partial y} \left( \frac{p}{\rho} + \overline{vv} \right)}_1 + \underbrace{\frac{\partial}{\partial z} (\overline{vw})}_1 - \underbrace{\nu \left\{ \frac{\partial^2 V}{\partial x^2} + \frac{\partial^2 V}{\partial y^2} + \frac{\partial^2 V}{\partial z^2} \right\}}_{\epsilon^2 (\epsilon, \epsilon^{-1}, \epsilon^{-1})} = 0 \quad (2) \\ & \underbrace{U \frac{\partial W}{\partial x}}_{\epsilon} + \underbrace{V \frac{\partial W}{\partial y}}_{\epsilon} + \underbrace{W \frac{\partial W}{\partial z}}_{\epsilon} + \underbrace{\frac{\partial}{\partial x} (\overline{uw})}_{\epsilon} + \underbrace{\frac{\partial}{\partial y} (\overline{vw})}_1 + \underbrace{\frac{\partial}{\partial z} \left( \frac{p}{\rho} + \overline{ww} \right)}_1 - \underbrace{\nu \left\{ \frac{\partial^2 W}{\partial x^2} + \frac{\partial^2 W}{\partial y^2} + \frac{\partial^2 W}{\partial z^2} \right\}}_{\epsilon^2 (\epsilon, \epsilon^{-1}, \epsilon^{-1})} = 0 \end{aligned}$$

If we retain terms of  $0(1)$ , two terms may be dropped in the x-momentum equation, but the only terms remaining in the y- and z-equations are those containing the Reynolds stresses! If terms of  $0(\epsilon)$  are also retained in the last two equations, then the resulting set of equations is similar to, but not identical with, the so-called 'PARTIALLY-PARABOLIC' or 'PARABOLIZED' REYNOLDS EQUATIONS (see Patankar and Spalding, 1972) in which all x-derivatives of the Reynolds and viscous stresses are neglected. Note that the difference between these and the present equations lies only in the terms  $\frac{\partial}{\partial x} (\overline{uv})$  and  $\frac{\partial}{\partial x} (\overline{uw})$  in the y- and z-momentum equations, respectively, and therefore the present approximations are consistent with the partially-parabolic approximations for laminar flow. The x-derivatives of the Reynolds stresses can be neglected only if it is assumed that the turbulent transport of

momentum in the x-direction is negligible. This is a question that can be settled only by experimental data. In the interim, we may make such an assumption and conclude that the equations of thick boundary layers are the same as the partially-parabolic equations, i.e.,

$$\begin{aligned}
 U \frac{\partial U}{\partial x} + V \frac{\partial U}{\partial y} + W \frac{\partial U}{\partial z} + \frac{\partial}{\partial x} \left( \frac{P}{\rho} \right) + \frac{\partial}{\partial y} (\overline{UV}) + \frac{\partial}{\partial z} (\overline{UW}) - \nu \left\{ \frac{\partial^2 U}{\partial y^2} + \frac{\partial^2 U}{\partial z^2} \right\} &= 0 \\
 U \frac{\partial V}{\partial x} + V \frac{\partial V}{\partial y} + W \frac{\partial V}{\partial z} + \frac{\partial}{\partial y} \left( \frac{P}{\rho} + \overline{VV} \right) + \frac{\partial}{\partial z} (\overline{VW}) - \nu \left\{ \frac{\partial^2 V}{\partial y^2} + \frac{\partial^2 V}{\partial z^2} \right\} &= 0 \\
 U \frac{\partial W}{\partial x} + V \frac{\partial W}{\partial y} + W \frac{\partial W}{\partial z} + \frac{\partial}{\partial y} (\overline{VW}) + \frac{\partial}{\partial z} \left( \frac{P}{\rho} + \overline{WW} \right) - \nu \left\{ \frac{\partial^2 W}{\partial y^2} + \frac{\partial^2 W}{\partial z^2} \right\} &= 0
 \end{aligned} \tag{3}$$

$$\frac{\partial U}{\partial x} + \frac{\partial V}{\partial y} + \frac{\partial W}{\partial z} = 0$$

The order of magnitude considerations indicate that the gradients of pressure in the x-direction may be of the first order, while those in the y- and z-directions are of  $O(\epsilon)$ . A simple example is the developing flow in a duct, where the pressure is essentially constant across the cross-section but varies with x. Equations (3) contain the pressure as an unknown and therefore provide a coupling with the external inviscid flow. They are termed partially-parabolic since they are elliptic in the y-z plane and parabolic in the x-direction. A numerical procedure for an iterative solution of such equations was first proposed by Patankar and Spalding (1972) and has been applied to the flow over ship sterns by Abdelmeguid et al. (1979) and Muraoka (1980, 1982). In this approach, an initial guess of  $\partial p / \partial x$  is first made, from a potential-flow solution say, the equations are integrated by a downstream-marching technique, and the pressure field is updated in successive solutions to satisfy the prescribed boundary conditions at the edge of the thick boundary layer. Thus, the complexity of equations (3) is intermediate to the exact elliptic Reynolds equations and the parabolic or hyperbolic thin boundary-layer equations.

In addition to the approximations considered above, there is yet another which has been employed in special classes of problems. This is the so-called 'thin-layer approximation' (Baldwin and Lomax, 1978), in which all viscous and Reynolds-stress terms except those which appear in the usual thin boundary-layer equations (i.e., the normal derivatives of the two primary shear stresses) are neglected. Thus, the pressure is again regarded as an unknown and the normal momentum equation is retained. The thin-

layer equations have been used by Pulliam and Steger (1980) and others in the calculation of three-dimensional flows over bodies and by Larsson and Chang (1980) for ship stern flows. The thick axisymmetric boundary-layer equations recommended by Patel (1974) and used subsequently by many other investigators also fall in this category. The thin-layer equations are obviously more restrictive than the partially-parabolic equations since they do not contain the transverse stress derivatives. Also, apart from the problem of modelling the additional turbulence terms, there is no computational advantage in making the restrictions concerning the stress gradients.

Thus far, we have considered the equations written in Cartesian coordinates. It is interesting to note that the various approximations have been discussed primarily by resort to experimental information, and the thick boundary-layer equations have been derived under the assumptions that the transverse and normal stress gradients are comparable, and much larger than the longitudinal gradients, and that the thickness  $\delta$  of the viscous, turbulent flow is small in comparison with a characteristic streamwise length of flow development. Although these physical features of thick boundary layers are usually observed on curved surfaces, it is also possible for such flows to occur on flat surfaces, e.g., the flow behind a vortex generator in a flat-plate boundary layer, or the flow along a streamwise corner. Consequently, the incorporation of surface or coordinate curvatures in the equations can be regarded as a geometrical problem rather than a physical one. This view is in contrast with the usual approach adopted in the derivation of the higher-order boundary-layer equations, where the Navier-Stokes or Reynolds equations are written in general curvilinear surface-fitted coordinates and terms of order higher than  $\kappa\delta$ , where  $\kappa$  is the largest surface curvature, are neglected. This procedure is described, for example, in Nash and Patel (1972) using a triply-orthogonal curvilinear coordinate system and, more recently, in Hirschel and Kordulla (1981), who employ generalized coordinates. However, as noted earlier, such higher-order equations should not be confused with either the thin-layer or the partially-parabolic equations although the techniques required for their solutions may be similar, or even identical.

In the treatment of thin three-dimensional boundary layers on arbitrary surfaces, it is possible to use a variety of orthogonal or non-orthogonal body-fitted coordinates since changes in the metrics in the direction normal to the surface are neglected. The equations then contain only the metrics and curvatures of the coordinate lines on the surface. Although this simplification is not possible in the case of thick boundary layers, the choice of coordinates is still vast if the restriction of orthogonality is not imposed. In the spirit of the assumptions made, the only requirement is that one of the coordinates, say  $x$ , should be

aligned with the primary flow direction, along which the stress gradients are neglected. However, if we seek an orthogonal body-fitted coordinate system, there is only one system, namely that in which two sets of coordinate surfaces intersect the body in its lines of principal curvature. The construction of such a system for an arbitrary body, such as an airplane fuselage or a ship form, is non-trivial and, in the final analysis, the resulting coordinates may not be the most convenient ones from a computational point of view. On the other hand, it may be possible to identify a convenient coordinate system for a class of shapes, e.g., ship sterns, without much loss of generality. An example is the distorted cylindrical-polar coordinated used by Muraoka (1980, 1982). In the following we shall derive the equations in a modified form of that system, eliminating one source of numerical inaccuracy in practical computations.

An examination of the available data in the flow over ship sterns (e.g., Nagamatsu, 1980; Wieghardt, 1982) indicates that, to a first approximation, the primary flow direction  $x$ , along which the stress gradients are neglected in equations (3), may be taken as the direction of ship motion rather than a coordinate along the hull. Suitable local corrections can be applied, for example in the near-wall region, to take into account significant departures from this assumption. For computational convenience and numerical accuracy it is also desirable to choose the grid net in the  $y$ - $z$  plane such that one coordinate coincides with the hull section and the other with a boundary just beyond the outer edge of the viscous flow. As shown by the various examples, the latter varies greatly in the transverse direction.

The above requirements can be accommodated in a variety of ways by adopting some of the recent numerical grid-generation techniques (Proceedings of Symposium on Numerical Generation of Curvilinear Coordinate Systems, etc., Mississippi State University, 1982). For the purposes of illustration, however, we consider a cylindrical polar coordinate system  $(x, r, \theta)$  distorted by the following transformations

$$\begin{aligned}\xi &= x \\ \eta &= \frac{r - r_s}{r_n - r_s} = \frac{r - r_s}{\Delta} \\ \zeta &= \theta / \psi\end{aligned}\tag{4}$$

where  $x$  is measured along the projection of the undisturbed water surface on to the center-plane and, as shown in Fig. 7,  $r_n$  and  $r_s$  represent the radial distances to the outer and inner (hull) boundaries, respectively, of the integration domain, and  $\psi = \pi/2$  is the extent of the domain in the circumferential direction.

Thus  $\eta$  and  $\zeta$  vary between 0 and 1, and boundary conditions are applied along  $\eta = 0, 1$  and  $\zeta = 0, 1$ .

The partially-parabolic equations, when transformed using equations (4), become

$$\frac{\partial U}{\partial \xi} + \frac{1}{\Delta} \frac{\partial}{\partial \eta} (V-FU-GW) + \frac{1}{h_3} \frac{\partial W}{\partial \zeta} + (K_{21})U + (k_{32})V + (k_{23} - k_{32}G)W = 0$$

$$U \frac{\partial U}{\partial \xi} + (V-FU-GW) \frac{1}{\Delta} \frac{\partial U}{\partial \eta} + \frac{W}{h_3} \frac{\partial U}{\partial \zeta} + \frac{\partial}{\partial \xi} \left( \frac{P}{\rho} \right) - \frac{F}{\Delta} \frac{\partial}{\partial \eta} \left( \frac{P}{\rho} \right) + \frac{1}{\Delta} \frac{\partial}{\partial \eta} (\overline{UV}) + \frac{1}{h_3} \frac{\partial}{\partial \zeta} (\overline{UW}) - \frac{G}{\Delta} \frac{\partial}{\partial \eta} (\overline{UW}) + k_{32} \overline{UV} - v \left\{ (1 + G^2) \frac{1}{\Delta^2} \frac{\partial^2 U}{\partial \eta^2} + \frac{1}{h_3^2} \frac{\partial^2 U}{\partial \zeta^2} + k_{32} \frac{1}{\Delta} \frac{\partial U}{\partial \eta} - \frac{2G}{\Delta} \frac{1}{h_3} \frac{\partial^2 U}{\partial \zeta \partial \eta} \right\} = 0$$

$$U \frac{\partial V}{\partial \xi} + (V-FU-GW) \frac{1}{\Delta} \frac{\partial V}{\partial \eta} + \frac{W}{h_3} \frac{\partial V}{\partial \zeta} - k_{32} W^2 + \frac{1}{\Delta} \frac{\partial}{\partial \eta} \left( \frac{P}{\rho} + \overline{V}^2 \right) + \frac{1}{h_3} \frac{\partial}{\partial \zeta} (\overline{VW}) - \frac{G}{\Delta} \frac{\partial}{\partial \eta} (\overline{VW}) + k_{32} (\overline{V}^2 - \overline{W}^2) - v \left\{ (1 + G^2) \frac{1}{\Delta^2} \frac{\partial^2 V}{\partial \eta^2} + \frac{1}{h_3^2} \frac{\partial^2 V}{\partial \zeta^2} + k_{32} \frac{1}{\Delta} \frac{\partial V}{\partial \eta} - \frac{2G}{\Delta} \frac{1}{h_3} \frac{\partial^2 V}{\partial \zeta \partial \eta} - 2k_{32} \left( \frac{1}{h_3} \frac{\partial W}{\partial \zeta} - \frac{G}{\Delta} \frac{\partial W}{\partial \eta} \right) - k_{32}^2 V \right\} = 0 \quad (5)$$

$$U \frac{\partial W}{\partial \xi} + (V-FU-GW) \frac{1}{\Delta} \frac{\partial W}{\partial \eta} + \frac{W}{h_3} \frac{\partial W}{\partial \zeta} + k_{32} WV + \frac{1}{h_3} \frac{\partial}{\partial \zeta} \left( \frac{P}{\rho} + \overline{W}^2 \right) - \frac{G}{\Delta} \frac{\partial}{\partial \eta} \left( \frac{P}{\rho} + \overline{W}^2 \right) + \frac{1}{\Delta} \frac{\partial}{\partial \eta} (\overline{VW}) + 2k_{32} \overline{VW} - v \left\{ (1 + G^2) \frac{1}{\Delta^2} \frac{\partial^2 W}{\partial \eta^2} + \frac{1}{h_3^2} \frac{\partial^2 W}{\partial \zeta^2} + k_{32} \frac{1}{\Delta} \frac{\partial W}{\partial \eta} - \frac{2G}{\Delta} \frac{1}{h_3} \frac{\partial^2 W}{\partial \zeta \partial \eta} + 2k_{32} \left( \frac{1}{h_3} \frac{\partial V}{\partial \zeta} - \frac{G}{\Delta} \frac{\partial V}{\partial \eta} \right) - k_{32}^2 W \right\} = 0$$

In the above equations, the coordinates are  $(\xi, \eta, \zeta)$  but the velocities  $(U, V, W)$  are in the original  $(x, r, \theta)$  directions, and the following abbreviations have been introduced

$$\begin{aligned}\Delta &= r_n - r_s \\ F &= \frac{\partial r_s}{\partial x} + \eta \frac{\partial \Delta}{\partial x} \\ G &= \frac{1}{r} \left\{ \frac{\partial r_s}{\partial \theta} + \eta \frac{\partial \Delta}{\partial \theta} \right\} = \frac{1}{r_s + \eta \Delta} \left\{ \frac{\partial r_s}{\partial \theta} + \eta \frac{\partial \Delta}{\partial \theta} \right\} \\ h_3 &= r\psi = (r_s + \eta \Delta)\psi \\ k_{21} &= \frac{1}{\Delta} \frac{\partial \Delta}{\partial \xi} = \frac{1}{\Delta} \frac{\partial \Delta}{\partial x} \\ k_{23} &= \frac{1}{h_3 \Delta} \frac{\partial \Delta}{\partial \zeta} = \frac{1}{(r_s + \eta \Delta)} \frac{1}{\Delta} \frac{\partial \Delta}{\partial \theta} \\ k_{32} &= \frac{1}{r} = \frac{1}{(r_s + \eta \Delta)}\end{aligned} \quad (6)$$

Note that the nonorthogonality of the coordinates is taken into account by the metrics  $\Delta$ ,  $h_3$  and the curvatures  $k_{21}$ ,  $k_{23}$ ,  $k_{32}$ , and these can be evaluated to any desired accuracy from the hull geometry and the thickness  $\Delta$  of the integration domain.

Equations (5) differ from those of Muraoka (1980) in two respects. The first is that an eddy-viscosity assumption has not been made to relate the Reynolds stresses to the mean rates of strain and the second is the introduction of the normalizing parameter  $\Delta$ . The latter serves to provide a better grid distribution in the regions where the boundary layer is thin (near the keel) and, at the same time, to define a match boundary between the viscous and inviscid flow. Thus,  $\Delta$  can be a pre-selected smooth boundary for the computation of the external inviscid flow with boundary conditions (e.g., normal velocities or singularity distribution) provided by the solution of the viscous flow. Such a technique has already been found to be quite successful in axisymmetric and two-dimensional flows (Nakayama et al., 1976; Mahgoub and Bradshaw, 1979).

#### IV. TURBULENCE MODELS

Comparison of the thin boundary-layer equations (1) with those for thick boundary layers (3,5) indicates that the former contain only two Reynolds stresses while the latter contain all six. Thus, for thick boundary layers, the turbulence models have to be, at



least in principle, more general. For a review of the various models that may be employed for the closure of the partially-parabolic equations, reference may be made to the recent article by Rodi (1982) and the literature cited therein. Instead of examining these, however, we shall address the question: What is the relative importance of the Reynolds-stress terms in the equations? Since detailed measurements required to evaluate the magnitude of each term in the equations are not yet available, we shall rely upon the available information and the now extensive experience with thin boundary layers and thick axisymmetric boundary layers to gain some insights. These could then be used to guide future experiments and select appropriate turbulence models and solution procedures for thick three-dimensional boundary layers.

Several sets (Lofdahl, 1982; Hatano and Hotta, 1982; Groves et al., 1982; Okuno and Himeno, 1982) of Reynolds-stress measurements in thick three-dimensional boundary layers have been reported in recent years. Among these, the data of Larsson (1974) and Lofdahl (1982) on a double model of a ship form are perhaps the most complete and best documented. Although a comprehensive analysis is beyond the scope of this paper, it is interesting to follow the flow development along streamline 5 which, as noted earlier, is in the region of maximum flow convergence and boundary-layer thickness.

The longitudinal and transverse surface-curvature parameters along this streamline are compared with those on the low-drag axisymmetric body tested by Patel and Lee (1977) in Fig. 8. Following the guidelines mentioned earlier, we note that both curvatures are large enough to influence the turbulence but only the transverse curvature is strong enough to have an appreciable effect on the mean flow. What is more interesting, however, is that the curvatures on the ship model are considerably smaller than those observed on the axisymmetric body over the last 20 percent of the body length.

Fig. 9 shows the parameter  $K_{31}\delta$  which is a measure of the rate of convergence or divergence of the streamlines. The continued convergence of the external streamlines in the axisymmetric case has been noted already. The corresponding convergence on the ship model is much smaller and the rate of growth of the boundary layer is therefore relatively slower. Also, the near-wall measurements indicate an important phenomenon, namely flow divergence close to the surface under the influence of convergence in the outer part of the boundary layer. In fact, the flow along streamline 5 resembles that along the leeward plane of symmetry of a body of revolution (Ramaprian, et al., 1981; Patel and Baek, 1982) where continued convergence of the external flow leads to flow divergence near the wall and eventually to a free-vortex separation. However, on the ship model, the divergence is not strong enough to lead to a decrease in the boundary layer thickness.

The mean-velocity and Reynolds-stress distributions in the boundary layer can now be examined in the framework of the curvature and flow-convergence parameters presented above. The velocity profiles measured by Larsson (1974) along streamline 5 are shown in the usual wall-layer coordinates in Fig. 10. As noted earlier, the crossflow along this streamline is very small and therefore we may set aside the arguments about the validity of the law of the wall. The figure shows that the usual law of the wall applies all the way upto the last measurement section 1,  $x/L = 0.95$  (see also Fig. 3). The most significant observation to be made here is that the region of validity of this law is nearly constant in terms of  $y^*$  ( $\sim 150$ ) but decreases from about  $0.05\delta$  at section 4 ( $x/L = 0.8$ ) to about  $0.02\delta$  at section 1 ( $x/L = 0.95$ ). Thus, the wall layer, through which we normally assume a linear variation of the turbulence length scale, has diminished from roughly  $0.15\delta$  in a thin boundary layer to about  $0.02\delta$  at the stern (2 mm in a 83 mm thick boundary layer at section 1 along streamline 5!). Thus, near-wall turbulence models developed for thin boundary layers appear to remain valid in thick boundary layers but in a much smaller fraction of the boundary-layer thickness.

Fig. 11 shows the profiles of the Reynolds stress  $\overline{uv}$  measured by Lofdahl (1982) along streamline 5. The other five components of the stress tensor show similar features and their relative magnitudes are similar to what would be expected in thin boundary layers. Note that, inspite of the thick boundary layers, measurements could not be made in the very thin logarithmic layer commented upon earlier. The turbulence measurements indicate the evolution of a distinct two-layer structure. This is already evident at section 5 ( $x/L = 0.75$ ), where the boundary layer is moderately thick (see Figs. 8 and 9) and is well developed at section 1 ( $x/L = 0.95$ ). It is also apparent in the mean-velocity profiles at sections 2 and 1, in Fig. 10, from the marked changes in the velocity gradient in the region  $200 < y^* < 500$ . Fig. 11 suggests that the inner one-fifth of the boundary layer contains relatively large stresses and stress gradients while the turbulence in the outer 80 percent remains at a low and nearly constant level. The stress distribution in the inner part is compatible with the wall shear-stress determined from the mean-velocity profiles and the local pressure gradients, and is quite similar to that in a thin boundary layer. The outer, low-turbulence layer appears to ride over the inner layer and continues to grow in thickness.

The foregoing observations raise two important questions: What is the origin of the two-layer structure and what are its implications relative to turbulence models for thick boundary layers? It has been apparent from almost all turbulence measurements in thick boundary layers, including those in axisymmetric flow, that the Reynolds stresses are much smaller over

a large part of the layer than would be expected in a thin boundary layer. As a consequence, eddy viscosities and mixing-lengths, when scaled by the boundary-layer thickness, show a marked decrease. The reduction in mixing length is shown in Fig. 12, where data from three sources are reproduced. The similarity among these, and the earlier axisymmetric data, is indeed striking but it should be noted that these results correspond only to regions when the crossflow is absent or small, there is as yet no satisfactory way of predicting the observed reductions in the mixing length, and such correlations are restricted only to one component of the stress tensor. Thus, the practical utility of the correlations in the closure of the partially-parabolic equations is severely limited. From the earlier observation concerning the law of the wall, we would expect  $\lambda \sim ky$ , where  $k$  is the Karman constant, over a very small region near the wall ( $y/\delta < 0.05$  say), and therefore the departures from this in what is usually regarded as the wall region ( $0.05 < y/\delta < 0.2$ ) should not be viewed in the context of the law of the wall. In other words, the turbulence measurements appear to indicate a thin layer close to the surface ( $y/\delta < 0.05$ ) where the usual law of the wall, or its extension to three-dimensional flow, applies, a layer adjacent to it ( $0.05 < y/\delta < 0.2$ ) in which the stresses and the stress gradients are large, and an extensive outer layer characterized by a low level of turbulence, small stress gradients, and nearly constant but small mixing length. The flow in the first two regions is similar to that in a thin boundary layer and therefore it may be possible to adopt a conventional turbulence model, including corrections for the extra rates of strain effects, to describe its dynamics. The total boundary layer thickness cannot, however, be used as a relevant length scale. The outer layer, on the other hand, is a product of the thickening boundary layer due to the strong convergence of the streamlines, and appears to be a region in which the turbulence produced upstream is convected and diluted simply by the increase in boundary layer thickness. Further analysis of the data and some supporting calculations are obviously required to confirm these preliminary observations.

## VI. STERN-FLOW CALCULATION METHODS

From the examples and characteristics of thick three-dimensional boundary layers discussed in the previous sections it is clear that simple extensions of thin boundary-layer calculation methods are unlikely to succeed in providing an adequate description of the flow over a ship stern. This was demonstrated at the SSPA-ITTC Workshop (Larsson, 1981). Among the major features of thick boundary layers to be addressed by calculation methods are the following:

- (a) an interaction between the viscous and inviscid flows leading to a modification of the pressure field from that predicted by potential-flow theory alone;

- (b) large transverse variations in the thickness of the viscous flow, implying strong cross-stream gradients of velocity and stresses;
- (c) a two-layer structure of the viscous flow: a small inner layer that resembles a thin boundary layer and a large outer layer which consists of weak mean shear and low turbulent stresses.

The partially-parabolic equations formally embody the first two features provided their solution is matched correctly to that of the external inviscid flow at the edge of the viscous-flow domain. However, the third feature must be reflected in the turbulence model that is selected to effect closure of the equations.

Solutions of the partially-parabolic equations, in conjunction with the basic  $k$ - $\epsilon$  model of turbulence, has been pursued by Abdelmeguid et al. (1979) and Muraoka (1980, 1982) with encouraging results. In the applications to date, however, the partially-parabolic solutions are obtained over a much larger domain than required by the local boundary-layer thickness and are matched at the outer edge of this domain with a potential-flow solution obtained in the absence of boundary layers. Thus, the matching between the viscous and inviscid regions is unrealistic and the numerical procedure is wasteful, and possibly inaccurate due to inadequate resolution in the region of thin boundary layers. The introduction of a normalizing parameter  $\Delta$  in equations (6), selection of a smooth match boundary just encompassing the boundary layer, and iterative matching with the external inviscid flow, taking into account the influence of the boundary layer, are some of the features which would lead to improvements in such methods. The performance of the  $k$ - $\epsilon$  model, and the isotropic eddy-viscosity assumption accompanying it, is also untested in thick boundary layers and modifications to the model may be needed to account for the observed turbulence behavior.

An attractive alternative to the direct numerical solution of the partially-parabolic thick boundary-layer equations is to develop approximate techniques that exploit the two-layer structure noted earlier. In such an approach, it may be assumed that the inner layer satisfies the usual thin boundary-layer equations and hence can be calculated using existing methods. These solutions have to be matched with those of the outer layer in which the flow may be treated as inviscid but rotational and fully three dimensional. Several methods exist for the solution of such problems. Conceptually, such an approach is feasible but its success would depend largely upon the solution of problems arising from matching the inner and outer layers, and the outer layer to

the external inviscid irrotational flow. This suggestion is somewhat similar to the assumptions implicit in the 'streamline curvature' method proposed by Dyne (1978) for the thick axisymmetric boundary layer and near wake, and being developed by Larsson (1982) for application to ship sterns.

## VII. CONCLUSIONS

Examination of the available experimental information on thick three-dimensional boundary layers over a variety of shapes indicates several common features. It is shown that the primary mechanism responsible for the thickening of the boundary layer is streamline convergence, and that prolonged convergence of the external flow leads to divergence close to the surface. Thus, the equation of continuity must be handled with special care in the numerical solutions. Thick boundary layers are accompanied by viscous-inviscid interaction and cross-stream gradients of velocity and stresses which cannot be neglected a priori as in the first-order equations. Also, the examples cited suggest an absence of singular separation or flow reversal in the primary direction. These features are embodied in the partially-parabolic equations, the coupling between the viscous and inviscid flow region being established through the unknown pressure field. The available turbulence data suggest that the thick boundary layer is composed of two layers: an inner layer whose properties are similar to those of a thin boundary layer, and a much larger outer layer in which the stresses and stress gradients are small. This characteristic may be exploited in the development of approximate solution procedures as an alternative to the numerical solution of the partially-parabolic equations. Finally, it appears that, in general, the success of prediction methods for thick boundary layers will be determined more by the manner in which the flow geometry and the pressure field are handled than by the precision of the turbulence model.

## VIII. ACKNOWLEDGEMENT

This research has been supported by the General Hydromechanics Research Program of the Naval Sea Systems Command of the U.S. Navy, administered by the David W. Taylor Naval Ship Research and Development Center, under Contract N00014-82-K0200.

The author is also grateful to the members of the 16th and 17th ITTC Resistance Committees for many fruitful discussions.

This paper is dedicated to the memory of Dr. M.R. Head, of Cambridge University Engineering Department, who passed away on 22 January 1982. Dr. Head made many innovative and lasting contributions to the development of practical boundary-layer calculation procedures which have found applications in aeronautics

as well as ship hydrodynamics. He was the author's thesis advisor during 1962-65 and was responsible for introducing the author to boundary-layer research.

## References

- Abdelmeguid, A.M., N.C. Markatos, K. Muraoka, and D.B. Spalding (1979). A comparison between the parabolic and partially-parabolic solution procedures for three-dimensional turbulent flows around ship's hulls, Appl. Math. Modelling, Vol. 3, p. 249.
- Baldwin, B.S. and H. Lomax (1978). Thin-layer approximation and algebraic model for separated turbulent flows, AIAA Paper 78-257.
- Dietz, M.S. (1980). An axisymmetric, strong interaction procedure to include large, normal pressure gradients, Applied Research Lab., Penn-State Univ., Tech. Memo. 80-160.
- Dyne, G. (1978). A streamline curvature method for calculating the viscous flow around bodies of revolution, Proc. Int. Sym. Ship Viscous Resistance, Goteborg, p. 6.1.
- Geller, E.W. (1979). Calculation of flow in the tail region of a body of revolution, AIAA, J. Hydronautics, Vol. 13.
- Groves, N.C., G.S. Belt, and T.T. Huang (1982). Stern boundary-layer flow on a three-dimensional body of 3:1 elliptic cross section, DT-NSRDC Rept. 82/022.
- Hatano, S., K. Mori, and T. Hotta (1978) Experimental and theoretical investigation of ship boundary layer and wake, Proc. 12th Sym. Naval Hydrodynamics, Nat. Acad. Sci, p. 169.
- Hatano, S. and T. Hotta (1982) Turbulence measurements in the thick boundary layer and near wake of a 3-dimensional body, 6th S.T.G. Meeting, Tokyo (unpublished).
- Hayashita, S. (1982). Flow around a spheroid at angle of attack, Trans. West Japan Soc. Nav. Arch., Vol. 63, p. 41.
- Hirschel, E.H. and W. Kordulla (1981). Shear Flow in Surface-Oriented Coordinates. Notes on Numerical Fluid Mechanics, Vol. 4, Vieweg, Braunschweig.
- Hoffman, G.H. (1980). A modified displacement-body method for treating the axisymmetric strong interaction problem, J. Ship Res., Vol. 24, p. 114.
- Hoffmann, H.P. (1976). Untersuchung der 3-dimensionalen, turbulenten grenzschicht an einem schiffdoppelmodell im windkanal, Inst. Schiffbau, Uni. Hamburg, Report 343.
- Huang, T.T., H.T. Wang, N. Santelli, and N.C. Groves (1976). Propeller/stern/boundary-layer interaction on axisymmetric bodies: theory and experiment, DT-NSRDC, Rept. 76-0113.
- Huang, T.T., N. Santelli, and G. Belt (1979). Stern boundary-layer flow on axisymmetric bodies, Proc. 12th Sym. Naval Hydrodynamics, Nat. Acad. Sci, p. 127.
- Huang, T.T., N.C. Groves, and G. Belt (1980). Boundary-layer flow on an axisymmetric body with an inflected stern, DT-NSRDC, Rept. 80/064.

- Larsson, L. (1974). Boundary layers of ships. Part III: an experimental investigation of the turbulent boundary layer on a ship model, SSPA, Goteborg, Report No. 46.
- Larsson, L. (ed). (1981). SSPA-ITTC workshop on ship boundary layers 1980. SSPA, Goteborg, Report No. 90.
- Larsson, L. (1982). A streamline curvature method for computing the flow near ship sterns. Private communication. (See paper at this Symposium). 14th Sym. Nav. Hydrodynamics, Ann Arbor.
- Larsson, L. and M.S. Chang (1980). Numerical viscous and wave resistance calculations including interaction, Proc. 13th Sym. Naval Hydrodynamics, Tokyo, Shipbuilding Res. Assoc. Japan, p. 707.
- Lofdahl, L. (1982). Measurements of the Reynolds stress tensor in the thick three-dimensional boundary layer near the stern of a ship model, Marintekniska Inst., SSPA, Goteborg, Allman Rept. 61.
- Mahgoub, H.E.H. and P. Bradshaw (1979). Calculation of turbulent-inviscid flow interactions with large normal pressure gradients, AIAA Journal, Vol. 17, p. 1025.
- Muraoka, K. (1980). Calculation of thick boundary layer and wake of ships by a partially parabolic method, Proc. 13th Sym. Naval Hydrodynamics, Tokyo, Shipbuilding Res. Assoc. Japan, p. 601.
- Muraoka, K. (1982). Calculation of viscous flow around ships with parabolic and partially parabolic flow solution procedure, Trans. West Japan Soc. Nav. Arch., Vol. 63, p. 13.
- Nagamatsu, T. (1980). Results of model experiments for the velocity measurement near the stern of M2058, Mitsubishi Expt. Tank, Nagasaki Tech. Inst, Rept. 2058.
- Nakayama, A., V.C. Patel, and L. Landweber (1976). Flow interaction near the tail of a body of revolution: parts I and II, ASME, J. Fluids Eng., Vol. 98, p. 531.
- Nash, J.F. and V.C. Patel (1972). Three Dimensional Turbulent Boundary Layers, SBC Tech. Books, Atlanta.
- Okuno, T. and Y. Himeno (1982). Turbulence measurement in ship-model flow, IUTAM Symposium, Berlin, March 29-April 1, Unpublished.
- Patankar, S.V. and D.B. Spalding (1972). A calculation procedure for heat, mass and momentum transfer in three-dimensional flows, Int. J. Heat Mass Transfer, Vol. 15, p. 1787.
- Patel, V.C. (1973). On the equations of a thick axisymmetric turbulent boundary layer, Iowa Inst. of Hydr. Research, IIHR Report 143.
- Patel, V.C., A. Nakayama, and R. Damian (1974). Measurements in the thick axisymmetric turbulent boundary layer near the tail of a body of revolution, J. Fluid Mech., Vol. 63, p. 345.
- Patel, V.C. and Y.T. Lee (1977). Thick axisymmetric turbulent boundary layer and near wake of a low-drag body of revolution, Iowa Inst. of Hydr. Research, IIHR Report 210.
- Patel, V.C. and J.H. Baek (1982). Calculation of three-dimensional boundary layers on bodies at incidence, 7th U.S. Air Force -

- Federal Republic of Germany Data Exchange Agreement Meeting, "Viscous and Interacting Flow Field Effects", U.S. Army BRL, Aberdeen Proving Grounds, Maryland, May 26-27, Unpublished.
- Pulliam, T.H. and J.L. Steger (1980). Implicit finite-difference simulations of three-dimensional compressible flow, AIAA Journal, Vol. 18, p. 159.
- Ramaprian, B.R., V.C. Patel, and D.H. Choi (1981). Mean-flow measurements in the three-dimensional boundary layer over a body of revolution at incidence. J. Fluid Mech., Vol. 103, p. 479.
- Rodi, W. (1982). Examples of turbulence models for incompressible flows, AIAA Journal, Vol. 20, p. 872.
- Wieghardt, K. (1982). Kinematics of ship wake flow, The Seventh David W. Taylor Lecture, DT-NSRDC, Rept. 81/093.



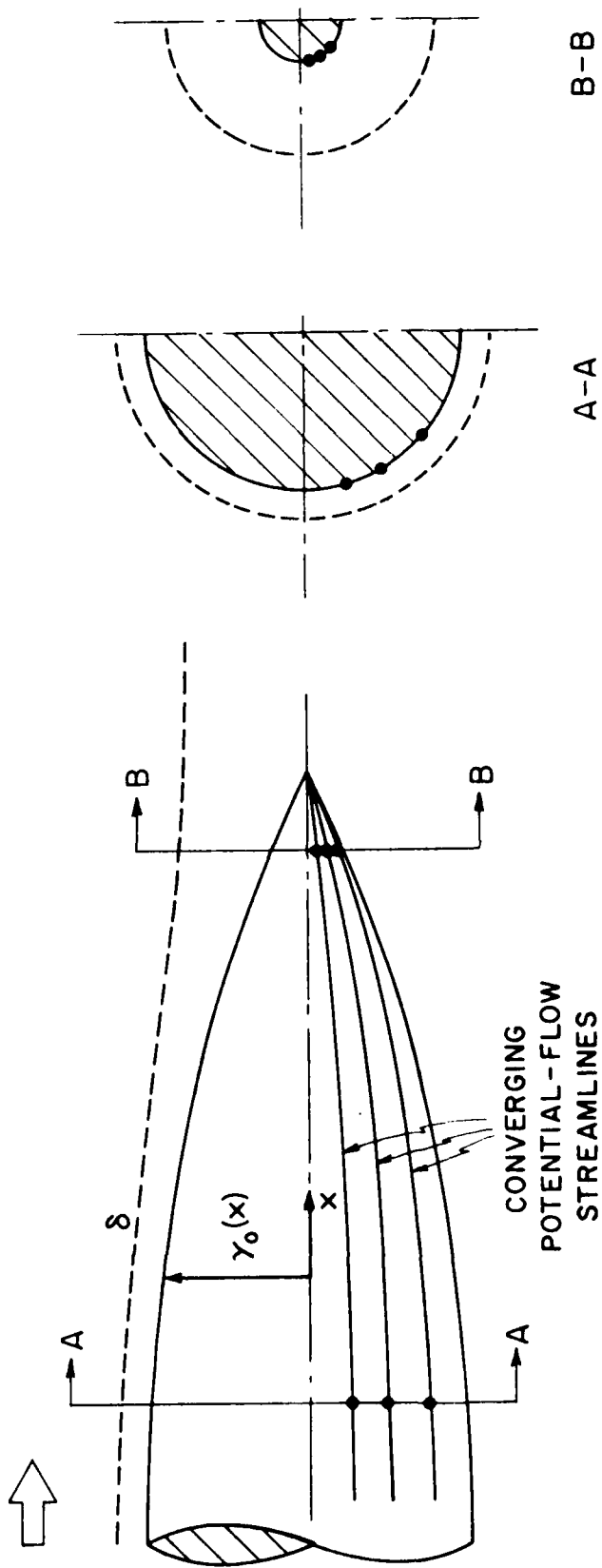


FIG. 1. THICK AXISYMMETRIC BOUNDARY LAYER.

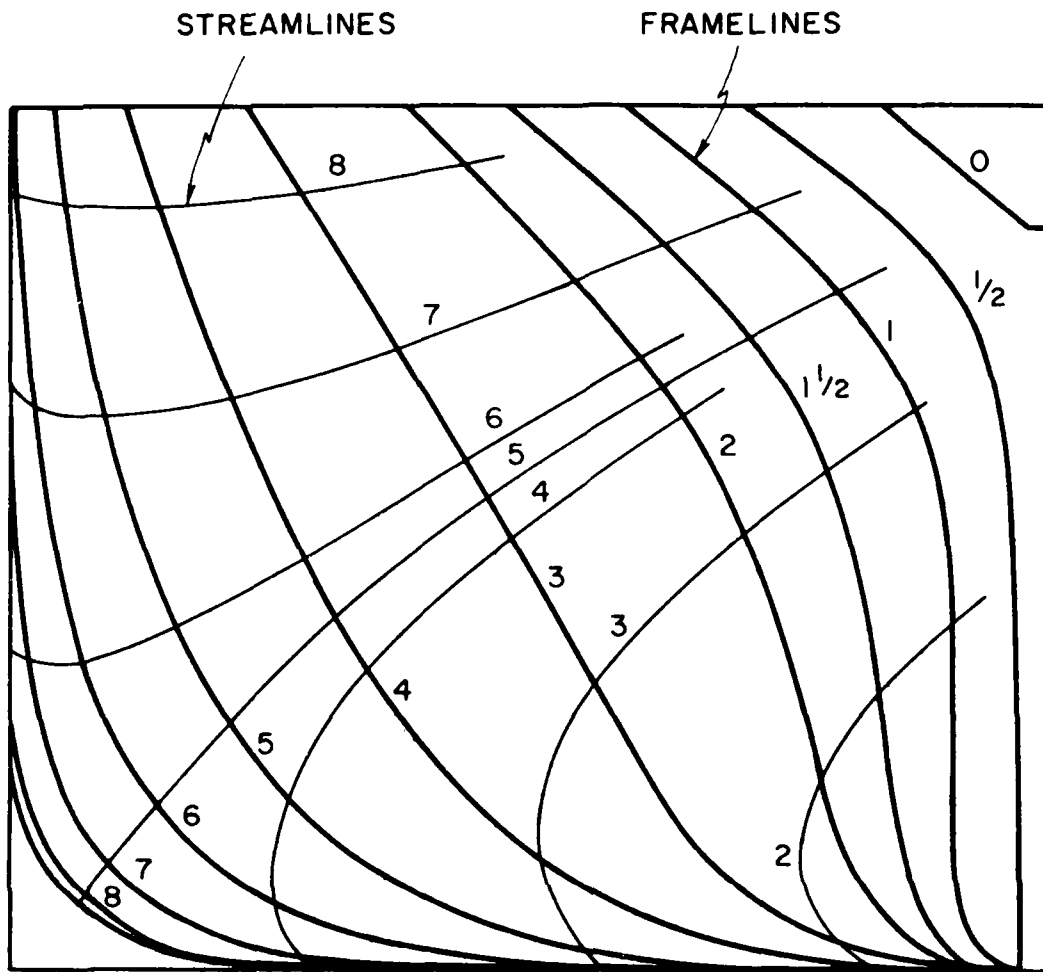


FIG. 2. GEOMETRY AND POTENTIAL-FLOW STREAMLINES  
ON SSPA MODEL 720 (LARSSON, 1974).

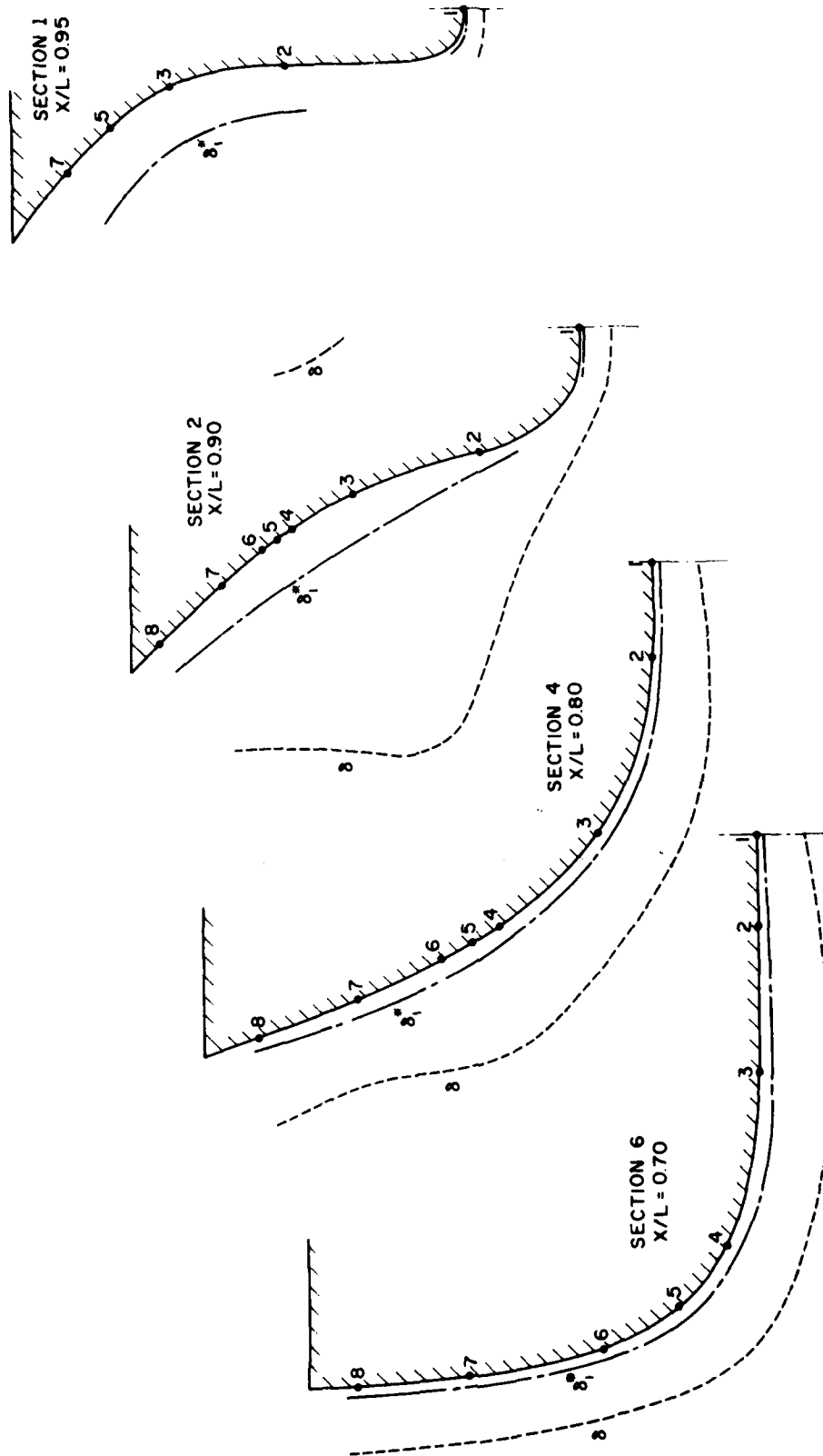


FIG. 3. STERN BOUNDARY LAYER ON SHIP MODEL. (LARSSON, 1974)

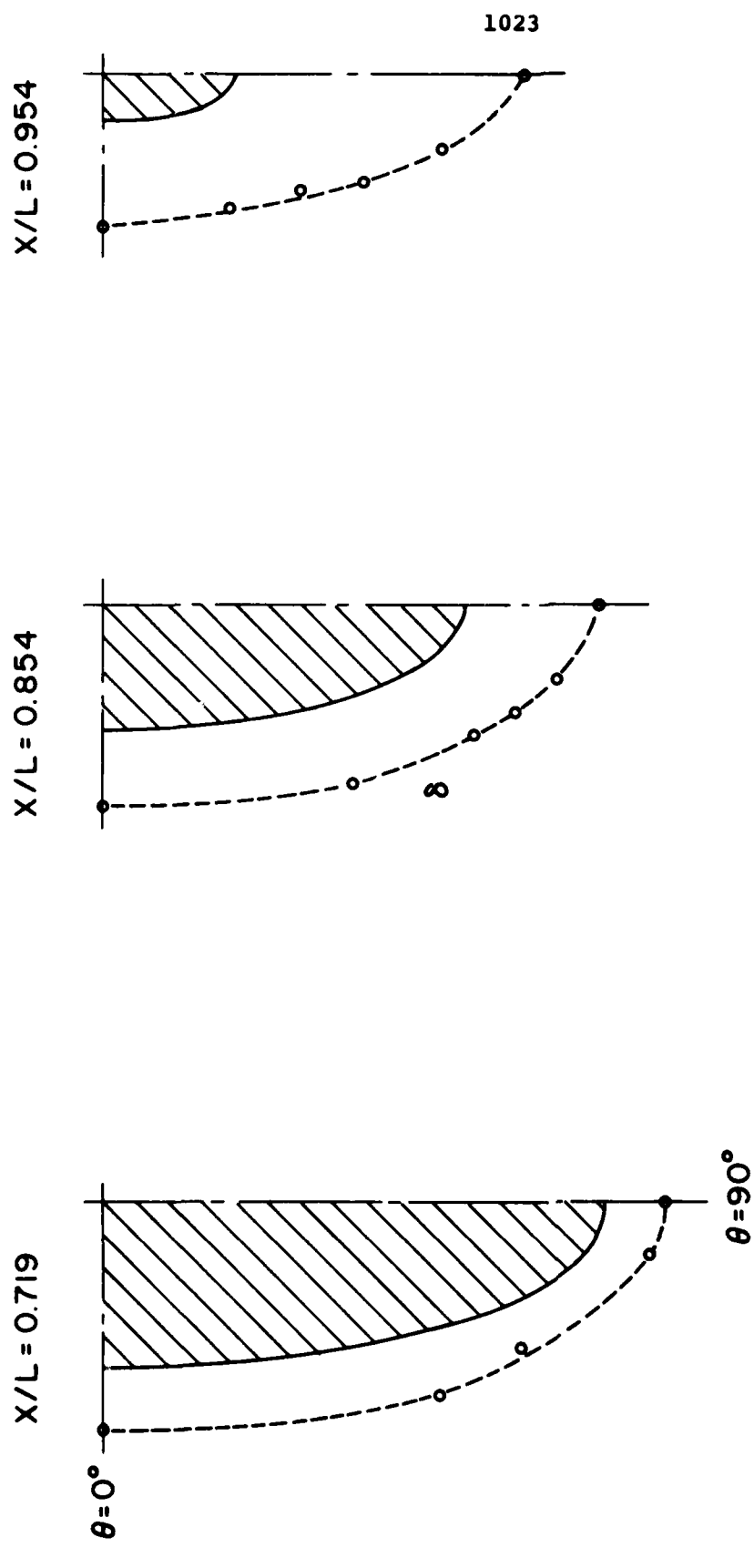


FIG. 4. THICK BOUNDARY LAYER ON A BODY OF ELLIPTIC CROSS SECTION.  
GROVES, BELT, AND HUANG (1982).

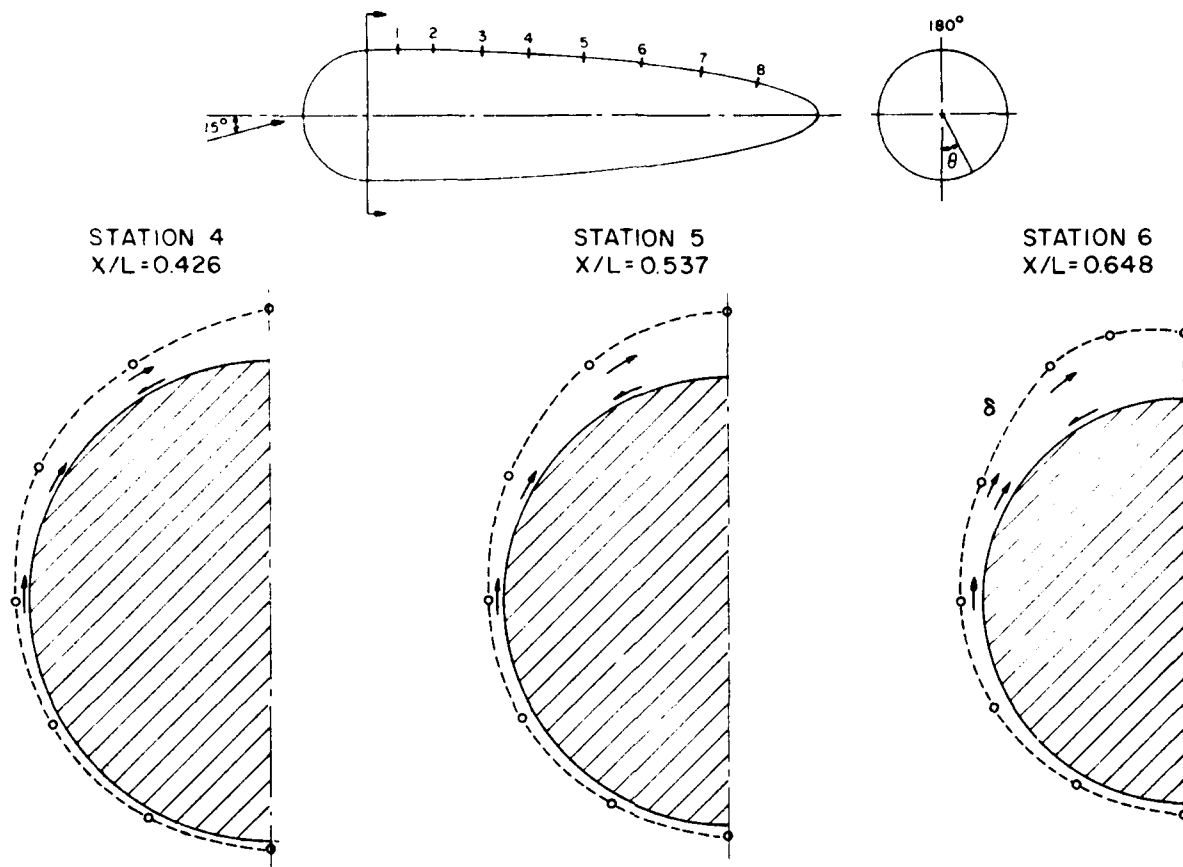


FIG. 5. THICK BOUNDARY LAYER ON A BODY OF REVOLUTION AT INCIDENCE. RAMAPRIAN, PATEL, AND CHOI (1981)

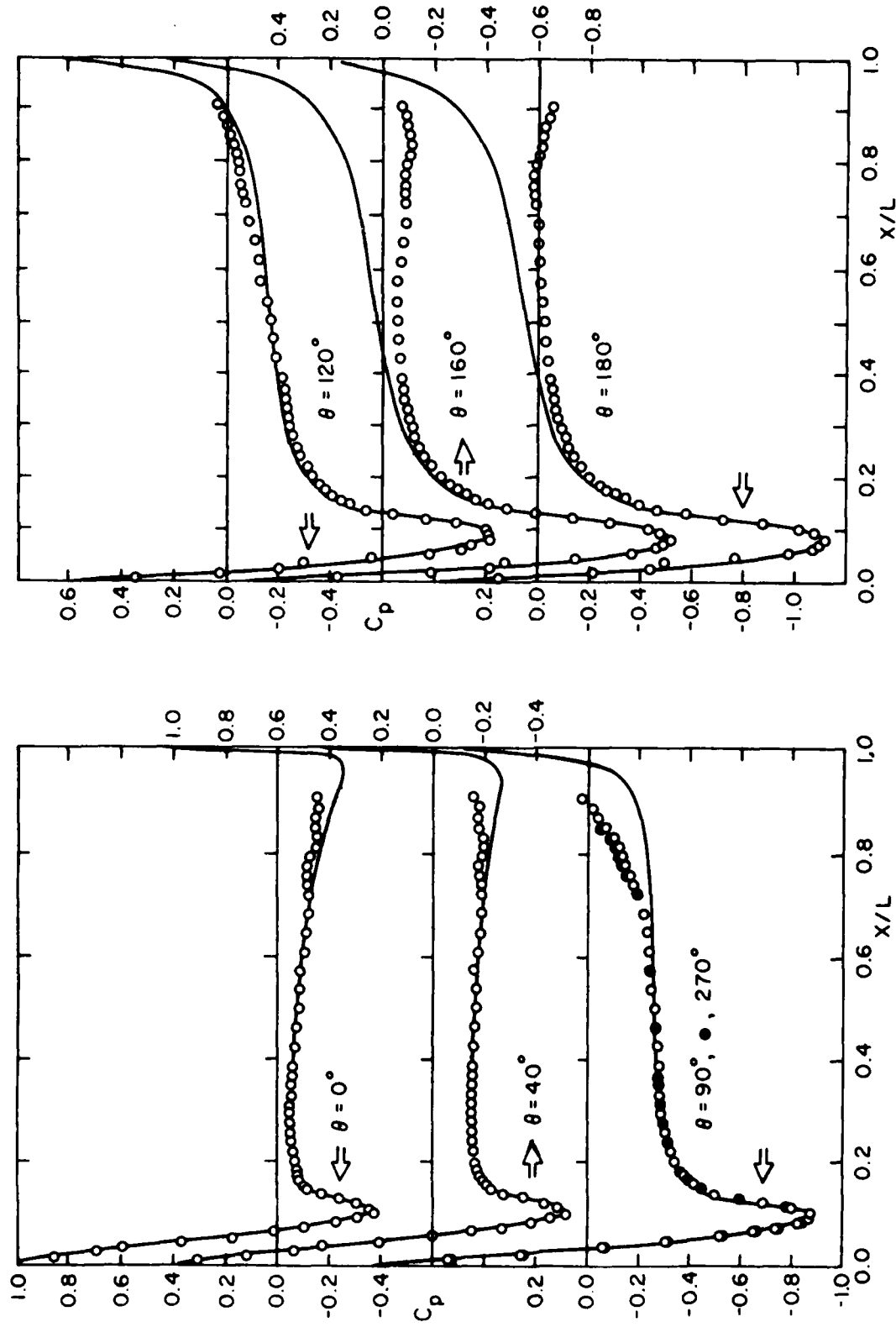


FIG. 6. PRESSURE DISTRIBUTION ON THE COMBINATION BODY AT 15° INCIDENCE.  $\circ, \bullet$  EXPERIMENT, — POTENTIAL FLOW.

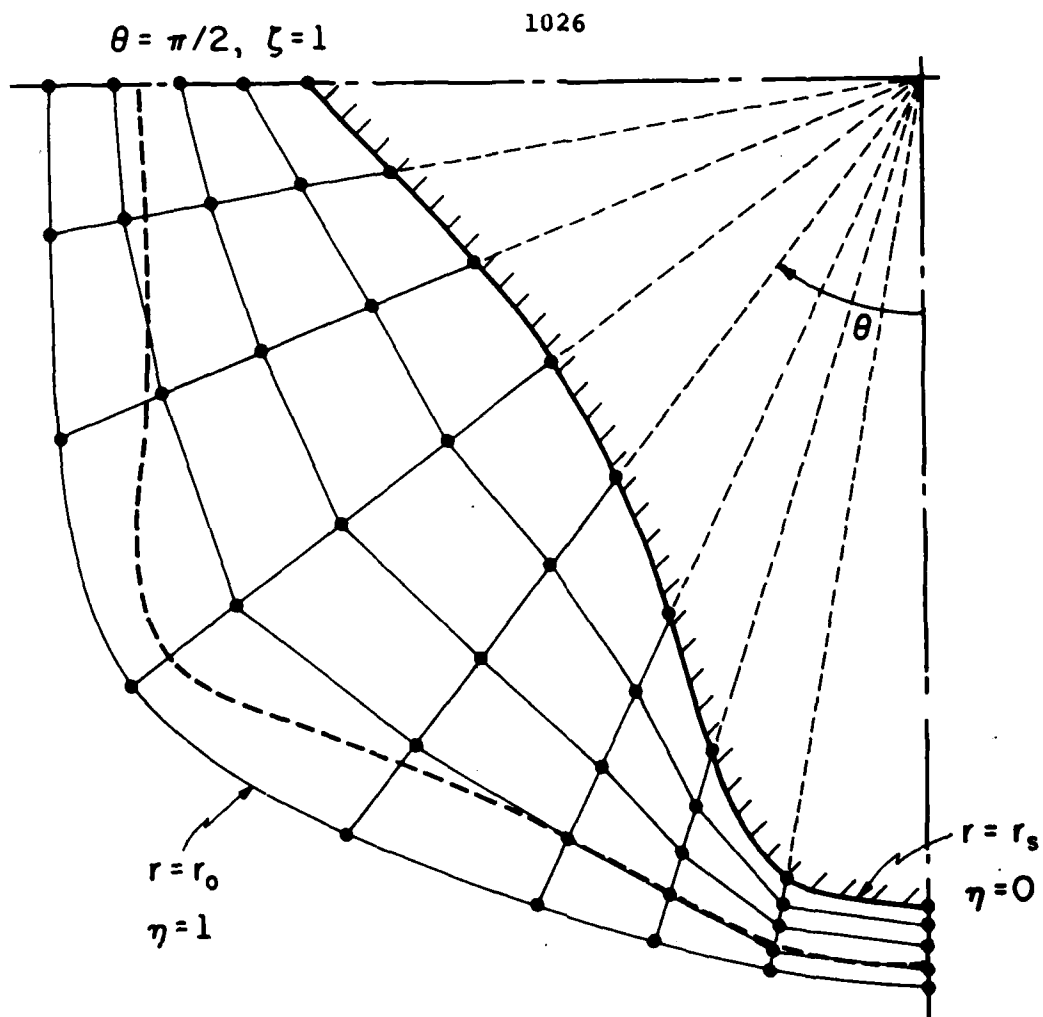


FIG. 7. A DISTORTED CYLINDRICAL POLAR COORDINATE SYSTEM.

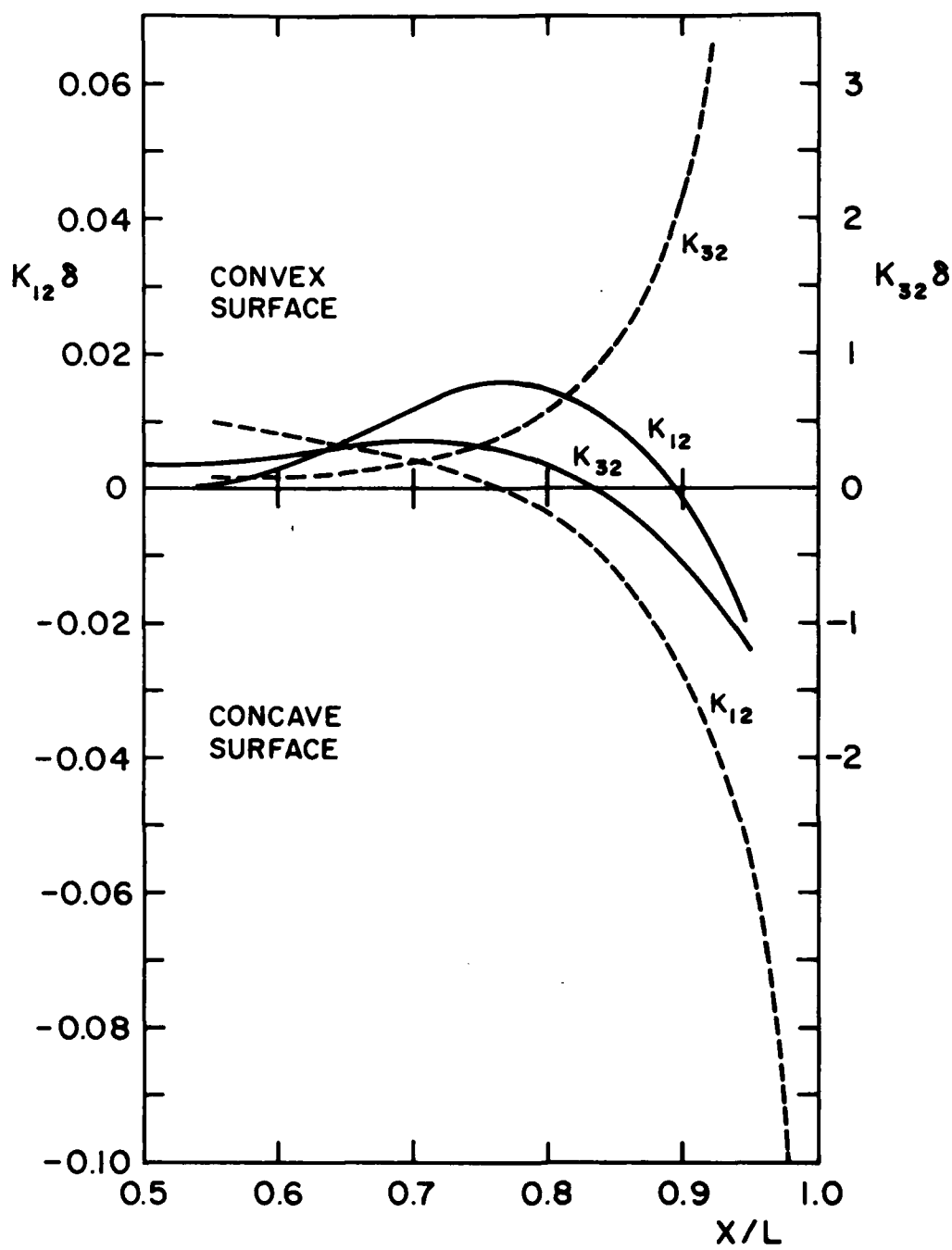


FIG. 8. LONGITUDINAL ( $K_{12}\delta$ ) AND TRANSVERSE ( $K_{32}\delta$ ) SURFACE CURVATURE PARAMETERS.  
 — SHIP, --- AXISYMMETRIC BODY.



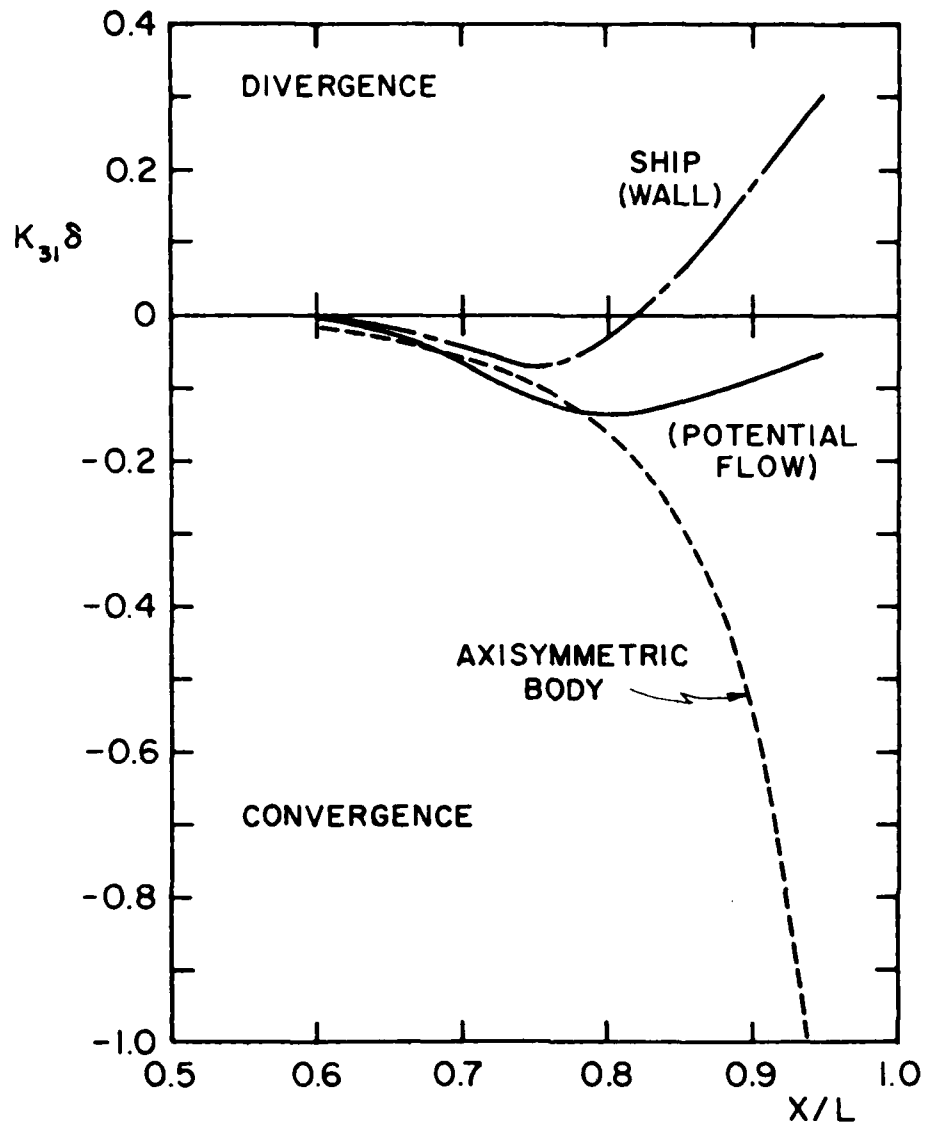


FIG. 9. STREAMLINE CONVERGENCE PARAMETER.

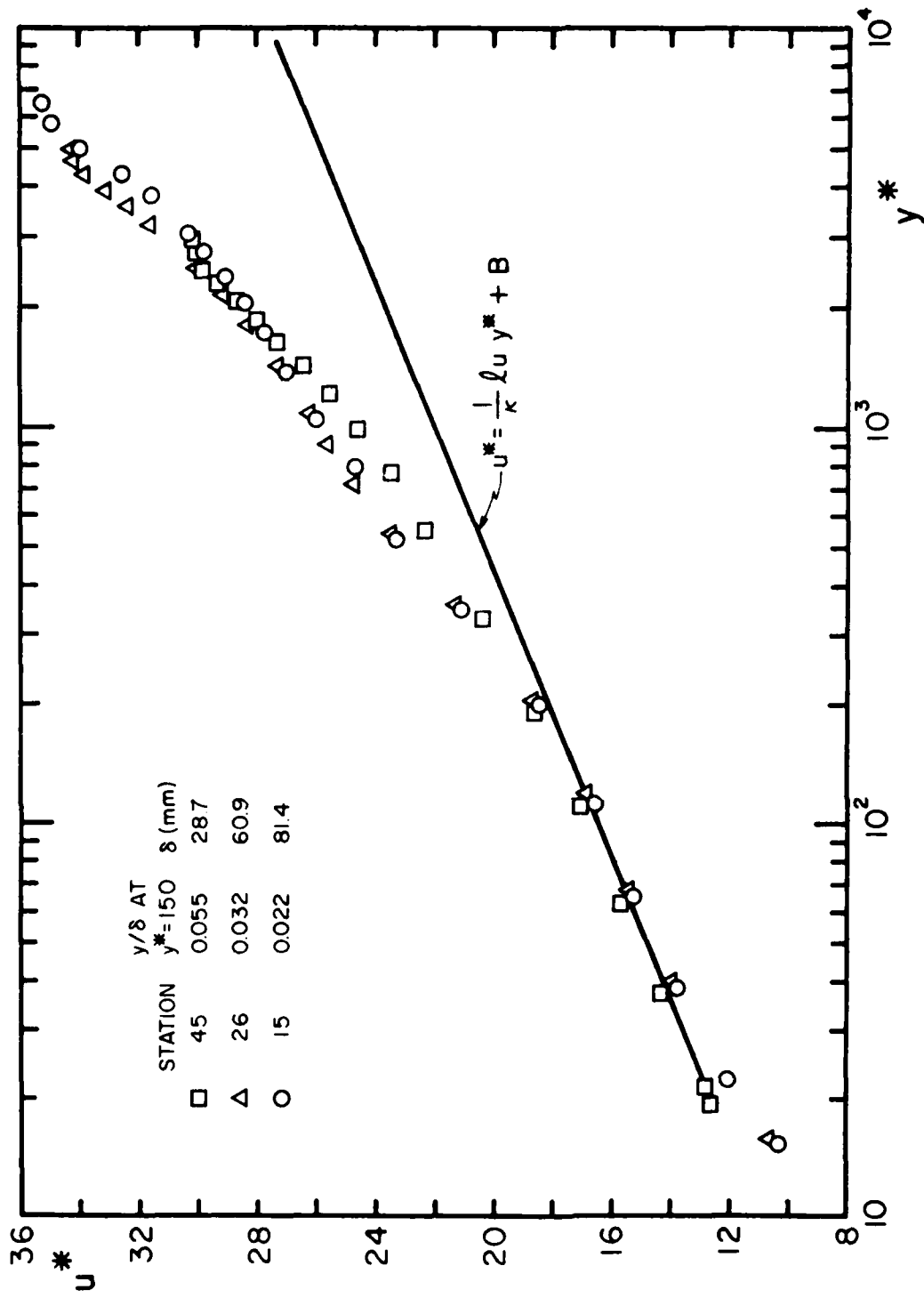


FIG. 10. VELOCITY PROFILES ALONG STREAMLINE 5. (LARSSON, 1974)

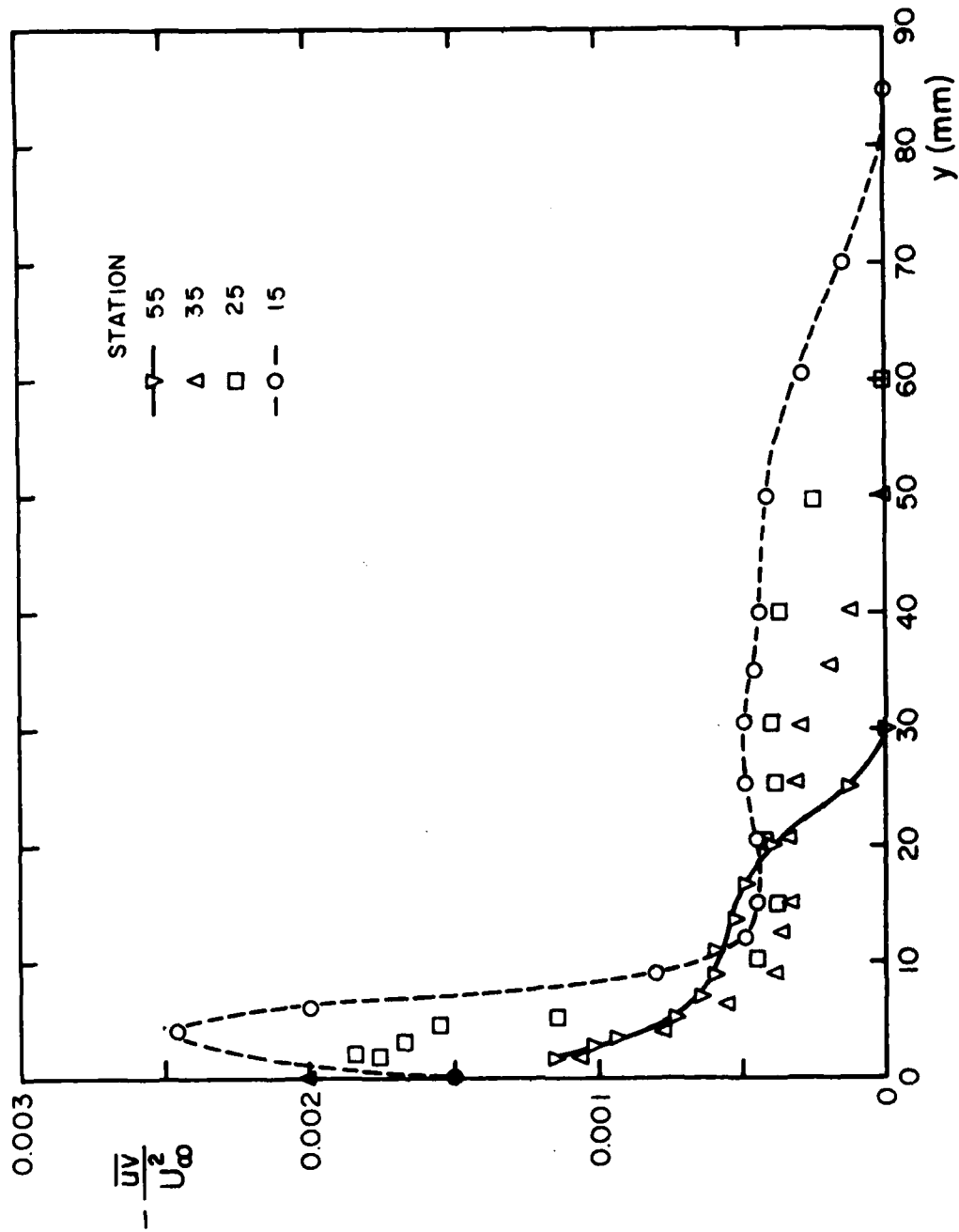
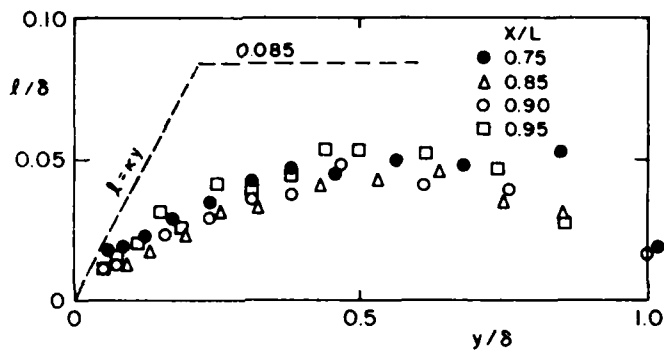
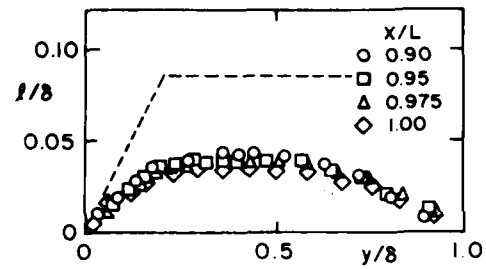


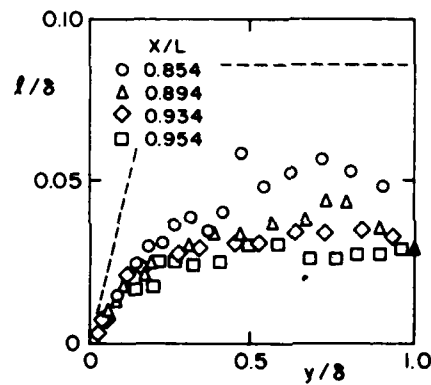
FIG. 11. REYNOLDS SHEAR-STRESS PROFILES ALONG STREAMLINE 5 ON SSPA MODEL 720 (LÖFDAHL, 1982)



(a) ALONG STREAMLINE 5 ON SHIP MODEL (LÖFDAHL)



(b) ALONG WATERLINE PLANE OF SYMMETRY OF WIGLEY DOUBLE MODEL (HATANO &amp; HOTTA).

(c) ALONG  $\theta=90^\circ$  PLANE OF SYMMETRY ON ELLIPTIC BODY (GROVES, BELT, & HUANG)FIG. 12. MIXING-LENGTH DISTRIBUTIONS IN THICK BOUNDARY-LAYERS.  
---- THIN BOUNDARY-LAYER CORRELATION.

## Discussion

K. Mori (Hiroshima University)

1. We can obtain the partially parabolic approximation consistently under the assumption

$$\frac{\partial}{\partial x} \sim O(1), \quad \frac{\partial}{\partial y} \quad \frac{\partial}{\partial z} \sim O(\epsilon^{-1}).$$

If the Reynolds stress can be expressed in terms of the mean velocity,  $\overline{uv}$ , for example, is written in the form of

$$\overline{uv} = -\nu_t \left( \frac{\partial v}{\partial x} + \frac{\partial u}{\partial y} \right)$$

where  $\nu_t$  is the kinematic eddy viscosity whose order we assume  $O(\epsilon^2)$ . Then we can have

$$\overline{uv} = -\nu_t \cdot \frac{\partial u}{\partial y} + O(\epsilon^2).$$

Similarly we can have

$$\overline{vv} = O(\epsilon^2), \quad \overline{vw} = O(\epsilon^2).$$

Now  $\overline{u_i u_j}$  is not of the same order any more;  $\overline{vw}$  is higher. This may be consistent with experiments.

Picking up the leading terms, we have the following equation for the y-equation:

$$u \frac{\partial v}{\partial x} + v \frac{\partial v}{\partial y} + w \frac{\partial v}{\partial z} + \frac{\partial}{\partial x} (\overline{uv}) + \frac{\partial}{\partial y} \left( \frac{p}{\rho} + \overline{vv} \right) + \frac{\partial}{\partial z} (\overline{vw}) \\ - \nu \left\{ \frac{\partial^2 v}{\partial y^2} + \frac{\partial^2 v}{\partial z^2} \right\} + O(\epsilon^2) = 0$$

Though Equation (5) seems still to have a transportation of the Reynolds stress in the x-direction, the fourth term of Equation (5) being given by Equation (3), we can conclude that Equation (5) has been parabolized.

Similarly we can have the parabolized z-equation.

2. The discussor supposes that, in the case of ship-like bodies, the important aspect of the partially parabolic approximation lies in retaining the pressure term rather than the  $\partial^2/\partial z^2$  term. This is because, first, in the two-dimensional case or the axisymmetry case, the partially parabolic equation is no more than the

boundary-layer equation except that it retains the pressure term; and also because the author has had experience calculating the near-wake flow of ships by making use of the vorticity transport equation with the same approximation as the boundary layer;

$$\vec{q} \cdot \nabla \vec{\omega} - \vec{\omega} \cdot \nabla \vec{q} = \nu_t \frac{\partial^2 \vec{\omega}}{\partial y^2},$$

where  $\vec{q}$  and  $\vec{\omega}$  are the velocity and the vorticity vectors, respectively, Equation (6) is the same as the boundary-layer equation except the pressure is released (kept unknown). The calculation was quite stable, and results were satisfactory.\*

Such equations, where just the pressure term is retained, can be obtained consistently under the assumption of orders

$$\frac{\partial}{\partial x} \sim O(1), \quad \frac{\partial}{\partial y} \sim O(\epsilon^{\frac{1}{2}}), \quad \partial/\partial z \sim O(\epsilon)$$

which is likely in the case of ship-like bodies. The equations must be similar to those used by Larsson and Chang (1980). Appreciable simplifications in numerical calculation can be expected.

3. What kind of scheme are you going to use for the Reynolds stresses instead of the mean rates of strains?

\*K. Mori; Mem. of Fac. of Eng., Hiroshima University, Vol. 7, No. 2 (1980).

A.Y. Odabasi (British Ship Research Association)

Professor Patel presents an excellent review of the state of the art on stern boundary layers, based on the information and data available to him, and proposes a possible calculation scheme based on these findings. Unfortunately, his data do not include the wind-tunnel measurements undertaken at NMI on three hull forms (one V-stern, one U-stern, and one bulbous stern form) nor does it include the analytical and numerical studies conducted at BSRA, apart from one by Odabasi and Saylan (1980), as this information was confidential to the sponsors of the research. I would therefore like to complement some of the points raised in this paper using the information available to us. Since a more detailed discussion of the flow structure will be presented in a paper by Odabasi and Davies (1983), the comments will be kept to a minimum here.

Potential Flow Computation The present paper pays little attention to the accuracy of potential flow calculations. Although for axisymmetric forms this is a relatively easy task to achieve, for the general forms encountered near the stern (or the bow) of the ship forms the accuracy of calculation depends very much on the method employed. The use of singularity panel methods does not automatically guarantee success since the choice of panels both in terms of aspect ratios and the area ratios of neighboring panels greatly influences the results.

A possible remedy to this problem is to link a surface representation with the potential flow and boundary-layer calculations and reduce the compound error. Although this may appear laborious at the outset if one remembers that a proper surface representation is needed both for detailed design and production, implementation of such a scheme does not add extra cost to the overall design or assessment program. At present, a hull surface representation using parametric spline surface patches (a program called HULLSURF) is being used for this purpose, which produces hull surface panels as well as their geometric features (i.e., areas, direction cosines of normal, and metric tensor) by mapping the principal curvature lines on the surface. These lines also form the coordinate lines on the hull surface ( $n = 0$  surface).

Coordinate System As pointed out in the paper, there exists a great deal of flexibility in the choice of a coordinate system for the boundary layer calculations, provided that they remain within the broad guidelines given by Wesseling (1969), i.e., one of the coordinates is aligned nearly with the mainstream direction and one of the other coordinates should be close to the surface normal. While the importance of the first requirement is self-evident, the need for the latter arises from the fact, in one form or another, that the governing equations are derived by employing assumption on the variation normal direction making the resulting equations semi-invariant with respect to coordinate transformations. Within this context the proposed coordinate system (Figure 7 of the paper) does not satisfy the second requirement unless a second transformation is conducted, which adds to the complication and introduces additional errors in the numerical execution of the transformation. Furthermore, for ships with bulbous stern a vertical shift of axis system is needed, which introduces further arbitrariness.

Modeling of Governing Equations Professor Patel vividly displays how the so-called order theories can be manipulated by choosing different assumptions on the order of magnitude of different terms. While this may look arbitrary, a more rational basis for the choice of assumptions may be conceived by considering the ratio of simple shear ( $\partial U / \partial n$ ) to the extra strain rates ( $e$ ) due to the effects of acceleration (deceleration), curvature, convergence, swirl, etc., cf. Bradshaw (1972), Odabasi (1980). Accordingly, one may broadly state that a layer is a

Simple shear layer if  $\partial U / \partial n \gg 10e$   
 Thin shear layer if  $\partial U / \partial n \gg e$   
 Fairly thin shear layer if  $\partial U / \partial y > 10e$   
 Strong distortion layer if  $\partial U / \partial y < 10e$   
 Rapid distortion layer if  $\partial U / \partial y < e$

where  $\gg$  implies a ratio between 10 and 100.

In principle, only in rapid distortion layers may one ignore the effect of Reynolds stresses, as proposed in the paper, and consider the flow field as ideal flow with vorticity. A glance at Figures 8 and 9 of the paper indicates that this assumption is quite justified for the axisymmetric body, since the distortion imposed by the external

potential flow will be far in excess of the simple shear, apart from a very small region near the wall. However, the same figures illustrate also that the situation is quite different for even a fairly fine V-form ship (SSPA model 720). In practice, depending on the form of the aft-end form, the flow in the stern region falls within the fairly thin shear-layer range, approaching a strong distortion layer when the angle of runs and convergence is high. Therefore, the assumptions related to the relative role of Reynolds stresses ceases to be valid. Figure 13 displays that turbulence production further downstream is quite evident. Wake and turbulence intensity measurements of HSVA tanker form, shown in Figure 14, also support BSRA.

When one combines this principle together with an order-of-magnitude of analysis of the wind tunnel data on ship forms, momentum transport equations show certain differences compared with the partially parabolic equations. For example, the transport equation in the normal direction becomes

$$U_1 \frac{\partial U_2}{\partial x_1} + U_1 \frac{\partial U_2}{\partial x_2} + U_3 \frac{\partial U_2}{\partial x_2} = - \frac{\partial}{\partial x_2} \left( \frac{P}{\rho} + \langle u_2^2 \rangle \right) - \frac{\partial}{\partial x_1} \langle u_1 u_2 \rangle - \frac{\partial}{\partial x_3} \langle u_2 u_3 \rangle.$$

which, in fact, is important in the computation of pressure in successive sweeps.

An important point, at least in our experience, is the role played by the extra strain rates imposed on the main flow. While the method proposed by Bradshaw (1972) is, in principle, not derived from a recognized principle, it at least produces results in the right direction, especially when used in conjunction with a dissipation length scale transport equation, cf. Odabasi and Davies (1983). It is therefore strongly suggested that this effect should be taken into account in a scheme for stern boundary-layer calculation.

It is also important to recognize that the mechanism gives rise to the formation of vortices in the wake, i.e., shear separation. Figure 15 displays measured velocity profiles at the location of shear separation, and Figure 15 shows the profiles along the same streamline in a further downstream location. The corresponding shear profiles (streamwise components) are demonstrated in Figure 17. In numerical computation one observes a weak singularity in the location of shear separation, which can be overcome by adopting a scheme similar to FLARE, cf. Odabasi (1981).

**Turbulence Models** While it is not possible to produce a universally valid turbulence model or assume that one can determine simpler equations than Navier-Stokes equations, within a fairly restricted class of flows an assessment may be possible. Experimental data on stern flow clearly indicate that an isotropic eddy viscosity assumption is not valid and therefore should be avoided. The assumption of Bradshaw on turbulence production generally holds, i.e., the shear-energy conversion constant  $\alpha$  varies between 0.17 and 0.18 depending on the pressure gradient. A dissipation length scale, or equivalently a dissipation rate, transport equation improves the performance of the calculation methods. Data also indicate that both convective and gradient diffusions assumption are not supported and a complete re-



thinking may be necessary for more realistic diffusion modeling, cf. Odabasi (1981).

Viscous-Inviscid Interaction While I would like to express my full support for the views expressed by Professor Patel, I would like to point out that early knowledge of this fact may help to introduce the interaction effect by modifying the potential flow computation results prior to the first iteration in boundary-layer calculations.

## References

- Bradshaw, P. (1972), The Understanding and Prediction of Turbulent Flow, *Aeronautical J.*, 76, 739, p. 403.
- Odabasi, A.Y. (1980), A Contribution to the Calculation of Flow Around the Aft-Ends of Ships, *Int. Shipbldg. Progress*, 27, 316, p. 316.
- Odabasi, A.Y. (1981), Analysis of NMI Wind Tunnel Data, BSRA Report SC/PHI 13.
- Odabasi, A.Y., and O. Saylan (1980), GEMAK--A Method for Calculating the Flow Around Aft-End of Ships, 13th Symp. on Naval Hydrodynamics, Tokyo.
- Odabasi, A.Y., and M.E. Davies (1983), Structure of the Turbulent Shear Flow in Ship Boundary Layers, Paper to be presented at Douglas Symp.
- Wessling, P. (1969), The Calculation of Incompressible Three-Dimensional Turbulent Boundary Layers, Part 1, Formulation of a System of Equations, National Aerospace Laboratory NLR, The Netherlands, Report AT-69-01.

## I. Tanaka (Osaka University)

In your Figures 2, 11, and 12(a), you referred to SSPA model 720, but, it seems to me, each figure has a different description about the measured locations in Square Stations. I would like to know the correspondence between them.

In Figure 11, assuming that station 55 is upstream (and station 15 downstream), let me ask the following:

1. Near the wall, why is the value at station 55 (upstream) smaller than the value at station 15 (downstream)?
2. Is it possible to give physical explanations for the difference of shapes of stresses between the two stations, noted above, near the wall?
3. What is the physical explanation about a sudden flat plateau formation of stress shape in outer layer? It seems to me that it may be homogeneous in the girthwise direction in this nature. Is it true?

In Figure 12:

1. How was  $\delta$  determined (in each figure)?

2. Among three figures, the configuration near  $y/\delta = 1.0$  is different. Could you show us the intermittency factor distributions for each figure? What is the main cause of different values of  $1/\delta$  at the edge of  $\delta$ ?

Mr. Fukuda of Mitsui's Akishima Lab made a measurement of stresses around a Series 60 model and published it in the Journal of the Society of Naval Architects of Japan, 1981.

H.T. Wang (Naval Research Laboratory)

I would like to thank Professor Patel for presenting an instructive overview of thick boundary layers. I would like to point out a calculation method that is not mentioned in the paper. I am referring to the potential flow/boundary-layer computer program developed at DTNSRDC by Dr. Thomas Huang and myself. It is an extremely simple calculation procedure, which nevertheless includes the essential thick boundary-layer features given in the paper.

Details of the program are given in Wang and Huang (1979). Briefly, the method uses the displacement body-wake concept to calculate the pressures on as well as off the body. The calculated pressure on the body is used to solve the thin boundary-layer momentum equation (but including the effect of transverse curvature) for the tangential velocity. The eddy viscosity is modified by a simple algebraic equation to account for the small shear stresses in the thick boundary-layer region. The calculated tangential velocities are then modified by the calculated off-body pressures such that, at the edge of the boundary layer, the modified tangential velocity is exactly equal to the potential flow value. Finally, the normal velocity is simply determined from the continuity equation. The procedure basically decouples the boundary-layer and pressure calculations. Also, the boundary-layer calculations are no more complex than those for the thin boundary-layer case.

The calculated results have been validated in the Reynolds number range  $10^6$  to  $10^7$  for a series of bodies, see Wang and Huang (1979). The paper presented by Dr. Coder at this symposium to some extent validates the program in the Reynolds number range  $10^7$  to  $10^8$ .

## Reference

- Wang, H.T., and T.T. Huang (1979), Calculation of Potential Flow/Boundary Layer Interaction on Axisymmetric Bodies, Turbulent Boundary Layers, ASME, New York, pp. 47-57.

## Author's Reply

V.C. Patel

To Prof. I. Tanaka

1. The correspondence between the notation used in Figure 2 and that in Figures 11 and 12 (a) is indicated in Figure 3. Since the mean flow was measured by Larsson (1974) and the turbulence measurements were made by Lofdahl (1982), both types of data are not available at all stations.
2. In Figure 11, station 55 is upstream ( $X/L = 0.75$ ) of station 15 ( $X/L = 0.95$ ).
  - a. The near-wall Reynolds stresses are increasing with downstream distance presumably owing to the increasing adverse pressure gradient along this streamline. Note that the wall shear stress is decreasing.
  - b. The evolution of the stress field in the wall region may be attributed to a variety of factors, including the local pressure gradients, streamline convergence and divergence, and possibly surface curvature. At this stage, it is not yet possible to isolate these effects, but, as indicated in the paper, it would be useful to perform additional analysis of the data and supporting calculations.
  - c. The plateau in the shear stress is not expected to be homogeneous in the girthwise direction since the boundary layer along the keel is still thin and may not indicate this feature. In the thick boundary layer, however, its presence may be attributed to the convection of turbulence from upstream rather than local production and diffusion.
3. In Figure 12:
  - a. The values of  $\delta$  are those quoted by the investigators using the usual definition based on either mean velocity or total-pressure profiles.
  - b. Intermittency measurements have not been reported in any of these investigations. The differences in  $1/\delta$  at the outer edge are most certainly due to lack of accuracy in the determination of  $l$  from experimental data, since it is the ratio of the square root of the diminishing Reynolds stress and the mean velocity gradient.
4. The turbulence measurements of Fukuda and Fujii (JSNA, Vol. 150, 1981) on a Series 60 model also show some of the qualitative features of thick boundary layers noted here. In a later, unpublished report (STG Meeting, Tokyo, May 1982), however, these authors presented a revised method for the analysis of hot-wire data that casts some doubt on the accuracy of the method used in the previous publication.

To Dr. H.T. Wang

The paper of Wang and Huang (1979) incorporates several additional features in the method of Huang, Wang, Santelli, and Groves (1976) referenced in my paper and could have been quoted in my brief survey of the analytical treatment of thick axisymmetric boundary layers in Section II of my paper. However, as the title suggests, the present paper is concerned primarily with thick three-dimensional boundary layers with special emphasis on experimental evidence.

To Prof. K. Mori

1. Any attempt at making an order-of-magnitude analysis of the terms involving Reynolds stresses in the equations of motion has to rely on experimental evidence. In this paper, I have assumed that all turbulent stresses are of the same order. Instead of using these measurable quantities, Professor Mori suggests the use of a derived quantity, namely an isotropic eddy viscosity. Once this is done, and a magnitude assigned to it, the equations reduce to those of a pseudo-laminar flow and the order-of-magnitude analysis can be made as if the flow were laminar. It is interesting to note that the net result is the same, although the eddy-viscosity approach enables the retention of the x-derivatives of the Reynolds stresses in the partially parabolic equations through relations such as Professor Mori's Equation (3) used in conjunction with continuity.
2. For ship-like bodies, the most important aspect of the partially parabolic equations may turn out to be their capability to relax the pressure field rather than the transverse gradients of stresses. This will be true if it can be shown that all the secondary motion (in the yz plane) is of the first kind, i.e., driven by the pressure forces. The partially parabolic equations are, however, more general insofar as they can be used also to describe secondary motion of the second kind, which is driven by the transverse gradients of Reynolds stresses (e.g., flow along a streamwise edge or corner). In view of this, it is perhaps better to work with the complete equations while recognizing that some terms may be small for an entire class of flows or in a subregion of a given flow. Professor Mori's Equation (6) results from the so-called thin-layer approximations, in which only the stresses responsible for transport normal to the shear layer are retained. The success of Professor Mori's solutions may be due more to the elimination of the pressure by the use of the vorticity transport equation rather than to the neglect of the extra turbulent transport terms. Needless to say, the solution of the vorticity equation poses other problems stemming largely from boundary conditions at solid walls.
3. It is apparent from the paper that the author has not yet made up his mind on any particular turbulence closure model since it is not clear at this stage which, if any, of the existing schemes would best reproduce the observed features.

To Dr. A.Y. Odabasi

The author does not have access to the confidential experimental and computational information noted by the discussor. The following response is confined to those items that can be addressed without recourse to that information.

Potential Flow I agree that the calculation of the external irrotational flow and its matching with the viscous flow is of crucial importance. However, it is not certain whether existing irrotational-flow calculation methods can be generalized to account for the thick boundary layer and near wake of arbitrary bodies with sufficient accuracy.

Coordinate System I do not see why the local surface normal has to be a coordinate for thick boundary layers of the type depicted in Figure 3. Once the appropriate equations are written down, e.g., the partially parabolic equations, the choice of coordinates is vast and must be determined by numerical considerations. The coordinates of Figure 7 have been chosen for illustration and may not be adequate for all sterns. Nevertheless, the example shows that it is not necessary to make further coordinate-related approximations once the basic governing equations have been selected and, in the case of partially parabolic equations, a marching direction decided on.

Modeling of Governing Equations The scheme proposed by Bradshaw for the classification of shear layers on the basis of "extra strain rates" is physically appealing for flows in which there is a primary strain rate. The examples of thick boundary layers shown in the paper indicate that it is not possible to put them in a single class since there are regions where the flow behaves as a thin shear layer next to regions where it may be regarded as a rapid distortion layer. As in my response 2 to Professor Mori's discussion, I believe it is safer to use the most general equations required to describe the various possibilities while recognizing that not all the terms in the equations may be important everywhere. With regard to the classification itself, I believe its most useful function is to provide a guide for the selection of turbulence models and further refinements therein.

Turbulence Models My conclusions concerning the relative importance of Reynolds stresses in the wall and outer regions of thick boundary layers have been derived from an examination of the published and readily available data. I believe that much more careful analysis of such data is required before endorsing or rejecting specific turbulence models. Unfortunately, experimenters do not always report all the details in a form required for such an analysis. This became apparent at the 1980 AFOSR-HTTM-Stanford Conference, where an attempt was made to select experiments that could be used as test cases for computation methods. Also, computers very seldom make comparisons with detailed turbulence data, even when those are available, and thereby forego the opportunity to advance the state of the art in turbulence modeling. I shall look forward to a detailed examination of the new BSRA data introduced by Dr. Odabasi at the discussion when they are reported in the open literature in full.

Viscous-Inviscid Interaction I agree with the discussor's comments.

# A Streamline-Iteration Method for Calculating Turbulent Flow Around the Stern of a Body of Revolution and Its Wake

Zhou Lian-di  
China Ship Scientific Research Centre  
Wuxi, Jiangsu, China

## Abstract

This paper presents a new numerical method for calculating viscous flow around the stern of a body of revolution and its wake using a two-equation ( $K-\epsilon$ ) model developed by Harlow and Nakayama (1968) and modelled by Launder and Spalding (1972). The features of this method are: 1) The grid points calculated are taken on mean-flow streamlines and on radial straight lines, thus the convection terms of the governing equations for total pressure, turbulent kinetic energy and its dissipation can be written in the form of their variations along streamlines. For static pressure the radial pressure gradient equation is used. These equations are convenient for numerical calculations. The mean-flow streamlines, however, are not known beforehand and must be determined by an iterative scheme. 2) By means of a system of coordinate transformations, the calculating region is extended to infinity in both radial and axial direction. By doing so, the free-stream condition and the parabolic flow condition may be used at the outer and the downstream boundary respectively. The flow in the boundary layer and the potential flow outside the boundary layer can be determined by a uniform equation system. 3) Assumptions for a thin boundary layer and partially parabolic flow, etc., are exempted.

The velocity profiles, the variations of static pressure and turbulent properties calculated theoretically at some axial stations are compared with the experiments by Huang et al. (1978), the agreements being satisfactory. For the wake, the accuracy of the present method is higher than that of Muraoka's method (Muraoka, 1980a, 1980b).

## NOMENCLATURE

## Alphabet Symbols

$C_1, C_2, C_D$	; constants of the (K- $\epsilon$ ) turbulence model
$C_p$	; pressure coefficient $(p-p_\infty)/\frac{1}{2} \rho V_\infty^2$
$f$	; distribution profile of K
$g$	; distribution profile of $\ell_m$
$K$	; turbulent kinetic energy
$\ell$	; distance along spatial streamline
$\vec{\ell}^\circ$	; unit vector in spatial streamline direction
$\ell_m$	; mixing length
$L$	; length of a body of revolution
$m$	; meridional streamline, distance along meridional streamline
$p$	; static pressure (time-averaged)
$p_o$	; total pressure $p + \frac{1}{2} \rho V^2$
$p_\infty$	; free-stream static pressure
$q$	; arbitrary spatial curve, distance along an arbitrary spatial curve
$Q$	; mass rate of flow
$r, \theta, z$	; cylindrical polar coordinates
$r_o$	; local radius of a body of revolution
$r_{\max}$	; maximum radius of a body of revolution
$R_e$	; Reynolds number
$S$	; distance from the leading edge
$u, v, w$	; axial, radial and circumferential velocity components in a cylindrical polar coordinate system (time-averaged)

$V$	; velocity $\sqrt{u^2+v^2+w^2}$
$V_m$	; meridional velocity $\sqrt{u^2+v^2}$
$V_\infty$	; free-stream velocity
$z$	; axial coordinate

## Greek Symbols

$\alpha$	; angle made by meridional streamlines with the z-axis
$\delta, \delta_r$	; boundary layer thickness
$\epsilon$	; dissipation rate of turbulence energy
$\eta, \xi$	; coordinate transformations of $\gamma$ and $z$
$\mu_l, \mu_t, \mu_{eff}, \nu$	; coefficients of viscosity
$\rho$	; density
$\sigma_{eff}, \kappa, \sigma_{eff}, \epsilon$	; Prandtl/Schmidt number
$\tau$	; stress
$\psi$	; a general fluid variable
$\omega$	; relaxation factor used to modify the location of streamlines



# A STREAMLINE-ITERATION METHOD FOR CALCULATING TURBULENT FLOW AROUND THE STERN OF A BODY OF REVOLUTION AND ITS WAKE

Zhou Lian-di  
China Ship Scientific Research Centre  
Wuxi, Jiangsu, China

## 1. INTRODUCTION

Theoretical predictions of flow field around ship stern and its wake are among the most important problems in naval hydrodynamics. In order to reduce cavitation erosion, vibration excitation and noise due to propeller-hull interaction and to prepare guidelines for aft-end design of ships, it is considered necessary to predict the flow around ship stern and its wake. Many research workers are engaged in this work. Among the methods for calculating turbulent flow around ship stern, the numerical method adopting two-equation turbulence model ( $K-\epsilon$ ) and partially parabolic flow assumption is the most effective and popular one at present. As mentioned by Markatos and Wills (1980), however, there is a serious limitation in the above method, namely, the necessity of prescribing the locations of the outer and the downstream boundary and of determining boundary conditions at these boundaries by potential flow solution. As a result, additional calculations have to be carried out to determine boundary conditions, and the accuracy of computed results also deteriorates. In this paper, the external flow field extended to infinity in both radial and axial directions is transformed into an internal flow field within a finite region by means of a system of coordinate transformations. By doing so, the free-stream condition and the parabolic flow condition may be used at the outer (infinity in radial direction) and the downstream boundary (infinity in axial direction), respectively; and the boundary layer flow and the potential flow outside the boundary layer can be determined by an uniform equation system, thus evading this serious limitation. Further steps will be taken to generalize this method to be applied to the case of ship stern.

In this paper the streamline-iteration method, which has been widely employed for calculating internal flow field in turbine machine channels, is further generalized to the calculation of turbulent flow around the stern of a body of revolution and its wake using the popular two-equation turbulence model ( $K-\epsilon$ ) by following our previous works (Jian and Zhou 1981 and Yan et al., 1982). A curvilinear nonorthogonal coordinate system is employed. One set of coordinate lines

coincide with the mean-flow streamlines, the other set are made of radial straight lines. So the convection terms of the governing equations for total pressure, turbulent kinetic energy and its dissipation in turbulent flow can be written in the form of their variations along streamlines. For static pressure the radial pressure gradient equation is used. These equations are convenient for numerical calculations. The mean-flow streamlines, however, are not known beforehand and must be determined by an iterative scheme. First, assume the initial locations of the streamlines and the initial distributions of the fluid variables along streamline, then solve the governing equations to evaluate the new distributions and the new locations of the streamlines. Repeat the calculation procedure until convergence is obtained. On solving differential equations, assumptions for a thin boundary layer and partially parabolic flow, etc., are exempted.

Calculations have been carried out by using the present method for a body of revolution which is named Afterbody 1 by Huang et al. (1978). The calculated results agree with Huang's experiment satisfactorily. For the wake, the accuracy of the computed results by using the present method is higher than that of Muraoka's (1980a, 1980b).

## II. BASIC EQUATION

In calculating the three-dimensional incompressible turbulent flow by two-equation turbulence model ( $K-\epsilon$ ), the unknown variables are:

$u, v, w$  ; axial, radial and circumferential time-averaged velocities in a cylindrical polar coordinate system

$p$  ; time-averaged static pressure

$K, \epsilon$  ; turbulent kinetic energy and its dissipation rate

In a cylindrical polar coordinate system, the time-averaged velocity components and static pressure are governed by following equations:

Continuity equation:

$$\frac{\partial u}{\partial z} + \frac{1}{r} \frac{\partial}{\partial r} (rv) + \frac{1}{r} \frac{\partial w}{\partial \theta} = 0 \quad (1)$$

Axial momentum equation:

$$\frac{\partial}{\partial z} (uu) + \frac{1}{r} \frac{\partial}{\partial r} (ruv) + \frac{1}{r} \frac{\partial}{\partial \theta} (uw) = -\frac{1}{\rho} \frac{\partial p}{\partial z} + \frac{1}{\rho} \left\{ \frac{\partial}{\partial z} (\tau_{zz}) + \right.$$

$$+ \frac{1}{r} \left[ \frac{\partial}{\partial r} (r \tau_{rz}) + \frac{\partial}{\partial \theta} (\tau_{\theta z}) \right] \}^* \quad (2)$$

Radial momentum equation:

$$\frac{\partial}{\partial z} (vu) + \frac{1}{r} \frac{\partial}{\partial r} (rvv) + \frac{1}{r} \frac{\partial}{\partial \theta} (vw) - \frac{w^2}{r} = - \frac{1}{\rho} \frac{\partial p}{\partial r} + \frac{1}{\rho} \left\{ \frac{\partial}{\partial z} (\tau_{rz}) + \frac{1}{r} \left[ \frac{\partial}{\partial r} (r \tau_{rr}) + \frac{\partial}{\partial \theta} (\tau_{r\theta}) \right] - \frac{\tau_{\theta\theta}}{r} \right\} \quad (3)$$

Circumferential momentum equation:

$$\frac{\partial}{\partial z} (wu) + \frac{1}{r} \frac{\partial}{\partial r} (rwv) + \frac{1}{r} \frac{\partial}{\partial \theta} (ww) + \frac{vw}{r} = - \frac{1}{\rho r} \frac{\partial p}{\partial \theta} + \frac{1}{\rho} \left\{ \frac{\partial}{\partial z} (\tau_{\theta z}) + \frac{1}{r} \left[ \frac{\partial}{\partial r} (r \tau_{r\theta}) + \frac{\partial}{\partial \theta} (\tau_{\theta\theta}) \right] + \frac{\tau_{r\theta}}{r} \right\} \quad (4)$$

where  $\rho$  is the density;  $\tau$  denotes the stress, which can be represented by the velocity gradient and the effective viscosity varied in the flow field. Its tensor form can be written as

$$[\tau] = \mu_{\text{eff}} (\nabla \vec{V} + \nabla \vec{V}^T) \quad (5)$$

where

$$\nabla \vec{V} = \frac{\partial \vec{V}}{\partial r} \vec{e}_r + \frac{1}{r} \frac{\partial \vec{V}}{\partial \theta} \vec{e}_\theta + \frac{\partial \vec{V}}{\partial z} \vec{e}_z = \begin{pmatrix} \frac{\partial v}{\partial r} & \frac{\partial w}{\partial r} & \frac{\partial u}{\partial r} \\ \frac{1}{r} \frac{\partial v}{\partial \theta} - \frac{w}{r} & \frac{1}{r} \frac{\partial w}{\partial \theta} + \frac{v}{r} & \frac{1}{r} \frac{\partial u}{\partial \theta} \\ \frac{\partial v}{\partial z} & \frac{\partial w}{\partial z} & \frac{\partial u}{\partial z} \end{pmatrix} \quad (6)$$

The components of  $\tau$  are:

$$\left. \begin{aligned} \tau_{rr} &= \mu_{\text{eff}} \left( 2 \frac{\partial v}{\partial r} \right) \\ \tau_{\theta\theta} &= \mu_{\text{eff}} \left[ 2 \left( \frac{1}{r} \frac{\partial w}{\partial \theta} + \frac{v}{r} \right) \right] \\ \tau_{zz} &= \mu_{\text{eff}} \left( 2 \frac{\partial u}{\partial z} \right) \\ \tau_{r\theta} &= \tau_{\theta r} = \mu_{\text{eff}} \left( \frac{\partial w}{\partial r} - \frac{w}{r} + \frac{1}{r} \frac{\partial v}{\partial \theta} \right) \\ \tau_{z\theta} &= \tau_{\theta z} = \mu_{\text{eff}} \left( \frac{1}{r} \frac{\partial u}{\partial \theta} + \frac{\partial w}{\partial z} \right) \\ \tau_{zr} &= \tau_{rz} = \mu_{\text{eff}} \left( \frac{\partial u}{\partial r} + \frac{\partial v}{\partial z} \right) \end{aligned} \right\} \quad (7)$$

\* In the formulas of this section, the underlined terms were neglected in the approximate assumption of the Spalding's partially parabolic flow (see Abdelmeguid et al., 1978).

In expressions (5) and (7),  $\mu_{\text{eff}}$  is the effective viscosity and defined by

$$\mu_{\text{eff}} = \mu_l + \mu_t = \mu_l + C_D \rho \frac{K^2}{\epsilon} \quad (8)$$

where  $\mu_l$  and  $\mu_t$  are the laminar and turbulent viscosity respectively.

The governing equations for turbulent kinetic energy  $K$  and its dissipation rate are:

$K$  - equation:

$$\begin{aligned} \frac{\partial}{\partial z} (uK) + \frac{1}{r} \frac{\partial}{\partial r} (rvK) + \frac{1}{r} \frac{\partial}{\partial \theta} (wK) = \frac{1}{\rho} \left\{ \frac{1}{r} \frac{\partial}{\partial r} \left( r \frac{\mu_{\text{eff}}}{\sigma_{\text{eff},K}} \frac{\partial K}{\partial r} \right) + \right. \\ \left. + \frac{1}{r^2} \frac{\partial}{\partial \theta} \left( \frac{\mu_{\text{eff}}}{\sigma_{\text{eff},K}} \frac{\partial K}{\partial \theta} \right) + \frac{\partial}{\partial z} \left( \frac{\mu_{\text{eff}}}{\sigma_{\text{eff},K}} \frac{\partial K}{\partial z} \right) + GE - \rho \epsilon \right\} \quad (9) \end{aligned}$$

$\epsilon$  - equation:

$$\begin{aligned} \frac{\partial}{\partial z} (u\epsilon) + \frac{1}{r} \frac{\partial}{\partial r} (rv\epsilon) + \frac{1}{r} \frac{\partial}{\partial \theta} (w\epsilon) = \frac{1}{\rho} \left\{ \frac{1}{r} \frac{\partial}{\partial r} \left( r \frac{\mu_{\text{eff}}}{\sigma_{\text{eff},\epsilon}} \frac{\partial \epsilon}{\partial r} \right) + \right. \\ \left. + \frac{1}{r^2} \frac{\partial}{\partial \theta} \left( \frac{\mu_{\text{eff}}}{\sigma_{\text{eff},\epsilon}} \frac{\partial \epsilon}{\partial \theta} \right) + \frac{\partial}{\partial z} \left( \frac{\mu_{\text{eff}}}{\sigma_{\text{eff},\epsilon}} \frac{\partial \epsilon}{\partial z} \right) + C_1 GE \frac{\epsilon}{K} - C_2 \rho \frac{\epsilon^2}{K} \right\} \quad (10) \end{aligned}$$

where

$$\begin{aligned} GE = \mu_t \left\{ 2 \left[ \left( \frac{\partial u}{\partial z} \right)^2 + \left( \frac{\partial v}{\partial r} \right)^2 + \left( \frac{1}{r} \frac{\partial w}{\partial \theta} + \frac{v}{r} \right)^2 \right] + \left( \frac{\partial w}{\partial r} - \frac{w}{r} + \frac{1}{r} \frac{\partial v}{\partial \theta} \right)^2 + \right. \\ \left. + \left( \frac{\partial u}{\partial r} + \frac{\partial v}{\partial z} \right)^2 + \left( \frac{1}{r} \frac{\partial u}{\partial \theta} + \frac{\partial w}{\partial z} \right)^2 \right\} \quad (11) \end{aligned}$$

In these equations,  $\sigma_{\text{eff},K}$  and  $\sigma_{\text{eff},\epsilon}$  are Prandtl/Schmidt numbers;  $C_1$ ,  $C_2$  and  $C_D$  are proportionality constants. The values of  $C_1$ ,  $C_2$ ,  $C_D$ ,  $\sigma_{\text{eff},K}$  and  $\sigma_{\text{eff},\epsilon}$  are given in Table 1.

Table 1. VALUES FOR PRANDTL/SCHMIDT NUMBERS AND PROPORTIONALITY CONSTANTS

$C_1$	$C_2$	$C_D$	$\sigma_{\text{eff},K}$	$\sigma_{\text{eff},\epsilon}$
1.44	1.92	0.09	1	1.23

Equations (1) through (4), (9) and (10) may be used to obtain the six unknown variables  $u$ ,  $v$ ,  $w$ ,  $p$ ,  $K$  and so they are closure. However, as these equations form a coupled system of non-linear equations, it is very difficulty to solve them straightforwardly. Based upon the partially parabolic flow assumption, these equations were solved by using the marching integral technique in the works of Spalding's group.

This paper does not adopt the partially parabolic flow assumption and the streamline-iteration method is used to solve above equations. Owing to the fact that the grid points calculated are situated on the mean-flow streamlines, these equations can be rewritten in following simple forms.

Continuity equation: We employ its integral form

$$\iint_A \vec{V} \cdot d\vec{A} = Q_0 = \text{const} \quad (12)$$

where  $A$  is the area of any cross section in the channel;  $Q_0$  is the mass rate of flow prescribed beforehand.

Energy equation: Substitute expression (7) and equation (1) into equations (2) through (4), then

$$u \frac{\partial u}{\partial z} + v \frac{\partial u}{\partial r} + \frac{w}{r} \frac{\partial u}{\partial \theta} = -\frac{1}{\rho} \frac{\partial p}{\partial z} + \frac{\mu_{\text{eff}}}{\rho} \left( \frac{\partial^2 u}{\partial z^2} + \frac{\partial^2 u}{\partial r^2} + \frac{1}{r} \frac{\partial u}{\partial r} + \frac{1}{r^2} \frac{\partial^2 u}{\partial \theta^2} \right) + \frac{1}{\rho} \left( \frac{\partial \log \mu_{\text{eff}}}{\partial r} \tau_{zr} + \frac{1}{r} \frac{\partial \log \mu_{\text{eff}}}{\partial \theta} \tau_{z\theta} + \frac{\partial \log \mu_{\text{eff}}}{\partial z} \tau_{zz} \right) \quad (13)$$

$$u \frac{\partial v}{\partial z} + v \frac{\partial v}{\partial r} + \frac{w}{r} \frac{\partial v}{\partial \theta} - \frac{w^2}{r} = -\frac{1}{\rho} \frac{\partial p}{\partial r} + \frac{\mu_{\text{eff}}}{\rho} \left( \frac{\partial^2 v}{\partial z^2} + \frac{\partial^2 v}{\partial r^2} + \frac{1}{r} \frac{\partial v}{\partial r} + \frac{1}{r^2} \frac{\partial^2 v}{\partial \theta^2} - \frac{v}{r^2} - \frac{2}{r^2} \frac{\partial w}{\partial \theta} \right) + \frac{1}{\rho} \left( \frac{\partial \log \mu_{\text{eff}}}{\partial r} \tau_{rr} + \frac{1}{r} \frac{\partial \log \mu_{\text{eff}}}{\partial \theta} \tau_{r\theta} + \frac{\partial \log \mu_{\text{eff}}}{\partial z} \tau_{rz} \right) \quad (14)$$

$$u \frac{\partial w}{\partial z} + v \frac{\partial w}{\partial r} + \frac{w}{r} \frac{\partial w}{\partial \theta} + \frac{vw}{r} = -\frac{1}{\rho r} \frac{\partial p}{\partial \theta} + \frac{\mu_{\text{eff}}}{\rho} \left( \frac{\partial^2 w}{\partial z^2} + \frac{\partial^2 w}{\partial r^2} + \frac{1}{r} \frac{\partial w}{\partial r} + \frac{1}{r^2} \frac{\partial^2 w}{\partial \theta^2} + \frac{2}{r^2} \frac{\partial v}{\partial \theta} - \frac{w}{r^2} \right) + \frac{1}{\rho} \left( \frac{\partial \log \mu_{\text{eff}}}{\partial r} \tau_{\theta r} + \frac{1}{r} \frac{\partial \log \mu_{\text{eff}}}{\partial \theta} \tau_{\theta\theta} + \frac{\partial \log \mu_{\text{eff}}}{\partial z} \tau_{\theta z} \right) \quad (15)$$

Equations (13) through (15) can be grouped as

$$(\vec{V} \cdot \nabla) \vec{V} = -\frac{1}{\rho} \nabla p + \frac{\mu_{\text{eff}}}{\rho} \nabla^2 \vec{V} + \frac{1}{\rho} \nabla \log \mu_{\text{eff}} \cdot [\tau] \quad (16)$$

Substitute the formula of vector operation

$$(\vec{V} \cdot \nabla) \vec{V} = \nabla \left( \frac{V^2}{2} \right) - \vec{V} \times (\nabla \times \vec{V}) \quad (17)$$

into equation (16), then

$$\nabla \left( p + \frac{V^2}{2} \right) = \vec{V} \times (\nabla \times \vec{V}) + \frac{1}{\rho} \{ \mu_{\text{eff}} \nabla^2 \vec{V} + \nabla \log \mu_{\text{eff}} \cdot [\tau] \} \quad (18)$$

Now if total pressure  $p_0$

$$p_o = p + \frac{\rho}{2} v^2 \quad (19)$$

is introduced and the following relations are utilized

$$\begin{aligned} \vec{\ell}^o \cdot \nabla \left( \frac{p}{\rho} + \frac{v^2}{2} \right) &= \vec{\ell}^o \cdot \nabla \left( \frac{p_o}{\rho} \right) = \frac{1}{\rho} \frac{dp_o}{d\ell} \Big|_{\text{along streamline}} \\ \vec{\ell}^o \cdot \vec{V} \times (\nabla \times \vec{V}) &= 0 \end{aligned}$$

where  $\vec{\ell}^o$  is an unit vector in spatial flow direction, then following equation can be obtained from equation (18)

$$\frac{dp_o}{d\ell} \Big|_{\text{along streamline}} = \vec{\ell}^o \cdot \{ \mu_{\text{eff}} \nabla^2 \vec{V} + \nabla \log \mu_{\text{eff}} \cdot [\tau] \} \quad (20)$$

Equation (20), which is called the energy equation of the incompressible turbulent flow, denotes the change of total pressure of turbulent flow along the streamline. When  $\mu_{\text{eff}} = 0$ , i.e., the fluid is inviscid, equation (20) becomes  $dp_o/d\ell|_{\text{along streamline}} = 0$ . It means that total pressure remains constant along the streamline and becomes the well-known Bernoulli's equation for ideal fluid.

Pressure gradient equation: After shifting the terms, equation (16) can be rewritten as

$$\nabla p = -\rho(\vec{V} \cdot \nabla) \vec{V} + \mu_{\text{eff}} \nabla^2 \vec{V} + \nabla \log \mu_{\text{eff}} \cdot [\tau] \quad (21)$$

Pressure gradients have to satisfy the above equation, which is called the pressure gradient equation. For any spatial curve  $q$ , equation (21) can be written in the form of direction derivative along curve  $q$

$$\frac{dp}{dq} = \vec{q}^o \cdot \{ -\rho(\vec{V} \cdot \nabla) \vec{V} + \mu_{\text{eff}} \nabla^2 \vec{V} + \nabla \log \mu_{\text{eff}} \cdot [\tau] \} \quad (22)$$

where  $\vec{q}^o$  is an unit vector in the direction of curve  $q$ . Curve  $q$  can take three arbitrary linear independent directions. If we take the direction of the streamline to be one of the directions of curve  $q$ , then the energy equation (20) can be obtained from equation (22).

For equations (9) and (10), if we utilize equation (1) and following relation

$$\left( u \frac{\partial \psi}{\partial z} + v \frac{\partial \psi}{\partial r} + w \frac{\partial \psi}{\partial \theta} \right) \Big|_{\text{along streamline}} = \left( v \frac{d\psi}{d\ell} \right) \Big|_{\text{along streamline}} \quad (23)$$

then the left-hand side of equations (9) and (10) can also be rewritten as direction derivative along the streamline

$$\begin{aligned} v \frac{dK}{d\ell} \Big|_{\text{along streamline}} &= \frac{1}{\rho} \left\{ \frac{1}{r} \frac{\partial}{\partial r} \left( r \frac{\mu_{\text{eff}}}{\sigma_{\text{eff},K}} \frac{\partial K}{\partial r} \right) + \frac{1}{r^2} \frac{\partial}{\partial \theta} \left( \frac{\mu_{\text{eff}}}{\sigma_{\text{eff},K}} \frac{\partial K}{\partial \theta} \right) + \right. \\ &\quad \left. + \frac{\partial}{\partial z} \left( \frac{\mu_{\text{eff}}}{\sigma_{\text{eff},K}} \frac{\partial K}{\partial z} \right) + GE - \rho \epsilon \right\} \quad (24) \end{aligned}$$

$$\begin{aligned}
v \frac{d\epsilon}{d\ell} \Big|_{\text{along streamline}} &= \frac{1}{\rho} \left\{ \frac{1}{r} \frac{\partial}{\partial r} \left( r \frac{\mu_{\text{eff}}}{\sigma_{\text{eff},\epsilon}} \frac{\partial \epsilon}{\partial r} \right) + \frac{1}{r^2} \frac{\partial}{\partial \theta} \left( \frac{\mu_{\text{eff}}}{\sigma_{\text{eff},\epsilon}} \frac{\partial \epsilon}{\partial \theta} \right) + \right. \\
&\quad \left. + \frac{\partial}{\partial z} \left( \frac{\mu_{\text{eff}}}{\sigma_{\text{eff},\epsilon}} \frac{\partial \epsilon}{\partial z} \right) + C_1^{\text{GE}} \frac{\epsilon}{K} - C_2^{\rho} \frac{\epsilon^2}{K} \right\} \quad (25)
\end{aligned}$$

For the turbulent flow around the stern of a body of revolution and its wake which is discussed in this paper, the flow is axisymmetric. Then  $w = 0$ , and partial derivatives of all flow variables with respect to  $\theta$  must be equal to zero. The above basic equations can be further simplified and we can discuss the flow case only in a meridian plane. For the axisymmetric turbulent flow, the basic equations are:

Continuity equation:

$$\begin{aligned}
&r_1(z) \\
&\int_{r_0(z)}^{} \rho \cdot 2\pi r \, u dr = Q_0 = \text{const} \quad (26)
\end{aligned}$$

where  $r_0(z)$  and  $r_1(z)$  are the locations of the lower and the upper boundary of the channel in the meridian plane  $(z, r)$ .

Energy equation: Since

$$v \frac{d\psi}{d\ell} \Big|_{\text{along streamline}} = v_m \frac{d\psi}{dm} \Big|_{\text{along streamline}} = u \frac{d\psi}{dz} \Big|_{\text{along streamline}} \quad (27)$$

where  $v_m$  is the meridian velocity,  $d\psi/dm|_{\text{along streamline}}$  and  $d\psi/dz|_{\text{along streamline}}$  denote the direction derivatives of  $\psi$  with respect to the meridian streamline  $m$  and  $z$  along the spatial streamline respectively, the axisymmetric form of equation (20) can be written as

$$\begin{aligned}
\frac{dp_0}{dz} \Big|_{\text{along streamline}} &= \frac{1}{u} \left\{ \mu_{\text{eff}} \left[ u \left( \frac{\partial^2 u}{\partial z^2} + \frac{\partial^2 u}{\partial r^2} + \frac{1}{r} \frac{\partial u}{\partial r} \right) + v \left( \frac{\partial^2 v}{\partial z^2} + \frac{\partial^2 v}{\partial r^2} + \right. \right. \right. \\
&\quad \left. \left. + \frac{1}{r} \frac{\partial v}{\partial r} - \frac{v}{r^2} \right) \right] + u \left[ \frac{\partial \mu_{\text{eff}}}{\partial z} \left( 2 \frac{\partial u}{\partial z} \right) + \frac{\partial \mu_{\text{eff}}}{\partial r} \left( \frac{\partial u}{\partial r} + \right. \right. \\
&\quad \left. \left. + \frac{\partial v}{\partial z} \right) \right] + v \left[ \frac{\partial \mu_{\text{eff}}}{\partial z} \left( \frac{\partial u}{\partial r} + \frac{\partial v}{\partial z} \right) + \frac{\partial \mu_{\text{eff}}}{\partial r} \left( 2 \frac{\partial v}{\partial r} \right) \right] \right\} \quad (28)
\end{aligned}$$

Radial pressure gradient equation: For an axisymmetric flow, we may discuss the pressure gradient equation (22) only in the radial direction. Thus we have

$$\begin{aligned} \frac{dp}{dr} = & -\rho u \left. \frac{dv}{dz} \right|_{\text{along streamline}} + \mu_{\text{eff}} \left( \frac{\partial^2 v}{\partial z^2} + \frac{\partial^2 v}{\partial r^2} + \frac{1}{r} \frac{\partial v}{\partial r} - \frac{v}{r^2} \right) + \\ & + \frac{\partial \mu_{\text{eff}}}{\partial z} \left( \frac{\partial u}{\partial r} + \frac{\partial v}{\partial z} \right) + \frac{\partial \mu_{\text{eff}}}{\partial r} \left( 2 \left( \frac{\partial v}{\partial r} \right) \right) \end{aligned} \quad (29)$$

K-equation:

$$\left. \frac{dK}{dz} \right|_{\text{along streamline}} = \frac{1}{\rho u} \left[ \frac{1}{r} \frac{\partial}{\partial r} \left( r \frac{\mu_{\text{eff}}}{\sigma_{\text{eff},K}} \frac{\partial K}{\partial r} \right) + \frac{\partial}{\partial z} \left( \frac{\mu_{\text{eff}}}{\sigma_{\text{eff},K}} \frac{\partial K}{\partial z} \right) + GE - \rho \epsilon \right] \quad (30)$$

$\epsilon$ -equation:

$$\begin{aligned} \left. \frac{d\epsilon}{dz} \right|_{\text{along streamline}} = & \frac{1}{\rho u} \left[ \frac{1}{r} \frac{\partial}{\partial r} \left( r \frac{\mu_{\text{eff}}}{\sigma_{\text{eff},\epsilon}} \frac{\partial K}{\partial r} \right) + \frac{\partial}{\partial z} \left( \frac{\mu_{\text{eff}}}{\sigma_{\text{eff},\epsilon}} \frac{\partial K}{\partial z} \right) \right. \\ & \left. + C_1 GE \frac{\epsilon}{K} - C_2 \rho \frac{\epsilon^2}{K} \right] \end{aligned} \quad (31)$$

where

$$GE = \mu_t \left\{ 2 \left[ \left( \frac{v}{r} \right)^2 + \left( \frac{\partial v}{\partial r} \right)^2 + \left( \frac{\partial u}{\partial z} \right)^2 \right] + \left( \frac{\partial u}{\partial r} + \frac{\partial v}{\partial z} \right)^2 \right\} \quad (32)$$

For an axisymmetric turbulent flow, the unknown variables are  $u$ ,  $v$ ,  $p$ ,  $K$  and  $\epsilon$ . So equations (26), (28), (29), (30) and (31) are closure, and can be used to evaluate these unknown variables numerically.

### III. COORDINATE TRANSFORMATIONS OF THE FLOW REGION AND CALCULATIONS OF THE DERIVATIVES OF FLOW VARIABLES

The physical flow region of the turbulent flow around the stern of body of revolution and its wake extends to infinity both in the radial and the axial direction (see figure 1). It is impossible to perform finite difference calculation in this infinite region. In practical numerical calculations, it is a common practice to cut off the infinite region with finite boundaries (dotted lines in figure 1), resulting a region for performing numerical calculations. However, this practice arouses some difficulties: how to determine the locations and boundary conditions of the radial outer boundary and the axial downstream boundary rationally. Additional calculations have to be carried out to determine these boundary conditions (in Maraoka's works the locations of the boundaries were prescribed empirically and the potential flow solutions were taken as the boundary conditions) and the accuracy of computed results also deteriorates. In this paper, we adopt a technique which transforms the infinite flow region into a finite region with a set of coordinate transformations. As a result,



the free-stream condition and the parabolic flow condition can be employed at the outer and the downstream boundary respectively. Coordinate transformations are realized by using following expressions

$$\left. \begin{aligned} \eta &= 1 - e^{-\frac{r}{C_r}} \\ \xi &= \frac{2}{\pi} \operatorname{arctg} \left( \frac{z}{C_z} \right) \end{aligned} \right\} \quad (33)$$

where  $C_r$  and  $C_z$  are radial and axial characteristic lengths.  $C_r$  is taken as the sum of the radius and the boundary layer thickness at the inlet station, and  $C_z$  is taken as the length of the stern. From expression (33), it is obvious that for  $\eta = 0.1$ ,  $r = 0, \infty$  and for  $\xi = 0, 0.5, 1$ ,  $z = 0, C_z, \infty$ , thereby, equations (26) and (28) through (32) can be solved in the transformed flow region in the coordinate system  $(\eta, \xi)$ , see figure 2. In this paper, the intersecting of the straight-lines in  $\eta$ -direction (corresponding the radial straight-lines in physical meridian plane) and the transformed meridian streamlines are taken as the grid points. At these grid points, the partial derivatives of flow variables with respect to  $r$  and  $z$  and the direction derivatives appeared in equations (28) through (31) can not be evaluated straightforwardly. Some operations must be made.

Let  $\psi$  denote a certain flow variable. The first and second derivatives of  $\psi$  with respect to  $\xi$  and  $\eta$  along the streamlines and the station-lines (straight-lines in  $\eta$ -direction),  $d\psi/d\xi$ ,  $d^2\psi/d\xi^2$ ,  $d\psi/d\eta$ ,  $d^2\psi/d\eta^2$  can be obtained by numerical differential method with the non-equidistant three point difference format (Jian, 1981). Then, by the derivation rule for compound functions, the direction derivatives of  $\psi$  can be obtained in the following form

$$\left. \begin{aligned} \frac{d\psi}{dr} \Big|_{\text{along station-line}} &= \frac{d\psi}{d\eta} \frac{(1-\eta)}{C_r} \\ \frac{d^2\psi}{dr^2} \Big|_{\text{along station-line}} &= \frac{d^2\psi}{d\eta^2} \left( \frac{1-\eta}{C_r} \right)^2 - \frac{d\psi}{d\eta} \left( \frac{1-\eta}{C_r} \right) \cdot \frac{1}{C_r} \\ \frac{d\psi}{dz} \Big|_{\text{along streamline}} &= \frac{d\psi}{d\xi} \cdot \frac{2}{\pi} \frac{1}{C_z} \cos^2 \left( \frac{\pi}{2} \xi \right) \\ \frac{d^2\psi}{dz^2} \Big|_{\text{along streamline}} &= \left[ \frac{2}{\pi} \frac{1}{C_z} \cos^2 \left( \frac{\pi}{2} \xi \right) \right]^2 \left[ \frac{d^2\psi}{d\xi^2} - \pi \frac{d\psi}{d\xi} \operatorname{tg} \left( \frac{\pi}{2} \xi \right) \right] \end{aligned} \right\} \quad (34)$$

In order to obtain the partial derivatives of flow variables with respect to  $r$  and  $z$  appeared in equations (28) through (31) the derivative properties and the meridian flow angle  $\alpha$  in physical meridian plane must be utilized. From figure 3, it is easy to obtain

$$\left. \begin{aligned} \frac{d\psi}{dz} \Big|_{\text{along streamline}} &= \frac{\partial\psi}{\partial r} \operatorname{tg} \alpha + \frac{\partial\psi}{\partial z} \\ \frac{d\psi}{dr} \Big|_{\text{along station-line}} &= \frac{\partial\psi}{\partial r} \end{aligned} \right\} \quad (35)$$

Thus, we have

$$\left. \begin{aligned} \frac{\partial\psi}{\partial r} &= \frac{d\psi}{dr} \Big|_{\text{along station-line}} \\ \frac{\partial\psi}{\partial z} &= \frac{d\psi}{dz} \Big|_{\text{along streamline}} - \frac{\partial\psi}{\partial r} \operatorname{tg} \alpha \end{aligned} \right\} \quad (36)$$

Perform the derivation operation once again on expression (35), we obtain

$$\frac{\partial^2\psi}{\partial r^2} = \frac{d^2\psi}{dr^2} \Big|_{\text{along station-line}} \quad (37)$$

$$\frac{\partial^2\psi}{\partial z^2} = \frac{d^2\psi}{dz^2} \Big|_{\text{along streamline}} - \frac{\partial^2\psi}{\partial r^2} \operatorname{tg}^2 \alpha - 2 \frac{\partial^2\psi}{\partial z \partial r} \operatorname{tg} \alpha - \frac{\partial\psi}{\partial r} \frac{d^2r}{dz^2} \Big|_{\text{along streamline}} \quad (38)$$

On the right-hand side of expression (38),  $\partial^2\psi/\partial z \partial r$  and  $d^2r/dz^2|_{\text{along streamline}}$  are still unsolved. With the obtained  $\partial\psi/\partial r$  and  $\partial^2\psi/\partial r^2$ ,  $\partial^2\psi/\partial z \partial r$  can be derived from the following expression

$$\frac{\partial^2\psi}{\partial z \partial r} = \frac{\partial}{\partial z} \left( \frac{\partial\psi}{\partial r} \right) = \frac{d}{dz} \left( \frac{\partial\psi}{\partial r} \right) \Big|_{\text{along streamline}} - \frac{\partial^2\psi}{\partial r^2} \operatorname{tg} \alpha \quad (39)$$

We can first obtain  $d/d\xi(\partial\psi/\partial r)|_{\text{along streamline}}$  by numerical differentiation of  $\partial\psi/\partial r$ , and then use the third equation of (34) to calculate  $d/dz(\partial\psi/\partial r)|_{\text{along streamline}}$  appeared on the righthand side of (39).  $d^2r/dz^2|_{\text{along streamline}}$  in (38) can be obtained by derivation of compound functions, employing the coordinates  $\eta, \xi$  of the grid points in the transformed meridian plane.

$$\frac{d^2r}{dz^2} \Big|_{\text{along stream line}} = \left[ \frac{2}{\pi} \frac{1}{C_z} \cos^2 \left( \frac{\pi}{2} \xi \right) \right]^2 \left\{ \left( \frac{d^2\eta}{d\xi^2} - \pi \frac{d\eta}{d\xi} \operatorname{tg} \left( \frac{\pi}{2} \xi \right) \right) \frac{C_r}{1-\eta} + \left( \frac{d\eta}{d\xi} \right)^2 \left( \frac{C_r}{1-\eta} \right)^2 \cdot \frac{1}{C_r} \right\} \quad (40)$$

Thus, being given the coordinates  $\eta, \xi$  of the grid points and flow variable  $\psi$  on these points, we may evaluate its direction derivatives and partial derivatives.

#### IV. BOUNDARY CONDITIONS

In order to solve the flow variables  $u, v, p, K$  and  $\epsilon$  from equations (26) and (28) through (31), it is necessary to determine the boundary conditions at each boundary of the flow region. They are defined as follows:

(1) Wall Surface

$$u = v = K = \epsilon = 0$$

(2) Wake Centreline

$$v=0 ; \quad \frac{\partial u}{\partial r} = \frac{\partial v}{\partial r} = \frac{\partial K}{\partial r} = \frac{\partial \epsilon}{\partial r} = \frac{\partial p}{\partial r} = 0$$

(3) Outer Boundary (infinity in the radial direction)

$$u=u_{\infty}, v=0 ; \quad p=p_{\infty} ; \quad \frac{\partial K}{\partial r} = \frac{\partial \epsilon}{\partial r} = 0$$

where  $v$  and  $p$  are free-stream velocity and static pressure respectively.

(4) Inlet Boundary

The inlet boundary may be located at about 75% of the length of a body of revolution, where thin boundary layer assumption is valid in general. Thus, the boundary layer thickness can be calculated either by the thin boundary layer theory or by Schlichting's formula for flat plate

$$\delta = 0.37 S \left( \frac{v_{\infty} S}{\nu} \right)^{-1/5} \quad (41)$$

where  $\nu$  is kinematic viscosity;  $S$  is the distance from the leading edge. The velocity components  $u$  and  $v$  are as follows

$$u = \begin{cases} v_{\infty} \left[ \frac{(r-r_0)}{\delta} \right]^{1/7} & r-r_0 \leq \delta \\ v_{\infty} & r-r_0 > \delta \end{cases} \quad (42)$$

$$v = 0$$

For static pressure  $p$ , either radial uniform distribution and  $p = p_{\infty}$  or uniform distribution within and linear variation outside

the boundary layer are assumed.

In order to predict turbulent properties in the flow region precisely, Muraoka improved the inlet conditions for  $K$  and  $\epsilon$  (Muraoka, 1980a). For  $K$ , this paper adopts his proposal, i.e.,

$$K = \begin{cases} f(r-r_0) \cdot V_\infty^2 & r-r_0 \leq \delta \\ \approx 0 & r-r_0 > \delta \end{cases}$$

where  $f(r-r_0)$  is determined from the experiment data of Klabanoff for flat plate (e.g., Rotta, 1972). For the mixing length  $\ell_m$ , we adopt the approximation proposed by Huang et al. (1978).

$$\ell_m = \ell_{mo} \cdot \frac{\sqrt{(r_0 + \delta)^2 - r_0^2}}{3.33\delta} \quad (43)$$

where  $\ell_{mo}$  is determined from the value of  $g(r-r_0)$  which Bradshaw et al., have given for thin boundary layer (Bradshaw et al, 1967)

$$\ell_{mo} = \begin{cases} g(r-r_0) & r-r_0 \leq 1.2 \delta \\ g(1.2 \delta) & r-r_0 > 1.2 \delta \end{cases}$$

The value of  $\epsilon$  is determined from the mixing length as follows

$$\epsilon = C_D^{3/4} \cdot K^{3/2} / \ell_m \quad (44)$$

(5) Exit Boundary (infinity in the axial direction)  
The parabolic flow conditions are used, i.e.,

$$\frac{\partial u}{\partial z} = \frac{\partial v}{\partial z} = \frac{\partial K}{\partial z} = \frac{\partial \epsilon}{\partial z} = 0 ; \quad \frac{\partial^2 u}{\partial z^2} = \frac{\partial^2 v}{\partial z^2} = \frac{\partial^2 K}{\partial z^2} = \frac{\partial^2 \epsilon}{\partial z^2} = 0$$

## V. CALCULATION PROCEDURE

As mentioned above, the present calculation method has to adopt an iterative scheme. The sequence of calculation steps is as follows:

- (1) Assumptions of the initial locations of the streamlines and of the initial distributions for  $u$ ,  $K$  and  $\epsilon$ .

The calculation is performed in the transformed flow region which is in the  $\xi$ - $\eta$  plane. Between interval  $[0,1]$  several straight-lines in  $\eta$ -direction are taken as calculating station-lines. According to a prescribed distribution principle of the mass rate of flow along

the station-line, the locations of streamlines at the inlet station can be determined from the known radial distribution of  $u$  at the same station by formula (26). Then, keeping the ratios of distances between streamlines at other stations to be the same as at the inlet station, the locations of corresponding streamlines at other stations can be assessed. Join the corresponding points for same streamlines at all stations with smooth curves, the initial calculating grid is formed by the intersecting points of station-lines and streamlines. For other stations, the initial radial distribution for  $u$ ,  $K$  and  $\epsilon$  on this grid are assumed to be the same as at the inlet station.

- (2) Calculations of the meridian flow angle and of the distribution for  $v$ .

According to its definition, the meridian flow angle  $\alpha$  can be obtained by derivation of compound functions

$$\operatorname{tg} \alpha = \left. \frac{dr}{dz} \right|_{\text{along streamline}} = \left. \frac{d\eta}{d\xi} \right|_{\text{along streamline}} \cdot \frac{2}{\pi} \frac{1}{C_z} \cos^2\left(\frac{\pi}{2} \xi\right) \cdot \frac{C_r}{1-\eta} \quad (45)$$

where  $d\eta/d\xi|_{\text{along streamline}}$  is calculated from the coordinates  $(\xi, \eta)$  of grid points by numerical differentiation method. Then,  $v$  can be obtained from

$$v = u \cdot \operatorname{tg} \alpha \quad (46)$$

- (3) Calculations of new distributions for  $K$ ,  $\epsilon$  and  $\mu_{\text{eff}}$ .

For each streamline (except on the wall surface and the wake centreline), equations (30) and (31) can be solved simultaneously to obtain the new values of  $K$  and  $\epsilon$  at the grid points on this streamline. Firstly, the terms appeared on the right-hand sides of equations (30) and (31) are calculated with the distributions for  $u$ ,  $K$  and  $\epsilon$  in previous iteration and the distribution for  $v$  in present iteration. Secondly, take the known values of  $K$  and  $\epsilon$  at the inlet station as the initial values of the integral, and solve equations (30) and (31) by marching integration along this streamline from upstream to downstream. The above calculation procedure is repeated for all the streamlines in the flow field. For wall surface and wake centreline,  $K$  and  $\epsilon$  can be obtained with conditions  $K = \epsilon = 0$  and  $\partial K / \partial r = \partial \epsilon / \partial r = 0$  respectively. Thus, new distributions for  $K$  and  $\epsilon$  are obtained. New distribution for  $\mu_{\text{eff}}$  is calculated from formula (8).

- (4) Calculation of the distribution for static pressure  $p$ .

Solve equation (29) for each station-line to obtain the distribution for  $p$ . On the right-hand side of this equation, the distribution for  $u$  should take values of the previous iteration and the distributions for  $v$  and  $\mu_{\text{eff}}$  should take the calculated results at steps (2) and (3) in present iteration. Those terms being known, equation (29) can be solved by ordinary numerical integration. The

interval of integration is from  $\eta = 1$  to the wall surface or to the wake centreline and the integral constant may take boundary condition  $p = p_0$  as its value.

(5) Calculation of the distribution for total pressure  $p_0$ .

For each streamline (except on the wall surface and the wake centreline), the energy equation (28) can be solved in the same way as in step (4). Here, all the terms on the right-hand side of equation (28) are known, so  $p_0$  can be evaluated by ordinary numerical integration. The integral constant may take the value of  $p_0$  at the inlet station on the corresponding streamline,  $p_0$  being calculated by expression (19) using the given radial distributions for  $u$ ,  $v$  and  $p$  at the inlet station.

For wall surface, the wall surface condition  $p_0 = p$  (i.e.,  $u=v=0$ ) is used directly. For wake centreline, the axisymmetric condition  $\partial u/\partial r = 0$  utilized to obtain the value of  $u$ , then  $p_0$  can be calculated by expression (19) using the obtained  $u$  and  $p$  and the axisymmetric condition  $v=0$ .

(6) Calculation of the new distribution for  $u$ ,  $p_0$ ,  $p$  and  $\tan \alpha$  being solved,  $V$  and  $u$  can be obtained as follows

$$v = \sqrt{\frac{2(p_0 - p)}{\rho}} \quad (47)$$

$$u = \frac{V}{\sqrt{1 + \tan^2 \alpha}} \quad (48)$$

(7) Calculation of the new locations of the streamlines.

From the obtained new distribution for  $u$ , the mass rates of flow at each station-line can be calculated by the formula (26). According to the prescribed distribution principle of the mass rate of flow along the station-line, the new locations of the streamlines on station-line,  $\eta_{cal}$ , can be obtained by inversive interpolation of the mass rate of flow. With a relaxation factor which is less than 1, the assumed new locations of the streamlines,  $\eta_{new}$ , can be obtained as follows. Re-

$$\eta_{new} = \eta_{old} + \omega(\eta_{cal} - \eta_{old}) \quad (49)$$

Repeating steps (2) through (7) until the maximum deviation between the locations of the streamlines in two successive iteration calculations is within prescribed accuracy. Then, these distributions for  $u$ ,  $v$ ,  $p$ ,  $K$  and  $\epsilon$  and the locations of streamlines are the final results for problem.

## VI. NUMERICAL RESULTS

Numerical calculations are carried out for a body of revolution which is named Afterbody 1 by Huang et al. (1978). The principal particulars of this body are given in table 2, and the afterbody configuration is shown in figure 1. Numerical calculations are executed

Table 2. PRINCIPAL PARTICULARS OF AFTERBODY 1

$L(m)$	$r_{\max}(m)$	$R_e$
3.066	0.1397	$6.6 \times 10^6$

in the transformed flow region which is in the  $(\xi-\eta)$  plane. The calculating inlet and exit station are placed at  $\xi = 0.4131$  ( $z/L = 0.7553$ ) and  $\xi = 0.9425$  ( $z/L = 11$ ) respectively. The number of the station-lines is 20 along  $\xi$ -direction and the number of the streamlines is 25 along  $\eta$ -direction. Station-lines are spaced more closely near the stern and so are the streamlines near the wall surface and the outer boundary (at  $\eta = 1$ ), see figure 2. The calculated results are shown in figure 1 to figure 6. The calculated mean-flow streamlines in the physical and the transformed flow region are shown in figure 1 and figure 2 respectively. From figure 1 it can be seen that in the region of  $z/L = 0.90$  the mean-flow streamlines are convex in shape and almost parallel to the surface of the body, and the boundary layer is thin. But in the region of the last 10% of the body length the mean-flow streamlines are concave in shape and divergent outwardly and the boundary layer becomes thick. This conclusion is consistent with that obtained by Huang et al. (1978) and Patel et al. (1974) from experiments.

Comparison of calculated and measured velocity components,  $u/V_\infty$  and  $-v/V_\infty$  is shown in figure 4 and comparison of pressure coefficient  $C_p$  is shown in figure 5. It can be seen that the calculated results by the present method have the same high accuracy as Muraoka's numerical results (Muraoka, 1980b) both being in fair agreement with experiments. The calculated axial velocity profile at  $z/L = 1.057$  by the present method is in better agreement with experiments than Muraoka's.

For turbulent properties, i.e., turbulent kinetic energy  $K$  and mixing length  $\ell_m$ , no comparison of calculated and measured results has been given in all the existent papers except Muraoka's (1980a). Muraoka improved the inlet conditions for  $K$  and  $\epsilon$  and compared calculated and measured results for the first time. The agreement was satisfactory in general, but the accuracy of calculation became worse as  $z/L$  increased. In figure 6 of the present paper, calculated results by the present method are compared with measured turbulent

properties by Huang et al. (1978). The agreement between them is satisfactory and the accuracy of calculation at  $z/L=1.057$  is better than Muraoka's.

The calculating exit boundary in Muraoka's calculation was located at  $z/L=1.182$  (Muraoka, 1980b). As the accuracy of his calculation became worse, thereby no comparison of calculated and measured results at  $z/L=1.182$  was given, though Huang et al., presented measured results at this station. This paper presents comparisons of calculated and measured results for velocity components, static pressure coefficient and turbulent properties at  $z/L=1.183$ , the agreement being satisfactory.

## VII. CONCLUDING REMARKS

From the calculated example in the previous section, it may be concluded that:

(1) Based upon the two-equation turbulence model ( $K-\epsilon$ ), the streamline-iteration method presented in this paper is effective for the theoretical prediction of the turbulent flow around the stern of a body of revolution and its wake on condition that no separation and recirculating flow are present. The agreement between measured and calculated results is encouraging.

(2) The coordinate transformation given in this paper can transform the external flow problem which is extended to infinity both in the radial and the axial direction into an internal flow problem in a finite region. Extending the calculating region to infinity in the radial direction, permits us to take the free-stream condition as the boundary condition at the outer boundary and the viscous flow in the boundary layer and the potential flow outside of that can be solved by an uniform equation system. The serious limitation in the existent differential method, namely the locations of the outer and the downstream boundary were empirically prescribed and the potential flow solution was taken as the boundary conditions at these boundaries, can be evaded. By extending the calculating region to infinity in the axial direction, not only the parabolic flow condition can be taken as the boundary condition at the exit boundary, but also the accuracy of calculation in wake can be improved.

Works will be continued to extend the present streamline-iteration method to calculations of three-dimensional turbulent flow around ship stern and of the turbulent flow around the stern of a body of revolution and its wake with propeller in operation.



## ACKNOWLEDGMENTS

Before closing this paper, the author wishes to express his heartfelt thanks to Professor Gu Mao-Xiang and Senior Engineer, Liu Xin of China Ship Scientific Research Centre for their advice and encouragements. The author is also grateful to Engineer. Wang Xi-liang of C.S.S.R.C. and to Lecturer. Jinang Jin-liang of Fudan University for their help during the preparation of this paper.

## References

- Abdelmeguid, A. M., N. C. G. Markatos, D. B. Spalding, and K. Muraoka (1978). A method of predicting three-dimensional turbulent flows around ship's hulls, Int. Symp. on Ship Viscous Resistance, SSPA, Goteborg.
- Bradshaw, P., D. H. Ferris, and N. P. Atwell (1967). Calculation of boundary-layer development using the turbulent equation, J. Fluid Mech. 20, p. 257.
- Harlow, F. H., and P. I. Nakayama (1968). Transport of turbulence energy decay rate, Los Alamos Sci. Lab., Univ. California, Rep. LA-3854.
- Huang, T. T., N. Santelli, and G. Belt (1978). Stern boundary-layer flow an axisymmetric bodies, 12th Symposium on Naval Hydrodynamic, Washington, D. C.
- Jian Jin-ling (1981). The method of streamline-iteration for calculating the two-dimensional viscous flow, Shanghai Mechanics 2, No. 1.
- Jian Jin-ling, and Zhou Lian-di (1981). Use streamline-iteration method to calculate viscous flow problems containing both internal and external flow field, Shanghai Mechanics, 2, No. 3, p. 30.
- Launder, B. E., and D. B. Spalding (1972). Mathematical Models of Turbulence, Academic Press, London and New York.
- Markatos, N. C., and C. B. Wills (1980). Prediction of viscous flow around a fully submerged appended body, 13th Symposium on Naval Hydrodynamic, Tokyo.
- Muraoks, K. (1979). Calculation of viscous flow around ship ship stern, Transaction of the West-Japan Society of Naval Architects, No. 58, p. 235.
- Muraoka, K. (1980a). Examination of a 2-equation model of turbulence for calculating the viscous flow around ships, Journal of the Society of Naval Architects of Japan, 147, p. 35.
- Muraoka, K. (1980b). Calculation of thick boundary layer and wake of ships by a partially parabolic method, 13th Symposium on Naval Hydrodynamics, Tokyo.
- Patel, V. C., A. Nakayama, and R. Damian (1974). Measurements in the thick axisymmetric turbulent boundary layer near the tail of a body of revolution, J. Fluid Mechanics 63, Part 2, p. 345.
- Rotta, Von. J. C. (1972). Turbulence Stromungen, B. G. Teuber.
- Yuan Jia-le, Zhou Lian-di, and Jian Jin-liang (1982). A streamline-iteration for calculating the viscous flow around a axisymmetric body, Shanghai Lixue 3, No. 1, p. 57.

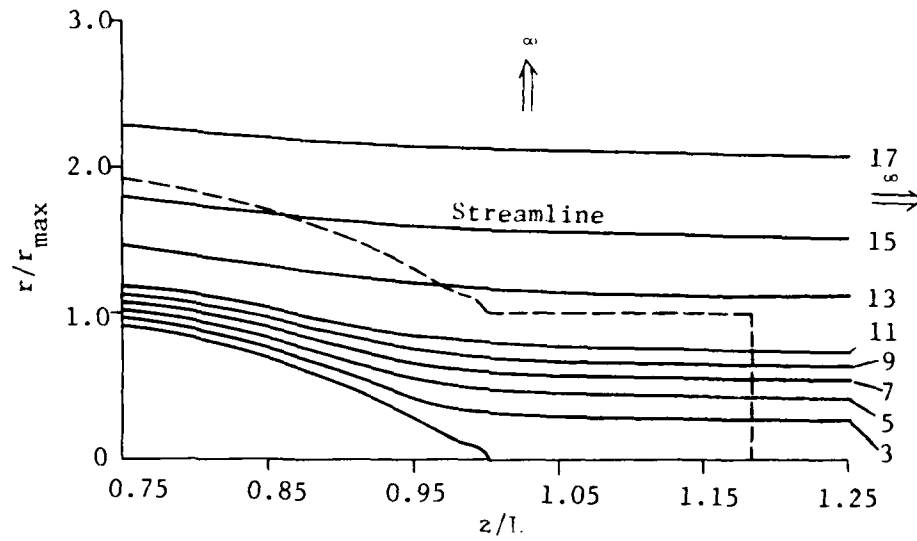


Figure 1. Afterbody Configuration and Calculated Streamlines for Afterbody 1

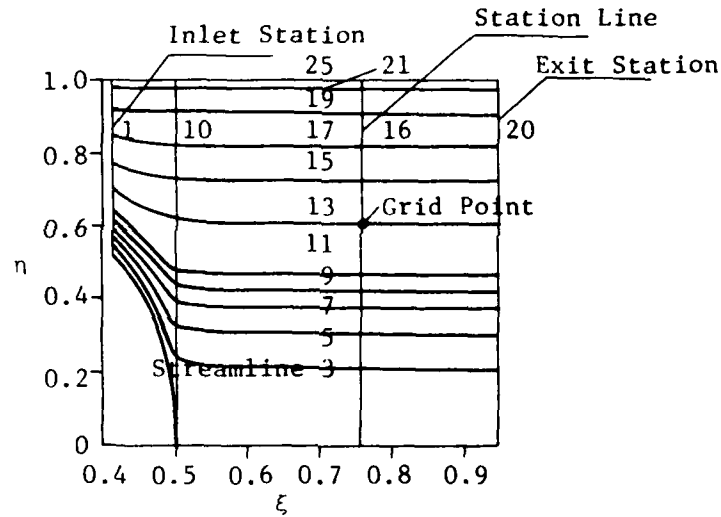


Figure 2. Transformed Flow Region and Calculated Streamlines for Afterbody 1

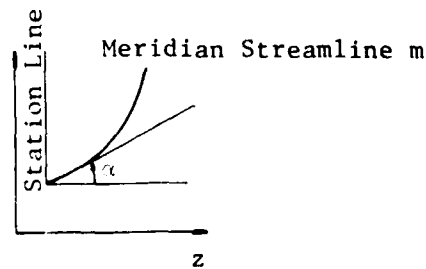


Figure 3. Meridian Flow Angle

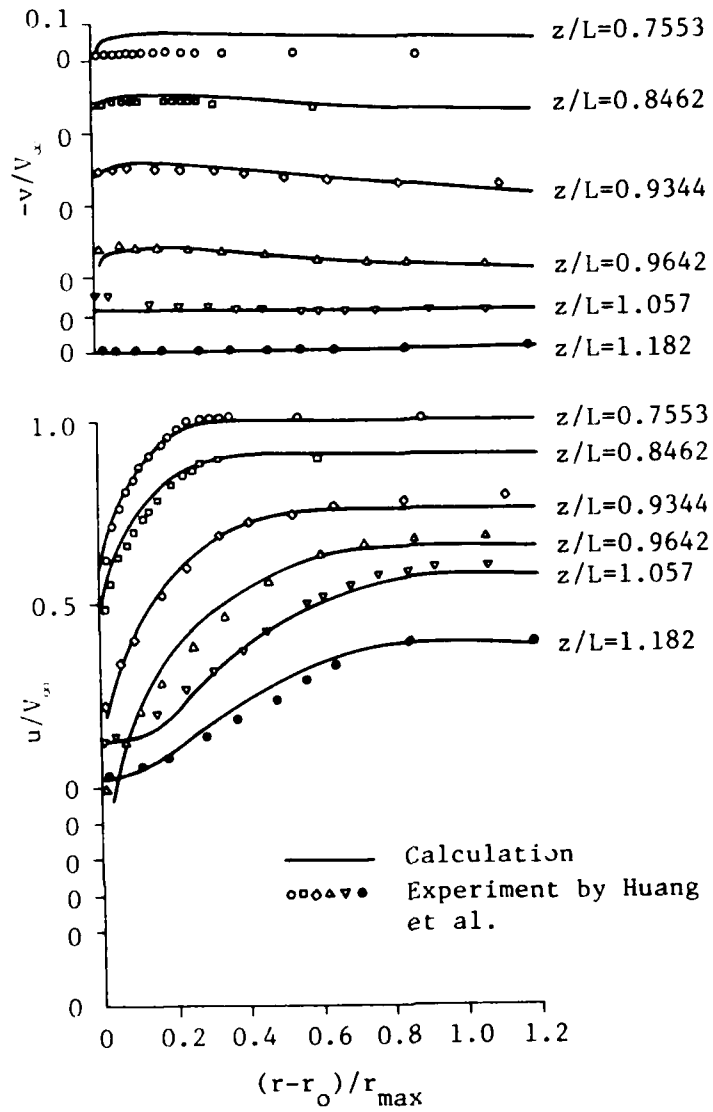


Figure 4. Comparison of Velocity Components  $u/V_\infty$  and  $-v/V_\infty$  for Afterbody 1

AD-A158 920

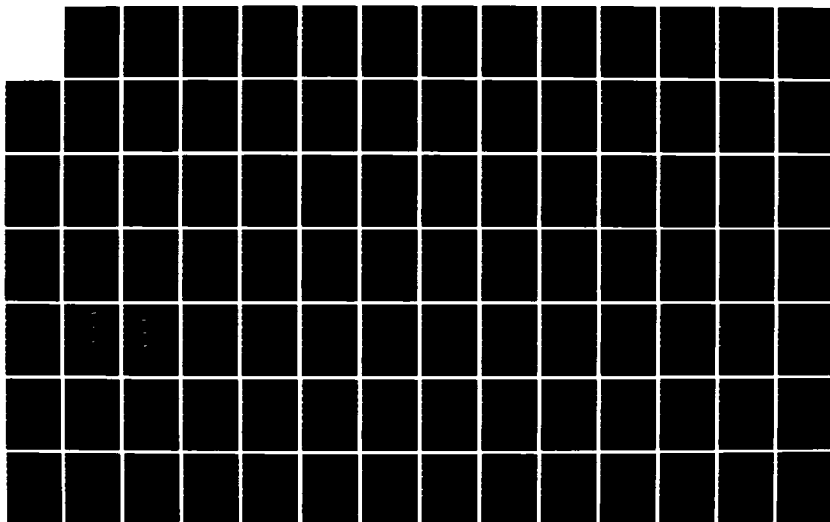
SYMPOSIUM OF NAVAL HYDRODYNAMICS (14TH) HELD AT ANN  
ARBOR MICHIGAN ON AUGUST 23-27 1982(U) OFFICE OF NAVAL  
RESEARCH ARLINGTON VA M P TULIN ET AL. 1982

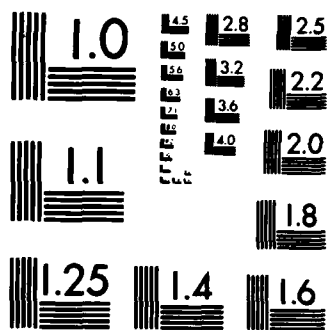
12/13

UNCLASSIFIED

F/G 20/4

NL





MICROCOPY RESOLUTION TEST CHART  
NATIONAL BUREAU OF STANDARDS-1963-A

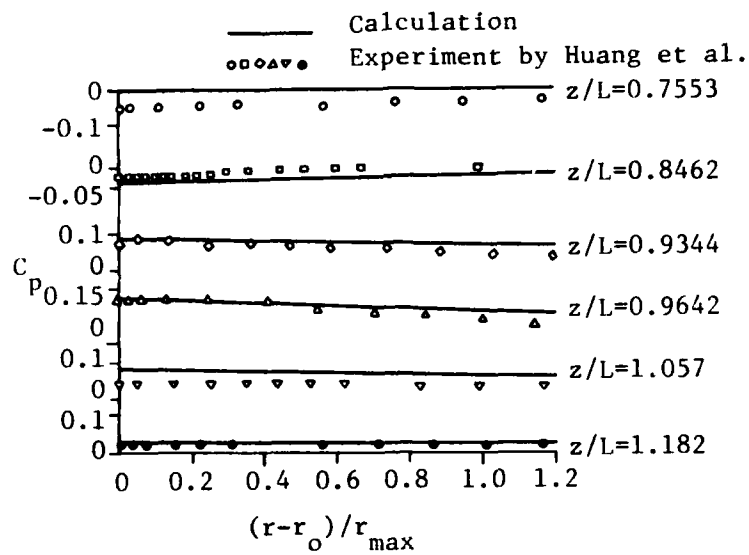


Figure 5. Comparison of Pressure Variations in the Flow Around Afterbody 1

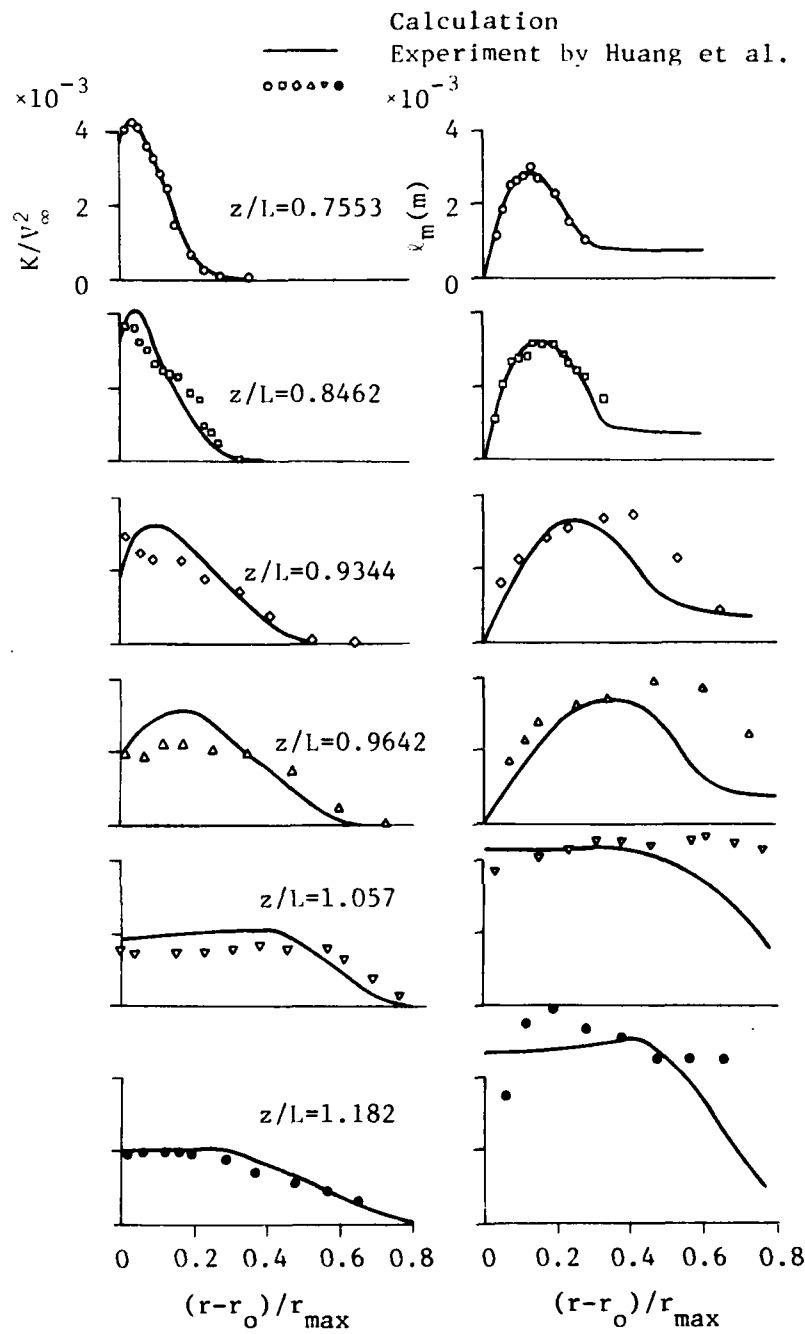


Figure 6. Comparison of Turbulent Properties for Afterbody 1



## Discussion

A.Y. Odabasi (British Ship Research Association)

The author makes a fine effort to make the K-E turbulence model of Launder and Spalding (1972) applicable to the calculation of stern and near-wake flow of ships. I fully agree with the use of a turbulent kinetic energy (K) and a dissipation rate (E) transport equations for modeling of turbulence, since both of these quantities are measurable and have physical meaning. The problem, however, is the use of the rather dramatic assumption of isotropic eddy viscosity, which unfortunately cannot be justified by experimental evidence. His Figures 7 and 8 display eddy viscosity distributions obtained from measured data in a wind tunnel, resolved into its streamwise and cross-flow components. The clear dissimilarity in streamwise and cross-flow direction is the proof of anisotropy. Under the flow conditions of small cross-flow this anisotropy may not be important and by small adjustment of certain terms and constants the results may agree with data. However, when the cross-flow becomes larger, the influence of isotropy becomes more pronounced, leading to substantial disagreements with the data. His Figure 9 displays a comparison of measured and computed velocity profiles (on top) by use of the K-L (L being the dissipation length scale) model with Bradshaw's turbulence modeling where the qualitative agreement is quite good and the quantitative differences may not be important for, at least, certain applications. In the same figure, results of three methods are compared with experimental data at three locations where computation of each method was performed by the association stated in the figure. This comparison clearly demonstrates that the K-E model with its partially parabolic application performs very badly owing to the isotropic eddy viscosity assumption, and only the BSRA model indicates the presence of flow retardation. While accepting that the method adopted by us may also need further improvements, the K-E model requires a complete rethinking on how the shear stresses are related to the turbulent kinetic energy.

T.F. Hogan (DTNSRDC)

The variable transformation of  $(z, r)$  to  $(\xi, \eta)$  together with integrating the equations along the streamlines is an interesting idea. Similar methods have been used by Patankar and Spalding (1967) and Markatos and Wells (1980) in connection with parabolic and partially parabolic flows. There are several key points of the present numerical technique that are not clear and I wish you could address. First, concerning the overall numerical iteration scheme, is the position of the streamlines first obtained for the entire domain, then is u ob-

tained for the entire field from equation (26), then  $V$ ,  $k$ - $\epsilon$ ,  $p$ ,  $p_0$ , and finally  $u$ ,  $v$ , and the new positions of the streamlines? That is, is each equation individually integrated over the entire domain separately? Or alternatively, given the upstream flow conditions at a particular station, is each equation integrated at the next downstream station and after this is done then the procedure is marched downstream to the next station?

Second, the system of equations are fully elliptic and, indeed, if we set the turbulent viscosity  $C_D k^2/\epsilon$  equal to zero, they are the exact Navier-Stokes equations. Does the elliptic nature of the flow with full upstream and downstream influences lead to any problems? Indeed, it would seem that a poor initial guess of any flow variable can lead to numerical instability especially when calculating the second derivative with respect to any flow variable that requires downstream information. In part (7) of the Calculation Procedure section a relaxation factor of less than 1 was mentioned. What does this apply to, and is it important in controlling the stability of the procedure? Also solving elliptic problems requires a considerably larger amount of computer time over parabolic problems. How many iterations were required to obtain a convergent solution?

Integrating the radial pressure Equation (29) downward from  $\eta = 1$  seems very risky. Do not small errors in the  $V$  field lead to large errors in the  $p$  field. In fact using a similar technique with the partially parabolic equations, we have found that integrating downward the pressure from a known streamline or from  $\infty$  leads to an instability with the pressure oscillating wildly on the body. This has been traced to small errors in the  $V$  field. We have avoided this problem by double sweeping the pressure (integrating down and then back up) by demanding that at each station the continuity equation is correct. Has any similar problem been encountered in the present work? Also, since the pressure field satisfies a Poisson equation, what is the exit boundary condition on  $p$ ?

Finally, concerning the  $k$ - $\epsilon$  model, it does not apply sufficiently close to the body (viscous sublayer and the matching layer). Other authors have typically placed the first point above the body far enough away from the body so that the model is accurate. Then they have used the law of the wall to obtain the values of  $k$  and  $\epsilon$  at this station above the body. Was a similar technique used here? If this is true, how was the model extended into the wake where the results agree extremely well with the experiment?

- Patankar, S.V., and D.B. Spalding (1967), A Finite Difference Procedure for Solving the Equations of the Two Dimensional Boundary Layer, Int. J. Heat Mass Transl., Vol. 10, p. 1389.
- Makatos, N.C., and C.B. Wells (1980), Prediction of Viscous Flow Around a Fully Submerged Appended Body, 13th Symposium on Naval Hydrodynamics, Tokyo.

## Author's Reply

Zhou Lian-di

To Y.A. Odabasi (BSRA)

In my opinion, some measured results of the turbulence structure were obtained recently either by flow visualization or hot-wire probe by using conditional sampling. However, at this time our understanding of the turbulence structure is not complete and investigations continue. The main objective of the present paper is to provide a numerical calculation method. As for the turbulence model, I merely adopted the  $k$ - $\epsilon$  model, which is a popular model at present. Of course, the present calculation method can also be used for turbulence models of the other transport equations.

To T.F. Hogan (DTNSRDC)

First, concerning the overall numerical iteration scheme, the initial distribution of  $u$  is first assumed, together with the positions of the streamlines, then  $v$ , the new distributions of  $k$ - $\epsilon$ ,  $p$ ,  $p_0$ , and finally the new distribution of  $u$  and the new positions of the streamlines are obtained. We employed the explicit formula in the iteration procedure, i.e., the right-hand sides of Equations (28), (29), (30), and (31) should take the values of the previous iteration. Equations (28) and (29) are individually integrated over the entire domain separately. Equations (30) and (31) are simultaneously integrated.

Second, as Dr. Hogan has rightly pointed out, in our calculation by the streamline iteration method a good or poor initial guess of the positions of the streamlines and of any flow variable will have a very important effect on the numerical stability. A relaxation factor is an important means in controlling the stability of the iteration procedure. But the value of the relaxation factor can only be chosen by experience and good judgment. It is very difficult to perform the stability analysis theoretically. On the other hand, owing to the fact that the system of equations employed by the present paper is fully elliptic, more computer time is required than that for parabolic and partially parabolic equations. About 50 iterations were required to obtain a convergent solution in our calculation. But as a result of that, the ellipticity of the equations is maintained, so the present method can be extended to the calculation of turbulent flows around and behind the stern of a body of revolution with propeller in operation, and of turbulent flow in channels of turbomachinery.

Third, as for solving the radial pressure-gradient Equation (29), our experience is the same as Dr. Hogan's, i.e., it is very difficult to compute the pressure accurately enough by integrating Equation (29)

downward from  $r = \infty$  (corresponding to  $\eta = 1$ ). Through the transformations we used, the accuracy of the calculated results can be improved only partially. In order to improve the accuracy further, a relaxation factor is also employed in solving the radial pressure gradient equation; however, the number of iteration is also increased. As to the exit boundary condition on  $p$ , because the exit boundary is located far downstream, we can assume that the streamlines at the exit boundary are straight, i.e.,

$$\frac{dr}{dz} \text{ exit boundary} = 0$$

This condition, together with the exit boundary conditions given in this paper, implies that  $p = p_\infty$  at the exit boundary from Equation (20), so that the exit-boundary condition on  $p$  is not given explicitly.

Finally, concerning the  $k-\epsilon$  model, it does not apply to the viscous sublayer, which is well known. Like other authors, we avoided the calculation of the flow in the viscous sublayer by using a numerical technique that is similar to that using a wall function, although the choice of applying the turbulence model to the region near the wake centerline is, up to now, quite debatable. However, after using the symmetric condition at the wake centerline appropriately, we have never experienced any trouble in calculating the flow in the wake by the  $k-\epsilon$  model. The calculated results at  $z/L = 1.057$  and  $1.182$  agree with experimental data satisfactorily. As for the far-field wake, so far we have no experimental results at hand, so no comparison was made.

# Reynolds Number Scaling of Velocities in Axisymmetric Turbulent Boundary Layers

David W. Coder

David Taylor Naval Ship Research and Development Center  
Bethesda, Maryland, U.S.A.

## ABSTRACT

Boundary layer and stern flow measurements were made for an axisymmetric body in the NASA/Ames Twelve-Foot Pressure wind tunnel at length Reynolds numbers from 12.2 to 150 million, about a decade higher in Reynolds number than previous experiments using the same shaped body. Measurements included body static pressure distribution and boundary layer and stern flow velocity profiles. In order to investigate tunnel wall effects more thoroughly the tunnel wall static pressure distribution throughout the test section and the wall boundary layer velocity profile at approximately the mid-model location were obtained.

The potential flow/boundary layer interaction computer program developed by Wang and Huang was utilized to calculate the boundary layer velocity profiles. The velocity profiles were calculated for an infinite fluid using computed pressure distributions and for the in-the-tunnel situation using the measured body static pressure distributions as input to the computer code.

Comparison of the experimental and infinite fluid calculated velocity profiles showed good agreement for the boundary layers on the parallel midbody but significant disagreement at the stern location. The discrepancy in the stern area was traced to an interference effect of the large floor-to-ceiling strut located aft of the model in the downstream diffuser section of the tunnel. When a tunnel blockage correction was applied to the measured stern velocity profiles, the corrected stern flow velocity profiles correlated reasonably well with the data of Huang et al. obtained at a Reynolds number of 6.6 million. The computed changes of velocity in the boundary layer on the parallel middle body and stern as a function of Reynolds number show good agreement with the experimental results.

## INTRODUCTION

While data on the flow field around full-scale ships are available for some isolated cases, in general these data are not available due to the difficulty and cost of obtaining them. Thus, most data are obtained from experiments with geosim models performed in towing tanks, water tunnels, and low speed atmospheric wind tunnels under scaled conditions. Due to velocity limitations of the facilities and the use of smaller-than-full-scale models, model Reynolds numbers are usually two orders of magnitude below those at full scale. Thus, computational methods, verified by lower Reynolds number experiments, are needed to extrapolate the lower Reynolds number results to full-scale Reynolds numbers. Such a computational method has been developed by Wang and Huang (1976, 1979) at DTNSRDC for fully wetted axisymmetric bodies in an infinite fluid. The method has been validated by experiments conducted at length Reynolds numbers of 6.6 million [Huang et al. (1978)], which is more than two orders of magnitude below full-scale Reynolds numbers of interest.

The present paper presents experimental data that were obtained in a large "pressure" wind tunnel for an axisymmetric body at Reynolds numbers from about 12.2 to 150 million, which is only one order of magnitude below the maximum full-scale Reynolds numbers of interest. Boundary layer velocity profiles were obtained at several axial positions along the body and at one location on the stern. Velocity profiles were also calculated using the above method and compared with the experimental results. These comparisons will be made and discussed, after a brief description, in the next two sections of the experimental and computational techniques employed.

## EXPERIMENTAL TECHNIQUE

The body of revolution model considered in the present paper is a 0.559 m (22 in.) diameter, 6.283 m (20.615 ft) long Series 58 body [Landweber and Gertler (1950)] modified with a parallel midbody and a stern sting (to accommodate a wake rake mechanism). The model, shown schematically in the test section of the NASA/Ames Pressure wind tunnel [NASA Publication (1974)] in Figure 1, produced about 2.3 percent blockage at the midmodel location. The model's nondimensional offsets are given in the Appendix. The cylindrical coordinate system used here is also shown in Figure 1. The radius ( $r$ ) is measured from the model centerline, the angle ( $\theta$ ) is positive clockwise from bottom looking aft, and axial distance ( $X$ ) is positive aftwards. Static pressure taps were located on the top of the model ( $\theta = 180$  deg) about every one-percent of model length and in the wall of the tunnel at a much larger spacing throughout the tunnel test section ( $\theta = 45$  and  $315$  deg). Boundary layer rakes consisting of total head tubes were located to measure model velocity profiles at  $(X/L, \theta) = (0.158, 270 \text{ deg})$ ,  $(0.357, 240 \text{ deg})$  and  $(0.595, 210 \text{ deg})$  and at about  $(0.54, 315 \text{ deg})$  on the tunnel wall.

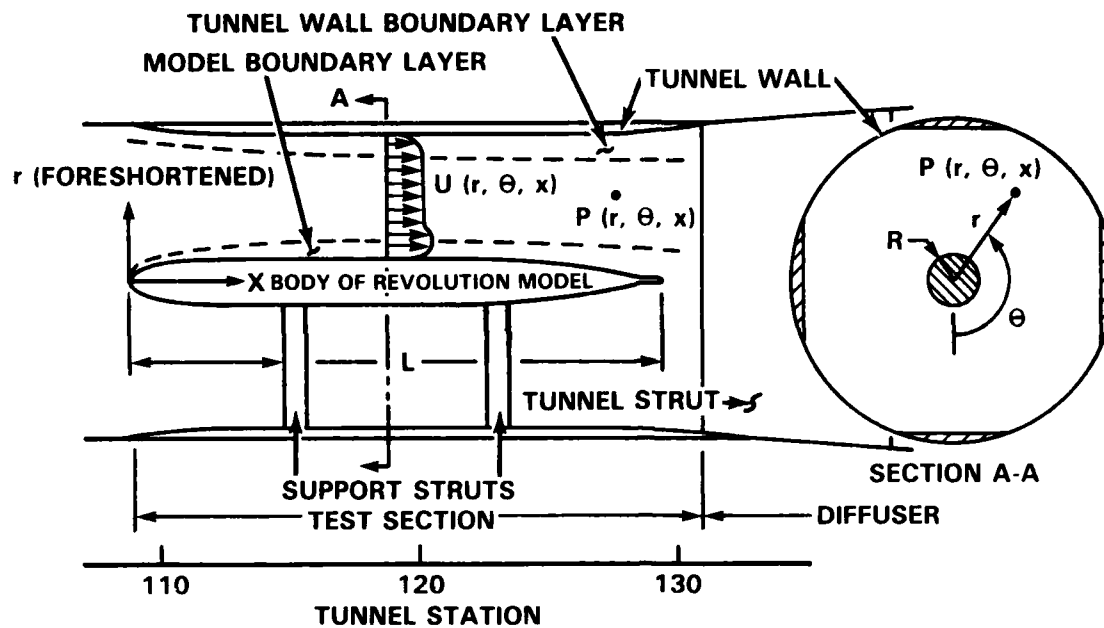


FIGURE 1. Schematic of model in test section of wind tunnel.

The wake rake located aft of the model on a stern sting was positioned to measure stern velocity profiles at  $(X/L, \Theta) = (0.967, 270 \text{ deg})$  with a five hole pitot tube (also known as a pitch-yaw probe) and at  $(X/L, \Theta) = (0.967, 90 \text{ deg})$  with a triaxial hot film probe.

Measurements were made at Reynolds numbers and Mach numbers of 12.2 million and 0.09, 22 million and 0.16, 40 million and 0.3, 60 million and 0.3, 100 million and 0.3, and 150 million and 0.3, respectively. The tunnel was operated at atmospheric pressure for the first three conditions and pressurized for the last three.

## THEORETICAL METHODS

### Transition

The location of transition from laminar to turbulent flow on the hydraulically smooth model was calculated using linearized stability theory and an  $e^N$  transition criterion [Smith and Gamberoni (1956)]. Locations of predicted disturbance amplification ratios ( $e^N$ ) versus Reynolds number for the model are shown in Figure 2 for various exponent values. McCarthy et al. (1976) show that for typical bodies of revolu-

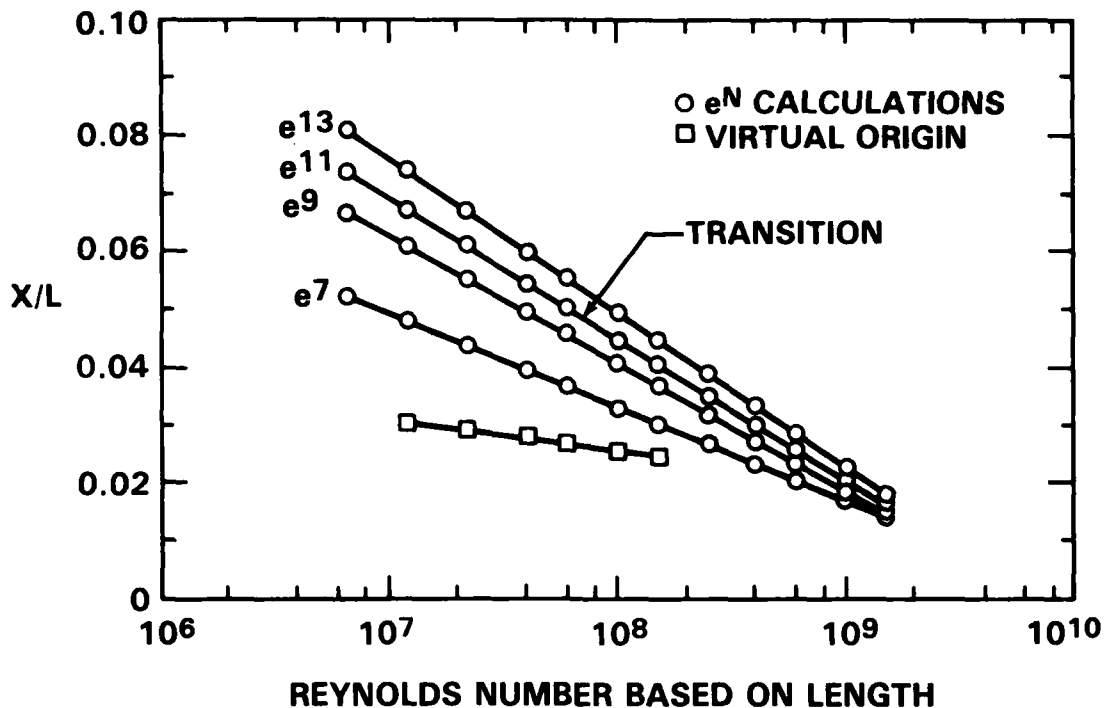


FIGURE 2. Prediction of location of natural transition and virtual origin.

tion,  $e^9$  amplification ratios correlate well with measured locations of the inception of Tollmien-Schlichting waves and  $e^{13}$  values correlate well with the existence of fully developed turbulence. Transition, or the occurrence of intermittent turbulent bursting, was found to correlate with an  $e^{11}$  criterion. From the figure, it is seen that the transition point is predicted to move forward from about 7 percent at a typical model Reynolds number of about 10 million, to about 2 percent at a full-scale Reynolds number of about 1000 million.

In order to move the model transition location forward, the model was fitted with a 0.25 mm (0.010 in.) diameter trip wire at  $X/L = 0.048$ . From McCarthy et al. (1976), the roughness Reynolds number has to be greater than 600 to insure transition. Calculations show that this condition is met for all but perhaps the lowest Reynolds number of about 12.2 million.



The virtual origins of turbulence for the trip wire were calculated according to the method outlined in McCarthy et al. (1976), values of trip wire drag coefficient were extrapolated to higher Reynolds number using the data of Kozlov (1969), and theoretical drag calculations were made as a function of transition location on the model in an infinite fluid using the program developed by Wang & Huang (described later). The values of virtual origin determined in this way are shown in Figure 2. Over the Reynolds number range of the experiment, 12.2 to 150 million, the effective transition location has been moved forward from about 4 to 7 percent to about 2.5 to 3 percent of the model length. Also notice that the effect of Reynolds number on the location of transition is minimized by the use of a trip wire. Thus, it is expected that the model will have a turbulent boundary layer over at least 97 percent of its length for the range of Reynolds numbers from 12.2 to 150 million.

#### Boundary Layer and Stern Flow Velocity Profiles

The theoretical method used to calculate the axisymmetric boundary layer velocity profiles was developed at DTNSRDC by Wang and Huang (1976, 1979). The method calculates the potential flow around the axisymmetric body using the method of Hess and Smith (1966). The potential flow velocity at the surface of the body is assumed to be the velocity at the edge of the boundary layer. The boundary layer over the body is then calculated using the differential, thin boundary layer method of Cebeci & Smith (1974). From these results, the boundary layer displacement thickness is computed and a "displacement body" is defined. Near the stern, the displacement body is faired into the displacement wake using a fifth degree polynomial. Use is made of the integral wake relations formulated by Granville (1953). The potential flow around the displacement body-wake configuration is calculated and used to re-define the boundary layer edge velocity. The boundary layer over the body is then re-calculated. Such calculations of the boundary layer and displacement body-wake are repeated three times to obtain the final results. The above method was used to calculate the infinite fluid case.

A modification of the program allows the experimentally (or otherwise) determined body static pressure distribution to be used as input. In this case the velocity at the edge of the boundary layer is determined from the inputted static pressure using the thin boundary layer assumption—that the pressure is constant across the boundary layer. The boundary layer calculations are only performed once since there is no need to improve the values of edge velocity. The modified version of the program was used to calculate the in-the-tunnel situation by inputting the experimentally determined body static pressure distribution.

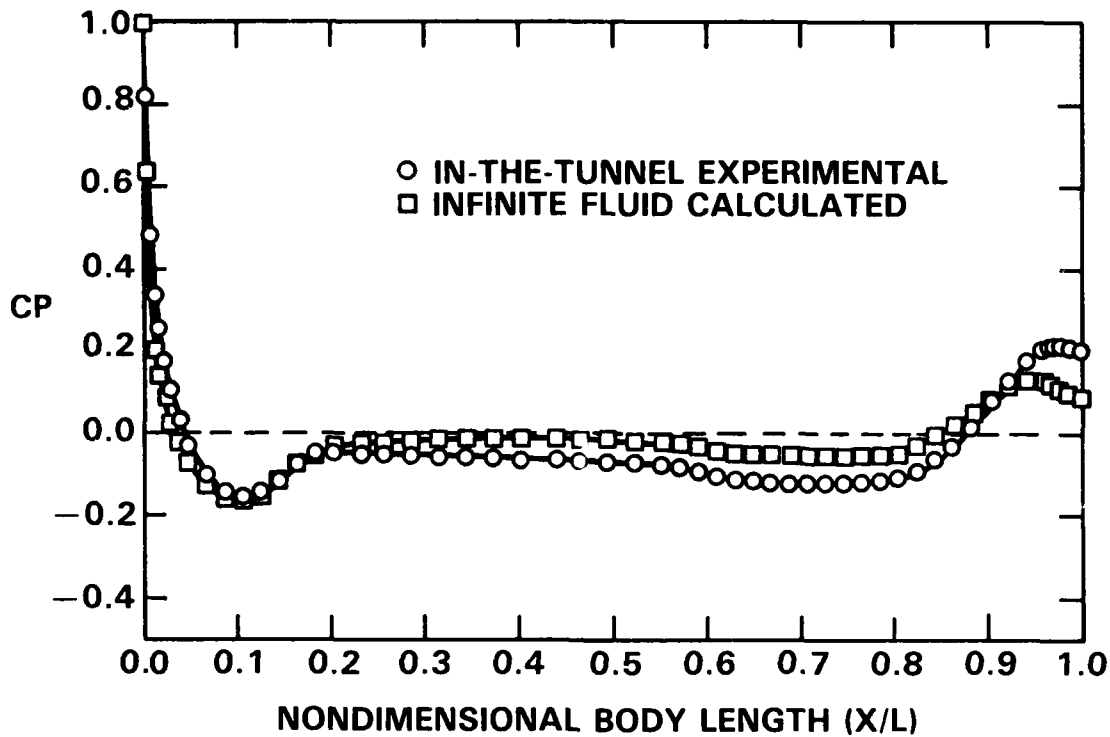


FIGURE 3. Measured and calculated distributions of static pressure over the axisymmetric body at a Reynolds number of 100 million.

#### PRESSURE DISTRIBUTIONS

The in-the-tunnel measured and calculated infinite-fluid model hull static pressure coefficient distributions for a Reynolds number of 100 million are shown in Figure 3. Results for other Reynolds numbers are similar with the difference between the two pressure distributions decreasing with increasing values of Reynolds number. In general, the measured in-the-tunnel velocities are lower (higher  $C_p$ ) than the infinite fluid velocities over the bow of the model and higher (lower  $C_p$ ) over much of the remaining hull except the region toward the end of the stern. For the stern region aft of about  $X/L > 0.90$ , velocities for the in-the-tunnel situation are much lower than for infinite flow. This may be attributed to the pressure field created by the large floor-to-ceiling strut permanently installed in the diffuser of the wind tunnel. While the strut creates a pressure distribution which is not axisymmetric, calculations for uniform irrotational flow around a 2-D strut show that the pressure field created by the strut is likely to be fairly flat in the region of the stern where the profiles were measured. At the location of the stern velocity profile measurements,  $C_p$  was calculated to be about 0.05 varying about 17 percent across the maximum

diameter of the model. Therefore, the disturbance effect is assumed to be approximately axisymmetric so that the axisymmetric calculational method used here can be employed. It is further assumed that the pressure distribution as measured on the top of the model at  $\phi = 180$  deg is representative of the axisymmetric situation.

Using the two pressure distributions, as described above, in-the-tunnel measured and infinite fluid calculated, the thin boundary layer velocity profiles at several positions along the parallel middlebody of the model and the thick boundary layer at one stern location were calculated. These results are presented next.

#### THIN BOUNDARY LAYER VELOCITY PROFILES

The calculated thin boundary layer velocity profiles at  $X/L = 0.158, 0.357, \text{ and } 0.595$  using the in-the-tunnel and infinite fluid pressure distributions are compared in Figure 4 with the experimentally determined profiles; experimental values of velocities are tabulated in the Appendix. The two sets of calculated profiles are not distinguishable from each other (and are shown together with a common curve in the figures) even though the static pressure distributions used to calculate them are somewhat different. However, all of the calculated velocity profiles are slightly fuller than the experimental profiles. The maximum difference in  $U/U_e$  between calculated and measured values is on the order of 0.02 to 0.04.

The effect of Reynolds number on the velocity profiles may be seen by examining the difference in nondimensional velocity from one Reynolds number to another. The difference in nondimensional velocity ( $\Delta U/U_e$ ) attained by an increase in Reynolds number from 22 to 150 million is shown in Figure 5. The differences obtained from experiments and calculations show good correlation over most of the profile. The main exception is for near the wall where the measured values are somewhat larger. Other comparisons, obtained by comparing any two Reynolds numbers, produce the same general results. This indicates that the computational method used can be expected to reflect the effect of Reynolds number on the change of velocity within a thin boundary layer profile. Thus the prediction method may be considered "validated" for the thin boundary layer situation and may be used to extrapolate low Reynolds number experimental profiles to full-scale.

○ EXPERIMENTAL

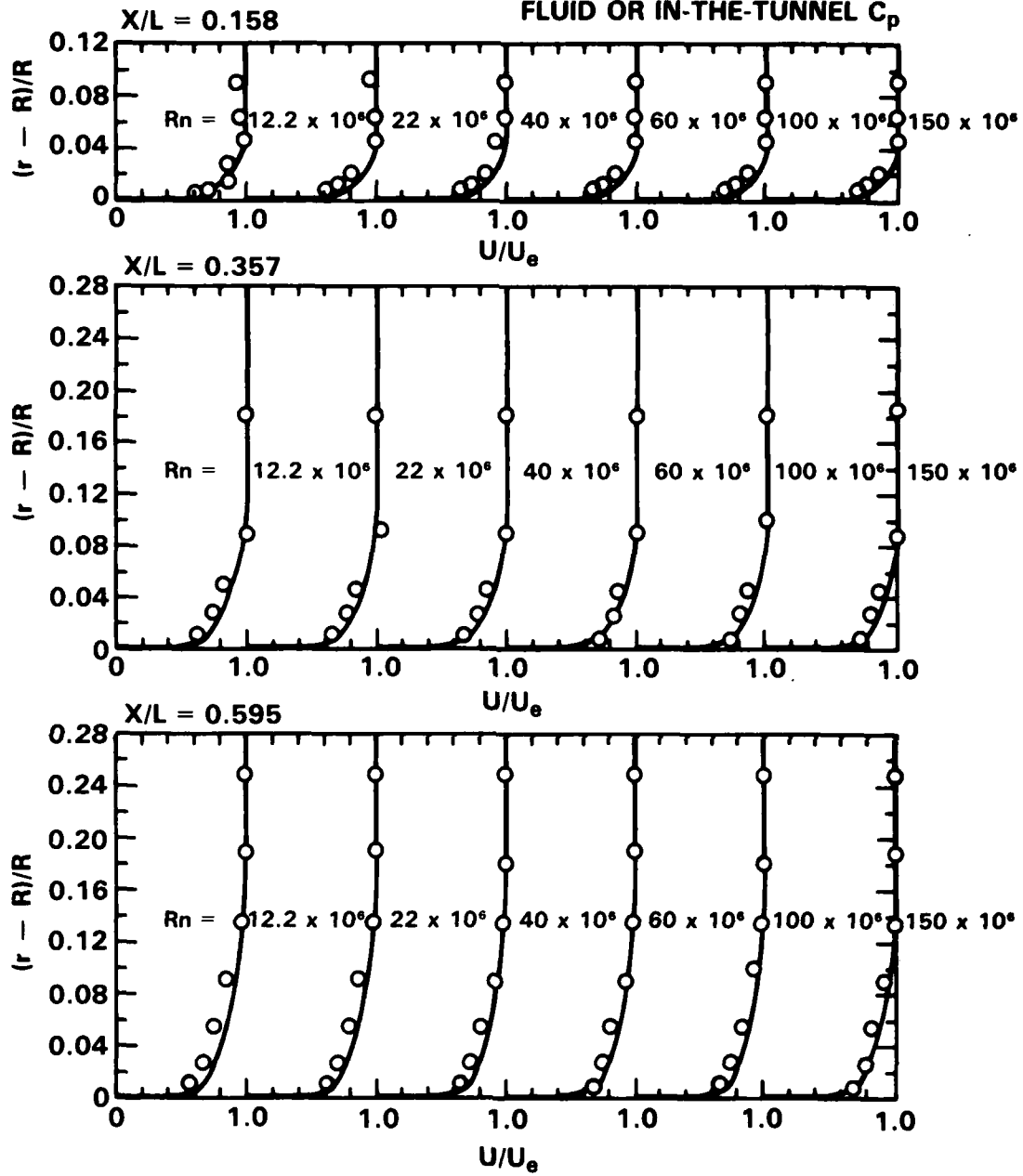
— CALCULATED FOR INFINITE  
FLUID OR IN-THE-TUNNEL  $C_p$ 

FIGURE 4. Measured and calculated thin boundary layer velocity profiles.

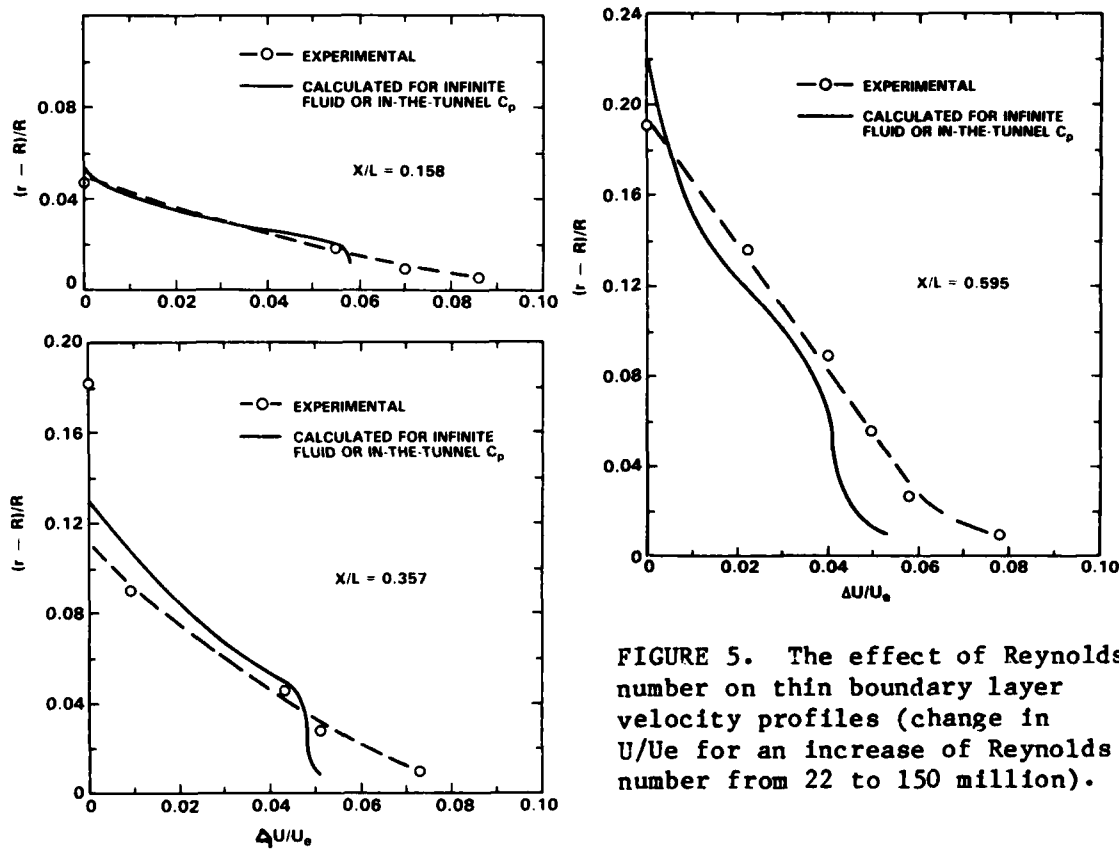


FIGURE 5. The effect of Reynolds number on thin boundary layer velocity profiles (change in  $U/U_e$  for an increase of Reynolds number from 22 to 150 million).

#### THICK STERN BOUNDARY LAYER VELOCITY PROFILES

The experimental and calculated thick stern boundary layer velocity profiles at  $X/L = 0.967$  are shown in Figure 6. Experimental values of velocities are also tabulated in the Appendix. Experimental profiles were obtained only for  $Rn = 12.2, 60$ , and  $100$  million. The experimental results represent averaged and smoothed values of velocity data obtained with the five hole pitot tube ( $\phi = 270$  deg) and the hot film probe ( $\phi = 90$  deg). It is seen that the velocity profiles calculated using the infinite fluid and in-the-tunnel model hull static pressure distributions are different from each other and from the experimental results.\*

\* The difference between the velocity profiles calculated for infinite fluid and in-the-tunnel situation can be attributed to tunnel blockage effects and may be used to obtain corrections for the measured profiles. The correction, as a function of radius is shown in the Appendix and may be applied to the nondimensional velocity as

$$(U/U_e)_{\text{corrected}} = (U/U_e)_{\text{measured}} + (\delta U/U_e)_{\text{correction}}$$

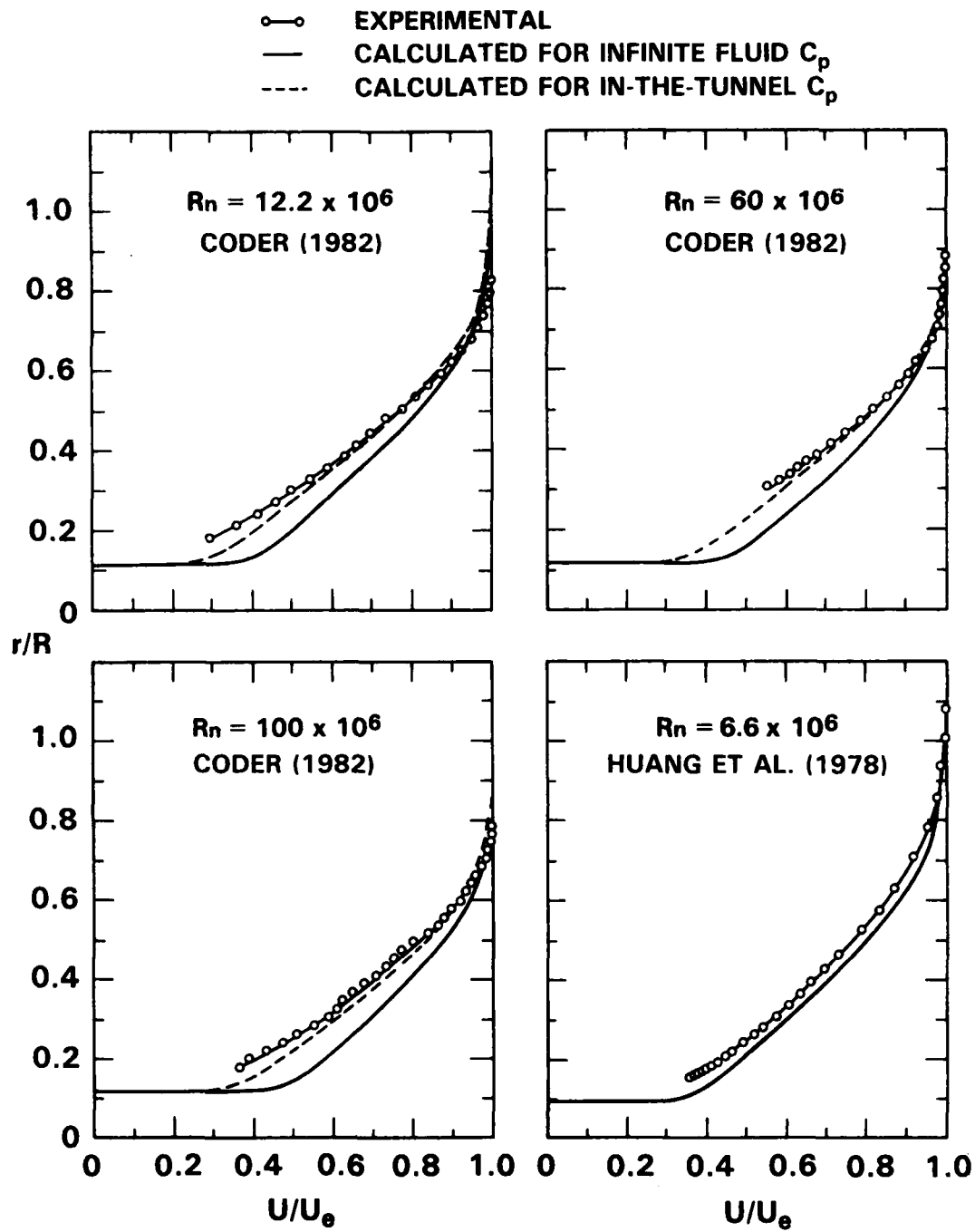


FIGURE 6. Measured and calculated thick stern boundary layer velocity profiles.

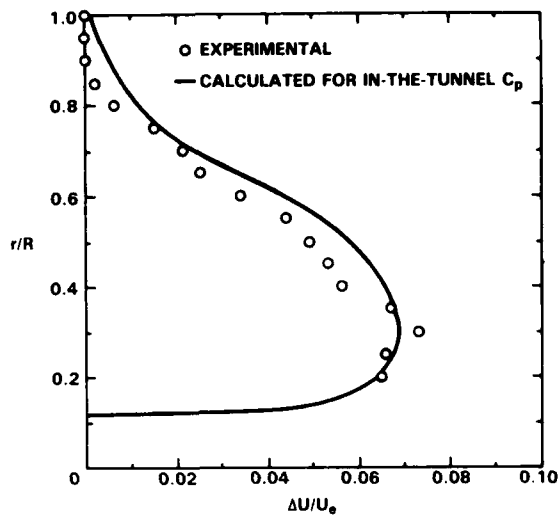


FIGURE 7. The effect of Reynolds number on thick stern boundary layer velocity profiles (change in  $U/U_e$  for an increase of Reynolds number from 12.2 to 100 million).

The stern flow velocity profiles calculated using the in-the-tunnel hull static pressure coefficient distributions are significantly closer to the experimental data than are the calculations made using the infinite fluid coefficients. Also included in Figure 6 and the Appendix are the results of Huang et al. (1978) at a Reynolds number of 6.6 million for a similar model but without the stern sting. The stern velocity profile of Huang et al. (1978) was obtained by interpolating between measured profiles at  $X/L$  values of 0.953 and 0.976 (corresponding of Huang's  $X/L$  values of 0.977 and 1.000, respectively). It is seen that all of the experimental velocity profiles are less full than the calculated profiles by about the same amount. The discrepancy in nondimensional velocity increases from zero at the edge of the boundary layer to about 0.05 at  $r/R$  of 0.3.

The effect of Reynolds number on the change in velocity profiles appears to show much better correlation between measured and calculated results. The difference in nondimensional velocities between Reynolds numbers of 12.2 and 100 million ( $\Delta U/U_e$ ), determined from the experimental velocity profiles and the in-the-tunnel calculated profiles, is shown as a function of radius in Figure 7. It is seen that the difference between the experimental and calculated values of  $\Delta U/U_e$  is on the order of 0.005 which is well below experimental error. These results indicate that the computational method may be used to predict the change in  $U/U_e$  as a function of Reynolds number change and to make full-scale extrapolations of stern flow velocity profile data obtained at lower Reynolds numbers.

## CONCLUSIONS

1. In-the-tunnel static pressure distributions on the model indicate that the velocity was lower over the bow and higher over most of the rest of the model than would be the case for an infinite fluid. The differences may be attributed to tunnel wall blockage effects and to a large strut located in the tunnel diffuser aft of the model.
2. Theoretical predictions of thin boundary layer velocity profiles along the parallel middlebody of the model are in good agreement with the experimental profiles, only slightly fuller. The measured and calculated changes of velocity in the boundary layer as a function of Reynolds number are in good agreement, indicating that calculated velocity differences due to Reynolds number changes may be used to extrapolate low Reynolds number thin boundary layer velocity profile data to full scale.
3. Theoretical predictions of the thick stern boundary layer velocity profiles using experimental pressure distributions are fuller than measured velocity profiles. This finding is in agreement with lower Reynolds number data reported by Huang et al. (1978). The measured and calculated changes in stern flow velocity profiles as a function of Reynolds number show good agreement, indicating that calculated velocity differences due to Reynolds number changes can be used to extrapolate lower Reynolds number thick boundary layer velocity profile data to full-scale.

## ACKNOWLEDGEMENTS

The author gratefully acknowledges the assistance of June E. Chappellear (DTNSRDC) and Nicholas Santelli (Consultant to Scientex Corp.) in the analysis of experimental data and theoretical calculations, respectively. Also appreciated are the support of the sponsors, Mark R. Henry and James J. Sejd (both of NAVSEA), and the technical discussions with Henry T. Wang (NRL) and Paul S. Granville (DTNSRDC). Special thanks are due Frank B. Peterson (NAVSEA) who provided the inspiration and encouragement for the work presented in this paper.

## References

- Cebeci, T. and A.M.O. Smith (1974). Analysis of Turbulent Boundary Layers, Academic Press, New York.
- Granville, P.S. (1953). Calculation of the Viscous Drag of Bodies of Revolution, DTMB Report 849.
- Hess, J.L. and A.M.O. Smith (1966). Calculation of Potential Flow about Arbitrary Bodies, Progress in Aeronautical Sciences, Volume 8, Pergamon Press, New York.



- Huang, T.T., N. Santelli, and G. Belt (1978). Stern Boundary-Layer Flow on Axisymmetric Bodies, Twelfth Symposium on Naval Hydrodynamics, Washington, D.C.
- Kozlov, L.F. (1969). Investigation of the Boundary Layer Turbulence Stimulation of the Ship Models, Proceedings of the Twelfth ITTC, Rome, Italy.
- Landweber, L. and M. Gertler (1950). Mathematical Formulation of Bodies of Revolution, David Taylor Model Basin Report 719.
- McCarthy, J.H., J.L. Power, and T.T. Huang (1976). The Roles of Transition, Laminar Separation, and Turbulence Stimulation in the Analysis of Axisymmetric Body Drag, Eleventh Symposium on Naval Hydrodynamics, London, England.
- NASA/Ames Research Center Brochure (1974). Ames Research Facilities Summary 1974.
- Smith, A.M.O. and N. Gamberoni (1956). Transition, Pressure Gradient and Stability Theory, Douglas Aircraft Report ES 26388.
- Wang, H.T. and T.T. Huang (1976). User's Manual for a FORTRAN IV Computer Program for Calculating the Potential Flow/Boundary Layer Interaction on Axisymmetric Bodies, DTNSRDC Report SPD-737-01.
- Wang, H.T. and T.T. Huang (1979). Calculation of Potential Flow/Boundary Layer Interaction on Axisymmetric Bodies, Proceedings of the 1979 Joint ASME/CSME Applied Mechanics - Fluid Engineering - Bioengineering Conference, Niagara Falls, New York.

## APPENDIX

TABLE A1. Model offsets.

X/L	r/R	Y/L	r/R	X/L	r/R	X/L	r/R
0.00000	0.00000	.16493	1.00000	.53844	1.00000	.81494	.76503
.00097	.09501	.17463	1.00000	.55300	1.00000	.82464	.73601
.00340	.17399	.18433	1.00000	.56270	1.00000	.83434	.70405
.00582	.23606	.19403	1.00000	.57240	1.00000	.84405	.66903
.00825	.28603	.20374	1.00000	.58210	1.00000	.85375	.63401
.01067	.32802	.21829	1.00000	.59180	1.00000	.86345	.59703
.01310	.36402	.23284	1.00000	.60150	1.00000	.87315	.55405
.01552	.39599	.24254	1.00000	.61121	.99902	.88285	.50998
.01795	.42697	.25709	1.00000	.62091	.99695	.89255	.46504
.02037	.45500	.27165	1.00000	.63061	.99498	.90420	.40362
.02425	.49635	.28620	1.00000	.64031	.99193	.91196	.36304
.02911	.54500	.30075	1.00000	.65001	.98702	.92166	.30599
.03008	.55383	.31530	1.00000	.65971	.98298	.93136	.25003
.03396	.58798	.32986	1.00000	.66942	.97796	.94106	.19199
.03881	.62900	.34441	1.00000	.67912	.97098	.95076	.14509
.04366	.66598	.35896	1.00000	.68882	.96400	.95561	.12905
.04851	.70099	.37351	1.00000	.69852	.95604	.95950	.11640
.05821	.76099	.38807	1.00000	.70822	.94600	.96241	.11640
.06791	.81302	.40262	1.00000	.71792	.93597	.96507	.11640
.07761	.85801	.41717	1.00000	.72763	.92495	.96716	.11640
.08732	.89342	.44143	1.00000	.73733	.91306	.97211	.11640
.09702	.92298	.45598	1.00000	.74703	.89997	.97550	.11640
.10672	.94698	.46568	1.00000	.75673	.88502	.98035	.11640
.11642	.96695	.48023	1.00000	.76643	.86800	.98520	.11640
.12612	.98102	.49479	1.00000	.77613	.85099	.99190	.10636
.13582	.99095	.50934	1.00000	.78584	.83299	.99588	.07276
.14553	.99596	.52389	1.00000	.79554	.81095	1.00000	0.00000
.15523	.99902			.80524	.78804		

TABLE A2. Experimental values of model boundary layer velocities.

X/L	(r-R)/R	U/U <sub>0</sub> FOR $R_n \times 10^{-6} =$					
		12	22	40	60	100	150
0.158	0.0909	0.964	0.982	0.990	1.000	1.000	1.000
	0.0636	0.986	1.000	1.000	0.997	0.998	0.997
	0.0455	1.000	0.999	0.963	0.996	0.997	0.997
	0.0273	—	—	—	—	—	—
	0.0182	0.851	0.824	0.849	0.857	0.870	0.879
	0.0091	0.722	0.708	0.730*	0.749	0.765	0.778
	0.0046	0.628	0.632	0.673	0.684	0.704	0.718
	—	—	—	—	—	—	—
0.357	0.1818	1.000	1.000	1.000	1.000	1.000	1.000
	0.1363	—	—	—	—	—	—
	0.0909	0.978	0.988	0.991	0.995	0.996	0.997
	0.0636	—	—	—	—	—	—
	0.0454	0.837	0.857	0.868	0.884	0.893	0.900
	0.0273	0.751	0.783	0.798	0.815	0.825	0.834
	0.0091	0.619	0.660	0.683	0.706	0.722	0.733
	—	—	—	—	—	—	—
0.595	0.2500	0.991	0.999	1.000	1.000	0.999	1.000
	0.1909	1.000	1.000	1.000	1.000	1.000	1.000
	0.1364	0.966	0.974	0.983	0.988	0.991	0.996
	0.0909	0.877	0.903	0.916	0.927	0.954	0.943
	0.0546	0.791	0.820	0.840	0.844	0.863	0.870
	0.0273	0.705	0.742	0.764	0.784	0.793	0.800
	0.0091	0.589	0.636	0.665	0.693	0.703	0.714
	—	—	—	—	—	—	—

X/L	$R_n = 6.6 \times 10^6 \ddagger$		$R_n = 12.2 \times 10^6$		$R_n = 60 \times 10^6$		$R_n = 100 \times 10^6$	
	r/R	U/U <sub>0</sub>	r/R	U/U <sub>0</sub>	r/R	U/U <sub>0</sub>	r/R	U/U <sub>0</sub>
0.967	0.157	0.360	0.185	0.290	0.237	†	0.180	0.362
	0.162	0.374	0.215	0.356	0.252	†	0.201	0.387
	0.168	0.384	0.244	0.408	0.266	†	0.222	0.429
	0.173	0.391	0.273	0.456	0.282	†	0.243	0.473
	0.179	0.400	0.302	0.493	0.296	†	0.264	0.507
	0.184	0.409	0.331	0.541	0.312	0.551	0.285	0.551
	0.195	0.424	0.360	0.582	0.325	0.580	0.305	0.584
	0.212	0.446	0.389	0.629	0.340	0.608	0.326	0.609
	0.224	0.463	0.418	0.659	0.355	0.628	0.347	0.623
	0.246	0.492	0.447	0.696	0.370	0.649	0.368	0.648
	0.268	0.520	0.476	0.733	0.385	0.675	0.390	0.675
	0.284	0.543	0.505	0.774	0.414	0.712	0.411	0.706
	0.312	0.574	0.535	0.807	0.443	0.748	0.432	0.733
	0.340	0.605	0.564	0.841	0.473	0.785	0.453	0.750
	0.368	0.635	0.593	0.874	0.503	0.818	0.474	0.770
	0.395	0.664	0.622	0.902	0.532	0.855	0.495	0.800
	0.431	0.699	0.651	0.923	0.561	0.882	0.516	0.835
	0.467	0.734	0.680	0.944	0.590	0.905	0.537	0.864
	0.523	0.789	0.709	0.962	0.620	0.925	0.557	0.874
	0.578	0.835	0.738	0.980	0.649	0.949	0.579	0.892
	0.633	0.874	0.767	0.987	0.678	0.968	0.600	0.920
	0.711	0.923	0.796	0.922	0.707	0.979	0.621	0.935
	0.788	0.959	0.825	1.000	0.737	0.985	0.642	0.948
	0.861	0.977	—	—	0.765	0.990	0.663	0.956
	0.939	0.988	—	—	0.795	0.992	0.684	0.972
	1.011	0.999	—	—	0.825	0.995	0.705	0.984
	1.083	1.000	—	—	0.855	0.997	0.725	0.987
	—	—	—	—	0.884	1.000	0.746	0.997
	—	—	—	—	—	—	0.767	0.999
	—	—	—	—	—	—	0.788	1.000

\*REYNOLDS NUMBER INTERPOLATED DATA  
AT SPECIFIC RADIUS

‡DATA INTERPOLATED FROM HUANG ET AL. (1978)

†QUESTIONABLE DATA

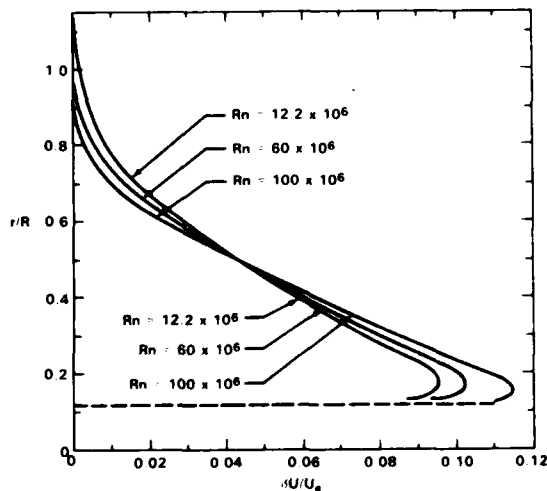


FIGURE A1. Strut interference correction for stern velocity profiles.

## Discussion

H.T. Wang (Naval Research Laboratory)

I would like to congratulate Dr. Coder on his success in obtaining boundary-layer measurements for Reynolds numbers that are one order of magnitude higher than those for previous measurements. As the co-author of the computer program used in this paper, I am pleased to see the close agreement between calculated and experimental results for the thin boundary-layer velocity profiles measured over the forward portion of the body. Since the theory for thin boundary layers is well developed, I take the viewpoint that this close agreement serves as a check on the correctness of the measurement technique and the existence of axisymmetric flow conditions in this region.

In the stern region, there is reasonably close agreement in the variation of velocity with Reynolds number, but only fair agreement in the absolute velocity profile. I pointed out to Dr. Coder that his original plots contained the calculated tangential velocities not the total velocities that would correspond with the experimentally measured velocities. Replotting served to bring the experimental and calculated results into the fair agreement shown in his Figure 6. One probable reason is the presence of the strut in the tunnel, which destroys both the infinite fluid and axisymmetric flow assumptions made in the program. Thus, the program is unable to duplicate the measured pressures on the body, and it was necessary to make a series of calculations in which the measured pressure was input. It is of interest to investigate how closely the calculated pressure using the resultant displacement body compares with the input measured pressure.

It would also be of interest to make a series of runs in which a portion of the displacement wake behind the stern is enlarged to various diameters to simulate the effect of the strut. A second possibility is that the algebraic correction to the eddy viscosity, which was previously validated at lower Reynolds numbers, may need to be revised for higher Reynolds numbers. The above revisions involve changing only a few lines of computer code and would not add to the complexity of the calculation procedure.

## Author's Reply

D.W. Coder (DTNSRDC)

Dr. Wang is the co-author (along with T.T. Huang of DTNSRDC) of the calculational method used in the paper to calculate the boundary-layer velocity profiles, so his remarks are especially welcome. I essentially agree with most remarks and wish to respond to four of them.

Dr. Wang has pointed out to me that the variable initially plotted in Figure 6 (in the preprints) is the nondimensional tangential velocity obtained with thin boundary-layer theory modified only to account for thick boundary-layer eddy viscosity (to agree with the Reynolds stresses measured in the stern region by Huang et al. [1978]). Figure 6 has been replotted and is shown in the present published version of the paper using the total nondimensional velocity, which includes both the tangential and normal velocities and also reflects additional thick boundary modifications as discussed by Wang and Huang (1979). These calculated velocity profiles (shown in Figure 6 here) are slightly less full than the previous ones (shown in the preprints) and give slightly better agreement between calculated and measured profiles.

The modified version of the program for which the body static pressure distribution can be used as input (instead of calculated) calculates the thin boundary layer (with modified eddy viscosity in the stern region) once (since there is no need to improve the thin boundary layer edge velocity). These results are used to obtain a displacement body-wake surface. The potential flow around this surface is calculated to obtain the off-body velocities used to make the additional thick boundary-layer modifications to the thin boundary calculations (with modified eddy viscosity). The comparison (suggested by Dr. Wang) of the on-body pressures in the stern area as calculated from this potential flow of the displacement surface with the input values shows little agreement. The calculated values are slightly higher than those calculated for an infinite fluid but significantly lower than the input values. Thus the correctness of the off-body velocities used to make the additional thick boundary-layer modifications is in question for the modified version of the program.

In order to obtain a purely calculational method to determine the tunnel strut interference effect (and resolve the above question), I have attempted to alter the calculated displacement wake by the addition of an axisymmetric body to simulate the tunnel strut interference effect. Axisymmetric bodies that have "equivalent tunnel blockage" as the strut or produce approximately the same potential flow upstream pressure field in the region of the stern as the strut have been defined. A few initial attempts in getting the program to run have failed so far. However, I am optimistic that results will soon be obtained.

Finally, Dr. Wang suggests that a modification to the eddy viscosity model for the thick boundary layer might be in order for the higher Reynolds numbers. I plan to modify the eddy viscosity model in the stern, if appropriate, based on stern Reynolds stress measurements made during the present experiment but not yet completely analyzed.

*Session VIII*

**VISCOUS FLUID  
PROBLEMS**

# Application of the Vortex-Lattice Concept to Flows with Smooth-Surface Separation

D. Fredd Thrasher

David W. Taylor Naval Research And Development Center  
Bethesda, Maryland 20084

## ABSTRACT

A nonlinear three-dimensional vortex-lattice method which treats the steady separated flow over an arbitrary body moving through an inviscid incompressible fluid at large incidence is developed. The method is not limited by body shape, interference pattern, or maneuver so long as the flow does not reattach, the locations of the separation lines are known, and vortex breakdown does not take place in the near field. Specifically, the problem of smooth-surface separation is considered in contrast to previous vortex-lattice methods which treated sharp-edge separation only. In the present case, flow separation is due to an adverse circumferential pressure gradient and is not associated with any geometric irregularity.

Following the vortex-lattice concept, we place a lattice of short straight vortex segments on the body and a number of semi-infinite non-intersecting curved vortex lines in each wake. Each of the wake vortex lines emanate from a separation line on the body and extend downstream along a streamline. Subsequently, each curved wake vortex line is replaced with a finite number of short straight connecting vortex segments with a straight semi-infinite vortex segment attached to the end of the last segment. These semi-infinite vortex lines are directed downstream parallel to the freestream.

A nonlinear iteration procedure is presented which solves for the circulation distribution that enforces the no-penetration condition at a finite number of collocation points on the body and simultaneously renders the wakes force-free. The pressure distribution on the body can then be calculated and numerically integrated to obtain distributed and total loads on the body.

As a numerical example, results are presented for an axisymmetric body, having a tangent-ogive nose and infinite parallel afterbody, at angle of attack. The shape of the wakes separating from the leeside of the afterbody are shown graphically. Comparisons of the resultant pressure distributions and distributed loads are made with results from other methods and experimental evidence.

## I. INTRODUCTION

Many problems in aero- and hydrodynamics involve potential flows where separation takes place on a smooth surface, such as a fuselage, rather than along a relatively sharp edge, such as the trailing edge of a wing. In the case of a smooth-surface, separation is due to adverse pressure gradients rather than geometric irregularities.

To date, most models of potential flows with smooth-surface separation have been based largely on two-dimensional crossflow analogies and frequently rely on empiricism. Recently, numerical schemes based on the vortex-lattice concept have had considerable success in treating the fully three-dimensional separated potential flow over low-aspect ratio thin wings at high incidence. So far, separation has been constrained to take place along the sharp edges of wings only. However, in principle the vortex-lattice method is not limited in application so long as the convection of vorticity dominates its diffusion and there is no destruction of vorticity by viscous effects.

For a discussion of the applicability of vortex methods, see J.H.B. Smith (1980).

We present a nonlinear vortex-lattice method which treats the steady flow past prolate bodies with open separation. We consider cases where the flow does not reattach and vortex breakdown does not take place near the body. We assume that the location of the separation lines on the body are known. Both the strength and shape of the body wake are found as part of the solution. Specific flows with smooth-surface separation are considered as opposed to flows with sharp-edge separation treated with vortex-lattice methods in the past.

To demonstrate the feasibility of the technique, we treat flow over an inclined axisymmetric body having a tangent-ogive nose and infinite parallel afterbody. The separation line is assumed to begin downstream of the nose but its circumferential location is fixed along the length of the body.

It is relevant to distinguish various flow phenomena at this point. Following Maskell (1955), we categorize separated flows into 'closed' and 'open' separation patterns as shown schematically in Figure 1. In flows with 'closed' separation there is a region in the flow field which is inaccessible to the oncoming flow. In flows with 'open' separation the fluid coming from upstream of the body wets both sides of the wake. Following J.H.B. Smith (1980), by 'reattachment' we mean that a shear layer, that has separated from the body at some upstream location, attaches to the body again downstream. The remainder of this section is devoted to a brief literature review.

Many methods in use may be loosely grouped under the heading of crossflow-plane analogies. These methods consider the impulsively started flow over a circular cylinder to be analogous to the flows viewed in a series of planes perpendicular to the body's longitudinal axis. Time in the former problem is related to axial distance of the crossflow plane in the latter problem. Hence, the problem reduces to finding the two-dimensional time dependent flow over an impulsively

started cylinder.

The most common formulation using the crossflow-plane analogy employs the discrete-vortex method to obtain the impulsive flow solution. Originally developed by Rosenhead (1932), the discrete-vortex method is based on replacing the Karman vortex streets behind the cylinder with point vortices. At each time step, a new point vortex is introduced into the outer flow at each separation point. The point vortices subsequently travel downstream under their mutual influence.

The discrete-vortex method has been used to calculate the flow over bodies at incidence with varying degrees of success. Unfortunately, the approach requires empirical guidance and considerable artwork on the part of the user. For examples of the discrete-vortex method and its application see Sarpkaya (1966), Gerrard (1967), Sarpkaya (1968), Larid (1971), and Sarpkaya and Schoaff (1979).

A similar approach, first suggested by Bryson (1959) and extended by Schindel (1965,1969), uses a lumped vortex crossflow model. Here, a point vortex is joined to the body with a feeding sheet of negligible strength. The system is adjusted such that it is globally force-free with the force on the feeding sheet balancing the force on the point vortex. In a modification of Bryson's model, called the multi-vortex model, a number of free point vortices are allowed to roll up and form a concentrated vortex in each crossflow plane (See Angelucci, 1971; Marshall and Deffenbaugh, 1974).

In the first fully three-dimensional approach to the problem, Hess and Smith (1962,1966) treated the non-lifting flow over arbitrary bodies with a distribution of constant source strength panels on the body surface. Asfar (1978) treated the same problem with a vortex-lattice method while Asfar et al., (1978) combined Asfar's vortex-lattice method with a surface distribution of sources of specified strength.

Atta and Nayfeh (1978) solved for the flow over wing-body combinations using a vortex-lattice method for both the body and the wings. They allowed for separation off the sharp edges of the wing only though.

Wing-body combinations were treated by Uchiyama et al., (1978) who used distributed sources on the surface of the body and a nonlinear vortex-lattice method similar to Rehbach (1974) to model the wings.

Maskew (1981) used a combination doublet-lattice and source model to solve for the flow over thick wings. Flow separation was not confined to the edges of the wing and thus he treated a problem similar to the one we consider here.

Fiddes (1980) solved for the separation angle on a cone at incidence by interacting F.T. Smith's (1978) extension of the two-dimensional triple-deck boundary-layer theory of Sychev (1972) with a sophisticated vortex-sheet model while using slender-body and conical flow assumptions.

The flow over thin wings with sharp-edge separation has been treated with nonlinear vortex-lattice methods by a number of authors over a wide variety of planforms. Steady flows were considered by Mook and Maddox (1974); Kandil et al. (1976); as well as Zorea and Rom (1978). Unsteady flows were considered by Belotserkovsky (1966); Atta et al. (1976); Thrasher et al. (1977); and Levin and Katz (1980).



Maskell (1955) was among the first to discuss plausible three-dimensional separation patterns in qualitative terms. Legendre (1956) proposed a mathematical framework to conceptualize limiting streamline patterns which were considered to have the properties of a continuous vector field; in particular, only one limiting streamline was allowed to pass through a regular point in the flow field.

Lighthill (1963) applied the concept of a continuous vector field to the pattern of skin-friction lines on a body's surface rather than to the limiting streamlines just above the surface as was done previously. Hunt et al., (1978) have shown that the notions of elementary singular points can be applied to the flow above the surface in planes of symmetry, in projections of conical flows (see J.H.B. Smith, 1969) and in crossflow planes (see Perry and Fairlie, 1974). Other extensions and applications can be found in Legendre (1972, 1977), and in excellent reviews by Tobak and Peak (1981a, 1981b) and Peake and Tobak (1980).

General reviews of three-dimensional separated flows were given by J.H.B. Smith (1975, 1978, 1980).

## II. HYDRODYNAMIC MODELING

We consider the steady inviscid incompressible flow past a body at an angle of attack. The fluid moves with a uniform freestream velocity far from the body and its extent is infinite. The angle of attack is sufficient to cause large scale separation on the leeside of the afterbody but is not so large as to precipitate unsteady vortex shedding. Hence, any asymmetry in the flow is due to geometry rather than to flow instabilities. Reattachment and secondary separation effects are neglected.

### A. Bound- and Free-Vortex Sheets

When the flow separates, vorticity generated within the boundary layer on the body is shed into the outer flow along separation lines. This shed vorticity forms the body wake. The resulting flow is fully three-dimensional and nonlinear. The wake shape and strength are important in determining the flow field surrounding the body and ultimately the loads.

If the Reynolds number is high, the wake is thin when compared with the overall dimensions of the body. Consequently, the vorticity in the flow is concentrated into the thin boundary layer on the body and thin vortical regions comprising the wake. The flow outside of these regions is essentially irrotational. As the Reynolds number tends toward infinity the thickness of each of these regions vanishes so that they may be represented as bound- and free-vortex sheets. The problem remains to specify the shape of the free-vortex sheets and the vorticity distribution on the bound- and free-vortex sheets.

### B. Kinematic Flow Conditions

There are a number of conditions which the solution must satisfy. First, there can be no penetration through the body surface:

$$(\vec{V}_{\infty} + \vec{V}_1) \cdot \vec{n} = 0 \quad \text{on the bound-vortex sheet} \quad (2.1)$$

where  $\vec{V}_{\infty}$  is the undisturbed freestream velocity,  $\vec{V}_1$  is the disturbance velocity, and  $\vec{n}$  is the unit normal to the body surface.

Second, vorticity is a divergenceless field by construction, or:

$$\text{div}(\vec{w}) = \text{div}(\text{curl } \vec{V}) = 0$$

In other words vorticity is spatially conserved.

Finally, according to the Kelvin-Helmholtz theory of vorticity, the substantial derivative of circulation,  $\Gamma$ , on a free-vortex sheet is zero or:

$$\frac{D\Gamma}{Dt} = 0 \quad (2.2)$$

Consequently, free vorticity is convected downstream with the local particle velocity and a steady free-vortex sheet is a stream surface.

### C. Separation Line Conditions

There are conditions along the separation lines as well. Since we are posing our problem in terms of the vorticity distribution we seek a condition on the vortex strength along a separation line. In terms of vorticity, the appropriate Kutta condition for the flow over two-dimensional airfoils is that the bound-vortex strength vanishes at the trailing edge. The vorticity generated within the boundary layer on a two-dimensional bluff body is swept into the outer flow at each of the separation points and the bound-vortex strength on the body vanishes there as well. In the vortex sheet model of the steady flow over three-dimensional thin wings with sharp-edge separation, the two-dimensional Kutta condition is applied in a localized manner. That is, on those edges where separation takes place the vorticity adjacent and parallel to the edge is immediately swept into the wake and the bound-vortex strength vanishes there. In a similar fashion, we apply the separation point condition for two-dimensional bluff bodies along the separation lines on three-dimensional bluff bodies in a localized manner. Therefore, the bound-vortex strength adjacent and parallel to a separation line

vanishes. Spatial conservation of vorticity demands that this vorticity be swept into the outer flow where it travels downstream to form the body wake.

### III. Numerical Modeling

The numerical model is based on the vortex-lattice concept of replacing continuous vortex sheets with arrangements of vortex segments. The physics of the flow dictates the placement of the vortex segments and their interaction. Here, we replace the bound- and free-vortex sheets with lattices of short straight vortex segments. The position of the segments in the free-vortex sheet and the strength of the segments in both the bound- and free-vortex sheets are then found via a nonlinear iteration procedure.

#### A. Bound-Vortex Lattice

We begin by replacing the continuous bound-vortex sheet with circumferential and longitudinal families of curved vortex lines which lie on the body's surface. The longitudinal vortex lines start at the nose of the body and continue back to the body's tail. The circumferential vortex lines form a series of axially spaced vortex rings which enclose the body. These two families of vortex lines intersect at various nodes to form rows and columns of vortex panels or elements which cover the entire body. The vortex lines are placed such that the resulting arrangement of vortex panels is regular and uniform. The panels which meet to form the nose and tail are three-sided, while the remaining panels are four-sided. Such an arrangement is shown schematically in Figure 2.

Short curved vortex segments which connect the various nodes on the body act as edges to the vortex panels. We replace these curved segments with straight segments connecting the nodes. These straight vortex segments make up the bound-vortex lattice.

The three-sided vortex panels are flat and triangular while the four-sided panels are generally nonplanar. In practical applications, however, the four-sided panels are almost flat.

The area of a four-sided panel is taken to be one-half the magnitude of, and its normal direction parallel to the cross product of the panel's diagonals. This approximation is exact if the panel is flat. The area and normal direction for a triangular panel are unambiguous.

We satisfy the no-penetration condition on the body in a collocation manner. That is, we enforce the no-penetration condition at a finite number of discrete points on the body and do not satisfy it elsewhere. (Indeed, large unrealistic normal velocities are induced between collocation points.) We call these collocation points 'control' points and place one on each panel.

We place the panel's control point on a plane that contains the centroid of the panel corners and is perpendicular to the panel's normal.

We refer to this plane as the panel plane. If the panel is nonplanar the centroid will not lie necessarily on the panel surface. In fact, the panel plane usually does not contain any of the panel's corners.

In their distributed-source method, Hess and Smith (1962) define a panel plane for each panel in the same manner as is done here and then project the panel's corners onto the panel plane along a direction parallel to the panel's normal. Thus, the corners of adjacent panels are not coincident as they are here but rather all the panels are flat.

We explore two choices for the placement of the control point on a panel plane. The first and most obvious choice is to place the control point at the panel's centroid. These control points are referred to as 'average' control points and are used by most authors. A second choice, investigated by Kelly (1977) and used by Asfar, et al., (1978), is to locate the control point such that the normal velocity induced by a unit loop circulation around the panel is a minimum. These control points are called to as 'optimal' control points and their use can have a profound effect on the results obtained.

We refer to the circulation around a vortex segment as a 'branch' circulation and denote it with the symbol ' $\Gamma$ '. Its sign and associated direction is taken according to the right-hand rule. Each vortex segment replaces the surface vorticity component parallel to and in an area immediately surrounding it. Thus, longitudinal segments replace the longitudinal components of vorticity on the body surface and likewise for the circumferential direction. Figure 3 illustrates this concept. If the two panels bordering a vortex segment have equal areas, the segment receives one-half of its strength from each of the two panels. However, if the panels have areas which are widely different, much more of the segment's strength originates from the panel with the larger surface area. In an attempt to account for this, we weight the branch circulation with the

appropriate panel areas when approximating the vorticity vector,  $\vec{w}$ , associated with a vortex panel, or:

$$\vec{w} = \frac{1}{A} \sum_{i=1}^m \frac{\vec{l}_i \Gamma_i A_i}{A + A_{i'}} \quad (3.1)$$

where  $\vec{l}_i$  denotes the vectors connecting consecutive nodes of the panel,

$\Gamma_i$  denotes the branch circulations of the corresponding vortex segments,

$A$  denotes the panel area,

$A_{i'}$  denotes the area of the adjoining panel on the  $i'$ th side,

and  $m$  is the number of panel edges ( either three or four ).

Authors in the past have simply used a one-half weighting for the branch circulation strength. As demonstrated later, weighting the branch circulations helps to alleviate some of the problems normally encountered with irregularly spaced lattices.

Spatial conservation of vorticity (or alternatively circulation) demands that the sum of the branch circulations at any node on a vortex-lattice vanish. A convenient way to satisfy this requirement is to define the branch circulations in terms of loop circulations. This is analogous to the familiar loop and branch currents in the analysis of electrical networks. We denote loop circulations with the letter 'G'. In Figure 4 we see that the branch circulation 'Γ' for the vortex segment bordering panels labeled 'i' and 'i+1' is given by:

$$\Gamma = G_i - G_{i+1} \quad (3.2)$$

We solve for the loop circulations as primary variables. We can then immediately write the branch circulations. We calculate the velocity field due to any vortex segment with its associated branch circulation by using the Biot-Savart law (See Section III.E). To find the total velocity, we add the freestream velocity to the combined velocity due to all the vortex segments in the flow. This includes the bound-vortex lattice in attached flow and both the bound- and free-vortex lattices in separated flow.

#### B. Attached Flow Solution Procedure

To enforce the no-penetration condition, we write a set of simultaneous linear equations for the loop circulations or:

$$\sum_{j=1}^N A_{ij} G_j = - \vec{V}_{\infty} \cdot \vec{n}_i \quad (3.3)$$

where  $A_{ij}$  are the influence coefficients,

$\vec{V}_{\infty}$  is the undisturbed freestream velocity,

$\vec{n}_i$  are the unit normal vectors for the panels,

and  $N$  is the number of panels on the body.

The influence coefficient  $A_{ij}$  is equal to the normal velocity induced at control point 'i' due to a unit loop circulation around panel 'j'. The solution of (3.3) is addressed in Section III.F. In the case of attached flow, once the no-penetration condition is satisfied we can calculate the loads on the body, as we describe in Section III.H.

### C. Free-Vortex Lattice

We use free-vortex lattices to replace the continuous free-vortex sheets in much the same way as we use a bound-vortex lattice to replace the bound-vortex sheet. Each free-vortex sheet joins the bound-vortex sheet along a prescribed separation line.

We first arrange the bound-vortex lattice such that each separation line coincides with one of the longitudinal vortex lines on the body. Furthermore, we place the circumferential vortex lines such that each separation line begins and ends on a node. Such an arrangement is shown in Figure 5.

We place a number of semi-infinite non-intersecting curved vortex lines on the free-vortex sheets. Each wake vortex line emanates from a node on the bound-vortex lattice on a separation line and extends downstream parallel to a streamline. These lines divide each free-vortex sheet into streamwise strips or 'ribbons' of surface vorticity. The vorticity distributed on each of these wake ribbons is subsequently concentrated into the vortex lines which border it in a fashion similar to the way we concentrate the bound vorticity into bound-vortex segments.

We now replace each curved vortex line in the wake with a number of short straight connected vortex segments. The first segment for each wake line attaches to the bound-vortex lattice, and the remainder extend downstream a finite distance. At the end of the last segment for each line we place a straight semi-infinite vortex line which extends downstream parallel to the undisturbed freestream.

The separation line condition demands that the bound vorticity adjacent and parallel to a separation line vanish. In view of the role the bound-vortex segments play in replacing the continuous bound-vortex sheet, we set the branch circulation around each of the longitudinal vortex segments along a separation line to zero. This is analogous to how we enforce the Kutta condition on the sharp edges of a thin wing in the vortex-lattice model appropriate for that problem. Spatial conservation of circulation then determines the strength of the free-vortex segments.

The problem remains of determining the orientation of the first wake segment in each line. J.H.B. Smith (1977) has shown that a free-vortex sheet leaves the body tangentially as the Reynolds number approaches infinity. We are unable to allow the sheet to do this due to numerical difficulties with the singular nature of vortex lines. To circumvent this problem we simply place the first segment in each wake line perpendicular to the body and make it short.

We include the wake lines in the calculation of the influence coefficients which correspond to the panels which border a separation line. This means that the influence coefficient matrix is now a function of

the wake shape.

The Kelvin-Helmholtz theory of vorticity requires that free vorticity travel downstream with the local particle velocity. If we view the steady state solution as a typical time step in the solution of an unsteady problem but with steady flow conditions, then each of the finite wake vortex segments represent an Euler step in the time integration of the path followed by a fluid particle. Thus, each wake vortex line is a pathline. We align each finite wake vortex segment with, and make its length proportional to the local particle velocity. This provides a force-free wake. The proportionality constant is the time increment, which we usually choose to be unity.

We use the velocity at the upstream end of a wake segment for directing and sizing the segment. Kelly (1977) investigated using other points along the segment and found that the fewest iterations were required and that the predicted loads were compared best with experiments when using the upstream end. Schroder (1978) used the average of the velocities calculated at the upstream and downstream ends but this practice almost doubles the computer time necessary for a solution.

#### D. Separated Flow Solution Procedure

We use the following scheme to obtain a solution:

1. Preset the wake position.
2. Calculate the influence coefficient matrix.
3. Solve for the loop circulations which enforce the no-penetration condition.
4. Position the wake vortex segments so that they are force-free.
5. Repeat steps 2-4 until convergence is achieved.

In step one, we set the wake either to be flat or at a previous solution. Step two involves changing only those columns in the influence coefficient matrix which correspond to panels bordering a separation line. Steps three and four require more elaborate calculations and are discussed in Sections III.F and III.G.

#### E. Velocity Calculations

We calculate the velocity field due to a vortex segment using the Biot-Savart law. For a single straight vortex segment, as shown in Figure 6, the velocity at a field point 'P' is given the following computationally advantageous form:

$$\vec{V} = \frac{\Gamma}{4\pi} \frac{\left| \begin{array}{cc} \vec{r}_{12} & \vec{r}_1 \\ \vec{r}_{12} & \vec{r}_2 \end{array} \right|}{\left| \begin{array}{cc} \vec{r}_{12} & \vec{r}_1 \\ \vec{r}_{12} & \vec{r}_2 \end{array} \right|^2} \left[ \vec{r}_{12} \cdot \left( \frac{\vec{r}_1}{|\vec{r}_1|} - \frac{\vec{r}_2}{|\vec{r}_2|} \right) \right] \quad (3.4)$$

where  $\vec{r}_1$ ,  $\vec{r}_2$  and  $\vec{r}_{12}$  are as shown in the figure.

The velocity due to a vortex segment tends towards infinity as we approach the segment. To avoid this problem, we insert a viscous core to replace the velocity field produced by the Biot-Savart law when we are close to a vortex segment. Here, we simply choose to set the induced velocity to zero within a certain radius of the vortex segment.

#### F. Solution of Simultaneous Linear Equations

The efficient solution of the arising set of simultaneous linear equations is important in solving for the flow over the body. This is especially true in the case of separated flow since we must do it once for every iteration between the wake position and loop circulations.

In general, iterative methods are particularly well suited for solving systems of equations when a good initial guess for the solution is available or when the number of equations prohibits complete storage of the coefficient matrix in high-speed memory. For an iterative method we use the modified Gauss-Seidel method (Johnson and Riess, 1977) or the modified Gauss-Seidel method with overrelaxation, sometimes called the SOR method (Goult et al. 1971).

In contrast, direct methods are particularly well suited for solving systems of equation when a good initial guess is not available and the number of equations allows for complete storage of the coefficient matrix in high-speed memory. For a direct method we use the Gauss-elimination method with partial pivoting (Johnson and Riess, 1977).

The number of operations (multiplications and divisions) for the Gauss-Seidel method is  $O(N^2)$  per iteration while the Gauss-elimination method requires  $O(N^3)$  operations for complete solution. Of course, considerable row exchanges may be necessary if pivoting is used.

A number of factors determine the structure and conditioning of [A] and thus govern the choice of the solution scheme. By inspection, we can show that if the body has a closed tail, then for any row 'i' in [A]:

$$\sum_{j=1}^N A_{ij} = 0 \quad (3.5)$$



Thus, every column of [A] is a linear combination of the remaining columns and the matrix is singular. This is because the loop circulations are taken as the unknowns in the problem while the branch circulations determine the velocity field. Since each of the branch circulations is defined as the difference between two loop circulations, the set of loop circulations which produce a particular velocity field are unique only within an additive constant vector or functionally:

$$\vec{V}([G]) = \vec{V}([G] + s[C]) \quad (3.6)$$

where  $s$  is a scalar and  $[C]$  is a vector of ones and is of the same length as  $[G]$ .

If the body has a open tail then we can show that for any row 'i' in [A]:

$$\sum_{j=1}^N A_{ij} = d_i \quad (3.7)$$

where  $d_i$  is the velocity induced normal to control point 'i' due to a unit branch circulation around each of the vortex segments in the last circumferential vortex ring.

For those rows which correspond to panels near the nose of the body,  $d_i$  can be of  $O(10^{-4})$  but it grows as we move to elements closer to the tail.

Even though the matrix is no longer singular, we found that partial pivoting was necessary to obtain a solution using Gauss-elimination.

In using the modified Gauss-Seidel method, we found that after several iterations, successive iterates of the loop circulations in both the singular and non-singular cases could be approximated by

$$[G]^{k+1} = [G]^k + s [C]^k \quad (3.8)$$

where the superscript indicates the iterate number and in this case  $s$  is a positive scalar. By monitoring the convergence of a few of the branch circulations during the Gauss-Seidel iteration, we were always able to find a solution. In most cases, the loop circulations eventually converged as well (that is,  $s$  would tend towards zero) but this usually required a large number of iterations.

If a good initial guess is available the number of Gauss-Seidel iterations is substantially reduced. A good initial guess can come from a previous solution at another angle of attack or from the previous wake iteration in the case of separated flow. However, in many cases the number of iterations was still large enough that Gauss-elimination was the preferred scheme.

Control point placement influences the structure of  $[A]$  and the resulting loads as well. Use of average control points does not necessarily result in  $[A]$  being strictly diagonal dominant. Nonetheless, the diagonal elements are always greater in absolute value than any of the off-diagonal elements. However, for the long thin panels near the nose of the body, the diagonal entries can overwhelm the off-diagonal elements and this seems to make the matrix product  $[A][G]$  sensitive to small changes in  $[G]$ . Using optimal control points minimizes the diagonal elements in  $[A]$  while leaving the off-diagonal elements essentially intact. Evidently, the use of optimal control points reduces the sensitivity of the system as fewer Gauss-Seidel iterations are needed. Also, the calculated loads are different near the nose of the body but not necessarily closer to experimental values. Numerical examples in Section IV illustrate this phenomena.

Another source of ill-conditioning is abrupt changes in the lattice spacing. A regularly spaced uniform lattice with gradual changes in panel size and aspect ratio is recommended for reliable and efficient solutions. There are also computer resource limitations. If an iterative scheme is used, the coefficient matrix can be stored on a low-speed device (disk or tape) and the matrix retrieved in row order. However, if a direct method is used, the coefficient matrix is changed (or destroyed) during the solution process. If the matrix cannot be stored in high-speed memory then successive rewrites of the matrix to low-speed storage are necessary. This is time consuming for a large system of equations and if pivoting is used, the penalties of retrieving the matrix in column and then row order are considerable. If memory limitations are severe then an iterative method should probably be used.

The choice of a solution technique for the system of equations depends on whether a good initial guess is available, the conditioning of the system, and the number of equations. We vary our choice of technique depending on the circumstances.

#### G. Wake Iteration Schemes

Once the no-penetration condition on the body is satisfied, we position the wake segments so that they are force-free. Since the influence of each wake segment is felt everywhere, moving any of the segments changes the force-free position of all the other wake segments and also results in the no-penetration condition on the body being violated. While this influence is minimal for those segments far away, the influence of near-by segments is substantial. Thus, the order of re-adjustment of the segments is important. We found that re-positioning the segments in turn converged faster than re-positioning all of them simultaneously. Typically, all the segments in the wake must be re-positioned three or four times for a fixed set of loop circulations before a reasonably force-free wake is obtained. In practice, the loads on the body are surprisingly insensitive to the wake position once the wake has begun to roll up.

The physics of the problem suggests judicious choices in the order of wake segment re-adjustment. If the flow is symmetric, we naturally re-adjust corresponding pairs of segments on either side of the plane of symmetry at the same time. Our experience indicates that it is best to adjust the furthest upstream segments first as their position seems to converge rather quickly. We do not adjust the position of the segments in the last two or three wake lines. Their converged position is difficult to find and their effect on the loads on the upstream portion of the body is small anyway. Evidently, the method tends to overestimate the distance that segments should be moved since underrelaxing the predicted changes in segment positions usually results in fewer iterations. Moreover, underrelaxation tends to stabilize the calculations, numerically. Relaxation factors as low as a tenth are not unreasonable, especially in the latter stages of the iteration.

As mentioned previously, our model of the wake corresponds to tracking the path of vorticity downstream with an Euler time integration scheme. Zorea and Rom (1978) used both an Euler method and a second order Runge-Kutta method to solve for the wake position, but they did not comment on the differences they may have encountered between the two methods. A Runge-Kutta scheme would certainly take more computer time.

Finding a converged wake position with vortex-lattice methods sometimes requires several trial iterative schemes in combination with under-relaxing the wake motion. Moreover, for some problems one combination of iteration parameters may induce convergence while another equally plausible combination, may not.

#### H. Calculation of Loads

We use the steady Bernoulli equation to calculate the pressure on the body:

$$C_p = \frac{P_\infty - P}{\frac{1}{2} \rho |\vec{V}_\infty|^2} = 1 - \frac{|\vec{V}|^2}{|\vec{V}_\infty|^2}$$

where  $C_p$  is the non-dimensional pressure coefficient,

$P_\infty$  is the freestream pressure,

$\vec{V}_\infty$  is the undisturbed freestream velocity,

$\rho$  is the fluid density,

and  $\vec{V}$  is the surface velocity.

We calculate the pressure coefficient on the body at the control points. We define the local normal force coefficient for a fixed axial location on the body as:

$$C_n = \frac{1}{r} \int_0^{2\pi} C_p \cos \theta d\theta$$

where  $r$  is the radius of the body and  $\theta$  is the circumferential angle measured from the windward meridian.

The total velocity on the bound-vortex sheet is the sum of the contributions due to the freestream, all of the vortex segments in the flow, and the jump in velocity across the vortex sheet. We calculate this jump as:

$$\vec{V} = \frac{1}{2} \vec{n} \times \vec{w}$$

where  $\vec{n}$  is the unit normal to the sheet and  $\vec{w}$  is the vorticity vector for the panel as defined in (3.1).

#### IV. NUMERICAL EXAMPLES

To demonstrate the numerical method, we treat the flow over a tangent-ogive cylinder at angle of attack with a nose length of three diameters. The circumferential angle and axial starting location of the separation line are given.

We measure the circumferential angle,  $\phi$ , from the windward meridian. The circumferential angle of the separation line we denote as

. All the cases considered here are symmetric flows so we show results for only one-half of the body. We specify a lattice with 'n' axial panels on the nose and 'm' circumferential panels everywhere on the body as a 'n x m' lattice.

We use a cosine circumferential distribution of elements and adjust it so that the separation line will fall on a longitudinal vortex line. By a cosine distribution of elements, we mean that the spacing in the circumferential direction is related to the difference in the cosines of equal increments of an angle. This provides a smooth variation in the size of adjacent panels. We specify the cosine spacing so that it is symmetric about the midplane of the body.

When comparing results from two different lattices or numerical with experimental values, pressures are rarely available from all sources at the same axial stations. We use a bi-cubic spline to interpolate the results of calculations to the experimental measurement locations or to a common axial station.

For the examples presented here, typical computation times for a Burroughs 7700 are from one to four hours for the separated flow cases starting with a flat wake. For additional angles of attack the computer time required is reduced about 40%.

#### A. Attached Flow Results

We first examine the effect of control point placement on the results. In Figure 7 we show the calculated results for the vortex-lattice method (VLM) for axisymmetric flow using both optimal and average control points together with experimental data from Faulker et al. (1964). The use of optimal control points has improved the accuracy of the results in this case. In Figure 8 we plot the normal-force co-

efficient vs. axial distance along the body for 15 angle of attack calculated with the present method and the source-distribution method (SM) of Hess and Smith (1966). The experimental results are from Tinling and Allen (1962). In this case, the use of average control points results in a better prediction of the forces. Similar behaviour is ob-

served at 10 and 20 angles of attack. It is not obvious why the suitability of the choice of control point placement is different in the two cases.

We next examine the effect of using area-weighted branch circulations in the definition of the panel vorticity vector on the pressure distribution obtained when the lattice has an irregularity. In Figure 9, a plan view view of two lattices is shown. Lattice 'a' has uniform spacing over the entire length of the body whereas lattice 'b' has a sudden refinement of the axial spacing immediately after the nose-cylinder junction. Both lattices have the same number of elements in the circumferential direction. In Figure 10 the pressure coefficient distribution obtained using both lattices with zero angle of attack are plotted along with the experimental results. Optimal control points were used in all calculations. As demonstrated by the figure, the use of area-weighting has all but removed any evidence of the lattice irregularity in the calculated pressures. The difference in pressures obtained by using and not using area weighting is indistinguishable for the uniform lattice.

#### B. Separated Flow Results

Here, we compare our results to the calculations of Jepps (1977) and the experimental results of Tinling and Allen (1962) for Reynolds numbers of 440,000 and 3,000,000. Jepps used the concentrated vortex core and feeding sheet model treating each separation line on the body as a locus of crossflow plane stagnation points. We have adjusted the separation angle such that the location of the control point just below the separation line is approximately the same in our case as in Jepps'. Since we used a circumferential spacing which was far coarser than Jepps', our separation angle is somewhat higher than Jepps'. That is, the separation line we use is located more towards the leeward side of the body.

In Figure 11, the wake off one side of the body is shown angle of attack ( $\alpha$ ) cases of 10°, 15°, and 20°. The separation angle in all cases is 140°.

There are 24 wake lines with the first line having 30 finite vortex segments and subsequent lines having one fewer than the one in front of it. This allows for many of the wake lines to end at approximately the same axial location. Figure 12 shows a front view of the same wakes. The first one or two wake lines do not converge to a smooth roll-up configuration in this example. Where the wake appears to have crossed itself, the longer more axially directed wake lines have extended beyond the envelope of the roll-up cone of wake lines and their direction has then been diverted outside of the organized vortex core. The last three wake lines were not adjusted to a force-free position and the two or three lines preceeding them also point away from the vortex core. If more elements had been used then all of the wake lines would have remained within the region of vortex roll up.

We see that there is a flattening of the wake lines near the plane of symmetry for the  $\alpha = 20^\circ$  case. This is because the wake has not yet fully rolled up.

In Figure 13, we show the surface velocity field for the attached and separated flow cases near a separation line. J.H.B. Smith (1978) showed that the surface velocity immediately behind a separation line is parallel to the separation line and that the surface velocity immediately in front of a separation line is inclined to the separation line. We can see that the velocities behind the separation line are more nearly parallel to the separation line in the separated case than they are in the attached case. In both cases the velocities in front of the separation line remain inclined to the separation line. This suggests that the method more or less predicts the proper behavior of the surface velocities near the separation line.

To demonstrate the behaviour of the circumferential pressure distribution as we move axially on the body from the attached flow region on the nose to the separated flow region on the afterbody, we compare the attached and separated circumferential pressure distributions for consecutive axial stations in Figure 14. The first wake vortex line attaches to the body between stations 12 and 13. After only a few stations, the shape of the pressure distribution becomes similar in shape from one station to the next. The presence of the separated vortex sheet increases the pressure in front of the separation line. The pressure behind the separation line falls off rapidly, but since there are only two panels behind the separation line we cannot expect the method to reproduce the flow details there.

Figures 15 through 17 display the circumferential pressure distributions computed by the present method and by Jepps, together with the experimental data of Tinling and Allen (1962), for  $\alpha = 10^\circ, 15^\circ$ , and

20 at  $x/d = 6$ . The separation angle for the present method was 149.1

which corresponds to to Jepps' angle of 144 . In all cases, both methods overpredicted the rise in the pressure in front of the separation line and display a sharp drop in the pressure behind the separation line. Neither method does well behind the separation line. Both do better for

$\alpha = 10$  and 15 than they do for  $\alpha = 20$  . Jepps' method does better than the present method on the windward plane. This is partly due to the coarseness of the lattice used in the present calculations. We see that the Reynolds number effect on the pressure distributions is larger at higher angles of attack.

Figures 18 through 20 display the normal-force coefficient vs. axial distance. Both the present method and Jepps' technique produces

forces which level off on the afterbody quickly at  $\alpha = 10$  but not at

$\alpha = 20$  . The sharp peaks in the results of the present method at the beginning of the separated region are present because of the sudden departure in the lattice configuration there due to the presence of the free-vortex sheet. The bound-vortex lattice for these examples was tested to ensure that no irregularities in the forces would be due to irregularities in the bound-vortex lattice spacing. Jepps mentioned that his method also fails at the beginning of the separation line and he smoothed the normal force coefficient values there using neighboring stations. We have not done such smoothing here.

Using a lattice which extended the afterbody a longer distance would probably result in the force leveling off for the higher angle of attack cases.

The results for the two separation angles used are shown in Figure 21 for  $\alpha = 15$  . The difference in control point location has caused some error in the normal force coefficient on the nose.

Figure 22 shows the normal-force coefficient vs. axial distance along the body for each iteration of the loop circulations. After only three iterations the normal-force coefficient has almost converged.

We could probably reduce the computer time needed somewhat by using the two-dimensional analogy results for vortex locations as a guide towards making a good initial guess for the wake position.

## V. CONCLUSIONS

We developed a nonlinear vortex-lattice method to treat the flow over prolate bodies with open separation. The strength and position of

the body wake is found as part of the solution. Specifically, flows with smooth-surface separation have been considered as opposed to flows with sharp-edge separation treated with vortex-lattice methods in the past. As a numerical example, we present results for the flow over a tangent-ogive cylinder at angle of attack.

Surprisingly, we found that using optimal control points produced more accurate results than average control points for the case of axisymmetric flow but less accurate results when the body was at an angle of attack. We showed that weighting the branch circulations with appropriate panel areas in the force calculation helps alleviate errors in the resultant pressure distributions due to a sudden change in the lattice spacing.

In separated flow cases, we found that the present method provided a somewhat more reliable estimate of the pressure distribution on the windward side of a separation line than does the two-dimensional method of Jepps. Neither method is successful behind a separation line. However, the present method is completely three-dimensional and accounts for the nonlinear behaviour of the body. It can be extended to treat appended bodies executing a variety of motions.

#### ACKNOWLEDGMENTS

This work is funded by NAVSEA Special Focus Project, Task Area SR023010B, Element No. 61153N. The illustrations were drawn by my wife, P.M. Thrasher, whose support and encouragement is deeply appreciated.

#### References

- Angelucci, S. B. (1971). A multivortex method for axisymmetric bodies at angle of attack, *J. of Aircraft*, 8, 12, December, pp. 959-96.
- Asfar, K. R. (1978). Application of the vortex-lattice technique to arbitrary bodies, M. S. Thesis, Dept. of Engineering Science and Mechanics, Virginia Polytechnic Institute and State University, Blacksburg, Virginia.
- Asfar, K. R., D. T. Mook, and A. H. Nayfeh (1978). Application of the vortex-lattice technique to arbitrary bodies, AIAA Paper No. 78-1205.
- Atta, E. H., O. A. Kandil, D. T. Mook, and A. H. Nayfeh (1976). Unsteady flow past wings having sharp edge separation, NASA SP-405, (Vortex-Lattice Utilization workshop), pp. 407-418.
- Atta, E. H. and A. H. Nayfeh (1978). Nonlinear aerodynamics of wing-body combinations, AIAA Paper No. 78-1206.
- Belotserkovsky, S. M. (1966). Gust effects on wings of complex planforms at subsonic speeds. *Mekanika Zhrdkosti i Craza*, 4, pp. 129-138.



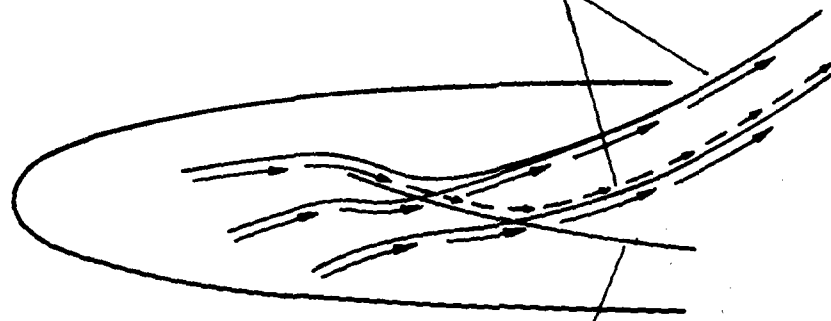
- Bryson, A. E. (1959). Symmetric vortex separation on circular cylinders and cones, J. of Applied Mechanics, 26, December, pp 643-648.
- Faulkner, S., J. L. Hess, and J. P. Giesing (1964). Comparison of experimental pressure distributions with those calculated by the Douglas-Neumann program, Douglas Aircraft Company, Report LB31831, December.
- Fiddes, S. P. (1980). A theory for the separated flow past a slender elliptic cone at incidence, RAE Tech Memo 1858.
- Gerrard, J. H., 1967. Numerical computation of the magnitude and frequency of the lift on a circular cylinder, Phil. Trans. Roy. Soc., 261, 1118, pp. 137-62.
- Goult, R. J., R. F. Hoskins, J. A. Milner, and M. J. Pratt (1974). Computational Methods in Linear Algebra, John Wiley & Sons, New York
- Hess, J. L. and A. M. O. Smith (1962). Calculation of nonlifting potential flow about arbitrary three-dimensional bodies, Douglas Aircraft Company Report No. E.S. 40622, March.
- Hess, J. L. and A. M. O. Smith (1966). Calculation of nonlifting potential flow about arbitrary three-dimensional bodies, Progress in Aeronautical Sciences, 8, Pergamon Press, New York. Also as Douglas Aircraft Company Engineering Paper 3327.
- Hunt, J. C. R., and C. J. Abell, J. A. Peterka, and H. Woo (1978). Kinematical studies of the flows around free or surface-mounted obstacles: Applying topology to flow visualization, J. of Fluid Mechanics, 86, pp. 179-200.
- Jepps, S. A. (1977). A theoretical investigation of the subsonic flow past an ogive-cylinder body, British Aircraft Corporation, Math Services Note 226, March.
- Johnson, Lee and R. Dean Riess (1977). Numerical Analysis, Addison-Wesley Publishing Company, Reading, Mass.
- Kandil, O. A., D. T. Mook, and A. H. Nayfeh (1976). A new convergence criterion for the vortex-lattice models of leading edge and wing-tip separation, NASA-SP-405 (Vortex-Lattice Utilization Workshop), pp. 285-300.
- Kelly, S. G. (1977). A systematic investigation of the parameters affecting the accuracy of the vortex-lattice method, M.S. Thesis, Dept. of Engineering Science and Mechanics, Virginia Polytechnic Institute and State University, Blacksburg, Virginia.
- Larid, A. D. K. (1971). Eddy formation behind circular cylinders, Proc. Am. Civil Engineering J. Hdy. Div., Hy6, pp. 763-75.
- Legendre, R. (1956). Separation de l'écoulement laminaire tridimensionnel. Recherche Aerospatiale, 54, pp. 3-8.
- Legendre, R. (1972). Separation de l'écoulement laminaire tridimensionnel. Recherche Aerospatiale, 54, pp. 241-248.
- Legendre, R. (1977). Lignes de courant d'un écoulement permanent: Decollement et separation, Recherche Aerospatiale, 6, pp. 327-355.
- Levin, D. and J. Katz (1980). A vortex-lattice method for the calculation of the nonsteady separated flow over delta wings, AIAA Paper No. 80-1803.

- Lighthill, M. J. (1963). Attachment and separation in three-dimensional flow, Laminar Boundary Layers, edited by L. Rosenhead Section 2.6, Oxford University, pp. 72-82.
- Marshall, F. J. and F. D. Deffenbaugh (1974). Separated flow over bodies of revolution using an unsteady discrete-vorticity cross wake, Part I Theory and application, NASA CR-2414, June.
- Maskell, E. C. (1955). Flow separation in three dimensions, RAE Aero Report 2565.
- Maskew, B. (1981). Prediction of subsonic aerodynamic characteristics-A case for low-order panel methods, AIAA Paper No. 81-0252.
- Mook, D. T., and S. A. Maddox (1974). Extension of a vortex-lattice method to include the effects of leading-edge separation, J. of Aircraft, 11, 2, p. 127.
- Peake, D. J. and M. Tobak (1980). Three-dimensional interactions and vortical flows with emphasis on high speeds, AGARDograph No. 252.
- Rehbach, C. (1974). Numerical investigation of vortex sheets issuing from a separation line near the leading edge, NASA TM-F 15,330.
- Rosenhead, L. (1932). Formation of vortices from a surface of discontinuity. Proc. Roy. Soc. A, 134, pp. 170-92.
- Perry, A. E., and B. D. Fairlie (1974). Critical points in flow patterns, Advances in Geophysics, 18B, Academic Press, New York, pp. 299-315.
- Sarpkaya, T. (1966). Separated flow about lifting bodies and impulsive flow about cylinders. AIAA J., 4, pp. 414-20.
- Sarpkaya, T. (1968). An analytical study of separated flow about circular cylinders, Transactions ASME J., Basic Engineering, 90, pp. 511-20.
- Sarpkaya, T. and R. L. Schoaff (1979). Inviscid model of two-dimensional vortex shedding of a circular cylinder, AIAA J., 17, 11, November, pp. 1193-1200.
- Schindel, L. (1965). Effects of vortex separation on lifting bodies of elliptic cross-section, MIT Tech Report 118, September.
- Schindel, L. (1969). Effects of vortex separation on lift distribution on elliptic cross section, J. of Aircraft, 6, 6, November-December, pp. 537-543.
- Schroder, W. (1978). Berechnung der nichtlinearen Beiwerte von Flugeln mit kleinem und mittlerem Seitenverhaltnis nach dem Wirbelleiterverfahren in inkompressibler Stromung. DFVLR-FB-78-26. Translated as ESA-TT-585.
- Smith, F. T. (1978). Three-dimensional viscous and inviscid separation of a vortex sheet from a smooth nonslender body, RAE Technical Report 78095.
- Smith, J. H. B. (1969). Remarks on the structure of conical flow, RAE TR-69119.
- Smith, J. H. B. (1975). A review of separation in steady three-dimensional flow, AGARD CP-168, Paper 31.
- Smith, J. H. B. (1977). Behaviour of a vortex sheet separating from a smooth surface, RAE Tech Report 77058, April.

- Smith, J. H. B. (1978). Inviscid fluid models for three-dimensional separation at high Reynolds numbers, AGARD LS-94.
- Smith, J. H. B. (1980). Vortical flows and their computation. Part of the von Karman Institute for Fluid Dynamics Lectures Series in Computational Fluid Dynamics, March.
- Sychev, V. V. (1972). On laminar separation. Izv. Akad. Nauk. Mekh. Zhid. Gaza, No. 3, pp. 47-59. Translated in Fluid Dynamics, Plenum, March/April 1974, pp. 407-417.
- Thrasher, D. F., D. T. Mook, O. A. Kandil, and A. H. Nayfeh (1977). Application of the vortex-lattice concept to general, unsteady lifting surface problems, AIAA Paper No. 77-1157.
- Tinling, B. E. and C. Q. Allen (1962). An investigation of the normal-force and vortex-wake characteristics of an ogive-cylinder body at subsonic speeds, NASA TN D-1297, April.
- Tobak, M. and D. J. Peake (1981a). Topology of three-dimensional separated flows, NASA TM-81294. Also to be published in Annual Review of Fluid Mechanics, 14, (1982).
- Tobak, M. and D. J. Peake (1981b). Topological structures of three-dimensional separated flows, AIAA Paper No. 81-1200.
- Uchiyama, N., R. P. Mikkilineni, and J. M. Wu, 1978. The analysis of wing-body combinations at moderate angles of attack. AIAA Paper No. 78-62,
- Zorea, C. R. and J. Rom (1978). The calculation of non-linear aerodynamic characteristics of wings and their wakes in subsonic flow, Israel Journal of Technology, 16, pp. 83-96.

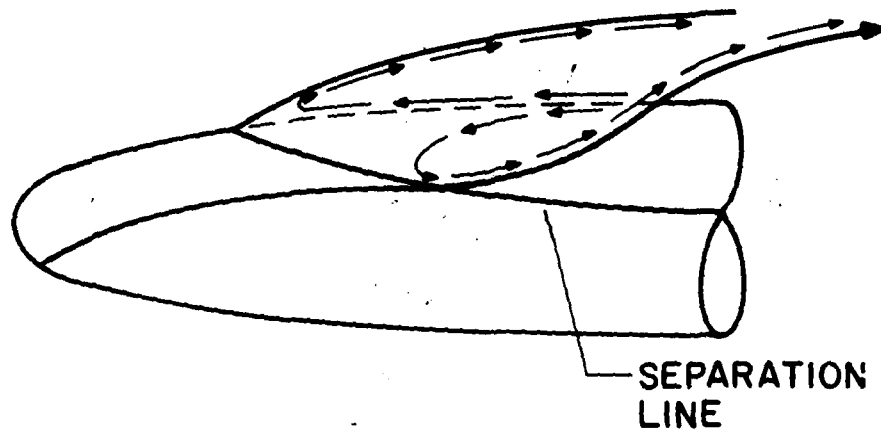
1111

FREE-VORTEX LINES



SEPARATION LINE

OPEN SEPARATION



SEPARATION  
LINE

CLOSED SEPARATION

Figure 1. Schematic views of open and closed separation patterns

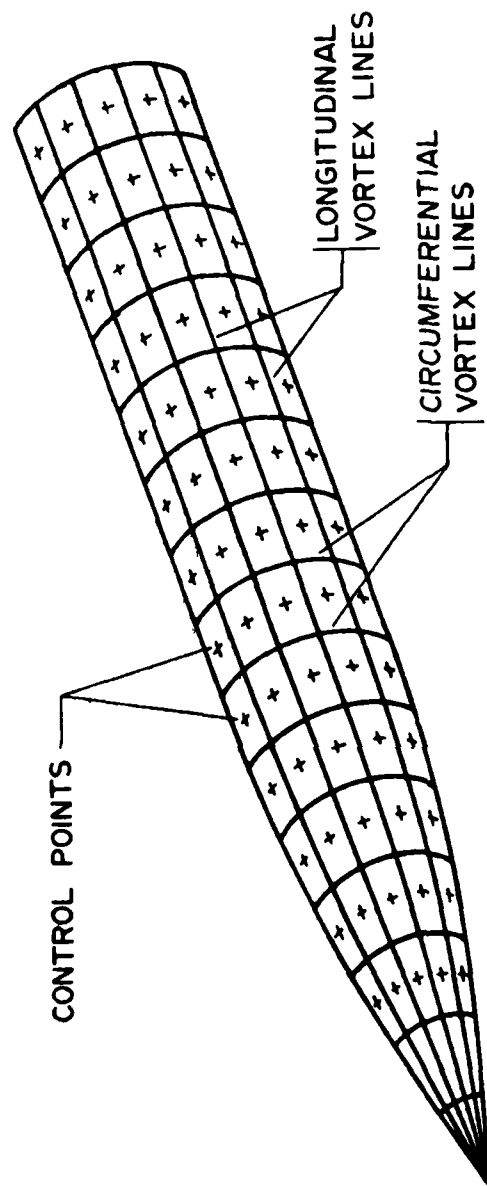


Figure 2. Schematic view of a bound-vortex lattice.

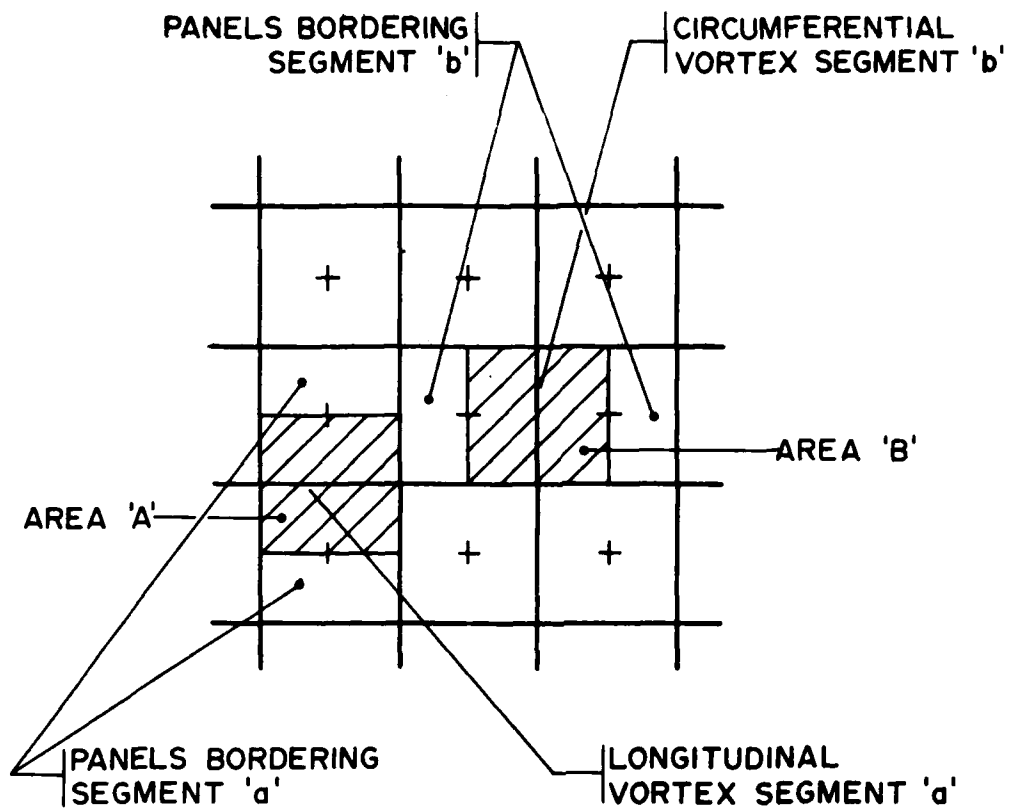


Figure 3. Representation of surface vorticity by bound-vortex segments.

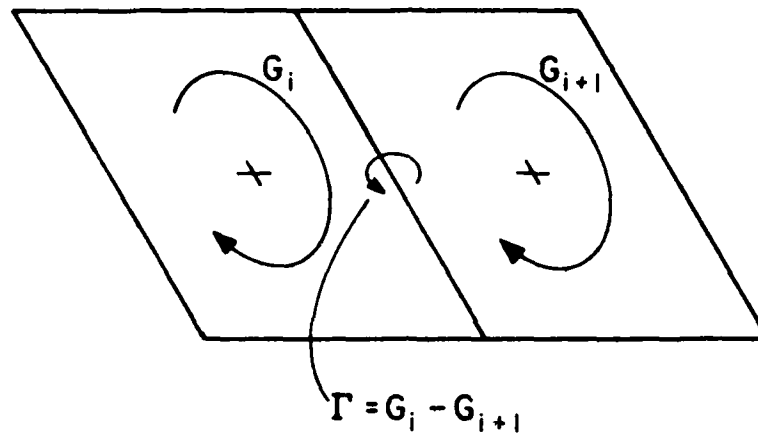


Figure 4. Definition of Loop and Branch circulations.

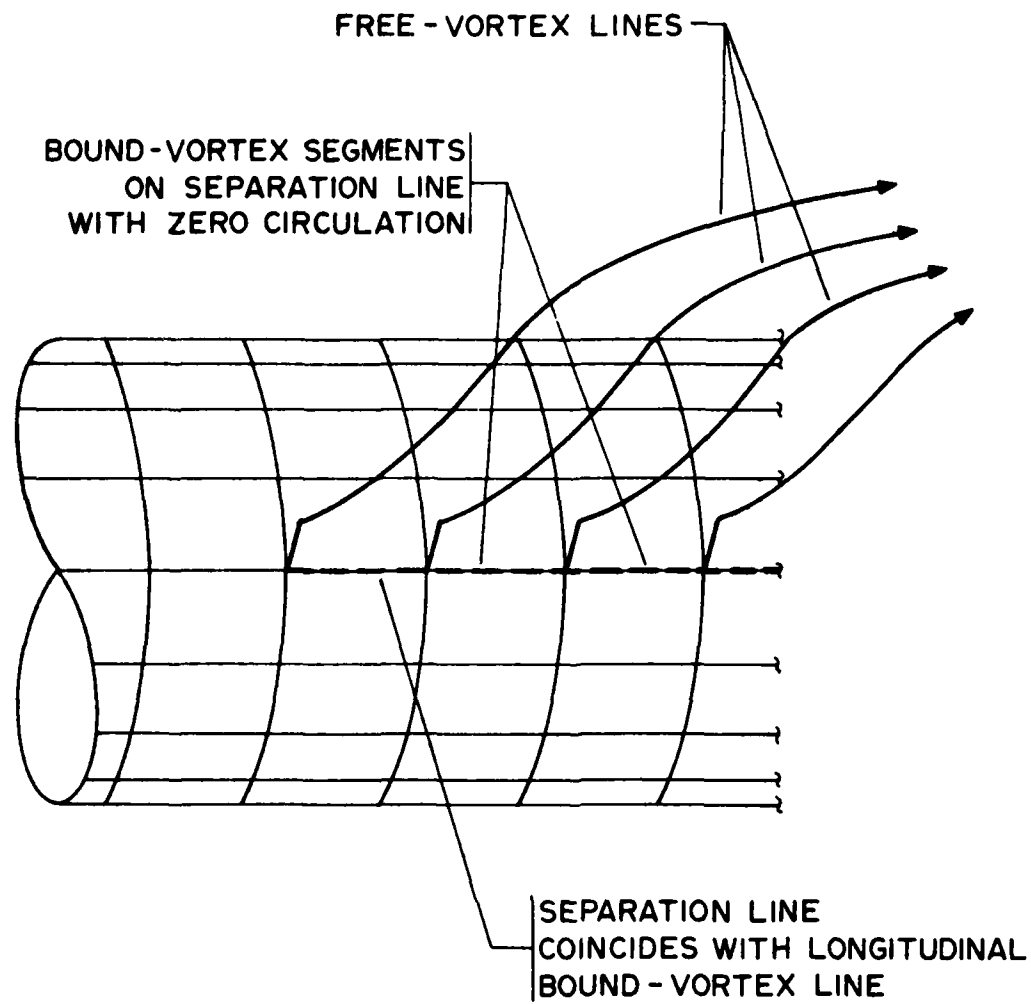


Figure 5. Schematic view of the attachment of a free- and bound-vortex lattice.



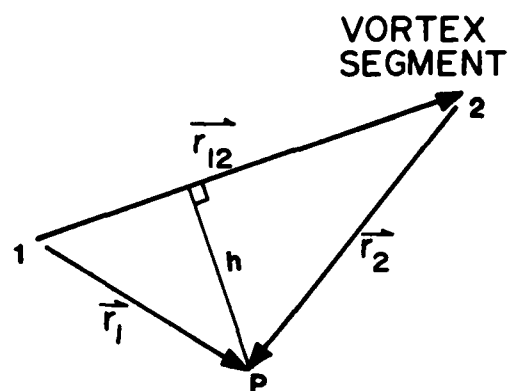


Figure 6. Definition sketch for Biot-Savart law velocity calculations.

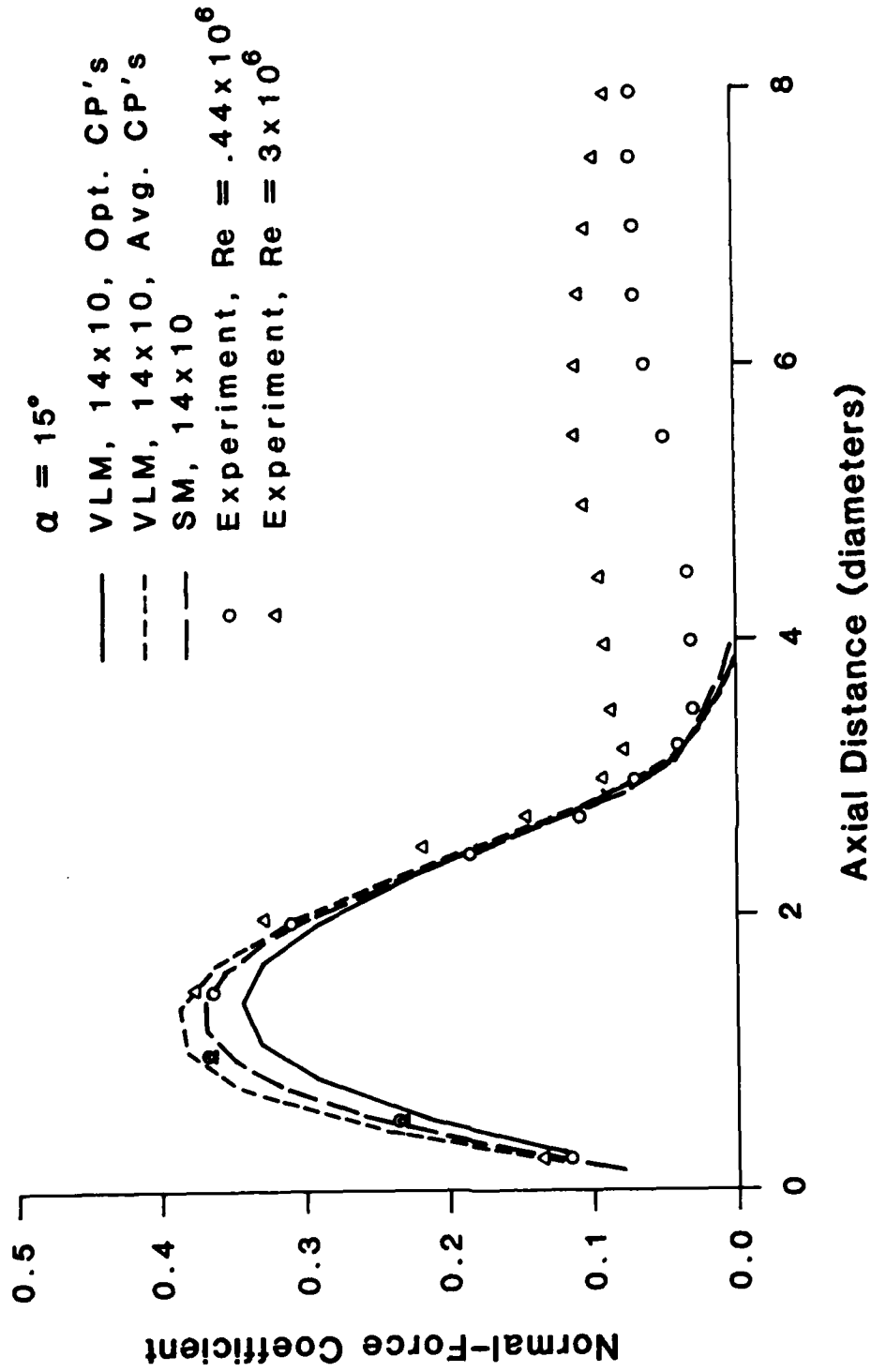


Figure 8. Effect of control point placement for  $\alpha = 15^\circ$ .

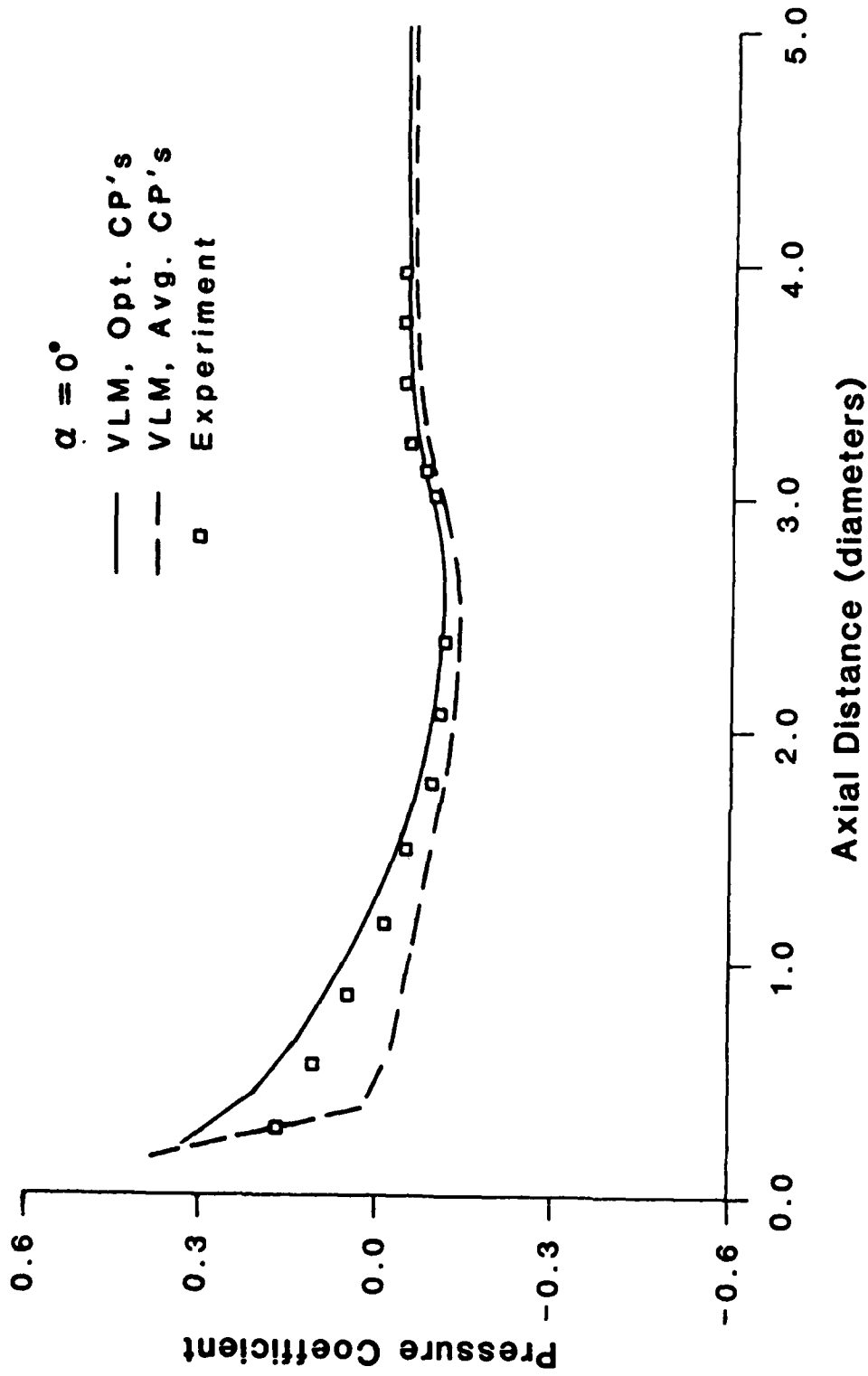


Figure 7. Effect of control point placement for  $\alpha = 0^\circ$ .

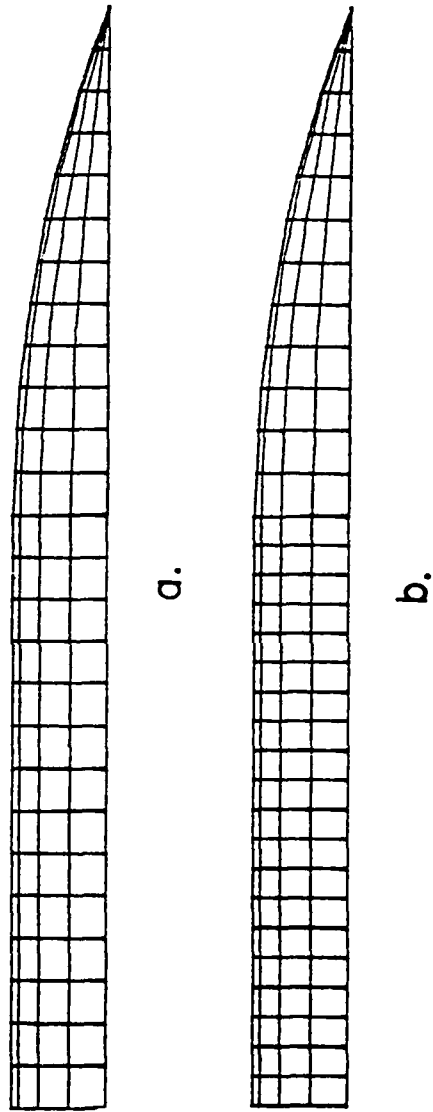


Figure 9. Planview of uniform and nonuniform lattices.

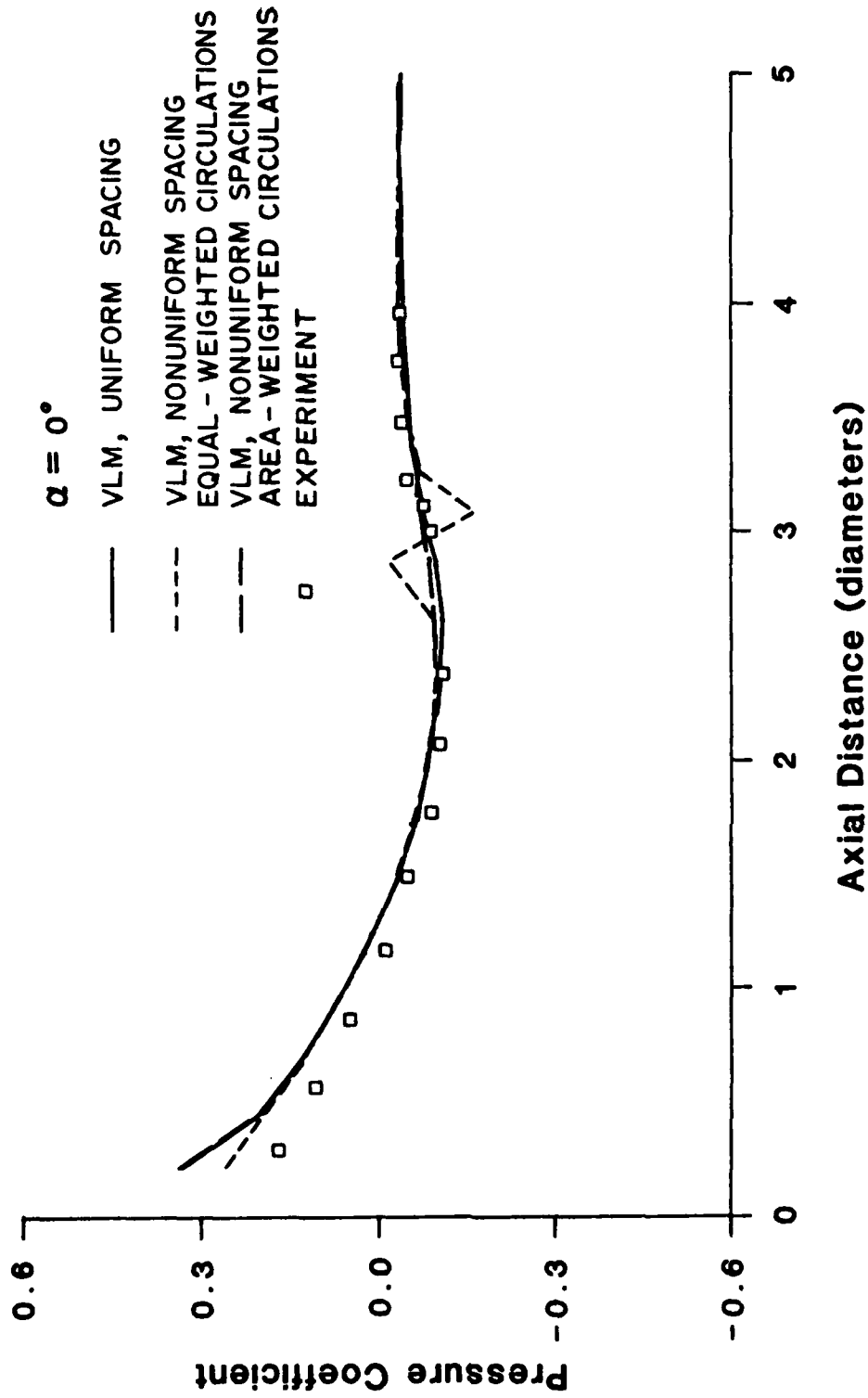


Figure 10. Effect of axial spacing and area-weighted circulations  
for  $\alpha = 0^\circ$ .

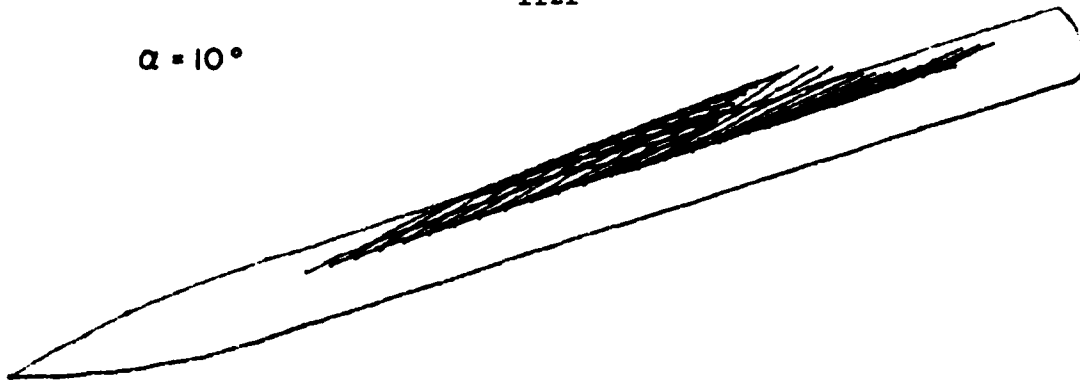
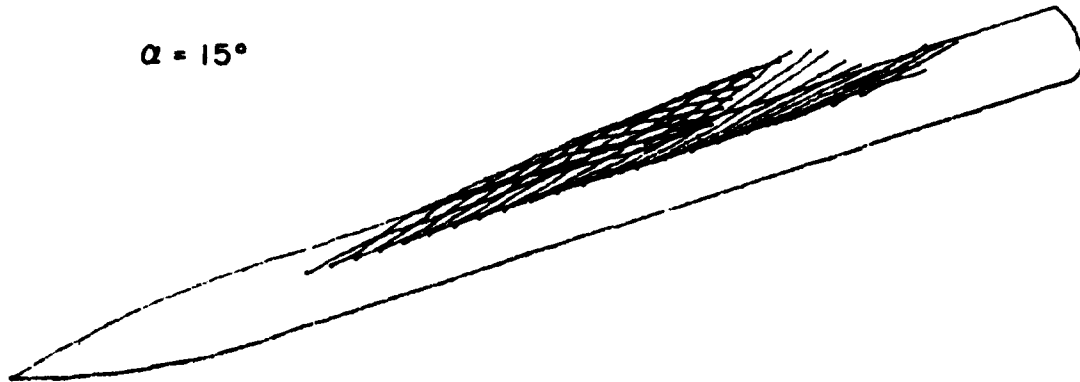
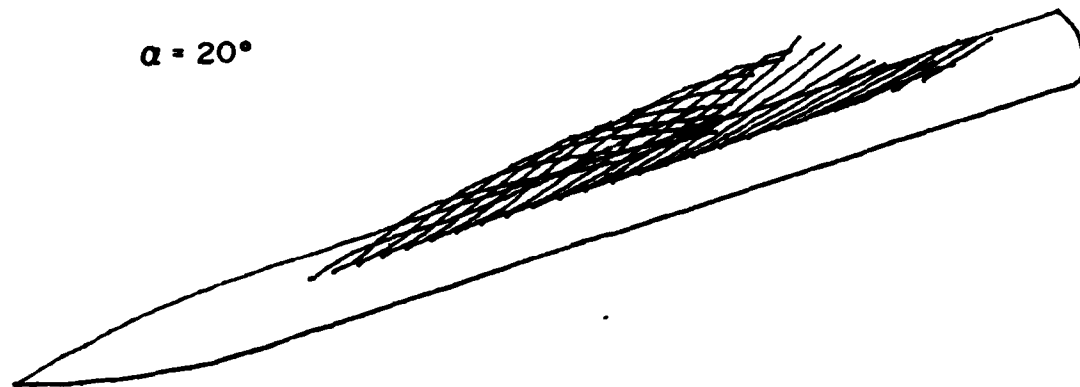
$\alpha = 10^\circ$  $\alpha = 15^\circ$  $\alpha = 20^\circ$ 

Figure 11. Perspective view of calculated wake shapes for  $\alpha = 10^\circ$ ,  $15^\circ$ ,  
and  $20^\circ$ .

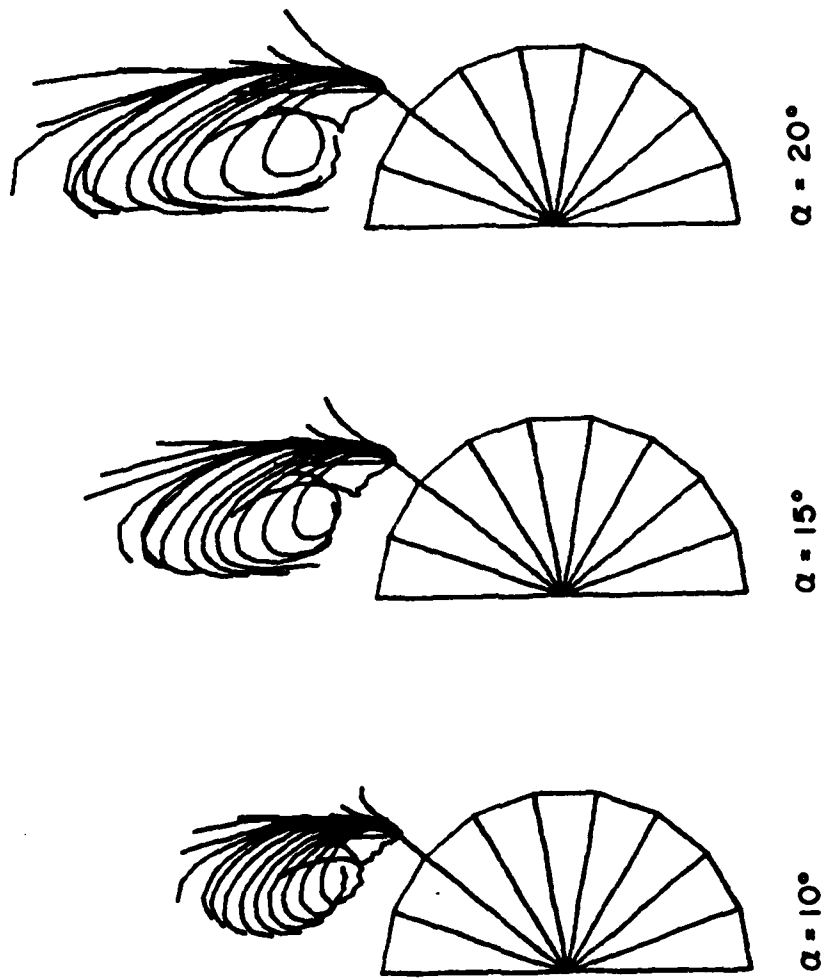
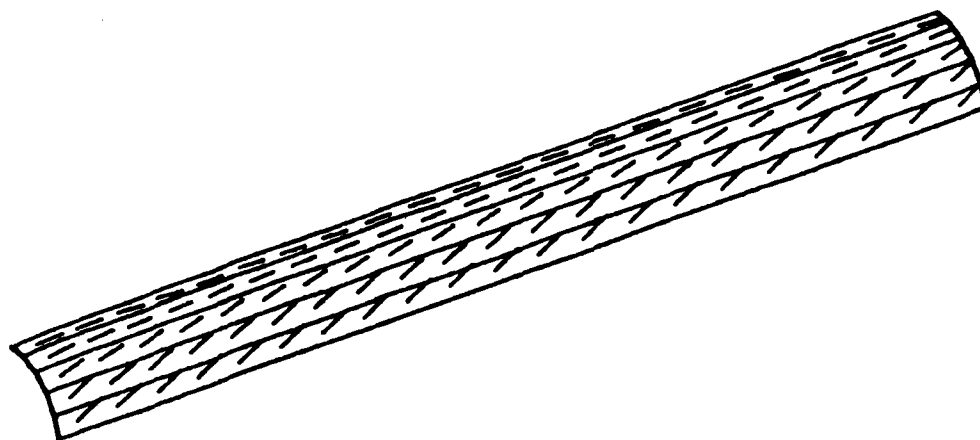
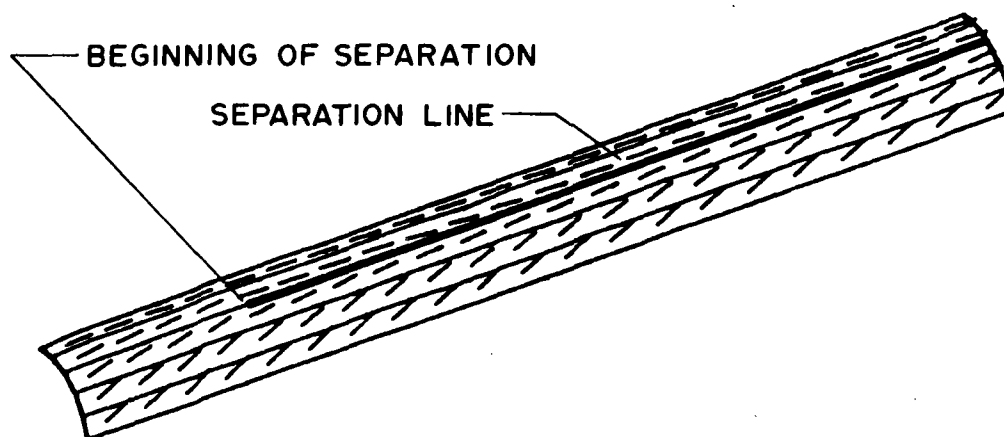


Figure 12. End view of calculated wake shapes for  $\alpha = 10^\circ$ ,  $15^\circ$ , and  $20^\circ$ .



ATTACHED FLOW



SEPARATED FLOW

Figure 13. Perspective view of surface velocity fields with and without separation.



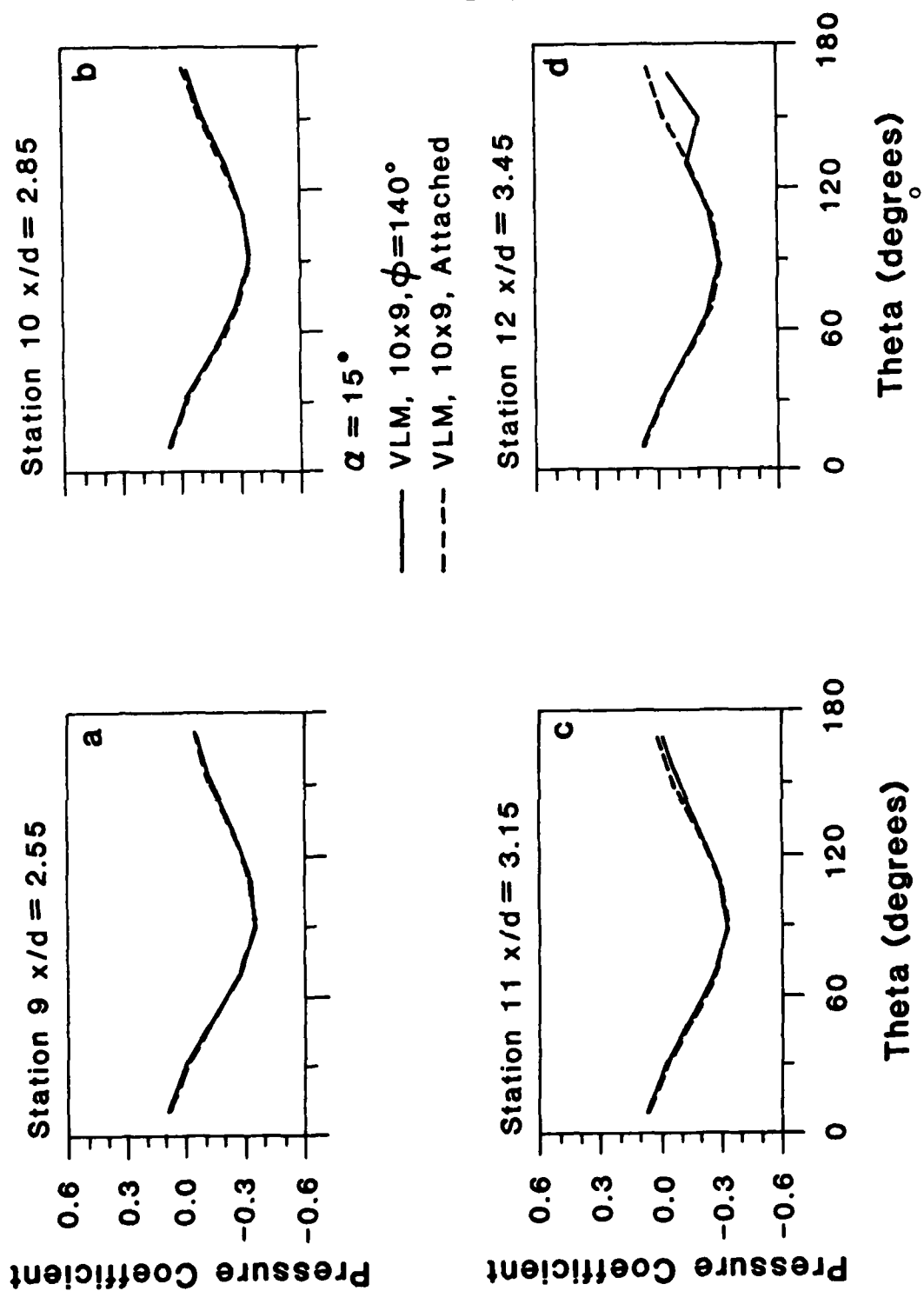
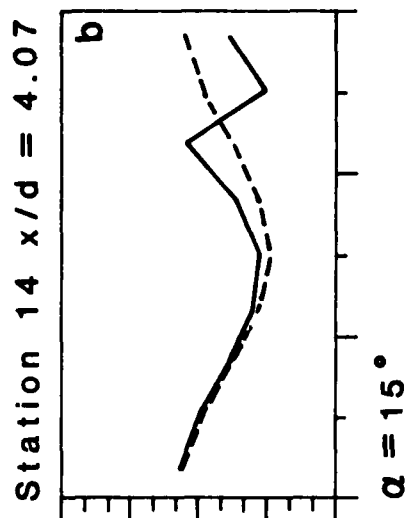
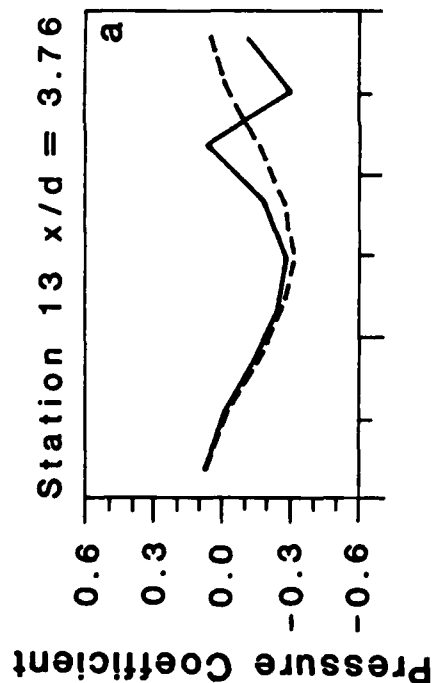
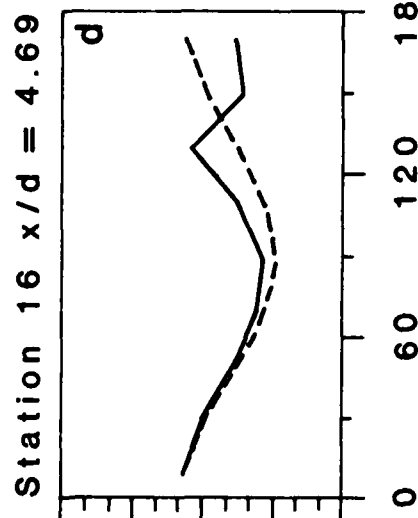
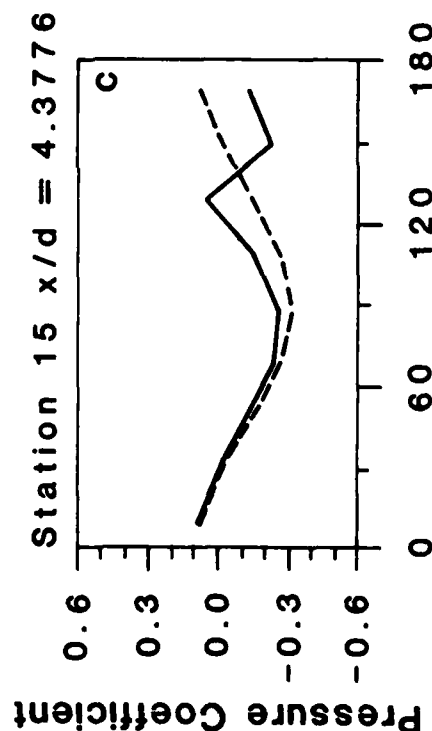


Figure 14. Comparison of separated pressure distributions for  $\alpha = 15^\circ$ , stations 9 through 16.



$\alpha = 15^\circ$

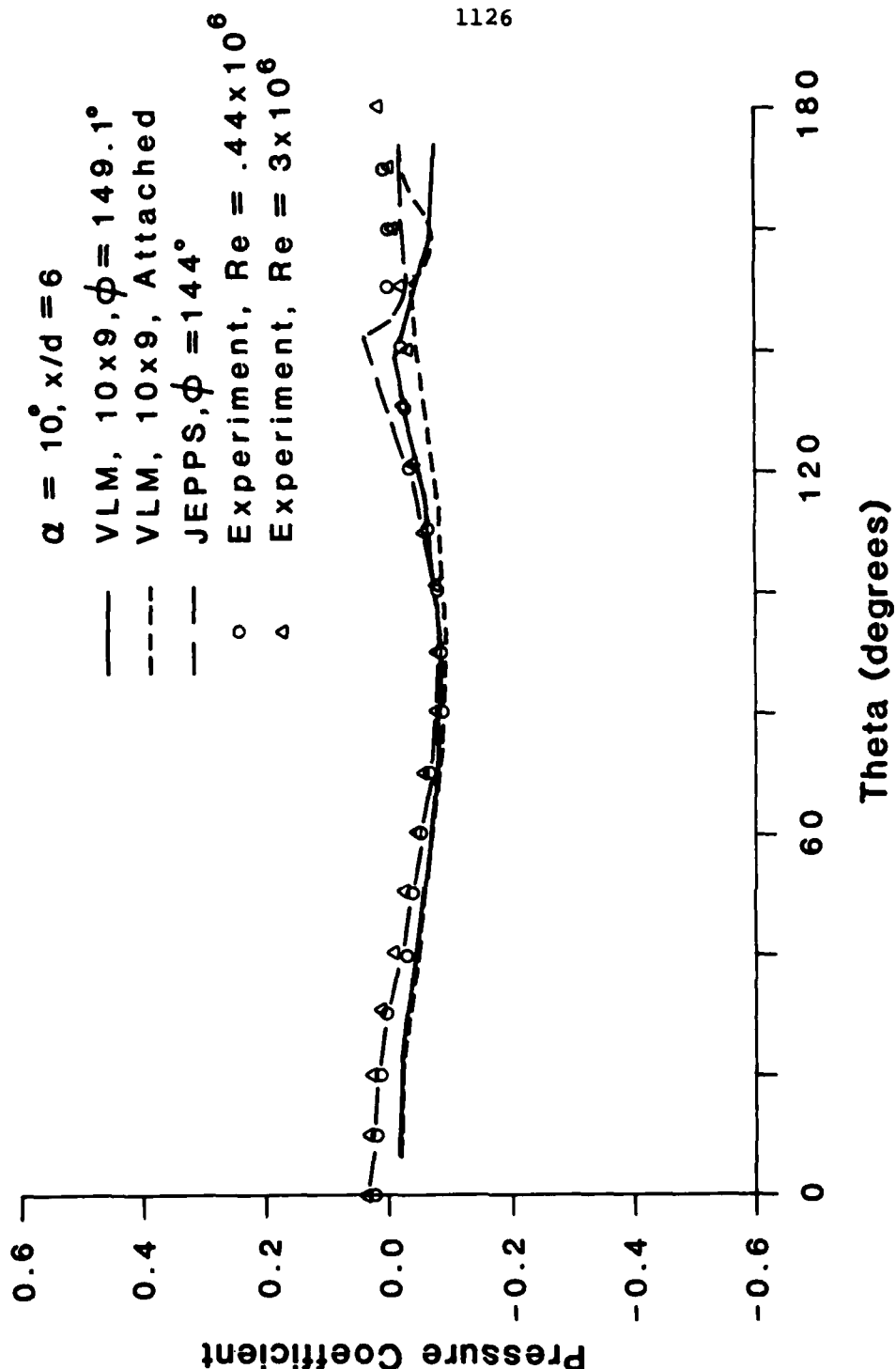
— VLM,  $10 \times 9$ ,  $\phi = 140^\circ$   
 --- VLM,  $10 \times 9$ , Attached



Theta (degrees)

Theta (degrees)

Figure 14. Cont'd.



1126

Figure 15. Comparison of calculated pressure distributions with experiments of Tinsling and Allen (1962) for  $\alpha = 10^\circ, x/d = 6$ .

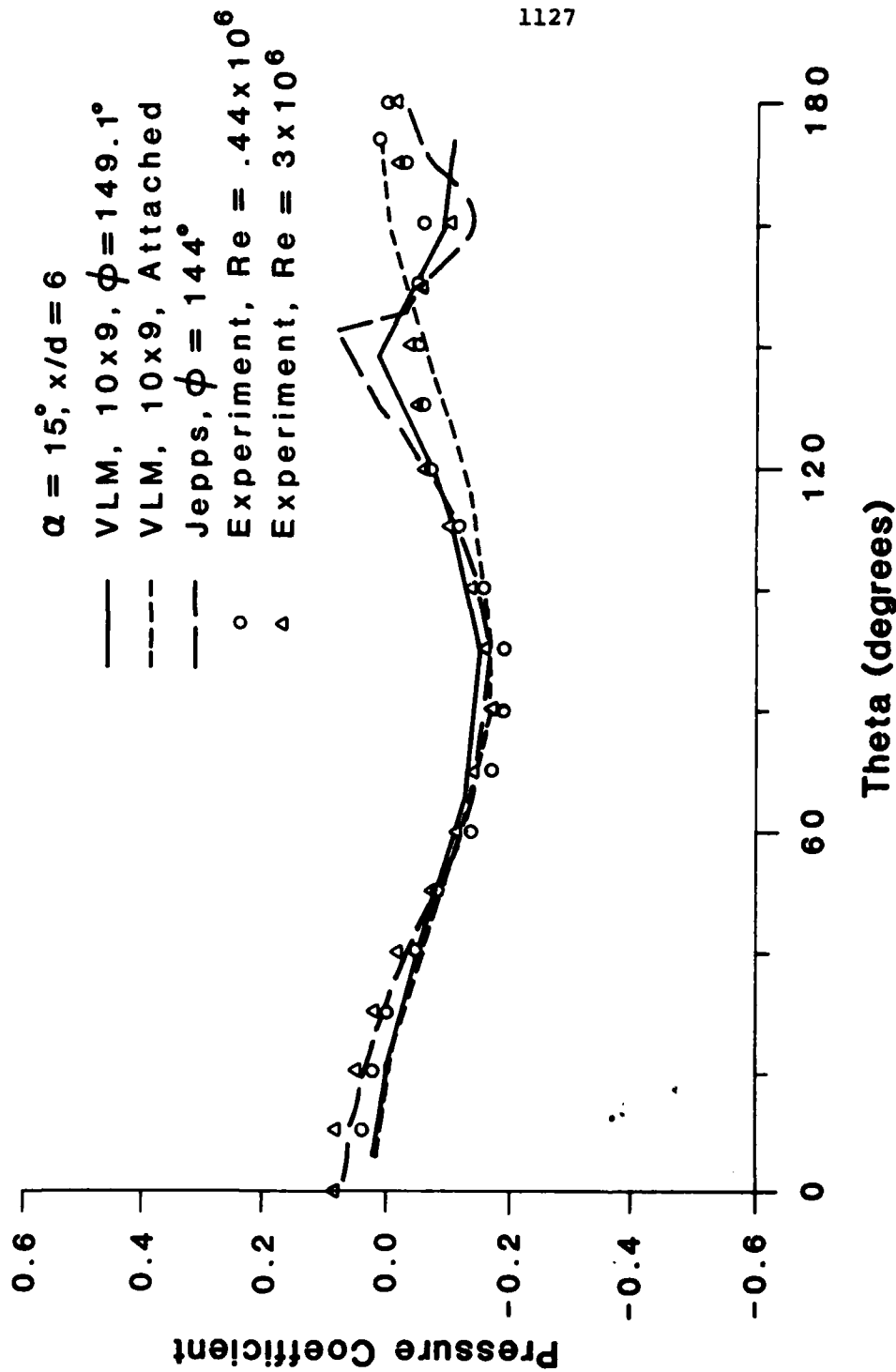


Figure 16. Comparison of calculated pressure distributions with experiments of Tinling and Allen (1962) for  $\alpha = 15^\circ$ ,  $x/d = 6$ .

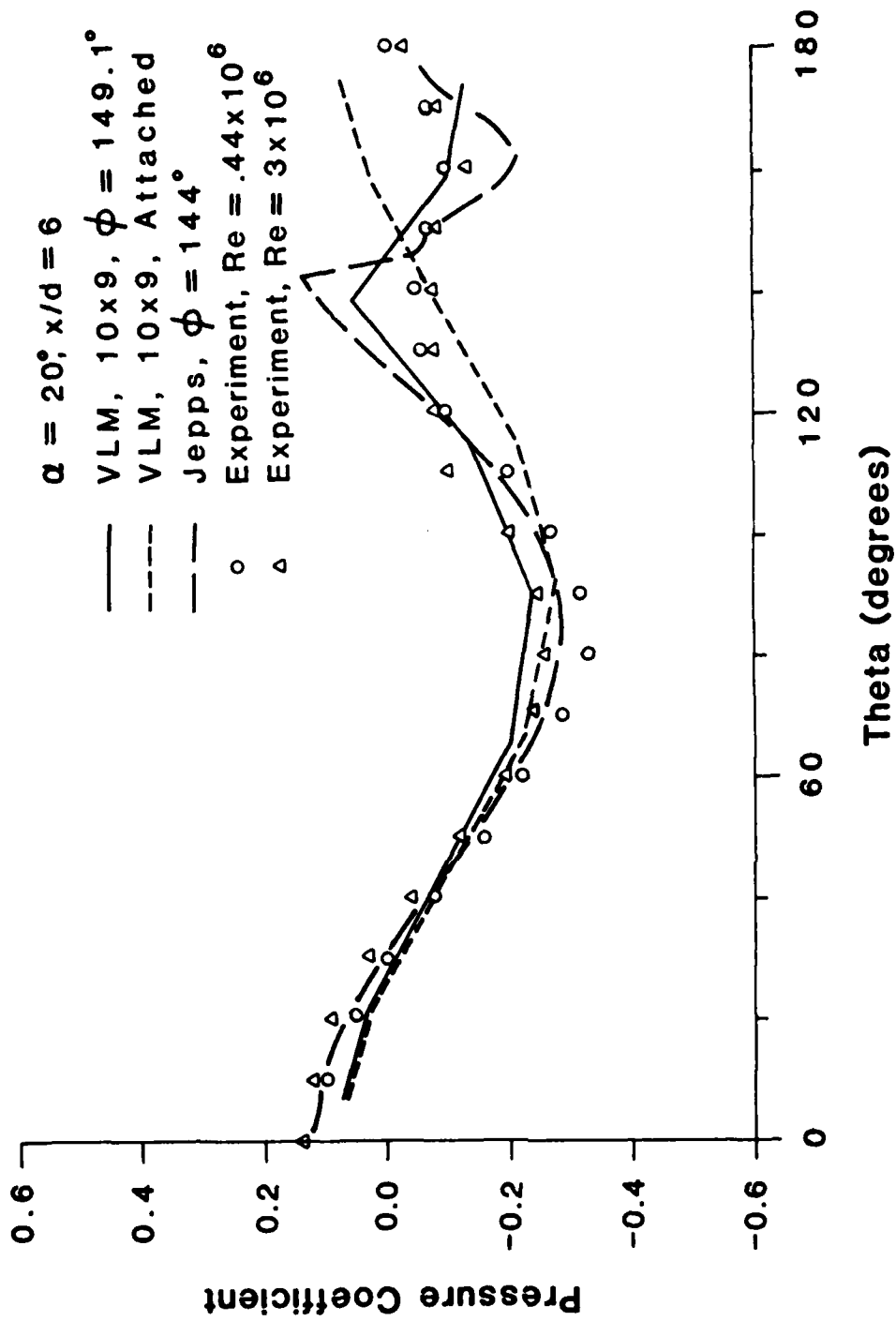


Figure 17. Comparison of calculated pressure distributions with experiments of Tinling and Allen (1962) for  $\alpha = 20^\circ, x/d = 6$ .

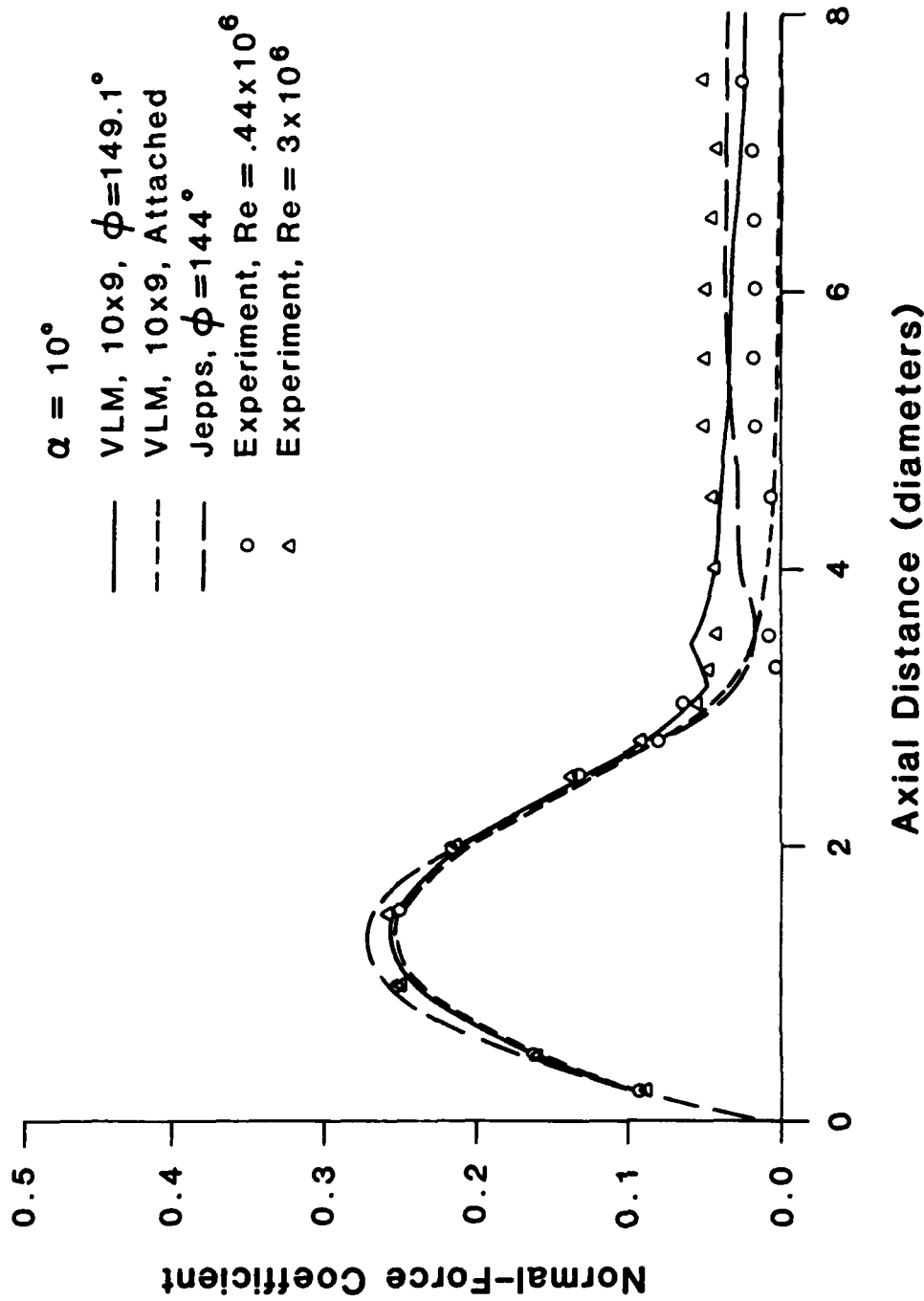


Figure 18. Comparison of calculated normal-force coefficient with experiments of Tinling and Allen (1962) for  $\alpha = 10^\circ$ .

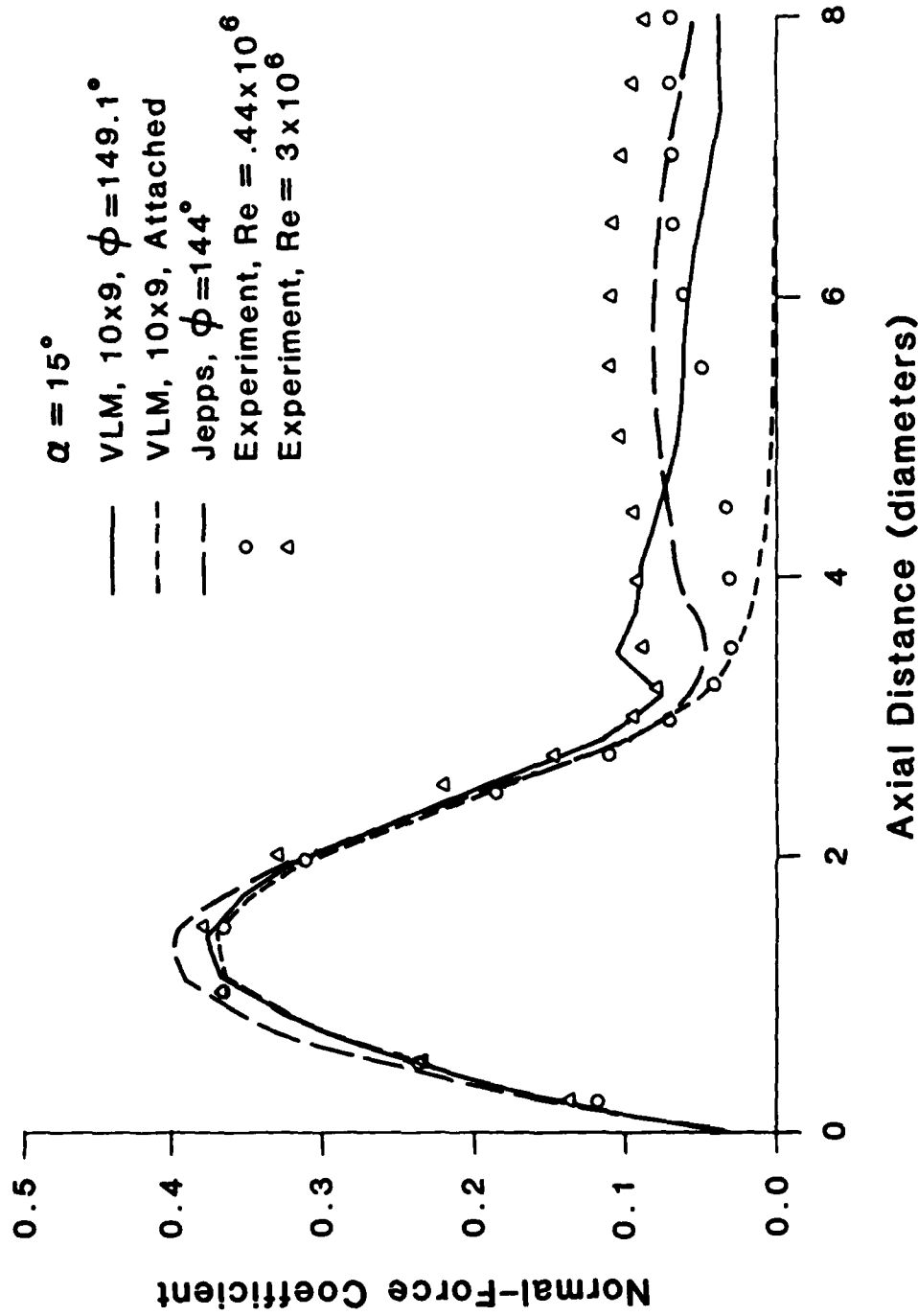


Figure 19. Comparison of calculated normal-force coefficient with experiments of Tinsling and Allen (1962) for  $\alpha = 15^\circ$ .

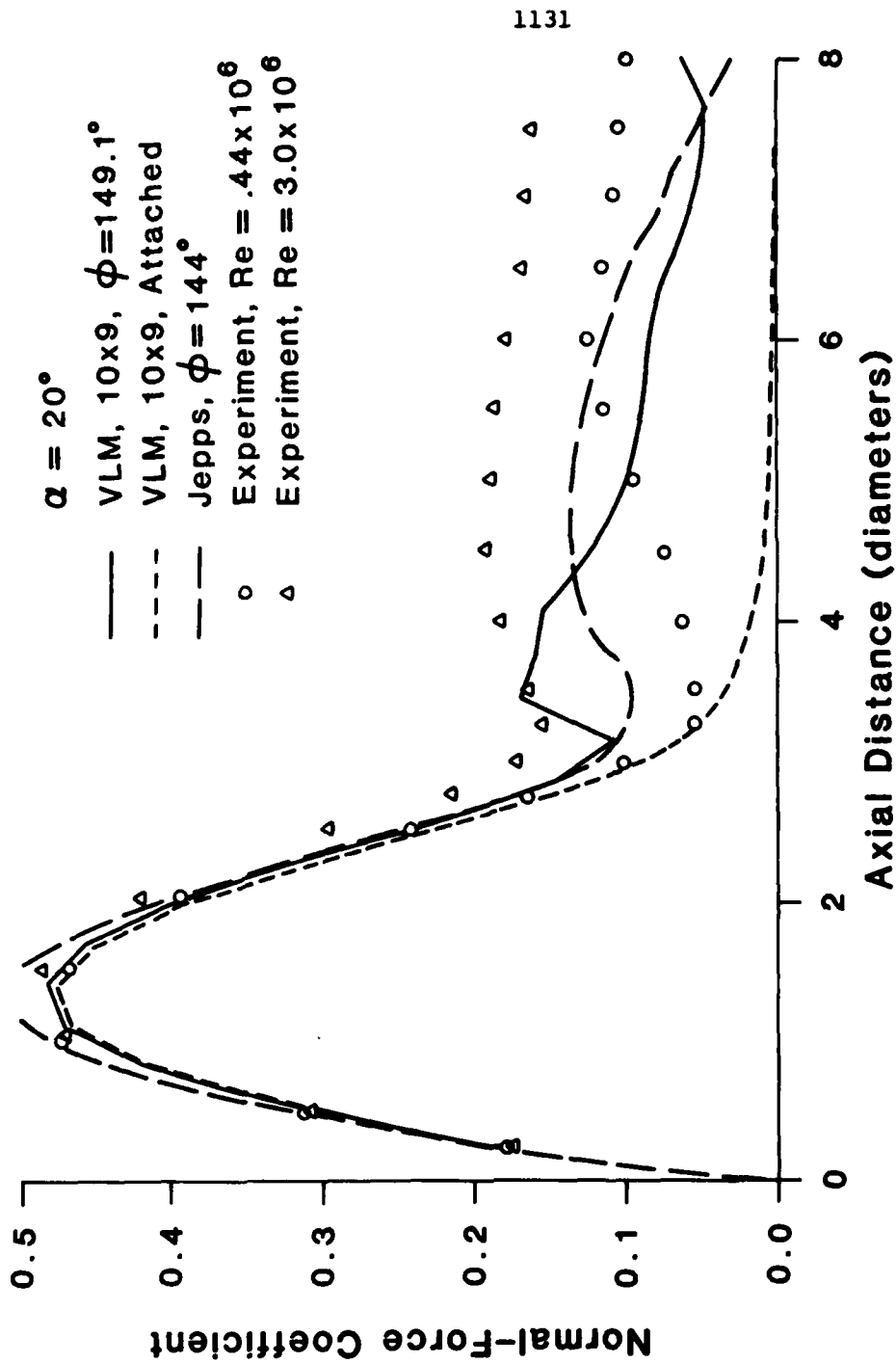


Figure 20. Comparison of calculated normal-force coefficient with experiments of Tinling and Allen (1962) for  $\alpha = 20^\circ$ .



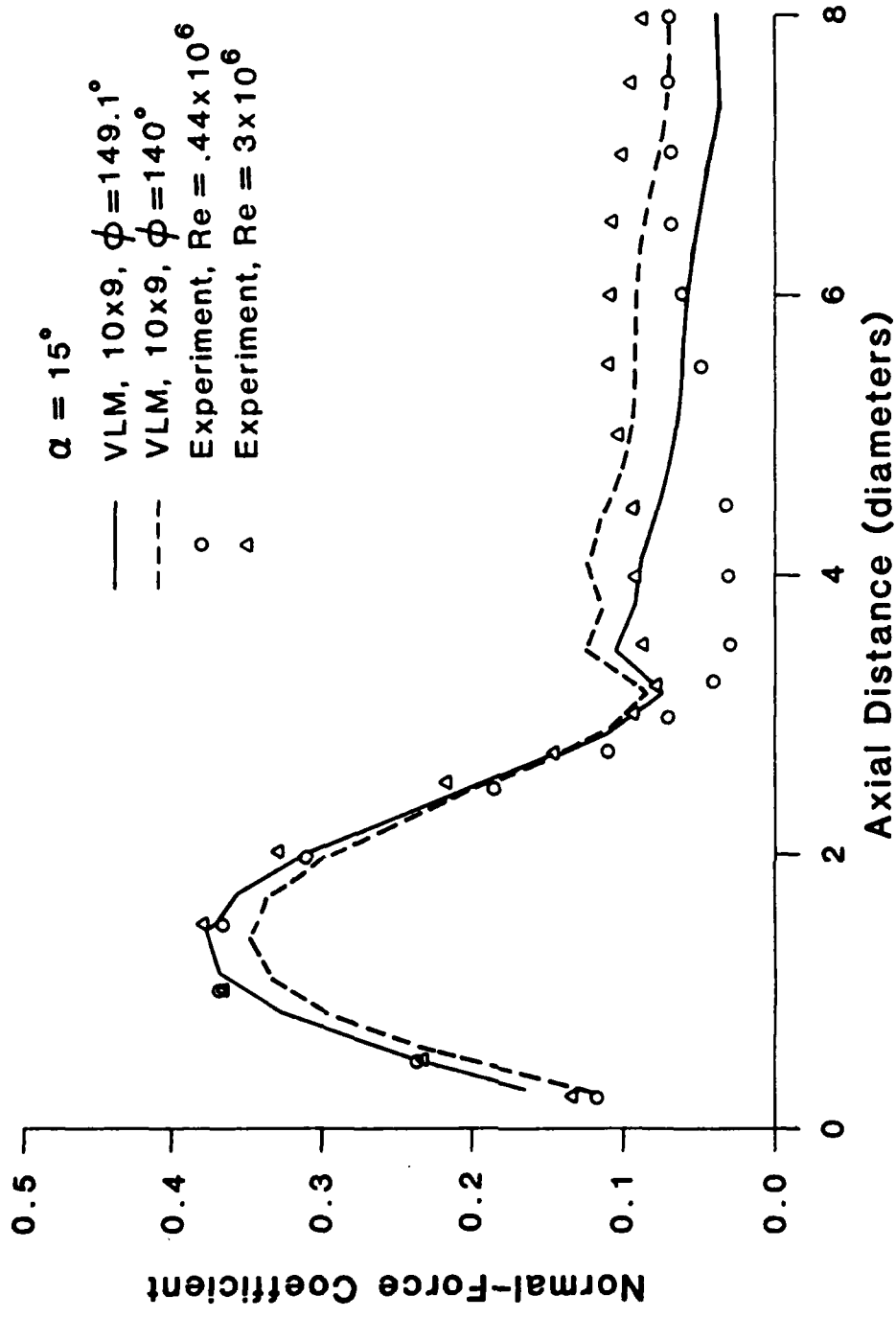


Figure 21. Comparison of calculated normal-force coefficient with experiments of Tinling and Allen (1962) for  $\alpha = 15^\circ$  with two different separation line angles.

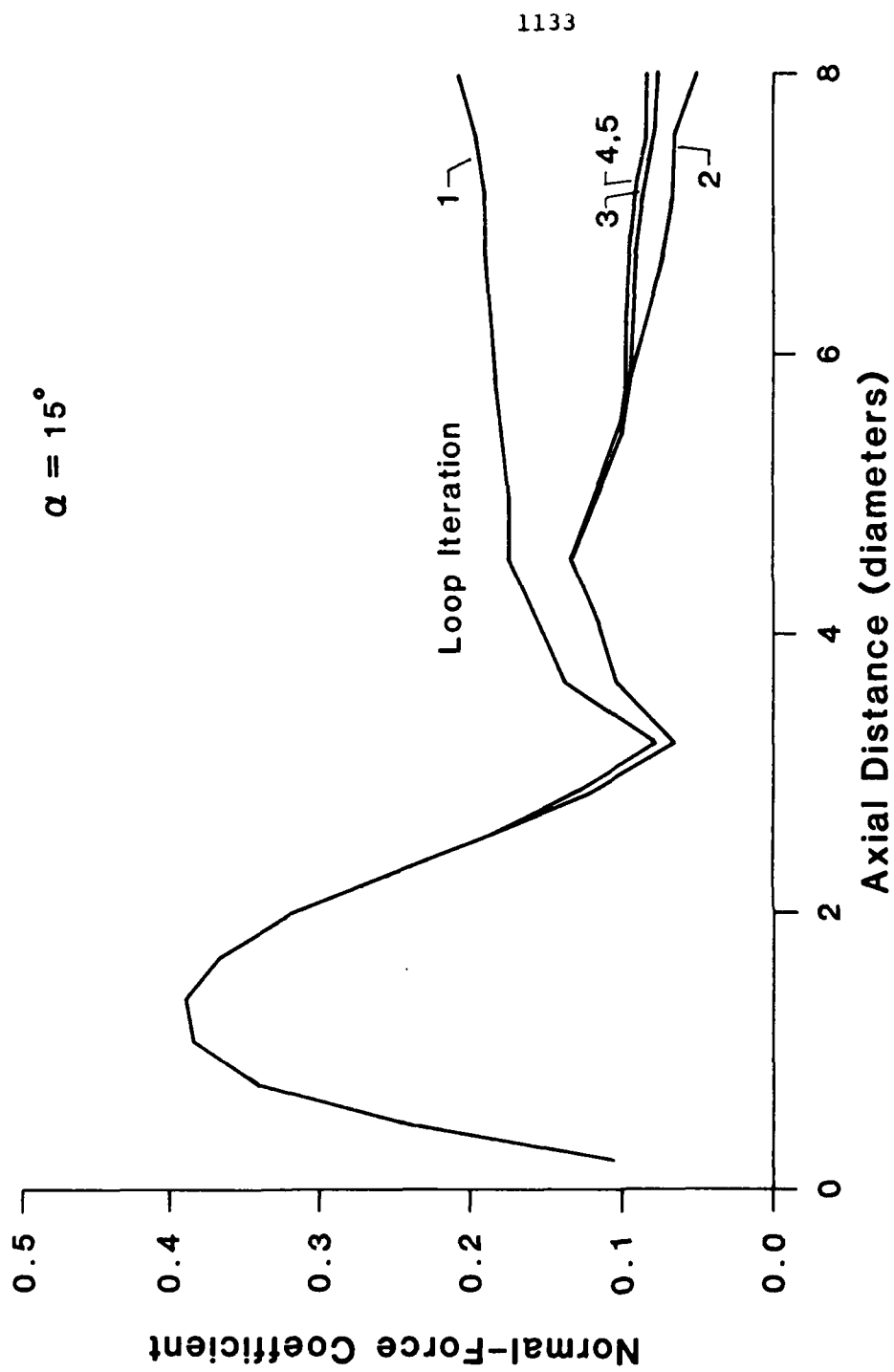


Figure 22. Convergence of calculated normal-force coefficient for  $\alpha = 15^\circ$ .

## Discussion

I. Tanaka (Osaka University)

What section does your Figure 12 signify? In this figure is the configuration of vortex filament closest to the section shown? What is the angle of the filament separating from the separation point? (The reason I am asking this is that the configuration is extremely important for pressure value.)

To the discussor, the configuration of the vortex sheet very close to the separation point is very important in calculating the pressure distribution over the wall because it has a very strong effect on pressure value. I would like to know the difference between the calculation presented here and the one with the vortex sheet shed from the same separation point tangentially. Also, I would welcome the comparison of these results with experiments, if any, in the pattern of vortex-rolling up motion (wake pattern with vortex motion).

## Author's Reply

D.F. Thrasher

The view in Figure 12 is a front view of all the wake lines separating from the body. That is, all the wake lines are collapsed onto the page and the diagram does not represent any one section of the body but rather all of them simultaneously.

On your second point, the configuration of the vortex sheet close to the body is indeed important in the resultant pressure and other calculated quantities. In this paper, all calculations were performed allowing the vortex sheet to leave the body normally. In fact, the sheet should leave tangentially (at least in the infinite Reynolds number limit). The only reason this was not done at this time was to circumvent numerical problems with the singular nature of vortex lines. At present, I am incorporating a scheme to allow the vortex lines to leave the body at any angle of choice.

# Investigation of Stern Flow Field by Boundary Layer Suction Technique

Ichiro Tanaka, Osaka University  
Toshio Suzuki, Osaka University

## 1. INTRODUCTION

As attention to the stern flow field has been intensified in these years, which is necessary for improvement of the propulsive efficiency of ship and estimation of the propeller exciting force as well as for study on cavitation of propeller, various measurements of characteristic quantities of the stern flow field have been done for a number of model ships. The optimum value of these quantities in relation to model ship forms can be obtained as the result of these measurements, but the question remains if the optimum value under the model ship condition could apply to the actual ship condition, because the law of correlation (scale effects) between them has not been fully clarified yet. In the meantime, due to the development of computers, accuracy of the numerical solution of the three-dimensional boundary layer equation has been improved, and numerous data on the scale effect has begun to be obtained. However, the behavior of the flow field within the thick boundary layer with three-dimensional separation vortices at the ship's stern has not been thoroughly investigated yet, so more studies would be necessary to make, e.g., an estimate of the wake distribution at the propeller plane. Although, attempts to investigate the scale effect experimentally are made with GEOSIM tests using large scale model ships and even the measurement on board of actual ship wake distributions are undertaken, the number of these experiments is so far still limited. (van Manen and Lap, 1958. Taniguchi and Fujita, 1970. Takahashi et al., 1971. Namimatsu et al., 1973. SR 107, 1973. Nilsson and Restad, 1976. Gadd, 1977. Fagerjord, 1978)

On the other hand, boundary layer suction technique is applicable to the purpose of making a boundary layer thickness thinner than as it is, i.e. same as actual ship in relative scale. This may be useful to the study of scale effect in wake distribution. (Kowalski, 1965. Tagori et al., 1968. Huse, 1977)

In view of the above-mentioned situation, authors made the investigation, as one of the means to get data for the scale effect of the stern flow field, on the change of the stern flow velocity distribution and the change of the propulsive characteristics induced thereby, when the boundary layer suction is applied at the stern. This

report is the summary of the results of the experiment and some theoretically calculated results.

## 2. MODEL SHIP AND APPARATUS OF EXPERIMENT

The model ship employed in the experiment is of the lines shown in figure 1. Her principal dimensions are shown in table 1. The model is the mother form of a research project done in Japan called SR 159. There is no actual ship corresponding to this lines. The fact that this model ship showed an unstable flow phenomena (Watanabe, 1969. Seo et al., 1978) during the self-propulsion test at 65% loaded condition was one of the reasons to adopt it as the model ship for the present research. The outline of the devices for boundary layer suction is illustrated in figure 2. Suction holes of 3 mm diameter with eight rows are set along the frame lines between square station (S.S.) 2 1/2 and 2 1/4 so that they would not directly affect the three-dimensional separation along the stern bilges which seems to occur at about S.S. 1. Items of investigation include; the measurement of velocity distribution along the frame line immediately abaft the suction holes; velocity distribution along a streamline at ship's side; wake distribution at the propeller plane; and the propeller-load variation test. Change of every items due to change of suction rate was investigated at two different rates. Experiments are all made at 65% loaded condition. Measurements of the flow field were carried out without propeller but with rudder.

## 3. ON BOUNDARY LAYER SUCTION AND SCALE EFFECT

In the past, the boundary layer suction technique has been employed as one of the means of boundary layer control for the purpose of preventing the separation of flow. But, in the present experiment, where simulation of flow field corresponding to higher Reynolds number is aimed at, the way of application of the boundary layer suction differs naturally from that in usual cases, and it must be noted whether the flow field itself could be simulated or not by the technique. If a flow in a fluid with very small coefficient of viscosity for the same ship length and velocity is considered as the flow field corresponding to higher Reynolds number, the difference in Reynolds number is presented in the equation of motion as the difference of the shearing stress. Therefore, in the stern flow field where pressure gradient takes large positive value and the proportion of the importance of the shearing stress to the pressure gradient is relatively small, the method of investigation to measure the flow abaft the suction devices by changing the boundary layer thickness by way of the boundary layer suction technique is considered to be effective means. Taking these consideration thus into account, boundary layer suction in the vicinity of S.S. 2 1/2 would be effective for flow at ship's side because the pressure appears minimum around S.S. 2 1/4. But, for bottom flow it may not work so good, because the flow turns

around the bilge where the pressure takes the minimum value, after travelling some distance from the point of suction. This situation may bring some disturbing effects of shearing stress term on Reynolds number similarity under suction. However, if the suction devices are placed very close to the bilge to relieve this defect, they might directly affect the three-dimensional separation that was generated in the vicinity of the bilge. Therefore, for investigation of the bottom flow, the suction devices were also placed at the same square station in this series of experiment.

The following consideration was made to determine the flow rate of suction. Assuming that the potential velocity at the boundary layer edge does not vary with the size of ship, a comparison is made between Sasajima-Tanaka's and Tanaka's methods for the scale effect of the flow field. (Sasajima and Tanaka, 1966. Sasajima et al., 1966. Tanaka, 1979) According to the former method, both the displacement thickness  $\delta^*$  and the momentum thickness  $\theta$  at a certain location are contracted altogether proportionally to the value of the frictional resistance coefficient  $C_F$ , as only the thickness of boundary layer is contracted proportionally to the value of  $C_F$ . On the other hand, if Tanaka's method is applied, and if specifically his upper bound ( $\sqrt{\quad}$ ) is adopted, the contraction ratio in the direction of the thickness of boundary layer becomes  $\sqrt{C_F}$ . But, simultaneously the velocity defect ( $U-u$ ) is also contracted proportionally to  $\sqrt{C_F}$ . Consequently,  $\delta^*$  is contracted proportionally to  $C_F$  which is quite similar to the former method. Therefore, the authors determined, as first approximation, the flow rate of the boundary layer suction is so adjusted that the ratio of  $\delta^*$  before and after suction equals to the ratio of  $C_F$ . Values of Reynolds number etc. calculated back from the flow rate of suction at the experiments are shown in table 2. As is shown, two values of suction quantity were adopted in the experiment; one is the case where  $\delta^*$  is a little bigger than the assumed actual ship ( $L=240$  m) and the other is the case where  $\delta^*$  is a little smaller than that. The former is written as P-1 and the latter P-3.

#### 4. RESULTS OF EXPERIMENTS AND THEIR DISCUSSION

In this chapter the results of measurements are described comparing with the results of three-dimensional turbulent boundary layer calculation. Calculation was made by Tanaka-Himeno's method (Tanaka and Himeno, 1975) for the cases without suction and with suction. In calculating the case with suction, potential flow is assumed to be the same as the case without suction, but the initial values of velocity distribution are changed following measured results. An empirical constant used in an auxiliary equation was also modified corresponding to both cases.

The points of measurement of the velocity distribution and the potential streamline calculated by Hess-Smith's method are also presented in figure 1. The velocity distribution within the boundary layer measurement at S.S. 2 which is just abaft the location of suction is shown in figure 3. It clearly demonstrates that due to absence of

low velocity fluid that is sucked away by the suction devices, the profile of the velocity distribution becomes steeper and the displacement thickness decreases. This tendency is plausible from the standpoint of variation of shape factor  $H$ , even if it is qualitatively. Figure 4 shows the value of displacement thickness  $\delta^*$  etc. calculated from these velocity distribution curves. The measured values vary reasonably with the change of the suction rate. Their change along the girth also shows good conformity with the results of calculation. Next, change of  $\theta$ ,  $\delta^*$  and  $H$  along a streamline are shown in figure 5. Figure 6 shows the comparison of momentum thickness between measured and calculated values. From this the deviation between measured and calculated values seems to be greater in ship condition, where it is to be anticipated that the calculated lines are in the middle of the measured points of P-1 and P-3. The reason of this discrepancy may be due to the effect of shearing stress term, which is not completely simulated to the actual ship's condition by boundary layer suction technique. The results of calculation along the streamlines at the bottom part are shown in figure 7. However, because the effect of three-dimensional separation is not taken into account in this calculation, obtained values may deviate from the actual velocity distribution. Figure 8 presents the change of wake distribution at the propeller plane. It shows that due to the effect of suction, the distribution region of the wake is gradually getting thinner and the plateau-like portion of the wake is shifting downward slightly. This trend agrees with that of the actual ship test conducted with SR 107, another project done in Japan under the sponsorship of Shipbuilding Research Association of Japan. Figure 9 presents the comparison of the wake distribution of the model ship with the boundary layer suction to that for actual ship estimated by upper bound value of Tanaka's method starting from the model condition without suction. Though the shapes of the curves show good conformity, the measured values at the plateau-like portion are not affected by suction and tend to follow the results obtained by Sasajima-Tanaka's method rather than Tanaka's. With regard to the scale effect of the mass of fluid that is entrained into this plateau-like portion of the wake, much is left to further study.

Finally as an example of application, an investigation is conducted on how the unstable phenomenon that occurs at the propeller-load changing test would be affected by the boundary layer suction. This phenomenon seems to occur for unusually full ship models under particular circumstances. For our particular model, this occurs at 65% loaded condition at some range of propeller load factor. The results of experiments are shown in figure 10. The amplitude of fluctuation of the wake fraction decreases according to the increase of the flow rate of suction. Ranges where the fluctuation occurs are also different according to the suction rate. These results suggest that the scaling law of wake fraction is very complicated for such models, so it is extremely important to know the inflow velocity distribution to propeller and its stableness in relation to model scale. From the figure one might also say that chances for occurrence of the unstable phenomena with large scale models would be less and very rare with

actual ships.

## 5. CONCLUSION

The results obtained in the investigation are summarized as follows :

- 1) The method of investigation of the stern flow field by way of the boundary layer suction is supposed to be effective for estimating the wake distributoion at the propeller plane of actual ships. In doing such investigation, the method to make the ratio of displacement thicknesses between model and ship equal to the ratio of frictional resistance coefficients seems to hold good as the first approximation for determining the flow rate of suction.
- 2) Using this method, the scale effect of the unstable phenomena at the self-propulsion test was also investigated. As its result, the model ship with suction shows trend to have less unstable characteristics. So it may be concluded that the actual ships are much stable than models.

The authors wish to express their gratitude to Messrs. Funaki, Shimamoto, Nakajima and Okajima for carrying out of experiment. The work was supported by the Grant-in-Aid for Scientific Research of the Ministry of Education, Science and Culture.

## References

- Fagerjord, O. (1978). Experience from Stern Wake Measurements during Sea Trial, Norwegian Maritime Research 6,37.
- Gadd, G.E. (1977). Scale Effect on Stern Separation and Resistance of Full Hull Form, The Naval Archt. 6,391.
- Huse, E. (1977). Bilge Vortex Scale Effect, Norwegian Maritime Research 5,9.
- Kowalski, T. (1965). Boundary Layer Suction Influence on Scale Effects of Self-Propelled Models, I.N.A. 107,273.
- van Manen, J.D., and A.J.W. Lap (1958). Scale Effect Experiments on Victory Ship and Models (2nd Report), I.N.A. 100,374.
- Namimatsu, M., K. Muraoka, S. Yamashita, and H. Kushimoto (1973). Wake Distribution of Ship and Model on Full Ship Form, J. Soc. Naval Architects Japan 134, 65.
- Nilsson, G., and K. Restad (1976). Problems in Full Scale Propulsion from a Shipbuilder's Viewpoint, I.S.P. 23,342.
- Sasajima, H., and I. Tanaka (1966). On the Estimation of Wake of Ships, Proc. 11th ITTC 140.
- Sasajima, H., I.Tanaka, and T.Suzuki (1966). Wake Distribution of Full Ships, J. Soc. Naval Architects Japan 120,1.
- Seo, T., Y. Nagashima, M. Sudo, I. Ashidate, R. Fujimoto, and H. Onogi (1978). Experimental Studies on Scale Effect of unstable Flow around the Stern, J.Soc. Naval Architects Japan 144,21.
- SR 107 Committee (1973). Investigation into the Speed Measurement and



- Improvement of Accuracy in Powering of Full Ships, Report of the Shipbuilding Research Association of Japan 73,1.
- Tagori, T., K.Masunaga, H.Okamoto, and N.Baba (1968). An Experimental study on the Stern Bilge Vortices of Full Hull Form, J. Soc. Naval Architects Japan 123,49.
- Takahashi, H., T. Ueda, M. Nakato, Y. Yamazaki, M. Ogura, K. Yokoo, H. Tanaka, and S. Omata (1971). Measurement of Velocity Distribution ahead the Propeller Disk of the Ship, J. Soc. Naval Architects West Japan 42,153.
- Tanaka, I. (1979). Scale Effects on Wake Distribution and Viscos Pressure Resistance of Ships, J. Soc. Naval Architects Japan 146,53.
- Tanaka, I., and Y. Himeno (1975). First Order Approximation to Three-Dimensional Turbulent Boundary Layer and Its Application to Model-Ship Correlation, J. Soc. Naval Architects Japan 138,63.
- Taniguchi, K., and T. Fujita (1970). Comparison of Velocity Distribution in the Boundary Layer between Ship and Model, J. Soc. Naval Architects Japan 127,1.
- Watanabe, K. (1969). Unstable Phenomenon in the Self-Propulsion Tests of Full Ship Form Models, J. Soc. Naval Architects Japan 126,45.

Table 1 Principal Dimensions of Model

L	B	d	C <sub>B</sub>
4.000	0.6667	0.2416	0.802
l <sub>cb</sub> = 1.48 % Lpp fore		Normal Bow	

Table 2 Effective Reynolds No., Ship Length and Ratio of  $C_f$ ,  $\delta^*$ ,  $\delta$

Pumps	Suct. Rate	Ratio (Cal.)		Effective	
		$\delta$	$\delta^* \& C_F$	Rn	Lpp
0	0 l/s	(1.0)	1.0	$4.0 \times 10^6$	4 m
1	5.8	(0.86)	0.62	$1.5 \times 10^8$	46
3	15.1	(0.68)	0.34	$4.1 \times 10^{10}$	> 400
Ship	—	(0.68)	0.45	$1.8 \times 10^9$	240

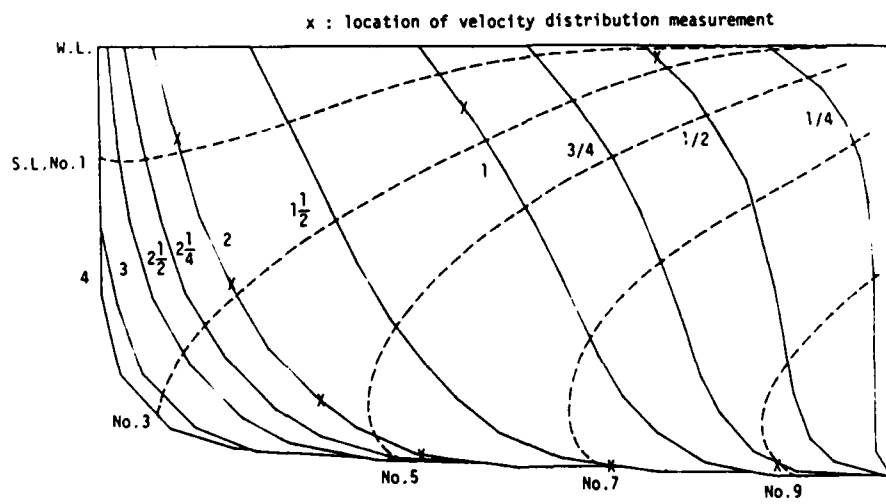


Figure 1 Body Plan and Streamlines of Potential Flow

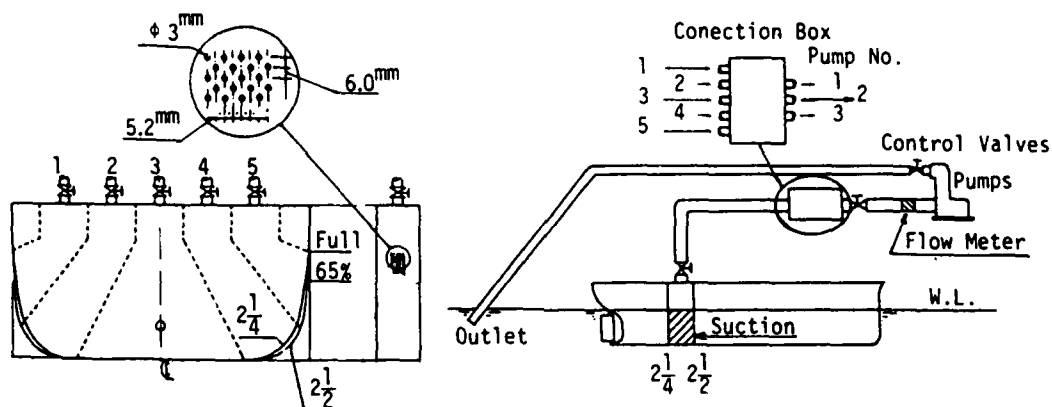


Figure 2 Arrangement of Boundary Layer Suction Device

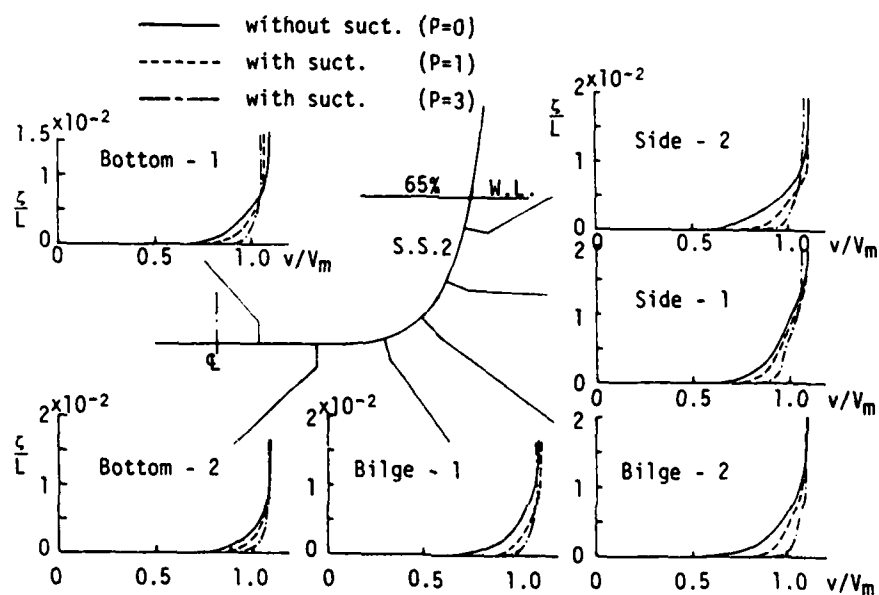


Figure 3 Measured Velocity Distributions with and without Suction at S.S.2

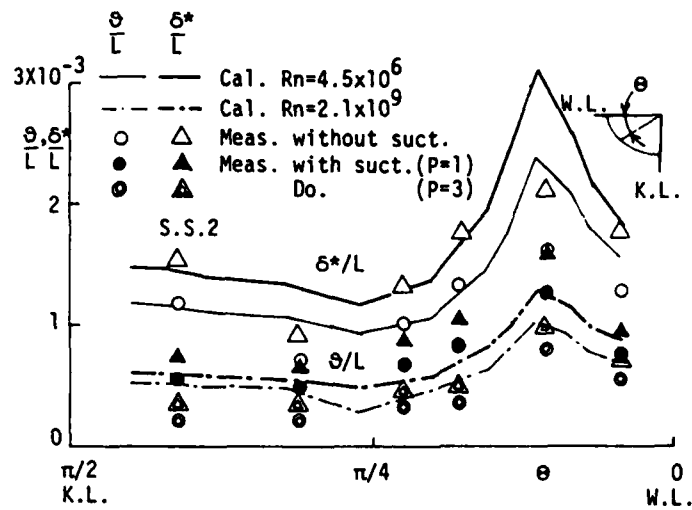


Figure 4 Calculated and Measured Displacement Thickness and Momentum Thickness at S.S.2

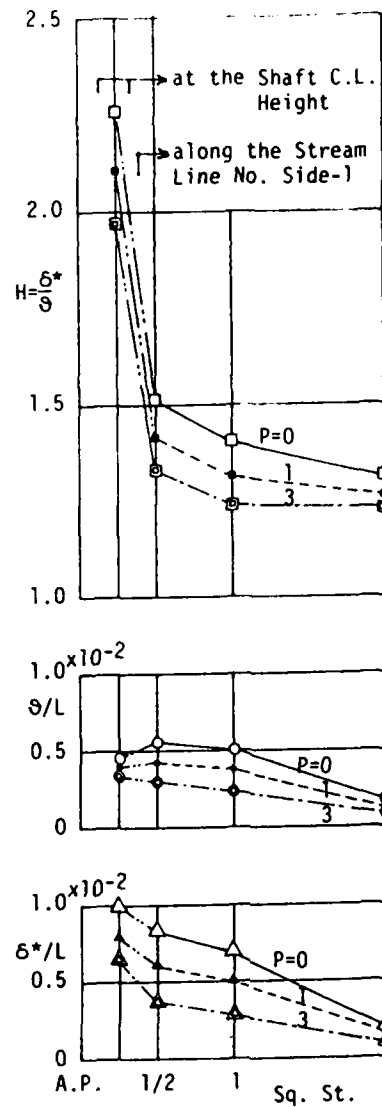


Figure 5 Measured Results of Displacement Thickness, Momentum Thickness and Shape Factor along the Streamline No. Side-1

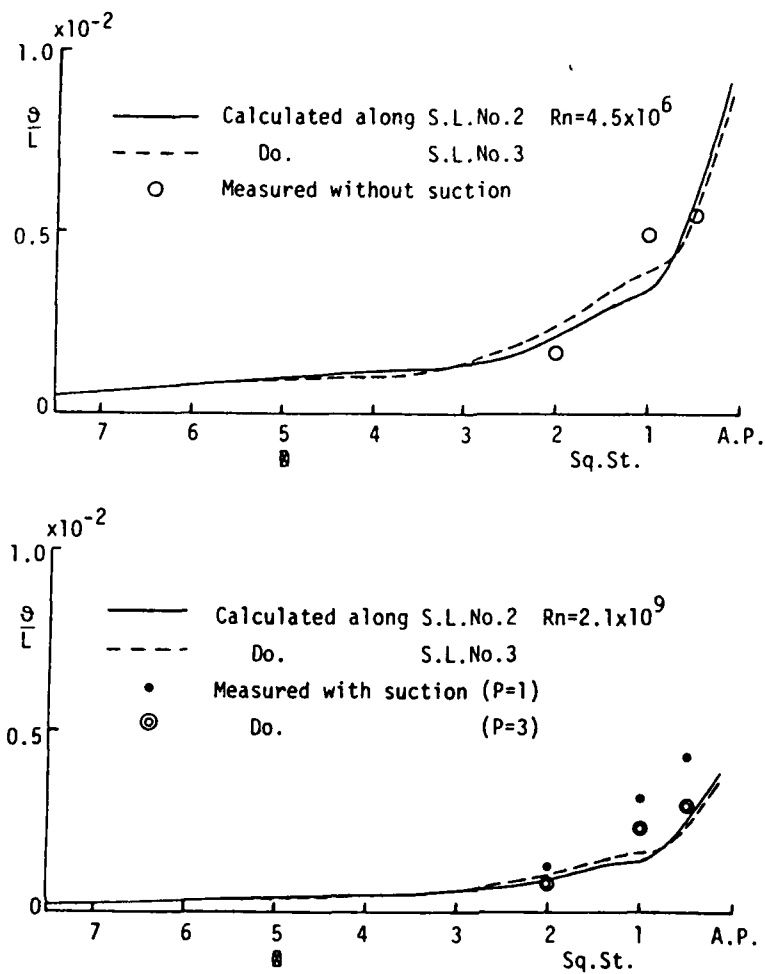


Figure 6 Calculated and Measured Momentum Thickness along S.L.No.2 and S.L.No.3

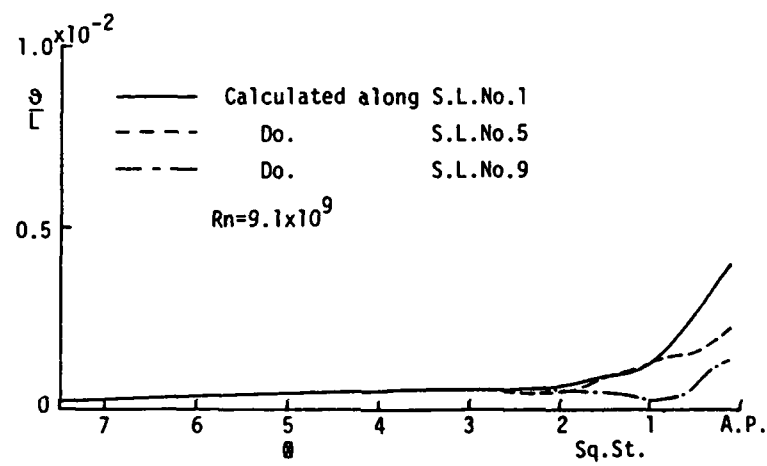
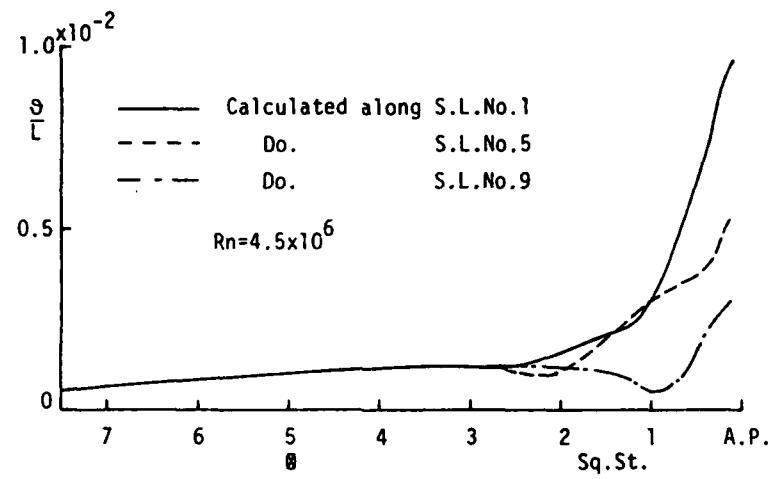


Figure 7 Calculated Momentum Thickness along Streamlines No.1, No.5, and No.9

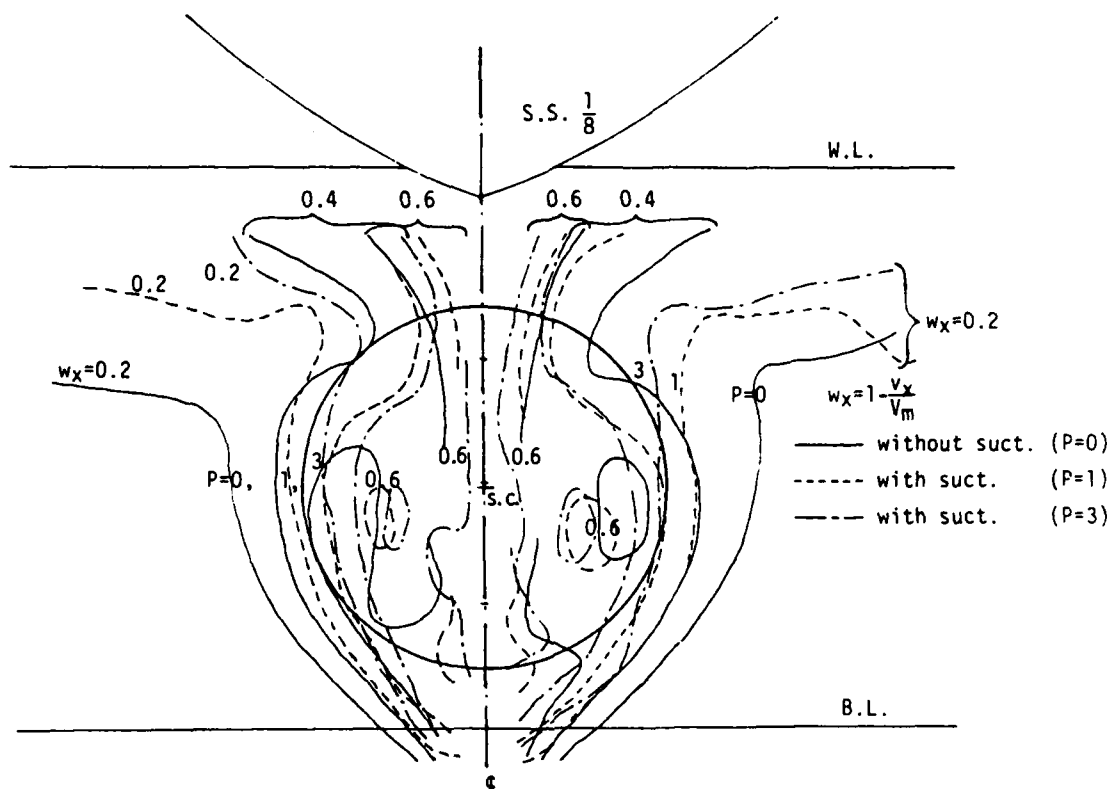


Figure 8 Measured Wake Distributions

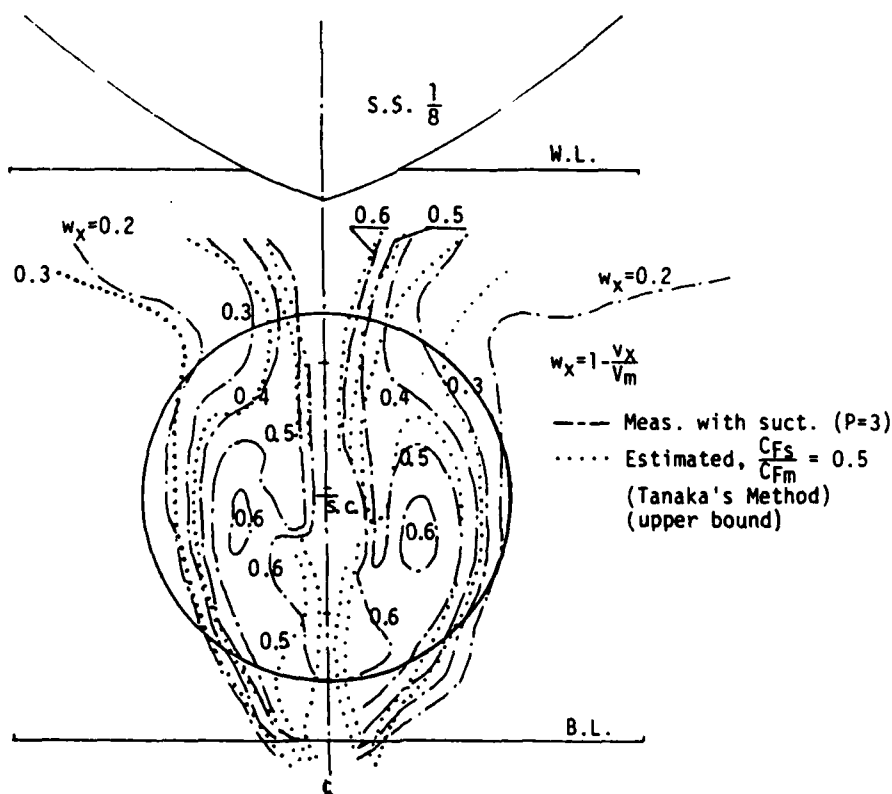


Figure 9 Measured and Estimated Wake Distributions



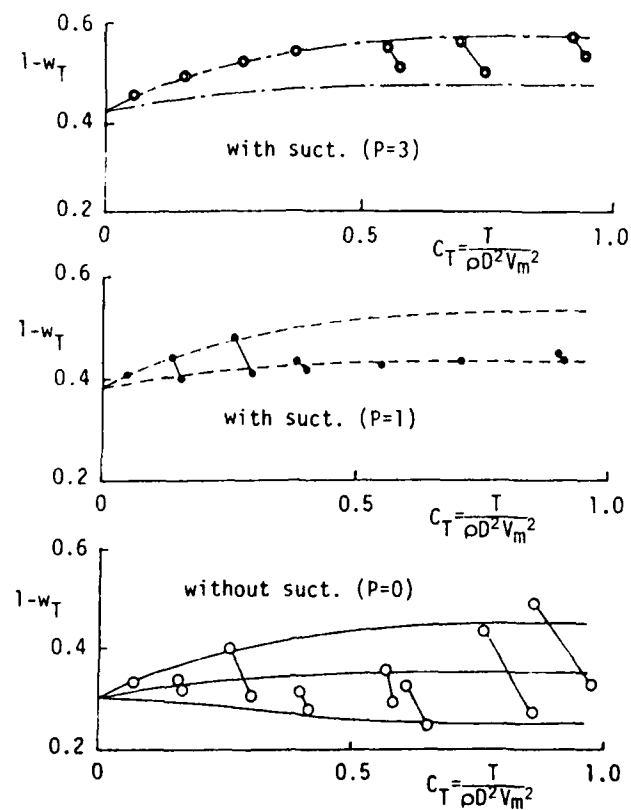


Figure 10 Results of Propeller-Load Variation Test with and without Suction

## Discussion

S. Calisal (University of British Columbia)

1. The authors reported a complex and apparently extensive experimental research. I would like to know if they also measured turbulence intensity or (RMS) values and its change with suction?
2. Another point of interest to me is the variation of  $\theta, \delta^*$  with suction. Calisal\* reported that for flat plate with slit suction these quantities had a logarithmic dependence on suction rate such as

$$\frac{\theta}{\theta_s} = A \ln(s) + B, \quad \frac{\delta^*}{\delta_s^*} = A \ln(s) + B$$

where A, B are constants, s is suction rate,  $\theta_s, \delta_s^*$  are  $\theta, \delta^*$  with suction. I would like to know if they observed similar relationships.

\*"Experimental Results with Slit Suction," Journal of Ocean Engineering, 1978.

## Author's Reply

I. Tanaka and T. Suzuki (Osaka University)

1. We did not measure the turbulence around the model ship. But we are now planning to measure it in wind tunnel with and without suction.
2. We do not have much data now. We only have two data points, so we cannot check your relationship. If we can add other suction rate conditions, we will try to check your formulas.

# Calculation Method for Separated Flows with Applications to Oscillatory Flow Past Cylinders and Roll Damping of Barges

P.W. Bearman, M.J. Downie and J.M.R. Graham  
Department of Aeronautics, Imperial College, London, UK

## 1. INTRODUCTION

The development of the offshore oil industry in recent years has been accompanied by a corresponding growth in the field of heavy marine transport. Ocean going deck cargo barges have come to play an increasingly important function in this field. These vessels, which are towed to their destination, are typically flat bottomed and rectangular in section. Their cargoes are generally secured to the decks by means of welded steel sea fastenings. The design of the fastenings, and in some cases the cargo structure itself, requires a knowledge of the stresses and accelerations to which they will be subjected as a result of the motion of the barge in a seaway. The need for reliable information concerning barge motion response is further accentuated by the continuing trend towards larger barges carrying heavier and more valuable cargoes.

The responses of conventional surface vessels in a seaway have commonly been predicted by methods which are based upon linear theory. In these methods, the variables in the equations representing displacements, velocities and accelerations are all of first order, and the excitation forces are assumed to be proportional to the wave amplitude. Under the assumptions that the responses are linear and harmonic, six linear coupled differential equations of motion may be written in the following form.

$$\sum (M_{jk} + A_{jk}) \ddot{\eta}_k + B_{jk} \dot{\eta}_k + C_{jk} \eta_k = F_j e^{i\omega t} \quad j = 1, 6 \quad (1)$$

where  $\eta_k$  represent the six degrees of freedom - surge, sway, heave, roll, pitch and yaw respectively,  $M_{jk}$  are the components for the generalised mass matrix for the ship,  $A_{jk}$  and  $B_{jk}$  are the added mass and damping coefficients,  $C_{jk}$  are the hydrostatic restoring coefficients. The forces and moments are given by the real part of  $F_j e^{i\omega t}$ ,  $\omega$  being the frequency of encounter and also of response. The ship's vertical plane responses are linearly coupled, as are the lateral plane responses, but in the case of symmetrical ships the two planes of motion are not coupled with respect to each other. The equations are referred to a right handed co-ordinate system fixed with respect to the mean position of the ship with  $y$  vertically downward through the centre of gravity of the ship,  $z$  in

the direction of the forward motion and the origin in the plane of the keel. The hydrodynamic forces, that is the added mass and damping, are calculated according to potential theory.

Experience has shown that such calculations produce realistic predictions of those degrees of freedom that are heavily damped, but that large discrepancies may occur between calculated and experimental results for lightly damped motions. In particular, the roll response of a vessel near resonance is considerably overestimated, or, to put it another way, the damping is considerably underestimated. The roll freedom is important, not only because it is the motion that is most difficult to predict accurately, but also because it is responsible for some of the most severe motions experienced by a marine barge under tow. Potential theory generally underpredicts the level of damping and this can lead to an expensive overdesign of the fastenings, hence more reliable prediction methods are required.

Two possible flow mechanisms that may be associated with the damping, yet which remain unaccounted for in the potential flow calculations are, firstly, viscous boundary layer effects due to the relative motion of the submerged surface of the vessel and the local fluid and, secondly, flows associated with vortex shedding. It may be concluded from the work carried on the frictional resistance to rolling ships (Kato, 1958) that the former mechanism plays a very small role in the overall damping. Similarly, it is reasonable for the most part, to assume that the effect of vortex shedding is also negligible in comparison with the dominant effects of wave damping. However, there is evidence to suggest that vortex shedding does become significant in the case of lightly damped motion near resonance, particularly if the vessel is sharp edged (Tanaka, 1961) as is the case with many ocean going barges.

It is with the evaluation of the non-linear damping brought about by the shedding of vortices from sharp-edged keels that this paper is chiefly concerned.

## 2. THE VISCOUS DAMPING TERM

The uncoupled rolling equation, corresponding to equation (1) with  $k = 4$ , may be written in the form

$$I\ddot{\eta}_4 + B(\dot{\eta}_4) + C\eta_4 = F_4 e^{i\omega t} \quad (2)$$

where the classical damping function is

$$B(\dot{\eta}_4) = B_1 \dot{\eta}_4 + B_{n1} |\dot{\eta}_4| \dot{\eta}_4. \quad (3)$$

In order to obtain realistic predictions of the motion response using linear theory, it is necessary to represent the non-linear character of the roll damping term within the linear equations. It is common practice to achieve this by writing the linear damping term as  $B_{44}\dot{\eta}_4$  and the non-linear damping term as an equivalent linear damping term  $B_{44}^* \dot{\eta}_4$ . The drawback of this approach as a theoretical tool is the determination of

a suitable equivalent linear damping term without resort to empirical methods.

One possible solution is to adopt a semi-empirical method based on the results of such investigations as Tanaka (1961) or Ikeda et al. (1977). Tanaka investigated the eddy making resistance to the rolling of ship hulls and developed a method of calculating the force resisting roll,  $R_{h(e+w)}$ , given by

$$R_{h(e+w)} = \frac{1}{2} \rho C S v^2, \quad (4)$$

where  $S$  is the wetted surface per unit length,  $v$  is the local velocity in the vicinity of the keel and  $C$  is a force coefficient that is a function of the ship geometry, its draft and the location of its centre of gravity. The form of the function defining the force coefficient for a wide range of ship sections was determined by conducting many forced roll model experiments and subtracting the effects of frictional resistance as calculated by Kato's method. Tanaka concluded that the resisting force calculated in this manner was principally due to the shedding of vortices from the bilge keels, particularly if they were sharp edged.

An equivalent linear damping term based on Tanaka's results may be obtained from an analysis of an equivalent energy dissipation, or as the describing function for the non-linearity which is the first harmonic in a Fourier series expansion. An example of a strip theory method embodying a viscous term calculated from Tanaka's results, is that of Salvesen et al. whose equivalent linear roll damping term took the form

$$B_{44}^* \dot{\eta}_4 = K \dot{\eta}_{4\max} \dot{\eta}_4 \quad (5)$$

where the maximum roll velocity,  $\dot{\eta}_{4\max}$ , is estimated initially and the motions are recalculated if the difference between the estimated and computed values is too large. The roll response calculated by this method is shown in Figure 1 which also shows the response calculated without viscous damping and compares both results with experiment.

More recently a method of representing the non-linear contributions to the roll damping, based on the concept of cross-flow drag, has been proposed by Kaplan et al. (1982). In this method an expression for the non-linear roll moment accounting for effects due to the skegs, bottom and sides of the barge, is derived in which the non-linear roll damping is proportional to  $|\dot{\eta}_4| \dot{\eta}_4$ . For the case of regular sinusoidal waves the non-linear damping term is approximated in equivalent form by

$$B_{n1} |\dot{\eta}_4| \dot{\eta}_4 = \frac{8}{3\pi} B_{n1} \omega_n \eta_{4\max} \dot{\eta}_4, \quad (6)$$

where  $\omega_n$  is the roll natural frequency.

Although the non-linearity of the roll damping term is generally held to be attributable to the generation of vortices from the ship's keel, to the authors' knowledge, there is no method in current usage which includes a viscous damping term that has been explicitly calculated from the forces experienced by the vessel due to vortex shedding.

Until recently there has been no available reliable method for performing a detailed calculation of this nature. The situation has changed with the development of the discrete vortex method, and the calculation of an equivalent linear damping coefficient based on this technique will be described in the succeeding sections.

### 3. THE DISCRETE VORTEX METHOD

The discrete vortex method is a technique that has been developed for the computation of flow fields in which the vorticity is confined to small sub-regions. Its most common application is to the calculation of two-dimensional separated flows around bluff bodies at high Reynolds number, in which it is assumed that viscous effects play little part other than in the initial generation of vorticity. In these calculations the separating shear layers are represented by arrays of isolated point vortices which, in the case of sharp-edged bodies, are introduced into the flow in the vicinity of the separation point so as to satisfy the Kutta-Joukowski condition ensuring smooth separation. The numerical method then follows the roll up of the discretised shear layers into large vortices and maps the passage of these conglomerations of vortices as they are convected by the flow field around the vorticity generating body. The forces on the body are obtained by integrating the pressures on the surface, via the unsteady Bernoulli equation, or directly through the application of the Blasius equation.

Many computations of this nature have been performed with varying degrees of success. Comprehensive reviews of the literature may be found in Clements (1977) and Downie (1981). Calculations involving flows analagous to barge motions have been carried out by Fink and Soh (1974), Ikeda and Himeno (1981) and Patel and Brown (1981). Two discrete vortex calculations will be mentioned briefly in this section the first by Bearman et al. (1981) because it incorporates many of the latest developments in the method and also demonstrates that forces and flow patterns are realistically predicted by the method even in difficult flow regimes, and the second, by Graham (1980) because it forms part of the work to be dealt with in the following sections.

Bearman et al. computed the flow around a two-dimensional flat plate normal to an oscillatory stream over a wide range of Keulegan-Carpenter number,  $KC$ , where  $KC = UT/D$ ,  $U$  being the flow velocity amplitude,  $T$  its period and  $D$  the cross flow width of the body. The time-dependent flow is calculated in a transformed circle plane by a method involving a fast Fourier transform solution of the Poisson equation over a mesh covering the flow field. This method has the advantage of being able to handle large numbers of discrete vortices. A typical flow pattern and a comparison of the results for the force coefficients with those obtained experimentally are shown in Figures 2 and 3. The prediction of the forces experienced by a body subjected to a flow of this nature requires a full discrete vortex calculation. However some flow configurations may be treated more simply by neglecting any interactions between vortices shed from different edges.

At small KC the maximum displacement of the fluid particles in the undisturbed flow is small in comparison with the scale of the body. Thus vortices may only move away from the edge under the influence of the velocity field of other vortices, and hence the shedding from a single edge may become independent from the shedding from other edges. In this instance, the local flow becomes equivalent to an infinite wedge subjected to an oscillatory flow. Experiments on sharp-edged bluff cylinders (Singh, 1979) have shown that at low KC the pattern of vortex shedding from a single isolated edge consists of one vortex pair shed per cycle. A vortex of the expected sense is shed on each half cycle. The vortex shed over the first half of the cycle is then swept back towards the growing vortex to form a pair, which moves rapidly away from the body when the two are of about equal strength.

The discrete point vortex analysis of shedding from an isolated edge carried out by Graham assumed that just such a stable and regular process occurs for separated flows below some value of KC of the order of 10. In this calculation point vortices were shed sequentially from an infinite edge and then traced as they moved with the fluid particles of an oscillatory flow. Groups of vortices which could be identified as representing completely rolled up sheets far from the body were progressively wound into a central core vortex. The main results for the case of a  $90^\circ$  edge, are as follows: by taking the appropriate Fourier integral of the in-line force over a cycle of the flow, the drag coefficient defined as

$$C_D = \frac{3\pi}{4T} \int_0^T \frac{F_v(t/T)}{\frac{1}{2}\rho \hat{U}^2 L} \cos\left(\frac{2\pi}{T} t\right) dt, \quad (7)$$

was found to be independent of KC and to have a value of 1.566. The vortex force,  $F_v$ , was shown to be directed at right angles to the bisector of the wedge angle and to be proportional to  $\frac{1}{2}\rho |U| UL$ , where  $L$  is a length scale that may be determined from the transformation, and the free stream velocity is given by

$$U = \hat{U} \cos\left(\frac{2\pi}{T} t\right).$$

The forces experienced by a barge rolling with small amplitude motion due to vortex shedding, then, may be calculated by matching the local flow in the vicinity of the barge keel with the oscillatory flow around the isolated edge at low KC, providing there is no interaction between vortices shed from opposite edges of the barges keel.

#### 4. MATCHING THE EDGE FLOWS

The method of matching the two flows will only be described in outline. A detailed account of the procedure is given in Downie et al. (1982). A rectangular barge floating in still water may be represented in a complex plane, the  $z$ -plane, by mapping a semi-rectangle into a half-plane by means of a Schwartz-Christoffel transformation. The

appropriate complex conformal transformation is given by

$$z = \int_0^{\zeta} \left( \frac{\zeta^2 - \zeta_d^2}{\zeta^2 - \zeta_e^2} \right)^{1/2} d\zeta \quad (8)$$

where the notation is consistent with Figure 4(a). If the body in the real plane is supposed to be rotating about the point 0 with an angular velocity  $\eta_4$ , the instantaneous boundary conditions may be represented in the transformed plane, the  $\zeta$ -plane, by a source distribution along the  $\xi$ -axis, whose strength per unit length may be shown to be

$$m(\xi) = 2 \left| \begin{array}{l} R\{z\} \\ \pm I\{z\} \end{array} \right| \frac{dz}{d\zeta} \dot{\eta}_4 \quad \begin{array}{l} y = 0 \\ x \leq 0 \end{array} \quad (9)$$

as shown in Figure 4(b), and where  $R\{z\}$  and  $I\{z\}$  are the real and imaginary parts of  $z$ . Thus the velocity at the point  $\xi_d$  in the transformed plane, corresponding to the shedding edge in the  $z$ -plane, and induced by the source distribution, is given by

$$q_d = \frac{1}{2\pi} \int_{\xi_b}^{\xi_e} \frac{m(\xi)}{\xi_d - \xi} d\xi. \quad (10)$$

The motion may be generalised to a rotation about any point P by the addition of a translational component in the  $z$ -plane, which gives rise to an extra component of the velocity in the  $\zeta$ -plane given by

$$U = q_d + h(1-\lambda)\dot{\eta}_4 \quad (11)$$

where  $U$  is the velocity in the transformed plane and  $h(1-\lambda)$  is the distance OP as shown in Figure 4(a). Hence if the roll motion is described by  $\eta_4 = \omega \hat{\eta}_4 \cos \omega t$ , the relationship between the rolling motion and the oscillatory motion in the transformed plane is given by

$$\hat{U} = a_U 1\omega \hat{\eta}_4 \quad (12)$$

where  $a_U$  is determined by the instantaneous boundary conditions.

In the immediate vicinity of the shedding edge, as  $z \rightarrow z_D$  and  $\zeta \rightarrow \zeta_d$ , the transformation given by equation (8) reduces to

$$z' = e^{-i\pi/2} \frac{2}{3} \left( \frac{2\zeta_d}{\zeta_e^2 - \zeta_d^2} \right)^{1/2} \zeta'^{3/2} \quad (13)$$

$$= e^{-i\pi/2} \left( a_L 1 \right)^{1/2} \zeta'^{3/2}, \quad (14)$$

where the primes denote a shift of origin to the shedding edge and  $a_L$  is defined solely by the barge geometry. The conformal transformation



that maps an infinite edge into a half-plane is given by

$$z = e^{-i\pi/2} L^{-1/2} \zeta^{3/2}. \quad (15)$$

Hence the transformations, and therefore the velocities in the vicinity of the shedding edge, become identical providing

$$L = a_L l \quad (16)$$

and the velocities in the respective transformed planes are the same.

Having determined the conditions necessary for the matching of the two flows, it is possible to express a damping coefficient for the rolling motion of the barge in terms of the drag coefficient obtained for oscillatory flow about an isolated edge.

## 5. CALCULATION OF THE DAMPING COEFFICIENT

The damping moment induced by vortex shedding,  $B_v$ , may be written in terms of the vortex force on a single edge,  $F_v$ , as follows

$$B_v(t/T) = a_R l F_v(t/T) \quad (16)$$

where  $a_R$  is determined by the location of the roll centre, the barge geometry and the direction of the vortex force, which is at right angles to the bisector of the edge angle.

If the damping moment is expressed as a Fourier series

$$B_v(t/T) = \rho l^4 \omega^2 \hat{\eta}_4^2 \sum \hat{B}_{vn} \cos(n\omega t) \quad (17)$$

and the barge motion is represented by the equation

$$I \ddot{\eta}_4 + (B_1 + B_v^*) \dot{\eta}_4 + C \eta_4 = F e^{i\omega t} \quad (18)$$

then the linear damping coefficient,  $B_v^*$ , is given by

$$B_v^* = \rho l^4 \omega \hat{\eta}_4 \hat{B}_{v1} = \rho l^4 \hat{B}_{v1} \dot{\eta}_{4\max}, \quad (19)$$

where the vortex damping factor,  $\hat{B}_{v1}$ , is given by

$$\hat{B}_{v1} = \frac{2}{T} \int_0^T \frac{B_v(t/T)}{\rho \omega^2 l^4 \hat{\eta}_4^2} \cos(\omega t) dt. \quad (20)$$

The vortex damping factor may now be written in terms of the drag coefficient for oscillatory flow about the isolated edge, given in equation (7), by matching the flow with the barge motion according to equations (12) and (16), and may be written as

$$\hat{B}_{v1} = \frac{4}{3\pi} a_U^2 a_L a_R C_D. \quad (21)$$

The vortex damping factor has been computed for a number of different flow cases and the results are presented in the following section.

## 6. DISCUSSION OF RESULTS

The value of the vortex damping factor,  $\hat{B}_{V1}$ , depends upon the aspect ratio of the barge,  $A = l/h$ , and the position of the roll centre, located a distance  $\lambda h$  measured downwards from the mean free surface. Full scale tests on a barge in a seaway (Stewart and Ewers, 1979) suggest that the roll centre may undergo large excursions, and so the value of  $\hat{B}_{V1}$  has been computed for barges of various aspect ratio ( $2 < A < 10$ ) over a range of roll centres ( $-10 < \lambda < 10$ ). The results are presented in Figure 5.

A physical interpretation of the results was gained by performing flow visualisation experiments involving forced roll model tests. The mathematical model predicts high damping factors due to the presence of large scale vortices of the opposite sense to the barge roll motion when the roll centre is well above the mean free surface, i.e.  $\lambda$  is large and negative. As  $\lambda$  goes positive, the scale of the vortices decreases until a situation is reached in which the roll centre coincides with the intersection of the vortex force vectors, and no vortex shedding occurs. This point should be attained with zero local flow relative to the shedding edge. Because the method assumes independence of each edge from the rest of the barge, this does not occur exactly and over a very small range of  $\lambda$  the model predicts a very small negative damping. Further increases of  $\lambda$  are accompanied by growing vortices, of the same sense as the body motion, giving rise to an increase in the damping factor. A comparison between the predicted scale of the vortices and the actual scale measured from photographs taken in the flow visualisation experiments is shown in Figure 6. Also shown is the flow pattern, taken straight from the computer print-out, predicted by the isolated edge calculation and which may be compared with the flow visualisation photograph of plate 1.

Further validation of the method was sought by comparing the results with a damping factor derived from Tanakas results, and which may be written as

$$\hat{B}_{T1} = \frac{2}{T} \int_0^T \frac{r R_h(e+w)}{\rho \omega^2 \hat{h}_4^2 l^4} \cos(\omega t) dt \quad (22)$$

$$= \frac{4}{3\pi} \frac{Sr^3}{l^4} C, \quad (23)$$

where  $r$  is the distance from the roll centre to the keel edge and the remaining notation is consistent with equation (4). The results are shown in Figure 7 and may be seen to show reasonable agreement when the roll centre lies between the keel and the mean free surface.

The results were also compared with data obtained from a series of model tests conducted by Atkins R & D in conjunction with the

National Maritime Institute for a consortium of companies organised by Noble Denton and Associates Ltd. Since the results are proprietary, they are expressed in arbitrary units in Figure 8, which shows the vortex damping compared with the overall damping (both given as a percentage of the critical damping) for barges rolling at their natural frequency over a range of amplitudes of oscillation.

The results are all in conformity with experimental trends and are of the expected order of magnitude. It is true that vortex damping is overpredicted, but this is not altogether unexpected. The technique of matching the isolated edge to the local flow around the shedding edge of a bluff body has been performed for a flat sharp-edged plate of finite thickness, a diamond cylinder and a square cylinder, all in low KC oscillatory flow. Although the force coefficients were in very good agreement with experimental values for the flat plate, the drag coefficient for the square cylinder (the worst case) was overpredicted by about 20% (Obasaja, 1982). If the damping factors are corrected by 20%, the calculated results for the vortex damping agree with the experimental results for the overall damping. This result lends credence to the assumptions made by those methods that base their viscous damping terms on Tanaka's results, namely that the roll damping of sharp-edged vessels at resonance is principally due to vortex shedding.

The overprediction of the damping might be attributed to a number of causes. The model assumes that there is no interaction between the vortices shed from opposite sides of the barge, or between the vortex shedding and surface wave effects. Nor does it make any allowance for end effects. Finally, Bearman et al. (1981) found that more realistic forces were predicted for a flat plate in oscillatory flow if due allowance was made for three-dimensional effects by the inclusion of a vortex decay parameter. No such technique was employed in the foregoing analysis.

## 7. EQUIVALENT LINEAR VORTEX DAMPING COEFFICIENTS

The calculation of barge motion response from the coupled equations (1) requires the evaluation of the components  $b_{jk}$  of the matrix of damping coefficients.

The contribution made by the viscous damping can be represented by equivalent linear vortex damping coefficients, each of which depends on the location of the roll centre.

The preparation of curves delineating the variation of such coefficients with the roll centre for the coupled equations of roll and sway is currently in progress.

## 8. FUTURE DEVELOPMENTS

The method described in this paper is fairly flexible with regard to the treatment of different barge geometries. Trial calculations have shown that the methods may readily be extended to barges with fin keels, for example.

The logical development of the method is a full scale calculation in which diffraction and viscous effects are considered simultaneously. The viability of such a method is currently under investigation.

## 9. CONCLUSIONS

A discrete vortex method has been developed for the prediction of the contribution made by vortex shedding towards the roll damping of barges. Equivalent linear vortex damping coefficients have been calculated for a number of barge geometries over a range of roll centres. The results, when compared with other methods of calculating vortex damping, and with experimental results, have been very encouraging. On the basis of this study, then, it may be concluded that the discrete vortex method shows great promise as a technique for the prediction of the viscous roll damping of barges.

## 10. ACKNOWLEDGEMENTS

This study has been jointly supported by the National Maritime Institute, Feltham, Middlesex, and the Science and Engineering Research Council Marine Technology Directorate. Their assistance and encouragement are gratefully acknowledged.

## 11. REFERENCES

- Bearman, P.W., J.M.R. Graham, P. Naylor and E.D. Obasaju (1981). The role of vortices in oscillatory flow about bluff cylinders, International Symposium on Hydrodynamics in Ocean Engineering, The Norwegian Institute of Technology.
- Clements, R.R. (1977). Flow representation, including separated regions, by discrete vortices. Computational Fluid Dynamics, AGARD, 86.
- Downie, M.J. (1981). An inviscid model for the fluid forces induced by vortex shedding from a circular cylinder. PhD Thesis, Royal Military College of Science, Shrivenham, U.K.
- Fink, P.T. and W.K. Soh (1974). Calculation of vortex sheets in unsteady flow and applications in ship hydrodynamics. 10th Symposium on Naval Hydrodynamics.
- Graham, J.M.R. (1980). Forces on sharp-edged cylinders in oscillatory flow at low Keulegan-Carpenter numbers. Fluid Mech., 97, 1.
- Ikeda, Y., Y. Himeno (1981) Calculation of vortex shedding flow around oscillating circular and Lewis form cylinders. 3rd International Conference on Numerical Ship Hydrodynamics, Paris.
- Ikeda, Y., Y. Himeno and N. Tanaka (1977). On eddy making component of roll damping force on naked hull, Soc. of Naval Arch. of Japan, J. 142.
- Kaplan, P., C.-W. Jiang and J. Bentson (1982). Hydrodynamic analysis of barge-platform systems in waves. Royal Institution of Naval Architects, Spring Meeting, Paper No. 8.

- Kato, H. (1958). On the frictional resistance to rolling of ships. Soc. of Naval Arch of Japan, J. 102, 115.
- Obasaju, E.D. (1982). Private Communication.
- Patel, M.H. and D.T. Brown (1981). The calculation of vorticity effects on the motion response of a flat bottomed barge to waves. Int. Symp. Hydr. Ocean Engg., The Norwegian Institute of Technology.
- Singh, S. (1979). Forces on bodies in oscillatory flow. PhD Thesis, University of London.
- Salvesen, N., E.O. Tuck and O. Faltinsen. (1970). Ship Motions and sea loads. Trans. SNAME., 78, 42]
- Tanaka, N. (1960). A study on bilge keels (Part 4. On the eddy making resistance to the rolling of a ship hull). Soc. of Naval Arch. of Japan, J. 109, 205.

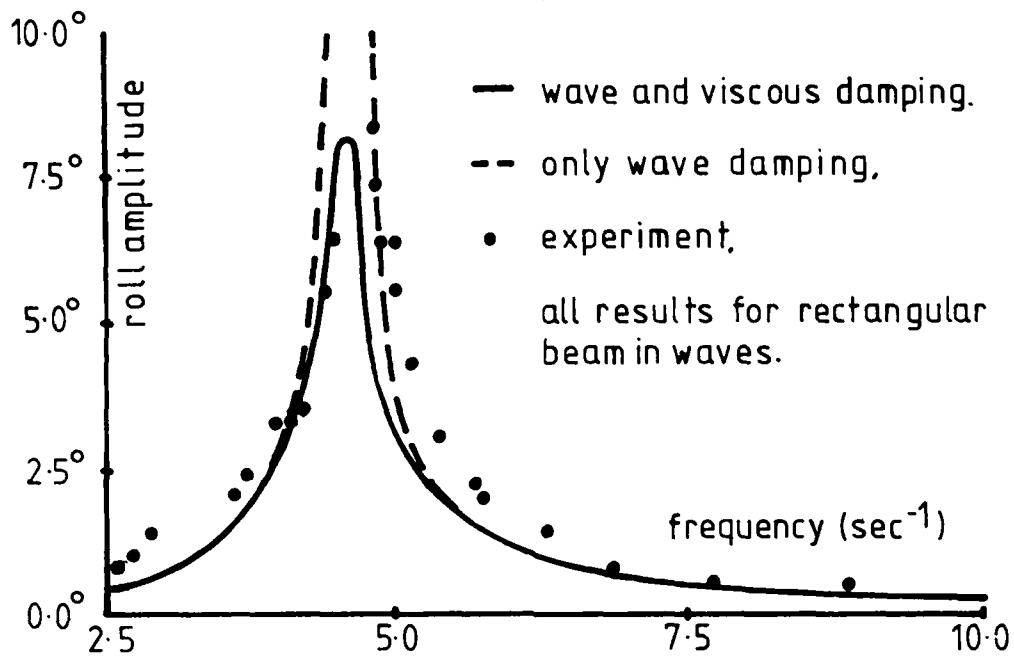


Figure 1: Roll Amplitude vs Frequency.

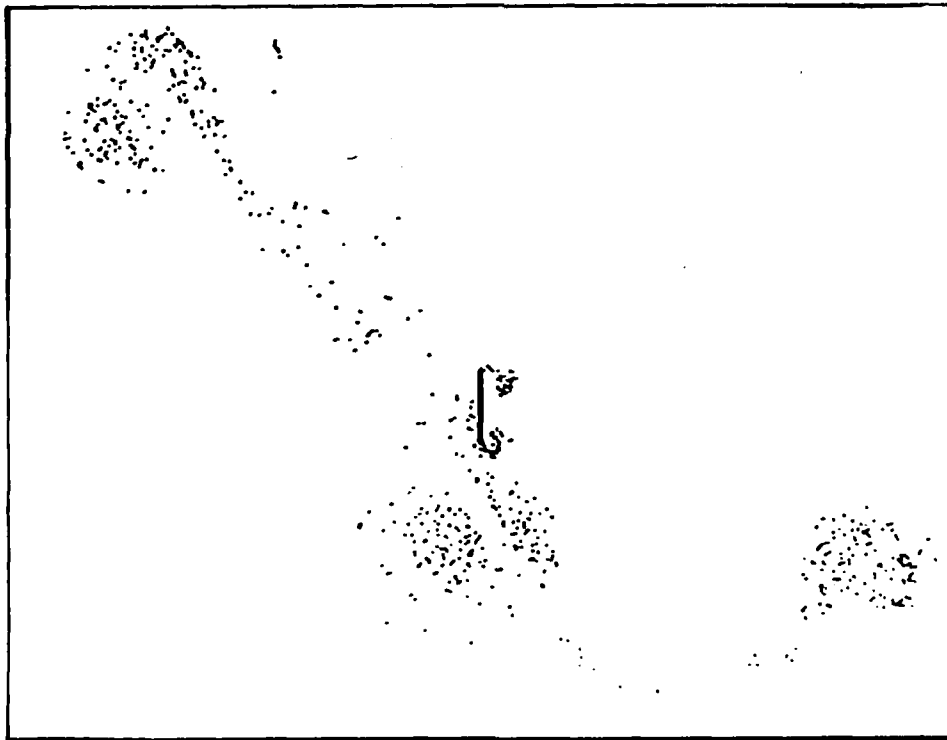
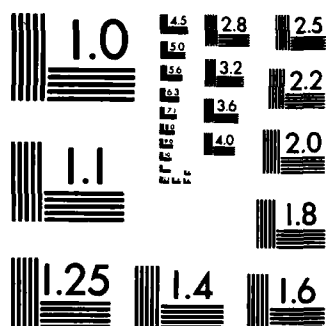


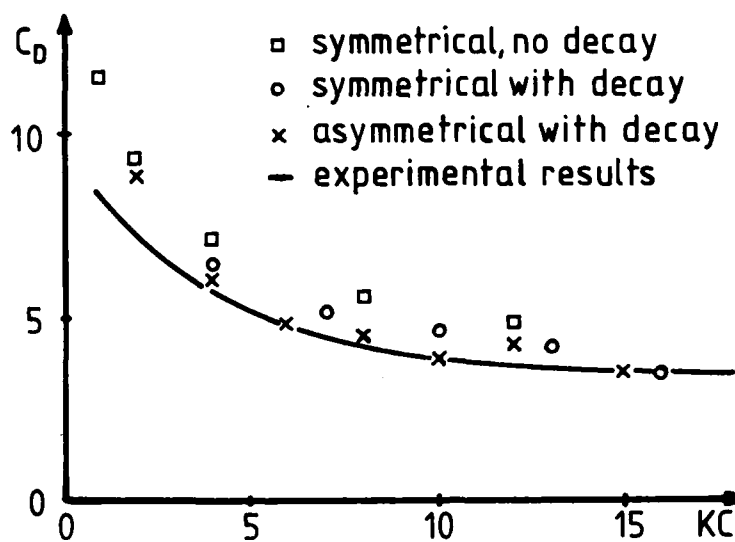
Figure 2: Computed Flow Pattern Around a Flat Plate at  $KC = 15$  After 2.2 Cycles.



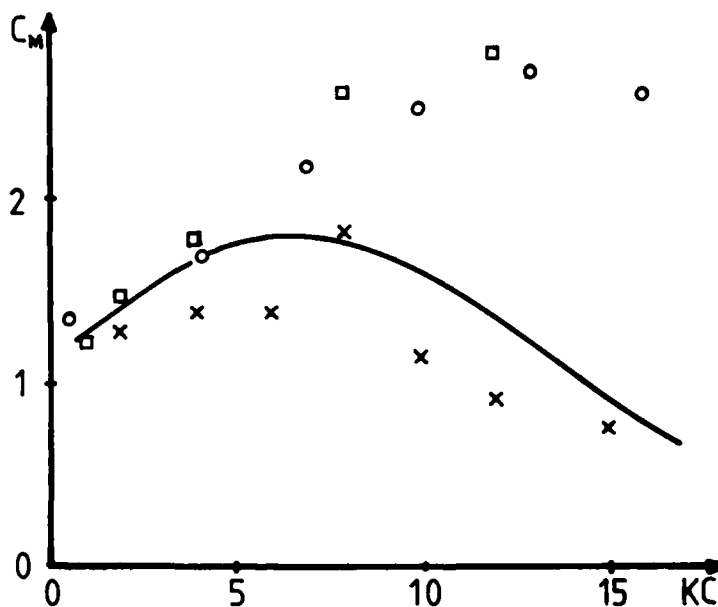


MICROCOPY RESOLUTION TEST CHART  
NATIONAL BUREAU OF STANDARDS-1963-A



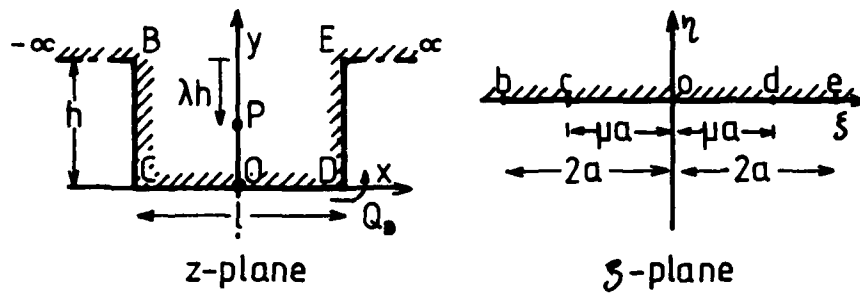


a) Drag Coefficient vs. Keulegan-Carpenter Number

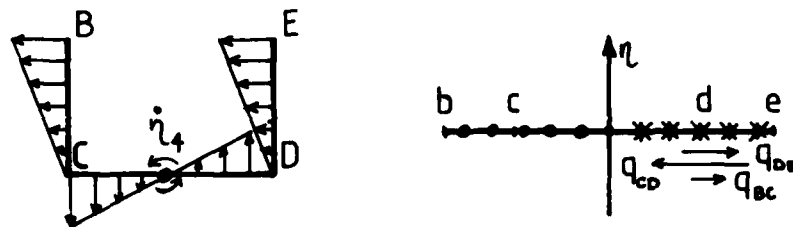


b) Inertia Coefficient vs. Keulegan-Carpenter Number

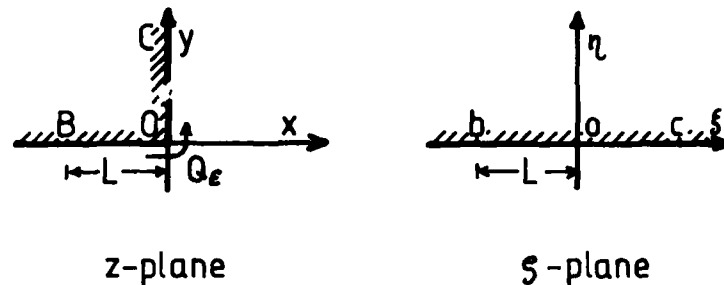
Figure 3



a) Barge Notation

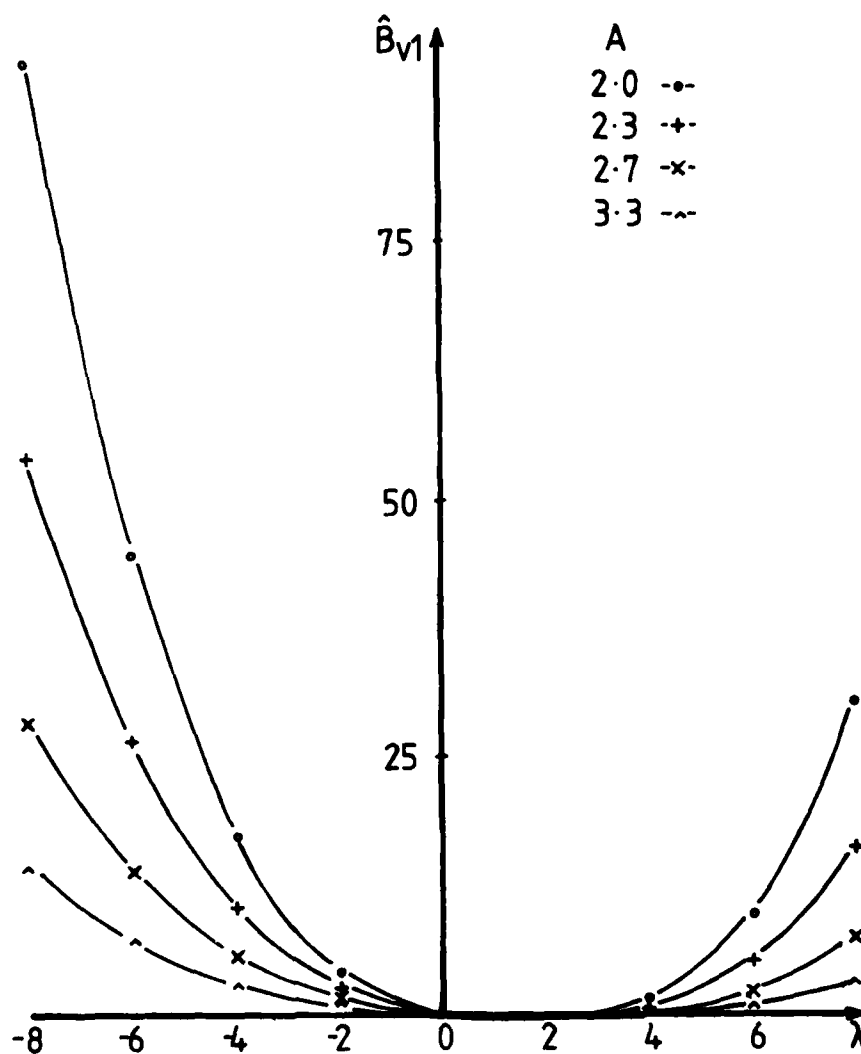
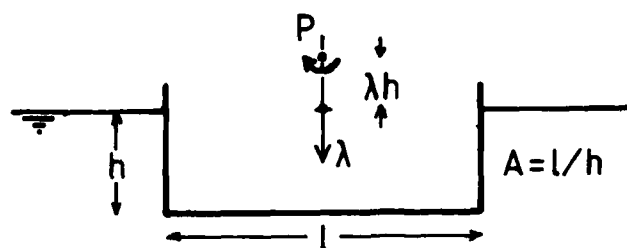


b) Instantaneous boundary conditions  
& source distribution in  $\zeta$ -plane



c) The Isolated Edge

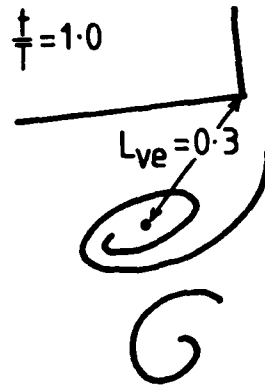
Figure 4



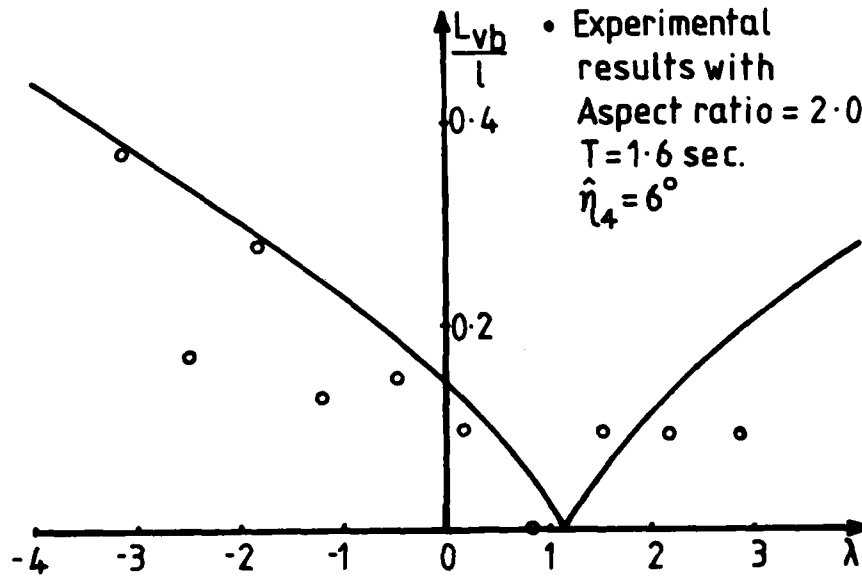
Damping Factor vs. Roll Centre & Aspect Ratio

Figure 5

$$L_{vb} = L_{ve,comp} a_L \left( \frac{U}{T} \right)^{3/4}$$



a) Computed Vortex Length Scale for Isolated Edge, KC=1

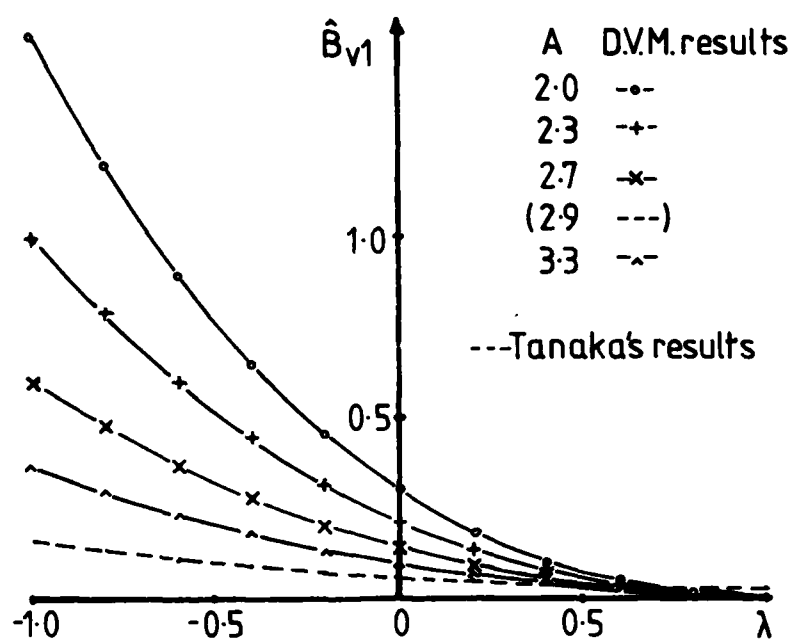


b) Computed Vortex Length Scale for Rolling Barge

Figure 6

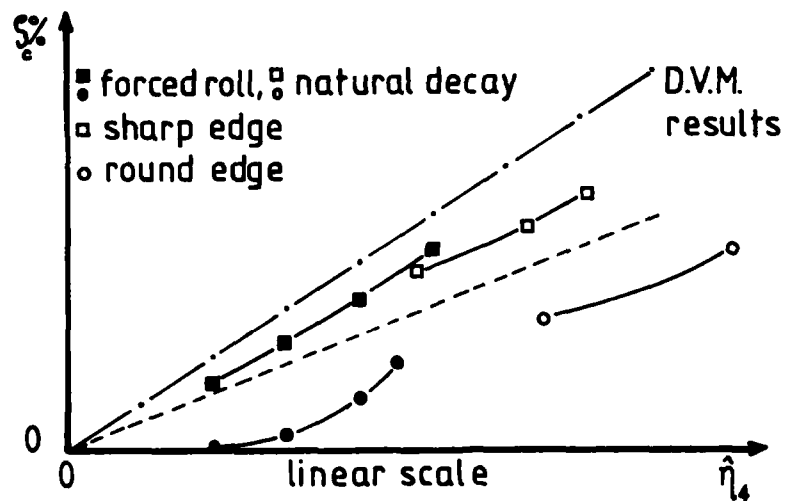


Vortex Shedding from Model Barge  
 $\lambda = -1.0, A = 2.0, \hat{\eta}_4 = 6^\circ, \omega = 4 \text{ Rad./sec.}$   
Plate 1



Damping Factor vs. Roll Centre & Aspect Ratio

Figure 7



Critical Damping Ratio vs. Roll Amplitude

Figure 8

## Discussion

A. Papanikolaou (Techn. University of Berlin)

In your potential flow calculations of the rolling barge you did not include the free-surface effects. Could you comment what the free-surface effects on the vortex flow are, especially for relatively flat barges (large B/T) rolling in waves? Could you include, in your scheme, Green's function method for the potential flow calculation? In your Figure 8, I miss some numbers.

G. McKee (Davidson Lab/SIT)

The one-degree-of-freedom equation for rolling is generally taken as being Equation (2) with the form of the damping taken as Equation (3). The authors are to be commended for determining the damping coefficient and checking it against experimental data. It would be a desirable extension of this research not only to continue refining the calculation of the equivalent linear damping coefficient but also to use the method to check the form of (3). Was the form of the damping against  $\eta_4$  suggestive of (3)?

## Author's Reply

Martin J. Downie

To Dr. Papanikolaou

The questions raised by Dr. Papanikolaou may be most conveniently answered by considering them in the reverse order to that in which they were asked. The experimental results shown in Figure 8 illustrate the relationship between the overall damping at resonance (i.e., damping due to wave radiation as well as other effects, such as vortex shedding) and the roll amplitude. These results were obtained from a series of model tests conducted on behalf of a consortium of private companies and are therefore proprietary. Nevertheless, although the figure does not provide actual numbers, it does provide a useful and meaningful comparison between the experimental overall damping and the computed vortex damping at resonance.

A method is currently being developed for matching the isolated edge solution to the rolling-barge problem using a Green's function representation of a point-wave source. Until this calculation has been carried out, the effect of the free surface on the vortex flow remains largely a matter of speculation. However, it is worth noting

that the computation predicts flow patterns that are similar to flow visualization photographs of a model barge of aspect ratio 2 and in which the vortices are of the correct scale (see Figure 6 and Plate 1). Furthermore, in these circumstances, a good discrete vortex model may generally be relied on to predict realistic forces.

Finally, the tests whose results are shown in Figure 8 were carried out on a scale model of a heavy transport barge typical of those used in and around the North Sea for offshore work. Since the computed and experimental results are in reasonable agreement, it might be concluded that the vortex flow is not influenced overmuch by surface-wave effects, at any rate for an aspect ratio of 2, and probably not for aspect ratios large enough to be appropriate to actual working barges.

To Dr. McKee

In reply to Dr. McKee's question relating to the form the damping force takes, it must be pointed out that the use of the matching technique presented in the paper obviates the explicit calculation of the vortex damping force. The vortex damping coefficients for the rolling barge were derived directly from the drag coefficient for an isolated edge in oscillatory flow, which had been computed by Graham (1980) in an earlier discrete vortex calculation. However, the results of this earlier analysis indicated that the vortex damping force is indeed proportional to  $|\dot{\eta}_4| \dot{\eta}_4$ , as implied by Equation (3), provided that the internal angles of the shedding edges of the keel are right angles. The result does not hold for significant departures from this proviso.



# Vortex Shedding Around Two-Dimensional Bodies at High Reynolds Number

Odd M. Faltinsen and Bjørnar Pettersen  
Norwegian Institute of Technology, Trondheim-NTH

## ABSTRACT

A method to predict the flow and associated vortex shedding around bluff bodies at high Reynolds number is presented. The velocity potential outside the free shear layers and boundary layers is expressed as a distribution of sources and dipoles. The Kutta condition, the starting condition and the numerical representation of the free shear layers is discussed. An alternative way to calculate the force on bluff bodies is presented. Numerical results for unsteady airfoil problems, oscillatory and steady cross-flow past a flat plate as well as steady cross-flow past a square cross-section is presented. Satisfactory agreement with other numerical results and flow visualization studies is documented.

## NOMENCLATURE

$\phi$	total velocity potential
$\phi^I$	incident undisturbed velocity potential
$\phi$	velocity potential due to the body
$(x,y)$	Cartesian coordinate system
$t$	time
$U$	free stream velocity
$U_{\max}$	maximum free stream velocity
$S_B$	body surface, see Figure 1
$S_V$	free shear layer surfaces, see Figure 1 (Both sides.) If only one side either + or - is used as index.
$S_R$	Riemann surfaces, see Figure 1. (Both sides.) If only one side either + or - is used as index.

$\alpha$	angle between the free stream velocity and the x-axis
$\phi^+ - \phi^-$	velocity potential jump across the free shear layer
$c$	chord length of airfoil
$\omega$	circular frequency of oscillation
$\Gamma$	circulation
$C_L$	$L / (\frac{1}{2} U^2 c)$
$L$	lift force on airfoil
$H$	half the height of a flat plate in unbounded fluid or the height of flat plate mounted to a wall (see Figure 16)
$C_N$	$F / (\frac{1}{2} U_{\max}^2 2H)$
$F$	force on a plate of height $2H$ with symmetric vortex shedding
$\Delta s_N$	length of elements describing the free shear layer
$KC$	Keulegan-Carpenter number
$\rho$	mass density of the fluid

## 1. INTRODUCTION

Flow around bluff bodies and associated vortex shedding is of importance in several marine hydrodynamic problems. Examples are wave and current induced loads on piles, jackets, risers and pipe lines, roll damping of ships and barges, slow drift oscillation damping of moored structures, anchor line damping, large amplitude maneuvering forces on ships and still water resistance of blunt ship forms.

The state of the art in calculating the loads on bluff bodies is not satisfactory. Traditionally the Morison's equation has been used in the offshore industry to calculate wave and current loads on cylindrical shapes applied in structural work. The formula is semi-empirical and its coefficients depend on many parameters like Reynolds number, Keulegan-Carpenter number and roughness ratio. Furthermore Morison's equation cannot at all predict the oscillatory forces due to vortex shedding, and it is questionable to generalize it to the case of non-fixed structures.

There have been attempts on more rationally based methods. (Bearman and Graham (1980)) The two-dimensional discrete vortex method is an example. A review has been given by Clements and Maull (1975). The discrete vortex method makes the assumption that the vorticity in the fluid

domain is fairly concentrated in thin boundary layers and thin free shear layers. But the numerical results of the free shear layer positions by the discrete vortex model are not impressive. Fink and Soh (1974) pointed out that this was due to the numerical representation of the free shear layers by discrete vortices. One should instead realize that there is a continuous distribution of vorticity in the free shear layers and that the discrete vortices used in the "discrete vortex methods" are a bad representation of the free shear layers. Fink and Soh (1974) applied their procedure for crossflow past flat plates and rectangular sections. Later Sarpkaya and Shoaff (1979) applied Fink and Soh's procedure for circular cross-sections. By using an empirically determined circulation reduction mechanism they come up with calculated results close to experimentally derived results for the case of steady incident flow on a two-dimensional circular cylinder.

In developing a theoretical model for flow around bluff bodies one should have in mind that the model should ultimately be able to handle

- a. General body configurations including several bodies in interaction as well as the effect of marine growth.
- b. Arbitrary motion of body and incident flow.
- c. Turbulent or laminar boundary layers.

Due to the complexity of the problem it seems wise to start out with a two-dimensional method, but one should have three-dimensional generalizations in mind. The latter may be important in studying correlation of wave loads along a pile.

We have decided to solve for the velocity potential instead of the velocity. The velocity potential is expected to be less singular than the velocity at possible singular points. Further we are using a distribution of sources and dipoles to represent the potential flow. This procedure can in principle be applied to any body configuration and it is possible to generalize it to three-dimensional problems. The latter is not true for the conformal mapping technique that is commonly used in vortex models. Further the conformal mapping technique is not easy to use for a general two-dimensional body-configuration. Our procedure leads to a Fredholm's integral equation of the second kind and not the first kind. A Fredholm's integral equation of the first kind may lead to numerical instability problems. This is not true for the Fredholm's integral equation of the second kind.

There are several difficult problems to solve in vortex shedding models. Some of the specific problems we will focus on are:

- a. What kind of Kutta condition is used?
- b. How is the vortex shedding process started?
- c. How do we represent a spiral with an infinite number of turns?
- d. How is the vorticity numerically convected?

Other important problems that we will not discuss are

- a. How is the separation point determined when the flow separates from a continuously curved surface.
- b. How is vorticity reduced in the free shear layer.

Both problems have been discussed by Sarpkaya and Shoaff (1979). Problems with how asymmetry is developed in the wake and how vorticity is annihilated due to interaction between different free shear layers have also been discussed by Sarpkaya and Shoaff (1979). The important problem of stability of free shear layers has been analyzed by Moore (1970).

We will in the following text first describe our theoretical approach and then how we numerically solve our problem. In the final chapter we will present numerical results including comparisons with analytical, experimental and other numerical results.

## 2. THEORY

The theory is based on a timestep integration method. It is assumed that the vorticity is concentrated in thin boundary layers and free shear layers. At each timestep we have to solve a potential flow problem outside the boundary layers and free shear layers. We will write the total velocity potential as

$$\phi = \phi^I + \phi \quad (1)$$

where  $\phi^I$  is the incident undisturbed velocity potential. Two-dimensional flow is assumed and we will write

$$\phi^I = U(t)\cos\alpha \cdot x + U(t)\sin\alpha \cdot y \quad (2)$$

Here  $(x,y)$  is a Cartesian coordinate system,  $t$  is the time variable,  $U(t)$  is the free stream velocity and  $\alpha$  is the angle between the free stream velocity and the  $x$ -axis.

A possible flow situation around a circular cylinder is presented in Figure 1, where the curves AC, EF and BD represent free shear layers. Our procedure will not be limited to a circular cylinder. In principle we want to be able to handle any number and types of bodies in interaction. In practice, however, large computer times may limit us. Further for a single body there may be one, two or more separation points.

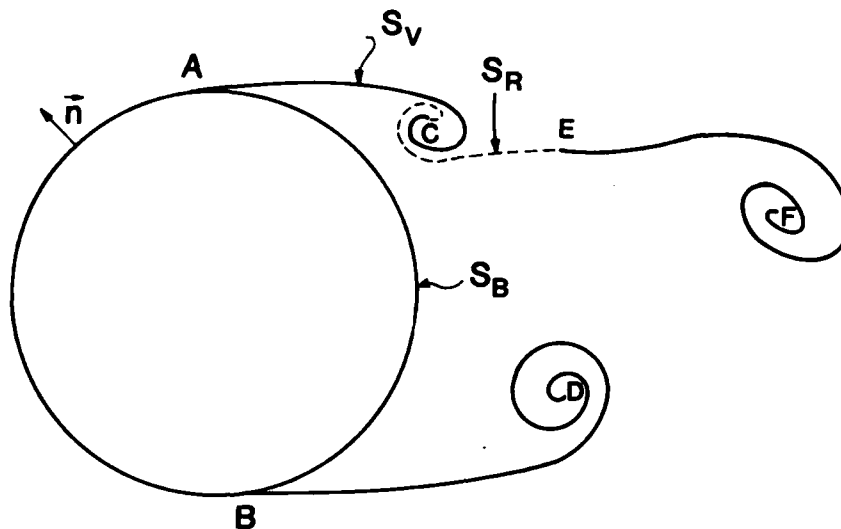


Figure 1 Flow situation around circular cylinder.

There are different ways to represent the potential flow. One way is to start out with Green's second identity and show that the velocity potential at a point  $(x_1, y_1)$  can be written as

$$\phi(x_1, y_1) = \frac{1}{2\pi} \int_{S_B + S_V + S_R} \left\{ \frac{\partial \phi}{\partial n} \log r - \phi \frac{\partial}{\partial n} \log r \right\} dS \quad (3)$$

where the normal direction  $n$  is shown in Figure 1 and

$$r = \sqrt{(x-x_1)^2 + (y-y_1)^2} \quad (4)$$

Further  $S_B$  is the wetted body surface,  $S_V$  both sides of the free shear layers and  $S_R$  both sides of the Riemann cuts. Expression (3) is based on that the total circulation around  $S_B + S_V + S_R$  is equal to zero. Let us explain what we mean by a Riemann cut by using Figure 1. Since the free shear layer EF has a non-zero circulation we have to

introduce a Riemann cut from C to E. Across the Riemann cut the velocity potential is discontinuous. The velocity potential jump will not vary along the cut. The Riemann cut is mathematical and not physical. This means that all physical quantities are continuous across the Riemann cut.

Equation (3) will be rewritten. We will use the body boundary condition

$$\frac{\partial \phi}{\partial n} = V_n \quad \text{on } S_B \quad (5)$$

where  $V_n = -\frac{\partial \phi^I}{\partial n}$  if the body is not moving. Otherwise it also includes the normal velocity component of the body motion. Further  $\partial \phi / \partial n$  is continuous across  $S_V$  and  $S_R$ . We can now write

$$\begin{aligned} \phi(x_1, y_1) = & -\frac{1}{2\pi} \int_{S_B} \phi \frac{\partial}{\partial n} \log r \, dS + \frac{1}{2\pi} \int_{S_B} V_n \log r \, dS \\ & - \frac{1}{2\pi} \int_{S_V^+ + S_R^+} [\phi^+ - \phi^-] \frac{\partial}{\partial n^+} \log r \, dS \end{aligned} \quad (6)$$

Here + and - refer to the two sides of a free shear layer or a Riemann cut. Equation (6) states that the velocity potential can be written as a distribution of sources and dipoles over the body surface and a distribution of dipoles over the free shear layers and the Riemann cuts. This is not a common way of writing the velocity potential when vorticity is involved.

It is more common to use vortices than dipoles. But by integrating by parts the dipole expressions in equation (6) it is possible to replace the dipole distribution by a vortex distribution. We can then write the resulting fluid velocity due to  $\phi$  as

$$\begin{pmatrix} \frac{\partial \phi}{\partial x_1} \\ \frac{\partial \phi}{\partial y_1} \end{pmatrix} = \frac{1}{2\pi} \int_{S_B} V_n \frac{1}{r^2} \begin{pmatrix} x_1 - x \\ y_1 - y \end{pmatrix} dS + \dots$$

cont. next page

$$\begin{aligned}
& + \frac{1}{2\pi} \int_{S_B} \frac{\partial \phi}{\partial s} \frac{1}{r^2} \begin{pmatrix} y_1 - y \\ -(x_1 - x) \end{pmatrix} dS \\
& + \frac{1}{2\pi} \int_{S_V^+} \left( \frac{\partial \phi^+}{\partial s} - \frac{\partial \phi^-}{\partial s} \right) \frac{1}{r^2} \begin{pmatrix} y_1 - y \\ -(x_1 - x) \end{pmatrix} dS \quad (7)
\end{aligned}$$

The first term on the right hand side represents a source distribution while the two last terms represent vortex distribution over the body surface and the free shear layers. There are no contributions from the Riemann cut since  $\partial \phi / \partial s$  is continuous across the Riemann cut. There are also other ways to represent the potential flow. The most common way in vortex shedding problems is to use a conformal mapping technique. Conformal mapping is not easy to apply for a general body configuration. Further it is only applicable in two-dimensional problems while equation (6) can be generalized to three-dimensional problems by replacing the two-dimensional source expression "logr" by the three-dimensional source expression. We have preferred to use equation (6) as our potential flow model. We will later argue more for our choice.

We should note that equation (6) is only a formal representation for each time step. Questions we have to discuss are how do we find the position of the free shear layers, the velocity potential jump across the free shear layers as well as the velocity potential on the body.

The position of the free shear layers away from the separation point is known by moving it with the convection velocity

$$\begin{aligned}
\vec{V}_c = & [U \cos \alpha + \frac{1}{2} (\frac{\partial \phi^+}{\partial x_1} + \frac{\partial \phi^-}{\partial x_1})] \vec{i} \\
& + [U \sin \alpha + \frac{1}{2} (\frac{\partial \phi^+}{\partial y_1} + \frac{\partial \phi^-}{\partial y_1})] \vec{j} \quad (8)
\end{aligned}$$

where  $\vec{i}$  and  $\vec{j}$  are unit vectors in the x- and y-direction, respectively. Expression (8) can be determined at each timestep by differentiating equation (6).

How the velocity potential jump  $\phi^+ - \phi^-$  across the free shear layer is convected, can be shown by using that the pressure is continuous across the free shear layer. It then follows by Bernoulli's equation that

$$\begin{aligned} \frac{\partial}{\partial t}(\phi^+ - \phi^-) + [U \cos \alpha + \frac{1}{2}(\frac{\partial \phi^+}{\partial x_1} + \frac{\partial \phi^-}{\partial x_1})] \frac{\partial}{\partial x_1}(\phi^+ - \phi^-) \\ + [U \sin \alpha + \frac{1}{2}(\frac{\partial \phi^+}{\partial y_1} + \frac{\partial \phi^-}{\partial y_1})] \frac{\partial}{\partial y_1}(\phi^+ - \phi^-) = 0 \end{aligned} \quad (9)$$

This means that  $\phi^+ - \phi^-$  is convected with the velocity  $\vec{V}$ .

Equation (9) is also valid at the separation points. It then tells us the rate of shedding of vorticity  $\phi^+ - \phi^-$  into the fluid. Further by integrating the equation with respect to time we will know the velocity potential jump at the separation point at each time instant. The same is true for the velocity potential jump across the free shear layers.

Equation (9) shows that the separation point cannot be a stagnation point for all time instants. Otherwise there will be no vortex shedding. In order to avoid a stagnation point on both sides of the free shear layers, it is necessary that the flow leaves the separation point parallel to the body surface on one of the sides of the free shear layer at the separation point (Maskell (1972)). What side the flow leaves tangentially depend on the sign of the shed vorticity. In the case of separation from a sharp corner with a non-zero apex angle there will be a stagnation point on the other side of the free shear layer at the separation point.

In the case of separation from a continuously curved surface one may combine potential theory and boundary layer theory in a quasi-steady manner to determine the separation point. This has been done by Deffenbaugh and Marshall (1976) and Sarpkaya and Shoaff (1979) in the case of laminar high Reynolds number flow past a circular cylinder. Pohlhausen method was used for the boundary layer calculations. Their approach is likely to be generalized to turbulent boundary layer including rough surfaces by employing a different integral method for the boundary layer calculations. But we will in this context only consider separation from sharp corners.

In the case of steady lifting flow around an airfoil one is using the wellknown Kutta condition to uniquely determine the circulation. The equivalence to a Kutta condition in this problem is that we require  $\phi^+ - \phi^-$  to be continuous at the separation point. Since the velocity potential jump is known at each time instant along the free shear layer, this is a constraint on the velocity potential along the body surface. In order to determine  $\phi$  at the body surface we are in addition using equation (6). By letting  $(x_1, y_1)$  in equation (6) approach points on the



body surface we obtain a Fredholm's integral equation of the second kind for the velocity potential. If we had instead used equation (7) with a source and vortex distribution and satisfied directly the body boundary condition, it will result in a Fredholm's integral equation of the first kind. The Fredholm's integral equation of the first kind is likely to cause numerical problems while this is not true for the Fredholm's integral equation of the second kind (Delves and Walsh (1974)). This means it is an advantage to use equation (6) instead of equation (7). Another advantage in using equation (6) instead of (7) is that we then solve for the velocity potential instead of the velocity. The velocity potential is less singular than the velocity at possible singular points. Further we need the velocity potential anyway when we want to calculate the pressure.

It should be stressed that our equation system is linear in the unknown velocity potential along the body, even if the flow is strongly nonlinear. Basu and Hancock (1978) solved a similar potential flow problem as ours for vortex shedding around airfoils. But their formulation of the boundary value problem ended up in a nonlinear equation system which is more inconvenient to solve than a linear equation system.

When the velocity potential is found as a function of time and space it is straightforward to use Bernoulli's equation to find the pressure and integrate the pressure properly to obtain the force. But there is also an alternative way to calculate the force, which is useful from a numerical comparison point of view. This will be derived below. We have based our derivation on Newman's derivation (1977) for the force on a body in non-separated potential flow.

We can write the hydrodynamic force on  $S_B$  as

$$\vec{F} = - \int_{S_B} p \vec{n} dS \quad (10)$$

where

$$p = - \rho \frac{\partial \phi}{\partial t} - \frac{\rho}{2} |\nabla \phi|^2 \quad (11)$$

where  $\phi$  is the total velocity potential. Since the pressure jump is zero across  $S_V$  and  $S_R$ , there cannot be any force on  $S_V + S_R$ , i.e.

$$\vec{F} = - \int_{S_B + S_V + S_R} p \vec{n} dS$$

We may now apply Gauss theorem on the fluid volume exterior to  $S_B + S_V + S_R$  and interior to a control surface  $S_\infty$  at infinity. Even if the control volume is different from Newman's case, the derivation of the force expressed is from now on similar as his. We will therefore only state the result

$$\vec{F} = \frac{d}{dt} \int_{S_B + S_V + S_R} \rho \vec{n} \, dS + \int_{S_\infty} \left( \rho \vec{v} \frac{\partial \phi}{\partial n} - \frac{1}{2} \rho |\vec{v}|^2 \vec{n} \right) dS \quad (12)$$

Since  $\phi \sim U \cos \alpha x + U \sin \alpha y$  at  $S_\infty$  it can be shown that equation (12) reduces to

$$\vec{F} = \frac{d}{dt} \int_{S_B + S_V + S_R} \rho \vec{n} \, dS \quad (13)$$

### 3. NUMERICAL ANALYSIS

Let us assume there are two separation points. The procedure will be similar for any number of separation points. Let us for simplicity assume no detached free shear layer. We will approximate the body surface and the free shear layer by straight line segments. On each element on the body we write

$$\phi = A_i, \quad i = 1, N \quad (14)$$

where  $A_i$ ,  $i = 1, N$  are unknown constants and  $V_n = V_n^i$  are known quantities. On each element on the free shear layer we write the velocity potential jump as a linear function, i.e.

$$\phi^+ - \phi^- = \frac{F_i - F_{i+1}}{s_i - s_{i+1}} (s - s_{i+1}) + F_{i+1} \quad (15)$$

where  $s$  is a curvilinear coordinate system along the free shear layer. Further  $s_i$  and  $s_{i+1}$  are  $s$ -coordinates of the ends of segment number  $i$ , and  $F_i$  is the velocity potential jump at  $s = s_i$ . For each time instant  $F_i$  are known quantities.

By letting  $(x_1, y_1)$  approach the midpoints of each segment on the body we can write the discretized resulting integral equation (6) as

$$A_j + \sum_{i=1}^N A_i \phi_{ji} = B^j + D^j \quad (16)$$

Here

$$\phi_{ji} = \frac{1}{2\pi} \int_{\Delta_i} \frac{\partial}{\partial n} \log r \, ds \quad (17)$$

The integration in (17) is over segment number  $i$  on the body with field point at the midpoint of body element number  $j$ . Further

$$B^j = \frac{1}{2\pi} \sum_{i=1}^N V_n^i \int_{\Delta_i} \log r \, ds \quad (18)$$

and

$$D^j = - \frac{1}{2\pi} \sum_{k=1}^2 \sum_{i=1}^{M_k} \left\{ \frac{F_i - F_{i+1}}{s_i - s_{i+1}} \int_{\Delta_i} (s - s_{i+1}) \frac{\partial}{\partial n^+} \log r \, ds \right. \\ \left. + F_{i+1} \int_{\Delta_i} \frac{\partial}{\partial n^+} \log r \, ds \right\} \quad (19)$$

where  $M_1$  and  $M_2$  are number of wake elements in each of the two free shear layers. The integrals in (17)-(19) has been exactly evaluated including asymptotic formulas valid for field points far from the elements.

Since we have two additional conditions which specify the potential jump at the separation points we cannot satisfy equation (16) at more than  $N-2$  midpoints. We choose to satisfy (16) at  $j=1, N1-1$  and  $j=N1+1, N-1$ . The two separation points are at the ends of segment  $N1$  and  $N$  (see Figure 2). We note that in the discretization of the integral equation we have set  $\phi$  equal to a constant over each element. Another possibility would be to set  $\phi$  equal to a linear function over each segment. Nothing is gained by using a linear variation of  $\phi$  over the segments which cannot satisfy the integral equation at midpoint but must be developed at both ends. The effort is unnecessary since the result is equivalent to the present method.

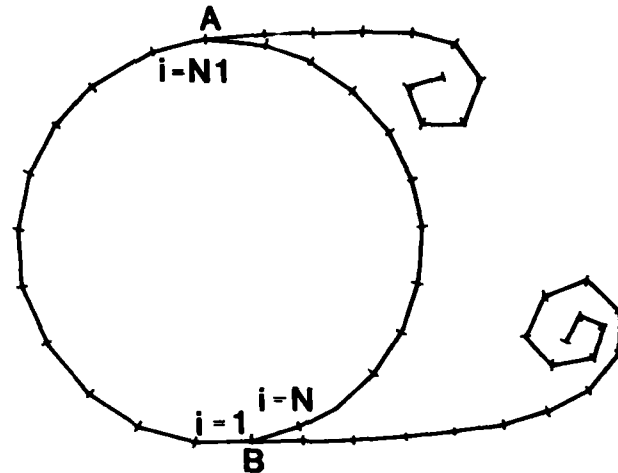


Figure 2 Numerical geometrical model of body and wake.

The two conditions that specifies the potential jump at the separation points can be written as

$$A_1 \left\{ -1 - \frac{s_1}{s_2 - s_1} \right\} + A_2 \left\{ \frac{s_1}{s_2 - s_1} \right\} + A_{N-1} \left\{ \frac{-s_N}{s_{N-1} - s_N} \right\} + A_N \left\{ 1 + \frac{s_N}{s_{N-1} - s_N} \right\} = (\phi^+ - \phi^-)_1 \quad (20)$$

$$A_{N1-1} \left\{ -\frac{s_{N1}}{s_{N1-1} - s_{N1}} \right\} + A_{N1} \left\{ 1 + \frac{s_{N1}}{s_{N1-1} - s_{N1}} \right\} + A_{N1+1} \left\{ -1 - \frac{s_{N1+1}}{s_{N1+2} - s_{N1+1}} \right\} + A_{N1+2} \left\{ \frac{s_{N1+1}}{s_{N1+2} - s_{N1+1}} \right\} = (\phi^+ - \phi^-)_2 \quad (21)$$

The indices on the right hand side of equation (20) and (21) indicates the two separation points. The other unexplained quantities in (20) and (21) are explained in Figure 3. In setting up equation (20) and (21) we have

linearly extrapolated  $\phi$  on the body to the separation points. We should note that our equation system (16), (20) and (21) are linear in the unknowns,  $A_j, j = 1, N$  even if the flow problem is basically nonlinear. When the unknowns  $A_j$  have been found by a standard method we can prepare for stepping forward in time.

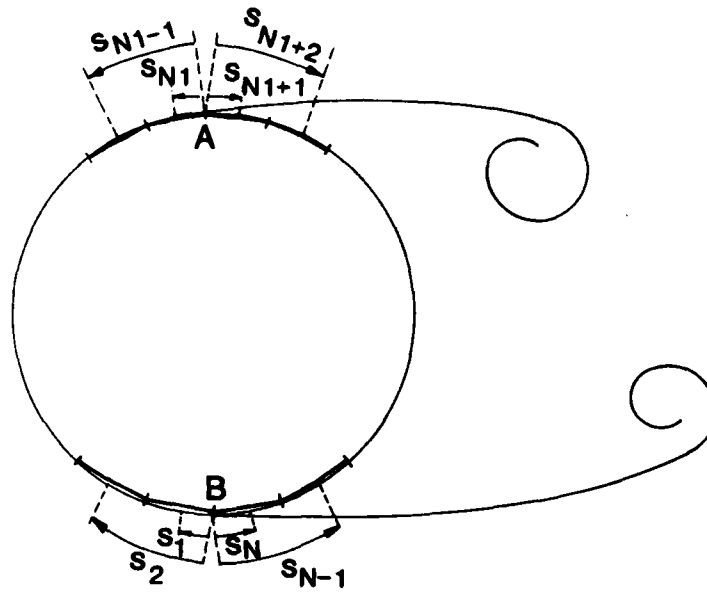


Figure 3 Coordinates used in specifying Kutta condition.

The convection velocity of the free shear layer at the midpoint of free shear layer element  $j$ , is given by (8) and can be written in discretized form as

$$\begin{aligned} \vec{V}_c = & \vec{i} [U \cos \alpha - \frac{1}{2\pi} \sum_{i=1}^N A_i \int_{\Delta_i} \frac{\partial}{\partial n} \left[ \frac{x_1 - x}{r^2} \right] ds + \frac{1}{2\pi} \sum_{i=1}^N v_n^i \int_{\Delta_i} \frac{x_1 - x}{r^2} ds \\ & - \frac{1}{2\pi} \sum_{\substack{i=1 \\ i \neq j}}^M \left\{ \frac{F_i - F_{i+1}}{s_i - s_{i+1}} \int_{\Delta_i} (s - s_{i+1}) \frac{\partial}{\partial n} \left[ \frac{x_1 - x}{r^2} \right] ds \right. \\ & \left. + F_{i+1} \int_{\Delta_i} \frac{\partial}{\partial n} \left[ \frac{x_1 - x}{r^2} \right] ds \right\} + \frac{\sin \psi (F_j + F_{j+1})}{\pi \Delta s_j} + \dots \end{aligned}$$

cont. next page

$$\begin{aligned}
& + j \left[ U \sin \theta - \frac{1}{2\pi} \sum_{i=1}^N A_i \int_{\Delta_i} \frac{Y_1 - Y}{r^2} ds + \frac{1}{2\pi} \sum_{i=1}^N V_n^i \int_{\Delta_i} \frac{Y_1 - Y}{r^2} ds \right. \\
& - \frac{1}{2\pi} \sum_{\substack{i=1 \\ i \neq j}}^M \frac{F_i - F_{i+1}}{s_i - s_{i+1}} \int_{\Delta_i} (s - s_{i+1}) \frac{Y_1 - Y}{r^2} ds \\
& \left. + F_{i+1} \int_{\Delta_i} \frac{Y_1 - Y}{r^2} ds \right] - \frac{\cos \psi (F_j + F_{j+1})}{\pi \Delta s_j} \quad (22)
\end{aligned}$$

The integrals in (22) have been exactly evaluated including asymptotic formulas valid for field points far from the elements. Further  $M$  is the total number of free shear layer elements,  $\psi$  is the angle between element number  $j$  and the  $x$ -axis and  $\Delta s_j$  is the length of element number  $j$ .

When  $\bar{V}$  has been found at the midpoints of each element, we perform a linear interpolation to find the convection velocity at the end points of each segment. The convection velocity of the end point coinciding with the separation points is extrapolated from velocities on the body and in accordance to Maskell's (1972) local flow behaviour around the separation points. At the free end of the free shear layers there exists different possibilities. One way is to directly evaluate the convection velocity by using that both the velocity potential jump and velocity jump is zero. Another possibility is that we have a spiral with infinite number of turns. In that case we will represent the inner core by a discrete vortex. The calculation of the convection velocity of the discrete vortex will be further discussed in connection with the starting process.

The end points of each element are then stepped forward in time, and according to equation (9) the velocity potential jump at the convected point will not change by this process. We have tried two different numerical time integration procedures. One is the simple Euler method. The other is Runge-Kutta of fourth order. It turns out that the Euler method is stable and provides sufficient accuracy.

The convection velocity may be quite different from element to element. This is for instance true within the spiral. If the convection procedure described above is allowed to go on for a long time, it may lead to quite different lengths of the free shear layer elements. To avoid this problem we are rediscrctizing the elements at every step so that all except the ones closest to the separation points are of equal length. The potential jump at the new segment ends are found by a linear interpolation.

To find the potential jump at the separation points at a new time step we are using equation (9) at the separation point at the preceeding time step.

One of the difficult problems is to start the whole process. In the case of an airfoil at small angle of attack it did not turn out to be any problem. We just started it up in accordance to the time stepping procedure described above. The solution will certainly be wrong at the start. The reason is that there is zero circulation around the foil which implies infinite velocities at the trailing edge. But the solution rapidly converges to a correct flow situation. In the case of a cross-flow past a plate for instance, we cannot follow this procedure. The potential flow situation with no circulation around the body would imply no rate of change of vorticity according to equation (9). But a solution to this problem can be derived if we look on the physical reality. From pictures in Batchelor (1970) for instance we see there is a small spiral at the separation point in a very small fraction of time. On the leeside we may therefore say that the velocity at the separation point is negligible compared to the velocity at the windward side of the separation point. Using this we can proceed with the timestepping procedure described above. But we should allow for small timesteps in the beginning accounting for the rapid change of the flow. Another possibility is to use Rott's (1956) similarity solution for corner flow as a starting solution. His solution is in the form of a discrete vortex with given position and circulation. The discrete vortex can in our solution procedure be represented in the following way. We can use a dipole distribution with constant strength over an element where one segment end coincide with the vortex position E, and the other end C is attached to the rest of the free shear layer (see Figure 4). The constant potential jump over this element will be equal to the circulation of the discrete vortex. The velocity contribution ( $\partial I / \partial x_1$ ,  $\partial I / \partial y_1$ ) from the segment can be written as

$$\begin{pmatrix} \frac{\partial I}{\partial x_1} \\ \frac{\partial I}{\partial y_1} \end{pmatrix} = - \frac{[\phi^+ - \phi^-]}{2\pi} \left[ \frac{1}{r_E^2} \begin{pmatrix} y_1 - y_E \\ -(x_1 - x_E) \end{pmatrix} - \frac{1}{r_C^2} \begin{pmatrix} y_1 - y_C \\ -(x_1 - x_C) \end{pmatrix} \right] \quad (23)$$

The first term can be interpreted as the velocity contribution from the discrete vortex while the last term has to be considered in connection with the contribution to the velocity from the rest of the source and dipole distribution.

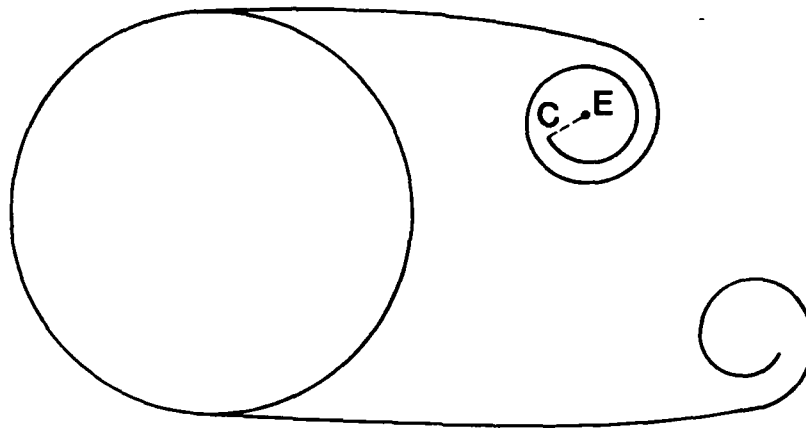


Figure 4 Representation of discrete vortex representing inner core of spiral.

In calculating the convection velocity of the discrete vortex we should in the conventional way exclude the first term of (23).

One could be attempted to use the more correct similarity solution of Pullin (1978) as a starting solution. But in our opinion it is too complicated and not necessary for that purpose. Pullin's solution will rather be used later as a control of the further development in time of our solution.

#### 4. NUMERICAL SOLUTION

As a test of the accuracy of our numerical model we started out with comparisons with analytical results for simple non-separated potential flows. We examined flow around ellipses of thickness-length ratios from 0.01 to 1.0 in currents of directions  $\alpha = 0^\circ, 45^\circ, 90^\circ$ . The agreement between numerical and analytical results was very good. We should note that our procedure will not work for zero thickness. But this does not represent a practical problem since the procedure works for very small thicknesses.

We have also tried to use a procedure based on equation (7), i.e. a distribution of sources and vortices over the body. By satisfying the body boundary condition we end up



with a Fredholm's integral equation of the first kind, where the tangential velocity  $\partial\phi/\partial s$  is the unknown. In the numerical discretization we assumed a linear variation of  $\partial\phi/\partial s$  over each straight line segment approximating the body surface. The boundary condition is satisfied at the midpoint of each segment. This procedure created some problems which worried us. In some cases there was an oscillatory tendency in the results. This is illustrated in Figure 5. We think the oscillations are due to the mathematical nature of the integral equation. We are solving Fredholm's integral equation of the first kind, which is known to have stability problems. One may argue that the oscillations do not seem too serious in the problem presented in Figure 5. But we did not like this tendency to instability and decided not to use the procedure.

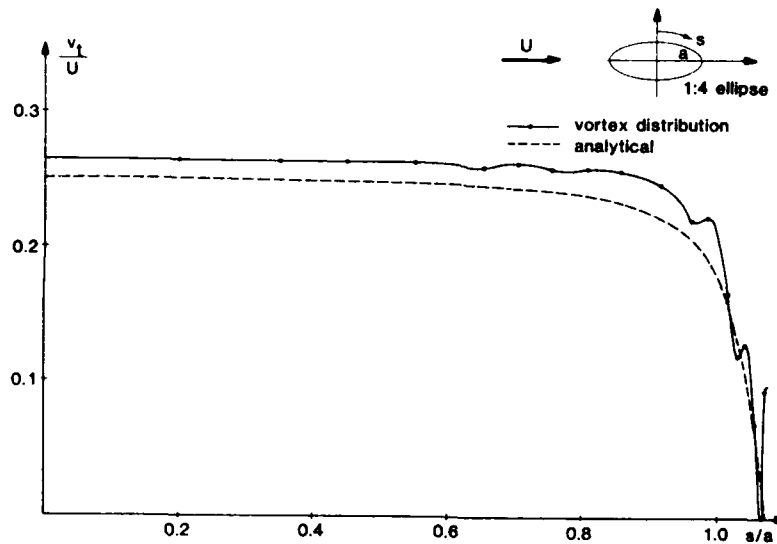


Figure 5 Calculation of tangential perturbation velocity for nonseparated flow around ellipse.

We have also compared our numerical solution procedure with analytical results for nonseparated potential flow around bodies with sharp corners. We then found that the solution for the velocity potential is not completely satisfactory for a segment adjacent to a sharp corner. We think the reason is that we assume a constant value of the velocity potential over the segment. Due to the singular nature of the solution around the sharp corner our assumption

about constant velocity potential is particularly bad for a segment adjacent to the sharp corner. We could probably circumvent this problem by using a local solution form around the sharp corner. But since this does not have relevance to the separated flow problem, we decided not to do it.

As a test of the accuracy in the evaluation of the integrals in the numerical solution procedure, the velocity field due to a circular vortex sheet of constant circulation was calculated. Analytically the velocity is zero inside the circle while the tangential velocity is

$$V_\theta = \frac{\Gamma}{2\pi} \frac{1}{r_0}$$

outside the circle. Here  $r_0$  is the radial distance from the centre of the circle and  $\Gamma$  is the circulation. The radial velocity field is zero outside the circle. Before the numerical evaluation we first integrated analytically the vortex distribution by parts. This gave a contribution from the ends of integration together with a dipole distribution with a linear density function. The velocity field due to the dipole distribution was calculated by dividing the circle into straight line segments and obtaining the contribution from each segment in the same way as described earlier. The results are presented in Figure 6 with a total number of only 20 elements around the circle surface.

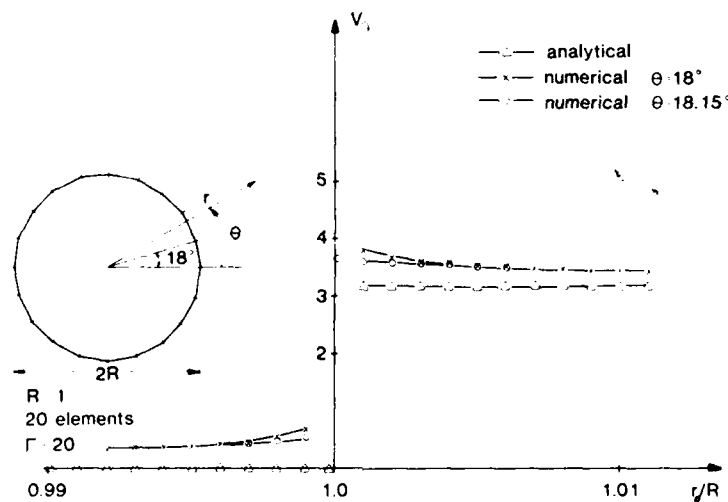


Figure 6 Tangential velocity field of a circular vortex sheet.

The most difficult place to calculate the velocities is close to the ends of the segments. But we note good agreement between analytical and numerical results even for a distance which is  $0.001 R$  from a segment end. This is an important result. The reason is that the velocity field due to an asymptotic spiral vortex is approximately equivalent to an infinite set of distinct uniform concentric vortex sheets. The results therefore tell us that we may be able to predict many turns of a vortex spiral with good accuracy even if the turns are quite close to each other.

The next step in our test procedure was to compare with the analytical solutions from linear unsteady airfoil theory (Newman (1977)). The comparisons for the Wagner problem for a flat plate of chord length  $c$  is shown in Figure 7.

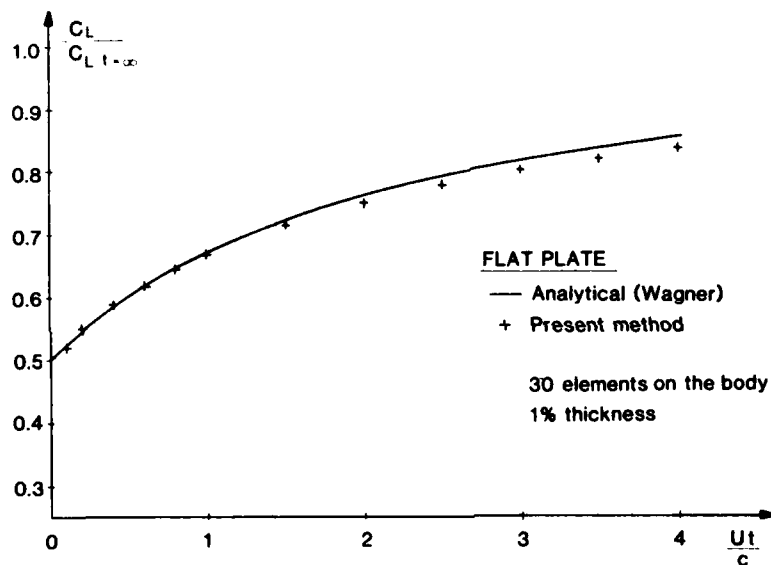


Figure 7 Comparison of calculated results with the Wagner function.

The Wagner function is the time history of the normalized circulatory lift on an airfoil that has been started impulsively from rest at an angle of attack. Even if we only used 30 elements totally on the body, the agreement between our numerical solution and the analytical solution is good. Giesing (1968) has also calculated the Wagner function for a 8.4% von Mises and 25.5% Joukowski profile at different angles of attack. The agreement between

Giesing's and our numerical results were similar good as for the plate shown in Figure 7.

We also compared with the Theodorsen function for a harmonic heaving flat plate in incident steady flow. The agreement was good.

We have also studied the nonlinear behaviour of a harmonic heaving airfoil in incident steady flow. This problem was studied earlier by Giesing (1968). He found good qualitative agreement with experimental picture of the wake. Giesing used discrete vortices to represent the free shear layer and in one extreme case which will be presented below, the wake has a "mushroom" - configuration. It is difficult to see from his results how he could have drawn a picture of the wake in this extreme case without having the experimental picture as a basis. Our results for the same situations as Giesing studied will be presented below. The airfoil is a NACA 0015. We used 30 elements to represent the foil numerically. The length of the foil was chosen to be 10 m and we chose the incident flow along the longitudinal axis of the airfoil to be 1 m/s. The incident flow normal to the longitudinal axis was of the form  $V \cos \omega t$ .

In the first case we used a circular frequency of oscillation of  $\omega = 0.43$  rad/s. The amplitude of heave oscillation corresponded to an angle of attack of  $4.5^\circ$ . We used a time step equal to 0.5 sec. in our numerical solution and the wake after 60 time step is presented in Figure 8.



Figure 8 Wake profile for heaving NACA 0015 airfoil.

In the other case we studied the circular frequency of oscillation were  $\omega = 1.7$  rad/s, and the amplitude of heave oscillation corresponded to an angle of attack of  $17.8^\circ$ . In this case we used a timestep of 0.05 s. The picture of the wake after 175 time steps is presented in Figure 9. We see very clearly a "mushroom" configuration in the wake, and that some of the details are very complicated. Both

of our results in Figure 8 and Figure 9 agree qualitatively with experimental pictures of the wake.

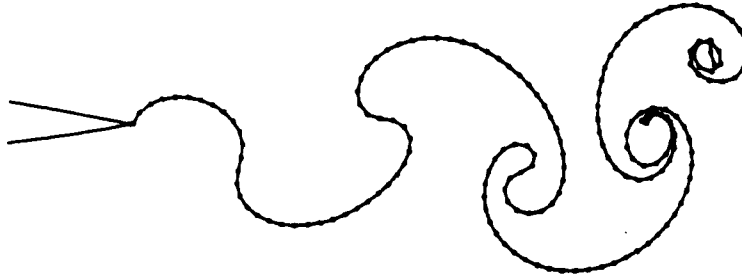


Figure 9 Wake profile for heaving NACA 0015 airfoil.

#### 4.1 Flat plate in steady cross-flow

In modelling the flat plate we used a total of 50 elements around the plate. Cosine-spacing was used on each side of the plate so that the elements were denser at the ends (see Figure 10). We cannot use zero plate thickness in our numerical model, but the procedure works for very small thicknesses. We used a thickness to length ratio of  $1/100$

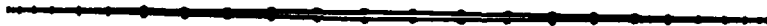


Figure 10 Distribution of body elements.

We used Rott's (1956) similarity solution for corner flows as a starting solution. His solution is in the form of a discrete vortex with given time-dependent position and circulation. We can write the vortex position for steady cross-flow past a flat plate with infinite initial acceleration as (see Figure 11)



Figure 11 Placement of discrete vortex at first timestep.

$$\frac{y_0}{H} = 0.395 \left( \frac{U_t}{H} \right)^{2/3} \quad (24)$$

$$\frac{x_0}{H} = 0.0 \quad (25)$$

Here  $2H$  is the height of the flat plate. The circulation can be written as

$$\frac{\Gamma}{2\pi UH} = 0.627 \left( \frac{U_t}{H} \right)^{1/3} \quad (26)$$

We started the solution at  $U_t/H = 0.004$ . The position of the discrete vortex at one end of the plate is shown in Figure 11. The dotted line is a Riemann surface connecting the discrete vortex and the plate end. In the following time steps the free shear layer was shed in a "continuous" manner. At successive time intervals of length  $U\Delta t/H = 0.01$  a new free shear layer segment was shed from each end of the flat plate. We tried with shedding vorticity only from the windward side and with shedding vorticity from both the windward and leeward side. The difference in the results was not important. The configuration of the free shear

layer after 100 time steps is shown in Figure 12 and after 150 time steps in Figure 13. We note there are no signs of instability in the free shear layer. This is in accordance with the stability analysis of Moore (1970).

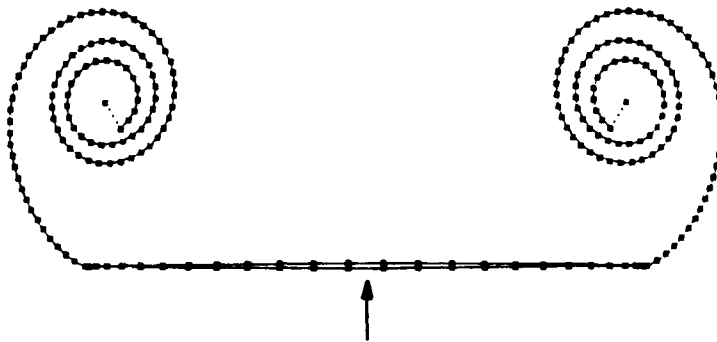


Figure 12 Two free shear layers with 101 wake elements in each layer.  $Ut/H = 0.994$ . Number of body elements 50.

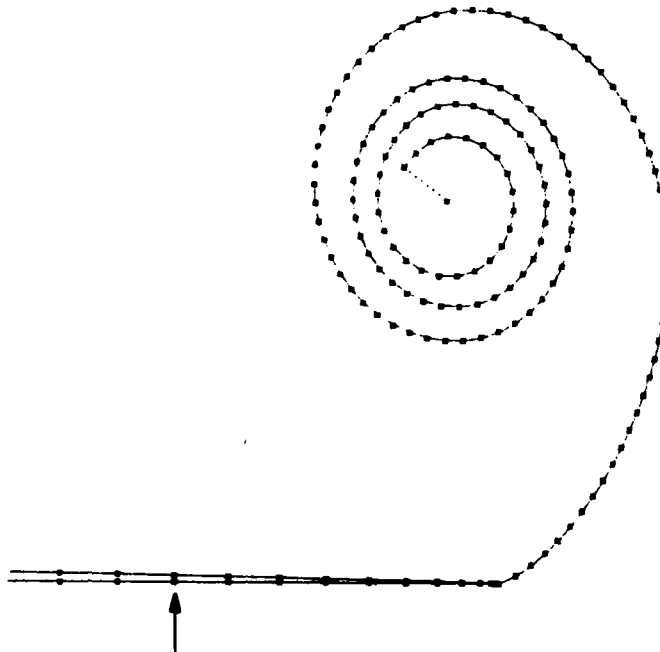


Figure 13 Free shear layer profile with 151 wake elements.  $Ut/H = 1.494$ . Number of body elements 50.

We could certainly have continued our solution and obtained more turns in the spiral. But there is a practical limit due to computer time when too many free shear layer segments are used. We therefore decided to redicretize the free shear layer after 100 time steps. There are many ways to do this. We did a rather substantial rediscrctization and reduced the number of wake elements from 100 to 14 (see Figure 14). It was done in the following way.

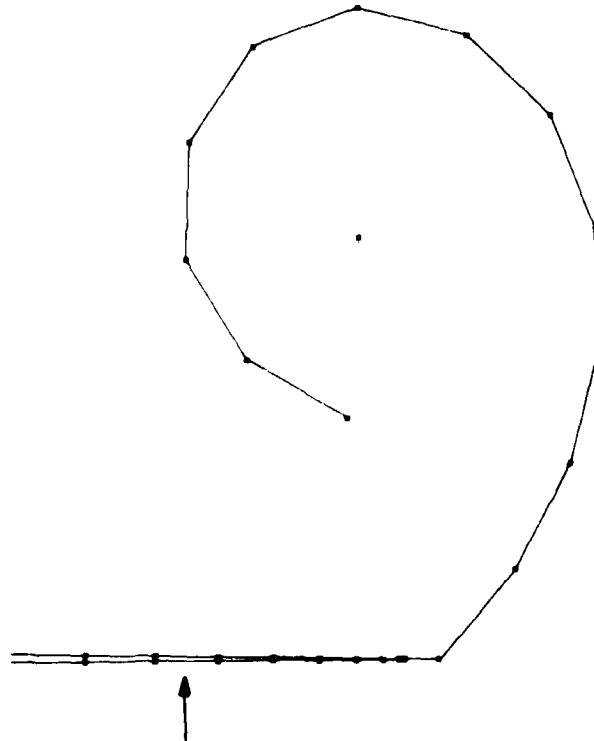


Figure 14 Free shear layer profile with 14 wake elements.  
 $Ut/H = 1.034$ . Number of body elements 50.

Since the inner turns of the spiral have nearly constant vortex strength and one complete turn is nearly circular, we can approximate one turn by a discrete vortex at the center of the spiral core. Two complete inner turns of the spiral was approximated in this way. The remaining free shear layer elements were changed by equalizing four original neighbour elements by one element. After the rediscrctization we used a time step of  $U\Delta t/H = 0.04$ . When a new complete turn of the spiral was created, we continued to



equalize it by a discrete vortex at the spiral core. The free shear layer after  $Ut/H = 7.39$  is shown in Figure 15.

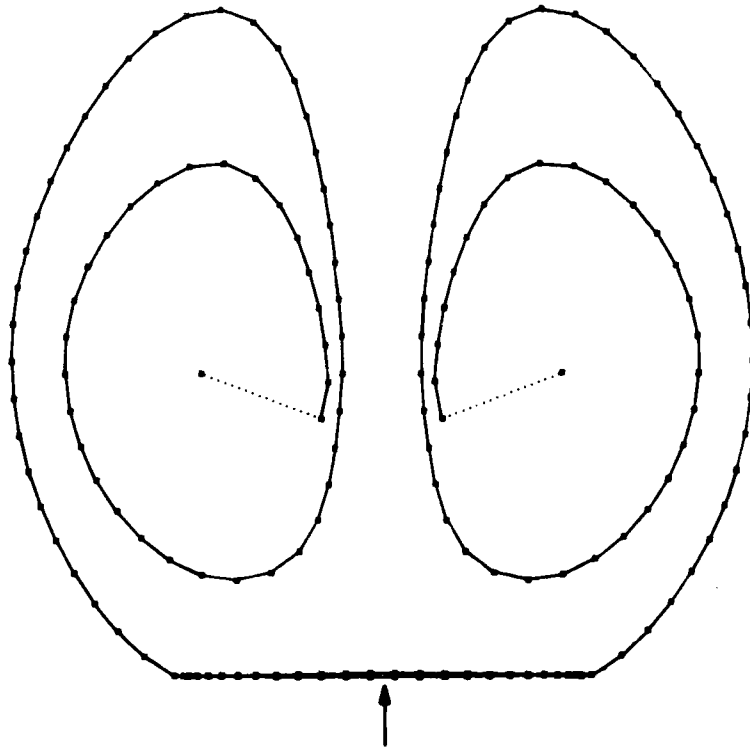


Figure 15 Two free shear layers with 66 wake elements in each layer.  $Ut/H = 7.39$ . Number of body elements 50.

We recognize that each free shear layer is no longer nearly circular in form. This is due to interaction with the other free shear layer and the plate. The noncircular form implies that the discrete vortex is not longer as good an approximation for the inner turns of the spiral. But even so the procedure seems to work. We should note that we have forced the flow to be symmetric. If we had made a perturbation of one of the free shear layer an asymmetry is likely to develop and cause vortex shedding. This has not yet been studied.

In Figure 16 is shown how circulation is developed in one of the free shear layers. Initially our results agree

well with Pullin's similarity solution but after some time it starts to deviate. This is expected since Pullin's results are for an infinitely long flat plate. We note that our results are in quite good agreement with Fink and Soh (1974) and Wedemeyers (1961) results for a finite flat plate.

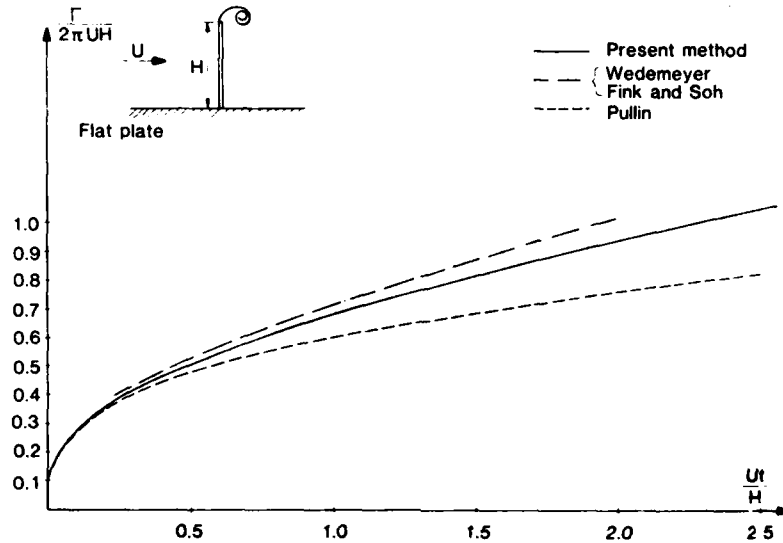
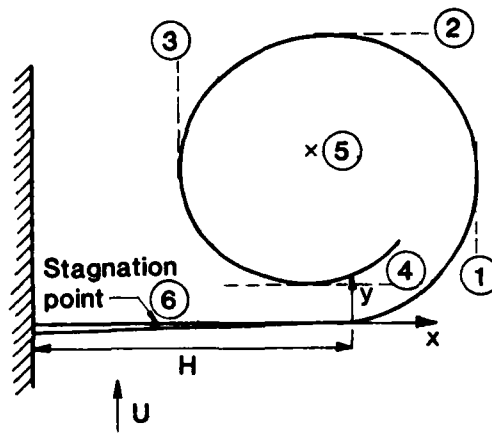


Figure 16 Time development of circulation shed into one shear layer for steady cross flow past a flat plate.

The results are not exactly the same, but the differences are similar as the differences between Fink and Soh's results in the initial state.

We have made more extensive comparisons between our solution and Pullin's similarity solution. We have compared the position of the outer turns of the spiral and the core of the spiral. This is shown in Table 1. The agreement is good, while the agreement on the position of the compared stagnation point on the lee side of the plate is less satisfactory.

We have also compared the results for the normal force on the flat plate with Fink and Soh's results (see Figure 17). We used two different ways to calculate the forces (see the chapter on the theory). The difference was generally in the third digit and is not shown in the figure.



$U\tau/H$	$x(1)/H$	$y(2)/H$	$x(3)/H$	$y(4)/H$	$x(5)/H$	$y(5)/H$	$x(6)/H$
0.2	0.09(0.1)	0.27(0.27)	-0.14(-0.13)	0.08(0.08)	-0.01(-0.03)	0.16(0.15)	-0.4(-0.28)
0.3	0.12(0.13)	0.36(0.35)	-0.16(-0.16)	0.12(0.11)	-0.04(-0.04)	0.24(0.19)	
0.4	0.15(0.16)	0.45(0.42)	-0.19(-0.2)	0.16(0.13)	-0.06(-0.05)	0.28(0.23)	
0.5	0.17(0.19)	0.52(0.49)	-0.22(-0.23)	0.19(0.15)	-0.05(-0.05)	0.33(0.26)	

Table 1 Initial free shear layer positions for steady cross-flow past a flat plate. Numbers in paranthesis are Pullin's (1978) similarity solution.

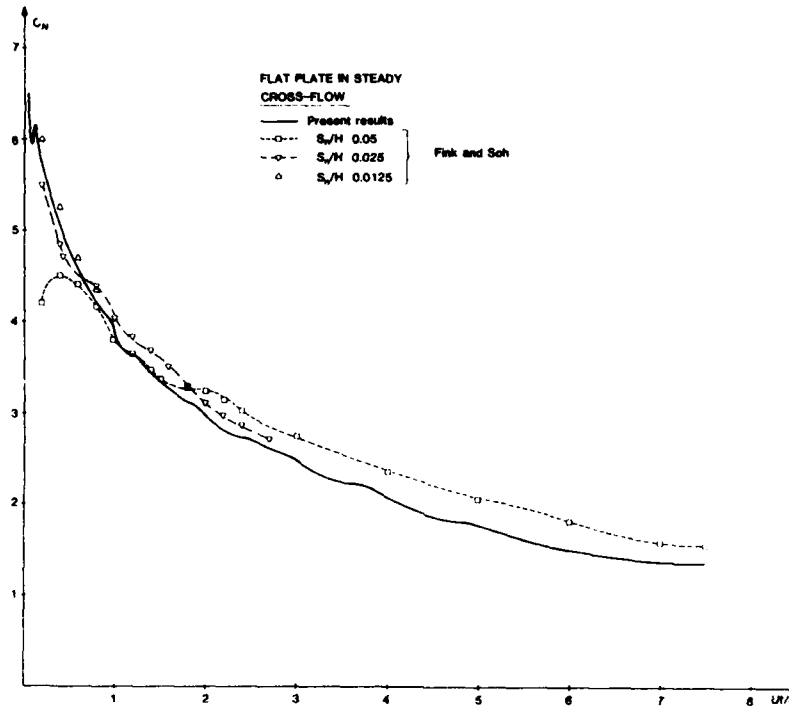


Figure 17 Normal force coefficient for a finite plate.

The good agreement between the results by the two force expressions is a good control of the accuracy of our numerical method. In Figure 17 are shown three different results by Fink and Soh (1974). The one lasting the shortest time is expected to be the most accurate and vice versa. The reason is that the one lasting shortest has a higher density of free shear layer segments than the one lasting longest. The agreement between our solution and the one lasting shortest is very good. We may note a small oscillation in our results around  $Ut/H = 0.01$ . This is due to difficulties in starting the flow. The small irregularities in our force results around  $Ut/H = 1.05, 1.83, 3.4, 4.3$  are due to the earlier described rediscrretization of the free shear layer (see Figure 14).

#### 4.2 Oscillatory cross-flow past a flat plate

The problems we have discussed in the preceeding text about steady cross flow past a flat plate apply also for

oscillatory cross-flow past a flat plate. In addition there are difficulties when the free shear layers are coming back and close to the body. Numerical inaccuracies may cause the vorticity to go through the plate and destroy the numerical solution. One reason for this happening is that we are only satisfying the body boundary conditions at discrete points. Between these discrete points the calculated normal velocity cannot be expected to be exactly zero. This problem can be avoided by imposing the analytical normal velocity on the part of the free shear layer which come very close to the body, for instance within a distance of  $|y|/H < 0.01$ . The timestep should also be kept relatively small when the free shear layer is close to the body.

Our studies were for a harmonic oscillatory cross-flow past a flat plate. The free stream velocity was written as

$$U(t) = U_{\max} \cos \omega t \quad (27)$$

The flow was started at  $t = 0$ . By writing

$$U_{\max} = \omega A$$

we can rewrite (27) as

$$U = U_{\max} \cos \left( \frac{H}{A} \frac{U_{\max} t}{H} \right)$$

where  $A/H$  can be interpreted as the ratio of the amplitude of the distance a fluid particle moves far away from the body relative to half the height of the flat plate. We can also write this amplitude ratio in terms of the Keulegan-Carpenter number  $KC$  as

$$KC = \pi \frac{A}{H}$$

We used Rott's similarity solution (see equations (24)-(26)) to start up the flow, and vorticity was shed from both the windward and leeward sides.

Results for positions of the free shear layer at different timesteps for  $A/H = 1$  is presented in Figure 18. The arrow indicates the free stream velocity. The correspondence between the timestep, the time  $t$  and the free shear velocity  $U$  is given in Table 2.  $U_{\max}$  was 1 m/s and  $H = 5$  m. In Table 2 is also shown the calculated force values by direct pressure integration and the alternative formula (13).

The satisfactory agreement between the two force results is a control of the accuracy of the numerical results.

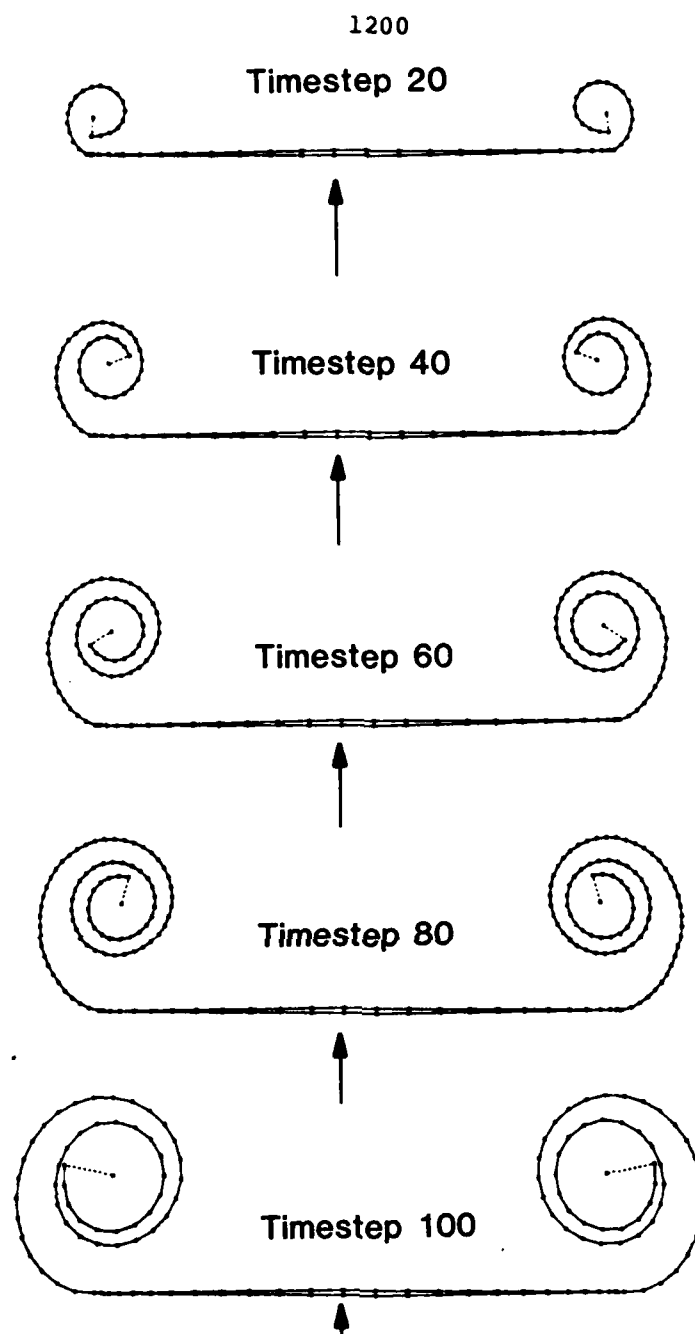
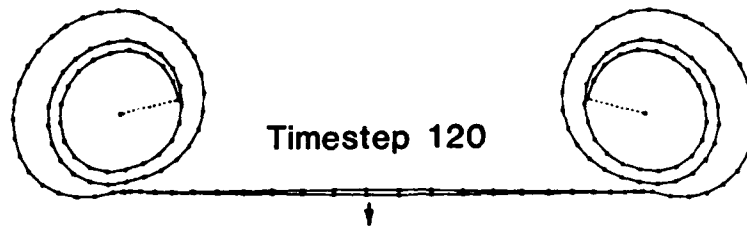
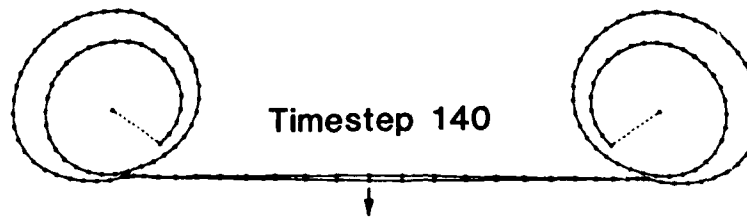


Figure 18 Free shear layer positions at different time-steps for oscillatory cross flow past flat plate ( $KC = \pi$ ).

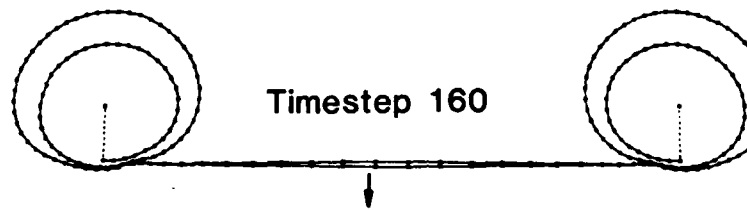
1201



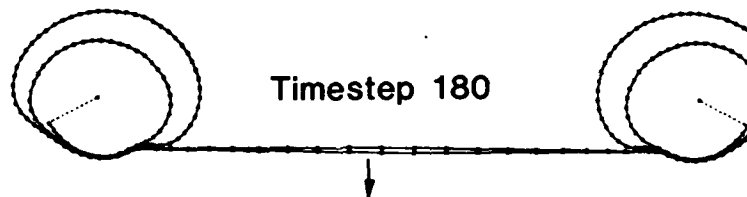
Timestep 140



Timestep 160



Timestep 180



Timestep 200

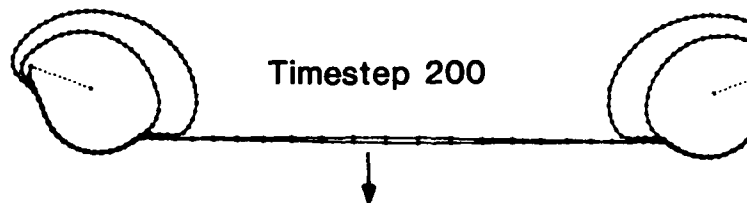


Figure 18 cont.

$$\left[ \frac{F}{\frac{1}{2} \rho U_{\max}^2 (2H)} \right]$$

Timestep	$\frac{U_{\max} t}{H}$	$U/U_{\max}$	pressure integration	alternative formula (13)
10	0.094	0.9956	5.8297	5.9181
20	0.194	0.9812	5.5094	5.6687
30	0.294	0.9571	5.1788	5.1882
40	0.394	0.9234	4.6753	4.6613
50	0.494	0.8804	4.2657	4.2536
60	0.594	0.8287	3.8684	3.8314
70	0.694	0.7687	3.4441	3.4024
80	0.794	0.7010	3.0142	2.9837
90	0.994	0.5453	2.1391	2.1381
100	1.194	0.3679	1.2098	1.1324
110	1.394	0.1759	- 0.0864	- 0.1875
120	1.594	- 0.0232	- 1.8486	- 1.9440
130	1.644	- 0.0731	- 2.7643	- 2.8613
140	1.694	- 0.1229	- 3.2218	- 3.2604
150	1.744	- 0.1723	- 3.6671	- 3.6457
160	1.794	- 0.2214	- 3.7207	- 3.6467
170	1.844	- 0.2698	- 3.4779	- 3.3331
180	1.894	- 0.3176	- 3.3014	- 3.1042
190	1.944	- 0.3646	- 3.0690	- 2.8187
200	1.994	- 0.4107	- 3.1540	- 2.9449
210	2.044	- 0.4557	- 2.9058	- 2.6389

Table 2 Comparison of force calculations for oscillating cross flow past flat plate. ( $KC = \pi$ .)



We note that parts of the free shear layers are coming very close to each other and the plate when the free shear layer are returning back towards the plate. An enlarged picture of the free shear layer at one side of the plate at time step 160 ( $U_{\max}t/H = 1.794$ ) is shown in Figure 19.

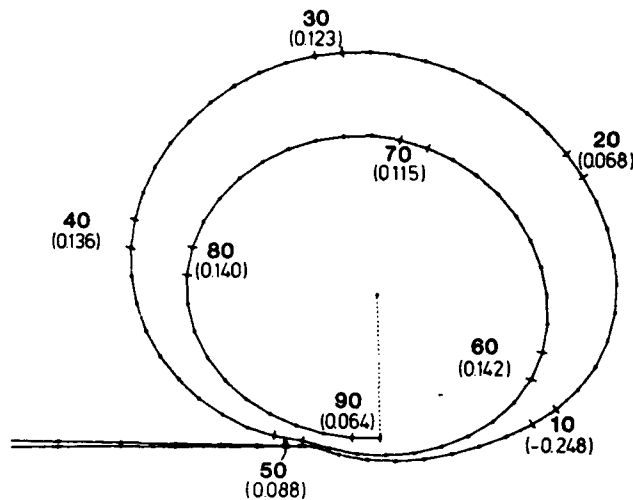


Figure 19 Enlarged picture of the free shear layer at  $U_{\max}t/H = 1.79$  for oscillatory cross-flow past flat plate.  $KC = \pi$ .

The vorticity of the different elements approximating the free shear layer at the same time step are given in Table 3. The vorticity for elements 10, 20 etc. are also given in brackets in Figure 19. We note that the vorticity is negative at the separation point and changes sign around element number 16. Visualization tests of the physical flow indicates that the part of the free shear layer with positive vorticity will in reality be detached and thereby shed. We have not yet incorporated this feature in our model. Another open question is to what extent the vorticity in the parts of the free shear layers which come close to each other or to the plate will in reality be annihilated. These questions should be studied before processing with the numerical solution further in time. For numerical studies with larger Keulegan-Carpenter number it is also importance to develop asymmetry of the shedding from the two separation points.

Wake element number	Element vorticity $d\Gamma$	Wake element number	Element vorticity $d\Gamma$
1	- 0.086	46	0.113
2	- 0.292	47	0.105
3	- 0.303	48	0.097
4	- 0.308	49	0.091
5	- 0.308	50	0.088
6	- 0.310	51	0.085
7	- 0.311	52	0.090
8	- 0.306	53	0.099
9	- 0.286	54	0.101
10	- 0.248	55	0.108
11	- 0.195	56	0.114
12	- 0.138	57	0.122
13	- 0.086	58	0.132
14	- 0.044	59	0.140
15	- 0.012	60	0.142
16	0.012	61	0.140
17	0.031	62	0.135
18	0.046	63	0.129
19	0.058	64	0.124
20	0.068	65	0.119
21	0.076	66	0.116
22	0.083	67	0.114
23	0.089	68	0.113
24	0.095	69	0.113
25	0.101	70	0.115
26	0.106	71	0.118
27	0.110	72	0.123
28	0.115	73	0.128
29	0.119	74	0.133
30	0.123	75	0.138
31	0.126	76	0.143
32	0.129	77	0.145
33	0.132	78	0.146
34	0.133	79	0.144
35	0.135	80	0.140
36	0.136	81	0.134
37	0.136	82	0.126
38	0.136	83	0.116
39	0.136	84	0.104
40	0.136	85	0.093
41	0.135	86	0.082
42	0.133	87	0.074
43	0.130	88	0.069
44	0.126	89	0.067
45	0.120	90	0.064

Jump in velocity potential  $[\phi^+ - \phi^-]$  at separation point: 17.919.  
Circulation of discrete vortex 12.8.

Table 3 Vorticity of wake elements at  $U_{\max}/H = 1.79$   
for oscillatory cross-flow past flat plate.

### 4.3 Steady cross-flow past a rectangular cross-section

As a guidance for our numerical solution we first performed flow-visualization experiments of a steady two-dimensional incident flow past a rectangular cross-section. We build a model that was 2.62 m high and of constant cross-sectional form. The lengths of the cross-dimensional sides were 0.5 m and 0.43 m. The model was towed vertically in the large towing tank of Norwegian Hydrodynamic Laboratoreis with the longest cross-sectional side in the towing direction. The submergence was 2.5 m, and the constant carriage velocity was 0.3 m/s. This is sufficiently low velocity to avoid influence of surface waves. Initially the acceleration of the carriage is 1 m/s<sup>2</sup>. The model was covered with plastic to avoid effect of roughness. Pictures of the flow around the cross-section is presented in Figure 20. An arrow indicates the free stream direction. These pictures were taken by covering the water surface by confetti. The pictures were taken successively. The exposure time was 1 sec. Unfortunately we do not have a relative time scale between the pictures. But the major intent was to get a qualitative picture of the flow. We do not have a good picture of what is happening in a very early stage, where the flow around both the leading and trailing edge are expected to be similar in form.

In picture number 2 of Figure 20 we note that the form of the free shear layer is quite different at the leading and trailing edge. The form of the shear layer is much more oval at the leading edge than at the trailing edge. A more detailed picture of the flow after the leading edge is presented in Figure 21. This picture is taken at a later timestep than the second picture in Figure 20. It is interesting to note what is happening as the free shear layer after the trailing edge grows stronger and bigger in form. Initially the free shear layer leaves tangentially from the windward side, but after some times it switches over to leave tangentially from the leeside. This causes a back-flow around the trailing edge. Later on we see that asymmetry is created in the wake causing alternate shedding of vorticity from each side.

In the numerical calculations a square section was studied. Rott's similarly solution was used to start the flow. The position of the discrete vortex for a square section is given by

$$\frac{r}{b} = 0.2685 \left( \frac{U t}{b} \right)^{3/4}$$

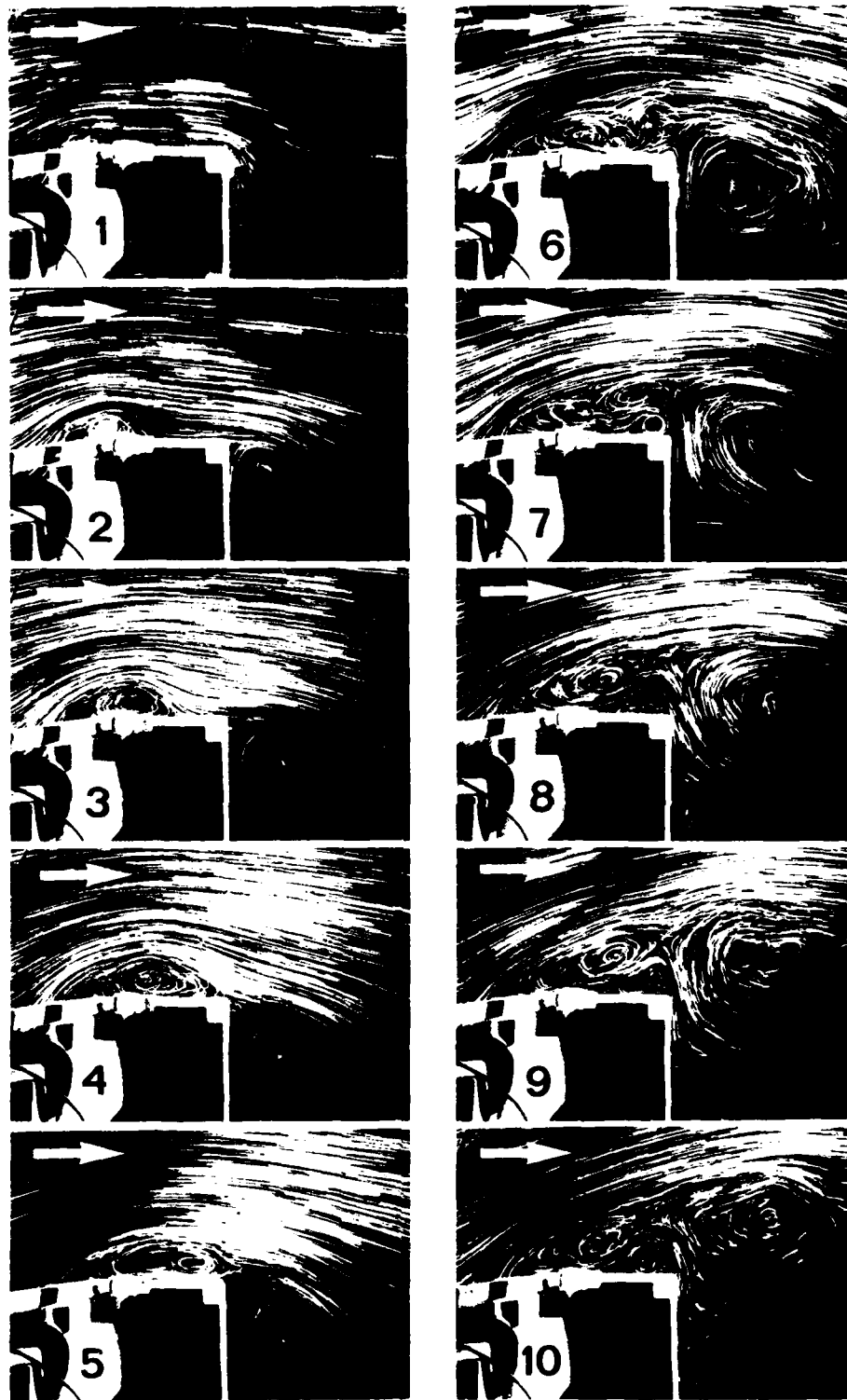


Figure 20 Visualization of initial flow around rectangular cross-section.

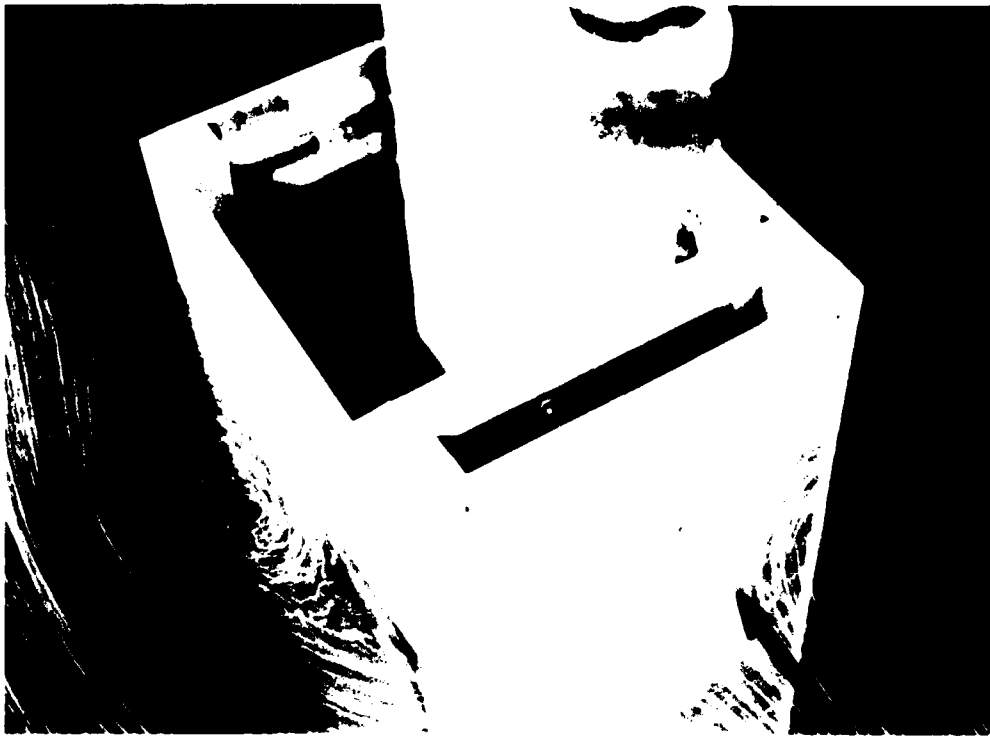


Figure 21 Visualization of flow around the leading edge of a rectangular cross-section.

and

$$\chi = 56.65^\circ$$

where  $2b$  is the length of one side of the square and the radius  $r$  and the angle  $\chi$  is defined in Figure 22. The strength of the discrete vortex is

$$\Gamma_S = 2.6309 Ub \left( \frac{Ut}{b} \right)^{0.5}$$

The offsetpoints describing the elements on one fourth of the cross-section are given in Table 4. Further  $U$  was chosen to be 1 m/s. We started the solution at  $t = 0.2$  s. Later on we used a timestep of 0.05 s.

It is quite difficult to describe properly numerically the flow around the leading edge. If we did not use a start vortex, the free shear layer went easily through the body surface. One also have to be careful with the

distribution of body elements to avoid the free shear layer to "crash" into the body around the leading edge.

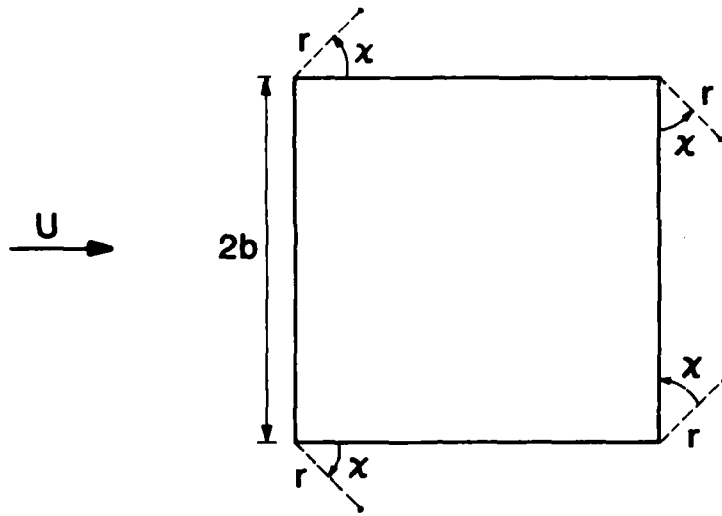


Figure 22 Definitions for starting solution of flow around square cross-section.

Our two different force calculation procedures were used to test the accuracy of our numerical results. The results are presented in Figure 23.

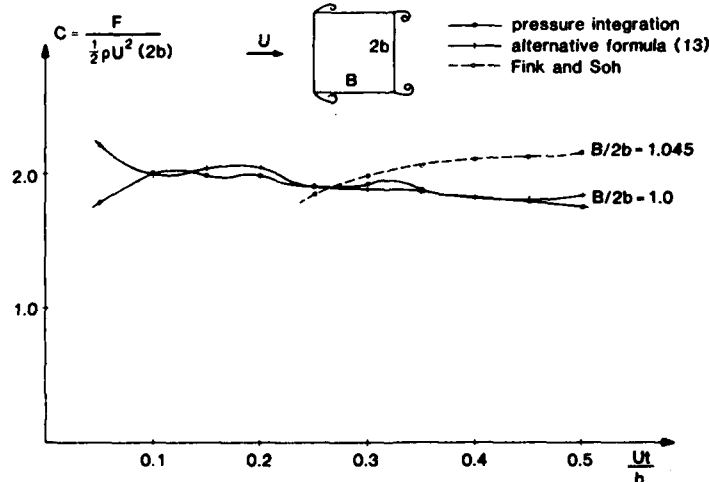
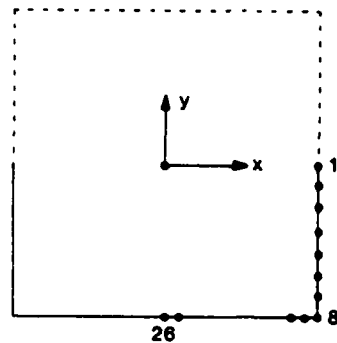


Figure 23 Force results for steady flow around rectangular cross-section.



Offset point number	x- coordinate	y- coordinate
1	5.0000	0.0
2	5.0000	-1.1126
3	5.0000	-2.1694
4	5.0000	-3.1174
5	5.0000	-3.9092
6	5.0000	-4.5048
7	5.0000	-4.8746
8	5.0000	-5.0000
9	4.9810	-5.0000
10	4.9240	-5.0000
11	4.8296	-5.0000
12	4.6985	-5.0000
13	4.5315	-5.0000
14	4.3301	-5.0000
15	4.0958	-5.0000
16	3.8302	-5.0000
17	3.5355	-5.0000
18	3.2139	-5.0000
19	2.8679	-5.0000
20	2.5000	-5.0000
21	2.1131	-5.0000
22	1.7101	-5.0000
23	1.2941	-5.0000
24	0.8682	-5.0000
25	0.4358	-5.0000
26	0.0	-5.0000

Table 4 Offset points for the square cross-section used in our numerical studies.

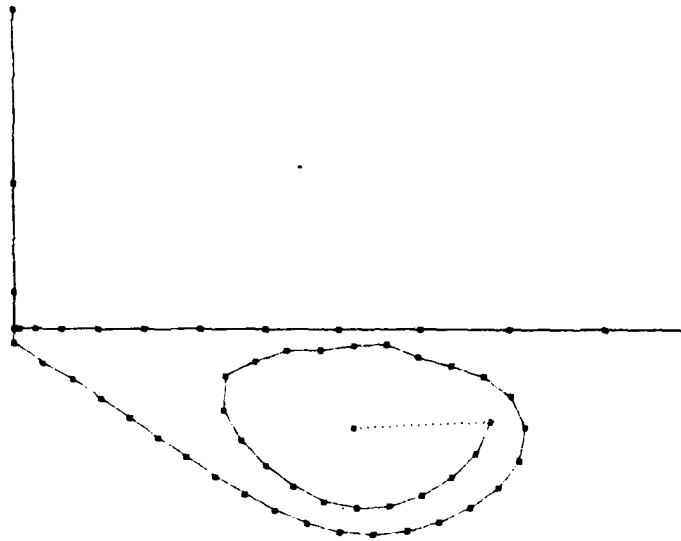


Figure 24 Numerical results for free shear layer position at leading edge of a square cross section ( $Ut/b = 0.43$ ).

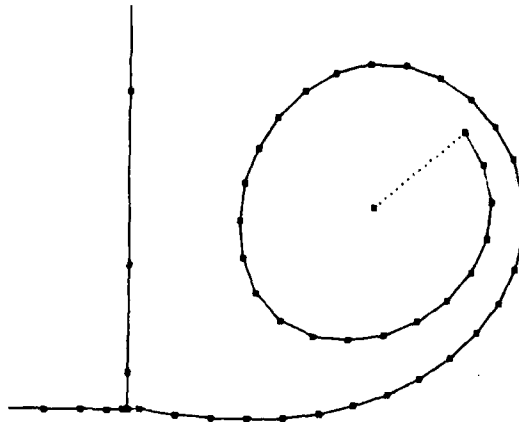


Figure 25 Numerical results for free shear layer at trailing edge of a square cross-section ( $Ut/b = 0.43$ ).



These results are in fair agreement with Fink and Soh's (1974) numerical results. The free shear layer position around the leading edge and the trailing edge at  $Ut/b = 0.43$  are presented in Figures 24 and 25. The points on the body are the offsetpoints defined in Table 4. These results are in qualitative agreement with the flow visualization studies presented in Figure 20. Our numerical results for the tangential velocity on the body indicate a singularity at the lee side of the leading edge. The reason to this is not clear. It may be either of mathematical nature or due to improper numerical approximation near the leading edge.

## 5. CONCLUSION

A method to predict the flow and associated vortex shedding around bluff bodies at high Reynold's number is presented. It is assumed that the vorticity is concentrated in thin boundary layers and free shear layers. Choice of solution technique for the potential flow problem is discussed, and it is decided to represent the solution for the velocity potential as a distribution of sources and dipoles over the body surface and the free shear layers. The equivalence to a Kutta condition is a prescribed velocity direction and continuity of the velocity potential at the separation points. Even if the problem is strongly nonlinear, the resulting equation system at each time instant is linear. The solution is started by using Rott's similarity solution to position a discrete vortex with known strength outside each separation point. The free shear layer is discretized at each time instant so that the length of the straight line elements approximating the continuous part of the free shear layer is kept equal. This is important in order to cope with the nonuniform stretching of the free shear layer. The inner core of a vortex spiral is represented by a discrete vortex. In order to reduce computer time complete inner turns of the free shear layer is approximated by a discrete vortex at different time intervals. A simple alternative way then calculating the force by integrating Bernoulli's equation is presented. This provides a control of the accuracy of the numerical calculations.

The method has been applied to linear and nonlinear unsteady airfoil problems. The agreement with results by other methods is good.

Steady crossflow past a flat plate has also been studied. The results are in agreement with Fink and Soh's results. The initial part of the solution agrees well with Pullin's similarity solution for an infinitely long flat plate.

Results for oscillatory cross flow past a flat plate and steady cross flow past a square section are also presented. The latter results are in qualitative agreement with presented flow visualization results.

#### ACKNOWLEDGEMENT

The authors are grateful to the funding provided by Conoco Norway, Inc. The authors appreciate discussions with professor J.N. Newman, MIT, and the help by O. Kjærland in arranging the experiments.

#### References

- Basu, B.C. and Hancock, G.J. (1978) "The unsteady motion of a two-dimensional aerofoil in incompressible inviscid flow", J. Fluid Mech., Vol. 87, part 1, pp. 159-178.
- Batchelor, G.K. (1970) "An Introduction to Fluid Dynamics", Cambridge University Press.
- Bearman, P.W. and Graham, J.M.R. (1980) "Vortex Shedding from Bluff Bodies in Oscillatory flow: A report on Euromech 119", J. Fluid Mech., Vol. 99, Part 2, pp 225-245.
- Clements, R.R. and Maull, D.J. (1975) "The Representation of Sheets of Vorticity by Discrete Vortices", Prog. Aerospace Sci. Vol. 16, No. 2, pp. 129-146.
- Deffenbaugh, F.D. and Marshall, F.J. (1976) "Time Development of the Flow About an Impulsively Started Cylinder", AIAA Journal, Vol. 14, No. 7, pp. 908-913.
- Delves, L.M. and Walsh, J., ed. (1974) "Numerical solution of integral equations", Clarendon Press, Oxford.
- Fink, P.T. and Soh, W.K. (1974) "Calculation of Vortex Sheets in Unsteady Flow and Applications in Ship Hydrodynamics", Tenth Symp. Naval Hydrodynamics, Cambridge, Mass., pp. 463-491.
- Giesing, J.P. (1968) "Nonlinear Two-Dimensional Unsteady Potential Flow with Lift", J. Aircraft, Vol. 5, No. 2, March-April, pp. 135-143.
- Maskell, E.C. (1972) "On the Kutta-Joukowski condition in two-dimensional unsteady flow", Roy. Aircraft Establishment, Farnborough, Techn. Memo Aero 1451.
- Moore, D.W. (1976) "The stability of an evolving two-dimensional vortex sheet", Mathematika, Vol. 23, pp. 35-44.
- Newman, J.N. (1977) "Marine Hydrodynamics", The MIT Press Cambridge, Massachusetts.
- Pullin, D.I. (1978) "The large-scale structure of unsteady self-similar rolled-up vortex sheets", J. Fluid Mech., Vol. 88, part 3, pp. 401-430.

- Rott, N. (1956) "Diffraction of a weak shock with vortex generation", J. Fluid Mech., Vol. 1, part 1, pp. 111-128.
- Sarpkaya, T. and Shoaff, R.L. (1979) "A discrete-vortex analysis of flow about stationary and transversely oscillating circular cylinders", NPS-69SL79011, Naval Postgraduate School, Monterey, California.
- Wedemeyer, E. (1961) "Ausbildung eines Wirbelpaares an den Kanten einer Platte", Ingenieur-Archiv, Band 30. pp. 187-200.

## Previous Books in the Naval Hydrodynamics Series

"First Symposium on Naval Hydrodynamics." National Academy of Sciences-National Research Council, Publication 515, 1957. Washington, D.C.; PB133732

"Second Symposium on Naval Hydrodynamics: Hydrodynamic Noise and Cavity Flow," Office of Naval Research, Department of the Navy, ACR-38, 1958; PA157668.

"Third Symposium on Naval Hydrodynamics: High Performance Ships," Office of Naval Research, Department of the Navy, ACR-65, 1960; AD430729.

"Fourth Symposium on Naval Hydrodynamics: Propulsion and Hydroelasticity," Office of Naval Research, Department of the Navy ACR-92, 1962; AD447732.

"The Collected Papers of Sir Thomas Havelock on Hydrodynamics," Office of Naval Research, Department of the Navy, ACR-103, 1963; AD623589.

"Fifth Symposium on Naval Hydrodynamics: Ship Motions and Drag Reduction," Office of Naval Research, Department of the Navy, ACR-112, 1964; AD640539.

"Sixth Symposium on Naval Hydrodynamics: Physics of Fluids, Maneuverability and Ocean Platforms, Ocean Waves, and Ship-Generated Waves and Wave Resistance," Office of Naval Research, Department of the Navy, ACR-136, 1966; AD676079.

"Seventh Symposium on Naval Hydrodynamics: Unsteady Propeller Forces, Fundamental Hydrodynamics, Unconventional Propulsion," Office of Naval Research, Department of the Navy, DR-148, 1968; AD721180.

"Eighth Symposium on Naval Hydrodynamics: Hydrodynamics in the Ocean Environment," Office of Naval Research, Department of the Navy, ACR-179, 1970; AD748721.

"Ninth Symposium on Naval Hydrodynamics: Unconventional Ships, Ocean Engineering, Frontier Problems," Office of Naval Research, Department of the Navy, ACR-203, 1972; Two Volumes; Vol. 1, ADA010505; Vol. 2, ADA010506.

"Tenth Symposium on Naval Hydrodynamics: Hydrodynamics for Safety, Fundamental Hydrodynamics," Office of Naval Research, Department of the Navy, ACR-204, 1974; ADA022379.

"Eleventh Symposium on Naval Hydrodynamics: Unsteady Hydrodynamics of Marine Vehicles," Office of Naval Research, Department of the Navy. Also available from Mechanical Engineering Publications Limited, London and New York.

"Twelfth Symposium on Naval Hydrodynamics: Boundary Layer Stability and Transition, Ship Boundary Layers and Propeller Hull Interaction, Cavitation, Geophysical Fluid Dynamics," Office of Naval Research, Department of the Navy. Also available from National Academy Press, 2101 Constitution Avenue, N.W., Washington, D.C. 20418

"Thirteenth Symposium on Naval Hydrodynamics: Impact of Hydrodynamics Theory upon Design Practice, With Emphasis on High Performance and/or Energy Saving Ships," Office of Naval Research, Department of the Navy. Also available from The Shipbuilding Research Association of Japan, The Senpaku-Shinko Bldg., 1-15-16 Toranomom, Minato-ku, Tokyo 105, Japan.

# List of Participants

## AUSTRALIA

Lawrence J. Doctors, University of South Wales

## AUSTRIA

Gerhard Strasser, Schiffbautechnische Versuchsanstalt

## BRAZIL

Antonio C. Fernandes, Instituto de Pesquisas Tecnologicas

## BULGARIA

Peter A. Bogdanov, Bulgarian Ship Hydrodynamics Centre

## CANADA

Sander M. Calisal, University of British Columbia  
Chi-Chao Hsiung, Memorial University of Newfoundland  
Tuomo O. Karppinen, National Research Council Canada  
Michael Mackay, Defence Research Establishment Atlantic

## DENMARK

M. Munk Nielsen, Skibsteknisk Laboratorium  
Keith R. Pucill, Danish Ship Research Laboratory

## FEDERAL REPUBLIC OF GERMANY

Fritz J. Bartels, Fraunhofer-Institut für Hydroakustik  
Harald G.G. Keil, Institut für Entwerfen von Schiffen  
Odo W. Krappinger, Hamburg Ship Model Basin  
Claus F.L. Kruppa, Technische Universität Berlin  
Bernt Lang, Versuchsanstalt für Wasserbau und Schiffbau  
Apostolos Papanikolaou, Technische Universität Berlin  
Bernd Remmers, Kempf & Remmers GmbH  
Michael Schmiechen, Versuchsanstalt für Wasserbau und Schiffbau  
Ernst A. Weitendorf, Hamburg Ship Model Tank

## FINLAND

Jerzy E. Matusiak, Ship Laboratory of Technical Research Centre of  
Finland  
Jaakko V. Pylkkänen, Helsinki University of Technology

## FRANCE

Christian Berhault  
Alain Bovis, Bassin d'Enais des Corenes  
Jean-Claude Dern, Bassin d'Enais des Corenes  
Yves Lecoffre, Alsthom-Atlantique  
Jean-Pierre Le Goff, D.R.E.T.

## INDIA

Vijay H. Arakeri, Indian Institute of Science  
Manohar L. Munjal, Indian Institute of Science

## ISRAEL

Gedeon Dagan, Tel Aviv University  
Touvia Miloh, Tel Aviv University  
Yona Yahalom, Solmat Systems Ltd.

## ITALY

Guglielmo A. Bellone, Cantieri Navali Riuniti  
Carmine Coppola, Istituto Nazionale per Studi ed Esperienze di  
Architettura Navale  
Rodolfo Pallabazzer, Universita di Pavia

## JAPAN

Mitsuhiro Abe, Mitsui Engineering & Shipbuilding Co., Ltd.  
Eiichi Baba, Misubishi Nagasaki Experimental Tank  
Takao Inui, University of Tokyo  
Hiroshi Isshiki, Technical Research Institute, Hitachi Zosen Corp.  
Hiroharu Kato, University of Tokyo  
Y. Kyojuka, National Defense Academy  
Michio Nakato, Hiroshima University  
Makoto Okusu, Kyushu University  
Toshio Suzuki, Osaka University  
Ichiro Tanaka, Osaka University  
Naoji Toki, Mitsubishi Heavy Industries, Inc.  
Koichi Yokoo, The Shipbuilding Research Center of Japan

## KOREA

Chang-Sup Lee, Korea Institute of Machinery and Metals

## THE NETHERLANDS

Martin Hoekstra, Maritime Research Institute Netherlands  
Arie J.W. Lap, Royal Institute for the Navy  
Marinus W.C. Oosterveld, Maritime Research Institute Netherlands  
Jan H.J. Van der Meulen, Maritime Research Institute Netherlands  
Willem Van Gent, Maritime Research Institute Netherlands  
Jan D. Van Manen, Maritime Research Institute Netherlands  
August G.P. Versmissen, Maritime Research Institute Netherlands

## NORWAY

Odd M. Faltinsen, Norwegian Institute of Technology  
John Grue, University of Oslo  
Kjell O. Holden, Norwegian Hydrodynamic Laboratories  
Jacques Lassabliere, Det Norske Veritas  
Jahn Henry Lovaas, Det Norske Veritas  
Knut J. Minsaas, Norwegian Hydrodynamic Laboratories  
Enoc J. Palm, University of Oslo  
Bjornar Pettersen, Norwegian Institute of Technology  
Tor Vinje, Norwegian Institute of Technology

## POLAND

Kazimierz Szponar, Ship Design and Research Center

## SCOTLAND

Mehmet Atlar, University of Glasgow  
Archibald M. Ferguson, University of Glasgow

## SPAIN

Jose A. Alaez, Pardo Tank-Carretera de la Sierra  
P. O'Dogherty, Canal de experiencias Hidrodinamicas

## SWEDEN

Gilbert I.F. Dyne, Swedish Maritime Research Centre, SSPA  
Lars A. Larsson, Swedish Maritime Research Centre, SSPA

## UNITED KINGDOM

Brian S. Bowden, National Maritime Institute  
William A. Crago, British Hovercraft Corp., Ltd.  
Martin J. Downie, Imperial College of Science and Technology  
Patrick A. Fitzsimmons, The British Ship Research Assoc.  
Edward J. Glover, The University of Newcastle upon Tyne  
Frank Haynes, Vickers Shipbuilding & Engineering Ltd.  
Charles P.J. Hirom, Admiralty Marine Technology Establishment  
Antony J. Musker, Admiralty Marine Technology Establishment  
Yucel A. Odabasi, The British Ship Research Assoc.



Stuart J. Pearce, Admiralty Marine Technology Establishment  
 Robert G. Standing, National Maritime Institute  
 Klaus R. Suhrbier, Vosper Thornycroft (UK) Ltd.  
 Clive M.R. Wills, Lloyd's Register of Shipping

# UNITED STATES

Roger E.A. Arndt, University of Minnesota  
 Robert F. Beck, University of Michigan  
 John P. Breslin, Stevens Institute of Technology  
 Terry E. Brockett, David W. Taylor Naval Ship Research & Development Center  
 Georges L. Chahine, Hydronautics, Inc.  
 Chu-Yung Chen, Naval Sea Systems Command  
 Hsi Cheng, David W. Taylor Naval Ship Research & Development Center  
 Allen T. Chwang, University of Iowa  
 David W. Coder, David W. Taylor Naval Ship Research & Development Center  
 Edward N. Comstock, Naval Sea Systems Command  
 Ralph D. Cooper, Flow Research Company  
 Bruce D. Cox, Hydrodynamics Research Associates, Inc.  
 Gabor F. Dobay, David W. Taylor Naval Ship Research & Development Center  
 Lawrence K. Forbes, University of Iowa  
 Martin J. Fritts, Naval Research Laboratory  
 Per Gabrielsen, Massachusetts Institute of Technology (Det Norske Veritas)  
 Philippe Genoux, Hydronautics, Inc.  
 Scott Gowing, David W. Taylor Naval Ship Research & Development Center  
 David S. Greeley, Bolt, Beranek and Newman Inc.  
 Charles J. Henry, General Dynamics Corp.  
 John L. Hess, McDonnell Douglas Corp.  
 Thomas T. Huang, David W. Taylor Naval Ship Research & Development Center  
 Lee M. Hunt, National Research Council  
 Stuart D. Jessup, David W. Taylor Naval Ship Research & Development Center  
 Bruce Johnson, U.S. Naval Academy  
 Paul Kaplan, Hydromechanics, Inc.  
 Justin E. Kerwin, Massachusetts Institute of Technology  
 Nan King, Department of the Navy  
 Tadeusz Kowalski, University of Rhode Island  
 Louis Landweber, The University of Iowa  
 George K. Lea, National Science Foundation  
 Choung M. Lee, Office of Naval Research  
 Wen-Chen Lin, David W. Taylor Naval Ship Research & Development Center  
 S. C. Ling, The Catholic University of America  
 Walter H. Livingston, Naval Sea Systems Command  
 Douglas J. Loeser, Science Applications, Inc.  
 Allen H. Magnuson, Virginia Polytechnic Institute  
 James M. Mays, Oceanroutes, Inc.

Justin H. McCarthy, David W. Taylor Naval Ship Research & Development Center

John McHugh, David W. Taylor Naval Ship Research & Development Center

Thomas G. McKee, Jr., Davidson Laboratories, Stevens Institute of Technology

Michael R. Mendenhall, Nielsen Engineering & Research, Inc.

William B. Morgan, David W. Taylor Naval Ship Research & Development Center

Kazuhiro Mori, The University of Iowa

Nicholas J. Newman, Massachusetts Institute of Technology

John A. Norton, Bird-Johnson Company

John F. O'Dea, David W. Taylor Naval Ship Research & Development Center

T. Francis Ogilvie, Massachusetts Institute of Technology

Michael G. Parsons, The University of Michigan

Virendra C. Patel, The University of Iowa

John H. Pattison, Naval Sea Systems Command

Alan Powell, David W. Taylor Naval Ship Research & Development Center

Arthur Reed, David W. Taylor Naval Ship Research & Development Center

Kenneth Remmers, David W. Taylor Naval Ship Research & Development Center

Nils Salvesen, Science Applications, Inc.

V. Otto Scherer, Hydronautics, Inc.

Paul D. Sclavounos, Massachusetts Institute of Technology

Frederick Stern, Science Applications, Inc.

Ming-Yang Su, Naval Ocean Research and Development Activity

Tsung-chow J. Su, Florida Atlantic University

Chao Ho Sung, David W. Taylor Naval Ship Research & Development Center

David F. Thrasher, David W. Taylor Naval Ship Research & Development Center

Marshall P. Tulin, Hydronautics, Inc.

Daniel T. Valentine, Hydrodynamics Research Associates, Inc.

Robert J. Van Houten, Massachusetts Institute of Technology

William S. Vorus, The University of Michigan

Robert L. Waid, Lockheed Missiles & Space Corp.

Quentin R. Wald, General Dynamics Corp.

David A. Walden, David W. Taylor Naval Ship Research & Development Center

Henry T. Wang, Naval Research Laboratory

William C. Webster, University of California, Berkeley

James A. White, U.S. Coast Guard

Robert E. Whitehead, Office of Naval Research

De-Ming Wu, California Institute of Technology

Theodore Y. Wu, California Institute of Technology

George T. Yates, California Institute of Technology

Shee-Mang Yen, University of Illinois

Chia-Shun Yih, The University of Michigan

Dick K. Yue, Science Applications, Inc.

#### YUGOSLAVIA

M. Molnar

**END**

**FILMED**

**10-85**

**DTIC**